Entrainment of Air into Thermal Spill Plumes

by

Roger Harrison

Supervised by

Michael Spearpoint and Charles Fleischmann

Fire Engineering Research Thesis

August 2009

A research thesis presented as partial fulfilment of the requirements for the degree of Doctor of Philosophy in Fire Engineering

Department of Civil and Natural Resources Engineering
University of Canterbury
Private Bag 4800
Christchurch
New Zealand

Abstract

The design of smoke management systems for buildings such as atria, covered shopping malls and sports arenas require appropriate calculation methods to predict the volume of smoky gases produced in the event of a fire. The volume of smoke must be calculated in order to determine the required fan capacity or ventilator area for a smoke management system.

In design, consideration is often given to entrainment of air into a smoke flow from a compartment opening that subsequently spills and rises into an adjacent atrium void. This type of plume is commonly known as a thermal spill plume. There has been much controversy over the validity of various entrainment calculation methods for the spill plume and there are considerable differences in the calculated smoke production rates using these methods. There are also scenarios involving the spill plume where design guidance is very limited. Whilst over-sizing of the required smoke exhaust can be uneconomical, under-sizing can compromise the design objectives.

This work attempts to rigorously characterises thermal spill plume entrainment using new data obtained from an extensive series of $1/10^{th}$ physical scale modelling experiments, supported by numerical modelling using Computational Fluid Dynamics.

Spill plume behaviour and subsequent entrainment appears to be specifically dependent on the characteristics of the layer flow below spill edge, particularly in terms of the width and the depth of the flow. Plumes generated from narrow, deep layer flows entrain air at a greater rate with respect to height compared to plumes generated from wide, shallow layers. The findings of this work go some way to explain and reconcile differences in entrainment reported between previous studies.

New guidance has been developed for the thermal spill plume in smoke management design, in the form of a range of new simplified design formulae, improvements to analytical calculation methods and an initial assessment of the use of numerical modelling using Computational Fluid Dynamics.

Acknowledgements

I would like to thank the following who have contributed to this research in various ways: From the University of Canterbury, Dr Mike Spearpoint for his support that has allowed me to continue this useful and interesting research, for his technical input and for acting as a sounding board when needed. Associate Professor Charley Fleischmann for his technical input, especially with the numerical modelling. Professor Andy Buchanan for his support that enabled me to return to Canterbury. Bob Wilsea-Smith and Grant Dunlop for their for their invaluable help with the construction of the experimental apparatus.

Professor Geoff Cox for his support and for seeding ideas that have driven some aspects of this research. Professor Suresh Kumar of BRE for collaborating with us and for his continued interest in this work.

Professor James Milke of the University of Maryland for providing me with information that has shed light on some aspects of the guidance given in NFPA 92B.

Education New Zealand, for providing funding in the form a New Zealand International Doctoral Research Scholarship. The National Fire Protection Association, USA, for the award of the David. B. Gratz Scholarship in 2006. The New Zealand Fire Service Commission for their continued support of the Fire Engineering programme at the University of Canterbury.

Gordon Garrad of Jeremy Gardner Associates, UK, for his guidance on the current practise of consulting fire engineers in smoke management design.

Dr Jerry Chang for keeping me entertained with his unique sense of humour and Pauline Anderson for her stupendous culinary delights.

Finally, to my family for their unwavering support from the other side of the world.

Table of Contents

List of Figures

List of Tables

Nomenclature

Symbol	Description
A	Area (m^2)
A_v	Area of natural smoke outlet (m^2)
A_i	Area of natural air inlet (m^2)
B	Entrainment coefficient (kg m s^{-1} $kW^{-1/3}$)
b	Balcony breadth (m)
c	Heat of combustion (kJ kg^{-1})
C	Entrainment coefficient (kg m s^{-1} $kW^{-1/3}$)
C_m	Dimensionless entrainment coefficient
C_e	Entrainment coefficient (kg $s^{-1}m^{-5/2}$)
c_p	Specific heat (J kg^{-1} K^{-1})
C_d	Coefficient of discharge
d	Depth of gas layer (m)
D^*	Characteristic plume dimension (m)
Fr	Froude number
g	Acceleration due to gravity (m s^{-2})
h	Height above floor (m)
k	Thermal conductivity (W m^{-1} K^{-1})
l	Characteristic length
L	Characteristic linear height of the model
$\dot{m}$	Mass flow rate of gases (kg s^{-1})
$\dot{m}_{ends}$	Mass flow rate entrained into the free ends of the plume (kg s^{-1})
$\dot{m}_{rot}$	Mass flow rate of air entrained into the rotation region (kg s^{-1})
n'	Number of gas molecules in the volume V
N	Avogadro's number
P	Gas pressure (Pa)
p	Fire perimeter (m)
ΔP	Pressure differential (Pa)
Re	Reynolds number

R_H	Hydraulic radius (m)
$\dot{Q}_c$	Convective heat flow in the gas layer below the spill edge (kW)
$\dot{Q}_t$	Total heat generated by the fire (kW)
R	Universal gas constant
T	Absolute gas temperature (K)
$\overline{T}$	Mass weighted average absolute gas temperature (K)
u	Velocity (m s^{-1})
V	Volume (m^3)
$\dot{V}$	Volume flow rate (m^3 s^{-1})
W	Width or lateral extent (m)
x_s	Horizontal distance perpendicular to the spill edge (m)
δx	Grid size (m)
y	Vertical distance (m)
z_s	Height of rise of plume above the spill edge (m)
z_0	Height of virtual line source below the spill edge (m)

Greek symbol	**Description**
α	Entrainment constant for plume
α'	Entrainment constant for air mixing into the rotation region
γ	Regression coefficient
δ	Regression coefficient
ε	Regression coefficient
θ	Temperature above ambient (^oC)
$\overline{\theta}$	Mass weighted average temperature above ambient (^oC)
ρ	Density (kg m^{-3})
$\overline{\rho}$	Mass weighted average density (kg m^{-3})
η	Smoke exhaust location factor
κ_m	Profile correction factor for mass flow rate of gases
κ_q	Profile correction factor for convective heat flow rate of gases
τ	Carbon dioxide concentration by volume above ambient
σ	Coefficient in Equations (2-8) and (5-4) (kg s^{-1} $m^{-5/2}$)

ω	The time scale
ν	Kinematic viscosity of air (m^2 s^{-1})
λ	An empirical thermal plume constant

List of subscripts	**Description**
amb	An ambient property
a	Variable evaluated in an atrium
acryl	A property of acrylic sheet
air	A property of air
b	A property of the balcony
CFI	A property of ceramic fibre insulation board
CO_2	A property of CO_2 gas
e	An effective property
f	A property evaluated on full scale
IMS	A property of Industrial Methylated Spirits
l	A property of a smoke layer
line	A property of a line plume
m	A property evaluated on model scale
max	A maximum value
o	A property of the fire compartment opening
p	Variable evaluated in the plume at an arbitrary height of rise
s	Variable evaluated in the gas layer flow below the spill edge
spill	A property of a spill plume
trans	Transition in the rate of entrainment from a balcony spill plume to axisymmetric
unchan	A property of a balcony spill plume without channelling screens below the balcony
v	A visual property
vent	A property of the gases in the vent of the smoke exhaust hood
w	Variable evaluated in the horizontal layer flow at the fire compartment opening
2D	Two-dimensional spill plume
3D	Three-dimensional spill plume

List of superscripts	Description
i	Regression coefficient
j	Regression coefficient
n	Regression coefficient

Chapter 1

1. Introduction

1.1 Background

Modern architectural and construction techniques have led to the increased design of novel, large undivided volume buildings such as covered shopping malls, airport terminals and sports arenas. These buildings typically contain large spaces or voids which can occupy many storeys in height. The generic term ‘atrium’ can be applied to the large voids within these types of buildings. The concept of an atrium dates back to Roman times when used as an entrance hall in a typical house. Atria are now commonly an integral part of modern office buildings, hotels, hospitals, museums and leisure facilities. They are designed with the intention of providing a visually and spatially external environment indoors, can potentially reduce energy consumption, improve the working environment (both physically and psychologically) and increase the available lettable space [1].

The traditional approach to fire protection is to provide compartmentation of the building in the form of floors, ceilings and partitions to limit the spread of fire and smoke. However, buildings with atria do not conform with this fundamental approach in terms of horizontal compartmentation and vertical separation. The lack of physical separations can allow smoke and hot gases to move unimpeded to locations far removed from the fire source in a relatively short period of time. Atrium buildings can contain large quantities of combustible materials and can also contain significant numbers of people which could be exposed to smoke, heat and toxic gases from a fire. The spread of fire and smoke can also cause a significant amount of property damage. Atrium buildings are commonly designed such that the atrium space is connected to adjacent rooms or spaces. The boundary between the atrium and the adjacent room can either be glazed or fully open.

Unprotected openings between the atrium and adjacent rooms are known as communicating spaces. Smoke and hot gases flowing from a communicating space can move unimpeded into an atrium, possibly affecting other areas of the building. Therefore, the use of a smoke management system in an atrium building is particularly important. An appropriate design of smoke management system can provide conditions to allow safe means of escape from a building, either by separating the occupants from the hot smoky gases produced or by providing tenable conditions for safe escape. Property protection can primarily be achieved by providing improved conditions for effective fire-fighting operations in addition to limiting the spread and temperature of the smoke. Atrium buildings generally require the use of performance based fire engineering principles to meet the requirements of local Building Regulations as they often cannot be dealt with using more restrictive prescriptive building codes (e.g. due to excessive lengths of egress to a place of safety).

1.2 Smoke hazards

A definition of the term 'smoke' is given in NFPA 92B [2], which states that "smoke consists of the airborne solid and liquid particulates and gases evolved when a material undergoes pyrolysis or combustion, together with the quantity of air that is entrained or otherwise mixed into the mass". Thus, smoke can be considered to be a mixture of the particulate and gaseous products from the burning fuel and any air entrained into the fire plume and into any subsequent smoke flow. It is generally recognised that the majority of fire deaths are due to the inhalation of smoke. UK fire statistics [3] show that the most common identified cause of death from fire, and approximately one-third of non-fatal fire incidents, was due to occupants being overcome by gas or smoke. Hall [4] reported that in the United States, most victims of fires died from the inhalation of smoke or toxic gases and not from burns. Smoke may reduce or eliminate the capacity of building occupants to escape due to reduced visibility, toxic and thermal hazards. For those who are subjected to smoke, these factors can be taken into account as part of a tenability analysis using methods described by Purser [5] and Milke *et al.* for smoke management applications [6].

1.2.1 Smoke visibility

Smoke particulates can cause direct visual obscuration by absorbing and scattering light, limiting visibility for those trying to escape and reducing the visibility of escape signs. Smoke properties which can affect visibility include particulate size, colour, spatial density and the level of irritancy. Reduced visibility in fire can cause people to become disorientated, delaying the time to escape to a place of safety as well as hindering fire service search and rescue operations. A tenability limit for visibility which is suitable for escape purposes is dependent upon the degree of familiarity of the occupants of the building. Jin [7] gives values between three to five metres for those familiar with the building, but up to 20 m for unfamiliar buildings. The Fire Code Reform Centre [8] recommends a design visibility tenability limit of five metres for small rooms and a ten metre visibility limit for other rooms which is consistent with other design guidance worldwide [9,10].

1.2.2 Smoke toxicity

Smoke from fires can have a toxic effect due to exposure to asphyxiant gases and irritant chemicals present in the combustion products. The toxic hazard of asphyxiant gases such as carbon monoxide (CO), carbon dioxide (CO_2) and hydrogen cyanide (HCN) is given by Purser [5]. Asphyxiant gases generally act to disturb the normal respiratory process. Inhaled CO is taken up by blood in the lungs and inhibits oxygen being supplied to body tissues, especially brain tissue [5]. HCN reduces the ability to use oxygen once delivered to the tissue [5]. Excess CO_2 stimulates breathing, thus increasing the uptake of fire gases, in addition to being an asphyxiant itself at concentrations above 5% [5]. Asphyxiant gases have no immediate effect to those exposed to fire gases, but when a sufficient dose has been inhaled, collapse and loss of consciousness is induced. If the person is not rescued immediately after incapacitation occurs, death is likely within a few minutes. For these reasons asphyxiant gases can be considered as having no significant effect on evacuation behaviour or movement speed but are a major determinant of the time when incapacitation is predicted [10].

Irritants such as hydrogen chloride, acrolein and formaldehyde are common in combustion products. Exposure to irritants reduces the efficiency of escape due to pain to the eyes and pain and breathing difficulties in the respiratory tract and the severity will depend upon the concentration and the potency of each irritant [10].

1.2.3 Thermal properties

Occupants who are subjected to heat from smoky gases in a fire may experience pain, shock, heat stroke (hyperthermia) and burns to the skin and/or the respiratory tract. These effects can be due to both radiant and convected heat when escaping beneath or within a smoke layer. Various tenability limits for radiant heat fluxes, temperatures and exposure times for skin pain and incapacitation due to thermal properties of smoke are given by Purser [5].

1.3 Objectives of atrium smoke management

Milke [11] gives five design objectives for smoke management systems in atrium buildings, these are:

1. Maintain a tenable environment in the means of egress in the atrium during the time required for evacuation.
2. Confine the smoke in the atrium to a limited region in that space.
3. Limit the migration of smoke into adjacent spaces from the atrium.
4. Provide conditions in the atrium to assist emergency response personnel in conducting search and rescue operations and locating and controlling the fire.
5. Contribute to the overall protection of life and reduction in property loss.

Milke states that a design may be to achieve either one, or a combination of these objectives. Milke also lists a number of ‘hazard parameters’ in which the design objectives can be evaluated in measurable terms, such as: smoke layer depth, visibility through the smoke layer, carbon monoxide concentration and temperature rise in the smoke layer. Milke states that an acceptable smoke management system is one which maintains the hazard parameter(s) of concern to within acceptable levels.

1.4 Smoke management in atria

There are a number of different smoke management methods available for atrium buildings [2,12,13]. Morgan *et al.* [12] present various alternative methods which are described below.

1.4.1 Smoke and heat exhaust ventilation

This approach utilises the buoyancy of the smoky gases from the fire to form and maintain a smoke layer above the heads of occupants of the building (with clear air beneath), providing a safe means of escape. This form of smoke management is pertinent to the research objectives in this work and is described in more detail in section 1.5.

1.4.2 Smoke filling

This approach can be applied to atria which have large volumes, such that smoke exhaust ventilation may not be necessary. This strategy becomes viable when smoke can be contained in a roof void for the duration of the required safe egress time for the occupants of the building. In this case, the height of the smoke layer may not reach an unacceptable value before the fire consumes the available fuel. This approach assumes that the fire grows at a predictable rate. Klote and Milke [13] provide empirical relationships to determine the smoke layer height above the fire with respect to time for both steady and growing fires. This strategy should only be used if the designer can demonstrate by calculation that smoke exhaust ventilation is not necessary.

1.4.3 Temperature control ventilation

This strategy is used when the height of the smoke layer above the floor is not a critical design parameter. In this case, smoke exhaust can be used to achieve a maximum value of the temperature of the layer of smoky gases. This approach allows the use of materials which would otherwise be damaged by hot gases (e.g. atrium façade materials which are not fire-resisting).

1.4.4 Smoke clearance

This approach provides sufficient ventilation to remove smoke from the atrium after the fire has been suppressed (typically by the fire service).

1.4.5 Smoke and heat exhaust from each storey separately

In some cases it may be impractical to provide smoke exhaust ventilation from the atrium space if the height of rise of the smoke layer above the floor is too large. It may be beneficial to prevent smoke from entering the atrium altogether (particularly for fully open atria). This can be achieved by the use of strategically placed smoke curtains around the atrium space at each storey, and providing smoke exhaust ventilation from each storey separately.

1.4.6 Atrium depressurisation

Where the boundary between the atrium space and the adjacent areas is linked by small openings (e.g. doors gaps, leaky façade), it is possible to prevent smoke from travelling through these openings by providing ventilation to locate the neutral pressure plane above the highest leakage path. This approach is known as depressurisation. The purpose of this technique is to prevent smoke from travelling into the adjacent spaces and does not necessarily provide protection to the atrium space [12]. This technique is similar to that employed for natural environmental ventilation in atrium buildings [14].

1.4.7 Combination of above strategies (hybrid smoke management)

Various combinations of the above strategies can also be applied, such as atrium depressurisation with smoke and heat exhaust ventilation.

1.5 Smoke and heat exhaust ventilation

Smoke management in atria is often provided by a Smoke and Heat Exhaust Ventilation System (SHEVS). This approach provides smoke and heat exhaust from the upper regions of a building to create a clear layer beneath a buoyant stratified smoke layer, thus providing conditions for safe means of escape. Some form of physical smoke containment may also be required, for example, using smoke curtains or downstands to create smoke reservoirs. For this approach to be effective, it is necessary for the temperature of the gas layer to be high enough to remain buoyant when at the design height. SHEVS may be naturally driven (due to buoyancy of the gases produced from the fire) or mechanically driven (mechanical exhaust fans).

Figure 1.1 shows the general principle of smoke and heat exhaust ventilation. Smoke from a fire will rise as a plume and entrain air as it rises. This entrainment will significantly increase the volume of smoky gases produced. The hot gases rise and form a buoyant layer within the enclosure. Smoke and heat will exhaust from ventilators in the roof of the enclosure either by natural or mechanical means. The hot gas layer will deepen until equilibrium is reached between the quantity of gases being ventilated and the quantity of gases entering the layer. For smoke ventilation to be effective it is necessary to provide an adequate amount of inlet air to replace the hot gases being removed.

The performance of SHEVS can depend on various factors [10] such as:

- Temperature of the smoke layer.
- Aerodynamic free area of natural ventilators.
- Volume of smoke exhausted by mechanical fans.
- Wind effects.
- Geometry, size and location of inlet air openings.
- Geometry, size and location of the smoke reservoir.

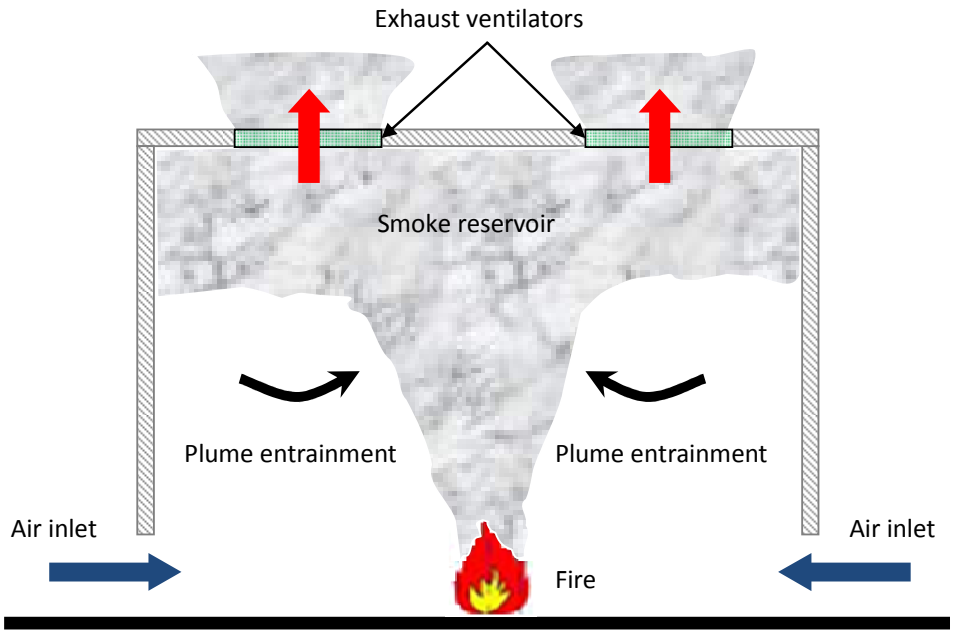

Figure 1.1: Principle of smoke and heat exhaust ventilation

SHEVS provides the safe use of escape routes which are in the same space as the fire. The amount of smoke exhaust must be calculated to ensure that the smoke layer is at a safe height above the occupants using these escape routes. In addition to providing conditions for safe means for escape, SHEVS also provide improved conditions for effective fire-fighting operations which can provide improved property protection.

1.5.1 Clear layer height

When considering life safety, a critical design parameter of SHEVS is the clear layer height. The clear layer height is the height between the level of the fire and the base of the buoyant smoke layer in the atrium. The design clear layer height will usually provide a layer with a safe height above the highest egress route open to the atrium. Figure 1.2 shows a schematic drawing of a design clear layer height for a multi-storey atrium. This clear layer height will provide a tenable environment for safe egress for the duration of the fire (provided the design fire is not exceeded). Milke [11] provides factors which must be taken into consideration when identifying a design clear layer height, these are: location of means of egress within the open space, separation of adjacent spaces from the open space and environmental and geometric factors.

Guidance on the recommended clear layer height for SHEVS varies worldwide. NFPA 101 [16] states that the design should "keep the smoke layer interface above the highest unprotected opening to adjoining spaces, or 1.83 m (i.e. 6 ft) above the highest floor level of exit access open to the atrium, for a period equal to 1.5 times the calculated egress time or 20 minutes, whichever is the greater".

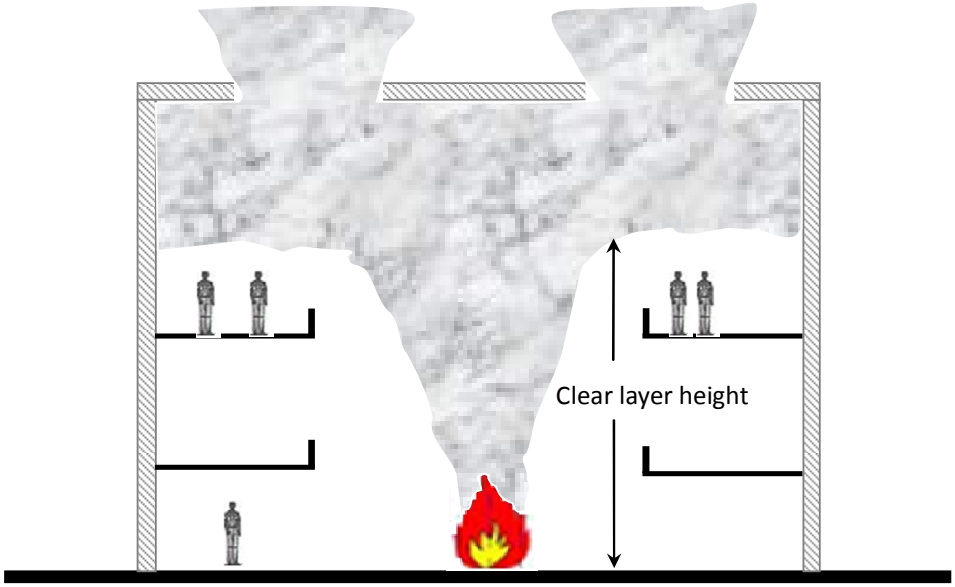

Figure 1.2: Schematic drawing of clear layer height

The history of guidance on acceptable clear layer heights in the UK is given by Morgan [18]. Current guidance in the UK [15] recommends a minimum clear height dependent upon the type of building. For public buildings (e.g. shopping malls) a minimum clear height of 3.0 m above the highest escape route is recommended. For non-public buildings (e.g. apartments, offices) a height of 2.5 m is given. Where the predicted smoke layer temperature is less than 50 ^{o}C above ambient temperature, the minimum clear heights should be increased by 0.5 m, as the smoke layer interface may not be well defined [15].

The current guidance within New Zealand [17] recommends a clear layer height of at least 2.0 m above the highest intermediate floor open to an atrium space.

1.6 Smoke movement and production

The controlling physical processes which govern the movement of smoke are: buoyancy forces due to the density difference between the hot gases and ambient air; air expansion forces generated by heat from the fire; and forced ventilation (e.g. smoke exhaust, HVAC and wind effects).

In design, the volume of smoky gases generated from a fire within an atrium is governed by the fire size (i.e. the design fire) and the amount of air entrained into the rising smoke plume. The volume of smoke must be calculated in order to determine the required fan capacity or vent area for a smoke ventilation system. The amount of air entrained into the plume will depend on the configuration of the plume produced.

Milke [11] identified five configurations of smoke plume which may exist within atrium buildings, these are:

1. Axisymmetric plume.
2. Wall plume.
3. Corner plume.
4. Spill plume.
5. Window plume.

A brief description of each of type of plume and the design fire is described below.

1.6.1 Axisymmetric plume

An axisymmetric plume is generally expected from a fire located near the centre of an atrium floor. This type of plume is typically remote from any walls and air is entrained around all sides of the plume. Entrainment of air will occur over the full height of the plume until it reaches the interface with a smoke layer which may have formed above.

A classical analysis of axisymmetric plumes has been carried out by Morton *et al.* [19]. This analysis has been extended for chemically reacting plumes due to fires in buildings [20,21]. Plume entrainment formulae for axisymmetric plumes are well established and will not be addressed further in this work.

1.6.2 Wall plume

A plume which is generated from a fire against a wall is known as a wall plume. Zukoski [22] developed a wall plume entrainment correlation based on "mirror symmetry". Work by Poreh and Garrad [23] has highlighted that further research on wall plume entrainment is desirable.

1.6.3 Corner plume

A plume which is generated from a fire located in the corner of a room, where the walls form a 90^{o} angle, is known as a corner plume. Zukoski [22] treated corner plumes in a similar manner to a wall plume with the use of "mirror symmetry" for plume entrainment. Again, work by Poreh and Garrad [23] has demonstrated that further research is desirable for corner plume entrainment.

1.6.4 Spill plume

A spill plume is generated from an initially horizontally moving smoke layer within a compartment which then subsequently rises at a spill edge (e.g. at an opening onto an atrium space). The behaviour of this type of plume is the major focus of this work and is described in more detail in the following section.

1.6.5 Window plume

A window plume is a plume which flows from a window (or doorway) into an atrium space [13]. Window plumes are often generated from post-flashover fires [24] although they can also occur from pre-flashover fires. An entrainment correlation has been developed by Heskestad, by comparing the air entrainment for a window plume with that of an axisymmetric plume. The window plume entrainment correlation is given by Klote and Milke [13].

1.6.6 The design fire

Calculation of the quantity of hot smoky gases produced in a fire requires knowledge of the fire size, either in terms of growth rate, area and heat release rate per unit area, or the expected maximum heat release rate. A design fire can either be specified with a constant heat release rate from ignition (i.e. a steady state fire) or a time dependent growing fire to which occupant egress time could be related. Steady state design fires have historically been used for SHEVS design [12] and various guidance documents and standards give suggested values for various occupancies [2,12,13]. Although it is recognised that a real fire does not reach steady state from ignition, it is convenient to assess the likely maximum size of fire to be expected for a scenario and design the smoke management system to deal with that. This approach allows the smoke management system to cater for all fires smaller than the accepted design fire and ignoring the growth period of the fire will introduce an element of conservatism in the design when considering mass entrainment (until the fire reaches the design fire size), but not necessarily for other performance parameters such as detection (i.e. it will give rise to false early detection being predicted). The use of time dependent growing fires has previously been less prevalent due to lack of robust and available data on fire growth for various occupancies and fire scenarios [12]. However, research has been carried out in the past few years to further characterise design fire growth rates for a variety of fire scenarios [25,26]. Therefore, it is likely that the use of time dependent design fires will become more common as the database of fire growth curves is increased. The use of a time dependent growing design fire could result in a more cost effective smoke management design. Guidance is available in the UK on the design of SHEVS using both steady state [15] and time dependent growing fires [27].

1.7 The thermal spill plume

If a fire were to occur in a communicating space within an atrium building (e.g. a shop or office unit), a horizontally moving buoyant layer of hot smoky gases will form within that space (see Figure 1.3). This layer will spread laterally and flow toward the opening connecting to the atrium space. If there are no smoke management measures to confine the smoke layer to the room of fire origin, this horizontally moving layer will flow out of the opening.

If a balcony exists beyond the compartment opening, smoke will flow beneath the balcony. The smoke flow will then rotate around the free edge of the balcony (i.e. the 'spill edge'). This region is often known as the 'rotation' region of the plume. The smoke will then rise as a plume into the atrium void. This type of plume is commonly known as a 'spill' or 'line' plume. The term 'line' is used, as immediately after the rotation region the plume is relatively long and narrow. As the rising plume consists of the convective flow of hot gases from the fire, these plumes are known as thermal spill plumes. Similar plumes which are generated from post-flashover fires, where flames project beyond the compartment and into the rising plume are known as flame spill plumes. The entrainment behaviour of flame spill plumes is not well understood and design guidance is limited (mainly the window plume correlation). However, most smoke management designs will generally concern pre-flashover fires (except for small rooms) and thermal spill plumes. The behaviour of flame spill plumes is outside the scope of this work.

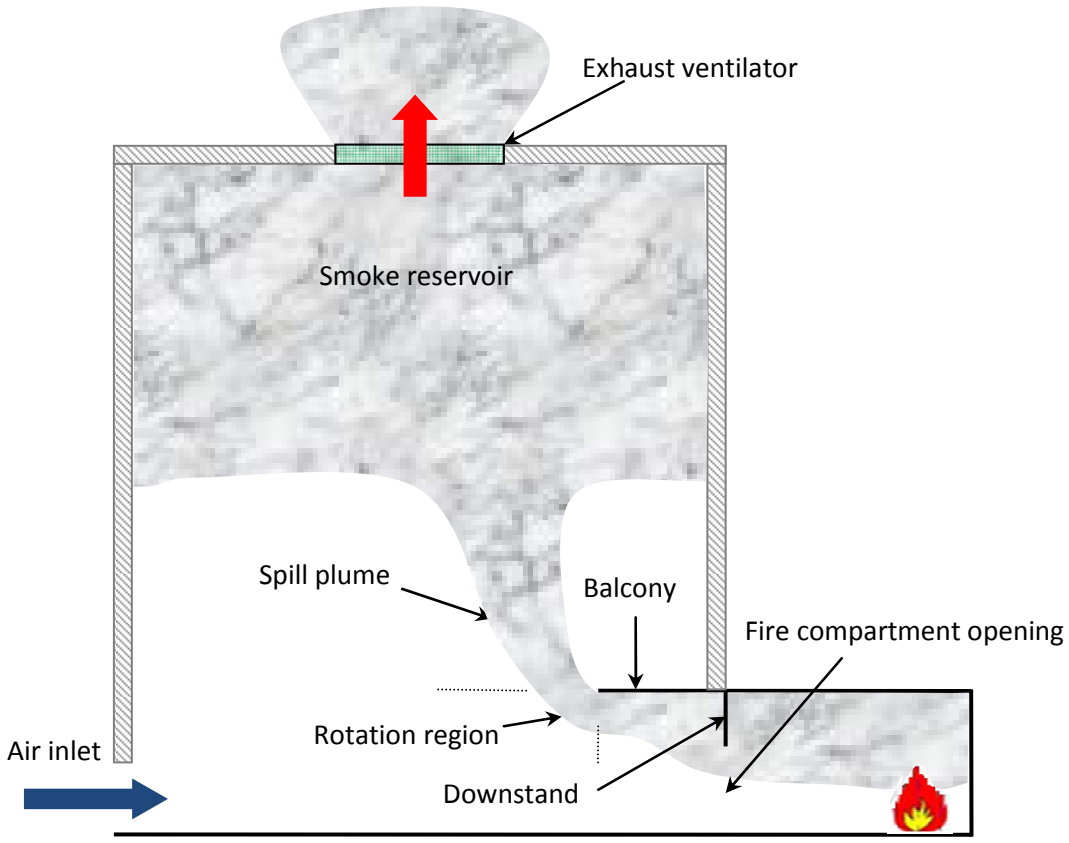

Figure 1.3: A spill plume with a SHEVS

Thermal spill plumes can generally be categorised into two groups, namely, balcony and adhered spill plumes.

Figure 1.4 shows a schematic drawing of a balcony spill plume. In this case, the smoke will flow from the compartment opening and then under a horizontal projection which may extend beyond the opening (e.g. a balcony). If there is a downstand at the compartment opening, then the smoke flow will rise from the opening and form a flowing layer beneath the balcony. The smoke layer below the balcony edge will then rotate at the spill edge (i.e. at the edge of the balcony) and rise as an unhindered plume in the atrium void. This type of plume is also known as a free spill plume.

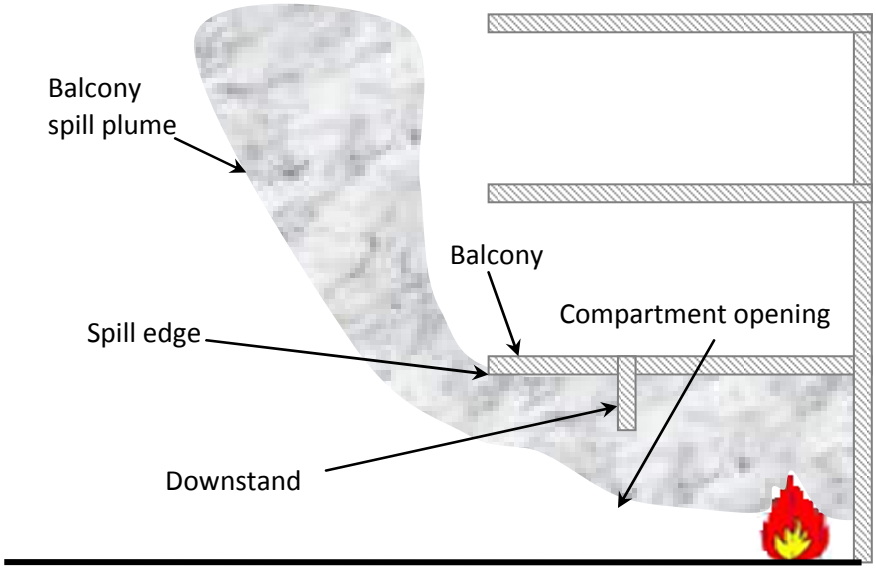

Figure 1.4: A balcony spill plume

Figure 1.5 shows a schematic drawing of an adhered spill plume. In this case, there is no balcony or horizontal projection beyond the compartment opening, and a wall projects vertically above the top of the opening. The smoke layer below the compartment opening will then rotate at the spill edge (i.e. the compartment opening in this case). The subsequent plume will then adhere to the vertical wall above the opening as it rises. This type of plume is also known as a single-sided spill plume.

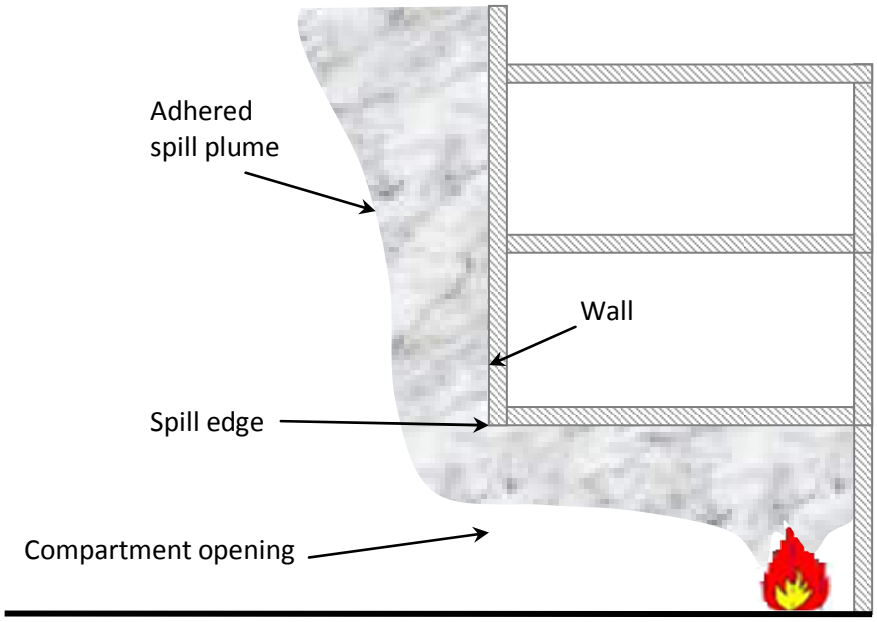

Figure 1.5: An adhered spill plume

1.7.1 Entrainment processes

The total mass flow rate of gases in a spill plume at the design clear layer height is dependent upon the total amount of entrainment occurring in the plume upstream of the design height. There are a number of possible entrainment processes that can take place depending upon the building geometry and spill plume type. In general, there are three regions where entrainment occurs for the spill plume scenario, namely: in the compartment of fire origin, between the fire compartment opening and the spill edge, and beyond the spill edge. Entrainment processes in each of these regions is briefly described below.

1.7.1.1 Entrainment in the compartment of fire origin

Figure 1.6 shows various entrainment processes which can occur within the compartment of fire origin. The mass flow rate of gases at the compartment opening can be considered to be made up of the combined total of the mass flow rate of the burning fuel, the air entrainment into the rising plume above the fire, the air entrainment due to impingement of the plume into the smoke layer interface above, and the entrainment of air into the horizontally moving layer in the fire compartment.

As the rising plume above the fire impinges with the ceiling, the flow will spread radially outward to form a ceiling jet [28]. If the compartment is small, then the ceiling jet can persist until it reaches the walls of the room, after which it becomes a wall jet. If the walls are cold and the smoke layer is sufficiently deep then a downward flowing convection current can also be generated [29]. The combination of the wall jet and convection current can cause the downward velocity flow to be large enough to be driven out of the gas layer and into the clear air beneath. The downward flow of the wall jet will be opposed by the buoyancy of the gases, forcing it to turn upward and return to the layer. This causes clear air to be entrained into the smoke layer in the compartment [29].

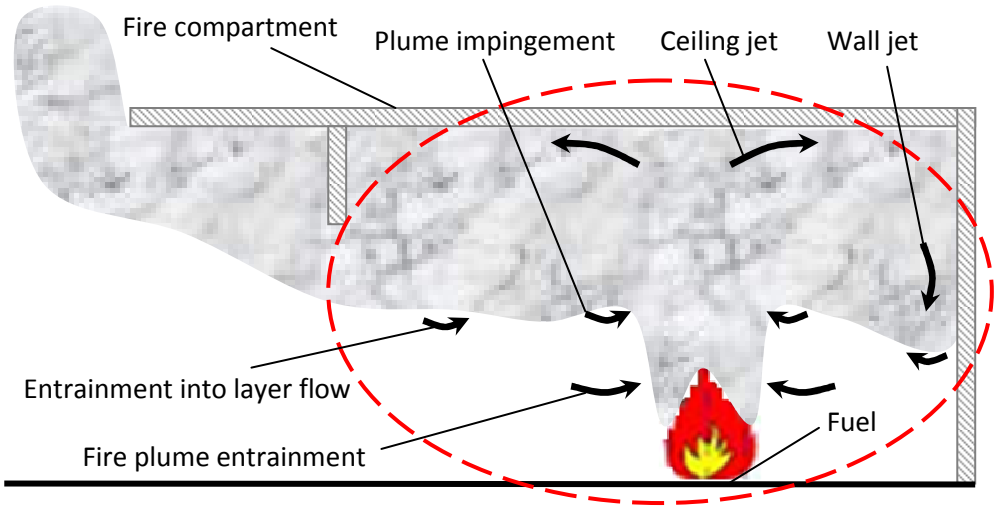

Figure 1.6: Entrainment in the compartment of fire origin

In general, the mass flow rate of the burning fuel and the air entrainment due to impingement of the plume into the smoke layer interface can be considered to be negligible [30,31]. The entrainment of air into the horizontally flowing layer can also be considered to be negligible [31], therefore the mass flow rate of gases at the compartment opening can be considered to be approximately equal to that generated from the plume above the fire (unless the effect of wall jets are significant). Entrainment of air into the rising plume is dependent on the compartment geometry, the location of ventilation openings and the location of the fire [32]. Methods used to determine the mass flow rate of gases at a fire compartment opening are described in Chapter 2.

1.7.1.2 Entrainment between the fire compartment opening and the spill edge

Figure 1.7 shows an entrainment process that can occur between the fire compartment opening and the spill edge. If a downstand and a higher projecting balcony exist at the compartment opening, then additional entrainment will occur into the flow as it rises beyond the compartment opening. The amount of entrainment is dependent on the width of the compartment opening and the depth of the downstand [33,34]. Methods used to determine the additional mass flow rate of gases between the compartment opening and the spill edge are described in Chapter 2. There will be no significant additional entrainment in the absence of a downstand at the compartment opening.

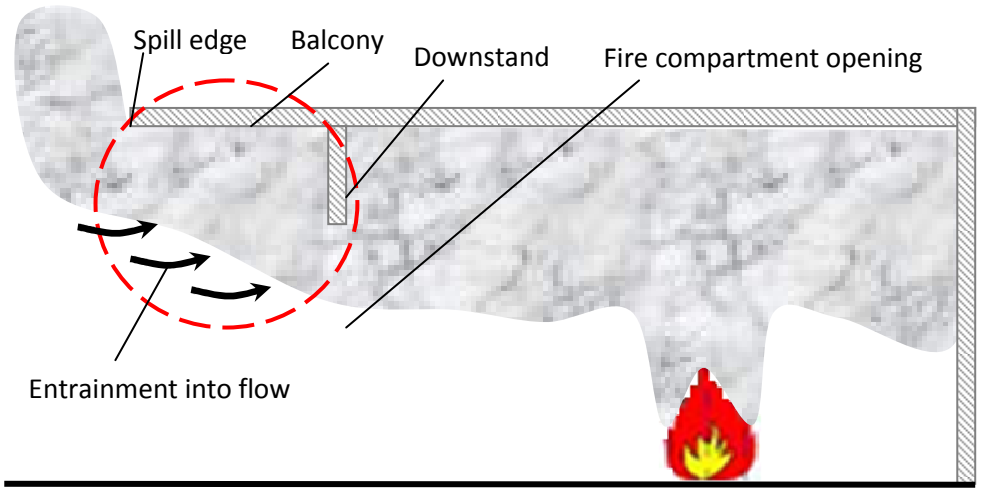

Figure 1.7: Entrainment between the fire compartment opening and the spill edge

1.7.1.3 Entrainment beyond the spill edge

Figure 1.8 shows the entrainment processes that can occur beyond the spill edge. The flowing layer below the spill edge (i.e. the balcony edge or the compartment opening) will rotate upwards around the top of the spill edge and rise into the atrium void with entrainment occurring in the rotation region. The subsequent amount of entrainment beyond the rotation region is dependent upon the type of spill plume generated. For a balcony spill plume (see Figure 1.8a), where the balcony sufficiently projects beyond any bounding walls (see section 2.4.3.3), entrainment will occur into both sides of the plume across its lateral extent. There will also be entrainment into the free ends of the plume over its full height of rise, unless the ends are bounded by walls.

For the adhered plume (see Figure 1.8b) entrainment will only occur into one side of the plume across its lateral extent. Entrainment will occur into both ends of the plume unless it is bounded by walls. Methods used to determine the mass flow rate of gases beyond the spill edge are described in Chapter 2.

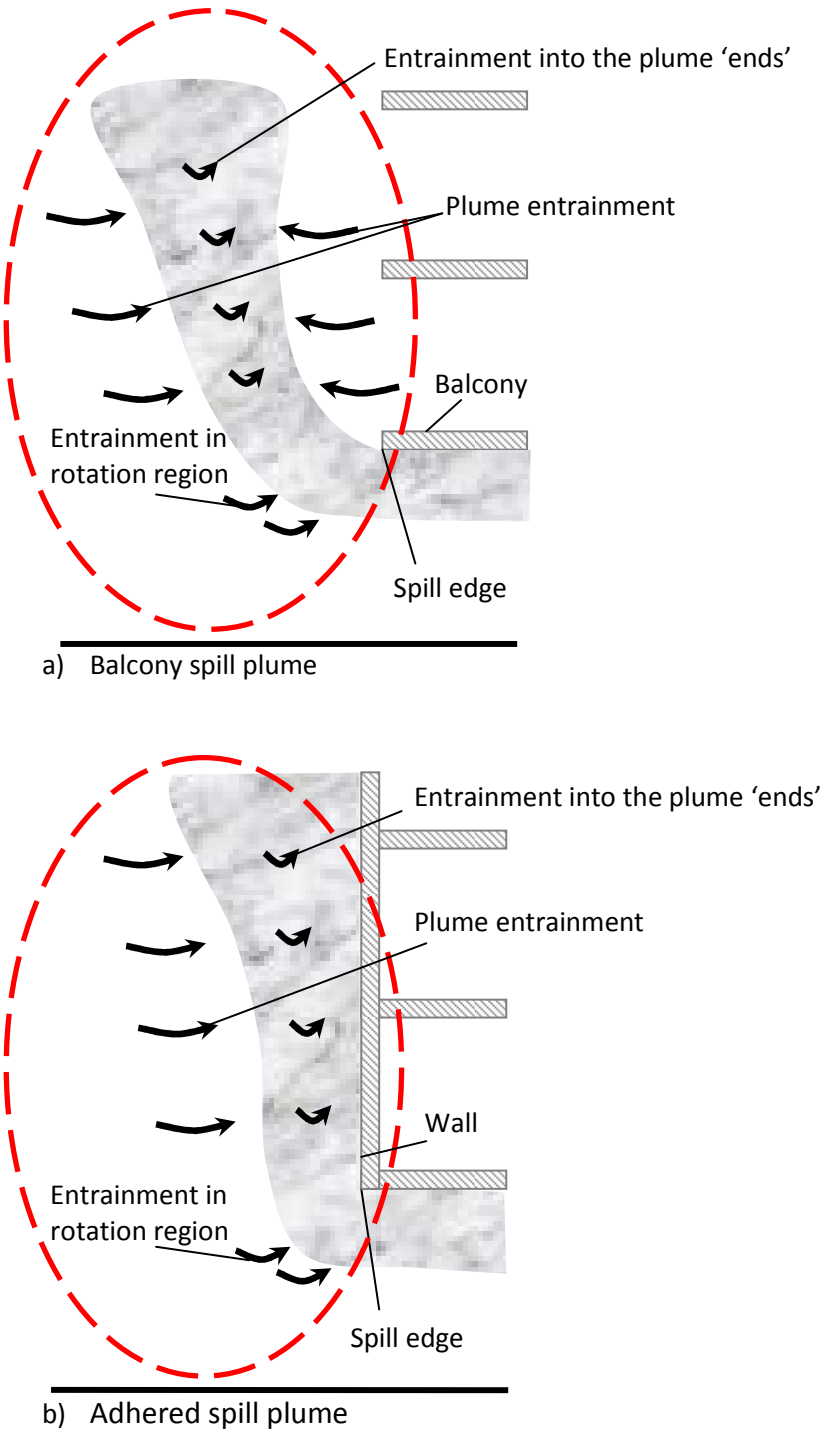

Figure 1.8: Entrainment beyond the spill edge

The spill edge can be at the end of a flat ceiling (i.e. a balcony edge) or at a downstand edge (see Figure 1.9). Harrison and Spearpoint [40] have shown that the subsequent amount of entrainment in the spill plume appears to be the same whether the spill edge is at a flat ceiling or at a downstand edge.

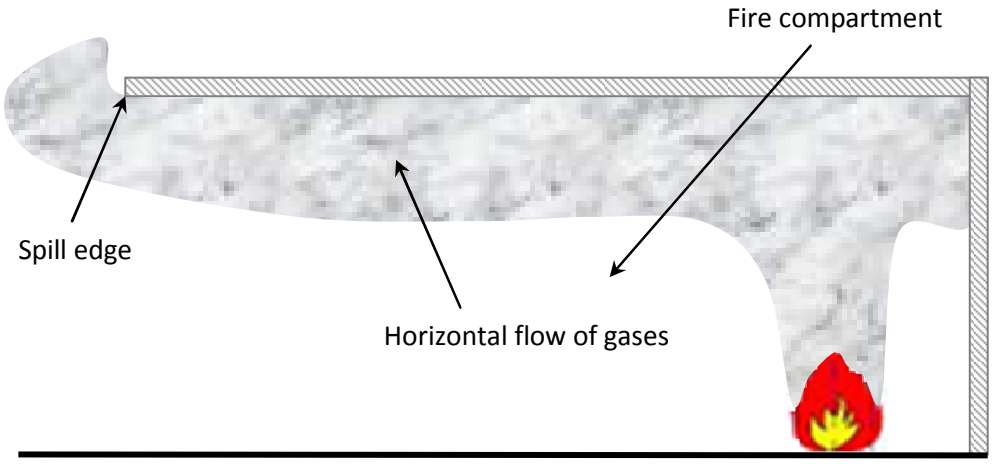

a)` Spill edge with a flat ceiling

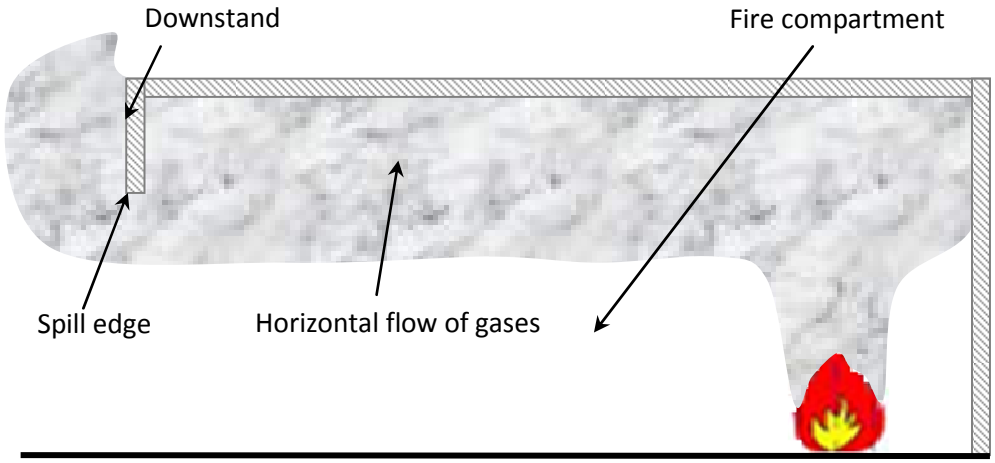

b) Spill edge at a downstand edge

Figure 1.9: Possible spill edge configurations

The governing factors which affect the amount of air entrainment into a spill plume are given by Morgan and Marshall [35], these are:

- The mass flow rate of the gases in the plume after rotation.
- The convective heat flow rate of the gases.
- The lateral extent of the spill plume entering the atrium, measured along the free edge past which the smoke spills.
- The height over which the plume must rise.

Spill plumes which do not include entrainment into the ends of the plume are known as two-dimensional (2-D) plumes and those which include end entrainment are known as three-dimensional (3-D) plumes.

1.7.2 Channelling screens

For adhered spill plumes, where there is no balcony or horizontal projection extending into the atrium void, the lateral extent of the rising plume is governed by the width of the opening at the spill edge. However, if the smoke flow from the compartment opening is allowed to pass unrestricted under a balcony, it will spread laterally. The flow will continue to spread laterally until it reaches an obstruction or loses sufficient buoyancy that it becomes stagnant. The smoke flow will spill at the balcony edge and rise into the atrium space as a wide spill plume with a large surface area over which entrainment of air occurs [12] (see Figure 1.10a). The amount of entrainment can be reduced by restricting the ability of the smoke flow to spread laterally beneath the balcony which will limit the lateral extent of the subsequent rising plume. This can be achieved with use of channelling screens (or draft curtains) beneath the balcony to 'channel' the flow to the balcony edge (see Figure 1.10b). Channelling screens can be part of the structure of the building or can be free hanging smoke curtains that are initially contained within a ceiling void and drop into position on detection of a fire. The minimum depth of a channelling screen can be calculated using a method given by Morgan *et al.* [12].

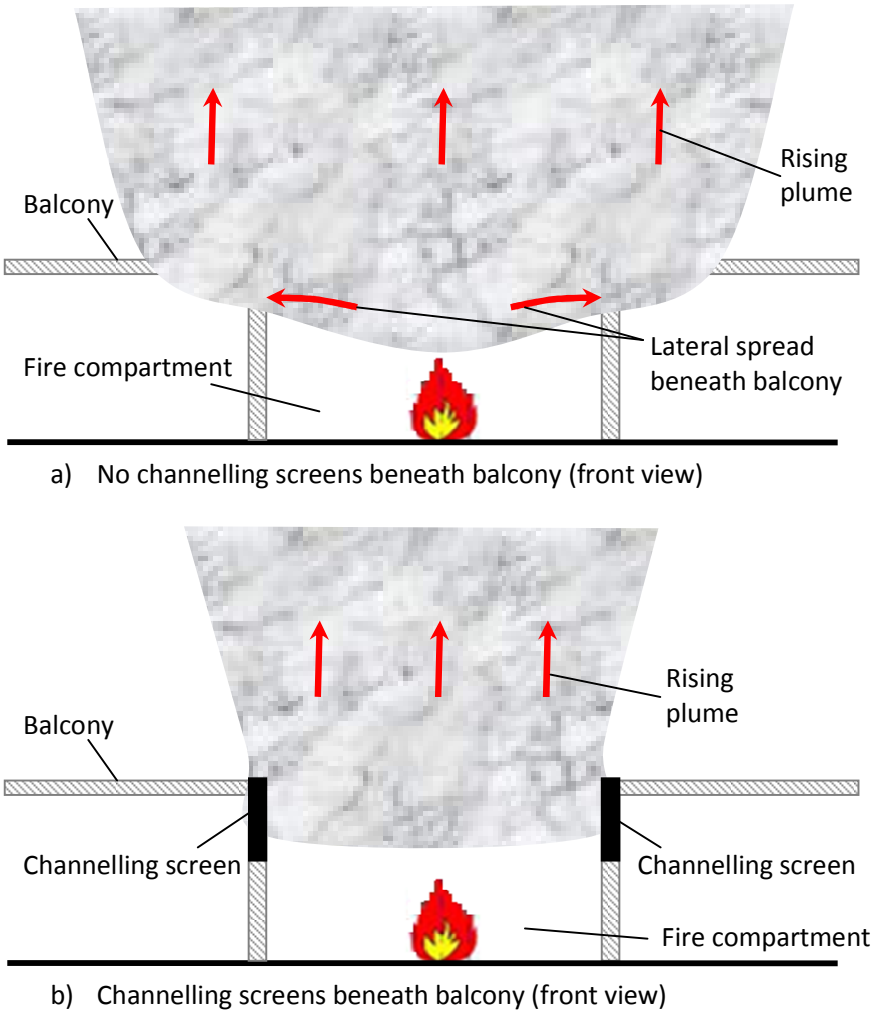

Figure 1.10: Channelling screens to limit the lateral extent of a balcony spill plume

1.7.3 Importance of the spill plume

A fire in a communicating space on the lowest level of a building will maximise the amount of air entrainment into a rising spill plume, this will result in the greatest quantity of smoky gases entering the layer above. In general, a spill plume provides the worst case condition for this scenario [12]. Milke [36] carried out a comparison between the smoke production rates for an axisymmetric plume with that of a variety of balcony spill plumes dependent upon the compartment geometry. The smoke production rate for the spill plume was determined using a formula by Law [36]. Milke states that this formula provides an approximation of the mass flow rate of gases generated by a spill plume. Comparison between each type of plume was made for a fire with a convective heat release rate of 5000 kW.

The smoke production rate for the spill plume was determined for a variety of balcony heights and spill plume lengths (i.e. the lateral extent of the plume at the balcony edge). Milke demonstrated that for the conditions studied, the balcony spill plume entrains a greater amount of air than an axisymmetric plume for a clear height of up to approximately 40 m (see Figure 1.11). The nomenclature for Figure 1.11 is such that H represents the height of the balcony above the floor and L represents the width of the plume at the balcony edge. Figure 1.11 suggests that wider openings entrain air at lower rate with respect to height compared to narrow openings, however, this is misleading as the the width of the plume is included in the calculation of the absolute value of volume flow rate. The entrainment coefficient assumed in the calculation of volume flow rate is the same for each width of plume.

At large heights of rise, spill and axisymmetric plumes are expected to behave similarly in terms of smoke production rate due to entrainment into the free ends of a spill plume causing it to eventually become axisymmetric in nature (see Chapter 9).

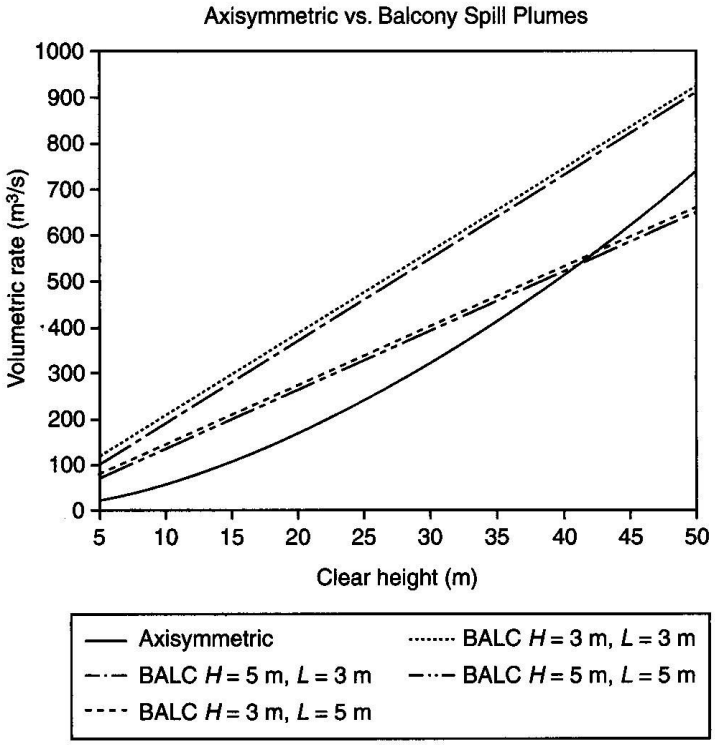

Figure 1.11: Comparison between an axisymmetric and balcony spill plumes [36]

1.7.4 Entrainment calculation methods for the thermal spill plume

Smoke management design requires appropriate entrainment calculation methods to predict the volume of smoky gases produced in a fire in order to determine the required exhaust fan capacity or ventilator area for a design clear layer height. There are various methods available for the thermal spill plume, which include a range of empirical simplified design formulae [2,31,38-40], more complex analytical methods [12,41] and numerical modelling using Computational Fluid Dynamics (CFD) for fire [e.g. 42,43]. A brief description of each of these general methods is described below with a more detailed description of specific methods in Chapter 2.

1.7.4.1 Simplified spill plume formulae

Simplified spill plume formulae typically consist of a single line equation to predict the mass flow rate of gases produced by a spill plume. These formulae are relatively quick to use and ease the task of designing a smoke management system. They are commonly used and are given within international guidance documents such as NFPA 92B [2] and the fire engineering guide produced by the Chartered Institution of Building Service Engineers (CIBSE), UK [38]. These simplified formulae are empirically based and therefore have specific limitations depending on the way the correlation was derived. Therefore, they generally apply for relatively idealised designs in line with the experiments from which they are based. These formulae are particularly useful for the early stages of design and for approving authorities as an initial assessment of calculations based on more complex methods. Simplified spill plume formulae are currently only available for a limited range of scenarios and recent research [40] has been carried out to develop formulae for a greater variety of spill plume geometries.

1.7.4.2 Analytical methods

The designer also has the option of using more complex analytical methods to calculate entrainment for a spill plume. The BRE spill plume method [12] developed at the Building Research Establishment, UK, has generally been the only method available for the past 30 years. An alternative method which differs in its treatment of the underlying physics has recently been developed by Kumar *et al.* [41]. This

alternative method currently applies for 2-D balcony spill plumes. The BRE method is more versatile than simplified spill plume formulae as it deals with both 2-D and 3-D spill plumes, balcony and adhered, and can take into account the presence of a downstand at the compartment opening. However, not all aspects of this method have been validated experimentally. This method has generally not been so widely used due to its complexity. It has mainly been used in the UK, parts of mainland Europe and Asia. In general, analytical methods are more complex and less user-friendly compared to simple formulae, typically requiring the designer to program the method into a computer. However, once this is successfully done, a result can quickly be achieved. All these methods have at least one empirical element that is required to achieve a result (i.e. an entrainment coefficient) similar to that used for entrainment into axisymmetric plumes given by Morton *et al.* [19]. Therefore, these methods generally apply to relatively idealised designs in line with the experiments from which the entrainment coefficient was determined.

1.7.4.3 Numerical modelling using CFD

The use of numerical modelling using CFD treats the geometry as a 3-D numerical grid and solves the underlying set of coupled equations for mass, momentum, energy and species concentration. There are various types of CFD model available which differ in the underlying turbulence model for the flows [e.g. 42,43]. Numerical modelling is best suited to more novel and complex buildings, where other more simple methods cannot be applied with confidence, although this does not preclude its use for simple buildings if required. There is currently limited validation of CFD for the spill plume in smoke management design [e.g. 41,44]. This approach is generally more time consuming to the designer, ranging from hours to weeks to achieve a result depending upon the building complexity, resolution of the grid size and computing power available. However, a more comprehensive and holistic analysis of the smoke flows are possible using this approach. The competency of the user of these models is essential and requires knowledge of fire science and numerical analysis to avoid misuse and the detailed results from these models can require careful analysis. The approach of numerical modelling using CFD is described in more detail in Chapter 3.

1.8 Research objectives

There has been much controversy over the validity of various entrainment calculation methods for the spill plume [45,46] and there are considerable differences in the smoke production rates predicted using these methods [40,47]. In design, there are possible scenarios involving the spill plume where guidance is very limited or does not exist. Whilst over-sizing of the required smoke exhaust can be uneconomical, under-sizing can compromise the design objectives.

This work aims to rigorously characterise thermal spill plume entrainment using experimental modelling (i.e. using a $1/10^{th}$ physical scale model) and numerical modelling (i.e. using CFD) to develop new and robust guidance to designers of smoke management systems. The main objectives of this research are described below which relate to Chapters 5 to 10 inclusive.

1.8.1 The horizontal flow of gases below the spill edge (Chapter 5)

Characteristics of the horizontally flowing layer below a spill edge in terms of mass flow rate, layer depth and convective heat flow rate are crucial input parameters to simple and analytical calculation methods. If there is no downstand prior to the spill edge the characteristics of the layer flow can be calculated using various methods to predict the flow from a fire compartment opening [e.g. 12,30,38,51].

The characteristics of the layer flow below the spill edge from a compartment with a flat ceiling, both with and without a vertical wall projecting above the spill edge (i.e. for an adhered or balcony spill plume) is determined experimentally as part of the subsequent analysis of entrainment into a spill plume.

These data will be used to assess the performance of various methods available to predict the flow of gases below the spill edge. This will enable recommendations to be made of the most appropriate method for design, for the specific spill edge and compartment geometries examined in this work.

1.8.2 Balcony spill plume entrainment (Chapter 6)

1.8.2.1 The 2-D plume

Experimental data to characterise entrainment into balcony spill plumes has mainly been obtained from $1/10^{th}$ physical scale model studies. The majority of these data concern the 2-D balcony spill plume with the measured entrainment between various studies generally being consistent [31,48]. However, all these experiments examined plumes which were generated from an identical width of fire compartment opening.

This work will provide additional experimental data for plumes generated from a variety of fire compartment opening widths to complement the existing data set. This will enable an assessment to be made of the general validity of existing empirical simplified design formulae and analytical methods for the 2-D plume. Development of new simplified design formulae and modifications to analytical methods (i.e. the empirical elements) will be proposed if necessary.

1.8.2.2 The 3-D plume with channelling screens

There is limited experimental data available to characterise entrainment into 3-D balcony spill plumes with the use of channelling screens below the balcony. Data obtained by Morgan and Marshall [35,81] and Hansell *et al.* [32] form the basis of the design guidance by NFPA 92B [2] (i.e. for heights of rise up to 15 m above the balcony) and CIBSE [38]. More recent data obtained by Harrison and Spearpoint [40] have led to the development of an alternative design formula. There are significant differences in the prediction of entrainment between these methods with the Harrison and Spearpoint formula predicting approximately 40% less entrainment than the guidance given by NFPA 92B and CIBSE [40]. Possible reasons for this may relate to differences in the nature of the plume, fire compartment geometry or smoke reservoir geometry between each experimental study. Thus, there is current uncertainty concerning an appropriate simple calculation method to predict entrainment for the 3-D plume.

Entrainment into 3-D plumes has not been systematically characterised for plumes generated from a variety of fire compartment opening widths. In shopping malls, shop fronts can vary from narrow openings (e.g. doorways) to wide shop units in large stores. The effect of the width of the fire compartment opening on the subsequent entrainment into the ends of the plume is currently unclear due to the lack of appropriate data.

This work aims to provide a comprehensive set of new experimental data to rigorously characterise 3-D plume entrainment by varying the width of the fire compartment opening, the fire size and the clear height of rise of the plume. The objective is to provide a better understanding of balcony spill plume entrainment in an attempt to explain and reconcile differences between previous studies. This will enable the development of improved empirical simplified design formulae which can be applied more generally than current guidance. The experimental data will also be used to validate (or modify where necessary) the prediction of entrainment using analytical methods.

1.8.2.3 The 3-D plume without channelling screens

Entrainment into 3-D balcony spill plumes which are not channelled by screens below the balcony is not well understood. A very limited data set obtained from $1/10^{th}$ physical scale model experiments by Hansell *et al.* [32] was subsequently analysed by Law [49] to give simplified design guidance for this scenario. This guidance is given by NFPA 92B [2] and CIBSE [38]. None of the current analytical methods deal with this scenario due to the complexity of the flow beneath the balcony.

This work aims to provide new experimental data to characterise entrainment into 3-D plumes without channelling screens by varying the width of the fire compartment opening, the fire size and the clear height of rise of the plume. This will enable an assessment to be made of the generality of the current design guidance. The experimental data will be used to develop improved simplified guidance if necessary.

1.8.3 Adhered spill plume entrainment (Chapter 7)

1.8.3.1 The 2-D plume

Recently published work by Poreh *et al.* [50] provides data on entrainment into 2-D adhered plumes from 1/10th physical scale model experiments. The Poreh *et al.* work proposes a simple design formula to predict entrainment for the 2-D adhered plume. The data shows that entrainment into a 2-D adhered plume is approximately half that of an equivalent 2-D balcony spill plume. However, all these experiments examined plumes which were generated from a single width of fire compartment opening.

This work will provide additional experimental data for plumes generated from a variety of fire compartment opening widths to complement the existing data set given by Poreh *et al.* This will enable an assessment to be made of the general validity of the existing simplified design formula and analytical methods for the 2-D plume. Development of new simplified design formulae and modifications to the analytical methods (i.e. the empirical elements) will be proposed if necessary.

1.8.3.2 The 3-D plume

Limited data from 1/10th physical scale model experiments by Hansell *et al.* [32] showed that entrainment into a 3-D adhered plume is approximately half that of an equivalent 3-D balcony spill plume. This was subsequently used to update the BRE spill plume method which is currently the most robust calculation method available for the 3-D adhered plume, although there is a simple approximation for this scenario given by CIBSE [38].

This work aims to provide new experimental data to systematically characterise entrainment into 3-D adhered plumes by varying the width of the fire compartment opening, the fire size and the clear height of rise of the plume. This will provide new data to assess and develop simplified design guidance and to assess the performance of analytical methods to predict entrainment for the 3-D adhered plume.

1.8.4 Numerical modelling of the spill plume using CFD (Chapter 8)

Validation of numerical modelling using CFD has mainly been carried out for the 2-D balcony spill plume [e.g. 44,52]. The extensive amount of experimental data from this work will enable a further assessment to be made of the validity of CFD to predict spill plume entrainment.

This work aims to provide an initial assessment of CFD to predict entrainment for the 3-D spill plume, for both balcony and adhered plumes using the CFD model Fire Dynamics Simulator (FDS), developed by the National Institute of Standards and Technology (NIST), USA [42].

As part of a collaborative effort, additional CFD modelling of selected experiments from this work, for the balcony spill plume, is carried out by researchers at BRE using their in-house model named JASMINE [43]. FDS and JASMINE differ in the underlying turbulence model assumed for the smoke flow.

This work will assess the performance of both CFD models to predict entrainment for a selected range of experiments and will provide guidance on appropriate use (e.g. grid resolution). The extensive amount of experimental data from this study will allow scope for more validation in further work.

1.8.5 Transition from a balcony spill plume to axisymmetric (Chapter 9)

All current simple and analytical calculation methods for the 3-D balcony spill plume assume that the mass flow rate of gases increases linearly with height of rise. For tall atrium voids where the design scenario involves a spill plume with a very large height of rise, it has been postulated that entrainment into the free ends of the plume will eventually cause it to behave like an axisymmetric plume [39] (i.e. the mass flow rate will increase according to a power law beyond the transition point). This can potentially lead to unsafe designs if the designer extrapolates the linear relationship between mass flow rate and height of rise beyond the point of transition.

Very limited and differing guidance on the location of the point of transition is given by NFPA 92B [2] and CIBSE [38]. The transition from a 3-D balcony spill plume to axisymmetric has not been rigorously studied and current guidance can only be considered to be an estimate. It is likely that the point of transition will be dependent upon the ratio between the height of rise of the plume and the lateral extent of the plume below the spill edge [39].

This work will examine this possible transition in entrainment behaviour for 3-D balcony spill plumes with large heights of rise. The experimental data will initially be analysed, with numerical modelling being used to extrapolate this analysis to much higher heights of rise than possible experimentally. The analysis will be used to develop improved guidance of the height or transition for design purposes.

1.8.6 Comparison with full scale data (Chapter 10)

This work will provide new data and design guidance obtained from the analysis of $1/10^{th}$ physical scale model experiments and numerical modelling using CFD. Although these analysis methods are well established, it is desirable to compare the new design guidance proposed in this work with any relevant full scale data on spill plumes.

Very limited full scale data is available from published experiments carried out by BRE and International Fire Safety Engineering and Technology S.A. (IFSET), Belgium [53,54]. These data are from "hot smoke tests" to assess the performance of smoke management systems in real buildings by burning fires 'in-situ' from two hot smoke tests will be considered in this work.

It is proposed to assess the relevant design guidance from this work with the data from these hot smoke tests. This will enable an assessment to be made of the general applicability of the guidance to full scale flows.

1.8.7 General

In general, this work aims to provide a better understanding of thermal spill plume entrainment mechanisms to provide improved design guidance for the analysis of the spill plume in smoke management design.

This work will aim to provide options to the designer in the form of a range of robust empirical simple formulae, suggested improvements and modifications to analytical methods and recommendations in the use of numerical modelling using CFD for appropriate design.

Chapter 2

2. Literature Review

This chapter presents various calculation methods which are used to predict entrainment of air into a thermal spill plume. Since the mass flow rate of gases in the spill plume is dependent upon the total amount of entrainment upstream of the design layer height, this chapter describes methods used to calculate the mass flow rate of gases in three regions, namely:

1. from the fire compartment opening.
2. between the fire compartment opening and the spill edge.
3. beyond the spill edge.

Details of previous experimental and computer modelling studies of the spill plume are also presented.

2.1 Mass flow rate from the fire compartment opening

There are various calculation methods available to determine the mass flow rate of gases from a fire compartment opening. These range from analytical methods to more simple engineering relationships which are commonly used in design. This section presents a summary of these methods.

2.1.1 Thomas, Hinkley, Theobald and Simms

Thomas *et al.* [30] developed the following equation to predict the flow of hot gases from a wide fire compartment opening with a deep downstand.

$$\dot{m}_w = \frac{2}{3} C_d \left(2g\theta_{\max,w} T_{amb}\right)^{1/2} \frac{W_o \rho_{amb}}{T_{\max,w}} d_w^{3/2} \qquad \textbf{(2-1)}$$

The approach applied Bernoulli's equation to the gas flow, with the assumption of zero initial velocity for the gases in the fire compartment. Bernoulli's equation was used to obtain an expression for the velocity distribution of the outflow and hence, the mass flow rate from the opening.

The derivation of this equation is not given here, but requires knowledge of the shape of the vertical temperature profile through the out flowing layer. Equation (2-1) was determined by taking into account the shape of the experimental temperature profiles, however, this equation generally holds for profiles which are described by a 'top-hat' function (i.e. a uniform vertical temperature profile). Agreement with experiments was achieved with a value of $C_d = 0.65$.

Similar equations (which are essentially identical to Equation (2-1)] have been developed by Rockett [55], Prahl and Emmons [56], Steckler *et al.* [57] and Quintiere and Denbraven [58], for flows from relatively narrow openings compared to their height (e.g. doorways) with the presence of a downstand at the opening.

2.1.2 Morgan

An alternative equation to calculate the mass flow rate of gases from a compartment opening has been developed by Morgan [51]. This approach is based on the assumption of a virtual 'vena contracta' outside the opening which ignores the upward acceleration of the buoyant gases. Morgan assumed that the gases are not accelerated from rest, but have an established velocity at the opening. He identified that the assumption of a virtual 'vena contracta' implies that the governing variable affecting the flow from the opening is the layer depth (i.e. the smaller dimension of the layer flow). From this, Morgan raised C_d to the same power as the layer depth over which it applies (i.e. to the power of 3/2). Morgan did not make the assumption of a uniform vertical temperature profile in the layer flow, as experiments showed that most layers are neither characterised by a 'top hat' nor a triangular profile, but part way between [51]. To account for the shape of the temperature profile, a correction factor, κ_m, was applied. The Morgan expression is given by Equation (2-2).

$$\dot{m}_w = \frac{2}{3} C_d^{3/2} \left(2g\theta_{\max,w} T_{amb}\right)^{1/2} \frac{W_o \rho_{amb}}{T_{\max,w}} d_w^{3/2} \kappa_m \qquad \textbf{(2-2)}$$

For a uniform temperature profile characterised by a 'top hat' function, $\kappa_m = 1$. For a triangular profile chosen to give the same smoke layer depth and buoyancy at the top of the opening as a 'top hat' function, Morgan determined by integration an expression for κ_m given by Equation (2-3).

$$\kappa_m = \frac{6}{5} \frac{T_{amb}^2}{\theta_{\max,w}^2} - 2 \frac{T_{amb} T_{\max,w}}{\theta_{\max,w}^2} + \frac{4 T_{\max,w}^{5/2}}{5 \theta_{\max,w}^2 T_{amb}^{1/2}} \qquad \textbf{(2-3)}$$

The value of κ_m for a triangular profile is dependent on the gas temperature. Morgan gives the following values: $\kappa_m = 1.51$ for $\theta_{max,w} = 10$ °C; $\kappa_m = 1.58$ for $\theta_{max,w} = 100$ °C and $\kappa_m = 2.16$ for $\theta_{max,w} = 1000$ °C.

For a realistic layer flow a value of κ_m is taken to be half way between $\kappa_m = 1$ and the value of κ_m for a triangular profile for the same $\theta_{max,w}$. Since many smoke flows of practical interest have $\theta_{max,w}$ below 300 °C [51], Morgan suggests a value of $\kappa_m = 1.3$ to be used in Equation (2-2) for design purposes.

Equation (2-2) can be applied to fire compartment geometry with either a downstand or a flat ceiling at the opening. Morgan suggests that for an opening with a downstand $C_d = 0.6$ and for an opening with a flat ceiling $C_d = 1.0$. For the case with a downstand at the opening Equation (2-2) reduces to an expression which is virtually identical to the reduced version of Equation (2-1) by Thomas *et al*. However, for a flat ceiling, the Morgan method predicts approximately 30% more mass flow than the Thomas *et al.* method.

Morgan also developed an expression for the convective heat flow rate in the layer given by Equation (2-4) which uses another, yet similar correction profile, κ_q.

$$\dot{Q}_c = \frac{2}{3} C_d^{3/2} \left(2g\theta_{\max,w} T_{amb}\right)^{1/2} \frac{W_o \rho_{amb}}{T_{\max,w}} d_w^{3/2} c_p \theta_{\max,w} \kappa_q \qquad \textbf{(2-4)}$$

The expression for κ_q for a triangular profile is given by Equation (2-5).

$$\kappa_q = \frac{T_{\max,w}^{5/2} T_{amb}^{1/2}}{\theta_{\max,w}^3} \left(\frac{16}{5} - 6\left(\frac{T_{amb}}{T_{\max,w}} \right)^{1/2} + 4\left(\frac{T_{amb}}{T_{\max,w}} \right)^{3/2} - \frac{6}{5}\left(\frac{T_{amb}}{T_{\max,w}} \right)^{5/2} \right) \quad \textbf{(2-5)}$$

Morgan suggests a value of $\kappa_q = 0.95$ for a layer flow between a 'top hat' function and a triangular profile and should be used in Equation (2-4) for design purposes.

Morgan also provides a relationship between the mass weighted average layer temperature above ambient $\overline{\theta}_w$ with $\theta_{\max,w}$ given by Equation (2-6).

$$\overline{\theta}_w = \frac{k_q}{k_m} \theta_{\max,w} \quad \textbf{(2-6)}$$

Thus, with the suggested values of κ_m and κ_q

$$\overline{\theta}_w = 0.73 \theta_{\max,w} \quad \textbf{(2-7)}$$

2.1.3 Hansell

The calculation methods by Thomas *et al.* [30] and Morgan [51] provide useful expressions to describe the horizontal flow of gases from a compartment opening. However, these methods have limited use in design as they are dependent on variables which may be unknown (e.g. the smoke layer depth and layer temperature). Because of this, more simplified empirical engineering relationships have been developed for design purposes.

A simplified equation [Equation (2-8)] has been developed by Hansell [59] using a method also described by Morgan and Hansell [60]. This equation was derived by combining Equation (2-2) with the 'large fire equation' given by Thomas *et al.* [30] for the mass flow from an axisymmetric plume within a compartment.

$$\dot{m}_w = \frac{C_e p W_o h_o^{3/2}}{\left(W_o^{2/3} + \frac{1}{C_d}\left(\frac{C_e p}{\sigma} \right)^{2/3} \right)^{3/2}} \qquad \textbf{(2-8)}$$

The denominator 'σ' in Equation (2-8) is a result of combining various parameters and has dimension, its value is often taken to be around 2.0. Hansell states a value of σ of 2.0 gives errors in predicted mass of less than 2% for a wide range of gas temperatures, and is deemed sufficiently accurate for design purposes.

Equation (2-8) is dependent upon an empirical entrainment coefficient, C_e, which takes into account various factors affecting entrainment in the fire compartment. C_e is dependent on the compartment geometry, incorporating the effect of possible wall jets, the proximity of walls to the fire, and the plume 'tilt' or 'lean' due to the location of the ventilation opening. These effects were quantified using data from Zukoski *et al.* [61] and Jaluria [29]. Equation (2-8) is also given in design guidance by Morgan *et al.* [12] and BS 7346 [15] which provide the following values of C_e and when it should be applied:

C_e = 0.19 ($kgs^{-1}m^{-5/2}$), for large area rooms such as auditoria, stadia, large open plan offices, atrium buildings, etc, where the ceiling is well above the fire.

C_e = 0.21 ($kgs^{-1}m^{-5/2}$), for large area rooms, such as open plan offices, where the ceiling is close to the fire (defined when the height of rise of the plume in the compartment is less than three times the square root of the floor area).

C_e = 0.34 ($kgs^{-1}m^{-5/2}$) for small rooms such as shop units, cellular offices and hotel bedrooms (prior to flashover). These rooms have a maximum dimension which is less than or equal to five times the diameter of the design fire and the incoming air can only enter from one direction.

For a compartment with a flat ceiling, a value of C_d = 1.0 should be used and for downstand at the opening C_d = 0.65.

2.1.4 CIBSE and BS 7974

CIBSE [38] and BS 7974 [85] provide a relationship to determine the mass flow rate of gases from a compartment opening [Equation (2-9)]. CIBSE state that this equation was developed using analysis of various data collected by Law [63] and data from Hansell *et al.* [32] and reviewed by Thomas [64]. BS 7974 attributes this equation to Thomas [64].

$$\dot{m}_w = 0.09\dot{Q}_c^{1/3} W_o^{2/3} h_o \qquad \textbf{(2-9)}$$

2.2 Mass flow rate between the fire compartment and the spill edge

As described in section 1.7.1.2 the presence of a downstand at a fire compartment opening from which a higher projecting balcony or canopy exists will cause additional entrainment into the smoke flow between the fire compartment and the spill edge. Limited design guidance to take account of this entrainment is described below.

2.2.1 Morgan and Hansell

Morgan and Hansell [60] referenced unpublished work by Marshall, which identified that this additional entrainment, when expressed as a percentage of the mass flow at the compartment opening, varied from 73% (+/- 19%) for a 7 m wide compartment opening to approximately 150% for a 14 m wide opening. This indicated that the amount of entrainment varied with the precise geometry involved. As there was insufficient data to accurately quantify the amount of entrainment for all likely geometries, an entrainment value of 100% was proposed as being representative for most cases. Therefore, for the purposes of engineering design, the mass flow rate of gases below the spill edge was recommended to be twice that at the compartment opening [i.e. see Equation (2-10)]. It was recognised that this assumption was crude and further work was necessary to quantify this entrainment. This advice is currently contained in guidance for smoke management design [12,15].

$$\dot{m}_s = 2\dot{m}_w \qquad \textbf{(2-10)}$$

2.2.2 Hansell

Hansell [32] developed an iterative calculation method to determine the entrainment of air from a compartment opening to a higher projecting balcony or canopy. This method was derived from limited full scale experimental data obtained from fires within a relatively narrow compartment opening (i.e. a maximum of 5 m wide by 3 m high). In all cases, channelling screens were used below the balcony. The Hansell method was including within previous design guidance given by BRE [65].

A subsequent analysis of this method was made by Garrad [66] who carried out fourteen calculations based on fire compartment openings with different widths ranging from 1 to 20 m. The height of the compartment was assumed to be 4 m, and the compartment opening height was assumed to be 3 m for all of the scenarios examined. Garrad showed that the Hansell method was unstable for many different scenarios and convergence to a solution was often not achieved. Convergence was also sensitive to the initial value chosen at the start of the iteration process. Garrad found that convergence to a result was not possible for large openings, although a reasonable result was possible for narrow openings similar to those in which the method was derived. He recommended that until further research was carried out, the guidance given by Equation (2-10) should remain as a conservative estimate of entrainment for design purposes. Following this analysis the Hansell method was removed from the updated design document given by BRE by Morgan *et al.* [12] and therefore the specific details of this method are not repeated here.

2.2.3 Harrison and Spearpoint

Harrison and Spearpoint [34,67] developed an empirical design formula given by Equation (2-11) to describe the under balcony entrainment. The analysis mainly involved the use of FDS (version 3) to simulate these flows for a variety of fire sizes, downstand depths, balcony breadths and compartment opening widths and heights, all modelled on $1/10^{th}$ scale. A limited set of selected experiments to validate the empirical formula were carried out using a $1/10^{th}$ physical scale model. The prediction of entrainment using Equation (2-11) agreed well with the experimental results.

$$\dot{m}_s = 0.89\left(\frac{h_o}{W_o}\right)^{-0.92}\left(\frac{h_b \dot{m}_w}{W_o}\right) \quad \textbf{(2-11)}$$

Equation (2-11) applies to a flow which is channelled and where the width of the compartment opening is the same as the width of the flow at the spill edge. It applies to a wide range of typical compartment opening geometries. Harrison [68] notes that this equation is only loosely dependent on W_o.

As Equation (2-11) is empirical in nature there are constraints on its use given by Equations (2-12) and (2-13).

$$1.16 < \left(\frac{h_o}{W_o}\right)^{-0.92}\left(\frac{h_b}{W_o}\right) < 2.23 \quad \textbf{(2-12)}$$

and,

$$\left(\frac{h_b}{h_o}\right)\left(\frac{b}{h_b - h_o}\right) \geq 2.5 \quad \textbf{(2-13)}$$

Harrison and Spearpoint state that entrainment into these flows is greatest for wide compartment openings with a deep downstand, and that the guidance given by Equation (2-10) is generally conservative.

The use of the term “conservative” in this thesis specifically applies to an over prediction in mass flow rate and that a larger smoke exhaust ventilation will be specified in design than required. It does not apply to toxic gas or temperature prediction.

2.2.4 Regev, Hassid and Poreh

Regev *et al.* [69] present a theoretical analysis of entrainment of air into horizontal smoke flows beyond a downstand by the formation of density jumps. The analysis shows that although the formation and intensity of such jumps are determined by the nature of the upstream flow, which may be characterised by the upstream Froude number. Regev *et al.* state that entrainment due to density jumps can double or even triple the entrainment between the downstand and the spill edge, similar to the crude guidance given by Morgan and Hansell.

2.2.5 Ko, Hadjisophocleous and Lougheed

Ko *et al.* [70] used FDS to develop an expression [Equation (2-14)] to describe the under balcony entrainment which specifically applies to a flow which is channelled by screens. No limits are provided for its use. The analysis simulated flows from a variety of fire sizes and compartment opening widths. A single depth of downstand, breadth of balcony and depth of channelling screen were examined.

$$\dot{m}_s = 1.2\left(\frac{h_b}{h_o}\right)^{0.5} \dot{m}_w \qquad \textbf{(2-14)}$$

Ko *et al.* also examined flows without a downstand or channelling screens below the balcony to provide an alternative simple expression given by Equation (2-15). This expression estimates entrainment dependent upon the specific geometry, with the use of an entrainment coefficient, *a*, with suggested values given in Table 2.1.

$$\dot{m}_s = a\dot{m}_w \qquad \textbf{(2-15)}$$

Scenario	Downstand	Channelling Screens	*a*
1	No	Yes	1.15
2	Yes	Yes	1.6
3	No	No	1.4
4	Yes	No	2

Table 2.1: Values of the entrainment coefficient *a* by Ko *et al.* [70]

For unchannelled flows, Equation (2-15) can only be considered to be an estimate as the width of the modelled balcony was limited and the flow beneath was such that gases were lost from the ends. The mass flow rate of gases lost from the ends of the balcony was estimated to determine values of *a* given in Table 2.1. If the width of the balcony had been increased, the true lateral extent of the flow beneath the balcony and the subsequent effect on entrainment could have been examined. Ko *et al.* report that this loss of gases from the ends of the balcony was also observed in full scale experiments by Lougheed *et al.* [71] which had the same geometry as the modelled compartment.

2.3 Mass flow rate beyond the spill edge

This section presents a summary of both simple and analytical calculation methods to predict entrainment beyond the spill edge and into a resulting spill plume. The available methods for both a balcony and an adhered spill plume are given and the basis behind the derivation of these existing methods is presented and discussed.

2.3.1 Single storey malls

For the specific case of a plume flowing into single storey mall, whose ceiling is not too much taller than the compartment opening onto the mall, the following simplified formula, which is an extension of the 'large fire equation' by Thomas *et al.* [30] is given by Morgan *et al.* [12]. Equation (2-16) is based on previous work by Heselden [72] and is given in earlier guidance by Morgan and Gardner [73].

$$\dot{m}_p = 0.38 p z_s^{3/2} \qquad \textbf{(2-16)}$$

It must be stressed that Equation (2-16) gives an approximate solution and is particularly case specific, as it only applies where z_s is less than 2 m above the top of the shop opening. Where z_s is greater than 2 m, the designer should employ other design methods detailed below.

2.3.2 Simplified design formulae for the balcony spill plume

The majority of simplified spill plume formulae have been developed using the assumption that the plume is generated from a line plume with a virtual source of zero width located below the spill edge (see Figure 2.1). Line plumes are generated from a source which is relatively long and narrow. Most simple formulae make the fundamental assumption of similarity between horizontal cross sectional distributions of velocity and temperature across the plume. These distributions are assumed to be Gaussian in nature. A constant empirical entrainment coefficient is also assumed to apply over the full height of rise of the plume.

This section firstly describes a brief summary of studies of line plume entrainment and then presents various simplified spill plume formulae that have been developed for the balcony spill plume, and are presented chronologically. A comparison of existing simplified formulae with the new experimental data obtained from this study is provided in section 6.6.

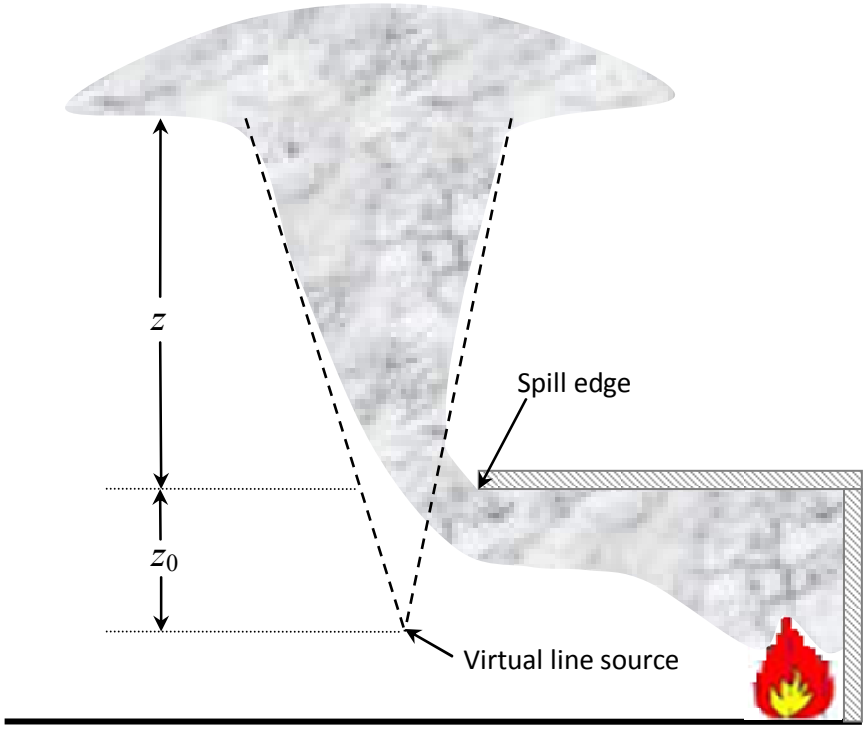

Figure 2.1: A balcony spill plume based on a virtual line source

2.3.2.1 Entrainment of air into a thermal line plume

The behaviour of line plumes was studied both experimentally and theoretically by Lee and Emmons [74]. Plumes were generated experimentally by burning methyl alcohol and acetone fires in a tray which was approximately 2 m long by 13 mm wide. The plumes produced were 2-D in nature, with full height channelling screens being used to prevent entrainment into the ends of the plume. The plumes were characterised by measuring horizontal temperature profiles with respect to height. The theoretical analysis assumed that velocity and temperature profiles across the horizontal cross-section of the plume were Gaussian in nature and self similar (i.e. Gaussian profiles remain Gaussian with height). The theory employs a constant empirical entrainment coefficient, α, over the height of rise of the plume (as per Morton *et al.* [19] for axisymmetric plumes), where entrainment into the plume is proportional to the centreline velocity.

The Lee and Emmons model for the mass flow rate per unit width in the plume is given by Equation (2-17) and assumes that the Boussinesq approximation applies (i.e. the plume temperature and density are both equal to ambient values in the mass and momentum terms, but not in the buoyancy term).

$$\frac{\dot{m}_p}{W} = C_m \left(\frac{\rho_{amb}^2 g \dot{Q}_c}{c_{p,air} W T_{amb}} \right)^{1/3} \left(z + z_0 \right) \qquad \textbf{(2-17)}$$

Where,

$$C_m = \sqrt{\pi} \alpha^{2/3} \left(1 + \lambda^2 \right)^{1/6} \qquad \textbf{(2-18)}$$

Lee and Emmons empirically determined values of the universal constants in Equation (2-17), with $\alpha = 0.16$ and $\lambda = 0.9$, which gives rise to $C_m = 0.58$. The mass flow rate of gases in the plume is given by Equation (2-19).

$$\dot{m}_p = C_m \left(\frac{\rho_{amb}^2 g}{c_{p,air} T_{amb}} \right)^{1/3} \dot{Q}_c^{1/3} W^{2/3} \left(z + z_0 \right) \qquad \textbf{(2-19)}$$

Typical values of $\rho_{amb,}$ g, $c_{p,air}$ and T_{amb} gives a value of $\left(\frac{\rho_{amb}^2 g}{c_{p,air} T_{amb}}\right)^{1/3}$ which is approximately constant at 0.36. Therefore it is convenient and common to see Equation (2-19) in the following form.

$$\dot{m}_p = C\dot{Q}_c^{1/3} W^{2/3} \left(z + z_0\right) \quad \textbf{(2-20)}$$

Where, $C = C_m \left(\frac{\rho_{amb}^2 g}{c_{p,air} T_{amb}}\right)^{1/3}$

Table 2.2 and Table 2.3 show that there is some variation in the proposed values of C_m and α in the literature from more recent line plume studies.

Author	C_m
Yuan and Cox [74]	0.51
Rouse et al [75]	0.57
Chen and Rodi [76] (from Rouse data)	0.48
Zukoski (Yokoi's data) [61]	0.52
Kotsovinos [77]	0.66
Ramparian and Chandrasekhara [78]	0.48

Table 2.2: Values of the dimensionless entrainment coefficient C_m

Author	α
Yuan and Cox [74]	0.126
Rouse et al [75]	0.162
Chen and Rodi [76] (from Rouse data)	0.126
Yokoi [79]	0.125
Kotsovinos [77]	0.20
Ramparian and Chandrasekhara [78]	0.117

Table 2.3: Values of entrainment coefficient α

Poreh *et al.* [31] note that differences in the proposed values of C_m and α depended on whether estimates were based on direct measurements of the mass flow rate, or calculated from velocity and temperature distributions. From the study of 2-D balcony spill plumes, Poreh *et al.* [31] determined the value of $C_m = 0.44$ with $\alpha = 0.11$. This

was lower than the value of $\alpha = 0.16$ proposed by Lee and Emmons [74]. In general, there is increasing evidence to suggest a reduced value of α from that originally proposed by Lee and Emmons.

2.3.2.2 Law

Law [37] developed a simplified spill plume formula by modifying a relationship developed by Yokoi [80] between the maximum gas temperature rise and the total heat release rate of the fire for flows from a window [see Equation (2-21)].

$$\theta_{\max} = \frac{6.89}{\left(z_s + z_0\right)}\left(\frac{\dot{Q}_t}{W_s}\right)^{2/3} \qquad \textbf{(2-21)}$$

Law used data from Morgan and Marshall [35] to correlate the maximum temperature rise in the spill plume, $\theta_{\max,\, p}$ versus $\left(\dot{Q}_t / W_s\right)$ at two specific heights of rise of plume. Law also correlated the maximum temperature rise in the gas layer below the spill edge, $\theta_{\max,\, s}$ versus $\left(\dot{Q}_t / W_s\right)$. These data provided relationships which obeyed a 2/3 power law as proposed by Yokoi. Law used these correlations to estimate the location of the virtual line source below the spill edge (i.e. z_0). When correlating $\theta_{\max,\, p}$ the virtual source was estimated to be a distance of $0.67h_b$ below the spill edge. However, when $\theta_{\max,\, s}$ was correlated the virtual source was estimated to be a distance of $0.5h_b$ below the spill edge.

Law used $\theta_{\max,\, s}$ and the conservation of heat to develop the following relationship for the mass flow rate of gases below the spill edge (i.e. under the balcony), as given by Equation (2-22).

$$\dot{m}_s = 0.025\left(\dot{Q}_t W^2\right)^{1/3} \qquad \textbf{(2-22)}$$

By analogy, Law proposed the following relationship for the mass flow rate of gases in the plume with respect to height above a virtual line source as given by Equation (2-23).

$$\dot{m}_p \propto \left(\dot{Q}_t W_s^2\right)^{1/3} \left(z_s + z_0\right) \quad \textbf{(2-23)}$$

Law then utilised further experimental data from Morgan and Marshall [81] to plot $\dot{m}_p \Big/ \left(\dot{Q}_t W_s^2\right)^{1/3}$ versus z_s. Law also used Equation (2-22) to determine the value of $\dot{m}_p$ when $z_s = 0$ (which was included with the experimental data in the correlation). From this analysis, Law developed a simple formula to determine $\dot{m}_{p,3D}$ for a 3-D balcony spill plume channelled by screens below the balcony, given by Equation (2-24).

$$\dot{m}_{p,3D} = 0.34\left(\dot{Q}_t W_s^2\right)^{1/3} \left(z_s + 0.075\right) \quad \textbf{(2-24)}$$

Law commented that the intercept value of 0.075 was equivalent to $0.15h_b$ which suggested that the virtual source of the plume was only a small distance below the spill edge. Equation (2-24) was therefore generalised, giving Equation (2-25).

$$\dot{m}_{p,3D} = 0.34\left(\dot{Q}_t W_s^2\right)^{1/3} \left(z_s + 0.15h_b\right) \quad \textbf{(2-25)}$$

Law proposed that Equation (2-25) could be used as an alternative to the BRE spill plume method [12] for interim use until further analysis had been carried out. Morgan [82] questioned the use of $\theta_{\max,\, s}$ in the development of Equation (2-25) due to its dependence on the flow behaviour upstream of the measuring region. Morgan commented that this result may not necessarily apply to other geometries. Morgan also stated that the use of Equation (2-22) to determine $\dot{m}_p$ when $z_s = 0$ appeared to be unjustified, and that this particular data point was given much greater weight than the experimental data. Morgan proposed a modified form of the Law correlation [see Equation (2-26)] by only using the experimental data points and applying the effective layer depth correction (see section 2.3.4.1) to adjust the height of rise.

$$\frac{\dot{m}_{p,3D}}{\left(\dot{Q}_t W_s^2\right)^{1/3}} = 0.40\left(h_a - 1.26d_l\right) + 0.061 \quad \textbf{(2-26)}$$

Morgan stated that Equation (2-26) implies that the virtual line source appears to be at a distance $0.3h_b$ below the spill edge. He suggested that Equation (2-26) could possibly be used for design purposes, however, due to the inconsistencies in the location of the virtual line source, the BRE spill plume method was recommended if greater accuracy was required. In response to these comments by Morgan, Law [83] agreed that the correlation given by Equation (2-25) need not necessarily pass through the data point generated from Equation (2-22). However, as the correlation was developed using an empirical approach, Law stated that Equation (2-25) could reasonably be used for design purposes. Law also questioned whether the BRE spill plume method gave greater accuracy due to reservations on the application of the effective layer depth correction.

2.3.2.3 Thomas

Thomas [84] used the experimental data from Morgan and Marshall [35,81] and a relationship by Lee and Emmons [74] describing temperature rise in a line plume with respect to height, to determine the location of the virtual source of a spill plume. This relationship reduced to a form which was virtually identical to that of Yokoi, as used by Law. Analysis of the data showed that the location of the virtual source varied between $0.32h_b$ and $0.66h_b$ depending on the region where the gas temperature was measured (i.e. the approach flow or the plume). Thomas also noted that the location of the virtual source was dependent on the experimental geometry.

Thomas developed a simple spill plume formula to determine $\dot{m}_{p,3D}$ by utilising the Lee and Emmons relationship given by Equation (2-19) and developing an explicit, yet approximate relationship for the entrainment into the free ends of the plume, by matching entrainment between a line plume and an axisymmetric plume at a large height of rise. This term was included into Equation (2-19) to give a simple formula for a 3-D balcony spill plume channelled by screens below the balcony given by Equation (2-27).

$$\dot{m}_{p,3D} = 0.58\left(\frac{\rho_{amb}^2 g}{c_{p,air} T_{amb}}\right)^{1/3} \dot{Q}_c^{1/3} W_s^{2/3} \left(z_s + z_0\right)\left(1 + \frac{0.22\left(z_s + 2z_0\right)}{W_s}\right)^{2/3} \quad \textbf{(2-27)}$$

Using typical values of $\rho_{amb,} g$, $c_{p,air}$ and T_{amb} this equation reduces to Equation (2-28).

$$\dot{m}_{p,3D} = 0.21\dot{Q}_c^{1/3}\left(z_s + z_0\right)\left(W_s + 0.22\left(z_s + 2z_0\right)\right)^{2/3} \quad \textbf{(2-28)}$$

One of the uncertainties in Equation (2-28) is the difficulty in selecting an appropriate location for the virtual origin. Thomas [84] provides a number of alternative locations. Morgan *et al.* [12] suggest that the location of the virtual line source, as explicitly defined by Poreh *et al.* [31] [see Equation (2-37)] could be used as a reasonable approximation. Morgan *et al.* [12] also state that the term which describes entrainment into the free ends of the plume in Equation (2-28) is a speculative correction and should be treated with caution.

2.3.2.4 Law

Law [49] used a similar analysis to that described in section 2.3.2.2 using further experimental data from Hansell *et al.* [32]. This analysis led to a revised formula given by Equation (2-29) which applies for a 3-D balcony spill plume channelled by screens below the balcony.

$$\dot{m}_{p,3D} = 0.31\left(\dot{Q}_t W_s^2\right)^{1/3}\left(z_s + 0.25h_b\right) \quad \textbf{(2-29)}$$

Law also noted that if no channelling screens were present beneath the balcony, the layer flow spread laterally and became diffuse and ill defined. Due to this lateral spread there was additional entrainment into the rising plume compared to a plume channelled by screens.

To take this additional entrainment into account, Law used limited data from Hansell *et al.* [32] to develop an effective width of the unchannelled flow at the spill edge given by Equation (2-30). This effective width can be used in Equation (2-29) to predict $\dot{m}_{p,3D}$ for unchannelled flow. Law states that Equation (2-30) does not represent the actual width of the flow below the spill edge, but it is an effective property which should be specifically used to predict entrainment for unchannelled flow.

$$W_{e,s} = W_o + b \tag{2-30}$$

Therefore, for unchannelled flow, the prediction of $\dot{m}_{p,3D}$ is given by Equation (2-31), which is generally recognised to be an approximate solution to a complex smoke flow.

$$\dot{m}_{p,3D,unchan} = 0.31\left(\dot{Q}_t \left(W_o + b\right)^2\right)^{1/3}\left(z_s + 0.25h_b\right) \tag{2-31}$$

2.3.2.5 CIBSE and BS 7974

A modified version of Equation (2-29) is included within guidance given by CIBSE [38] and BS 7974 [85] but with the use of $\dot{Q}_c$ instead of $\dot{Q}_t$ [see Equation (2-32)]. Equation (2-32) can also be applied for unchannelled flow using the effective width of plume given by Equation (2-30). BS 7974 states that Equation (2-32) is based on relatively few data and is intended for the assessment of smoke mass flow rates only.

$$\dot{m}_{p,3D} = 0.36\left(\dot{Q}_c W_s^2\right)^{1/3}\left(z_s + 0.25h_b\right) \tag{2-32}$$

Equation (2-32) should be applied within the limit given by Equation (2-33).

$$\frac{z}{W} < 5 \tag{2-33}$$

2.3.2.6 Poreh, Morgan, Marshall and Harrison

Poreh *et al.* [31] used dimensional analysis to deduce a relationship between $\dot{m}_p$ and $\dot{Q}_c$ for a line plume. This assumed that the volumetric flux of ambient air into a unit length of the plume in the far field is a function of the buoyant flux per unit length and the distance from the virtual line source. The following relationship to determine $\dot{m}_p$ for a spill plume was developed [see Equation (2-34)] which is virtually identical to the Lee and Emmons line plume relationship given by Equation (2-20).

$$\dot{m}_p = C\dot{Q}_c^{1/3} W_s^{2/3} \left(z_s + z_0 \right) \quad \textbf{(2-34)}$$

Where,

$$C = 0.3 C_m \rho_{amb} \quad \textbf{(2-35)}$$

Poreh *et al.* derived an explicit expression to determine the location of the virtual line source of the spill plume by examining the scenario when the height of rise of layer in the smoke reservoir was the same as the layer base at the spill edge (i.e. $z_s = -d_s$). In this case there is no additional entrainment into the smoke flow beyond the spill edge (i.e. $\dot{m}_p = \dot{m}_s$). Therefore, Poreh *et al.* deduced from Equation (2-34) that,

$$\dot{m}_s = C\dot{Q}_c^{1/3} W_s^{2/3} \left(-d_s + z_0 \right) \quad \textbf{(2-36)}$$

Hence,

$$z_0 = d_s + \frac{\dot{m}_s}{C\dot{Q}_c^{1/3} W_s^{2/3}} \quad \textbf{(2-37)}$$

By substituting Equation (2-37) into Equation (2-34), Poreh *et al.* derived the following simplified formula to determine the mass flow rate of gases due to a spill plume [see Equation (2-38)].

$$\dot{m}_p = C\dot{Q}_c^{1/3} W_s^{2/3} \left(z_s + d_s + \frac{\dot{m}_s}{C\dot{Q}_c^{1/3} W_s^{2/3}} \right) \quad \textbf{(2-38)}$$

To determine the value of C, Poreh *et al.* correlated experimental data produced from four separate experimental studies of 2-D spill plumes described by Marshall and Harrison [48]. The correlation gave rise to C = 0.16, from which C_m = 0.44 [using Equation (2-35)]. This was smaller than proposed values of C_m from various line plume studies given in Table 2.2. Poreh *et al.* deduced that for C_m = 0.44, the

entrainment coefficient α = 0.11, which was lower than the value of α = 0.16 proposed by Lee and Emmons [74]. It is convenient to rearrange Equation (2-38) to express the amount of air entrained into the plume beyond the spill edge (i.e. $\dot{m}_p - \dot{m}_s$), which is given by Equation (2-39). When expressed in this form, this method deals with the entrainment into the rotation region (i.e. $\dot{m}_p - \dot{m}_s$ at z_s = 0) by assuming it is the same as the entrainment into the virtual region of the plume, with the origin located at the base of the layer below the spill edge (i.e. $z_0 = d_s$).

$$\left(\dot{m}_p - \dot{m}_s\right) = C\dot{Q}_c^{1/3} W_s^{2/3} \left(z_s + d_s\right) \quad \textbf{(2-39)}$$

Equation (2-40) gives the Poreh *et al.* simplified formula to predict $\dot{m}_{p,2D}$ specifically for a 2-D balcony spill plume channelled by screens below the balcony. This method is given within guidance on balcony spill plumes in BS 7974 [85].

$$\left(\dot{m}_{p,2D} - \dot{m}_s\right) = 0.16 Q_c^{1/3} W_s^{2/3} \left(z_s + d_s\right) \quad \textbf{(2-40)}$$

As Equation (2-40) applies to 2-D balcony spill plumes, Morgan *et al.* [12] comment that this is likely to severely limit the range of scenarios in which this method can be applied.

2.3.2.7 Thomas, Morgan and Marshall

Thomas *et al.* [39] used a rigorous dimensional analysis in the development of a simplified spill plume formula. This method does not require an explicit term to specify the location of the virtual source, nor does it make the assumption of self-similar flow profiles in terms of temperature and velocity throughout the plume or a constant entrainment coefficient. The dimensional analysis produced the following general formula based on dimensionless variables as given by Equation (2-41), where γ, δ and ε are regression coefficients.

$$\frac{\dot{m}'_p}{\dot{Q}'_c} = \gamma \frac{z_s}{\dot{Q}'^{2/3}_c} + \delta \frac{\dot{m}'_s}{\dot{Q}'_c} + \varepsilon \qquad \textbf{(2-41)}$$

Where,

$$\dot{m}'_p = \frac{\dot{m}_p}{W_s} \qquad \dot{m}'_b = \frac{\dot{m}_s}{W_s} \qquad \dot{Q}'_c = \frac{\dot{Q}_c}{W_s} \qquad \textbf{(2-42)}$$

Thomas *et al.* statistically analysed the experimental data given by Marshall and Harrison [48] as used by Poreh *et al.* [31] to develop the following formula for the 2-D balcony spill plume,

$$\frac{\dot{m}'_{p,2D}}{\dot{Q}'_c} = 0.16 \frac{z_s}{\dot{Q}'^{2/3}_c} + 1.2 \frac{\dot{m}'_s}{\dot{Q}'_c} + 0.0027$$

$$\Rightarrow \dot{m}'_{p,2D} = 0.16 \dot{Q}_c^{1/3} W_s^{2/3} z_s + 1.2 \dot{m}_s + 0.0027 \dot{Q}_c \qquad \textbf{(2-43)}$$

Thomas *et al.* also provided an alternative version of the spill plume formula provided by Poreh *et al.* [31] so that it was in the same form as Equation (2-43) . To achieve this, the following empirical relationship to describe d_s was derived, using the data given by Poreh *et al.* and the method by Morgan [51] to predict the mass flow rate of gases from a fire compartment opening.

$$\frac{d_s \left(\frac{\dot{Q}_c}{W_s} \right)}{\left(\frac{\dot{m}_s}{W_s} \right)} = 2.5 \left(1 + \frac{\dot{Q}_c}{c_{p,air} T_{amb} \dot{m}_s} \right) \qquad \textbf{(2-44)}$$

Thomas then substituted Equation (2-44) into Equation (2-40) to remove an element of redundancy requiring the calculation of both $\dot{m}_s$ and d_s. This then gave Equation (2-45) which Thomas states as being an acceptable alternative to Equation (2-40). This form of the Thomas method is given within the guidance for 2-D balcony spill plumes in BS 7974 [85].

$$\frac{\dot{m}'_{p,2D}}{\dot{Q}'_c} = 0.16\frac{z_s}{\dot{Q}'^{2/3}_c} + 1.4\frac{\dot{m}'_s}{\dot{Q}'_c} + 0.0014$$

$$\Rightarrow \dot{m}'_{p,2D} = 0.16\dot{Q}_c^{1/3}W_s^{2/3}z_s + 1.4\dot{m}_s + 0.0014\dot{Q}_c \quad \textbf{(2-45)}$$

Thomas *et al.* also analysed the experimental data from Hansell *et al.* [32] for the 3-D balcony spill plume to give,

$$\frac{\dot{m}'_{p,3D}}{\dot{Q}'_c} = 0.34\frac{z_s}{\dot{Q}'^{2/3}_c} + 2.64\frac{\dot{m}'_s}{\dot{Q}'_c} - 0.0083$$

$$\Rightarrow \dot{m}'_{p,3D} = 0.34\dot{Q}_c^{1/3}W_s^{2/3}z_s + 2.64\dot{m}_s - 0.0083\dot{Q}_c \quad \textbf{(2-46)}$$

With the limit,

$$\frac{z_s}{W_s} < 3 \quad \textbf{(2-47)}$$

Equation (2-46) has an entrainment coefficient (i.e. the value of γ) of 0.34 which is similar to that of Law [i.e. the 0.31 in Equation (2-29)] and CIBSE [i.e. the 0.36 in Equation (2-32)] when correlating the same experimental data by Hansell *et al.*

Thomas also proposed an alternative expression to describe the total amount of entrainment into the free ends of a 3-D balcony spill plume using the data from Hansell *et al.* given by,

$$\dot{m}_{ends} = 0.09z_s\left(\frac{\dot{Q}_c}{W_s}\right)^{1/3} \quad \textbf{(2-48)}$$

Thomas *et al.* state that Equation (2-48) should be treated with caution as it applies when values of z_s/W_s are 'not too large' and the limit of this criterion remains unknown until further data is available.

2.3.2.8 Harrison and Spearpoint

Harrison and Spearpoint [40,67] carried out a series of experiments using a 1/10th physical scale model to provide new data describing entrainment into a 3-D balcony spill plume channelled by screens below the balcony. The experiments examined the scenario of both a flat ceiling and a downstand at the spill edge and are described in more detail in section 2.4.6.

Harrison and Spearpoint determined the following simplified formula to predict $\dot{m}_{p,3D}$ using the method by Poreh *et al.* [31] described in section 2.3.2.6.

$$\dot{m}_{p,3D} = 0.20\dot{Q}_c^{1/3} W_s^{2/3} \left(z_s + d_s\right) + \dot{m}_s \qquad \textbf{(2-49)}$$

Harrison and Spearpoint [86] statistically analysed the data using the dimensional analysis by Thomas *et al.* [Equation (2-41)] which gives an alternative design formula given by Equation (2-50).

$$\frac{\dot{m}'_{p,3D}}{\dot{Q}'_c} = 0.22\frac{z_s}{\dot{Q}'^{2/3}_c} + 1.92\frac{\dot{m}'_s}{\dot{Q}'_c} - 0.0042$$

$$\Rightarrow \dot{m}'_{p,3D} = 0.22\dot{Q}_c^{1/3} W_s^{2/3} z_s + 1.92\dot{m}_s - 0.0042\dot{Q}_c \qquad \textbf{(2-50)}$$

These formulae apply to a flow with either a flat ceiling or a downstand at the spill edge and should be applied within the limit given by Equation (2-51).

$$\frac{z_s}{W_s} < 2 \qquad \textbf{(2-51)}$$

The values of the dominant entrainments coefficient from the Harrison and Spearpoint data (i.e. the 0.20 and 0.22) are significantly lower than the values obtained from correlating the Hansell *et al.* data (i.e. 0.31 to 0.36) for the 3-D balcony spill plume. This has given rise to further uncertainty in the prediction of entrainment for this scenario.

2.3.2.9 Valkist

Valkist [87] used numerical modelling to develop simple formulae for 3-D balcony spill plumes channelled by screens from wide compartment openings (i.e. greater than 7 m in width). These formulae were determined using data obtained from fourteen simulations using FDS (see section 2.5.8). Valkist used the predictions of $\dot{m}_{p,3D}$ to determine values of regression coefficients in the form given by Equation (2-52).

$$\dot{m}_{p,3D} = B\dot{Q}_c^{1/3} W_s^i z_s + \dot{m}_{p,z_s=0} \qquad \textbf{(2-52)}$$

Equation (2-52) is of a similar form to the majority of spill plume models, but with the use of $\dot{m}_{p,z_s=0}$ (i.e. the value of $\dot{m}_p$ at $z_s = 0$) to describe the entrainment below the balcony without resorting to the assumption of a virtual line source. Correlating the data gave rise to Equation (2-53) which Valkist states as being a simple method to predict $\dot{m}_{p,3D}$.

$$\dot{m}_{p,3D} = 0.1936\dot{Q}_c^{1/3} W_s^{0.6174} z_s + \dot{m}_{p,z_s=0} \qquad \textbf{(2-53)}$$

The values of the regression coefficients are stated to an accuracy of four decimal places, as given by Valkist, although this is probably unjustified considering the uncertainty in the prediction of $\dot{m}_{p,3D}$ from fourteen simulations. Equation (2-53) gives a similar result to the formulae produced by Harrison and Spearpoint given in section 2.3.2.8.

Valkist also provides a modified method, similar to Equation (2-53), but with the use of an additional term to take into account the aspect ratio of the layer flow below the spill edge given by Equation (2-54).

$$\dot{m}_{p,3D} = B\dot{Q}_c^{1/3} W_s^i \left(\frac{d_s}{W_s}\right)^j z_s + \dot{m}_{p,z_s=0} \qquad \textbf{(2-54)}$$

Correlating the data according to Equation (2-54) gave rise to the values of regression coefficients given in Equation (2-55).

$$\dot{m}_{p,3D} = 0.1060\dot{Q}_c^{1/3} W_s^{1.2523} \left(\frac{d_s}{W_s}\right)^{0.4151} z_s + \dot{m}_{p,z_s=0} \quad \textbf{(2-55)}$$

Valkist states that the modified method given by Equation (2-55) should be used in preference to the simple method given by Equation (2-53).

The above equations require the user to determine $\dot{m}_{p,z_s=0}$. Valkist provides a general expression to determine this given by Equation (2-56).

$$\dot{m}_{p,z_s=0} = B\dot{Q}_c^{1/3} W_s^{\,i} d_s^{\,j} \dot{m}_s^{\,n} \quad \textbf{(2-56)}$$

Correlating the data according to Equation (2-56) gave rise to the values of regression coefficients given in Equation (2-57) .

$$\dot{m}_{p,z_s=0} = 2.2628\dot{Q}_c^{1/3} W_s^{0.4923} d_s^{0.2426} \dot{m}_s^{0.5780} \quad \textbf{(2-57)}$$

2.3.2.10 NFPA 92B

Guidance on balcony spill plume entrainment in NFPA 92B [2] has recently been updated following full scale experiments and numerical modelling carried out by Lougheed *et al.* [71] of the National Research Council (NRC), Canada.

The guidance is dependent upon z_s and W_s and is as follows:

For a 3-D balcony spill plume with $z_s < 15$ m,

$$\dot{m}_{p,3D} = 0.36\dot{Q}_t^{1/3} W_s^{2/3} \left(z_s + 0.25h_b\right) \quad \textbf{(2-58)}$$

For a 3-D balcony spill plume where $z_s \geq 15$ m and $W_s < 10$ m,

$$\dot{m}_{p,3D} = 0.59\dot{Q}_c^{1/3} W_s^{1/5} \left(z_s + 0.17 W_s^{7/15} h_b + 10.35 W_s^{7/15} - 15 \right) \quad \textbf{(2-59)}$$

For a balcony spill plume where $z_s \geq 15$ m and $10 \text{ m} \leq W_s \leq 14$ m,

$$\dot{m}_{p,3D} = 0.2\dot{Q}_c^{1/3} W_s^{2/3} \left(z_s + 0.51 h_b + 15.75 \right) \quad \textbf{(2-60)}$$

Equation (2-58) is identical to the guidance in the 2005 version of NFPA 92B [88], with the exception that there is now a limit on its use (i.e. $z_s < 15$ m). Equation (2-58) is almost identical to the guidance given by CIBSE [Equation (2-32)], but with the use of $\dot{Q}_t$ in Equation (2-58) instead of $\dot{Q}_c$ in Equation (2-32). Equation (2-58) can be described in terms of $\dot{Q}_c$ and is given by Equation (2-61) [71].

$$\dot{m}_{p,3D} = 0.41\dot{Q}_c^{1/3} W_s^{2/3} \left(z_s + 0.25 h_b \right) \quad \textbf{(2-61)}$$

NFPA 92B states that the NRC experiments show that Equation (2-58) provides reasonable but conservative estimates for values of z_s below 15 m. This statement appears hard to justify as the ceiling height of the experimental atrium was 12.2 m and the height of the balcony was 5 m. Therefore, the height the atrium ceiling above the spill edge was approximately 7 m, with z_s generally ranging from 2 to 4 m in the experiments due to the limited smoke exhaust capacity of the experimental facility.

The NRC experimental results are anomalously high compared with measured entrainment from previous experimental studies, and they do not appear to support the statement that Equation (2-58) is conservative (see section 2.4.7). This anomalously high entrainment is partially attributed to recirculation of the ceiling jet flow in the atrium space, as was also reported in one set of experiments by Marshall and Harrison [48] using a small collecting hood (see section 2.4.4.1).

However, the NRC results still produce significantly higher entrainment than the Marshall and Harrison 'small hood' experiments. Lougheed *et al.* [71] also attribute this additional entrainment to the trajectory of the plume in the near field, which is contrary to the findings reported by Harrison and Spearpoint [40] from small scale experiments. Lougheed *et al.* state that there are a number of factors that contributed to variation and uncertainty in the results. These uncertainties are further discussed in section 2.4.7, which describes the experiments in more detail.

For z_s above 15 m, Equations (2-59) and (2-60) predict a lower rate of entrainment with respect to height of rise compared to predictions using Equation (2-58) for z_s below 15 m. The justification for a reduced rate of entrainment for z_s above 15 m is unclear in the report by Lougheed *et al.* [71]. However, Lougheed [89] states that this height was chosen as a conservative estimate of the point of intersection between the simplified spill plume formula by Law [49] [Equation (2-29)] and a line plume entrainment approximation. This analysis makes the assumption that the entrainment behaviour of the 3-D spill plume approaches that of a line plume at a height when the plume rises vertically into the atrium void, thus giving rise to a reduction in the rate of entrainment. However, this assumption neglects the effect of entrainment into the free ends of the plume on the overall entrainment behaviour and is not supported by the numerical modelling predictions by Lougheed *et al.* [71] which show that the rate of entrainment was constant (both below and above a height of 15 m) for z_s up to 50 m (see section 2.5.9).

Equations (2-59) and (2-60) were derived by adjusting the term describing the virtual source so that they matched the prediction of entrainment using Equation (2-58) at a height of 15 m. It is interesting to note that the location of the virtual source is dependent on h_b in Equations (2-58) and (2-60), yet it is dependent on both h_b and W_s in Equation (2-59). It is unclear why there is inconsistency in the terms to describe the location of the virtual source between these equations.

NFPA 92B states that a design based on Equations (2-59) and (2-60) (i.e. z_s > 15 m) should be compared with predictions for an axisymmetric plume scenario and the higher mass flow rate used for the design of the atrium smoke management system. It is also recommended that this scenario is supported by a CFD modelling study.

NFPA 92B states that the NRC experiments demonstrate that the above equations can be applied for unchannelled flows for compartment opening widths between 5 m and 14 m using the effective lateral extent of the flow given by Equation (2-30). This statement should be treated with caution as Ko *et al.* [70] report that mass loss was observed from the ends of the balcony in the NRC experiments, therefore it was not possible to examine the true lateral extent of the unchannelled flow and plume.

2.3.3 Simplified design formulae for the adhered spill plume

There is limited experimental data on entrainment into adhered plumes with a single simplified formula developed by Poreh *et al.* [50] for the 2-D adhered plume. There are no robust simplified formulae to predict entrainment for the 3-D adhered plume, however, CIBSE [38] give a formula to provide an approximate solution for this scenario. These formulae are described below. A comparison of these formulae with the new experimental data obtained from this study is provided in sections 7.2.3 and 7.3.4.

2.3.3.1 Poreh, Marshall and Regev

Poreh *et al.* [50] give a simplified formula for a 2-D adhered spill plume based on limited experimental data obtained by Marshall [90]. Poreh *et al.* correlated the data using the method described in section 2.3.2.6 to determine the value of the entrainment constant, C. Equation (2-62) shows the Poreh *et al.* formula, which gives a value of $C = 0.075$.

$$\dot{m}_{p,2D} = 0.075 Q_c^{1/3} W_s^{2/3} \left(z_s + d_s\right) + \dot{m}_s \qquad \textbf{(2-62)}$$

It is interesting to note that the value of *C* is approximately half that of a 2-D balcony spill plume (i.e. 0.16). This is not surprising considering that entrainment only occurs into one side of an adhered plume, compared to two sides in a balcony spill plume.

2.3.3.2 CIBSE

CIBSE [38] provides a formula to determine the mass flow rate of a spill plume above a compartment opening without a balcony [see Equation (2-63)]. CIBSE states that this equation can be used whether or not there is a wall above the opening, so therefore can apply to the adhered plume scenario.

$$\dot{m}_{p,3D} = 0.23 Q_c^{1/3} W_s^{2/3} \left(z_s + h_o \right) \quad \textbf{(2-63)}$$

Equation (2-63) was derived using the adhered plume experimental data from Hansell *et al.* [32] which was subsequently increased by 50%, and data from Porter [91] from post-flashover fires. It is unclear why the Hansell *et al.* data was increased by 50% (presumably to be conservative), nor is the derivation of this formula published elsewhere.

2.3.4 Analytical methods

The BRE spill plume method is the only analytical method that has been used for design purposes over the past 30 years. However, as this method is rather complex it has not been as widely used as simplified spill plume formulae for design. An alternative, yet still complex method has recently been developed by Kumar *et al.* [41] of BRE, which differs from the original BRE method in the underlying physics. The Kumar *et al.* method is known as "the curved plume method" and currently only applies to 2-D balcony spill plumes. The basis behind each of these analytical methods is described below.

2.3.4.1 The BRE spill plume method

Morgan and Marshall [35,81] first developed the BRE spill plume method. Modifications have subsequently been made to extend the method, such that it deals with both 2-D and 3-D spill plumes, balcony and adhered, and can take into account the presence of a downstand at the fire compartment opening. However, not all aspects of this method have been validated experimentally. The BRE spill plume method was first developed from a series of $1/10^{th}$ physical scale model experiments (see section 2.4.1). This method is complicated and the calculation procedure is not fully reproduced herein. For full details of the calculation procedure, reference should be made to the original paper by Morgan and Marshall [35] and the current design document detailing a user guide to this calculation method [12]. A summary of the key features of the method and some of the fundamental assumptions are described below. The calculation method deals with the spill plume in four discrete regions:

1. The horizontally flowing buoyant layer of smoky gases below the spill edge.
2. The rotation region, as the horizontally moving layer rotates around the spill edge (i.e. as the gases change from a horizontally to a vertically moving flow).
3. The vertically moving smoke flow in the form of a 2-D line plume.
4. Entrainment of air into the free ends of the line plume.

The method applies to an approach flow of a horizontally flowing thermal buoyant layer toward an opening, through which the gases then rise at the spill edge. The following assumptions are made for the approach flow [12].

- The flow is from beneath a flat ceiling (or a downstand) at the spill edge.
- The flow is channelled by walls or channelling screens.
- The flow has flow-lines which are everywhere parallel and which approach the spill edge at a right angle.
- The approach flow is assumed to be fully turbulent.
- There is no immersed ceiling jet.
- The velocity of the clear air below the smoke layer has a value smaller than that of the layer itself.

At least two key parameters of the approach flow below the spill edge must initially be determined, such as the following combinations:

- Mass flow rate and convective heat flow rate.
- Mass flow rate and mean layer temperature.
- Mass flow rate and ceiling temperature.
- Convective heat flow rate and mean layer temperature.
- Convective heat flow rate and layer temperature at its highest point.
- Convective heat flow rate and layer depth.
- Layer depth and mean layer temperature.
- Layer depth and layer temperature at its highest point.

If there is additional entrainment between a compartment opening and the spill edge (e.g. due to the presence of a downstand prior to the spill edge), this must be taken into account using the guidance in section 2.2 when specifying the key parameters of the flow below the spill edge.

The method then calculates the required remaining approach flow parameters below the spill edge using the theory by Morgan [51] to describe the horizontal flow of gases toward an opening (see section 2.1.2). Therefore, the mass flow rate of gases below the spill edge can be determined using Equation (2-64) .

$$\dot{m}_s = \frac{2}{3} C_d^{3/2} \left(2g\theta_{\max,s} T_{amb}\right)^{1/2} \frac{W_s \rho_{amb}}{T_{\max,s}} d_s^{3/2} \kappa_m \qquad \textbf{(2-64)}$$

The amount of air entrainment into the gases which rotate around the spill edge are then determined using Equation (2-65).

$$\dot{m}_{rot} = \frac{2}{3} \rho_{amb} W_s \alpha' \left(\frac{2g\theta_{\max,s}}{T_{amb}} \right)^{1/2} d_s^{3/2} \qquad \textbf{(2-65)}$$

Morgan and Hansell [60] empirically derived the entrainment constant (i.e. α') in the rotation region to be 1.1, updating the original value of 0.9 found by Morgan and Marshall [35]. Morgan and Hansell recognised that this high value for α' infers an anomalously large amount of entrainment into the rotating flow of gases at the spill edge. This large value of α' is a result of treating all anomalous entrainment above the spill edge as if it occurred in the rotation region [12]. This aspect of the BRE spill plume method has led to some controversy and debate. Subsequent work by Miles *et al.* [44] and Yii [92] indicate only a small degree of entrainment into the rotation region. However, the BRE spill plume method is recognised to be empirical in nature, with the overall calculation package adjusted to provide good agreement with experimental results [60].

Combining Equations (2-64) and (2-65) and provides the mass flow rate of gases rising in a vertical flow at the spill edge (i.e. the value of $\dot{m}_p$ at $z_s = 0$) and is given by Equation (2-66). This is used in the subsequent analysis of entrainment of air into the vertically rising plume.

$$\dot{m}_{p,z_s=0} = \dot{m}_{rot} + \dot{m}_s \qquad \textbf{(2-66)}$$

Morgan and Marshall utilised the theory of Lee and Emmons [74] in the calculation of a virtual 'Equivalent Gaussian Source' (EGS) in the horizontal plane. The EGS provides the source of the vertically rising thermal plume at the spill edge. This plume is a 2-D line plume rising from a 'retarded source' [35, 74]. Morgan and Marshall modified the Lee and Emmons approach to determine the source parameters of the EGS from the characteristics of the vertical flow at the spill edge (i.e. at $z_s = 0$). They also used the Lee and Emmons approach in the subsequent analysis of entrainment into the rising plume. This incorporated the use of the entrainment constant, α, empirically determined by Lee and Emmons to have a value of 0.16. For a particular height of rise above the spill edge, this method then allows the mass flow rate of gases to be determined ignoring any entrainment of air into the ends of the plume. This method makes the fundamental assumption that the entrainment coefficient is constant, and profiles of velocity and temperature across the plume are Gaussian throughout.

Morgan and Marshall [81] provide an updated expression to determine entrainment of air into the ends of the plume, which is based on the simplified assumption that the ends of the plume are rectangular in shape, rather than conical, as assumed in the original derivation. The expression for end entrainment also utilises the entrainment constant, α, with a value of 0.16.

The methods for calculating the EGS, the entrainment of air into the rising plume and into the ends of the plume are given in the user guide [12]. The total mass flow rate of gases of the spill plume, at a particular height of rise, is the sum of the entrainment into the plume and the entrainment into the ends.

The user guide [12] also provides details of a calculation procedure for adhered spill plumes which requires an entrainment constant, α, of 0.077, as determined from experiments of adhered spill plumes by Hansell *et al.* [32], assuming that horizontal profiles of temperature and velocity across the plume are half Gaussian. This value of α is close to that determined by Grella and Faeth [93] in a more fundamental study of adhered line plumes. They found that adhered line plumes are not truly half Gaussian in nature, resulting in a value of α of 0.068.

Experiments by Hansell *et al.* [32] suggest that the BRE method should not be used for approach flow temperatures in excess of approximately 350 °C. At present, accurate calculation methods for high temperature flows do not exist.

Morgan and Marshall found that the BRE method over predicted entrainment in a series of scale model experiments which simulated a two-storey shopping mall [81]. They attributed the poor agreement between the prediction and the experiment due to a violation of one of the assumptions of the Lee and Emmons line plume theory, namely that the ambient air through which the plume rises was not at a uniform ambient temperature. Experimental studies [32,81] have shown that this fundamental assumption can be violated depending upon the geometry of the smoke reservoir and the smoke layer depth. To take this possible effect into account, Morgan *et al.* [12] provide an empirical correction, called ‘the effective layer depth correction’ when using the BRE spill plume method.

This correction reduces the design height of rise of plume above the spill edge (i.e. z_s). The reduced value is taken to be the design value minus 26% of the design layer depth. If the reduced clear height is less than 0.75 m, then the correction should be ignored. Morgan *et al.* [12] give classification criteria between 'large' and 'small' area smoke reservoirs to determine when this correction should be applied. The correction is required for 'large' area smoke reservoirs, namely when the design smoke layer depth is less than two-thirds of the characteristic width of the smoke reservoir (i.e. the square root of the cross-sectional area of the smoke reservoir). Where the design smoke layer depth is greater than two-thirds of the characteristic width of the smoke reservoir, the reservoir can be classed as 'small' and no correction applies.

When using the BRE spill plume method, it is crucial that the designer identifies whether the effective layer depth correction applies to the particular design in question. Harrison and Spearpoint [40] found that the use of the effective layer depth correction did not always provide good agreement with their experimental results. They suggest that this correction may not be reliable when applied to scenarios dissimilar to that from which it was derived. Harrison and Spearpoint also state that the classification criteria between 'large' and 'small' area smoke reservoirs may not be reliable for all scenarios and should be used with caution.

There has been some criticism of the BRE spill plume method, with Thomas [46] expressing his concerns in an open letter to the Fire Engineers Journal in the UK. Thomas states that his criticism is based on elementary fluid mechanics rather than safety or cost, with the main issue being the procedure to determine the characteristics of the EGS. Thomas states that there is an error in the physics which assumes that the potential energy of the flow beneath the balcony is equated to the kinetic energy at the EGS to a vertical flow, with the associated error being that all the energy at the EGS refers to vertical motion. In reality, the horizontal momentum is not completely lost and consequently the rising plume never becomes truly vertical. Thomas states that the use of an energy balance, instead of a momentum balance, is wrong in principle where there are changes in the degree of turbulence over a distance. Thomas states that these errors do not affect the safety or the cost of the design using the BRE method because the theory has been adjusted to fit the experimental results.

Morgan [94] provides a response to this letter in which he states that he was not in dispute with Thomas as to the role of kinetic energy and momentum for the flow at and around the spill edge to determine the characteristics of the EGS. However, he states that the flow in the rotation region is characterised by a simplified approximation [i.e. Equation (2-65)] employing an empirical entrainment constant. It was explicitly stated in the method that the sole justification of this approach was that the overall package was adjusted so that the prediction matched the experiment, as recognised by Thomas in his letter. Morgan states that it is acceptable to use empirical relationships within the limits which are themselves established empirically, even in the absence of theory, and that this justified the continued use of the BRE method.

2.3.4.2 The curved plume method

Kumar *et al.* [41] have developed 'the curved plume method' for calculating entrainment into a 2-D balcony spill plume. This method provides an alternative to the BRE method for the 2-D plume. It builds on the 2-D 'strong' plume analysis of Thomas [95] and Thomas and Delichatsios [96] and therefore incorporates density variations in the plume. It applies the conservation of momentum in the plume from the horizontal flow of gases below the spill edge.

Figure 2.2 shows a schematic drawing of a 2-D balcony spill plume emerging from underneath a balcony as given by Kumar *et al.* [41]. The entrainment into both the upper and lower sides of the plume is assumed to be constant and a 'top hat' profile (or step function) assumed. $\dot{M}'_p$, ρ, u, w and D represent the momentum per unit width, the density, the horizontal and vertical components of velocity and the cross-stream dimension of the plume respectively. $\dot{M}'_s$, ρ_s, u_s and D_s represent respectively initial momentum, density, velocity and depth of the layer at the spill edge, and ds represents the incremental distance along the axis (trajectory) of the spill plume and ϕ represents its angle of rotation from the horizontal. The terms used in this section are consistent with those given by Kumar *et al.* [41] and are separate from the nomenclature given in this thesis.

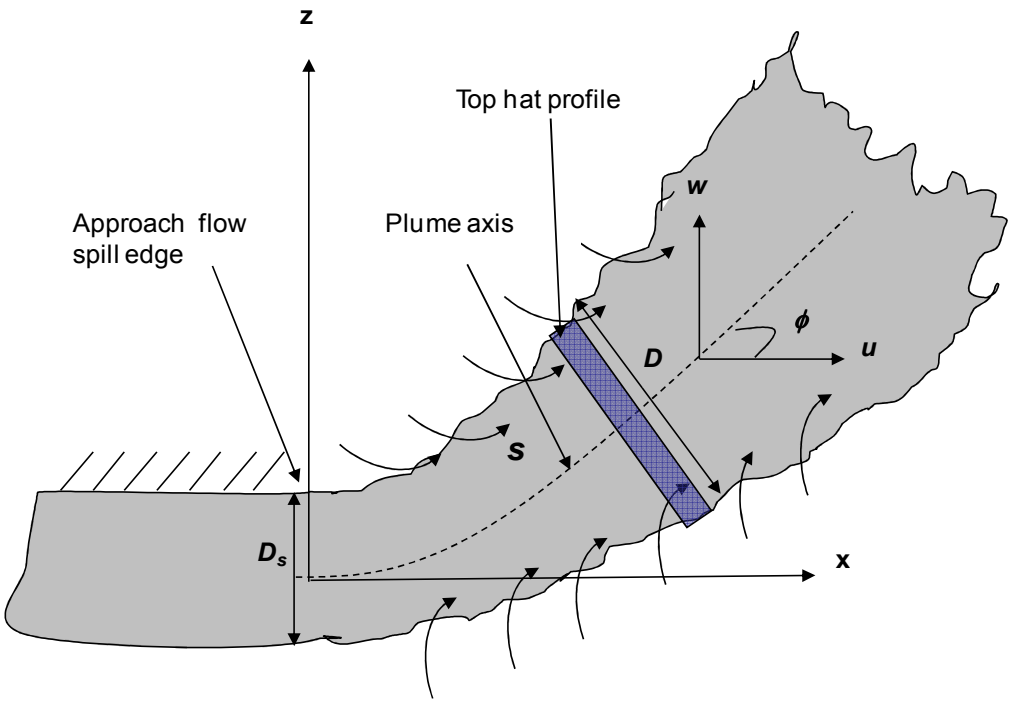

Figure 2.2: Schematic of smoke flowing below a horizontal ceiling into a void [41]

The mass flow rate per unit width and momentum per unit width are given by Equations (2-67) and (2-68).

$$\dot{m}'_p = \rho D\left(u^2 + w^2\right)^{1/2} \quad \textbf{(2-67)}$$

$$\dot{M}'_p = \rho D\left(u^2 + w^2\right) \quad \textbf{(2-68)}$$

The entrainment rate into the spill plume is defined by top hat profile approximation is given by,

$$\frac{d\dot{m}'_p}{ds} = 2\rho_{amb} ED\left(u^2 + w^2\right)^{1/2} \quad \textbf{(2-69)}$$

Where ρ_{amb} is the ambient density and E is the top hat entrainment coefficient which is the same on both upper and lower sides of the plume.

Thomas and Delichatsios [96] have shown that E is $\sqrt{2}\alpha$, where α is the Gaussian entrainment coefficient, which Kumar *et al.* took to be 0.11 from Poreh *et al.* [31]. The continued mathematical derivation of the curved plume method is particularly complex and is not repeated herein. For further details of this derivation, reference should be made to the original paper by Kumar *et al.* [41]. The derivation provides a generalised solution for the balcony spill plume between mass flow rate per unit width and momentum per unit width given by Equation (2-70).

$$\beta\left(\dot{m}'^{3} - \dot{m}_s'^{3}\right) = \dot{M}_p'^{3}\left(1 - \frac{\dot{M}_s'^{2}}{\dot{M}_p'^{2}}\right)\left(1 + \frac{2\dot{M}_s'^{2}}{\dot{M}_p'^{2}}\right) \qquad \textbf{(2-70)}$$

Where,

$$\beta = \frac{g\dot{Q}_c'}{2E\rho_{amb}c_{p,air}T_{amb}} \qquad \textbf{(2-71)}$$

The derivation also provides expressions to describe the plume trajectory given by Equations (2-72) and (2-73).

$$z = \frac{1}{2E\rho_{amb}\beta}\int_{\dot{M}_s'}^{\dot{M}_P'} \frac{\dot{M}_p' d\dot{M}_p'}{\dot{m}_p'} \qquad \textbf{(2-72)}$$

$$x = \frac{\dot{M}_s'}{2E\rho_{amb}\beta}\int_{\dot{M}_s'}^{\dot{M}_P'} \frac{d\dot{M}_p'}{\dot{m}_p'\left(1 - \dot{M}_s'^{2}/\dot{M}_p'^{2}\right)^{1/2}} \qquad \textbf{(2-73)}$$

Kumar *et al.* also express Equations (2-71) to (2-73) in non-dimensional form. These equations can be used simultaneously to achieve a solution, by providing input values of the approach flow below the spill edge and a range of trial values of the mass flow rate of gases in the plume. These calculations require the method to be programmed into a computer to achieve solution by integration.

2.4 Experimental studies of the spill plume

There have been a number of experimental studies of the thermal spill plume. This section gives an overview of relevant studies and their findings, which are presented chronologically.

2.4.1 Morgan and Marshall

Morgan and Marshall [35] conducted a series of 1/10th scale model experiments according to the scaling principles set out by Thomas *et al.* [30]. The model simulated smoke flow from a shop unit in the form of a balcony spill plume. Flows from two fire compartments were examined with opening widths of 0.7 and 1.4 m respectively (see Figure 2.3). The fire compartments were each 0.5 m deep by 0.5 m high, with a 0.16 m deep downstand located at the opening for selected tests. A balcony (0.4 m in breadth) extended across the fire compartment opening. Channelling screens were located beneath the balcony, in line with the compartment opening, to prevent lateral spread and to achieve a more uniform flow across the spill edge.

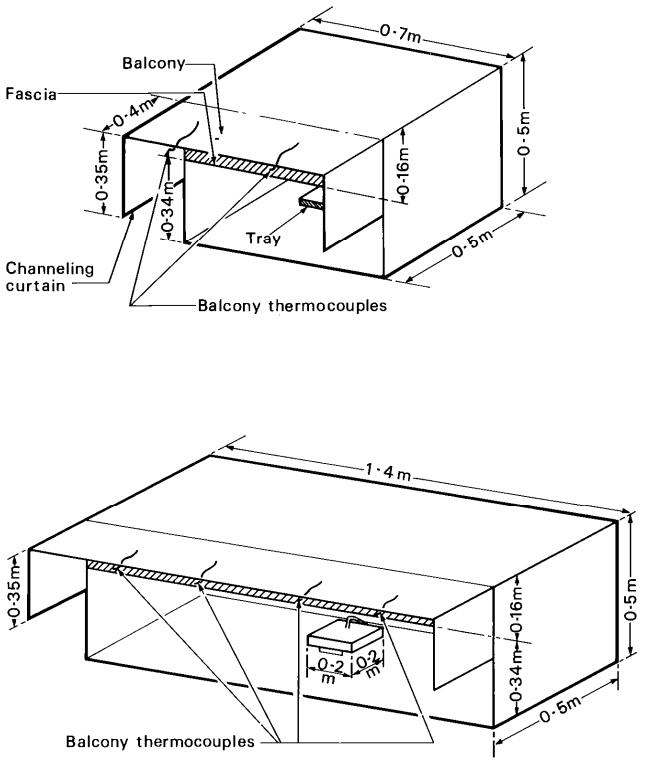

Figure 2.3: The scale model used by Morgan and Marshall [35]

The hot gases were produced by burning Industrial Methylated Spirits (IMS) at a controlled and measured rate into a tray. The emerging balcony spill plume was allowed to freely flow into the laboratory. Measurements of gas temperatures were made 10 mm below the spill edge. A horizontal array of thermocouples was located above the spill edge to determine the maximum axial plume temperature. This array was generally located 0.31 m above the spill edge, however, for some experiments the array was located at a height of 0.40 m. The experimental results were used in the development of the BRE spill plume method (see section 2.3.4.1). Morgan and Marshall empirically determined the entrainment coefficient α' to be 0.90 from these experiments. Good agreement was obtained between the experiment (based on the temperature measurements) and the prediction using the BRE spill plume method. Morgan and Marshall noted that much larger smoke exhaust rates were required for safe means of escape than had previously been thought. To limit the required smoke exhaust capacity, Morgan and Marshall recommended the use of channelling screens to prevent lateral spread.

2.4.2 Morgan and Marshall

Morgan and Marshall [81] conducted another series of $1/10^{th}$ physical scale model experiments which simulated smoke flow from a shop unit into a two storey mall (see Figure 2.4). The majority of the experiments examined a shop with a width of 0.7 m. Four circular exhaust vents were located in the ceiling of the mall. These outlets were connected to an axial fan which provided mechanical exhaust. The model had an array of inlet vents which could be individually closed. The hot gases were produced from a series of convector heaters. This produced a balcony spill plume from the shop unit. The mass flow rate of gases in the mall was measured directly using a carbon dioxide tracer gas technique. Columns of thermocouples were located at strategic locations to determine the smoke layer depth. The fire size, compartment width, clear layer height and number of inlet vents were varied. The BRE spill plume method was used to compare the theoretical mass flow rates with those produced from the experiment.

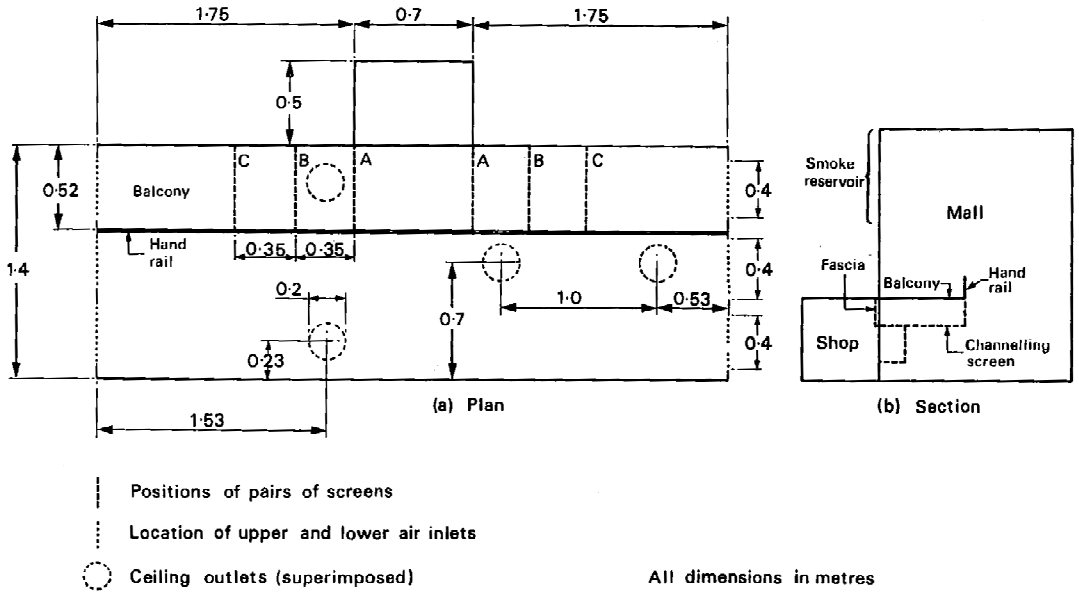

Figure 2.4: The scale model used by Morgan and Marshall [81]

The results of this study gave rise to the development of the effective layer depth correction (see section 2.3.4.1) due to the poor agreement between the experiment and the prediction using the BRE spill plume method. The use of channelling screens was also shown to be effective in reducing the required quantity of smoke to be exhausted.

2.4.3 Hansell, Morgan and Marshall

Hansell *et al.* [32] describe a series of experiments within a $1/10^{th}$ scale model atrium building. The geometry of the model atrium was relatively tall and narrow with approximate dimensions of 1.0 m deep by 1.6 m wide by 3.3 m high. The hot gases were produced from a spatially distributed electrical heater within a fire compartment. The opening width of the compartment was fixed at approximately 0.4 m. Mechanical smoke exhaust was provided from the top of the atrium void to maintain the required clear layer height. Air inlet to the atrium was provided by four asymmetric openings, which could have been the cause for an observed swirling of the rising plumes. This swirling plume behaviour could explain the higher entrainment coefficient determined by from this work [e.g. the 0.34 in Equation (2-46)] compared to other studies [e.g. the 0.22 in Equation (2-50)]. A brief summary of the findings of this work is described below.

2.4.3.1 Horizontal flow of gases toward a compartment opening

A study of the approach flow of gases beneath the spill edge confirmed the assumption made by Morgan [51], that a horizontal flow of gases approaching a flat ceiling with a free edge experiences an effective discharge coefficient of 1.0.

2.4.3.2 Comparison between visually and buoyancy derived smoke layer depths

This work demonstrated that the relationship between visually and buoyancy derived smoke layer depths was different to that observed in earlier work. This relationship appeared to be dependent on the smoke layer geometry (i.e. relationship between the layers depth to its width). This difference was linked to the aspect ratio of the smoke reservoir. A tentative proposal for reconciling these differences with respect to the aspect ratio of the smoke reservoir was presented. This has been taken into account when defining the criteria for applying the effective layer depth correction when using the BRE spill plume method (see section 2.3.4.1). Hansell *et al.* state that further work in this area was highly desirable.

2.4.3.3 Effect of balcony breadth and channelling screens

Hansell *et al.* examined the effect of changing the breadth of the balcony from the fire compartment opening. Three balcony breadths were examined, 0.125, 0.25 and 0.5 m respectively (i.e. 1.25, 2.5 and 5 m full-scale equivalent). For unchannelled flow, they suggest that lateral smoke spread beneath the balcony is minimal for balconies not more than 1.5 m (full-scale equivalent) in breadth for 'large' fires (e.g. 5 MW) or not more than 1.0 m for smaller fires (e.g. 1 MW). It was recommended that channelling screens should be used with broader balconies. Hansell *et al.* suggest that from the conditions studied, balconies broader than or equal to 2 m (full-scale equivalent) will allow the plume to rise through the atrium space as an unhindered balcony spill plume (see Figure 2.5).

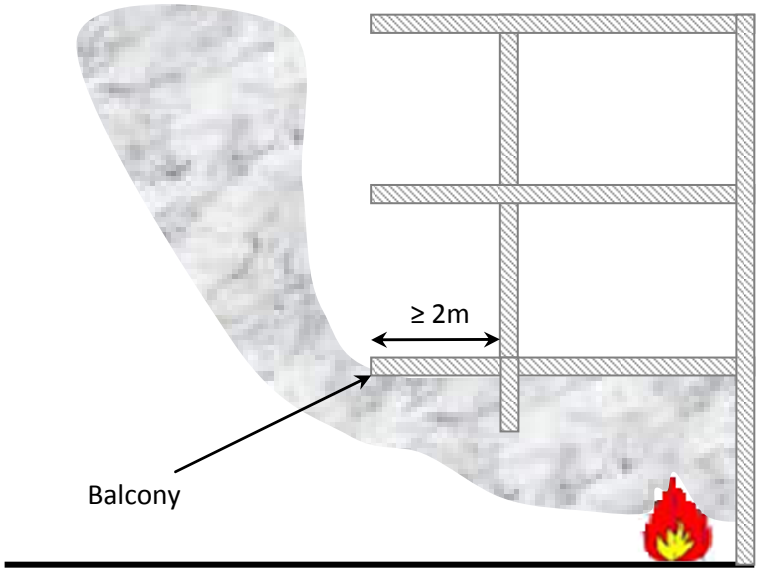

Figure 2.5: Typical smoke flow for balconies broader than 2 m

They also suggest that balconies narrower than 2 m will cause smoke logging between the plume and the wall behind (see Figure 2.6). It was not possible to examine the effect of W_s on the likelihood smoke logging in this work, although Hansell *et al.* state that attachment to the wall above the opening is more likely to occur with wider plumes. Thus, the 2 m balcony breadth criterion may not apply generally for plumes generated from a variety of compartment opening widths.

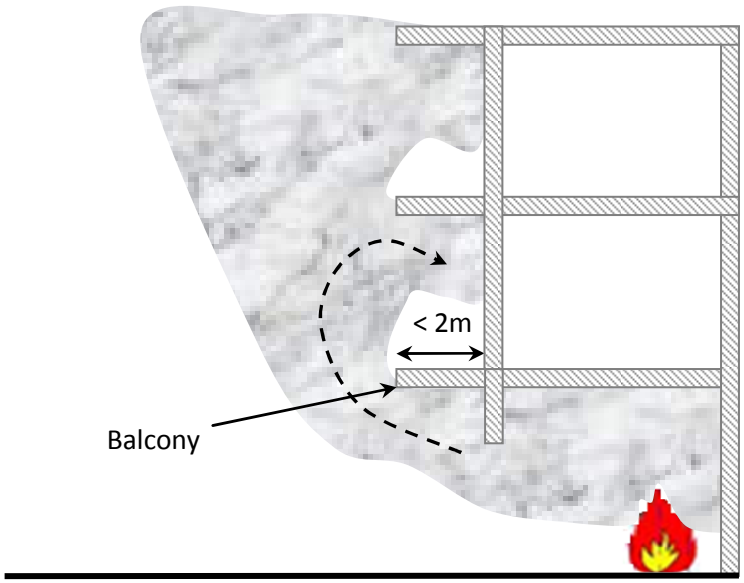

Figure 2.6: Typical smoke flow for balconies narrower than 2 m

2.4.3.4 Temperature limitation of the BRE spill plume method

Hansell *et al.* found that there was a critical temperature of the approach flow, above which the BRE spill plume method breaks down. This was due to the a sharp reduction (up to 50%) in the required empirical entrainment constant, α , for the method to match the experiment. Hansell *et al.* state that it was not possible to identify whether this critical high-temperature failure of the model was related to α or α' and that the analysis could equally well to suggest a breakdown in the model of the rotation region as in the subsequent plume, and that further research was needed. These limiting temperature criteria are dependent on W_s and the type of spill plume and are given in Table 2.4.

Plume type	W_s (m)	$\theta_{\max,\, s}$ (°C)
3-D Balcony	4 to 5	250
3-D Balcony	7	330
3-D Adhered	4	280

Table 2.4: Limiting temperature criteria for the BRE spill plume method

2.4.3.5 Adhered plume entrainment and the BRE spill plume method

Hansell *et al.* suggest that the BRE spill plume method can be used to predict entrainment for adhered plumes by using an entrainment coefficient, α, with a value of 0.077. This value of α is approximately half that for a balcony spill plume and should only be used with 'Gaussian profile' plume models.

2.4.4 Marshall and Harrison

Marshall and Harrison [48] have summarised the results of five separate series of experiments mainly examining 2-D balcony spill plume entrainment using a $1/10^{th}$ physical scale model. In all of these studies the scale model consisted of a fire compartment to generate the spill plume and a smoke collecting hood to measure entrainment. These experiments did not recreate a scale model representation of a shopping mall or an atrium building as in the previous studies by Morgan and Marshall [81] and Hansell *et al.* [32], but utilised a collecting hood to specifically

measure entrainment in the plume. The smoke layer within the hood was adjusted so that it was just contained within the hood and allowed fresh air to be entrained unrestricted into the plume below the layer with no significant warming of the air beneath. The plumes were generated by burning IMS at a controlled and measured rate within compartment which was 1.0 m deep by 0.91 m wide by 0.59 m high. The geometry of the smoke collected hood varied between each study.

The data produced from four of these studies was used in the development of the calculation method described by Poreh *et al.* [31] for 2-D balcony spill plumes (see section 2.3.2.6). A summary of the general findings of this work is given below.

2.4.4.1 Geometry of smoke collecting hood

This work demonstrated that a relatively small collecting hood with a low ceiling height caused additional air entrainment to be measured compared to that using larger hoods with higher ceilings from identical fire conditions. Marshall and Harrison observed that the flow within the small hood was more turbulent than that observed in larger hoods, with the rising plume causing ceiling jet and wall jet effects leading to an unstable and fluctuating smoke layer causing additional entrainment. This additional entrainment may not be a significant issue in real design as the full scale equivalent dimensions of the small hood were 10 m wide by 10 m deep by 10 m high (i.e. height above the spill edge) and is not truly representative of the size of a typical atrium voids found in reality.

2.4.4.2 Counter flow at the compartment opening

One of the fundamental assumptions of the BRE spill plume method is that the velocity of incoming air at the fire compartment opening is much smaller than the outward flowing hot gas layer. To ensure that this condition occurred, a sliding shutter was installed at the fire compartment opening (for two experimental series) to prevent the passage of free air to the fire without significantly affecting the outward flowing gases. The height of this shutter was adjusted so that it was just beneath the observed smoke layer. The fire drew air in through ducts, at the rear and base of the compartment, allowing the inflow of air to be measured. However, for the other

experimental series, the shutter was removed and free air was allowed to pass into the compartment beneath the smoke layer. This created a counter flow to the outward flowing gas layer from the compartment opening. Marshall and Harrison showed that a counter flow at a compartment opening produced a 30% increase in the layer depth and mass flow rate of gases at the opening. This led to a 15% increase in the mass flow rate of gases entering the layer in the smoke reservoir. Marshall and Harrison suggested that this increase was possibly due to the inflow of air affecting the plume behaviour within the fire compartment. Visual observations showed that the inflow of air caused the fire plume to lean towards the rear wall of the compartment. Earlier work [32,97] has suggested that a leaning fire plume within a room will entrain more air than an upright fire plume. Marshall and Harrison utilised Equation (2-8) developed by Hansell [32] to demonstrate that the experimental measurements of the mass flow rate of gases at the compartment opening were comparable with the theoretical predictions for a leaning plume. The results suggest that the BRE method could be successfully used with counter flow at the compartment opening.

2.4.4.3 Air entrainment into the free ends of a balcony spill plume

Marshall and Harrison demonstrated that from very limited data, entrainment of air into a balcony spill plume was increased by approximately 30% when air was allowed to enter into the free ends of the plume (i.e. the difference in entrainment between the 2-D and 3-D plumes). This conclusion was drawn from data for plumes generated from a single width of fire compartment opening and may not apply generally for plumes generated from a variety of opening widths.

2.4.4.4 Helium as an alternative method

Marshall and Harrison demonstrated the feasibility of using Helium gas as an alternative source to heated air for studying the flow of hot gases within physical scale models. This technique was originally suggested in unpublished work by Poreh. Helium has an advantage over thermal methods in that there is no heat transfer from the simulated fire source or from the resulting plume. Experiments could also be carried out over shorter time durations, since there is no need to wait for thermal equilibrium. The main disadvantage of Helium was its high cost.

2.4.5 Yii

Yii [92] carried out a study of the balcony spill plume using salt water modelling and a Laser Induced Fluorescence (LIF) flow visualisation technique. The experiments were carried out within a $1/20^{th}$ physical scale model. Salt water modelling can only simulate relatively small density differences, corresponding to relatively low temperatures above ambient (i.e. 30 to 50 °C above ambient).

Yii demonstrated that good flow visualisation of the spill plume could be achieved using the LIF technique. He showed that there was a small degree of entrainment into the rotation region of the spill plume. It was also observed that the presence of a downstand at a compartment opening resulted in significant entrainment in the under balcony layer flow. Yii also showed that smoke logging on an upper balcony was found to be more severe for a short balcony compared to a long balcony. This study only identified flow features of the spill plume as the LIF technique was the only method used for investigation. Measurements of the mass flow rate of the spill plume were not made.

2.4.6 Harrison and Spearpoint

Harrison and Spearpoint [40] carried out a series of $1/10^{th}$ physical scale model experiments to provide new data to characterise entrainment into 3-D balcony spill plumes channelled by screens below the balcony.

The scale model utilised a fire compartment to generate the spill plume and a collecting hood to measure entrainment, similar to that used in the experiments by Marshall and Harrison [48] (see Figure 2.7). The dimensions of the collecting hood were 1.0 m wide by 2.0 m deep by 2 m high. The dimensions of the fire compartment were 1.0 m wide by 1.0 m deep by 0.5 m high. Walls were inserted at the open face of the fire compartment to reduce the opening width to 0.6 m so that the resulting spill plume was contained within the collecting hood above. A 0.3 m broad balcony was attached to the fire compartment opening and extended across its full width. The experiments examined the scenario of both a flat ceiling and a downstand at the spill edge, with downstand depths of 0.1 m and 0.2 m respectively.

Figure 2.7: The scale model used by Harrison and Spearpoint [40]

The hot gases were generated by burning IMS in a tray within the compartment. The total heat release rate of the fire was varied, which in turn varied the mass flow rate and convective heat flow rate of the gases below the spill edge, in addition to varying the depth of the resulting smoke layer. The height of rise of the plume was also varied.

Harrison and Spearpoint used the data to develop a new simplified spill plume formula as described in section 2.3.2.8. They concluded that entrainment of air into a 3-D balcony spill plume appeared to be the same, whether the spill edge was at a downstand edge or a flat balcony edge. However, the presence of a deep downstand at the spill edge caused the emerging plume to rise vertically from the opening, which has significant implications for smoke logging on higher storeys due to partial impingement of the plume with the balconies above.

Harrison and Spearpoint also used the data to assess the performance of the BRE spill plume method. They found that the classification criteria between 'large' and 'small' area smoke reservoirs given by Morgan *et al.* [12] (see section 2.3.4.1) may not be reliable for all scenarios and should be used with caution. They also found that the use of the effective layer depth correction did not always provide good agreement with the experimental results and should also be used with caution.

For a flat ceiling at the spill edge, the BRE spill plume method gave reasonably good agreement with the experimental results when using an entrainment constant α, with a value of 0.11 (rather than 0.16) and not applying the effective layer depth correction. Harrison and Spearpoint state that it may be more reliable to apply the BRE method using this approach rather than adjusting the height of rise of the plume. When a downstand was present at the spill edge, the BRE spill plume method did not give good agreement with the experimental results, however, the predicted results were conservative.

2.4.7 Lougheed, McCartney and Gibbs

Lougheed *et al.* [71] have recently carried out a series of full scale experiments examining entrainment into 3-D balcony spill plumes to support new guidance within NFPA 92B. The experiments were carried out within the NRC full-scale burn hall test facility which was used to simulate an atrium space. The simulated atrium space in the experiments used part of the burn hall facility with a footprint of 16.8 by 30.5 by 12.2 m high. Mechanical smoke exhaust was provided from the atrium using a duct system with eight circular vents located near the ceiling with a variable capacity up to a maximum of 25 $m^3 s^{-1}$. A fire compartment was located near one end of the atrium with dimensions 5 m deep by 13.8 m wide by 5 m high. The front wall of the compartment was modular in construction to allow for multiple opening widths. All openings were located on the compartment centreline. A removable downstand could be installed at the top of the compartment opening. Removable channelling screens could be installed in line with the sides of the compartment opening. These channelling screens were originally 2 m in depth, but their depth was increased to 2.9 m due to minor leakage under them during experiments with a downstand. A 4 m broad balcony was installed over the entire width of the fire compartment. The balcony was 5 m above the floor and 7.2 m below the ceiling of the atrium. The fire source was generated from a variable area propane burner system with dimensions of up to 3 m by 3 m located at the centre of the fire compartment.

The experiments carried out an extensive parametric analysis, with the total heat release rate of the fire being varied between 0.5 and 5 MW. The fire compartment opening width was varied with values of 5, 7.5, 10 and 12 m. Smoke flows with and without a downstand at the compartment opening were examined as well as flows with and without channelling screens. As the exhaust fan capacity of the facility was limited, only very low heights of rise of plume were able to be examined in this work. In some cases, the smoke layer within the atrium was below the spill edge and additional smoke exhaust (to that already being provided mechanically) was provided by natural means into adjacent areas of the burn hall laboratory. It is unclear if the amount of additional smoke exhaust was measured. The height of rise of plumes examined in the experiments was generally 1 to 2 m above the spill edge, up to a maximum of approximately 4 m. The height of rise of the plume was estimated from temperature profiles through the layer in the atrium as the hot gases from the propane burner could not be easily observed. Lougheed *et al.* provide various methods to determine the layer depth from the temperature measurements, all of which gave slightly different results.

The calculated entrainment coefficients for those experiments with channelling screens below the balcony are shown in Figure 2.8, with a line showing the entrainment coefficient given in the 2005 version of NFPA 92B [88] (i.e. 0.41) based on the formula using the convective heat flow rate of the gases [Equation (2-61)].

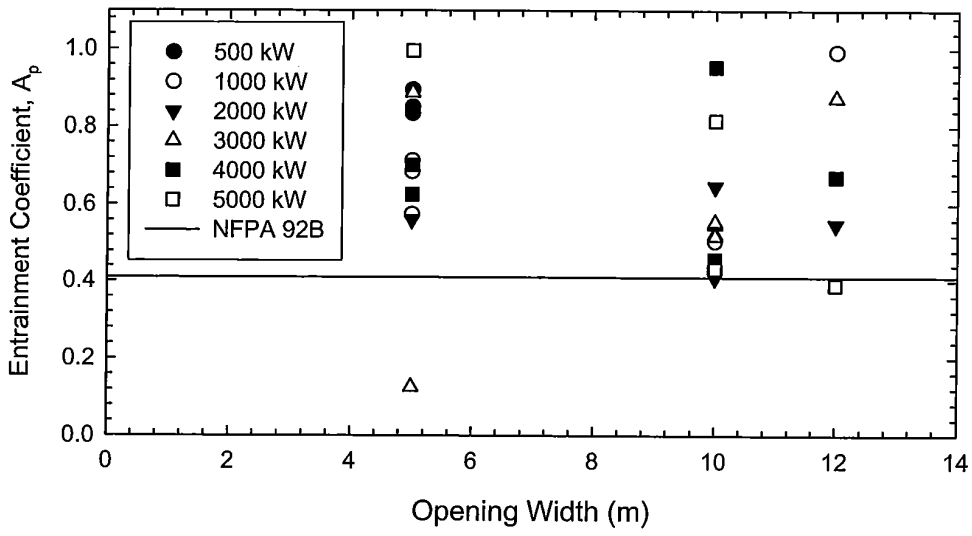

Figure 2.8: Entrainment coefficient for experiments with channelling screens [71]

Lougheed *et al.* appear to give conflicting statements regarding the experimental results, they first state that "the linear entrainment coefficient determined using the experimental data is higher than that used in NFPA 92B particularly for the experiments with a 5 m opening". They then state that "the experimental results indicate that the linear entrainment coefficient used in NFPA 92B is conservative for most scenarios". This last statement appears hard to justify as Figure 2.8 shows that there is considerable scatter of the data, with the majority giving entrainment coefficients much higher than the value of 0.41 given in NFPA 92B.

The entrainment coefficients in Figure 2.8 range from approximately 0.4 to 1.0 for all widths examined and are anomalously high compared with entrainment coefficients from previous studies. A maximum entrainment coefficient of 1.0 is approximately three times greater than the value of 0.34 from the data by Hansell *et al.* [see Equation (2-46)] and approximately five times greater than the value of 0.22 from Harrison and Spearpoint [see Equation (2-50)]. Lougheed *et al.* partially attribute this additional entrainment to recirculation of the ceiling jet flow in the atrium space and to the trajectory of the plume in the near field, although it is unlikely that the additional entrainment can be reconciled due to these factors alone. These differences are more likely due to uncertainties in determining the entrainment coefficients. Lougheed *et al.* state that "there are a number of factors that contributed to the variation in the results including the uncertainty in estimating the variation in the smoke layer interface. Other factors include leakage of the smoke under the draft curtain separating the simulated atrium space from the remainder of the test facility, the height limitations in the atrium area and the height above the balcony at which the entrainment coefficient was determined". The uncertainty is most likely due to the combined effect of the limited height of rise of plume over which the entrainment coefficient was determined and the uncertainty in the location of height of rise of plume. Clearly, a relatively small uncertainty in the location of the height of rise of plume (e.g. 0.5 m) for a limited height of rise of plume (e.g. 2 m) will have a significant effect on the calculated entrainment coefficient (determined from the change in mass flow rate with respect to height of rise of the plume), than if calculated over a wide range of heights.

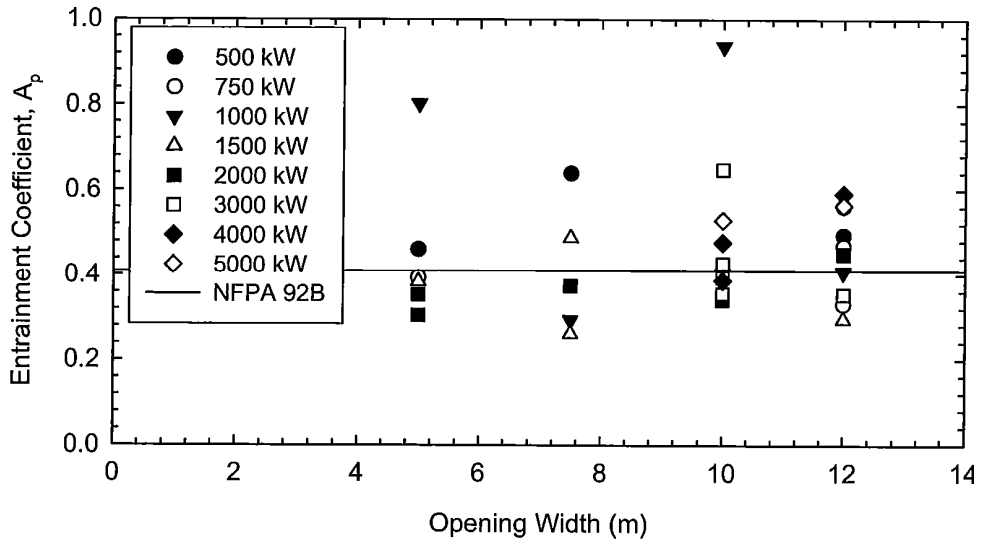

Figure 2.9: Entrainment coefficient for experiments without channelling screens [71]

Lougheed *et al.* also provide results of the calculated entrainment coefficients for those experiments without channelling screens below the balcony (see Figure 2.9). The entrainment coefficients were determined using the effective lateral extent of the flow at the spill edge given by Equation (2-30). Figure 2.9 shows that there is a considerable amount of scatter in these results, however, there is generally a better agreement between the calculated entrainment coefficients and the value given in NFPA 92B compared to the results with channelling screens.

Lougheed *et al.* state that the experimental results demonstrate that the equations in NFPA 92B can be applied for unchannelled flows using the effective lateral extent of the flow given by Equation (2-30). Again, this statement should be treated with caution as Ko *et al.* [70] report that mass loss was observed from the ends of the balcony in the experiments, such that it was not possible to examine the true lateral extent of the unchannelled flow below the balcony and subsequent plume entrainment.

2.5 Computer modelling studies of the spill plume

There have been a number of computer modelling studies of the spill plume which have used either CFD modelling or simpler zone models in the analysis. A summary of these studies are described below, all of which examined the balcony spill plume.

2.5.1 Miles, Kumar and Cox

Miles *et al.* [44] used CFD modelling to examine entrainment into a 2-D balcony spill plume channelled by screens below the balcony. The CFD model, JASMINE, was used in the analysis to simulate experiments within a $1/10^{th}$ physical scale model described by Marshall and Harrison [48].

The plumes were generated by utilising the temperature and velocity profiles of the flow below the spill edge (as measured experimentally by Marshall and Harrison) as the fire source. This enabled the plumes to be simulated without modelling the fire and the compartment.

Miles *et al.* suggested that there was only a small degree of entrainment into the rotation region of the spill plume. The predictions agreed well with the experimental data from Marshall and Harrison for low heights of rise of plume, but appeared to diverge at greater heights. Miles *et al.* suggest that this divergence could be due to the unrealistic assumption of a horizontal layer within the smoke collecting hood (which was observed at high heights of rise of plume). Alternatively, this divergence could have been due to the application of an inappropriate turbulence model for this flow. The predictions generally agreed well with the correlations developed by Poreh *et al.* [31] and Thomas *et al.* [39].

2.5.2 Chow and Cui

Chow [98] used CFD modelling to examine entrainment into a 2-D balcony spill plume channelled by screens. Simulations were carried out of the scale model experiments described by Marshall and Harrison [48] using the model CC-EXACT. A linear correlation was derived from the predicted results between the mass flow rates in the plume with respect to height of rise. This correlation provided a result similar to that described by Poreh *et al.* [31]. Chow suggests that CC-EXACT model is a suitable tool to study smoke filling in atria from a spill plume.

2.5.3 Chow

Chow [99] again simulated the 2-D balcony spill plume experiments described by Marshall and Harrison [48]. The CFD model PHOENICS 3.1 was used in this work. A fixed fire size of 17 kW was examined with 6 different exhaust rates from the smoke collecting hood. The location of the neutral plane in the smoke reservoir was examined with respect to each smoke exhaust rate.

2.5.4 Chow and Li

Chow and Li [100] developed a two-layer zone model named CL-Atrium to examine smoke filling in an atrium due to a 2-D balcony spill plume The simulated atrium had a floor to ceiling height of 15 m and a horizontal cross-sectional area of 100 m^2. A fire compartment with a height of 3 m and an opening width of 6 m was modelled, with a balcony extending across the full width of the compartment opening. A range of both steady state and growing fires were used in the analysis.

The design formulae given by Poreh *et al.* [31], Thomas *et al.* [39] and NFPA 92B [101] were each used in the model to predict the rate of smoke filling in the atrium. Comparisons were made between predictions using the CL-Atrium model and the CFAST zone model [102]. The results from the model indicated that the predicted layer temperature and interface height in the simulated atrium were similar either when using the Poreh *et al.* or Thomas *et al.* methods. The results based on the formula in NFPA 92B were similar to those predicted by CFAST, but produced much greater predicted mass flow rates compared to that using the formulae by Poreh *et al.* and Thomas *et al.* This is partially attributed to the additional entrainment into the ends of the plume assumed in the NFPA 92B formula.

2.5.5 Li and Chow

Li and Chow [103] used the CFD model PHOENICS 3.1 to simulate a balcony spill plume within an atrium building. In this study, the effect of smoke filling within a thermally stratified atrium space 30 m high, 20 m long and 10 m wide was examined.

Li and Chow demonstrated the effect of stratification of smoke from a balcony spill plume prior to reaching the ceiling of the atrium space. They provide an expression to determine the minimum fire size required such that stratification does not occur. The maximum height that the spill plume will reach can also be calculated.

2.5.6 Shi, Lu, Chow and Huo

Shi *et al.* [104] describe computer modelling to simulate smoke filling within a full scale atrium due to a 3-D balcony spill plume generated from a fire within a shop unit. The analysis used numerical modelling using FDS (version 3) and zone modelling using CFAST. Although CFAST does not include a balcony spill plume model, the spill plume was simulated by assuming an equaivalent axisymmetric source at the base of the atrium. Shi *et al.* propose an alternative zone model to estimate smoke filling due to a spill plume, which includes a transport time lag. The modelling was supported with data from two full scale experiments.

The modelling and the experiments examined a spill plume generated from a shop unit 4 m by 3 m by 3 m high. The shop contained a narrow doorway opening, 1.6 m wide by 1.4 m high from which the plumes were produced. The shop unit was located in an atrium with dimensions of 22.4 m by 11.0 m by 27 m high. The hot gases were produced from diesel pool fires.

Predictions of smoke filling using the alternative zone model provided reasonably good agreement with the experimental results. Shi *et al.* state that this model performed slightly better than FDS, especially during the growth stage of the fire, and much better than CFAST, in which the transport lag time was not considered and the spill plume was treated as an axisymmetric plume. Shi *et al.* state that the experimental results and the predictions demonstrate that smoke filling can be rapid and that smoke management is necessary and important for atria.

2.5.7 Li and Chow

Li and Chow [105] used the CFD model PHOENICS to examine entrainment into 2-D and 3-D balcony spill plumes channelled by screens below the balcony. The source of the plumes was generated by simulating temperature and velocity profiles of the out flowing hot gas layer below the spill edge, similar to the approach used by Miles *et al.* [44]. Li and Chow assumed uniform profiles for the flow below the spill edge both horizontally and vertically, in the absence of experimentally derived profiles. This assumption does not reflect the realistic characteristics of a flow below a flat spill edge, where temperature and velocity decrease with depth [33,34]. However, this assumption should be sufficient to provide general conclusions on entrainment into balcony spill plumes.

For the 2-D plume, a computational domain with dimensions of 25 by 10 by 45 m high was simulated. The height of the balcony from the floor was 6 m, with the balcony extending 6 m into the domain, with its width the same as that of the domain. The sides of the domain in line with the rising plume contained walls to prevent entrainment into the ends of the plume, with the remaining sides of the domain being open boundaries. The lateral extent of the flow below the spill edge was 10 m with a depth of 1.5 m. The temperature of the flow below the spill edge was 250 °C with the velocity of the flow varied with values of 2.0, 2.5, and 3.0 m s^{-1}.

For the 3-D plume, a domain with dimensions of 25 by 20 by 45 m high was simulated. The balcony geometry was the same as that used for the 2-D plume analysis. The lateral extent of the flow below the spill edge was varied by modelling channelling screens separated by a distance of 5, 8 and 10 m with a depth of 1.5 and 3.0 m respectively. The temperature of the flow below the spill edge was varied with values of 250, 300 and 320 °C with the velocity of the flow varied with values of 3.0 and 3.5 m s^{-1}.

Predictions of mass flow rate were obtained by integration over the horizontal cross-sectional area of the plume with height. The CFD predictions were compared with predictions using the BRE spill plume method [2] and the simple formulae given by Thomas [84], Poreh *et al.* [31], Thomas *et al.* [39] and NFPA 92B [88].

For the 2-D plume, the CFD predictions of mass flow rate provided good agreement with those obtained using the formulae by Poreh *et al.* and Thomas *et al.* The BRE method predictions were much higher than those obtained using CFD when an entrainment coefficient, α, with a value of 0.16 was used. However, Li and Chow state that reasonably good agreement was achieved when α was assumed to be 0.11, as also found by Poreh *et al.* [31] and Harrison and Spearpoint [34]. The predictions using the formulae by Thomas and NFPA 92B were much greater than the CFD predictions, however, this is not surprising as these formulae apply to 3-D plumes.

For the 3-D plume, Li and Chow provide predictions of the entrainment coefficient for the various plumes examined. The predicted entrainment coefficients ranged from 0.22 for wide plumes to 0.29 for narrow plumes. These entrainment coefficients are lower than the value in the NFPA 92B formula (i.e. 0.41) which tended to over predict entrainment. The CFD predictions of mass flow rate provided good agreement with the formula by Thomas at low heights of rise, however, there were discrepancies at greater heights. The BRE method predictions provided reasonable agreement with CFD when a value of α of 0.11 was used, instead of 0.16. The formulae by Poreh *et al.* and Thomas *et al.* provided lower predictions of entrainment compared to those obtained using CFD as these formulae only apply for the 2-D plume.

Figure 2.10 shows predictions of mass flow rate with respect to height for a 3-D balcony spill plume generated from a flow that was 5 m wide by 3.0 m deep. Figure 2.10 shows that CFD predicts a rate of entrainment that initially obeys a linear relationship, however, at greater heights the predictions begin to depart from this linear relationship. Li and Chow attribute this to the plume being more 3-D in nature at greater heights of rise.

Li and Chow do not comment on the location of this transition in entrainment behaviour, although it can be inferred for this specific case that the point of transition occurs when the height of rise above the spill edge is approximately 4 to 5 times the width of the flow below the spill edge. This appears to be the only data to partially support the hypothesis described in section 1.8.5 that a 3-D balcony spill plume eventually becomes axisymmetric in nature due to end entrainment.

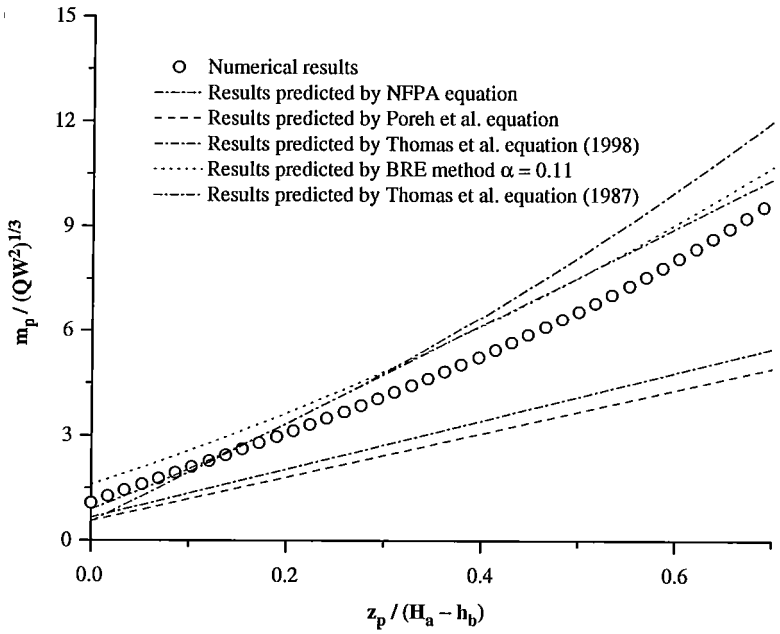

Figure 2.10: Mass flow rate with respect to height for a 3-D balcony spill plume [103]

2.5.8 Valkist

Valkist [87] carried out CFD modelling using FDS (version 4) to develop simple design formulae for 3-D balcony spill plumes generated from wide compartment openings. Fourteen simulations were carried out examining plumes generated from compartment opening widths of 7.2, 14.4, 40.0 and 87.2 m respectively, with and without a 1.0 m deep downstand at the opening. The fire compartment was 31 m deep, with a fixed height of 5.0 m. The horizontal distance between the fire source and the compartment opening was varied, with values of 7.8 and 22.4 m examined. The fire source was modelled as a propane burner with a total heat release rate ranging between approximately 3.5 and 7.0 MW.

The plumes were allowed to rise unhindered into a domain with open boundary conditions, with the mass flow rate in the plume determined at heights of rise above the spill edge up to 56.8 m. The predictions generally demonstrated a linear relationship between mass flow rate and height of rise for the spill plumes examined. These predictions were used to develop the simple formulae shown in section 2.3.2.9.

2.5.9 Lougheed, McCartney and Gibbs

Lougheed *et al.* [71] carried out CFD modelling using FDS (version 3) to examine entrainment into 3-D balcony spill plumes. The modelling simulated plumes generated from a range of compartment geometries which had identical dimensions to that examined in the series of full scale experiments already described in section 2.4.7. However, the modelling examined entrainment at much greater heights of rise than was possible experimentally.

The modelling examined plumes rising unhindered from a compartment into a 50 m cubic computational domain with open boundary conditions. Hence, no smoke layer formed within the domain and the plume did not interact with any smoke reservoir ceiling or walls. The mass flow rate in the spill plume was calculated by integration across entire horizontal cross-sections of the flow domain at 0.5 m height intervals.

A grid sensitivity analysis was performed to determine the most efficient grid size to ensure accuracy of the simulations. Simulations were carried out with the grid size being systematically reduced until a grid independent solution was achieved. The predictions of mass flow rate in the plume with height were similar when a grid size of either 0.25 or 0.5 m was used. Therefore, a grid size of 0.5 m was chosen to be appropriate for the parametric analysis. The grid sensitivity analysis did not utilise the data from the full scale experiments (obtained at low heights of rise of plume) for validation purposes.

The FDS predictions have been used by Lougheed *et al.* to develop new simplified design formulae in NFPA 92B [2] but only for plumes in the far field with a height of rise at or above 15 m [see Equations (2-59) and (2-60) in section 2.3.2.10]. It unclear why the new correlations derived from the FDS simulations only apply to plumes above the 15 m criterion, as the predictions show a constant entrainment rate both below and above a height of 15 m (see Figure 2.11 and Figure 2.12).

Figure 2.11 shows predictions of mass flow rate with height for a 3-D balcony spill plume generated from a 5 m wide opening. Predictions were obtained from "NFPA 92B" using the formula given the 2005 version [88] which is also included in the current version [2]. Predictions using a "line plume" approximation are shown, and also for a "new correlation" based on the FDS predictions, represented by Equation (2-59).

Figure 2.11 shows that the "new correlation" predicts a constant and lower rate of entrainment compared to the predictions using "NFPA 92B" both below and above a height of rise of 15 m. The predictions using the "new correlation" are higher that the "line plume" predictions due to the entrainment into the ends of the plume.

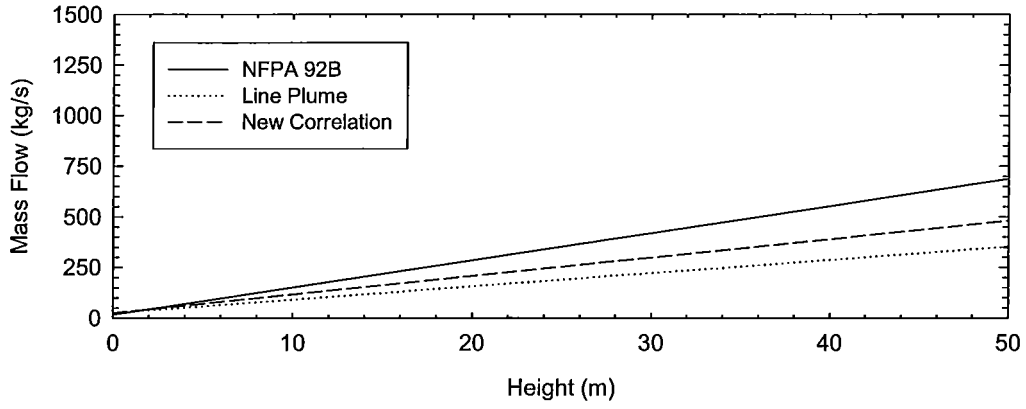

Figure 2.11: Mass flow rate with height for a plume from a 5 m wide opening [71]

Figure 2.12 shows a similar analysis given by Lougheed *et al.* but for a plume generated from a 10 m wide opening. In this case, as the plume is wider, the "new correlation" prediction is given by Equation (2-60). Again, the "new correlation" prediction gives a constant and significantly lower rate of entrainment compared to the "NFPA 92B" prediction (both below and above a height of rise of 15 m). However, in this case, the "new correlation" gives predictions which are almost identical to that obtained using a "line plume" approximation. The FDS predictions indicate that plume entrainment appears to be dependent on the width of plume, as also indicated by Li and Chow in section 2.5.7.

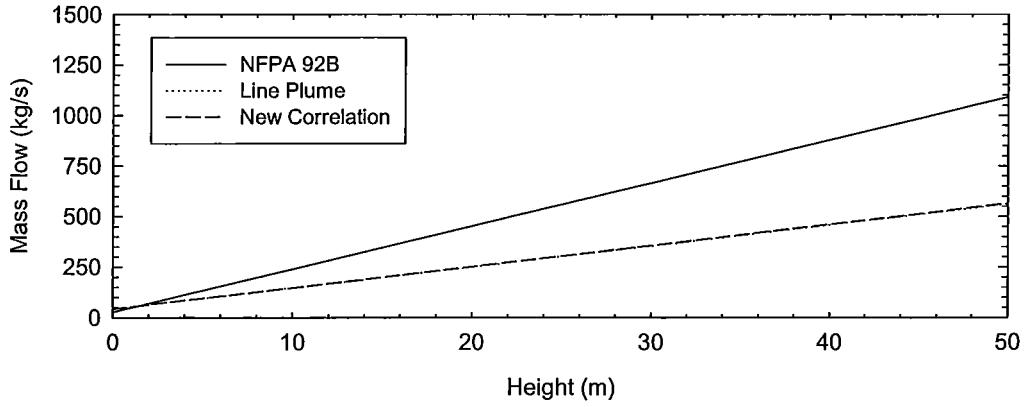

Figure 2.12: Mass flow rate with height for a plume from a 10 m wide opening [71]

The predictions provide a linear rate of entrainment over the full height of rise of plume and do not show a departure from this relationship at greater heights due to end entrainment. This behaviour is not consistent with the predictions obtained by Li and Chow shown in Figure 2.10. This could possibly be due to differences in the CFD model being used, or that Lougheed *et al.* obtained predictions of mass flow by integration over entire horizontal cross-sections of the flow domain rather than from cross-sections of the plume as done by Li and Chow. These differences add further uncertainty regarding the transition from a balcony spill plume to axisymmetric.

Chapter 3

3. Approach

This work involves the use of physical scale modelling and numerical modelling using CFD in the analysis. A brief description of each approach is given below.

3.1 Physical scale modelling

The approach of physical scale modelling using Froude number scaling is well established and has been used in many studies of smoke movement in buildings. The approach described in this work was primarily developed at the Fire Research Station in the UK [30,106]. Physical scale modelling is also described by Quintiere [107], Klote and Milke [13] and in NFPA 92B [2] which recognises its use as an appropriate method for the analysis of smoke movement in atria.

The approach typically takes the form of reduced scale fires within a physical model. Measurements are generally made of temperature, velocity and gas concentrations, in addition to visual observations. Measurements can be extrapolated to full scale using the appropriate scaling laws for turbulent flow which are described below.

3.1.1 The scaling laws for turbulent flow

To ensure that the experimental results can be extrapolated to full scale, the physical scale model used in this study was designed to meet the scaling principles set out by Thomas *et al.* [30]. This is effectively a modified Froude number scaling which requires that equivalent flows are fully turbulent on both full and model scale (i.e. turbulent flow is achieved for flows with Reynolds numbers ≥ 4000 [108] analogous to flow in a pipe). For an example calculation of the Reynolds number for a typical flow in the scale model, see section 4.1.2.6.

The Froude number is the ratio of the inertial forces to gravity forces, given by Equation (3-1).

$$Fr = \frac{u}{\sqrt{gl}} \tag{3-1}$$

As buoyancy is a gravity force and dominates the flow resulting from fires, a modified Froude number [given by Equation (3-2)] must be preserved between full and model scale [109].

$$Fr = \frac{u}{\sqrt{\left(\frac{\Delta\rho}{\rho}\right)gl}} \tag{3-2}$$

Based upon the work by Thomas *et al.* [30], Morgan *et al.* [110] derived dimensional relationships between fluid dynamic variables from first principles in a more explicit and simpler manner. The derivation of the scaling laws is given as follows [110]:

Fully developed turbulent flows of incompressible fluids can be described by equations of the general form of D'Arcy's formula where the pressure difference driving the flow is approximately proportional to the flow velocity squared.

$$\Delta P \propto u^2 \rho \tag{3-3}$$

The power of u can vary for different scenarios, and is a function of the Reynolds number [30]. However, for most cases, Equation (3-3) is a good approximation. For the special case of fluid flows driven only by buoyancy, the pressure difference depends only on the buoyant head, i.e.

$$\Delta P = \Delta\rho g d = \rho_{amb} \frac{\theta}{T} g d \tag{3-4}$$

Combining Equations (3-3) and (3-4), gives, in terms of the length scale (i.e. the ratio between the full and model scale equivalent length).

$$\theta L \propto u^2 \tag{3-5}$$

The expression for the volume rate of flow across an area (A) normal to the flow is,

$$\dot{V} = uA \tag{3-6}$$

In dimensional terms this becomes,

$$\dot{V} = uL^2 \tag{3-7}$$

The convected heat flow across this area due to the flow is given by,

$$\dot{Q}_c = \dot{m}c_p\theta = \rho\dot{V}c_p\theta = \rho_{amb}T_{amb}c_p\dot{V}\frac{\theta}{T} \tag{3-8}$$

In dimensional terms, this is,

$$\dot{Q}_c \propto \theta\dot{m} \propto \frac{\theta\dot{V}}{T} \tag{3-9}$$

Provided that each variable is assumed to refer to similar points in both the full scale system and in the small scale model, these dimensional relationships can be used to derive the scaling laws.

From Equations (3-5) and (3-7) and eliminating u,

$$\dot{V} \propto L^{5/2}\theta^{1/2} \tag{3-10}$$

From Equations (3-9) and (3-10), and eliminating $\dot{V}$,

$$\dot{Q}_c \propto \frac{L^{5/2}\theta^{3/2}}{T} \tag{3-11}$$

These relationships can be simplified by holding one of these variables constant. For experimental modelling, it is convenient to keep the temperature above ambient equal on both full and model scale. Hence, the same temperature must apply to the corresponding points in the flow system, irrespective of scale. Therefore, if the temperature above ambient is constant, the scaling laws become,

$$\begin{aligned}
&\dot{Q}_c \propto L^{5/2} \Rightarrow \dot{Q}_{c,f} = \dot{Q}_{c,m}\left(\frac{l_f}{l_m}\right)^{5/2} \\
&\dot{m} \propto L^{5/2} \Rightarrow \dot{m}_f = \dot{m}_m\left(\frac{l_f}{l_m}\right)^{5/2} \\
&\dot{V} \propto L^{5/2} \Rightarrow \dot{V}_f = \dot{V}_m\left(\frac{l_f}{l_m}\right)^{5/2} \\
&u \propto L^{1/2} \Rightarrow u_f = u_m\left(\frac{l_f}{l_m}\right)^{1/2}
\end{aligned} \tag{3-12}$$

and the time scale ω, which is described for the flow system by,

$$\omega \propto \frac{L}{u} \propto L^{1/2} \tag{3-13}$$

Hence, if the length scale is changed by a factor of 9, the time scale will change by a factor of 3, the mass flow rate by a factor of 243.

Alternatively, one can hold the length scale L constant. This is useful for extrapolating the results from a given size flow system for a particular heat input, to other values of heat input for the same size system. In this case, where $\theta \leq T$, Equation (3-11) becomes,

$$\dot{Q}_c \propto \frac{\theta^{3/2}}{T} \tag{3-14}$$

The constant of proportionality can be found using experimental results and a new value of θ found for another value of the heat input. The scaling laws now become,

$$\begin{aligned} \dot{V} &\propto \theta^{1/2} \\ \dot{m} &\propto \frac{\theta^{1/2}}{T} \\ u &\propto \theta^{1/2} \\ \omega &\propto \theta^{-1/2} \end{aligned} \tag{3-15}$$

For 'cool' models, where θ << T, Equations (3-14) and (3-15) reduce to,

$$\begin{aligned} \dot{Q}_c &\propto \theta^{3/2} \\ \dot{V} &\propto \theta^{1/2} \\ m &\propto \theta^{1/2} \\ u &\propto \theta^{1/2} \\ \omega &\propto \theta^{-1/2} \end{aligned} \tag{3-16}$$

The above scaling laws do not describe either conductive or radiative heat transfer processes. If either is present to a significant extent in the flow system, the scaling laws given here cannot be applied. The modelling technique used for this application was designed to minimise both of these, but a method of partial scaling of conductive heat transfer is described by Quintiere [107] and Klote and Milke [13]. For this particular study, the temperature above ambient has been assumed to be equal on both full and model scale. Therefore, those equations given by (3-12) apply. It should be noted that all of the above applies only to a flow that is fully turbulent. For truly 2-D problems, one length scale, the width of the flow remains effectively infinite, and the scaling laws would be more appropriately expressed in terms of per unit width.

Similar scaling laws for laminar flow can be derived by replacing Equation (3-3) with an equation of the form of Poiseulle's formula (i.e. $\Delta P \propto u$) and then proceeding by similar methods to those above.

3.1.1.1 Validation of the scaling laws

Thomas *et al.* [30] carried out a series of scale model experiments to check the validity of the scaling laws derived in the same study. The experiments examined smoke flows in models with differing scales with the results providing temperature measurements consistent with the predictions made using the scaling laws. Kumar and Cox [111] applied a 2-D, steady state, finite difference model for smoke movement within compartment fires to the problem of scaling prototype fire test experiments. They demonstrated that the scaling laws held satisfactorily over a range of scale, heat release rate, compartment and fire source geometry. Morgan [112] describes similarities between small scale and full scale experiments of roof venting. The experimental data also agreed well with predictions using a calculation method for roof venting derived from small scale experiments using the scaling laws. Klote and Milke [13] report work by Tsujimoto *et al.* [113] which validated the use of the scaling laws for smoke movement in atria. Quintiere *et al.* [114] also validated the scaling laws by comparing temperature data from full scale and $1/7^{th}$ scale model experiments examining smoke flows in a room and corridor.

Harrison and Miles [115] used the scaling laws as part of a series of $1/5^{th}$ physical scale model experiments examining smoke ventilation of fire-fighting shafts. Numerical modelling using CFD was also used to support and extend the findings of the experiments to full scale. In an attempt to determine if the CFD predictions gave results consistent with the scaling laws, a simulation was carried out of a scale model experiment and a full scale equivalent. Analysis of the CFD predictions between model and full scale were consistent with the correct application of the various scaling laws, with minor differences being attributed to phenomena such as boundary heat losses which were not included in the scaling analysis. Although this CFD analysis does not validate the scaling laws, it provides further confidence in their use by demonstrating consistency in the predictions between model and full scale.

A similar analysis using was carried by Valkist [87] as part of a series of one-third scale model experiments examining smoke flows from a fire compartment opening. CFD predictions were made of four scale model experiments and of the full scale equivalent. The CFD predictions were again consistent with the predictions obtained using the scaling laws.

3.2 Numerical modelling using Computational Fluid Dynamics

Numerical modelling based on the technique of CFD provides detailed predictions of the fluid flow and heat transfer processes associated with applications from across a wide range of science and engineering fields. These include smoke movement studies which are being undertaken increasingly with CFD fire models in design, especially for cases where the assumptions made in simple engineering calculations and zone models may no longer apply. The approach of CFD divides the geometrical space into a 3-D numerical grid (or mesh) containing a large number of control volumes (ranging from thousands to millions of grid elements). At each numerical grid element, the model approximates the solution to the underlying set of coupled conservation equations for mass, momentum, energy and species concentrations (i.e. the Navier-Stokes equations). CFD models specifically developed for application to fire contain sub-models to describe the influence of factors such as combustion and radiation heat transfer on fire and smoke spread. A summary of CFD modelling and its applications are provided by Versteeg and Malalasekera [116]. There are different types of CFD model which differ in the underlying turbulence modelling for the flows. The majority of commercially available CFD models treat turbulence by solving the Reynolds-averaged Navier-Stokes equations (RANS) numerically. RANS models solve the fundamental equations by time average the turbulent transfer processes. In order to solve the RANS equations, additional equations are necessary to describe the contribution of turbulent mixing and influences on chemical kinetics that need to be modelled [13,117]. In the majority of RANS models, this is achieved by implementing the two equation k-ε turbulence model, where k is the kinetic energy of the turbulence and ε is its rate of dissipation. An alternative approach to modelling turbulence is to use Large Eddy Simulation (LES) methods described by McGrattan *et al.* [118] which deals with the turbulent eddies more explicitly, without resorting to

time averaging of the Navier-Stokes equations. CFD is suitable for various aspects of this study and complements the physical scale modelling work. It is used to extrapolate the analysis, by examining spill plume entrainment at much higher heights of rise than were possible experimentally. A brief description of the CFD models used in this work is described below.

3.2.1 FDS

The CFD model mainly used in this study was FDS (version 5.1.4) developed by McGrattan *et al.* [42] of NIST. This model numerically solves a unique form of the Navier-Stokes equations that incorporates compressibility effects sufficient for thermally driven flows of smoke and hot gases generated in a fire [13]. The fundamental equations and the numerical algorithm within the model are given by McGrattan *et al.* [42] and are not repeated herein. In this study, FDS was set to treat turbulence by means of the Smagorinsky form of Large Eddy Simulation (LES) without resorting to Reynolds averaging of the Navier-Stokes equations. FDS has been used extensively for a wide range of fire applications and has been compared with experimental data for validation purposes [42]. The results of the model have been visualised using a 3-D imaging post processing software tool called Smokeview, developed by Forney [119].

3.2.2 JASMINE

As part of a collaborative effort, selected CFD predictions of the experiments carried out in this work have been obtained by researchers at the BRE, UK, using their in-house model, JASMINE [43], which is a RANS CFD model implementing the k-ε turbulence model. Standard wall functions for enthalpy and momentum describe the turbulent boundary layer adjacent to solid surfaces. The fundamental equations and numerical algorithm within the model are given by Cox and Kumar [42] and are not repeated herein. JASMINE has undergone continual development over the past 20 years, during which various combustion, radiation and other fire related sub-models have been added. It has extensively been compared with measured data for validation purposes [e.g. 115,120].

Chapter 4

4. Experimental methodology

Physical scale modelling experiments were carried out using a 1/10th scale model to systematically examine entrainment of air into both balcony and adhered spill plumes. Details of the experiments are described in this chapter, including the experimental apparatus, instrumentation, method and data reduction techniques.

4.1 Balcony spill plume experiments

4.1.1 The physical scale model

Figures 4.1 and 4.2 show the 1/10th physical scale model used in this work. The model simulated a fire within a room adjacent to an atrium void and consisted of two main units, the fire compartment and a smoke collecting hood. The model employed a similar technique to that used by Zukoski *et al.* [61] when measuring entrainment of air into unbounded axisymmetric plumes. The model was designed to meet the scaling principles set out by Thomas *et al.* [30] (see section 4.1.2.6).

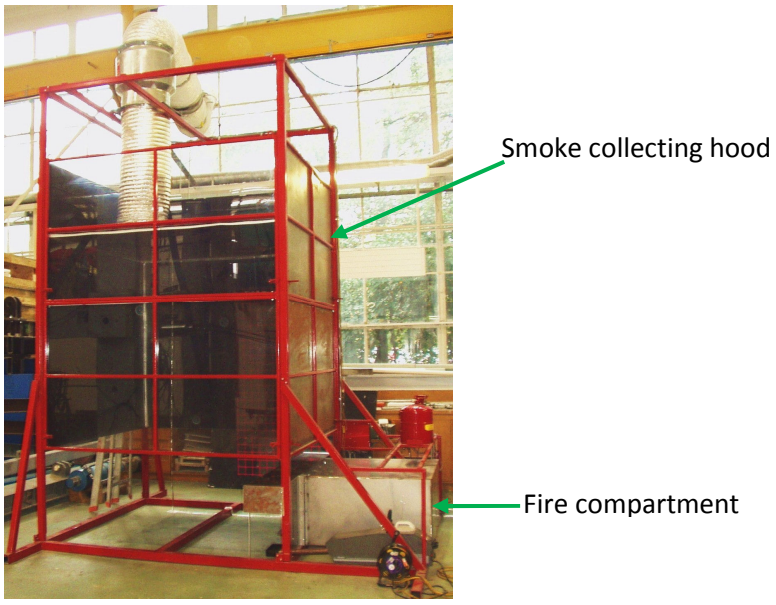

Figure 4.1: The 1/10th physical scale model

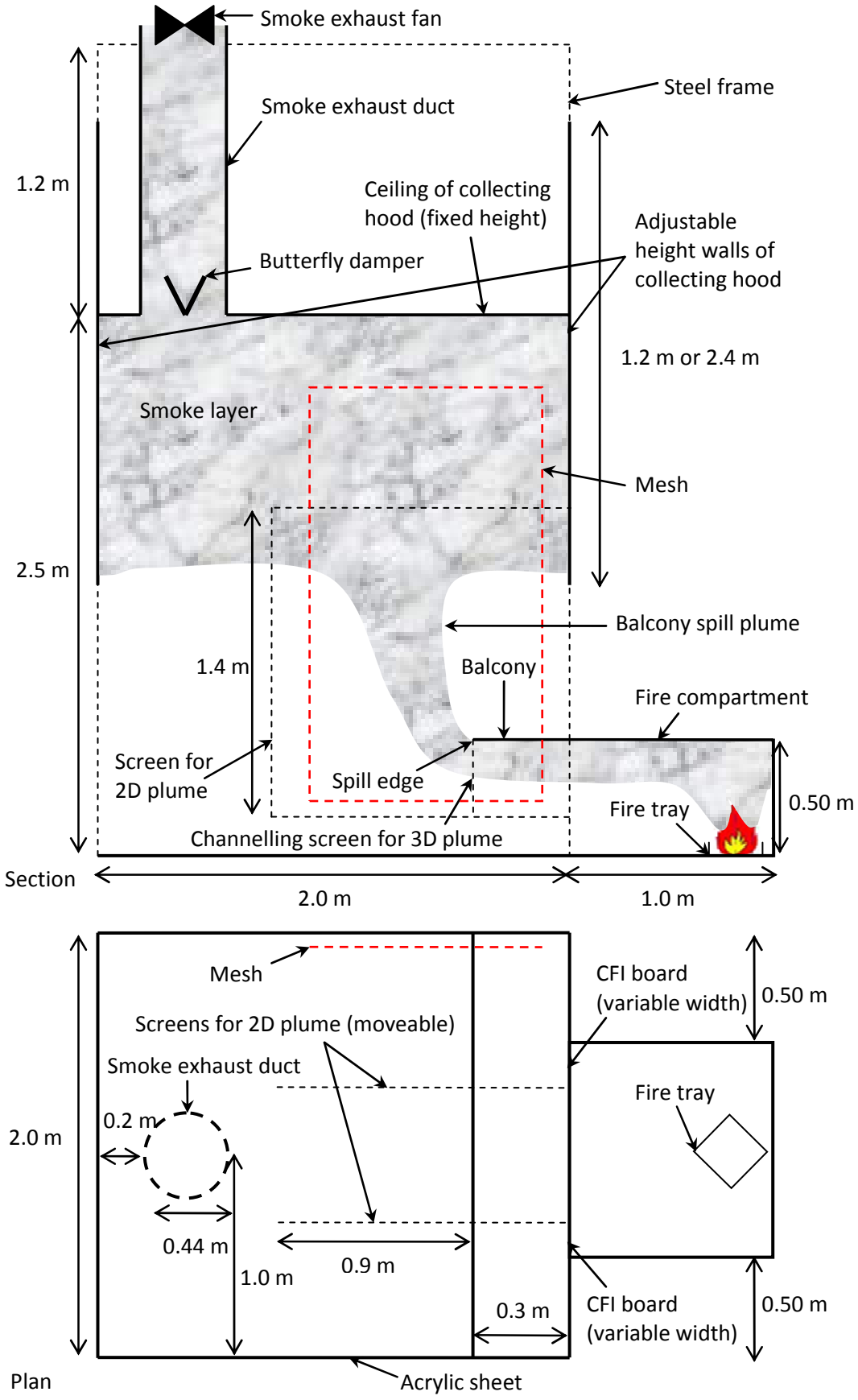

Figure 4.2: Schematic of the 1/10th physical scale model

4.1.1.1 The fire compartment

The fire compartment (see Figure 4.3) was constructed from 25 mm thick Ceramic Fibre Insulation (CFI) board with a 1 mm thick steel substrate on each external face. The dimensions of the fire compartment were 1.0 by 1.0 by 0.5 m high. The height of the compartment opening was equal to the height of the compartment. The width of the opening was varied by inserting walls of equal width at either end. The inserted walls had widths of 0.1, 0.2, 0.3 and 0.4 m and were constructed from 25 mm thick CFI board with a 1 mm thick steel substrate on the non-fire side of the compartment. A 0.3 m broad balcony constructed from 10 mm thick CFI board with a 1 mm thick steel substrate on its upper face was attached to the top of the fire compartment opening. The balcony extended 0.5 m beyond each side of the fire compartment. Full height walls made from 1 mm thick steel sheet extended 0.3 m beyond the side walls of the compartment in line with the open face, with 0.15 m deep walls (below the rear edge of the balcony) extending a further 0.2 m on either side.

For the majority of experiments channelling screens were located in line with each side of the compartment opening and projected across the full breadth of the balcony. The screens were made from 10 mm thick CFI board with a 1 mm thick steel substrate on the external face. The screens used were either 0.2 or 0.3 m deep, depending on the compartment geometry and fire size examined.

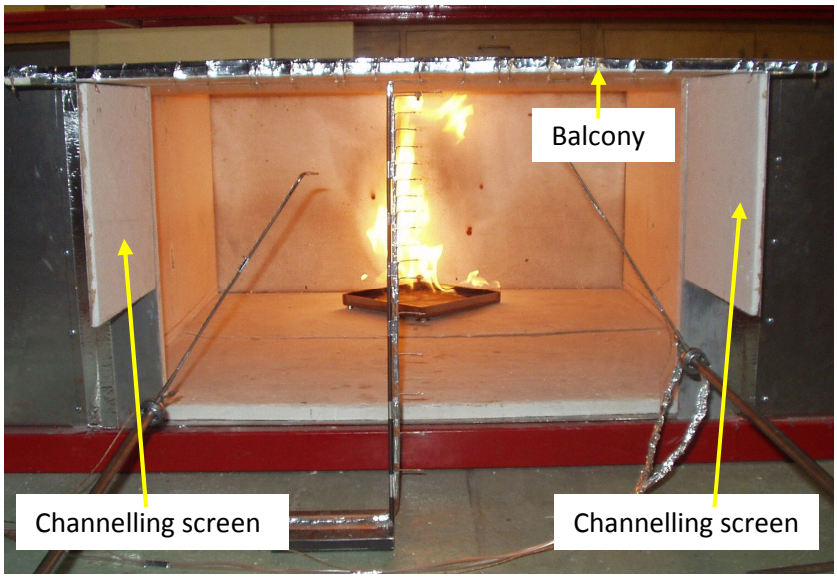

Figure 4.3: The fire compartment and IMS fire source

4.1.1.2 The fire source

A steady state fire source (see Figure 4.3) was generated by supplying IMS into a metal tray within the fire compartment at a controlled and measured rate. The fuel was supplied to the fire compartment continuously into a metal tray, via a fuel reservoir, flowmeter, tap and copper tubing (see Figure 4.4). The flow of fuel was controlled by a needle valve on the flowmeter. To maintain a constant flow, the fuel reservoir contained a constant pressure head device [35]. This incorporated a steel tube which passed into the fuel reservoir such that air was drawn in to replace the burning fuel. This caused fuel at the same height as the end of the steel tube (20 mm from the base of the reservoir) to be at atmospheric pressure.

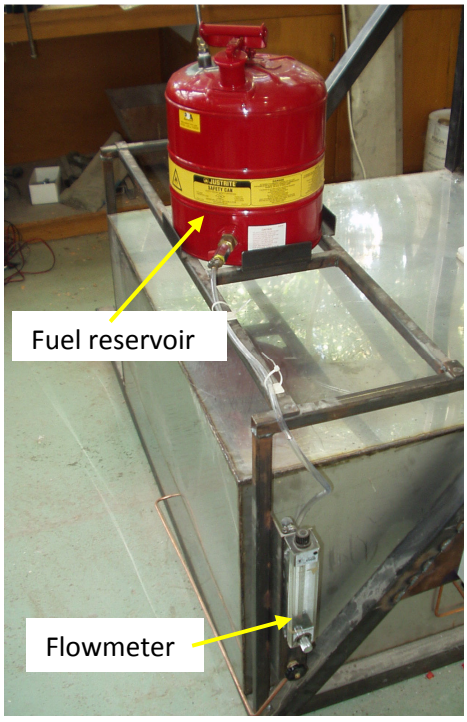

Figure 4.4: The fuel supply system

The tray was located at the rear of the fire compartment. Since the fuel did not occupy the full area of the tray, the tray was tilted toward the back of the compartment at an angle of 45 degrees to the walls of the compartment. Hence, the sides of the fire tray channelled the fuel such that its surface remained reasonably uniform and automatically adjusted to match the burning rate to the inflow of fuel. The tray was 0.25 by 0.25 by 0.015 m high.

The total heat release rate of the fire was determined from the heat of combustion and the volume flow rate of the fuel (see section 4.1.4.1) and assumes a combustion efficiency of 100%. The flowmeter was calibrated by collecting and measuring the quantity of fuel over known time intervals for a range of flow settings. Details of the flowmeter calibration are given in Appendix A. The hot gases from the fire were visualised by injecting smoke from a commercial smoke generator into the fire compartment. This highlighted the flowing gas layer from the compartment and the subsequent spill plume and smoke layer in the collecting hood.

4.1.1.3 The smoke collecting hood

The side walls of the smoke collecting hood were generally constructed from 10 mm thick CFI board with a 1 mm thick steel sheet substrate on each external face. However, one of the side walls was constructed from 10 mm thick transparent acrylic sheet to enable visual observations to be made of the smoke layer within the hood. The model was designed such that the walls could freely move in a vertical direction within a supporting steel frame. Each side wall contained locking bolts close to its base which could connect to the supporting frame at regular height intervals via holes in the frame (see Figure 4.5). This enabled the base of each wall to be moved independently to just below the base of the desired height of rise of plume allowing unrestricted fresh air to be entrained into the rising plume. This effectively simulated an unbounded balcony spill plume and prevented warming of the air beneath the observed smoke layer.

Figure 4.5: Locking mechanism for the walls of the smoke collecting hood

The supporting steel frame was designed such that each side wall could contain up to two, smaller modular walls each 2.0 m wide by 1.2 m high, which could be bolted together. This would then form a single wall on each face when examining deep smoke layers within the hood. The internal walls of the hood (except the acrylic wall) were painted black to aid visual observations of the smoke behaviour. A section of steel reinforcing mesh (painted red) was hung next to one wall of the collecting hood (see Figures 4.2 and 4.6) to provide a point of reference for visual observations for the plume behaviour. The individual grid size of the mesh was 75 by 75 mm, with 22 grids extending above the spill edge (i.e. the balcony edge in these experiments) and three below. There were nine grids horizontally projecting beyond the spill edge, with three grids prior to the edge.

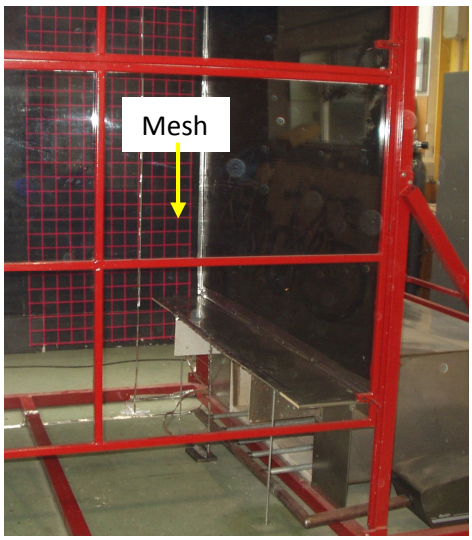

Figure 4.6: Mesh to assist visual observations of plume behaviour

For those tests which examined 2-D balcony spill plumes, screens were suspended from the ceiling of the collecting hood, in line with each side of the fire compartment opening to prevent the lateral spread of the plume both below and above the balcony (see Figure 4.7). These screens prevented air from entering the ends of the plume over its full height of rise. The dimensions of these screens were 1.2 m wide by 1.4 m high, made from 10 mm thick CFI board with a 1 mm thick steel sheet substrate on the external face. The screens were moveable and projected horizontally across the breadth of the balcony and continued 0.9 m beyond the spill edge. The screens projected 0.3 m below and 1.1 m above the spill edge.

Figure 4.7: Screens to prevent entrainment into the ends of the plume

The mechanical smoke exhaust system from the hood consisted of a 0.44 m diameter bifurcated fan attached to the hood exhaust vent using temperature resistant flexible ducting. The gases were exhausted to the outside of the laboratory through flexible ducting connected to the exhaust end of the fan (see Figure 4.8). The fan speed was controllable, which enabled different exhaust rates, and hence, variation in the height of rise of the plume to be examined.

The vent within the smoke exhaust hood contained a 'butterfly' damper which could be adjusted to alter the size of the vent from the hood. This was necessary for those experiments which required very low smoke exhaust rates from the hood.

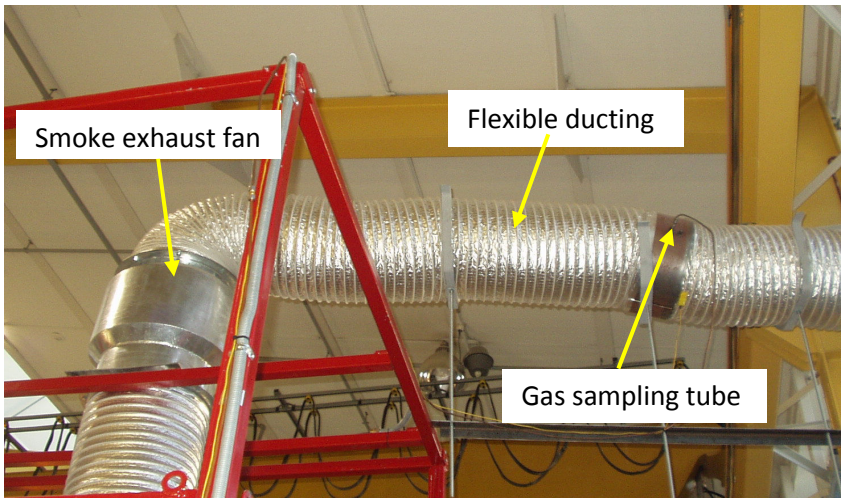

Figure 4.8: The smoke exhaust fan and ducting

4.1.2 Instrumentation

Measurements of temperature, velocity and carbon dioxide concentration of the gases within the model were made, in addition to visual and photographic records. Details of the instrumentation used are given below.

4.1.2.1 Gas temperatures

Gas temperatures were measured using 0.5 mm diameter chromel/alumel (K-type) thermocouples positioned at various locations in the model, as follows:

- Two columns of 15 thermocouples (Columns A and B) located within the smoke collecting hood.
- One column of 18 thermocouples (Column C) located below the centreline of the spill edge.
- An array of 23 thermocouples (Array A) spaced across the width of the spill edge, projecting 10 mm below the edge. The thermocouples were spaced to ensure that a minimum of five thermocouples were located across a flow of any width examined below the spill edge.
- For selected experiments, an array of 18 thermocouples (Array B) attached to an adjustable height steel stand to measure horizontal temperature profiles along the centreline of the plume (perpendicular to the spill edge) at incremental heights of rise (see Figure 4.9).
- Five thermocouples located in the throat of the exhaust vent in the smoke collecting hood.
- One thermocouple located centrally within the smoke exhaust duct (5 m downstream of the exhaust vent) adjacent to the gas sampling tube.
- Two thermocouples, one located next to each of two pitot-static tubes measuring the velocity of the gas flow below the spill edge.

Figure 4.10 and Appendix B detail the thermocouple locations and spacings.

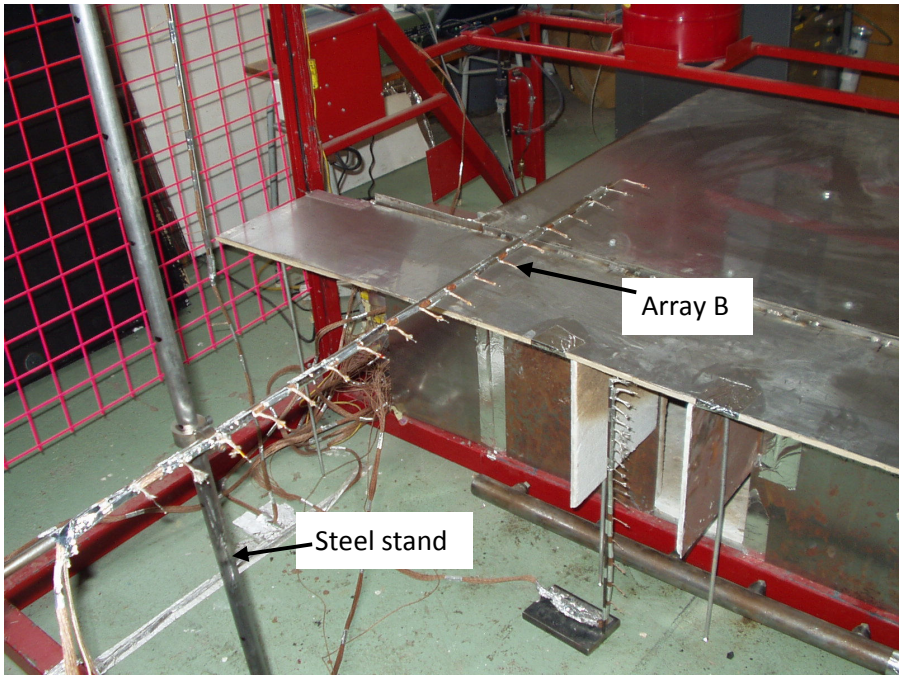

Figure 4.9: Array B to measure temperature profiles across the plume

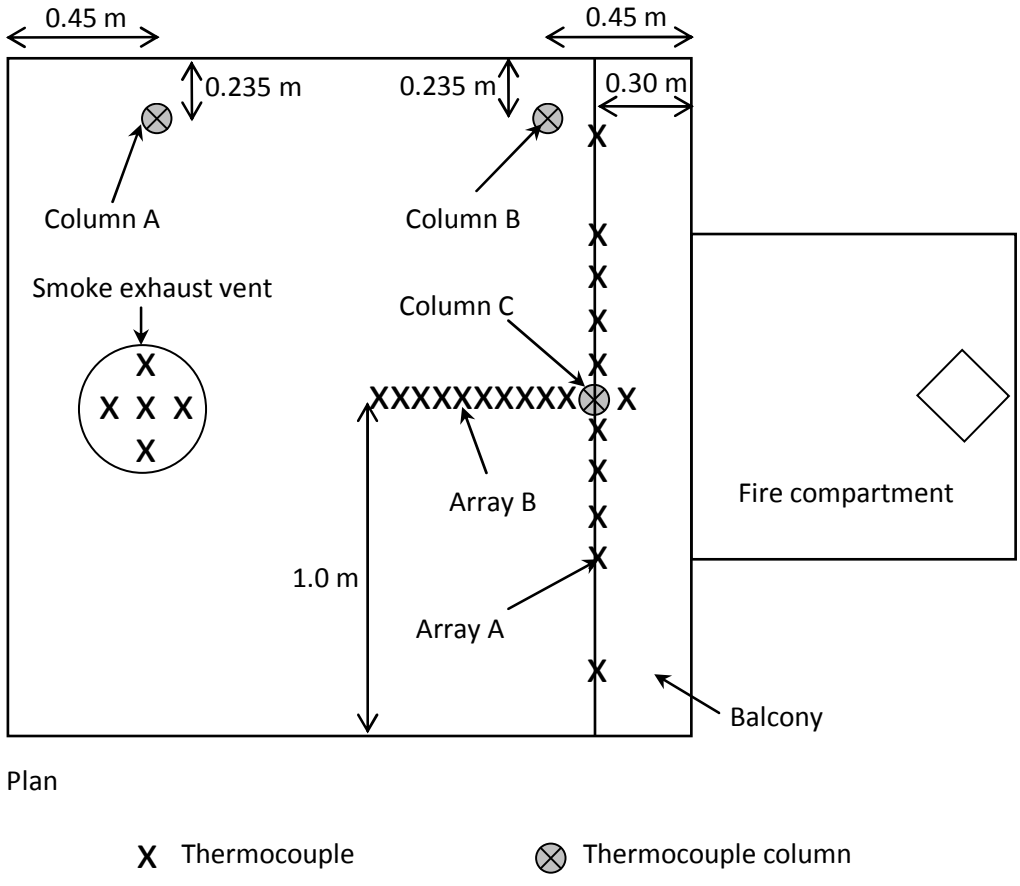

Figure 4.10: Thermocouple locations

4.1.2.2 Gas concentration

A perforated gas sampling tube was located across the horizontal diameter of the exhaust duct approximately 5.0 m downstream of the exhaust vent in the smoke collecting hood. This enabled measurement of the CO_2 gas concentration of the gas flow in the duct to be made using an infra red gas analyser (Siemens, Ultramat 6, accuracy ± < 1 %) which was calibrated on a daily basis. This measurement enabled the mass flow rate of gases in the smoke collecting hood to be determined (see section 4.1.4.5). The location of the gas sampling tube was chosen to ensure that sampling was from a flow that was homogeneous. A homogeneous gas flow would allow the gas concentration to be measured over a single diameter of the duct.

A study by Marshall [121] showed that for a fire below a naturally ventilated hood and vertical duct arrangement, without any flow baffles or bends, homogeneity was achieved at a height of approximately twelve duct diameters above the top of the hood. In this work, the sampling tube was located approximately eleven duct diameters from the exhaust vent. However, the configuration of the smoke exhaust system included additional factors to promote mixing of the flow, such as the 'butterfly' damper in the throat of the vent, the rotating fan blades of the mechanical exhaust and a 90° bend in the flexible ducting approximately 2 m downstream of the exhaust vent in the hood.

As a check to ensure that homogeneity was achieved at the sampling location, a test fire was carried out to measure temperature and CO_2 concentration profiles across horizontal and vertical diameters of the duct. Measurements were made at the centre of the duct, and at a distance of 0.11 and 0.21 m on either side of the centre for both horizontal and vertical diameters (for a 0.44 m diameter duct). The total heat release rate of the fire was 10 kW, for a plume produced from a 0.6 m wide compartment opening channelled by screens below the balcony. The height of rise of plume in the collecting hood was 0.9 m above the spill edge. The measured profiles across the duct in terms of gas CO_2 concentration and temperature (above ambient) are shown in Figures 4.11 and 4.12 respectively. The profiles show uniformity in the flow across the duct. This demonstrates that the flow at the sampling location was homogeneous, such that it was appropriate to measure the gas concentration using a perforated sampling tube across a single duct diameter.

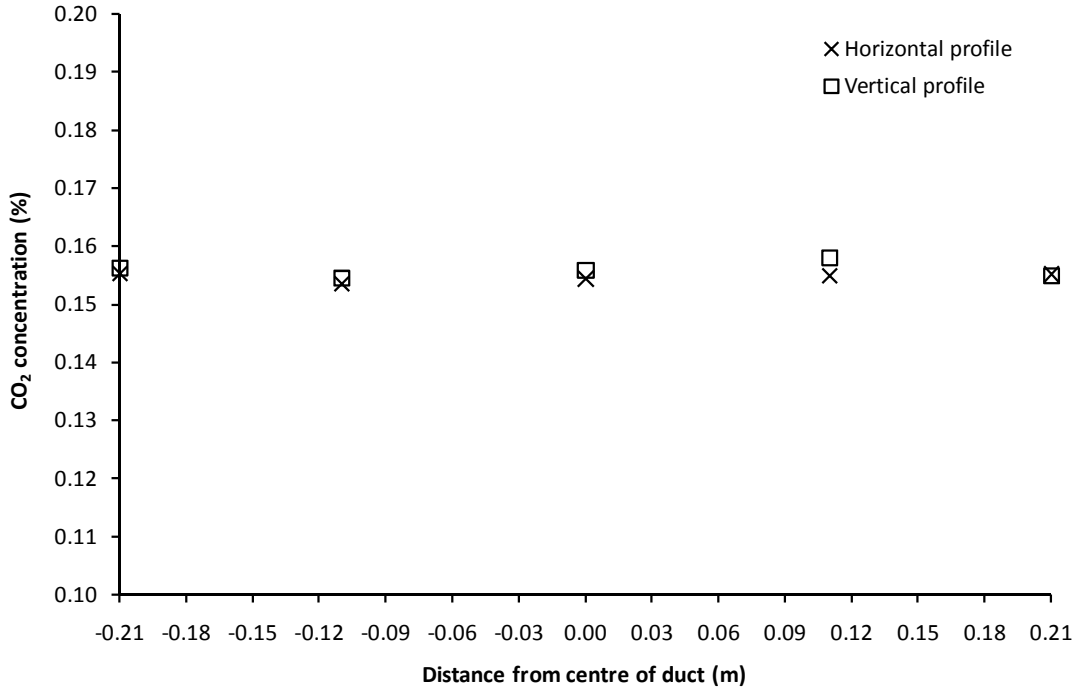

Figure 4.11: Profiles of CO_2 concentration at the gas sampling location

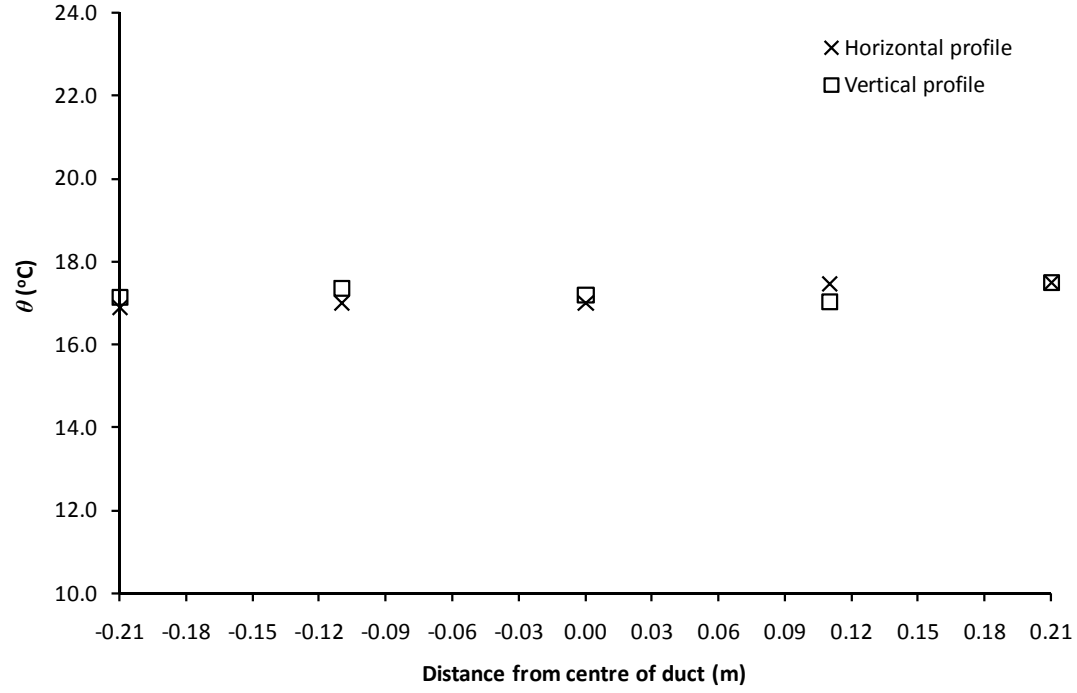

Figure 4.12: Profiles of temperature above ambient at the gas sampling location

4.1.2.3 Gas velocities

Vertical velocity profiles of the buoyant gas layer flow below the spill edge were made using two pitot-static tubes with a thermocouple attached to each tube. The gas velocity was calculated from the measured pressure differential from the pitot-tube and the gas temperature as given by Equation (4-1).

$$u = \sqrt{\frac{2\Delta PT}{\rho_{amb} T_{amb}}} \qquad \textbf{(4-1)}$$

The pitot-tubes were attached to a specially built steel stand which enabled vertical traverses to be made through the gas flow (see Figure 4.13). The pitot-tubes were each located a distance of one-third of the compartment opening width from each side of the opening. Each pitot-tube was connected to a sensitive differential pressure transducer (Furness Controls FCO 012, ± 1 and ± 10 Pa full scale range, accuracy ± 0.25 %).

Gas velocity measurements were made at each location every 10 mm below the spill edge until the base of the smoke layer was reached (i.e. from visual observations and until a negative flow, from the inflow, was measured). This measurement, in addition to the temperature profiles, enabled the mass flow rate and convective heat flow rate of the gas layer to be determined for a flow channelled by screens below the balcony (see sections 4.1.4.3 and 4.1.4.4). The use of channelling screens provides uniformity across the flow (i.e. horizontally) in terms of layer depth, velocity and temperature as demonstrated by Harrison [33] for flows which used the same fire compartment as in this work.

The mass flow rate and convective heat flow rate of layer flow below the spill edge for flows which were not channelled by screens was not determined, as lateral spread below the balcony caused the flow to become diffuse and non-uniform. Therefore, it was not practical to use velocity and temperature measurements in this case due to the excessive number of measurements points that would be required to characterise the flow below the spill edge.

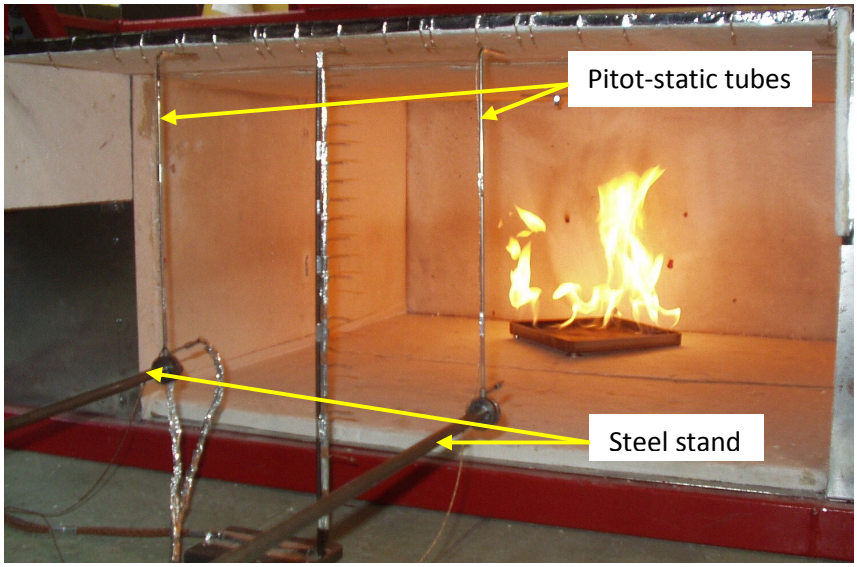

Figure 4.13: The pitot-tube arrangement

4.1.2.4 Data recording

All the instrument readings were recorded using University of Canterbury data logging boxes associated with the Universal Data Logging (UDL) software package. The data were stored directly on to the hard disc of a PC in the form of an EXCEL spreadsheet, from which the data could be further processed and analysed.

4.1.2.5 Visual records

Visual observations of each test were carried out, including the plume behaviour and the smoke layer depth below the spill edge and within the collecting hood. Cosmetic, non-toxic smoke was used to visualise the hot gas flow (as IMS burns with no visible smoke). Photographic and video records were made for selected tests.

4.1.2.6 Reynolds number of typical flows

As described in section 3.1.1, this particular form of scaling requires that the equivalent flows are turbulent on both full and model scale, (i.e. that turbulent flow is achieved for flows with Reynolds numbers ≥ 4000 [108] analogous to flow in a pipe).

The Reynolds number can be calculated using the following equation.

$$\mathrm{Re} = \frac{ul}{\upsilon} \qquad \textbf{(4-2)}$$

In this series of experiments the Reynolds number of the horizontally flowing layer flows below the spill edge were determined, with values to ranging between approximately 8100 and 20400 (see example calculation below). This demonstrated that the significant flows were fully turbulent and that scaling laws could be applied with confidence for the range of flows generated in the physical scale model.

Example of Reynolds number calculation

The Reynolds number determined in this example is for a layer flow channelled by screens below the spill edge, generated from a 5 kW fire with a compartment opening width of 1.0 m (i.e. Experiment C1).

The characteristic velocity used to determine the Reynolds number was the average velocity of the flowing layer below the spill edge, calculated using Equation (4-3).

$$\overline{u}_s = \frac{\dot{m}_s}{W_s d_s \overline{\rho}_s} \qquad \textbf{(4-3)}$$

Where, from Charles's Law,

$$\overline{\rho}_s = \frac{353}{\overline{\theta}_s + T_{amb}} \qquad \textbf{(4-4)}$$

Where, from the conservation of energy,

$$\overline{\theta}_s = \frac{\dot{Q}_c}{\dot{m}_s c_{p,air}} \qquad \textbf{(4-5)}$$

For the conditions studied, the following was measured in the model,

$\dot{m}_s$ = 0.059 kg s^{-1}

d_s = 0.10 m

$\dot{Q}_c$ = 3.60 kW

W_s = 1.0 m

T_{amb} = 294 K

Hence, using Equations (4-3), (4-4) and (4-5),

$\overline{u}_s$ = 0.59 m s^{-1}

$\overline{\rho}_s$ = 0.99 kg m^{-3}

$\overline{\theta}_s$ = 61 K

To determine the Reynolds number, the kinematic viscosity, υ, is required. The kinematic viscosity is temperature dependent, and for air at a temperature of 355 K (i.e. 61 K + 294 K) is given by,

υ = 20.91 x 10^{-6} m^2 s^{-1} [122]

The characteristic distance, *l*, is dependent on the shape and boundary conditions of the flow. A gas layer flow from a compartment opening which is channelled by screens is analogous to flow of a fluid in an open channel, as one surface of the flow is subjected to the atmosphere (i.e. the smoke layer base). For this type of flow, the hydraulic radius must be determined, which is the cross-sectional area of the flow divided by the perimeter of the flow in contact with the surface of the channelling boundaries [123], given by Equation (4-6).

$$R_H = \frac{W_s d_s}{(W_s + 2d_s)} \qquad \textbf{(4-6)}$$

The characteristic distance, l, for the layer flow is given as $4R_H$ [see Equation (4-7)], as this value obeys the same Reynolds number criterion for the onset of turbulence as in pipe flow (i.e. Re ≥ 4000) [123].

$$l = \frac{4W_s d_s}{(W_s + 2d_s)} \qquad \textbf{(4-7)}$$

Therefore, in this case, l = 0.333 m

Therefore, from Equation (4-2), the Reynolds number for this flow is,

$$\mathrm{Re} = \frac{(0.59)(0.333)}{(20.91 \times 10^{-6})} = 9405$$

4.1.3 Method

4.1.3.1 Parameters of interest

Some of the parameters of interest which may affect entrainment of air into a balcony spill plume are listed below:

- Total heat release rate of the fire.
- Mass flow rate of gases below the spill edge.
- Convective heat flow rate of the gases below the spill edge.
- Depth of gas layer below the spill edge.
- Height of rise of the spill plume.
- Type of balcony spill plume (e.g. channelled, unchannelled, 2-D and 3-D).
- Lateral extent of the plume at the spill edge (e.g. distance between channelling screens).
- Entrainment into the free ends of the plume.

4.1.3.2 Parameter variation

For the majority of the experiments, a 3-D balcony spill plume channelled by screens below the balcony was examined. The total heat release rate of the fire was varied with three fire sizes of 5, 10 and 15 kW examined. This equates to a fire size of 1.6, 3.2 and 4.7 MW respectively for a full scale equivalent using the scaling laws. The width of the fire compartment opening was varied with widths of 0.2, 0.4, 0.6, 0.8 and 1.0 m examined. Varying the total heat output of the fire in turn varied the mass flow rate, convective heat flow rate and depth of the gas layer flow below the spill edge. The conditions studied were chosen to provide a range of flows below the spill edge (i.e. from relatively cool, shallow and wide layer flows to hot, deep and narrow flows) which could conceivably be generated from a range of possible geometries upstream of the spill edge. The height of rise of plume above the spill edge was also varied with six different heights examined between 0 to 1.25 m.

The same conditions were examined for 3-D balcony spill plumes generated from a flow that was not channelled by screens below the balcony. However, the majority of experiments examined plumes generated from fires with a total heat release rate of 5 and 10 kW, as the lateral spread beneath the balcony for 15 kW fires was so great, that gases could not be collected in the hood above, thus, these experiments were not continued.

Selected experiments were carried out for a 2-D balcony spill plume to confirm and extend findings from previous work. For these experiments, the height of rise of plume above the balcony edge was varied with five different heights examined between 0 to 1.02 m. The width of the fire compartment opening was varied with widths of 0.2, 0.4, 0.6, 0.8 and 1.0 m examined. The total heat output of the fire remained fixed at 10 kW for the experiments without end entrainment.

The cross sectional area of the smoke collecting hood remained fixed (2.0 m long by 2.0 m wide) for the series of experiments. The breadth of the balcony was also fixed at 0.3 m.

4.1.3.3 The series of experiments

The series of experiments was carried out in three parts:

1. A series of 15 experiments to characterise the flow of hot gases below the spill edge, channelled by screens below the balcony (see Table 4.1).
2. A series of 3 experiments, to characterise the horizontal temperature profiles along the centreline of the plume (perpendicular to the spill edge) at incremental heights of rise above the spill edge (see Table 4.2).
3. A series of 182 experiments to systematically characterise entrainment of air into a balcony spill plume (see Table 4.3).

Experiment	$\dot{Q}_t$ (kW)	W_s (m)	Channelling screen depth (m)
C1	5.0	1.0	0.2
C2	10.0	1.0	0.2
C3	15.0	1.0	0.2
C4	5.0	0.8	0.2
C5	10.0	0.8	0.2
C6	15.0	0.8	0.2
C7	5.0	0.6	0.2
C8	10.0	0.6	0.2
C9	15.0	0.6	0.2
C10	5.0	0.4	0.2
C11	10.0	0.4	0.2
C12	15.0	0.4	0.2
C13	5.0	0.2	0.2
C14	10.0	0.2	0.2
C15	15.0	0.2	0.3

Table 4.1: The series of experiments to characterise the flow below the spill edge

Experiment	$\dot{Q}_t$ (kW)	W_s (m)	Channelling screen depth (m)
T1	10.0	1.0	0.2
T2	10.0	0.6	0.2
T3	10.0	0.2	0.2

Table 4.2: The series of experiments to characterise plume temperature profiles

Experiment	Plume type	$\dot{Q}_t$ (kW)	W_s (m)	z_s (m)	Channelling screen depth (m)
E1	3-D Balcony	5.0	1.0	0.00 ± 0.02	0.2
E2	3-D Balcony	10.0	1.0	0.00 ± 0.02	0.2
E3	3-D Balcony	15.0	1.0	0.00 ± 0.02	0.2
E4	3-D Balcony	5.0	1.0	0.00 ± 0.02	No screens
E5	3-D Balcony	10.0	1.0	0.00 ± 0.02	No screens
E6	3-D Balcony	15.0	1.0	0.00 ± 0.02	No screens
E7	3-D Balcony	5.0	0.8	0.00 ± 0.02	0.2
E8	3-D Balcony	10.0	0.8	0.00 ± 0.02	0.2
E9	3-D Balcony	15.0	0.8	0.00 ± 0.02	0.2
E10	3-D Balcony	5.0	0.8	0.00 ± 0.02	No screens
E11	3-D Balcony	10.0	0.8	0.00 ± 0.02	No screens
E12	3-D Balcony	15.0	0.8	0.00 ± 0.02	No screens
E13	3-D Balcony	5.0	0.6	0.00 ± 0.02	0.2
E14	3-D Balcony	10.0	0.6	0.00 ± 0.02	0.2
E15	3-D Balcony	15.0	0.6	0.00 ± 0.02	0.2
E16	3-D Balcony	5.0	0.6	0.00 ± 0.02	No screens
E17	3-D Balcony	10.0	0.6	0.00 ± 0.02	No screens
E18	3-D Balcony	15.0	0.6	0.00 ± 0.02	No screens
E19	3-D Balcony	5.0	0.4	0.00 ± 0.02	0.2
E20	3-D Balcony	10.0	0.4	0.00 ± 0.02	0.2
E21	3-D Balcony	15.0	0.4	0.00 ± 0.02	0.2
E22	3-D Balcony	5.0	0.4	0.00 ± 0.02	No screens
E23	3-D Balcony	10.0	0.4	0.00 ± 0.02	No screens
E24	3-D Balcony	15.0	0.4	0.00 ± 0.02	No screens
E25	3-D Balcony	5.0	0.2	0.00 ± 0.02	0.2
E26	3-D Balcony	10.0	0.2	0.00 ± 0.02	0.2
E27	3-D Balcony	15.0	0.2	0.00 ± 0.02	0.3
E28	3-D Balcony	5.0	0.2	0.00 ± 0.02	No screens
E29	3-D Balcony	10.0	0.2	0.00 ± 0.02	No screens
E30	3-D Balcony	15.0	0.2	0.00 ± 0.02	No screens
E61	3-D Balcony	5.0	0.2	0.30 ± 0.03	0.2
E62	3-D Balcony	10.0	0.2	0.30 ± 0.03	0.2
E63	3-D Balcony	15.0	0.2	0.30 ± 0.03	0.3
E64	3-D Balcony	5.0	0.2	0.30 ± 0.03	No screens
E65	3-D Balcony	10.0	0.2	0.30 ± 0.03	No screens
E66	3-D Balcony	15.0	0.2	0.30 ± 0.03	No screens
E67	3-D Balcony	5.0	0.4	0.30 ± 0.03	0.2
E68	3-D Balcony	10.0	0.4	0.30 ± 0.03	0.2
E69	3-D Balcony	15.0	0.4	0.30 ± 0.03	0.2
E70	3-D Balcony	5.0	0.4	0.30 ± 0.03	No screens
E71	3-D Balcony	10.0	0.4	0.30 ± 0.03	No screens
E72	3-D Balcony	15.0	0.4	0.30 ± 0.03	No screens
E73	3-D Balcony	5.0	0.6	0.30 ± 0.03	0.2
E74	3-D Balcony	10.0	0.6	0.30 ± 0.03	0.2
E75	3-D Balcony	15.0	0.6	0.30 ± 0.03	0.2

Table 4.3: The series of experiments to characterise balcony spill plume entrainment

Experiment	Plume type	$\dot{Q}_t$ (kW)	W_s (m)	z_s (m)	Channelling screen depth (m)
E76	3-D Balcony	5.0	0.6	0.30 ± 0.03	No screens
E77	3-D Balcony	10.0	0.6	0.30 ± 0.03	No screens
E78	3-D Balcony	5.0	0.8	0.30 ± 0.03	0.2
E79	3-D Balcony	10.0	0.8	0.30 ± 0.03	0.2
E80	3-D Balcony	15.0	0.8	0.30 ± 0.03	0.2
E81	3-D Balcony	5.0	0.8	0.30 ± 0.03	No screens
E82	3-D Balcony	10.0	0.8	0.30 ± 0.03	No screens
E83	3-D Balcony	5.0	1.0	0.30 ± 0.03	0.2
E84	3-D Balcony	10.0	1.0	0.30 ± 0.03	0.2
E85	3-D Balcony	15.0	1.0	0.30 ± 0.03	0.2
E86	3-D Balcony	5.0	1.0	0.30 ± 0.03	No screens
E87	3-D Balcony	10.0	1.0	0.30 ± 0.03	No screens
E88	3-D Balcony	5.0	1.0	0.50 ± 0.05	0.2
E89	3-D Balcony	10.0	1.0	0.50 ± 0.05	0.2
E90	3-D Balcony	15.0	1.0	0.50 ± 0.05	0.2
E91	3-D Balcony	5.0	1.0	0.50 ± 0.05	No screens
E92	3-D Balcony	10.0	1.0	0.50 ± 0.05	No screens
E93	2-D Balcony	10.0	1.0	0.55 ± 0.05	End screens
E94	3-D Balcony	5.0	0.8	0.50 ± 0.05	0.2
E95	3-D Balcony	10.0	0.8	0.50 ± 0.05	0.2
E96	3-D Balcony	15.0	0.8	0.50 ± 0.05	0.2
E97	3-D Balcony	5.0	0.8	0.50 ± 0.05	No screens
E98	3-D Balcony	10.0	0.8	0.50 ± 0.05	No screens
E99	2-D Balcony	10.0	0.8	0.55 ± 0.05	End screens
E100	3-D Balcony	5.0	0.6	0.50 ± 0.05	0.2
E101	3-D Balcony	10.0	0.6	0.50 ± 0.05	0.2
E102	3-D Balcony	15.0	0.6	0.50 ± 0.05	0.2
E103	3-D Balcony	5.0	0.6	0.50 ± 0.05	No screens
E104	3-D Balcony	10.0	0.6	0.50 ± 0.05	No screens
E105	2-D Balcony	10.0	0.6	0.55 ± 0.05	End screens
E106	3-D Balcony	5.0	0.4	0.50 ± 0.05	0.2
E107	3-D Balcony	10.0	0.4	0.50 ± 0.05	0.2
E108	3-D Balcony	15.0	0.4	0.50 ± 0.05	0.2
E109	3-D Balcony	5.0	0.4	0.50 ± 0.05	No screens
E110	3-D Balcony	10.0	0.4	0.50 ± 0.05	No screens
E111	2-D Balcony	10.0	0.4	0.55 ± 0.05	End screens
E112	3-D Balcony	5.0	0.2	0.50 ± 0.05	0.2
E113	3-D Balcony	10.0	0.2	0.50 ± 0.05	0.2
E114	3-D Balcony	15.0	0.2	0.50 ± 0.05	0.3
E115	3-D Balcony	5.0	0.2	0.50 ± 0.05	No screens
E116	3-D Balcony	10.0	0.2	0.50 ± 0.05	No screens
E117	2-D Balcony	10.0	0.2	0.55 ± 0.05	End screens
E158	3-D Balcony	5.0	1.0	0.73 ± 0.05	0.2
E159	3-D Balcony	10.0	1.0	0.73 ± 0.05	0.2
E160	3-D Balcony	15.0	1.0	0.73 ± 0.05	0.2

Table 4.3: (continued)

Experiment	Plume type	$\dot{Q}_t$ (kW)	W_s (m)	z_s (m)	Channelling screen depth (m)
E161	3-D Balcony	5.0	1.0	0.73 ± 0.05	No screens
E162	3-D Balcony	10.0	1.0	0.73 ± 0.05	No screens
E163	2-D Balcony	10.0	1.0	0.79 ± 0.05	End screens
E164	3-D Balcony	5.0	0.8	0.73 ± 0.05	0.2
E165	3-D Balcony	10.0	0.8	0.73 ± 0.05	0.2
E166	3-D Balcony	15.0	0.8	0.73 ± 0.05	0.2
E167	3-D Balcony	5.0	0.8	0.73 ± 0.05	No screens
E168	3-D Balcony	10.0	0.8	0.73 ± 0.05	No screens
E169	2-D Balcony	10.0	0.8	0.79 ± 0.05	End screens
E170	3-D Balcony	5.0	0.6	0.73 ± 0.05	0.2
E171	3-D Balcony	10.0	0.6	0.73 ± 0.05	0.2
E172	3-D Balcony	15.0	0.6	0.73 ± 0.05	0.2
E173	3-D Balcony	5.0	0.6	0.73 ± 0.05	No screens
E174	3-D Balcony	10.0	0.6	0.73 ± 0.05	No screens
E175	2-D Balcony	10.0	0.6	0.79 ± 0.05	End screens
E176	3-D Balcony	5.0	0.4	0.73 ± 0.05	0.2
E177	3-D Balcony	10.0	0.4	0.73 ± 0.05	0.2
E178	3-D Balcony	15.0	0.4	0.73 ± 0.05	0.2
E179	3-D Balcony	5.0	0.4	0.73 ± 0.05	No screens
E180	3-D Balcony	10.0	0.4	0.73 ± 0.05	No screens
E181	2-D Balcony	10.0	0.4	0.79 ± 0.05	End screens
E182	3-D Balcony	5.0	0.2	0.73 ± 0.05	0.2
E183	3-D Balcony	10.0	0.2	0.73 ± 0.05	0.2
E184	3-D Balcony	15.0	0.2	0.73 ± 0.05	0.3
E185	3-D Balcony	5.0	0.2	0.73 ± 0.05	No screens
E186	3-D Balcony	10.0	0.2	0.73 ± 0.05	No screens
E187	2-D Balcony	10.0	0.2	0.79 ± 0.05	End screens
E223	3-D Balcony	5.0	0.2	1.25 ± 0.05	0.2
E224	3-D Balcony	10.0	0.2	1.25 ± 0.05	0.2
E225	3-D Balcony	15.0	0.2	1.25 ± 0.05	0.3
E226	3-D Balcony	5.0	0.2	1.25 ± 0.05	No screens
E227	3-D Balcony	10.0	0.2	1.25 ± 0.05	No screens
E228	3-D Balcony	5.0	0.4	1.25 ± 0.05	0.2
E229	3-D Balcony	10.0	0.4	1.25 ± 0.05	0.2
E230	3-D Balcony	15.0	0.4	1.25 ± 0.05	0.2
E231	3-D Balcony	5.0	0.4	1.25 ± 0.05	No screens
E232	3-D Balcony	10.0	0.4	1.25 ± 0.05	No screens
E233	3-D Balcony	5.0	0.6	1.25 ± 0.05	0.2
E234	3-D Balcony	10.0	0.6	1.25 ± 0.05	0.2
E235	3-D Balcony	15.0	0.6	1.25 ± 0.05	0.2
E236	3-D Balcony	5.0	0.6	1.25 ± 0.05	No screens
E237	3-D Balcony	10.0	0.6	1.25 ± 0.05	No screens
E238	3-D Balcony	5.0	0.8	1.25 ± 0.05	0.2
E239	3-D Balcony	10.0	0.8	1.25 ± 0.05	0.2
E240	3-D Balcony	15.0	0.8	1.25 ± 0.05	0.2

Table 4.3: (continued)

Experiment	Plume type	$\dot{Q}_t$ (kW)	W_s (m)	z_s (m)	Channelling screen depth (m)
E241	3-D Balcony	5.0	0.8	1.25 ± 0.05	No screens
E242	3-D Balcony	10.0	0.8	1.25 ± 0.05	No screens
E243	3-D Balcony	5.0	1.0	1.25 ± 0.05	0.2
E244	3-D Balcony	10.0	1.0	1.25 ± 0.05	0.2
E245	3-D Balcony	15.0	1.0	1.25 ± 0.05	0.2
E246	3-D Balcony	5.0	1.0	1.25 ± 0.05	No screens
E247	3-D Balcony	10.0	1.0	1.25 ± 0.05	No screens
E248	3-D Balcony	5.0	1.0	0.95 ± 0.05	0.2
E249	3-D Balcony	10.0	1.0	0.95 ± 0.05	0.2
E250	3-D Balcony	15.0	1.0	0.95 ± 0.05	0.2
E251	3-D Balcony	5.0	1.0	0.95 ± 0.05	No screens
E252	3-D Balcony	10.0	1.0	0.95 ± 0.05	No screens
E253	2-D Balcony	10.0	1.0	1.02 ± 0.05	End screens
E254	3-D Balcony	5.0	0.8	0.95 ± 0.05	0.2
E255	3-D Balcony	10.0	0.8	0.95 ± 0.05	0.2
E256	3-D Balcony	15.0	0.8	0.95 ± 0.05	0.2
E257	3-D Balcony	5.0	0.8	0.95 ± 0.05	No screens
E258	3-D Balcony	10.0	0.8	0.95 ± 0.05	No screens
E259	2-D Balcony	10.0	0.8	1.02 ± 0.05	End screens
E260	3-D Balcony	5.0	0.6	0.95 ± 0.05	0.2
E261	3-D Balcony	10.0	0.6	0.95 ± 0.05	0.2
E262	3-D Balcony	15.0	0.6	0.95 ± 0.05	0.2
E263	3-D Balcony	5.0	0.6	0.95 ± 0.05	No screens
E264	3-D Balcony	10.0	0.6	0.95 ± 0.05	No screens
E265	2-D Balcony	10.0	0.6	1.02 ± 0.05	End screens
E266	3-D Balcony	5.0	0.4	0.95 ± 0.05	0.2
E267	3-D Balcony	10.0	0.4	0.95 ± 0.05	0.2
E268	3-D Balcony	15.0	0.4	0.95 ± 0.05	0.2
E269	3-D Balcony	5.0	0.4	0.95 ± 0.05	No screens
E270	3-D Balcony	10.0	0.4	0.95 ± 0.05	No screens
E271	2-D Balcony	10.0	0.4	1.02 ± 0.05	End screens
E272	3-D Balcony	5.0	0.2	0.95 ± 0.05	0.2
E273	3-D Balcony	10.0	0.2	0.95 ± 0.05	0.2
E274	3-D Balcony	15.0	0.2	0.95 ± 0.05	0.3
E275	3-D Balcony	5.0	0.2	0.95 ± 0.05	No screens
E276	3-D Balcony	10.0	0.2	0.95 ± 0.05	No screens
E277	2-D Balcony	10.0	0.2	1.02 ± 0.05	End screens
E278	2-D Balcony	10.0	1.0	0.31 ± 0.03	End screens
E279	2-D Balcony	10.0	0.8	0.31 ± 0.03	End screens
E280	2-D Balcony	10.0	0.6	0.31 ± 0.03	End screens
E281	2-D Balcony	10.0	0.4	0.31 ± 0.03	End screens
E282	2-D Balcony	10.0	0.2	0.31 ± 0.03	End screens
E288	2-D Balcony	10.0	0.2	0.00 ± 0.02	End screens
E289	2-D Balcony	10.0	0.4	0.00 ± 0.02	End screens
E290	2-D Balcony	10.0	0.6	0.00 ± 0.02	End screens
E291	2-D Balcony	10.0	0.8	0.00 ± 0.02	End screens
E292	2-D Balcony	10.0	1.0	0.00 ± 0.02	End screens

Table 4.3: (continued)

4.1.3.4 Experimental procedure

The experimental procedure for the series of 15 test fires to characterise the flow below the spill edge was as follows:

1. The required fire compartment geometry to be examined was set up.
2. The pitot-tube arrangement was then set up.
3. The mechanical exhaust fan was switched on to provide exhaust from the hood.
4. IMS was then fed into the fire tray at a controlled and measured rate.
5. The fuel was ignited and the fire within the compartment was allowed to burn until the gas temperature below the spill edge had reached stability.
6. The smoke generator was switched on and smoke was injected just below the gas layer in the compartment.
7. The speed of the mechanical exhaust fan was adjusted so that the smoke layer in the collecting hood was approximately 1.2 m above the spill edge.
8. Visual observations were made of the smoke behaviour below the spill edge.
9. The smoke generator was switched off.
10. Gas velocity and temperature measurements were made at each location every 10 mm below the spill edge until the base of the smoke layer was reached (i.e. from visual observations and when a negative velocity, from the inflow, was measured). These data were stored directly to a PC and recorded for a period of 60 s for each measurement point, sampling at a rate of every 1 s.

The experimental procedure for the series of 3 test fires to characterise the horizontal temperature profiles across the plume with respect to height of rise was as follows:

1. The required fire compartment geometry and smoke collecting hood height (i.e. height of rise of the spill plume) was set up.
2. The thermocouple array (Array B) was located at a height level with the spill edge (i.e. 0.5 m above the floor).
3. The mechanical exhaust fan was switched on to provide exhaust from the hood.
4. IMS was then fed into the fire tray at a controlled and measured rate.
5. The fuel was ignited and the fire within the compartment was allowed to burn until the gas temperature below the spill edge had reached stability.

6. The smoke generator was switched on and smoke was injected just below the gas layer in the compartment.
7. The speed of the mechanical exhaust fan was adjusted so that the smoke layer in the collecting hood was approximately 1.0 m above the spill edge.
8. Visual observations were made of the smoke behaviour and depth.
9. The smoke generator was switched off.
11. Gas temperature measurements were made using the thermocouple array at heights of rise between 0 and 1.0 m above the spill edge, at 0.1 m intervals (i.e. 11 measurement locations). These data were stored directly to a PC and recorded for a period of 60 s for each measurement point, sampling at a rate of every 1 s.

The experimental procedure for the series of 182 test fires to examine entrainment of air into a balcony spill plume was as follows:

1. The required fire compartment geometry and smoke collecting hood height (i.e. height of rise of the spill plume) was set up.
2. The mechanical exhaust fan was switched on to provide exhaust from the hood.
3. IMS was fed into the fire tray at a controlled and measured rate.
4. The fuel was ignited and the fire within the compartment was allowed to burn until the gas temperatures had reached stability.
5. The smoke generator was switched on and smoke was injected just below the gas layer in the compartment.
6. Visual observations were made of the smoke layer depth beneath the spill edge and the behaviour of the plume as it flowed into the collecting hood.
7. The speed of the mechanical exhaust fan was adjusted until the base of the smoke layer was contained with smoke collecting hood (approximately 60 mm above the base of the hood).
8. The smoke generator was switched off.
9. Measurements were made of the gas temperatures and the concentration of CO_2 in the duct. These data were stored directly to a PC and recorded for a period of 60 s, sampling at a rate of every 1 s.

4.1.4 Data reduction

4.1.4.1 Heat output of IMS fuel source

The heat output of the IMS fuel source was determined from the measured flow rate of fuel through the flowmeter and the heat of combustion and the density of IMS [124,125] (see Appendix A). The total heat release rate of the fire was calculated using Equation (4-8).

$$\dot{Q}_t = c_{IMS}\rho_{IMS}\dot{V}_{IMS} \qquad \textbf{(4-8)}$$

4.1.4.2 Gas layer depth

The gas layer depth was generally determined from visual observations, however, it was also determined from vertical temperature profiles using a method given by Thomas *et al.* [30] [see Equation (4-9)]. The temperature measurements enabled buoyancy [i.e. (θ/T)] profiles with respect to height above the floor to be determined. The method essentially converts the area beneath the buoyancy profile into an equivalent "top hat" profile to determine the layer depth. Hansell *et al.* [32] demonstrated that the performance of this method was dependent on the aspect ratio of the layer, with good agreement obtained with visual observations for broad, shallow layers, but not so good for narrow, deep layers. The performance of this method is likely to be dependent on the shape of the buoyancy profile, as profiles that significantly depart from a "top hat" (e.g. a triangular profile) give poorer agreement with visual observations [59].

$$d_l\theta_{\max} = T_{\max}\int_0^{h_{ceil}}(\theta/T)(y)dy \qquad \textbf{(4-9)}$$

To determine the layer depth, (θ/T) versus y was plotted. An integration of the resulting curve $\int_0^{h_{ceil}}(\theta/T)(y)dy$ was found using the trapezoid rule in a spreadsheet. This area was divided by $(\theta_{\max}/T_{\max})$ to determine the layer depth.

4.1.4.3 Calculation of the mass flow rate of gases below the spill edge

The mass flow rate of gases below the spill edge (for channelled flow) was determined from vertical velocity and temperature profiles of the gas layer below the spill edge, obtained from the pitot-tube traverses. To determine total mass flow rate of gases below the spill edge, an integration of the plot of $W_s \rho u$ with respect to d_s (determined from visual observations and when the velocity of the flow was zero) was performed as given by Equation (4-10). The integration was done using the trapezoid rule in a spreadsheet and assumes a uniform profile in terms of temperature and velocity across the lateral extent of the flow below the spill edge.

$$\dot{m}_s = W_s \int_0^{d_s} \rho u(y)\, dy \qquad \textbf{(4-10)}$$

4.1.4.4 Calculation of the convective heat flow rate of gases below the spill edge

Similarly, the convective heat flow of the gases below the spill edge (for channelled flow) was determined using the results of the vertical velocity and temperature profiles, by performing an integration of the plot of $W_s \rho u c_{p,air} \theta$ with respect to d_s as given by Equation (4-11). The integration was done using the trapezoid rule in a spreadsheet and assumes a uniform profile in terms of temperature and velocity across the lateral extent of the flow below the spill edge.

$$\dot{Q}_c = W_s\, c_{p,air} \int_0^{d_s} \theta \rho u(y)\, dy \qquad \textbf{(4-11)}$$

4.1.4.5 Calculation of the mass flow rate of gases in the collecting hood

The mass flow rate of gases entering the buoyant gas layer in the smoke collecting hood, and therefore leaving the hood, was found by using a tracer gas technique and calculation method. In this study the tracer gas was CO_2 produced from the fire and by monitoring its concentration from the source, the amount of mixing can be calculated.

Properties of tracer gases are [126]:

- A density similar to that of air.
- Not normally present in air.
- A concentration that can accurately and easily be measured when diluted.
- Readily available and cheap.
- Non-flammable and non-explosive.
- Non-toxic in the concentration used.
- Non-reactive, non-absorbed or non-decomposed.

This technique has been used in many previous studies of smoke movement [e.g. 34,48,81,90,106,126], is detailed by Marshall [106], and is described here for completeness:

In the combustion of IMS, the gas layer in the hood can be considered to consist of hot air and tracer CO_2 produced by the fire. Although CO_2 is present in air, it is only approximately 0.03% by volume. The ambient CO_2 concentration can be measured and taken into account.

Dalton's law of partial pressures states "the pressure exerted by a mixture of gases behaving perfectly is the sum of the pressures exerted by the individual gases occupying the same volume alone". Hence, taking this law and the perfect gas equation of state, when CO_2 mixes with air it moves with the air and contributes to the overall gas pressure, as given by Equation (4-12).

$$\left(P_{air} + P_{CO_2}\right)V = \frac{n'_{air} + n'_{CO_2}}{N} RT \qquad \textbf{(4-12)}$$

Where n' is the number of gas molecules in the volume V. As air is a mixture of gases including CO_2, n'_{air} is taken to include the ambient CO_2 present in air, consequently n'_{CO_2} is the number of additional (i.e. tracer) molecules of CO_2 present.

Equation (4-12) can also be written as,

$$\left(V_{air} + V_{CO_2}\right)P = \frac{n'_{air} + n'_{CO_2}}{N} RT \qquad \textbf{(4-13)}$$

Considering the CO_2 tracer gas on its own,

$$PV_{CO_2} = \frac{n'_{CO_2}}{N} RT \qquad \textbf{(4-14)}$$

Therefore, the CO_2 gas concentration above ambient (τ) by volume is, from Equations (4-13) and (4-14),

$$\tau = \frac{n'_{CO_2}}{n'_{air} + n'_{CO_2}} = \frac{V_{CO_2}}{V_{air} + V_{CO_2}} \qquad \textbf{(4-15)}$$

A concentration by volume is equivalent to a molar concentration and is not dependent on changes in temperature in a sample of gases removed from the model.

From Equation (4-15), and replacing V with $\dot{V}$ gives the volume flow rate of air through the model, such that,

$$\dot{V}_{air} = \frac{\left(1-\tau\right)}{\tau} \dot{V}_{CO_2} \qquad \textbf{(4-16)}$$

The mass flow rate of air is given by,

$$\dot{m}_{air} = \dot{V}_{air} \rho_{air,amb}$$

$$\Rightarrow \dot{m}_{air} = \dot{V}_{air} \frac{\rho_{air,T} T}{T_{amb}} \qquad \textbf{(4-17)}$$

Substituting Equation (4-16) into Equation (4-17) gives,

$$\dot{m}_{air} = \frac{(1-\tau)\rho_{air,T} T \dot{V}_{CO_2}}{\tau T_{amb}} \quad \textbf{(4-18)}$$

The mass flow rate of CO_2 is given by,

$$\dot{m}_{CO_2} = \dot{V}_{CO_2} \frac{\rho_{CO_2,T}\, T}{T_{amb}} \quad \textbf{(4-19)}$$

The total mass flow rate of gases is given by $\dot{m}_{air} + \dot{m}_{CO_2}$, hence,

$$\dot{m} = \frac{\dot{V}_{CO_2} T}{T_{amb}} \left[\rho_{CO_2,T} + \frac{(1-\tau)\rho_{air,T}}{\tau} \right] \quad \textbf{(4-20)}$$

Where, $\rho_{air,T}$ and $\rho_{CO_2,T}$ are evaluated at standard temperature, T = 273 K and $\dot{V}_{CO_2}$ is evaluated at T_{amb}. $\dot{V}_{CO_2}$ was calculated from the mass of fuel burnt. IMS is essentially denatured ethanol. A material safety data sheet for this fuel is given in Appendix C. The chemical equation for the combustion of ethanol is given by,

$$C_2H_5OH + 3O_2 \rightarrow 3H_2O + 2CO_2 \quad \textbf{(4-21)}$$

Therefore, one mole of ethanol produced two moles of CO_2. One mole of CO_2 will occupy 22.4 x 10^{-3} m^3 at standard temperature and pressure. One mole of ethanol weighs 0.046 kg. Hence, burning 0.046 kg of IMS produces 44.8 x 10^{-3} m^3 of CO_2. Therefore,

$$\dot{V}_{CO_2} = \frac{0.0448}{0.046} \dot{m}_{IMS} \quad \textbf{(4-22)}$$

Where $\dot{m}_{IMS}$ was determined from the fuel flowmeter calibration.

4.1.4.6 Error analysis

Although the experimental measurements were made during steady state conditions, fluctuations in various measurements (e.g. temperature, velocity, mass flow rate) occurred during the sampling period. Therefore, the experimental results were determined in terms of a time averaged mean value with an associated standard error. The standard error was determined by dividing the standard deviation of the sample by the square root of the number of samples. The standard deviations of the mean values were determined using the relevant function given in the EXCEL spreadsheet package.

4.2 Adhered spill plume experiments

4.2.1 The physical scale model

The physical scale model was essentially the same as that described in section 4.1.1 with minor modifications made to the geometry of the fire compartment and the smoke collecting hood as shown in Figures 4.14 and 4.15 and described below. The spill edge is defined as the top of the fire compartment opening for the adhered plume experiments.

Figure 4.14: The 1/10th physical scale model

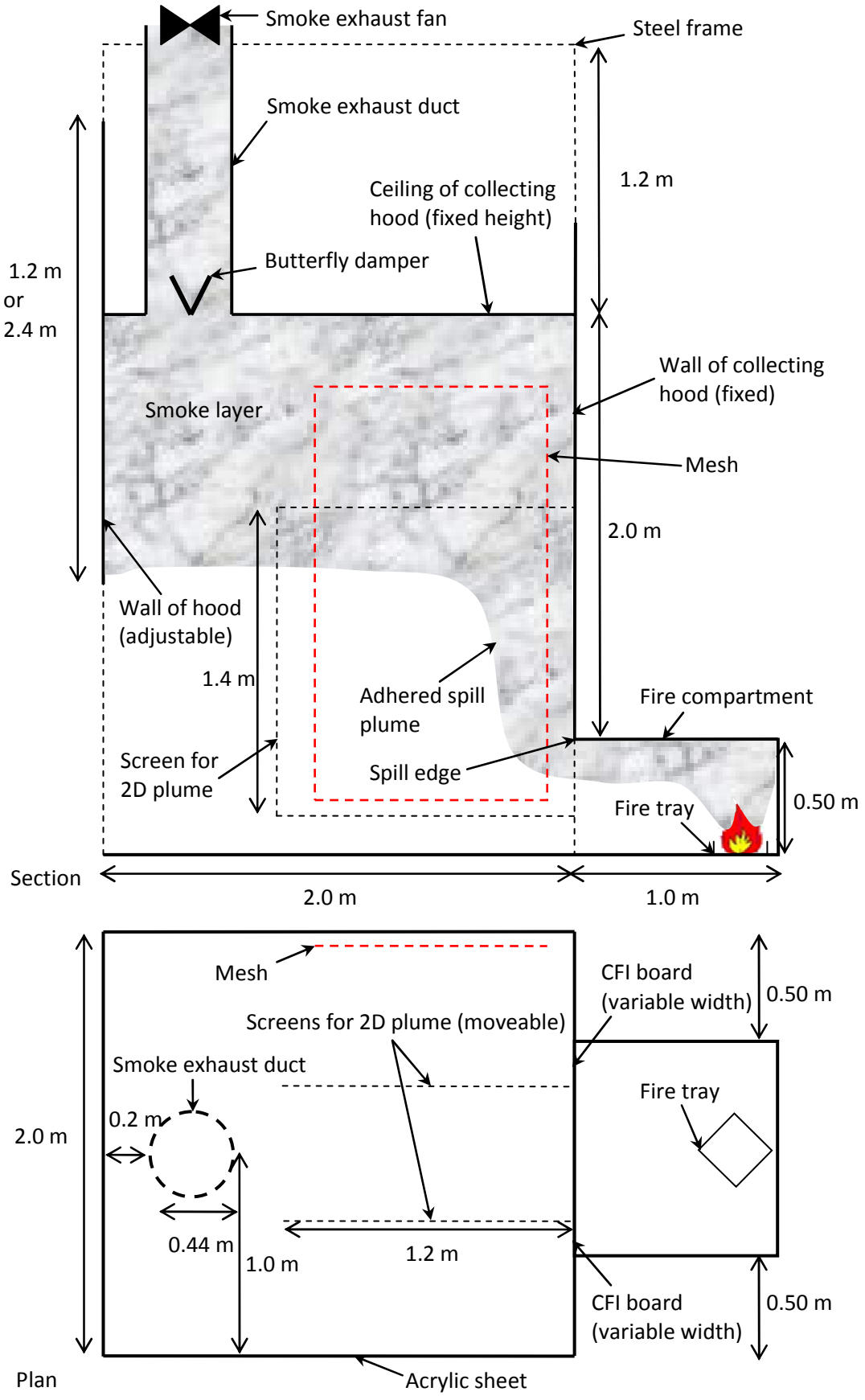

Figure 4.15: Schematic of the physical scale model

4.2.1.1 The fire compartment

The fire compartment was identical to that described in section 4.1.1.1 with the exception that there was no balcony or under balcony channelling screens located beyond the opening (see Figure 4.16).

Figure 4.16: The fire compartment

4.2.1.2 The smoke collecting hood

The smoke collecting hood was essentially the same as described in section 4.1.1.3. However, the wall of the collecting hood directly above the fire compartment opening was lowered so that it extended from the top of the compartment and beyond the ceiling of the hood. This simulated a vertically projecting wall above the spill edge as required for the adhered plume scenario (see Figures 4.14 to 4.16).

The mesh that was used to aid visual observations within the hood for the balcony spill plume experiments was also used for the adhered plume experiments. The mesh was located 75 mm from the wall of the hood above the fire compartment, with twelve grids projecting horizontally, 22 grids extending vertically above the spill edge and three below.

For those tests which examined 2-D adhered plumes, identical screens to that described in section 4.1.1.3 were used within the collecting hood to prevent entrainment into the ends of the plume (see Figure 4.17). The screens horizontally projected a distance of 1.2 m from the spill edge, and vertically projected 0.3 m below and 1.1 m above the spill edge.

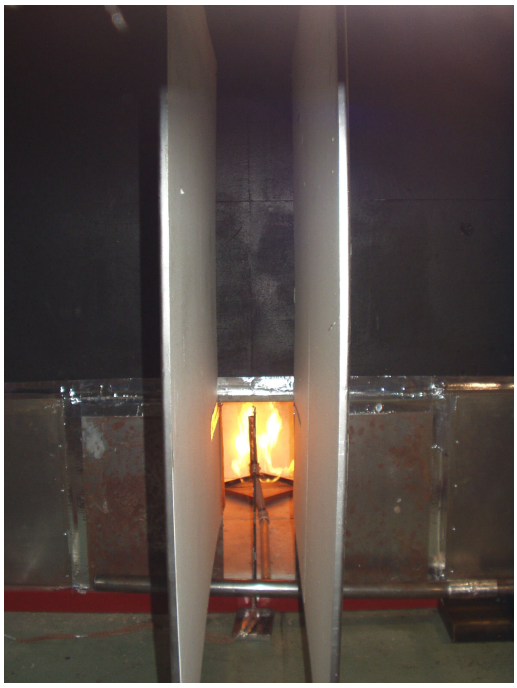

Figure 4.17: Screens to prevent entrainment into the ends of the plume

4.2.2 Instrumentation

Measurements of temperature, velocity and carbon dioxide concentration of the gases within the model were made, in addition to visual and photographic records. Details of the instrumentation used are given below.

4.2.2.1 Gas temperatures

Gas temperatures in the model were measured using 0.5 mm diameter K-type thermocouples at identical locations to that described in section 4.1.2.1 (the only difference is that the spill edge is defined as the top of the compartment opening).

Additional temperature measurements were made using a column of 18 thermocouples (Column D) above the spill edge along the centreline of the plume, 5 mm from the wall of the collecting hood above the spill edge.

For selected experiments, Array B was again used to measure horizontal temperature profiles along the centreline of the plume (perpendicular to the spill edge) at incremental heights of rise above the spill edge. Figure 4.18 and Appendix B details the thermocouple locations and spacings.

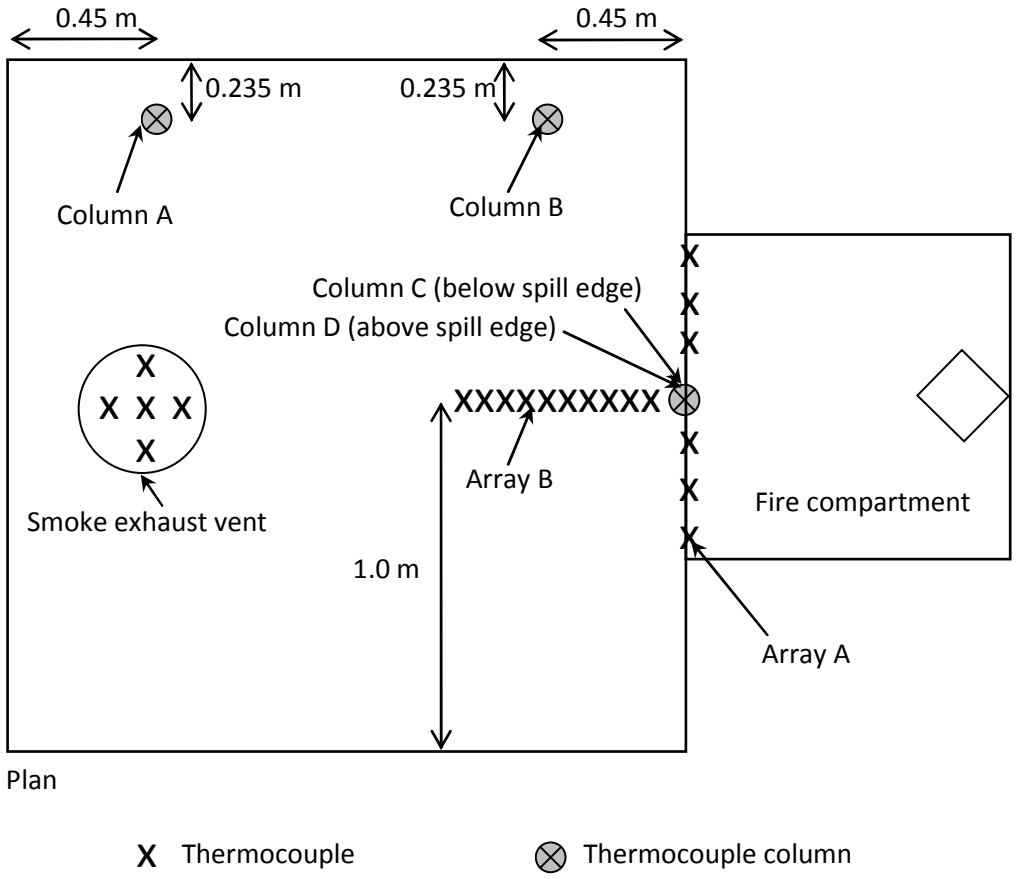

Figure 4.18: Thermocouple locations

4.2.2.2 Gas concentration

The measurement of gas concentration in the smoke exhaust duct was the same as that described in section 4.1.2.2.

4.2.2.3 Gas velocities

Measurement of vertical velocity profiles of the gas layer below the spill edge used the same technique as described in section 4.1.2.3.

4.2.2.4 Data recording and visual records

The methods used for data recording and to obtain visual records were the same as described in sections 4.1.2.4 and 4.1.2.5.

4.2.2.5 Reynolds number of typical flows

The Reynolds number of the horizontally flowing layer flows below the spill edge had values to ranging between approximately 7000 and 12500, using the same calculation method described in section 4.1.2.6. This demonstrated that the significant flows were fully turbulent and that scaling laws could be applied with confidence.

4.2.3 Method

4.2.3.1 Parameters of interest

Some of the parameters of interest which may affect entrainment of air into an adhered spill plume are listed below:

- Total heat release rate of the fire.
- Mass flow rate of gases below the spill edge.
- Convective heat flow rate of the gases below the spill edge.
- Depth of gas layer below the spill edge.
- Height of rise of the spill plume.
- Type of adhered spill plume (e.g. 2-D and 3-D).
- Lateral extent of the plume at the spill edge.
- Entrainment into the free ends of the plume.

4.2.3.2 Parameter variation

The majority of experiments examined a 3-D adhered spill plume. The total heat release rate of the fire was varied with fire sizes of 5, 10 and 15 kW examined. Varying the total heat output of the fire in turn varied the mass flow rate, convective heat flow rate and depth of the gas layer below the spill edge. The width of the fire compartment opening was varied with widths of 0.2, 0.4, 0.6, 0.8 and 1.0 m examined. The conditions studied were again chosen to provide a range of flows below the spill edge as in the balcony spill plume experiments. The height of rise of plume above the spill edge was also varied with six different heights examined between 0 to 1.25 m.

Selected experiments were carried out to examine 2-D adhered spill plumes to confirm and extend findings from previous work. For these experiments, the height of rise of plume above the balcony edge was varied with five different heights examined between 0 to 1.10 m. The width of the fire compartment opening was varied with widths of 0.2, 0.4, 0.6, 0.8 and 1.0 m examined. The total heat output of the fire remained fixed at 10 kW for the experiments without end entrainment.

The cross sectional area of the smoke collecting hood remained fixed (2.0 m long by 2.0 m wide) for the series of experiments.

4.2.3.3 The series of experiments

The series of experiments was carried out in three parts:

1. A series of 15 experiments to characterise the flow of hot gases below the spill edge (see Table 4.4).
2. A series of 3 experiments, to characterise the horizontal temperature profiles along the centreline of the plume (perpendicular to the spill edge) at incremental heights of rise above the spill edge (see Table 4.5).
3. A series of 110 experiments to systematically characterise entrainment of air into an adhered spill plume (see Table 4.6).

Experiment	$\dot{Q}_t$ (kW)	W_s (m)
C16	5.0	0.2
C17	10.0	0.2
C18	15.0	0.2
C19	5.0	0.4
C20	10.0	0.4
C21	15.0	0.4
C22	5.0	0.6
C23	10.0	0.6
C24	15.0	0.6
C25	5.0	0.8
C26	10.0	0.8
C27	15.0	0.8
C28	5.0	1.0
C29	10.0	1.0
C30	15.0	1.0

Table 4.4: The series of experiments to characterise the flow below the spill edge

Experiment	$\dot{Q}_t$ (kW)	W_s (m)
T4	10.0	1.0
T5	10.0	0.6
T6	10.0	0.2

Table 4.5: The series of experiments to characterise plume temperature profiles

Experiment	Plume type	$\dot{Q}_t$ (kW)	W_s (m)	z_s (m)
E31	3-D Adhered	5.0	0.2	0.00 ± 0.02
E32	3-D Adhered	10.0	0.2	0.00 ± 0.02
E33	3-D Adhered	15.0	0.2	0.00 ± 0.02
E34	3-D Adhered	5.0	0.4	0.00 ± 0.02
E35	3-D Adhered	10.0	0.4	0.00 ± 0.02
E36	3-D Adhered	15.0	0.4	0.00 ± 0.02
E37	3-D Adhered	5.0	0.6	0.00 ± 0.02
E38	3-D Adhered	10.0	0.6	0.00 ± 0.02
E39	3-D Adhered	15.0	0.6	0.00 ± 0.02
E40	3-D Adhered	5.0	0.8	0.00 ± 0.02
E41	3-D Adhered	10.0	0.8	0.00 ± 0.02
E42	3-D Adhered	15.0	0.8	0.00 ± 0.02

Table 4.6: The series of experiments to characterise adhered spill plume entrainment

Experiment	Plume type	$\dot{Q}_t$ (kW)	W_s (m)	z_s (m)
E43	3-D Adhered	5.0	1.0	0.00 ± 0.02
E44	3-D Adhered	10.0	1.0	0.00 ± 0.02
E45	3-D Adhered	15.0	1.0	0.00 ± 0.02
E46	3-D Adhered	5.0	1.0	0.30 ± 0.02
E47	3-D Adhered	10.0	1.0	0.30 ± 0.02
E48	3-D Adhered	15.0	1.0	0.30 ± 0.02
E49	3-D Adhered	5.0	0.8	0.30 ± 0.02
E50	3-D Adhered	10.0	0.8	0.30 ± 0.02
E51	3-D Adhered	15.0	0.8	0.30 ± 0.02
E52	3-D Adhered	5.0	0.6	0.30 ± 0.02
E53	3-D Adhered	10.0	0.6	0.30 ± 0.02
E54	3-D Adhered	15.0	0.6	0.30 ± 0.02
E55	3-D Adhered	5.0	0.4	0.30 ± 0.02
E56	3-D Adhered	10.0	0.4	0.30 ± 0.02
E57	3-D Adhered	15.0	0.4	0.30 ± 0.02
E58	3-D Adhered	5.0	0.2	0.30 ± 0.02
E59	3-D Adhered	10.0	0.2	0.30 ± 0.02
E60	3-D Adhered	15.0	0.2	0.30 ± 0.02
E118	3-D Adhered	5.0	0.2	0.50 ± 0.05
E119	3-D Adhered	10.0	0.2	0.50 ± 0.05
E120	3-D Adhered	15.0	0.2	0.50 ± 0.05
E121	2-D Adhered	10.0	0.2	0.50 ± 0.05
E122	3-D Adhered	5.0	0.4	0.50 ± 0.05
E123	3-D Adhered	10.0	0.4	0.50 ± 0.05
E124	3-D Adhered	15.0	0.4	0.50 ± 0.05
E125	2-D Adhered	10.0	0.4	0.56 ± 0.05
E126	3-D Adhered	5.0	0.6	0.50 ± 0.05
E127	3-D Adhered	10.0	0.6	0.50 ± 0.05
E128	3-D Adhered	15.0	0.6	0.50 ± 0.05
E129	2-D Adhered	10.0	0.6	0.56 ± 0.05
E130	3-D Adhered	5.0	0.8	0.50 ± 0.05
E131	3-D Adhered	10.0	0.8	0.50 ± 0.05
E132	3-D Adhered	15.0	0.8	0.50 ± 0.05
E133	2-D Adhered	10.0	0.8	0.56 ± 0.05
E134	3-D Adhered	5.0	1.0	0.50 ± 0.05
E135	3-D Adhered	10.0	1.0	0.50 ± 0.05
E136	3-D Adhered	15.0	1.0	0.50 ± 0.05
E137	2-D Adhered	10.0	1.0	0.56 ± 0.05
E138	3-D Adhered	5.0	1.0	0.73 ± 0.05
E139	3-D Adhered	10.0	1.0	0.73 ± 0.05
E140	3-D Adhered	15.0	1.0	0.73 ± 0.05
E141	2-D Adhered	10.0	1.0	0.83 ± 0.05
E142	3-D Adhered	5.0	0.8	0.73 ± 0.05
E143	3-D Adhered	10.0	0.8	0.73 ± 0.05
E144	3-D Adhered	15.0	0.8	0.73 ± 0.05
E145	2-D Adhered	10.0	0.8	0.83 ± 0.05

Table 4.6: (continued)

Experiment	Plume type	$\dot{Q}_t$ (kW)	W_s (m)	z_s (m)
E146	3-D Adhered	5.0	0.6	0.73 ± 0.05
E147	3-D Adhered	10.0	0.6	0.73 ± 0.05
E148	3-D Adhered	15.0	0.6	0.73 ± 0.05
E149	2-D Adhered	10.0	0.6	0.83 ± 0.05
E150	3-D Adhered	5.0	0.4	0.73 ± 0.05
E151	3-D Adhered	10.0	0.4	0.73 ± 0.05
E152	3-D Adhered	15.0	0.4	0.73 ± 0.05
E153	2-D Adhered	10.0	0.4	0.83 ± 0.05
E154	3-D Adhered	5.0	0.2	0.73 ± 0.05
E155	3-D Adhered	10.0	0.2	0.73 ± 0.05
E156	3-D Adhered	15.0	0.2	0.73 ± 0.05
E157	2-D Adhered	10.0	0.2	0.83 ± 0.05
E188	3-D Adhered	5.0	0.2	0.95 ± 0.05
E189	3-D Adhered	10.0	0.2	0.95 ± 0.05
E190	3-D Adhered	15.0	0.2	0.95 ± 0.05
E191	2-D Adhered	10.0	0.2	1.10 ± 0.05
E192	3-D Adhered	5.0	0.4	0.95 ± 0.05
E193	3-D Adhered	10.0	0.4	0.95 ± 0.05
E194	3-D Adhered	15.0	0.4	0.95 ± 0.05
E195	2-D Adhered	10.0	0.4	1.10 ± 0.05
E196	3-D Adhered	5.0	0.6	0.95 ± 0.05
E197	3-D Adhered	10.0	0.6	0.95 ± 0.05
E198	3-D Adhered	15.0	0.6	0.95 ± 0.05
E199	2-D Adhered	10.0	0.6	1.10 ± 0.05
E200	3-D Adhered	5.0	0.8	0.95 ± 0.05
E201	3-D Adhered	10.0	0.8	0.95 ± 0.05
E202	3-D Adhered	15.0	0.8	0.95 ± 0.05
E203	2-D Adhered	10.0	0.8	1.10 ± 0.05
E204	3-D Adhered	5.0	1.0	0.95 ± 0.05
E205	3-D Adhered	10.0	1.0	0.95 ± 0.05
E206	3-D Adhered	15.0	1.0	0.95 ± 0.05
E207	2-D Adhered	10.0	1.0	1.10 ± 0.05
E208	3-D Adhered	5.0	1.0	1.25 ± 0.05
E209	3-D Adhered	10.0	1.0	1.25 ± 0.05
E210	3-D Adhered	15.0	1.0	1.25 ± 0.05
E211	3-D Adhered	5.0	0.8	1.25 ± 0.05
E212	3-D Adhered	10.0	0.8	1.25 ± 0.05
E213	3-D Adhered	15.0	0.8	1.25 ± 0.05
E214	3-D Adhered	5.0	0.6	1.25 ± 0.05
E215	3-D Adhered	10.0	0.6	1.25 ± 0.05
E216	3-D Adhered	15.0	0.6	1.25 ± 0.05
E217	3-D Adhered	5.0	0.4	1.25 ± 0.05
E218	3-D Adhered	10.0	0.4	1.25 ± 0.05
E219	3-D Adhered	15.0	0.4	1.25 ± 0.05

Table 4.6: (continued)

Experiment	Plume type	$\dot{Q}_t$ (kW)	W_s (m)	z_s (m)
E220	3-D Adhered	5.0	0.2	1.25 ± 0.05
E221	3-D Adhered	10.0	0.2	1.25 ± 0.05
E222	3-D Adhered	15.0	0.2	1.25 ± 0.05
E283	2-D Adhered	10.0	0.2	0.31 ± 0.03
E284	2-D Adhered	10.0	0.4	0.31 ± 0.03
E285	2-D Adhered	10.0	0.6	0.31 ± 0.03
E286	2-D Adhered	10.0	0.8	0.31 ± 0.03
E287	2-D Adhered	10.0	1.0	0.31 ± 0.03

Table 4.6: (continued)

4.2.3.4 Experimental procedure

The experimental procedure for the series of 15 test fires to characterise the flow below the spill edge was the same as that described in section 4.1.3.4.

The experimental procedure for the series of 3 test fires to characterise the horizontal temperature profiles across the plume with respect to height of rise was the same as that described in section 4.1.3.4.

The experimental procedure for the series of 115 test fires to examine entrainment of air into an adhered spill plume was the same as that described in section 4.1.3.4.

4.2.4 Data reduction

The same data reduction and error analysis techniques described in section 4.1.4 were used for the adhered plume experiments.

Chapter 5

5. The horizontal flow of gases below the spill edge

The characteristics of the horizontal flow of gases below the spill edge are key input parameters to simple and analytical entrainment calculation methods for the spill plume. In this work, measurements have been made in the physical scale model to determine the mass flow rate, layer depth and convective heat flow rate of the horizontal flow of hot gases below the spill edge which will subsequently be used in the analysis of entrainment beyond the spill edge for both balcony and adhered spill plumes. These data also provide useful information to assess the performance of various calculation methods to determine the mass flow rate of gases below the spill edge.

As the horizontal flow of gases in the experiments was generated from a fire compartment with a flat ceiling (i.e. there was no downstand upstream of the spill edge), the compartment opening and the spill edge can be considered to be at the same location. Therefore, the mass flow rate of gases below the spill edge can be calculated using the methods given in section 2.1 which predict the mass flow rate of gases from a compartment opening. All these calculation methods have been derived for a flow emerging from a free spill edge, where there is no wall vertically extending above the edge (although the spill edge may be a downstand edge). It is unclear if these calculation methods apply to flow at a spill edge which is not free, where a wall projects vertically above the edge (i.e. for the adhered plume scenario).

This chapter presents the experimental results to characterise the horizontal flow of gases below the spill edge. It also presents an analysis of the performance of various calculation methods used to predict the mass flow rate of gases at a spill edge with a flat ceiling, both with and without a vertical wall projecting above the spill edge (i.e. for an adhered or balcony spill plume scenario).

5.1 Horizontal flow of gases without a wall above the spill edge

Those experiments which examined balcony spill plume entrainment were generated from a horizontal flow of hot gases from a spill edge with flat ceiling (i.e. the balcony edge), without a wall above the edge. This section considers those experiments to characterise the horizontal flow gases below the spill edge for this scenario, where the flow below the balcony is channelled by screens (i.e. Experiments C1 to C15). A schematic of the observed gas flow behaviour for this scenario is shown in Figure 5.1.

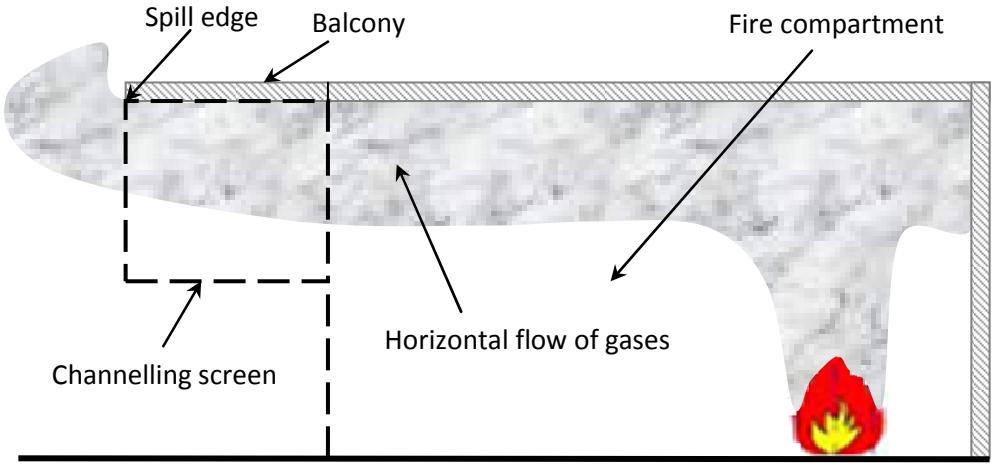

Figure 5.1: Horizontal gas layer flow for the balcony spill plume experiments

5.1.1 Uniformity of the gas layer flow across the spill edge

Uniformity of the gas layer below the spill edge enables the mass flow rate and convective heat flow rate of the layer to be determined from vertical profiles of temperature and velocity through the layer, without mapping the entire flow. Previous work by Harrison [33] demonstrated that a flow channelled by screens provided a uniform flow across the spill edge for the fire compartment used in this work. To examine if this conclusion applies for the conditions studied in this work, Figure 5.2 shows temperature profiles (above ambient) across the flow, 10 mm below the spill edge, normalised according to each W_s examined, for an intermediate fire size with $\dot{Q}_t$ = 10 kW (i.e. Experiments C2, C5, C8, C11 and C14).

The standard errors in the temperature measurements are encompassed by the size of marker used and are not explicitly shown in any of the temperature plots in this thesis.

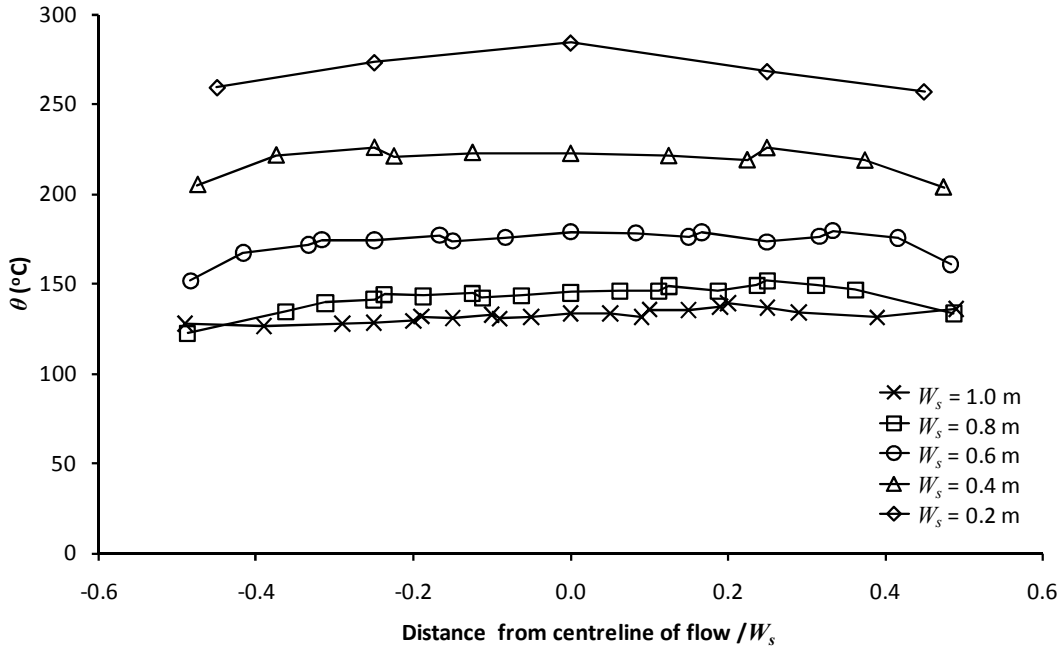

Figure 5.2: Temperature profiles across the layer flow

Figure 5.2 shows that the temperature profiles across the flow were reasonably uniform for each W_s examined. However, for those experiments where W_s was less than the width of the fire compartment (i.e. where $W_s \leq 0.8$ m), slightly lower temperatures were measured at the extremities of the flow close to the channelling screens, mostly likely due to the thermocouples at these locations being in the boundary layer of the flow. The boundary layer effect is not apparent for a flow where $W_s = 1.0$ m, as W_s was the same as the width of the fire compartment for this scenario. The profile across the narrowest flow (i.e. $W_s = 0.2$ m) is the least uniform of the flows examined and is characterised by a symmetric profile with a peak temperature at the centreline. However, since the key parameters of the flow were determined from vertical profiles at a distance of one-third of the flow width from each side of flow, the measurements at these locations can be considered to be 'average' values and are reasonably representative of the entire flow. Uniformity can also be assessed from the similarity between the vertical profiles of temperature and velocity through the layer flow below the spill edge (to the base of the layer flow, when the velocity is

zero). Figures 5.3 and 5.4 show that these profiles, in terms of temperature and velocity respectively, were virtually identical at each measurement location for a wide flow with an intermediate fire size (i.e. Experiment C2, W_s = 1.0 m, $\dot{Q}_t$ = 10 kW).

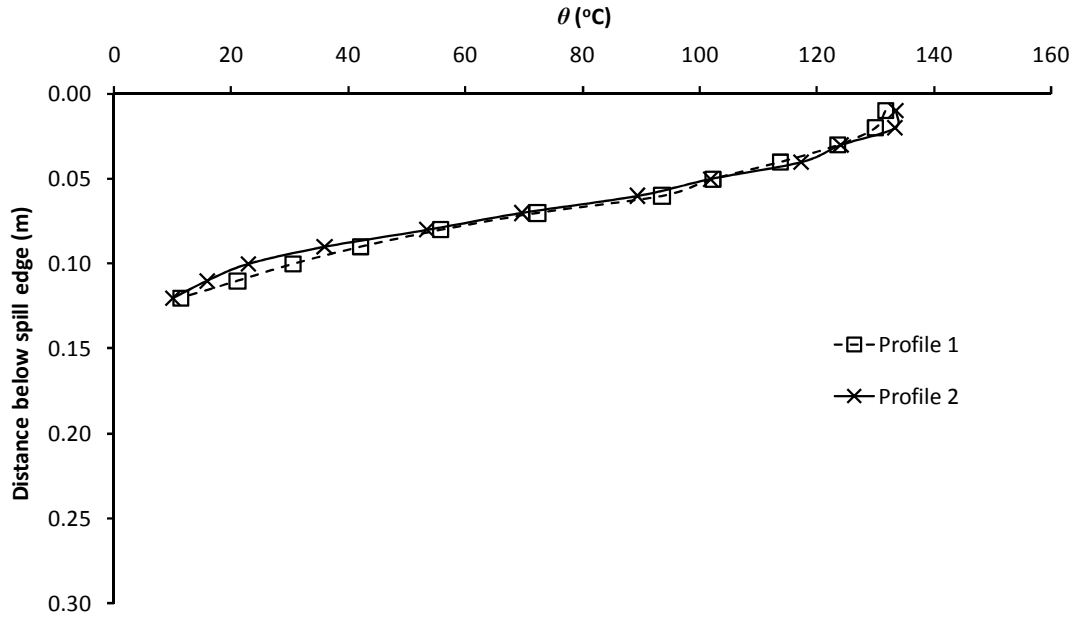

Figure 5.3: Comparison of temperature profiles below the spill edge (Experiment C2)

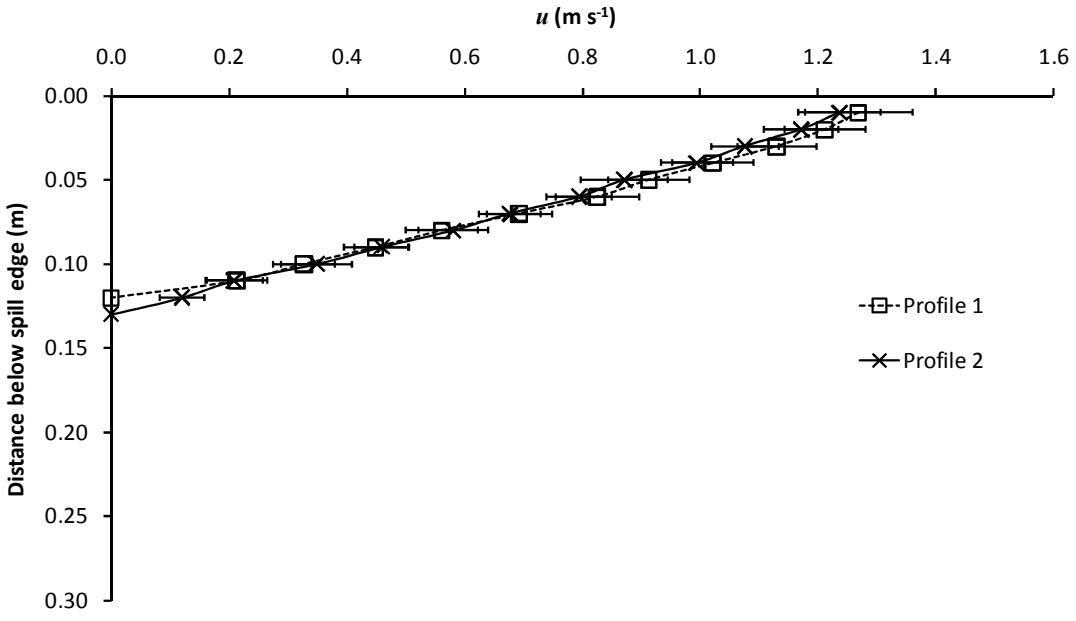

Figure 5.4: Comparison of velocity profiles below the spill edge (Experiment C2)

Figures 5.5 and 5.6 also show similarity between the profiles in terms of temperature and velocity respectively, for a narrow flow with an intermediate fire size (i.e. Experiment C14, W_s = 0.2 m, $\dot{Q}_t$ = 10 kW).

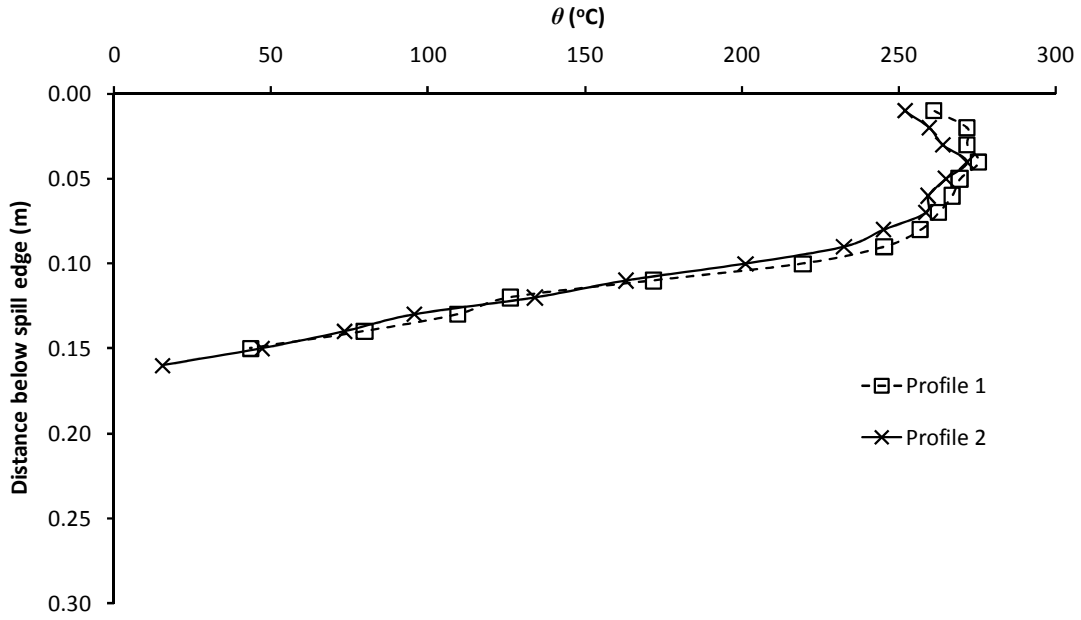

Figure 5.5: Comparison of temperature profiles below the spill edge (Experiment C14)

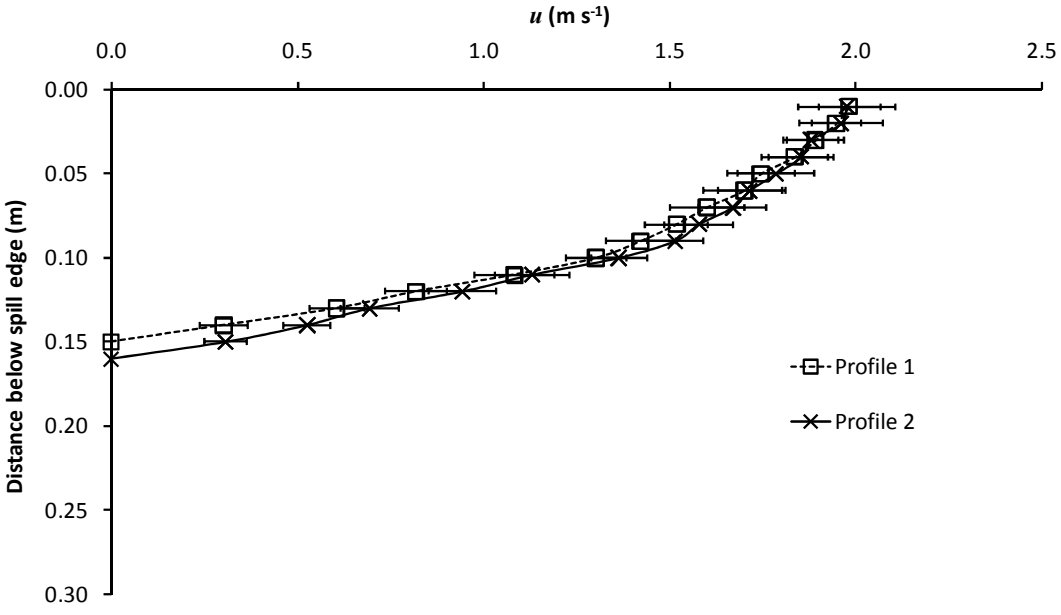

Figure 5.6: Comparison of velocity profiles below the spill edge (Experiment C14)

This behaviour was typical for the range of flows generated below the spill edge as shown in Appendix D which gives the vertical profiles of temperature and velocity for Experiments C1 to C15 inclusive, including the temperature profiles from Column C.

The above results provided the confidence to enable an integration to be performed through the gas layer flow from the average of the two profiles (for both temperature and velocity) to determine the mass flow rate and convective heat flow rate of the flow below the spill edge using Equations (4-10) and (4-11).

5.1.2 Experimental results

Table 5.1 shows a summary of the experimental results to characterise the horizontal flow of gases below the spill edge (for Experiments C1 to C15) in terms of the convective heat flow rate and mass flow rate, visual and buoyancy derived layer depths, the maximum temperature of the gas layer (above ambient) and the ambient temperature. It should be noted that the ambient temperature was taken to be a local ambient at the base of the thermocouple column below the spill edge to partially account for radiative warming of the bare wire thermocouples, as done in previous work [32,33].

Experiment	$\dot{Q}_t$ (kW)	$\dot{Q}_c$ (kW)	$\dot{m}_s$ (kg s^{-1})	$d_{v,s}$ (m)	$d_{buoy,s}$ (m)	$\theta_{\max,s}$ (^{o}C)	T_1 (K)
C1	5.0 ± 0.3	3.6 ± 0.2	0.059 ± 0.005	0.100 ± 0.005	0.079 ± 0.003	92.3 ± 0.6	294.1
C2	10.0 ± 0.3	8.0 ± 0.6	0.082 ± 0.007	0.115 ± 0.005	0.099 ± 0.003	132.4 ± 0.6	297.8
C3	15.0 ± 0.3	12.2 ± 1.0	0.099 ± 0.009	0.125 ± 0.005	0.117 ± 0.003	154.1 ± 1.0	298.8
C4	5.0 ± 0.3	3.7 ± 0.3	0.052 ± 0.005	0.105 ± 0.005	0.087 ± 0.003	99.4 ± 0.4	292.1
C5	10.0 ± 0.3	7.8 ± 0.6	0.069 ± 0.006	0.115 ± 0.005	0.106 ± 0.003	145.7 ± 0.8	295.8
C6	15.0 ± 0.3	12.8 ± 0.8	0.091 ± 0.007	0.135 ± 0.005	0.130 ± 0.002	176.6 ± 1.1	296.8
C7	5.0 ± 0.3	3.9 ± 0.2	0.042 ± 0.004	0.110 ± 0.005	0.089 ± 0.003	126.7 ± 0.3	295.8
C8	10.0 ± 0.3	7.7 ± 0.5	0.058 ± 0.005	0.120 ± 0.005	0.107 ± 0.002	175.6 ± 0.7	298.1
C9	15.0 ± 0.3	12.2 ± 0.7	0.070 ± 0.005	0.140 ± 0.005	0.133 ± 0.002	217.3 ± 1.6	300.4
C10	5.0 ± 0.3	3.6 ± 0.2	0.034 ± 0.002	0.115 ± 0.005	0.096 ± 0.003	155.1 ± 0.6	296.0
C11	10.0 ± 0.3	7.2 ± 0.4	0.043 ± 0.003	0.125 ± 0.005	0.119 ± 0.003	222.0 ± 0.6	300.9
C12	15.0 ± 0.3	10.9 ± 0.6	0.052 ± 0.004	0.145 ± 0.005	0.137 ± 0.004	264.8 ± 1.8	301.5
C13	5.0 ± 0.3	3.5 ± 0.2	0.024 ± 0.002	0.135 ± 0.005	0.114 ± 0.004	173.8 ± 2.4	292.3
C14	10.0 ± 0.3	6.6 ± 0.4	0.028 ± 0.002	0.155 ± 0.005	0.140 ± 0.004	274.9 ± 3.1	298.1
C15	15.0 ± 0.3	9.9 ± 0.6	0.033 ± 0.002	0.170 ± 0.005	0.165 ± 0.003	352.4 ± 4.5	302.0

Table 5.1: Summary of results for the horizontal flow of gases below the spill edge

5.1.3 Mass weighted average layer temperature

The horizontal flow theory by Morgan [51] (described in section 2.1.2) provides a relationship between $\overline{\theta}_w$ and $\theta_{\max,w}$ [see Equation (2-6)] which is useful in smoke management design to reduce equations which are solely dependent on $\theta_{\max,w}$ (which in many cases is unknown). For the experiments in this work, $\overline{\theta}_w = \overline{\theta}_s$, therefore Equation (2-6) becomes,

$$\overline{\theta}_s = 0.73\theta_{\max,s} \qquad \textbf{(5-1)}$$

The performance of Equation (5-1) can be assessed using the experimental measurements of the gas layer flow below the spill edge. Figure 5.7 shows a plot of $\overline{\theta}_s$ versus $\theta_{\max,s}$ for Experiments C1 to C15, where $\overline{\theta}_s$ was determined using the experimental data within Equation (4-5).

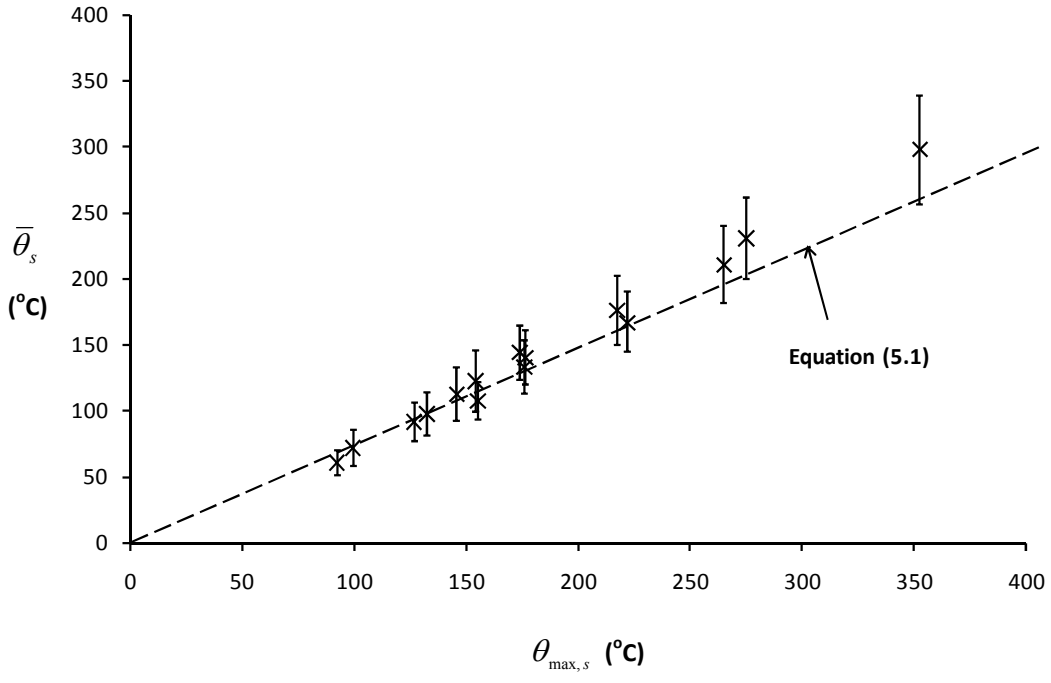

Figure 5.7: Plot of $\overline{\theta}_s$ versus $\theta_{\max,s}$ for Experiments C1 to C15

Figure 5.7 shows that Equation (5-1) gives a prediction which generally agrees with the experimental data (i.e. equal to within one standard error). The agreement is not quite so good for flows where $\theta_{\max,s}$ was above 250 ^{o}C (i.e. for flows produced from narrow openings), where Equation (5-1) somewhat tends to under predict $\overline{\theta}_s$. This is unsurprising as the Morgan theory primarily applies to flows which are wider than their depth (i.e. $W_s >> d_s$). However, for design purposes, it appears that the use of Equation (5-1) provides a reasonable approximation to determine $\overline{\theta}_s$ for the majority of layer flows.

5.1.4 Froude number of the horizontal flow of gases

Figure 5.8 shows the characteristic Froude number (i.e. *Fr*) for the flows below the spill edge for Experiments C1 to C15 inclusive. The *Fr* was determined using Equation (3-2) with the characteristic length taken to be the depth of the layer below the spill edge. Figure 5.8 shows that for the range of flows examined the *Fr* is approximately constant with a value of around 1.3, which is typical of plume flows generated from natural fires which have a *Fr* of approximately 1.0 [127].

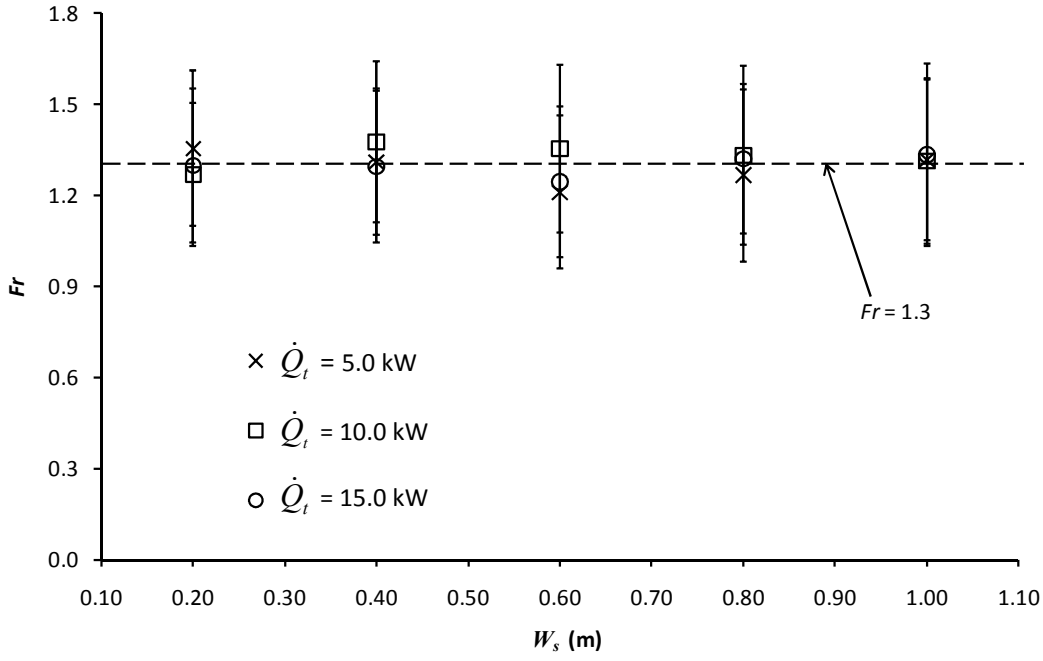

Figure 5.8: *Fr* below the spill edge for Experiments C1 to C15

5.1.5 Prediction of the mass flow rate of gases below the spill edge

5.1.5.1 Analytical methods

Figure 5.9 shows a comparison between the experimental results and the predictions of $\dot{m}_s$ using the analytical methods by Thomas *et al.* (see section 2.1.1) and Morgan (see section 2.1.2) which in this case are given by Equations (5-2) and (5-3) respectively. The predictions were made assuming C_d = 1.0 as recommended by Morgan [51] for a flow with a flat ceiling at the spill edge. The visually derived layer depths below the spill edge were used in Equations (5-2) and (5-3).

$$\dot{m}_s = \frac{2}{3} C_d \left(2g\theta_{\max,s} T_{amb}\right)^{1/2} \frac{W_s \rho_{amb}}{T_{\max,s}} d_s^{3/2} \qquad \textbf{(5-2)}$$

$$\dot{m}_s = \frac{2}{3} C_d^{3/2} \left(2g\theta_{\max,s} T_{amb}\right)^{1/2} \frac{W_s \rho_{amb}}{T_{\max,s}} d_s^{3/2} \kappa_m \qquad \textbf{(5-3)}$$

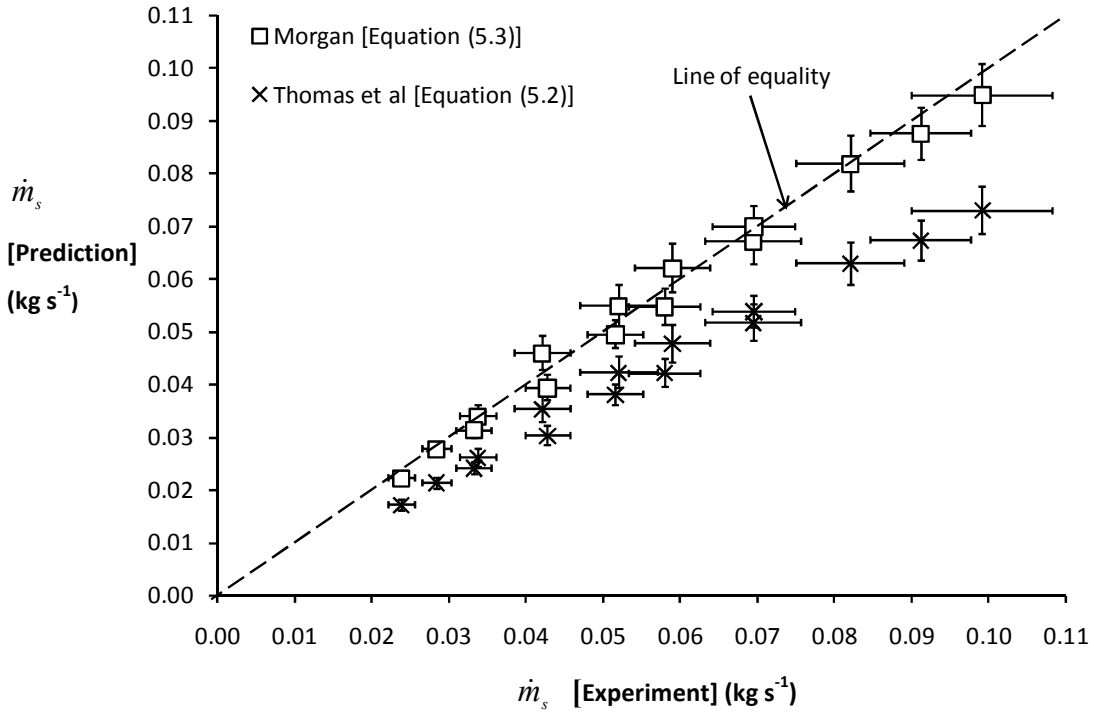

Figure 5.9: Comparison of the prediction of $\dot{m}_s$ with experiment

Figure 5.9 shows that the predictions of $\dot{m}_s$ using the Morgan method gives excellent agreement with the experimental results. The Thomas *et al.* method gives predictions which are approximately 30% lower than the Morgan method and the experimental results, consistent with the findings of previous work by Harrison [40]. The difference in the predictions between the two methods is most likely due to the use of the profile correction factor, κ_m, in the Morgan method which is recommended to have value of 1.3 for design purposes. This correction factor takes into account the shape of the buoyancy profile in the calculation and is assumed to be approximately half way between a 'top hat' and a triangular profile (rather than a 'top-hat' profile assumed in the Thomas *et al.* method). In the development of the expression to describe κ_m [Equation (2-3)], Morgan chose the shape of the triangular profile to give the same gas layer depth [using Equation (4-9)] and the same buoyancy at the top of the flow as a 'top hat' profile (see Figure 5.10).

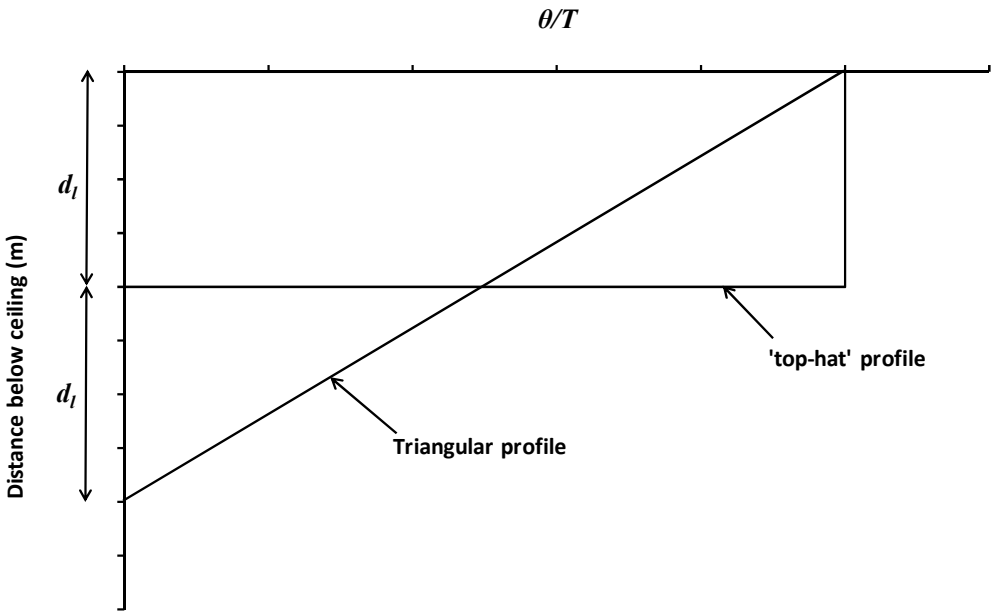

Figure 5.10: Triangular and 'top-hat' buoyancy profiles assumed by Morgan [51]

Figures 5.11 to 5.13 show a comparison between some typical experimental buoyancy profiles with the assumed triangular and top hat profiles in the Morgan method.

The experimental buoyancy profiles shown are for wide, intermediate and narrow flows respectively, for an intermediate fire size (i.e. Experiments C2, C8, C14, where W_s = 0.2, 0.6, 1.0 m and $\dot{Q}_t$ = 10 kW).

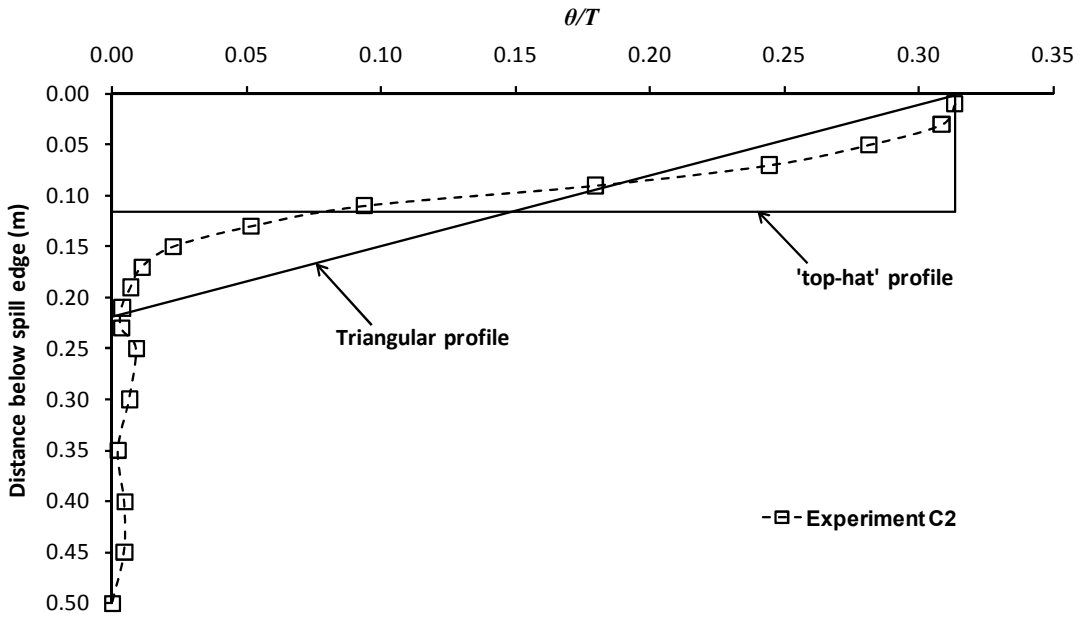

Figure 5.11: Comparison of buoyancy profiles for Experiment C2 (W_s = 1.0 m)

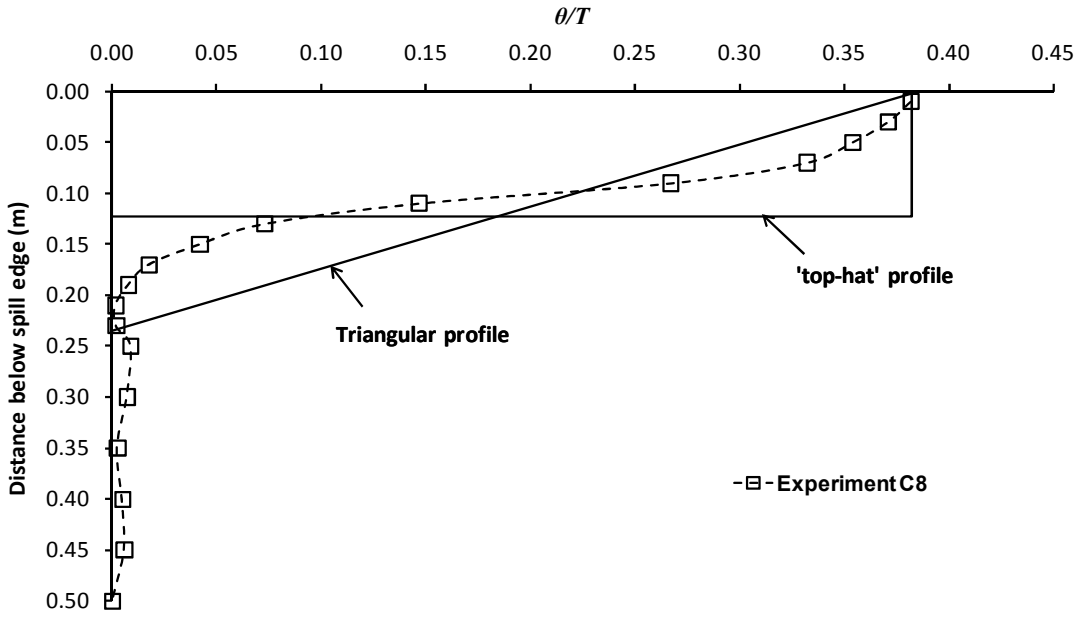

Figure 5.12: Comparison of buoyancy profiles for Experiment C8 (W_s = 0.6 m)

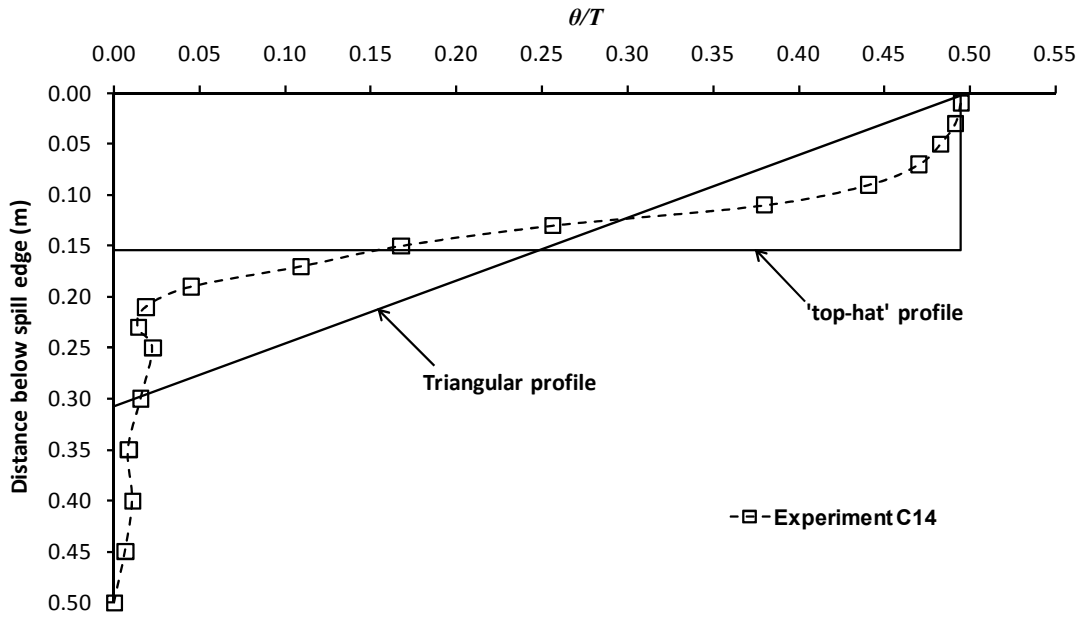

Figure 5.13: Comparison of buoyancy profiles for Experiment C14 (W_s = 0.2 m)

Figure 5.11 to 5.13 show that the experimental buoyancy profiles are generally part way between the triangular and 'top-hat' profiles. Therefore, the use of the profile correction factor, κ_m, in the Morgan method appears to be appropriate for the flows examined in this work and most likely explains why the Morgan method gives predictions which provide excellent agreement with the experimental results compared with the predictions made by the Thomas *et al.* method. As W_s approaches zero it would seem reasonable to assume that a 'top-hat' profile will give a best approximation for the layer profile from the opening.

If C_d is taken to be approximately 1.3 for the conditions studied, then the Thomas *et al.* method will give a good prediction of the experiment. However, this value can be considered to be non-physical as C_d is an empirical modifying factor to represent the actual flow, and a value of 1.3 suggests that the aerodynamic free area of the opening below the spill edge is greater than the actual cross-sectional area.

5.1.5.2 Simple empirical formulae

Figure 5.14 shows a comparison of the experimental results with the predictions of $\dot{m}_s$ using the simple formulae given by Hansell (section 2.1.3) and CIBSE/BS 7974 (section 2.1.4) which in this case are given by Equations (5-4) and (5-5) respectively.

$$\dot{m}_s = \frac{C_e p W_s h_s^{3/2}}{\left(W_s^{2/3} + \frac{1}{C_d}\left(\frac{C_e p}{\sigma} \right)^{2/3} \right)^{3/2}} \quad \textbf{(5-4)}$$

$$\dot{m}_s = 0.09 \dot{Q}_c^{1/3} W_s^{2/3} h_s \quad \textbf{(5-5)}$$

The predictions made using Equation (5-4) assumed a C_d = 1.0 (for a flat ceiling at the spill edge) and C_e = 0.34 (as the fire compartment represents a small room, and the incoming air can only enter from one direction) as recommended by Morgan *et al.* [12].

Although the fire perimeter (p) is a length scale, it was not clear if this fire property directly obeys the scaling laws. Therefore, it was unclear if it was appropriate to use the fire perimeter determined from model scale as an input into Equation (5-4), especially as the Hansell method is essentially empirical in nature and was derived using data from full scale experiments. The performance of this method has never previously been assessed using reduced scale data. To examine this, the perimeter of the fire in the model was compared with the calculated full scale equivalent perimeter (which were both determined from the heat release rate of the fire, a property that does obey the scaling laws). As the burning area of IMS did not occupy the full surface area of the fire tray, the perimeter of the fire in the model was determined from the perimeter of an equivalent square burning area (i.e. $p = 4\sqrt{A_{fire}}$), as the fuel was channelled by the straight edges of the fire tray. The area of the fire was determined by dividing $\dot{Q}_t$ by the value of $\dot{Q}_t''$ for IMS (i.e. 527 kW m^{-2} [126]). The full scale equivalent fire areas and perimeters were determined in the same way.

Table 5.2 shows the calculated areas and perimeters of the fire sizes examined in the model (which agreed well with visual observations) and their full scale equivalent.

$\dot{Q}_{t,m}$ (kW)	$\dot{Q}_{t,f}$ (kW)	$A_{fire,m}$ (m^2)	$A_{fire,f}$ (m^2)	$\frac{A_{fire,f}}{A_{fire,m}}$	p_m (m)	p_f (m)	$\frac{p_f}{p_m}$	$p_{m,v}$
5.0 ± 0.3	1581 ± 95	0.0095 ± 0.001	3.00 ± 0.18	316	0.39 ± 0.04	6.90 ± 0.20	17.7	0.40 ± 0.05
10.0 ± 0.3	3162 ± 95	0.0190 ± 0.001	6.00 ± 0.18	316	0.55 ± 0.02	9.80 ± 0.14	17.8	0.50 ± 0.05
15.0 ± 0.3	4743 ± 95	0.0285 ± 0.001	9.00 ± 0.18	316	0.68 ± 0.02	12.12 ± 0.12	17.8	0.70 ± 0.05

Table 5.2: Fire areas and perimeters used on model scale and their full scale equivalent.

As the fire size is governed by the area, the ratio of $A_{fire,f}/A_{fire,m}$ should be consistent with the appropriate scaling law for heat release rate [given by Equation (3-12)]. Therefore, for the calculated fire areas to be consistent with the scaling laws, the ratio of $A_{fire,f}/A_{fire,m}$ should be of the order of 316 [i.e. $10^{(5/2)}$] and Table 5.2 shows that this is the case. Since the perimeter of the fire is a length, the ratio of p_f/p_m should be of the order of 10 to be consistent with the scaling assumed for this study (i.e. $1/10^{th}$ scale), however, Table 5.2 shows that this ratio is approximately 18. This indicates that the perimeter of the fire on model scale is approximately $1/18^{th}$ of the full scale equivalent and is not consistent with the scaling laws. Therefore, it appears that the fire perimeter is not a property that directly obeys the scaling laws. If the fire perimeter on model scale were to be used within Equation (5-4), it will give a significantly lower prediction of $\dot{m}_s$ than the full scale equivalent fire perimeter (by approximately 30 to 40%). As the Hansell method has been validated using full scale data, the predictions of $\dot{m}_s$ were made using full scale equivalent values of the fire perimeter and the compartment geometry. These predictions were then subsequently scaled down to model scale to enable comparison to be made with the experimental results and the predictions made using the CIBSE/BS 7974 method.

Figure 5.14 shows that for relatively low values of $\dot{m}_s$ produced from narrow width flows, the predictions using the Hansell method are generally conservative by up to approximately 30%.

However, for larger values of $\dot{m}_s$ (produced from wider flows) there is good agreement between the predictions and the experiment, which are generally equal to within one standard error. It is unsurprising that this method is more reliable for these flows as Hansell states that this method specifically applies to layer flows which are wider than their depth (i.e. $W_s >> d_s$) [59]. Considering that the predictions of $\dot{m}_s$ are either conservative or appropriate for the range of flows examined, the use of the Hansell method seems suitable for design purposes.

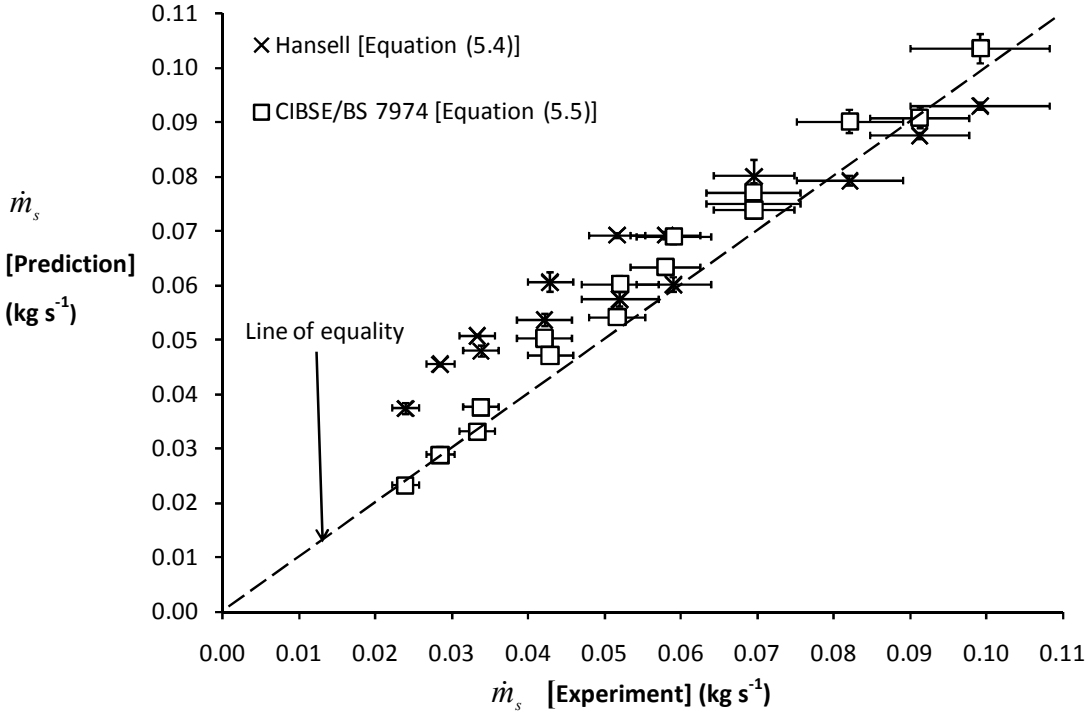

Figure 5.14: Comparison of the prediction of $\dot{m}_s$ with experiment

Figure 5.14 shows that the predictions of $\dot{m}_s$ using the CIBSE/BS 7974 method generally provides excellent agreement with the experimental results for the range of flows examined. Those predictions which do not agree with the experiment to within one standard error are generally conservative by approximately 5 to 10 %. It appears that the use of this method is also suitable for design purposes, and may be preferential to the Hansell method, considering its relative simplicity (i.e. less 'adjustment' parameters) and that it generally performs better for the range of conditions studied.

5.2 Horizontal flow of gases with a wall above the spill edge

Those experiments which examined adhered spill plume entrainment were generated from a horizontal flow of hot gases from a spill edge with flat ceiling (i.e. the compartment opening) with a wall above the edge. This section considers those experiments to characterise the horizontal flow of gases below the spill edge for this scenario (i.e. Experiments C16 to C30). A schematic of the observed gas flow behaviour for this scenario is shown in Figure 5.15.

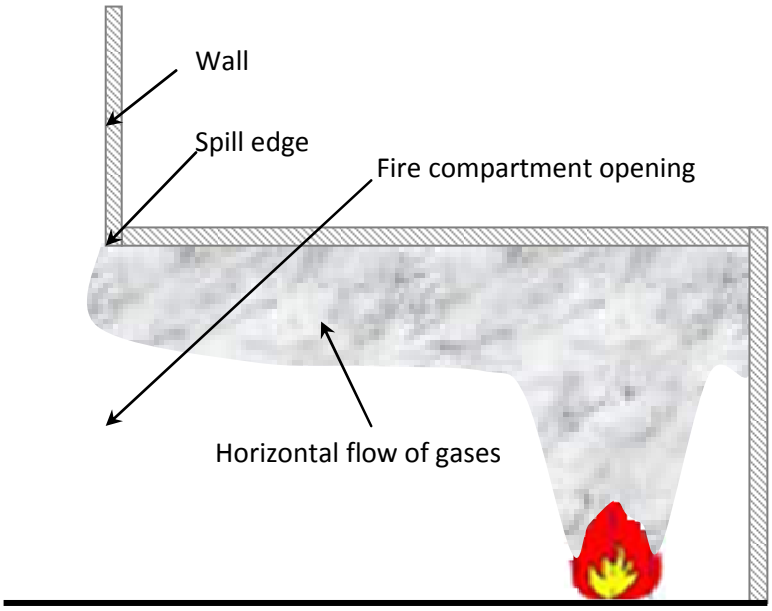

Figure 5.15: Horizontal gas layer flow for the adhered spill plume experiments

5.2.1 Uniformity of the gas layer flow across the spill edge

To examine uniformity of the gas layer flow across the spill edge this scenario, and to assess if the mass flow rate and convective heat flow rate of the flow could be successfully determined from vertical temperature and velocity profiles of the flow, Figure 5.2 shows temperature profiles (above ambient) across the flow, 10 mm below the spill edge, normalised according to each W_s examined, for an intermediate fire size with $\dot{Q}_t$ =10 kW (i.e. Experiments C17, C20, C23, C26 and C29).

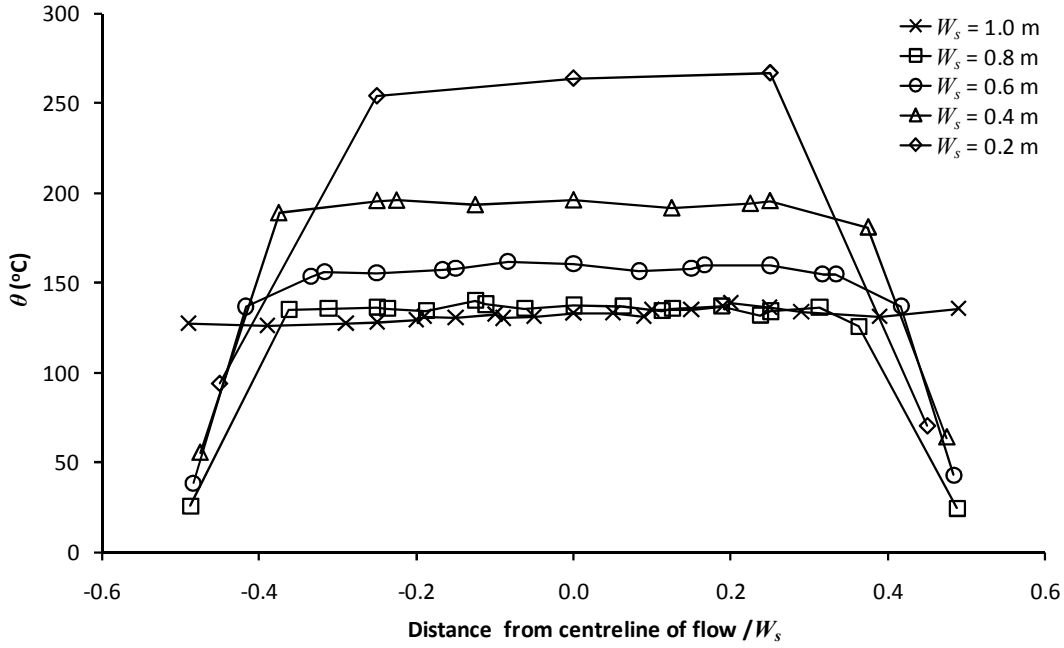

Figure 5.16: Temperature profiles across the layer flow

Figure 5.16 shows that the temperature profiles across the flow for this scenario were reasonably uniform for each W_s examined. However, for those experiments where W_s was 0.8 m or less, the boundary layer effect on the temperatures at the extremities of the flow (i.e. a lower measured temperature) close to the sides of the fire compartment opening is more pronounced compared to the flows shown in Figure 5.2 which had been channelled by screens prior to the spill edge.

As the boundary layer only affects the temperature at the extremities of the flow (i.e. 10 mm from each side), the vast majority of the flow can be considered to be uniform in nature and errors in the mass flow rate and convective heat flow rate from the vertical temperature and velocity profiles can be considered to be minimal.

To further examine uniformity of the flow, Figures 5.17 and 5.18 show the vertical profiles through the layer below the spill edge (to the base of the layer), in terms of temperature and velocity respectively, for a wide flow with an intermediate fire size (i.e. Experiment C29, W_s = 1.0 m and $\dot{Q}_t$ =10 kW).

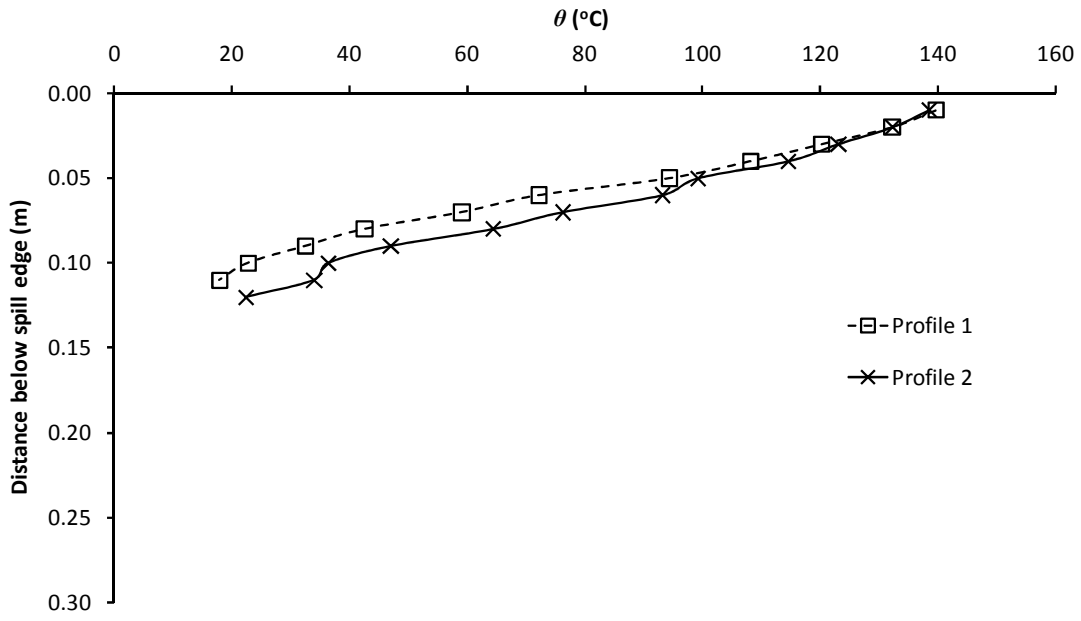

Figure 5.17: Comparison of temperature profiles for Experiment C29

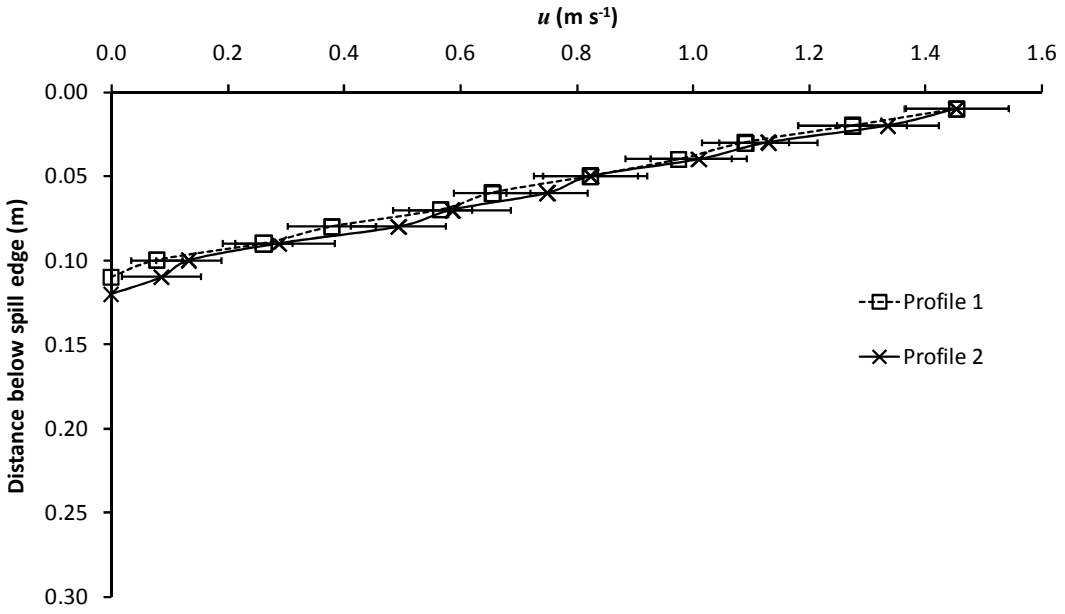

Figure 5.18: Comparison of velocity profiles for Experiment C29

Figures 5.17 and 5.18 show that the profiles at each measurement location were very similar in terms of both temperature and velocity, thus, the average of these two profiles can be considered to be representative of the flow.

Figures 5.19 and 5.20 show similar profiles of temperature and velocity respectively, at each measurement location, for a narrow flow with an intermediate fire size (i.e. for Experiment C17, W_s = 0.2 m and $\dot{Q}_t$ =10 kW).

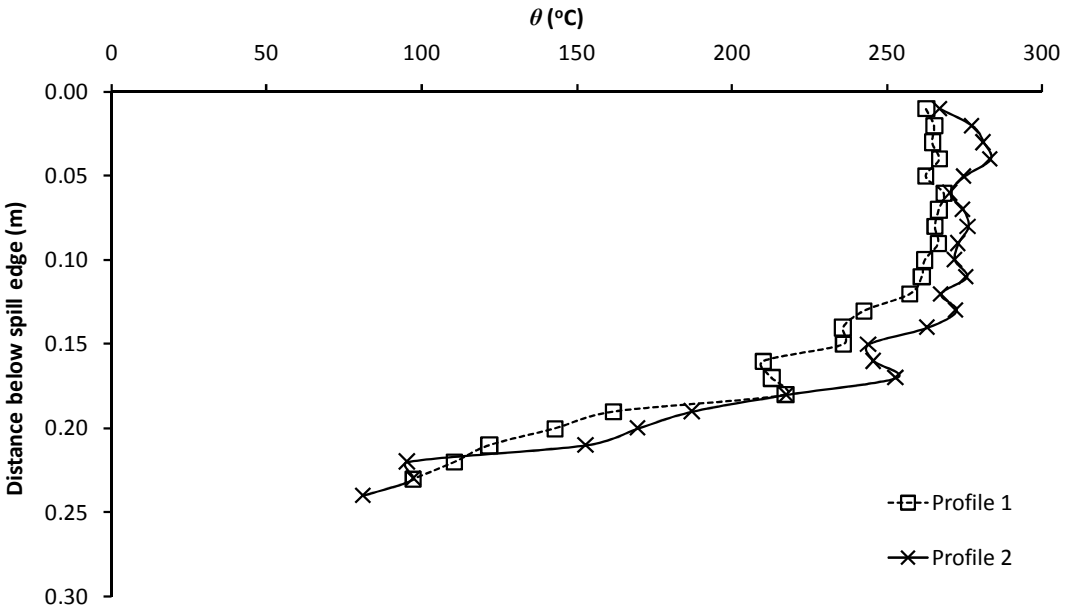

Figure 5.19: Comparison of temperature profiles for Experiment C17

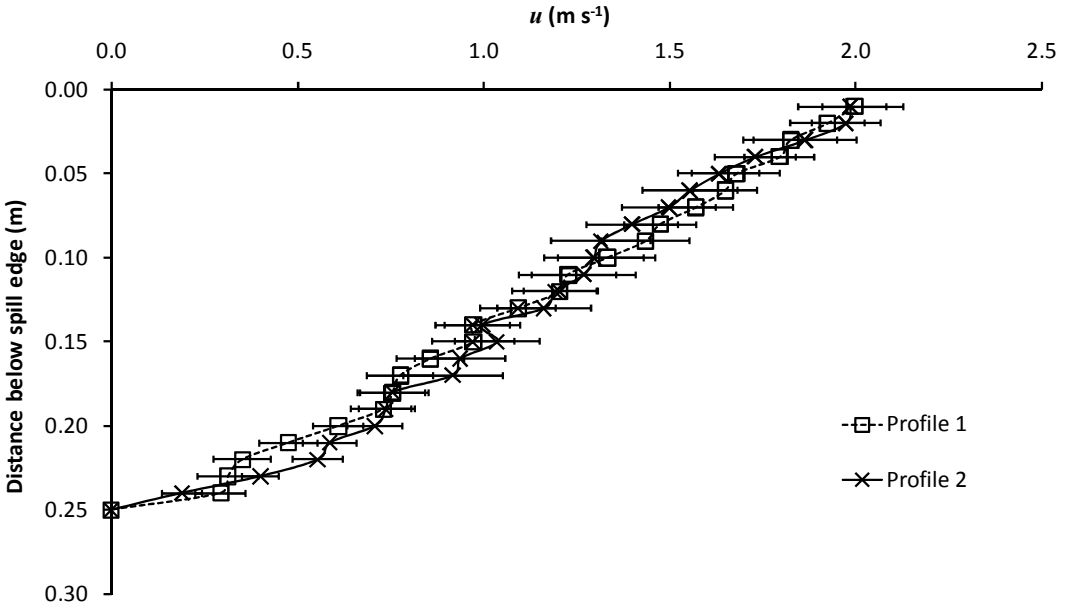

Figure 5.20: Comparison of velocity profiles for Experiment C17

This behaviour was typical for the range of flows generated below the spill edge as shown in Appendix E which gives the vertical profiles of temperature and velocity for Experiments C16 to C30 inclusive, including the temperature profiles from Column C.

The above results provided the confidence to enable an integration to be performed through the gas layer flow from the average of the two profiles (for both temperature and velocity) to determine the mass flow rate and convective heat flow rate of the flow below the spill edge using Equations (4-10) and (4-11).

5.2.2 Experimental results

Table 5.3 shows a summary of the experimental results to characterise the horizontal flow of gases below the spill edge (for Experiments C16 to C30), in terms of the convective heat flow rate and mass flow rate, visual and buoyancy derived layer depths, the maximum temperature of the gas layer and the ambient temperature. The ambient temperature was again taken to be a local ambient at the base of the thermocouple column below the spill edge.

Experiment	$\dot{Q}_t$ (kW)	$\dot{Q}_c$ (kW)	$\dot{m}_s$ (kg s^{-1})	$d_{v,s}$ (m)	$d_{buoy,s}$ (m)	$\theta_{\max,s}$ (^{o}C)	T_l (K)
C16	5.0 ± 0.3	4.1 ± 0.3	0.0259 ± 0.002	0.195 ± 0.005	0.183 ± 0.004	183.8 ± 0.7	299.2
C17	10.0 ± 0.3	9.0 ± 0.8	0.0365 ± 0.003	0.245 ± 0.005	0.233 ± 0.006	264.4 ± 3.1	306.5
C18	15.0 ± 0.3	13.1 ± 1.1	0.0400 ± 0.003	0.260 ± 0.005	0.270 ± 0.006	332.2 ± 3.7	321.8
C19	5.0 ± 0.3	4.0 ± 0.3	0.0377 ± 0.004	0.160 ± 0.005	0.130 ± 0.004	140.5 ± 0.6	299.3
C20	10.0 ± 0.3	8.5 ± 0.8	0.0517 ± 0.005	0.195 ± 0.005	0.173 ± 0.004	196.9 ± 1.2	303.4
C21	15.0 ± 0.3	13.6 ± 1.1	0.0642 ± 0.006	0.225 ± 0.005	0.205 ± 0.004	238.8 ± 1.4	309.9
C22	5.0 ± 0.3	4.1 ± 0.3	0.0465 ± 0.004	0.135 ± 0.005	0.101 ± 0.003	119.3 ± 0.3	299.6
C23	10.0 ± 0.3	8.0 ± 0.7	0.0635 ± 0.006	0.160 ± 0.005	0.139 ± 0.003	157.7 ± 0.7	302.4
C24	15.0 ± 0.3	13.3 ± 1.3	0.0779 ± 0.008	0.185 ± 0.005	0.175 ± 0.003	195.8 ± 1.6	309.9
C25	5.0 ± 0.3	4.0 ± 0.4	0.0493 ± 0.006	0.105 ± 0.005	0.088 ± 0.005	106.7 ± 0.5	299.3
C26	10.0 ± 0.3	7.9 ± 0.7	0.0709 ± 0.007	0.135 ± 0.005	0.121 ± 0.004	139.5 ± 0.6	301.8
C27	15.0 ± 0.3	12.7 ± 1.2	0.0902 ± 0.010	0.155 ± 0.005	0.136 ± 0.002	169.5 ± 1.5	304.2
C28	5.0 ± 0.3	3.3 ± 0.3	0.0472 ± 0.006	0.085 ± 0.005	0.064 ± 0.004	97.0 ± 0.8	296.9
C29	10.0 ± 0.3	7.9 ± 0.7	0.0732 ± 0.008	0.105 ± 0.005	0.086 ± 0.003	135.4 ± 0.5	300.8
C30	15.0 ± 0.3	11.6 ± 1.1	0.0888 ± 0.010	0.120 ± 0.005	0.104 ± 0.002	162.0 ± 1.1	303.2

Table 5.3: Summary of results for the horizontal flow of gases below the spill edge

5.2.3 Mass weighted average layer temperature

The performance of Equation (5-1) by Morgan [51] can again be assessed using the experimental measurements of the layer flow below the spill edge for the conditions studied. Figure 5.21 shows a plot of $\overline{\theta}_s$ versus $\theta_{max,s}$ for Experiments C16 to C30, where $\overline{\theta}_s$ was determined using Equation (4-5).

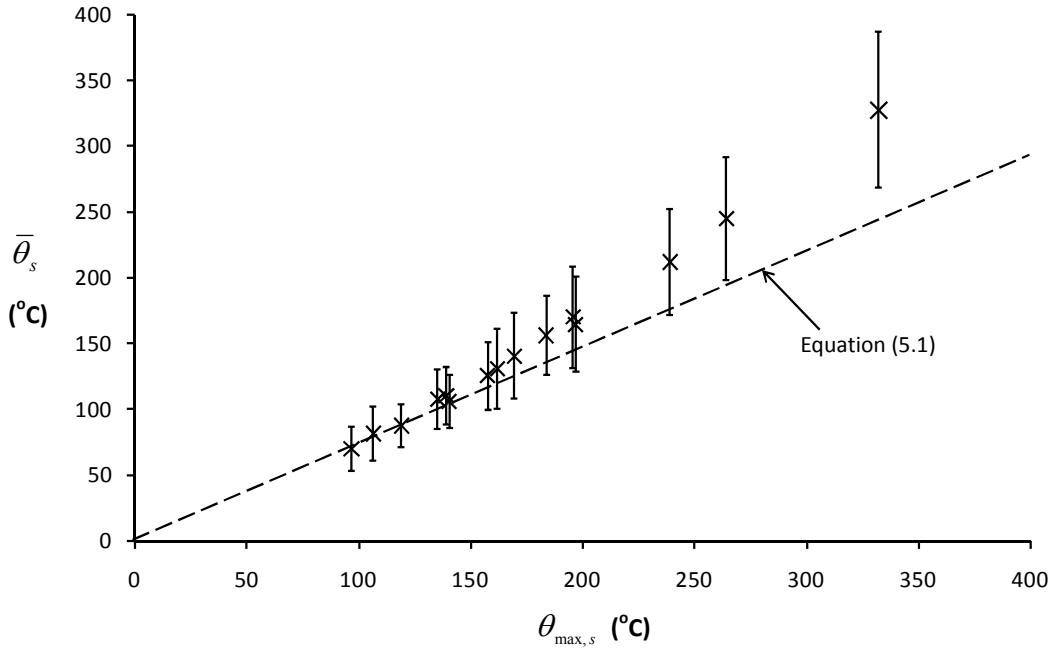

Figure 5.21: Plot of $\overline{\theta}_s$ versus $\theta_{max,s}$ for Experiments C16 to C30

Figure 5.21 shows that Equation (5-1) gives a prediction which agrees reasonably well with the majority of the experimental data for values of $\theta_{max,s}$ below 200 °C. However, there is a general trend for Equation (5-1) to under predict $\overline{\theta}_s$ for flows at higher temperatures (i.e. for flows produced from narrow openings). This is likely to be due to the shape of the temperature profiles for narrow flows being more similar to 'top hat' in nature (e.g. Figure 5.19) such that the value of $\overline{\theta}_s$ is comparable to $\theta_{max,s}$ (as is the case for the highest value of $\theta_{max,s}$ shown in Figure 5.21). However, for design purposes, the use of Equation (5-1) can still be considered to provide a reasonably approximation of $\overline{\theta}_s$ for values of $\theta_{max,s}$ below 200 °C.

5.2.4 Froude number of the horizontal flow of gases

Figure 5.22 shows the *Fr* for the range of flows examined below the spill edge for Experiments C16 to C30 inclusive.

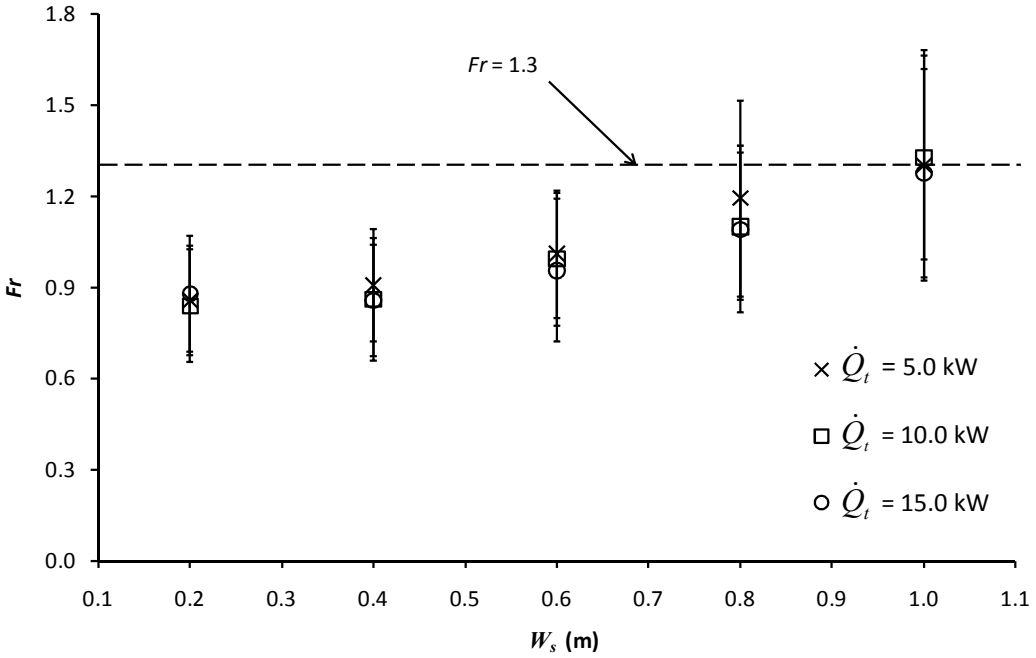

Figure 5.22: *Fr* of the flow below the spill edge for Experiments C16 to C30

Figure 5.22 shows that the *Fr* of the flow is not constant for the range of conditions studied, contrary to that shown in Figure 5.8 when there was no wall above the spill edge. Figure 5.22 shows that the *Fr* varies with W_s but appears to be independent of $\dot{Q}_t$ for each width of flow examined. For wide flows with W_s = 1.0 m the *Fr* is approximately 1.3 consistent with the equivalent flows without a wall above the spill edge. However, for flows with W_s less than 1.0 m the *Fr* gradually decreases to a value of approximately 0.9 where it is remains reasonably constant for values of W_s of 0.2 and 0.4 m respectively.

Comparison of Figures 5.8 and 5.24 suggests that the presence of a wall above the spill edge affects the characteristics of the flow below the edge as this is essentially the only significant difference between the two scenarios.

To examine the effect of a wall above the spill edge, a comparison is made between the vertical profiles of temperature and velocity below the spill edge (to the base of the layer), with and without a wall, for a wide, intermediate and narrow width flow respectively.

Figures 5.23 and 5.24 show a comparison of the profiles of temperature and velocity respectively, for a wide flow with an intermediate fire size, with and without a wall above the spill edge (i.e. Experiments C2 and C29, W_s = 1.0 m and $\dot{Q}_t$ = 10 kW).

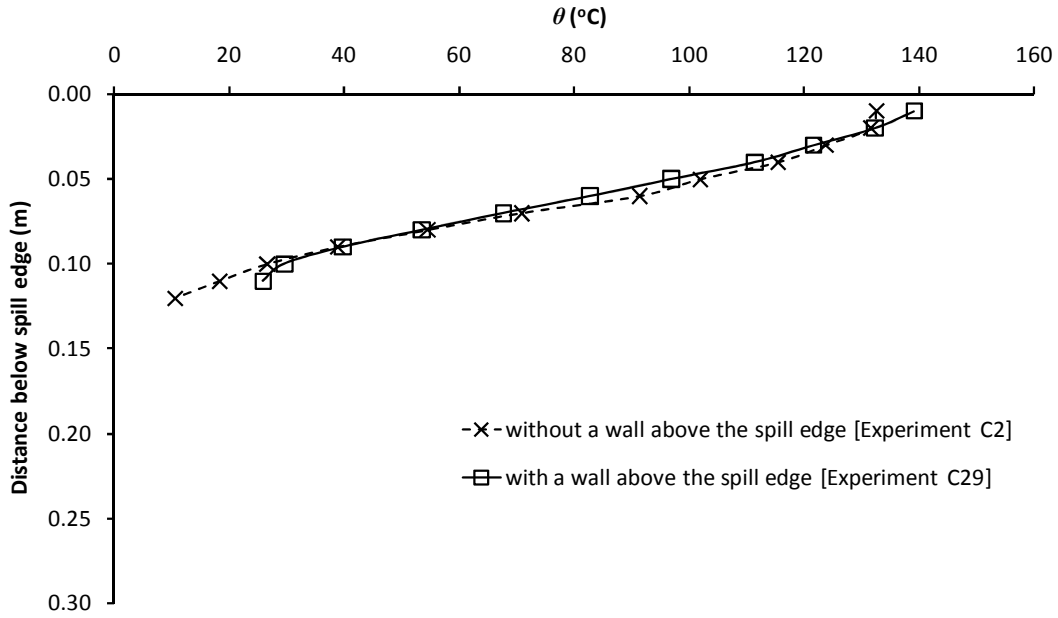

Figure 5.23: Comparison of temperature profiles for Experiments C2 and C29

Figure 5.23 shows that the temperature profiles of the flows were very similar, both with and without a wall above the edge. Figure 5.24 shows that the velocity profiles were also similar, but with the peak velocity being slightly higher just below the spill edge for a flow with a wall above. The observed layer depths below the edge were also similar, with depths of 0.105 m and 0.115 m for flows with and without a wall respectively. Therefore, it is unsurprising that the characteristic *Fr* for wide flows were similar (i.e. 1.3), both with and without a wall above the edge.

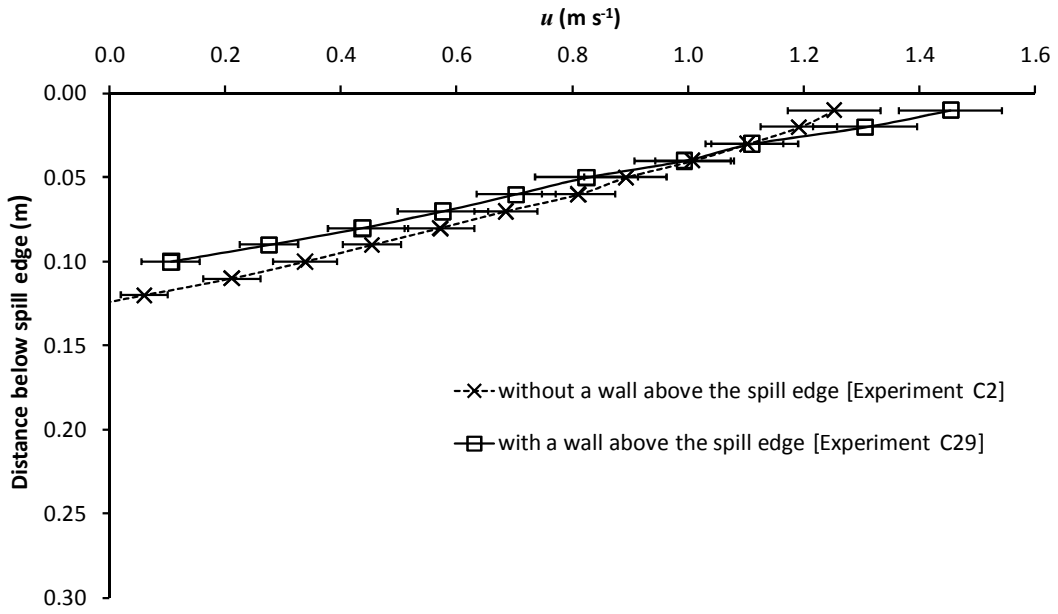

Figure 5.24: Comparison of velocity profiles for Experiments C2 and C29

Figures 5.25 and 5.26 show a comparison of the profiles of temperature and velocity respectively, for an intermediate width flow with an intermediate fire size, with and without a wall above the spill edge (i.e. Experiments C8 and C23, W_s = 0.6 m and $\dot{Q}_t$ = 10 kW).

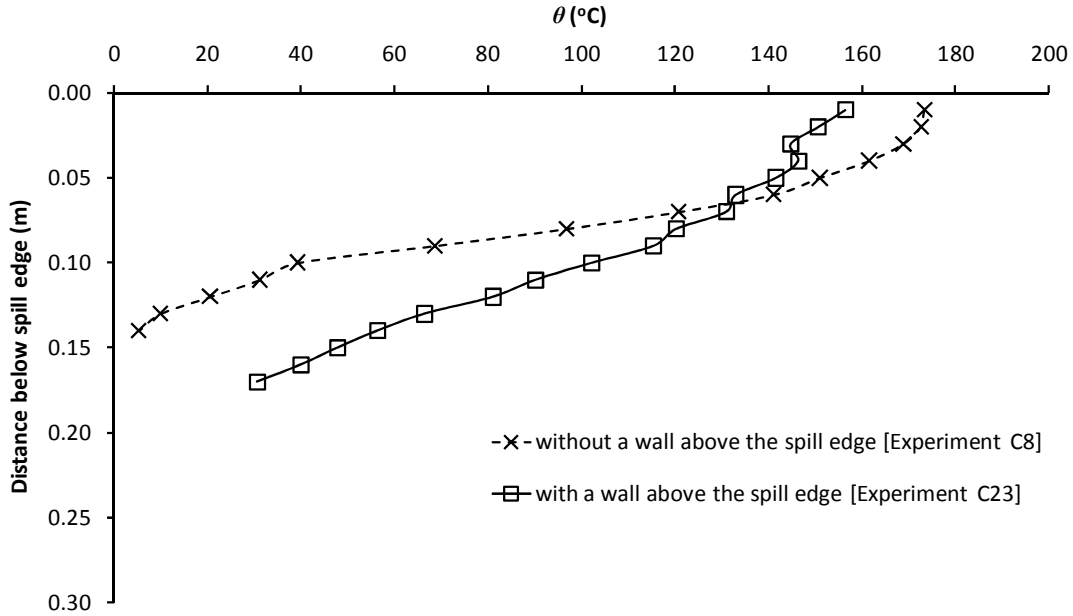

Figure 5.25: Comparison of temperature profiles for Experiments C8 and C23

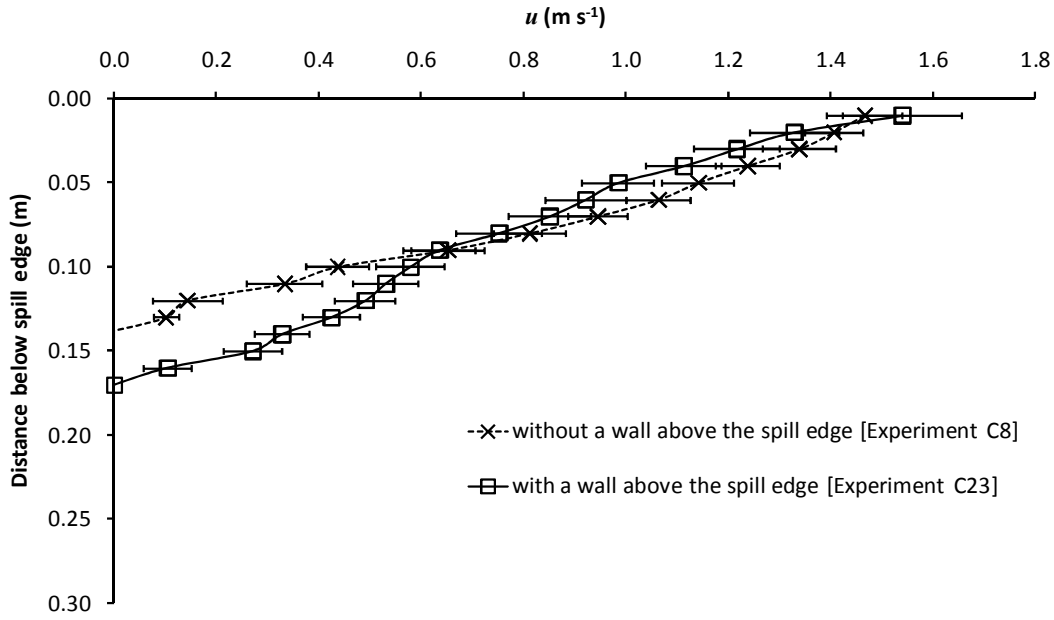

Figure 5.26: Comparison of velocity profiles for Experiments C8 and C23

Figure 5.25 shows differences between the temperature profiles, both with and without a wall above the edge. The temperature just below the edge tends to be lower for a flow with a wall compared to a flow without a wall. However, higher temperatures were measured at greater distances below the spill edge compared to the flow without a wall, indicating a deeper layer flow below the edge. This is supported when considering Figure 5.26 which shows that the velocity profile for a flow with a wall above, gives rise to higher velocities being measured at greater distances below the edge compared to the flow without a wall. The analysis is further supported if the observed layer depth below the edge is considered, which shows that the depth of the flow with a wall (i.e. 0.160 m) was deeper than the flow without a wall (i.e. 0.120 m).

As the presence of a wall above the edge gives rise to a deeper layer flow below the edge for an intermediate width flow, and that this appears to be the only significant difference between the profiles, it is unsurprising that the characteristic *Fr* was lower than without a wall [with reference to Equation (3-2)].

Figures 5.27 and 5.28 show a comparison of the profiles of temperature and velocity respectively, for narrow flow with an intermediate fire size, with and without a wall above the spill edge (i.e. for Experiments C14 and C17, W_s = 0.2 m and $\dot{Q}_t$ = 10 kW).

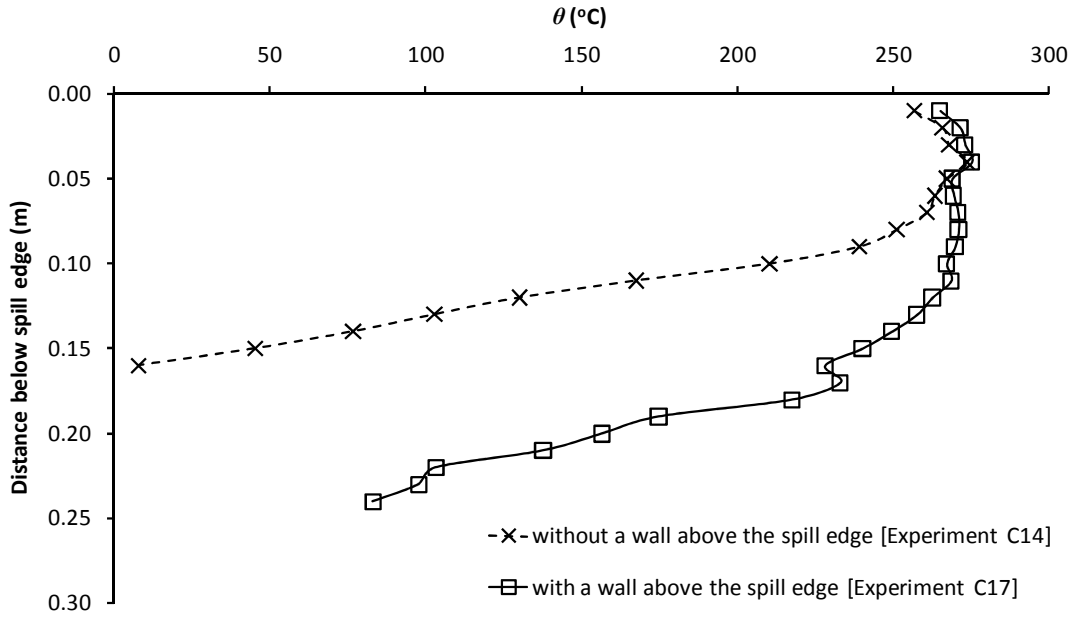

Figure 5.27: Comparison of temperature profiles for Experiments C14 and C17

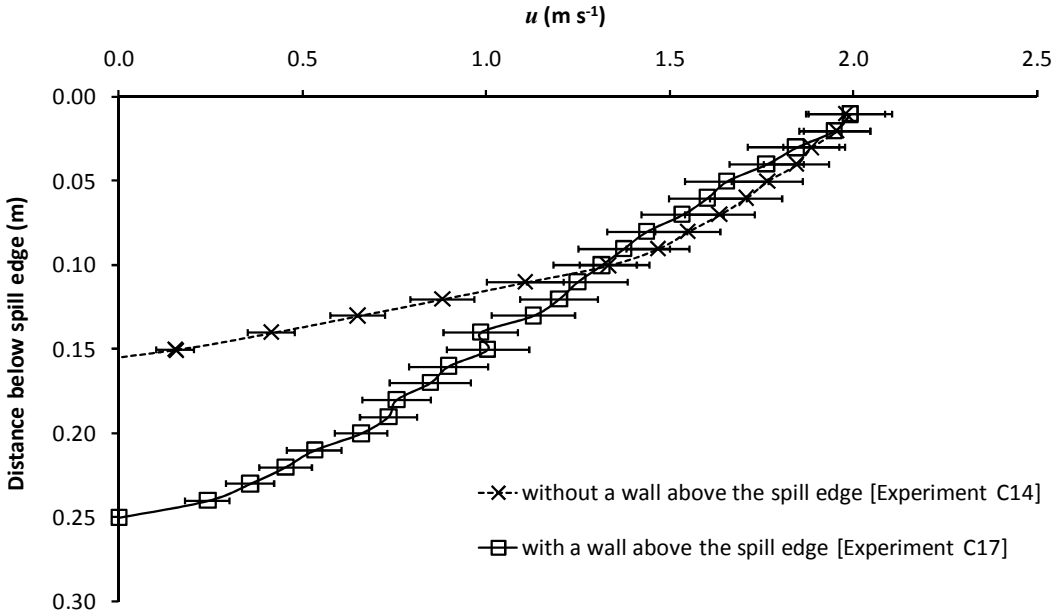

Figure 5.28: Comparison of velocity profiles for Experiments C14 and C17

Figures 5.27 and 5.28 show significant differences between the temperature and velocity profiles below the spill edge which are consistent with an increase in the depth of the layer flow when a wall is present above the spill edge. The observed layer depth below the edge with a wall above (i.e. 0.245 m) was much deeper than the flow without a wall (i.e. 0.155 m). Again, as the increase in layer depth appears to be the significant difference between the profiles for a narrow width flow, it is unsurprising that the characteristic *Fr* was lower than for flows without a wall above.

These differences in the flow behaviour can possibly be explained by considering the behaviour of the plume beyond the spill edge, when a wall is present above the edge. The plume behaviour beyond the spill edge is specifically explained in Chapter 7, however, in an attempt to explain the differences described above, a brief is description is given here.

The plume behaviour beyond the spill edge was highly dependent on the width of plume examined. Plumes generated from a wide flow (e.g. W_s = 1.0 m) were observed to adhere to the wall above the opening almost immediately (see Figure 5.29a). Plumes generated from intermediate width openings (e.g. W_s = 0.6 to 0.8 m) were initially observed to horizontally project beyond the opening, before curling back and reattaching to the wall above, after which the plume adhered to the wall (see Figure 5.29b). The height of reattachment above the spill edge tended to increase as W_s decreased and when the fire size and depth of the layer below the spill edge increased. Plumes generated from narrow width openings (e.g. W_s = 0.2 to 0.4 m) were observed to project beyond the opening and not reattach to the wall above (see Figure 5.29c).

This behaviour is similar to that observed by Yokoi [80] who examined the trajectory of flames from windows from post-flashover fires. Yokoi characterised the behaviour of the flame plumes by considering the characteristics of the flow at the window opening in terms of width and depth.

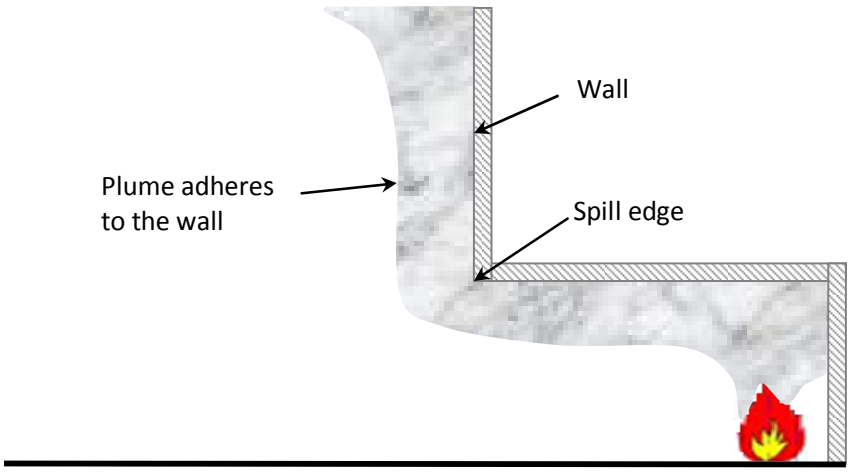

a) Plume from a wide flow (e.g. W_s = 1.0 m)

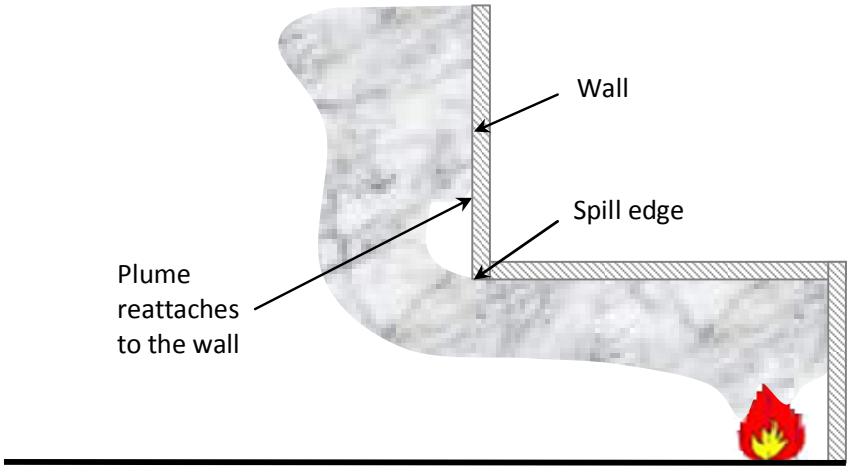

b) Plume from an intermediate width flow (e.g. W_s = 0.6 and 0.8 m)

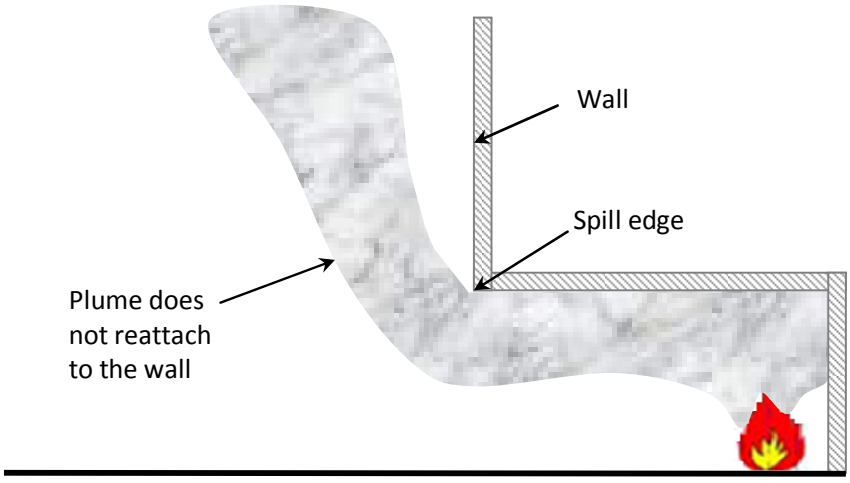

c) Plume from a narrow width flow (e.g. W_s = 0.2 and 0.4 m)

Figure 5.29: Plume behaviour beyond the spill edge with a wall above the edge

It appears that the behaviour of the plume beyond the spill edge affects the characteristics of the flow below the edge for plumes which subsequently reattach or do not attach to the wall above. The plume behaviour downstream of the spill edge appears to create impedance to the flow which affects the characteristics of the flow upstream (i.e. below the spill edge). This proposed phenomenon is analogous to flow behaviour described by McCaffrey and Quintiere [129] and Quintiere *et al.* [130] on how an obstruction downstream of a flow can cause counter-currents causing impedance to the flow upstream. It is also analogous to the simple case of a flow over an obstacle described by Turner [131] who states that the flow behaviour is dependent upon the *Fr*. For $Fr > 1$ small disturbances cannot propagate upstream against the flow and any obstacle will only have a local effect, however, for $Fr < 1$ short waves can remain at rest relative to the obstacle (i.e. stationary waves) which can give rise to longer waves which propagate upstream, causing an increase in the depth of the flow upstream of the obstacle. Although there were no physical obstructions in the flow beyond the spill edge in this work (apart from the ceiling of the hood), it is possible that the plume behaviour could have given rise to the propagation of waves upstream, which in turn created impedance and an increase in the depth of the flow below the spill edge. The experimental method meant that it was not possible to identify the exact mechanism for the flow behaviour observed in this work, although it is encouraging to note that similar behaviour has been reported in previous studies.

The flow below the spill edge can be characterised by following a similar analysis to that of Yokoi, by considering the out flowing layer in terms of the width and depth in non-dimensional terms (i.e. W_s/d_s) and the *Fr* (see Figure 5.30). Figure 5.30 shows that the behaviour of the plume beyond the spill edge can be described by the characteristics of the flow below the spill edge. The plume did not reattach to the wall above when W_s/d_s was less than approximately 3 and this gave rise to a constant *Fr* below the spill edge of approximately 0.9. The plume reattached to the wall above the spill edge when W_s/d_s was between approximately 3 and 8, where the *Fr* below the edge increases from 0.9 to 1.3 according to a linear relationship. The plume adheres to the wall when W_s/d_s was greater than 8.0, where the *Fr* below the spill edge remained reasonably constant with a value of approximately 1.3.

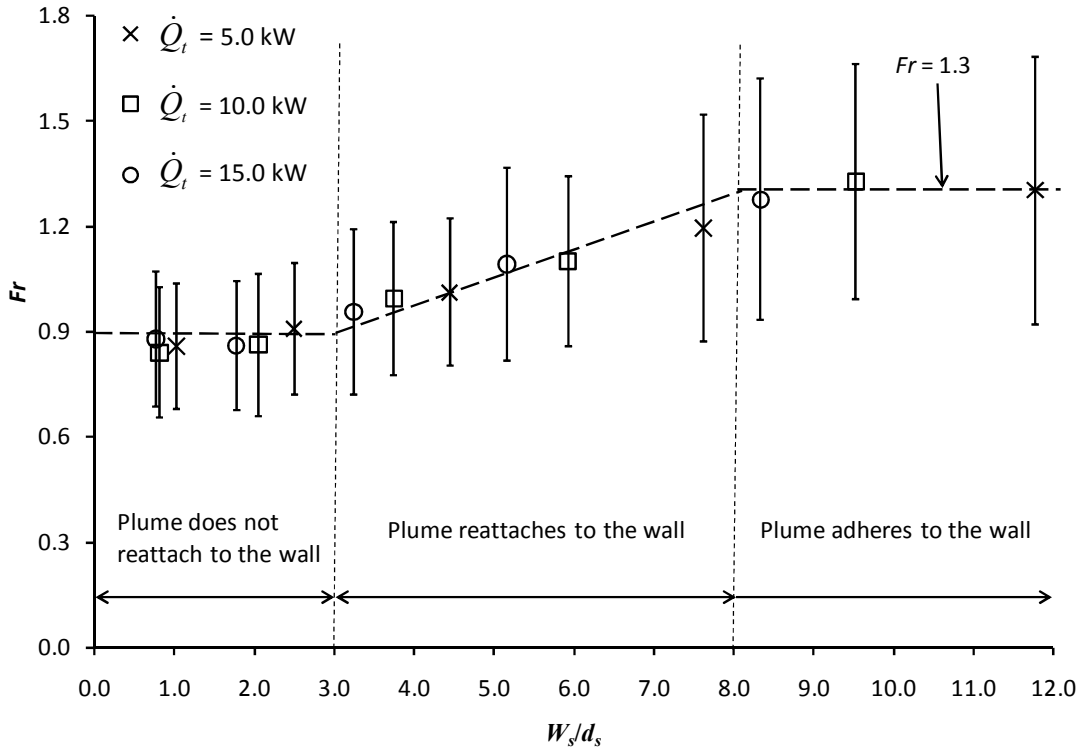

Figure 5.30: Plot of *Fr* versus W_s/ d_s for Experiments C16 to C30

5.2.5 Prediction of the mass flow rate of gases below the spill edge

5.2.5.1 Analytical methods

Figure 5.31 shows a comparison between the experimental results with the predictions of $\dot{m}_s$ using the analytical methods by Thomas *et al.* [Equation (5-2)] and Morgan [Equation (5-3)] respectively. The predictions were again made assuming C_d = 1.0, with the visually derived layer depths below the spill edge being used.

Figure 5.31 shows that the predictions of $\dot{m}_s$ using both the Morgan and Thomas *et al.* methods provide much more scatter compared to the equivalent predictions shown in Figure 5.9 (for flows without a wall above the spill edge). In general, the Morgan method provides conservative predictions of $\dot{m}_s$ although a few predictions give very good agreement with the experiment. The Thomas *et al.* method generally under predicts the experiment, although there are some predictions which match the experiment.

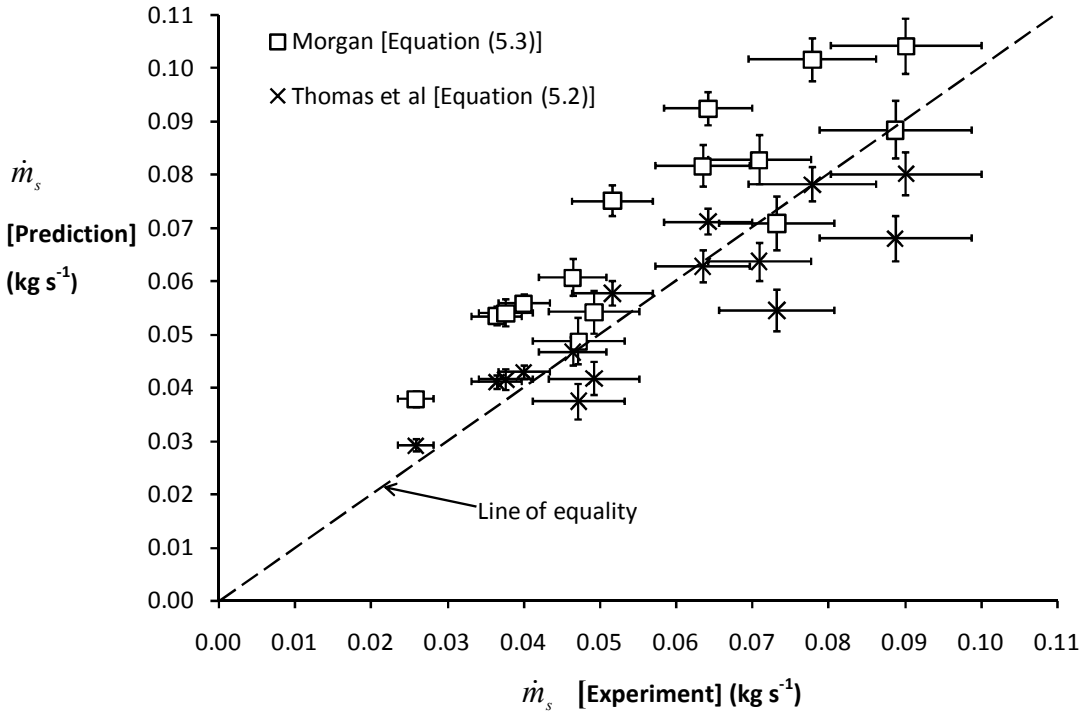

Figure 5.31: Comparison of the prediction of $\dot{m}_s$ with experiment

The reason for the difference in the predictions of $\dot{m}_s$ between these methods has already been described in section 5.1.5.1 (i.e. the use of the profile correction factor, κ_m, in the Morgan method) and is not repeated here.

As the Thomas *et al.* method generally under predicts $\dot{m}_s$ the value of C_d required in Equation (5-2) to provide a good match with the experiment will be greater than 1.0, which is non-physical, therefore the Thomas *et al.* method is not considered further and the performance of the Morgan method is dealt with in the analysis that follows.

In an attempt to explain why there is greater scatter in the predictions of $\dot{m}_s$ using the Morgan method, the predictions are shown again in Figure 5.32, however, the values of W_s examined for each prediction are shown in this case.

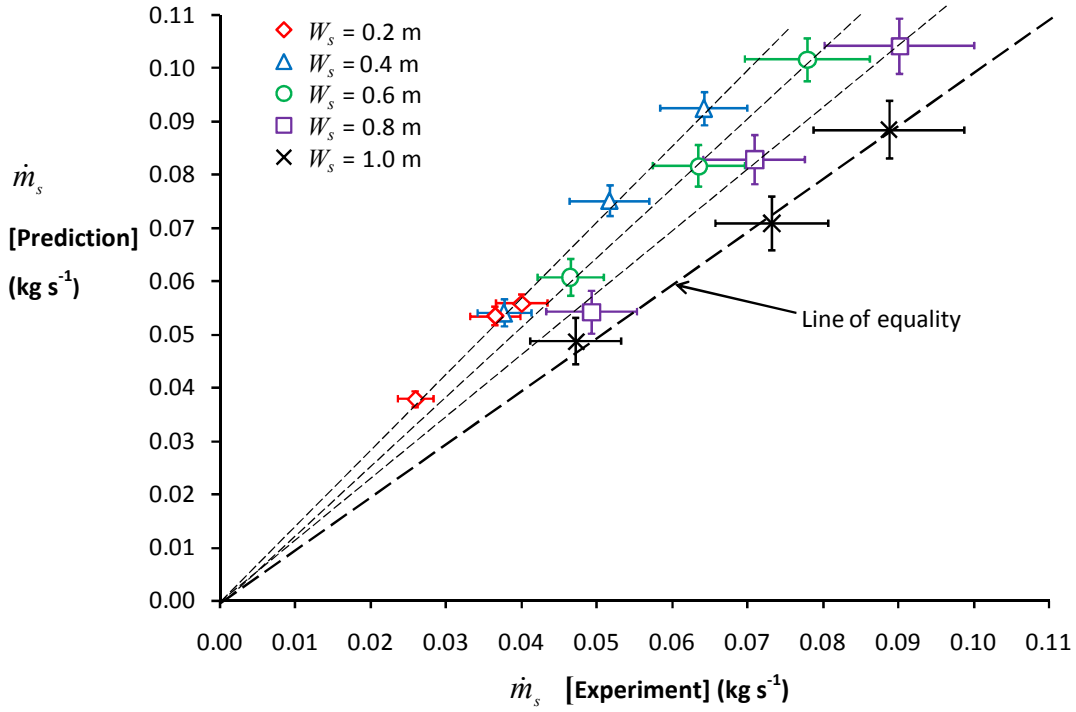

Figure 5.32: Comparison of the prediction of $\dot{m}_s$ by Morgan [51] with experiment

Figure 5.32 clearly shows that the prediction of $\dot{m}_s$ appears to be dependent on W_s. For flows with W_s = 1.0 m there is excellent agreement between the prediction and the experiment. However, as W_s decreases the discrepancy between the prediction and the experiment increases. Figure 5.32 shows separate linear relationships describing the level of agreement between the prediction and the experiment for flows with W_s = 0.8 and 0.6 m respectively. The predictions for flows with W_s = 0.4 and 0.2 m are described by a common linear relationship.

There appears to be some dependency between the plume behaviour beyond the spill edge and the prediction of $\dot{m}_s$ as each linear relationship shown in Figure 5.32 is common to those values of W_s which give differences in the observed plume behaviour (i.e. the plume adheres to the wall above the edge for W_s = 1.0 m, it reattaches to the wall at different heights above the edge for W_s = 0.8 and 0.6 m respectively, and it does not reattach to the wall for W_s = 0.4 and 0.2 m).

Those predictions which were conservative (i.e. for flows with W_s = 0.2 to 0.8 m) require a C_d of less than 1.0 to be used in Equation (5-3) to provide a prediction to match the experiment. This supports the above analysis that plumes which reattach or do not attach to the wall above cause impedance to the flow which will necessarily reduce the C_d of the flow below the spill edge. This could also explain the increased boundary layer effect observed in Figure 5.16 for flows with W_s between 0.2 to 0.8 m.

The values of C_d required to provide predictions of $\dot{m}_s$ to match the experiment were determined. These were then plotted against W_s/d_s as this non-dimensional parameter can be used to describe the plume behaviour beyond the spill edge following the analysis of Yokoi (see Figure 5.33).

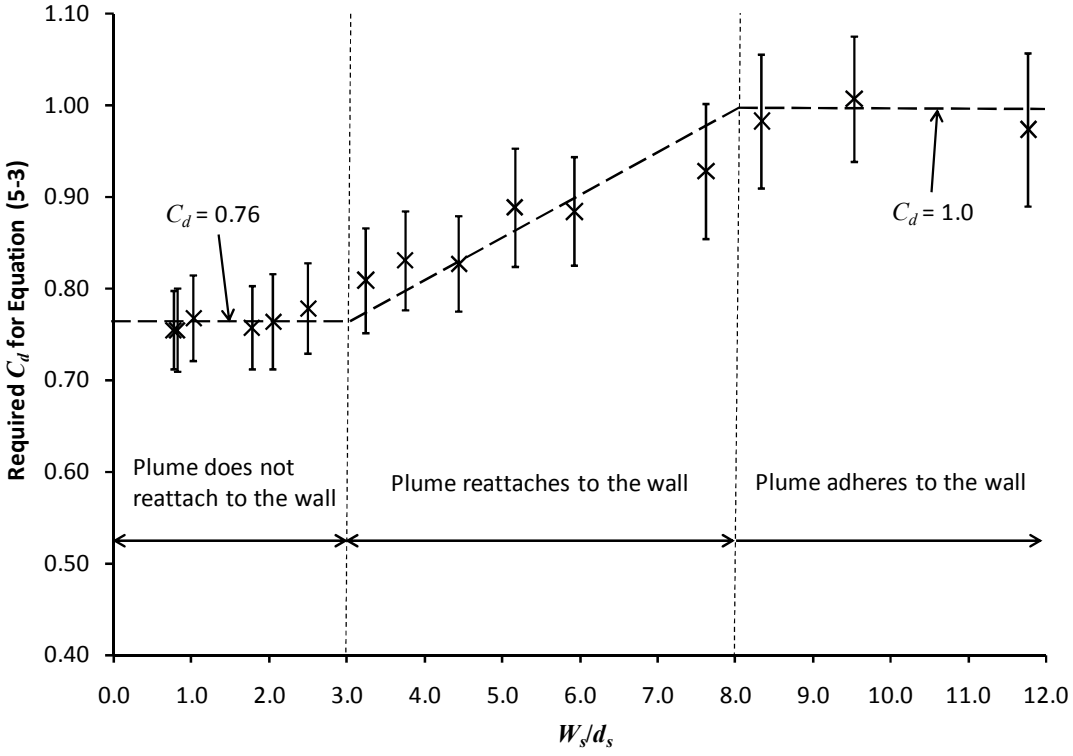

Figure 5.33: Plot of required C_d in Equation (5-3) to match the experiment (κ_m =1.3)

Figure 5.33 shows a similar behaviour to that shown in Figure 5.30 (when considering Fr with respect to W_s/d_s). Figure 5.33 shows that when W_s/d_s was less than approximately 3, when the plume did not reattach to the wall above, the required C_d was approximately constant with a value of 0.76. For values of W_s/d_s greater than 8.0, when the plume adheres to the wall, the required C_d was approximately constant with a value of 1.0 (similar to flows without a wall). For values of W_s/d_s between 3 and 8, when the plume reattaches to the wall, the required C_d can be described by the following linear relationship.

$$\text{If } 3 < \left(\frac{W_s}{d_s}\right) < 8 \qquad C_d = 0.048\left(\frac{W_s}{d_s}\right) + 0.616 \tag{5-6}$$

Thus, when using the Morgan method [Equation (5-3)] the required value of C_d to give an appropriate prediction of $\dot{m}_s$ for a flow with a vertical wall projecting above a spill edge with a flat ceiling is given by,

$$\text{If } \left(\frac{W_s}{d_s}\right) \le 3 \quad \text{then } C_d = 0.76$$

$$\text{If } 3 < \left(\frac{W_s}{d_s}\right) < 8 \quad \text{then } C_d = 0.05\left(\frac{W_s}{d_s}\right) + 0.62 \tag{5-7}$$

$$\text{If } \left(\frac{W_s}{d_s}\right) \ge 8 \quad \text{then } C_d = 1.0$$

Alternatively, assuming a C_d of 1.0 will give rise to give either an appropriate or conservative (by up to approximately 30%) prediction of $\dot{m}_s$.

5.2.5.2 Simple empirical formulae

Figure 5.34 shows a comparison of the experimental results with the predictions of $\dot{m}_s$ using the simple formulae given by Hansell [Equation (5-4)] and CIBSE/BS 7974 [Equation (5-5)].

The predictions made using Equation (5-4) again assumed a C_d = 1.0 and C_e = 0.34 and were determined using full scale equivalent values of the fire perimeter and the compartment geometry which were subsequently scaled down to model scale (see section 5.1.5.2).

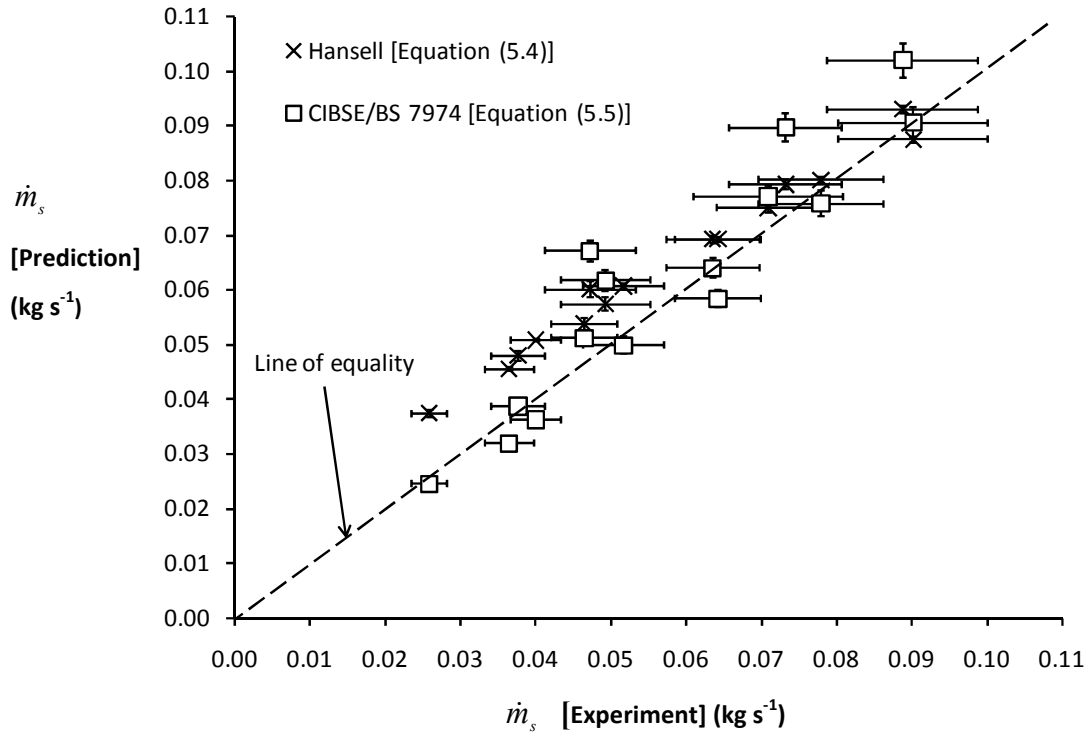

Figure 5.34: Comparison of the prediction of $\dot{m}_s$ with experiment

Figure 5.34 shows that for relatively low values of $\dot{m}_s$ produced from narrow width flows, the predictions using the Hansell method are generally conservative by up to approximately 25%. However, for larger values of $\dot{m}_s$ (produced from wider flows) there is very good agreement between the predictions and the experiment which are generally equal to within one standard error.

Again, it is unsurprising that this method is more reliable for wide flows as Hansell states that this method specifically applies to layer flows which are much wider than their depth.

Figure 5.34 shows that the predictions of using the CIBSE/BS 7974 method generally provides excellent agreement with the experimental results for the majority of flows examined. However, there are a few predictions which are conservative (by up to approximately 25%) which were determined from wide flows.

As the predictions are mostly appropriate (or conservative in some cases) for the range of flows examined, the use of either method seems suitable for design purposes, although the CIBSE/BS 7974 method may be preferential due to its relative simplicity.

5.3 Conclusions

This chapter provides experimental data to characterise the horizontal flow of gases below a spill edge with a flat ceiling, with and without a vertical wall above the edge, for a range of fire sizes and compartment geometries. Analysis of these results has provided the following conclusions:

The formula given by Morgan [Equation 5.1] to predict $\overline{\theta}_s$ generally gives good agreement with the experiment for the range of conditions studied. It appears to be suitable for design purposes to reduce formulae which are dependent on $\theta_{\max,s}$ and applies to geometries with or without a wall above the spill edge.

The empirical formulae given by Hansell [Equation (5-4)] to predict $\dot{m}_s$ generally gives good agreement with the experiment for geometries with and without a wall above the edge, however, the performance of this method is better for layer flows that are wider than their depth. The CIBSE/BS 7974 method [Equation (5-5)] generally provides good agreement with the experiment for the range of conditions studied. Either of these formulae appear to be suitable for design purposes, although, the CIBSE/BS 7974 formula may be preferential due to its relative simplicity and that it generally performs better for the range of conditions studied.

For flows without a wall above the spill edge, the analytical method given by Morgan [Equation (5-3)] gives an excellent prediction of $\dot{m}_s$. The method by Thomas *et al.* [Equation (5-2)] gives predictions which are approximately 30% lower than the Morgan method and the experimental results. The difference in the predictions appears to be due to the profile correction factor used in the Morgan method to take into account the shape of the buoyancy profile of the flow in the integration to calculate $\dot{m}_s$.

The presence of a wall can affect the behaviour of the plume beyond the spill edge which in turn affects the characteristics of the flow below the edge. It appears that the plume behaviour downstream of the edge can create impedance to the flow which affects the characteristics of the flow upstream. The plume behaviour appears to be dependent on W_s and d_s consistent with the findings of Yokoi [80].

For flows with a wall above the spill edge, Equation (5-3) by Morgan generally gives a conservative prediction of $\dot{m}_s$ whereas Equation (5-2) by Thomas *et al.* tends to under predict $\dot{m}_s$. The predictions using both methods were dependent on the plume behaviour beyond the edge. To achieve good prediction of $\dot{m}_s$ using the Morgan method, a modification to C_d is proposed which is dependent on W_s and d_s given by,

$$\text{If } \left(\frac{W_s}{d_s}\right) \leq 3 \quad \text{then } C_d = 0.76$$

$$\text{If } 3 < \left(\frac{W_s}{d_s}\right) < 8 \quad \text{then } C_d = 0.05\left(\frac{W_s}{d_s}\right) + 0.62$$

$$\text{If } \left(\frac{W_s}{d_s}\right) \geq 8 \quad \text{then } C_d = 1.0$$

Alternatively, assuming a discharge coefficient of 1.0 will give rise to give either an appropriate or conservative (by up to approximately 30%) prediction of $\dot{m}_s$.

Chapter 6

6. Balcony spill plume experiments

This chapter presents the results and discussion for the series of experiments examining entrainment of air into a balcony spill plume. Both 2-D plumes and 3-D plumes (with and without channelling screens below the balcony) are considered in the analysis.

Some aspects of this chapter have been published in a paper presented at the 9th International Symposium on Fire Safety Science in September 2008 [86]. The paper is given in Appendix F and was accepted for publication following a peer review by three anonymous referees.

6.1 Experimental results

A summary of the key results for the series of experiments examining entrainment of air into a balcony spill plume is given in Table 6.1. Table 6.1 details the measured mass flow rate of gases entering the layer in the collecting hood due to the spill plume ($\dot{m}_p$) and the temperature (above ambient) of the gases in the throat of the exhaust vent (θ_{vent}) determined from the average of the five thermocouples in the vent. Selected results for the associated horizontal flow of gases below the spill edge for each experiment are also included for completeness (already given in Table 5.1). The results are presented in terms of the time averaged mean value with associated standard errors.

As it was not possible to directly measure the properties of the horizontal flow of gases below the spill edge for flows without channelling screens below the balcony, the relevant results for these experiments are marked as non-applicable (i.e. n/a) in Table 6.1.

For those experiments which examined plumes with a relatively high height of rise (i.e. $z_s \geq 0.95$ m), visual observations indicated that in some cases fresh air was possibly being entrained into the exhaust vent from directly below the smoke layer. This effect is more commonly known as "plug-holing" and generally occurs for smoke layers that are relatively cool and shallow, where smoke exhaust is provided by a dominant vent, as was the case for those experiments with a high height of rise.

As the measurement technique to determine $\dot{m}_p$ is based on the dilution of CO_2 from the IMS fire source, the effect of "plug-holing" will give rise to an anomalous amount of dilution at the gas sampling location which will give rise to an erroneously high value of $\dot{m}_p$. Due to the thin nature of the smoke layer in the collecting hood at high heights of rise, it was difficult to determine if "plug-holing" was occurring based on visual observations alone. Therefore, Equation (6-1) given by Klote and Milke [13] was used to determine the maximum mass flow rate of gases that can efficiently be exhausted using a single exhaust vent ($\dot{m}_{\max}$) without "plug-holing" occurring (a new equation to determine "plug-holing" is given in the latest version of NFPA 92B [2]).

$$\dot{m}_{\max} = 3.13\eta d_l^{5/2}\left(\frac{\theta_l}{T_l}\right)^{1/2}\left(\frac{T_{amb}}{T_l}\right)^{1/2} \qquad \textbf{(6-1)}$$

The visually derived smoke layer depth below the exhaust vent was used in Equation (6-1) and the temperature of the gases in the throat of the exhaust vent was assumed to represent the smoke layer temperature. The value of η was taken to be 2.0 as recommended by Klote and Milke for an exhaust vent near a wall.

For those experiments where the value of $\dot{m}_p$ was greater than $\dot{m}_{\max}$ it can be concluded that "plug-holing" was likely to be occurring (as it is not possible for $\dot{m}_p$ to be greater than $\dot{m}_{\max}$ without "plug-holing") and that the measured values of $\dot{m}_p$ are erroneous. These experiments are marked with an asterisk in Table 6.1. Therefore the values of $\dot{m}_p$ from these experiments have been neglected from the entrainment analysis that follows and should not be used in any subsequent analysis.

Expt	$\dot{Q}_t$ (kW)	$\dot{Q}_c$ (kW)	$\dot{m}_s$ (kg s^{-1})	$d_{v,s}$ (m)	$\dot{m}_p$ (kg s^{-1})	θ_{vent} (^{o}C)	T_1 (K)
E1	5.0 ± 0.3	3.6 ± 0.2	0.059 ± 0.005	0.100 ± 0.005	0.074 ± 0.004	25.62 ± 0.05	289.8
E2	10.0 ± 0.3	8.0 ± 0.6	0.082 ± 0.007	0.115 ± 0.005	0.094 ± 0.003	47.90 ± 0.06	291.6
E3	15.0 ± 0.3	12.2 ± 1.0	0.099 ± 0.009	0.125 ± 0.005	0.115 ± 0.002	66.85 ± 0.05	292.5
E4	5.0 ± 0.3	n/a	n/a	n/a	0.081 ± 0.004	24.75 ± 0.03	289.5
E5	10.0 ± 0.3	n/a	n/a	n/a	0.103 ± 0.003	44.72 ± 0.06	290.2
E6	15.0 ± 0.3	n/a	n/a	n/a	0.123 ± 0.002	62.71 ± 0.06	291.3
E7	5.0 ± 0.3	3.7 ± 0.3	0.052 ± 0.005	0.105 ± 0.005	0.072 ± 0.004	25.95 ± 0.03	290.5
E8	10.0 ± 0.3	7.8 ± 0.6	0.069 ± 0.006	0.115 ± 0.005	0.093 ± 0.003	46.02 ± 0.05	291.0
E9	15.0 ± 0.3	12.8 ± 0.8	0.091 ± 0.007	0.135 ± 0.005	0.109 ± 0.002	67.08 ± 0.06	292.2
E10	5.0 ± 0.3	n/a	n/a	n/a	0.073 ± 0.004	23.40 ± 0.03	288.9
E11	10.0 ± 0.3	n/a	n/a	n/a	0.103 ± 0.003	42.59 ± 0.07	289.6
E12	15.0 ± 0.3	n/a	n/a	n/a	0.122 ± 0.002	60.69 ± 0.06	290.9
E13	5.0 ± 0.3	3.9 ± 0.2	0.042 ± 0.004	0.110 ± 0.005	0.058 ± 0.003	27.19 ± 0.05	290.3
E14	10.0 ± 0.3	7.7 ± 0.5	0.058 ± 0.005	0.120 ± 0.005	0.079 ± 0.002	50.57 ± 0.04	291.3
E15	15.0 ± 0.3	12.2 ± 0.7	0.070 ± 0.005	0.140 ± 0.005	0.094 ± 0.002	75.90 ± 0.09	292.9
E16	5.0 ± 0.3	n/a	n/a	n/a	0.065 ± 0.004	29.09 ± 0.03	291.0
E17	10.0 ± 0.3	n/a	n/a	n/a	0.091 ± 0.003	49.16 ± 0.05	292.4
E18	15.0 ± 0.3	n/a	n/a	n/a	0.104 ± 0.002	69.83 ± 0.15	292.8
E19	5.0 ± 0.3	3.6 ± 0.2	0.034 ± 0.002	0.115 ± 0.005	0.045 ± 0.002	29.88 ± 0.02	290.0
E20	10.0 ± 0.3	7.2 ± 0.4	0.043 ± 0.003	0.125 ± 0.005	0.063 ± 0.002	56.01 ± 0.05	290.6
E21	15.0 ± 0.3	10.9 ± 0.6	0.052 ± 0.004	0.145 ± 0.005	0.072 ± 0.001	80.46 ± 0.08	292.4
E22	5.0 ± 0.3	n/a	n/a	n/a	0.061 ± 0.003	28.05 ± 0.03	290.5
E23	10.0 ± 0.3	n/a	n/a	n/a	0.085 ± 0.002	46.84 ± 0.04	291.0
E24	15.0 ± 0.3	n/a	n/a	n/a	0.100 ± 0.002	65.28 ± 0.08	292.3
E25	5.0 ± 0.3	3.5 ± 0.2	0.024 ± 0.002	0.135 ± 0.005	0.034 ± 0.002	32.37 ± 0.05	289.5
E26	10.0 ± 0.3	6.6 ± 0.4	0.028 ± 0.002	0.155 ± 0.005	0.046 ± 0.001	62.59 ± 0.04	291.0
E27	15.0 ± 0.3	9.9 ± 0.6	0.033 ± 0.002	0.170 ± 0.005	0.055 ± 0.001	86.30 ± 0.08	292.4
E28	5.0 ± 0.3	n/a	n/a	n/a	0.058 ± 0.002	28.43 ± 0.03	290.5
E29	10.0 ± 0.3	n/a	n/a	n/a	0.076 ± 0.002	47.26 ± 0.03	292.1
E30	15.0 ± 0.3	n/a	n/a	n/a	0.090 ± 0.002	63.72 ± 0.06	292.1
E61	5.0 ± 0.3	3.5 ± 0.2	0.024 ± 0.002	0.135 ± 0.005	0.079 ± 0.004	23.00 ± 0.03	289.0
E62	10.0 ± 0.3	6.6 ± 0.4	0.028 ± 0.002	0.155 ± 0.005	0.114 ± 0.003	36.95 ± 0.05	289.4
E63	15.0 ± 0.3	9.9 ± 0.6	0.033 ± 0.002	0.170 ± 0.005	0.133 ± 0.002	50.08 ± 0.06	290.6
E64	5.0 ± 0.3	n/a	n/a	n/a	0.172 ± 0.009	15.19 ± 0.03	289.0
E65	10.0 ± 0.3	n/a	n/a	n/a	0.211 ± 0.006	25.21 ± 0.05	289.7
E66	15.0 ± 0.3	n/a	n/a	n/a	0.259 ± 0.005	32.21 ± 0.05	290.5
E67	5.0 ± 0.3	3.6 ± 0.2	0.034 ± 0.002	0.115 ± 0.005	0.102 ± 0.006	21.53 ± 0.03	288.5
E68	10.0 ± 0.3	7.2 ± 0.4	0.043 ± 0.003	0.125 ± 0.005	0.146 ± 0.004	35.50 ± 0.03	289.0
E69	15.0 ± 0.3	10.9 ± 0.6	0.052 ± 0.004	0.145 ± 0.005	0.175 ± 0.003	48.72 ± 0.08	289.0
E70	5.0 ± 0.3	n/a	n/a	n/a	0.161 ± 0.009	15.87 ± 0.03	289.0
E71	10.0 ± 0.3	n/a	n/a	n/a	0.225 ± 0.006	26.19 ± 0.05	289.0
E72	15.0 ± 0.3	n/a	n/a	n/a	0.269 ± 0.005	34.68 ± 0.05	289.5
E73	5.0 ± 0.3	3.9 ± 0.2	0.042 ± 0.004	0.110 ± 0.005	0.114 ± 0.006	19.89 ± 0.03	289.0
E74	10.0 ± 0.3	7.7 ± 0.5	0.058 ± 0.005	0.120 ± 0.005	0.172 ± 0.005	31.95 ± 0.05	289.5
E75	15.0 ± 0.3	12.2 ± 0.7	0.070 ± 0.005	0.140 ± 0.005	0.204 ± 0.004	45.14 ± 0.05	290.7

Table 6.1: Summary of results for the series of balcony spill plume experiments

Expt	$\dot{Q}_t$ (kW)	$\dot{Q}_c$ (kW)	$\dot{m}_s$ (kg s^{-1})	$d_{v,s}$ (m)	$\dot{m}_p$ (kg s^{-1})	θ_{vent} (^{o}C)	T_1 (K)
E76	5.0 ± 0.3	n/a	n/a	n/a	0.159 ± 0.009	17.21 ± 0.05	289.5
E77	10.0 ± 0.3	n/a	n/a	n/a	0.228 ± 0.006	27.15 ± 0.05	290.5
E78	5.0 ± 0.3	3.7 ± 0.3	0.052 ± 0.005	0.105 ± 0.005	0.140 ± 0.008	16.99 ± 0.03	290.5
E79	10.0 ± 0.3	7.8 ± 0.6	0.069 ± 0.006	0.115 ± 0.005	0.192 ± 0.005	28.98 ± 0.05	291.0
E80	15.0 ± 0.3	12.8 ± 0.8	0.091 ± 0.007	0.135 ± 0.005	0.230 ± 0.004	39.64 ± 0.04	292.0
E81	5.0 ± 0.3	n/a	n/a	n/a	0.167 ± 0.009	16.20 ± 0.04	289.9
E82	10.0 ± 0.3	n/a	n/a	n/a	0.235 ± 0.006	26.80 ± 0.05	290.5
E83	5.0 ± 0.3	3.6 ± 0.2	0.059 ± 0.005	0.100 ± 0.005	0.161 ± 0.004	15.74 ± 0.03	287.9
E84	10.0 ± 0.3	8.0 ± 0.6	0.082 ± 0.007	0.115 ± 0.005	0.218 ± 0.006	26.06 ± 0.05	288.5
E85	15.0 ± 0.3	12.2 ± 1.0	0.099 ± 0.009	0.125 ± 0.005	0.255 ± 0.005	36.04 ± 0.07	289.0
E86	5.0 ± 0.3	n/a	n/a	n/a	0.177 ± 0.005	14.06 ± 0.03	289.0
E87	10.0 ± 0.3	n/a	n/a	n/a	0.254 ± 0.007	24.49 ± 0.05	289.0
E88	5.0 ± 0.3	3.6 ± 0.2	0.059 ± 0.005	0.100 ± 0.005	0.232 ± 0.013	13.12 ± 0.03	289.6
E89	10.0 ± 0.3	8.0 ± 0.6	0.082 ± 0.007	0.115 ± 0.005	0.306 ± 0.008	20.82 ± 0.04	290.6
E90	15.0 ± 0.3	12.2 ± 1.0	0.099 ± 0.009	0.125 ± 0.005	0.369 ± 0.007	27.75 ± 0.05	291.0
E91	5.0 ± 0.3	n/a	n/a	n/a	0.251 ± 0.014	12.49 ± 0.02	290.6
E92	10.0 ± 0.3	n/a	n/a	n/a	0.354 ± 0.001	19.09 ± 0.07	291.5
E93	10.0 ± 0.3	8.0 ± 0.6	0.082 ± 0.007	0.115 ± 0.005	0.277 ± 0.008	22.63 ± 0.04	290.8
E94	5.0 ± 0.3	3.7 ± 0.3	0.052 ± 0.005	0.105 ± 0.005	0.221 ± 0.012	12.05 ± 0.04	288.2
E95	10.0 ± 0.3	7.8 ± 0.6	0.069 ± 0.006	0.115 ± 0.005	0.294 ± 0.008	20.25 ± 0.05	288.8
E96	15.0 ± 0.3	12.8 ± 0.8	0.091 ± 0.007	0.135 ± 0.005	0.353 ± 0.006	28.11 ± 0.05	289.3
E97	5.0 ± 0.3	n/a	n/a	n/a	0.242 ± 0.013	13.41 ± 0.04	288.9
E98	10.0 ± 0.3	n/a	n/a	n/a	0.327 ± 0.009	20.36 ± 0.05	289.2
E99	10.0 ± 0.3	7.8 ± 0.6	0.069 ± 0.006	0.115 ± 0.005	0.250 ± 0.007	24.10 ± 0.05	289.1
E100	5.0 ± 0.3	3.9 ± 0.2	0.042 ± 0.004	0.110 ± 0.005	0.178 ± 0.010	13.47 ± 0.03	288.5
E101	10.0 ± 0.3	7.7 ± 0.5	0.058 ± 0.005	0.120 ± 0.005	0.248 ± 0.007	23.44 ± 0.04	289.1
E102	15.0 ± 0.3	12.2 ± 0.7	0.070 ± 0.005	0.140 ± 0.005	0.301 ± 0.005	31.92 ± 0.06	289.1
E103	5.0 ± 0.3	n/a	n/a	n/a	0.216 ± 0.012	15.54 ± 0.03	289.4
E104	10.0 ± 0.3	n/a	n/a	n/a	0.312 ± 0.009	20.66 ± 0.06	290.0
E105	10.0 ± 0.3	7.7 ± 0.5	0.058 ± 0.005	0.120 ± 0.005	0.211 ± 0.006	27.26 ± 0.04	289.3
E106	5.0 ± 0.3	3.6 ± 0.2	0.034 ± 0.002	0.115 ± 0.005	0.161 ± 0.009	15.59 ± 0.03	288.3
E107	10.0 ± 0.3	7.2 ± 0.4	0.043 ± 0.003	0.125 ± 0.005	0.228 ± 0.006	26.10 ± 0.05	288.7
E108	15.0 ± 0.3	10.9 ± 0.6	0.052 ± 0.004	0.145 ± 0.005	0.287 ± 0.005	35.27 ± 0.06	289.2
E109	5.0 ± 0.3	n/a	n/a	n/a	0.250 ± 0.014	16.72 ± 0.04	288.7
E110	10.0 ± 0.3	n/a	n/a	n/a	0.326 ± 0.009	21.96 ± 0.05	289.1
E111	10.0 ± 0.3	7.2 ± 0.4	0.043 ± 0.003	0.125 ± 0.005	0.159 ± 0.004	33.22 ± 0.05	289.5
E112	5.0 ± 0.3	3.5 ± 0.2	0.024 ± 0.002	0.135 ± 0.005	0.106 ± 0.006	18.84 ± 0.03	289.2
E113	10.0 ± 0.3	6.6 ± 0.4	0.028 ± 0.002	0.155 ± 0.005	0.165 ± 0.005	28.99 ± 0.05	290.0
E114	15.0 ± 0.3	9.9 ± 0.6	0.033 ± 0.002	0.170 ± 0.005	0.198 ± 0.004	36.42 ± 0.05	290.5
E115	5.0 ± 0.3	n/a	n/a	n/a	0.222 ± 0.012	16.03 ± 0.09	289.5
E116	10.0 ± 0.3	n/a	n/a	n/a	0.298 ± 0.008	21.41 ± 0.03	289.6
E117	10.0 ± 0.3	6.6 ± 0.4	0.028 ± 0.002	0.155 ± 0.005	0.091 ± 0.003	39.74 ± 0.06	289.6
E158	5.0 ± 0.3	3.6 ± 0.2	0.059 ± 0.005	0.100 ± 0.005	0.321 ± 0.017	10.58 ± 0.04	286.8
E159	10.0 ± 0.3	8.0 ± 0.6	0.082 ± 0.007	0.115 ± 0.005	0.404 ± 0.011	16.74 ± 0.04	287.0
E160	15.0 ± 0.3	12.2 ± 1.0	0.099 ± 0.009	0.125 ± 0.005	0.488 ± 0.009	22.33 ± 0.04	287.5
E161	5.0 ± 0.3	n/a	n/a	n/a	0.351 ± 0.019	10.91 ± 0.03	287.5
E162	10.0 ± 0.3	n/a	n/a	n/a	0.471 ± 0.013	15.24 ± 0.04	287.5

Table 6.1: (continued)

Expt	$\dot{Q}_t$ (kW)	$\dot{Q}_c$ (kW)	$\dot{m}_s$ (kg s^{-1})	$d_{v,s}$ (m)	$\dot{m}_p$ (kg s^{-1})	θ_{vent} (^{o}C)	T_1 (K)
E163	10.0 ± 0.3	8.0 ± 0.6	0.082 ± 0.007	0.115 ± 0.005	0.361 ± 0.010	18.73 ± 0.03	287.5
E164	5.0 ± 0.3	3.7 ± 0.3	0.052 ± 0.005	0.105 ± 0.005	0.299 ± 0.016	9.52 ± 0.04	285.5
E165	10.0 ± 0.3	7.8 ± 0.6	0.069 ± 0.006	0.115 ± 0.005	0.386 ± 0.010	16.04 ± 0.04	286.0
E166	15.0 ± 0.3	12.8 ± 0.8	0.091 ± 0.007	0.135 ± 0.005	0.468 ± 0.008	22.40 ± 0.06	286.3
E167	5.0 ± 0.3	n/a	n/a	n/a	0.336 ± 0.018	11.63 ± 0.04	285.9
E168	10.0 ± 0.3	n/a	n/a	n/a	0.436 ± 0.012	16.71 ± 0.04	286.3
E169	10.0 ± 0.3	7.8 ± 0.6	0.069 ± 0.006	0.115 ± 0.005	0.341 ± 0.009	19.26 ± 0.05	286.4
E170	5.0 ± 0.3	3.9 ± 0.2	0.042 ± 0.004	0.110 ± 0.005	0.247 ± 0.013	11.25 ± 0.02	287.0
E171	10.0 ± 0.3	7.7 ± 0.5	0.058 ± 0.005	0.120 ± 0.005	0.338 ± 0.009	18.55 ± 0.05	287.3
E172	15.0 ± 0.3	12.2 ± 0.7	0.070 ± 0.005	0.140 ± 0.005	0.396 ± 0.007	25.01 ± 0.06	287.5
E173	5.0 ± 0.3	n/a	n/a	n/a	0.350 ± 0.019	10.93 ± 0.02	287.4
E174	10.0 ± 0.3	n/a	n/a	n/a	0.436 ± 0.012	16.18 ± 0.05	287.5
E175	10.0 ± 0.3	7.7 ± 0.5	0.058 ± 0.005	0.120 ± 0.005	0.273 ± 0.007	23.57 ± 0.05	287.1
E176	5.0 ± 0.3	3.6 ± 0.2	0.034 ± 0.002	0.115 ± 0.005	0.224 ± 0.012	12.02 ± 0.04	285.3
E177	10.0 ± 0.3	7.2 ± 0.4	0.043 ± 0.003	0.125 ± 0.005	0.283 ± 0.008	20.77 ± 0.04	285.6
E178	15.0 ± 0.3	10.9 ± 0.6	0.052 ± 0.004	0.145 ± 0.005	0.345 ± 0.006	27.14 ± 0.04	286.5
E179	5.0 ± 0.3	n/a	n/a	n/a	0.308 ± 0.017	11.88 ± 0.03	285.8
E180	10.0 ± 0.3	n/a	n/a	n/a	0.396 ± 0.011	16.57 ± 0.05	286.1
E181	10.0 ± 0.3	7.2 ± 0.4	0.043 ± 0.003	0.125 ± 0.005	0.197 ± 0.005	26.99 ± 0.04	286.3
E182	5.0 ± 0.3	3.5 ± 0.2	0.024 ± 0.002	0.135 ± 0.005	0.155 ± 0.008	14.32 ± 0.02	287.1
E183	10.0 ± 0.3	6.6 ± 0.4	0.028 ± 0.002	0.155 ± 0.005	0.221 ± 0.006	22.72 ± 0.04	287.5
E184	15.0 ± 0.3	9.9 ± 0.6	0.033 ± 0.002	0.170 ± 0.005	0.261 ± 0.005	29.94 ± 0.04	287.8
E185	5.0 ± 0.3	n/a	n/a	n/a	0.328 ± 0.018	11.22 ± 0.03	287.5
E186	10.0 ± 0.3	n/a	n/a	n/a	0.400 ± 0.011	16.14 ± 0.05	287.5
E187	10.0 ± 0.3	6.6 ± 0.4	0.028 ± 0.002	0.155 ± 0.005	0.116 ± 0.011	34.69 ± 0.06	287.3
E223*	5.0 ± 0.3	3.5 ± 0.2	0.024 ± 0.002	0.135 ± 0.005	0.323 ± 0.017*	9.51 ± 0.04	287.0
E224*	10.0 ± 0.3	6.6 ± 0.4	0.028 ± 0.002	0.155 ± 0.005	0.388 ± 0.011*	14.67 ± 0.04	287.5
E225*	15.0 ± 0.3	9.9 ± 0.6	0.033 ± 0.002	0.170 ± 0.005	0.461 ± 0.008*	18.72 ± 0.08	287.5
E226*	5.0 ± 0.3	n/a	n/a	n/a	0.513 ± 0.028*	8.18 ± 0.06	287.5
E227*	10.0 ± 0.3	n/a	n/a	n/a	0.629 ± 0.017*	10.38 ± 0.08	287.5
E228*	5.0 ± 0.3	3.6 ± 0.2	0.034 ± 0.002	0.115 ± 0.005	0.429 ± 0.023*	6.44 ± 0.07	282.5
E229*	10.0 ± 0.3	7.2 ± 0.4	0.043 ± 0.003	0.125 ± 0.005	0.501 ± 0.014*	11.64 ± 0.12	287.4
E230*	15.0 ± 0.3	10.9 ± 0.6	0.052 ± 0.004	0.145 ± 0.005	0.645 ± 0.012*	13.83 ± 0.10	287.7
E231*	5.0 ± 0.3	n/a	n/a	n/a	0.504 ± 0.027*	7.05 ± 0.11	282.5
E232*	10.0 ± 0.3	n/a	n/a	n/a	0.664 ± 0.018*	8.34 ± 0.12	283.1
E233*	5.0 ± 0.3	3.9 ± 0.2	0.042 ± 0.004	0.110 ± 0.005	0.528 ± 0.029*	4.85 ± 0.07	282.7
E234*	10.0 ± 0.3	7.7 ± 0.5	0.058 ± 0.005	0.120 ± 0.005	0.648 ± 0.018*	8.58 ± 0.08	282.7
E235*	15.0 ± 0.3	12.2 ± 0.7	0.070 ± 0.005	0.140 ± 0.005	0.767 ± 0.014*	11.35 ± 0.10	283.4
E236*	5.0 ± 0.3	n/a	n/a	n/a	0.524 ± 0.028*	5.52 ± 0.06	283.4
E237*	10.0 ± 0.3	n/a	n/a	n/a	0.698 ± 0.019*	7.56 ± 0.07	283.6
E238*	5.0 ± 0.3	3.7 ± 0.3	0.052 ± 0.005	0.105 ± 0.005	0.580 ± 0.031*	4.75 ± 0.05	283.1
E239*	10.0 ± 0.3	7.8 ± 0.6	0.069 ± 0.006	0.115 ± 0.005	0.731 ± 0.020*	7.55 ± 0.06	283.3
E240*	15.0 ± 0.3	12.8 ± 0.8	0.091 ± 0.007	0.135 ± 0.005	0.850 ± 0.015*	10.15 ± 0.11	283.7
E241*	5.0 ± 0.3	n/a	n/a	n/a	0.634 ± 0.034*	4.32 ± 0.08	283.9

*"plug-holing"

Table 6.1: (continued)

Expt	$\dot{Q}_t$ (kW)	$\dot{Q}_c$ (kW)	$\dot{m}_s$ (kg s^{-1})	$d_{v,s}$ (m)	$\dot{m}_p$ (kg s^{-1})	θ_{vent} (^{o}C)	T_1 (K)
E242*	10.0 ± 0.3	n/a	n/a	n/a	0.828 ± 0.022*	6.72 ± 0.09	284.0
E243*	5.0 ± 0.3	3.6 ± 0.2	0.059 ± 0.005	0.100 ± 0.005	0.646 ± 0.035*	3.93 ± 0.08	283.9
E244*	10.0 ± 0.3	8.0 ± 0.6	0.082 ± 0.007	0.115 ± 0.005	0.829 ± 0.022*	6.36 ± 0.08	284.0
E245*	15.0 ± 0.3	12.2 ± 1.0	0.099 ± 0.009	0.125 ± 0.005	0.941 ± 0.017*	9.14 ± 0.10	284.0
E246*	5.0 ± 0.3	n/a	n/a	n/a	0.685 ± 0.037*	3.84 ± 0.05	284.0
E247*	10.0 ± 0.3	n/a	n/a	n/a	0.841 ± 0.023*	6.52 ± 0.10	284.0
E248*	5.0 ± 0.3	3.6 ± 0.2	0.059 ± 0.005	0.100 ± 0.005	0.441 ± 0.024*	7.49 ± 0.05	284.0
E249*	10.0 ± 0.3	8.0 ± 0.6	0.082 ± 0.007	0.115 ± 0.005	0.539 ± 0.015*	11.81 ± 0.06	284.5
E250*	15.0 ± 0.3	12.2 ± 1.0	0.099 ± 0.009	0.125 ± 0.005	0.647 ± 0.012*	15.65 ± 0.08	284.5
E251*	5.0 ± 0.3	n/a	n/a	n/a	0.487 ± 0.026*	8.75 ± 0.05	284.1
E252*	10.0 ± 0.3	n/a	n/a	n/a	0.611 ± 0.017*	11.46 ± 0.04	284.7
E253	10.0 ± 0.3	8.0 ± 0.6	0.082 ± 0.007	0.115 ± 0.005	0.443 ± 0.012	15.31 ± 0.05	285.0
E254	5.0 ± 0.3	3.7 ± 0.3	0.052 ± 0.005	0.105 ± 0.005	0.348 ± 0.019	9.93 ± 0.02	284.5
E255	10.0 ± 0.3	7.8 ± 0.6	0.069 ± 0.006	0.115 ± 0.005	0.475 ± 0.013	13.96 ± 0.06	285.0
E256	15.0 ± 0.3	12.8 ± 0.8	0.091 ± 0.007	0.135 ± 0.005	0.593 ± 0.011	17.42 ± 0.07	285.5
E257	5.0 ± 0.3	n/a	n/a	n/a	0.421 ± 0.023	9.36 ± 0.04	285.4
E258	10.0 ± 0.3	n/a	n/a	n/a	0.557 ± 0.015	11.68 ± 0.05	285.5
E259	10.0 ± 0.3	7.8 ± 0.6	0.069 ± 0.006	0.115 ± 0.005	0.385 ± 0.010	16.52 ± 0.05	285.5
E260	5.0 ± 0.3	3.9 ± 0.2	0.042 ± 0.004	0.110 ± 0.005	0.292 ± 0.016	8.61 ± 0.04	284.6
E261	10.0 ± 0.3	7.7 ± 0.5	0.058 ± 0.005	0.120 ± 0.005	0.374 ± 0.010	15.74 ± 0.06	284.0
E262	15.0 ± 0.3	12.2 ± 0.7	0.070 ± 0.005	0.140 ± 0.005	0.460 ± 0.008	21.26 ± 0.06	284.0
E263	5.0 ± 0.3	n/a	n/a	n/a	0.347 ± 0.019	10.40 ± 0.02	284.5
E264	10.0 ± 0.3	n/a	n/a	n/a	0.465 ± 0.013	13.45 ± 0.04	284.8
E265	10.0 ± 0.3	7.7 ± 0.5	0.058 ± 0.005	0.120 ± 0.005	0.302 ± 0.008	19.79 ± 0.03	284.7
E266	5.0 ± 0.3	3.6 ± 0.2	0.034 ± 0.002	0.115 ± 0.005	0.246 ± 0.013	10.91 ± 0.03	283.8
E267	10.0 ± 0.3	7.2 ± 0.4	0.043 ± 0.003	0.125 ± 0.005	0.335 ± 0.009	18.08 ± 0.04	284.0
E268	15.0 ± 0.3	10.9 ± 0.6	0.052 ± 0.004	0.145 ± 0.005	0.410 ± 0.007	23.39 ± 0.05	284.0
E269	5.0 ± 0.3	n/a	n/a	n/a	0.389 ± 0.021	11.03 ± 0.04	284.1
E270	10.0 ± 0.3	n/a	n/a	n/a	0.495 ± 0.013	13.68 ± 0.04	284.7
E271	10.0 ± 0.3	7.2 ± 0.4	0.043 ± 0.003	0.125 ± 0.005	0.234 ± 0.006	24.27 ± 0.06	284.8
E272	5.0 ± 0.3	3.5 ± 0.2	0.024 ± 0.002	0.135 ± 0.005	0.196 ± 0.011	13.30 ± 0.03	284.8
E273	10.0 ± 0.3	6.6 ± 0.4	0.028 ± 0.002	0.155 ± 0.005	0.277 ± 0.008	18.88 ± 0.03	284.8
E274	15.0 ± 0.3	9.9 ± 0.6	0.033 ± 0.002	0.170 ± 0.005	0.327 ± 0.006	24.14 ± 0.05	285.5
E275	5.0 ± 0.3	n/a	n/a	n/a	0.344 ± 0.018	11.40 ± 0.02	285.0
E276	10.0 ± 0.3	n/a	n/a	n/a	0.327 ± 0.013	13.47 ± 0.04	285.0
E277	10.0 ± 0.3	6.6 ± 0.4	0.028 ± 0.002	0.155 ± 0.005	0.145 ± 0.004	31.23 ± 0.07	285.0
E278	10.0 ± 0.3	8.0 ± 0.6	0.082 ± 0.007	0.115 ± 0.005	0.221 ± 0.006	23.03 ± 0.05	284.5
E279	10.0 ± 0.3	7.8 ± 0.6	0.069 ± 0.006	0.115 ± 0.005	0.188 ± 0.005	28.44 ± 0.06	284.5
E280	10.0 ± 0.3	7.7 ± 0.5	0.058 ± 0.005	0.120 ± 0.005	0.153 ± 0.004	31.20 ± 0.06	285.2
E281	10.0 ± 0.3	7.2 ± 0.4	0.043 ± 0.003	0.125 ± 0.005	0.113 ± 0.003	37.34 ± 0.05	285.0
E282	10.0 ± 0.3	6.6 ± 0.4	0.028 ± 0.002	0.155 ± 0.005	0.070 ± 0.002	45.32 ± 0.07	285.5
E288	10.0 ± 0.3	6.6 ± 0.4	0.028 ± 0.002	0.155 ± 0.005	0.048 ± 0.001	61.29 ± 0.10	287.6
E289	10.0 ± 0.3	7.2 ± 0.4	0.043 ± 0.003	0.125 ± 0.005	0.065 ± 0.002	61.79 ± 0.05	288.0
E290	10.0 ± 0.3	7.7 ± 0.5	0.058 ± 0.005	0.120 ± 0.005	0.076 ± 0.002	55.07 ± 0.06	288.9
E291	10.0 ± 0.3	7.8 ± 0.6	0.069 ± 0.006	0.115 ± 0.005	0.088 ± 0.002	50.92 ± 0.04	289.0
E292	10.0 ± 0.3	8.0 ± 0.6	0.082 ± 0.007	0.115 ± 0.005	0.094 ± 0.003	52.79 ± 0.03	289.1

*"plug-holing"

Table 6.1: (continued)

The thermocouple columns within the smoke collecting hood (Columns A and B) provided temperature profiles through the smoke layer for each height of rise of plume examined. Although visual observations were used to define the height of the smoke layer above the spill edge in the experiment, the temperature (and hence, buoyancy) profiles also enabled the smoke layer depth in the collecting hood to be calculated if required.

Figure 6.1 shows the temperature profiles in the collecting hood for Experiment E101, where the height of rise of plume was approximately 0.5 m above the spill edge (with the depth of the layer 1.5 m below the ceiling of the collecting hood) and are generally typical of all the profiles measured in the hood.

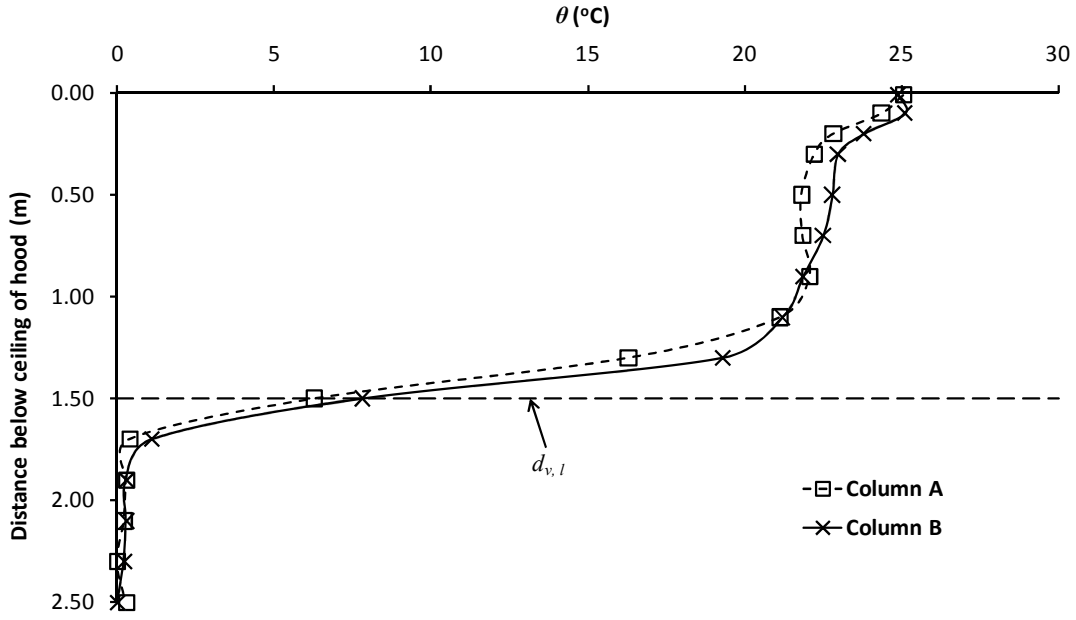

Figure 6.1: Temperature profiles in the smoke collecting hood (Experiment E101)

Appendix G shows the temperature profiles in the smoke collecting hood for the series of balcony spill plume experiments.

6.2 The 2-D plume

6.2.1 Plume behaviour

The horizontal flow of gases within the fire compartment was observed to flow from the opening, under the balcony, rotate at the spill edge (i.e. the balcony edge) and then rise as a 2-D balcony spill plume between the screens used to prevent entrainment into the ends of the plume. Figure 6.2 shows a schematic drawing of the typical plume behaviour observed.

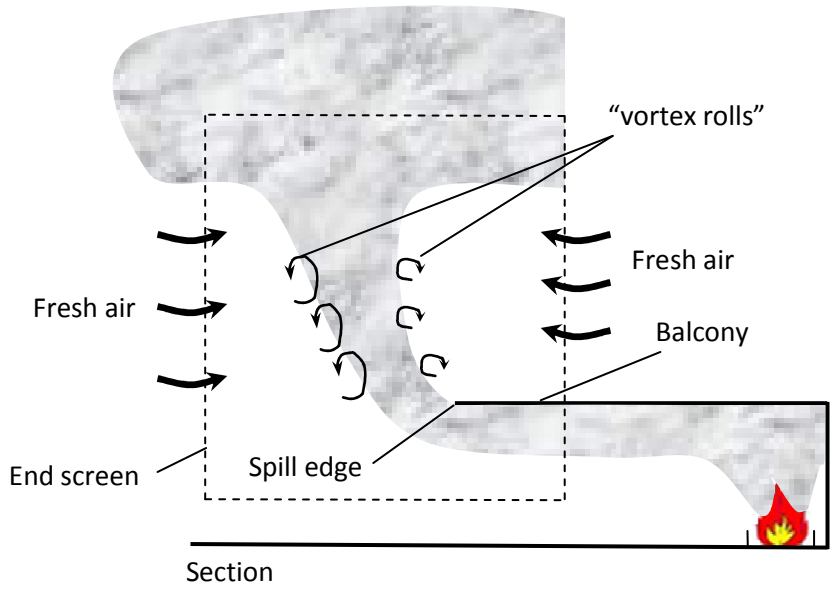

Figure 6.2: Typical 2-D balcony spill plume behaviour

The momentum of the flow of hot gases initially caused the flow beyond the spill edge to project horizontally before rising as a plume into the collecting hood above. The amount of horizontal projection tended to increase as the fire size increased and/or the width of the fire compartment opening decreased, this in turn caused subtle changes to the trajectory of the rising plume. Visual observations identified that entrainment of air occurred across the lateral extent of the plume by the generation of vortices (known as "vortex rolls") being shed from each side of the rising plume exposed to ambient air. Larger, slower moving vortices were observed on the front side of the spill plume (furthest from the spill edge) as the temperature and velocity of the gases were lower in this region compared to the rear side of the plume.

6.2.2 Smoke layer in the collecting hood

Visual observations showed that the height of the smoke layer in the collecting hood was not entirely uniform for those experiments which examined heights of rise of plume with $z_s > 0$. In these experiments the height of the smoke layer between the end screens was slightly higher (up to 0.07 m higher) than the height of the layer between the walls of the collecting hood and the screens. Figure 6.3 shows a schematic diagram and photographs of the smoke layer behaviour in the collecting hood.

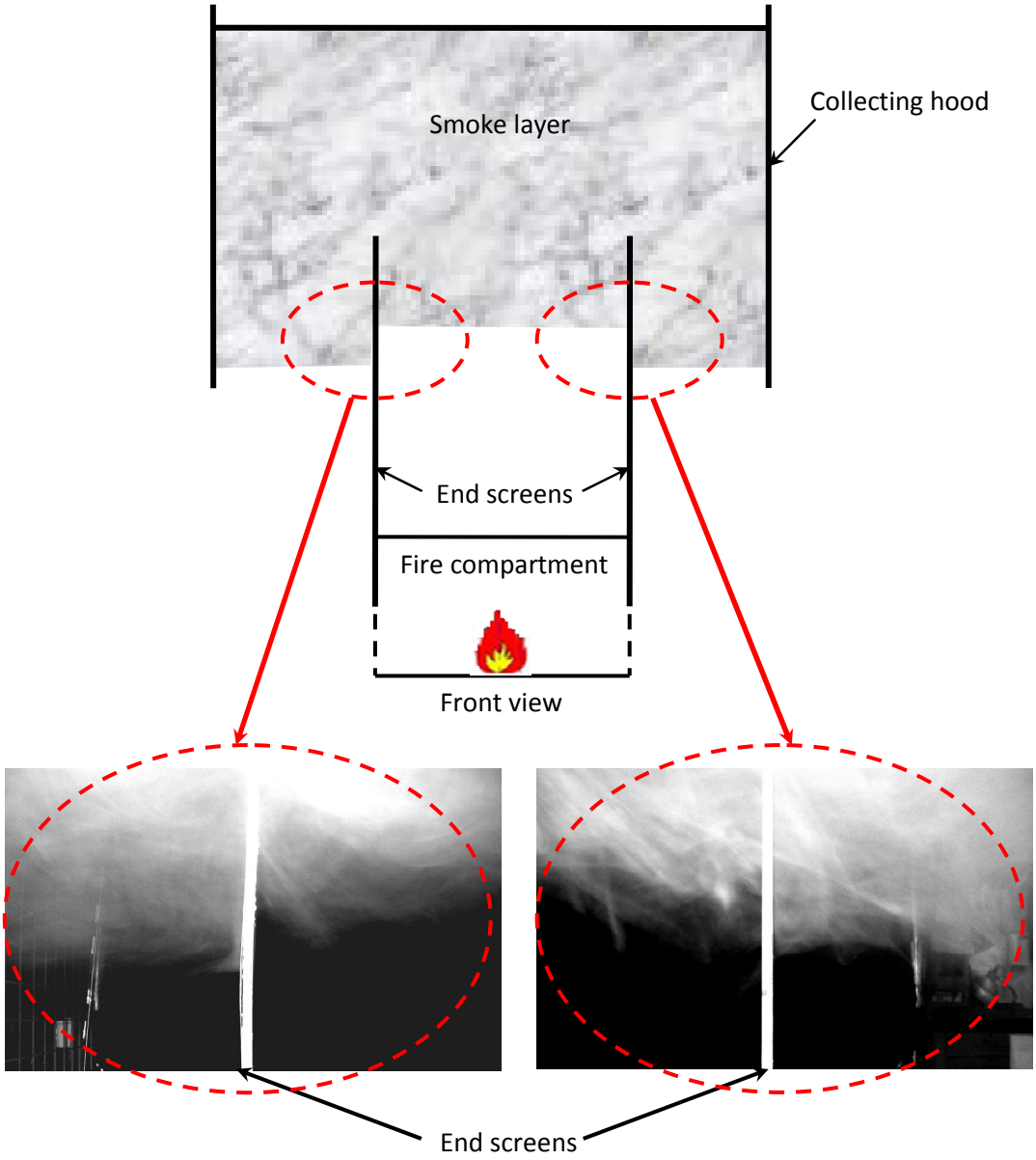

Figure 6.3: The smoke layer behaviour in the collecting hood

The smoke layer behaviour shown in Figure 6.3 has previously been identified and theoretically analysed by Poreh [128] who suggests that the difference in layer height is dependent upon local density differences in the layer in the hood and the density of ambient air.

This smoke layer behaviour led to higher heights of rise being used in the analysis of 2-D spill plumes (given in Table 4.3) compared to the equivalent 3-D plumes (where the height of the smoke layer in the collecting hood was reasonably uniform).

6.2.3 Entrainment analysis

The analysis of the experimental results utilises the more robust simplified spill plume entrainment models that have been developed for the 2-D balcony spill plume. The generalised form of the methods by Thomas *et al.* [39] and Poreh *et al.* [31] are used in the analysis.

Previous 1/10th physical scale modelling work, from separate studies described by Marshall and Harrison [48] has provided data to characterise entrainment of air into 2-D balcony spill plumes. From the statistical analysis of these data, Thomas *et al.* used multiple linear regression to determine [according to Equation (2-41)] that;

$$\frac{\dot{m}'_{p,2D}}{\dot{Q}'_c} = 0.16\frac{z_s}{\dot{Q}'^{2/3}_c} + 1.2\frac{\dot{m}'_s}{\dot{Q}'_c} + 0.0027 \qquad \textbf{(6-2)}$$

Hence, $\gamma = 0.16$, $\delta = 1.2$ and $\varepsilon = 0.0027$.

Poreh *et al.* correlated the same data to determine [according to Equation (2-39)] that;

$$\frac{\dot{m}'_{p,2D} - \dot{m}'_s}{\dot{Q}'_c} = 0.16\left(\frac{z_s + d_s}{\dot{Q}'^{2/3}_c}\right) \qquad \textbf{(6-3)}$$

Hence, $C = 0.16$.

Equations (6-2) and (6-3) were determined for fires with $\dot{Q}_c$ ranging between 6 to 34 kW. However, W_s was fixed in these experiments at 0.91 m. Therefore, in this study a selected number of experiments were carried out to complement the Marshall and Harrison data to determine if Equations (6-2) and (6-3) apply generally for a range of W_s.

Figure 6.4 shows the data obtained from this study and the data obtained by Marshall and Harrison [48] plotted in a form consistent with the dimensional analysis given by Thomas *et al.* [39]. A line representing Equation (6-2) is shown for an intermediate value of $\dot{Q}_c$ from the Marshall and Harrison data, as it is weakly dependent on $\dot{Q}_c$.

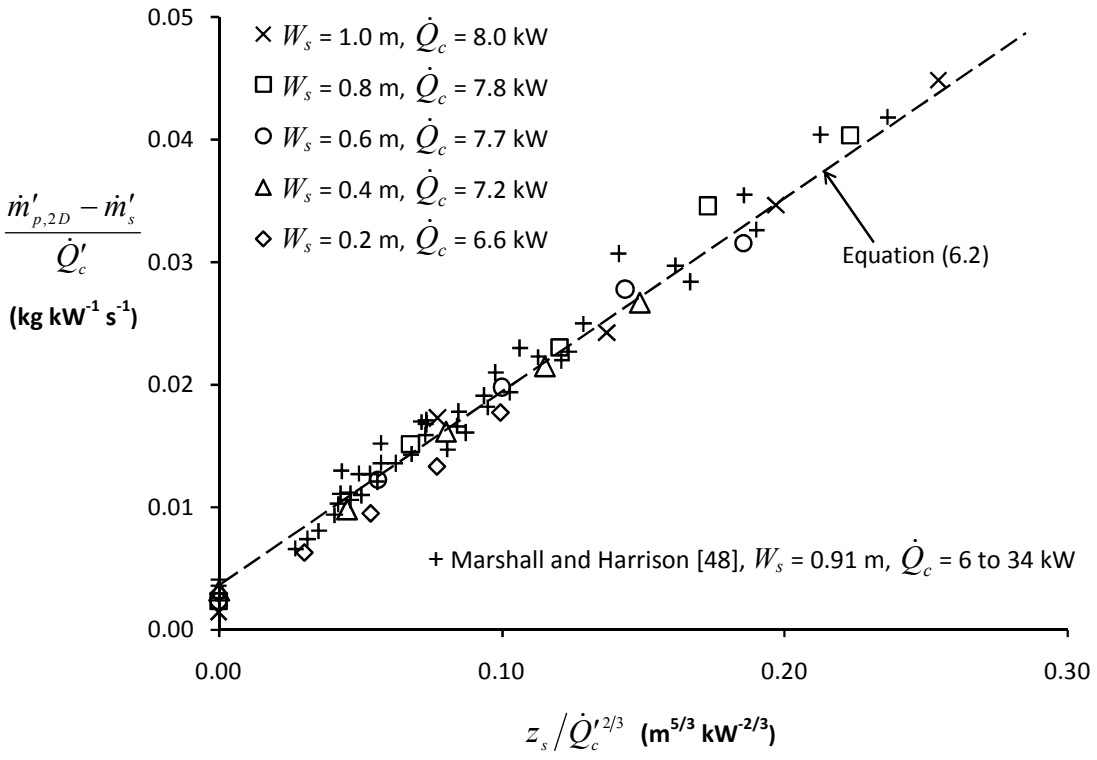

Figure 6.4: Experimental results for the 2-D plume plotted according to Thomas *et al.*

Figure 6.4 shows that all the data generally follow a common linear relationship. The intercept on the vertical axis represents the amount of entrainment in the rotation region of the plume. The slope of the linear relationship represents the rate of entrainment above the spill edge which appears to be independent of $\dot{Q}_c$ and W_s. This indicates that the observed differences between the plume trajectories (due to changes in $\dot{Q}_c$ and W_s) have little effect on the subsequent rate of entrainment, presumably due to subtle changes in the dynamics of the entrainment process with trajectory.

The same data are plotted in Figure 6.5 according to the method by Poreh *et al.* [31] which includes a line representing Equation (6-3).

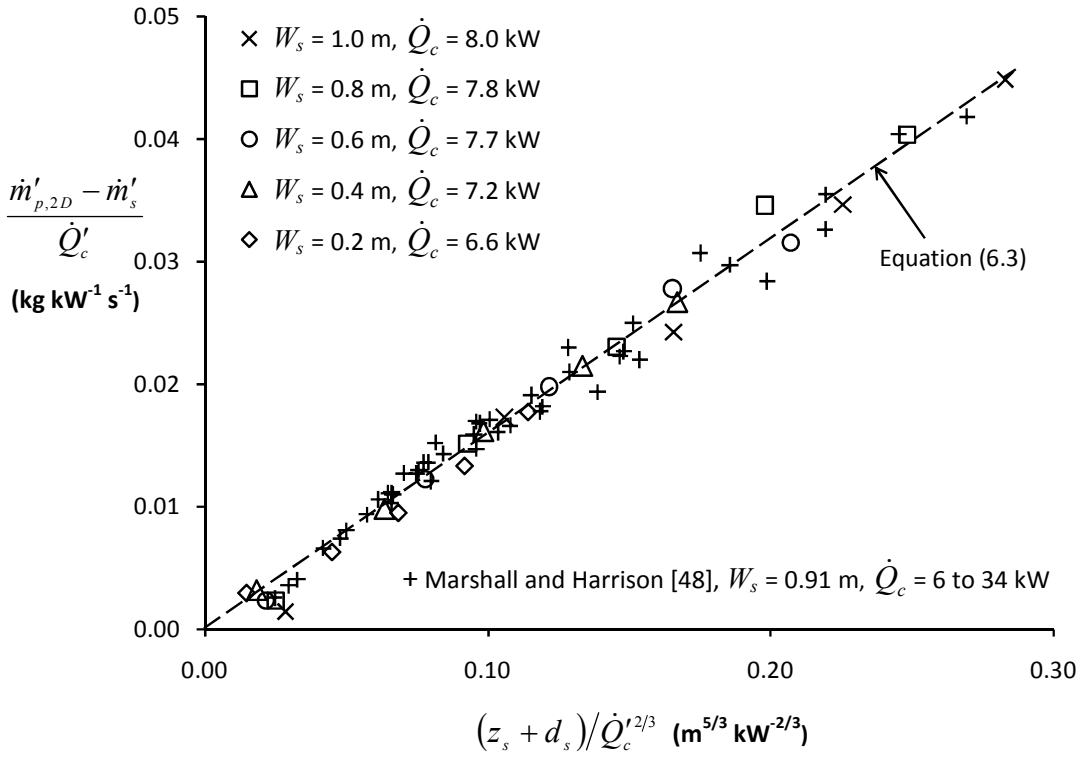

Figure 6.5: Entrainment results for the 2-D plume plotted according to Poreh *et al.*

Figures 6.4 and 6.5 indicate that the data from this study, obtained from a range of W_s, is broadly consistent with the data from previous work. It is not surprising that those data points close to the origin tend to lie just below the lines representing Equations (6-2) and (6-3) as these points represent experiments for plumes where $z_s = 0$ which describe the entrainment in the rotation region (i.e. where entrainment occurs into only one side of the flow) which is different in nature to the flows where $z_s > 0$ (i.e. where entrainment occurs into two sides).

Performing linear regression for each complete data set shown in Figures 6.4 and 6.5 respectively gives $\alpha = 0.163$ and $C = 0.159$ with standard errors of 0.003 and 0.001 respectively. Therefore, the additional data from this study is consistent with the dominant regression coefficients in Equations (6-2) and (6-3) (representing the rate of entrainment above the spill edge) being equal to within one standard error, with a value of 0.16. It appears that both Equations (6-2) and (6-3) can generally be applied for 2-D balcony spill plumes.

Comparison of Equations (6-2) and (6-3) shows that the term describing the rate of entrainment above the spill edge in each equation are identical (i.e. $0.16 z_s / \dot{Q}_c'^{2/3}$). The difference between them is the term(s) describing the total amount of entrainment below the height of the spill edge (i.e. $\dot{m}_p$ at $z_s = 0$). Existing experimental data describing the mass flow rate in the plume at $z_s = 0$ is particularly sparse and entrainment into these flows has not been characterised in a robust manner. The Marshall and Harrison data statistically analysed by Thomas *et al.* and Poreh *et al.* only contained three data points at $z_s = 0$, therefore, to potentially further improve and simplify these design formulae for the terms describing the amount of entrainment below the spill edge, additional experimental data has been obtained from this work which is described below.

6.2.3.1 Entrainment in the plume at $z_s = 0$

In this work, a more extensive data set from 20 experiments was obtained to determine $\dot{m}_p$ at $z_s = 0$ for a variety of $\dot{Q}_c$ and W_s in an attempt to characterise and decouple entrainment into the flow below the height of the spill edge (which includes entrainment into the rotation region). Figure 6.6 shows a plot of $\dot{m}'_p/\dot{Q}'_c$ versus $\dot{m}'_s/\dot{Q}'_c$ at $z_s = 0$ consistent with the dimensional analysis by Thomas *et al.* [39]. The data shown in Figure 6.6 was from those tests which had channelling screens used for the 2-D plume (i.e. screens both above and below the balcony) and those screens used for the 3-D plume (i.e. channelling screens only below the balcony), as at $z_s = 0$ it is expected that the effect of end entrainment into the rotation region will be negligible for the 3-D plume scenario (also assumed by Thomas *et al.* [39]). Data from previous work by Harrison and Spearpoint [40] and Marshall and Harrison [48] obtained at $z_s = 0$ is also included in the analysis. These data are presented in terms of the time averaged mean values with associated standard errors.

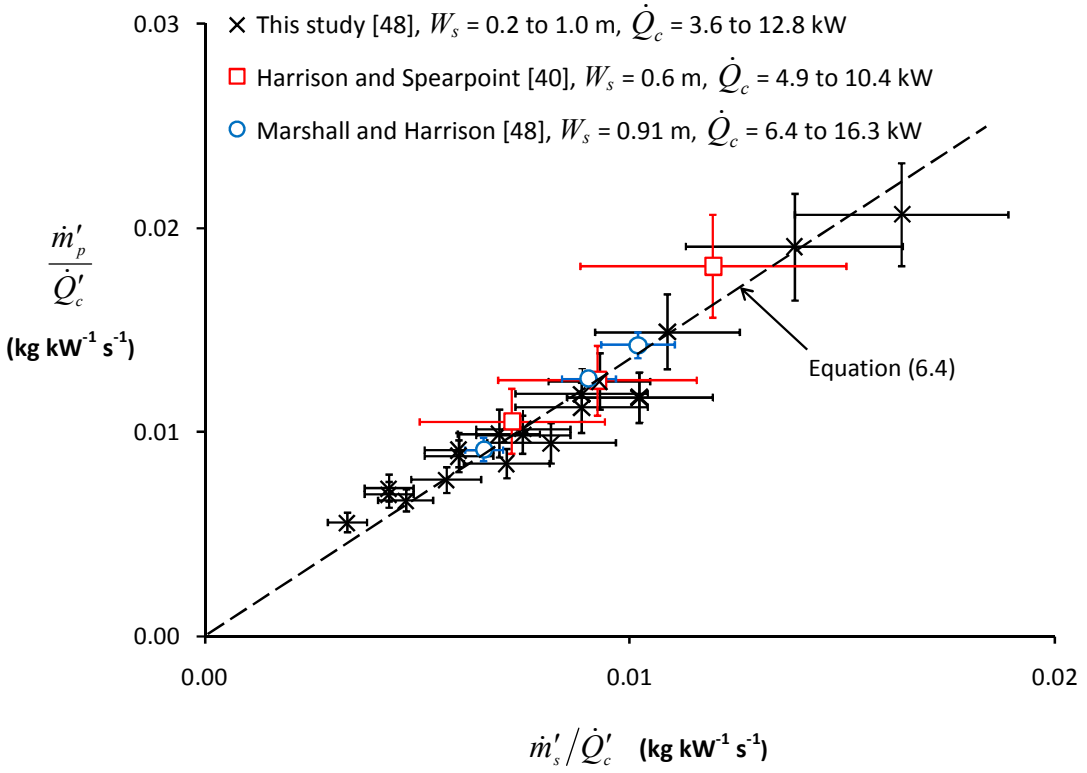

Figure 6.6: Correlation between $\dot{m}'_p/\dot{Q}'_c$ and $\dot{m}'_s/\dot{Q}'_c$ at $z_s = 0$

Figure 6.6 shows that all of the data obtained from a range of $\dot{Q}_c$ and W_s generally follow a relationship described by Equation (6-4) which passes through the origin with regression coefficients of δ = 1.34 and ε = 0. This is similar to that suggested by Thomas *et al.* [39] (i.e. δ = 1.4) from the analysis of much fewer data points. The standard error of the regression coefficient δ is 0.023.

$$\frac{\dot{m}'_p}{\dot{Q}'_c} = 1.34\left(\frac{\dot{m}'_s}{\dot{Q}'_c}\right) \qquad \textbf{(6-4)}$$

It seems reasonable to use Equation (6-4) to describe the entrainment of air in the plume at z_s = 0 instead of the regression coefficients δ = 1.2 and ε = 0.0027 given in Equation (6-2) which were determined using multiple linear regression from data mainly obtained above the balcony. Equation (6-4) provides a simple equation to describe the decoupled entrainment below the height of the spill edge and is not specific to 2-D balcony spill plumes. It is obtained from a more robust data set than the Thomas *et al.* statistical analysis, is not determined from data obtained above the spill edge, nor is it weakly dependent on $\dot{Q}_c$.

6.2.3.2 A new design formula for the 2-D plume

From the above analysis, Equation (6-2) can be more simply described by replacing the values of the regression coefficients δ and ε with 1.34 and 0 respectively (instead of the δ =1.2 and ε = 0.0027). This gives rise to Equation (6-5) which is proposed as a new simplified design formula for the 2-D balcony spill plume.

$$\frac{\dot{m}'_{p,2D}}{\dot{Q}'_c} = 0.16\frac{z_s}{\dot{Q}'_c} + 1.34\frac{\dot{m}'_s}{\dot{Q}'_c} \qquad \textbf{(6-5)}$$

$$\Rightarrow \dot{m}_{p,2D} = 0.16\dot{Q}_c^{1/3}W_s^{2/3}z_s + 1.34\dot{m}_s$$

Equation (6-5) is made up of two terms, one describing the mass flow rate of gases generated above the spill edge, the other describing the mass flow rate of gases below the height of the spill edge (as shown in Figure 6.7). It is a simpler, modified version of the Thomas *et al.* method and appears to apply generally with respect to variation in $\dot{Q}_c$ and W_s and does not require the calculation of both $\dot{m}_s$ and d_s as required by the Poreh *et al.* method.

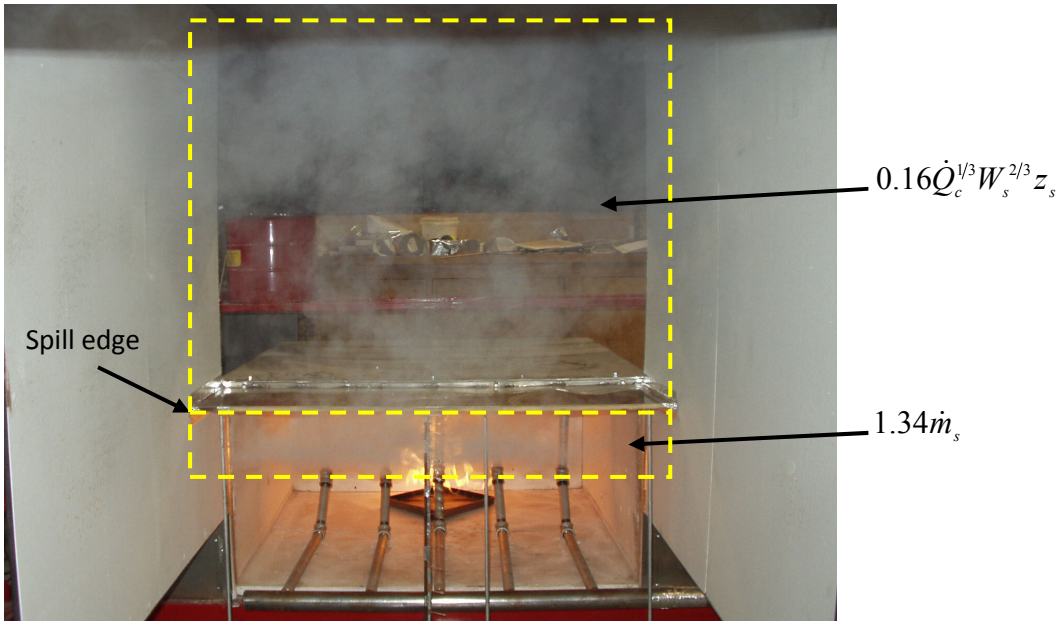

Figure 6.7: Entrainment regions described by Equation (6-5)

6.3 The 3-D plume with channelling screens

6.3.1 Plume behaviour

The behaviour of the plume emerging beyond the spill edge and the subsequent entrainment processes occurring across its lateral extent were similar to that described for the 2-D balcony spill plume, with the exception that additional entrainment also occurred into the free ends of the plume. The entrainment into the ends was observed to be more 3-D in nature compared to that across its lateral extent due to more of a 'shear' flow at the ends. Figures 6.8 to 6.10 show photographs of the typical plume behaviour beyond the spill edge (from a side and front view) generated from a wide, intermediate and narrow width of compartment opening respectively.

a) Side view b) Front view

Figure 6.8: Plume behaviour (W_s = 1.0 m)

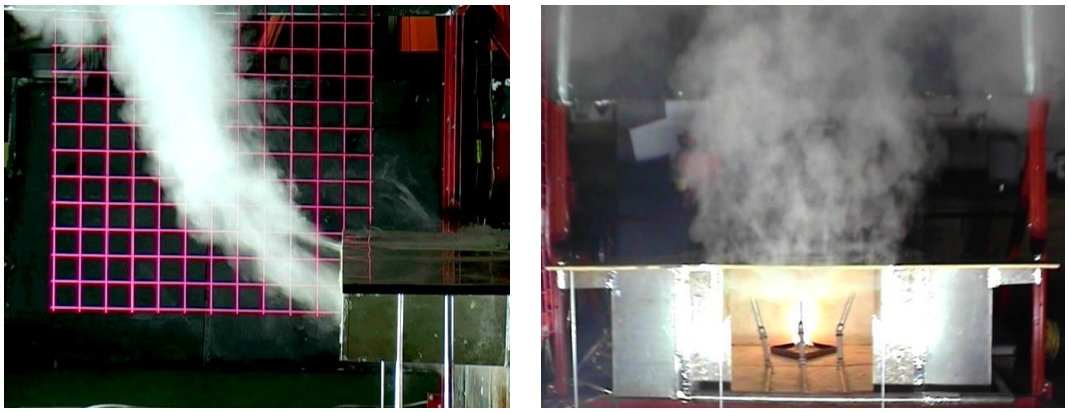

a) Side view b) Front view

Figure 6.9: Plume behaviour (W_s = 0.6 m)

a) Side view b) Front view

Figure 6.10: Plume behaviour (W_s = 0.2 m)

Figures 6.8a to 6.10a show that the plume behaviour from a side view was similar to that described for the 2-D plume. When the width of the compartment opening decreased (and also when the fire size increased) the amount of horizontal projection and the breadth of the ends of the plume tended to increase.

Figures 6.8b to 6.10b show a broadening of the lateral extent of the plume with respect to height of rise above the spill edge. The rate of broadening tended to increase as the width of the compartment opening decreased, most likely due to the increased amount of end entrainment occurring in the plume.

6.3.2 Horizontal temperature profiles across the plume

Figure 6.11 shows a plot of the horizontal temperature profiles across the centreline of the plume, perpendicular to the spill edge, with respect to height of rise above the edge for Experiment T1 (i.e. W_s = 1.0 m, $\dot{Q}_t$ = 10 kW).

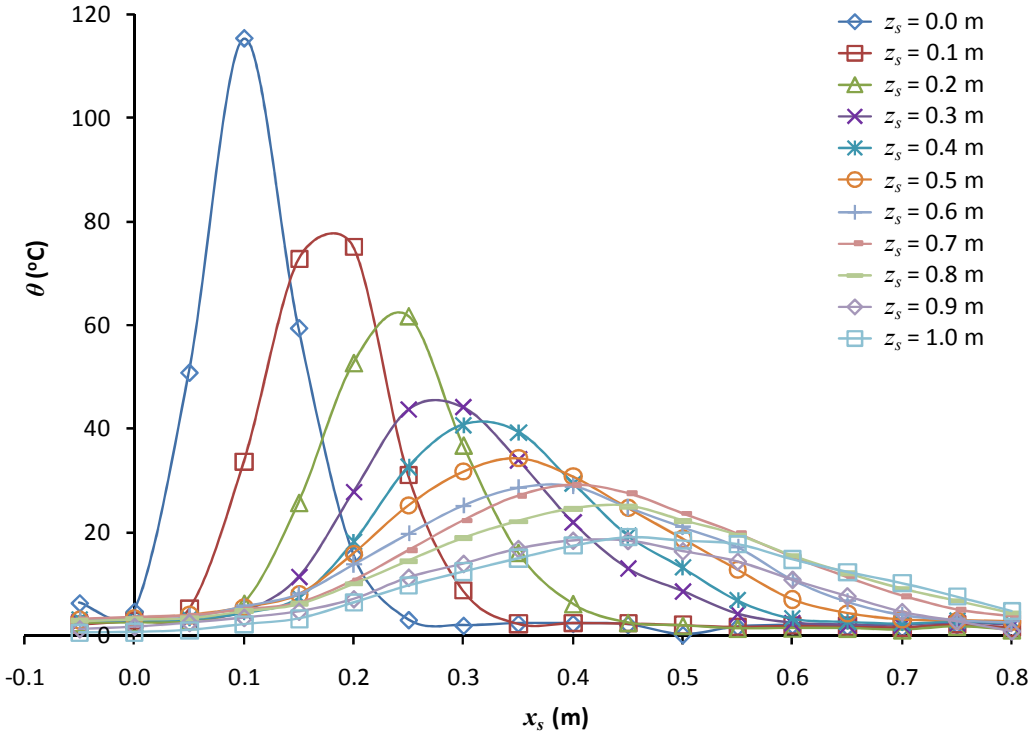

Figure 6.11: Horizontal temperature profiles across the plume for Experiment T1

Figure 6.11 show that the characteristic shape of these profiles are generally Gaussian in nature, however the profiles with $z_s \leq 0.3$ m are similar to Gaussian but appear to be slightly skewed as the plume was not fully established over a short height of rise (i.e. from a horizontal layer flow to a vertically rising two-sided plume), consistent with a similar analysis carried out by Marshall and Harrison [48].

These profiles can be expressed in non-dimensional form by plotting θ/θ_{max} with respect to x_s/z_s consistent with the analysis by Yokoi [80] on the study of vertically rising line plumes. Yokoi demonstrated when plotted in this form that the temperature data for line plumes collapse to a single characteristic profile demonstrating self-similarity with respect to height of rise. Figure 6.12 shows that when the temperature data for Experiment T1 are plotted in this form the shape of the profiles are similar, however, they do not collapse to a single profile due to an horizontal offset between the profiles.

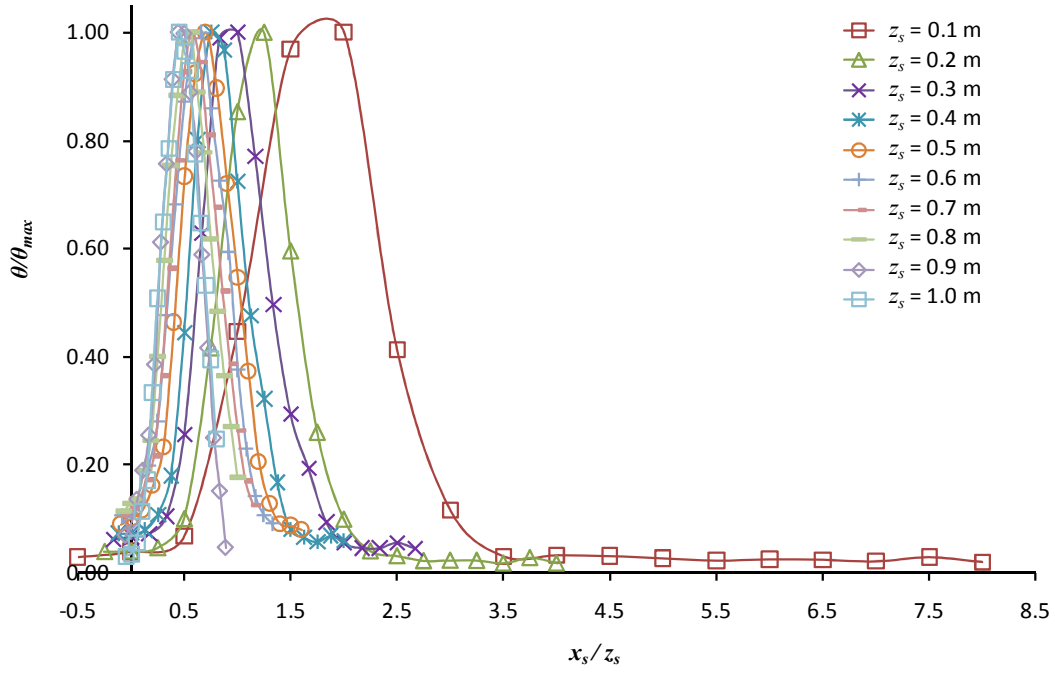

Figure 6.12: Plot of θ/θ_{max} with respect to x_s/z_s for Experiment T1

This is not surprising as the Yokoi analysis was for vertically rising line plumes, where θ/θ_{max} was a maximum directly above the plume centreline with respect to height of rise. However, as spill plumes possess horizontal momentum, the maximum value of θ/θ_{max} shifts horizontally with respect to height of rise of plume.

To take this into account (x_s/z_s) is normalised in terms of $(x_s/z_s)^*$ such that θ/θ_{max} is a maximum (i.e. 1) when $(x_s/z_s)^*$ is 1 for each profile (see Figure 6.13).

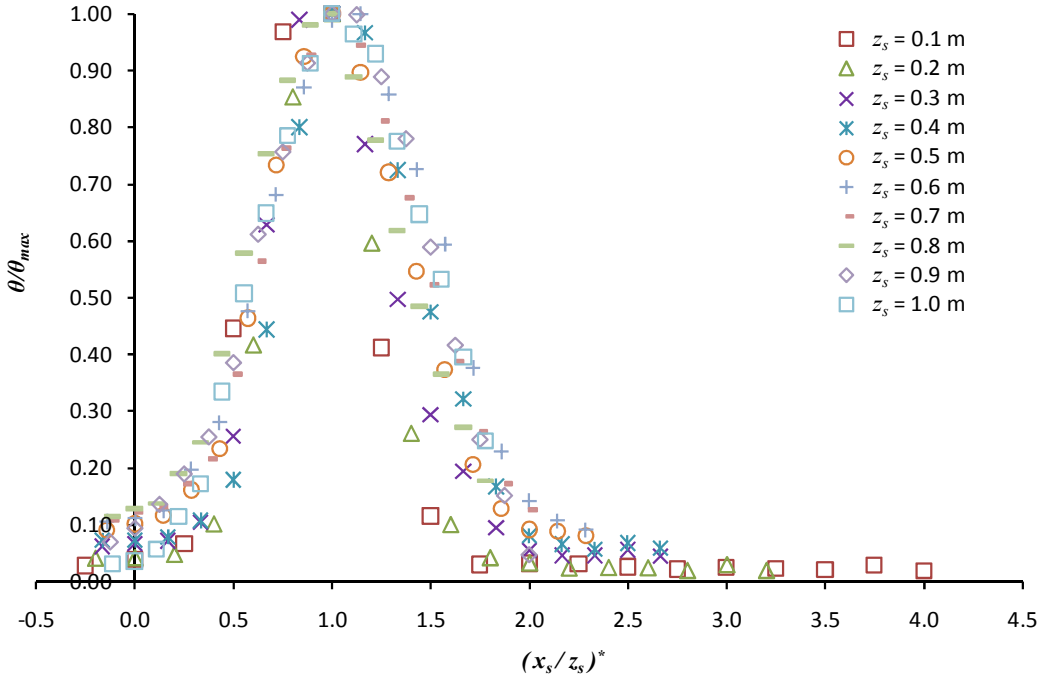

Figure 6.13: Plot of θ/θ_{max} with respect to $(x_s/z_s)^*$ for Experiment T1

Figure 6.13 shows that when plotted in a normalised form the data collapse reasonably well for the majority of z_s to a single characteristic temperature profile which demonstrates self-similarity. Again, the profiles for $z_s \leq 0.3$ m are slightly skewed and do not perfectly collapse in line with the other profiles due to the plume not being so well established at low heights of rise.

Figure 6.14 shows that the profiles for $z_s \geq 0.4$ m plotted separately collapse to a common Gaussian distribution.

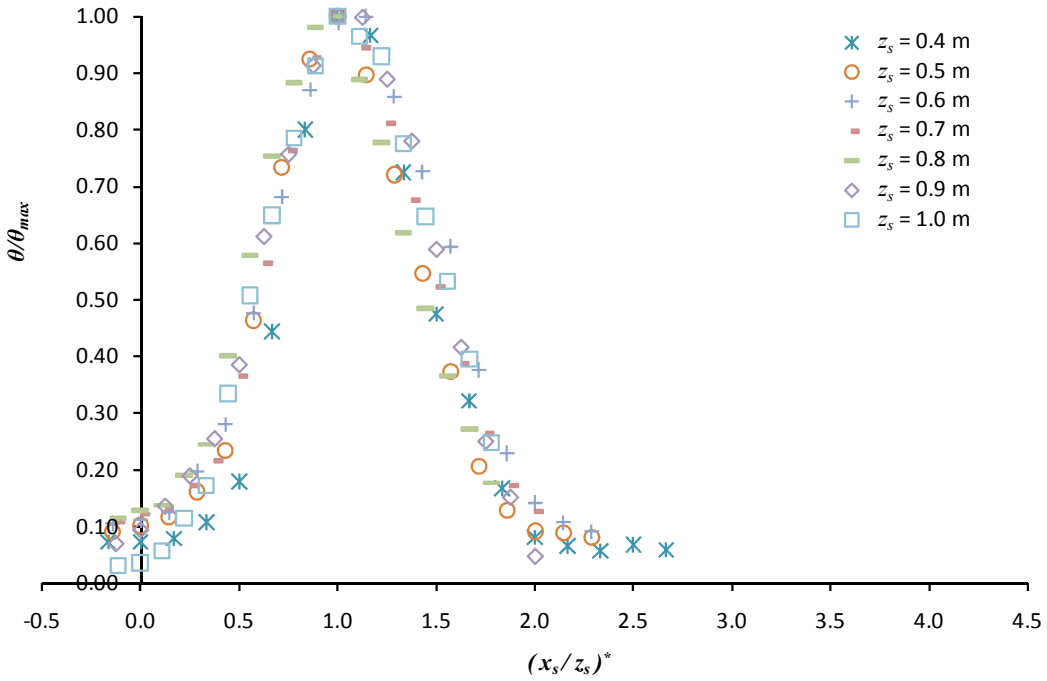

Figure 6.14: Plot of θ/θ_{max} with respect to $(x_s/z_s)^*$ for Experiment T1 (z_s = 0.4 to 1.0 m)

This analysis gives confidence in the use of spill plume entrainment models which assume a constant entrainment coefficient and a virtual line source, which make the fundamental assumption of self-similarity between profiles with respect to height of rise.

Appendix H shows both the temperature and non-dimensional normalised temperature profiles for Experiments T1 to T3 inclusive which demonstrate the same general behaviour as described above for plumes generated from a wide, intermediate and narrow width compartment opening (i.e. W_s = 1.0, 0.6 and 0.2 m, $\dot{Q}_t$ = 10 kW).

6.3.3 Entrainment analysis

The analysis of the experimental results will use the same methods as used for the 2-D plume by encompassing the additional entrainment into the free ends of the 3-D plume into the empirical entrainment coefficient(s). Hence, the methods by Thomas *et al.* [39] [Equation (2-41)] and Poreh *et al.* [31] [Equation (2-39)] are used in the analysis.

There is a limited amount of experimental data currently available to describe 3-D balcony spill plume entrainment. The most robust data available, obtained from 1/10th physical scale model studies, is provided in work by Hansell *et al.* [32] and Harrison and Spearpoint [40], which includes data describing the characteristics of the layer flow below the spill edge. If the Hansell *et al.* data (which essentially forms the basis of the guidance given by CIBSE [38] and NFPA 92B [2]) is correlated according Equation (2-41), then,

$$\frac{\dot{m}'_{p,3D}}{\dot{Q}'_c} = 0.34\frac{z_s}{\dot{Q}'^{2/3}_c} + 2.64\frac{\dot{m}'_s}{\dot{Q}'_c} - 0.0083 \qquad \textbf{(6-6)}$$

Similarly, the Harrison and Spearpoint data correlates to,

$$\frac{\dot{m}'_{p,2D}}{\dot{Q}'_c} = 0.22\frac{z_s}{\dot{Q}'^{2/3}_c} + 1.92\frac{\dot{m}'_s}{\dot{Q}'_c} - 0.0042 \qquad \textbf{(6-7)}$$

The difference in γ between Equations (6-6) and (6-7) (i.e. the 0.22 and the 0.34) provides significant differences in predicted entrainment. Possible reasons for this may relate to differences in the nature of the plume, fire compartment geometry or smoke reservoir geometry between each experimental study. To address this uncertainty the experimental results from this work provide new data to systematically characterise entrainment of air into 3-D balcony spill plumes. Figure 6.15 shows a plot of all the data from this study in a form consistent with the dimensional analysis by Thomas *et al.* [39].

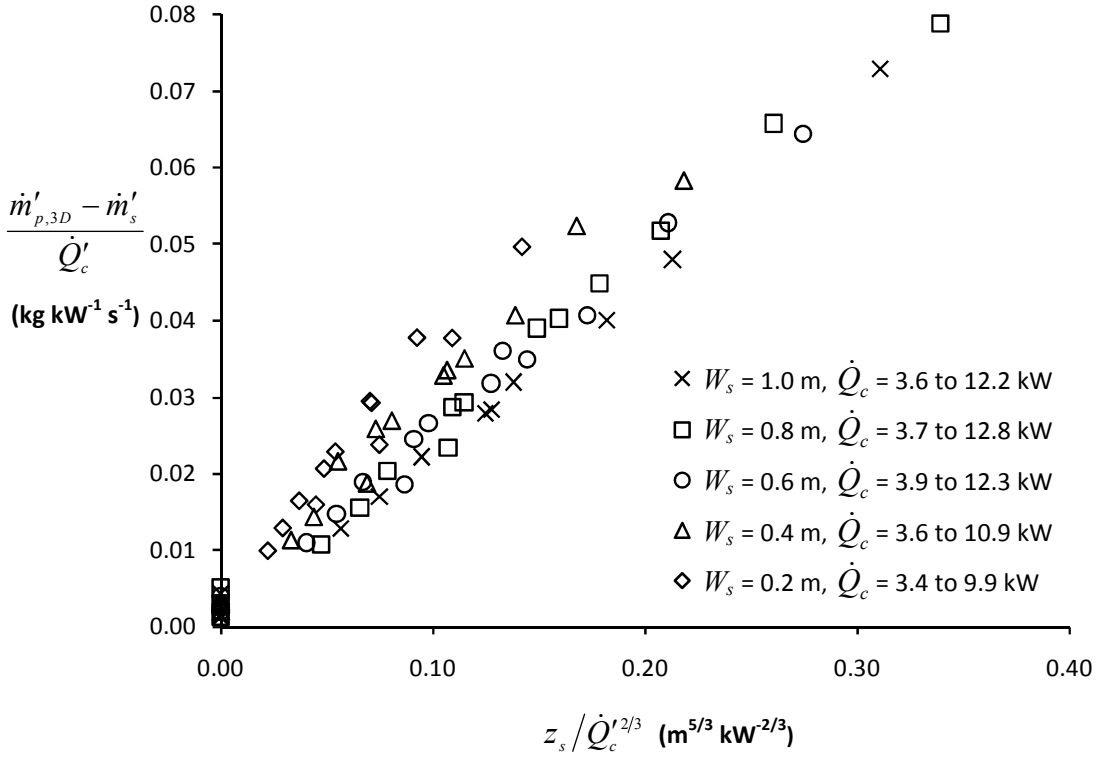

Figure 6.15: Results for the 3-D plume correlated using the Thomas *et al.* analysis

Figure 6.15 shows some scatter of the data which appears to be dependent on W_s. The data exhibits linearity with the representative slope of the line through each data set, for each value of W_s, appearing to increase as W_s decreases. The slope of the line represents the rate of entrainment with respect to height above the spill edge. Figure 6.15 indicates that plumes generated from narrower openings tend to entrain air at a greater rate with respect to height, compared to plumes generated from wider openings. The difference in entrainment appears to be dependent on the nature of the rising plume. Figure 6.16 shows photographs of plumes generated in the scale model from both a wide (i.e. W_s = 1.0 m) and a narrow (i.e. W_s = 0.2 m) opening. Figure 6.16 shows that entrainment into the plume rising above the balcony can be considered in distinct regions (marked in yellow in Figure 6.16). The first region consists of entrainment into the 2-D region of the plume, rising above and in line with the compartment opening. The second region is entrainment into both ends of the plume, which appeared to be more 3-D in nature as the lateral extent of the plume increased with the height above the spill edge. It seems reasonable to expect that the rate of entrainment into the ends of the plume is greater than in the 2-D region of the plume.

Figure 6.16 shows that the majority of the plume from the wide opening consists of the 2-D region, with entrainment into the ends of the plume being less significant in the overall entrainment process. However, for the narrow opening, entrainment into the ends of the plume is more significant.

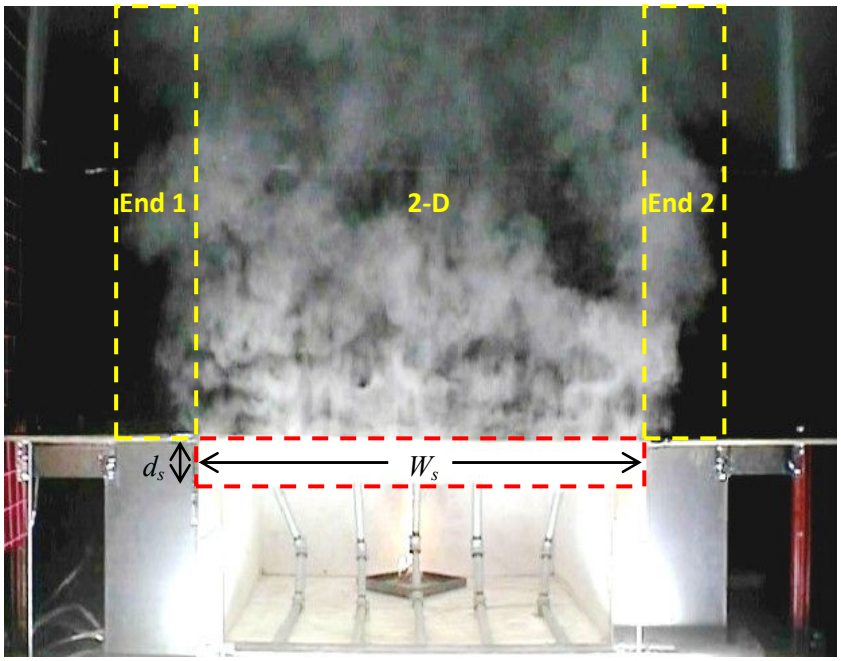

a) W_s = 1.0 m

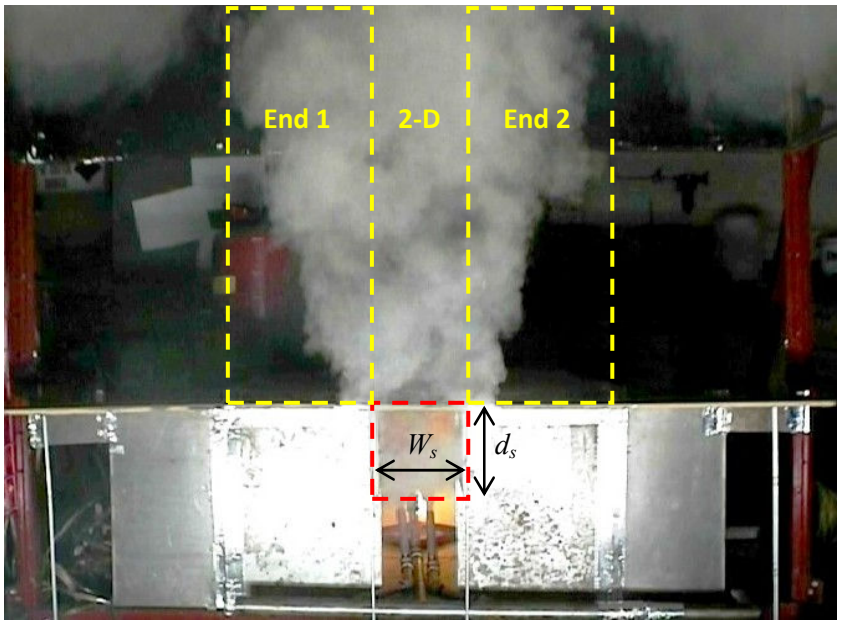

b) W_s = 0.2 m

Figure 6.16: The 3-D balcony spill plume and entrainment regions

This analysis is further supported if we consider the aspect ratio of the layer flow below the spill edge (marked in red in Figure 6.16), which can be considered to be representative of the shape of the resulting horizontal rectangular source of the plume after rotation at $z_s = 0$ (see Figure 6.17). Figures 6.16a and 6.17a show that for a wide opening the layer flow is wide and shallow, which suggests that entrainment will mostly occur over the long length of the rectangular source (i.e. the 2-D region) with only a small amount of entrainment occurring over the short length (i.e. the free ends).

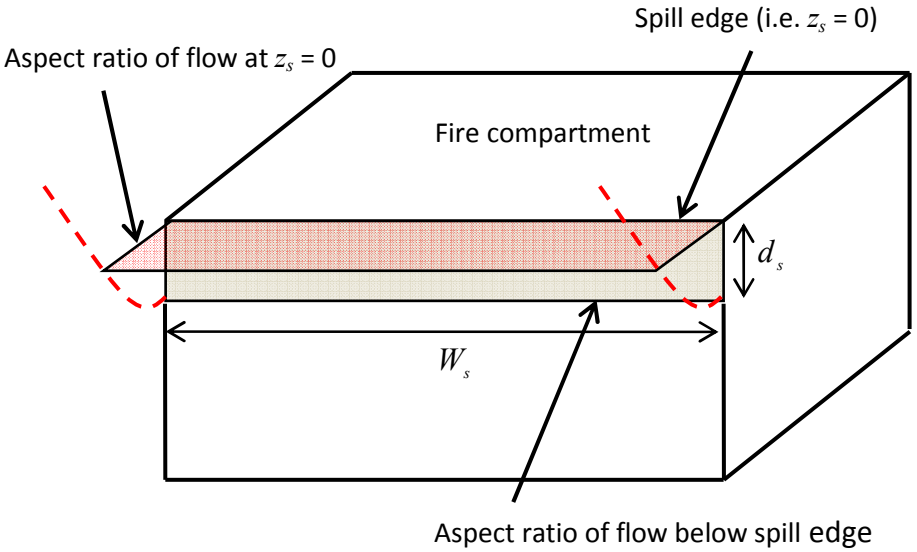

a) Flow from a wide opening

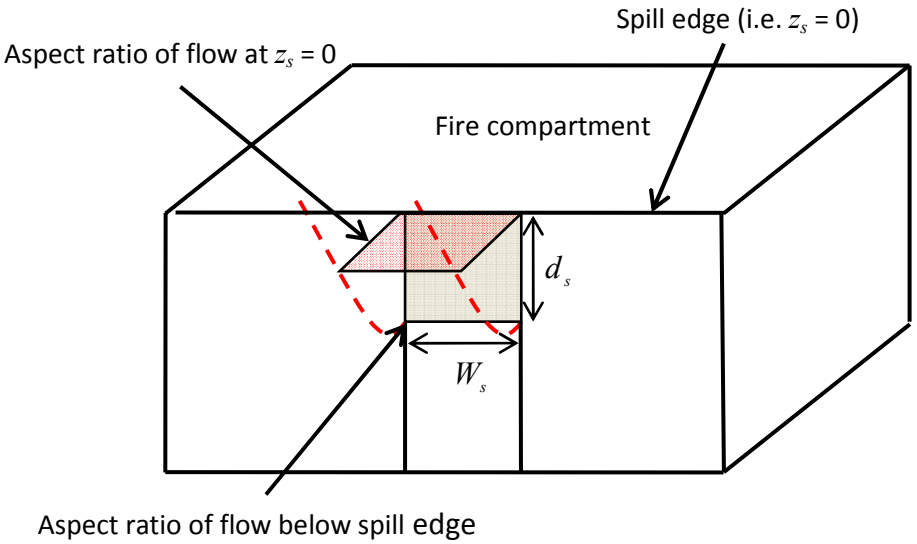

b) Flow from a narrow opening

Figure 6.17: Aspect ratio of the flow at and below the spill edge

However, Figure 6.16b and 6.17b show that for a narrow opening the aspect ratio of the layer flow is more square than rectangular in nature, which again suggests that entrainment into the ends of the plume is more significant in the overall entrainment process. Therefore, it seems reasonable that plumes generated from narrow, deep layer flows entrain air at a greater rate with respect to height compared to plumes generated from wide, shallow layers.

Figure 6.18 shows the same experimental data a plotted according to the Poreh *et al.* method given by Equation (2-39).

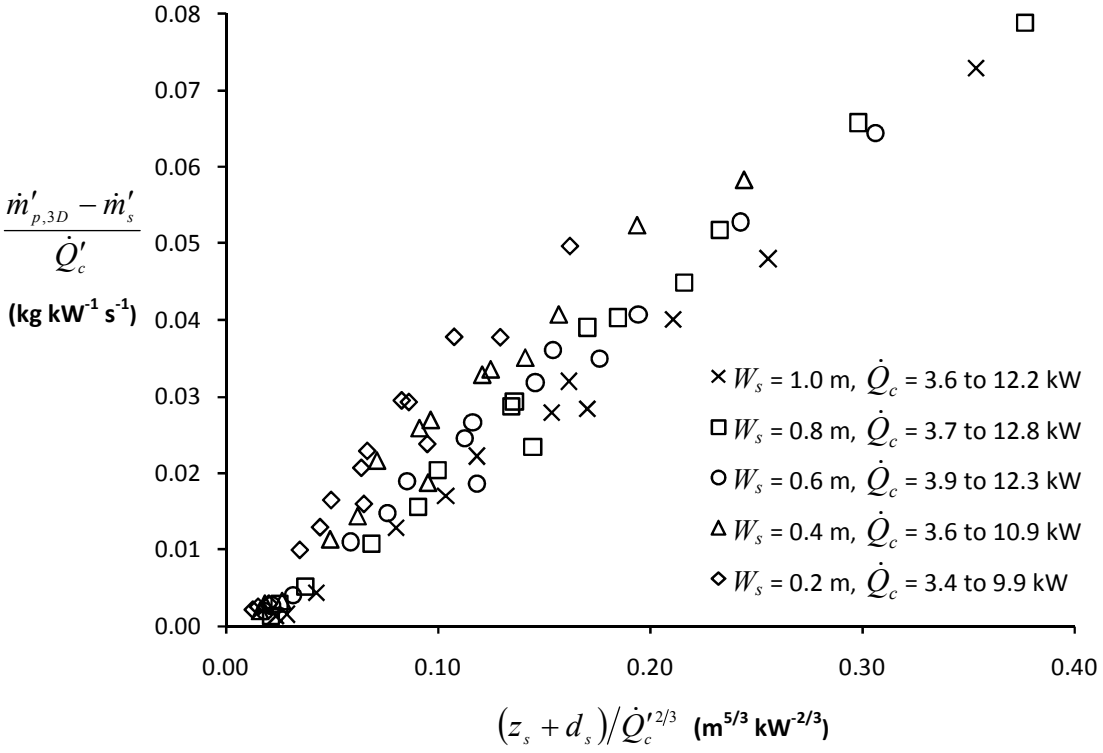

Figure 6.18: Results for the 3-D plume correlated using the Poreh *et al.* analysis

Figure 6.18 shows that although the data demonstrates the same trend in entrainment as the analysis using the Thomas *et al.* method, the general data set does not conveniently pass through the origin (as seen in Figure 6.5 for the 2-D plume) when an adjustment is made to the height of rise of the plume (assuming $z_0 = d_s$).

Figure 6.18 indicates that any line of best fit through each data set, for each value of W_s, would give rise to a negative intercept on the vertical axis. This negative intercept infers negative entrainment in the rotation region, which is implausible. It appears that for the 3-D plume, the additional entrainment into the ends of the plume gives rise to a different location of virtual line source (based on data mainly obtained above the balcony) to that assumed in Equation (2-39). The location of this virtual source is likely to be dependent on W_s as the contribution of the end entrainment changes. The location of the virtual source of the spill plume is analysed and discussed in more detail in section 6.8. Therefore, the use of Equation (2-39) which was developed for a 2-D plume may not be appropriate for a 3-D plume, when encompassing the additional end entrainment into a 'lumped' entrainment coefficient for the entire plume above the spill edge. Therefore, the Poreh *et al.* method will not be considered further for the analysis of the 3-D balcony spill plume.

The above analysis of the experimental results indicates that a general expression needs to be developed to describe 3-D balcony spill plume entrainment to take into account the variation in entrainment with W_s. The Thomas *et al.* method given by Equation (2-41) will be used in the further analysis of the 3-D plume as it does not make the fundamental assumption of a virtual source to deal with entrainment below the height of the spill edge.

As the results in Figure 6.15 show some scatter with respect to W_s there is little benefit in statistically analysing the complete data set according to Equation (2-41) as this will give a correlation that represents the average amount of entrainment for the series of experiments and will not appropriately describe differences in entrainment with respect to W_s. Therefore, the results were correlated for each data set (i.e. for each W_s) separately to determine the values of the regression coefficients given in Equation (2-41) (see Table 6.2).

Experiment	W_s (m)	γ	δ	ε
E1-E3, E83-85, E88-E90, E158-160	1.0	0.219	1.216	-0.0009
E7-E9, E78-80, E94-96, E164-166, E254-E256	0.8	0.233	1.025	0.0020
E13-15, E73-75, E100-102, E170-172, E260-E262	0.6	0.231	0.818	0.0040
E19-21, E67-69, E106-108, E176-178, E266-E268	0.4	0.276	0.626	0.0056
E25-27, E61-63, E112-114, E182-184, E272-E274	0.2	0.352	-0.049	0.0074

Table 6.2: Regression coefficients for the 3-D plume according to Equation (2-41)

Table 6.2 shows that the regression coefficient, γ, which represents the rate of entrainment above the spill edge (i.e. the slope of the line of best fit), increases from approximately 0.22 to 0.35 as W_s decreases. This range of values of γ is generally consistent with the entrainment coefficients measured in previous work by Hansell *et al.* [32] and Harrison and Spearpoint [40] given in Equations (6-6) and (6-7) (i.e. 0.34 and 0.22 respectively) where W_s was fixed (but with different values) in each study.

If the entrainment below the height of the spill edge is next considered, Table 6.2 shows that the regression coefficients δ and ε do not remain constant with respect to W_s and are dissimilar to those already given in Equation (6-4) (i.e. $\delta = 1.34$ and $\varepsilon = 0$). Table 6.2 shows that as W_s decreases, δ decreases from 1.2 to approximately zero and ε increases slightly, but remains close to zero. Values of δ less than unity infer a negative amount of entrainment in the rotation region, which is implausible. As the values of δ and ε were determined from data mainly obtained above the spill edge, it is possible that the differences in entrainment that occur above the spill edge have been taken into account by modifying δ and ε (as well as γ) when linear regression is performed, giving rise to some implausible values for these regression coefficients. It seems reasonable to assume that Equation (6-4) is more appropriate to describe entrainment below the height of the spill edge for the 3-D plume, rather than the values of δ and ε given in Table 6.2, as Equation (6-4) was determined for flows that were decoupled from the entrainment above the spill edge. Because of this, the entrainment above the spill edge has been treated separately in the analysis that follows.

To decouple the entrainment above the spill edge, the measured mass flow rates were modified by subtracting the mass flow rate in the plume at $z_s = 0$ for each W_s and $\dot{Q}_t$ (and hence, $\dot{Q}_c$) examined. Thus, for each W_s the data set passes through the origin, with the slope of each line representing the regression coefficient, γ (see Figure 6.19).

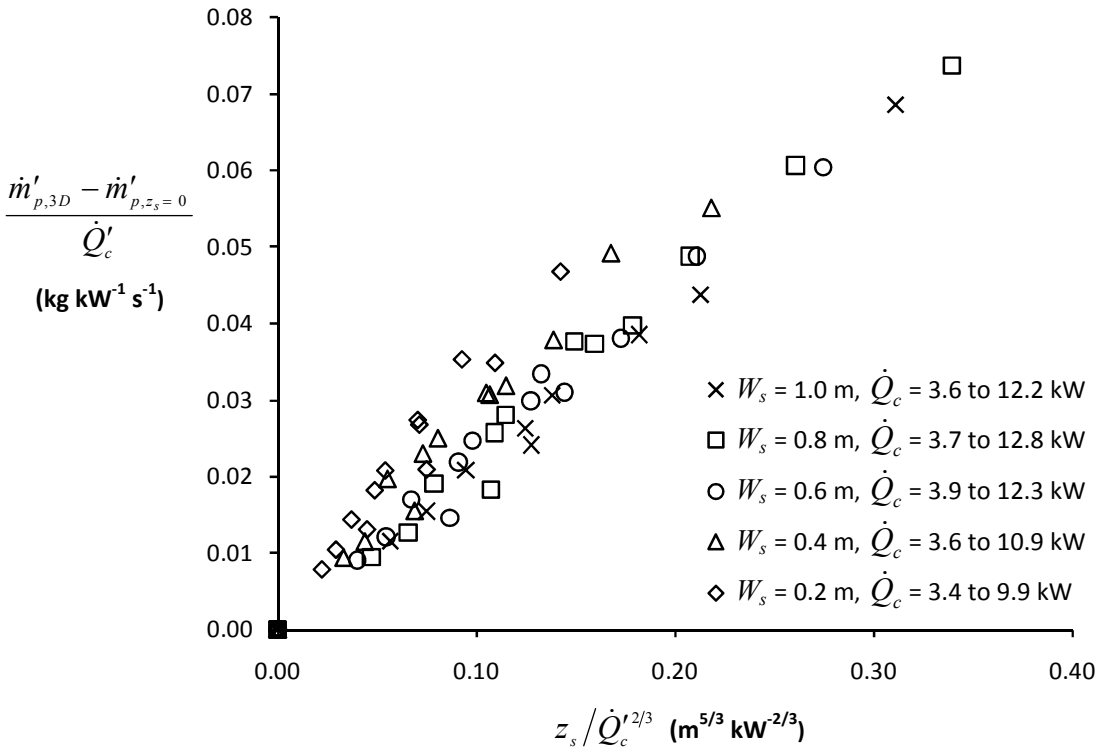

Figure 6.19: Decoupled entrainment above the spill edge according to Thomas *et al.*

Each data set shown in Figure 6.19 (i.e. for each W_s) is made up of data obtained from three different fire sizes examined. To assess if entrainment is dependent on $\dot{Q}_t$ (and hence, $\dot{Q}_c$) as well as W_s, Figures 6.20 to 6.22 show separate plots of the data for flows from a wide, intermediate and narrow width opening respectively (i.e. W_s = 1.0, 0.6 and 0.2 m) for each $\dot{Q}_t$ examined. Figure 6.20 shows that for a wide flow the characteristic slope of the line of best fit through the data (i.e. γ) appears to be relatively independent of $\dot{Q}_t$. However, Figures 6.21 and 6.22 show that for flows from intermediate and narrow width openings, there is some scatter in the data and the characteristic slope appears to become more dependent on $\dot{Q}_t$ as W_s decreases.

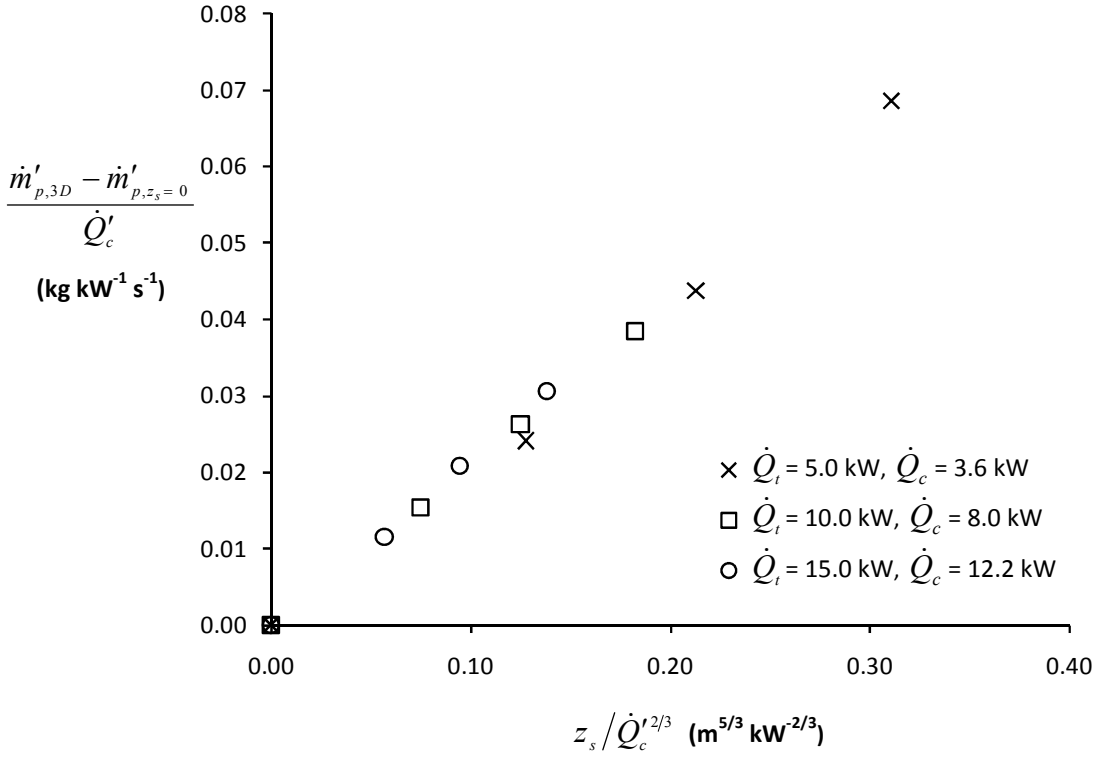

Figure 6.20: Decoupled entrainment above the spill edge (W_s = 1.0 m)

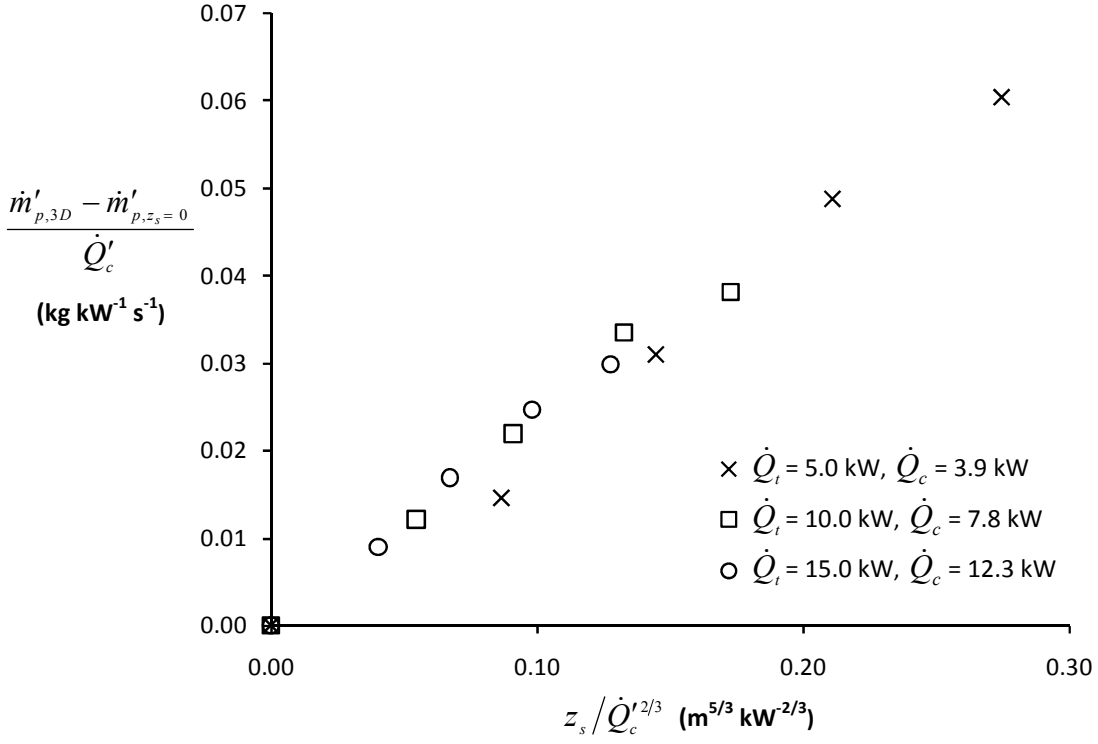

Figure 6.21: Decoupled entrainment above the spill edge (W_s = 0.6 m)

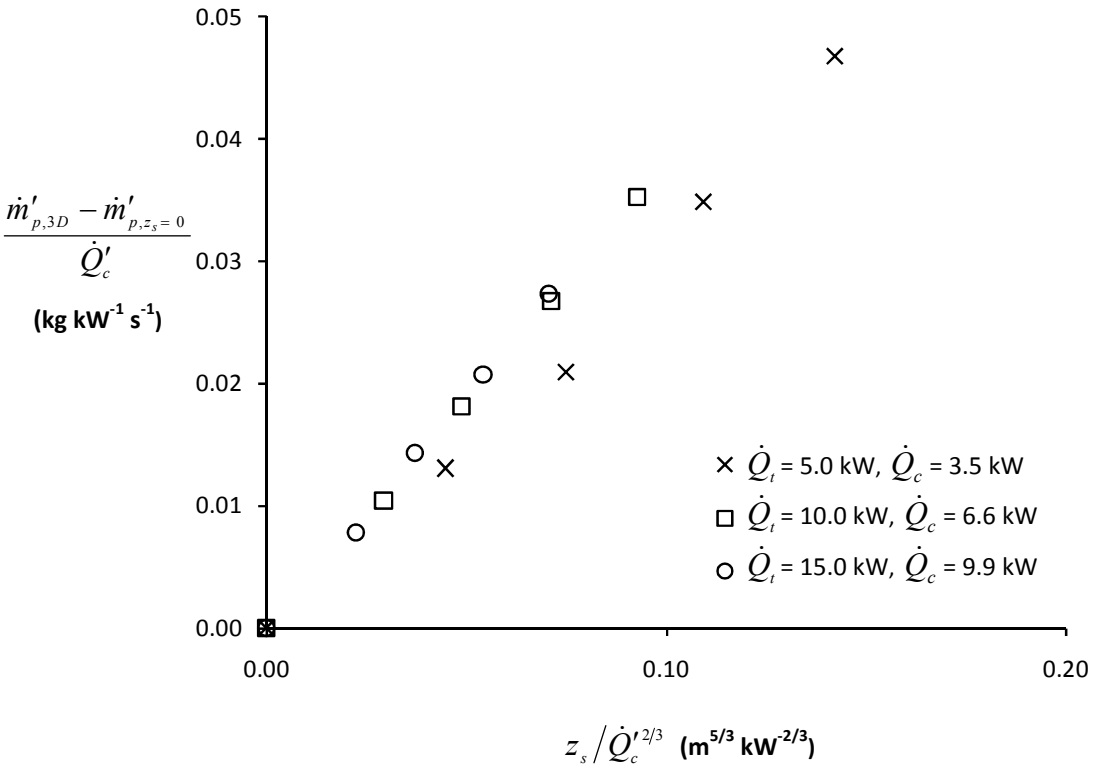

Figure 6.22: Decoupled entrainment above the spill edge (W_s = 0.2 m)

To further examine this, linear regression was performed to determine γ for each W_s and $\dot{Q}_t$ examined. Figure 6.23 shows the results of the linear regression with values of γ (and associated standard errors) plotted with respect to W_s. The fixed value of γ for the 2-D plume (i.e. 0.16) is also shown. Figure 6.23 shows that when W_s = 1.0 m, $\gamma \approx 0.21$, which is higher than γ for the 2-D plume (i.e. 0.16) due to the additional entrainment into the ends of the plume. As W_s decreases, γ generally increases, with a maximum value of approximately 0.38. The difference in γ between the 2-D and 3-D plumes is representative of the amount of entrainment into the ends of the plume. Figure 6.23 shows that as W_s decreases, the contribution of end entrainment in the overall entrainment process increases, thus increasing the value of γ, which is consistent with the entrainment analysis described above. However, as W_s increases the value of γ approaches 0.16, thus, 3-D plumes from very wide openings are likely to behave similarly to 2-D plumes in terms of entrainment as the contribution of end entrainment becomes less significant for wide and shallow layer flows below the edge.

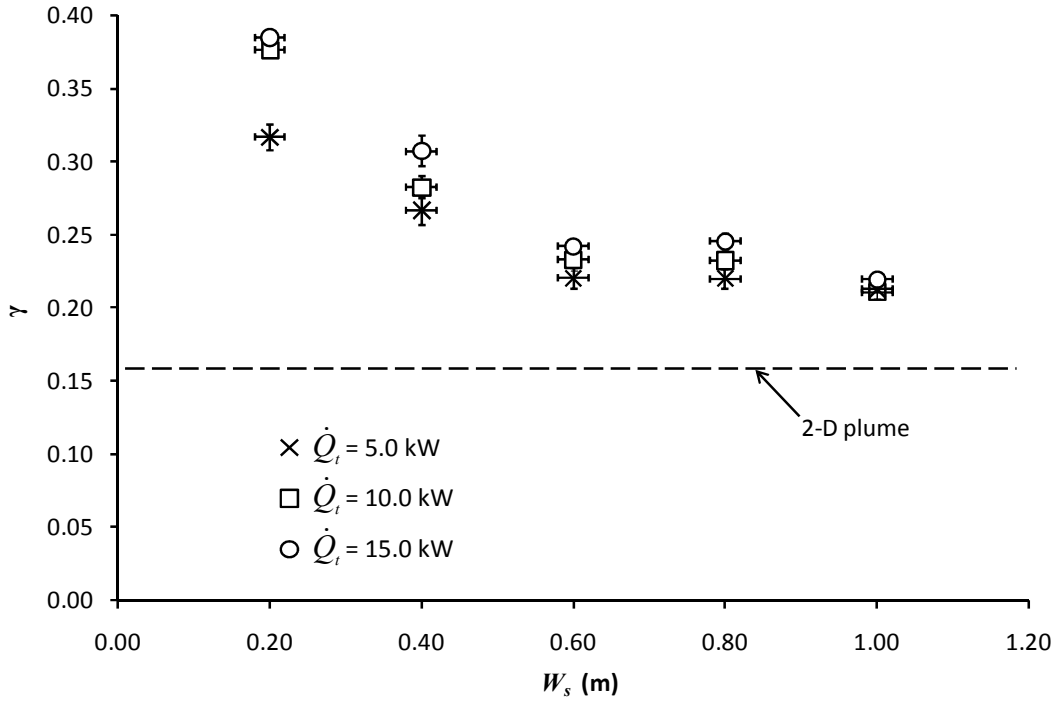

Figure 6.23: Plot of γ versus W_s for entrainment above the spill edge

Figure 6.23 again shows that γ appears to be independent of $\dot{Q}_t$ for flows from a wide opening (i.e. W_s = 1.0), but for narrower openings there is clearly some dependency on $\dot{Q}_t$ which becomes more pronounced as W_s decreases. This is contrary to that observed for the 2-D plume where γ was independent of W_s and $\dot{Q}_t$. It is likely that this dependency is not primarily due to changes in $\dot{Q}_t$ itself, but is more likely due to changes to the nature of the 3-D plume as $\dot{Q}_t$ changes (that do not occur for the 2-D plume). It is possible that this dependency is due to variation in d_s (with respect changes in W_s and $\dot{Q}_t$) and that the amount of end entrainment is directly proportional d_s (as also postulated by Thomas *et al.* [39]). For wide openings d_s was reasonably insensitive to changes in $\dot{Q}_t$, however, for narrow openings d_s was more sensitive to changes in $\dot{Q}_t$. Clearly, a deep layer flow emerging from the spill edge will give rise to a 3-D spill plume with broader ends compared to a shallow layer flow (see section 6.3.1), thus entraining more air.

Figure 6.24 shows a plot of ($\gamma_{3D} - \gamma_{2D}$) versus ($W_s/d_s$) to express the contribution of entrainment into the ends of the plume and to take into account the effect of d_s. Figure 6.23 shows that all the data shown in Figure 6.23 now collapse to the relationship given by Equation (6-8).

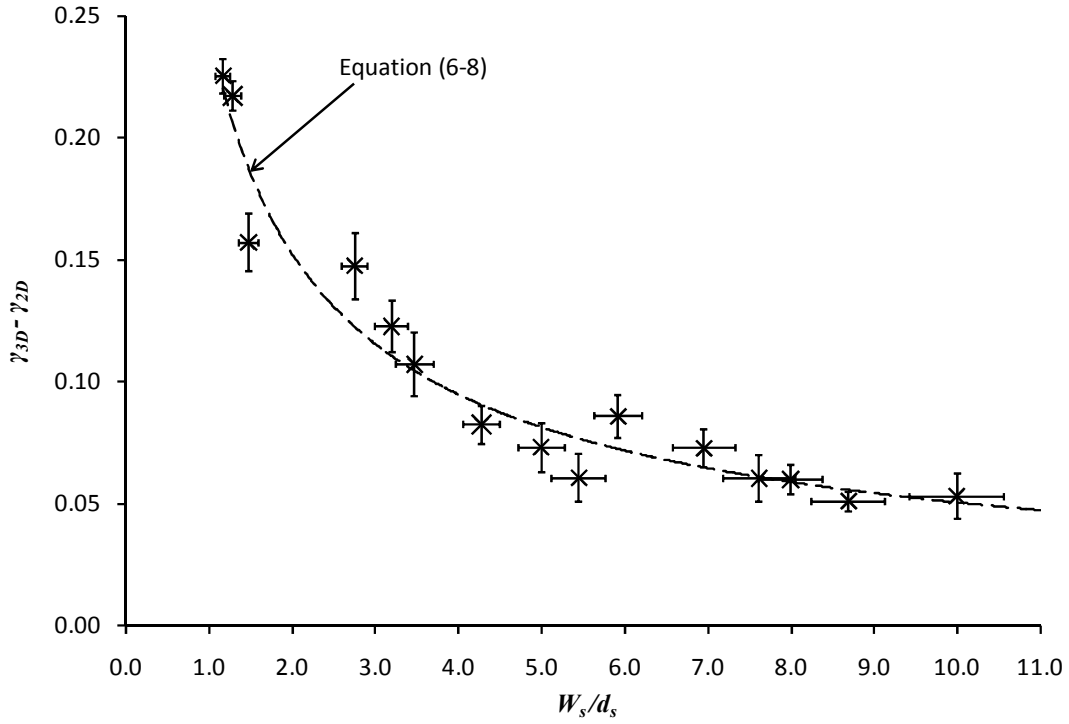

Figure 6.24: Plot of ($\gamma_{3D} - \gamma_{2D}$) versus ($W_s/d_s$) for entrainment above the spill edge

$$\left(\gamma_{3D} - \gamma_{2D}\right) = 0.246\left(\frac{W_s}{d_s}\right)^{-0.687} \qquad \textbf{(6-8)}$$

The standard errors of the regression coefficients 0.246 and -0.687 are 0.020 and 0.048 respectively. Therefore, for design purposes it seems reasonable and convenient to express Equation (6-8) by Equation (6-9).

$$\left(\gamma_{3D} - \gamma_{2D}\right) = 0.25\left(\frac{W_s}{d_s}\right)^{-2/3} \qquad \textbf{(6-9)}$$

It appears that it is not appropriate to assign a universal value of γ to represent the total amount of entrainment above the spill edge due to the varying contribution of end entrainment. Therefore, to develop a general simplified design formula for the 3-D balcony spill plume, it is necessary to develop an expression to explicitly describe the mass flow rate of gases into the ends of the plume ($\dot{m}_{ends}$) above the spill edge. This can be determined from the difference in $\dot{m}_p$ between the 3-D and 2-D spill plumes for the decoupled flow above the spill edge and is described by Equation (6-10).

$$\frac{\dot{m}'_{p,3D} - \dot{m}'_{p,2D}}{\dot{Q}'_c} = \frac{\dot{m}'_{ends}}{\dot{Q}'_c} = \left(\gamma_{3D} - \gamma_{2D}\right)\frac{z_s}{\dot{Q}'^{2/3}_c} \qquad \textbf{(6-10)}$$

If Equation (6-9) is substituted into Equation (6-10), this gives an explicit term to describe the mass flow rate of gases into the ends of the plume [Equation (6-11)], which suggests that the amount of end entrainment is indeed proportional to d_s.

$$\dot{m}_{ends} = 0.25\dot{Q}_c^{1/3} d_s^{2/3} z_s \qquad \textbf{(6-11)}$$

It is interesting to note that Equation (6-11) is similar in nature to the general expression that describes the rate of entrainment above the spill edge, but with the lateral extent of the plume given by d_s instead of W_s, which suggests that the breadth (i.e. the short length) of the horizontal rectangular source after rotation at $z_s = 0$ is related to d_s.

Equation (6-11) was determined from data which exhibited linearity. It is expected that at higher heights of rise of plume, the effect of end entrainment will cause the plume to be more axisymmetric in nature and linearity will no longer apply. Therefore, as Equation (6-11) is empirical in nature, there will be a limit its use which is developed and given in Chapter 9 [i.e. Equation (9-14)].

6.3.3.1 A new design formula for the 3-D spill plume

A simplified design formula for the 3-D plume can now be deduced by simply appending Equation (6-11) to the design formula for the 2-D plume [given by Equation (6-5)]. Equation (6-12) describes the sum of entrainment of air into the flow below the height of the spill edge, entrainment into the 2-D region of plume above the spill edge and entrainment into the ends of the plume above the spill edge. It applies to a flow which is channelled by screens beneath the balcony, with the limit given by Equation (9-14) (see Chapter 9). The overall uncertainty in the use of Equation (6-12) will be dependent on the nature of the plume and hence, the relative contribution of each term and the associated standard error of each regression coefficient.

$$\dot{m}_{p,3D} = 0.16\dot{Q}_c^{1/3} W_s^{2/3} z_s + 1.34\dot{m}_s + 0.25\dot{Q}_c^{1/3} d_s^{2/3} z_s \qquad \textbf{(6-12)}$$

$$\Rightarrow \dot{m}_{p,3D} = 0.16\dot{Q}_c^{1/3}\left(W_s^{2/3} + 1.56 d_s^{2/3}\right) z_s + 1.34\dot{m}_s$$

This work suggests that entrainment of air into a 3-D balcony spill plume is dependent on the characteristics of the layer flow below the spill edge (in terms of W_s and d_s) and may explain differences between measured entrainment from previous studies. The Harrison and Spearpoint [40] data was determined from a flow with W_s = 0.6 m, whereas the Hansell *et al.* [32] data was determined from a flow which was narrower with $W_s \approx 0.43$ m. Thus, it appears that currently available simplified formulae for the 3-D plume, based on these data (e.g. [2,38]), apply specifically to the range of conditions studied in these experiments and do not apply generally for a wide range of W_s (also see section 6.6). Following the analysis of this work, it is not surprising that value of γ obtained from Hansell *et al.* is greater than that obtained from Harrison and Spearpoint as the plumes were generated from narrower, deeper flows below the spill edge. This may explain the differences in entrainment between these previous studies and the use of Equation (6-12) may be appropriate to reconcile these differences. Therefore, Equation (6-12) was applied to the data from these previous studies, using the measured results for the layer flow below the spill edge as the input. Figure 6.25 shows that Equation (6-12) provides a good prediction of the Harrison and Spearpoint results and also provides a reasonably good prediction of the Hansell *et al.* data for smaller values of mass flow rate, obtained at low heights of rise.

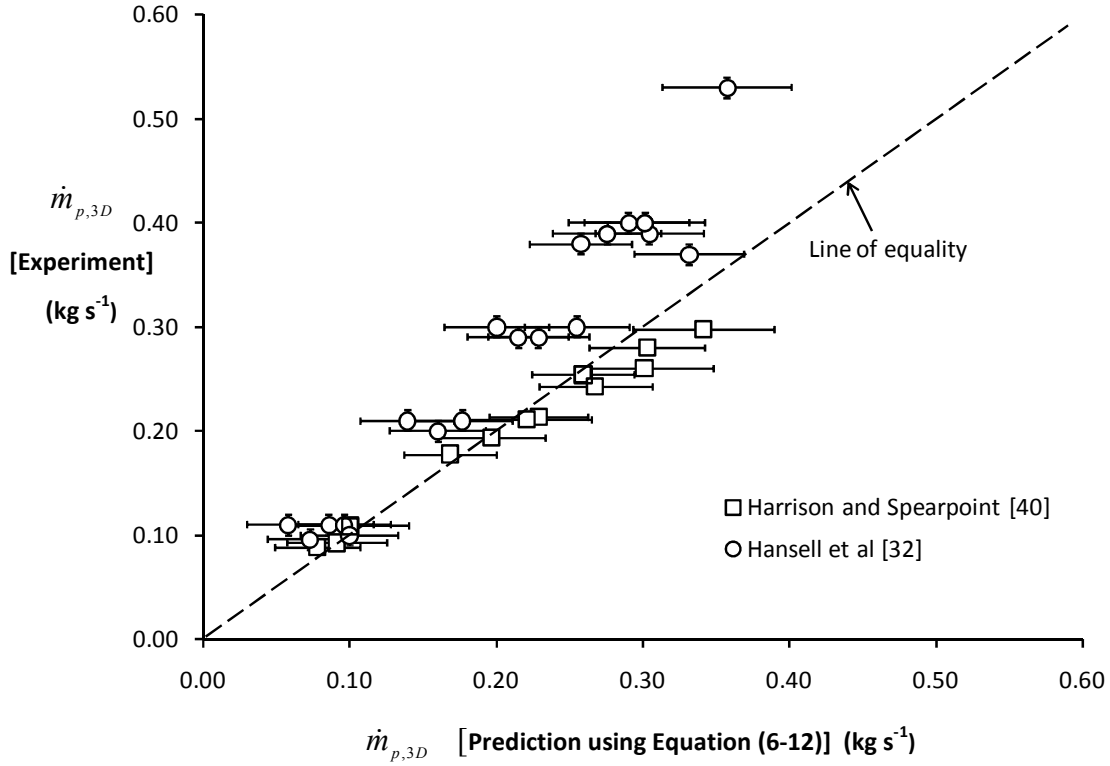

Figure 6.25: Prediction using Equation (6-12) with data from previous work

However, for larger values obtained at higher height of rise, there is divergence between the experimental results and the prediction, with a general trend to under predict the experimental results. However, the experimental boundary conditions in the Hansell *et al.* work were such that the nature of the plume was different to the unbounded plumes generated in this work and by Harrison and Spearpoint. The plumes generated by Hansell *et al.* were obtained from a model which had four asymmetric openings for inlet air, with the resulting plume having a tendency to become more axisymmetric in nature due to the observed swirling of rising plume in the smoke reservoir [31,32]. Therefore, due to the different nature of the plume, it is possible that the Hansell *et al.* can be considered to be anomalously high (particularly for larger heights of rise of plume) compared to the data obtained from the unbounded spill plumes in this work and by Harrison and Spearpoint. Therefore, it appears that Equation (6-12) goes some way to reconcile the differences in entrainment between previous work and can be applied more generally compared to currently available simplified design formulae.

6.4 The 3-D plume without channelling screens

6.4.1 Plume behaviour

To demonstrate the difference in plume behaviour without the use of channelling screens below the balcony, Figures 6.26 to 6.28 show a comparison between plumes generated both with and without screens for a wide, intermediate and narrow width fire compartment opening respectively (i.e. W_o = 1.0, 0.6 and 0.2 m). Without channelling screens there was lateral spread of the layer flow below the balcony which was not well defined. The depth of this layer flow was not uniform and was generally deeper at the centreline of the flow and shallower near the extremities. The shallow layer flow at the extremities tended to be stagnant in nature and lacked sufficient buoyancy to rise as part of a plume into the collecting hood above due to the cooling of these gases after lateral spread. The spread of the flow below the balcony subsequently gave rise to plumes with a greater lateral extent above the spill edge compared to plumes generated with the use of channelling screens.

The lateral spread of gases beneath the balcony for those experiments where $\dot{Q}_t$ was 15 kW was so great that the flow horizontally projected beyond the ends of the balcony such that the true lateral extent of the flow and the mass flow rate in the subsequent plume could not be measured, hence, these experiments were not continued.

Figures 6.26 to 6.28 show that the relative increase in the lateral extent of the rising plume (when compared to W_o) increased as W_o decreased (which also occurred when $\dot{Q}_t$ increased). To quantify the increase in the lateral extent of the plume for flows without channelling screens, visual observations were made of the lateral extent of the flow below the spill edge (i.e. W_s) for each W_o and $\dot{Q}_t$ examined (see Table 6.3).

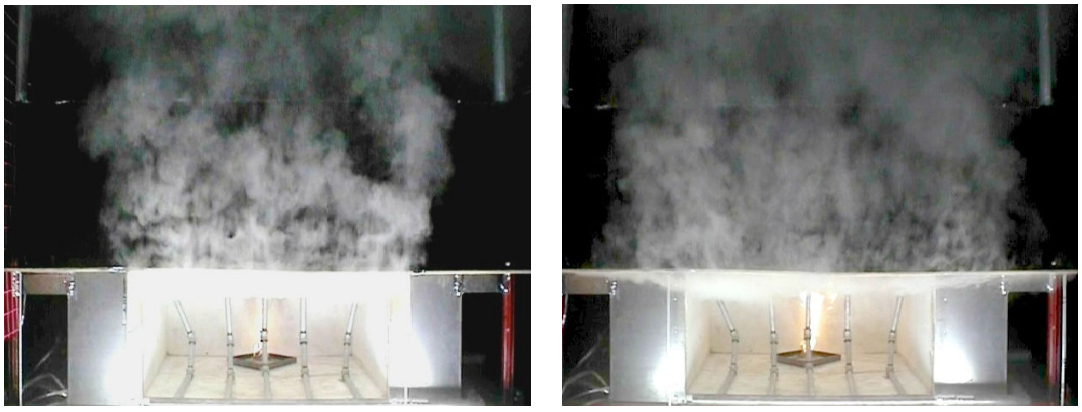

a) with channelling screens b) without channelling screens

Figure 6.26: Plume behaviour (W_o = 1.0 m)

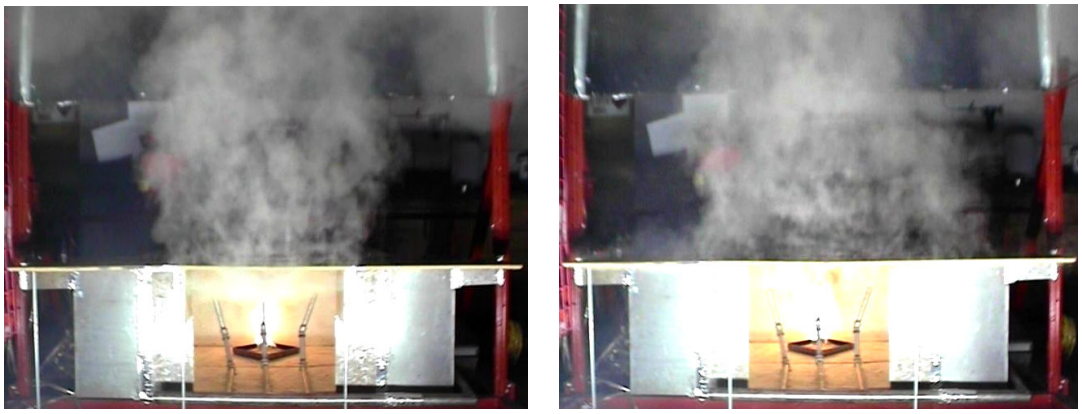

a) with channelling screens b) without channelling screens

Figure 6.27: Plume behaviour (W_o = 0.6 m)

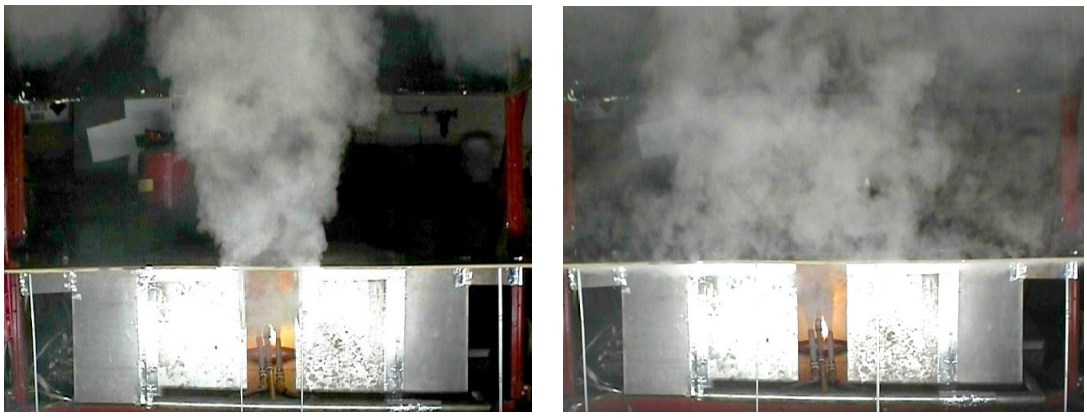

a) with channelling screens b) without channelling screens

Figure 6.28: Plume behaviour (W_o = 0.2 m)

Experiment	$\dot{Q}_t$ (kW)	W_o (m)	W_s (m)	W_s/W_o
E4, E86, E91 and E161	5.0	1.0	1.35 ± 0.10	1.35
E5, E87, E92 and E162	10.0	1.0	1.70 ± 0.10	1.70
E10, E81, E97, E167 and E257	5.0	0.8	1.30 ± 0.10	1.60
E11, E82, E98, E168 and E258	10.0	0.8	1.60 ± 0.10	2.00
E16, E76, E103, E173 and E263	5.0	0.6	1.30 ± 0.10	2.20
E17, E77, E104, E174 and E264	10.0	0.6	1.70 ± 0.10	2.80
E22, E70, E109, E179 and E269	5.0	0.4	1.35 ± 0.10	3.40
E23, E71, E110, E180 and E270	10.0	0.4	1.75 ± 0.10	4.40
E28, E64, E115, E185 and E275	5.0	0.2	1.35 ± 0.20	6.75
E29, E65, E116, E186 and E276	10.0	0.2	1.70 ± 0.20	8.50

Table 6.3: Visually observed values of W_s for flows without screens

The values of W_s in Table 6.3 specifically apply to the region of the flow below the spill edge that contained sufficient buoyancy to rise as a plume and did not include the stagnant gases at the extremities. It is interesting to note that the absolute values of W_s in Table 6.3 remain reasonably constant for each $\dot{Q}_t$ examined with respect to changes in W_o. However, Table 6.3 shows that the ratio of W_s/W_o increases significantly as W_o decreases (and as $\dot{Q}_t$ increases). For the conditions studied, W_s was approximately 35 to 70% greater than W_o for flows from a wide opening (i.e. W_o = 1.0 m), however, for flows from a narrow opening (i.e. W_o = 0.2 m) W_s was approximately 6 to 9 times greater than W_o.

The extensive amount of lateral spread below the balcony for flows from a narrow opening gave rise to subsequent plumes above the spill edge that were particularly complex and relatively unstable in nature compared to plumes from wider openings.

It appears that the amount of lateral spread below the balcony is dependent upon the velocity of the gas flow emerging from the fire compartment opening which increases when W_o decreases and $\dot{Q}_t$ increases (see Figure 6.29). An increase in velocity in all components of the flow from the compartment opening (both parallel and perpendicular to the opening) appears to cause an increase in lateral spread.

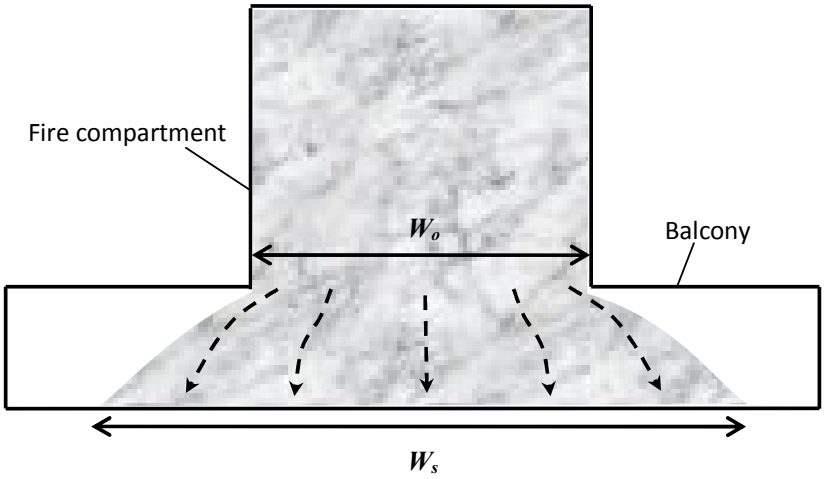

a) Flow without channelling screens from a wide compartment opening (i.e. W_o = 1.0 m)

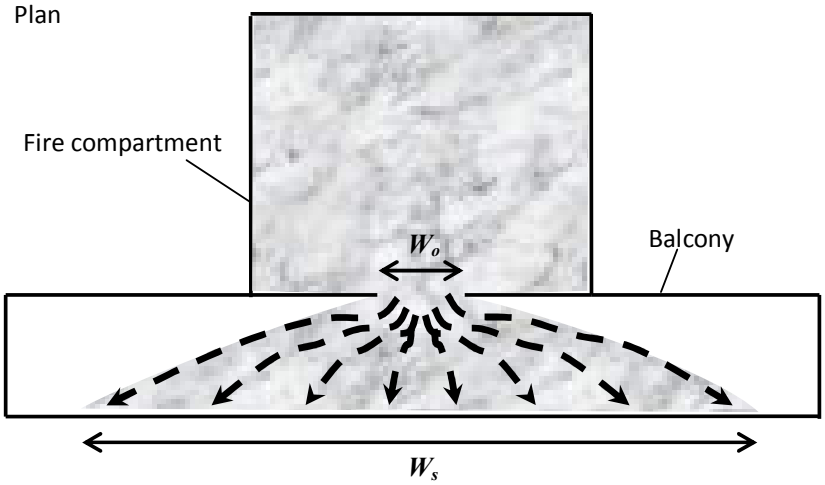

b) Flow without channelling screens from a narrow compartment opening (i.e. W_o = 0.2 m)

Figure 6.29: Schematic of the lateral spread below the balcony without screens

Although the absolute values of W_s in Table 6.3 remain reasonably constant for each $\dot{Q}_t$ examined with respect to changes in W_o, the nature of the plumes rising above the edge were different when considering the temperature profiles across the flow just below the spill edge. Figure 6.30 shows a comparison of typical temperature profiles across the spill edge, 10 mm below the edge, for a flow from a wide, intermediate and narrow width compartment opening respectively without the use of channelling screens below the balcony (i.e. Experiments E246, E236 and E226, W_o = 1.0, 0.6 and 0.2 m, $\dot{Q}_t$ = 5 kW).

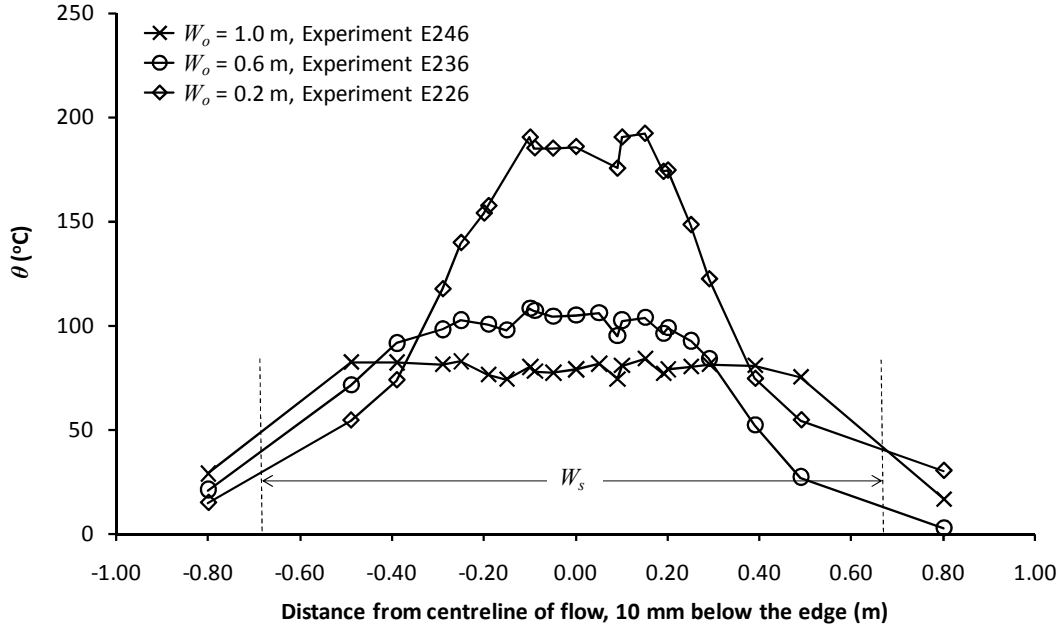

Figure 6.30: Typical temperature profiles across the spill edge without screens

Figure 6.30 shows that the temperature profiles for each W_o examined approach ambient at a similar distance from the centreline of the flow consistent with the visual observations of W_s. However, the nature of these profiles for each W_o are different. The profile across the flow from a wide opening was reasonably uniform for majority of the flow (apart from at the extremities), but for a narrow opening the profile is characterised by a single peak at the flow centreline. An intermediate width opening gives rise to a profile part way between that from a wide and narrow compartment opening. Appendix I shows the temperature profiles of the flow across and below the spill edge for the range of conditions examined without channelling screens.

As the plumes generated without channelling screens generally do not provide a uniform temperature profile across the flow below the spill edge, and that the depth of these flows were not uniform, any subsequent plume will violate the fundamental assumption made for all empirical and analytical spill plume entrainment calculation methods (i.e. uniformity across the flow below the spill edge in terms of temperature, velocity and depth). Thus, only an approximate solution to predict entrainment for this scenario can be applied (or by using numerical modelling) such as the method proposed by Law [Equation (2-30)] and the analysis in the following section.

Figure 6.31 shows a comparison of the plume behaviour both with and without screens from a side view, this behaviour was generally typical for plumes generated from the range of fire compartment opening widths examined.

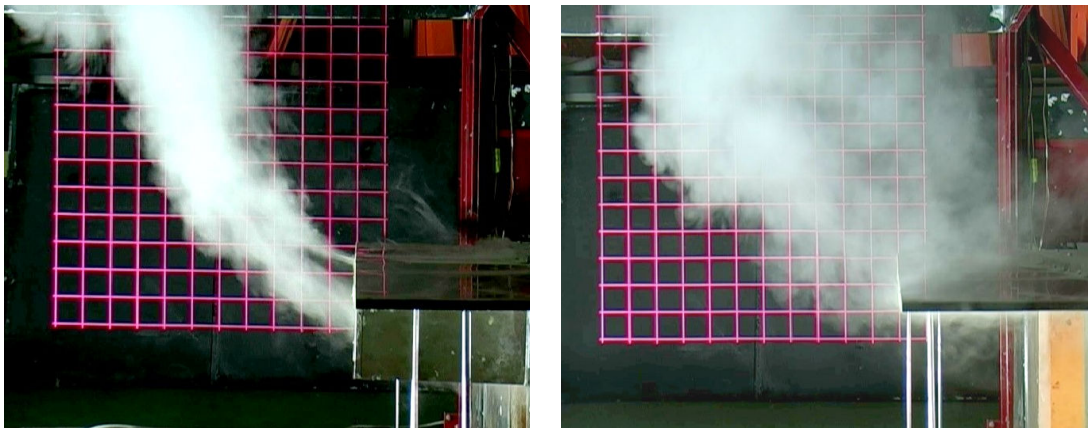

a) with channelling screens b) without channelling screens

Figure 6.31: Comparison of typical plume behaviour from a side view

Figure 6.31 shows that the plume generated without screens below the balcony is less well defined compared to an equivalent plume produced with screens.

Without channelling screens the plume tended to curl back above the spill edge to cause smoke contamination local to the area above the balcony in line with the fire compartment opening. In addition, the relatively stagnant smoke at the extremities of the flow below the balcony caused smoke to accumulate just above the balcony edge. This stagnant smoke was observed to be subsequently entrained back towards the rear of the rising plume via the area above the balcony causing further smoke contamination.

This plume behaviour is an important consideration for the design of smoke management systems, particularly when addressing the tenability of the smoke local to the area just above the balcony, which could be designated as an escape route. This study has not examined the tenability of the smoke contamination above the balcony, however, this is planned in a further study using numerical modelling [132].

6.4.2 Entrainment analysis

Since the characteristics of the layer flow below the spill edge (i.e. $\dot{Q}_c$ $\dot{m}_s$ and d_s) could not be directly measured in the experiments without channelling screens, the methods used in the entrainment analysis described above (i.e. The Thomas *et al.* [39] and Poreh *et al.* [31] methods) cannot be applied here. Therefore, in an attempt to quantify entrainment into plumes produced without screens, Figure 6.32 shows a direct comparison of the measured values of $\dot{m}_{p,3D}$ for equivalent plumes with and without screens below the balcony.

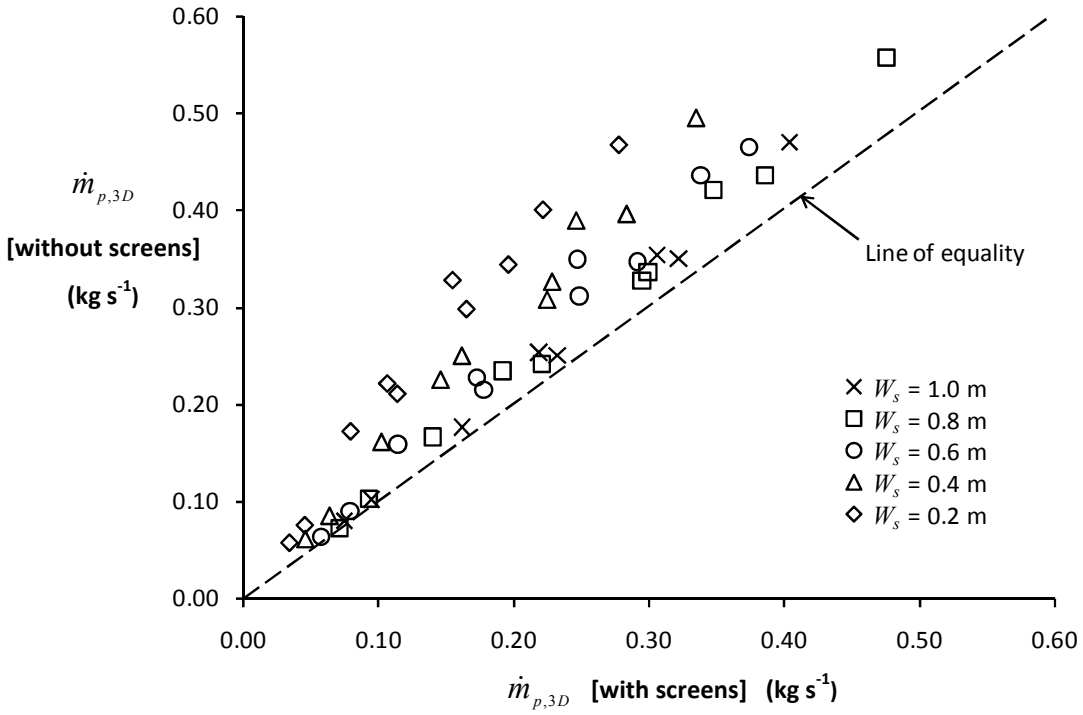

Figure 6.32: Comparison of $\dot{m}_{p,3D}$ for equivalent plumes with and without screens

Figure 6.32 shows little difference in entrainment between plumes generated with or without screens for values of $\dot{m}_{p,3D}$ less than approximately 0.10 kg s^{-1}. However, these data were measured at z_s = 0 and describe the entrainment below the height of the spill edge. Therefore, it appears that the only significant difference in the flow of gases below the spill edge, with or without screens, is how these flows are distributed below the balcony (in terms of width and depth).

Figure 6.32 shows that for values of $\dot{m}_{p,3D}$ greater than 0.10 kg s^{-1} obtained at $z_s > 0$, the measured entrainment for plumes generated without screens is generally greater than the measured entrainment for equivalent plumes with screens. The difference in entrainment tends to increase as W_o decreases consistent with the relative increase in W_s (as W_o decreases) described above due to lateral spread of gases below the balcony. For the conditions studied, plumes generated without screens from a wide opening (e.g. W_o = 1.0 m) tended to provide an increase in measured entrainment of approximately 10% compared to plumes with screens. Plumes generated without screens from a narrow opening (e.g. W_o = 0.2 m) tended to provide an increase in measured entrainment of approximately 80% compared to plumes with screens. The relative increase in entrainment measured in this work is specific to the breadth of balcony examined and is likely to vary for different balcony breadths. As the balcony breadth was fixed in this study, further work is desirable to examine plumes generated without screens for a variety of balcony breadths.

As the nature of the flow below the spill edge without screens generally violates the fundamental assumption for spill plume calculation methods in terms of uniformity of the flow, an approximate solution to determine entrainment for this complex flow can be developed using a similar analysis to that carried out by Law [49]. Thus, this entrainment can be determined by using an effective lateral extent of the plume below the spill edge (i.e. $W_{e,s}$) similar to Equation (2-30) determined by Law for use within the design equation given by CIBSE [Equation (2-32)] (also in NFPA 92B [2]).

However, in this case it seems more appropriate to determine $W_{e,s}$ for use within the new design equation for the 3-D balcony spill plume proposed in this work [i.e. Equation (6-12)] as it appears to be more general in nature. Values of $W_{e,s}$ were determined using Equation (6-12) from the measured values of $\dot{m}_{p,3D}$ for plumes without screens with $z_s > 0$. Since Equation (6-12) requires values of $\dot{Q}_c$, $\dot{m}_s$ and d_s which could not be measured experimentally for plumes without screens, these values were assumed to be the same as those determined with screens in the analysis. Table 6.4 shows the values of $W_{e,s}$ determined using Equation (6-12) for the range of conditions studied.

Experiment	$\dot{Q}_t$ (kW)	z_s (m)	W_o (m)	$W_{e,s}$ (m)	$W_{e,s}/W_o$	W_o/b
E86	5.0	0.30	1.0	1.00	1.00	3.33
E91	5.0	0.50	1.0	1.10	1.10	3.33
E161	5.0	0.73	1.0	1.28	1.28	3.33
E87	10.0	0.30	1.0	1.20	1.20	3.33
E92	10.0	0.50	1.0	1.24	1.24	3.33
E162	10.0	0.73	1.0	1.27	1.27	3.33
E81	5.0	0.30	0.8	0.93	1.16	2.67
E97	5.0	0.50	0.8	1.06	1.32	2.67
E167	5.0	0.73	0.8	1.19	1.49	2.67
E257	5.0	0.95	0.8	1.21	1.52	2.67
E82	10.0	0.30	0.8	1.18	1.48	2.67
E98	10.0	0.50	0.8	1.16	1.45	2.67
E168	10.0	0.73	0.8	1.17	1.46	2.67
E258	10.0	0.95	0.8	1.26	1.57	2.67
E76	5.0	0.30	0.6	1.01	1.68	2.00
E103	5.0	0.50	0.6	0.87	1.44	2.00
E173	5.0	0.73	0.6	1.38	2.30	2.00
E263	5.0	0.95	0.6	0.80	1.33	2.00
E77	10.0	0.30	0.6	1.32	2.20	2.00
E104	10.0	0.50	0.6	1.15	1.92	2.00
E174	10.0	0.73	0.6	1.27	2.12	2.00
E264	10.0	0.95	0.6	0.86	1.44	2.00
E70	5.0	0.30	0.4	1.32	3.30	1.33
E109	5.0	0.50	0.4	1.47	3.69	1.33
E179	5.0	0.73	0.4	1.14	2.86	1.33
E269	5.0	0.95	0.4	1.16	2.90	1.33
E71	10.0	0.30	0.4	1.70	4.25	1.33
E110	10.0	0.50	0.4	1.57	3.94	1.33
E180	10.0	0.73	0.4	1.18	2.94	1.33
E270	10.0	0.95	0.4	1.16	2.90	1.33
E64	5.0	0.30	0.2	1.87	9.35	0.67
E115	5.0	0.50	0.2	1.24	6.21	0.67
E185	5.0	0.73	0.2	1.42	7.11	0.67
E275	5.0	0.95	0.2	0.92	4.60	0.67
E65	10.0	0.30	0.2	1.78	8.92	0.67
E116	10.0	0.50	0.2	1.45	7.27	0.67
E186	10.0	0.73	0.2	1.32	6.61	0.67
E276	10.0	0.95	0.2	1.09	5.43	0.67

Table 6.4: Values of $W_{e,s}$ using Equation (6-12) for plumes generated without screens

In an attempt to develop a general relationship to describe $W_{e,s}$, a similar analysis can be carried out to that of Law [49] by plotting $W_{e,s}$, W_o and b (i.e. balcony breadth) in non-dimensional form. Figure 6.33 shows a plot of $W_{e,s}/W_o$ with respect to W_o/b.

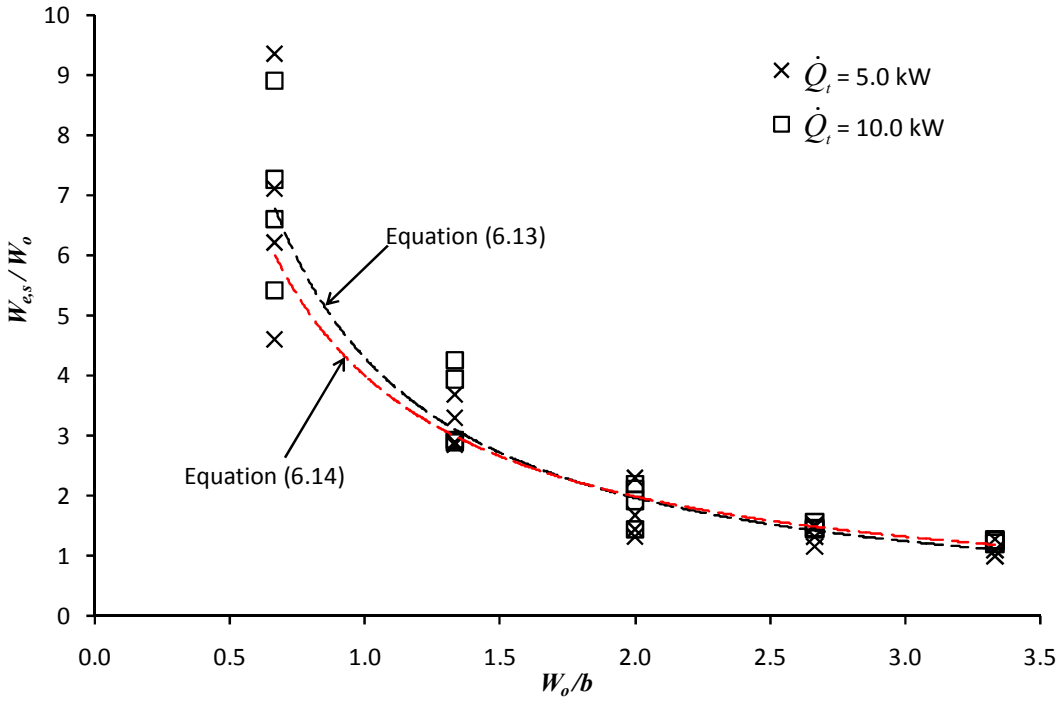

Figure 6.33: Plot of $W_{e,s}/W_o$ versus W_o/b

Figure 6.33 shows that the data collapse reasonable well to a power law relationship given by Equation (6-13), however, the scatter in the data increases significantly for $W_o/b < 2$ (i.e. for plumes from narrow openings). The relationship also appears to be independent of $\dot{Q}_t$ consistent with Equation (2-30) by Law, although only two values of $\dot{Q}_t$ were examined in this work.

$$\frac{W_{e,s}}{W_o} = 4.3\left(\frac{W_o}{b}\right)^{-1.1} \qquad \textbf{(6-13)}$$

As there is considerable scatter in the data for flows with $W_o/b < 2$ it seems reasonable and convenient to simplify Equation (6-13) to,

$$\frac{W_{e,s}}{W_o} \approx 4\left(\frac{W_o}{b}\right)^{-1} \qquad \textbf{(6-14)}$$

Lines representing Equations (6-13) and (6-14) are shown in Figure 6.33.

Equation (6-14) then becomes,

$$W_{e,s} \approx 4b \qquad \textbf{(6-15)}$$

Equation (6-15) provides a surprising result as it infers that $W_{e,s}$ is solely dependent on b and provides a constant value of $W_{e,s}$ for a specified b (for any W_o and $\dot{Q}_t$). This is possibly analogous to the constant value of W_s observed for each W_o and $\dot{Q}_t$ examined (see Table 6.3). However, Equation (6-15) should be treated with extreme caution as $W_{e,s}$ is dependent on a parameter (i.e. b) which was not varied in the experiments. Thus, at this stage there is little confidence that Equation (6-15) applies generally for a range of b and therefore it is currently not recommended for design purposes until further work is carried out.

It may be more appropriate to assess the performance of Equation (2-30) by Law to describe $W_{e,s}$ [but for use within Equation (6-12)], namely,

$$W_{e,s} = W_o + b$$

Although Equation (2-30) was determined from very few data points, it was empirically derived from flows with a variety of b and is currently used for design purposes. Figure 6.34 shows a comparison between a line representing Equation (2-30) and the data already shown in Figure 6.33.

Figure 6.34 shows that Equation (2-30) provides a reasonably good prediction of $W_{e,s}/W_o$ for $W_o/b \geq 2$. However, for $W_o/b < 2$, Equation (2-30) significantly under predicts the required $W_{e,s}/W_o$ [to be used in Equation (6-12)]. This is not surprising as Equation (2-30) was not developed from flows from narrow openings. Since plumes from narrow openings are complex and unstable in nature it may not be suitable to predict entrainment for these flows using a simple approximation and numerical modelling may be more appropriate.

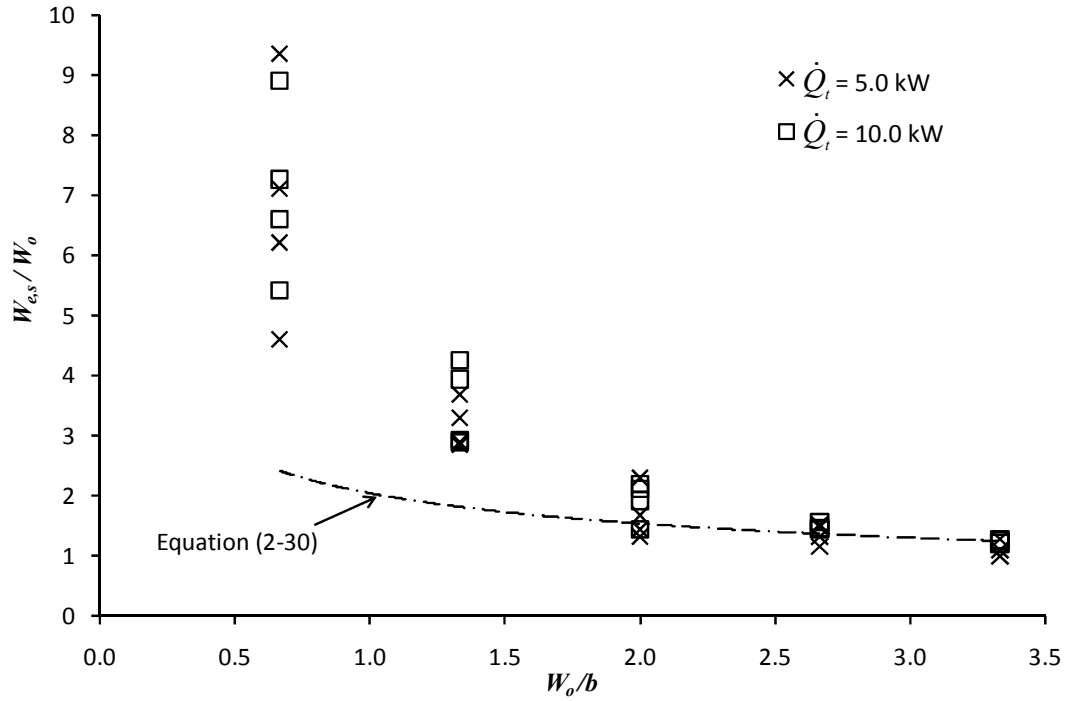

Figure 6.34: Plot of $W_{e,s}/W_o$ versus W_o/b and comparison with Equation (2-30)

6.4.2.1 A new design formula for the 3-D plume without channelling screens

As Equation (2-30) by Law provides a relationship to suitably describe $W_{e,s}$ for use within Equation (6-12) for flows where $W_o/b \geq 2$, the following formula is proposed as a simple approximation to predict entrainment for the 3-D balcony spill plume without channelling screens below the balcony.

$$\dot{m}_{p,3D,unchan} = 0.16\dot{Q}_c^{1/3}\left[(W_o + b)^{2/3} + 1.56 d_s^{2/3}\right] z_s + 1.34\dot{m}_s \qquad \textbf{(6-16)}$$

With the strict limit that,

$$\frac{W_o}{b} \geq 2 \qquad \textbf{(6-17)}$$

This is further supported in Figure 6.35 which shows a plot of the prediction of $\dot{m}_{p,3D}$ [using Equation (6-16)] versus the experiment.

It must be stressed that Equation (6-16) is an approximate solution to a complex smoke flow and should ideally be used in the early stages of design.

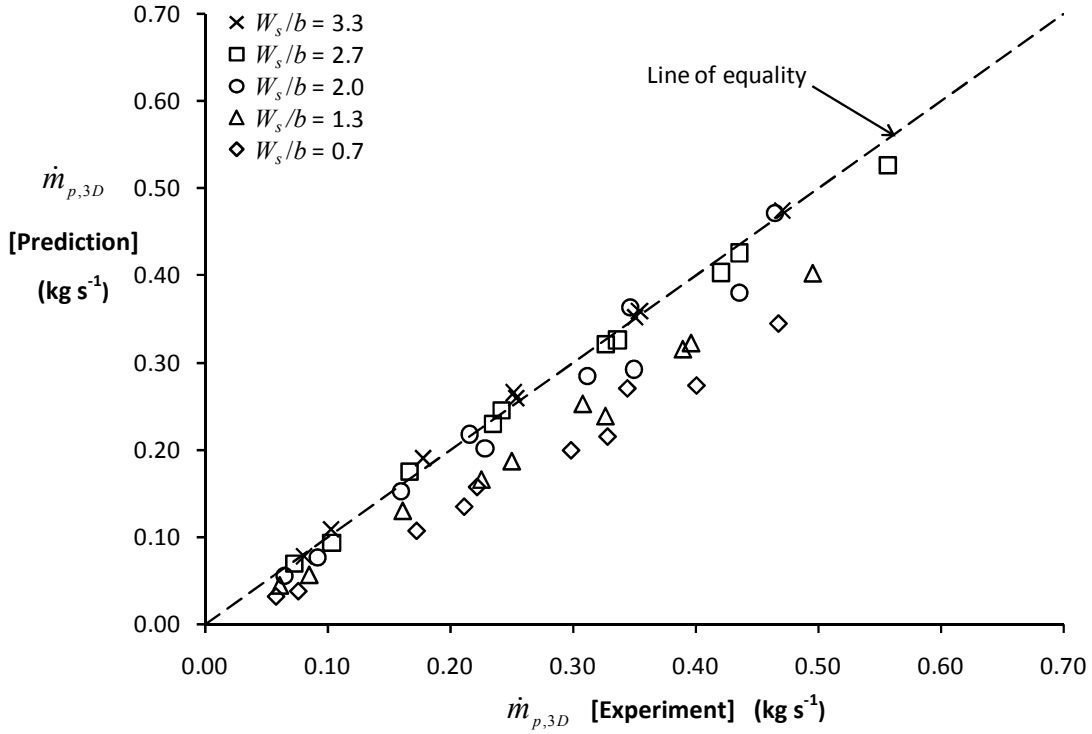

Figure 6.35: Prediction of $\dot{m}_{p,3D}$ using Equation (6-16) versus the experiment

Since the smoke flow behaviour of plumes generated without channelling screens is likely to be susceptible to factors such as internal air movement (particularly for stagnant smoke at the flow extremities) and local geometry effects (e.g. presence of downstands, upstands, etc) the entrainment analysis should ideally be supported by numerical modelling.

Numerical modelling is recommended to predict entrainment into plumes generated from unchannelled flows where $W_o/b < 2$ (at least until further experiments and analysis have been carried out) and Equation (6-16) should not be applied. An assessment of the performance of numerical modelling to predict plumes without channelling screens (using the experimental data from this study) is currently in progress as part of a further study [132].

6.5 Input parameters to the new design formulae

The new simplified design formulae proposed in this chapter require some of the following list of input parameters to achieve a result:

- The convective heat flow rate of gases below the spill edge, $\dot{Q}_c$
- The mass flow rate of gases below the spill edge, $\dot{m}_s$
- The depth of the gas layer flow below the spill edge, d_s
- The height of rise of the plume above the spill edge, z_s
- The lateral extent of the spill plume below the spill edge, W_s
- The width of the fire compartment opening, W_o
- The balcony breadth, b

The input parameters W_o and b are easily determined from the given geometry in question. W_s has the same value as W_o for flows with channelling screens in line with the fire compartment opening (assumed in this study). z_s is generally determined from the clear layer height required from standards or local regulations (see section 1.5.1).

$\dot{Q}_c$ is determined by assuming a suitable convective component of the gas flow (typically $\dot{Q}_c \approx 0.7\dot{Q}_t$ [13]) based on the type of fuel assumed in the design fire.

$\dot{m}_s$ is dependent upon the specific geometry upstream of the spill edge and may involve a single or many entrainment processes. If the flow below the spill edge is directly from a fire compartment opening (without any subsequent entrainment between the opening and the spill edge, i.e. $\dot{m}_s = \dot{m}_w$**)** then the methods given by CIBSE [Equation (5-5)] or Hansell [Equation (5-4)] can be used, although the analysis given in sections 5.1.5.2 and 5.2.5.2 suggests that Equation (5-5) (shown again below) may be preferential due to its relative simplicity. Hence,

$$\dot{m}_s = 0.09\dot{Q}_c^{1/3} W_s^{2/3} h_s$$

If there is additional entrainment between the fire compartment opening and the spill edge such as from a compartment opening below a downstand to a higher projecting balcony [i.e. $\dot{m}_s \neq \dot{m}_w$] then this can be accounted for using the methods described in section 2.2, such as that given by Harrison and Spearpoint [34] [Equation (2-11)] (shown again below) to predict $\dot{m}_s$. Hence,

$$\dot{m}_s = 0.89\left(\frac{h_o}{W_o}\right)^{-0.92}\left(\frac{h_b \dot{m}_w}{W_o}\right)$$

Where $\dot{m}_w$ can be determined from Equations (2-8) or (2-9).

d_s can be determined using the following equation given by Morgan *et al.* [12],

$$d_s = \frac{0.36}{C_d}\left[\frac{\dot{m}_s \overline{T}_s}{\overline{\theta}_s^{\,0.5} W_s T_1^{0.5}}\right]^{2/3} \qquad \textbf{(6-18)}$$

Morgan *et al.* recommend that C_d = 1.0 for flows with a flat ceiling at the spill edge and C_d = 0.65 if a deep downstand is present at the edge. Equation (6-18) requires properties of the average layer temperature below the spill edge which can be determined from $\dot{Q}_c$ and $\dot{m}_s$ [e.g. Equation (4-5)]. An alternative approximated version of Equation (6-18) is given by Hansell [59] [Equation (6-19)] which reduces the $\overline{T}_s / \overline{\theta}_s^{\,0.5}$ term to a 'constant' value of approximately 39 for a wide range of gas temperatures likely to be found in design (i.e. 65 K < $\overline{\theta}_s$ < 1200 K) and also by assuming T_{amb} = 293 K Equation (6-18) reduces to,

$$d_s \approx \frac{1}{C_d}\left[\frac{\dot{m}_s}{2W_s}\right]^{2/3} \qquad \textbf{(6-19)}$$

The performance of Equations (6-18) and (6-19) to predict d_s can be assessed against the experimental results from this study (i.e. $d_{v,s}$) for flows channelled by screens below a balcony with a flat ceiling (i.e. assuming $C_d = 1.0$) as shown in Figure 6.36.

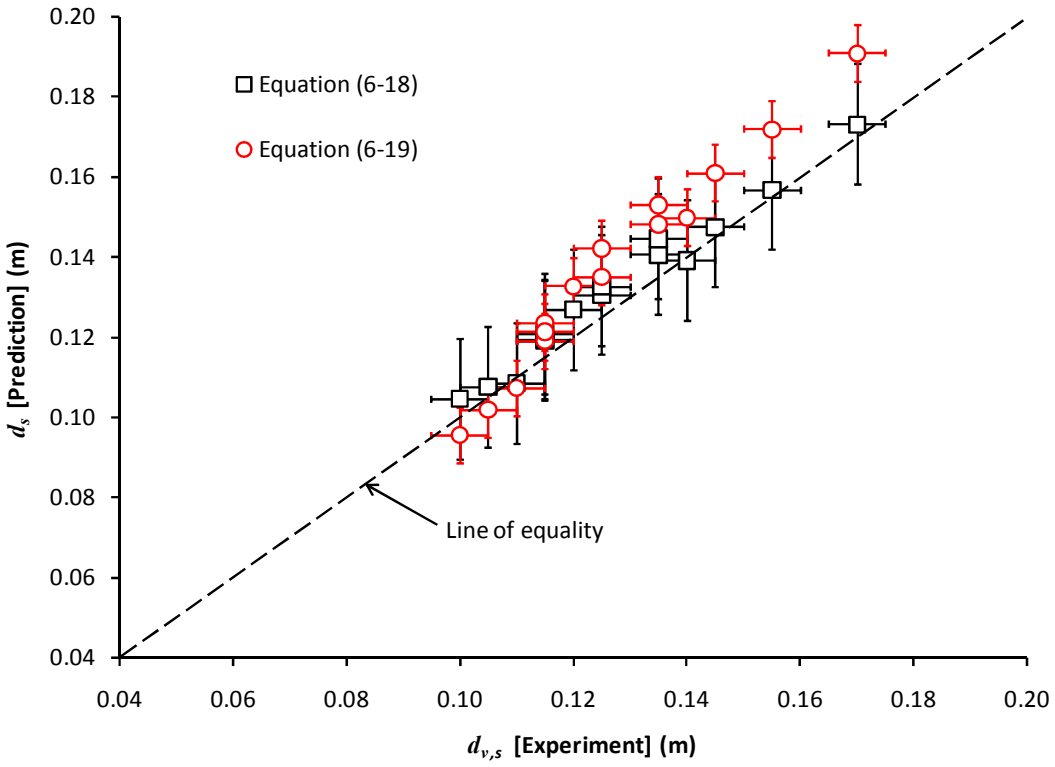

Figure 6.36: Comparison of the prediction of d_s with experiment

Figure 6.36 shows that the use of Equation (6-18) by Morgan *et al.* provides an excellent prediction of d_s and is generally equal to the experiment within one standard error. Equation (6-19) by Hansell provides a reasonably good prediction of the experiment and is generally equal (within one standard error) to the predictions made using Equation (6-18). However, Equation (6-19) tends to provide a slightly conservative prediction (by approximately 10%) for deeper layer flows generated from narrow openings. Considering the relative simplicity of Equation (6-19) and that it provides either an appropriate or slightly conservative prediction, this equation appears to be suitable for design purposes. If a more accurate prediction of d_s is required then Equation (6-18) by Morgan *et al.* should be used.

6.6 Comparison with existing simplified design formulae

The prediction of $\dot{m}_p$ using existing simplified design formulae can be compared with the experimental results to assess the performance of these methods. The experimental results have already been compared with existing formulae as part of the analysis for the 2-D plume and therefore this is not repeated again here. The following analysis presents a comparison for the 3-D plume with channelling screens as the very limited simple guidance for plumes without screens has been assessed above.

The predictions using the formulae given by CIBSE/BS 7974 [38] [Equation (2-32)], NFPA 92B [2] [Equation (2-61)] and Harrison and Spearpoint [40] [Equation (2-50)] are compared with the experiment. The CIBSE and NFPA 92B formulae were chosen as these are given in current design guidance that is commonly used worldwide and the Harrison and Spearpoint formula was chosen as it is based on experiments that effectively form a subset of this work. The relevant NFPA 92B formula was chosen for the range of z_s examined in the experiment (z_s < 1.5 m, i.e. z_s < 15 m full scale equivalent) in a form dependent on $\dot{Q}_c$ to enable easy comparison with the other formulae (which are dependent on $\dot{Q}_c$).

Figure 6.37 shows a comparison between the experiment results and the prediction for the decoupled entrainment above the spill edge in a form consistent with the dimensional analysis by Thomas *et al.* [39]. The decoupled entrainment above the spill edge was chosen to simplify the comparison as this is generally the most significant entrainment region that needs to be considered in design, and as the Harrison and Spearpoint method would yield five, slightly different predictions (of equal slope) for each W_s examined if entrainment below the height of the spill edge is included (as it dependent on $\dot{m}_s$).

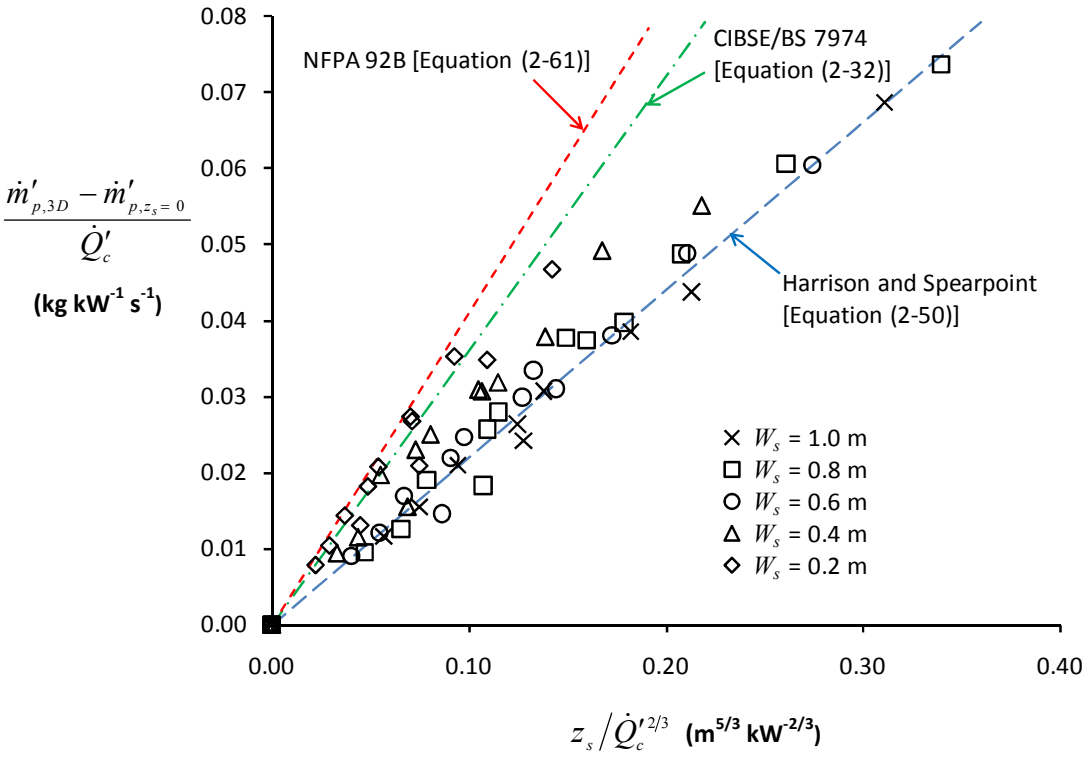

Figure 6.37: Comparison of experiment with prediction of $\dot{m}_p$ using existing formulae

Figure 6.37 shows that the NFPA 92B formula provides the highest prediction of entrainment and provides a good prediction of the experiment for plumes generated from a narrow opening (i.e. W_s = 0.2 m), however, it provides an increasingly conservative prediction as W_s increases. The NFPA 92B formula provides a prediction that is approximately 80% higher than the experiment for plumes generated from the widest flow examined (i.e. W_s = 1.0 m).

As the design of smoke management systems involving the spill plume often considers plumes generated from wide openings as a reasonable worst case, it appears that the NFPA 92B formula will provide a particularly conservative prediction of entrainment for most cases. A similar prediction of entrainment is given by the CIBSE/BS 7974 formula, although it is approximately 15% lower than that of NFPA 92B.

The Harrison and Spearpoint formula predicts a much lower rate of entrainment and provides a good prediction for plumes generated from intermediate to wide openings (i.e. W_s = 0.6 to 1.0 m), however, it under predicts entrainment for plumes from narrow openings. The Harrison and Spearpoint formula will generally provide a more cost effective smoke management solution for plumes from wide openings compared to the NFPA 92B and CIBSE/BS 7974 formulae, however, it should not be used to predict entrainment for plumes from narrow openings (i.e. W_s < 6 m full scale).

The above analysis confirms the view (given in section 6.3.3.1) that none of the existing simplified design formulae apply generally for a range of W_s and are specific to the conditions studied in the original experiments from which they were derived. This analysis gives further support for the use of the new design formulae proposed in this work as they have been derived generally for plumes for a range of W_s.

A comparison is not made with the raw data obtained from the full scale experiments carried out by NRC due to the considerable scatter in the calculated entrainment coefficients shown in section 2.4.7, the lack of robust data describing the layer flow below the spill edge, uncertainties in the measurements (given by Lougheed et al [71]) in terms of the clear layer height, the mass flow rate of gases and the very limited height of rise over which the entrainment coefficients were determined.

6.7 Comparison with existing analytical methods

6.7.1 The curved plume method

A summary of the curved plume method is given in section 2.3.4.2 and is described in more detail by Kumar *et al.* [41]. It applies specifically to the 2-D balcony spill plume.

Kumar *et al*. [41] provides predictions of entrainment using the curved plume method for the relevant experiments carried out in this work. As some of the predictions were not made at exactly the same heights of rise as the experiment, the predictions and experimental results are shown in Figure 6.38 as two separate data sets plotted according to the dimensional analysis by Thomas *et al*. [39].

Figure 6.38 shows that the predictions using the curved plume method are generally consistent with the experimental results for the range of W_s examined and therefore this method provides an excellent prediction of entrainment for the 2-D plume. This method seems suitable for design purposes for the rare occasions when the design scenario involves a 2-D plume, although it is a more complex method compared to simplified design formulae.

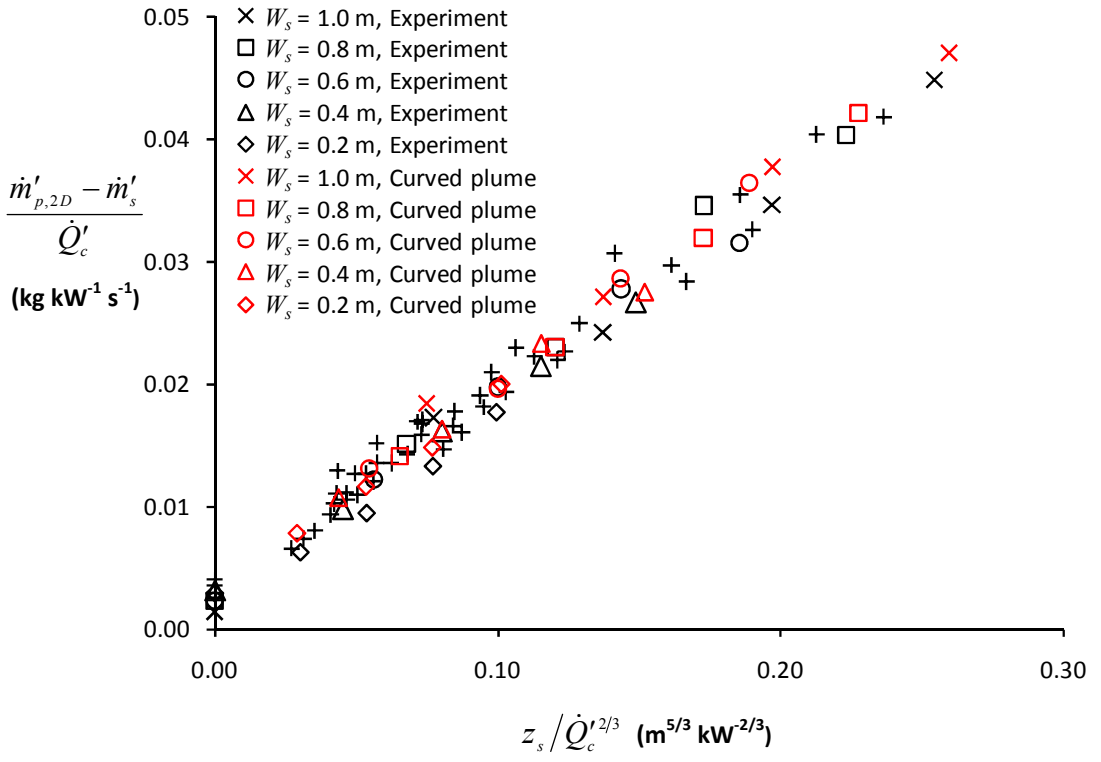

Figure 6.38: Comparison of experiment with prediction using the curved plume method

6.7.2 The BRE spill plume method

The BRE spill plume method (see section 2.3.4.1) can provide predictions of both 2-D and 3-D balcony spill plumes which are channelled by screens below the balcony. Figure 6.39 shows a comparison of the predictions of $\dot{m}_p$ against the experiment for the 2-D and 3-D plumes examined in this work, assuming α = 0.16, α' = 1.1 and not applying the effective layer depth correction. The predictions were determined using the relevant program (i.e. CP 4875) from an in-house suite of programs known as ASKHPM [133] which was developed at The Fire Research Station, BRE.

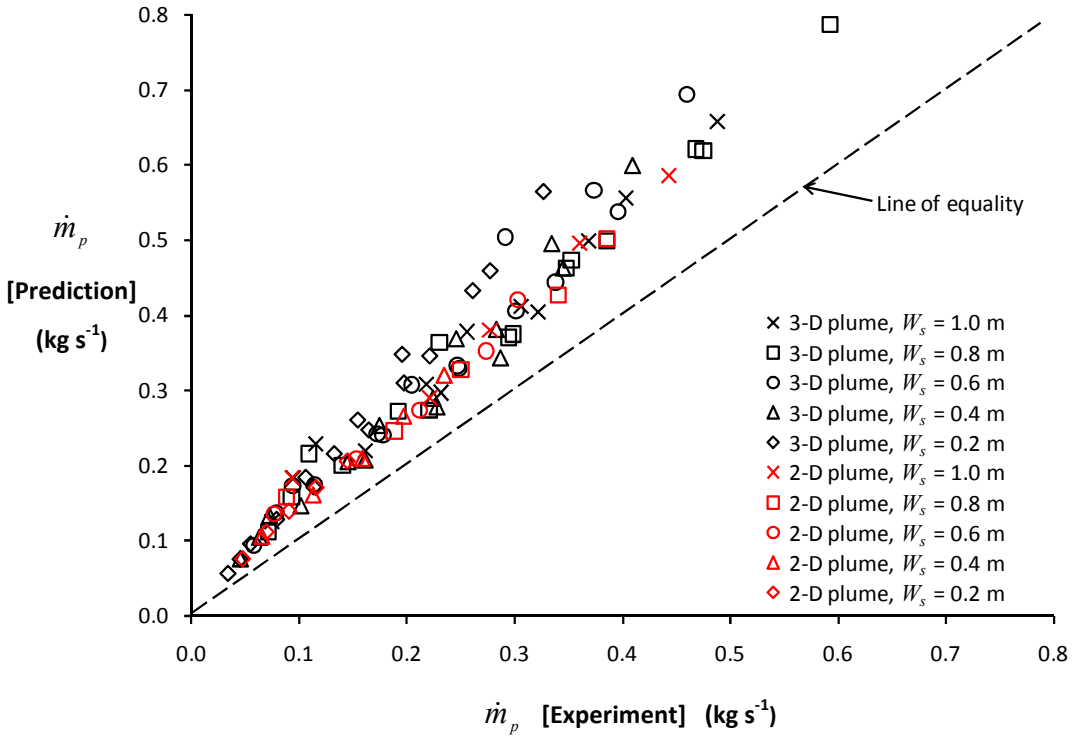

Figure 6.39: Prediction of $\dot{m}_p$ versus experiment (α = 0.16, α' = 1.1, effective layer depth correction <u>not</u> applied)

Figure 6.39 shows that the BRE method over predicts $\dot{m}_p$ by approximately 30 to 40% for the 2-D plume and by approximately 20 to 70% for the 3-D plume depending upon the conditions studied. This behaviour is similar to that found in the experiments by Morgan and Marshall [81] which led to the development of the effective layer depth correction to adjust the predictions to match the experimental results. However, the experimental arrangement in this present work was specifically designed to allow fresh air to enter the rising plume directly below the smoke layer in the collecting hood to prevent significant warming of the air below the layer base (i.e. see temperature profile in Figure 6.1). Therefore it is possible that formation of an effective layer below the visual layer is more apparent than real. Nevertheless, the predictions using the BRE method still require some form of adjustment to match the experimental results.

The criterion for when the effective layer depth correction should be applied (i.e. when the smoke layer depth is less than two-thirds of the characteristic width of the smoke reservoir) suggests that only those experiments which examined $z_s > 0.7$ m should require the use of this correction to match the experiment. However, Figure 6.39 suggests that all of the predictions need to be adjusted. Therefore, Figure 6.40 shows the predictions of $\dot{m}_p$ by applying the effective layer depth correction for all the experiments examined and assuming $\alpha = 0.16$ and $\alpha' = 1.1$.

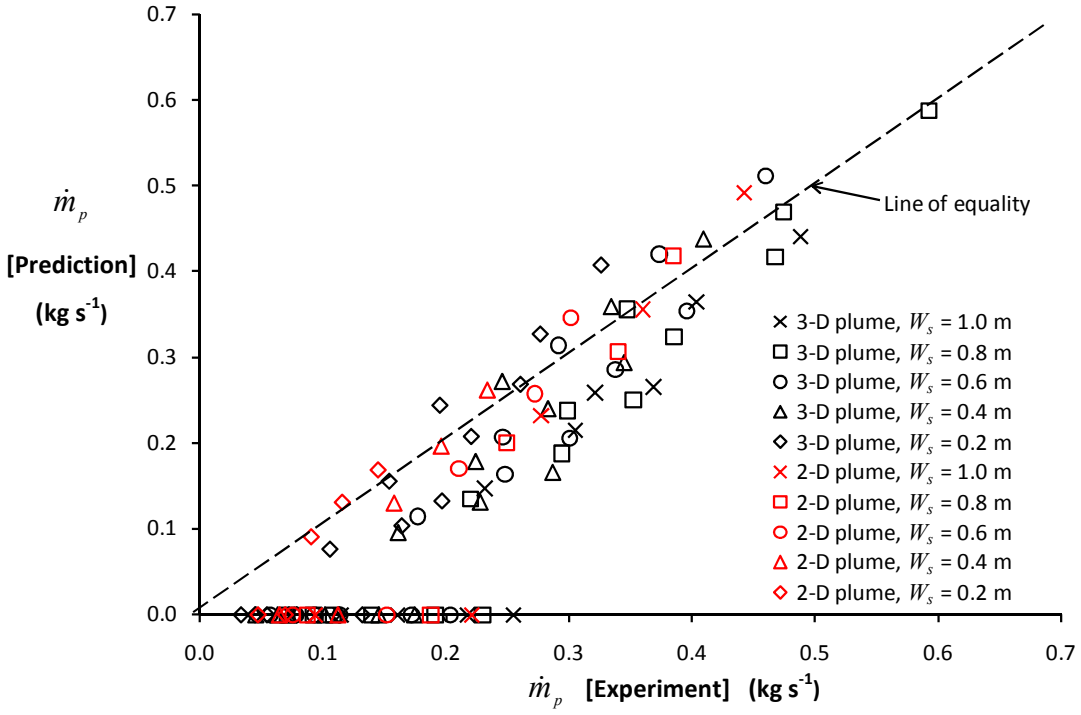

Figure 6.40: Prediction of $\dot{m}_p$ versus experiment ($\alpha = 0.16$, $\alpha' = 1.1$, effective layer depth correction applied)

When the effective layer depth correction was applied to those experiments with relatively deep layers in the collecting hood (i.e. with $z_s \leq 0.3$ m), this gave rise to effective layers that were below the spill edge and therefore a prediction of $\dot{m}_p$ could not be achieved (as shown by the data points on the horizontal axis in Figure 6.40). For those experiments where a prediction was achieved, Figure 6.40 shows that there is good agreement with the experiment for some predictions.

However, the majority tend to under predict the experiment (by as much as 40%) when using the effective layer depth correction. This suggests that this correction may not provide a reliable result for a wide range of possible plume scenarios and should be used with caution. It is possible that the effective layer depth correction accounts for differences in measured entrainment between previous studies, but was attributed to differences in the geometry of the smoke reservoir rather than the nature of the plume in terms of W_s and d_s (as identified in this work).

The above analysis suggests that it may be more appropriate to correct the predictions by modifying the empirical entrainment coefficients (i.e. α and α') and not applying the effective layer depth correction at all. Work by Poreh et al [31] and Harrison and Spearpoint [40] suggest a more appropriate value of α of 0.11 based on recent experiments of 2-D and 3-D balcony spill plumes. Therefore, Figure 6.41 shows the predictions of $\dot{m}_p$ assuming $\alpha = 0.11$ and $\alpha' = 1.1$ and not applying the effective layer depth correction.

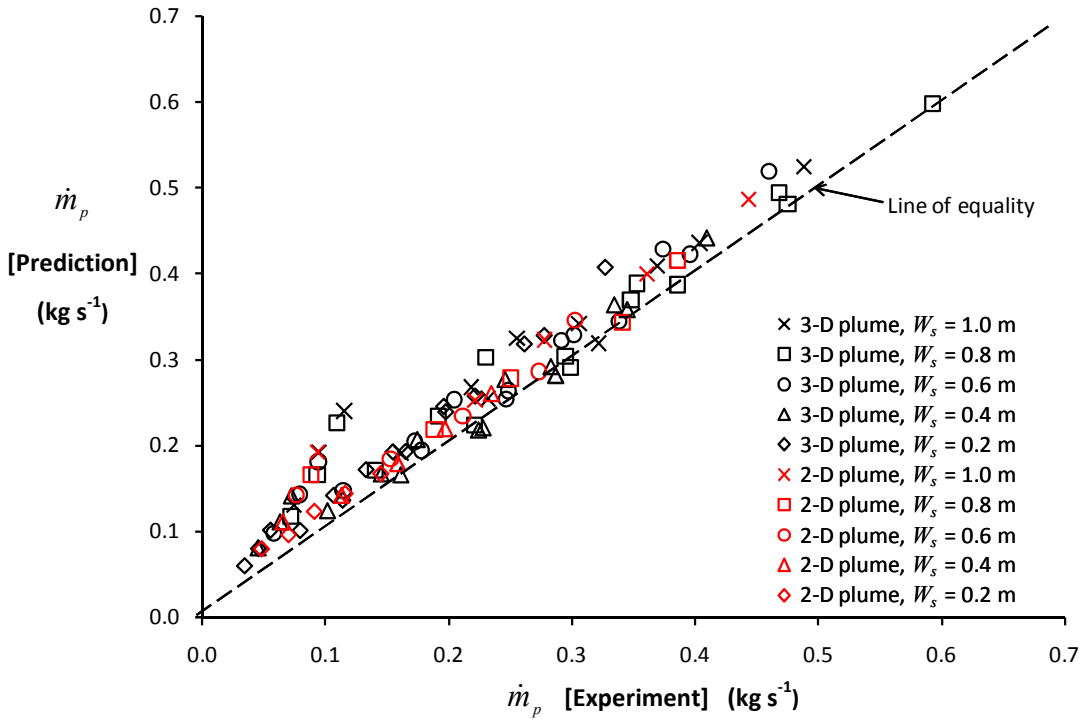

Figure 6.41: Prediction of $\dot{m}_p$ versus experiment ($\alpha = 0.11$, $\alpha' = 1.1$, effective layer depth correction <u>not</u> applied)

Figure 6.41 shows that there is much better agreement between the predictions and the experiment when α is assumed to be 0.11. The majority of predictions are generally conservative by approximately 10 to 20%, however, for small values of $\dot{m}_p$ obtained at relatively low height of rise the predictions are conservative by as much as 80%.

At low heights of rise the effect of the assumed value of α' (to account for entrainment in the rotation region of the plume) is more significant in overall plume entrainment process. The recommended value of α' (i.e. 1.1) is recognised to be high as the BRE method treats all anomalous entrainment above the spill edge (perhaps due inadequacies in the simplistic term describing entrainment into the free ends of the plume) as if it occurred in the rotation region.

However, the nature of the experiments in this work allows a value of α' to be explicitly determined from the difference between the mass flow rate in the plume at $z_s = 0$ and the mass flow rate of gases below the spill edge, which gives the decoupled entrainment in the rotation region of the plume (i.e. $\dot{m}_{rot} = \dot{m}_{p,z_s=0} - \dot{m}_s$). This has not been achieved in any previous experimental work. The value of α' was empirically determined to be 0.28 ± 0.02 for the decoupled flow in the rotation region for the range of plumes examined in this work. This provides a much lower, but more sensible value of α' (i.e. less than unity) compared to the current value of 1.1.

Furthermore, as this work has developed an explicit empirical expression to describe the entrainment into the free ends of the plume [i.e. Equation (6-11)], this can be used to better deal with entrainment above the spill edge, instead of the simplified assumption in the BRE method of a plume with rectangular ends, which has never been validated experimentally. Therefore, a modified version of the BRE method is proposed (named "BRE [UC] method" for the purposes of this thesis) as summarised in Table 6.5.

Entrainment coefficient/correction	BRE method (current)	BRE [UC] method (proposed)
α	0.16	0.11
α'	1.1	0.28
End entrainment	Rectangular end relationship [12]	Equation (6 -11)
Other	Effective layer depth correction	No correction applies

Table 6.5: Summary of current and proposed versions of the BRE spill plume method

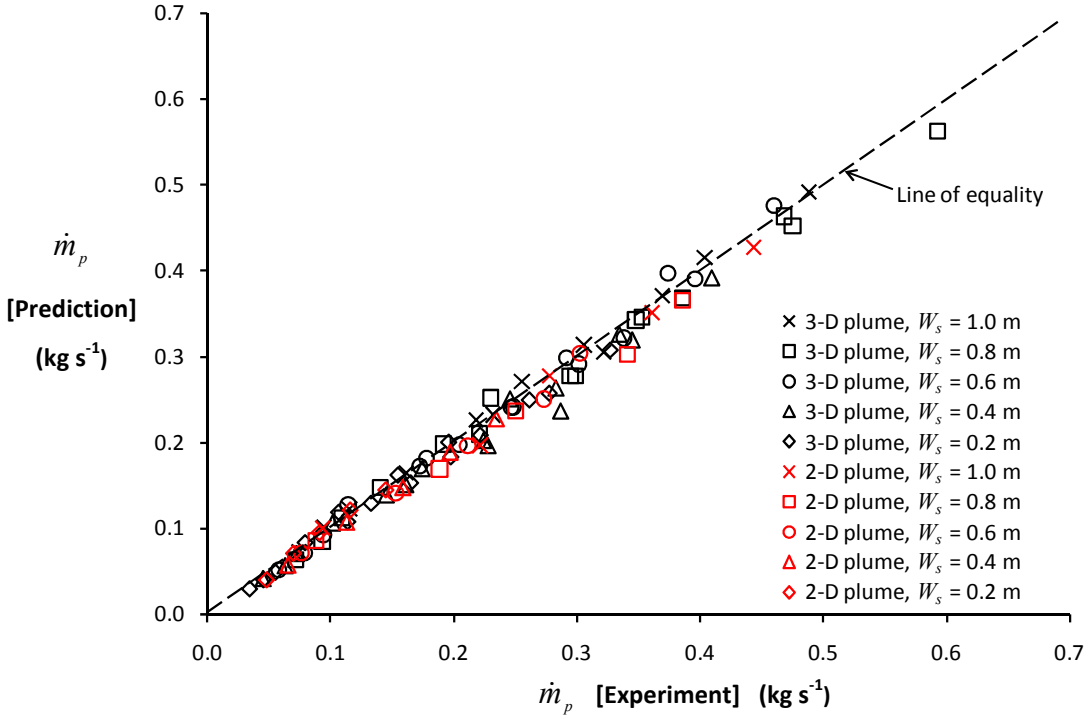

Figure 6.42: Prediction of $\dot{m}_p$ versus experiment (α = 0.11, α' = 0.28, effective layer depth correction <u>not</u> applied)

Figure 6.42 shows that the proposed modifications to the BRE spill plume method (i.e. BRE [UC] method) provides an excellent prediction of $\dot{m}_p$ for both 2-D and 3-D balcony spill plumes for the range of conditions examined in the experiments. Therefore, these modifications are proposed to provide an improved analytical method for the balcony spill plume.

6.8 The virtual line source

The majority of existing simplified spill plume formulae have been developed by assuming that the plume is generated from a virtual line source of zero width located below the spill edge [2,31,36,40,49,84]. The location of this virtual source has been a matter of much debate and uncertainty. Although a virtual source was not assumed in the development of the new simplified design formulae proposed in this work, the experiments provide data to determine a simple, general expression to describe the location of this source.

The location of the virtual source is dependent upon many factors such as the size of the fire, the fire compartment geometry and the geometry upstream of the spill edge (e.g. presence of a downstand) [84]. A virtual line source (i.e. z_0) can be used as a modifier to the height of rise of the plume (i.e. z_s) to describe the total amount of entrainment below the height of the spill edge. It is commonly described in a form consistent with the Lee and Emmons line plume model given by Equation (2-20) such that,

$$\dot{m}_p = C\dot{Q}_c^{1/3} W_s^{2/3} \left(z_s + z_0 \right) \qquad \textbf{(6-20)}$$

The importance of specifying an appropriate location of the virtual source is dependent upon the design scenario in question. For those scenarios with a spill plume with a high height of rise, the entrainment below the height of the spill edge is relatively insignificant in the overall entrainment process and uncertainties in the location of the source are not so important (see Figure 6.43a). However, for plumes with a low height of rise the total amount of entrainment below the edge is significant in the overall entrainment process and specifying an appropriate location of the source is important design (see Figure 6.43b).

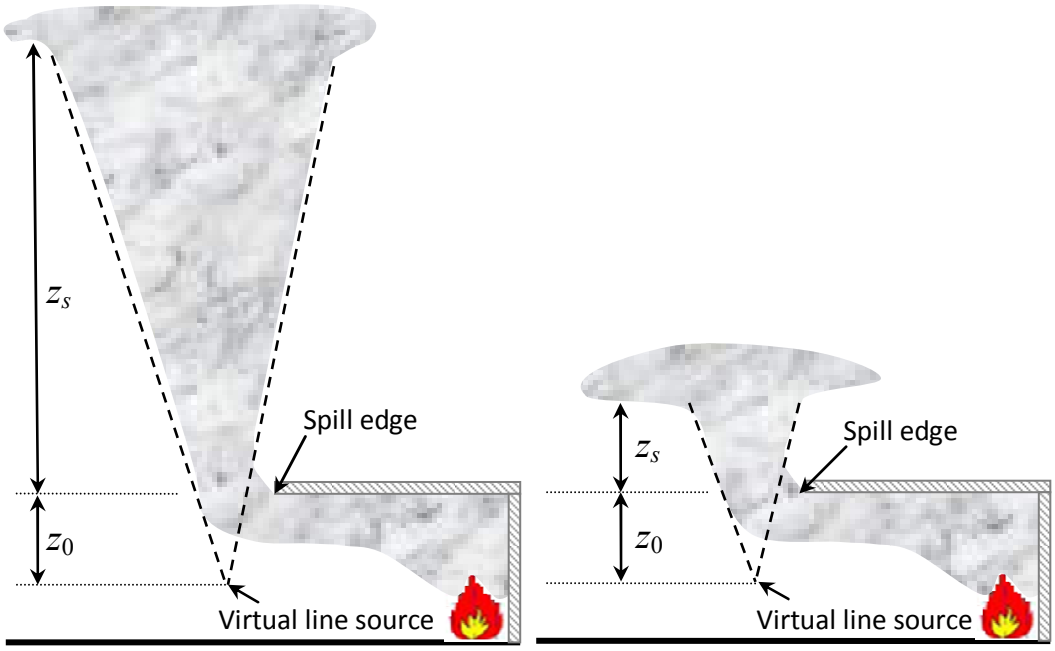

Figure 6.43: Spill plumes assuming a virtual line source

A simple expression to describe the location of the virtual source was first determined empirically by Law [36] who expressed z_0 as a fraction of the height of the spill edge above the fire, h_s (or more specifically the height of the balcony, h_b). Law analysed the experimental data by Morgan and Marshall [35,81] and estimated that z_0 varied between $0.15h_b$ and $0.67h_b$ (see section 2.3.2.2). Thomas [84] analysed the same data (see section 2.3.2.3) and concluded that z_0 varied between $0.32h_b$ and $0.66h_b$ depending on whether temperature or mass flow rate measurements were used. Thomas states that "the values of the virtual source from different measurements are not at all consistent". The most commonly used existing simplified formulae (e.g. given by CIBSE/BS 7974 [Equation (2-32)] and NFPA 92B [Equation (2-61)]) assume $z_0 = 0.25h_b$.

This approach does not relate z_0 to a parameter that directly relates to the fire or the flow below the spill edge. It provides a fixed value of z_0 for a specified h_s (or h_b) for any design fire size or the width of the fire compartment opening. Thus, the empirically determined values of z_0 based on h_s are only likely to apply for the range of conditions examined in the original experiments and may not apply generally.

A further analysis by Thomas *et al.* [39] suggest that it more appropriate to relate z_0 to the depth of the layer flow below the spill edge (i.e. d_s) as "for small values of d_s/h_s (or d_s/h_b) z_0 is expected from dimensional grounds, to be related primarily to d_s". Thomas then states that "when d_s/h_s is large, the layer interacts with the inflow and d_s needs to be expressed as a fraction of h_s (or h_b)". Therefore, it is generally recognised that it is more appropriate to express z_0 in terms of d_s as the ratio of d_s/h_s is likely to be small (i.e. less than unity) in smoke management design unless the design involves post–flashover fires or plumes generated from very narrow compartment openings.

Poreh *et al.* [31] provide an explicit expression to describe z_0 based on the characteristics of the flow below the spill edge as given by Equation (2-37) which is shown again below,

$$z_0 = d_s + \frac{\dot{m}_s}{C\dot{Q}_c^{1/3} W_s^{2/3}}$$

Kumar et al [41] have reduced Equation (2-37) in a form given that is dependent upon d_s and the gas density, by using the experimental data from Marshall and Harrison [48] which is given by,

$$\frac{z_0}{d_s} = 1 + 2.6\frac{\overline{\rho}_s}{\rho_1} \qquad \textbf{(6-21)}$$

If the experimental results from this work are considered, the location of z_0 can first be determined by performing an analysis similar to that carried out by Law [36] by plotting the data according to Equation (6-20) and plotting $\dot{m}_p \big/ \dot{Q}_c^{1/3} W_s^{2/3}$ against z_s. The intercept on the horizontal axis represents the absolute value of z_0 for the particular experiment in question, as shown in Figure 6.44 for flows with W_s = 1.0 m and $\dot{Q}_t$ = 10 kW for both the 2-D and 3-D spill plume.

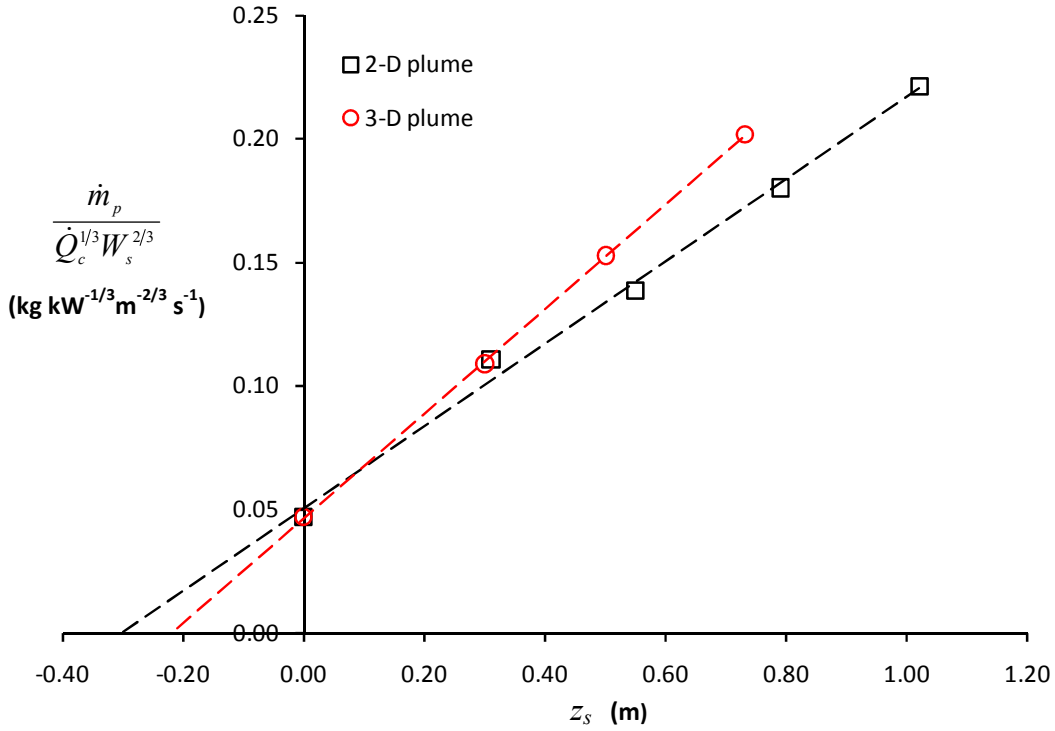

Figure 6.44: Plot of $\dot{m}_p / \dot{Q}_c^{1/3} W_s^{2/3}$ against z_s (W_s = 1.0 m, $\dot{Q}_t$ = 10 kW)

Figure 6.44 shows that for plumes which subsequently become either 2-D or 3-D above the edge, the absolute values of z_0 (i.e. from the intercept on the horizontal axis) are different with z_0 being closer to the spill edge for the 3-D plume (z_0 = 0.22 m) than for the 2-D plume (z_0 = 0.30 m). This is because z_0 was determined using data mainly obtained above the spill edge, and for the 3-D plume includes additional entrainment into the free ends, in addition to the lateral extent of the plume broadening with respect to the height above the edge. This was not the case for the 2-D plume where there was no additional entrainment into the ends and the lateral extent of the plume remained constant above the edge. The difference between the locations of z_0 using this approach is likely to be dependent on W_s as the contribution of end entrainment changes above the spill edge (similar to the analysis describe in section 6.3.3). This is demonstrated in Figure 6.45 which shows a similar plot for both the 2-D and 3-D plume with W_s = 0.2 m and $\dot{Q}_t$ = 10 kW. Figure 6.45 shows a greater difference between the values of z_0 (i.e. z_0 = 0.18 m for the 3-D plume, z_0 = 0.45 m for the 2-D plume) for plumes from a narrow opening due to the reasons described above.

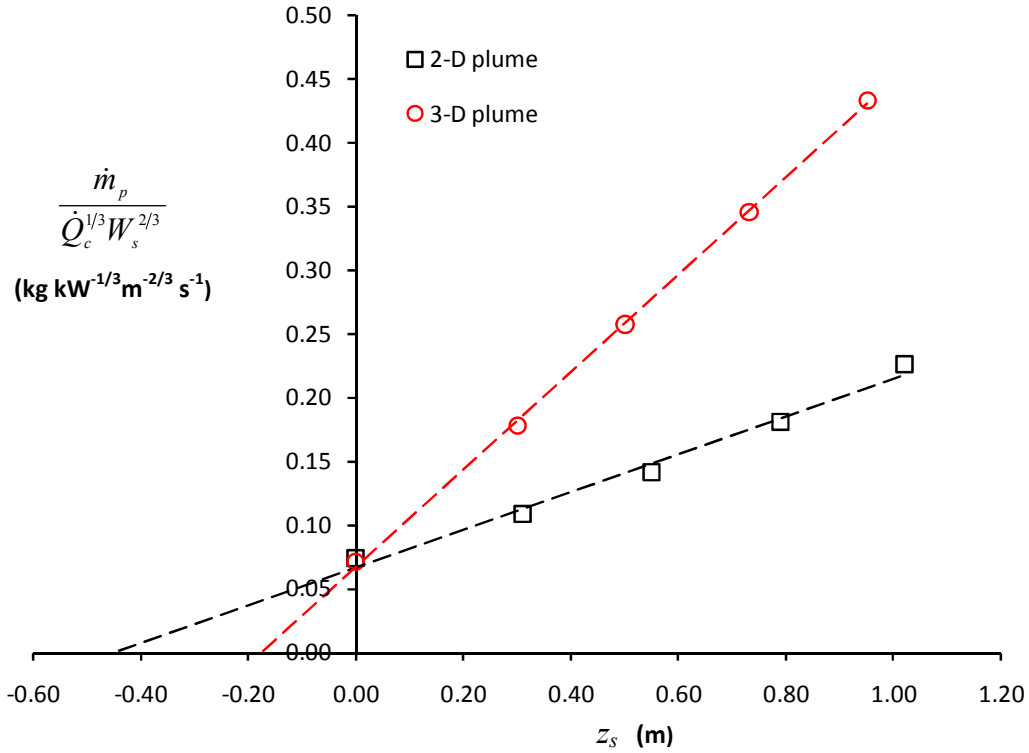

Figure 6.45: Plot of $\dot{m}_p / \dot{Q}_c^{1/3} W_s^{2/3}$ against z_s (W_s = 0.2 m, $\dot{Q}_t$ = 10 kW)

Therefore, it appears that correlating the data according to the Equation (6-20) to determine z_0 may not be entirely appropriate using data from 3-D plumes. Hence, the locations of z_0 using this approach have only been determined for 2-D plumes and are given in Table 6.6.

Experiment	W_s (m)	$\dot{Q}_t$ (kW)	z_0 (m)	z_0/d_s	z_0/h_s
E93,E163,E253,E278 and E292	1.0	10.0	0.30	2.6	0.61
E99,E169,E259,E279 and E291	0.8	10.0	0.31	2.7	0.61
E105,E175,E265,E280 and E290	0.6	10.0	0.36	3.0	0.72
E111,E181,E271,E281 and E289	0.4	10.0	0.38	3.1	0.77
E117,E187,E277,E282 and E288	0.2	10.0	0.45	2.9	0.91

Table 6.6: Values of z_0 determined using Equation (6-20) for the 2-D spill plume

Table 6.6 shows that the absolute value of z_0 increases as W_s decreases. When expressed as a factor of d_s, z_0 varies between $2.6d_s$ and $3.1d_s$. If expressed in terms of h_s (or h_b) z_0 increases as W_s decreases from approximately $0.6h_s$ to $0.9h_s$ for the conditions studied. This demonstrates that z_0 does not remain constant for a variety of W_s when expressed in this form and is greater than the $0.25h_b$ currently recommended by CIBSE/BS 7974 and NFPA 92B. Therefore, it is possible that these formulae may underestimate entrainment at low heights of rise of plume for flows from narrow openings. Although this is likely to be a rare design scenario, Figure 6.46 shows that the CIBSE/BS 7974 and NFPA 92B formulae do tend to under predict entrainment for plumes generated from a narrow opening (i.e. W_s = 0.2 m) for z_s < 0.3 m when plotted according to Equation (6-20). However, Figure 6.47 shows that they do not under predict entrainment for plumes from a wide opening (i.e. W_s = 1.0 m) for z_s < 0.3 m. Therefore, these formulae should be treated with caution for design scenarios with very low heights of rise of plume generated from narrow openings even though they provide a conservative or appropriate prediction for z_s well above the spill edge.

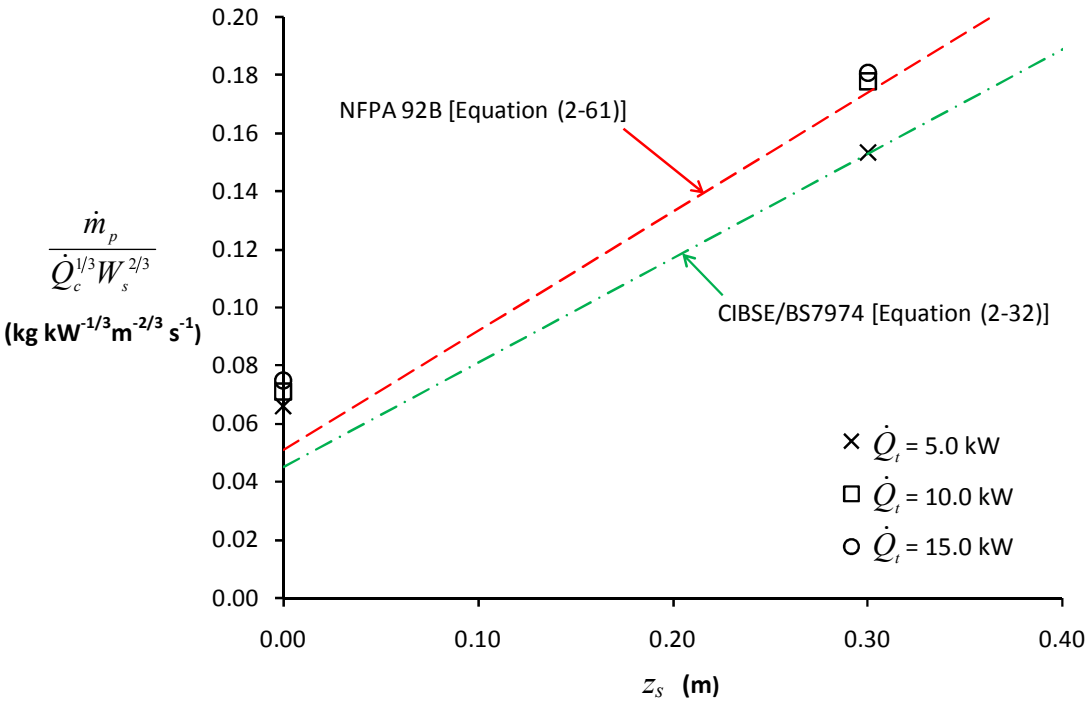

Figure 6.46: Plot of $\dot{m}_p / \dot{Q}_c^{1/3} W_s^{2/3}$ against z_s and comparison with CIBSE/BS 7974 and NFPA 92B (W_s = 0.2 m)

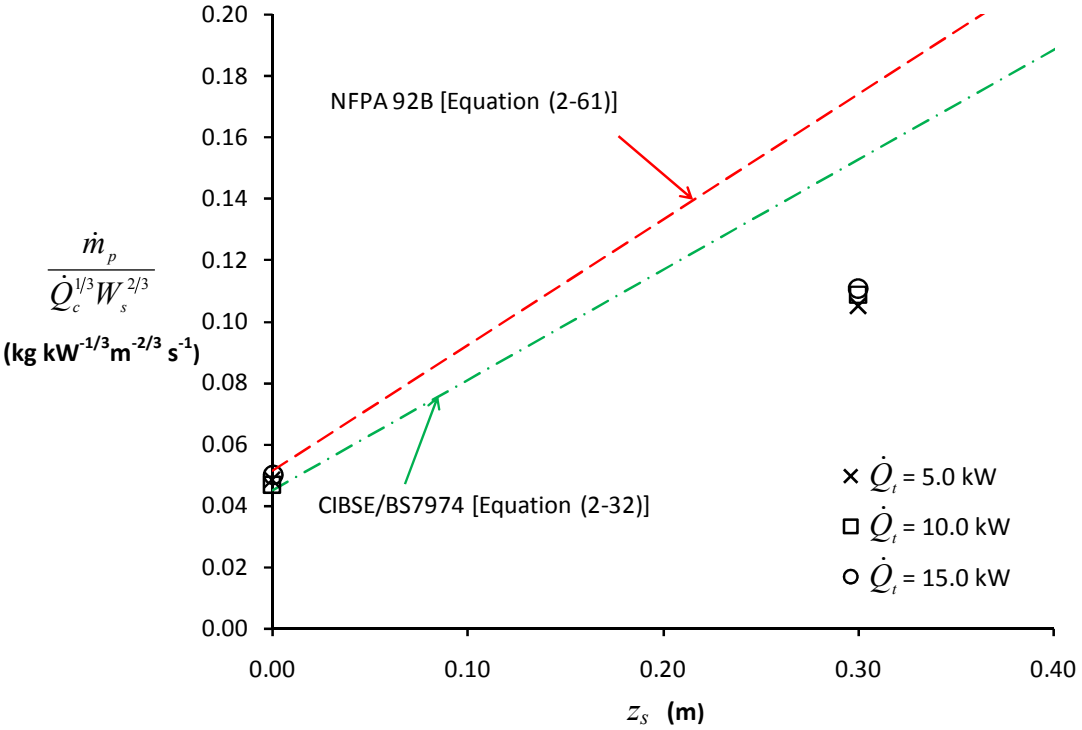

Figure 6.47: Plot of $\dot{m}_p / \dot{Q}_c^{1/3} W_s^{2/3}$ against z_s and comparison with CIBSE/BS 7974 and NFPA 92B (W_s = 1.0 m)

It may be more appropriate to determine z_0 by using the explicit term given by Poreh *et al.*[31] [Equation (2-37)] from the measured characteristics of the flow below the spill edge without resorting to using data obtained above the edge. The location of the virtual source can then be described in terms of d_s as suggested by Thomas *et al.* [39].

In an attempt to develop a simple general expression to describe the location of z_0, Figure 6.48 shows a plot in non-dimensional form of z_0/d_s versus ρ_s/ρ_1 using the experimental data [i.e. in a similar form to Equation (6-21)], where z_0 was determined using Equation (2-37) and assumed that C = 0.16 as recommended by Poreh *et al.*

Figure 6.48 shows that $z_0/d_s \approx 3$ for the range of ρ_s/ρ_1 examined, however, there is a slight tendency for z_0/d_s to decrease a ρ_s/ρ_1 decreases. This is most likely due to the upward source momentum being higher for gas flows with high temperatures, thus causing z_0 to be a little closer to the spill edge, although this effect is probably insignificant for design purposes.

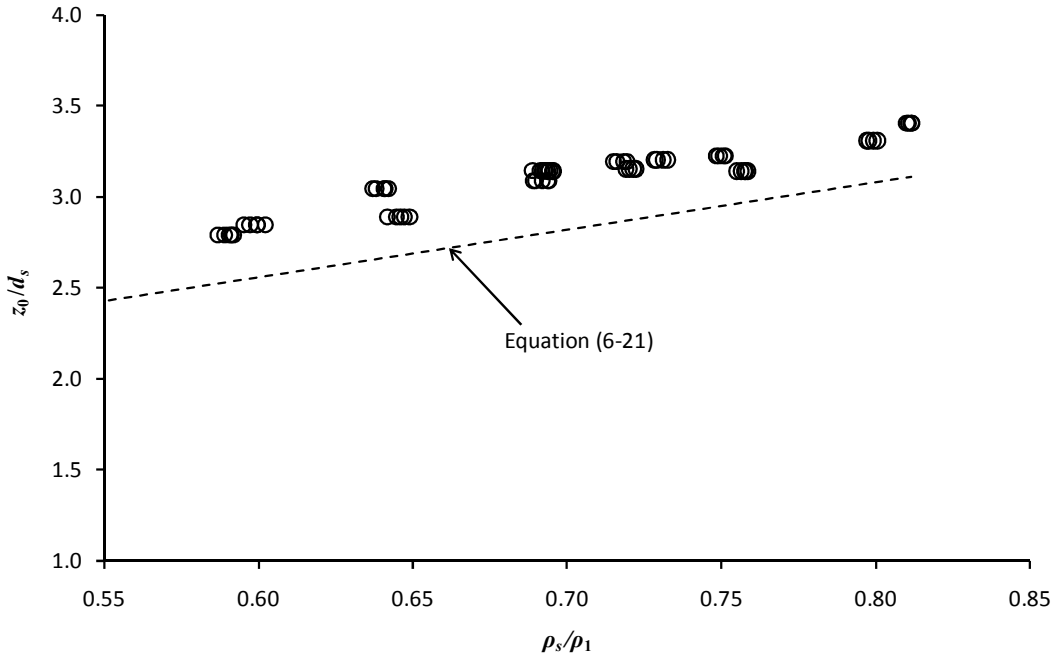

Figure 6.48: Plot of z_0/d_s versus ρ_s/ρ_1

Figure 6.48 shows that the data from this study provides values of z_0/d_s which are slightly higher than that given by Equation (6-21) which was partially derived using data from Marshall and Harrison [48]. Therefore, to aid the analysis, Figure 6.49 shows a comparison of the data with previous work by Marshall and Harrison [48], Hansell *et al.* [32] and Harrison and Spearpoint [40]. Figure 6.49 shows that the data from Hansell *et al.* and Harrison and Spearpoint are broadly consistent with the data from this study. The data from Marshall and Harrison gives slightly lower values of z_0/d_s for reasons that are not clear, and unsurprisingly provide a better fit with Equation (6-21).

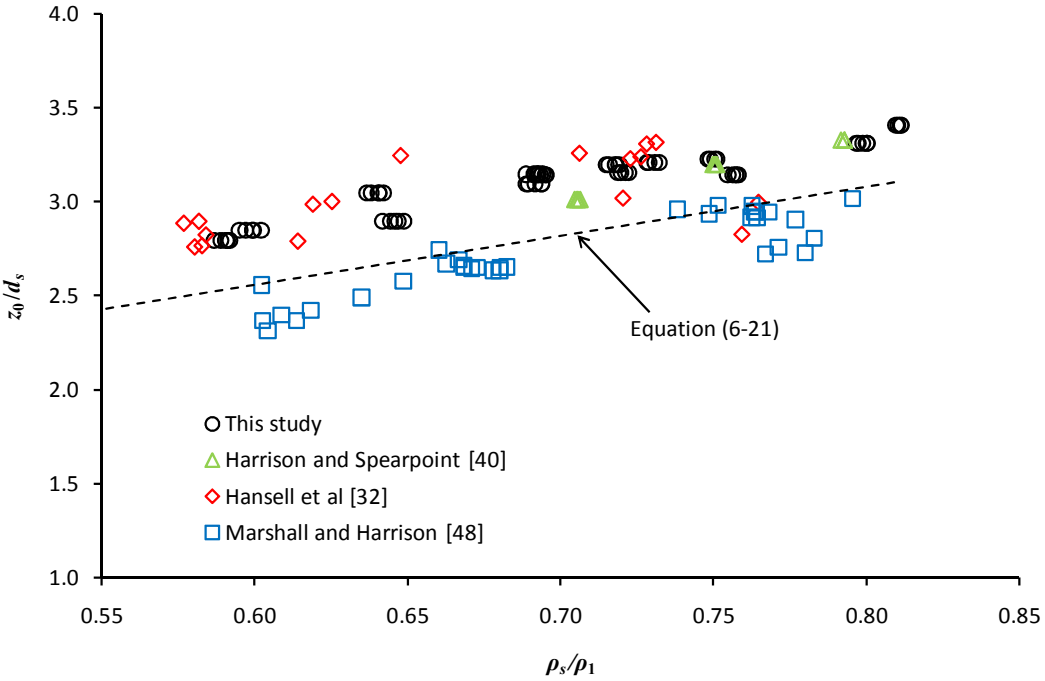

Figure 6.49: Plot of z_0/d_s versus ρ_s/ρ_1 and comparison with previous work

When considering all the data shown in Figure 6.49 it seems reasonable to express z_0/d_s in general terms by,

$$\frac{z_0}{d_s} \approx 3 \qquad \textbf{(6-22)}$$

Thus, for design purposes it is proposed that,

$$z_0 \approx 3d_s \qquad \textbf{(6-23)}$$

This provides the same result as given by Kumar *et al.* [41] following an independent analysis of the location of the virtual source.

6.8.1 Alternative simplified design formulae

The development of Equation (6-23) allows alternative simplified design formulae to be developed for both 2-D and 3-D balcony spill plumes (with channelling screens below the balcony). The Lee and Emmons line plume model can be utilised expressed in a form for the spill plume as given by Equation (6-20) such that,

$$\dot{m}_p = C\dot{Q}_c^{1/3} W_s^{2/3} \left(z_s + z_0\right)$$

Thus, for the 2-D plume and from the analysis in section 6.2.3, $C = 0.16$, hence,

$$\dot{m}_p = 0.16\dot{Q}_c^{1/3} W_s^{2/3} \left(z_s + z_0\right) \quad \textbf{(6-24)}$$

Thus, using Equation (6-23) to describe z_0 gives the following alternative simplified design formula for the 2-D plume,

$$\dot{m}_{p,2D} = 0.16\dot{Q}_c^{1/3} W_s^{2/3} \left(z_s + 3d_s\right) \quad \textbf{(6-25)}$$

Hence, a similar formula for the 3-D plume can be developed by adding the expression describing the entrainment into the free ends [Equation (6-11)] to Equation (6-25) to give,

$$\dot{m}_{p,3D} = 0.16\dot{Q}_c^{1/3} W_s^{2/3} \left(z_s + 3d_s\right) + 0.25\dot{Q}_c^{1/3} d_s^{2/3} z_s \quad \textbf{(6-26)}$$

Since the above analysis has made some simplifying assumptions/rounding in the development of the various new simplified formulae proposed in this work, the performance of these alternative equivalent equations are compared against each other and the experiment to give confidence in their use. Figure 6.50 shows a comparison between Equations (6-5), (6-25) and the experiment for the 2-D plume. Figure 6.51 shows a comparison between Equations (6-12) and (6-26) and the experiment for the 3-D plume.

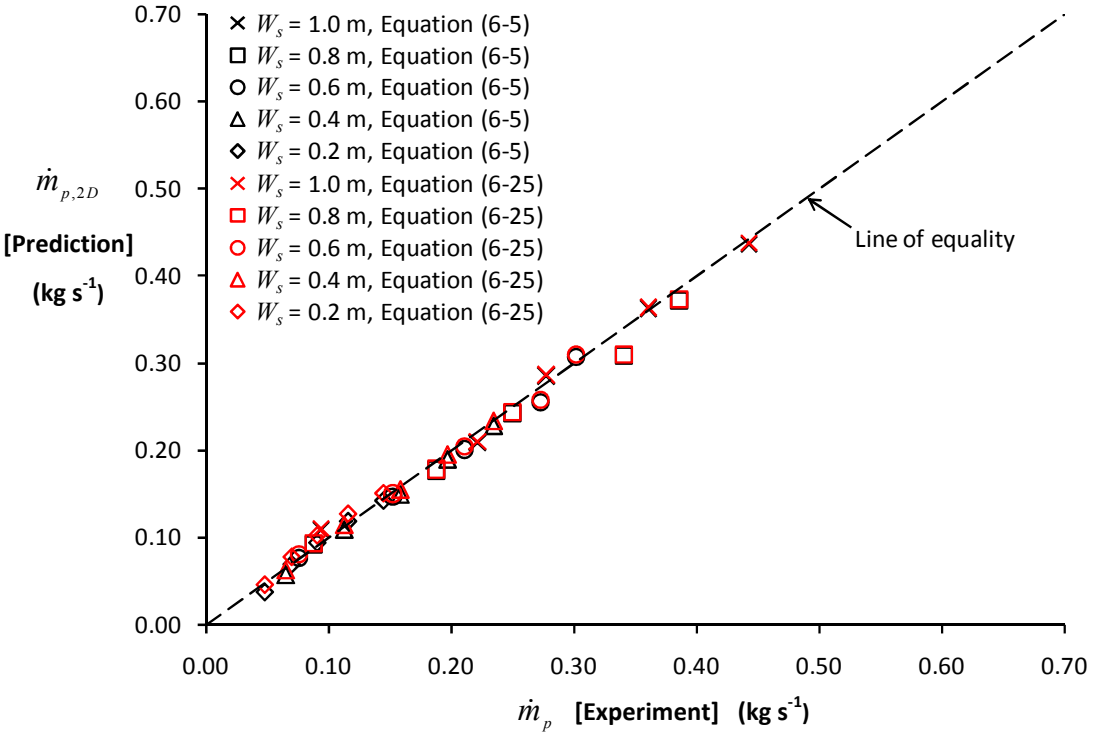

Figure 6.50: Comparison of Equations (6-5) and (6-25) with the experiment

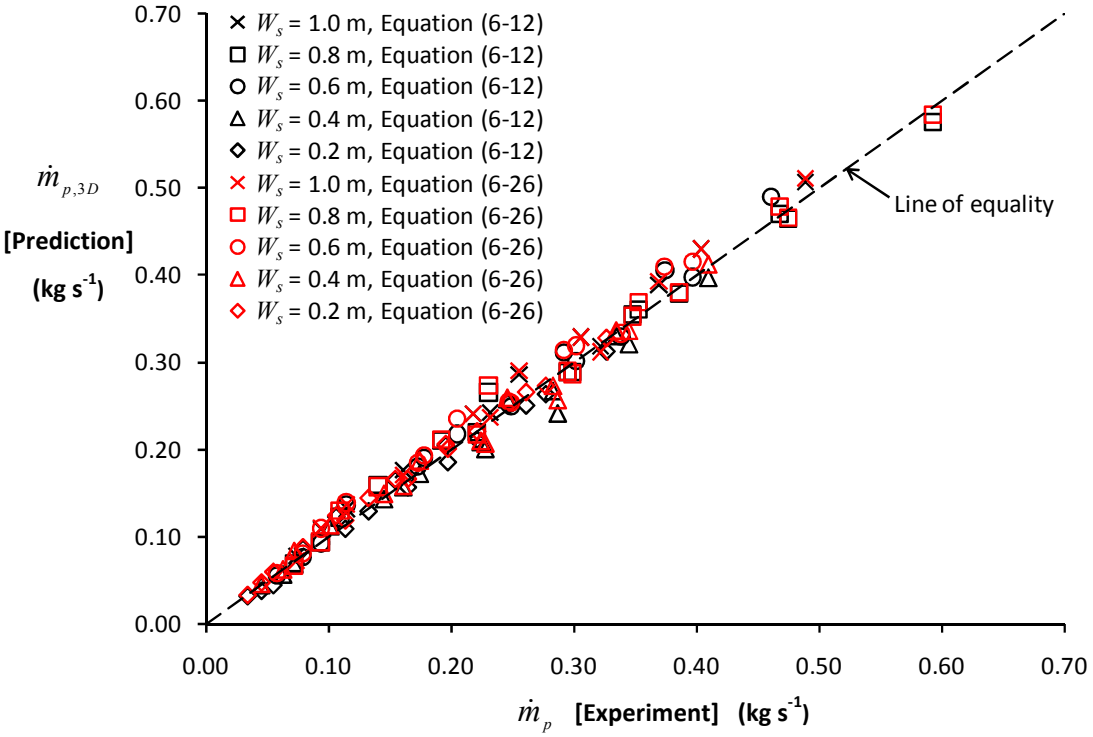

Figure 6.51: Comparison of Equations (6-12) and (6-26) with the experiment

Figures 6.50 and 6.51 show that the new and alternative simplified design formulae proposed in this work provide a prediction of entrainment that are consistent with each other and the experiment for both 2-D and 3-D balcony spill plumes respectively. The vast majority of predictions of using these formulae are generally within less than 10% of the experiment as expected. This provides further confidence in the use of these equations for design purposes.

6.9 Conclusions

This chapter provides a comprehensive set of new experimental data to rigorously characterise balcony spill plume entrainment. Analysis of the results has provided the following conclusions.

6.9.1 The 2-D plume

This work has demonstrated that existing simplified design formulae for the 2-D balcony spill plume [i.e. Equations (6-2) and (6-3)] appear to apply generally for the range of $\dot{Q}_c$ and W_s examined in the experiments.

The following empirical relationship is proposed to describe the decoupled entrainment in the plume below the height of the spill edge (i.e. at $z_s = 0$) and appears to apply generally. It is not specific to 2-D plumes as it effectively describes the amount of entrainment in any spill plume after rotation as it has been determined from a decoupled flow.

$$\dot{m}_s = 1.34\dot{m}_s$$

A new simplified design formula is proposed for the 2-D plume, using the above empirical relationship describing the entrainment below the height of the spill edge. This formula appears to apply generally and is given by,

$$\dot{m}_{p,2D} = 0.16\dot{Q}_c^{1/3} W_s^{2/3} z_s + 1.34\dot{m}_s$$

6.9.2 The 3-D plume with channelling screens

Entrainment into a 3-D balcony spill plume appears to be specifically dependent on the characteristics of the layer flow below spill edge, particularly in terms of W_s and d_s, such that plumes generated from narrow, deep layer flows entrain air at a greater rate with respect to height compared to plumes generated from wide, shallow layers. The rate of entrainment also appears to be dependent on the contribution of the end entrainment in the overall entrainment process. The findings go some way to explain and reconcile differences in entrainment reported between previous studies.

A new simplified design formula is proposed for the 3-D plume channelled by screens below the balcony, by developing a general empirical expression to explicitly describe the entrainment of air into the ends of the plume. This simplified formula can be applied more generally compared to currently available formulae for the 3-D plume and is given by,

$$\dot{m}_{p,3D} = 0.16\dot{Q}_c^{1/3}\left(W_s^{2/3} + 1.56d_s^{2/3}\right)z_s + 1.34\dot{m}_s$$

There is a limit to its use which has been developed and explained in Chapter 9 and given below for information purposes, such that the above equation applies when $z_s \le z_{trans}$, where,

$$z_{trans} = 3.4\left(W_s^{2/3} + 1.56d_s^{2/3}\right)^{3/2}$$

The analysis shows that none of the existing simplified design formulae (e.g. NFPA 92B, CIBSE) apply generally for a range of W_s and are specific to the conditions studied in the original experiments from which they were derived. This analysis gives further support for the use of the new design formula proposed in this work as they have been derived generally for plumes for a range of W_s.

6.9.3 Analytical methods

The curved plume method provides an excellent prediction of entrainment for the 2-D balcony spill plume. This method seems suitable for design purposes for the rare occasions when the design scenario involves a 2-D plume.

The BRE spill plume method over predicts entrainment by approximately 30 to 40% for the 2-D balcony spill plume and by approximately 20 to 70% for the 3-D balcony spill plume depending upon the conditions studied. The use of the effective layer depth correction did not always provide a reliable prediction and should be used with caution. It also appears that that formation of an effective layer below the visual layer is more apparent than real.

A modified version of the BRE method is proposed for the 3-D balcony spill plume (named "BRE [UC] method") to provide a prediction of entrainment that matches the experimental results, without resorting to the using the effective layer depth correction.

6.9.4 The virtual line source

This work has demonstrated that it is more appropriate to describe the location of the virtual line source below the spill edge in terms of the depth of the layer flow below the spill edge, rather than the height of the spill edge (or balcony) above the floor. The experimental results from this study and data from previous work suggests that for design purposes,

$$z_0 \approx 3d_s$$

The development of this general expression to describe z_0 has allowed alternative simplified design formulae to be developed for both 2-D and 3-D balcony spill plume. Hence, for the 2-D balcony spill plume the following alternative formula is proposed,

$$\dot{m}_{p,2D} = 0.16\dot{Q}_c^{1/3} W_s^{2/3} \left(z_s + 3d_s\right)$$

An alternative formula for the 3-D balcony spill plume is given by,

$$\dot{m}_{p,3D} = 0.16\dot{Q}_c^{1/3} W_s^{2/3} \left(z_s + 3d_s\right) + 0.25\dot{Q}_c^{1/3} d_s^{2/3} z_s$$

The new and alternative simplified design formulae proposed in this work provide a prediction of entrainment that are consistent with each other and the experiments for both 2-D and 3-D balcony spill plumes respectively.

6.9.5 The 3-D plume without channelling screens

Plumes generated without channelling screens caused lateral spread of the layer flow below the balcony. This spread gave rise to plumes with a greater lateral extent above the spill edge compared to plumes with screens below the balcony. The amount of lateral spread appears to be dependent upon the velocity of the flow from the fire compartment opening which increases when W_o decreases and $\dot{Q}_t$ increases. There was also smoke contamination local to the area above the balcony in line with the fire compartment opening.

The measured entrainment for plumes generated without screens was greater than that from equivalent plumes with screens. The difference in entrainment increases as W_o decreases due to the increased spread of gases below the balcony.

The entrainment can be approximated by using an effective lateral extent of the plume below the spill edge. The following formula is proposed as a simple approximation to predict entrainment,

$$\dot{m}_{p,3D,unchan} = 0.16\dot{Q}_c^{1/3} \left[\left(W_o + b\right)^{2/3} + 1.56 d_s^{2/3}\right] z_s + 1.34\dot{m}_s$$

With the strict limit that,

$$\frac{W_o}{b} \geq 2$$

This is an approximate solution to a complex smoke flow and should be used in the early stages of design. Ideally, the entrainment analysis of these plumes should be supported by numerical modelling. Numerical modelling is recommended to predict entrainment into plumes where $W_o/b < 2$, at least until further experiments and analysis have been carried out.

Chapter 7

7. Adhered spill plume experiments

This chapter presents the results and discussion for the series of experiments examining entrainment of air into an adhered spill plume, both 2-D and 3-D plumes are considered in the analysis.

7.1 Experimental results

A summary of the key results for the series of experiments to characterise entrainment of air into an adhered spill plume is given in Table 7.1. Table 7.1 shows the mass flow rate of gases entering the layer in the collecting hood due to the spill plume ($\dot{m}_p$) and the temperature (above ambient) of the gases in the throat of the exhaust vent (θ_{vent}) determined from the average of the five thermocouples in the vent. Selected results for the associated horizontal flow of gases below the spill edge for each experiment are also included for completeness (already given in Table 5.3). The results are presented in terms of the time averaged mean value with associated standard errors.

Similar to the analysis described in section 6.1, visual observations suggested that "plug-holing" was possibly occurring for those experiments which examined plumes at high heights of rise. Therefore, Equation (6-1) was again used to determine the maximum mass flow rate of gases that can efficiently be exhausted using a single exhaust vent ($\dot{m}_{\max}$) without "plug-holing" occurring. Those experiments where "plug-holing" was deemed to be occurring are marked with an asterisk in Table 7.1. The measured values of $\dot{m}_p$ for these experiments have therefore been neglected from the entrainment analysis described below and should not be used in any subsequent analysis of this work.

Expt	$\dot{Q}_t$ (kW)	$\dot{Q}_c$ (kW)	$\dot{m}_s$ (kg s^{-1})	$d_{v,s}$ (m)	$\dot{m}_p$ (kg s^{-1})	θ_{vent} (^{o}C)	T_1 (K)
E31	5.0 ± 0.3	4.1 ± 0.3	0.026 ± 0.002	0.195 ± 0.005	0.036 ± 0.002	33.03 ± 0.05	289.5
E32	10.0 ± 0.3	9.0 ± 0.8	0.037 ± 0.003	0.245 ± 0.005	0.046 ± 0.001	59.51 ± 0.05	291.5
E33	15.0 ± 0.3	13.1 ± 1.1	0.040 ± 0.003	0.260 ± 0.005	0.054 ± 0.001	82.19 ± 0.07	292.5
E34	5.0 ± 0.3	4.0 ± 0.3	0.038 ± 0.004	0.160 ± 0.005	0.045 ± 0.002	34.55 ± 0.04	291.0
E35	10.0 ± 0.3	8.5 ± 0.8	0.052 ± 0.005	0.195 ± 0.005	0.055 ± 0.002	63.10 ± 0.06	292.4
E36	15.0 ± 0.3	13.6 ± 1.1	0.064 ± 0.006	0.225 ± 0.005	0.067 ± 0.001	83.58 ± 0.10	293.5
E37	5.0 ± 0.3	4.1 ± 0.3	0.047 ± 0.004	0.135 ± 0.005	0.051 ± 0.003	32.40 ± 0.04	291.5
E38	10.0 ± 0.3	8.0 ± 0.7	0.064 ± 0.006	0.160 ± 0.005	0.070 ± 0.002	57.13 ± 0.09	292.5
E39	15.0 ± 0.3	13.3 ± 1.3	0.078 ± 0.008	0.185 ± 0.005	0.083 ± 0.002	79.43 ± 0.06	294.1
E40	5.0 ± 0.3	4.0 ± 0.4	0.049 ± 0.006	0.105 ± 0.005	0.063 ± 0.003	28.30 ± 0.02	288.0
E41	10.0 ± 0.3	7.9 ± 0.7	0.071 ± 0.007	0.135 ± 0.005	0.085 ± 0.002	50.49 ± 0.07	289.0
E42	15.0 ± 0.3	12.7 ± 1.2	0.090 ± 0.010	0.155 ± 0.005	0.106 ± 0.002	69.94 ± 0.07	290.8
E43	5.0 ± 0.3	3.3 ± 0.3	0.047 ± 0.006	0.085 ± 0.005	0.063 ± 0.003	27.96 ± 0.02	290.5
E44	10.0 ± 0.3	7.9 ± 0.7	0.073 ± 0.008	0.105 ± 0.005	0.095 ± 0.003	48.56 ± 0.06	291.7
E45	15.0 ± 0.3	11.6 ± 1.1	0.089 ± 0.010	0.120 ± 0.005	0.114 ± 0.002	66.27 ± 0.06	292.5
E46	5.0 ± 0.3	3.3 ± 0.3	0.047 ± 0.006	0.085 ± 0.005	0.097 ± 0.005	22.93 ± 0.02	290.5
E47	10.0 ± 0.3	7.9 ± 0.7	0.073 ± 0.008	0.105 ± 0.005	0.151 ± 0.004	36.50 ± 0.05	291.0
E48	15.0 ± 0.3	11.6 ± 1.1	0.089 ± 0.010	0.120 ± 0.005	0.187 ± 0.003	49.61 ± 0.04	291.2
E49	5.0 ± 0.3	4.0 ± 0.4	0.049 ± 0.006	0.105 ± 0.005	0.087 ± 0.005	22.20 ± 0.04	289.5
E50	10.0 ± 0.3	7.9 ± 0.7	0.071 ± 0.007	0.135 ± 0.005	0.133 ± 0.004	39.49 ± 0.05	290.0
E51	15.0 ± 0.3	12.7 ± 1.2	0.090 ± 0.010	0.155 ± 0.005	0.162 ± 0.003	53.69 ± 0.05	291.0
E52	5.0 ± 0.3	4.1 ± 0.3	0.047 ± 0.004	0.135 ± 0.005	0.085 ± 0.005	26.29 ± 0.02	290.0
E53	10.0 ± 0.3	8.0 ± 0.7	0.064 ± 0.006	0.160 ± 0.005	0.126 ± 0.003	41.43 ± 0.05	291.0
E54	15.0 ± 0.3	13.3 ± 1.3	0.078 ± 0.008	0.185 ± 0.005	0.148 ± 0.003	58.53 ± 0.05	291.0
E55	5.0 ± 0.3	4.0 ± 0.3	0.038 ± 0.004	0.160 ± 0.005	0.070 ± 0.004	27.34 ± 0.03	289.7
E56	10.0 ± 0.3	8.5 ± 0.8	0.052 ± 0.005	0.195 ± 0.005	0.105 ± 0.003	45.26 ± 0.05	290.8
E57	15.0 ± 0.3	13.6 ± 1.1	0.064 ± 0.006	0.225 ± 0.005	0.124 ± 0.002	62.43 ± 0.03	291.4
E58	5.0 ± 0.3	4.1 ± 0.3	0.026 ± 0.002	0.195 ± 0.005	0.074 ± 0.004	25.87 ± 0.03	288.0
E59	10.0 ± 0.3	9.0 ± 0.8	0.037 ± 0.003	0.245 ± 0.005	0.099 ± 0.003	45.21 ± 0.04	289.0
E60	15.0 ± 0.3	13.1 ± 1.1	0.040 ± 0.003	0.260 ± 0.005	0.119 ± 0.002	62.63 ± 0.08	290.0
E118	5.0 ± 0.3	4.1 ± 0.3	0.026 ± 0.002	0.195 ± 0.005	0.106 ± 0.006	19.17 ± 0.04	289.0
E119	10.0 ± 0.3	9.0 ± 0.8	0.037 ± 0.003	0.245 ± 0.005	0.155 ± 0.004	31.23 ± 0.04	289.4
E120	15.0 ± 0.3	13.1 ± 1.1	0.040 ± 0.003	0.260 ± 0.005	0.185 ± 0.003	42.06 ± 0.06	290.1
E121	10.0 ± 0.3	9.0 ± 0.8	0.037 ± 0.003	0.245 ± 0.005	0.074 ± 0.002	52.55 ± 0.07	290.5
E122	5.0 ± 0.3	4.0 ± 0.3	0.038 ± 0.004	0.160 ± 0.005	0.104 ± 0.006	20.62 ± 0.05	290.4
E123	10.0 ± 0.3	8.5 ± 0.8	0.052 ± 0.005	0.195 ± 0.005	0.152 ± 0.004	34.69 ± 0.04	290.9
E124	15.0 ± 0.3	13.6 ± 1.1	0.064 ± 0.006	0.225 ± 0.005	0.184 ± 0.003	46.47 ± 0.05	291.5
E125	10.0 ± 0.3	8.5 ± 0.8	0.052 ± 0.005	0.195 ± 0.005	0.110 ± 0.003	43.62 ± 0.04	291.0
E126	5.0 ± 0.3	4.1 ± 0.3	0.047 ± 0.004	0.135 ± 0.005	0.125 ± 0.007	18.37 ± 0.03	288.0
E127	10.0 ± 0.3	8.0 ± 0.7	0.064 ± 0.006	0.160 ± 0.005	0.189 ± 0.005	30.57 ± 0.04	288.7
E128	15.0 ± 0.3	13.3 ± 1.3	0.078 ± 0.008	0.185 ± 0.005	0.239 ± 0.004	39.18 ± 0.03	289.2
E129	10.0 ± 0.3	8.0 ± 0.7	0.064 ± 0.006	0.160 ± 0.005	0.150 ± 0.004	35.64 ± 0.04	289.0
E130	5.0 ± 0.3	4.0 ± 0.4	0.049 ± 0.006	0.105 ± 0.005	0.132 ± 0.007	17.15 ± 0.03	284.0
E131	10.0 ± 0.3	7.9 ± 0.7	0.071 ± 0.007	0.135 ± 0.005	0.181 ± 0.005	30.97 ± 0.04	284.0
E132	15.0 ± 0.3	12.7 ± 1.2	0.090 ± 0.010	0.155 ± 0.005	0.237 ± 0.004	40.47 ± 0.03	284.5
E133	10.0 ± 0.3	7.9 ± 0.7	0.071 ± 0.007	0.135 ± 0.005	0.169 ± 0.005	33.11 ± 0.03	284.5

Table 7.1: Summary of results for the series of adhered spill plume experiments

Expt	$\dot{Q}_t$ (kW)	$\dot{Q}_c$ (kW)	$\dot{m}_s$ (kg s^{-1})	$d_{v,s}$ (m)	$\dot{m}_p$ (kg s^{-1})	θ_{vent} (^{o}C)	T_1 (K)
E134	5.0 ± 0.3	3.3 ± 0.3	0.047 ± 0.006	0.085 ± 0.005	0.140 ± 0.008	20.42 ± 0.03	284.5
E135	10.0 ± 0.3	7.9 ± 0.7	0.073 ± 0.008	0.105 ± 0.005	0.200 ± 0.005	29.85 ± 0.04	285.3
E136	15.0 ± 0.3	11.6 ± 1.1	0.089 ± 0.010	0.120 ± 0.005	0.262 ± 0.005	37.48 ± 0.04	286.3
E137	10.0 ± 0.3	7.9 ± 0.7	0.073 ± 0.008	0.105 ± 0.005	0.181 ± 0.005	32.53 ± 0.04	285.5
E138	5.0 ± 0.3	3.3 ± 0.3	0.047 ± 0.006	0.085 ± 0.005	0.148 ± 0.008	16.44 ± 0.07	288.5
E139	10.0 ± 0.3	7.9 ± 0.7	0.073 ± 0.008	0.105 ± 0.005	0.230 ± 0.006	25.84 ± 0.04	289.0
E140	15.0 ± 0.3	11.6 ± 1.1	0.089 ± 0.010	0.120 ± 0.005	0.299 ± 0.005	32.18 ± 0.06	289.5
E141	10.0 ± 0.3	7.9 ± 0.7	0.073 ± 0.008	0.105 ± 0.005	0.216 ± 0.006	28.46 ± 0.04	289.0
E142	5.0 ± 0.3	4.0 ± 0.4	0.049 ± 0.006	0.105 ± 0.005	0.131 ± 0.007	19.26 ± 0.03	289.0
E143	10.0 ± 0.3	7.9 ± 0.7	0.071 ± 0.007	0.135 ± 0.005	0.208 ± 0.006	29.31 ± 0.03	289.6
E144	15.0 ± 0.3	12.7 ± 1.2	0.090 ± 0.010	0.155 ± 0.005	0.269 ± 0.005	36.34 ± 0.04	290.6
E145	10.0 ± 0.3	7.9 ± 0.7	0.071 ± 0.007	0.135 ± 0.005	0.198 ± 0.005	31.68 ± 0.04	289.4
E146	5.0 ± 0.3	4.1 ± 0.3	0.047 ± 0.004	0.135 ± 0.005	0.152 ± 0.008	16.71 ± 0.04	289.0
E147	10.0 ± 0.3	8.0 ± 0.7	0.064 ± 0.006	0.160 ± 0.005	0.242 ± 0.006	25.20 ± 0.05	289.2
E148	15.0 ± 0.3	13.3 ± 1.3	0.078 ± 0.008	0.185 ± 0.005	0.307 ± 0.006	31.23 ± 0.08	289.4
E149	10.0 ± 0.3	8.0 ± 0.7	0.064 ± 0.006	0.160 ± 0.005	0.187 ± 0.005	31.97 ± 0.06	289.1
E150	5.0 ± 0.3	4.0 ± 0.3	0.038 ± 0.004	0.160 ± 0.005	0.135 ± 0.007	16.57 ± 0.06	289.5
E151	10.0 ± 0.3	8.5 ± 0.8	0.052 ± 0.005	0.195 ± 0.005	0.206 ± 0.006	26.26 ± 0.05	289.9
E152	15.0 ± 0.3	13.6 ± 1.1	0.064 ± 0.006	0.225 ± 0.005	0.261 ± 0.005	34.53 ± 0.09	290.0
E153	10.0 ± 0.3	8.5 ± 0.8	0.052 ± 0.005	0.195 ± 0.005	0.138 ± 0.004	39.36 ± 0.05	289.8
E154	5.0 ± 0.3	4.1 ± 0.3	0.026 ± 0.002	0.195 ± 0.005	0.144 ± 0.008	14.66 ± 0.08	287.5
E155	10.0 ± 0.3	9.0 ± 0.8	0.037 ± 0.003	0.245 ± 0.005	0.215 ± 0.006	23.82 ± 0.08	288.0
E156	15.0 ± 0.3	13.1 ± 1.1	0.040 ± 0.003	0.260 ± 0.005	0.263 ± 0.005	31.79 ± 0.04	288.5
E157	10.0 ± 0.3	9.0 ± 0.8	0.037 ± 0.003	0.245 ± 0.005	0.081 ± 0.002	48.70 ± 0.08	288.5
E188	5.0 ± 0.3	4.1 ± 0.3	0.026 ± 0.002	0.195 ± 0.005	0.185 ± 0.010	13.01 ± 0.03	287.0
E189	10.0 ± 0.3	9.0 ± 0.8	0.037 ± 0.003	0.245 ± 0.005	0.263 ± 0.007	20.69 ± 0.03	287.5
E190	15.0 ± 0.3	13.1 ± 1.1	0.040 ± 0.003	0.260 ± 0.005	0.292 ± 0.005	27.27 ± 0.06	288.0
E191	10.0 ± 0.3	9.0 ± 0.8	0.037 ± 0.003	0.245 ± 0.005	0.094 ± 0.003	44.77 ± 0.06	287.5
E192	5.0 ± 0.3	4.0 ± 0.3	0.038 ± 0.004	0.160 ± 0.005	0.197 ± 0.011	15.43 ± 0.03	287.5
E193	10.0 ± 0.3	8.5 ± 0.8	0.052 ± 0.005	0.195 ± 0.005	0.270 ± 0.007	23.58 ± 0.04	287.5
E194	15.0 ± 0.3	13.6 ± 1.1	0.064 ± 0.006	0.225 ± 0.005	0.323 ± 0.006	30.18 ± 0.06	288.0
E195	10.0 ± 0.3	8.5 ± 0.8	0.052 ± 0.005	0.195 ± 0.005	0.160 ± 0.004	36.93 ± 0.05	287.5
E196	5.0 ± 0.3	4.1 ± 0.3	0.047 ± 0.004	0.135 ± 0.005	0.222 ± 0.012	13.61 ± 0.02	286.0
E197	10.0 ± 0.3	8.0 ± 0.7	0.064 ± 0.006	0.160 ± 0.005	0.349 ± 0.010	19.19 ± 0.04	287.1
E198	15.0 ± 0.3	13.3 ± 1.3	0.078 ± 0.008	0.185 ± 0.005	0.425 ± 0.008	24.69 ± 0.05	287.5
E199	10.0 ± 0.3	8.0 ± 0.7	0.064 ± 0.006	0.160 ± 0.005	0.213 ± 0.006	29.70 ± 0.06	287.5
E200	5.0 ± 0.3	4.0 ± 0.4	0.049 ± 0.006	0.105 ± 0.005	0.176 ± 0.001	15.39 ± 0.03	285.4
E201	10.0 ± 0.3	7.9 ± 0.7	0.071 ± 0.007	0.135 ± 0.005	0.294 ± 0.008	22.54 ± 0.04	285.5
E202	15.0 ± 0.3	12.7 ± 1.2	0.090 ± 0.010	0.155 ± 0.005	0.380 ± 0.007	27.54 ± 0.06	286.0
E203	10.0 ± 0.3	7.9 ± 0.7	0.071 ± 0.007	0.135 ± 0.005	0.256 ± 0.007	26.02 ± 0.04	285.5
E204	5.0 ± 0.3	3.3 ± 0.3	0.047 ± 0.006	0.085 ± 0.005	0.188 ± 0.010	18.63 ± 0.04	285.9
E205	10.0 ± 0.3	7.9 ± 0.7	0.073 ± 0.008	0.105 ± 0.005	0.302 ± 0.008	23.67 ± 0.04	286.2
E206	15.0 ± 0.3	11.6 ± 1.1	0.089 ± 0.010	0.120 ± 0.005	0.388 ± 0.007	27.01 ± 0.09	286.7
E207	10.0 ± 0.3	7.9 ± 0.7	0.073 ± 0.008	0.105 ± 0.005	0.266 ± 0.007	25.92 ± 0.06	287.1

Table 7.1: (continued)

Expt	$\dot{Q}_t$ (kW)	$\dot{Q}_c$ (kW)	$\dot{m}_s$ (kg s^{-1})	$d_{v,s}$ (m)	$\dot{m}_p$ (kg s^{-1})	θ_{vent} (^{o}C)	T_1 (K)
E208*	5.0 ± 0.3	3.3 ± 0.3	0.047 ± 0.006	0.085 ± 0.005	0.268 ± 0.014*	9.44 ± 0.05	286.0
E209*	10.0 ± 0.3	7.9 ± 0.7	0.073 ± 0.008	0.105 ± 0.005	0.408 ± 0.011*	14.57 ± 0.07	286.5
E210*	15.0 ± 0.3	11.6 ± 1.1	0.089 ± 0.010	0.120 ± 0.005	0.545 ± 0.010*	15.72 ± 0.07	287.5
E211*	5.0 ± 0.3	4.0 ± 0.4	0.049 ± 0.006	0.105 ± 0.005	0.260 ± 0.014*	12.37 ± 0.03	286.5
E212*	10.0 ± 0.3	7.9 ± 0.7	0.071 ± 0.007	0.135 ± 0.005	0.412 ± 0.011*	15.51 ± 0.10	286.8
E213*	15.0 ± 0.3	12.7 ± 1.2	0.090 ± 0.010	0.155 ± 0.005	0.587 ± 0.011*	16.66 ± 0.08	287.4
E214*	5.0 ± 0.3	4.1 ± 0.3	0.047 ± 0.004	0.135 ± 0.005	0.364 ± 0.020*	8.40 ± 0.04	286.5
E215*	10.0 ± 0.3	8.0 ± 0.7	0.064 ± 0.006	0.160 ± 0.005	0.497 ± 0.013*	12.45 ± 0.06	287.0
E216*	15.0 ± 0.3	13.3 ± 1.3	0.078 ± 0.008	0.185 ± 0.005	0.652 ± 0.012*	14.95 ± 0.09	287.5
E217*	5.0 ± 0.3	4.0 ± 0.3	0.038 ± 0.004	0.160 ± 0.005	0.291 ± 0.016*	9.44 ± 0.05	287.3
E218*	10.0 ± 0.3	8.5 ± 0.8	0.052 ± 0.005	0.195 ± 0.005	0.421 ± 0.011*	14.66 ± 0.10	287.5
E219*	15.0 ± 0.3	13.6 ± 1.1	0.064 ± 0.006	0.225 ± 0.005	0.545 ± 0.010*	16.72 ± 0.10	288.0
E220*	5.0 ± 0.3	4.1 ± 0.3	0.026 ± 0.002	0.195 ± 0.005	0.290 ± 0.016*	9.48 ± 0.05	287.5
E221*	10.0 ± 0.3	9.0 ± 0.8	0.037 ± 0.003	0.245 ± 0.005	0.406 ± 0.011*	14.83 ± 0.05	287.5
E222*	15.0 ± 0.3	13.1 ± 1.1	0.040 ± 0.003	0.260 ± 0.005	0.499 ± 0.009*	18.37 ± 0.08	288.2
E283	10.0 ± 0.3	9.0 ± 0.8	0.037 ± 0.003	0.245 ± 0.005	0.059 ± 0.002	50.48 ± 0.06	287.0
E284	10.0 ± 0.3	8.5 ± 0.8	0.052 ± 0.005	0.195 ± 0.005	0.091 ± 0.003	47.14 ± 0.04	287.0
E285	10.0 ± 0.3	8.0 ± 0.7	0.064 ± 0.006	0.160 ± 0.005	0.118 ± 0.003	44.11 ± 0.05	288.2
E286	10.0 ± 0.3	7.9 ± 0.7	0.071 ± 0.007	0.135 ± 0.005	0.126 ± 0.003	41.30 ± 0.03	287.5
E287	10.0 ± 0.3	7.9 ± 0.7	0.073 ± 0.008	0.105 ± 0.005	0.135 ± 0.004	40.10 ± 0.04	287.9
E293	10.0 ± 0.3	9.0 ± 0.8	0.037 ± 0.003	0.245 ± 0.005	0.048 ± 0.001	61.29 ± 0.10	287.6
E294	10.0 ± 0.3	8.5 ± 0.8	0.052 ± 0.005	0.195 ± 0.005	0.065 ± 0.002	61.79 ± 0.05	288.0
E295	10.0 ± 0.3	8.0 ± 0.7	0.064 ± 0.006	0.160 ± 0.005	0.076 ± 0.002	55.07 ± 0.06	288.9
E296	10.0 ± 0.3	7.9 ± 0.7	0.071 ± 0.007	0.135 ± 0.005	0.088 ± 0.002	50.92 ± 0.04	289.0
E297	10.0 ± 0.3	7.9 ± 0.7	0.073 ± 0.008	0.105 ± 0.005	0.094 ± 0.003	52.79 ± 0.03	289.1

*"plug-holing"

Table 7.1: (continued)

The thermocouple columns within the smoke collecting hood (Columns A and B) provided temperature profiles through the smoke layer for each height of rise of plume examined. Figure 7.1 shows the temperature profiles in the collecting hood for Experiment E127, where the height of rise of plume was approximately 0.5 m above the spill edge (1.5 m below the ceiling of the collecting hood). These profiles are generally typical of all the profiles measured in the hood.

Appendix J shows the temperature profiles in the smoke collecting hood for the series of adhered spill plume experiments.

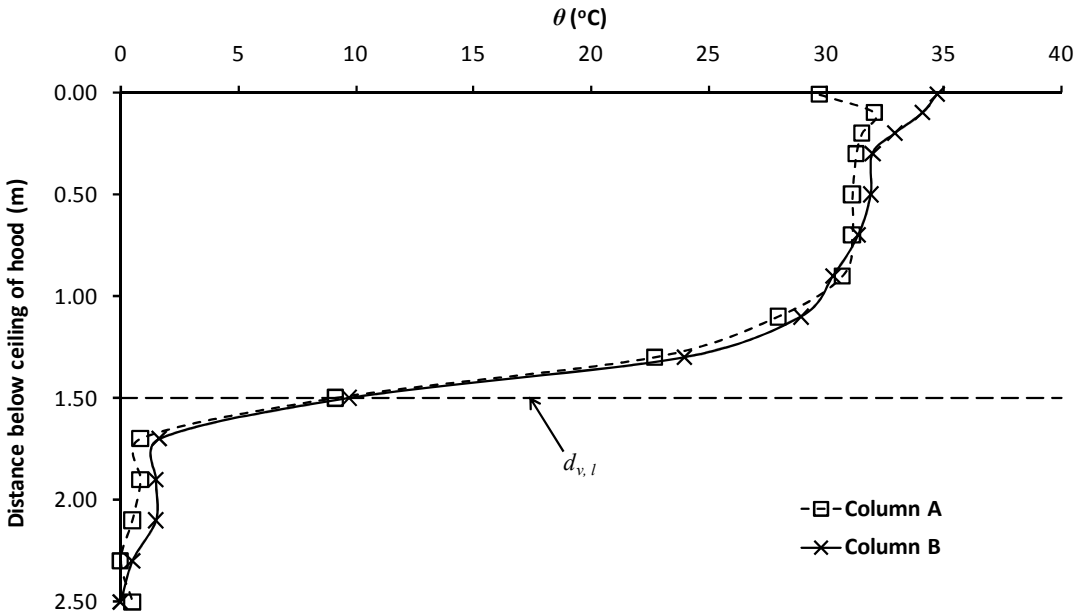

Figure 7.1: Typical temperature profile in the smoke collecting hood (Experiment E127)

7.2 The 2-D adhered spill plume

7.2.1 Plume behaviour

The horizontal flow of gases within the fire compartment was observed to flow out from the opening, rotate at the spill edge (i.e. the top of the fire compartment opening) and then rise as a 2-D adhered spill plume between the screens used to prevent entrainment into the ends of the plume. As the plume was bounded by these end screens and the vertical wall directly above the spill edge, the plume subsequently adhered to the wall above the opening for all widths of plume examined.

Recent work by Poreh *et al.* [50] based on experiments using heated smoke in a scale model, states that the 2-D plume will detach from the wall for horizontal layer flows with *Fr* greater than unity. This behaviour was not observed in this work for flows with *Fr* up to 1.3. However, in the Poreh *et al.* work the *Fr* was measured upstream of the spill edge, where in this work it was measured below the spill edge. It is unclear how the 2-D plume can detach from the wall if air is prevented from entering the rear of the plume due to the presence of bounding walls and screens.

Visual observations identified that entrainment of air occurred across the lateral extent of the plume by the generation of "vortex rolls" being shed from the front side of the rising plume exposed to ambient air. Figure 7.2 shows a schematic drawing of the typical plume behaviour observed for all of the 2-D adhered spill plume experiments.

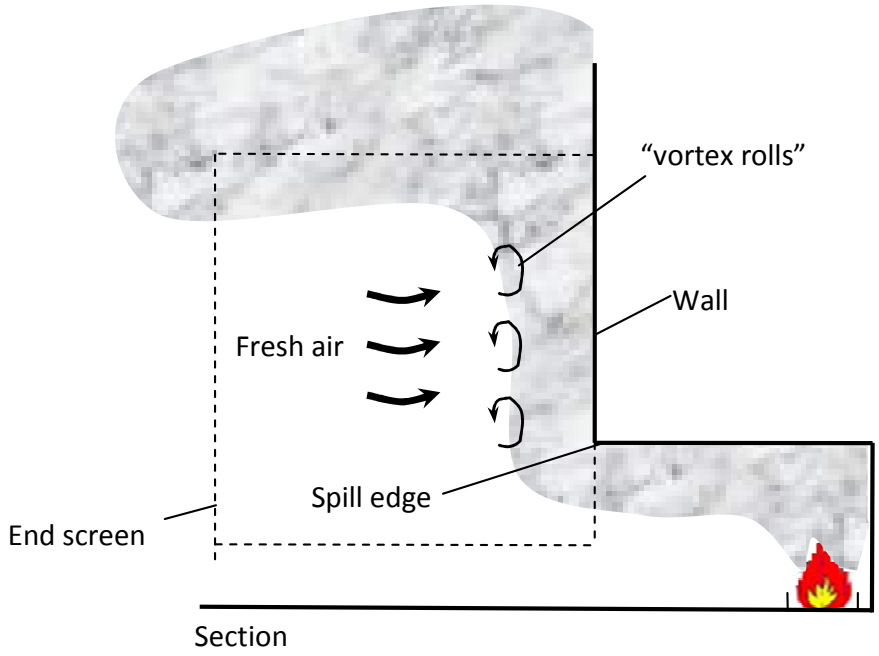

Figure 7.2: Typical 2-D adhered plume behaviour

7.2.2 Smoke layer in the collecting hood

Visual observations again showed that the height of the smoke layer in the collecting hood was not entirely uniform, with the height of the smoke layer between the end screens being slightly higher (up to 0.15 m higher) than the height of the layer between the walls of the collecting hood and the screens. Reasons for this have already been described in section 6.2.2 and are not repeated here. This smoke layer behaviour led to higher heights of rise being used in the analysis of 2-D spill plumes (given in Table 4.6) compared to the equivalent 3-D plumes (where the smoke layer in the collecting hood was reasonably uniform).

7.2.3 Entrainment analysis

The analysis of the experimental results utilises the same simplified entrainment models that were used in the analysis of the 2-D balcony spill plume, with the difference in entrainment accounted for in the empirical entrainment coefficient(s). Hence, the generalised form of the methods by Thomas *et al.* [39] [Equation (2-41)] and Poreh *et al.* [31] [Equation (2-39)] will be used in the analysis.

Previous 1/10th physical scale modelling work described by Poreh *et al.* [50] provide limited data for 2-D adhered spill plumes. Poreh *et al.* correlated their data according to Equation (2-39) to determine that,

$$\frac{\dot{m}'_{p,2D} - \dot{m}'_s}{\dot{Q}'_c} = 0.075\left(\frac{z_s + d_s}{\dot{Q}'^{2/3}_c}\right) \qquad \textbf{(7-1)}$$

Hence, $C = 0.075$.

Equation (7-1) was determined from fires with $\dot{Q}_c$ ranging between 2.9 to 11.9 kW. However, W_s was fixed in these experiments at 0.91 m. Therefore, in this study a selected number of experiments were carried out to complement the Poreh *et al.* data to determine if Equation (7-1) applies generally for a range of W_s. Figure 7.3 shows the data obtained from this study and the data given by Poreh *et al.*, plotted in a form according to Equation (2-39). A line representing Equation (7-1) is also shown.

Figure 7.3 shows the data from this study being broadly in line with the previous data, although the Poreh *et al.* data exhibits much greater scatter. The data from this work correlates to a line (through the origin) such that $C = 0.080$ with a standard error of 0.001. The Poreh *et al.* data correlates to a line with $C = 0.072$ with standard error of 0.003. Performing linear regression in the complete data set gives $C = 0.074$ with a standard error of 0.002, which is consistent with Equation (7-1) given by Poreh *et al.*

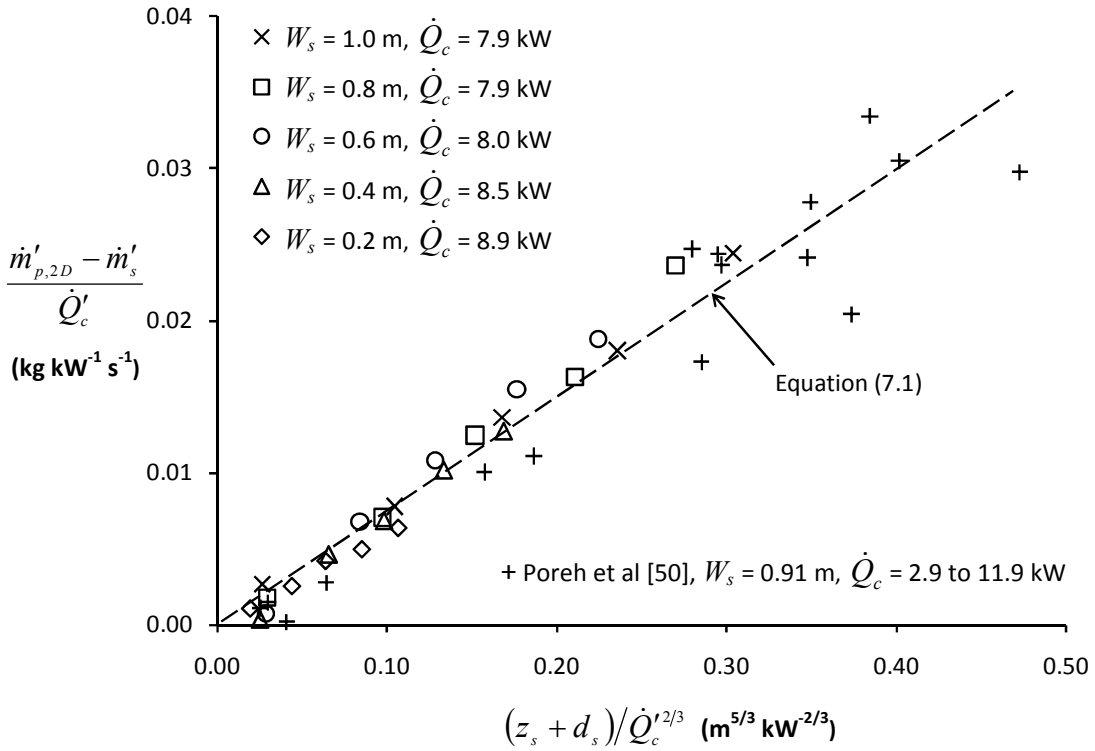

Figure 7.3: Experimental results for the 2-D plume according to Poreh *et al.*

Therefore it appears that Equation (7-1) applies generally and is independent of $\dot{Q}_c$ and W_s. However, considering the greater amount of scatter in the Poreh *et al.* data compared to the data obtained from this study it would seem reasonable to describe Equation (7-1) by the following equation for the 2-D adhered plume (i.e. $C = 0.08$) for design purposes.

$$\frac{\dot{m}'_{p,2D} - \dot{m}'_s}{\dot{Q}'_c} = 0.08\left(\frac{z_s + d_s}{\dot{Q}'^{2/3}_c}\right) \qquad \textbf{(7-2)}$$

The characteristic slope of the linear relationship given by Equation (7-2) (i.e. C) represents the rate of entrainment above the spill edge. The value of C is half that of an equivalent 2-D balcony spill plume (i.e. $C = 0.16$) and gives a result consistent with the findings of previous work [i.e. 32,50]. This is unsurprising considering that entrainment only occurs into one side of a 2-D adhered plume, compared to two sides in a 2-D balcony spill plume.

These data can also be analysed according to the Thomas *et al.* method [39] given by Equation (2-41) to be consistent with the analysis carried out for 2-D balcony spill plumes. Figure 7.4 shows the same data correlated according to this method.

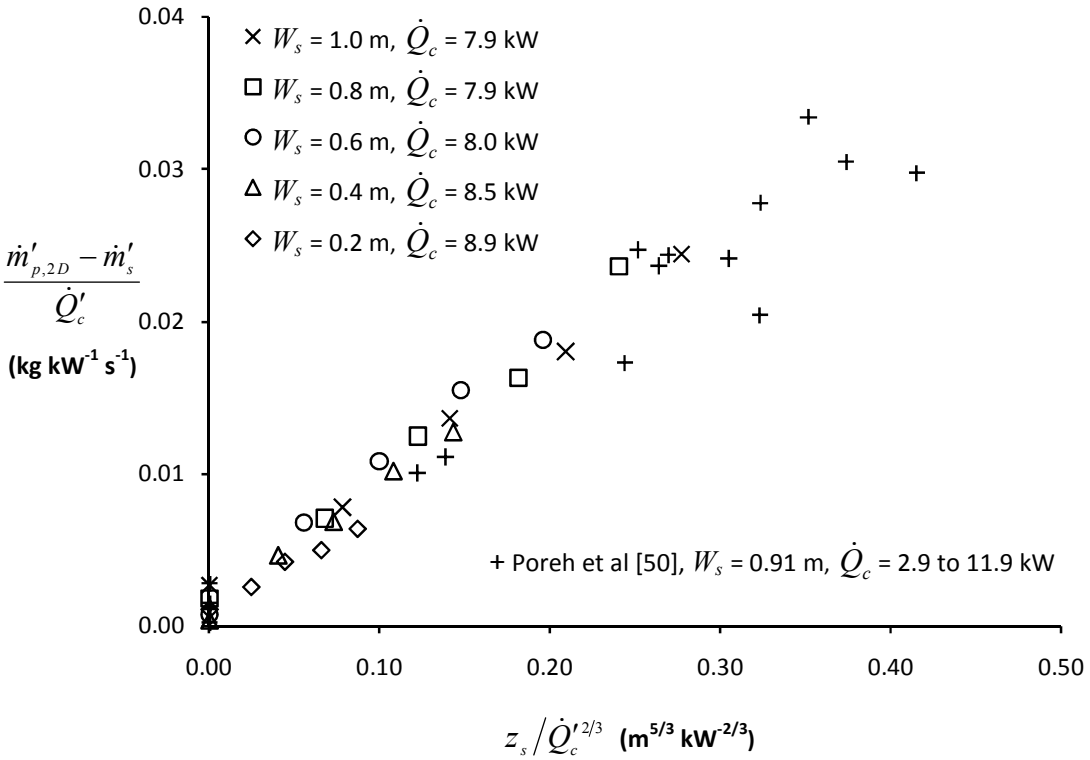

Figure 7.4: Entrainment results for the 2-D plume according to Thomas *et al.*

Using multiple linear regression the data obtained from this study correlates to,

$$\frac{\dot{m}'_{p,2D}}{\dot{Q}'_c} = 0.083\frac{z_s}{\dot{Q}'^{2/3}_c} + 1.35\frac{\dot{m}'_s}{\dot{Q}'_c} - 0.0012 \qquad \textbf{(7-3)}$$

Hence, γ = 0.083, δ = 1.35 and ε = -0.0012. The standard error of γ (representing the rate of entrainment above the spill edge) is 0.003.

Similarly, the Poreh *et al.* data correlates to,

$$\frac{\dot{m}'_{p,2D}}{\dot{Q}'_c} = 0.076\frac{z_s}{\dot{Q}'^{2/3}_c} + 0.645\frac{\dot{m}'_s}{\dot{Q}'_c} + 0.0068 \qquad \textbf{(7-4)}$$

Hence, $\gamma = 0.076$, $\delta = 0.645$ and $\varepsilon = 0.0068$. The standard error of γ is 0.004.

The complete data set correlates according to,

$$\frac{\dot{m}'_{p,2D}}{\dot{Q}'_c} = 0.081\frac{z_s}{\dot{Q}'^{2/3}_c} + 0.825\frac{\dot{m}'_s}{\dot{Q}'_c} + 0.0029 \qquad \textbf{(7-5)}$$

Hence, $\gamma = 0.081$, $\delta = 0.825$ and $\varepsilon = 0.0029$. The standard error of γ is 0.002.

Therefore, the regression coefficient γ can be considered to be the same (to within one standard error) with a value of 0.08, which is identical to the equivalent regression coefficient (i.e. C) proposed in Equation (7-2).

As described in section 6.2.3.1 the regression coefficients δ and ε describe the total amount of entrainment below the height of the spill edge (i.e. $\dot{m}_p$ at $z_s = 0$). The analysis described in section 6.2.3.1 also applies here, as at $z_s = 0$ the entrainment in the adhered plume can be considered to be the same for this decoupled flow. Therefore it again seems reasonable to describe this entrainment with regression coefficients $\delta = 1.34$ and $\varepsilon = 0$. Hence, combining with the regression coefficient describing the entrainment above the spill edge (i.e. γ), Equation (7-6) gives a simplified formula to predict 2-D adhered spill plume entrainment consistent with the dimensional analysis by Thomas *et al.*

$$\frac{\dot{m}'_{p,2D}}{\dot{Q}'_c} = 0.08\frac{z_s}{\dot{Q}'^{2/3}_c} + 1.34\frac{\dot{m}'_s}{\dot{Q}'_c} \qquad \textbf{(7-6)}$$

$$\Rightarrow \dot{m}_{p,2D} = 0.08\dot{Q}_c^{1/3}W_s^{2/3}z_s + 1.34\dot{m}_s$$

7.2.3.1 A new simplified design formula for the 2-D adhered spill plume

It appears that both Equations (7-2) and (7-6) can generally be applied for 2-D adhered spill plumes. However, as Equation (7-6) does not require the calculation of both $\dot{m}_s$ and d_s it can be considered to be simpler. Thus, the following equation is proposed as a new simplified design formula for the 2-D adhered plume. It is in a similar form to the new formula proposed in this work for the 2-D balcony spill plume [Equation (6-5)] and predicts half the entrainment of an equivalent 2-D balcony plume.

$$\dot{m}_{p,2D} = 0.08\dot{Q}_c W_s^{2/3} z_s + 1.34\dot{m}_s \qquad \textbf{(7-7)}$$

Since the above analysis has made some simplifying assumptions, Figure 7.5 shows a plot of the prediction of $\dot{m}_{p,2D}$ versus the experimental results from this study and demonstrates that Equation (7-7) provides a good prediction of the experiment, with the vast majority within less than 10% of the experiment. This gives further confidence in the use of Equation (7-7) for design purposes.

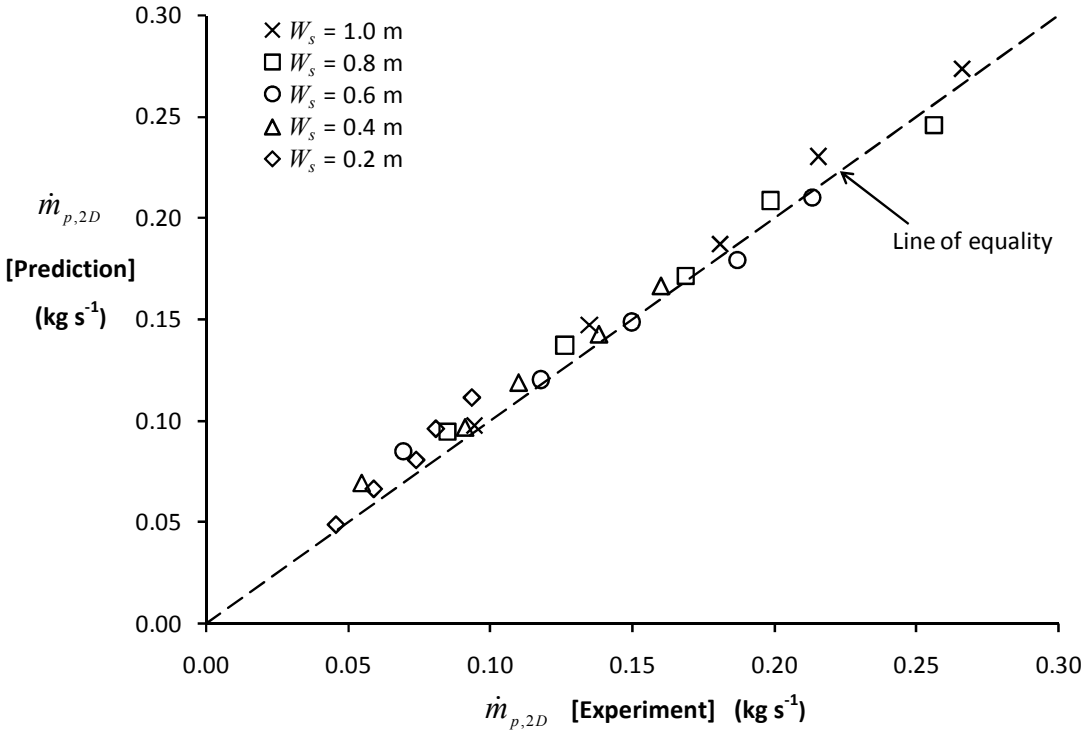

Figure 7.5: Prediction of $\dot{m}_{p,2D}$ using Equation (7-7) versus the experiment

7.3 The 3-D adhered spill plume

7.3.1 Plume behaviour

The behaviour of the 3-D adhered plume was highly dependent on the width of the fire compartment opening. Plumes generated from a wide opening (e.g. W_s = 1.0 m) were observed to adhere to the wall above almost immediately (see Figure 7.6a). Entrainment of air occurred into the front side of the plume exposed to ambient air (due to the shedding of "vortex rolls") and also into the free ends of the plume.

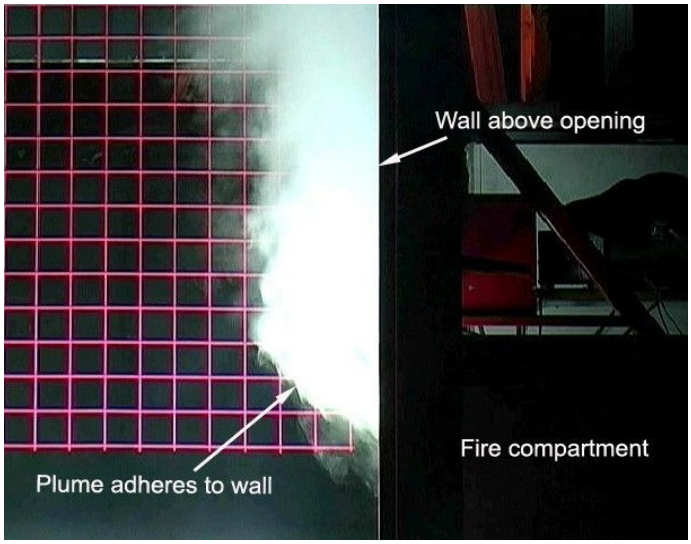

a) Side view

b) Front view

Figure 7.6: Plume behaviour (W_s = 1.0 m)

Figure 7.7b shows that from a front view the lateral extent of the plume tended to narrow slightly due to the action of entrainment into the ends of the plume, before broadening above as end entrainment became more significant.

Plumes generated from intermediate width openings (e.g. W_s = 0.6 to 0.8 m) were initially observed to horizontally project beyond the opening, before curling back and reattaching to the wall above, after which the plume adhered to the wall (see Figure 7.7a).

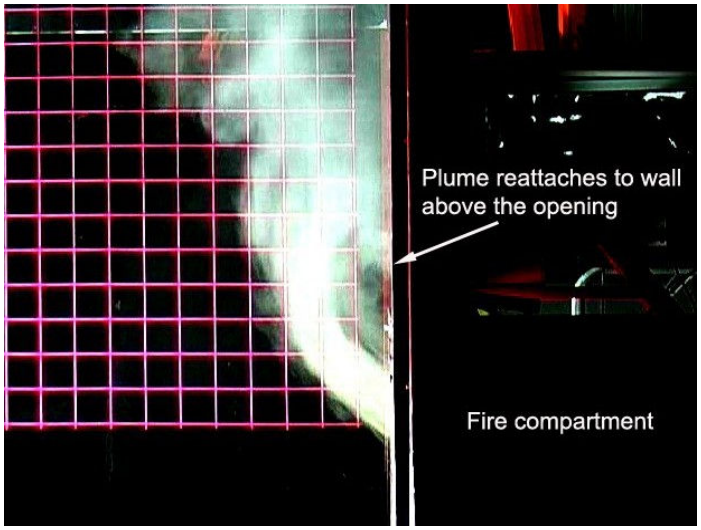

a) Side view

b) Front view

Figure 7.7: Plume behaviour (W_s = 0.6 m)

The height of reattachment above the spill edge tended to increase as W_s decreased and when the fire size and depth of the layer below the spill edge (i.e. d_s) increased. Entrainment of air was observed into front and rear side of the plume (via the sides) in the region where it was detached and also into the free ends. After the plume had reattached to the wall above, entrainment only occurred into the front side of the plume and the free ends. The mechanism causing reattachment of the plume to the wall above the opening is described by Zukoski [22] and is due to the decrease in static pressure between the wall and the plume (in the region where the plume is detached). This reduction in pressure occurs when the supply of ambient air cannot be easily supplied to the rear of the plume in this region and the entrainment process causes the static pressure to fall close to the wall. This low pressure region causes the plume to be pulled back toward the wall and reattachment occurs. This behaviour is more commonly known as the Coanda effect.

Figure 7.6b shows that from a front view the lateral extent of the plume narrowed in the region where the plume was detached from the wall due to entrainment into the ends and into the rear of the plume via the ends. The plume was observed to broaden again above the point of reattachment due to end entrainment becoming more significant.

Plumes generated from narrow width openings (see Figure 7.8a) were observed to project beyond the opening and not reattach to the wall above, with entrainment occurring on both sides of the plume and the free ends over the full height of rise. This is most likely due to the combined effect of the increased momentum of the flow from the opening and the relative narrow width of the plume are not enough to create a small enough pressure drop at the rear of the plume and the Coanda effect does not occur. The observed trajectory of the rising plume was rather diagonal in nature, and different to that observed for the balcony spill plume, presumably due to the dynamics of the flow being different due to the entrainment of fresh air into the rear side of the plume coming via the sides in this case.

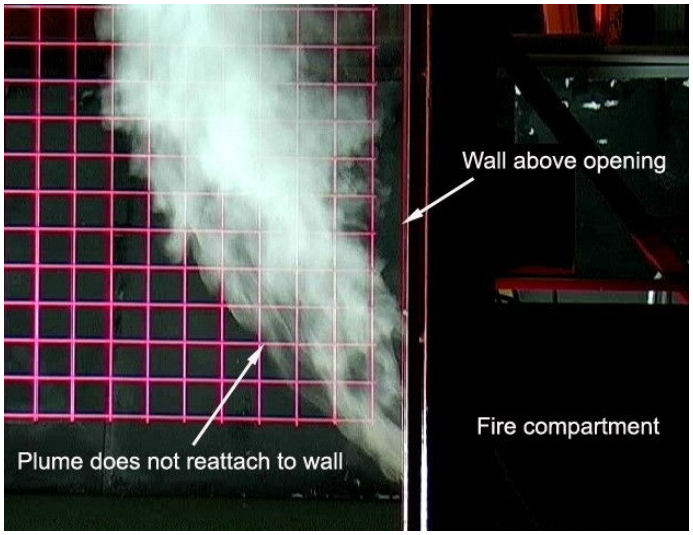

a) Side view

b) Front view

Figure 7.8: Plume behaviour (W_s = 0.2 m)

Figure 7.8b shows that from a front view the lateral extent of the plume tended to broaden above the spill edge due to the contribution of end entrainment and was similar to that observed for the equivalent balcony spill plume (see Figure 6.10b).

The general behaviour described above is similar to that observed in previous work which examined the trajectory of flames from windows from post-flashover fires. This was first studied experimentally by Yokoi [80] and later studied numerically by Galea *et al.* [134]. These studies highlighted that the behaviour of the flame plumes from windows were dependent upon the geometry of the window. When the window was narrow compared to its height, the flame plumes tended to project beyond the opening and sometimes reattach to a wall above. However, for windows that were wide compared to their height, the flames adhered immediately to the wall above the window.

Yokoi characterised the behaviour of window flame plumes by considering the characteristics of the flow at the window opening. A geometric parameter was defined to describe the plume behaviour from the window, which was the ratio of twice the width of the opening to the height of the opening. Zukoski [22] suggests that as the Yokoi experiments were for post flashover fires, the depth of the outflow from the window was approximately half the window height. Hence, this geometric parameter can be considered to be the ratio of the width over the depth of the out flow (i.e. width of the window over half the window height).

The behaviour of the 3-D adhered plumes observed in this work can be characterised by following a similar analysis to that of Yokoi, by considering the out flowing layer in terms of the width and depth of the layer flow below the spill edge (i.e. W_s and d_s).

The height at which the plume first reattaches to the wall above the spill edge (i.e. z_{attach}) was determined from visual observations. Table 7.2 gives the values of z_{attach} observed for the range of W_s and d_s examined, for those experiments with a high height of rise plume (i.e. Experiments E208 to E222, z_s = 1.25 m) as these gave the maximum height over which the rising plume could be observed.

Experiment	$\dot{Q}_t$ (kW)	$\dot{Q}_c$ (kW)	W_s (m)	d_s (m)	z_{attach} (m)	W_s/d_s
E208	5.0 ± 0.3	3.3 ± 0.3	1.0	0.085 ± 0.005	0.050 ± 0.050	11.76 ± 0.65
E209	10.0 ± 0.3	7.9 ± 0.7	1.0	0.105 ± 0.005	0.075 ± 0.050	9.52 ± 0.43
E210	15.0 ± 0.3	11.6 ± 1.1	1.0	0.120 ± 0.005	0.150 ± 0.050	8.33 ± 0.33
E211	5.0 ± 0.3	4.0 ± 0.4	0.8	0.105 ± 0.005	0.100 ± 0.050	7.62 ± 0.35
E212	10.0 ± 0.3	7.9 ± 0.7	0.8	0.135 ± 0.005	0.200 ± 0.050	5.93 ± 0.21
E213	15.0 ± 0.3	12.7 ± 1.2	0.8	0.155 ± 0.005	0.225 ± 0.075	5.16 ± 0.16
E214	5.0 ± 0.3	4.1 ± 0.3	0.6	0.135 ± 0.005	0.200 ± 0.050	4.44 ± 0.16
E215	10.0 ± 0.3	8.0 ± 0.7	0.6	0.160 ± 0.005	0.300 ± 0.050	3.75 ± 0.11
E216	15.0 ± 0.3	13.3 ± 1.3	0.6	0.185 ± 0.005	0.500 ± 0.100	3.24 ± 0.09
E217	5.0 ± 0.3	4.0 ± 0.3	0.4	0.160 ± 0.005	No attachment	2.50 ± 0.08
E218	10.0 ± 0.3	8.5 ± 0.8	0.4	0.195 ± 0.005	No attachment	2.05 ± 0.05
E219	15.0 ± 0.3	13.6 ± 1.1	0.4	0.225 ± 0.005	No attachment	1.78 ± 0.04
E220	5.0 ± 0.3	4.1 ± 0.3	0.2	0.195 ± 0.005	No attachment	1.03 ± 0.03
E221	10.0 ± 0.3	9.0 ± 0.8	0.2	0.245 ± 0.005	No attachment	0.82 ± 0.02
E222	15.0 ± 0.3	13.1 ± 1.1	0.2	0.260 ± 0.005	No attachment	0.77 ± 0.01

Table 7.2: Observed values of z_{attach} for Experiments E208 to E222

The observed values of z_{attach} are supported by temperature measurements from Column D above the spill edge close to the wall. As an example, Figure 7.9 shows that the temperature profile above the spill edge increases rapidly just above a height that coincides with z_{attach} (for Experiment E215).

Appendix K shows that the observed values of z_{attach} were generally in line with the height above which an increase in temperature occurs for the range of plumes examined in Experiments E208 to E222 respectively. This gives further confidence in the use of z_{attach} to characterise the plume behaviour.

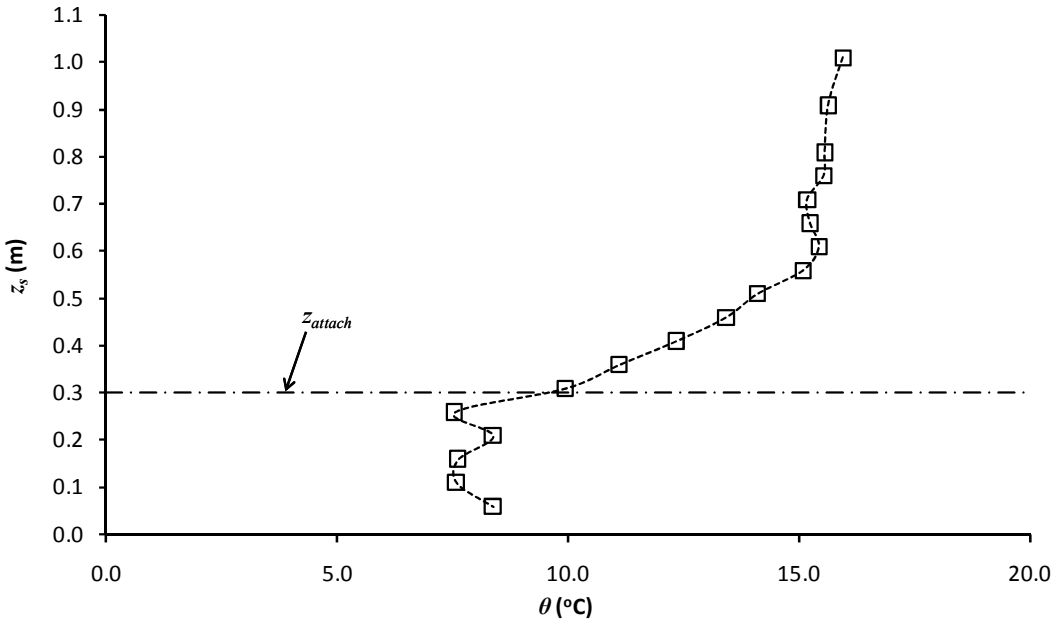

Figure 7.9: Temperature profile close to wall (Column D, Experiment E215)

In an attempt to describe the plume behaviour beyond the spill edge, a similar analysis to that of Yokoi can be carried out. Figure 7.10 shows a plot in non-dimensional form of z_{attach}/W_s with respect to W_s/d_s.

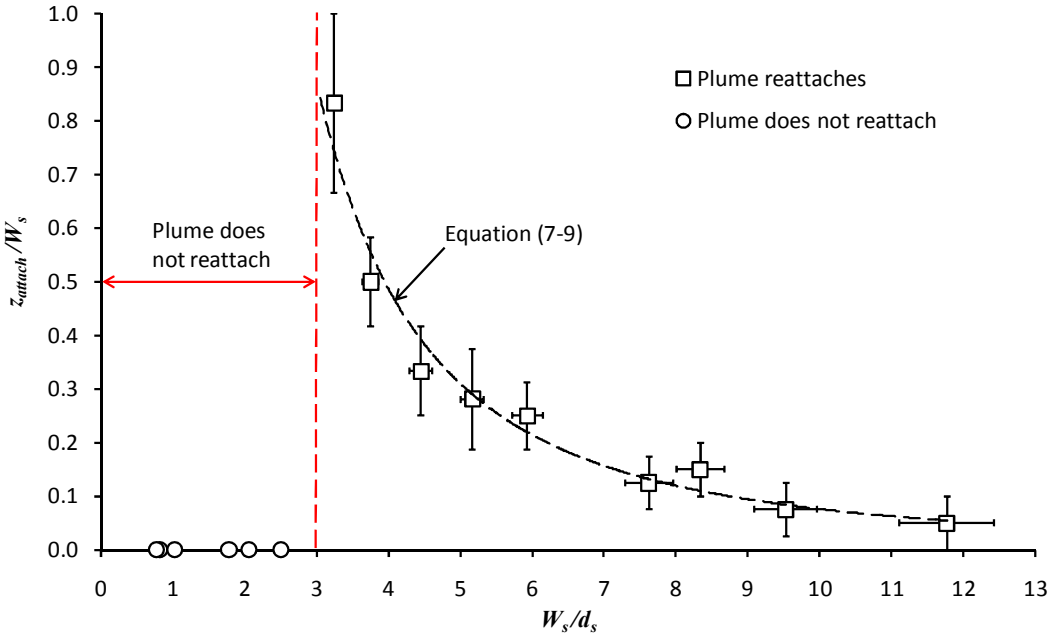

Figure 7.10: Plot of z_{attach}/W_s with respect to W_s/d_s for Experiments E208 to E222

Figure 7.10 shows a clear relationship between z_{attach}/W_s and W_s/d_s which suggests that the behaviour of the 3-D adhered plume is dependent on the characteristics of the layer flow below the spill edge (in terms of W_s and d_s). In general, a layer flow below the spill edge that is shallow compared to its width will tend to adhere to the wall above the opening compared to flows whose depth approaches its width, and this is supported by the visual observations.

It appears that when $W_s/d_s > 3$ the plume reattaches to the wall above the spill edge and z_{attach} can be determined from the line of best fit through the data described by the following power law.

$$\frac{z_{attach}}{W_s} = 7.99\left(\frac{W_s}{d_s}\right)^{-2.02} \qquad \textbf{(7-8)}$$

The standard errors of the regression coefficients 7.99 and -2.02 are 1.74 and 0.13 respectively. Therefore it seems reasonable and convenient to describe Equation (7-8) by,

$$\frac{z_{attach}}{W_s} = 8\left(\frac{W_s}{d_s}\right)^{-2} \qquad \textbf{(7-9)}$$

$$\Rightarrow z_{attach} = \frac{8d_s^2}{W_s}$$

Plumes did not reattach to the wall above the spill edge when $W_s/d_s \leq 3$. The threshold criterion of $W_s/d_s = 3$ was chosen as in Experiment E216 (where $W_s/d_s = 3.24$) the plume was observed to intermittently detach from the wall, which indicated that characteristics of the layer flow below the spill edge was close to the threshold of a detached plume. Therefore, it seems reasonable to set the criterion just below 3.24.

7.3.2 Horizontal temperature profiles across the plume

Figure 7.11 shows a plot of the horizontal temperature profiles across the centreline of the plume, perpendicular to the spill edge, with respect to height of rise above the edge for Experiment T4 (i.e. W_s = 1.0 m, $\dot{Q}_t$ = 10 kW).

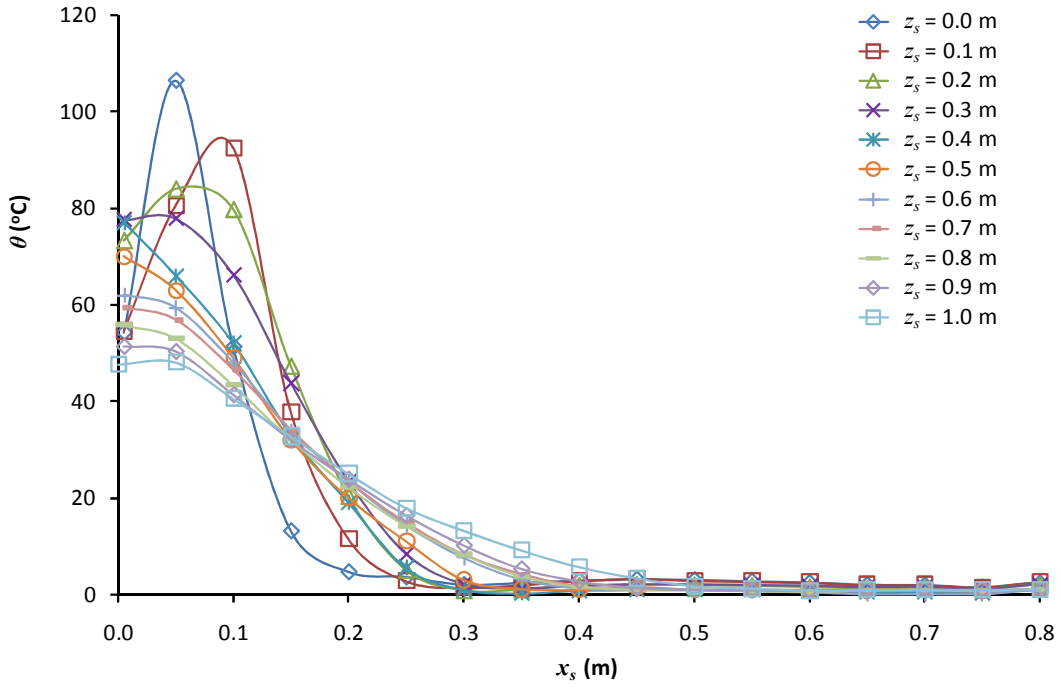

Figure 7.11: Horizontal temperature profiles across the plume for Experiment T4

Figure 7.11 shows that the characteristic shape of the majority of these profiles are approximately half Gaussian in nature with the maximum temperature generally being directly above the spill edge (i.e. at x_s = 0) due to the plume adhering to the wall above. However, the profiles with $z_s \leq 0.3$ m are part way between half Gaussian and Gaussian as the plume had not fully adhered to the wall over a short height of rise.

These profiles can be expressed in non-dimensional form by plotting θ/θ_{max} with respect to x_s/z_s consistent with the analysis given in section 6.3.2. As the adhered plume generally rises vertically, with little horizontal momentum, it was not necessary to normalise the horizontal axis to reflect a shift in the maximum value of θ/θ_{max} with respect to height as required for the balcony spill plume.

Figure 7.12 shows that with the exception of the profiles obtained at $z_s \leq 0.3$ m, the data collapse reasonably well to a single characteristic profile when expressed in non-dimensional form. Figure 7.13 shows the profiles for $z_s \geq 0.4$ m plotted separately to demonstrate this.

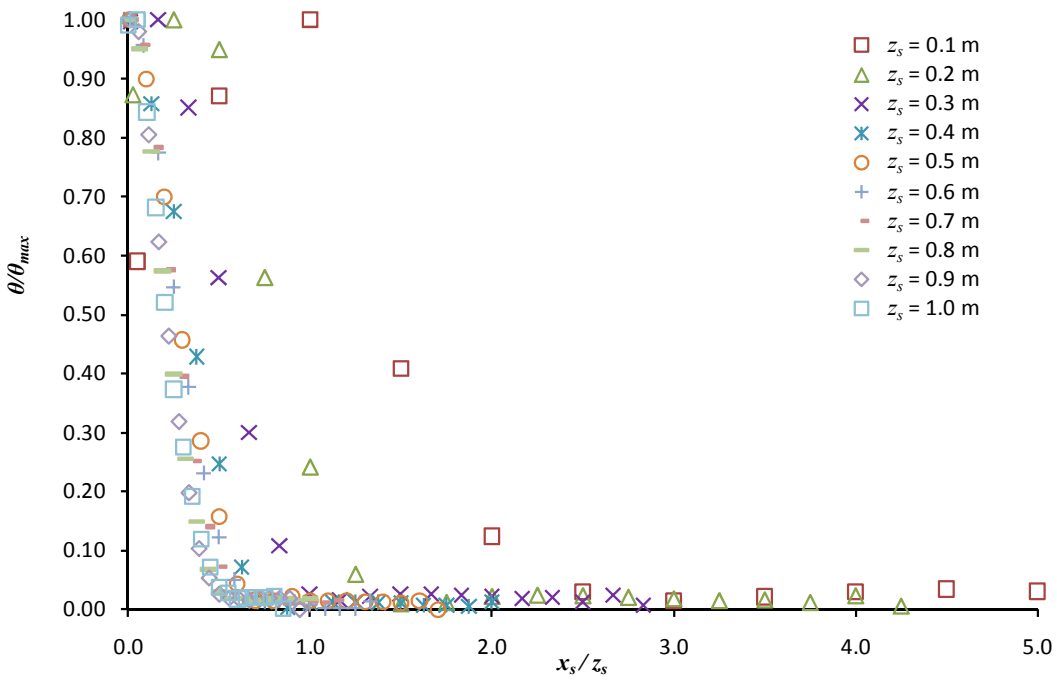

Figure 7.12: Plot of θ/θ_{max} with respect to x_s/z_s for Experiment T4

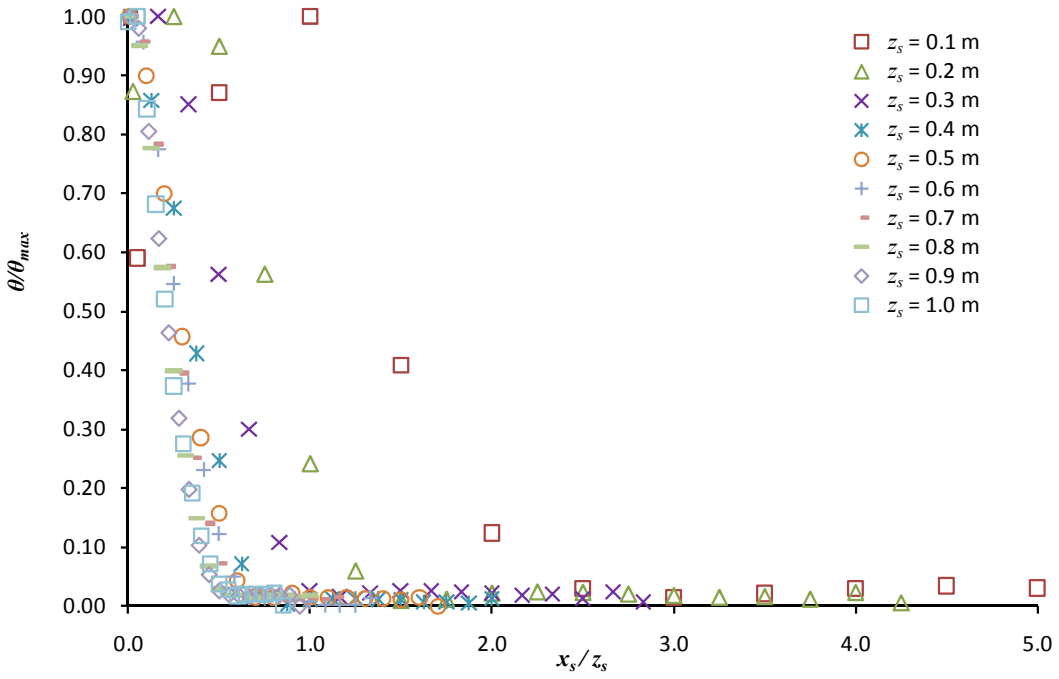

Figure 7.13: Plot of θ/θ_{max} with respect to x_s/z_s for Experiment T4 (z_s = 0.4 to 1.0 m)

This analysis gives confidence in the use of spill plume entrainment models which assume a constant entrainment coefficient and a virtual line source, which make the fundamental assumption of self-similarity between profiles with respect to height of rise.

Appendix L shows both the temperature and non-dimensional normalised temperature profiles for Experiments T4 to T6 inclusive (i.e. W_s = 1.0, 0.6 and 0.2 m, $\dot{Q}_t$ = 10 kW) which demonstrate that the profiles approach Gaussian (from half Gaussian) when the width of the compartment opening decreases (due to the plume tending to detach from the wall for narrow flows).

7.3.3 Entrainment analysis

Unfortunately, the difference in plume behaviour observed between 2-D and 3-D adhered plumes meant that it was not possible to carry out a similar analysis to that for the 3-D balcony spill plume by decoupling and characterising the amount of end entrainment to develop a new simplified design formula (i.e. by subtracting the 2-D plume entrainment from 3-D plume entrainment above the spill edge). This is because the inherent difference in the nature of the 3-D plume (which reattaches to the wall above the spill edge or completely detaches) leads to additional entrainment into the rear side of the plume which did not occur for the 2-D plume.

The generalised form of the method by Thomas *et al.* [39] [Equation (2-41)] is used in the analysis to be consistent with approach used for the 3-D balcony spill plume. Figure 7.14 shows a plot of all the data in a form consistent with the dimensional analysis by Thomas *et al.* describing the total amount of entrainment in the plume. Figure 7.14 shows some scatter of the data which appears to be dependent on W_s. The representative slope of the line through each data set, for each value of W_s, generally appears to increase as W_s decreases. The data very generally exhibits linearity, although there is some scatter in the data (or non-linearity) as in some cases due to the entrainment behaviour of the plume varying with respect to height of rise (e.g. when the plume detaches and then reattaches to the wall above, and due to narrowing of the plume [i.e. W_s = 0.6 m]).

Figure 7.14 indicates that plumes generated from narrower openings (that tend to detach from the wall) entrain air at a greater rate with respect to height compared to plumes generated from wider openings (that tend to adhere to the wall). This is unsurprising when considering the plume behaviour described above and it appears that the amount of entrainment into the plume is specifically linked to the plume behaviour (i.e. whether it adheres, reattaches or is detached from the wall).

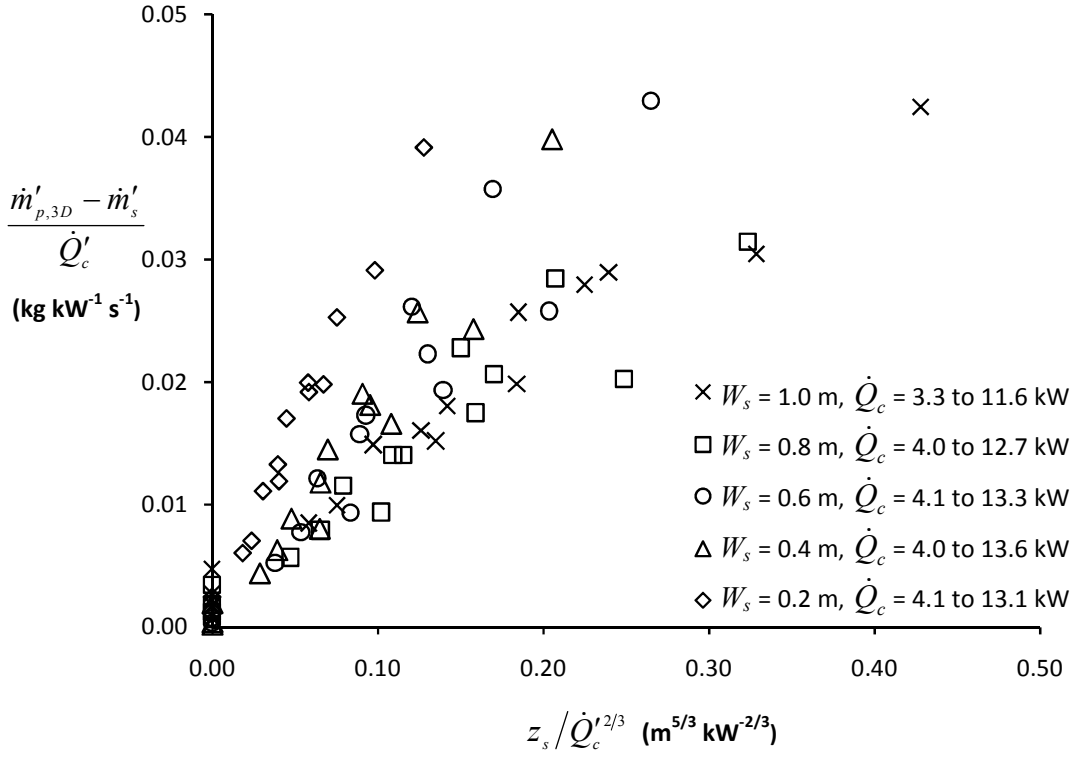

Figure 7.14: Experimental results for the 3-D plume according to Thomas *et al.*

To develop a general expression to describe 3-D adhered spill plume entrainment, the following analysis examines the total amount of entrainment above the spill edge, decoupled from the entrainment below the height of the spill edge (which has already been characterised in section 6.2.3.1). To decouple the entrainment above the spill edge, the measured mass flow rates were modified by subtracting $\dot{m}_p$ at z_s = 0 for each W_s and $\dot{Q}_t$ (and hence, $\dot{Q}_c$ and d_s) examined. Thus, for each W_s, the data set passes through the origin (see Figure 7.15).

As the amount of entrainment appears to be specifically linked to the plume behaviour the results were then correlated with respect to W_s/d_s as the above analysis demonstrates that this non-dimensional parameter can be successfully used to describe the plume behaviour. Therefore, linear regression was performed to determine the value of γ for each W_s/d_s examined.

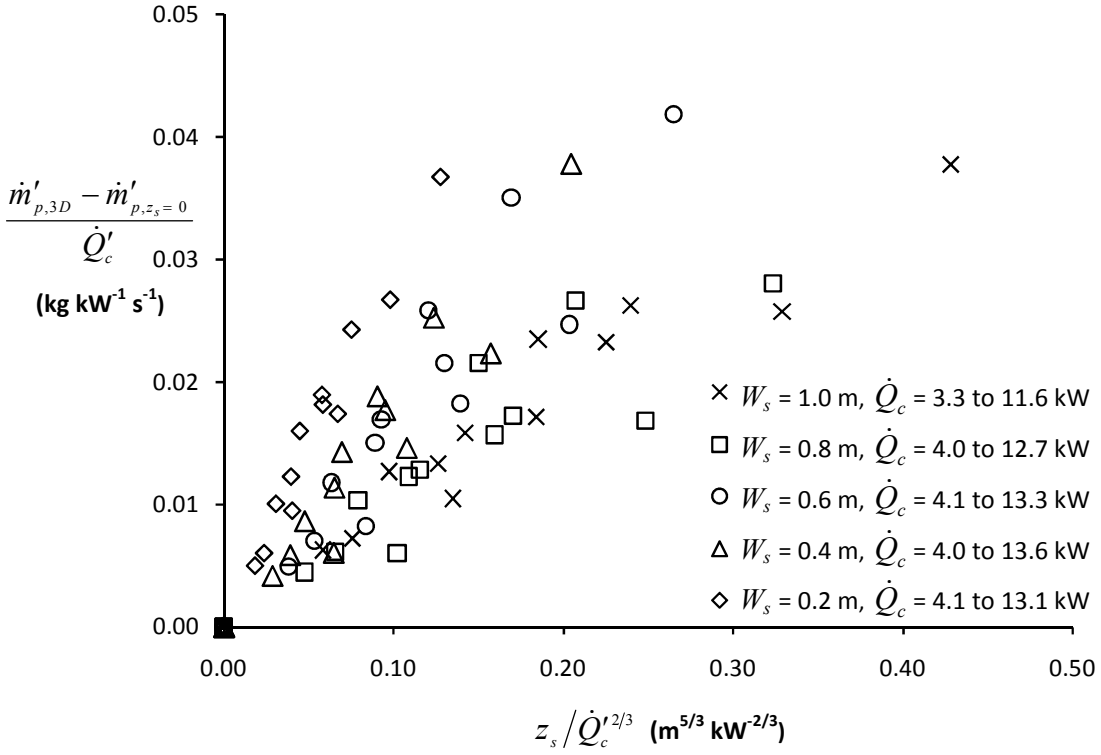

Figure 7.15: Decoupled entrainment above the spill edge according to Thomas *et al.*

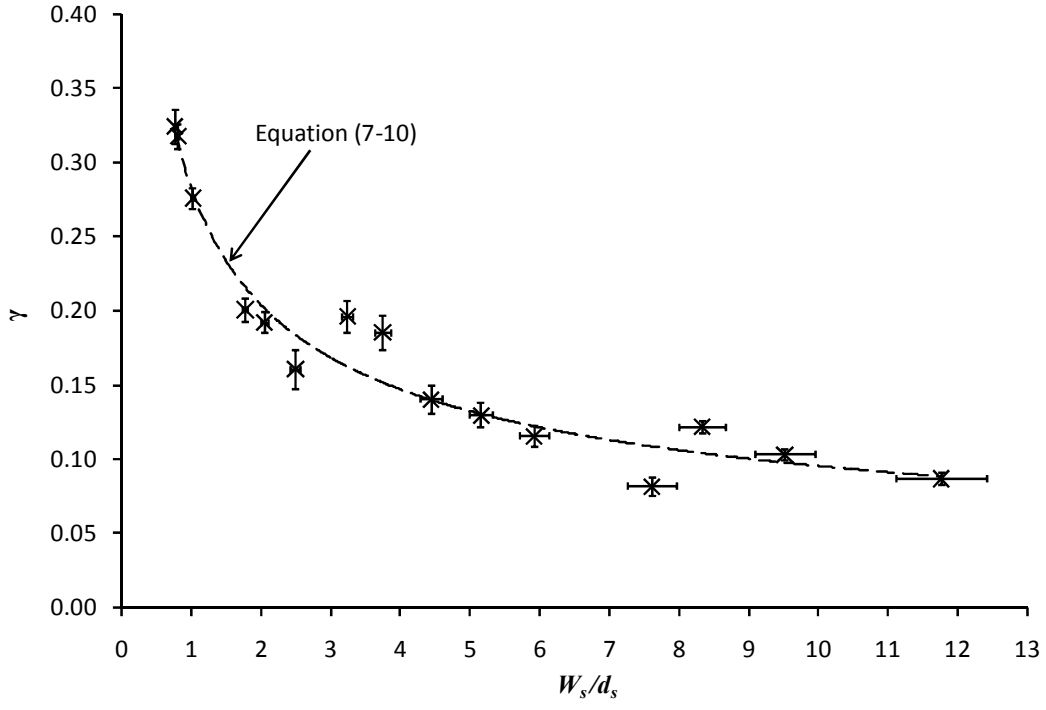

Figure 7.16: Plot of γ versus W_s/d_s for entrainment above the spill edge

Figure 7.16 shows that the values of γ determined for each W_s/d_s examined collapse to the relationship given by,

$$\gamma = 0.284\left(\frac{W_s}{d_s}\right)^{-0.48} \quad \textbf{(7-10)}$$

The standard errors of the regression coefficients 0.284 and -0.48 are 0.02 and 0.04 respectively. Therefore, considering there was some scatter (or non-linearity) in the data in some cases, it seems reasonable and convenient to be slightly conservative and simplify Equation (7-10) to,

$$\gamma = 0.3\left(\frac{W_s}{d_s}\right)^{-1/2} \quad \textbf{(7-11)}$$

Equation (7-11) indicates that for a layer flow below the spill edge that is shallow compared to its width (e.g. $W_s/d_s \approx 12$) where the subsequent spill plume adheres almost immediately to the wall above, $\gamma \approx 0.09$ which is approximately half that of an equivalent balcony spill plume where $\gamma \approx 0.20$. For a layer flow below the spill edge whose depth is similar to its width (e.g. $W_s/d_s \approx 1.0$), where the subsequent plume did not reattach to the wall, $\gamma \approx 0.3$. This value of γ is comparable to that of an equivalent balcony spill plume, where $\gamma \approx 0.32$. Intermediate width openings give rise to values of γ between these upper and lower bounds. Therefore, the rate of entrainment is dependent on the behaviour of the plume, which is in turn dependent on the characteristics of the layer flow at the opening. There is a limit to the use of Equation (7-11) as it is expected that for large W_s/d_s the value of γ should approach that of the 2-D spill plume (i.e. 0.08). However, Equation (7-11) predicts values of γ below 0.08 for $W_s/d_s > 13$, therefore the following limit applies to its use.

$$\left(\frac{W_s}{d_s}\right) \leq 13 \quad \textbf{(7-12)}$$

7.3.3.1 A new design formula for the 3-D adhered spill plume

Since γ represents the total rate of entrainment above the spill edge (including end entrainment), the mass flow rate of gases in the plume above the spill edge can by described by,

$$\frac{\dot{m}'_{p,3D} - m'_{p,z_s=0}}{\dot{Q}'_c} = \gamma \frac{z_s}{\dot{Q}'^{2/3}_c} = 0.3\left(\frac{W_s}{d_s}\right)^{-1/2}\left(\frac{z_s}{\dot{Q}'^{2/3}_c}\right) \quad \textbf{(7-13)}$$

A new design for the 3-D adhered plume can be developed by summing the decoupled entrainment both above and below the spill edge [i.e. Equations (7-13) and (6-4)] to give Equation (7-14) which is consistent with the dimensional analysis by Thomas *et al.*

$$\frac{\dot{m}'_{p,3D}}{\dot{Q}'_c} = 0.3\left(\frac{W_s}{d_s}\right)^{-1/2}\left(\frac{z_s}{\dot{Q}'^{2/3}_c}\right) + 1.34\frac{\dot{m}'_s}{\dot{Q}'_c} \quad \textbf{(7-14)}$$

$$\Rightarrow \dot{m}_{p,3D} = 0.3\dot{Q}_c^{1/3} W_s^{1/6} d_s^{1/2} z_s + 1.34\dot{m}_s$$

With the limit,

$$\left(\frac{W_s}{d_s}\right) \leq 13$$

For flows where $W_s/d_s > 13$, then Equation (7-7) for the 2-D plume should be used.

It is expected that at higher heights of rise of plume, the effect of end entrainment will cause the plume to be more axisymmetric in nature and Equation (7-14) will no longer apply. Therefore, as a conservative estimate the limit given by Equation (9-14) (see Chapter 9) applies for its use consistent with that for the 3-D balcony spill plume. Further work is required to determine the limit which linearity applies for the 3-D adhered plume.

Since the above analysis has made some simplifying assumptions, Figure 7.17 shows a plot of the prediction of $\dot{m}_{p,3D}$ using Equation (7-14) versus the experimental results from this study.

Figure 7.17 demonstrates that Equation (7-14) provides a good (if slightly conservative) prediction of the experiment, with the majority of predictions within less than 15% of the experiment. This gives further confidence in the use of Equation (7-14) for design purposes. The predictions can be considered slightly conservative due to the rounding up of the regression coefficients, as there was some scatter (or non-linearity) in the data due to narrowing and reattachment of the plume to the wall above the spill edge in some cases.

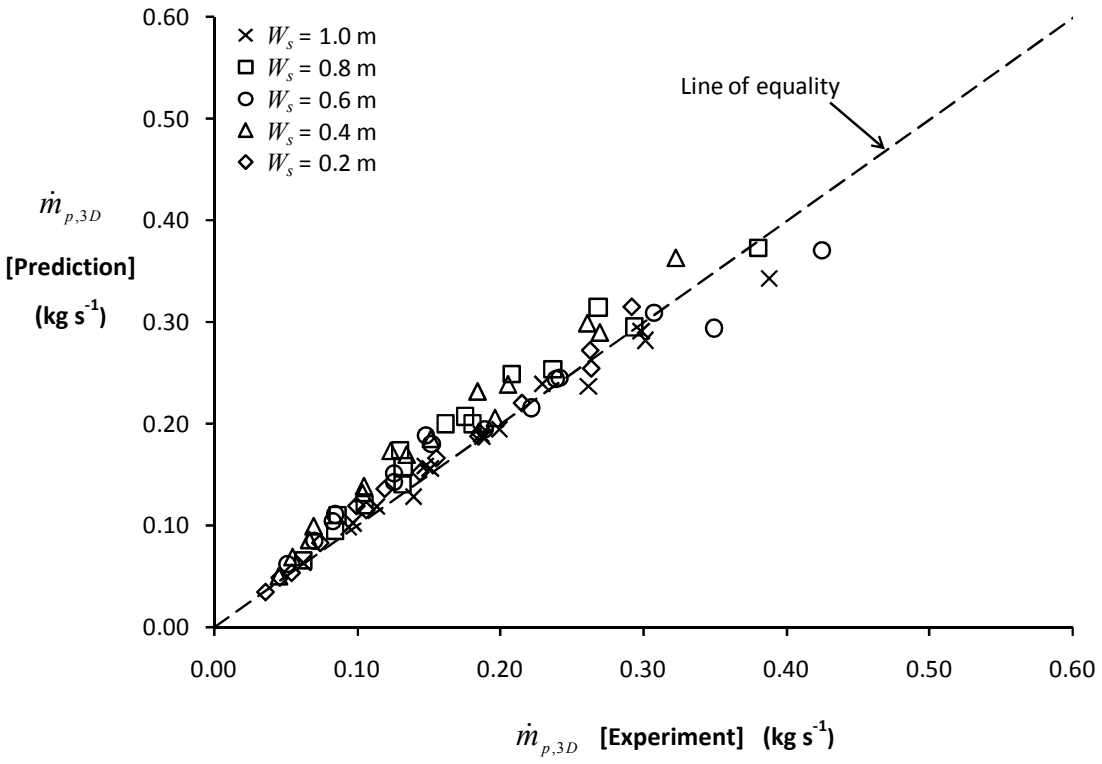

Figure 7.17: Prediction of $\dot{m}_{p,3D}$ using Equation (7-14) versus the experiment

7.3.4 Comparison with an existing simplified formula

Figure 7.18 shows a comparison between the experimental results and prediction of $\dot{m}_{p,3D}$ using the simplified formula for the 3-D adhered plume given by CIBSE [38] [see Equation (2-63)].

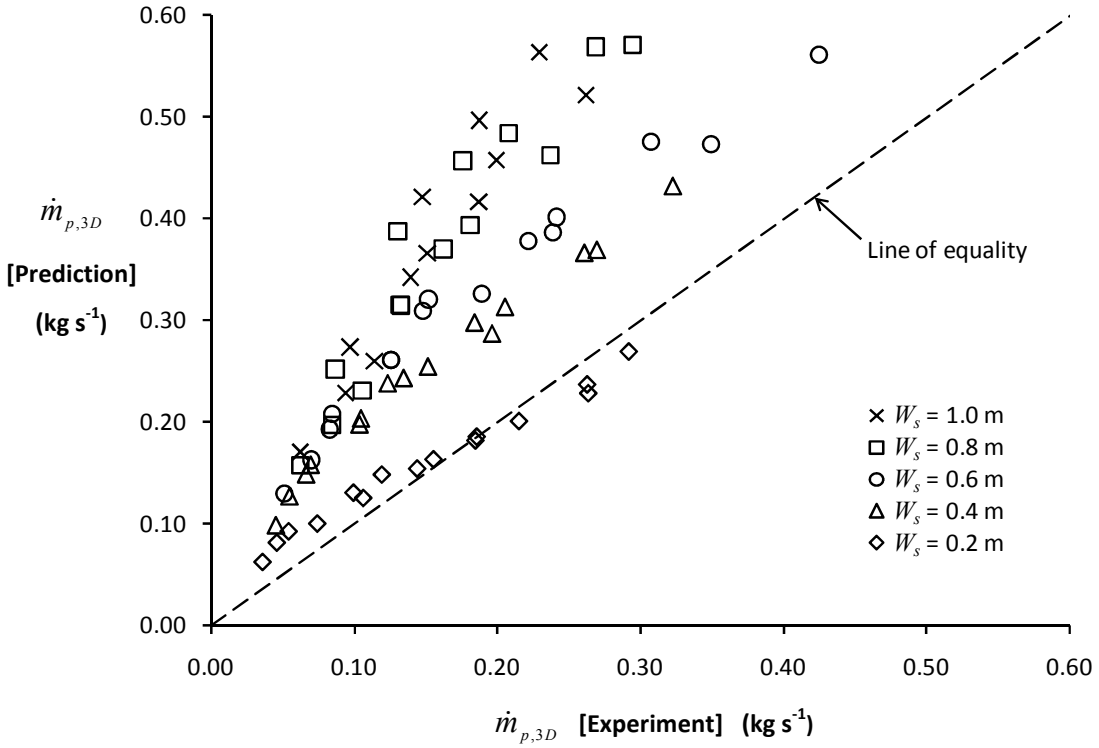

Figure 7.18: Comparison of experiment with prediction of $\dot{m}_{p,3D}$ using Equation (2-63)

Figure 7.18 shows that the CIBSE formula generally provides a highly conservative prediction of $\dot{m}_{p,3D}$ particularly for flows from wide openings where the plume adheres to the wall above, where the prediction is up to 200% higher than the experiment. The predictions tend to become less conservative as W_s decreases, due to the additional entrainment that occurs in plumes from narrower openings. The CIBSE formula provides a reasonably good prediction of $\dot{m}_{p,3D}$ for flows from the narrowest opening (i.e. W_s = 0.2 m) and appears to apply best to plumes that do not reattach or adhere to the wall, such that entrainment occurs into both sides of the rising plume.

7.3.5 Comparison with existing analytical methods

The BRE spill plume method is the only analytical method for the 2-D and 3-D adhered plume. However, it does not cater for the range of adhered plume behaviour observed in this work as it effectively assumes that the plume always adheres to the wall above the spill edge. Therefore the entrainment coefficient, α, is taken to be 0.077 which is approximately half that used for the balcony spill plume (i.e. 0.16).

Figure 7.19 shows a comparison of the predictions of $\dot{m}_p$ against the experiment for the 2-D and 3-D plumes examined in this work, assuming $\alpha = 0.077$, $\alpha' = 1.1$ and not applying the effective layer depth correction.

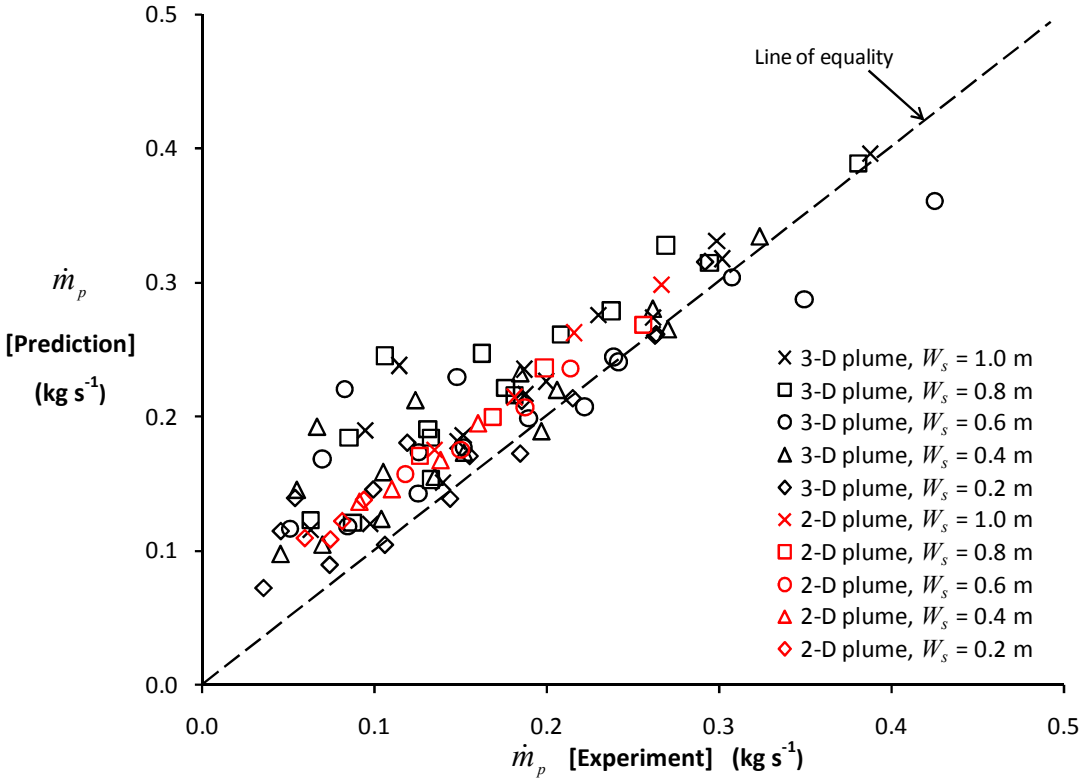

Figure 7.19: Prediction of $\dot{m}_p$ versus experiment (α = 0.16, α' = 1.1, effective layer depth correction <u>not</u> applied)

Figure 7.19 shows that the BRE method generally over predicts $\dot{m}_p$ by up to 15% for the 2-D plume and up to 20 to 30 % for the 3-D plume. However, many of the 3-D plume predictions give a reasonably good match with the experiment, with the exception of those obtained at $z_s = 0$ (with values of $\dot{m}_p$ less than 0.1 kg s^{-1}) which are particularly conservative. In general, there appears to be less need to correct the predictions to match the experiment when compared with the predictions for the balcony spill plume in section 6.7.2. This could possibly be due to the effect of the wall above the spill edge on the calculation of the horizontal flow of gases beneath the edge using the theory by Morgan [51] (see section 5.2.5.1) which is incorporated into the BRE spill plume method.

As the effective layer depth correction has been shown to be unreliable, it has not been applied here. Also, since it was not possible to derive an explicit expression to describe the amount of end entrainment into a 3-D adhered plume, modifications similar to that given by the BRE (UC) method are not proposed.

Therefore, if an analytical method is required to predict adhered spill plume entrainment, it appears that the original BRE spill plume method should continue to be used (without applying the effective layer depth correction) as it will provide either a conservative or an appropriate prediction of entrainment.

7.4 Input parameters to the new design formulae

The input parameters for the new design formulae presented in this chapter are the same as those for the new formulae proposed for balcony spill plume, therefore the formulae given in section 6.5 to determine these input parameters are also recommended for the adhered spill plume.

7.5 Conclusions

This chapter provides a comprehensive set of new experimental data to rigorously characterise adhered spill plume entrainment. Analysis of the results has provided the following conclusions.

7.5.1 The 2-D plume

This work has demonstrated that the existing simplified design formula for the 2-D adhered spill plume [i.e. Equation (7-1)] appears to apply generally for the range of $\dot{Q}_c$ and W_s examined in the experiments. The rate of entrainment with respect to height above the spill edge is approximately half that of an equivalent 2-D balcony spill plume.

The following is proposed as a new simplified design formula for the 2-D adhered plume. It is in a similar form to the new formula proposed in this work for the 2-D balcony spill plume [Equation (6-5)] and predicts half the entrainment of an equivalent 2-D balcony spill plume.

$$\dot{m}_{p,2D} = 0.08\dot{Q}_c^{1/3} W_s^{2/3} z_s + 1.34\dot{m}_s$$

It can be considered to be simpler version of the existing simplified design formula as it does not require the calculation of both $\dot{m}_s$ and d_s.

7.5.2 The 3-D plume

The behaviour of the 3-D adhered plume was highly dependent on the width of the fire compartment opening. Plumes generated from a wide opening were observed to adhere to the wall above almost immediately. Plumes generated from intermediate width openings were initially observed to horizontally project beyond the opening, before reattaching to the wall above, after which the plume adhered to the wall. Plumes generated from narrow width openings were observed to project beyond the opening and not reattach to the wall above.

The plume behaviour observed in this work has been characterised in terms of the width and depth of the layer flow below the spill edge (i.e. W_s and d_s). In general, a layer flow below the spill edge that is shallow compared to its width will tend to adhere to the wall above the opening compared to flows whose depth approaches its width.

For $W_s/d_s > 3$, the height at which the plume first reattaches to the wall above the spill edge (z_{attach}) can be determined from the following empirical relationship given by,

$$z_{attach} = \frac{8 d_s^2}{W_s}$$

Plumes did not reattach to the wall above the spill edge when $W_s/d_s \leq 3$.

The amount of entrainment into the 3-D adhered plume is specifically linked to the plume behaviour, such that plumes generated from narrower openings (that tend to detach from the wall) entrain air at a greater rate with respect to height compared to plumes generated from wider openings (that tend to adhere to the wall).

The following is proposed as a new simplified design formula for the 3-D adhered plume,

$$\dot{m}_{p,3D} = 0.3 \dot{Q}_c^{1/3} W_s^{1/6} d_s^{1/2} z_s + 1.34 \dot{m}_s$$

With the limit,

$$\left(\frac{W_s}{d_s} \right) \leq 13$$

For flows where $W_s/d_s > 13$, then the new simplified formula for the 2-D adhered plume should be used. As a conservative estimate, the upper limit given for the 3-D balcony spill plume should be also be used [i.e. Equation (9-14)].

The formula given by CIBSE that can be used for the 3-D adhered plume scenario [Equation (2-63)] generally provides a highly conservative prediction of entrainment, particularly for flows from wide openings. The predictions tend to become less conservative as W_s decreases. The CIBSE formula provides a reasonably good prediction for flows from the narrow openings where the plume does not reattach or adhere to the wall.

7.5.3 Analytical method

The BRE spill plume method generally provided a conservative prediction of entrainment for both the 2-D and 3-D adhered plume. However, many of the 3-D adhered plume predictions gave a reasonably good match with the experiment. Therefore, it appears that the original BRE spill plume method should continue to be used (without applying the effective layer depth correction) as it will provide either a conservative or an appropriate prediction of entrainment.

Chapter 8

8. Numerical modelling of the experiment

This chapter describes numerical modelling using CFD of a selected number experiments carried out in this work to enable an initial assessment to be made of the validity of CFD to predict spill plume entrainment. The extensive amount of experimental data collected from this study will allow scope for more validation in future work.

CFD predictions of the experiments were mainly obtained using FDS (version 5.1.4) with additional predictions made using JASMINE (v3.23). The modelling procedure, assumptions made and the predictions of plume entrainment are described below.

8.1 FDS modelling

As the majority of previous CFD modelling studies have examined 2-D balcony spill plume entrainment, this work used FDS to model those experiments which examined 3-D spill plumes, both balcony and adhered, as these are more likely to be found in design. The balcony spill plume simulations only examined the scenario of plumes generated from flows channelled by screens below the balcony. As part of a separate study, work is currently in progress (using FDS) to model plumes without channelling screens below the balcony using the experimental data from this study for validation purposes [132].

All of the FDS modelling described below did not employ the use of a mirror symmetry boundary which is often used in RANS models to reduce computational run times for symmetric flows. Mirror symmetry boundaries are not recommended to be used along the centreline of turbulent fire plumes in FDS [42]. This is because an LES model does not compute a time averaged symmetric solution and a mirror boundary along the centreline of a fire plume will change the dynamics of the flow so that it is similar to a flow field adjacent to a vertical wall [42].

8.1.1 Computing facility

The vast majority of the simulations were carried out using the parallel processing version of FDS which was run on the University of Canterbury Super Computer (UCSC) facility. The UCSC allows multiple concurrent users and consists of 160 processors. Further details of the specification of the UCSC facility are described by Cheong [135]. Parallel processing allows the use of several processors to divide the problem up into multiple computational domains which are simultaneously computed (using one processor per domain) to reduce run times. This was generally required for many of the simulations due to the large number of numerical grid elements specified (e.g. up to 6.1 million grid elements). A small number of simulations were carried out using the serial version of FDS using a conventional workstation with a single processor (Pentium 4, 2.4 GHz, 2.0 GB RAM), for those simulations where it was not possible to obtain a result using the UCSC (e.g. due to numerical instabilities).

8.1.2 The horizontal flow of gases below the spill edge

Previous CFD modelling studies have used alternative approaches to describe the source of the spill plume (i.e. the horizontal flow of gases below the spill edge). Some studies have modelled the fire source and flows from the compartment of fire origin [e.g. 71], others, to reduce computational run times, have specified the characteristic vertical temperature and velocity profiles of the out flowing gas layer below the spill edge and have not modelled the flows from fire compartment [e.g. 44,105]. Both of these approaches could possibly be applied in this study to define the plume source. It was decided to characterise the spill plume source by modelling the fire and flows from the compartment of fire origin to be consistent with the approach typically used in design. For the predictions of entrainment above the spill edge to be meaningful, the source of the plume below the edge should be representative of that measured in the experiments. Therefore, the flows from the fire compartment opening and just beyond the spill edge were initially modelled separately, prior to the detailed modelling of the plumes above the spill edge. This was done to determine the most appropriate grid resolution to satisfactorily describe the spill plume source and to give confidence in the subsequent prediction of entrainment above the spill edge.

8.1.2.1 Modelled geometry

FDS was used to model the flows generated from the fire compartment of the 1/10th physical scale model. The geometry examined was for a flow resulting in a balcony spill plume and hence modelled a balcony extending beyond the fire compartment opening with channelling screens beneath. An intermediate fire compartment opening width was chosen for the grid sensitivity analysis (i.e. W_s = 0.6 m). The walls of the compartment were assumed to be made from 25 mm thick CFI board. The balcony and channelling screens were assumed to be made from 10 mm thick CFI board. The following thermal properties were assumed for CFI board as given by Drysdale [109] for fibre insulating board and also used by Miles *et al.* [44]:

k_{CFI} = 0.041 W m^{-1} K^{-1}; ρ_{CFI} = 229 kg m^{-3}; $c_{p,\,CFI}$ = 2.09 kJ kg^{-1} K^{-1}.

8.1.2.2 Computational domain

A single computational domain was specified which was 1.8 m long by 1.2 m wide by 0.6 m high (see Figure 8.1). The domain extended horizontally beyond and vertically above the spill edge (i.e. the balcony edge) by a distance of 0.5 and 0.1 m respectively and extended 0.1 m beyond the side walls of the fire compartment. The dimensions of the domain were chosen so that the number of grids chosen in each dimension could be factored by 2's, 3's and 5's to not unduly slow down the calculation, as required by the Poisson solver in FDS [42].

The exterior boundaries of the computational domain (except the lower boundary) were set as 'OPEN', which assumes a passive opening to the outside at ambient conditions. The lower exterior boundary of the domain was specified as a solid surface. The ambient temperature was assumed to be 20 ^{o}C.

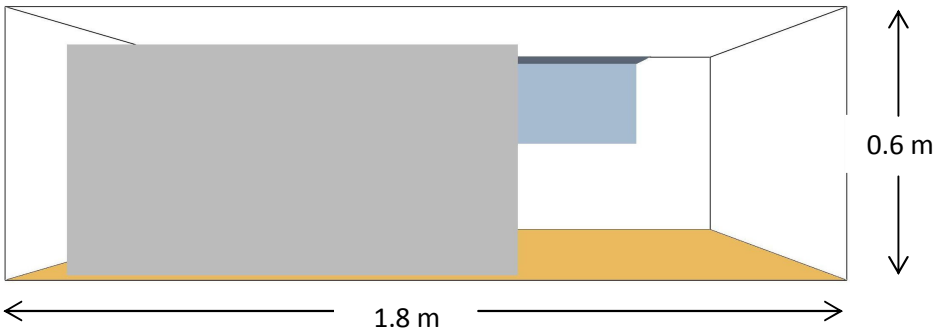

a) Side view

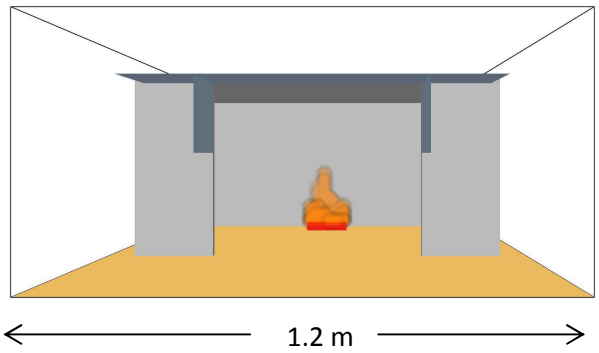

b) Front view

Figure 8.1: The modelled geometry and computational domain

8.1.2.3 Fire source

As the total heat release rate of the fire in the experiment was well characterised and controlled, the fire source in FDS was characterised by a burner with a specified heat release rate per unit area (HRRPUA) located in the same position as the fire tray in the experiment. This assumption simplified the fire source without resorting to the use of the combustion model in FDS. The HRRPUA was set at 527 kW m^{-2} for IMS [126]. The area of the burner was set to the same as the area of the fire in the experiment (see fire areas in Table 5.2) to give an intermediate fire size (i.e. $\dot{Q}_t$ =10 kW). The height of the burner was set at 25 mm from the floor of fire compartment, as in the experiment the fire tray was raised at one end. The radiative fraction of the fire was set at 0.2, which is appropriate for burning ethanol [109], without resorting to the use of the radiation transport model in FDS or the default radiative fraction which is 0.35.

8.1.2.4 Predictions

Gas temperatures were predicted by assuming a column of thermocouples at the same location and with the same spacings as that of Column C in the physical scale model (see section 4.1.2.1). Gas velocities were predicted in the same locations as that measured in the experiment, every 10 mm below the spill edge, to a maximum depth of 0.2 m below the edge.

The mass flow rate of out flowing gas layer below the spill edge (i.e. $\dot{m}_s$) was predicted using the 'MASS FLOW +" command, which utilises the temperature and velocity predictions to integrate over a specified planar area to determine the mass flow rate of gases, with the "+" specifying the direction of the flow.

Preliminary simulations were also carried out to determine the simulation time within FDS such that the predictions of temperature and velocity below the spill edge remained reasonably steady state. A simulation time of 900 seconds was deemed appropriate and used for the series of grid sensitivity simulations for the plume source.

8.1.2.5 The series of grid sensitivity simulations for the plume source

To determine the optimum grid size for subsequent simulations of the plume source, Table 8.1 shows the series of seven simulations carried out and the physical values of the grid sizes used. Appendix M gives an example of the FDS input file used for these simulations (Simulation SC6).

Simulation	$\dot{Q}_t$ (kW)	W_s (m)	Grid size (mm)	Total number of grid elements
SC1	10.0 ± 0.3	0.6	100	1296
SC2	10.0 ± 0.3	0.6	60	6000
SC3	10.0 ± 0.3	0.6	50	10368
SC4	10.0 ± 0.3	0.6	40	20250
SC5	10.0 ± 0.3	0.6	30	48000
SC6	10.0 ± 0.3	0.6	25	82944
SC7	10.0 ± 0.3	0.6	20	162000

Table 8.1: The series of grid sensitivity simulations for the plume source

8.1.2.6 FDS simulation results

Although the burner fire source in FDS was assumed to be steady state, it was first necessary to confirm when reasonably steady conditions were predicted for the gas layer below the spill edge. Figures 8.2 and 8.3 shows graphs of temperature and velocity with respect to time for Simulations SC1 to SC7 respectively, determined from the average of the two profiles 10 mm below the spill edge.

Figures 8.2 and 8.3 show that the predictions of temperature and velocity appear to converge to similar solution as the grid size is reduced and that conditions below the spill edge can be considered to be steady after approximately 600 s. Therefore, the predictions for each simulation were time averaged between 600 and 900 s to enable a comparison to be made with the experiment.

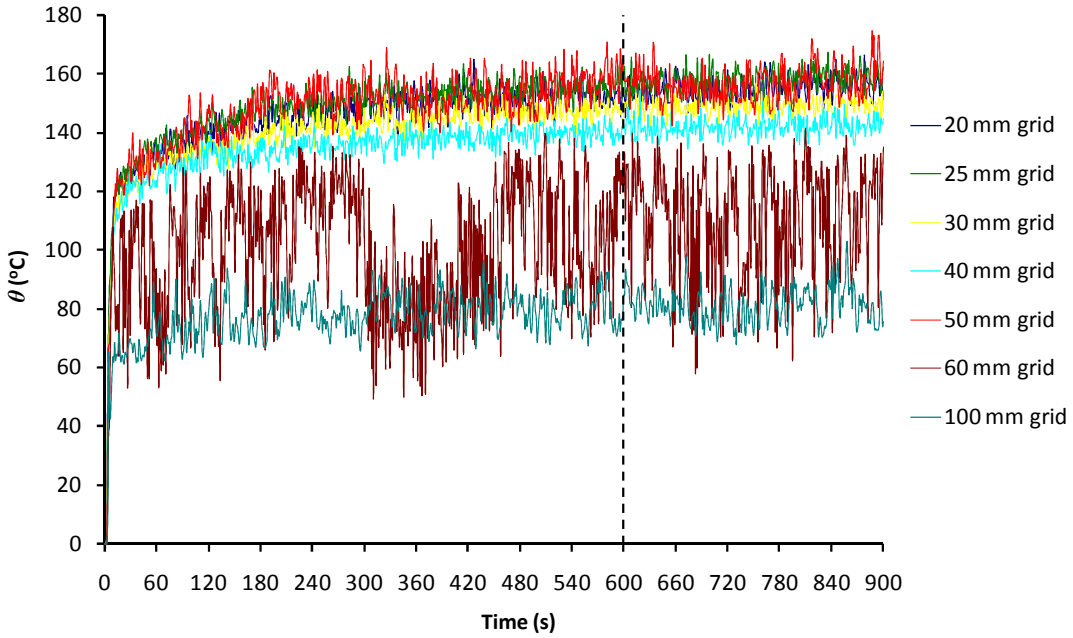

Figure 8.2: Temperature above ambient 10 mm below the spill edge versus time

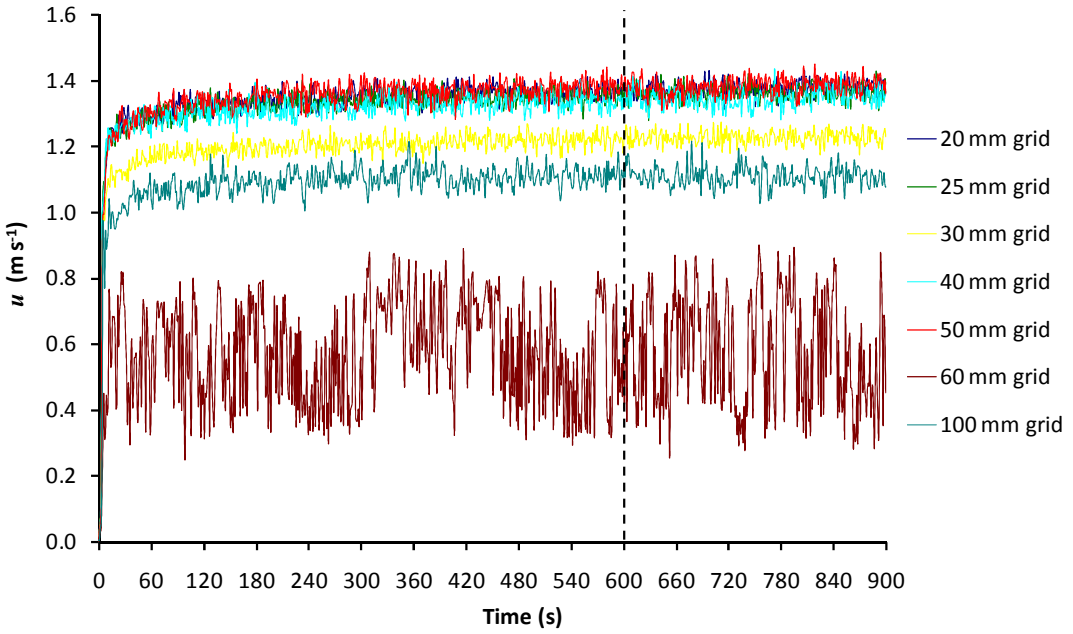

Figure 8.3: Velocity 10 mm below the spill edge versus time

A comparison between the prediction and the experiment in terms of the vertical temperature profiles (above ambient) below the spill edge is shown over two figures to enable a comparison to be more easily made. Figure 8.4 shows a comparison of the predictions with grid sizes of 100, 60 and 50 mm respectively (i.e. Simulations SC1 to SC3). Figure 8.5 shows a comparison of the predictions with grid sizes of 40, 30, 25 and 20 mm respectively (i.e. Simulations SC4 to SC7).

Figure 8.4 shows that for coarse grid sizes, namely 100 mm and 60 mm, there is poor agreement between the prediction and the experiment in terms of the shape and absolute values of the predicted temperature profiles. There is reasonable agreement between the prediction and the experiment when a 50 mm grid size was used, however, the resolution of the shape of the profile is rather discrete in nature, due to the relatively coarseness of the grid compared to the measurement interval below the spill edge in the experiment (i.e. every 10 mm).

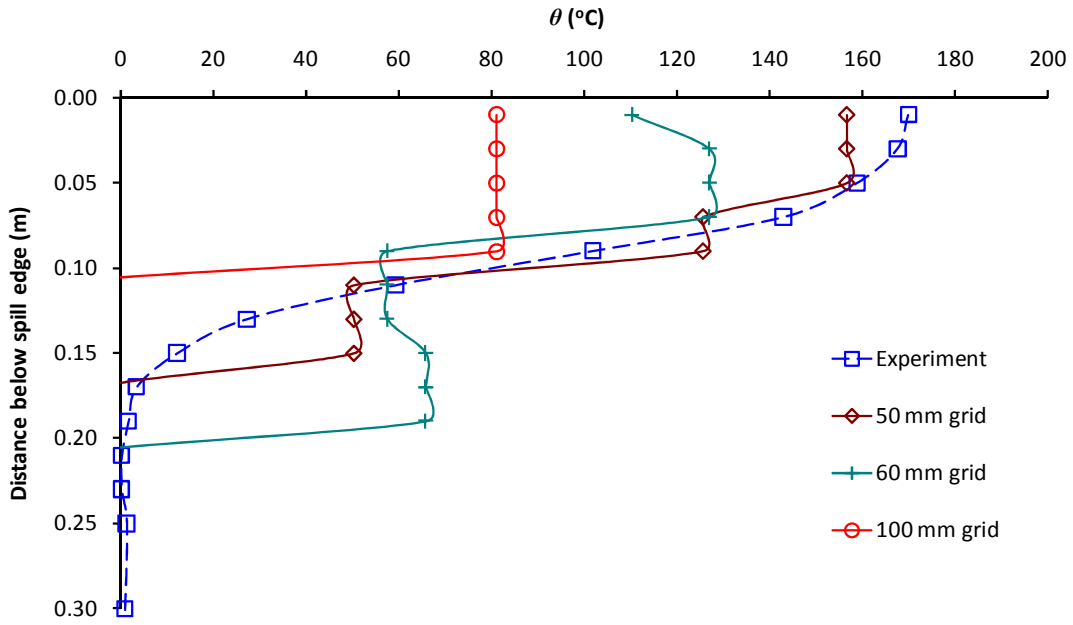

Figure 8.4: Comparison of predicted temperature profiles with experiment

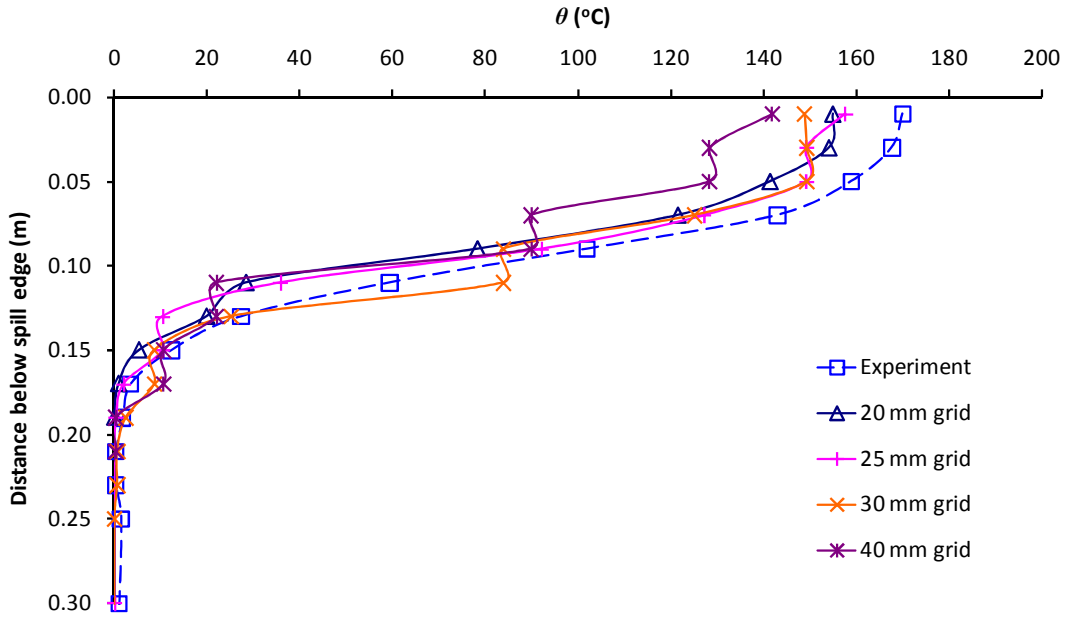

Figure 8.5: Comparison of predicted temperature profiles with experiment

Figure 8.5 shows that the agreement between the prediction and the experiment generally improves as the grid size is reduced, with the predictions for grid sizes of 20 and 25 mm being very similar, with the shape of these profiles also being similar to the experiment. However, these profiles tend to slightly under predict the temperature in the experiment. It is possible that this slight under prediction may be due to radiative warming of the bare wire thermocouples in the experiment, which have only been partially accounted for by using a local ambient at the base of Column C, giving rise to slightly higher measured temperatures that are not accounted for in FDS. The under prediction could also be due to the assumption made for radiative fraction of IMS in FDS, as a lower radiative fraction would give rise to a higher predicted temperature. Varying the assumed thermal properties of CFI board may provide a better prediction of the experiment, although a sensitivity analysis was not done here. Considering these uncertainties, the predicted temperature profiles of the flow below the spill edge for simulations with grid sizes of 20 and 25 mm can be considered to representative of the experiment.

A similar comparison can be made between the prediction and the experiment in terms of velocity profiles below the spill edge. Figure 8.6 shows a comparison of the predictions with grid sizes of 100, 60 and 50 mm respectively (i.e. Simulations SC1 to SC3). Figure 8.7 shows a comparison of the predictions with grid sizes of 40, 30, 25 and 20 mm respectively (i.e. Simulations SC4 to SC7). Figure 8.6 shows that for coarse grid sizes of 100 mm and 60 mm there is poor agreement between the prediction and the experiment in terms of the shape and the absolute values of the predicted velocity profiles. There is reasonable agreement between the prediction and the experiment in terms of peak velocity when a 50 mm grid size was used, however, the resolution of the shape of the profile is again very discrete in nature, due to the relatively coarseness of the grid compared to the measurement interval below the spill edge in the experiment.

Figure 8.7 shows that agreement between the prediction and the experiment generally improves when the grid size is reduced, with predictions for grid sizes of 20 and 25 mm both providing very good agreement with the experiment, with the shape of these profiles also being similar to the experiment, if a little more discrete in nature.

The predicted velocity profiles of the flow below the spill edge for simulations with grid sizes of 20 and 25 mm can be considered to representative of the experiment.

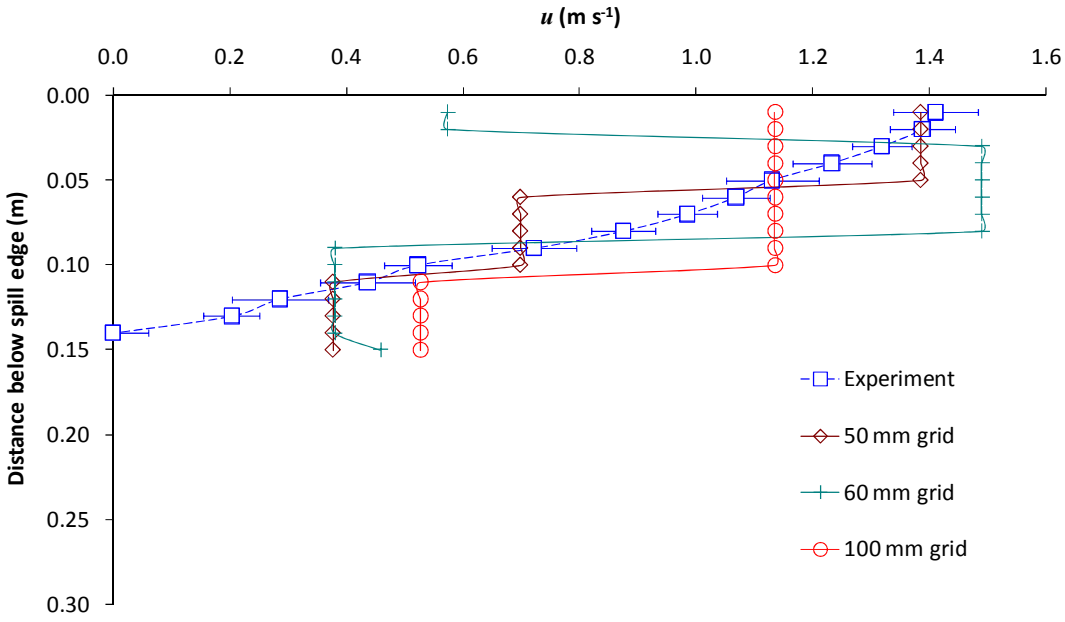

Figure 8.6: Comparison of predicted velocity profiles with experiment

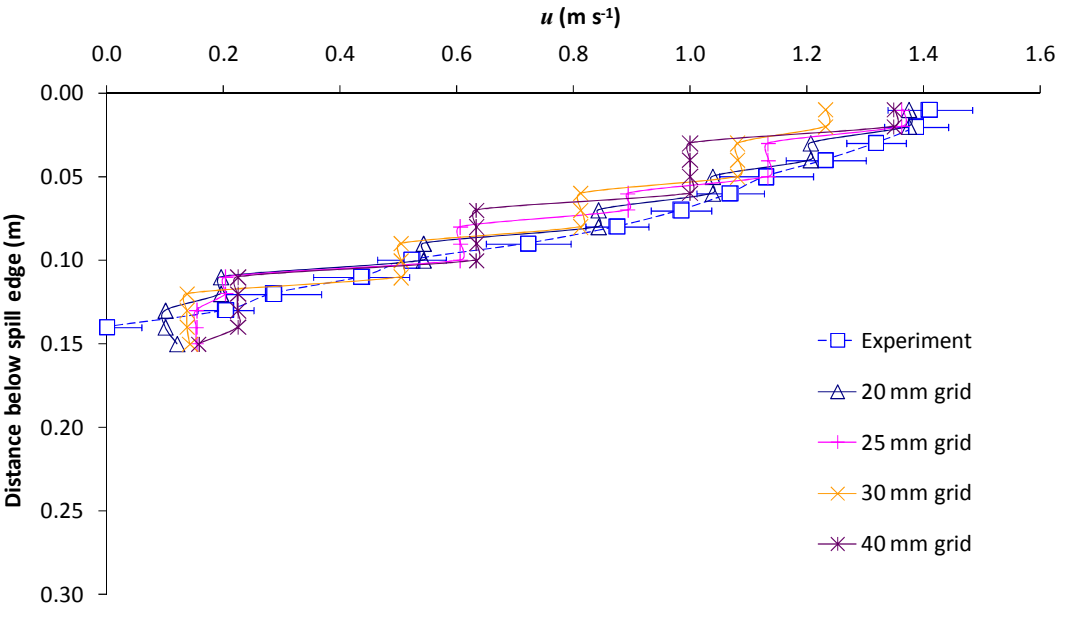

Figure 8.7: Comparison of predicted velocity profiles with experiment

Figure 8.8 shows a comparison between the prediction and experiment in terms of $\dot{m}_s$, with predictions made with grid sizes of 20 and 25 mm respectively. Figure 8.8 shows that steady conditions for $\dot{m}_s$ are predicted earlier than for velocity and temperature (i.e. from approximately 150 s). It appears that this bulk measurement is not so sensitive to differences in velocity and temperature when combined in the integration.

Figure 8.8 shows that the predictions of $\dot{m}_s$ tend to under predict the experiment by approximately 15%, with the simulation using a 25 mm grid size giving a slightly better match with the experiment. This under prediction is possibly due to differences in the assumed location of the layer base below the spill edge between the prediction (using the "MASS FLOW +" command) and the experiment (where the measured velocity was zero). However, since the velocity and temperature profiles below the spill edge (which are used in the planar integration to predict $\dot{m}_s$) are close to the experiment, simulations with grid sizes of 20 and 25 mm can still be considered to representative of the plume source below the spill edge.

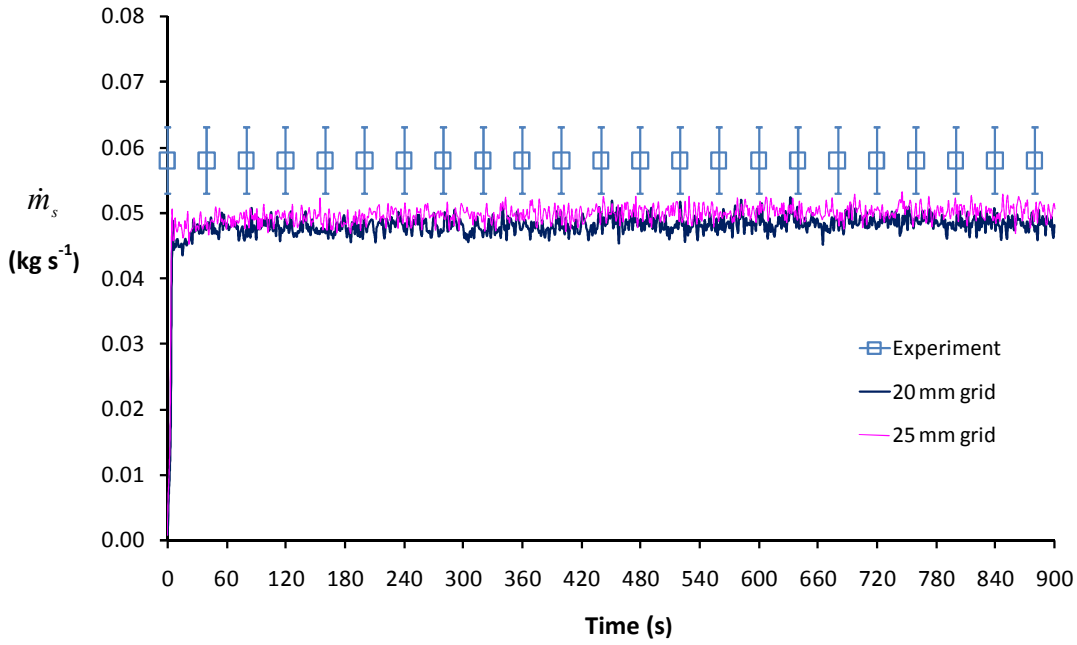

Figure 8.8: Comparison of $\dot{m}_s$ with experiment for Simulations SC6 to SC7

The above analysis indicates that when grid sizes of 20 or 25 mm are used there are no significant differences in the prediction of the flow below the spill edge and either could be used in subsequent simulations of the spill plume. However, if computational run times are considered, simulations with a grid size of 20 mm took approximately 70 hours to complete, whereas simulations with a grid size of 25 mm took approximately 25 hours to complete (using a single processor). There appears to be little benefit in using a 20 mm grid size over a 25 mm grid considering that the required computational run time is almost three times longer. Therefore, a 25 mm grid size was chosen for all subsequent simulations of the flows from the fire compartment and below the spill edge to describe the plume source.

8.1.3 3-D balcony spill plume entrainment

Previous experimental work [40,48,68] and an earlier JASMINE study [44] that utilised a smoke collecting hood to measure (or predict) entrainment, highlighted an interaction between the plume and the hood in some cases. This interaction caused a recirculation of the flow in the hood, additional entrainment to occur and the layer base in the hood was observed to be non-uniform. This effect occurred in hoods which were relatively narrow, with a width similar to the fire compartment opening. In this study the hood was made deliberately larger than in previous work and was double the cross-sectional area of the hood used by Harrison and Spearpoint [40]. The effect of increasing the size of the hood minimised any significant recirculation and the layer base was observed to be reasonably uniform for the majority experiments. Some recirculation and non–uniformity of the layer base was observed for those experiments with a very high height of rise where "plug-holing" was occurring, however, these have been ignored in the analysis. Therefore, as the hood appeared to have a minimal effect on the measured mass flow rate, the FDS predictions did not require a hood to be modelled as it could be more efficiently obtained from integration of the velocity and temperature predictions over specified horizontal planar areas of the flow domain at specific heights of rise. This allowed multiple predictions of $\dot{m}_{p,3D}$ to be obtained from a single simulation. Details of the modelling procedure used and the assumptions made using this approach are described below.

8.1.3.1 Modelled geometry

The modelled geometry and assumptions made for the fire compartment of the scale model were the same as described in section 8.1.2.1. However, a greater range of fire compartment geometries were examined in this aspect of the modelling.

8.1.3.2 Computational domain

A larger computational domain than that described in section 8.1.2.2 was required to capture the rising plume above the spill edge for the heights of rise of plume examined in the experiment. Preliminary simulations were carried out to determine (by inspection) the required size of the domain so that the rising plume was contained within the domain over the height of rise examined with no mass loss from the sides.

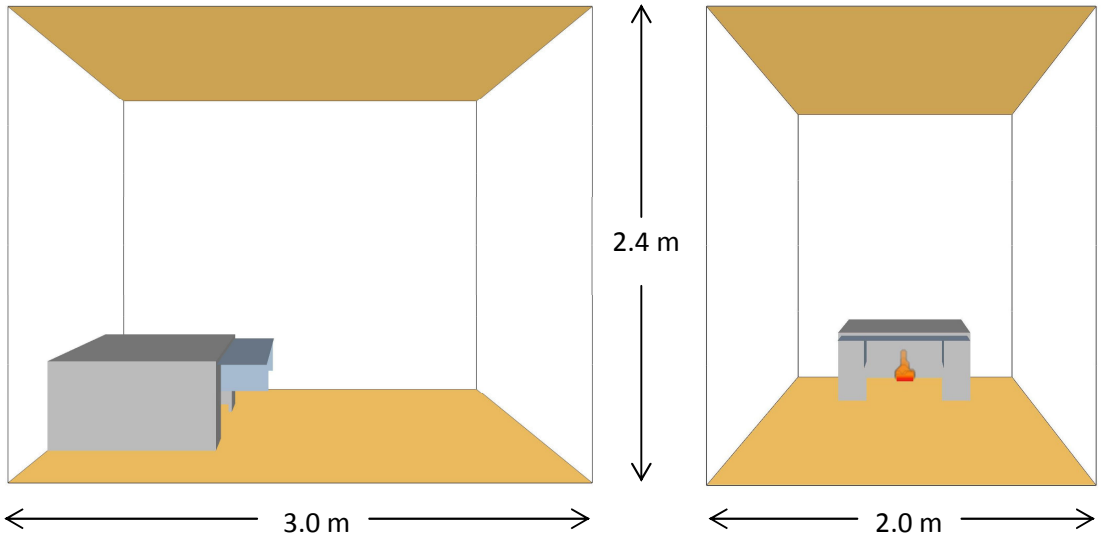

Figure 8.9: An example of the modelled geometry and computational domain

The size of computational domain used was 3.0 m long by 2.0 m wide by 2.4 m high (see Figure 8.9). The domain extended horizontally beyond and vertically above the spill edge by a distance of 1.7 and 1.9 m respectively and extended 0.5 m beyond the side walls of the fire compartment. The dimensions of the domain were again chosen so that the number of grids in each dimension could be factored by 2's, 3's and 5's. The sides of the exterior boundaries of the domain were set as open boundaries and the upper and lower exterior boundaries were set as solid inert surfaces to simulate a floor and ceiling of an atrium space. The assumption of a solid ceiling to the domain

also minimised numerical instabilities of the solution which occurred when an open boundary was assumed for the upper boundary in preliminary simulations.

The computational domain was then divided up into several separate domains to enable parallel processing of the problem to reduce computational run times. A number of different domain configurations were attempted, particularly dividing the flow domain surrounding the fire compartment, such that areas remote from the compartment could be assigned a coarser grid size. This led to difficulties in achieving any sort of result using the parallel version of FDS using the UCSC due to numerical instabilities causing the simulation to abort almost immediately. These numerical instabilities continued to occur even when later versions of FDS were compiled on the UCSC (e.g. version 5.1.6).

When identical input files (that gave numerical instabilities using the parallel version) were run using the serial version of FDS, no numerical instabilities occurred. Unfortunately, the computational run times using the serial version of FDS was so large (in the order of several weeks) that this approach was not viable for the series of simulations. It is unclear why there was inconsistency in the running of FDS for identical input files, possibly due to differences in the operating systems used for the serial and parallel versions. However, through trial and error, a computational domain configuration was identified that enabled a result to be achieved using the parallel version of FDS on the UCSC and shown in Figure 8.10.

Figure 8.10 shows that the domain was split in four separate computational domains each with dimension of 3.0 m long by 2.0 m wide by 0.6 m high. It was necessary for the volume and aspect ratio of each domain to be identical to achieve a result. Domain 1 encompassed the flow from the fire compartment, below the spill edge and in the rotation region. Domains 2 to 4 dealt with the plume above the spill edge and into the free ends of the plume.

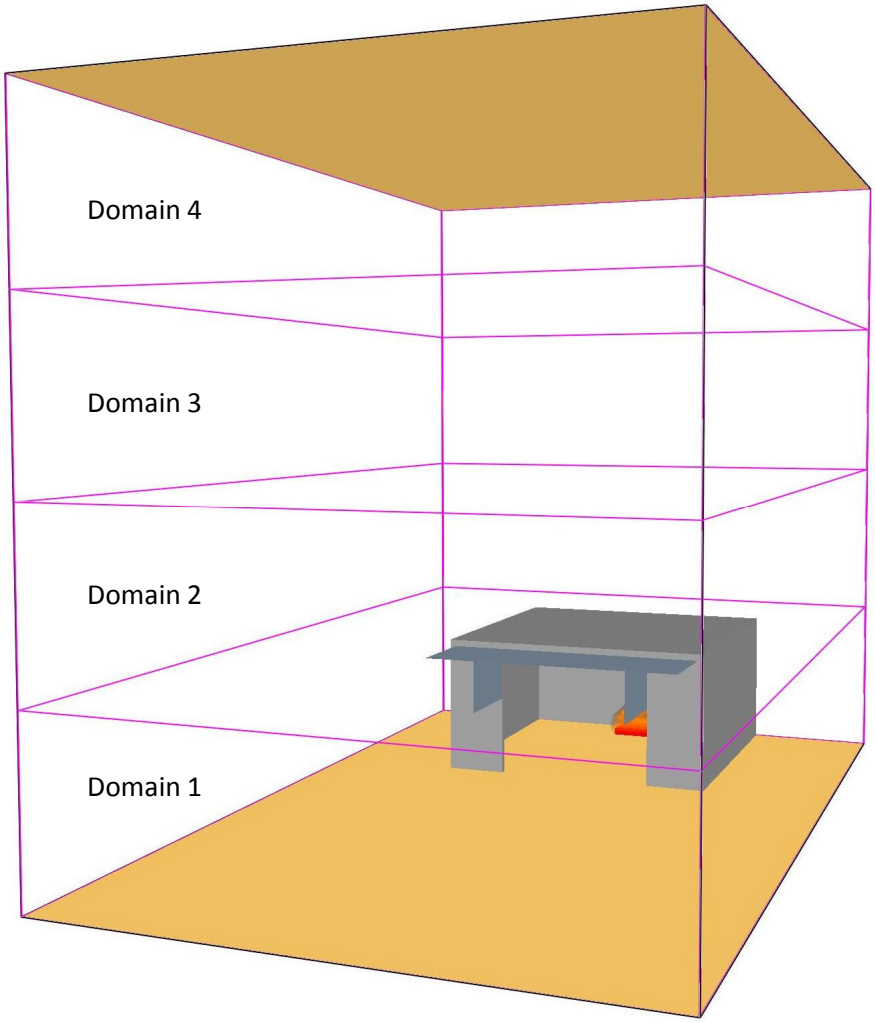

Figure 8.10: Configuration of the multiple computational domains

8.1.3.3 Fire source

The fire source within the compartment was assumed to be the same as that described in section 8.1.2.3 (i.e. a burner). The area of the burner was varied to give the desired total heat output (see fire areas in Table 5.2) as part of the parametric analysis.

8.1.3.4 Predictions

Temperature and velocity slices were generated in Smokeview in horizontal planes at each height of rise examined, and in a vertical plane centrally through the domain. The slices provided an overall velocity and temperature map throughout a plane.

Predictions of $\dot{m}_{p,3D}$ were obtained at heights of rise above the spill edge common to the experiment. These were obtained using the "MASS FLOW" command in FDS over a specified rectangular planar area, similar to the approach used in the FDS modelling by Lougheed *et al.* [71]. However, Lougheed *et al.* determined $\dot{m}_{p,3D}$ over the horizontal cross-sectional area of the entire domain, whereas in this study the area specified was for the cross-sectional area occupied by the plume at each height of rise (similar to the approach used by Chow and Li [100]). Preliminary simulations demonstrated that $\dot{m}_{p,3D}$ was up to 50 % higher (at low heights of rise of plume) if the cross-sectional area of the entire domain was used in the integration rather than that of the plume. This additional mass is due to the movement of ambient air in the domain remote from the plume which is incorporated in the integration when considering the entire flow domain.

The maximum cross-sectional area occupied by the plume was determined by inspection using slice files of temperature at each height of rise during the simulation (see Figure 8.11). A temperature contour of two degrees above ambient was used in the analysis to highlight this area. When considering $\dot{m}_{p,3D}$ a simulation time of 240 s was deemed sufficient for steady state conditions to be reached and was used for the series of simulations (see below).

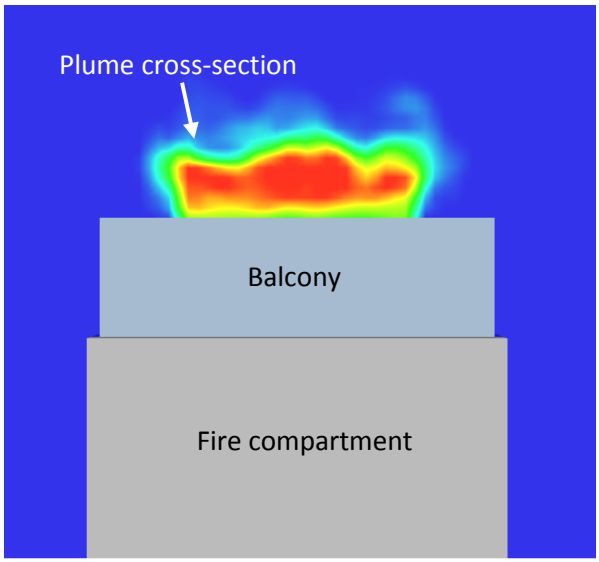

Figure 8.11: Plan view of the cross-sectional area occupied by the plume

8.1.3.5 Grid sensitivity analysis for Domains 2 to 4

Following the above analysis a grid size of 25 mm was used for Domain 1. However, as a larger grid size could be appropriate for the plume above the spill edge due to the larger turbulent eddies produced, a grid sensitivity analysis was carried out to determine the optimum grid size for Domains 2 to 4. As FDS requires that the alignment of grids in abutting domains should have the same cross-sectional area or integral ratios, grid sizes of 25 and 50 mm were used for Domains 2 to 4 inclusive. The grid sensitivity analysis examined a geometry with an intermediate width of fire compartment opening and the same fire sizes as in the experiment (i.e. W_s = 0.6 m and $\dot{Q}_t$ = 5, 10 and 15 kW). Predictions of $\dot{m}_{p,3D}$ were made at each height of rise common to the experiment. Table 8.2 show the series of six FDS simulations for the grid sensitivity analysis for Domains 2 to 4.

Simulation	$\dot{Q}_t$ (kW)	W_s (m)	z_s (m)	Domain 1 Grid size (mm)	Domains 2 to 4 Grid size (mm)	Total number of grid elements
SE1	5.0	0.6	0.00	25	50	316800
			0.30			
			0.50			
			0.73			
			0.95			
SE2	10.0	0.6	0.00	25	50	316800
			0.30			
			0.50			
			0.73			
			0.95			
SE3	15.0	0.6	0.00	25	50	316800
			0.30			
			0.50			
			0.73			
			0.95			
SE4	5.0	0.6	0.00	25	25	921600
			0.30			
			0.50			
			0.73			
			0.95			
SE5	10.0	0.6	0.00	25	25	921600
			0.30			
			0.50			
			0.73			
			0.95			
SE6	15.0	0.6	0.00	25	25	921600
			0.30			
			0.50			
			0.73			
			0.95			

Table 8.2: The series of grid sensitivity simulations for Domains 2 to 4

Figure 8.12 shows a plot of $\dot{m}_{p,3D}$ with respect to time at each height of rise of plume examined in Simulation SE5 and demonstrates that a simulation time of 240 s was sufficient for steady state conditions to be reached. Figure 8.12 shows that the predictions of $\dot{m}_{p,3D}$ are reasonably steady after approximately 120 s and therefore the predictions were time averaged over a 60 s time interval (as in the experiment) between 180 and 240 s.

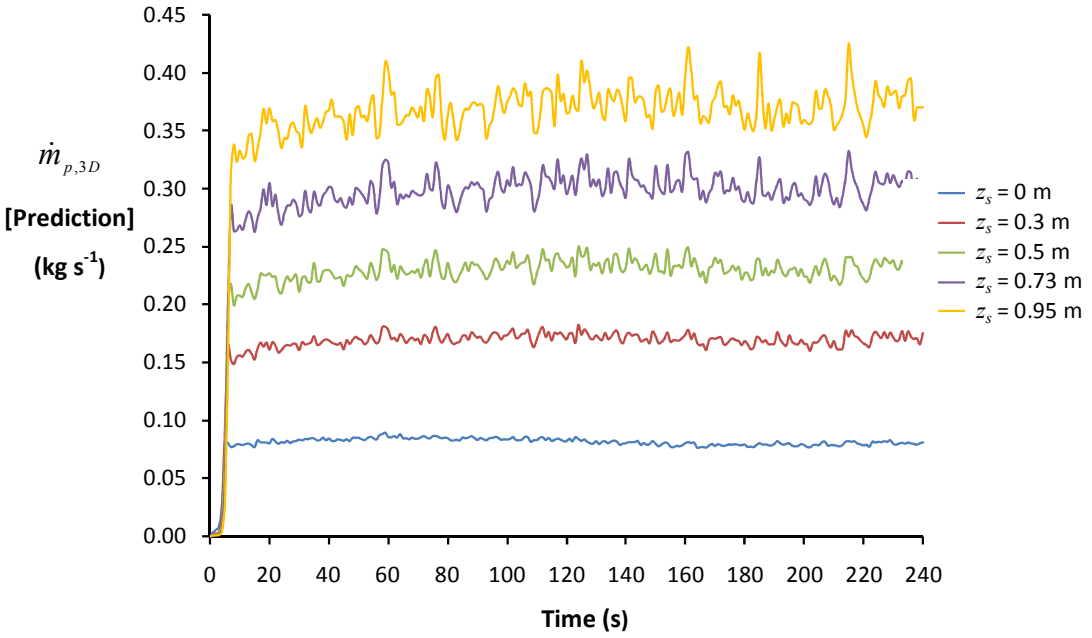

Figure 8.12: $\dot{m}_{p,3D}$ with respect to time for each z_s examined (Simulation SE5)

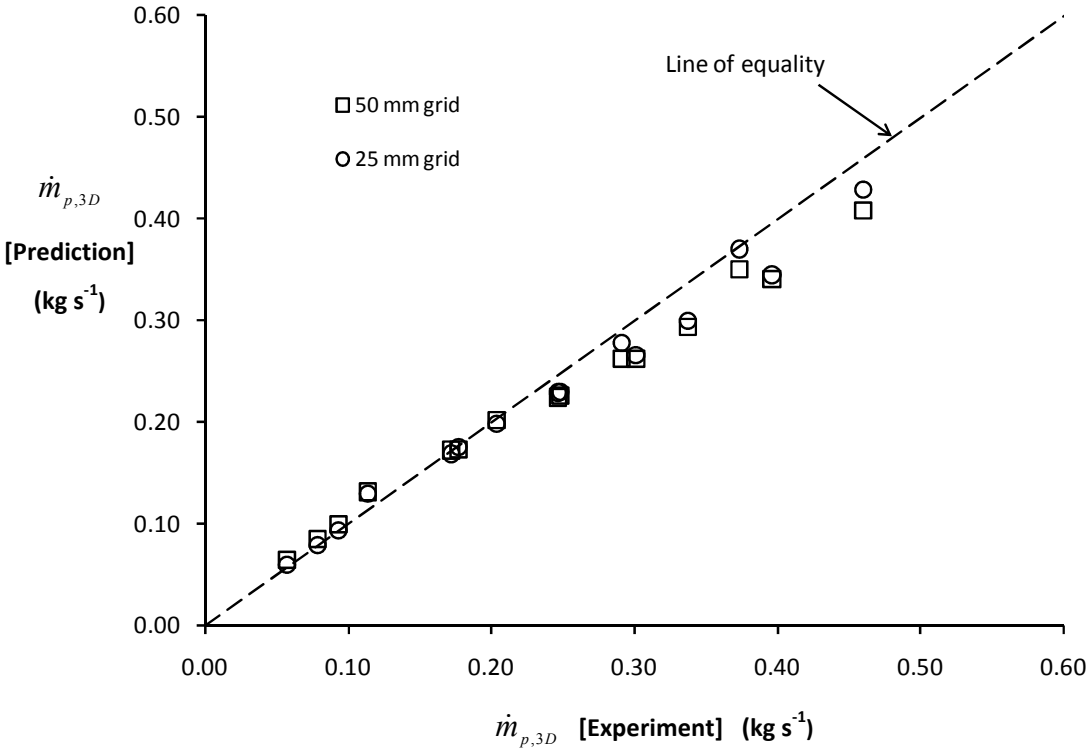

Figure 8.13: Comparison of $\dot{m}_{p,3D}$ with the experiment (Simulations SE1 to SE6)

Figure 8.13 shows the predictions of $\dot{m}_{p,3D}$ when either a 25 or 50 mm grid size was used for Domains 2 to 4, which are plotted against the experiment. Figure 8.13 shows that for values of $\dot{m}_{p,3D}$ below 0.25 kg s^{-1} (which were obtained at relatively low heights of rise of plume) there is little difference in the predictions when either a 25 or 50 mm grid was used. All of these predictions provide excellent agreement with the experiment.

For values of $\dot{m}_{p,3D}$ above 0.25 kg s^{-1} (which were obtained at higher heights of rise), there is a general trend for the predictions to somewhat under predict entrainment (up to approximately 10%) with the predictions using a 50 mm grid being slightly lower than when a 25 mm grid was used. This could possibly be due to the 25 mm grid providing a better resolution of the entrainment into the ends of the plume which become more significant at higher heights of rise. Therefore, following this analysis a 25 mm grid size was chosen to be appropriate for Domains 2 to 4 as it provides a reasonably good prediction of the experiment for the conditions studied. Thus, the main series of FDS simulations used a uniform grid size of 25 mm for the entire computational domain (i.e. Domains 1 to 4 inclusive) giving a total of 921,600 grid elements. Four processors were used for these simulations (one processor per domain) giving rise to an execution time of approximately 5.5 days.

8.1.3.6 The series of FDS simulations

The series of FDS simulations complemented those already carried out as part of the grid sensitivity analysis. The simulations examined plumes generated from a wide, intermediate and narrow compartment opening (i.e. W_s = 1.0, 0.6 and 0.2 m) with the same range of fire sizes as examined in the experiment (i.e. $\dot{Q}_t$ = 5, 10 and 15 kW). Predictions of $\dot{m}_{p,3D}$ were determined at identical heights of rise to the experiment (i.e. z_s = 0 to 0.95 m). Table 8.3 shows the series of nine simulations, including those which used a 25 mm grid size in the sensitivity analysis for completeness.

Appendix N gives an example of the FDS input file used for these simulations (Simulation SE5).

Simulation	$\dot{Q}_t$ (kW)	W_s (m)	z_s (m)	Domains 1 to 4 Grid size (mm)
SE4	5.0	0.6	0.00	25
			0.30	
			0.50	
			0.73	
			0.95	
SE5	10.0	0.6	0.00	25
			0.30	
			0.50	
			0.73	
			0.95	
SE6	15.0	0.6	0.00	25
			0.30	
			0.50	
			0.73	
			0.95	
SE7	5.0	0.2	0.00	25
			0.30	
			0.50	
			0.73	
			0.95	
SE8	10.0	0.2	0.00	25
			0.30	
			0.50	
			0.73	
			0.95	
SE9	15.0	0.2	0.00	25
			0.30	
			0.50	
			0.73	
			0.95	
SE10	5.0	1.0	0.00	25
			0.30	
			0.50	
			0.73	
SE11	10.0	1.0	0.00	25
			0.30	
			0.50	
			0.73	
S12	15.0	1.0	0.00	25
			0.30	
			0.50	
			0.73	

Table 8.3: The series of FDS simulations for the 3-D balcony spill plume

8.1.3.7 FDS simulation results

The predictions of plume behaviour (in Smokeview) were very similar to observed in the experiment (see section 6.3.1) and therefore a detailed description is not repeated here. Figures 8.14 and 8.15 show a 3-D velocity contour plot (0.5 m s^{-1} contour) to highlight the shape of the rising plume generated from a wide and narrow compartment opening respectively (Simulations SE11 and SE9). Predictions of $\dot{m}_{p,3D}$ for each simulation are shown in Table 8.4.

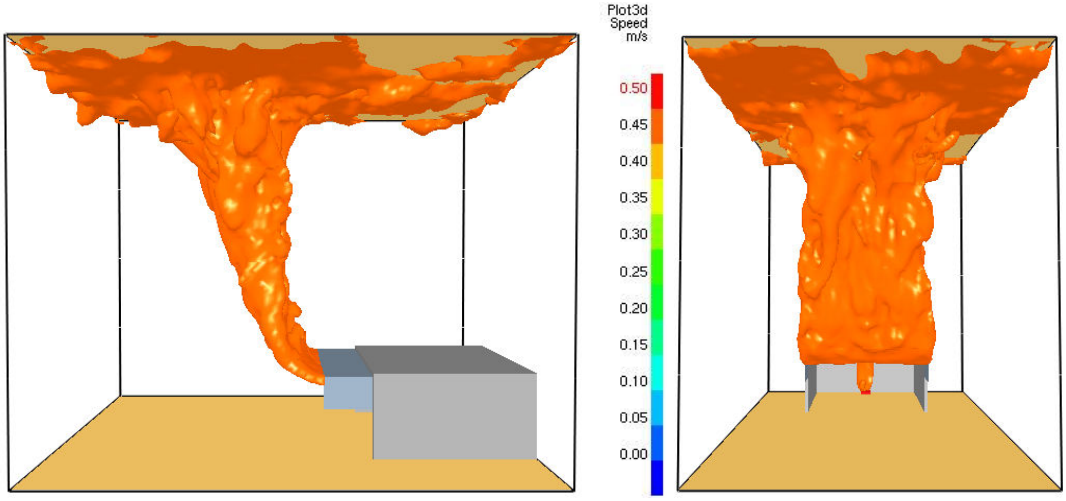

Figure 8.14: Predicted plume behaviour (W_s = 1.0 m, Simulation SE11)

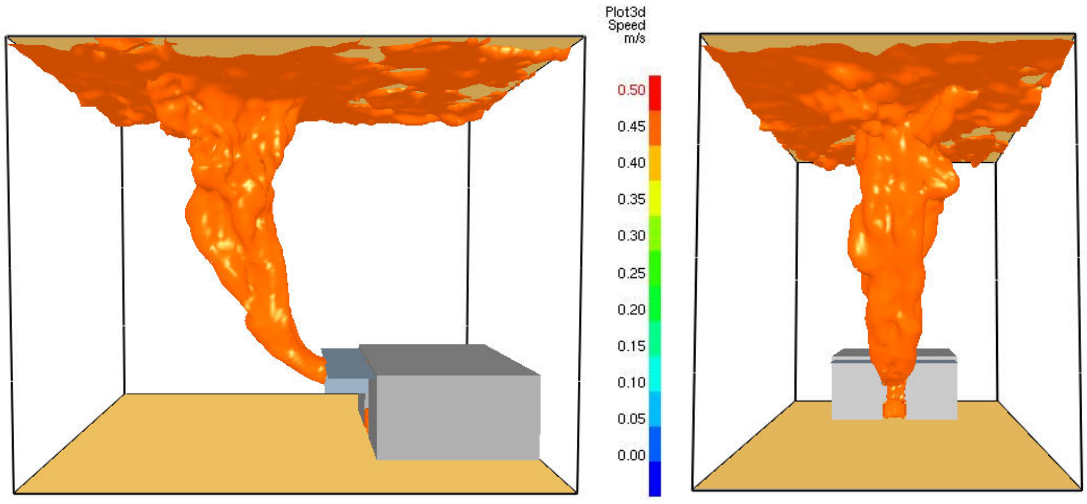

Figure 8.15: Predicted plume behaviour (W_s = 0.2 m, Simulation SE9)

Simulation	$\dot{Q}_t$ (kW)	W_s (m)	z_s (m)	$\dot{m}_{p,3D}$ (kg s^{-1})
SE4	5.0	0.6	0.00	0.061
			0.30	0.130
			0.50	0.176
			0.73	0.230
			0.95	0.279
SE5	10.0	0.6	0.00	0.079
			0.30	0.169
			0.50	0.231
			0.73	0.300
			0.95	0.371
SE6	15.0	0.6	0.00	0.095
			0.30	0.199
			0.50	0.267
			0.73	0.345
			0.95	0.429
SE7	5.0	0.2	0.00	0.038
			0.30	0.077
			0.50	0.106
			0.73	0.145
			0.95	0.181
SE8	10.0	0.2	0.00	0.054
			0.30	0.105
			0.50	0.152
			0.73	0.212
			0.95	0.270
SE9	15.0	0.2	0.00	0.057
			0.30	0.121
			0.50	0.166
			0.73	0.225
			0.95	0.288
SE10	5.0	1.0	0.00	0.077
			0.30	0.174
			0.50	0.227
			0.73	0.288
SE11	10.0	1.0	0.00	0.102
			0.30	0.223
			0.50	0.299
			0.73	0.381
S12	15.0	1.0	0.00	0.122
			0.30	0.254
			0.50	0.342
			0.73	0.434

Table 8.4: Summary of results for the series of FDS simulations

Figure 8.16 shows the predictions of $\dot{m}_{p,3D}$ for Simulations SE4 to SE12 plotted against the measured values from the experiment.

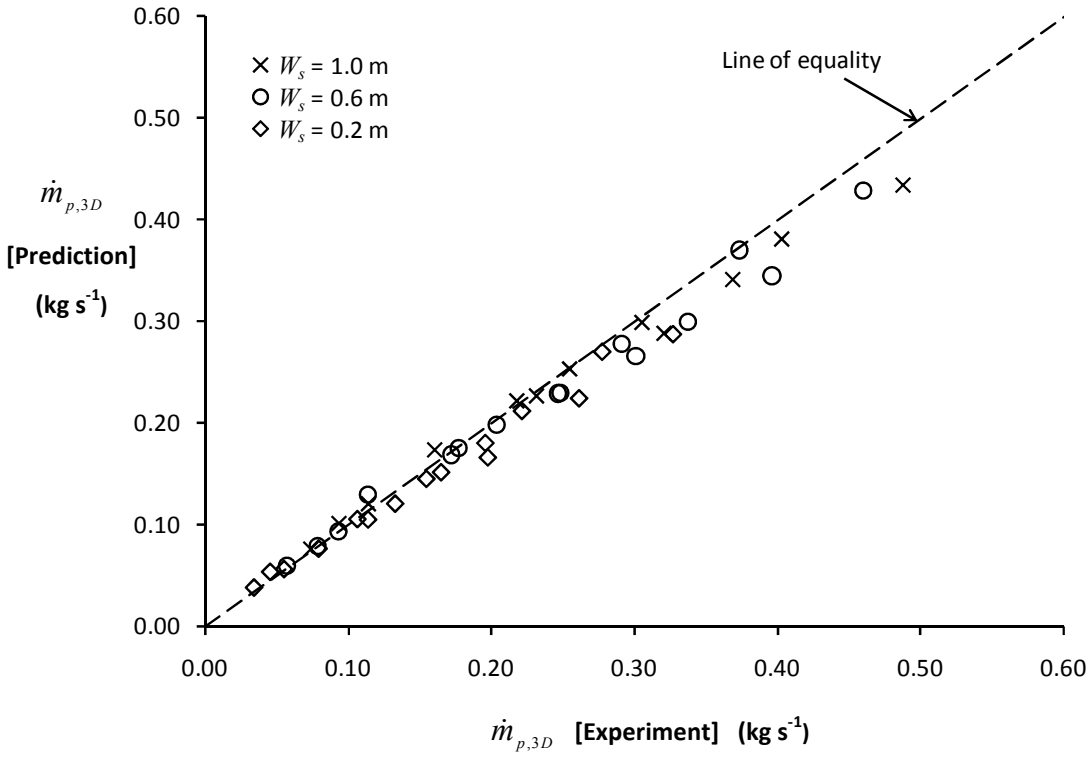

Figure 8.16: Comparison of prediction of $\dot{m}_{p,3D}$ with experiment

Figure 8.16 shows excellent agreement between the prediction and the experiment for values of $\dot{m}_{p,3D}$ below approximately 0.25 kg s^{-1} for each W_s examined. For larger values of $\dot{m}_{p,3D}$ which were mainly obtained at high heights of rise, the prediction of $\dot{m}_{p,3D}$ is slightly lower than the experiment by up to approximately 10%. However, Figure 8.16 does not reflect the greater experimental uncertainty in the height of rise of the plume at high heights of rise due to the thin nature of the smoke and fluctuations of the layer in the collecting hood. Therefore, considering these uncertainties, it appears that FDS generally provides a good prediction of 3-D balcony spill plume entrainment using a 25 mm grid size (on model scale), therefore, for full scale modelling a grid size of 0.25 m would seem reasonable for design purposes. A suitable grid size expressed in non-dimensional form is presented in section 8.1.3.9.

8.1.3.8 Modelling with a smoke collecting hood

As a check to confirm that the FDS also provides a prediction of $\dot{m}_{p,3D}$ consistent with the experimental method used (i.e. with a collecting hood above the fire compartment), the complete experimental setup described in section 4.1 was modelled for a single experiment. The simulation modelled Experiment E101 which examined a plume generated from an intermediate fire compartment opening width, fire size and height of rise of plume (i.e. $W_s = W_o = 0.6$ m, $\dot{Q}_t = 10$ kW and $z_s = 0.5$ m).

The assumptions made for the modelling of the fire compartment and fire source were the same as described in section 8.1.2. The walls and ceiling of the smoke collecting hood were assumed to be made from 10 mm thick CFI board except one of the walls which was assumed to be made from 10 mm thick acrylic sheet with the following properties [109]:

$k_{acryl} = 0.19$ W m^{-1} K^{-1}, $\rho_{acryl} = 1190$ kg m^{-3}, $c_{p,\,acryl} = 1.42$ kJ kg^{-1} K^{-1}.

The base of the collecting hood was set at 65 mm below the height of the smoke layer in the experiment. Therefore, for the prediction of $\dot{m}_{p,3D}$ to be consistent with the experimental method, the predicted layer should be just contained within the collecting hood.

The smoke exhaust vent in the hood was modelled as square exhaust vent with an equivalent area to the circular vent used in the experiment. Previous versions of FDS only allowed an exhaust vent to be specified in terms of a velocity normal to the vent surface. The version used in this study (FDS 5) allows the vent to be specified in terms of volume or mass flow rate (as well as velocity) to better deal with vent areas that do not align exactly with grid elements. FDS converts the specified volume flow rate into a velocity from the area of the vent, and for mass flow rate converts to velocity using the area of the vent and a local gas density. Therefore, for convenience, the vent was specified according to the mass flow rate measured in the experiment (i.e. $\dot{m}_{p,3D} = 0.248$ kg s^{-1}). Appendix O gives an example of the FDS input file used for this simulation (Simulation SR1).

The computational domain had dimensions of 3.1 by 2.2 by 2.75 m high so that it extended just beyond the walls and ceiling of the collecting hood (approximately 0.2 m beyond). The exterior domain boundaries were set as open boundaries except the lower boundary which was modelled as a solid inert surface. A uniform grid size of 25 mm and a simulation time of 240 s were used to be consistent with the modelling without a collecting hood.

The simulations were initially run using the parallel version of FDS on the UCSC, however, the more complex geometry again led to numerical instabilities with the simulations aborting immediately. Therefore these simulations were instead run successfully using the serial version of FDS by assuming a single domain. Each simulation took approximately 9 days to complete.

Thermocouples were modelled in locations identical to the experiment, including within the smoke collecting hood, the exhaust vent and horizontally across the plume. Temperature and velocity slices were generated in Smokeview in a vertical plane centrally through the domain. Figure 8.17 shows the modelled geometry, computational domain and thermocouples (in green).

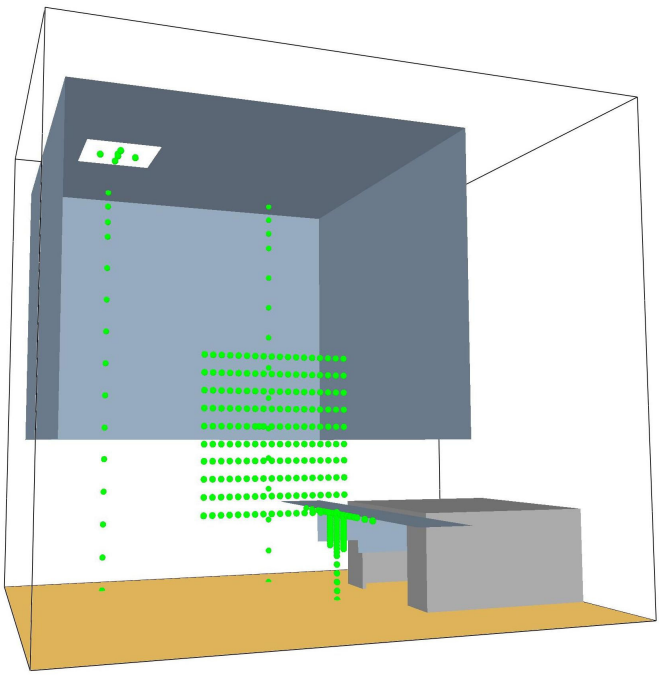

Figure 8.17: The modelled geometry, computational domain and thermocouples

Figure 8.18 shows the predicted vertical slice file in terms of temperature through the centreline of the plume for Simulation SR1.

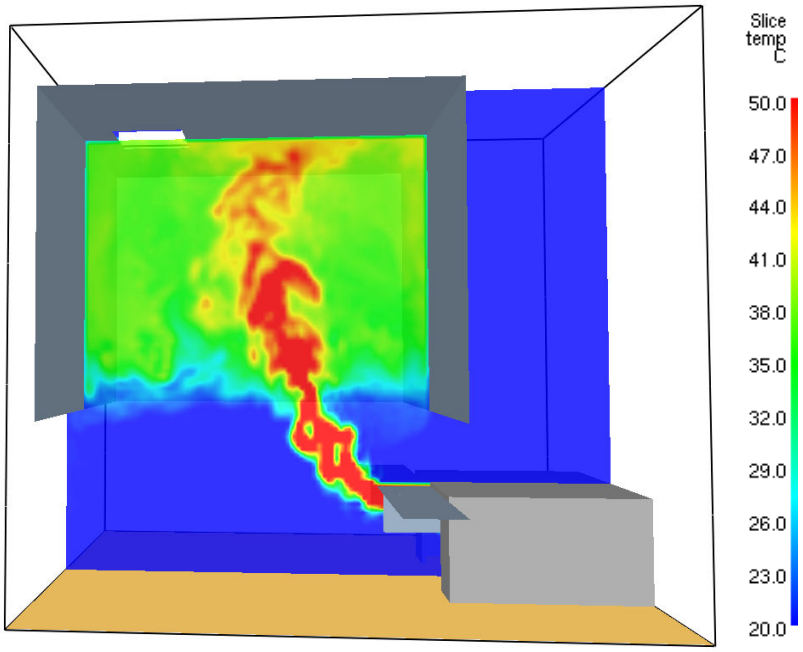

Figure 8.18: Temperature slice through centreline of plume (Simulation SR1)

Figure 8.18 shows that the smoke layer was just contained with the hood and indicates that FDS provides a prediction of entrainment that is consistent with the experiment and the numerical modelling without a collecting hood. As the exhaust vent can be specified in alternative ways, two more simulations of the same experiment were carried out, one assigned the vent in terms of volume flow rate (Simulation SR2) the other according to velocity (Simulation SR3). The volume flow rate and velocity were determined by converting the measured mass flow rate in the experiment (i.e. 0.248 kg s^{-1}) from the vent area (i.e. 0.152 m^2) and the measured temperature of the gases in the throat of the vent (i.e. 312.5 K) with specified values of 0.219 m^3 s^{-1} and 1.45 ms^{-1}. A prediction of the mass flow rate from the vent was also determined (across the horizontal planar area). Figures 8.19 and 8.20 show the predicted vertical slice files in terms of temperature through the centreline of the plume for Simulations SR2 and SR3 respectively, and demonstrate that when the vent was specified in terms of either volume flow rate or velocity the smoke layer was just contained within the collecting hood as observed in the experiment.

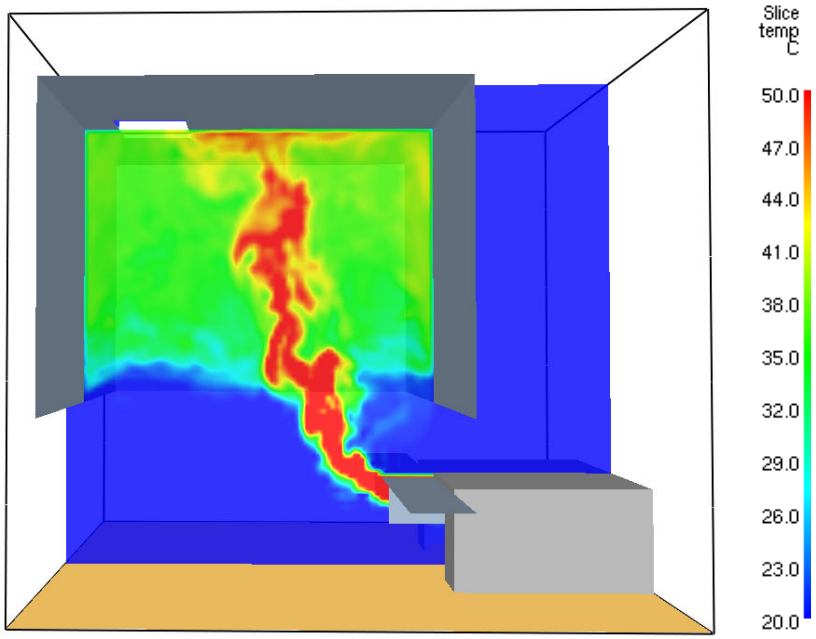

Figure 8.19: Temperature slice through centreline of plume (Simulation SR2)

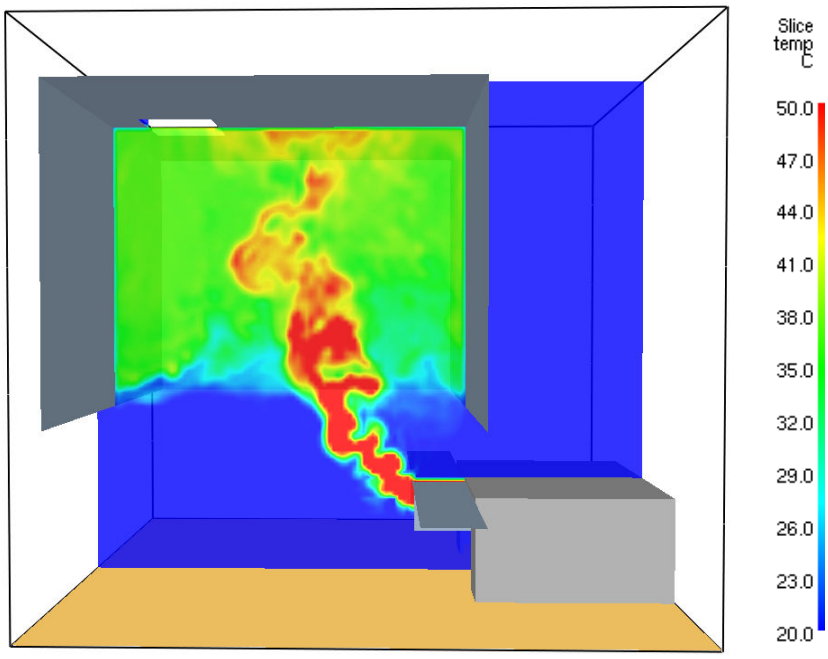

Figure 8.20: Temperature slice through centreline of plume (Simulation SR3)

The predicted mass flow rate from the vent was 0.26 kg s^{-1} for Simulations SR2 and SR3 respectively. This provided good agreement with the specified mass flow rate (i.e. 0.248 kg s^{-1}) considering that there were small differences between the modelling and the experiment in terms of the vent area (i.e. 0.008 m^2, as the modelled geometry aligns to the closest grid line) and the temperature of the gases in the vent (i.e. up to 5 °C difference). This demonstrates that FDS provides a prediction of entrainment that is consistent with the experiment and the numerical modelling without a collecting hood if the vent is specified in terms of either volume flow rate or velocity.

A full analysis of the temperature predictions in the hood is not given here as the simulation time was limited to 240 s to provide steady conditions to primarily consider mass entrainment. However, Figure 8.21 shows a comparison between the predicted temperature profiles in the hood (Columns A and B) with the experiment, and demonstrates that although the predicted temperatures in the hood were lower than the experiment, the predicted profiles approach ambient at a similar depth below the ceiling of the hood as in the experiment, which indicates a good prediction of the layer depth. Better agreement between the prediction and the experiment may be achieved if the simulation time were to be increased.

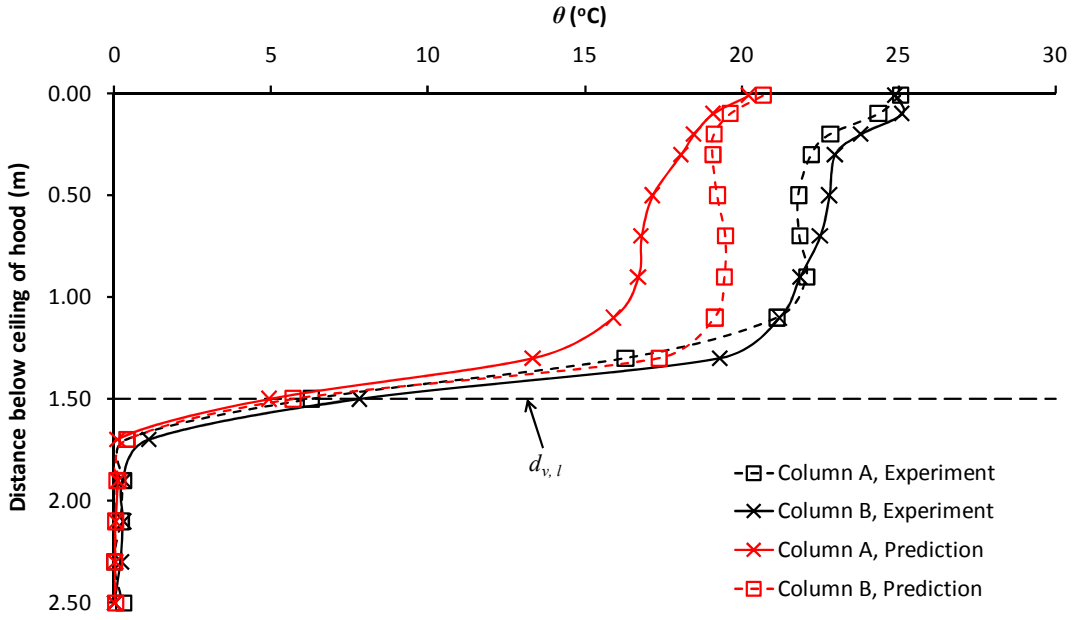

Figure 8.21: Comparison of predicted temperature profiles in the hood with experiment

8.1.3.9 Non-dimensional characteristic grid size

A suitable grid size of 0.25 m been proposed for the FDS modelling of full scale spill plumes above the spill edge (see section 8.1.3.7). The characteristic grid size can be described by the following non-dimensional expression for buoyant plumes [42]:

$$n^* = \frac{D^*}{\delta x} \qquad \textbf{(8-1)}$$

Where D^* is a characteristic plume dimension in metres [see Equation (8-2)] and δx is the grid size.

$$D^* = \left(\frac{\dot{Q}_c}{\rho_{amb} c_{p,air} T_{amb} \sqrt{g}} \right)^{2/5} \qquad \textbf{(8-2)}$$

However, Equation (8-2) essentially applies to axisymmetric plumes. An equivalent expression to describe the characteristic dimension for a line plume is given by Quintiere and Grove [136] [see Equation (8-3)].

$$D_{line}{}^* = \left(\frac{\dot{Q}'_c}{\rho_{amb} c_{p,air} T_{amb} \sqrt{g}} \right)^{2/3} \qquad \textbf{(8-3)}$$

$\dot{Q}'_c$ is the convective heat flow rate per unit length of the line plume (kW m^{-1}).

Hence, by analogy for a spill plume,

$$D^*_{spill} = \left(\frac{\frac{\dot{Q}_c}{W_s}}{\rho_{amb} c_{p,air} T_{amb} \sqrt{g}} \right)^{2/3} \quad \text{and} \quad n^*_{spill} = \frac{D_{spill}{}^*}{\delta x} \qquad \textbf{(8-4)}$$

For the range of conditions examined in the analysis D^*_{spill} ranged between 0.02 and 0.13 m. Hence, for a grid size of 25 mm (i.e. 0.025 m) the equivalent non-dimensional expression for a spill plume n^*_{spill} ranged between 0.9 and 5.1. As the minimum value of n^*_{spill} represents the coarsest grid resolution from which the prediction provides good agreement with the experiment it appears that a grid resolution of $n^*_{spill} \geq 0.9$ can be considered to be appropriate for design purposes.

8.1.4 3-D Adhered spill plume entrainment

The modelling approach used for the 3-D adhered plume was essentially the same as that used for the 3-D balcony spill plume. The assumptions made for the fire source and compartment were the same with the exception that no balcony or channelling screens were modelled. The only significant difference was the modelling of a wall above the top of the fire compartment opening (i.e. the spill edge) which extended across the full width and height of the domain and was assumed to be made from 10 mm thick CFI board. The size and characteristics of the computational domain (i.e. four separate domains) were also the same and a uniform grid size of 25 mm was used for the simulations. Figure 8.22 shows an example of the modelled geometry and computational domain.

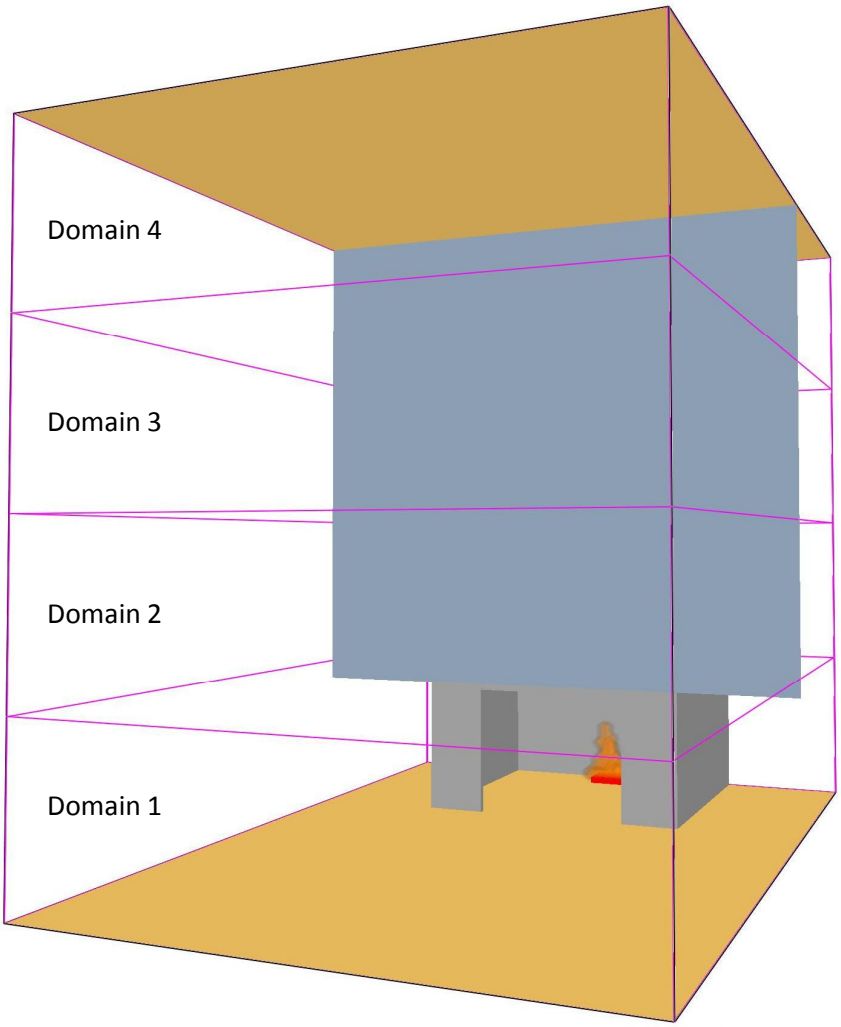

Figure 8.22: An example of the modelled geometry and computational domain

8.1.4.1 The series of FDS simulations

The series of FDS simulations examined plumes generated from a wide, intermediate and narrow compartment opening (i.e. W_s = 1.0, 0.6 and 0.2 m) with the same range of fire sizes as examined in the experiment (i.e. $\dot{Q}_t$ = 5, 10 and 15 kW). Predictions of $\dot{m}_{p,3D}$ were determined from horizontal planar areas of the domain occupied by the plume at identical heights of rise to the experiment (i.e. z_s = 0 to 0.95 m).

Table 8.5 shows the series of nine simulations. Appendix P gives an example of the FDS input file used for these simulations (Simulation SE14).

Simulation	$\dot{Q}_t$ (kW)	W_s (m)	z_s (m)	Domains 1 to 4 Grid size (mm)
SE13	5.0	0.6	0.00	25
			0.30	
			0.50	
			0.73	
			0.95	
SE14	10.0	0.6	0.00	25
			0.30	
			0.50	
			0.73	
			0.95	
SE15	15.0	0.6	0.00	25
			0.30	
			0.50	
			0.73	
			0.95	
SE16	5.0	0.2	0.00	25
			0.30	
			0.50	
			0.73	
			0.95	
SE17	10.0	0.2	0.00	25
			0.30	
			0.50	
			0.73	
			0.95	
SE18	15.0	0.2	0.00	25
			0.30	
			0.50	
			0.73	
			0.95	
SE19	5.0	1.0	0.00	25
			0.30	
			0.50	
			0.73	
			0.95	
SE20	10.0	1.0	0.00	25
			0.30	
			0.50	
			0.73	
			0.95	
SE21	15.0	1.0	0.00	25
			0.30	
			0.50	
			0.73	
			0.95	

Table 8.5: The series of FDS simulations for the 3-D adhered plume

8.1.4.2 FDS simulation results

The predictions of plume behaviour (in Smokeview) were very similar to observed in the experiment (see section 7.3.1) and therefore a detailed description is not repeated here.

Figures 8.23 to 8.25 show 3-D velocity contour plots (0.5 ms^{-1} contour) of plumes generated from a wide, intermediate and narrow compartment opening width respectively (Simulations SE20, SE14 and SE17) and demonstrate that the plume tends to detach from the wall as the width of the opening decreases. For a plume generated from an intermediate width opening, Figure 8.24 shows a narrowing of the plume above the spill edge, consistent with the experiment (see Figure 7.7b).

Figures 8.26 to 8.28 show vertical velocity slice files through the centreline of the plume and demonstrate that the predicted behaviour close to wall above the spill edge was very similar to the experiment for plumes generated from a wide, intermediate and narrow compartment opening width (i.e. Simulations SE20, SE14 and SE17 and Experiments E209, E215 and E221 respectively). The layer flows below the spill edge appear to be shallower in the slice file images compared to the experiment, however, this is misleading due to the velocity being chosen as the parameter in question (as this best shows the detachment close to the wall), the range of the scale used and the perspective of the image. The predicted approach flow layer depths were very similar to that in the experiment, for example, see Figure 8.29 which shows the the vertical temperature slice file for Simulation SE17.

Predictions of $\dot{m}_{p,3D}$ for each simulation are shown in Table 8.6.

Figure 8.30 shows the predictions of $\dot{m}_{p,3D}$ for Simulations SE13 to SE21 plotted against the measured values from the experiment.

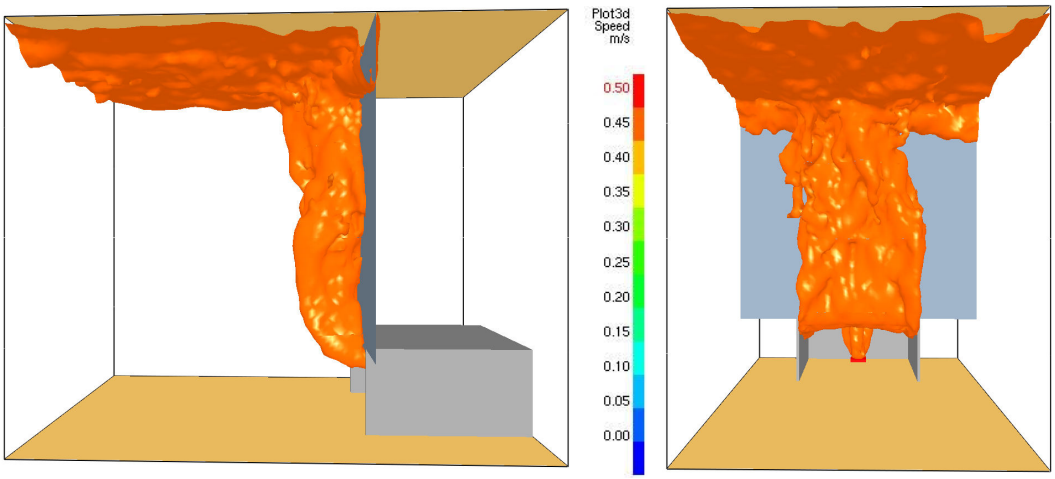

Figure 8.23: Predicted plume behaviour (W_s = 1.0 m, Simulation SE20)

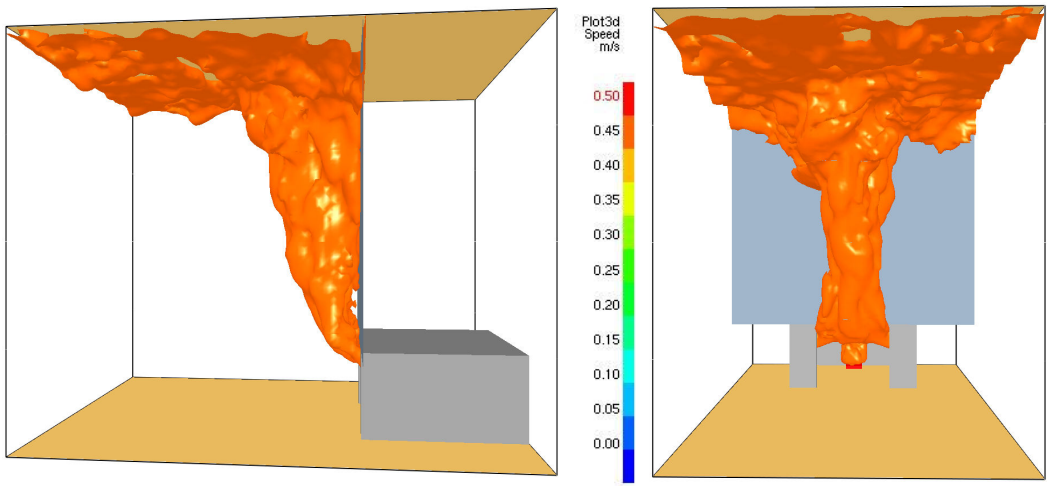

Figure 8.24: Predicted plume behaviour (W_s = 0.6 m, Simulation SE14)

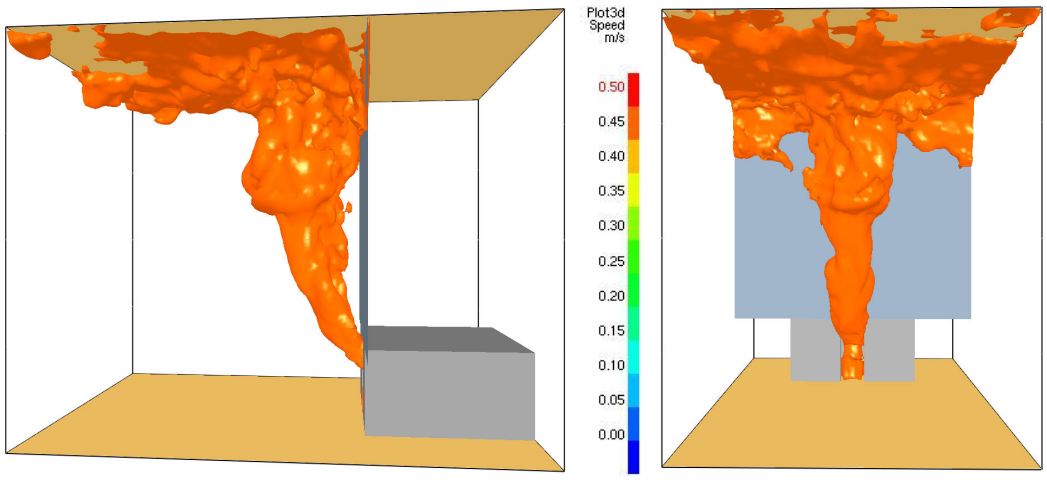

Figure 8.25: Predicted plume behaviour (W_s = 0.2 m, Simulation SE17)

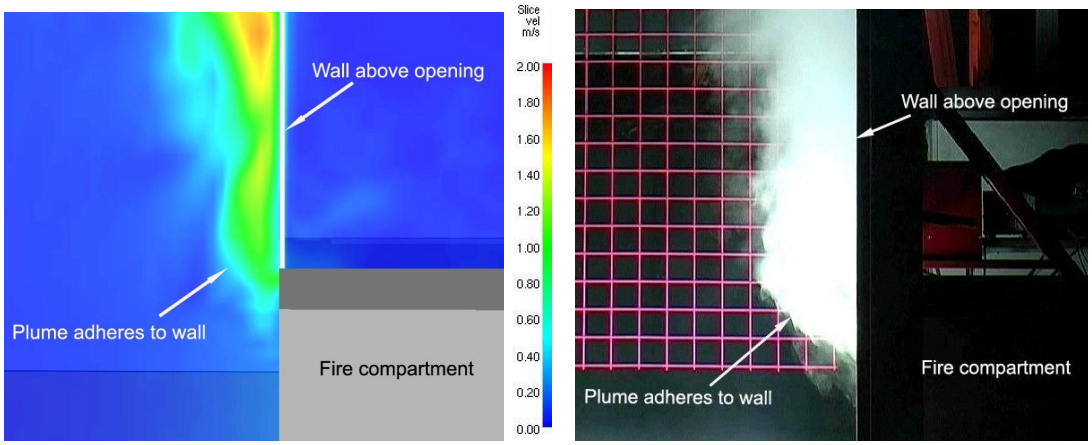

a) Simulation SE20 b) Experiment E209

Figure 8.26: Comparison of predicted plume behaviour with experiment (W_s = 1.0 m)

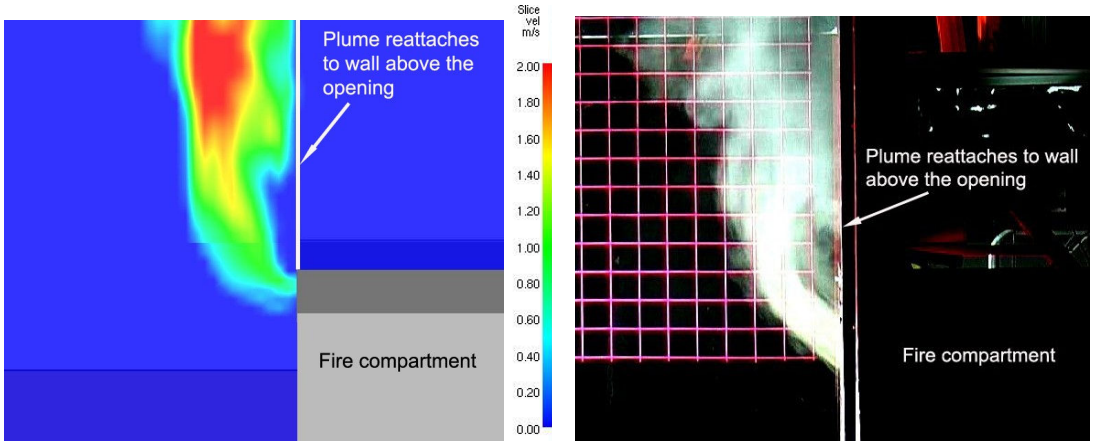

a) Simulation SE14 b) Experiment E215

Figure 8.27: Comparison of predicted plume behaviour with experiment (W_s = 0.6 m)

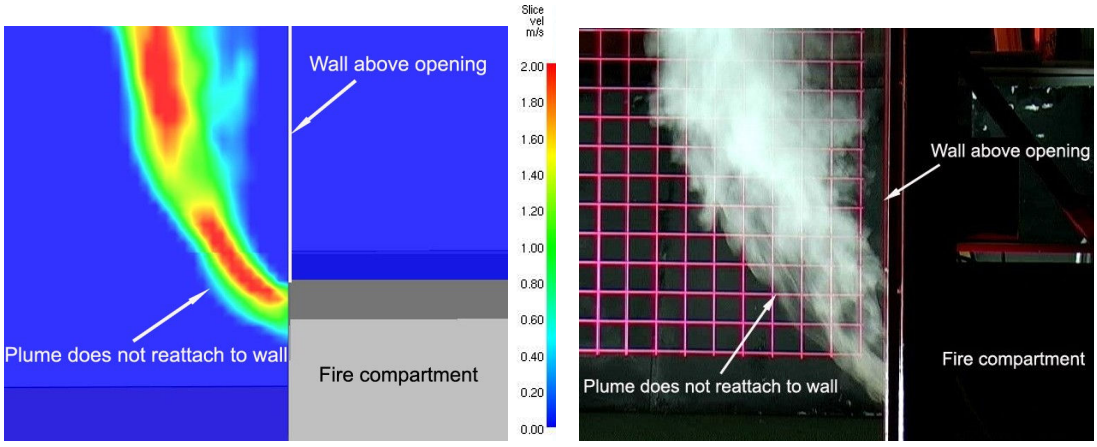

a) Simulation SE17 b) Experiment E221

Figure 8.28: Comparison of predicted plume behaviour with experiment (W_s = 0.2 m)

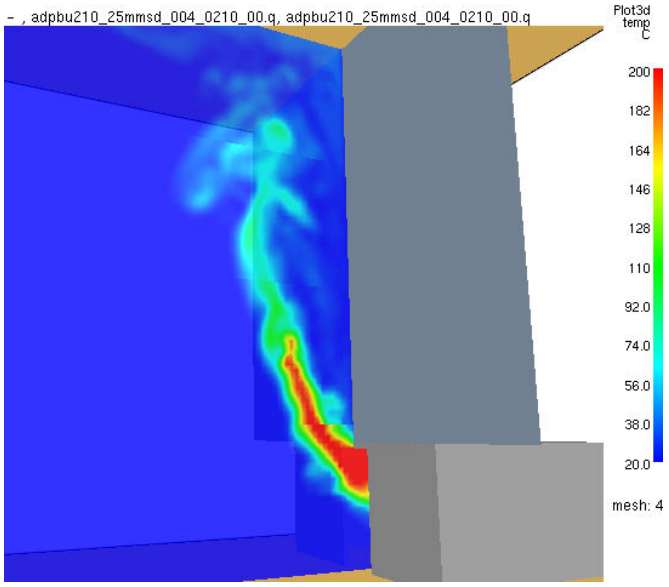

Figure 8.29: Predicted vertical temperature slice file (Simulation SE17, W_s = 0.2 m)

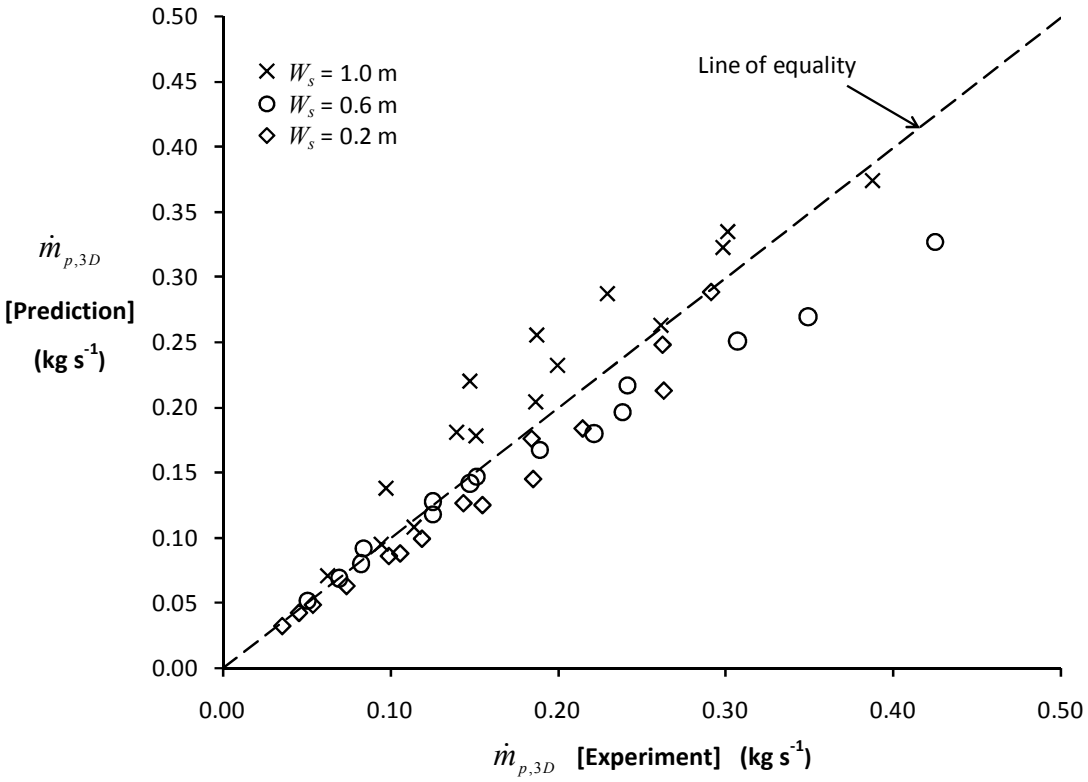

Figure 8.30: Comparison of prediction of $\dot{m}_{p,3D}$ with experiment

Simulation	$\dot{Q}_t$ (kW)	W_s (m)	z_s (m)	$\dot{m}_{p,3D}$ (kg s^{-1})
SE13	5.0	0.6	0.00	0.052
			0.30	0.092
			0.50	0.118
			0.73	0.147
			0.95	0.180
SE14	10.0	0.6	0.00	0.069
			0.30	0.128
			0.50	0.168
			0.73	0.217
			0.95	0.269
SE15	15.0	0.6	0.00	0.081
			0.30	0.142
			0.50	0.196
			0.73	0.251
			0.95	0.327
SE16	5.0	0.2	0.00	0.033
			0.30	0.064
			0.50	0.089
			0.73	0.127
			0.95	0.177
SE17	10.0	0.2	0.00	0.043
			0.30	0.084
			0.50	0.126
			0.73	0.184
			0.95	0.248
SE18	15.0	0.2	0.00	0.049
			0.30	0.100
			0.50	0.146
			0.73	0.213
			0.95	0.289
SE19	5.0	1.0	0.00	0.071
			0.30	0.138
			0.50	0.181
			0.73	0.220
			0.95	0.256
SE20	10.0	1.0	0.00	0.096
			0.30	0.179
			0.50	0.232
			0.73	0.288
			0.95	0.335
SE21	15.0	1.0	0.00	0.108
			0.30	0.205
			0.50	0.264
			0.73	0.323
			0.95	0.375

Table 8.6: Summary of results for the series of FDS simulations

Figure 8.30 shows good agreement between the prediction and the experiment for values of $\dot{m}_{p,3D}$ below 0.10 kg s^{-1} for each W_s examined. However, these predictions were mainly obtained at the height of the spill edge (i.e. at $z_s = 0$). For larger values of $\dot{m}_{p,3D}$ obtained above the spill edge the prediction appears to be dependent on W_s and hence the plume behaviour.

Figure 8.30 shows that for plumes that adhere to the wall above the spill edge (i.e. $W_s = 1.0$ m), the prediction tends to be conservative by up to approximately 30 %. This could be due to FDS not dealing appropriately with the flow close to the surface of the wall and hence, the boundary layer effect on the subsequent plume velocity. In FDS (LES version), the velocity at the wall is set as a fraction of the value in the grid element adjacent to the wall. This fraction can be altered by adjusting a parameter called the 'SLIP FACTOR' which can be used to represent the surface roughness [42].

A default 'SLIP FACTOR' of 0.5 was used in the simulations (it can be varied with values between -1 and 1). The FDS user guide [42] recommends that the default 'SLIP FACTOR' should only be changed using experimental data or an empirical correlation to examine its effect on the overall flow. Variation in the 'SLIP FACTOR' has been shown to have an important effect on fluid flows in numerical modelling by McBryde [137]. It is possible that a better prediction of entrainment could be achieved by varying the 'SLIP FACTOR', although this was not done here. It is also possible that a finer grid resolution could be required to provide a better prediction of entrainment for plumes that adhere to walls. The boundary layer effect is dealt with differently in RANS models which employ universal wall laws to describe the transition from turbulent to laminar flow close to walls. These are used to reduce the computational cost and effort, as a very fine grid resolution would be required in the boundary layer region to properly capture the flow behaviour numerically. A comparison of the performance of the approaches used in LES and RANS models to deal with the boundary layer for the adhered plume case would be useful in further work.

For plumes that detach and then reattach to the wall (i.e. W_s = 0.6 m), Figure 8.30 shows that FDS tends to under predict the experiment by up to approximately 20%. It is possible that the more complex behaviour of these plumes may require a finer grid resolution, particularly in the region where the plume is detached from the wall, where entrainment occurs into the rear of the plume via the ends.

For plumes that do not reattach to the wall above the spill edge (i.e. W_s = 0.2 m), Figure 8.30 shows that FDS provided a reasonably good prediction of the experiment. However, in some cases, there is a tendency to under predict entrainment by approximately 10 to 15%. It is possible that a finer grid resolution may achieve a better prediction of entrainment for these plumes.

In general, although FDS provides an excellent prediction of 3-D adhered plume behaviour, it appears that further work is desirable to provide improved guidance on the use of FDS to better quantify entrainment.

8.2 JASMINE modelling

Kumar *et al*. [41] provide predictions of entrainment using JASMINE for the series of experiments carried out in this work examining 2-D balcony spill plumes. The modelling procedure and assumptions made were not identical to that assumed in the FDS modelling carried out in this work, therefore, they are summarised below along with a comparison between the predictions of $\dot{m}_{p,2D}$ with the experimental results.

The JASMINE simulations modelled the experimental setup described in section 4.1. Figure 8.31 shows an example of the modelled geometry, with the use of screens to prevent entrainment into the ends of the plume.

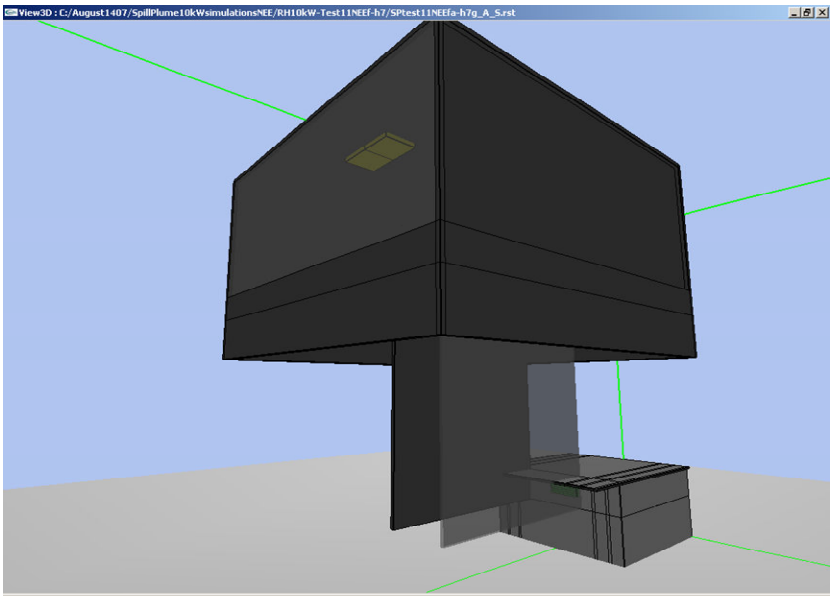

Figure 8.31: An example of the modelled geometry in JASMINE [41]

Fixed-pressure (open) boundary conditions were imposed at the limits of the computational domain, set remotely from the modelled geometry (up to several metres). These boundaries were imposed at all domain limits except at the bottom (a solid floor). A mirror symmetry boundary condition was employed along the plume centreline such that only half the geometry was modelled.

A non-uniform numerical grid was used, with a fine grid (typically 10 mm minimum grid dimension) in the region of the rising plume and a coarser grid remote from the modelled apparatus. A total number of 315,000 grid elements were used (see Figure 8.32).

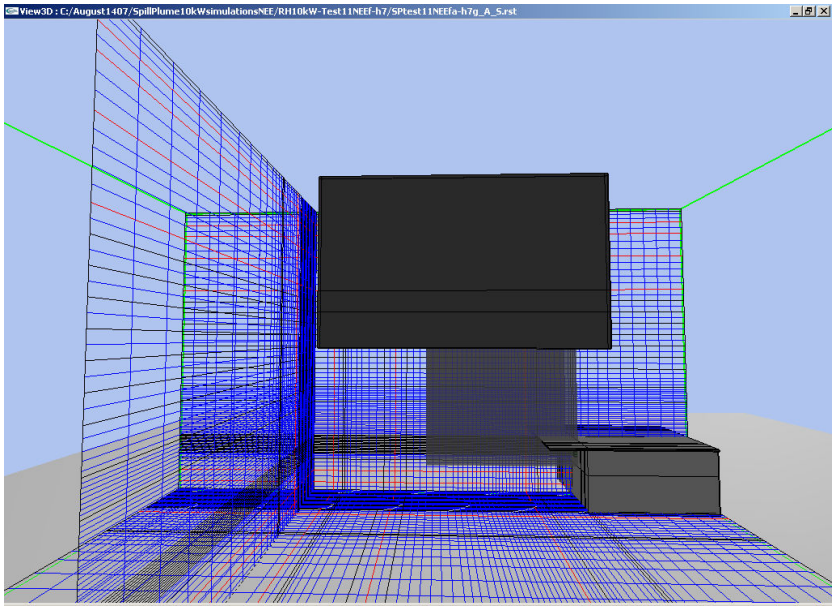

Figure 8.32: Non- uniform numerical grid used for the simulations [41]

The flows within the fire compartment were not modelled. Instead, the measured vertical profiles of temperature and velocity below the spill edge were assigned as the inlet boundary condition to define the plume source. The mass exhaust rate from the vent in the collecting hood was initially set to the value obtained using the curved plume method (see section 2.3.4.2). This was then adjusted by 5% increments until the iso-surface of 1°C temperature rise, characterising the smoke layer interface, coincided the bottom of hood as shown in Figure 8.33. This then provided a prediction of $\dot{m}_{p,2D}$ for the balcony spill plume.

As some of the predictions were not always made at exactly the same height of rise as the experiment (up to 0.02 m difference), the predictions and experimental results are shown as two separate data sets in Figure 8.34, plotted according to the dimensional analysis by Thomas *et al*. [39].

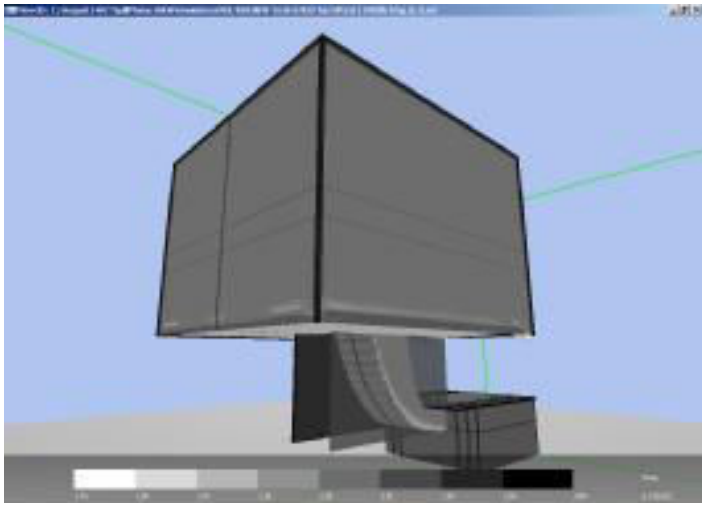

Figure 8.33: Typical predicted iso-surface of 1°C temperature rise [41]

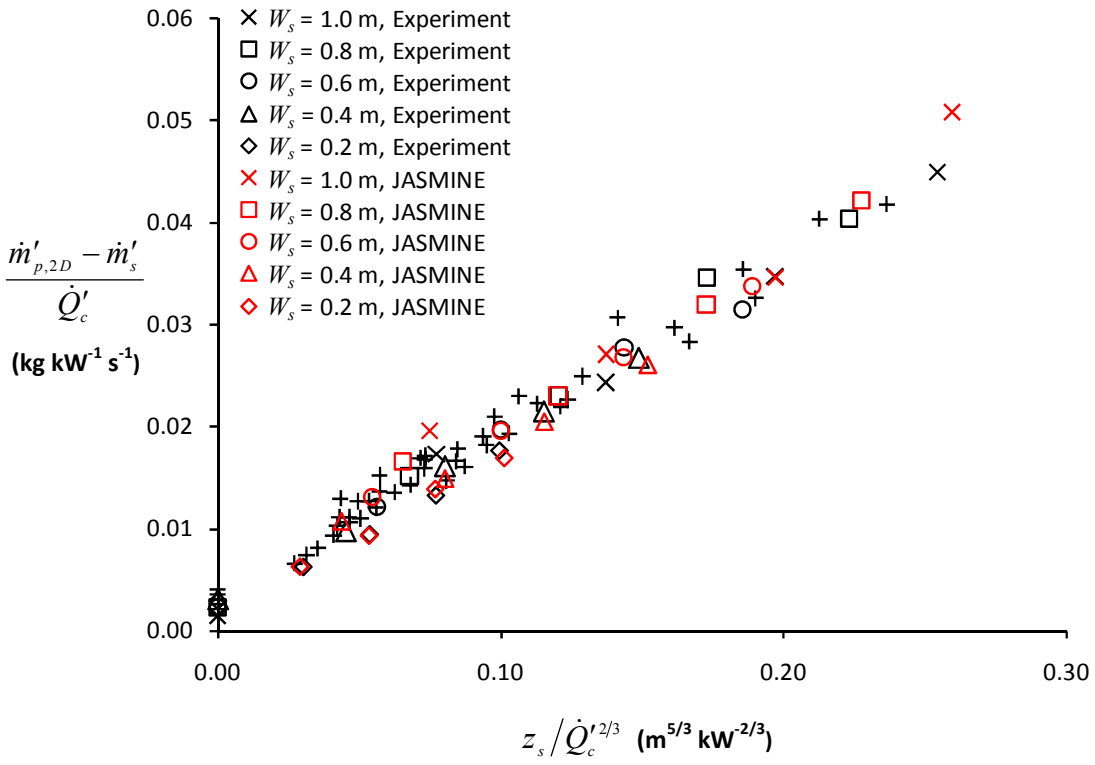

Figure 8.34: Comparison of the JASMINE prediction of $\dot{m}_{p,2D}$ with experiment

Figure 8.34 shows that the JASMINE predictions are generally consistent with the experimental results for the range of W_s examined and therefore provides an excellent prediction of entrainment for the 2-D plume.

As part of a collaborative effort, additional JASMINE predictions have been obtained by Kumar [138] for the experiments carried out of this work examining the 3-D balcony spill plume channelled by screens below the balcony. The modelling procedure and the assumptions made were the same as that described above, except that the screens used to prevent end entrainment were not modelled.

Figure 8.35 shows a typical iso-surface of 1°C temperature rise, characterising the smoke layer interface for the 3-D plume.

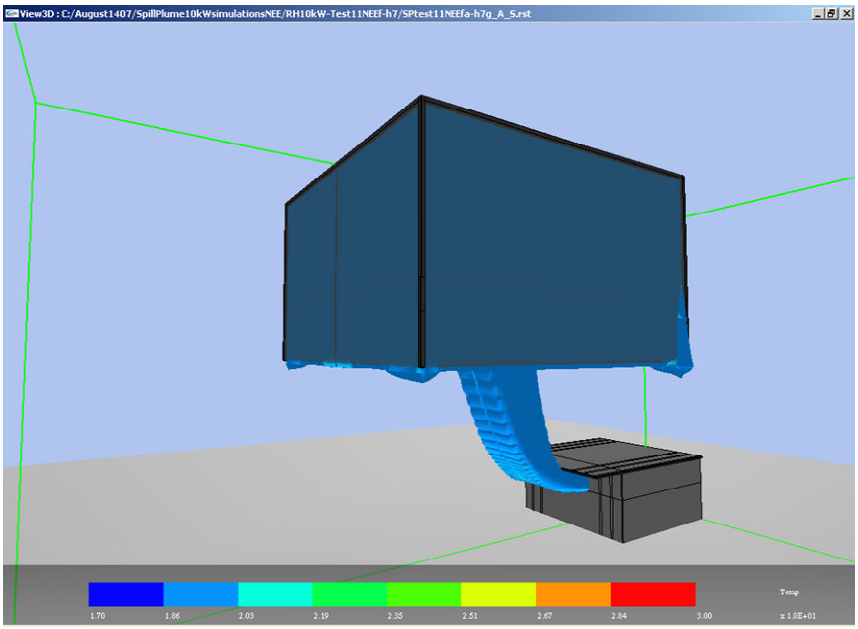

Figure 8.35: Typical predicted iso-surface for 1°C rise for the 3-D plume [138]

Figure 8.36 shows the JASMINE predictions of $\dot{m}_{p,3D}$ and the experimental results plotted according to the dimensional analysis by Thomas *et al*. [39].

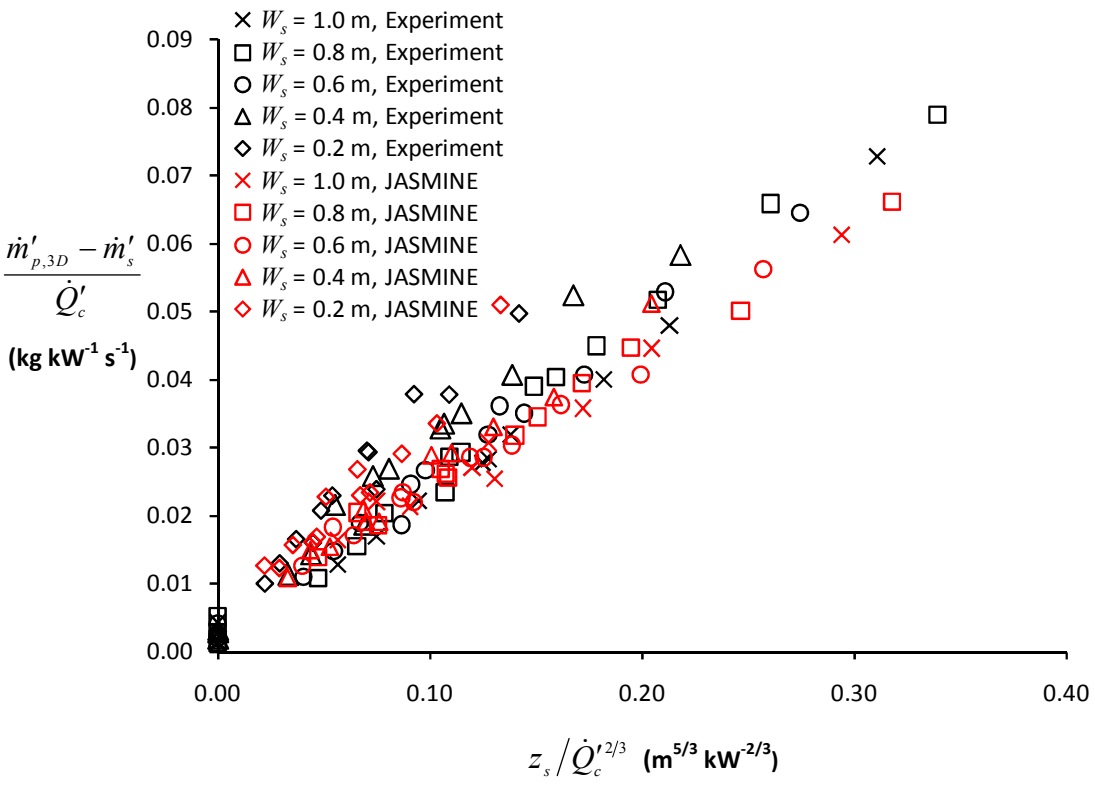

Figure 8.36: Comparison of experiment with the JASMINE prediction of $\dot{m}_{p,3D}$

Figure 8.36 shows that JASMINE predicts an increase in the rate of entrainment with respect to z_s as W_s decreases, which is consistent with the experiment. The JASMINE predictions are generally in line with the experimental results at relatively low values of z_s (or more specifically $z_s / \dot{Q}'^{2/3}_c$). However, at higher values there is a general trend to somewhat under predict the experiment by approximately 10 to 15%, although there was also greater uncertainty in z_s at higher heights of rise in the experiment. In general, JASMINE can be considered to provide a reasonably good prediction of 3-D balcony spill plume entrainment, particularly at relatively low heights of rise.

8.3 Conclusions

This chapter provides predictions of spill plume entrainment using CFD modelling for a selected number experiments carried out in this work. Predictions were mainly obtained using FDS (version 5.1.4) with additional predictions made using JASMINE (v3.23). Analysis of the results has provided the following conclusions.

8.3.1 FDS modelling

8.3.1.1 The 3-D balcony spill plume

Following a grid sensitivity analysis, FDS generally provides a good prediction of the flow from a fire compartment opening and subsequent spill plume behaviour and entrainment when using a grid size of 25 mm (on model scale). Thus, the equates to a grid size of 0.25 m for full scale flows.

From the conditions studied, a suitable grid size for design has been developed in non-dimensional form (i.e. n^*_{spill}). The chosen grid size must meet the following criterion for the design in question, such that the grid size can be considered to be appropriate when,

$$n^*_{spill} \geq 0.9$$

Where,

$$n^*_{spill} = \frac{D^*_{spill}}{\delta x} \quad \text{and} \quad D^*_{spill} = \left(\frac{\frac{\dot{Q}_c}{W_s}}{\rho_{amb} c_{p,air} T_{amb} \sqrt{g}} \right)^{2/3}$$

As a general rule, it is recommended that grid size of 0.25 m should initially be chosen for design, and that this should be reduced if the above non-dimensional criterion is not met.

8.3.1.2 The 3-D adhered plume

FDS provided an excellent prediction of 3-D adhered plume behaviour when a grid size of 25 mm (on model scale) was used. However, its performance in predicting the amount of entrainment appeared to be dependent on the plume behaviour. It is possible that the complex nature of these plumes may require a finer grid resolution and/or the effect of the boundary layer close to the wall on the subsequent plume velocity needs to be better dealt with. In general, it appears that further work is desirable to provide improved guidance on the use of FDS to better quantify entrainment for the 3-D adhered spill plume.

8.4 JASMINE modelling

8.4.1 The 2-D balcony spill plume

For the conditions studied, JASMINE provided an excellent prediction of 2-D plume balcony spill plume entrainment. The minimum grid dimension used in the region encompassing the rising plume was approximately 0.01 m on model scale (i.e. 0.1 m full scale equivalent).

8.4.2 The 3-D balcony spill plume

In general, JASMINE provided a good prediction of 3-D balcony spill plume entrainment when using the same grid resolution as that used for the 2-D plume. The predictions provided excellent agreement with the experiment at relatively low heights of rise, however, at higher values there was a general trend to somewhat under predict the experiment by approximately 10 to 15%.

Chapter 9

9. Transition from a balcony spill plume to axisymmetric

This chapter presents a further analysis of 3-D balcony spill plume entrainment, but over a much greater range of heights of rise than were possible experimentally. All current simple and analytical entrainment calculation methods (including the new design formula proposed from this study) predict that entrainment increases linearly with respect to the height of rise of plume. It has been postulated [39] that entrainment into the free ends of the plume will eventually cause it to become axisymmetric in nature at high heights of rise. It is expected that entrainment will increase according to $z_s^{5/3}$ at a height beyond the transition in plume behaviour. This could potentially lead to an unsafe design if a linearly based design equation is extrapolated beyond the height of transition.

The analysis in this chapter utilises a similar approach to that carried out in previous work to determine a general expression for the height of transition in entrainment behaviour from a 3-D balcony spill plume to axisymmetric (i.e. z_{trans}). The analysis is further supported with a limited number of FDS simulations examining identical plumes to that produced in the experiment, but over a much greater height of rise.

9.1.1 Previous analysis

Thomas [84] first presented an analysis to determine a general expression for z_{trans} by matching design equations for a 3-D balcony spill plume and an axisymmetric plume to give equivalency in terms of entrainment behaviour at high heights of rise.

Thomas used the Lee and Emmons line plume model [Equation (2.19)] and assumed $C_m = 0.58$ to give,

$$\dot{m}_p = 0.58\left(\frac{\rho_{amb}^2 g}{c_{p,air} T_{amb}}\right)^{1/3} \dot{Q}_c^{1/3} W^{2/3}\left(z + z_0\right) \tag{9-1}$$

$$\Rightarrow \dot{m}_p = 0.21\dot{Q}_t^{1/3} W_s^{2/3}\left(z_s + z_0\right)$$

To describe axisymmetric plume entrainment, Thomas used the following formula given by Zukoski [61].

$$\dot{m}_p = 0.21\left(\frac{g}{\rho_{amb} c_{p,air} T_{amb}}\right)^{1/3} \dot{Q}_c^{1/3}\left(z + z_0\right)^{5/3} \tag{9-2}$$

$$\Rightarrow \dot{m}_p = 0.071\dot{Q}_c^{1/3}\left(z + z_0\right)^{5/3}$$

Thomas determined that at high heights of rise Equations (9-1) and (9-2) become equivalent when,

$$W = W_s + 0.22\left(z + 2z_0\right) \tag{9-3}$$

This analysis was used to develop a formula for 3-D balcony spill plume entrainment already given by Equation (2-28) which is shown again below.

$$\dot{m}_{p,3D} = 0.21\dot{Q}_c^{1/3}\left(z_s + z_0\right)\left(W_s + 0.22\left(z_s + 2z_0\right)\right)^{2/3}$$

Thomas states that Equation (2-28) exhibits linearity in entrainment for small z_s/W_s but becomes axisymmetric in nature (i.e. dependent on $z_s^{5/3}$) beyond $z_s/W_s \approx 5$. Therefore,

$$z_{trans} = 5W_s \tag{9-4}$$

Heskestad [139] employed a similar approach to that of Thomas but did not use the Lee and Emmons model to describe balcony spill plume entrainment. Instead, Heskestad used the 3-D balcony spill plume formula by Law [36] already given by Equation (2-25) which is shown again below.

$$\dot{m}_{p,3D} = 0.34\left(\dot{Q}_t W_s^2\right)^{1/3}\left(z_s + 0.15h_b\right)$$

As Equation (2-25) is dependent on $\dot{Q}_t$, it was assumed that $\dot{Q}_c = 0.7\dot{Q}_t$ so that it becomes,

$$\dot{m}_{p,3D} = 0.38\left(\dot{Q}_c W_s^2\right)^{1/3}\left(z_s + 0.15h_b\right) \quad \textbf{(9-5)}$$

To further simplify the analysis, Heskestad assumed that the terms describing the location of the virtual source in Equations (9-2) and (9-5) (i.e. the z_0 and $0.15h_b$) could be neglected as these become insignificant at high heights of rise. Thus, Equation (9-2) for the axisymmetric plume becomes,

$$\dot{m}_p = 0.071\dot{Q}_c^{1/3} z_s^{5/3} \quad \textbf{(9-6)}$$

(assuming $z = z_s$)

Equation (9-5) for the 3-D balcony spill plume becomes,

$$\dot{m}_{p,3D} = 0.38\dot{Q}_c^{1/3} W_s^{2/3} z_s \quad \textbf{(9-7)}$$

Heskestad then expressed Equation (9-7) in a form compatible with Equation (9-6) given by,

$$\dot{m}_{p,3D} = 0.071\dot{Q}_c^{1/3} z_s^{5/3} / \left(0.08 z_s / W_s\right)^{2/3} \quad \textbf{(9-8)}$$

Therefore, Equation (9-8) reduces to similar form to Equation (9-6) when,

$$0.080\, z_s / W_s = 1$$

$$\Rightarrow z_s / W_s = 12.5 \qquad \textbf{(9-9)}$$

Hence,

$$z_{trans} = 12.5 W_s \qquad \textbf{(9-10)}$$

This criterion is essentially the same as that given within an earlier version of NFPA 92B [88] when using Equation (2-58) (i.e. $z_{trans} = 13 W_s$).

Clearly, there are significant differences in the general expressions to describe z_{trans} from the Thomas and Heskestad analyses which is also reflected in differing guidance given by CIBSE [38] and NFPA 92B [88]. The only significant difference between each analysis is the entrainment coefficient assumed for the 3-D balcony spill plume [i.e. the 0.21 in Equation (9-1) and the 0.38 in Equation (9-5)]. Since the analysis methods were essentially the same, it is unsurprising that different expressions for z_{trans} were obtained if different entrainment coefficients were assumed for the 3-D balcony spill plume. The 0.21 assumed by Thomas was for line plume entrainment, yet the 0.38 assumed by Heskestad was determined from empirical 3-D balcony spill plume data where end entrainment was more significant than in a line plume. This analysis suggests that expressing z_{trans} simply as a factor W_s may not be entirely appropriate as it will not give a general expression that applies for a variety of 3-D balcony spill plumes where the contribution of end entrainment varies. The analysis described in Chapter 6 demonstrates that entrainment into 3-D balcony spill plumes is dependent upon W_s and d_s and it appears that a general expression to describe z_{trans} should include both of these terms (see below).

9.1.2 Matching axisymmetric entrainment with the experiment

Although the experimental data from this study exhibited linear entrainment behaviour for the range of heights of rise examined, a similar analysis to that described above can be carried out to determine z_{trans} by matching the new simplified design formula proposed from this work [i.e. Equation (6-12), shown again below] with the entrainment formula for an axisymmetric plume.

$$\dot{m}_{p,3D} = 0.16\dot{Q}_c^{1/3}\left(W_s^{2/3} + 1.56d_s^{2/3}\right)z_s + 1.34\dot{m}_s$$

The analysis can be simplified by only considering the rate of entrainment above the spill edge (consistent with the approach by Heskestad), as the entrainment below the spill edge is relatively insignificant in the overall entrainment process at large heights of rise and end entrainment only becomes significant above the edge. As it is not possible to specify entrainment above the spill edge according to $(\dot{m}_{p,3D} - 1.34\dot{m}_s)$ and then subsequently make this compatible with Equation (9-6), the last term in Equation (6-12) is neglected as a simplifying assumption to give,

$$\dot{m}_{p,3D} = 0.16\dot{Q}_c^{1/3}\left(W_s^{2/3} + 1.56d_s^{2/3}\right)z_s \qquad \textbf{(9-11)}$$

Equation (9-11) can be expressed in a form compatible with Equation (9-6) (for the axisymmetric plume) such that,

$$\dot{m}_{p,3D} = \frac{0.071\dot{Q}_c^{1/3}\left(W_s^{2/3} + 1.56d_s^{2/3}\right)z_s^{5/3}}{0.44z_s^{2/3}} \qquad \textbf{(9-12)}$$

Therefore, Equation (9-12) reduces to Equation (9-6) when,

$$\frac{\left(W_s^{2/3} + 1.56d_s^{2/3}\right)}{0.44z_s^{2/3}} = 1 \qquad \textbf{(9-13)}$$

Hence, z_{trans} is given by,

$$z_{trans} = 3.4\left(W_s^{2/3} + 1.56 d_s^{2/3}\right)^{3/2} \quad \textbf{(9-14)}$$

Equation (9-14) is dependent on W_s and d_s (rather than W_s alone) which seems reasonable following the analysis described in Chapter 6.

Table 9.1 shows the prediction of z_{trans} (in metres) using Equation (9-14) for the range of W_s and d_s examined in the experiment. Table 9.1 also shows the transition in entrainment expressed in non-dimensional form consistent with Thomas and Heskestad (i.e. in terms of z_{trans}/W_s).

$\dot{Q}_t$ (kW)	$\dot{Q}_c$ (kW)	W_s (m)	d_s (m)	z_{trans} (m)	z_{trans}/W_s
5.0 ± 0.3	3.6 ± 0.2	1.0	0.100 ± 0.005	5.3	5.3
10.0 ± 0.3	8.0 ± 0.6	1.0	0.115 ± 0.005	5.5	5.5
15.0 ± 0.3	12.2 ± 1.0	1.0	0.125 ± 0.005	5.6	5.6
5.0 ± 0.3	3.7 ± 0.3	0.8	0.105 ± 0.005	4.5	5.6
10.0 ± 0.3	7.8 ± 0.6	0.8	0.115 ± 0.005	4.7	5.9
15.0 ± 0.3	12.8 ± 0.8	0.8	0.135 ± 0.005	4.9	6.1
5.0 ± 0.3	3.9 ± 0.2	0.6	0.110 ± 0.005	3.8	6.3
10.0 ± 0.3	7.7 ± 0.5	0.6	0.120 ± 0.005	3.9	6.5
15.0 ± 0.3	12.2 ± 0.7	0.6	0.140 ± 0.005	4.1	6.8
5.0 ± 0.3	3.6 ± 0.2	0.4	0.115 ± 0.005	3.0	7.5
10.0 ± 0.3	7.2 ± 0.4	0.4	0.125 ± 0.005	3.1	7.8
15.0 ± 0.3	10.9 ± 0.6	0.4	0.145 ± 0.005	3.3	8.3
5.0 ± 0.3	3.5 ± 0.2	0.2	0.135 ± 0.005	2.2	11.0
10.0 ± 0.3	6.6 ± 0.4	0.2	0.155 ± 0.005	2.4	12.0
15.0 ± 0.3	9.9 ± 0.6	0.2	0.170 ± 0.005	2.5	12.5

Table 9.1: Values of z_{trans} for the range of W_s and d_s examined in the experiment

Table 9.1 shows that in general the absolute value (in metres) of z_{trans} tends to decrease as W_s decreases. This is expected as narrower plumes will tend to become axisymmetric in nature at lower heights of rise compared to wider plumes due to end entrainment being more significant in the overall entrainment process.

However, Table 9.1 shows a small increase in z_{trans} as d_s increases (due to the increase in $\dot{Q}_t$ and hence $\dot{Q}_c$) for each W_s examined. This is somewhat counter intuitive as it is expected that as d_s approaches W_s then z_{trans} should decrease, as the aspect ratio of the flow below the spill edge becomes more square than rectangular in nature (hence, a greater contribution of end entrainment above the spill edge). This is most likely due to the assumption of neglecting the term describing the entrainment below the spill edge in Equation (6-12) (i.e. the $1.34\dot{m}_s$) which should ideally be subtracted from $\dot{m}_{p,3D}$ when considering the entrainment above the spill edge. The value of $1.34\dot{m}_s$ will increase as $\dot{Q}_t$ increases and neglecting this subtraction probably explains the increase in z_{trans}. However, as these differences are small and Equation (9-14) is an approximate solution, it seems reasonable that these differences can be ignored in the analysis.

Table 9.1 shows that if the transition in entrainment is expressed in non-dimensional form dependent only upon W_s, then z_{trans}/W_s varies between approximately 5 and 13. It is encouraging to note that for spill plumes where $W_s >> d_s$ (i.e. for spill plumes similar in nature to line plumes) then $z_{trans}/W_s \approx 5$ which is consistent with the analysis by Thomas, and for plumes where $W_s \approx d_s$ then $z_{trans}/W_s \approx 13$ similar to that determined by Heskestad. This variation in z_{trans}/W_s with respect to W_s demonstrates that it is not appropriate to generally describe the transition in entrainment in terms of W_s alone. This gives further support in the use of Equation (9-14) to describe z_{trans} which is dependent on W_s and d_s. Equation (9-14) describes the upper limit in terms that Equation (6-12) (or any linear based entrainment formula) should be applied, and at a height beyond z_{trans} the entrainment in the plume should be determined using Equation (9-6) for an axisymmetric plume.

9.1.3 FDS Modelling

As already described in section 8.1.4, FDS provided a good prediction of $\dot{m}_{p,3D}$ when compared against the experiment. This gives confidence in the further use of FDS to examine 3-D balcony spill plume entrainment, from identical plumes to that produced in the experiment, but over a much greater height of rise.

Therefore, Table 9.2 shows the series of four FDS simulations carried out to examine 3-D plume entrainment up to a height of rise of 5.0 m on model scale (i.e. 50 m full scale). The analysis will also enable the performance of Equation (9-14) to predict the height in transition behaviour to be assessed against the FDS predictions.

Simulation	$\dot{Q}_t$ (kW)	W_s (m)	z_s (m)
STR1	10.0	0.2	0 to 5.0
STR2	10.0	0.4	0 to 5.0
STR3	10.0	0.6	0 to 5.0
STR4	10.0	1.0	0 to 5.0

Table 9.2: The series of FDS simulations

The modelling procedure and assumptions made were essentially the same as that described in section 8.1.3 (i.e. without modelling a collecting hood) and therefore a description is not repeated here. The only significant difference was the increased size of computational domain to encompass the rising plume. The domain had dimensions of 4.0 by 4.0 by 6.0 m high (all dimensions are $1/10^{th}$ scale), encompassing ten separate domains (each 4.0 by 4.0 by 0.6 m high) for parallel processing purposes. This allowed heights of rise of plume of up to 5.0 m to be examined due to a shallow smoke layer forming under the ceiling of the domain.

Figure 9.1 shows the modelled geometry, the computational domain and a typical plume produced showing a velocity contour (0.5 m s^{-1}) for Simulation STR3.

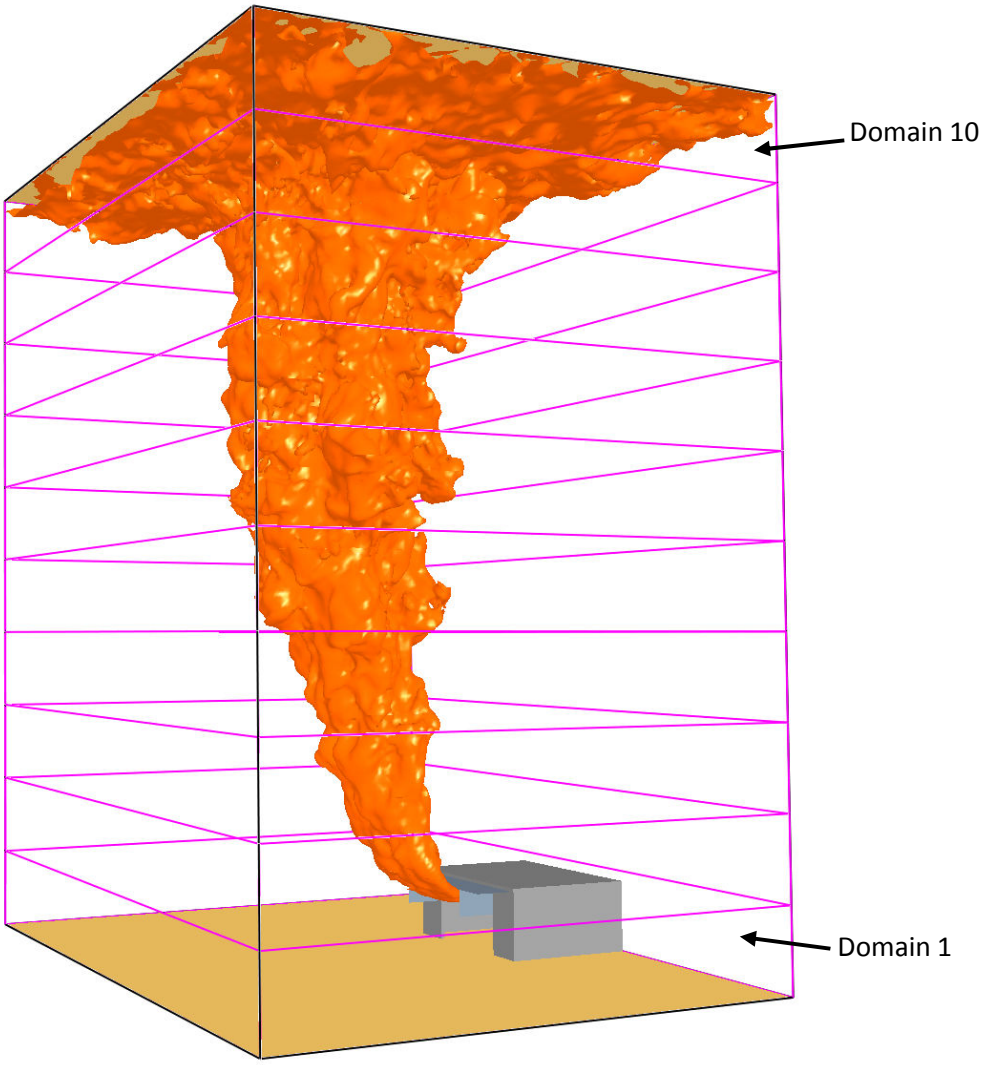

Figure 9.1: The geometry, computational domain and plume (Simulation STR3)

A uniform grid size of 25 mm was used for each domain encompassing a total of approximately 6.1 million grid elements. Each simulation took approximately 30 days to complete.

Predictions of $\dot{m}_{p,3D}$ were obtained from specified planar areas occupied by the plume every 0.1 m above the spill edge up to a maximum height of 5.0 m. Appendix Q gives the predictions of $\dot{m}_{p,3D}$ at each height of rise examined for Simulations STR1 to STR4 respectively.

9.1.3.1 Plume behaviour

Figure 9.2 shows a plan view of horizontal velocity slice files through the plume with increasing height above the spill edge for Simulation STR3 (i.e. W_s = 0.6 m). These slice files highlight the shape of the plume cross-section with increasing height.

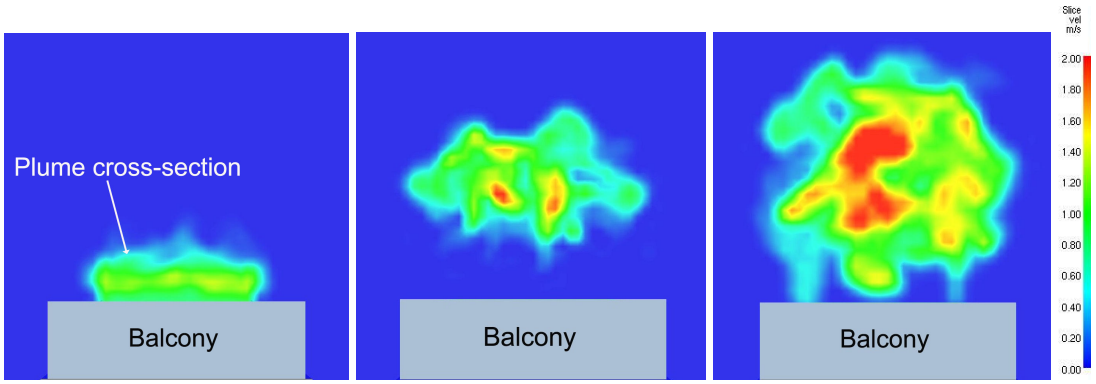

a) z_s = 0 m b) z_s = 0.5 m c) z_s = 1.0 m

Figure 9.2: Horizontal cross-sectional area of the plume with height (Simulation STR3)

Figure 9.2 shows an important change in the shape of the cross-sectional area of the plume as it rises. Close to the balcony (see Figure 9.2a), the plume can be considered to be wide and narrow and similar in nature to a line plume. However, as z_s increases (see Figures 9.2b and c), it appears that the action of entrainment into the ends of the plume causes the cross-section to become more circular in nature, similar to an axisymmetric plume. The velocity tends to a maximum close to the plume centreline with increasing height. The cross-sectional area shown in Figure 9.2c was generally typical for the plume at z_s > 1.0 m. This change in the cross-sectional area gives further support to the hypothesis that a 3-D balcony spill plume will eventually behave like an axisymmetric plume due to end entrainment. This analysis assumes that the plume rises unhindered into the atrium void. The behaviour of the plume at higher heights of rise could be influenced by the presence of bounding walls such that it becomes confined.

9.1.3.2 Entrainment analysis

In order to examine the entrainment behaviour of the 3-D balcony spill plume at high heights of rise, the FDS predictions of $\dot{m}_{p,3D}$ are plotted against z_s on a log-log scale, as changes in the characteristic slope of the predictions will demonstrate if and when a transition in entrainment behaviour occurs.

Figures 9.3 to 9.6 show plots of the predictions of $\dot{m}_{p,3D}$ with respect to z_s for Simulations STR1 to STR4 respectively. A line representing z_{trans} determined from Equation (9-14) is shown to enable an assessment to be made of its applicability to predict the transition in entrainment behaviour. A line representing the new simplified design formula proposed from this work [Equation (6-12)] is also shown to assess the height limit beyond which this equation should not be applied. A line with a slope representing axisymmetric plume entrainment [i.e. according to Equation (9-6)] is also shown.

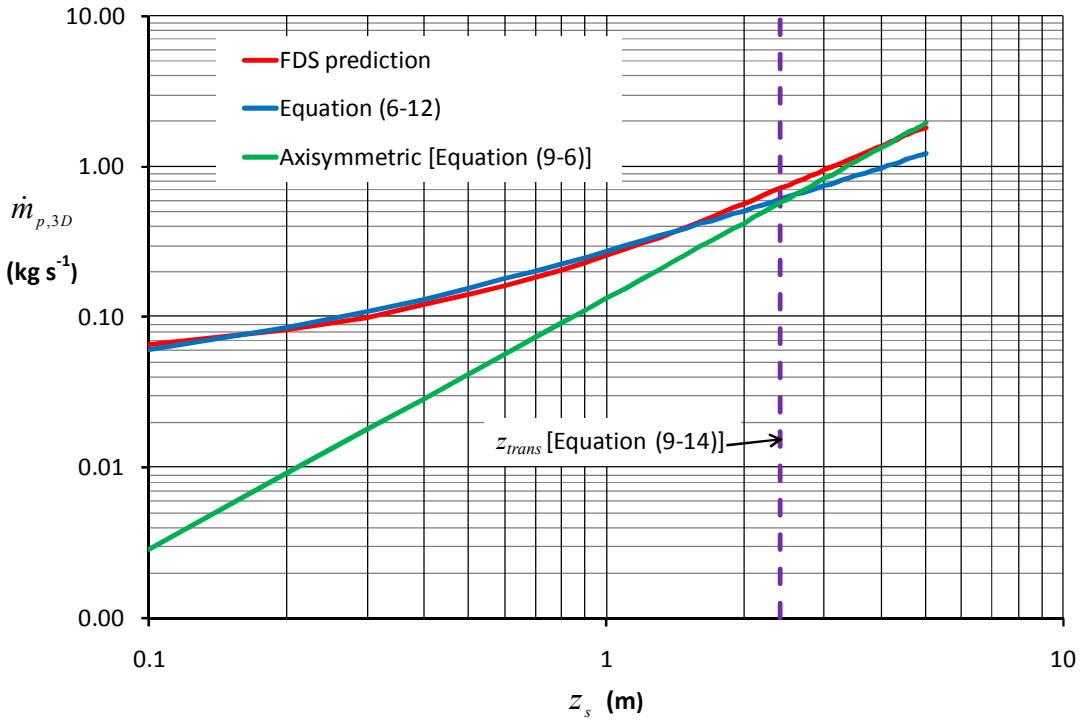

Figure 9.3: Predictions of $\dot{m}_{p,3D}$ with respect to z_s (Simulation STR1)

Figure 9.3 shows that for Simulation STR1 (i.e. W_s = 0.2 m) the FDS predictions of $\dot{m}_{p,3D}$ generally obey the linearly based relationship given by Equation (6-12) up to a height of rise of approximately 2.0 m. However, Figure 9.3 shows that above this height the FDS prediction departs from the predictions using Equation (6-12), characterised by a line with a steeper slope (i.e. entrainment according to a power law). This indicates that FDS predicts a transition in entrainment behaviour due to entrainment into the ends of the spill plume. The height at which the transition in entrainment behaviour occurs is close to the prediction of z_{trans} using Equation (9-14) (i.e. 2.4 m). It is encouraging to note that the predicted value of z_{trans} coincides with point of intersection between the lines representing Equations (6-12) and (9-6). The FDS predictions follow a similar yet slightly shallower slope to that of an axisymmetric plume beyond the point of intersection which indicates a rate of entrainment somewhere between linearity and $z_s^{5/3}$. Figures 9.4 and 9.5 shows that for Simulations STR2 and STR3 (i.e. W_s = 0.4 and 0.6 m) the predictions of $\dot{m}_{p,3D}$ with respect to height of rise demonstrate similar behaviour to that described above, but with the transition in entrainment behaviour occurring at a greater height of rise due to end entrainment being less significant for wider plumes. Again the prediction of z_{trans} using Equation (9-14) gives a good approximation of the location of the height of transition for each simulation.

Figure 9.6 shows that for Simulation STR2 (i.e. W_s = 1.0 m) the predictions of $\dot{m}_{p,3D}$ with respect to z_s are broadly in line with Equation (6-12) over the full height of rise examined without any significant difference in entrainment behaviour. This because the width of the plume was such that the transition in entrainment behaviour does not occur over the height of rise examined due to end entrainment being less significant. Equation (9-14) predicts a value of z_{trans} of approximately 5.5 m which is higher than maximum height of rise examined in the simulations. Therefore it is not surprising that no transition in entrainment is observed. It would have been useful to extend the height of the domain, however, the simulation run time would have been excessive. As the predicted plume temperature close to z_{trans} was approximately 2^{o}C above ambient, it is expected that stratification of smoke at high level is more likely to be an issue for wide plumes rather than a change in the rate of entrainment.

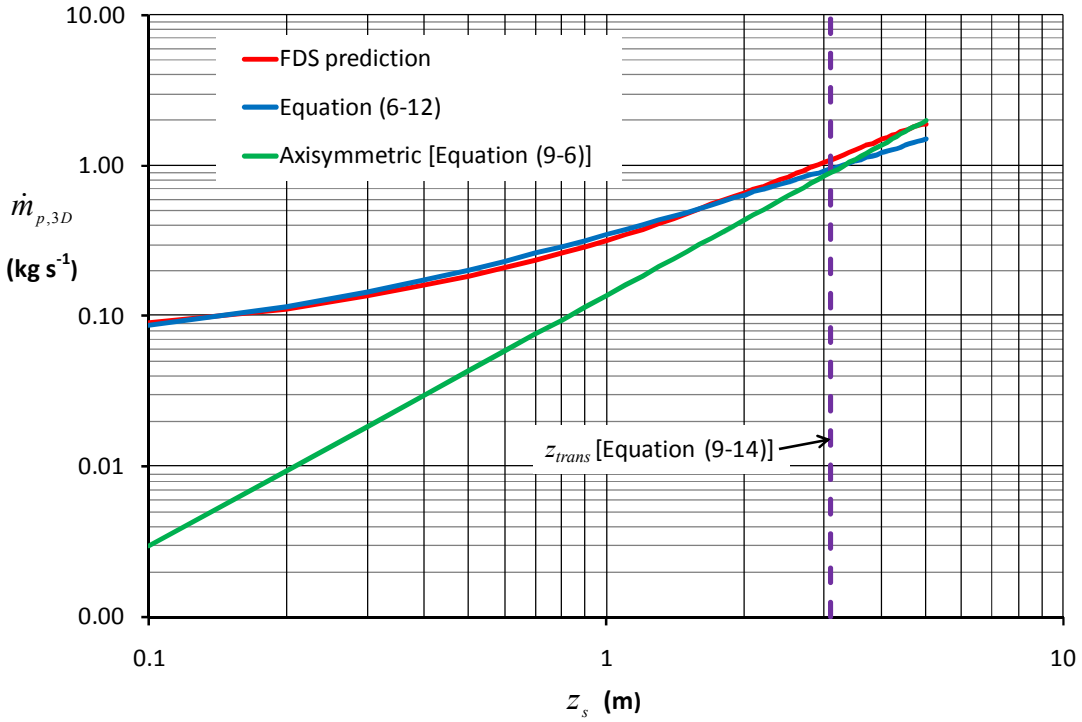

Figure 9.4: Predictions of $\dot{m}_{p,3D}$ with respect to z_s (Simulation STR2)

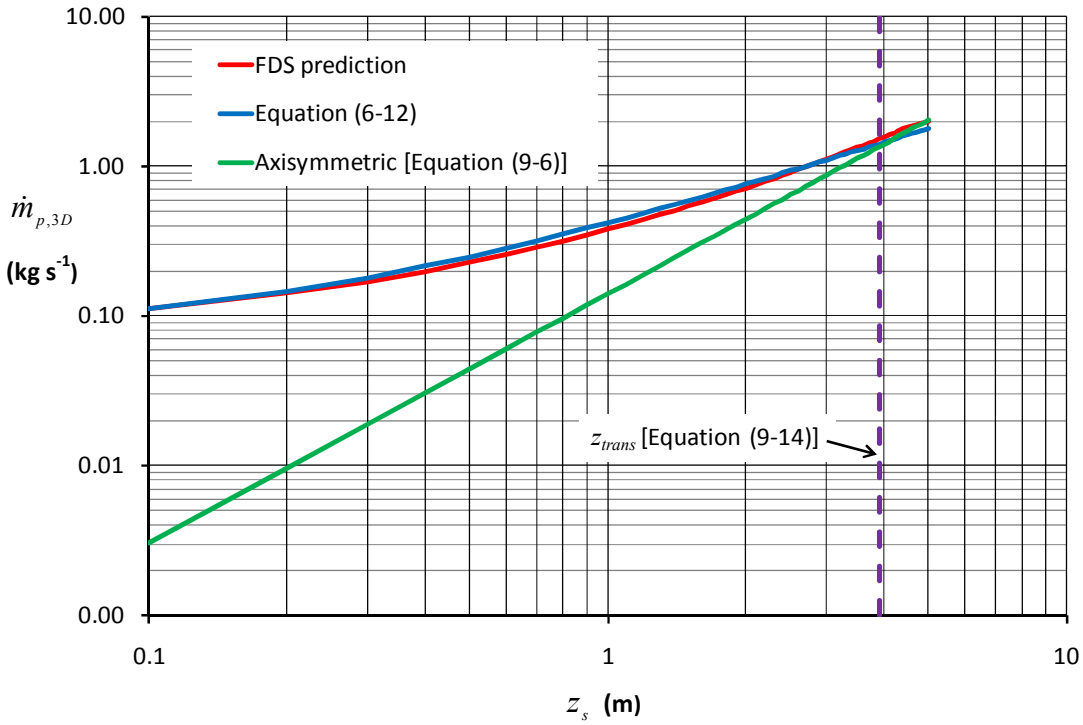

Figure 9.5: Predictions of $\dot{m}_{p,3D}$ with respect to z_s (Simulation STR3)

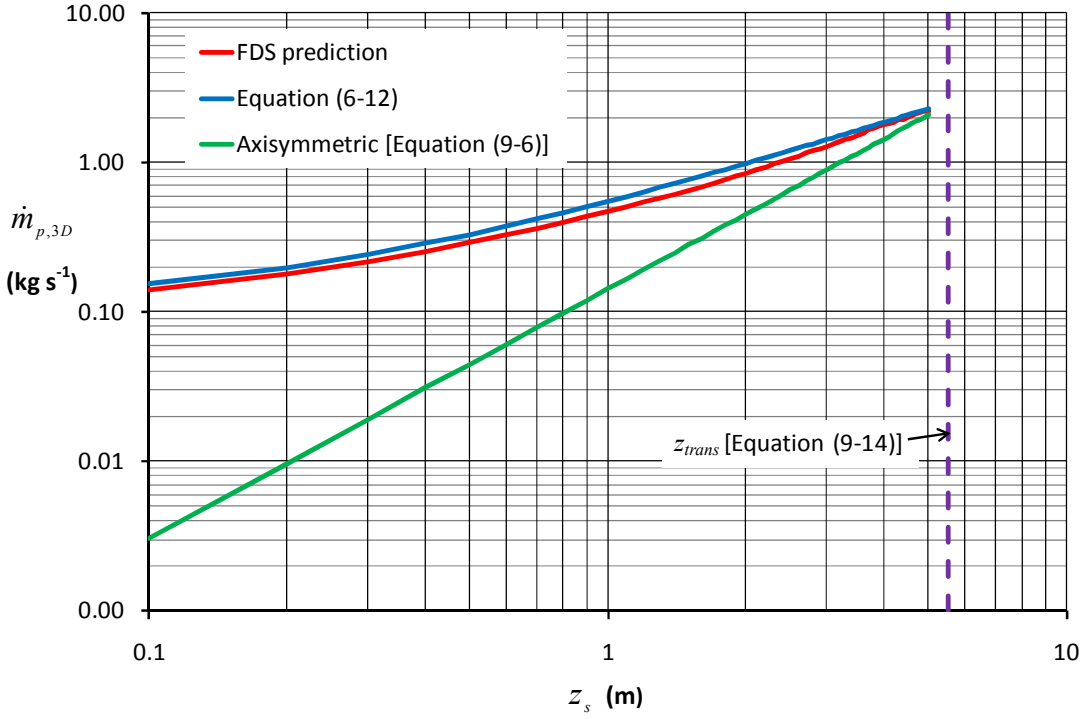

Figure 9.6: Predictions of $\dot{m}_{p,3D}$ with respect to z_s (Simulation STR4)

The above analysis indicates that FDS provides a prediction of $\dot{m}_{p,3D}$ that is broadly in line with Equation (6-12) for plumes generated from a variety of W_s up to a height of z_{trans}. Beyond z_{trans}, FDS appears to predict a rate of entrainment that is greater than described by Equation (6-12) but slightly less than for an axisymmetric plume (for the conditions studied). Therefore it seems reasonable to use Equation (9-14) to provide the upper limit for which Equation (6-12) should be applied (i.e. z_{trans}). For design scenarios where the height of rise of plume is greater than z_{trans} the entrainment beyond this height should be according to an axisymmetric plume formula. Hence, if, $z_s \leq z_{trans}$ then $\dot{m}_{p,3D}$ can be predicted using Equation (6-12), such that

$$\dot{m}_{p,3D} = 0.16\dot{Q}_c^{1/3}\left(W_s^{2/3} + 1.56d_s^{2/3}\right)z_s + 1.34\dot{m}_s$$

If $z_s > z_{trans}$ then Equation (9-6) should be used, such that,

$$\dot{m}_{p,3D} = 0.071\dot{Q}_c^{1/3}z_s^{5/3}$$

9.1.3.3 Comparison with NFPA 92B

The current version of NFPA 92 B [2] provides new simplified formulae to predict 3-D balcony spill plume entrainment. The new guidance is dependent upon z_s and W_s and gives separate design formulae which apply above and below z_s = 15 m (full scale). The design formula for z_s < 15 m is essentially the same as the previous guidance in NFPA 92B [88] and is given by Equation (2-61) [and Equation (2-58)]. The design formulae for $z_s \geq 15$ m are given by Equations (2-59) and (2-60) and were derived from a series of FDS3 simulations. As previously discussed in section 2.5.9, these simulations did not predict a transition in entrainment behaviour to that of an axisymmetric plume for z_s up to 50 m full scale (i.e. 5 m on 1/10th scale), contrary to that predicted from the FDS modelling in this study.

Figure 9.7 show a comparison of the predictions of $\dot{m}_{p,3D}$ using the NFPA 92B [2] formulae with the predictions already shown in Figure 9.3 for Simulation STR1 (i.e. W_s = 0.2 m). These data are plotted on a linear scale in this case due to negative predictions of $\dot{m}_{p,3D}$.

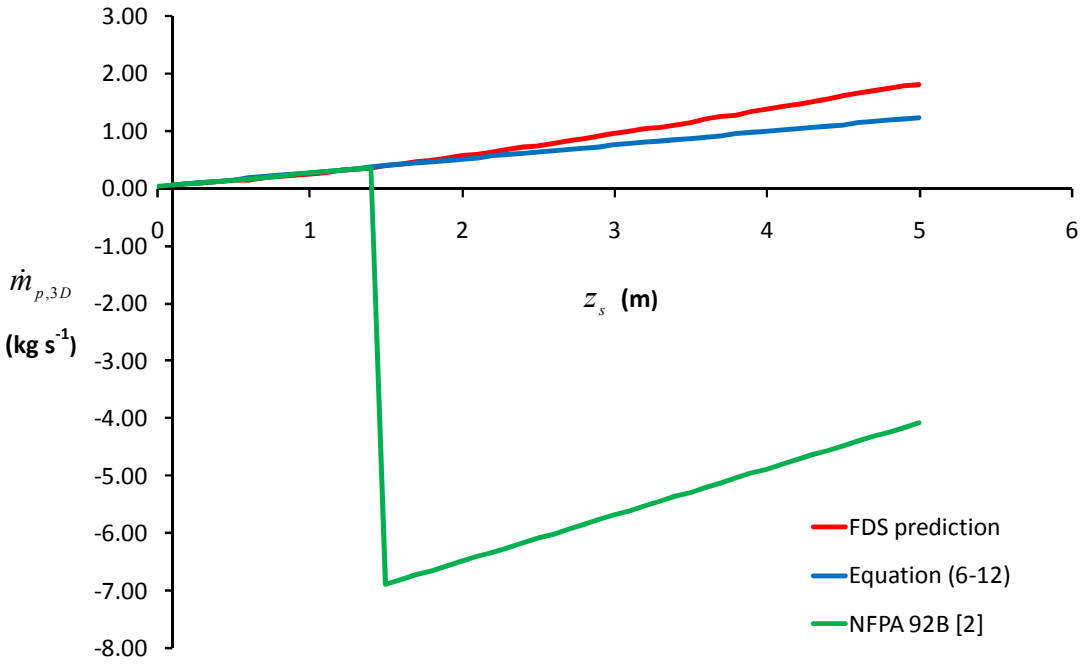

Figure 9.7: Comparison of predictions of $\dot{m}_{p,3D}$ with NFPA 92B (Simulation STR1)

Figure 9.7 shows that the NFPA 92B predictions beyond 1.5 m (i.e. 15 m full scale) give rise to negative predictions of $\dot{m}_{p,3D}$. This is because Equation (2-59) contains a constant "-15" term, which means that it is not general in nature and gives a nonsensical result if attempting to predict $\dot{m}_{p,3D}$ from reduced scale data. Therefore, it appears that Equation (2-59) [and Equation (2-60)] only truly apply to full scale scenarios over the range of conditions examined to derive these correlations.

To enable a comparison to be made with the FDS predictions and the predictions using Equation (6-12), all the NFPA 92B predictions were initially determined using full scale equivalent input parameters which were then subsequently scaled down (i.e. to 1/10th scale).

Figures 9.8 to 9.11 show a comparison of these predictions on a log-log scale for Simulations STR1 to STR4 respectively.

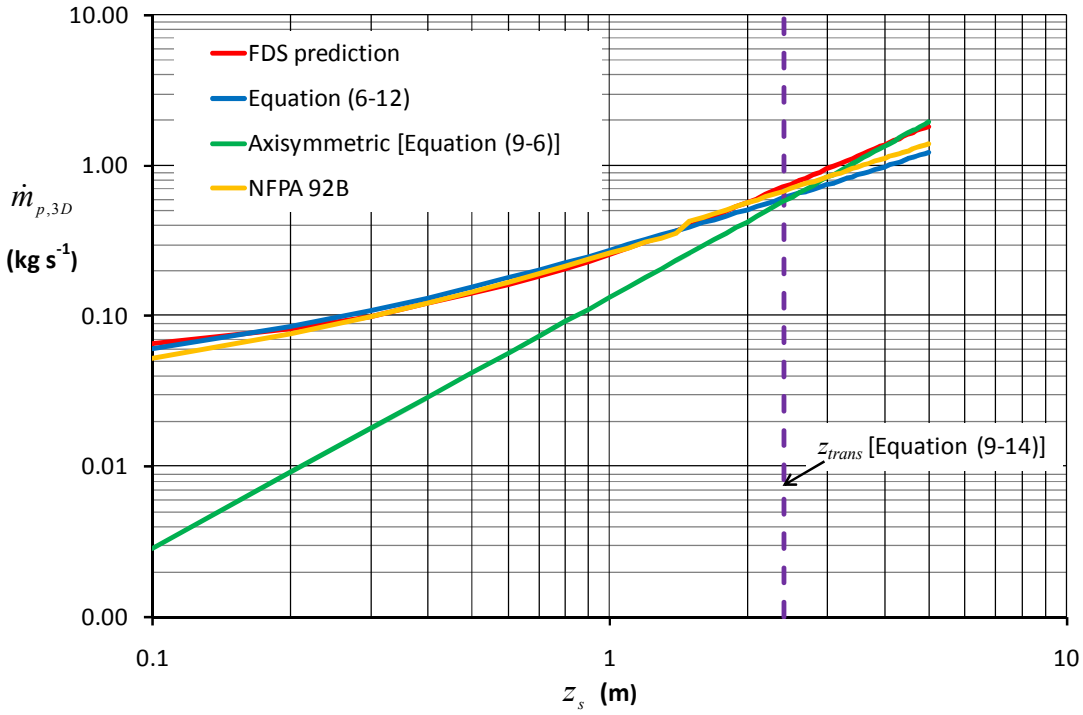

Figure 9.8: Comparison of predictions of $\dot{m}_{p,3D}$ with NFPA 92B (Simulation STR1)

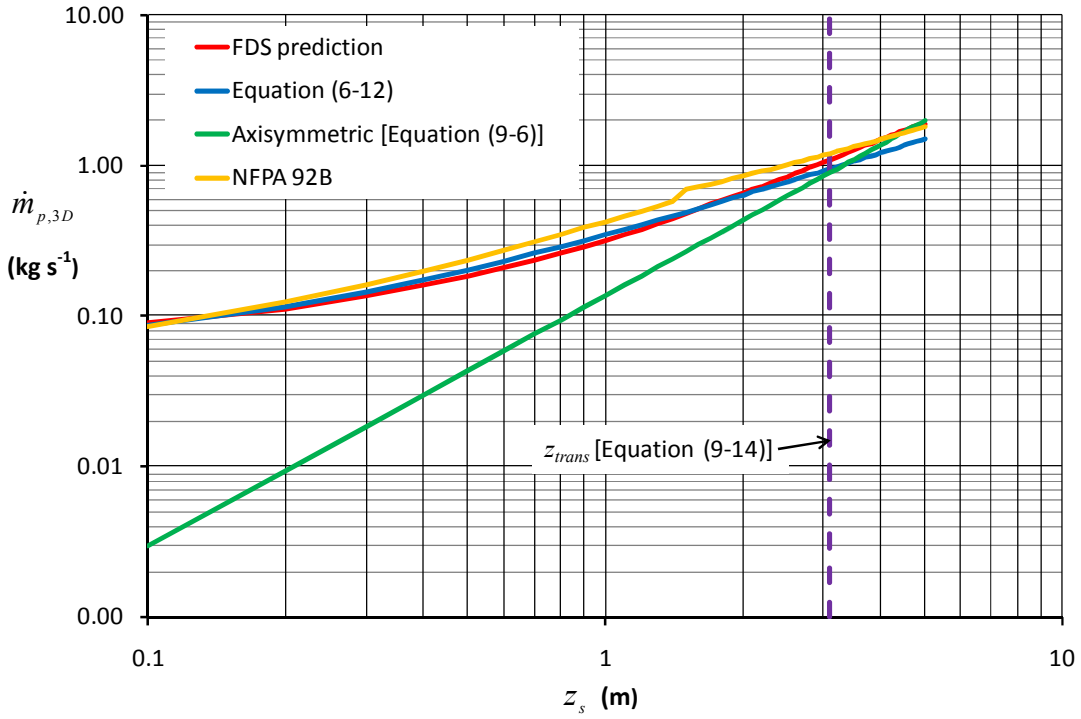

Figure 9.9: Comparison of predictions of $\dot{m}_{p,3D}$ with NFPA 92B (Simulation STR2)

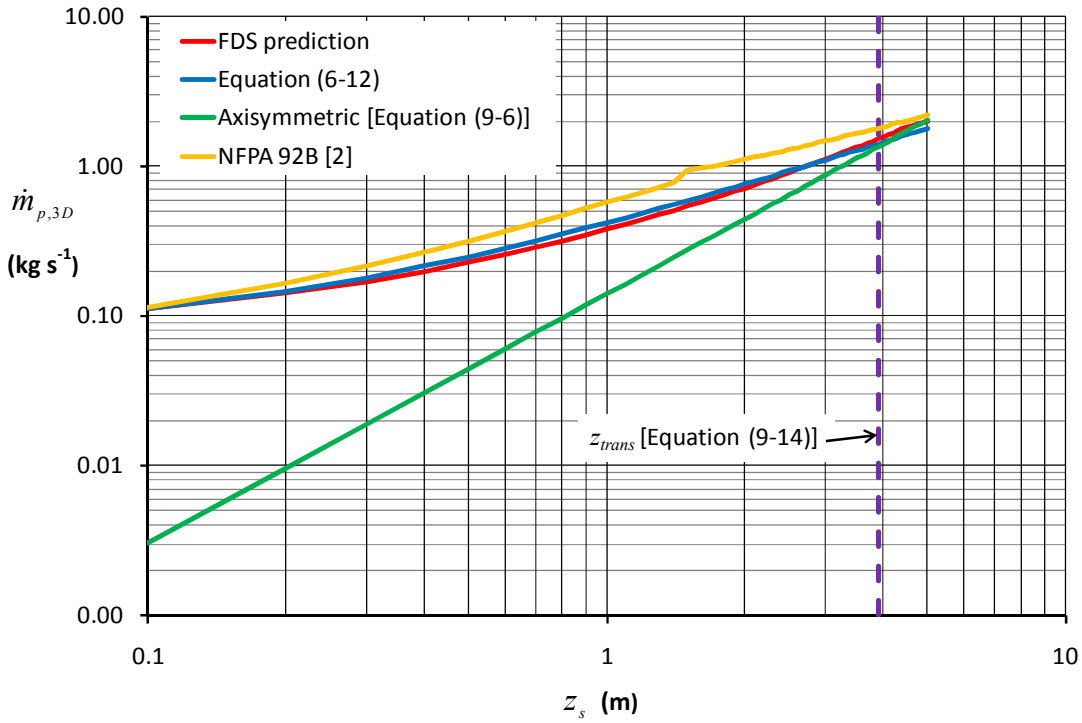

Figure 9.10: Comparison of predictions of $\dot{m}_{p,3D}$ with NFPA 92B (Simulation STR3)

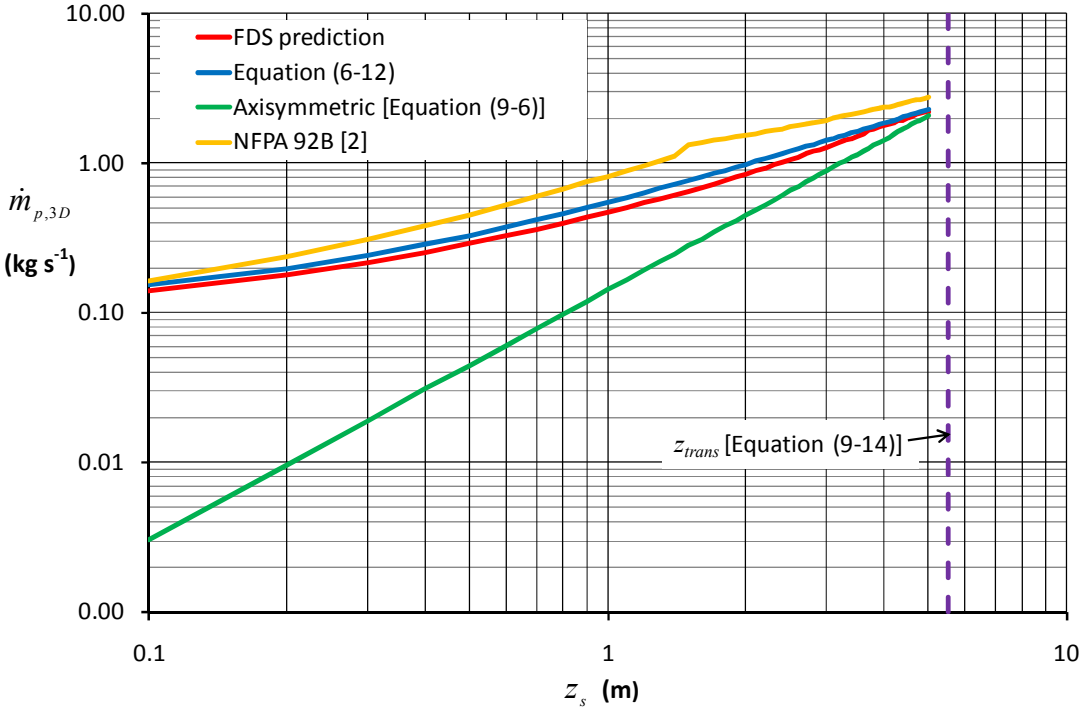

Figure 9.11: Comparison of predictions of $\dot{m}_{p,3D}$ with NFPA 92B (Simulation STR4)

Figure 9.8 shows that the NFPA 92B predictions agree well with the FDS predictions and Equation (6-12) up to the height of z_{trans} (although there is a slight discontinuity in the predictions at z_s = 1.5 m at the threshold between the different design equations). This is consistent with the analysis in section 6.6 which showed that the NFPA 92B provides a prediction of entrainment that is appropriate for narrow width plumes. However, beyond z_{trans} the NFPA 92B prediction is lower than the FDS prediction and does not predict a transition in entrainment behaviour to axisymmetric.

Figures 9.9 to 9.11 demonstrates the NFPA 92B formula provides an increasingly conservative prediction of entrainment as W_s increases (again with a discontinuity in the predictions at z_s = 15 m). The NFPA 92B formulae provides a prediction that is approximately 80% higher than the FDS prediction and Equation (6-12) for plumes generated from the widest flow examined (i.e. Simulation STR4) at z_s = 1.5 m (see Figure 9.11), although the level of conservativeness reduces (to approximately 20%) at z_s = 5.0 m.

As the design of smoke management systems involving the spill plume often considers plumes generated from wide openings as a reasonable worst case, it appears that the NFPA 92B formula will provide a conservative prediction of entrainment in most cases.

9.2 Conclusions

This chapter provides a further analysis of 3-D balcony spill plume entrainment, but at much higher heights of rise than were possible experimentally. The analysis is based on the results from the physical scale model experiments, supported by FDS modelling. Analysis of the results has provided the following conclusions:

The following formula is proposed to describe the height of transition in entrainment behaviour from a balcony spill plume to axisymmetric. This was determined by matching the new design formula proposed in this work [Equation (6-12)] with an axisymmetric plume formula so that they become equivalent at a high height of rise. The formula is given by,

$$z_{trans} = 3.4\left(W_s^{2/3} + 1.56 d_s^{2/3}\right)^{3/2}$$

z_{trans} is dependent on W_s and d_s (rather than W_s alone) which seems reasonable following the analysis described in Chapter 6.

The absolute value (in metres) of z_{trans} tends to decrease as W_s decreases. This is expected as narrower plumes will tend to become axisymmetric in nature at lower heights of rise compared to wider plumes due to end entrainment being more significant in the overall entrainment process.

The predicted value of z_{trans} coincides with point of intersection between the relationships representing the rate of entrainment for the 3-D balcony spill plume [Equation (6-12)] and that for an axisymmetric plume [Equation (9-6)] for the range of fire compartment opening widths examined.

The proposed formula to determine z_{trans} describes the upper limit that Equation (6-12) (or any linear based entrainment formula) should be applied, and at a height beyond z_{trans} entrainment should be determined using a formula for the axisymmetric plume.

Hence, if, $z_s \le z_{trans}$ then entrainment can be predicted using Equation (6-12), such that

$$\dot{m}_{p,3D} = 0.16\dot{Q}_c^{1/3}\left(W_s^{2/3} + 1.56d_s^{2/3}\right)z_s + 1.34\dot{m}_s$$

However, if $z_s > z_{trans}$ then Equation (9-6) should be used, such that,

$$\dot{m}_{p,3D} = 0.071\dot{Q}_c^{1/3}z_s^{5/3}$$

The analysis is supported by a limited number of FDS simulations which demonstrate a transition in entrainment behaviour that departs from a linear relationship. The FDS predictions follow a similar yet slightly shallower slope to that of an axisymmetric plume beyond the point of transition which indicates a rate of entrainment somewhere between linearity and $z_s^{5/3}$. The predicted height of transition in entrainment in FDS broadly coincides with the predicted value of z_{trans} for the range of fire compartment opening widths examined. This gives further confidence in its use for design purposes.

The FDS predictions highlight that stratification of smoke at high level is more likely to be an design issue for wide spill plumes rather than a change in the rate of entrainment.

Comparison of the FDS predictions [and the predictions using Equation (6-12)] with the new guidance given in the NFPA 92B [2] shows that the NFPA 92B formulae will generally provide a particularly conservative prediction of entrainment for many cases found in design.

Chapter 10

10. Case studies with full scale data

This work has developed new guidance for the spill plume in smoke management design, in the form of a range simplified design formulae, improvements to analytical calculation methods and initial guidance on the use of CFD modelling. This guidance has been developed using $1/10^{th}$ physical scale modelling experiments and numerical modelling using CFD. Although these analysis methods are well established, it is desirable to assess the performance of the proposed guidance against any relevant full scale experimental data on spill plumes.

Full scale data to describe thermal spill plume entrainment is very limited. However, data is available from published experiments carried out by BRE and IFSET [53,54]. These data were obtained from two separate "hot smoke tests" to assess the performance of smoke management systems in real buildings by burning fires '*in-situ*'. The first hot smoke test was carried out in the atrium space of the new terminal building at Brussels Airport in 1994 [53] where the design fire scenario involved a 3-D balcony spill plume channelled by screens below the balcony. The second test was carried out in an atrium space within the new European Parliament Building, Brussels, in 1996 [54] where the design scenario involved a 3-D adhered spill plume. These tests provided visual and temperature measurements of the flow from the fire compartment and of the subsequent spill plume and smoke layer in the atrium space.

This chapter assesses the performance of guidance proposed in this work relevant to the scenarios examined in the hot smoke tests. A description of each test and the predictions made using the proposed new guidance are described below.

10.1 Hot Smoke Test at the Brussels Airport terminal building

Morgan *et al.* [53] provide a detailed description of the hot smoke test carried out in the atrium space of the (then unfinished) terminal building at Brussels Airport. A summary of the test is described below, including a description of the building, the test fires and the results.

10.1.1 The building

The terminal building at Brussels Airport includes an atrium space (i.e. a shopping mall) that is approximately 85 m long (the length of two reservoirs) by 12 m wide by 17 m high (to the top the glazed barrel vault roof). This part of the building is known as the "Lightstreet". There are two floors, the ground floor (the departure level) and the first floor (the mezzanine level). Figure 10.1 shows a photograph of the atrium space at the time of the hot smoke test. Figure 10.2 shows a schematic drawing of the departure area (incorporating the smoke test area) in plan view.

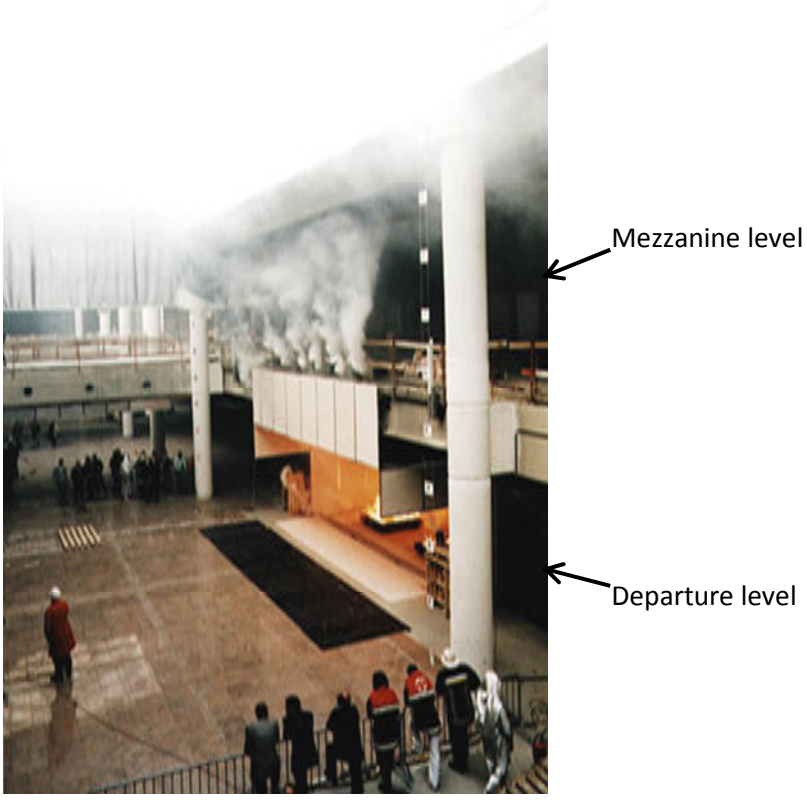

Figure 10.1: The atrium space in the terminal building [12]

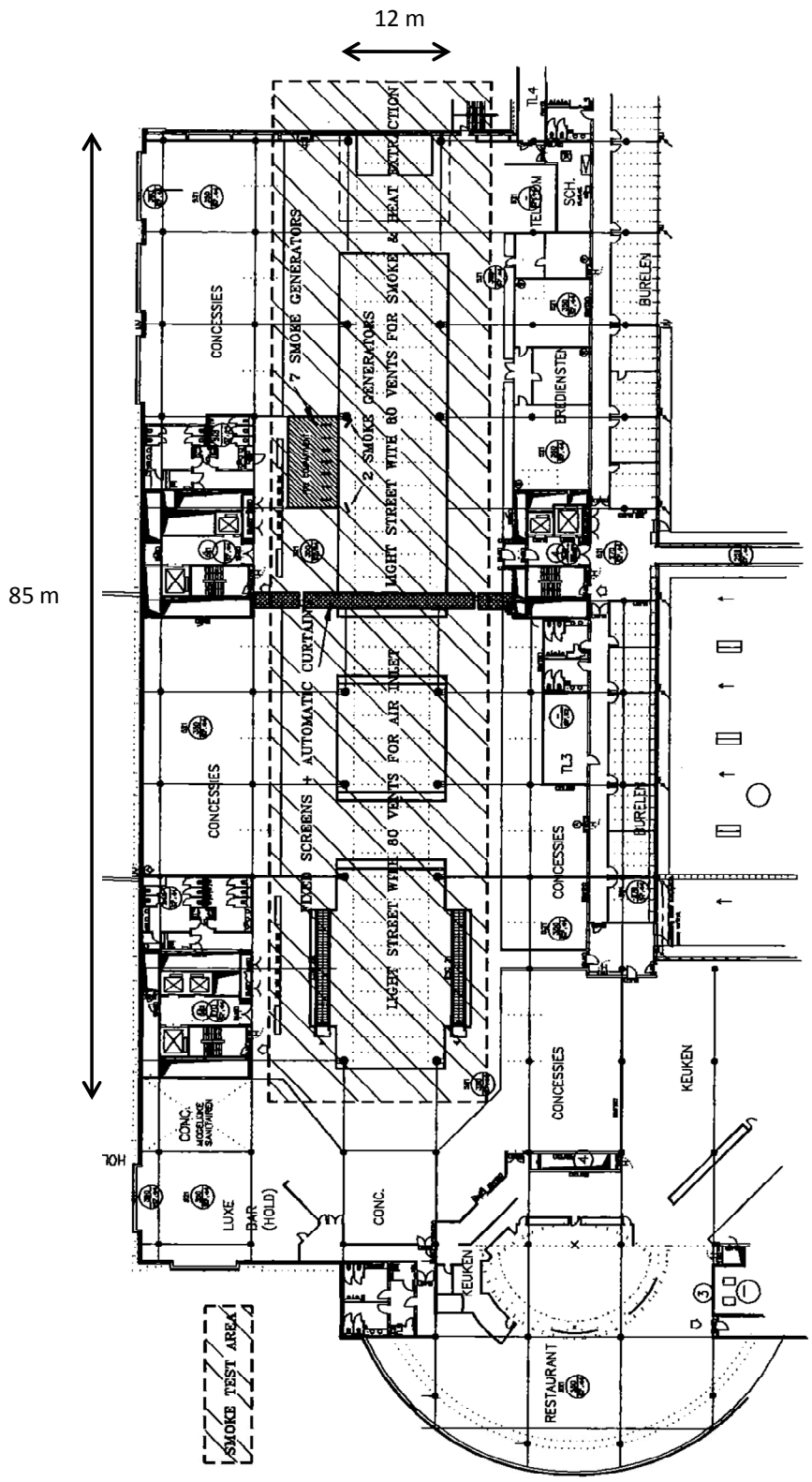

Figure 10.2: Schematic plan view of the departure level (adapted from [53])

10.1.2 The fire compartment

A fire compartment made of 10 mm calcium silicate board (Promatect-H) attached to an angle iron structure was built on the departure level and fronted onto the atrium space (see Figure 10.3). The compartment was 9.6 m wide by 3.5 m deep by 3.5 m high. The front of the compartment was open on the 9.6 m width face and there was a channelling screen at either side of the compartment projecting forward by a distance of 2.0 m. This represented a shop unit. The compartment structure was continued upwards by 1.5 m to the level of the mezzanine floor. This was to simulate the final architectural finish and to protect the building structure against exposure to hot gases.

Figure 10.3: The fire compartment and IMS test fire [53]

10.1.3 The test fire

The hot buoyant layer was produced by burning IMS pool fires in the compartment. The fuel was burnt in two square steel fire trays, 1.5 m by 1.5 m, each of which was floated on a larger tray of water, 1.75 m by 1.75 m. The convective heat flow in the fire gases from each tray was 965 kW, to give a test fire with a total of 1930 kW. White oil-mist cosmetic smoke from seven commercial smoke generators was fed into the plume above the spill edge to mark the hot gases for visual and photographic observations. These generators were placed on the mezzanine above the compartment (see Figure 10.3).

10.1.4 The SHEVS

The SHEVS was naturally (i.e. buoyancy) driven, with 160 natural smoke ventilators located 13.5 m above the floor (to mid-vent, see Figure 10.4) running either side of the barrel vault roof (80 vents on the each side). The 85 m reservoir was equally divided by smoke curtains and fixed screens (see Figure 10.2) to form two reservoirs each having 80 m^2 of vent area (48 m^2 aerodynamic free area). The vents in the reservoir containing the fire compartment acted as outlets and the vents in the adjacent reservoir acted as inlets.

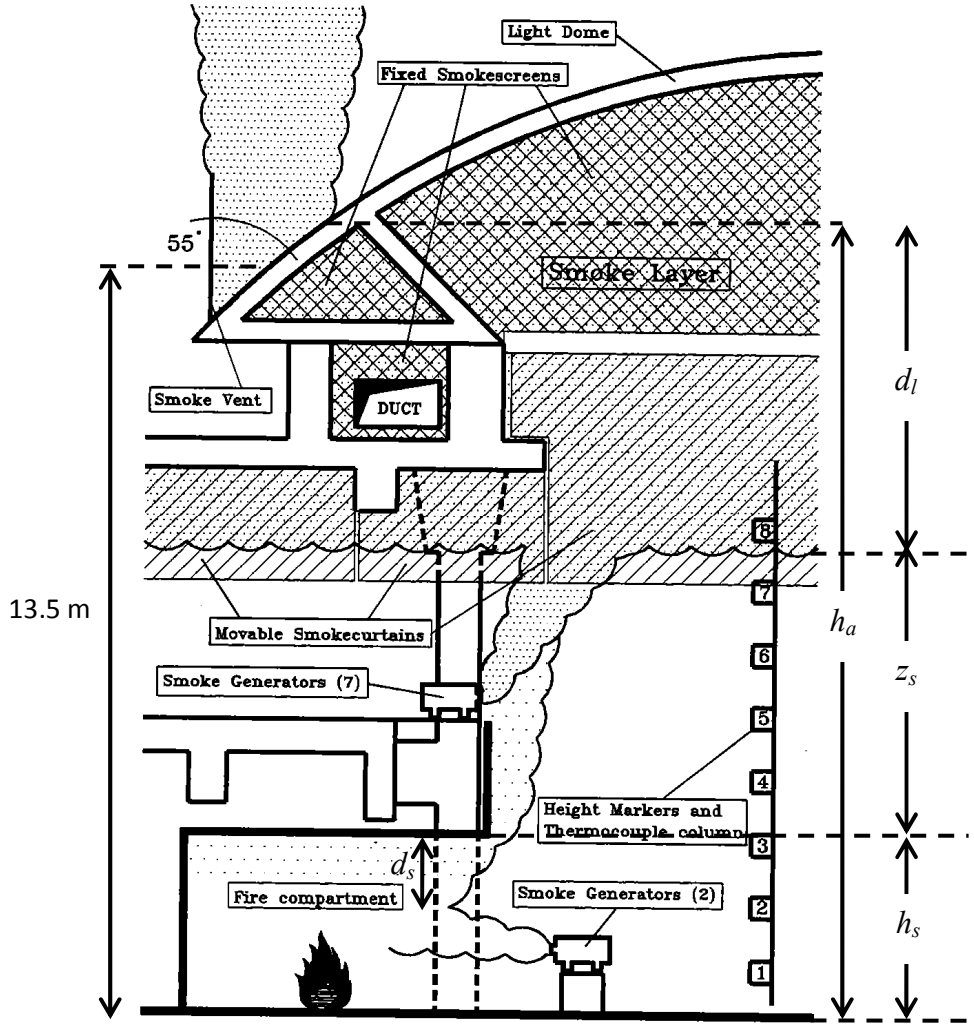

Figure 10.4: Half-section of the atrium (adapted from [53])

10.1.5 Instrumentation

A thermocouple column was hung from the barrel vault roof to measure the smoke layer temperature and also to determine the smoke layer depth. The location of these thermocouples is given by Morgan *et al.* [53]. Height markers were also hung from the roof so that observers could visually assess the smoke layer depth. There was extensive video and stills camera coverage of the tests.

10.1.6 Results

The SHEVS maintained the smoke layer base in the atrium at a height of 10.5 ± 0.5 m above floor level.

Morgan *et al.* provide a prediction of the height of the layer base using the BRE spill plume method (assuming a 3-D balcony spill plume) by applying the 'effective layer depth correction'. The predicted height of the layer was determined to be 9.05 m. Morgan *et al.* explain that the discrepancy in layer height between the test and the prediction was most likely due to the balcony spill plume not being 'ideal' in nature (i.e. free directly above the spill edge) as the geometry of the compartment was such that the plume was possibly adhered (or partially adhered) over the first 1.5 m of its rise and then was free above that, thus the prediction was expected to be somewhat conservative. Therefore it was concluded that the BRE method provided a good prediction of the hot smoke test to give confidence in extrapolating the calculations to the full design fire (as it will provide a slightly conservative result). Extrapolated calculations showed that the SHEVS would work successfully for the full design fire of 5 MW.

The hot smoke test identified a number of design features which allowed smoke to accumulate or travel through unforeseen leakage paths. However, these issues required relatively simple remedial action and are not discussed here.

10.1.7 Prediction of the hot smoke test using new guidance

As the hot smoke test essentially involved a 3-D balcony spill plume channelled by screens below the balcony, the relevant design guidance proposed in this work for this scenario are:

- The simplified design formula for the 3-D balcony spill plume channelled by screens below the balcony [Equation (6-12)] (see section 6.3.3.1).
- The BRE (UC) method (see section 6.7.2).
- FDS modelling with a grid size of 0.25 m (see section 8.1.3.7).

The key criterion used to assess the performance of the new guidance proposed in this work is taken to be the height of the smoke layer above the floor of the atrium. However, the nature of FDS modelling allows a more holistic prediction of the smoke behaviour to be achieved and this is assessed against the visual observations and measurements made during the test. A prediction of the hot smoke test using each of these methods is described below.

10.1.7.1 New simplified design formula [Equation (6-16)]

As the SHEVS was a natural system, the specification is given in terms of the total ventilation area for smoke exhaust (i.e. A_v = 80 m^2). Thus, the calculation to determine z_s (from which the height of the layer above the floor can be determined) is somewhat problematic as it cannot be directly obtained using Equation (6-12) as it requires the value of $\dot{m}_{p,3D}$ which is currently unknown. Therefore the following approach is taken:

Firstly, Equation (6-12) shown below, can be reduced using the known values of the input parameters from the hot smoke test, therefore,

$$\dot{m}_{p,3D} = 0.16\dot{Q}_c^{1/3}\left(W_s^{2/3} + 1.56d_s^{2/3}\right)z_s + 1.34\dot{m}_s$$

$\dot{m}_s$ can be determined using Equation (5-5) such that,

$$\dot{m}_s = 0.09\dot{Q}_c^{1/3} W_s^{2/3} h_s$$

As $\dot{Q}_c$ = 1930 kW, W_s = 9.6 m and h_s = 3.5 m, then,

$$\dot{m}_s = 0.09(1930)^{1/3}(9.6)^{2/3}(3.5) = 17.7 \text{ kg s}^{-1}$$

d_s can be determined using Equation (6-19), such that,

$$d_s = \frac{1}{C_d}\left[\frac{\dot{m}_s}{2W_s}\right]^{2/3}$$

As there was a flat ceiling at the spill edge of the fire compartment C_d = 1.0 [59], thus,

$$d_s = \frac{1}{1.0}\left[\frac{17.7}{2(9.6)}\right]^{2/3} = 0.95 \text{ m}$$

Therefore, Equation (6-12) becomes,

$$\dot{m}_{p,3D} = 0.16(1930)^{1/3}\left([9.6]^{2/3} + 1.56[0.95]^{2/3}\right)z_s + 1.34(17.7)$$

$$\Rightarrow \dot{m}_{p,3D} = \left(12z_s + 23.7\right) \quad \textbf{(10-1)}$$

The following formula given by Klote and Milke [13] which describes $\dot{m}_{p,3D}$ in terms of A_v can then be utilised,

$$\dot{m}_{p,3D} = \frac{C_d A_v \rho_{amb}\left[2gd_l\overline{\theta}_l\left(\frac{T_{amb}}{\overline{T}_l}\right)\right]^{1/2}}{\left[\overline{T}_l + \left(A_v/A_i\right)^2 T_{amb}\right]^{1/2}} \quad \textbf{(10-2)}$$

d_l can be expressed in terms of z_s by (also see Figure 10.4),

$$d_l = h_a - h_s - z_s = (14.0 - 3.5 - z_s) = (10.5 - z_s) \quad \textbf{(10-3)}$$

As the ceiling of the atrium was not flat, the height of the ceiling (h_a) for the calculation of natural exhaust was taken to be the height from the floor to top of the vents (i.e. 14.0 m).

Morgan *et al*. [53] give T_{amb} = 291 K, thus, ρ_{amb} = 1.21 kg m^{-3}.

$\overline{\theta}_l$ can be determined from [12],

$$\overline{\theta}_l = \frac{\dot{Q}_c}{\dot{m}_{p,3D} c_{p,air}}$$

Assuming $c_{p,air}$ = 1.0 kJ kg^{-1} K^{-1} [12] gives,

$$\overline{\theta}_l = \frac{1930}{\dot{m}_{p,3D}} = \frac{1930}{(12 z_s + 23.7)} \quad \textbf{(10-4)}$$

From which,

$$\overline{T}_l = \overline{\theta}_l + T_{amb} = \left[\frac{1930}{(12 z_s + 23.7)} + 291 \right] \quad \textbf{(10-5)}$$

Other input parameters given by Morgan *et al.* [53] are A_v = 80 m^2, (A_v / A_t) = 1.0 and C_d = 0.6. Therefore, Equations 10.3 to 10.5 and the known input parameters can be substituted into Equation (10-2) to reduce it to a form that is only dependent on z_s, such that,

$$12z_s + 23.7 = \frac{58\left[19.6(10.5 - z_s)\left(\frac{1930}{12z_s + 23.7}\right)\left(\frac{291}{\left[\frac{1930}{(12z_s + 23.7)} + 291\right]}\right)\right]^{1/2}}{\left[\left(\frac{1930}{(12z_s + 23.7)} + 291\right) + 291\right]^{1/2}} \quad \textbf{(10-6)}$$

Equation (10-6) can be solved in a spreadsheet to give,

z_s = 6.0 m

Finally, as a check to confirm that Equation (6-12) is not being applied beyond the height of transition in entrainment behaviour to axisymmetric, z_s must be below the limit (z_{trans}) given by Equation (9-14), such that,

$$z_{trans} = 3.4\left(W_s^{2/3} + 1.56 d_s^{2/3}\right)^{3/2} = 3.4\left(\left[9.6\right]^{2/3} + 1.56\left[0.95\right]^{2/3}\right)^{3/2} = 50.3 \text{ m}$$

Hence, $z_s << z_{trans}$ and therefore it is appropriate to use Equation (6-12) in the analysis. Thus, the height of the layer base above the floor is predicted to be,

$z_s + h_s$ = 6.0 + 3.5 = 9.5 m

The prediction provides good agreement with the observed height of layer in the hot smoke test of 10.5 ± 0.5 m, considering that a slightly conservative prediction is expected due to the presence of the upstand above the compartment which is not taken to account in the prediction. As the plume is assumed to be free above the spill edge in the prediction, the additional mass flow of gases over the 1.5 m upstand height was determined to be 13.7 kg s^{-1} from the difference between a balcony spill plume and an adhered spill plume using Equations (6-12) and (7-14) respectively. This additional mass is approximately 15% of the total mass flow rate in the plume (i.e. 97 kg s^{-1}) and is comparable to the predicted layer height being approximately 10% lower than the observed clear layer height in the test. This gives further confidence in the use of Equation (6-12) to predict entrainment for full scale 3-D balcony spill plumes.

10.1.7.2 BRE (UC) method

The suggested modifications to the BRE spill plume method given in section 6.7.2 [to give the BRE (UC) method] were programmed into ASKHPM [133] to provide a prediction of z_s for the test. The values of $\dot{Q}_c$ (1930 kW) and $\dot{m}_s$ (17.7 kg s^{-1}) were used as input parameters. The BRE (UC) method predicts z_s to be 5.6 m and therefore gives a height of smoke layer above the atrium floor of 9.1 m. This is similar to the prediction made above using Equation (6-12) and again is slightly conservative due to the effect of the upstand not being taken into account in the prediction. Therefore, it appears that the BRE (UC) method provides a good prediction of the test and gives further confidence in its use to predict entrainment for full scale 3-D balcony spill plumes.

10.1.7.3 FDS modelling

Figure 10.5 shows an overview of the computational domain and geometry used in the FDS modelling. The domain was 55 by 47 by 18 m high and primarily incorporated the outlet smoke reservoir. The domain extended 6 m beyond the glazed screen into the inlet reservoir and 1 m above the top of the glazed roof. All of the domain boundaries were open apart from the floor which was a solid surface. The open domain boundary on the inlet side of the reservoir provided the inlet air.

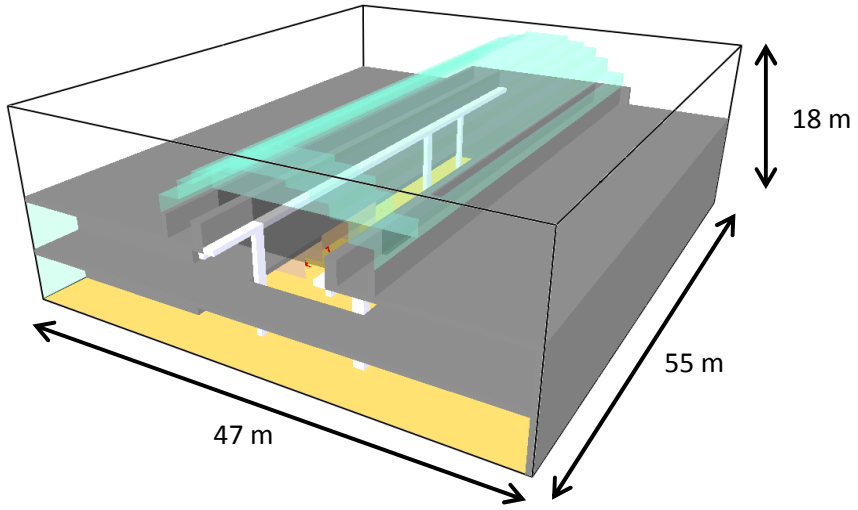

Figure 10.5: An overview of the computational domain and modelled geometry

The areas of the building adjacent to the atrium on both the departure and mezzanine levels were modelled (see Figure 10.6). The floors and walls of the structure were assumed to be made from concrete (0.5 m thick) and the glazed roof was assumed to be made from 5 mm thick glass, as well as the fixed screen used to partition the atrium space. Smoke curtains were also modelled below the screen as in the test, with the bottom of the curtain being 7.5 m above the floor. Other architectural features (e.g. columns) were also modelled and assumed to be made from concrete.

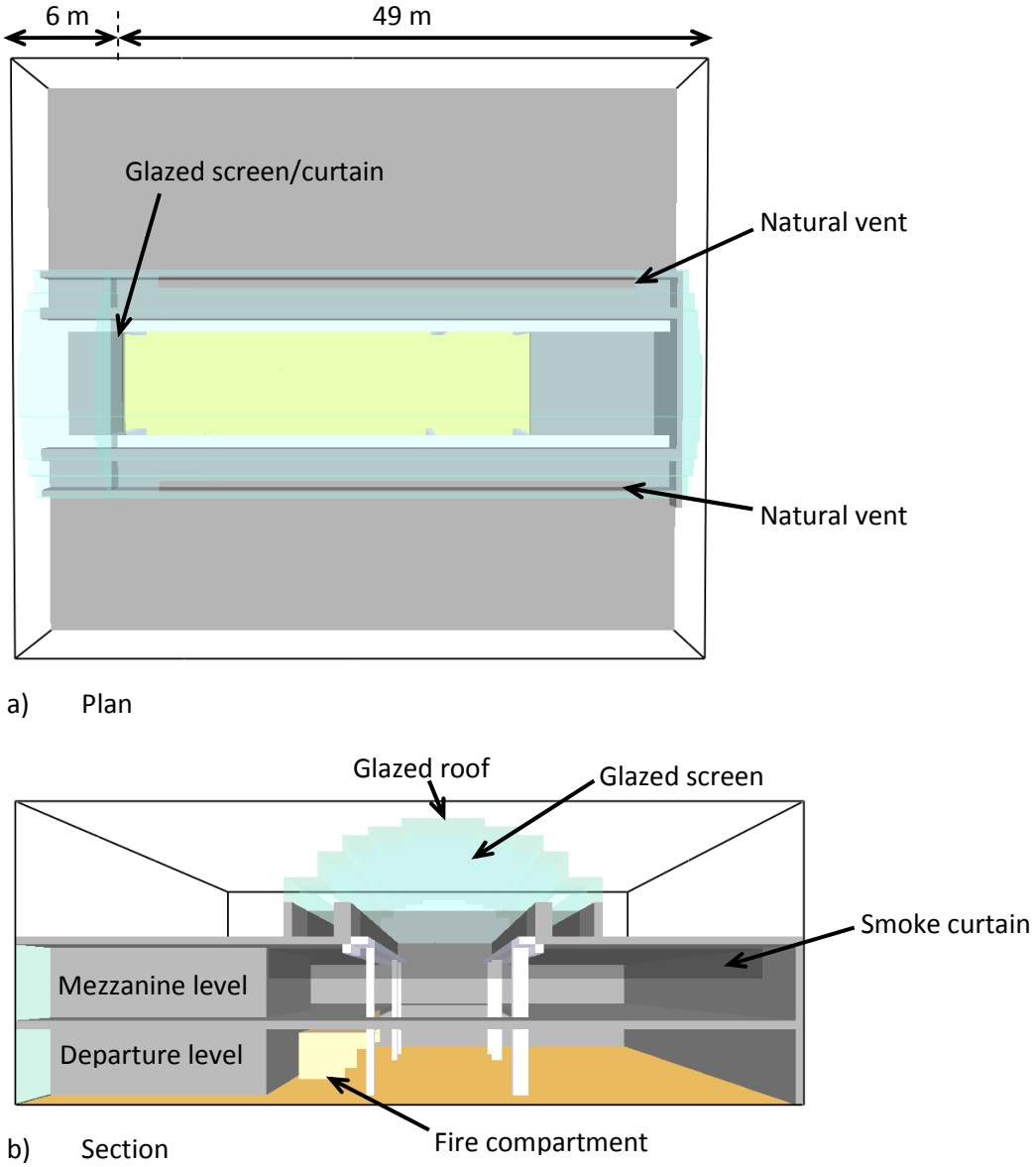

Figure 10.6: Plan and section view of the modelled geometry

The curved glazed roof was approximated to a stepped geometry (see Figure 10.6b) as it is not possible to model curved surfaces in FDS. The natural smoke exhaust was modelled as two separate open vents along each side of the glazed roof (see Figure 10.6a) with dimensions of 40 m long by 1 m wide (at a height of 13.5 m above the floor of the atrium) providing a total of 80 m^2 of vent area.

The fire compartment was assumed to be made from 10 mm thick calcium silicate board with the same dimensions as the compartment used in the test (see Figure 10.7). The fire source was modelled as two separate burners with the same dimensions and in the same locations as the fire trays used in the test. Each burner was assigned with a HRRPUA of 527 kW m^{-2} [126] and a radiative fraction of 0.2 [109]. The thermal properties of the materials modelled in the simulation are given in Table 10.1, with the smoke curtain material assumed to be glass fibre in the absence of any other data.

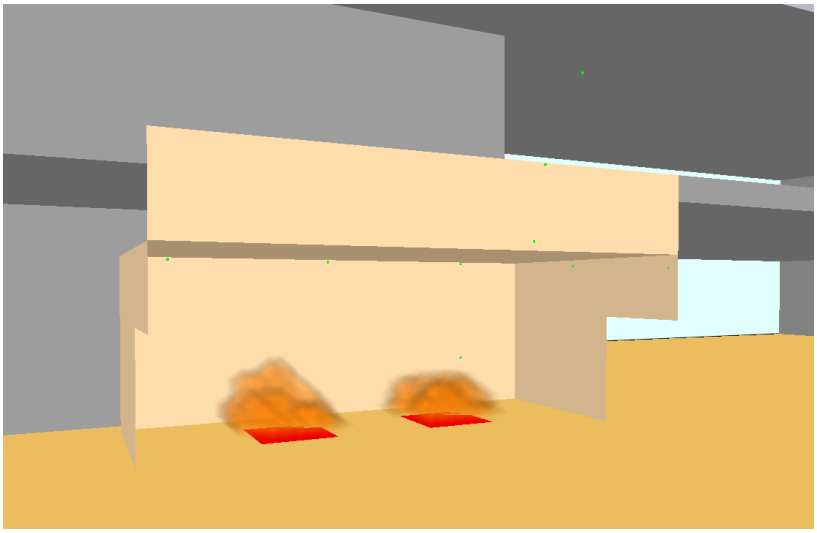

Figure 10.7: The modelled fire source and compartment

Material	k	ρ	c_p
	W m^{-1} K^{-1}	kg m^{-3}	kJ kg^{-1} K^{-1}
Concrete [139]	1.0	2100	0.88
Glass plate [108]	0.76	2700	0.84
Calcium silicate board [140]	0.19	870	0.92
Smoke curtain (glass fibre) [120]	0.036	105	0.80

Table 10.1: Thermal properties of materials modelled in the simulation

The grid size distribution in the computational domain was varied to provide a coarser grid in areas remote from the fire compartment and plume (see Figure 8.10) which is recommended in areas of less importance in the flow domain [42]. Therefore, a region of the domain with dimensions of 13.5 by 47 by 18 m high, which incorporated the fire compartment and the spill plume, was assigned with a grid size of 0.25 m. This region extended 2 m beyond each side of the fire compartment to encompass the broadening of the plume and extended the full height and breadth (perpendicular to the spill edge) of the domain. The other two regions of the domain were assigned with a coarser grid size of 0.5 m (see Figure 10.8). This resulted in a total of 1,011,816 grid elements within the whole of the domain. The ambient temperature in the simulation was set to be 18 °C to be consistent with the test. The simulation time was set to 600 s (consistent with the time when steady conditions were reached in the test [53]) and took approximately 3.5 days to run using the serial version of FDS.

A detailed description of the modelled geometry and computational domain is given in Appendix R which shows the FDS input file used for the simulation.

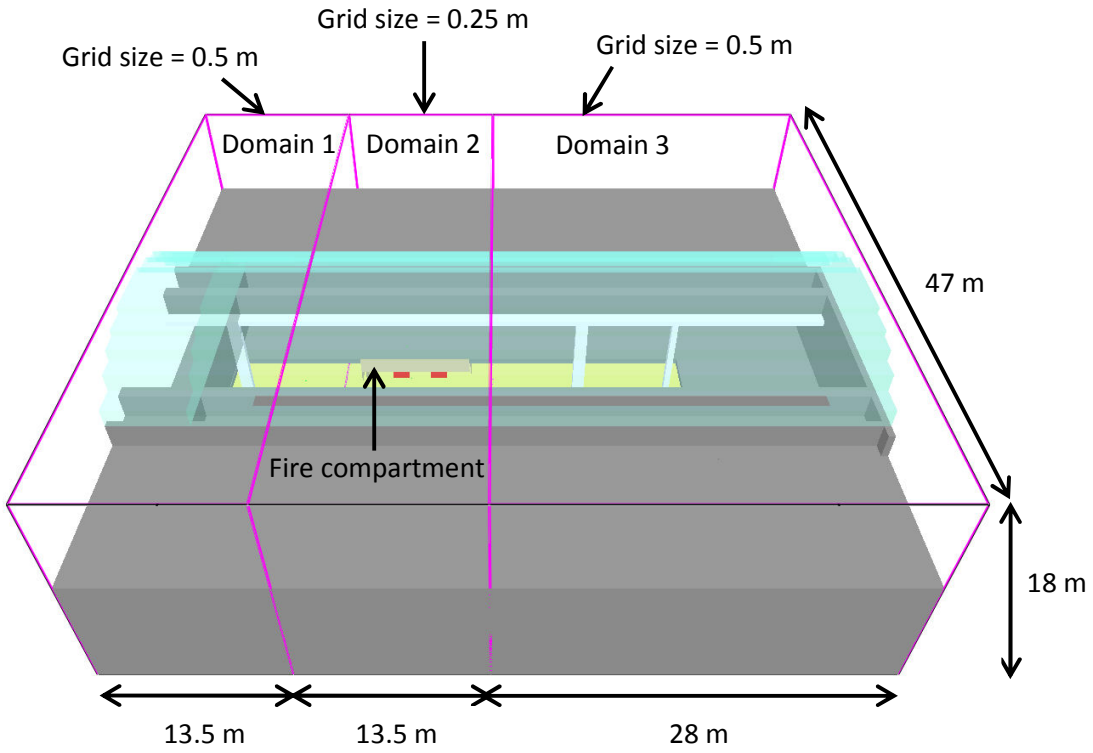

Figure 10.8: Grid size distribution in the computational domain

To confirm that a grid size of 0.25 m is appropriate to predict plume entrainment for the conditions studied, then the grid size must meet the criterion recommended in section 8.1.3.9 (i.e. $n^*_{spill} \geq 0.9$) where,

$$n^*_{spill} = \frac{D_{spill}{}^*}{\delta x} \quad \text{and} \quad D^*_{spill} = \left(\frac{\frac{\dot{Q}_c}{W_s}}{\rho_{amb} c_{p,air} T_{amb} \sqrt{g}} \right)^{2/3}$$

Hence,

$$D^*_{spill} = \left(\frac{\frac{1930}{9.6}}{1103} \right)^{2/3} = 0.32 \quad \text{and} \quad n^*_{spill} = \frac{0.32}{0.25} = 1.29$$

Thus, as n^*_{spill} is greater than 0.9 then a grid size of 0.25 m is suitable in modelling the plume for the conditions studied.

Figure 10.9 shows the predicted vertical temperature slice file through the centreline of the plume in the atrium, and shows that the plume appears to adhere to the 1.5 m upstand above the fire compartment before rising as a balcony (i.e. free) spill plume above that. The prediction also shows partial impingement of the plume with the architectural feature extending beyond the ceiling of the mezzanine level which projected (by approximately 1.0 m) into the atrium space. This is discussed further later.

Figure 10.9 shows smoke exhaust from the natural vents in the glazed roof and the location of the smoke layer base in the atrium space. The predicted smoke layer is approximately in line with the ceiling of the mezzanine level which was at a height of 10 m above the floor of the atrium, and agrees very well with visually derived height of layer during the hot smoke test of 10.5 ± 0.5 m.

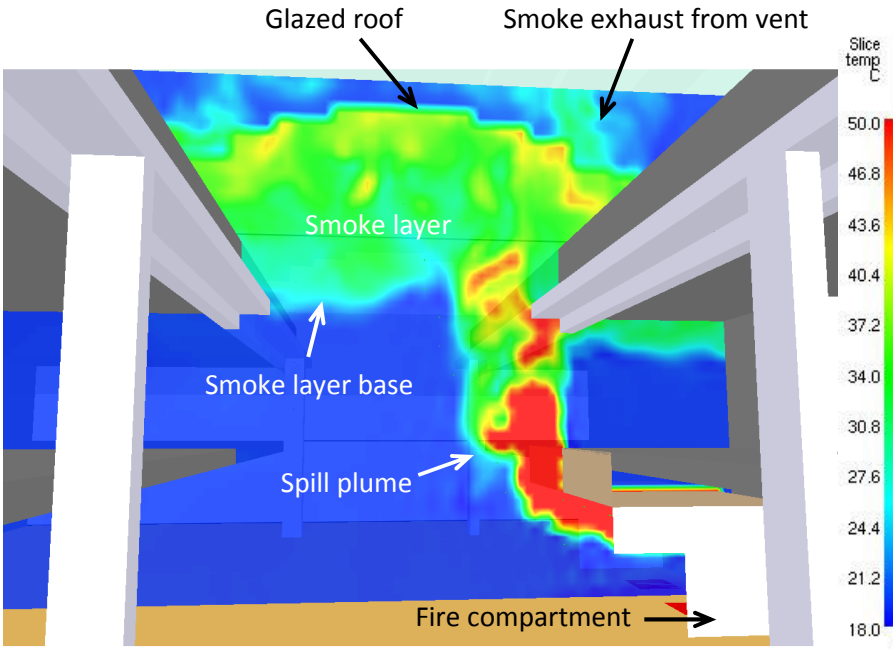

Figure 10.9: Vertical temperature slice file through centreline of the plume

Figure 10.10 shows a slice file of the predicted temperature through the centreline of the atrium, parallel to the long length, and demonstrates that the height smoke layer was reasonably uniform along the reservoir, apart from some local deepening at the ends due to interaction with the partition screen/wall.

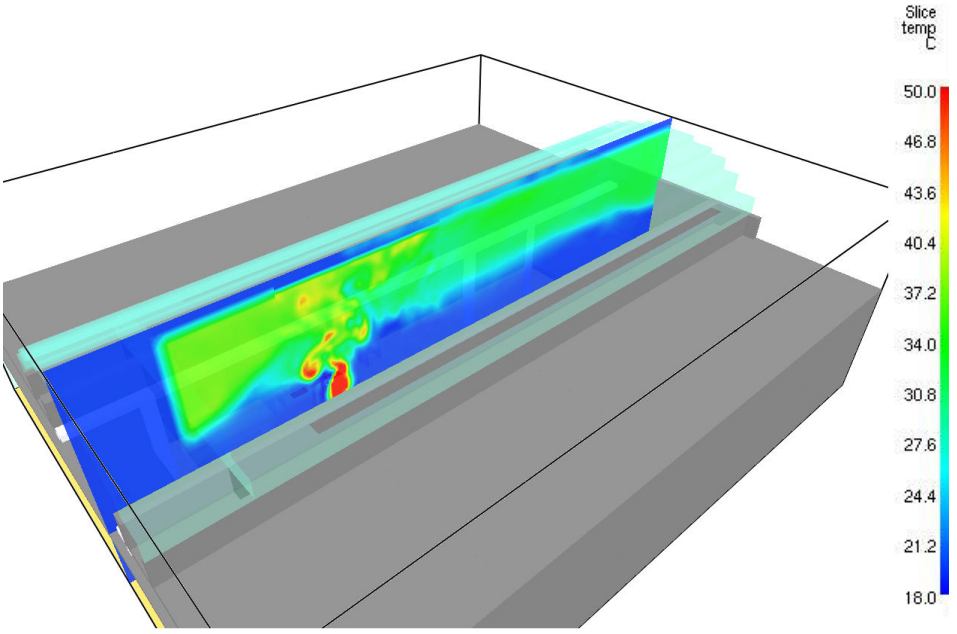

Figure 10.10: Vertical temperature slice file through the centreline of the atrium

The analysis of the smoke layer height can be further supported from the predicted temperatures of the column of thermocouples in the atrium space. Figure 10.10 shows a comparison of the predicted buoyancy profiles in the atrium with the measured values in the test. The predicted buoyancy was time averaged over the last 60 s of the simulation during steady conditions.

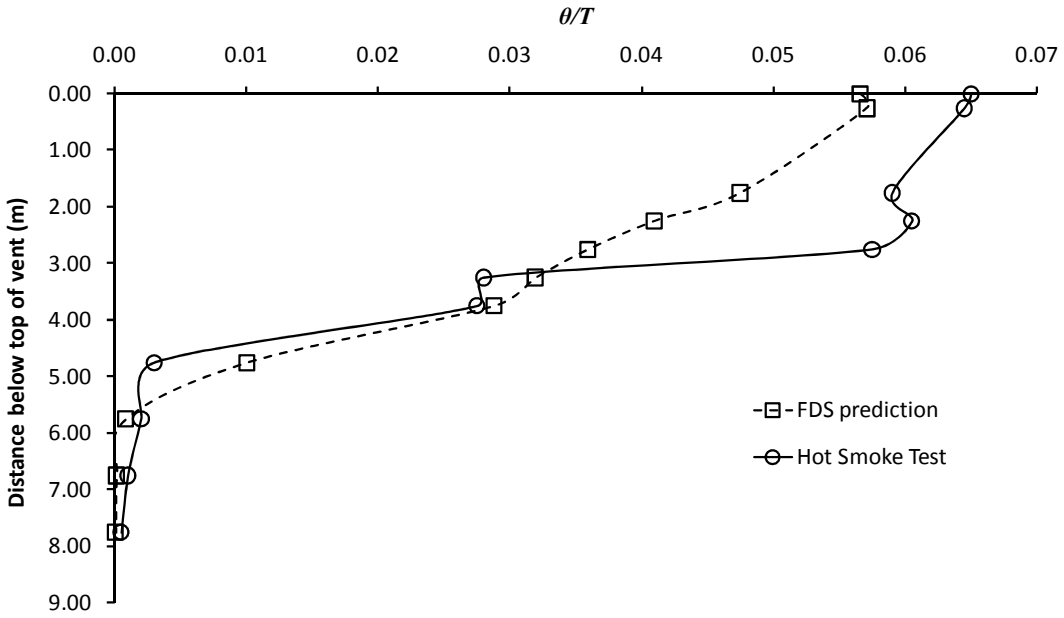

Figure 10.11: Comparison of buoyancy profiles in the atrium

Figure 10.11 shows that the predicted buoyancy close to the top of the vent is somewhat lower than was measured in the test, possibly due to differences in the heat transfer to the boundaries between the prediction and the test. However, the profiles approach ambient at a similar depth below the vent. The buoyancy profiles can be utilised to calculate the height of the smoke layer above the atrium floor from the measurements/predictions using Equation (4-9). The buoyancy derived height of layer from the predictions was determined to be 10.6 m which provides excellent agreement with the calculated height from the test measurements of 10.5 m. Therefore, the above analysis demonstrates that FDS provides an excellent prediction of the smoke layer height in the atrium and hence, 3-D balcony spill plume entrainment (with channelling screens below the balcony).

As mentioned above, the predicted temperature slice file showed plume impingement with a horizontal projection which extended beyond the ceiling of the mezzanine level. This caused part of the plume to be directed beneath the ceiling of the mezzanine from which a buoyant smoke layer formed. The predicted smoke flow behaviour was very similar to that observed in the hot smoke test as shown in Figure 10.12, which shows a direct comparison between the prediction and the test in terms of the smoke behaviour on the mezzanine level above the fire compartment.

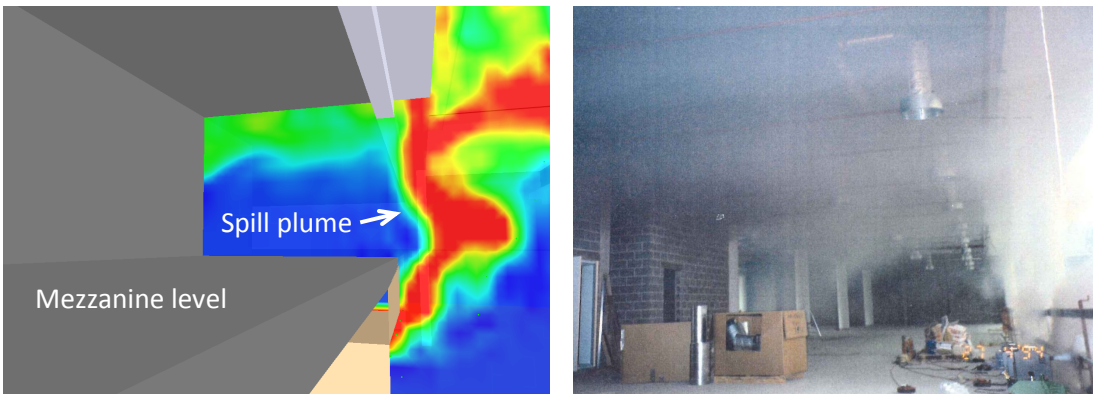

a) FDS prediction b) The hot smoke test

Figure 10.12: Comparison of predicted smoke behaviour on the mezzanine with the test

Therefore, it appears that FDS provides an excellent prediction of balcony spill plume behaviour and entrainment, when using a grid size of 0.25 m in the region of the rising plume and grid size of 0.5 m in regions remote from the plume.

The analysis also demonstrates that there can be additional benefits in using CFD modelling in terms of providing a more general assessment of the smoke flow behaviour which is not possible using simple/analytical calculation methods.

10.2 Hot Smoke Test at the European Parliament Building, Brussels

Harrison *et al.* [54] provide a detailed description of the hot smoke test carried out in an atrium space of the (then unfinished) European Parliament building in Brussels. A summary of the test is described below, including a description of the building, the test fires and the results.

10.2.1 The building

The hot smoke test was carried out in part of the 'D3 Espace Leopold Building' of the European Parliament building. The test area was approximately 74 m long by 12 m wide by 27 m high and contained two reservoirs (or atrium spaces). The fire reservoir was designated as Reservoir 1 and the adjacent reservoir as Reservoir 2. A plan view of the test area is shown in Figure 10.13.

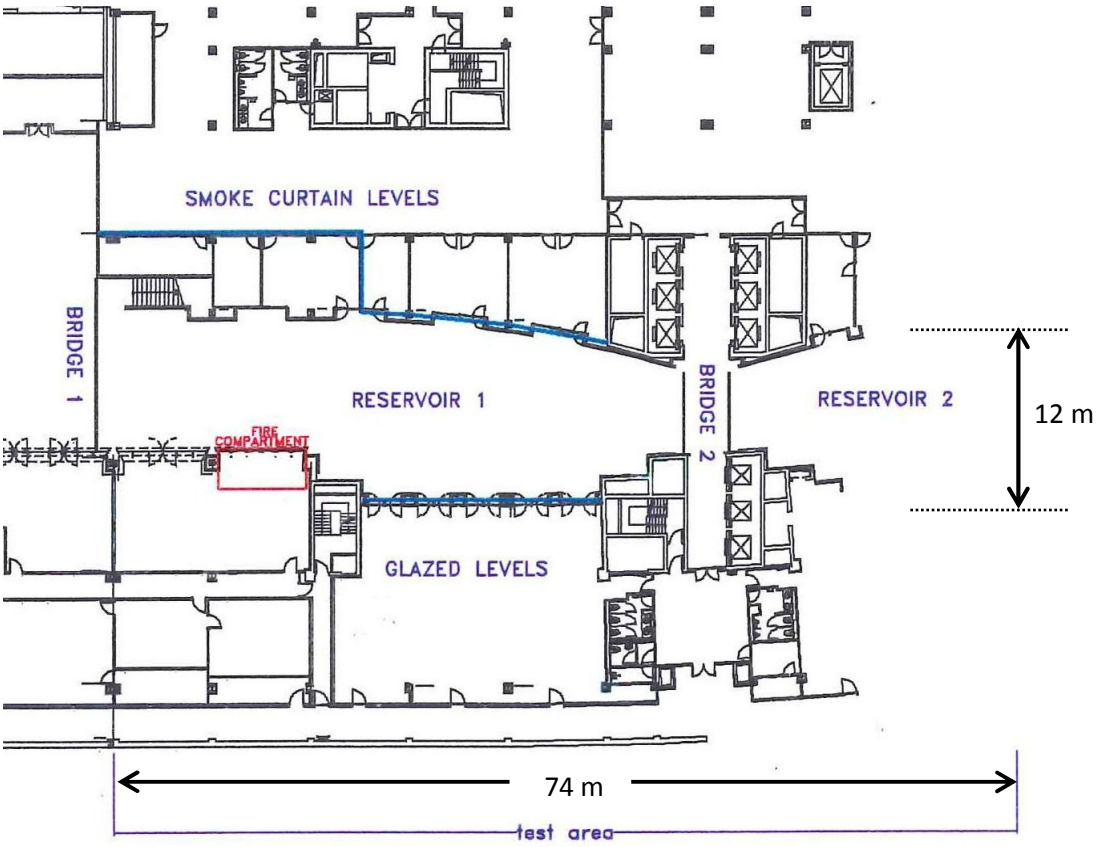

Figure 10.13: Schematic plan view of the test area (adapted from [54])

Figure 10.14 shows a section of Reservoir 1. Directly above the fire compartment were six levels of glazed offices up to the glazed roof level, designated Levels 1 to 6. There were more office levels beyond the glazed roof. On the opposite side of the reservoir were three levels of foyers up to roof level designated Levels 1, 3 and 5. Figure 10.14 shows a photograph of the finished building.

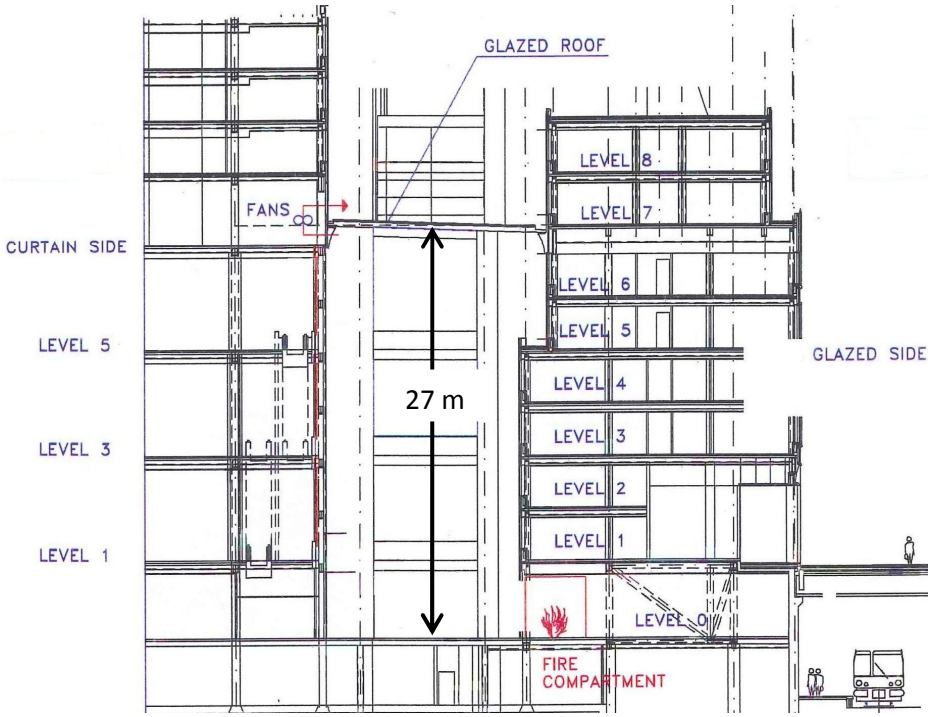

Figure 10.14: Schematic of a section of Reservoir 1 (adapted from [54])

Figure 10.15: The D3 Espace Leopold Building in its finished state (adapted from [12])

10.2.2 The fire compartment

A fire compartment made of 10 mm calcium silicate board (Promatect-H) attached to an angle iron structure was built on ground level beneath the glazed offices and fronted onto the atrium space to simulate the design scenario (see Figure 10.16). The compartment was 6.5 m wide by 3.5 m deep by 2.75 m high. The front of the compartment was open on the 6.5 m width face. This represented a shop/office unit. The compartment structure continued upwards to a height of 9 m above the spill edge to protect the building structure against exposure to hot gases.

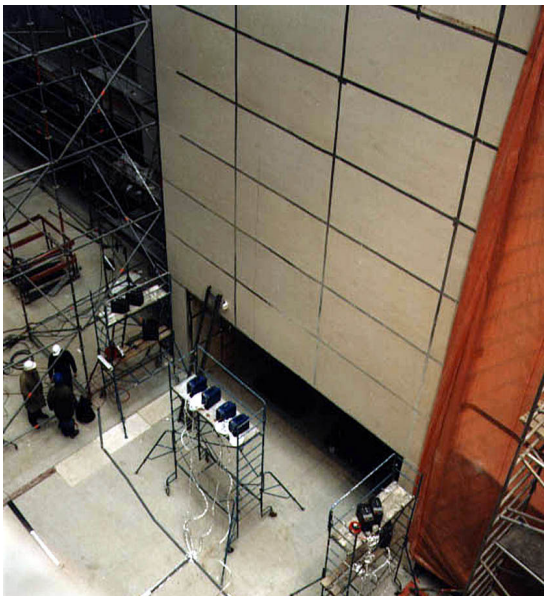

Figure 10.16: The fire compartment and smoke generators

10.2.3 The test fire

The hot buoyant layer was produced by burning IMS pool fires in the compartment. The fuel was burnt in two square steel fire trays, 1.0 m by 1.0 m, each of which was floated on a larger tray of water, 1.5 m by 1.5 m. The convective heat flow in the fire gases from each tray was 420 kW, to give a test fire with a total of 840 kW. Oil-mist cosmetic smoke from eight commercial smoke generators was fed into the plume above the spill edge to mark the hot gases for visual and photographic observations. These generators were placed on scaffolding at locations shown in Figure 10.16 and 10.17 to inject smoke into the front side of the plume.

Figure 10.17: The IMS test fire [54]

10.2.4 The SHEVS

The SHEVS was mechanically driven using two fans located approximately 1 m below the roof of the reservoir. The actual fan capacities of each of the two fans was found from a fan test to be 22.2 m^3 s^{-1} and 16.7 m^3 s^{-1}, thus giving a total volumetric exhaust rate of 38.9 m^3 s^{-1}. Inlet air was provided via low level openings distributed around the building.

The smoke reservoir in the atrium was formed by full height smoke curtains and the structure of the building. The foyer side of the reservoir contained smoke curtains intended to prevent smoke from entering these levels. There were full height smoke curtains across the connecting bridges on either side of the fire reservoir which divided the length of the test area into two separate reservoirs. The building at the time of the test was not in its finished state with much of the cladding material was not in place, leaving in some places wider gaps between smoke curtains and walls or columns than would have been the case in the finished building. In many places temporary curtaining of polythene had been installed.

Morgan *et al.* state that the curtains on Level 5 were originally specified to overlap, but a design change created a curved edge which removed the overlap. Due to the incomplete and partially temporary nature of much of the smoke curtaining, the curtains were dropped into their fire positions prior to the test.

During the test, smoke entered the Level 5 foyer through curtain/curtain and curtain/structure gaps and beneath the smoke curtains which caused the foyer and connecting lobby to fill with smoke. Smoke also passed through the gaps between the curtain and the structure on Level 5 (Bridge 2) due to deflection of the curtain such that smoke also accumulated within Reservoir 2. Therefore, the effective smoke exhaust from the atrium was higher than the specified 38.9 $m^3 s^{-1}$ from the mechanical fans alone due to additional natural exhaust through the curtain gaps. Hence, there was some uncertainty on the total amount of smoke exhaust from the reservoir. The quantity of the additional natural exhaust from the reservoir was approximated by Morgan *et al.* [140] from the total gap area on the Level 5 foyer and on Bridge 2 on Level 5. The total gap area on the Level 5 foyer was determined by inspection to be 6.5 m^2, and from the pressure drop measured across the curtains (0.2 Pa) and the gas density (1.2 kg m^{-3}) gave a volume exhaust rate of 3.7 $m^3 s^{-1}$. The total gap area on Bridge 2, Level 5 was determined to be 1.4 m^2 and from the pressure drop across the curtain (3 Pa) and the gas density (1.2 kg m^{-3}) gave a volume exhaust rate of 3.1 $m^3 s^{-1}$, to give a total additional smoke exhaust of 6.8 $m^3 s^{-1}$. Therefore the total smoke exhaust from the reservoir during the test was approximately 46 $m^3 s^{-1}$.

10.2.5 Instrumentation

A column of thermocouples was also installed below the atrium ceiling to measure the smoke layer temperatures and to determine the smoke layer depth. The location of these thermocouples is given by Harrison *et al.* [53]. The pressure drop across the smoke curtains on Level 5 and on Bridge 2 (Level 5) was measured during the test. The height of the smoke layer in the atrium above the floor was also determined visually with the aid of height markers which were hung from the roof. Video and stills photographic coverage of the test and observers' records were taken.

10.2.6 Results

The SHEVS maintained the smoke layer base in the atrium at a visually observed height of 15.0 ± 1.0 m above floor level. This agreed with the predicted result using the BRE method (applying the effective layer depth correction) within experimental error, although the additional smoke exhaust through the curtain gaps on Level 5 was not considered in the prediction. By extrapolation from the test results, it was shown that the SHEVS would work successfully in keeping the smoke layer base above that allowed for in the design fire scenario.

The tests did identify a number of design features which allowed smoke to travel through unforeseen leakage paths which needed relatively simple remedial action, however, they are not discussed here.

10.2.7 Prediction of the hot smoke test using new guidance

As the hot smoke test involved a 3-D adhered spill plume, the relevant guidance proposed in this work for this scenario are:

- The simplified design formula for the 3-D adhered plume [Equation (7-14)] (see section 7.3.5).
- The original BRE spill plume method (see section 7.3.5).

Although the analysis in section 8.1.4 demonstrated that further work is necessary to provide improved guidance on the use of FDS to quantify 3-D adhered plume entrainment, the hot smoke test was also modelled in FDS to assess its performance in predicting a full scale adhered spill plume.

Therefore, a prediction of the test using each of these methods is described below.

10.2.7.1 New simplified design formula [Equation (7-14)]

The simplified design formula proposed in this work for the 3-D adhered plume [Equation (7-14)] is shown below,

$$\dot{m}_{p,3D} = 0.3\dot{Q}_c^{1/3} W_s^{1/6} d_s^{1/2} z_s + 1.34\dot{m}_s$$

There is a limit on its use given by Equation (7-12) (given below), which first needs to be checked.

$$\left(\frac{W_s}{d_s}\right) \leq 13$$

Therefore, d_s can be determined using Equation (6-19), such that,

$$d_s = \frac{1}{C_d}\left[\frac{\dot{m}_s}{2W_s}\right]^{2/3}$$

$\dot{m}_s$ can be determined using Equation (5-5) such that,

$$\dot{m}_s = 0.09\dot{Q}_c^{1/3} W_s^{2/3} h_s = 0.09(840)^{1/3}(6.5)^{2/3}(2.75) = 8.1 \text{ kg s}^{-1}$$

As there was a flat ceiling at the spill edge of the fire compartment $C_d = 1.0$ [59], thus,

$$d_s = \frac{1}{1.0}\left[\frac{8.1}{2(6.5)}\right]^{2/3} = 0.7 \text{ m}$$

Hence,

$$\left(\frac{W_s}{d_s}\right) = \left(\frac{6.5}{0.7}\right) = 9.3 \leq 13$$

Therefore, the limit given by Equation (7-12) is met, hence,

$$z_s = \frac{\dot{m}_{p,3D} - 1.34\dot{m}_s}{0.3\dot{Q}_c^{1/3} W_s^{1/6} d_s^{1/2}}$$

$$z_s = \frac{46 - 1.34(8.1)}{0.3(840)^{1/3}(6.5)^{1/6}(0.7)^{1/2}}$$

$$z_s = 10.9 \text{ m}$$

Therefore, the height of the smoke layer above the floor is predicted to be 13.6 m (as h_s = 2.75 m). This compares well with height of the layer visually observed in the test of 15.0 ± 1.0 m, however, as explained in section 7.3.3.1 it is expected that Equation (7-14) will provide a slightly conservative prediction in some cases (by up to 10 to 15%) due to a rounding up of the dominant regression coefficient. Therefore, considering this, and the uncertainty in the total smoke exhaust rate due to leakage through curtain gaps, Equation (7-14) provides a good prediction of the hot smoke test and gives further confidence in its use to predict full scale 3-D adhered spill plume entrainment for design purposes.

10.2.7.2 BRE spill plume method

The values of $\dot{Q}_c$ (840 kW) and $\dot{m}_s$ (8.1 kg s^{-1}) were used as input parameters to the BRE spill plume method (without applying the effective layer depth correction). The total amount of smoke exhaust from the atrium (i.e. 46 m^3 s^{-1}) was used in the calculation, but converted to a mass flow rate of 55 kg s^{-1} from the gas density of the smoke layer in the atrium (i.e. 1.2 kg m^{-3}). This gave rise a predicted value of z_s to be 11.5 m. Therefore, the height of smoke layer above the atrium floor is predicted to be 14.3 m which provides excellent agreement layer height in the test of 15.0 ± 0.5 m. Therefore, the BRE spill plume method provides a good prediction of the test and gives further confidence in its use to predict entrainment for full scale 3-D adhered spill plumes.

10.2.7.3 FDS modelling

Figure 10.18 shows an overview of the computational domain and geometry used in the FDS modelling. The domain was 48 by 17.5 by 28 m high and modelled the reservoir which contained the fire compartment (Reservoir 1). The domain extended 1 m beyond the bridges at either end of the reservoir, 1 m above the roof, and up to approximately 4 m into the foyer and office levels from the atrium space. All of the domain boundaries were open apart from the floor which was a solid surface. The open domain boundaries were used to simulate inlet air at low level from the ends of the reservoir and to simulate open spaces in the foyers and office levels as these areas were open to other areas of the building.

The floors and walls of the structure were assumed to be made from concrete (0.5 m thick) and the roof was assumed to be made from 5 mm thick glass. Full height smoke curtains were also modelled in position on the foyers and on the bridges. Other architectural features (e.g. columns) were assumed to be made from concrete.

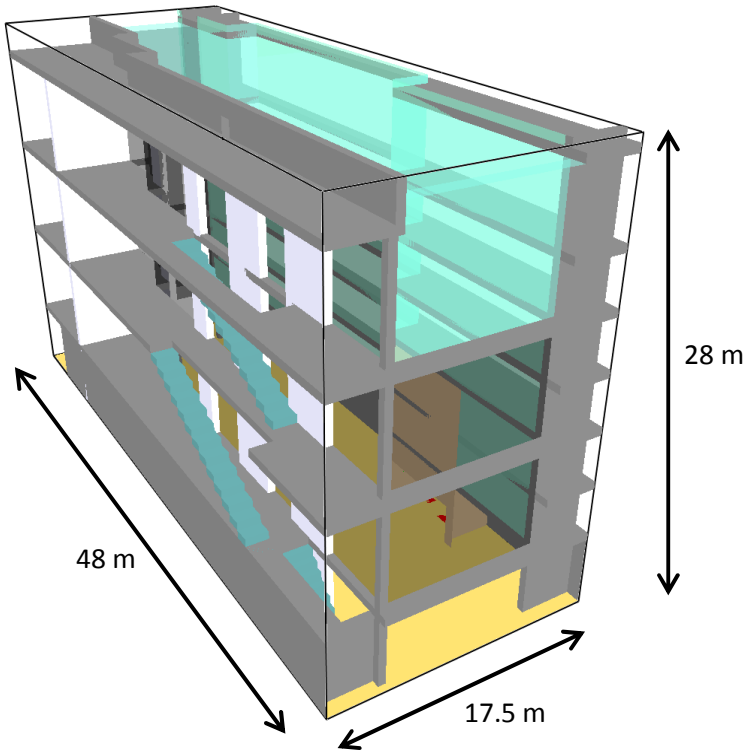

Figure 10.18: An overview of the computational domain and modelled geometry

Mechanical smoke exhaust was provided by modelling two separate fans, each 1 m high by 1 m wide, located approximately 1/3rd of the length of the atrium from each end (in the absence of the exact locations of these fans), 1 m below the glazed roof (see Figure 10.19). Each fan was assigned with a volumetric exhaust flow rate which matched that measured in the fan test.

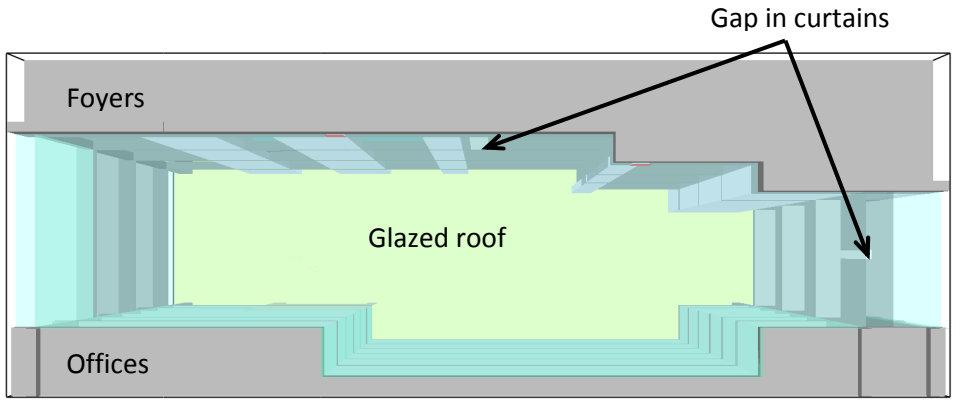

a) Plan

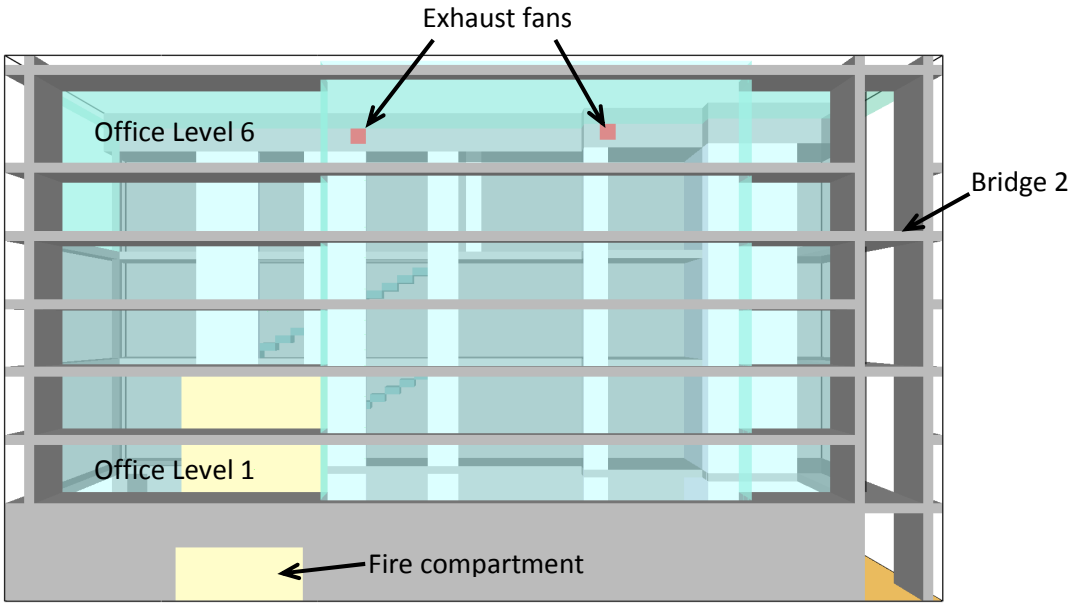

b) Section

Figure 10.19: Plan and section views of the modelled geometry

The smoke curtain gaps on the Level 5 foyer and on Bridge 2 of Level 5 were modelled as a single gap in each location, with a combined area of the total gap size (as the exact resolution of these gaps could not be modelled with the chosen grid size). The gap on the foyer was modelled as a 'hole' in FDS with dimensions of 1.0 m wide by 6.5 m high, the gap on Bridge 2 was 0.5 m wide by 3 m high. Each gap was located centrally in each area.

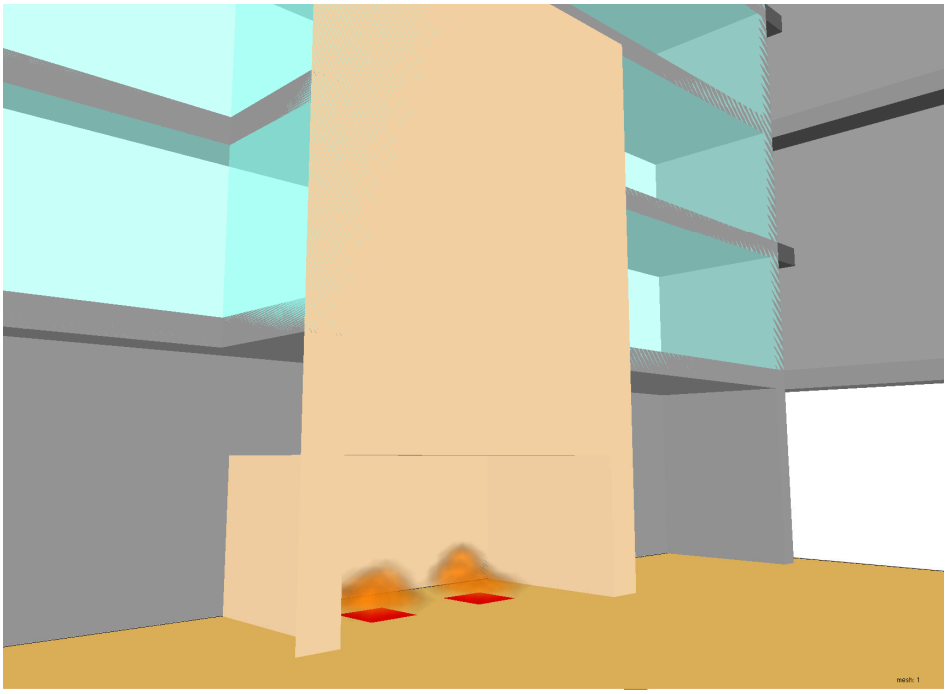

Figure 10.20: The modelled fire source and compartment

The fire compartment was assumed to be made from 10 mm thick calcium silicate board with the same dimensions as the compartment used in the test. The fire source was modelled as two separate burners with the same dimensions and in the same locations as the fire trays used in the test (see Figure 10.20). Each burner was assigned with the same characteristics for burning IMS (or ethanol) as used in the Brussels Airport simulation.

The thermal properties of the materials modelled in the simulation were the same as those given in Table 10.1.

Although the analysis in section 8.1.4 recommends that further work is required on the use of FDS to model 3-D adhered plume entrainment, for the purposes of this simulation a grid size of 0.25 m was chosen to model the plume (consistent with the Brussels Airport simulation). The grid size distribution in the domain was again varied to provide a coarser grid in areas remote from the plume. Therefore, part of the domain with dimensions of 8 by 17.5 by 28 m high which incorporated the fire compartment and the rising plume was assigned with a grid size of 0.25 m (see Figure 10.21). This region of the domain extended 1.25 m beyond either side of the fire compartment and extended the full height and breadth of the domain (perpendicular to the spill edge). The other regions of the domain were assigned with a grid size of 0.5 m. This resulted in a total number of 407,680 grid elements. The ambient temperature in the simulation was set at 7°C to match that measured in the test. The simulation time was set to 600 s (consistent with the time when steady conditions were reached in the test [54]) and took approximately 2.5 days to complete.

A detailed description of the modelled geometry and computational domain is given in Appendix S which shows the FDS input file used for the simulation.

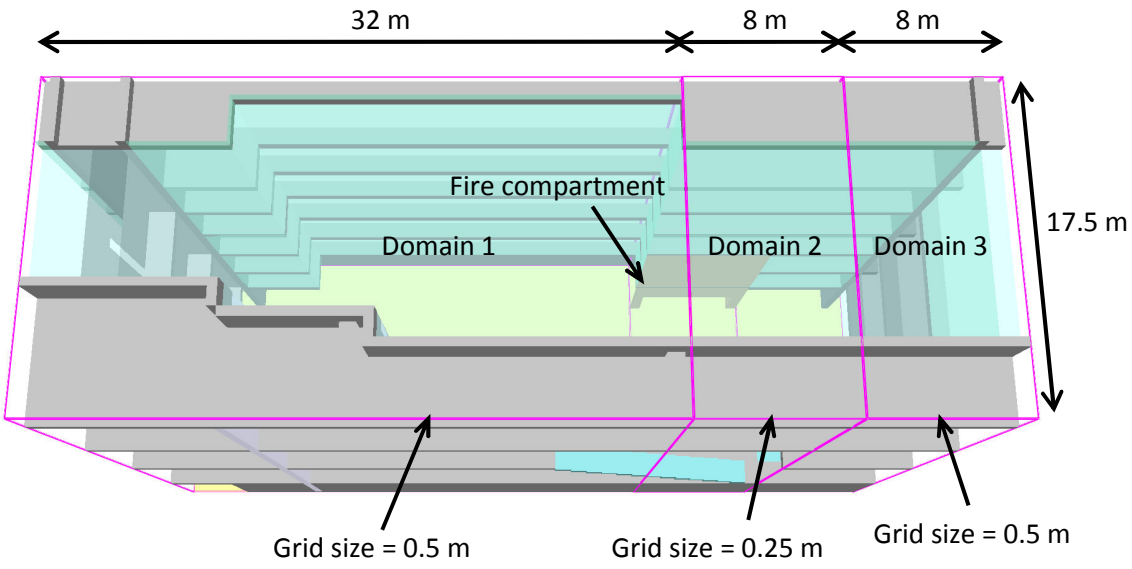

Figure 10.21: Grid size distribution in the computational domain

Figure 10.22 shows the predicted vertical temperature slice file through the centreline of the plume in the atrium, which shows that the plume adheres almost immediately to the wall above the spill edge (i.e. the top of the fire compartment opening). The predicted plume behaviour also agrees well with that observed during the test when compared with Figure 10.23 which shows a photograph of the plume from a side view.

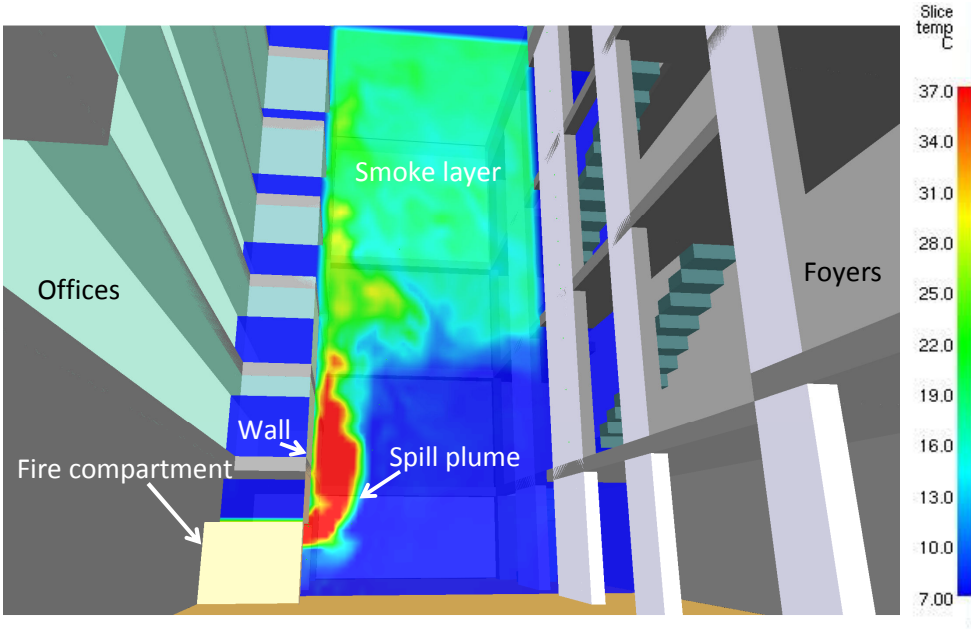

Figure 10.22: Vertical temperature slice file through centreline of the plume

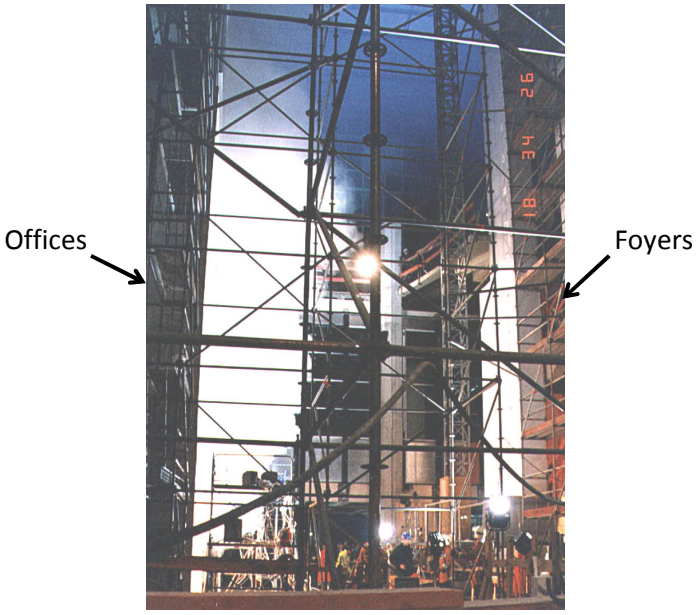

Figure 10.23: Photograph of the plume during the test (side view) [54]

The performance of Equation (7-9) (shown again below) to predict the height of reattachment of the plume above the spill edge (i.e. z_{attach}) can be assessed against the prediction (and the hot smoke test).

$$z_{attach} = \frac{8d_s^2}{W_s}$$

For the conditions studied, the value of d_s was the same, whether it was determined from the visual observations during the test [54], from inspection of the temperature slice files in FDS or from the calculation using Equation (6-19). All of these methods gave rise to a value of d_s of approximately 0.7 m. Hence,

$$z_{attach} = \frac{8(0.7)^2}{6.5} = 0.6\,\text{m}$$

Therefore, z_{attach} was determined to be 0.6 m, which is very close to the spill edge and consistent with that observed during the test and in the FDS simulation. This is further supported if the velocity slice file through the centreline of the plume is examined (see Figure 10.24) which also indicates that the plume adheres almost immediately above the edge. Therefore this analysis provides further confidence in the use of Equation (7-9) to predict the height of reattachment of a 3-D adhered spill plume.

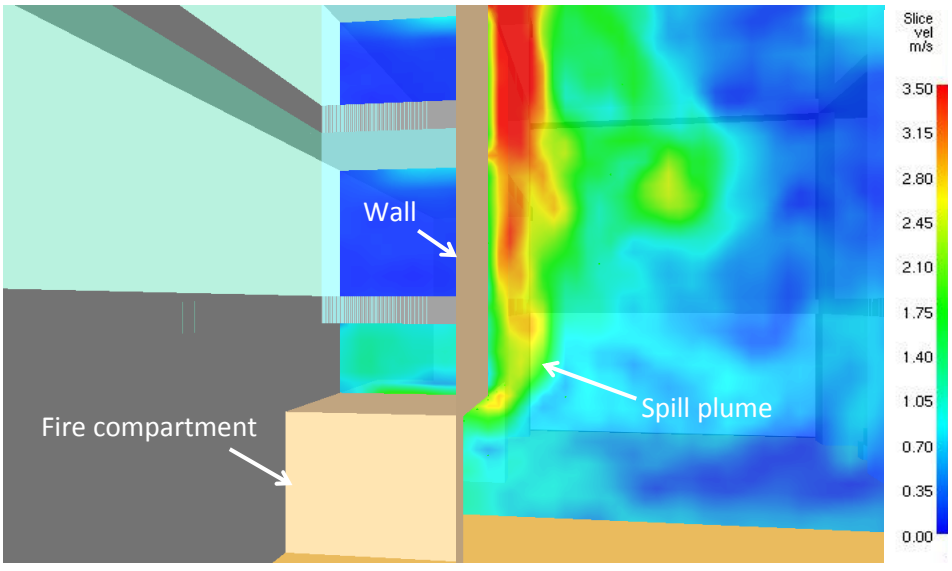

Figure 10.24: Vertical temperature slice file through centreline of the plume

Figure 10.22 also shows that the predicted smoke layer base in the atrium is approximately in line with the ceiling of the Level 1 Foyer at a height of approximately 11.5 m above the floor of the atrium. Figure 10.25 shows a vertical temperature slice file parallel to the long length of the atrium and demonstrates that the height of the smoke layer was reasonably uniform.

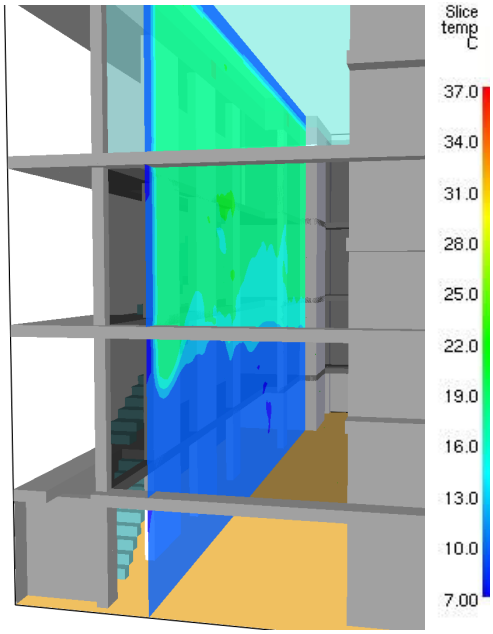

Figure 10.25: Vertical temperature slice file along the atrium

The smoke layer is lower than the visually derived height of layer in the test of 15.0 ± 0.5 m and therefore gives a conservative prediction by approximately 25%.

The analysis of the layer height can be further supported from the predicted temperatures of the column of thermocouples in the atrium space. Figure 10.10 shows a comparison of the predicted buoyancy profiles in the atrium with the measured values from the test. The predicted buoyancy was time averaged over the last 60 s of the simulation during steady conditions. Figure 10.26 shows that although the predicted buoyancy close to the glazed roof is similar to that measured in the test, the profiles approach ambient at different depths below the roof, and indicates a lower height of layer from the FDS prediction compared to the hot smoke test. This supports the above analysis from the temperature slice file.

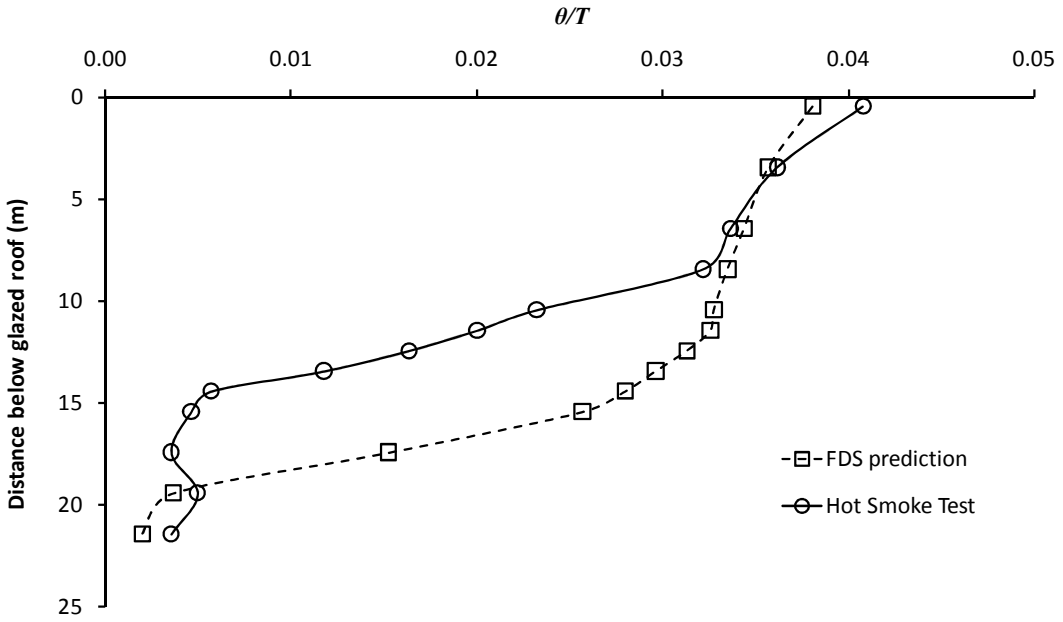

Figure 10.26: Comparison of buoyancy profiles in the atrium

The buoyancy derived height of layer from the predictions [using Equation (4-9)] was determined to be 11.7 m which is lower than the buoyancy derived height of layer from the test measurements of 15.5 ± 0.5 m [54]. Therefore, the above analysis demonstrates that FDS provides a lower prediction of the clear layer height and therefore a higher amount of entrainment in the plume by approximately 20 to 25% .

As a further check, the predicted volume flow rate of gases entering the smoke layer at the plume/layer interface (i.e. at 11.7 m) was determined over the horizontal planar area occupied by the plume. This gave rise to a predicted volumetric exhaust rate of 57 m^{-3} s^{-1} which is approximately 25% higher than the volumetric exhaust from the atrium in the hot smoke test (i.e. 46 m^{-3} s^{-1}), thus giving rise to a lower layer height above the atrium floor.

A further simulation was carried out to determine if varying the distribution of the grid size in the domain had any effect on the predicted entrainment. Thus, a grid size of 0.25 m was assigned to the whole of the computational domain (to give 1,505,280 grid elements). This had no effect on the predicted layer height in the atrium.

Therefore, it appears that the FDS modelling of the hot smoke test is consistent with the modelling of the scale model experiments, which demonstrate that FDS tends to over predict entrainment for plumes which adhere to the wall above the edge. Possible reasons for this are already given in section 8.1.4.2. This analysis give further support for need to carry further work to provide improved guidance for the use of FDS to predict 3-D adhered spill plume entrainment.

10.3 Conclusions

The performance of the new design guidance proposed in this work has been assessed against relevant full scale spill plume data from two hot smoke tests carried out by BRE/IFSET.

The new guidance proposed in this work, in the form of simplified design formulae, analytical calculation methods and numerical modelling using FDS generally provided a good prediction of the clear layer height in each hot smoke test. This gives further confidence in the use of these methods to predict entrainment for full scale flows involving both a balcony and an adhered 3-D spill plume. However, the analysis did identify that further work is desirable on the appropriate use of FDS to predict 3-D adhered spill plume entrainment, consistent with the findings from the FDS modelling of the experiments in this work.

The analysis has demonstrated that the use of numerical modelling can allow a more general analysis of smoke flow behaviour that cannot be achieved using simplified design formulae. However, simplified formulae are particularly useful in the early stages of design, prior to any detailed numerical modelling and best apply to simple, idealised geometries. The hot smoke tests examined in this work examined scenarios which were relative idealised (i.e. a simple fire compartment fronting onto an atrium space). Clearly, if the design geometry is more complex or novel (e.g. a curved spill edge, or if the plume trajectory is obstructed in some way) then there will be less confidence in the use of these simple formulae/analytical methods and the use of numerical modelling is likely to be more appropriate for design purposes.

.

Chapter 11

11. Conclusions

This work has rigorously characterised thermal spill plume entrainment from an extensive number of physical scale modelling experiments, supported by numerical modelling using CFD. The analysis has led to the development of a range of new simplified design formulae that provide an appropriate prediction of entrainment for wide range of conditions, these formulae can be applied more generally than any existing design formulae. Analysis of the results has provided the following conclusions that relate to Chapters 5 to 10 inclusive:

11.1 The horizontal flow of gases below the spill edge

The formula given by Morgan [Equation 5.1] to predict $\overline{\theta}_s$ generally gives good agreement with the experiment for the range of conditions studied. It appears to be suitable for design purposes to reduce formulae which are dependent on $\theta_{\max,s}$ and applies to geometries with or without a wall above the spill edge.

The empirical formulae given by Hansell [Equation (5-4)] to predict $\dot{m}_s$ generally gives good agreement with the experiment for geometries with and without a wall above the edge, however, the performance of this method is better for layer flows that are wider than their depth. The CIBSE/BS 7974 method [Equation (5-5)] generally provides good agreement with the experiment for the range of conditions studied. Either of these formulae appear to be suitable for design purposes, although, the CIBSE/BS 7974 formula may be preferential due to its relative simplicity and that it generally performs better for the range of conditions studied.

For flows without a wall above the spill edge, the analytical method given by Morgan [Equation (5-3)] gives an excellent prediction of $\dot{m}_s$. The method by Thomas *et al.* [Equation (5-2)] gives predictions which are approximately 30% lower than the Morgan method and the experimental results. The difference in the predictions appears to be due to the profile correction factor used in the Morgan method to take into account the shape of the buoyancy profile of the flow in the integration to calculate $\dot{m}_s$.

The presence of a wall can affect the behaviour of the plume beyond the spill edge which in turn affects the characteristics of the flow below the edge. It appears that the plume behaviour downstream of the edge can create impedance to the flow which affects the characteristics of the flow upstream. The plume behaviour appears to be dependent on W_s and d_s consistent with the findings of Yokoi [80].

For flows with a wall above the spill edge, Equation (5-3) by Morgan generally gives a conservative prediction of $\dot{m}_s$ whereas Equation (5-2) by Thomas *et al.* tends to under predict $\dot{m}_s$. The predictions using both methods were dependent on the plume behaviour beyond the edge. To achieve good prediction of $\dot{m}_s$ using the Morgan method, a modification to C_d is proposed which is dependent on W_s and d_s given by,

$$\text{If } \left(\frac{W_s}{d_s}\right) \leq 3 \quad \text{then } C_d = 0.76$$

$$\text{If } 3 < \left(\frac{W_s}{d_s}\right) < 8 \quad \text{then } C_d = 0.05\left(\frac{W_s}{d_s}\right) + 0.62$$

$$\text{If } \left(\frac{W_s}{d_s}\right) \geq 8 \quad \text{then } C_d = 1.0$$

Alternatively, assuming a discharge coefficient of 1.0 will give rise to give either an appropriate or conservative (by up to approximately 30%) prediction of $\dot{m}_s$.

11.2 Balcony spill plume entrainment

11.2.1 The 2-D plume

This work has demonstrated that existing simplified design formulae for the 2-D balcony spill plume [i.e. Equations (6-2) and (6-3)] appear to apply generally for the range of $\dot{Q}_c$ and W_s examined in the experiments.

The following empirical relationship is proposed to describe the entrainment in the plume below the height of the spill edge (i.e. at $z_s = 0$) and appears to apply generally. It is not specific to 2-D plumes as it effectively describes the amount of entrainment in any spill plume after rotation as it has been determined from a decoupled flow.

$$\dot{m}_s = 1.34\dot{m}_s$$

A new simplified design formula is proposed for the 2-D plume, using the above empirical relationship describing the entrainment below the height of the spill edge. This formula appears to apply generally and is given by,

$$\dot{m}_{p,2D} = 0.16\dot{Q}_c^{1/3} W_s^{2/3} z_s + 1.34\dot{m}_s$$

11.2.2 The 3-D plume with channelling screens

Entrainment into a 3-D balcony spill plume appears to be specifically dependent on the characteristics of the layer flow below spill edge, particularly in terms of W_s and d_s, such that plumes generated from narrow, deep layer flows entrain air at a greater rate with respect to height compared to plumes generated from wide, shallow layers. The rate of entrainment also appears to be dependent on the contribution of the end entrainment in the overall entrainment process. The findings goes some way to explain and reconcile differences in entrainment reported between previous studies.

A new simplified design formula is proposed for the 3-D plume channelled by screens below the balcony, by developing a general empirical expression to explicitly describe the entrainment of air into the ends of the plume. This simplified formula can be applied more generally compared to currently available formulae for the 3-D plume and is given by,

$$\dot{m}_{p,3D} = 0.16\dot{Q}_c^{1/3}\left(W_s^{2/3} + 1.56d_s^{2/3}\right)z_s + 1.34\dot{m}_s$$

There is a limit to it use which has been developed and explained in Chapter 9 and given below for information purposes, such that the above equation applies when $z_s \le z_{trans}$, where,

$$z_{trans} = 3.4\left(W_s^{2/3} + 1.56d_s^{2/3}\right)^{3/2}$$

The analysis shows that none of the existing simplified design formulae (e.g. NFPA 92B, CIBSE) apply generally for a range of W_s and are specific to the conditions studied in the original experiments from which they were derived. This analysis gives further support for the use of the new design formulae proposed in this work as they have been derived generally for plumes for a range of W_s.

11.2.3 Analytical methods

The curved plume method provides an excellent prediction of entrainment for the 2-D balcony spill plume. This method seems suitable for design purposes for the rare occasions when the design scenario involves a 2-D plume.

The BRE spill plume method over predicts entrainment by approximately 30 to 40% for the 2-D balcony spill plume and by approximately 20 to 70% for the 3-D balcony spill plume depending upon the conditions studied. The use of the effective layer depth correction did not always provide a reliable prediction and should be used with caution. It also appears that that formation of an effective layer below the visual layer is more apparent than real.

A modified version of the BRE method is proposed for the 3-D balcony spill plume (named "BRE [UC] method") to provide a prediction of entrainment that matches the experimental results, without using the effective layer depth correction.

11.2.4 The virtual line source

This work has demonstrated that it is more appropriate to describe the location of the virtual line source below the spill edge in terms of the depth of the layer flow below the spill edge, rather than the height of the spill edge (or balcony) above the floor. The experimental results from this study and data from previous work suggests that for design purposes,

$$z_0 \approx 3d_s$$

The development of this general expression to describe z_0 has allowed alternative simplified design formulae to be developed for both 2-D and 3-D balcony spill plume. Hence, for the 2-D balcony spill plume the following alternative formula is proposed,

$$\dot{m}_{p,2D} = 0.16\dot{Q}_c^{1/3} W_s^{2/3} \left(z_s + 3d_s\right)$$

An alternative formula for the 3-D balcony spill plume is given by,

$$\dot{m}_{p,3D} = 0.16\dot{Q}_c^{1/3} W_s^{2/3} \left(z_s + 3d_s\right) + 0.25\dot{Q}_c^{1/3} d_s^{2/3} z_s$$

The new and alternative simplified design formulae proposed in this work provide a prediction of entrainment that are consistent with each other and the experiment for both 2-D and 3-D balcony spill plumes respectively.

11.2.5 The 3-D plume without channelling screens

Plumes generated without channelling screens caused lateral spread of the layer flow below the balcony. This spread gave rise to plumes with a greater lateral extent above the spill edge compared to plumes with screens below the balcony. The amount of lateral spread appears to be dependent upon the velocity of the flow from the fire compartment opening which increases when W_o decreases and $\dot{Q}_t$ increases. There was also smoke contamination local to the area above the balcony in line with the fire compartment opening.

The measured entrainment for plumes generated without screens was greater than that from equivalent plumes with screens. The difference in entrainment increases as the width of the fire compartment decreases due to the increased spread of gases below the balcony.

The entrainment can be approximated by using an effective lateral extent of the plume below the spill edge. The following formula is proposed as a simple approximation to predict entrainment,

$$\dot{m}_{p,3D,unchan} = 0.16\dot{Q}_c^{1/3}\left[(W_o + b)^{2/3} + 1.56d_s^{2/3}\right]z_s + 1.34\dot{m}_s$$

With the strict limit that,

$$\frac{W_o}{b} \geq 2$$

This is an approximate solution to a complex smoke flow and should be used in the early stages of design. Ideally, the entrainment analysis of these plumes should be supported by numerical modelling. Numerical modelling is recommended to predict entrainment into plumes where $W_o/b < 2$, at least until further experiments and analysis have been carried.

11.3 Adhered spill plume entrainment

11.3.1 The 2-D plume

This work has demonstrated that the existing simplified design formula for the 2-D adhered spill plume [Equation (7-1)] appears to apply generally for the range of $\dot{Q}_c$ and W_s examined in the experiments. The rate of entrainment with respect to height above the spill edge is approximately half that of an equivalent 2-D balcony spill plume.

The following is proposed as a new simplified design formula for the 2-D adhered plume. It is in a similar form to, and predicts half the entrainment of the new formula proposed for the 2-D balcony spill plume.

$$\dot{m}_{p,2D} = 0.08\dot{Q}_c^{1/3} W_s^{2/3} z_s + 1.34\dot{m}_s$$

It can be considered to be simpler version of the existing simplified design formula as it does not require the calculation of both $\dot{m}_s$ and d_s.

11.3.2 The 3-D plume

The behaviour of the 3-D adhered plume was highly dependent on the width of the fire compartment opening. Plumes generated from a wide opening were observed to adhere to the wall above almost immediately. Plumes generated from intermediate width openings were initially observed to horizontally project beyond the opening, before reattaching to the wall above, after which the plume adhered to the wall. Plumes generated from narrow width openings were observed to project beyond the opening and not reattach to the wall above. The plume behaviour observed in this work has been characterised in terms of the width and depth of the layer flow below the spill edge (i.e. W_s and d_s). In general, a layer flow below the spill edge that is shallow compared to its width will tend to adhere to the wall above the opening compared to flows whose depth approaches its width.

For $W_s/d_s > 3$, the height at which the plume first reattaches to the wall above the spill edge (z_{attach}) can be determined from the following empirical relationship given by,

$$z_{attach} = \frac{8d_s^2}{W_s}$$

Plumes did not reattach to the wall above the spill edge when $W_s/d_s \leq 3$.

The amount of entrainment into the 3-D adhered plume is specifically linked to the plume behaviour, such that plumes generated from narrower openings (that tend to detach from the wall) entrain air at a greater rate with respect to height compared to plumes generated from wider openings (that tend to adhere to the wall).

The following is proposed as a new simplified design formula for the 3-D adhered plume,

$$\dot{m}_{p,3D} = 0.3\dot{Q}_c^{1/3} W_s^{1/6} d_s^{1/2} z_s + 1.34\dot{m}_s$$

With the limit,

$$\left(\frac{W_s}{d_s}\right) \leq 13$$

For flows where $W_s/d_s > 13$, then the new simplified formula for the 2-D adhered plume should be used. As a conservative estimate, the upper limit given for the 3-D balcony spill plume should be used [Equation (9-14)].

The formula given by CIBSE for the 3-D adhered plume scenario [Equation (2-63)] generally provides a highly conservative prediction of entrainment, particularly for flows from wide openings. The predictions tend to become less conservative as W_s decreases. The CIBSE formula provides a reasonably good prediction for flows from the narrow openings where the plume does not reattach or adhere to the wall.

11.3.3 Analytical method

The BRE spill plume method generally provided a conservative prediction of entrainment for both the 2-D and 3-D adhered plume. However, many of the 3-D adhered plume predictions gave a reasonably good match with the experiment. Therefore, it appears that the original BRE spill plume method should continue to be used (without applying the effective layer depth correction) as it will provide either a conservative or an appropriate prediction of entrainment.

11.4 Numerical modelling using CFD

This chapter provides predictions of spill plume entrainment using CFD modelling for a selected number experiments carried out in this work. Predictions were mainly obtained using FDS (version 5.1.4) with additional predictions made using JASMINE (v3.23). Analysis of the results has provided the following conclusions.

11.4.1 FDS modelling

11.4.1.1 The 3-D balcony spill plume

Following a grid senility analysis, FDS generally provides a good prediction of the flow from a fire compartment opening and subsequent spill plume behaviour and entrainment when using a grid size of 25 mm (on model scale). Thus, the equates to a grid size of 0.25 m for full scale flows. From the conditions studied, a suitable grid size for design has been developed in non-dimensional form (i.e. n^*_{spill}). The chosen grid size must meet the following criterion for the design in question, such that the grid size can be considered to be appropriate when $n^*_{spill} \geq 0.9$.

Where,

$$n^*_{spill} = \frac{D_{spill}^{\ *}}{\delta x} \quad \text{and} \quad D^*_{spill} = \left(\frac{\dot{Q}_c}{\rho_1 c_{p,air} T_1 \sqrt{g}} \right)^{2/3}$$

As a general rule, it is recommended that grid size of 0.25 m should initially be chosen for design, and that this should be reduced if the above non-dimensional criterion is not met.

11.4.1.2 The 3-D adhered plume

FDS provided an excellent prediction of 3-D adhered plume behaviour when a grid size of 25 mm (on model scale) was used. However, its performance in predicting the amount of entrainment appeared to be dependent on the plume behaviour. It is possible that the complex nature of these plumes may require a finer grid resolution and/or the effect of the boundary layer close to the wall on the subsequent plume velocity needs to be better dealt with. In general, it appears that further work is desirable to provide improved guidance on the use of FDS to better quantify entrainment for the 3-D adhered spill plume.

11.4.2 JASMINE modelling

11.4.3 The 2-D balcony spill plume

For the conditions studied, JASMINE provided an excellent prediction of 2-D plume balcony spill plume entrainment. The minimum grid dimension used in the region encompassing the rising plume was approximately 0.01 m on model scale (i.e. 0.1 m full scale equivalent).

11.4.4 The 3-D balcony spill plume

In general, JASMINE provided a good prediction of 3-D balcony spill plume entrainment when using the same grid resolution as that used for the 2-D plume. The predictions provided excellent agreement with the experiment at relatively low heights of rise, however, at higher values there was a general trend to somewhat under predict the experiment by approximately 10 to 15%.

11.5 Transition from a balcony spill plume to axisymmetric

The following formula is proposed to describe the height of transition in entrainment behaviour from a balcony spill plume to axisymmetric. This was determined by matching the new design formula proposed in this work [Equation (6-12)] with an axisymmetric plume formula so that they become equivalent at a high height of rise. The formula is given by,

$$z_{trans} = 3.4\left(W_s^{2/3} + 1.56 d_s^{2/3}\right)^{3/2}$$

z_{trans} is dependent on W_s and d_s (rather than W_s alone) which seems reasonable following the analysis described in Chapter 6.

The absolute value of z_{trans} tends to decrease as W_s decreases. This is expected as narrower plumes will tend to become axisymmetric in nature at lower heights of rise compared to wider plumes due to end entrainment being more significant in the overall entrainment process.

The predicted value of z_{trans} coincides with point of intersection between the relationships representing the rate of entrainment for the 3-D balcony spill plume [Equation (6-12)] and that for an axisymmetric plume [Equation (9-6)] for the range of fire compartment opening widths examined.

The proposed formula to determine z_{trans} describes the upper limit that Equation (6-12) (or any linear based entrainment formula) should be applied, and at a height beyond z_{trans} entrainment should be determined using a formula for the axisymmetric plume. Hence, if, $z_s \le z_{trans}$ then entrainment can be predicted using Equation (6-12), such that

$$\dot{m}_{p,3D} = 0.16\dot{Q}_c^{1/3}\left(W_s^{2/3} + 1.56d_s^{2/3}\right)z_s + 1.34\dot{m}_s$$

However, if $z_s > z_{trans}$ then Equation (9-6) should be used, such that,

$$\dot{m}_{p,3D} = 0.071\dot{Q}_c^{1/3}z_s^{5/3}$$

The analysis is supported by a limited number of FDS simulations which demonstrate a transition in entrainment behaviour that departs from a linear relationship. The FDS predictions follow a similar yet slightly shallower slope to that of an axisymmetric plume beyond the point of transition which indicates a rate of entrainment somewhere between linearity and $z_s^{5/3}$. The predicted height of transition in entrainment in FDS broadly coincides with the predicted value of z_{trans} for the range of fire compartment opening widths examined. This gives further confidence in its use for design purposes.

The FDS predictions highlight that that stratification of smoke at high level is more likely to be an design issue for wide spill plumes rather than a change in the rate of entrainment.

Comparison of the FDS predictions [and the predictions using Equation (6-12)] with the new guidance given in the NFPA 92B [2] shows that the NFPA 92B formulae will generally provide a particularly conservative prediction of entrainment for most cases found in design.

11.6 Comparison with full scale data

The performance of the new design guidance proposed in this work has been assessed against relevant full scale spill plume data from two hot smoke tests carried out by BRE/IFSET.

The new guidance proposed in this work, in the form of simplified design formulae, analytical calculation methods and numerical modelling using FDS generally provided a good prediction of the clear layer height in each hot smoke test. This gives further confidence in the use of these methods to predict entrainment for full scale flows involving both a balcony and an adhered 3-D spill plume. However, the analysis did identify that further work is desirable on the appropriate use of FDS to predict 3-D adhered spill plume entrainment, consistent with the findings from the FDS modelling of the experiments in this work.

The analysis has demonstrated that the use of numerical modelling can allow a more general analysis of smoke flow behaviour that cannot be achieved using simplified design formulae. However, simple formulae are particularly useful in the early stages of design, prior to any detailed numerical modelling and best apply to simple, idealised geometries. The hot smoke tests examined in this work examined scenarios which were relative idealised (i.e. a simple fire compartment fronting onto an atrium void). Clearly, if the design geometry is more complex or novel (e.g. a curved spill edge, or if the plume trajectory is obstructed in some way) then there will be less confidence in the use of these simple formulae/analytical methods and the use of numerical modelling is likely to be more appropriate for design purposes.

Chapter 12

12. Further work

This work has further characterised entrainment into 3-D balcony spill plumes without channelling screens below the balcony and provides an approximate formula to predict entrainment for design purposes. However, as the balcony breadth was fixed in the experiments, further work is desirable to characterise these flows for a variety of breadths to develop more general guidance for this scenario. As these plumes can be particularly complex in nature, this work has recommended that simple design guidance should ideally be supported by numerical modelling, particularly for plumes generated from narrow openings which tend to be unstable in nature. An assessment of the performance of numerical modelling (using FDS) to predict plume entrainment without channelling screens (using the experimental data from this study) is currently in progress as part of a further study [132]. The modelling will examine the effect of varying the balcony breadth on entrainment and the tenability of smoke that may accumulate on the balcony directly above the fire compartment (as observed in the experiments in this work).

This work has demonstrated that the performance of FDS to predict 3-D adhered plume entrainment appears to be dependent on the plume behaviour. To provide improved guidance to better quantify entrainment for this scenario further work is desirable to examine the effect of the wall (i.e. the boundary layer effect) on the plume velocity and the subsequent prediction of entrainment in FDS. A further grid sensitivity analysis may be required to recommend an appropriate grid size for design purposes. Following this, a numerical analysis of adhered spill plume behaviour at high heights of rise can provide guidance on the upper limit to when current simplified formulae no longer apply.

This work has examined entrainment into unbounded balcony spill plumes. In design, the balcony spill plume may not always be free from bounding walls and factors such as the breadth of the balcony and the width of the spill plume will govern whether the plume rises unhindered into the atrium space or curls back and reattaches to a wall above, causing smoke logging on higher balconies. The current guidance available is limited and may not apply generally for a range of geometries. A series of physical scale modelling experiments are currently in progress as part of a further study [143] to provide improved simple design guidance in predicting balcony spill plume behaviour and the likelihood of smoke contamination on upper balconies.

This work has specifically examined entrainment of air into thermal spill plumes and the guidance proposed in this work may not apply to plumes where flames project beyond the fire compartment opening into the atrium void. Further work is desirable to examine entrainment of air into flame plumes from post-flashover fires as guidance for this scenario is very limited (i.e. the window plume formula).

As the NRC full scale experiments only examined entrainment into 3-D balcony spill plumes at very low heights of rise, and given the uncertainties in the experimental results, further work is desirable to examine air entrainment into full scale (or close to full scale) spill plumes, as also recommended by Lougheed *et al.* [71]. Of particular interest is entrainment into the free ends of a spill plume at high heights of rise to provide experimental data to characterise when a transition in entrainment behaviour occurs from a balcony spill plume to axisymmetric. This will enable a comparison to be made with the guidance proposed from this study.

Chapter 13

13. References

1. Saxon R. *Atrium buildings, development and design*. The Architectural Press. London, 1983.
2. National Fire Protection Association. *Smoke management systems in malls, atria and large areas*. (2009 edition). Publication No.92B. Quincy MA, 2009.
3. *United Kingdom Fire Statistics 2006*. Communities and Local Government, London, 2008.
4. Hall J R. *Burns, toxic gases, and other hazards associated with fires: Deaths and injuries in fire and non-fire situations*. NFPA, Fire Analysis and Research Division, Quincy, MA, 2001.
5. Purser D A. *Toxicity assessment of combustion products*, Chapter 6, Section 2, SFPE Handbook of Fire Protection Engineering, 3rd Edition, NFPA, Quincy, MA, 2002.
6. Milke J A, Carroll J P, Hoskins B L, Hugue D E. *Overview of tenability analyses in smoke management applications*. ASHRAE Transactions, 112, pp 379-386, 2006.
7. Jin T. *Visibility through fire smoke. Part 5. Allowable smoke density for escape from fire.* Report of Fire Research Institute of Japan. No.42, 1976.
8. *Fire Engineering Guidelines*. Fire Code Reform Centre Ltd, Sydney, Australia, 1996.
9. Spearpoint M J, Editor. *Fire Engineering Design Guide*. Centre for Advanced Engineering, New Zealand, 2008.
10. British Standards Institution. *PD 7974: Application of fire safety engineering principles to the design of buildings. Part 6: Human factors: Life safety strategies - Occupant evacuation, behaviour and condition*. London, BSI, 2004.
11. Milke J A. *Smoke management for covered malls and atria*. Fire Technology, vol. 26, no. 3, pp 223-243, 1990.

12. Morgan H P, Ghosh B K, Garrad G, Pamlitschka R, De Smedt J-C and Schoonbaert L R. *Design methodologies for smoke and heat exhaust ventilation*. BRE Report 368, 1999.
13. Klote J H and Milke J A. *Principles of smoke management*. American Society of Heating, Refrigerating and Air-conditioning Engineers, Atlanta, GA, 2002.
14. Williams C, Perera E, Morgan H P, Harrison R, Caplen B and Ferguson A. *Natural ventilation in atria for environment and smoke control: an introductory guide*. BRE Report 375, 1999.
15. British Standard Institution. *BS7346 Part 4: Components for smoke and heat control systems. Functional recommendations and calculation methods for smoke and heat exhaust ventilation systems, employing steady-state design fires*. Code of practice. London, BSI, 2003.
16. National Fire Protection Association. *NFPA 101*, *Life Safety Code,* (2005 Edition). Quincy, MA, 2005.
17. Department of Building and Housing. *Compliance Document for New Zealand Building Code, Clauses C1-C4, Fire Safety*. Wellington, New Zealand. 2008.
18. Morgan H P. *A brief note on the history of 'acceptable clear heights' for smoke and heat exhaust ventilation systems in the UK*. International Journal on Engineering Performanced Based Fire Codes, vol. 5, no. 2, pp 43-44, 2003.
19. Morton B R, Taylor G I and Turner J S. *Turbulent gravitational convection from maintained and instantaneous sources*. Proc. Royal Society, A234, pp 1-23, 1956.
20. Cetegen B M, Zukoski E E and Kubota T. *Entrainment in the near and far field of fire plumes*. Combustion Science and Technology, vol. 39, pp 305-331, 1984.
21. Heskestad G. *Engineering relations for fire plumes*. Fire Safety Journal, vol. 7, no. 1, pp 25-32, 1984.
22. Zukoski E E. *Properties of fire plumes*. Combustion Fundamentals of Fire, Cox G, Editor. Academic Press, London, 1995.
23. Poreh M and Garrad G. *A study of wall and corner fire plumes.* Fire Safety Journal, vol. 34, no. 1, pp 81-98, 2000.
24. Klote J H. *An overview of atrium smoke management*. Fire Protection Engineering, no. 7, SFPE, pp 24-34, 2000.
25. *Design fires database, version 1.2*. Building Research Establishment, UK, 2003.

26. Hadjisophocleous G V and Zalok E. *Development of design fires for performance-based fire safety designs*. Proceedings of the 9th Symposium of the International Association of Fire Safety Science, pp 63-78, Germany, 2008.
27. British Standard Institution. *BS7346 Part 5: Components for smoke and heat control systems. Functional recommendations and calculation methods for smoke and heat exhaust ventilation systems, employing time-dependent design fires*. Code of practice. London, BSI, 2005.
28. Alpert R L. *Turbulent ceiling-jet induced by large scale fires*. Combustion Science and Technology, vol. 11, no. 5, pp 197-293, 1975.
29. Jaluria Y. *Natural convection wall flows*. Chapter 7, Section 1, SFPE Handbook of Fire Protection Engineering, 1st Edition, NFPA, Quincy, MA, 1988.
30. Thomas P H, Hinkley P L, Theobald C R and Simms D L. *Investigations into the flow of hot gases in roof venting*. Fire Research Technical Paper No 7, London, The Stationary Office, 1963.
31. Poreh M, Morgan H P, Marshall N R and Harrison R. *Entrainment by two dimensional spill plumes in malls and atria*. Fire Safety Journal, vol. 30, no.1, pp 1-19, 1998.
32. Hansell G O, Morgan H P and Marshall N R. *Smoke flow experiments in a model atrium*. Building Research Establishment Occasional Paper, OP 55, 1993.
33. Harrison R. *Smoke Control in Atrium Buildings: A study of the thermal spill plume*. Fire Engineering Research Thesis 04/1, University of Canterbury, New Zealand, April 2004.
34. Harrison R and Spearpoint M. *The Balcony Spill Plume: Entrainment of air into a flow from a compartment opening to a higher projecting balcony*. Fire Technology, vol. 43, no. 4, pp 301 -317, 2007.
35. Morgan H P and Marshall N R. *Smoke hazards in covered multi-level shopping malls: an experimentally-based theory for smoke production*. BRE Current Paper 48/75, BRE, 1975.
36. Milke J A. *Smoke management in covered malls and atria*. Chapter 13, Section 4, SFPE Handbook of Fire Protection Engineering, 3rd Edition, NFPA, Quincy, MA, 2002.
37. Law M. *A note on smoke plumes from fires in multi-level shopping malls*. Fire Safety Journal, vol. 10, no. 3, pp 197-202, 1986.

38. Chartered Institution of Building Services Engineers, *CIBSE Guide Volume E: Fire Engineering*, London, CIBSE, 2003.
39. Thomas P H, Morgan H P and Marshall N R. *The spill plume in smoke control design*. Fire Safety Journal, vol. 30, no. 1, pp 21-46, 1998.
40. Harrison R and Spearpoint M J. *Entrainment of air into a balcony spill plume.* Journal of Fire Protection Engineering, vol. 16, no. 3, pp 211-245, 2006.
41. Kumar S, Thomas P H, and Cox G. *Novel analytical approach for characterising air entrainment into a balcony spill plume*. Proceedings of the 9th Symposium of the International Association of Fire Safety Science, Karlsruhe, Germany, pp 739-750, 2008.
42. McGrattan K B, Klein B, Hostikka S, Floyd F E, and Prasad K. *Fire Dynamics Simulator (Version 5) - User Guide*. NIST Special publication 1019-5, 2008.
43. Cox G and Kumar S. *Field Modelling of Fire in Forced Ventilated Enclosures*. Combustion Science and Technology, vol. 52, no.7, 1987.
44. Miles S, Kumar S and Cox G. *The balcony spill plume – Some CFD simulations*. Fire Safety Science – Proceedings of the 5th Symposium of the International Association of Fire Safety Science, pp 237-247, Melbourne, Australia.
45. Kealy M, Thomas P H, Law M, Porter A, Drysdale D, Barnfield J, Marchant E, Charters D, Slattery M, Hansell G, England I Grzyb R and Smith I. *Concern over design guide endorsement*. Fire Engineers Journal, pp 8-9, January 2001.
46. Thomas P. *Criticism of the BRE method*. Fire Engineers Journal and Fire Prevention, p 8, August 2002.
47. Sanderson I. *The Validity and Applicability of Fire Models used to Predict the Production of Smoke within the Built Environment*, PhD Thesis, Glasgow Caledonian University, 2007.
48. Marshall N R and Harrison R. *Experimental studies of thermal spill plumes*. Building Research Establishment Occasional Paper, OP1, 1996.
49. Law M. *Measurements of balcony smoke flow*. Fire Safety Journal, vol. 24, no.2, pp 189-195, 1995.
50. Poreh M, Marshall N R and Regev A. *Entrainment by adhered two-dimensional plumes*. Fire Safety Journal, vol. 43, no. 5, pp 344-350, July 2008.
51. Morgan H P. *The horizontal flow of buoyant gases toward an opening*. Fire Safety Journal, vol. 11, no.3, pp 193-200, 1986.

52. Chow W K. *CFD simulations on balcony spill plume*. Journal of Fire Sciences, vol. 16, no. 6, pp 468-485, 1998.
53. Morgan H P, Williams C, Harrison R, Shipp M and De Smedt J C. *BATC - hot smoke ventilation test at Brussels Airport*. Proceedings of the international conference on fire research and engineering, Orlando, Florida, 10-15 September 1995.
54. Harrison R, Williams C, Morgan H P, Shipp M and De Smedt J C. *A hot smoke ventilation test in an atrium in the new European Parliament Building*. Proceedings of the 2nd International conference on fires in large enclosed spaces, Geneva, Switzerland, June 1998.
55. Rockett J A. *Fire induced gas flow in an enclosure*. Combustion Science and Technology, vol.12, no. 4, pp 165-175, 1976.
56. Prahl J and Emmons H W. *Fire induced flow through an opening*. Combustion and Flame, vol. 25, no. 3, pp 369-385, 1975.
57. Steckler K D, Quintiere J G and Rinkinen W J. *Flow induced by a fire in a compartment*. Proceedings of the 19th international symposium on combustion. The Combustion Institute, pp 913-920, 1982.
58. Quintiere J G and DenBraven K. *Some theoretical aspects of fire induced flows through doorways in a room-corridor scale model*. NBSIR 78-1512, National Bureau of Standards, Washington D.C., 1978.
59. Hansell G O. *Heat and mass transfer process affecting smoke control in atrium buildings*. PhD thesis, South Bank University, 1993.
60. Morgan H P and Hansell G O. *Atrium buildings: Calculating smoke flows in atria for smoke control design*. Fire Safety Journal, vol. 12, no. 1, pp 9-25, 1987.
61. Zukoski E E, Kubota T and Cetegen B. *Entrainment in fire plumes*. Fire Safety Journal, vol. 3, no.3, pp 107-121, 1980.
62. Chartered Institution of Building Services Engineers, *CIBSE Technical Memorandum 19, Relationships for smoke control calculations*, London, CIBSE, 1995.
63. Law M. *Design formulae for hot gases from narrow openings- points for consideration*. Technical seminar: Flow of smoke through openings. Fire Research Station, Borehamwood, 1989.

64. Thomas P H. *Two-dimensional Smoke Flows from Fires in Compartments: Some Engineering Relationships*. Fire Safety Journal, vol. 18, no. 2, pp 125-137, 1992.
65. Hansell G O and Morgan H P. *Design approaches for smoke control in atrium buildings*. BR 258, 1994.
66. Garrad G. *Calculations based on the Hansell method for calculating entrainment into hot gases flowing beneath a downstand and rising to a projecting canopy*. Private communication, BRE, 1996.
67. Harrison R and Spearpoint M. *Spill Over*. Fire Prevention and Fire Engineers Journal, vol. 65, no. 258, pp 33-35, July 2005.
68. Harrison R. *Smoke Control in Atrium Buildings: A study of the thermal spill plume*. Fire Engineering Research Thesis 04/1, Department of Civil Engineering, University of Canterbury, New Zealand, April 2004.
69. Regev A, Hassid S and Poreh M. *Density jumps in smoke flow along horizontal ceilings*. Fire Safety Journal, vol 39, pp 465-479, 2004.
70. Ko Y, Hadjisophocleous G and Lougheed G D. *CFD study of the air entrainment of balcony spill plumes at the balcony edge*. ASHRAE transactions 114, pp 344-354, July 2008.
71. Lougheed G D, McCartney C J and Gibbs E. *Balcony spill plumes*. Final Research Project Report 1247. National Research Council, Canada, 2006.
72. Heselden A J M. *Fire problems of pedestrian precincts: Part 1. The smoke production of various materials*. Fire Research Note 856, Fire Research Station, Borehamwood, 1971.
73. Morgan H P and Gardner J P. *Design principles for smoke ventilation in enclosed shopping centres*. BR 186, BRE, 1990.
74. Shao-Lin Lee and Emmons H W. *A study of natural convection above a line fire. Journal of Fluid Mechanics*, vol. 11, no. 3, pp 353-368, 1961.
75. Yuan L U and Cox G. *An experimental study of some line fires*. Fire Safety Journal, vol. 27, no. 2, pp 123-139, 1996.
76. Rouse H, Yih C S and Humphreys H W. *Gravitational convection from a boundary source*. Tellus, 4, pp 201-210, 1952.
77. Chen C and Rodi W. *A review of experimental data of vertical turbulent buoyant jets*. University of Karlsruhe Report No SFB 80/T/69, 1975.

78. Kotsovinos N E. *A study of the entrainment and turbulence in a plane buoyant jet*. W M Keck Laboratory of Hydraulics and Water Resources Report KH-R-32, California Institute of Technology, Pasedena, CA, 1975.
79. Ramaprian B R and Chandrasekhara M S. *Measurements in vertical plane turbulent plumes*. Journal of Fluids Engineering, vol. 111, no. 1, pp 69-77, 1989.
80. Yokoi S. *Study on the prevention of fire spread by hot upward current*. Building Research Institute Report 34, Japan, 1960.
81. Morgan H P and Marshall N R. *Smoke control measures in a covered two-storey shopping mall having balconies and pedestrian walk ways*. BRE Current paper 11/79, BRE, 1979.
82. Morgan H P. *Comments on "A note on smoke plumes from fires in multi-level shopping malls"*. Letters to the Editor, Fire Safety Journal, vol. 12, no.1, pp 83-84, 1987.
83. Law M. *Reply to Comments on "A note on smoke plumes from fires in multi-level shopping malls"*. Letters to the Editor, Fire Safety Journal, vol.12, no.1, p 85, 1987.
84. Thomas P H. *On the upward movement of smoke and related shopping mall problems*. Fire Safety Journal, vol.12, no. 3, pp 191-203, 1987.
85. British Standards Institution. *PD 7974: Application of fire safety engineering principles to the design of buildings. Part 2: Spread of smoke and toxic gases within and beyond the enclosure of origin*. London, BSI, 2002.
86. Harrison R and Spearpoint M. *Characterisation of balcony spill plume entrainment using physical scale modelling*. Proceedings of the 9th Symposium of the International Association of Fire Safety Science, Karlsruhe, Germany, pp 727-738, 2008.
87. Valkist M B S. *New engineering principles for atrium smoke management*. PhD thesis. Technical University of Denmark, 2007.
88. National Fire Protection Association. *Smoke management systems in malls, atria and large areas*. 2005 edition. Publication No.92B. Quincy MA, 2005.
89. Lougheed G. Private Communication. January 2009.
90. Marshall N R. *Adhered thermal line plume: a small scale study*. Private Communication, BRE, 1997.

91. Porter A M. *Large scale tests to evaluate mass flow of smoke in a line plume*. Technical Seminar: Flow of smoke through openings, Fire Research Station, Borehamwood, June 1989.
92. Yii E H. *Exploratory salt water experiments of balcony spill plume using laser induced fluorescence technique*. Fire Engineering Research Report, University of Canterbury, 1998.
93. Grella J J and Faeth G M. *Measurements in a two-dimensional thermal plume along a vertical adiabatic wall*. Journal of Fluid Mechanics, vol.71, no.4, pp 701-710, 1975.
94. Morgan H P. *Response to letter by Dr Thomas*. Fire Engineers Journal and Fire Prevention, p 8, August 2002.
95. Thomas P H. *On strong two-dimensional plumes*. Fire Safety Journal, vol.34, no.1, pp 47- 53, 2000.
96. Thomas P H and Delichatsios M. *Notes on the similarity of turbulent buoyant fire plumes*. Fire Safety Journal, vol. 42, no.1, pp 43- 50, 2007.
97. Quintiere J G, Rinkinen W J and Jones W W. *The effects of room openings on fire plume entrainment*. Combustion Science and Technology, vol. 26, no.5, pp 193-201, 1981.
98. Chow W K and Cui E. *CFD simulations on balcony spill plume*. Journal of Fire Sciences, vol.16, no. 6, pp 468-485, 1998.
99. Chow W K. *Numerical simulations on balcony spill plume*. Fire and Materials, vol. 23, no. 6, pp 91-99, 1999.
100. Chow W K and Li J. *Simulation on natural smoke filling in atrium with a balcony spill plume*. Journal of Fire Sciences, vol. 19, no. 4, pp 258-277, 2001.
101. National Fire Protection Association. *Smoke management systems in malls, atria and large areas*. 1995 edition. Publication No.92B. Quincy MA, 1995.
102. Jones W W, Forney G P, Peacock R D, Reneke P A. *A technical reference for CFAST: an engineering tool for estimating fire and smoke transport.* National Institute of Standards and Technology, NIST TN 1431, Building and Fire Research Laboratory, Maryland, USA, 2000.
103. Li J and Chow W K. *Line plume approximation on atrium smoke filling with thermal stratified environment*. Journal of Heat Transfer, vol. 125, no. 2, pp 289-300, 2003.

104. Shi C L, Lu W Z, Chow W K and Huo R. *An investigation on spill plume development and natural filling in large full-scale atrium under retail shop fire*. International Journal of Heat and Mass Transfer, vol. 50, no. 3, pp 513–529, 2007.
105. Li J and Chow W K. *Numerical simulations on aerodynamics of thermally induced plumes*. Journal of Fire Sciences, vol. 25, no.2, pp 119 - 160, 2007.
106. Marshall N R. *The behaviour of hot gases flowing within a staircase*. Fire Safety Journal, vol. 9, no. 3, pp 245-255, 1985.
107. Quintiere J G. *Scaling applications in fire research*. Fire Safety Journal, vol. 15, no. 1, pp 3-29, 1989.
108. Massey B S. *Mechanics of fluids*. Van Nostrand Reinhold Company, London, 1990.
109. Drysdale D. *An introduction to fire dynamics*. 2nd Edition. Wiley Press.
110. Morgan H P, Marshall N R and Goldstone B M. *Smoke hazards in covered multi-level shopping malls: some studies using a model 2-storey mall*. BRE Current Paper, CP45/76, BRE, 1976.
111. Kumar S and Cox G. *The application of a numerical field model of smoke movement to the physical scaling of compartment fires*. Proceedings of the Third International Conference of Numerical Methods in Thermal Problems, pp 837- 848. Editors, Lewis R W, Johnson J A and Smith W R., Pineridge Press, Swansea, 1983.
112. Morgan H P. *Roof venting – similarities between large and small scale calculations*. Fire Prevention, no. 198, April 1987.
113. Tsujimoto M, Takenouchi T and Uehara S. *A scaling law of smoke movement in atrium*. 11th Joint panel meeting of the UJNR panel on fire research and safety. NIST. 1990.
114. Quintiere J G, McCaffrey, B W, and Kashiwagi T. *A scaling study of a corridor subject to a room fire.* Combustion Science and Technology, vol. 18, no. 1, pp 1-19, 1978.
115. Harrison R and Miles S. *Smoke shafts protecting fire-fighting shafts: their performance and design*. BRE Report 79204, March 2002.

116. Versteeg H K and Malalasekera W. *An introduction to Computational Fluid Dynamics - the finite volume method*. Longman Scientific and Technical, 1995.
117. Cox G and Kumar S. *Modeling Enclosure Fires using CFD*. Chapter 8, Section 3, SFPE Handbook of Fire Protection Engineering, 3rd Edition, NFPA, Quincy, MA, 2002.
118. McGrattan K B, Baum H R and Rehm R G. *Large Eddy Simulations of smoke movement*. Fire Safety Journal, vol. 30, no. 2, pp 161-178, 1998.
119. Forney G P. *User's guide for Smokeview version 5 – a tool for visualizing fire dynamics simulation data*. NIST Special publication 1017-1, 2008.
120. Cox G, Kumar S, and Markatos N C. *Some field model validation studies*. Proceedings of the 1st Symposium of the International Association of Fire Safety Science, University of Berkeley, USA, pp 159-171, 1986.
121. Marshall N R. *Homogenisation of buoyant gases in a vertical duct*. Fire Safety Journal, vol. 13, no 23, pp 155 -162, 1988.
122. Incropera F P and Dewitt D P. *Fundamentals of heat and mass transfer*. 5th Edition, Wiley Press.
123. Streeter V L. *Fluid Mechanics*, 3rd edition , McGraw-Hill.
124. B P Chemicals, Hull Research and Technology Centre, Saltend, Hull, UK.
125. British Standard Institution. *BS3591: British Standard Specification for Industrial Methylated Spirits.* London, BSI, 1985.
126. Williams C. *The downward movement of smoke due to a sprinkler spray*. PhD thesis. South Bank University, 1993.
127. Cox G. *Basic considerations*. Combustion Fundamentals of Fire, Cox G, Editor. Academic Press, London, 1995.
128. Poreh M. *Beware of communicating elevated smoke layers*. Fire Technology, vol.35, no. 2, pp 170-178, 1999.
129. McCaffrey B J and Quintiere J G. *Buoyancy driven counter-current flows generated by a fire source*. In: Spalding D B and Afgan N. Heat Transfer and Turbulent Buoyant Convection, pp 457-472, Hemisphere, USA, 1977.
130. Quintiere J G, McCaffrey B J and Rinkinen W. *Visualisation of room fire-induced smoke movement and flow in a corridor*. Fire and Materials, vol. 2, no. 1, pp 18-24, 1978.
131. Turner J S. *Buoyancy effects in fluids*. Cambridge University Press, 1973.

132. Tiong H Y. *Numerical simulation of unchannelled balcony spill plume*. University of Canterbury research report, New Zealand. In preparation.
133. Morgan H P, Carrington C and Marshall N R. *ASKHPM – a suite of programs for use in smoke ventilation calculations.* Private Communication, BRE, 1994.
134. Galea E R, Berhane D and Hoffmann N. CFD anlaysis of fire plumes emerging from windows in high-rise buildings. Proceedings of Fire Safety by Design, vol. 3, University of Sunderland, pp 111-120, 1995.
135. Cheong M K. *Assessment of credible vehicle fires in road tunnels*. PhD thesis, University of Canterbury, 2008.
136. Quintiere J G and Grove A. *Unified analysis for fire plumes*. 27th Symposium on Combustion. The Combustion Institute, Pittsburgh, 1998, pp 2757-2766, 1998.
137. McBryde J D. *Experimental and numerical modelling of gravity currents preceding backdraft*. Fire Engineering Research Report 08/1, University of Canterbury, New Zealand, 2008.
138. Kumar S. Private Communication. BRE, 2008.
139. Heskestad G. *Fire plume entrainment and related problems in venting of fire smoke from large open spaces*. NFPA 92A subcommittee paper, December 1987.
140. Morgan H P, Williams C, Harrison R, Shipp M and De Smedt J C. *A hot smoke ventilation test in the new European Parliament building, Brussels*. Private Communication, April 1996.
141. Quintiere J G. *Fundamentals of fire phenomena*. Wiley Press, 2006.
142. Promatect H board technical data sheet, http://www.promat.it/AlteTemperature/docs/PROMATECT%20H%20-%20eng.pdf. Accessed, July 2008.
143. Tan F. *Physical scale modelling of smoke contamination in upper balconies by a balcony spill plume*. University of Canterbury Research Report, New Zealand. To be published.

Appendix A: Fuel flowmeter calibration

The volume of IMS flowing through the flowmeter was measured over a fixed time period for each setting number examined. This was repeated five times, giving an average fuel volume flow rate. The heat of combustion (26.58 MJ kg^{-1} [124]) and density of IMS 99 (739.2 kg m^{-3} in air at 20 ^{o}C [125]) were then used to determine a relationship between the total heat output of the fire and the flowmeter setting number. The results of the calibration were as follows:

Setting number	Time (s)	Vol 1 (cc)	Vol 2 (cc)	Vol 3 (cc)	Vol 4 (cc)	Vol 5 (cc)
2	240	42	40	40	41	41
4	180	89	90	89	90	90
6	120	99	98	98	97	98
8	120	137	136	137	136	137
10	120	174	174	175	175	174

Table A1: Raw data from the fuel flowmeter calibration

Setting number	Volume flow rate (cc/s)	Mass flow rate (kg/s)	Heat Output (kW)
2	0.17	0.00013	3.6
4	0.50	0.00039	10.5
6	0.82	0.00065	17.2
8	1.14	0.00090	24.0
10	1.45	0.00115	30.6

Table A2: Processed data from the fuel flowmeter calibration

Appendix B: Thermocouple locations

Column A	
Thermocouple number	Distance below ceiling of smoke exhaust hood (mm)
1	10
2	100
3	200
4	300
5	500
6	700
7	900
8	1100
9	1300
10	1500
11	1700
12	1900
13	2100
14	2300
15	2500

Table B1: Thermocouple spacings for Column A

Column B	
Thermocouple number	Distance below ceiling of smoke exhaust hood (mm)
16	10
17	100
18	200
19	300
20	500
21	700
22	900
23	1100
24	1300
25	1500
26	1700
27	1900
28	2100
29	2300
30	2500

Table B2: Thermocouple spacings for Column B

Column C	
Thermocouple number	Distance below spill edge (mm)
31	10
32	30
33	50
34	70
35	90
36	110
37	130
38	150
39	170
40	190
41	210
42	230
43	250
44	300
45	350
46	400
47	450
48	500

Table B3: Thermocouple spacings for Column C

Column D (Adhered spill plume only)	
Thermocouple number	Distance above spill edge (mm)
94	1.01
95	0.91
70	0.81
71	0.76
72	0.71
73	0.66
74	0.61
75	0.56
76	0.51
77	0.46
78	0.41
79	0.36
80	0.31
81	0.26
82	0.21
83	0.16
84	0.11
85	0.06

Table B4: Thermocouple spacings for Column D

Array A	
Thermocouple number	Distance from centreline of flow (mm)
96*	-800
49	-490
50	-390
51	-290
52	-250
53	-200
54	-190
55	-150
56	-100
57	-90
58	-50
59	0
60	50
61	90
62	100
63	150
64	190
65	200
66	250
67	290
68	390
69	490
97*	800

* only used for 3-D balcony spill plume experiments

Table B5: Thermocouple spacings for Array A

Thermocouple number	Location
86	Throat of vent,1
87	Throat of vent,2
88	Throat of vent,3
89	Throat of vent,4
90	Throat of vent,5
91	CO_2 sampling tube
92	Pitot tube (LHS)
93	Pitot tube (RHS)

Table B6: Other thermocouple locations

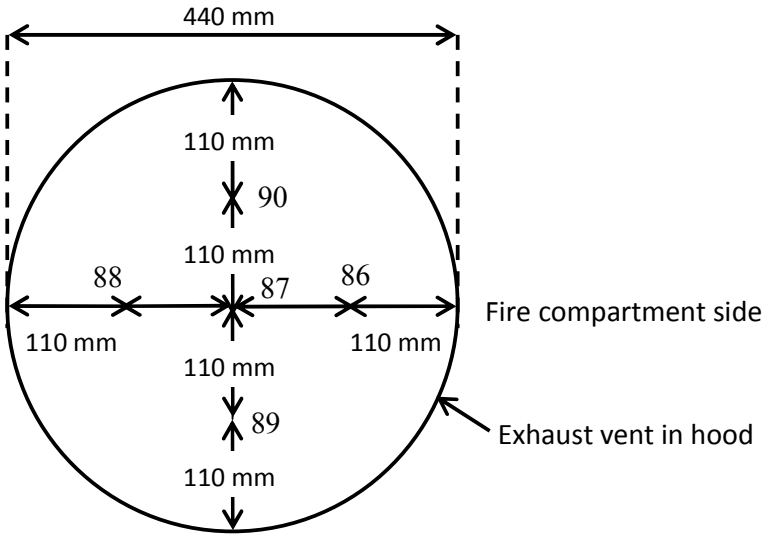

Figure B1: Plan view of thermocouple locations in exhaust vent

Array B		
Thermocouple number	Perpendicular distance from spill edge (Balcony spill plume) (mm)	Perpendicular distance from spill edge (Adhered spill plume) (mm)
98	-50	5
99	0	50
100	50	100
101	100	150
102	150	200
103	200	250
104	250	300
105	300	350
106	350	400
107	400	450
108	450	500
109	500	550
110	550	600
111	600	650
112	650	700
113	700	750
114	750	800
115	800	850

Table B7: Thermocouple spacings for Array B

Appendix C: IMS safety data sheet

Methylated Spirits Industrial

Infosafe No. ACPCT **Issue Date** June 2007 **Status** ISSUED by APSSC

Not classified as hazardous according to criteria of NOHSC

COMPANY DETAILS

Company Name	Asia Pacific Specialty Chemicals Limited (ABN 32000316138)
Address	15 Park Road SEVEN HILLS NSW 2147
Emergency Tel.	1800 022 037 (24H)
Tel/Fax	Tel: (02) 9839 4000 Fax: (02) 9674 6225
Other Information	New Zealand: Asia Pacific Specialty Chemicals (NZ) Limited 119 Carbine Road Mt Wellington, Auckland 6 Emergency Tel: 0800 243 622 (24H) Telephone: (09) 276 4019 Fax: (09) 276 7231

IDENTIFICATION

Product Name	Methylated Spirits Industrial
Proper Shipping Name	ETHANOL (ETHYL ALCOHOL)
UN Number	1170
DG Class	3
Packing Group	II
Hazchem Code	2[Y]E
Poisons Schedule	S5
Product Use	General industrial solvent

Physical Data

Appearance	Clear colourless liquid.
Melting Point	-117°C
Boiling Point	78°C
Vapour Pressure	44 mmHg @ 20°C
Specific Gravity	0.79-0.89 (H2O=1)
Flash Point	13°C (Abel closed cup)
Flamm. Limit LEL	3.5%
Flamm. Limit UEL	19.0%
Solubility in Water	Complete

Other Properties

Volatile Component	100%
Autoignition Temp.	392°C
Evaporation Rate	2.53 (n-Butyl Acetate = 1)
Vapour Density	1.59 (air=1)
Odour Threshold	Characteristic ethanol odour 5 ppm
Stability	Stable under normal conditions.
Haz. Polymerization	Will not occur.
Materials to Avoid	Strong oxidising agents.

Ingredients

Ingredients	**Name**	**CAS**	**Proportion**
	Ethanol	64-17-5	95.8-99.8 %
	Water	7732-18-5	0.2-4.2 %
	Denaturants		0-1 %

Appendix D: Temperature and velocity profiles below the spill edge (Experiments C1 to C15)

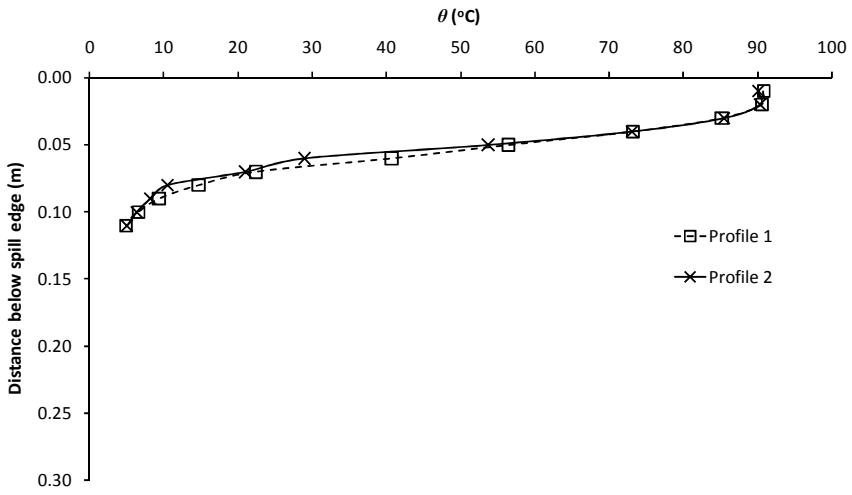

Figure D1: Temperature profiles, Experiment C1

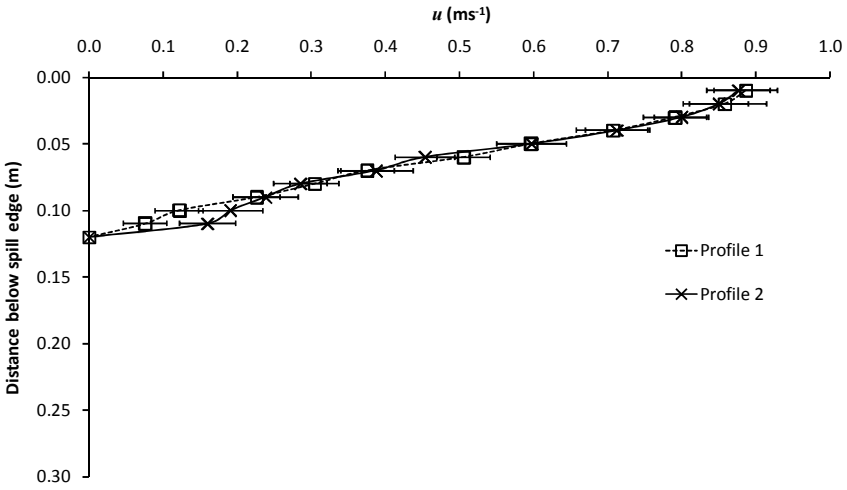

Figure D2: Velocity profiles, Experiment C1

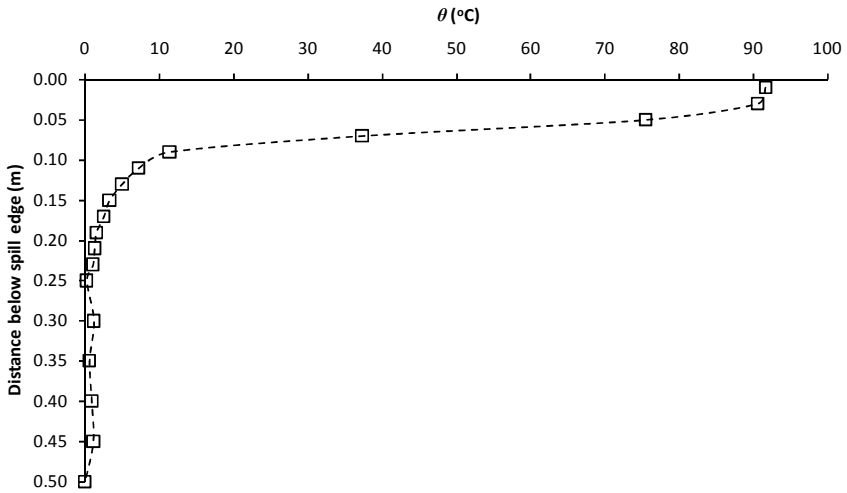

Figure D3: Temperature profile from Column C, Experiment C1

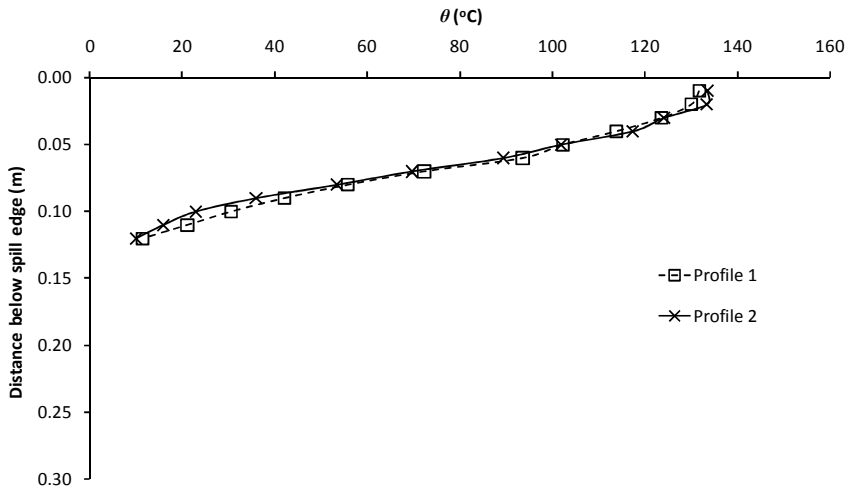

Figure D4: Temperature profiles, Experiment C2

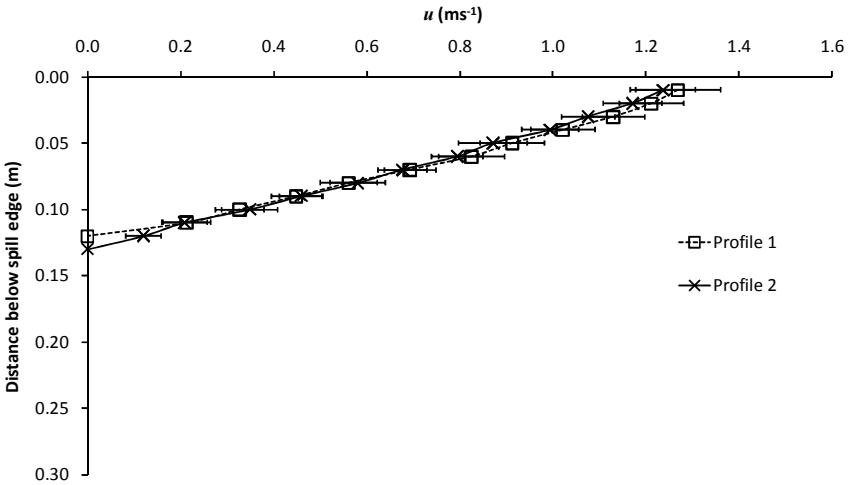

Figure D5: Velocity profiles, Experiment C2

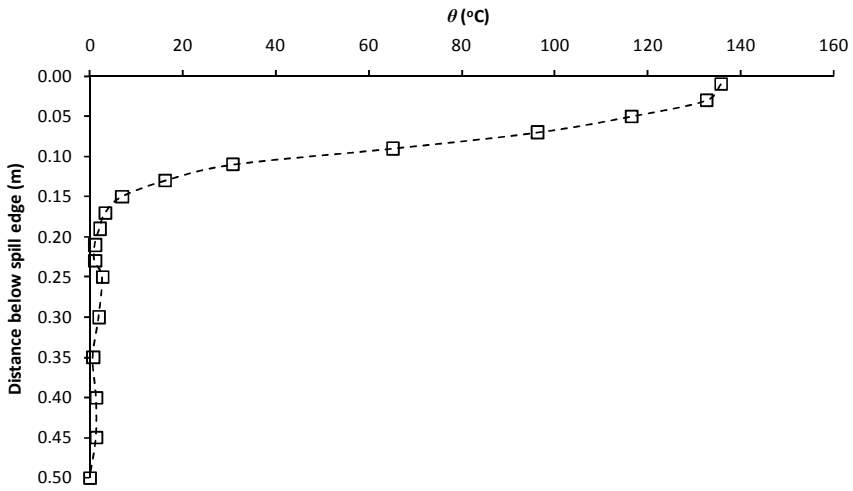

Figure D6: Temperature profile from Column C, Experiment C2

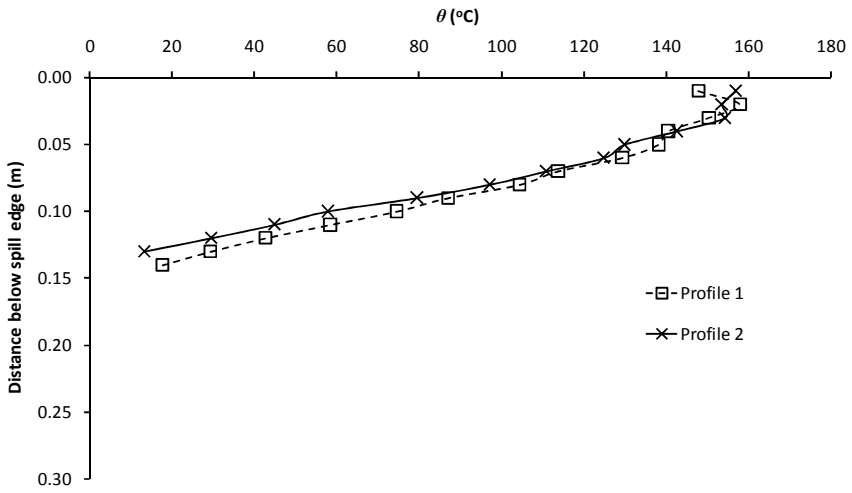

Figure D7: Temperature profiles, Experiment C3

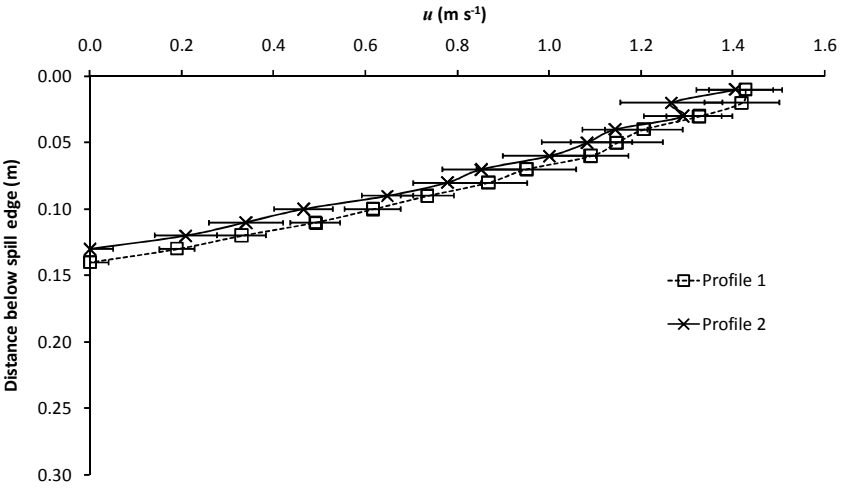

Figure D8: Velocity profiles, Experiment C3

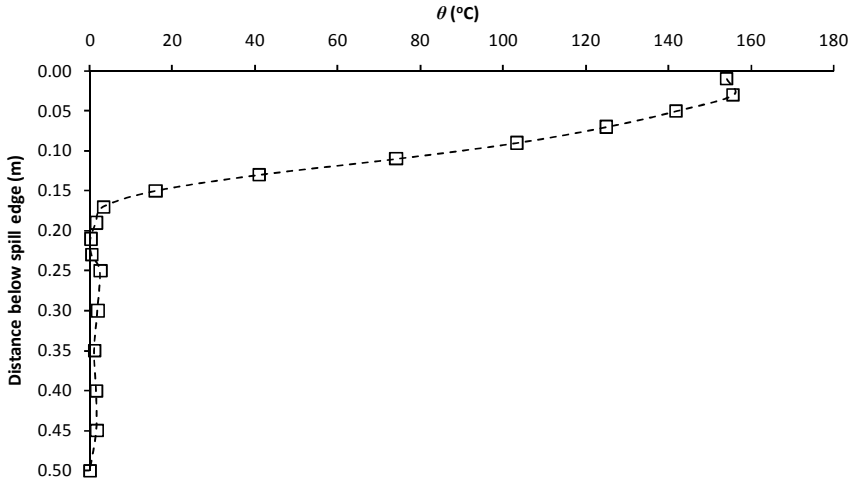

Figure D9: Temperature profile from Column C, Experiment C3

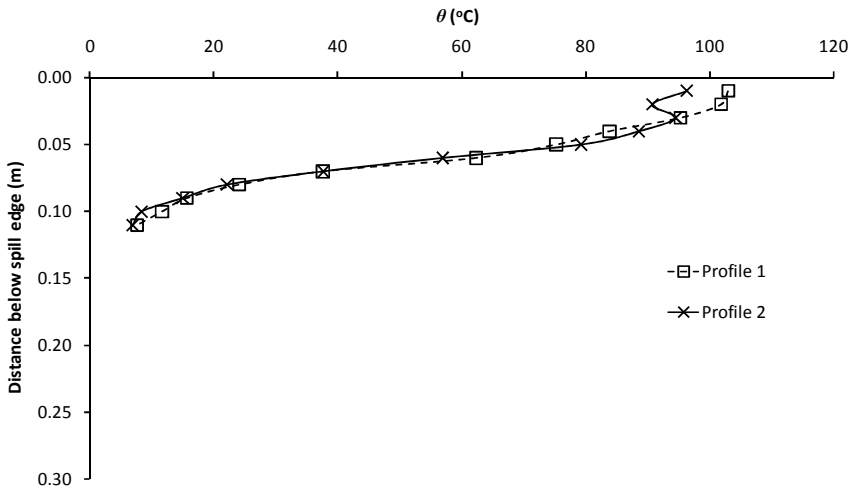

Figure D10: Temperature profiles, Experiment C4

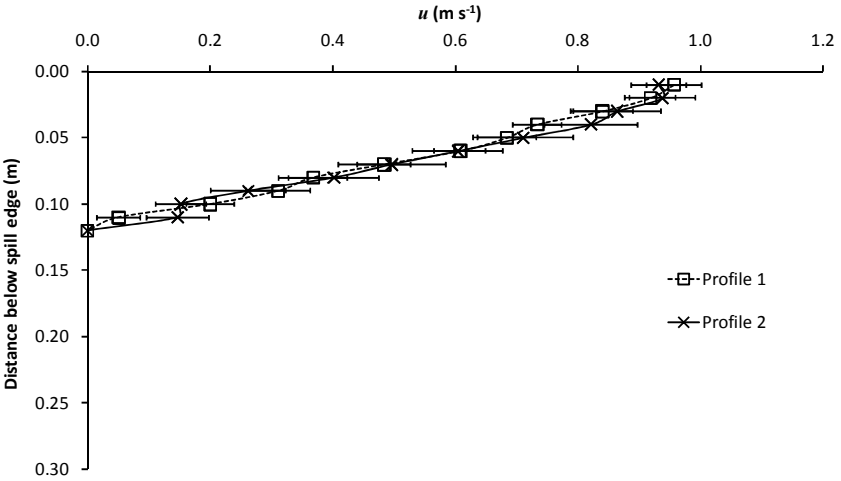

Figure D11: Velocity profiles, Experiment C4

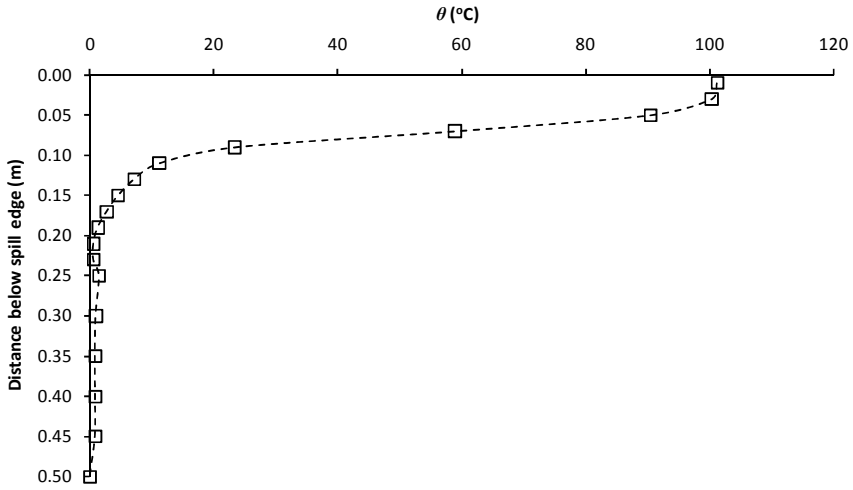

Figure D12: Temperature profile from Column C, Experiment C4

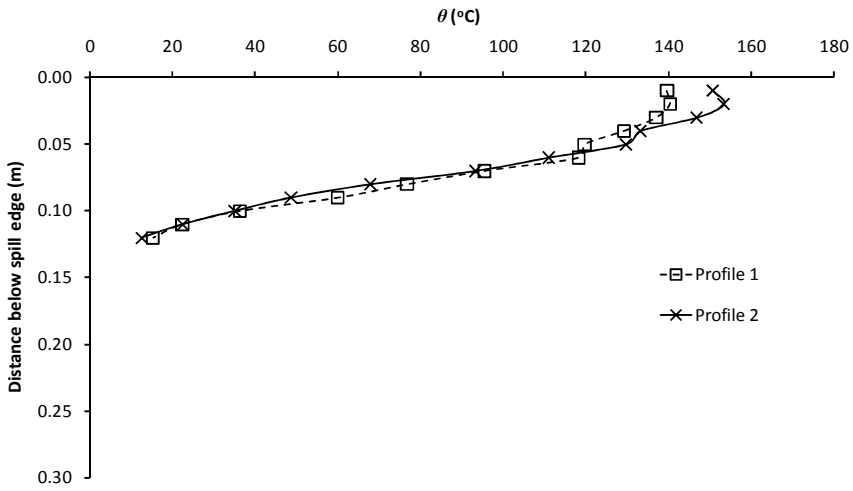

Figure D13: Temperature profiles, Experiment C5

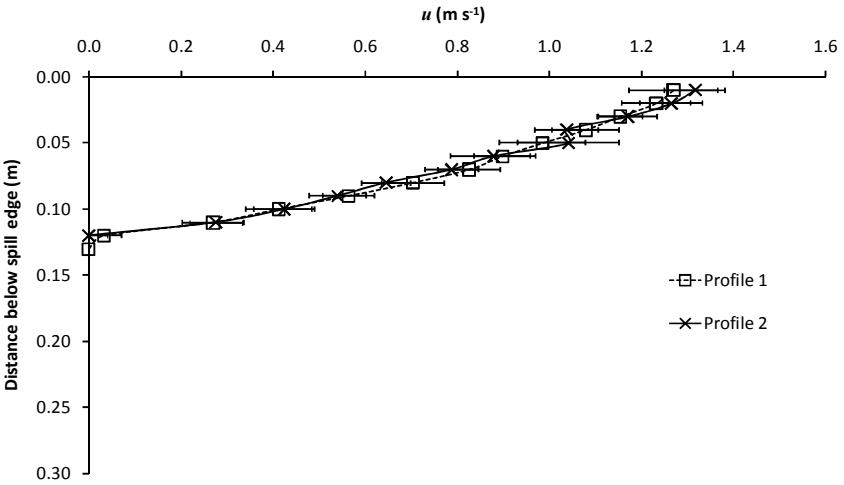

Figure D14: Velocity profiles, Experiment C5

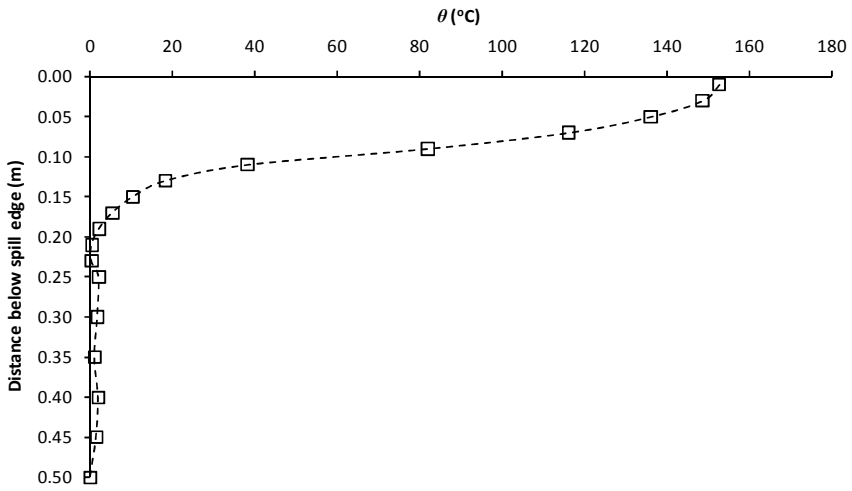

Figure D15: Temperature profile from Column C, Experiment C5

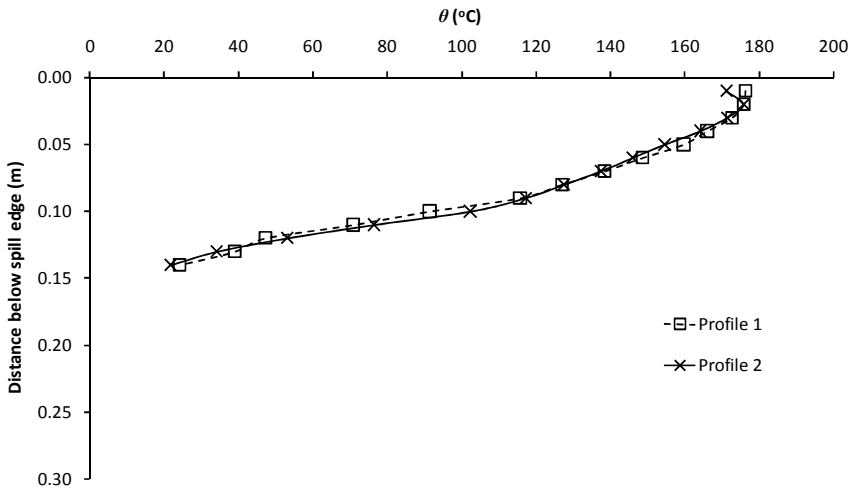

Figure D16: Temperature profiles, Experiment C6

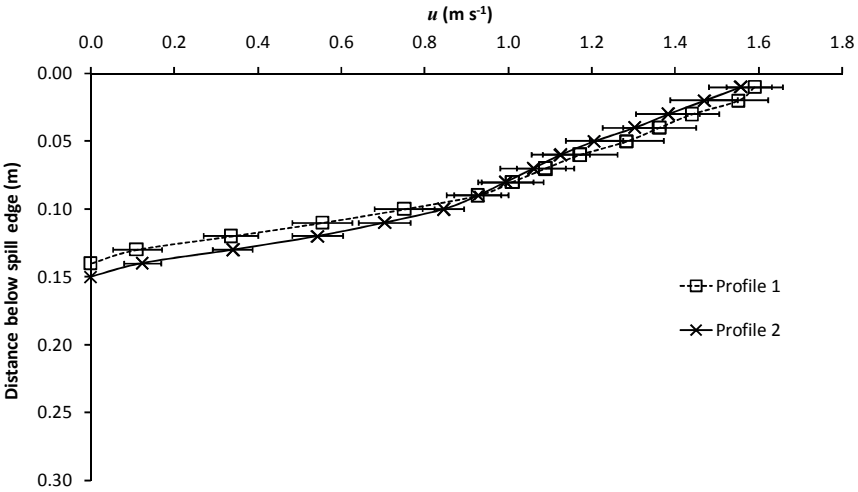

Figure D17: Velocity profiles, Experiment C6

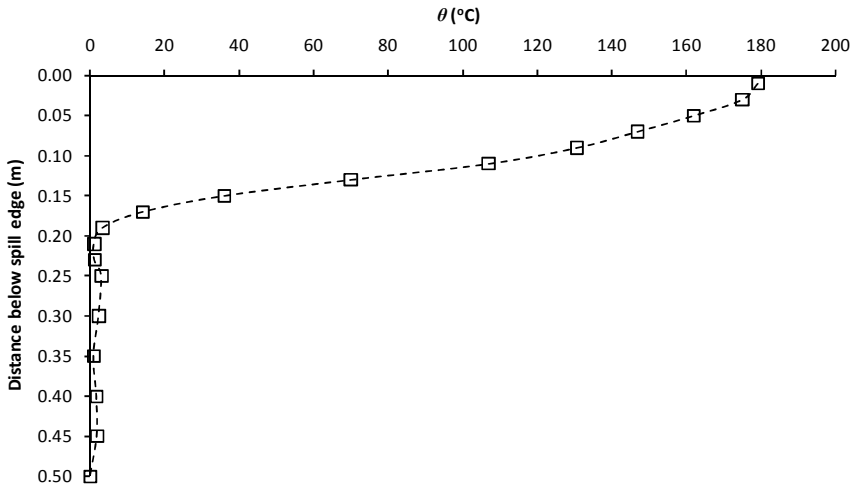

Figure D18: Temperature profile from Column C, Experiment C6

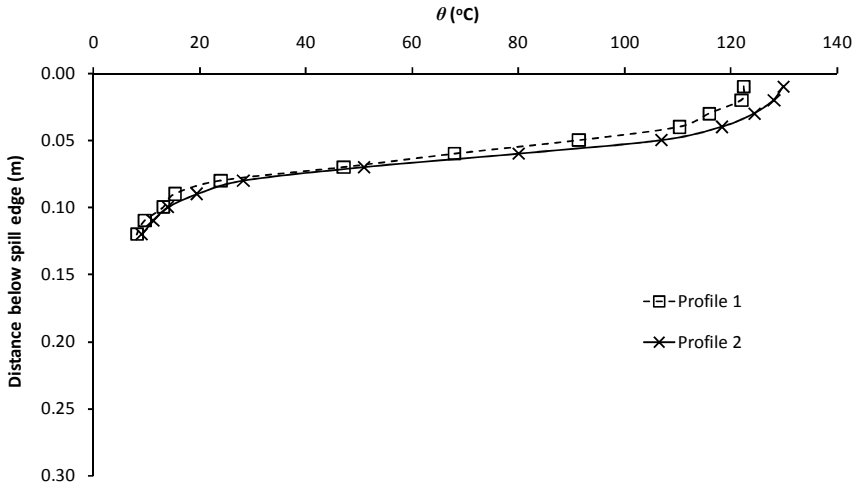

Figure D19: Temperature profiles, Experiment C7

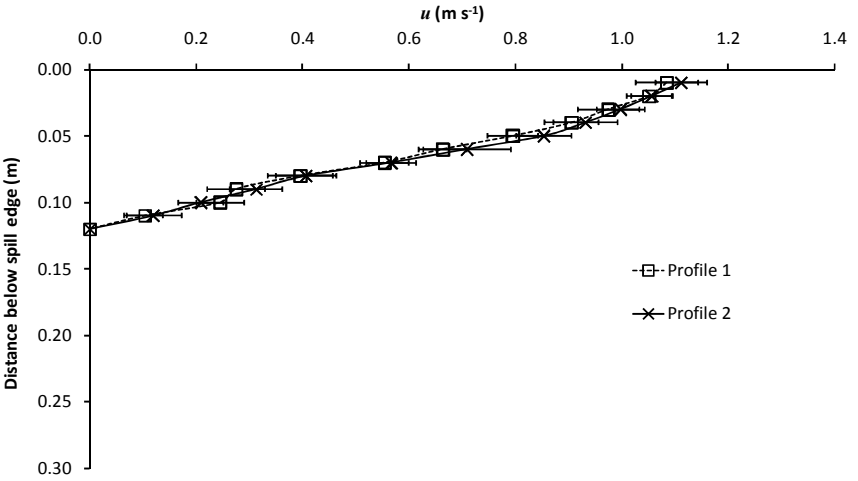

Figure D20: Velocity profiles, Experiment C7

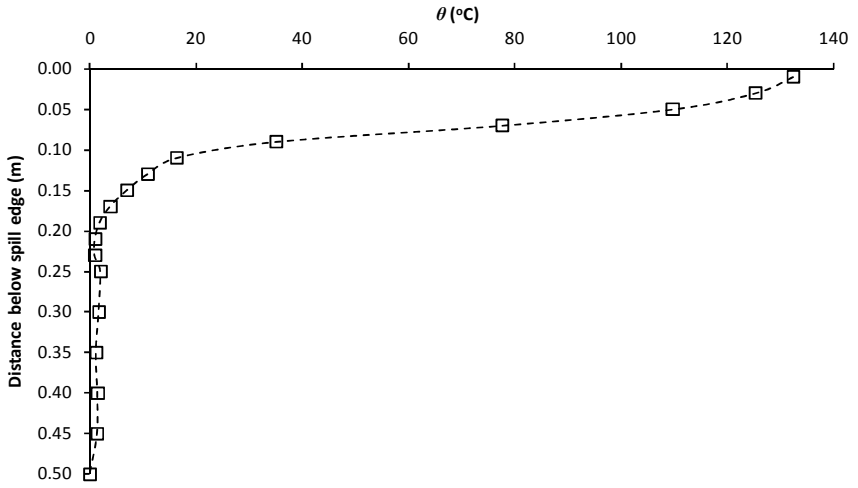

Figure D21: Temperature profile from Column C, Experiment C7

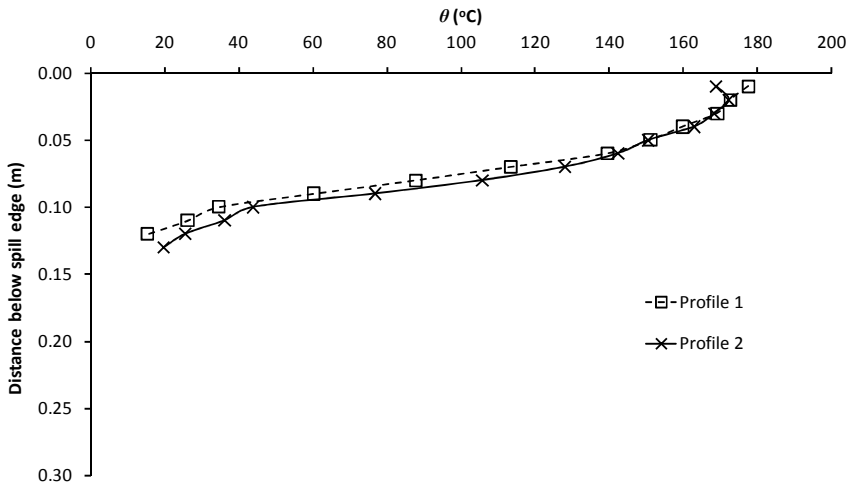

Figure D22: Temperature profiles, Experiment C8

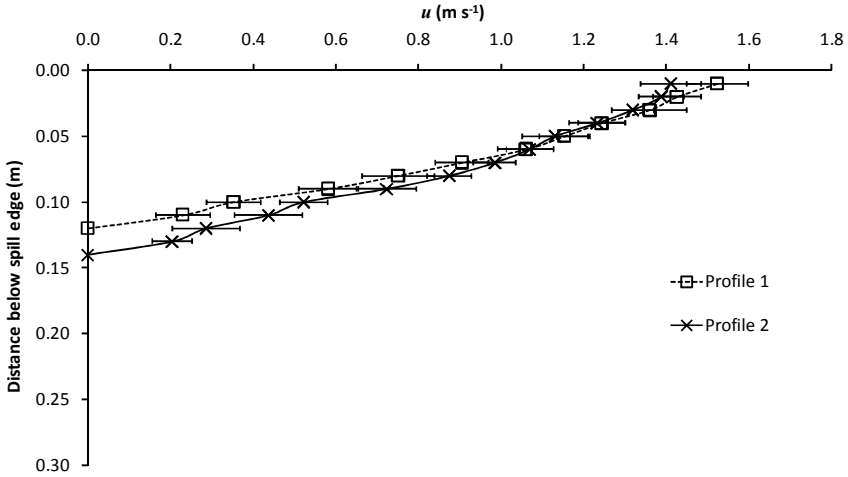

Figure D23: Velocity profiles, Experiment C8

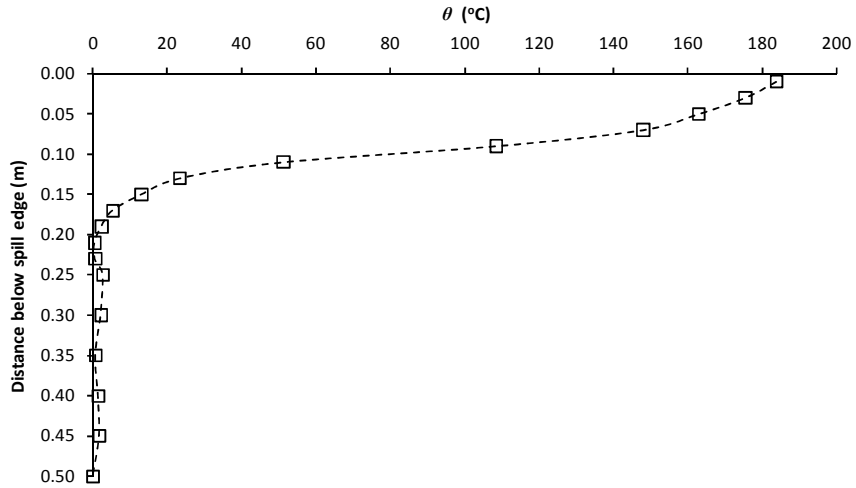

Figure D24: Temperature profile from Column C, Experiment C8

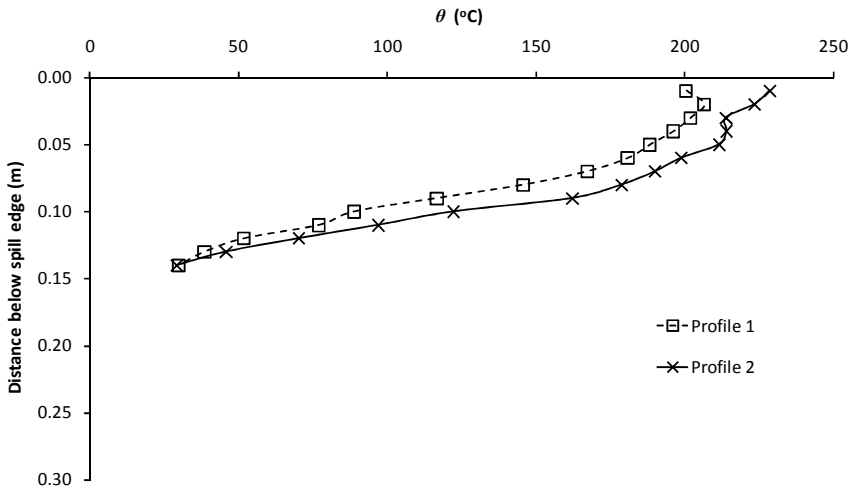

Figure D25: Temperature profiles, Experiment C9

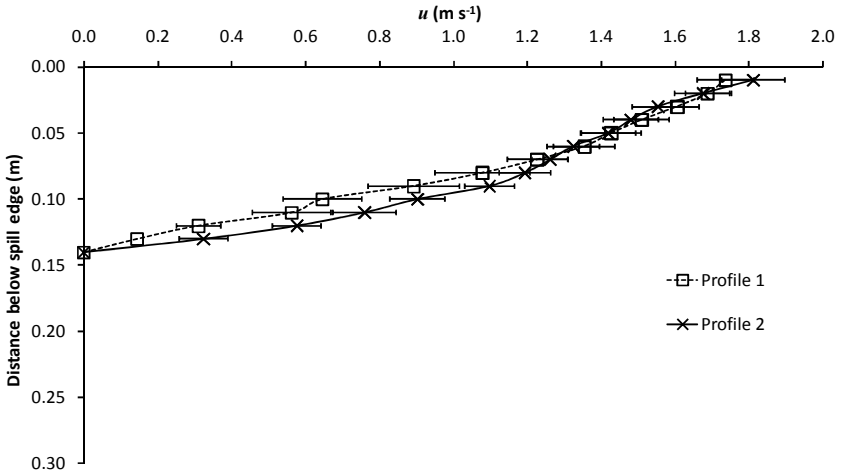

Figure D26: Velocity profiles, Experiment C9

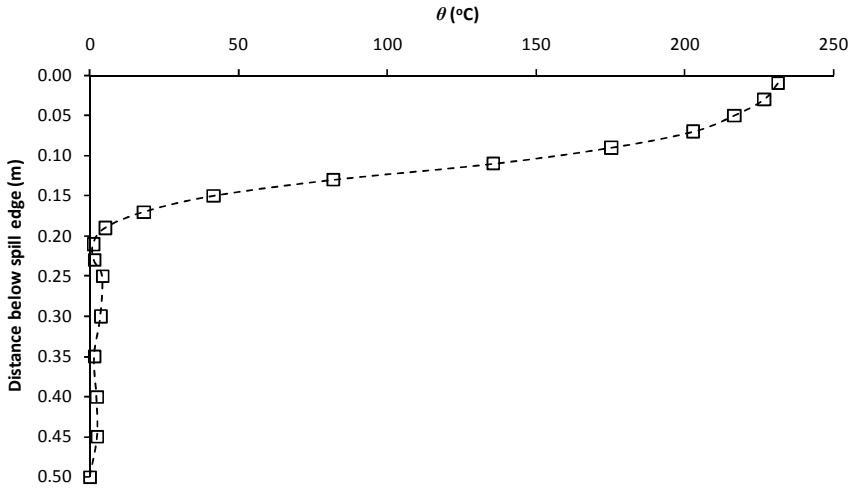

Figure D27: Temperature profile from Column C, Experiment C9

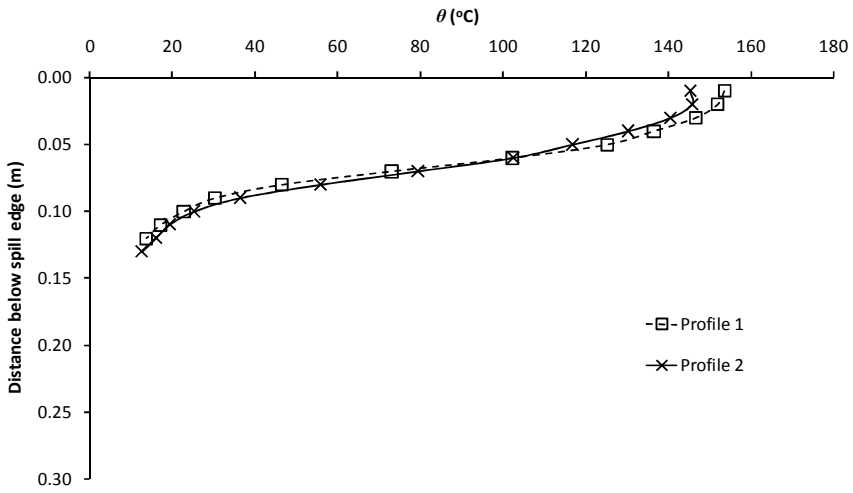

Figure D28: Temperature profiles, Experiment C10

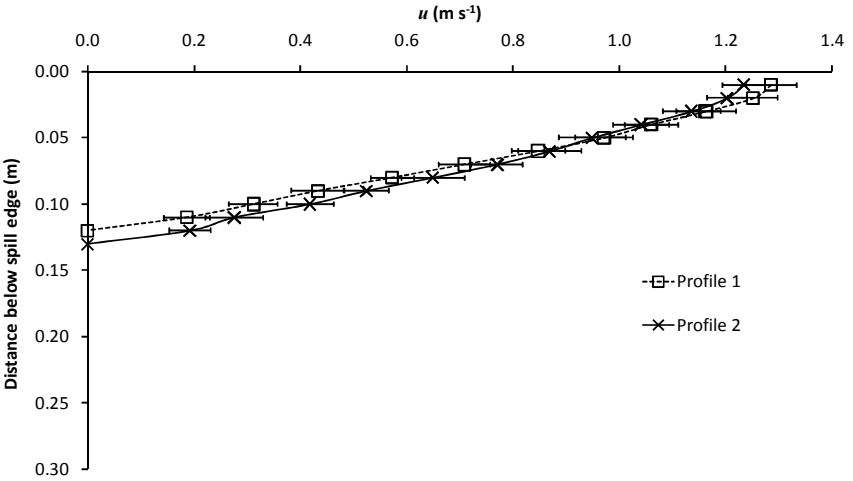

Figure D29: Velocity profiles, Experiment C10

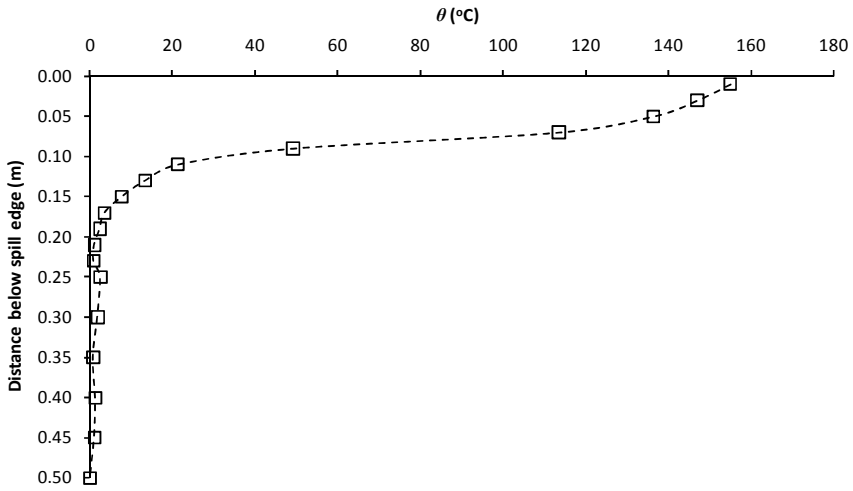

Figure D30: Temperature profile from Column C, Experiment C10

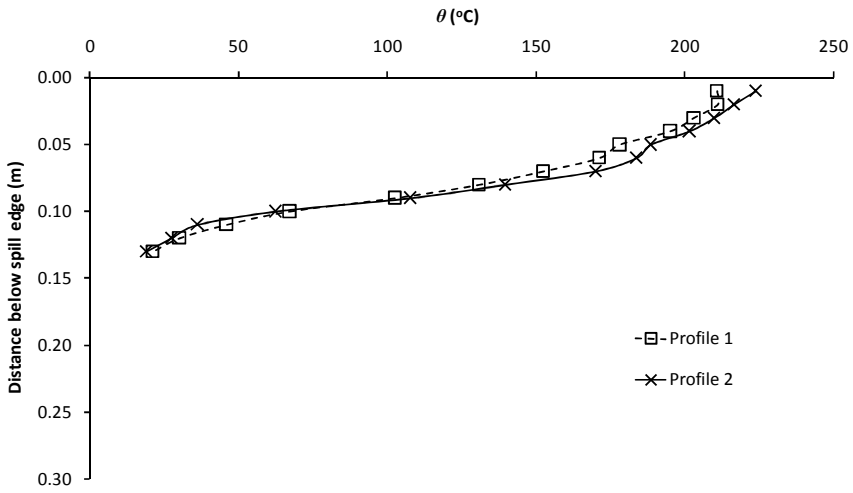

Figure D31: Temperature profiles, Experiment C11

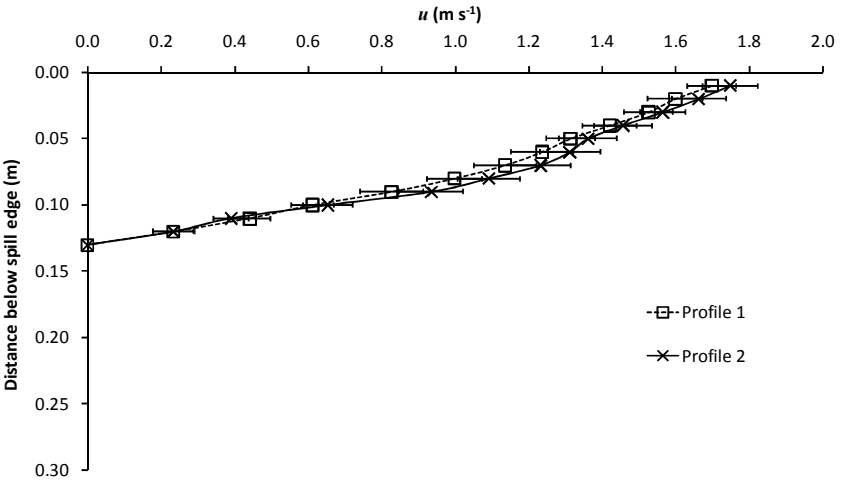

Figure D32: Velocity profiles, Experiment C11

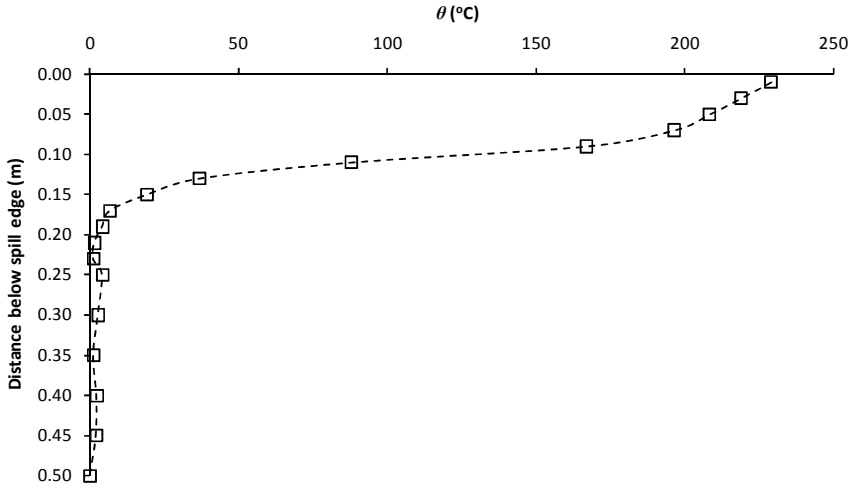

Figure D33: Temperature profile from Column C, Experiment C11

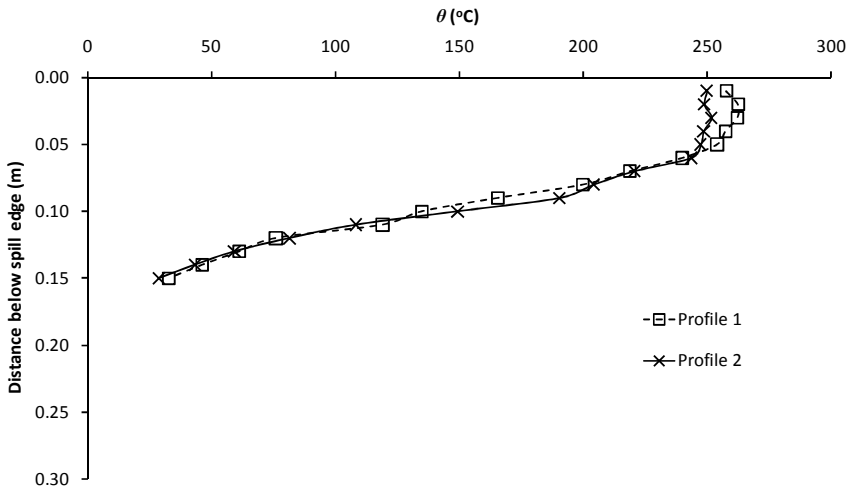

Figure D34: Temperature profiles, Experiment C12

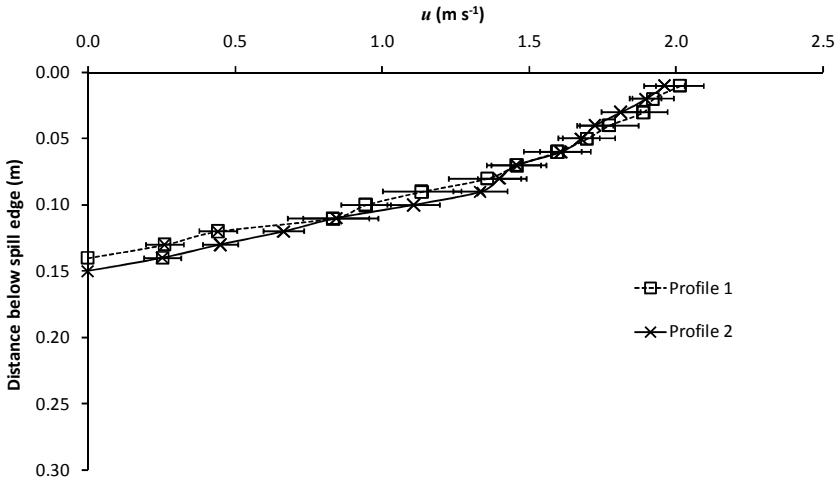

Figure D35: Velocity profiles, Experiment C12

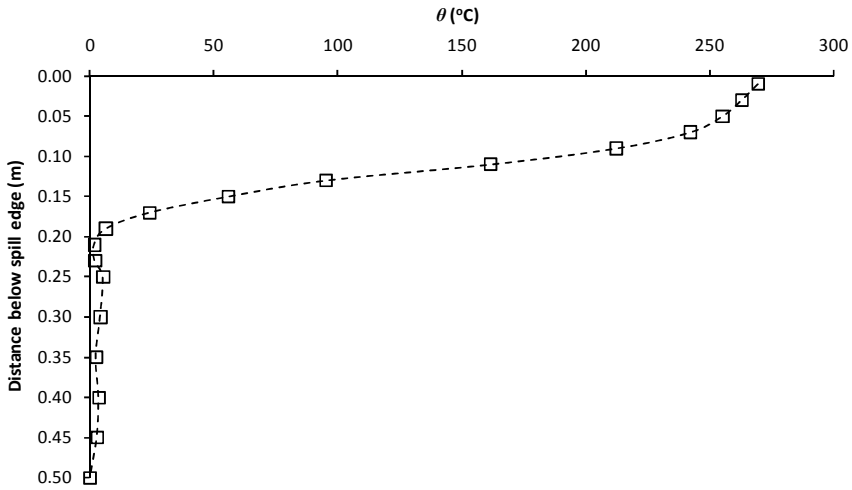

Figure D36: Temperature profile from Column C, Experiment C12

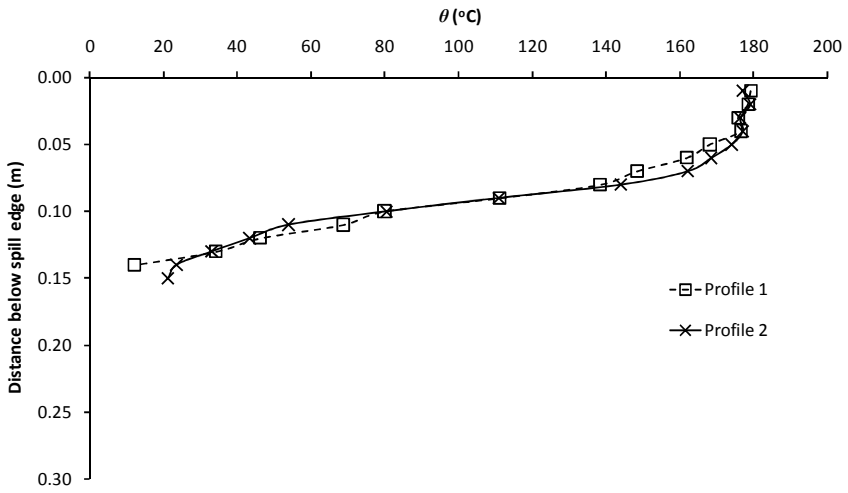

Figure D37: Temperature profiles, Experiment C13

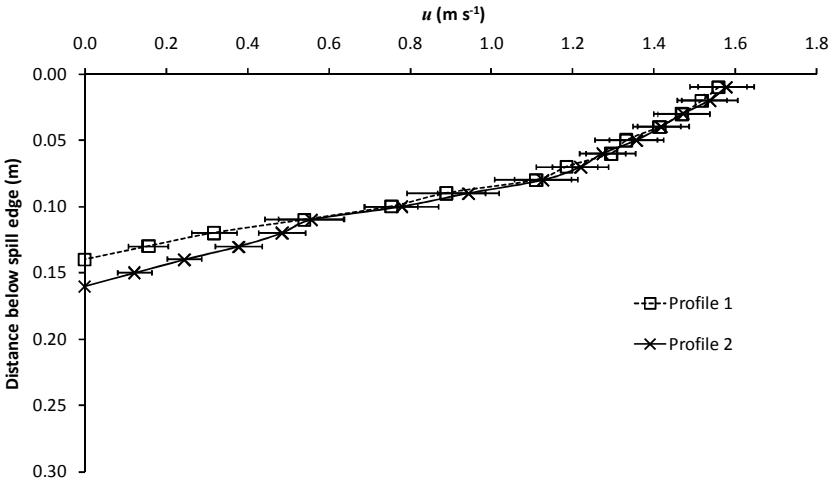

Figure D38: Velocity profiles, Experiment C13

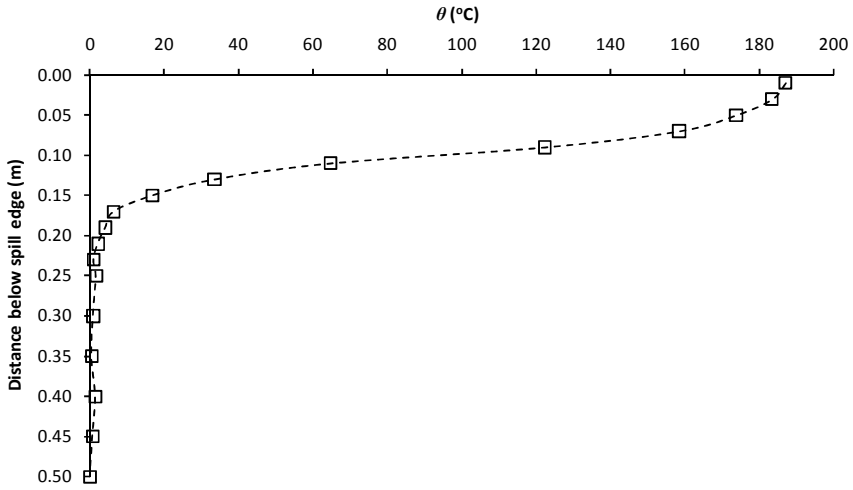

Figure D39: Temperature profile from Column C, Experiment C13

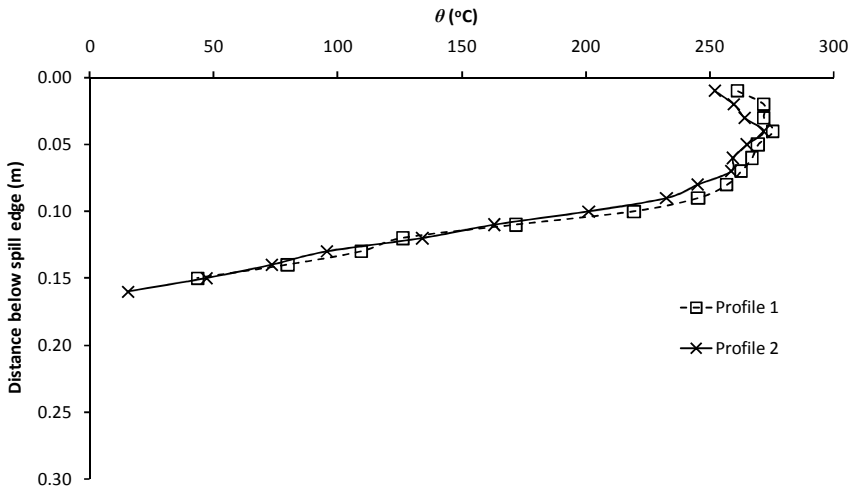

Figure D40: Temperature profiles, Experiment C14

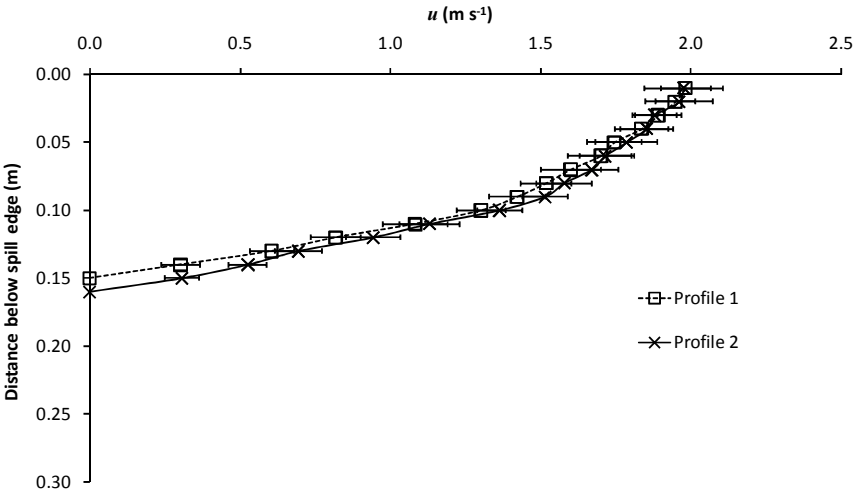

Figure D41: Velocity profiles, Experiment C14

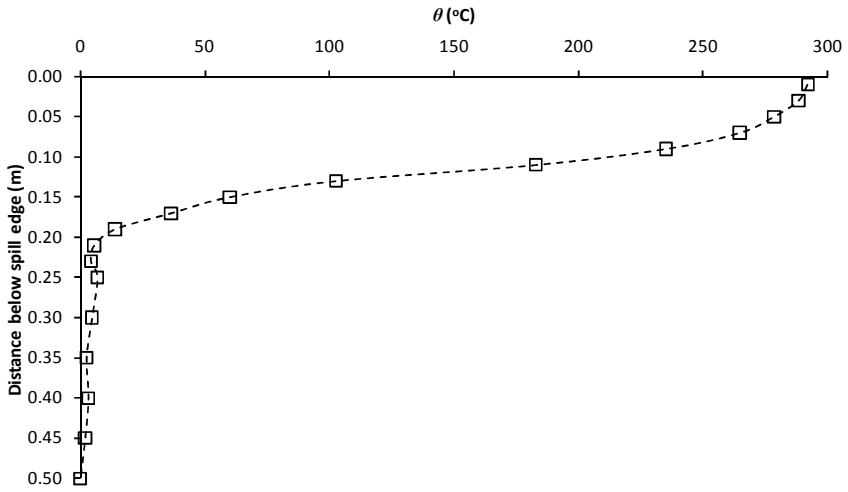

Figure D42: Temperature profile from Column C, Experiment C14

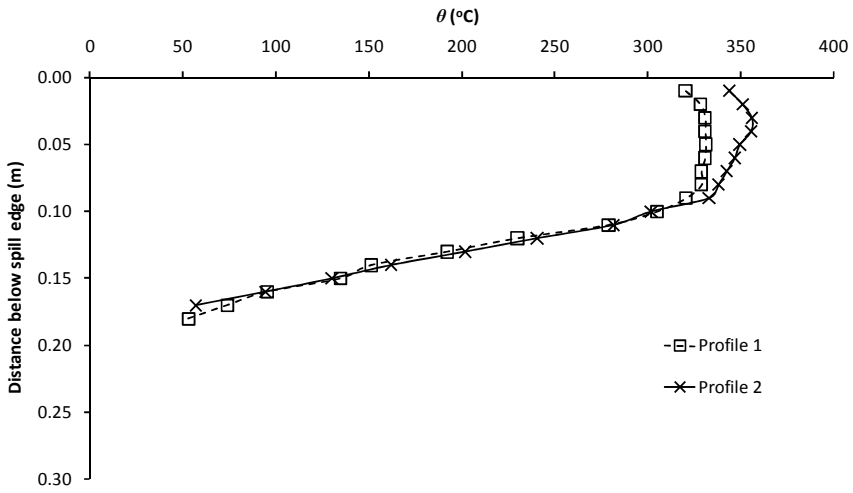

Figure D43: Temperature profiles, Experiment C15

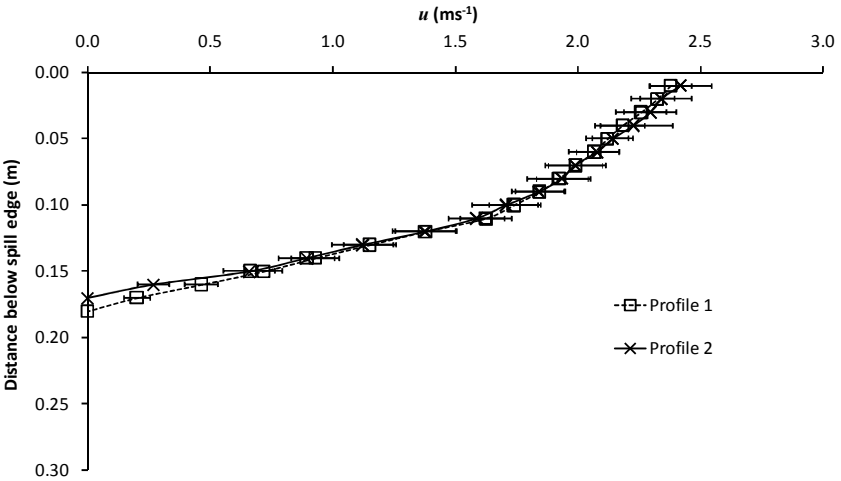

Figure D44: Velocity profiles, Experiment C15

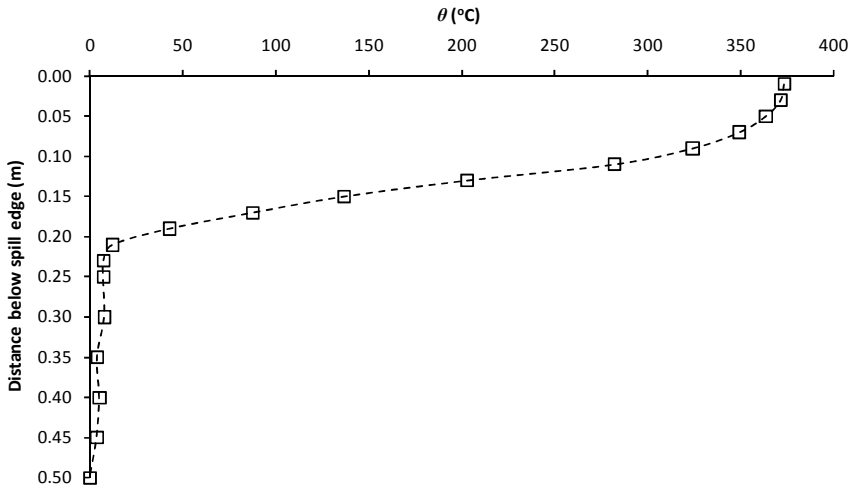

Figure D45: Temperature profile from Column C, Experiment C15

Appendix E: Temperature and velocity profiles below the spill edge (Experiments C16 to C30)

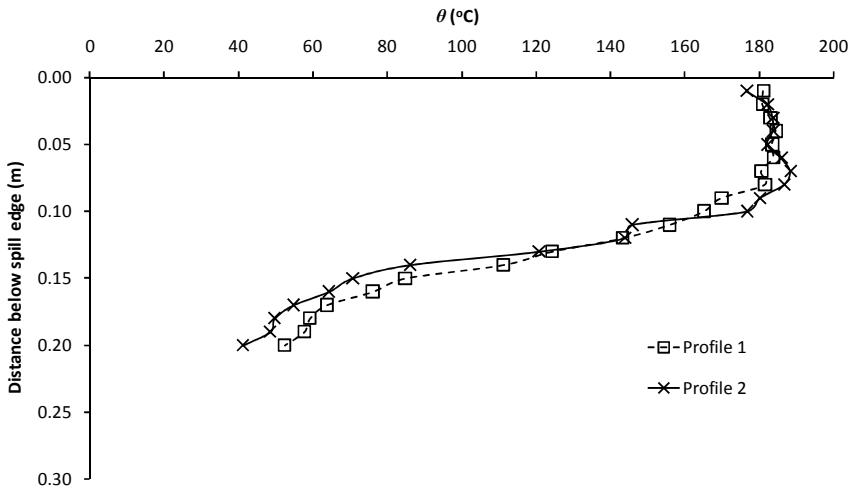

Figure E1: Temperature profiles, Experiment C16

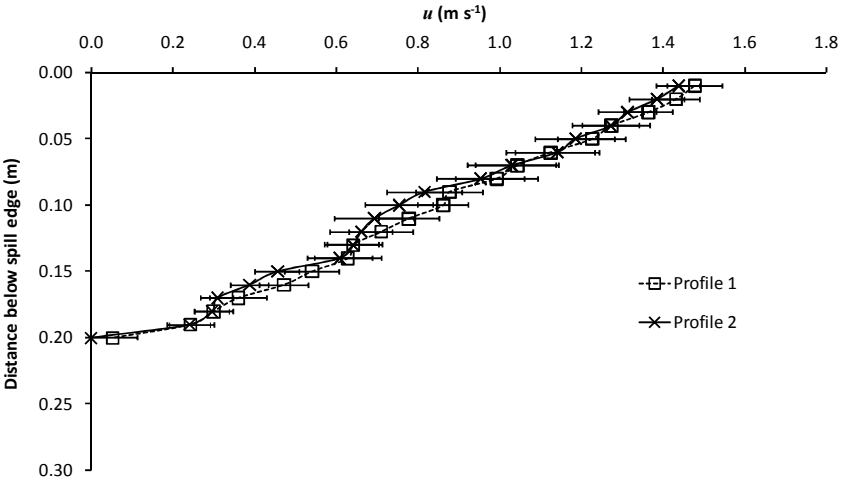

Figure E2: Velocity profiles, Experiment C16

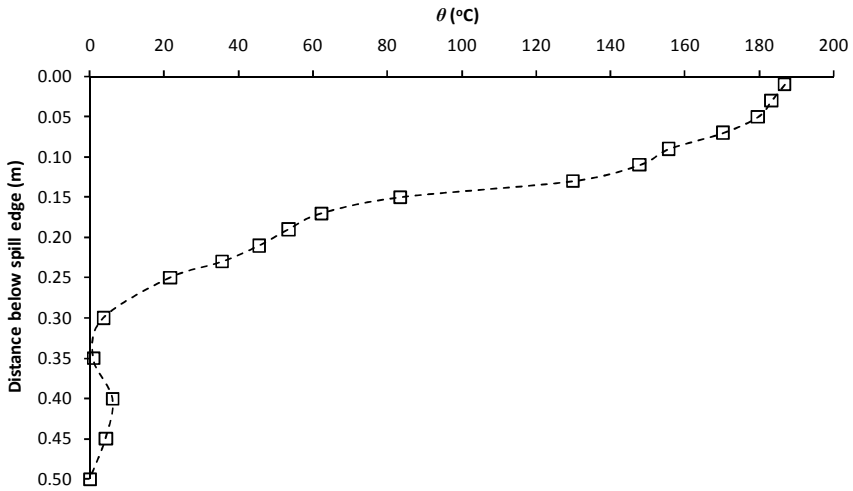

Figure E3: Temperature profile from Column C, Experiment C16

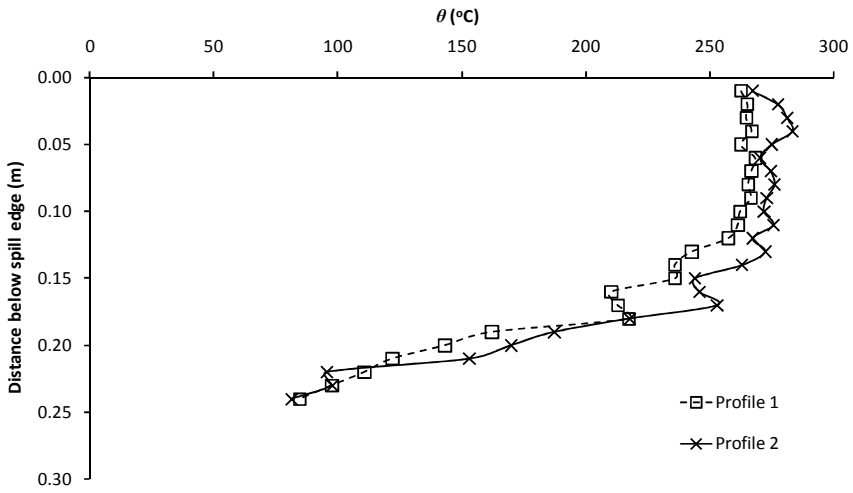

Figure E4: Temperature profiles, Experiment C17

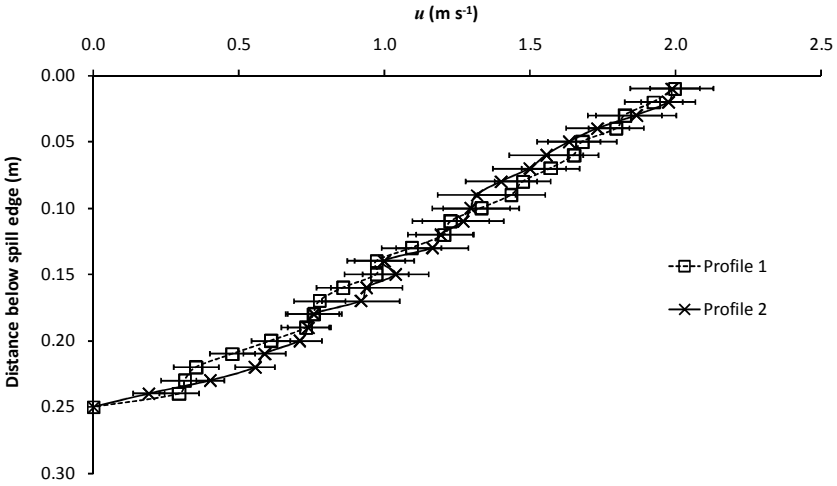

Figure E5: Velocity profiles, Experiment C17

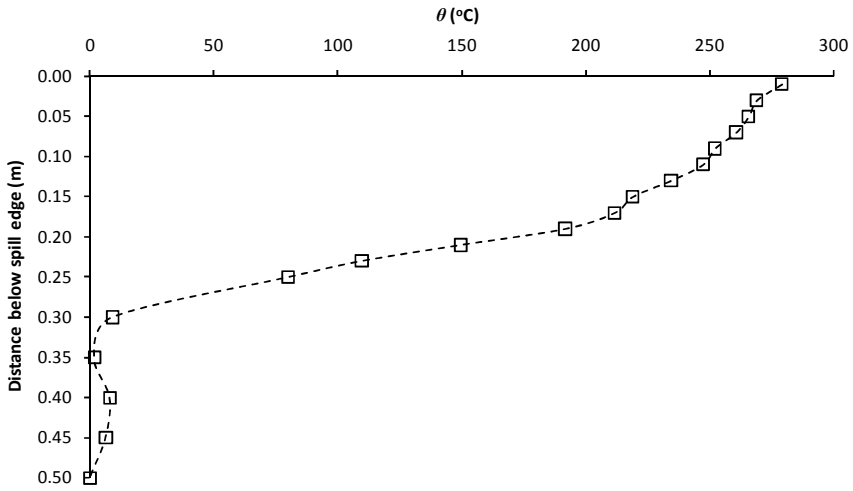

Figure E6: Temperature profile from Column C, Experiment C17

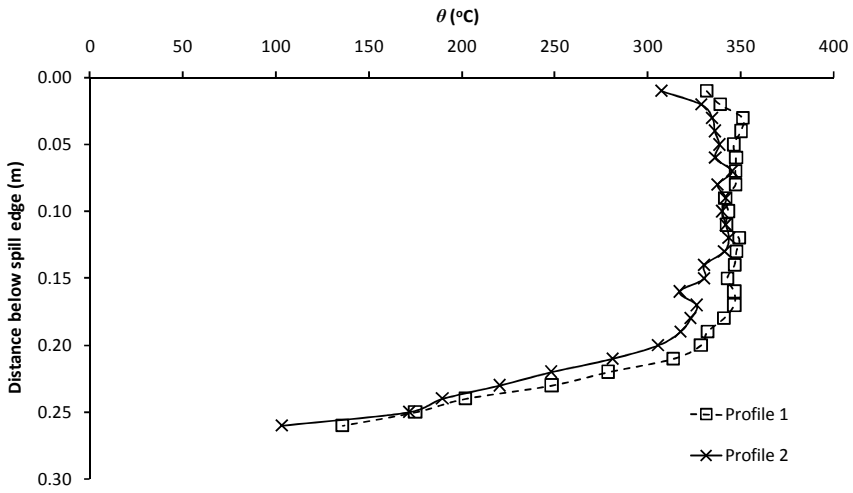

Figure E7: Temperature profiles, Experiment C18

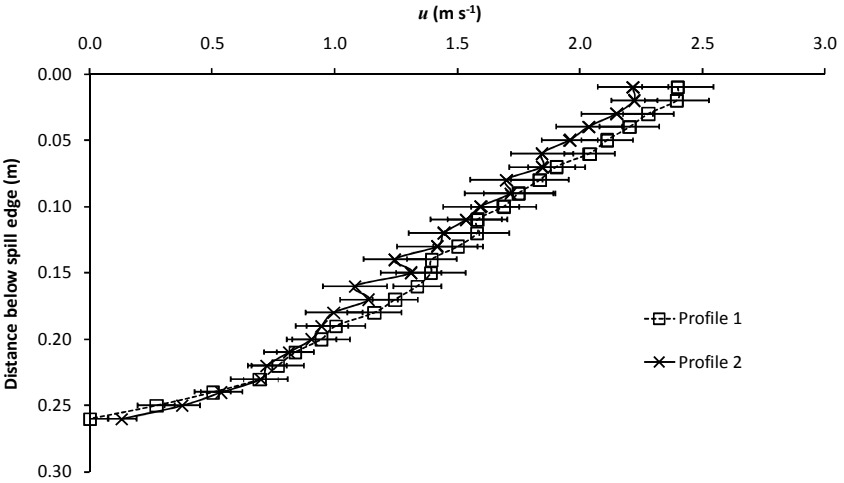

Figure E8: Velocity profiles, Experiment C18

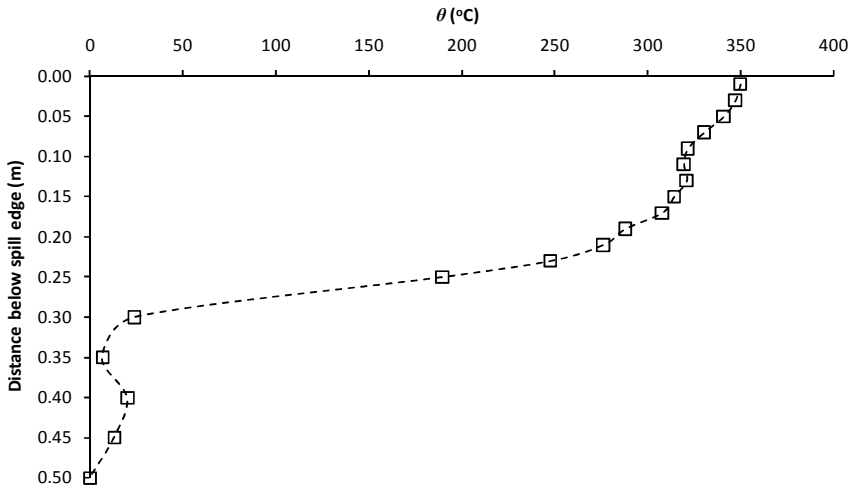

Figure E9: Temperature profile from Column C, Experiment C18

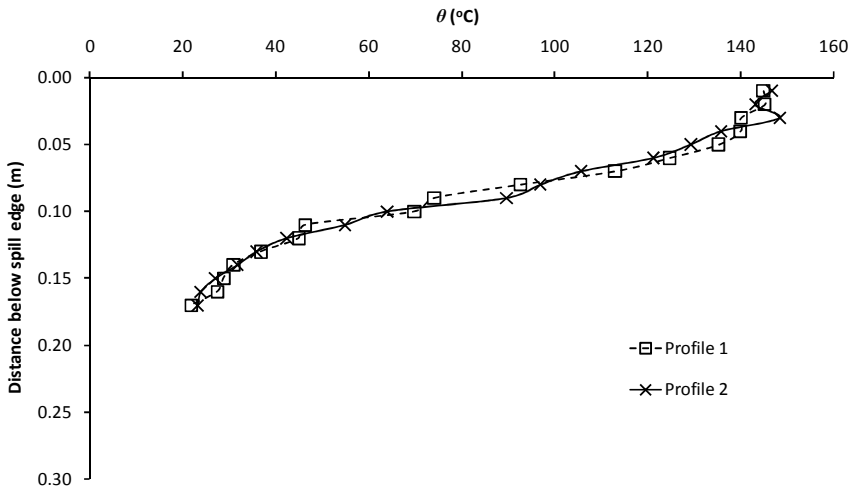

Figure E10: Temperature profiles, Experiment C19

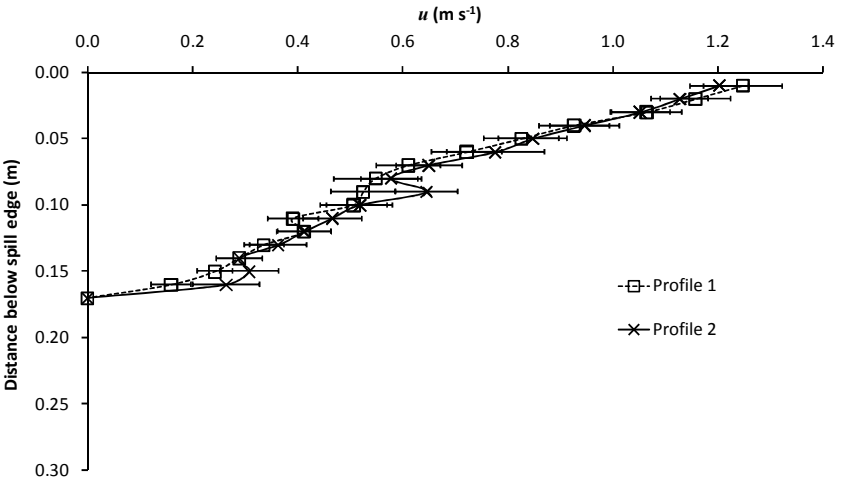

Figure E11: Velocity profiles, Experiment C19

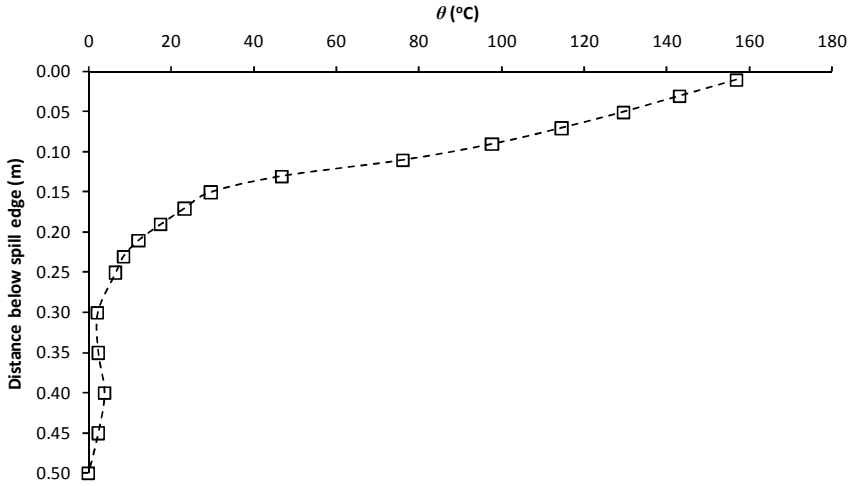

Figure E12: Temperature profile from Column C, Experiment C19

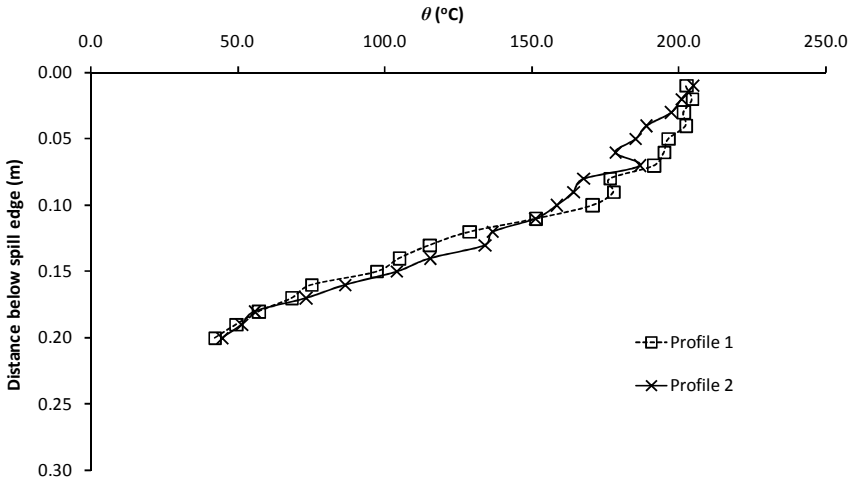

Figure E13: Temperature profiles, Experiment C20

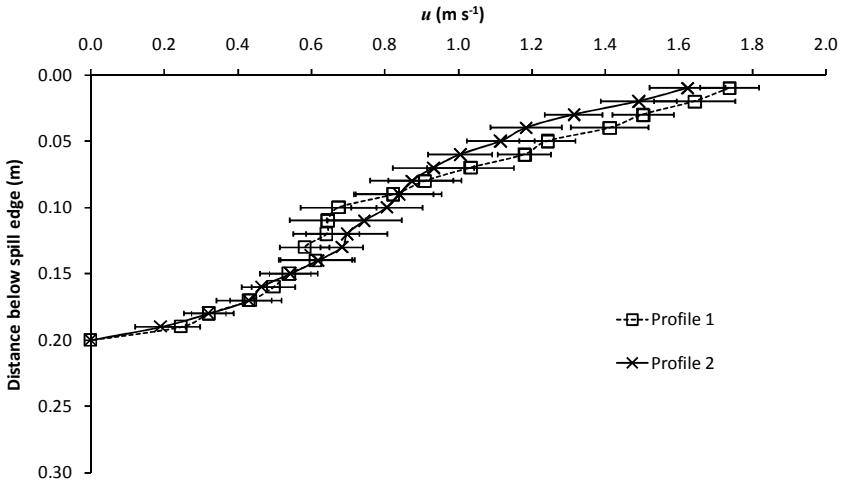

Figure E14: Velocity profiles, Experiment C20

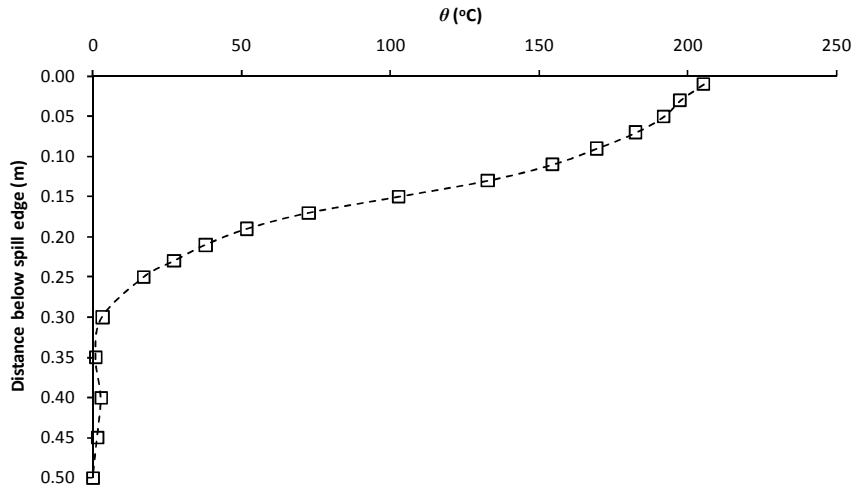

Figure E15: Temperature profile from Column C, Experiment C20

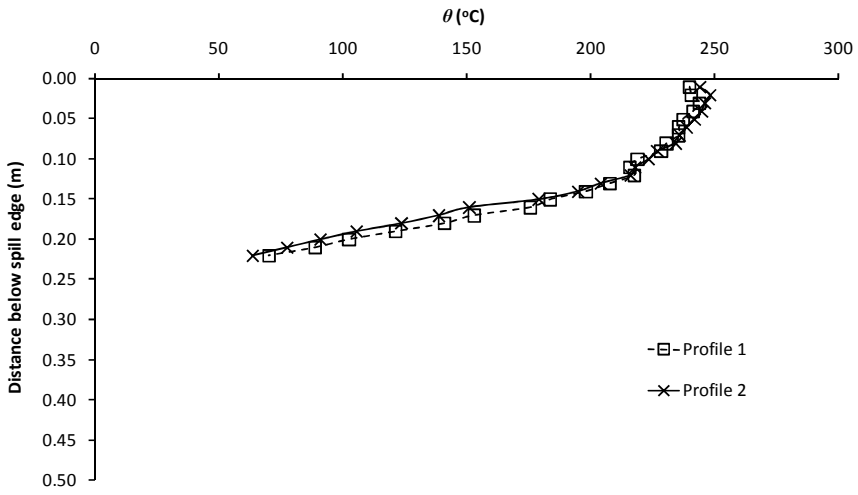

Figure E16: Temperature profiles, Experiment C21

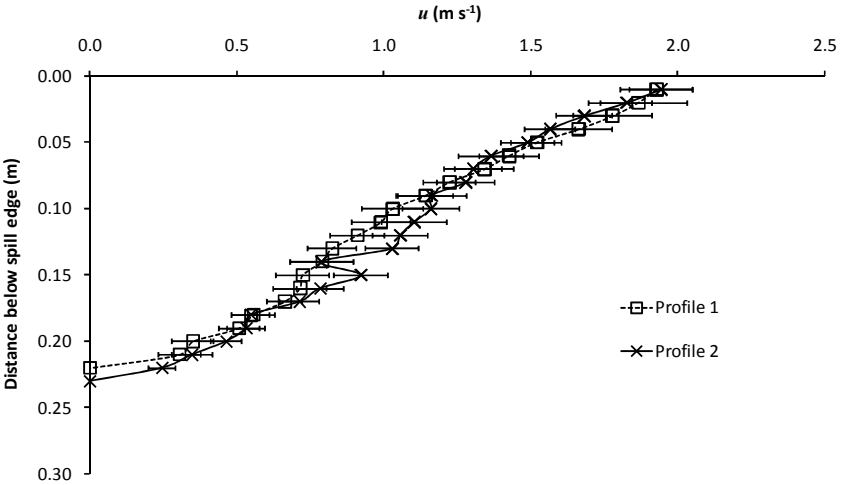

Figure E17: Velocity profiles, Experiment C21

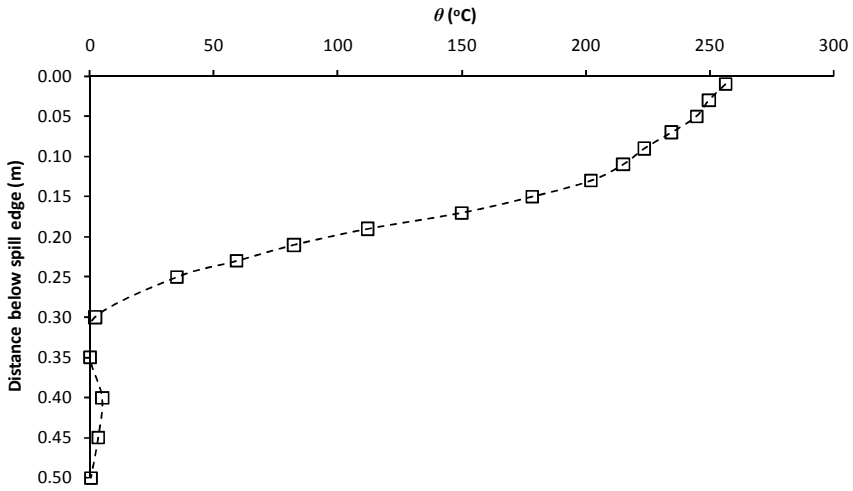

Figure E18: Temperature profile from Column C, Experiment C21

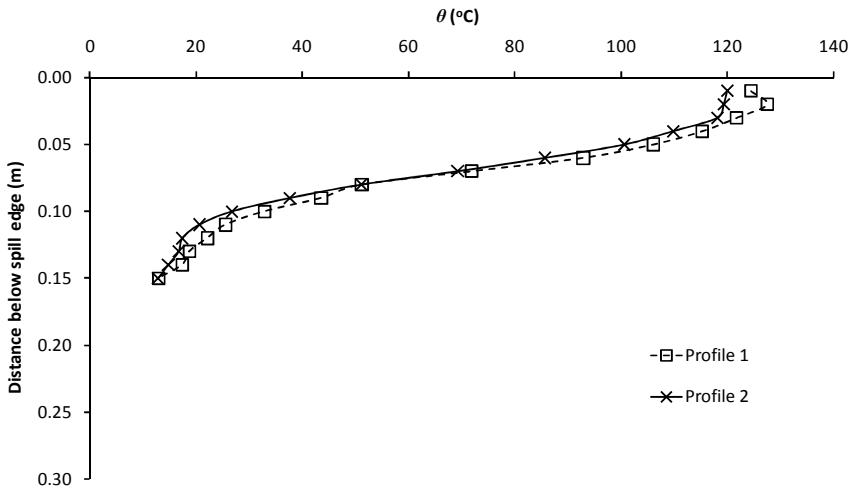

Figure E19: Temperature profiles, Experiment C22

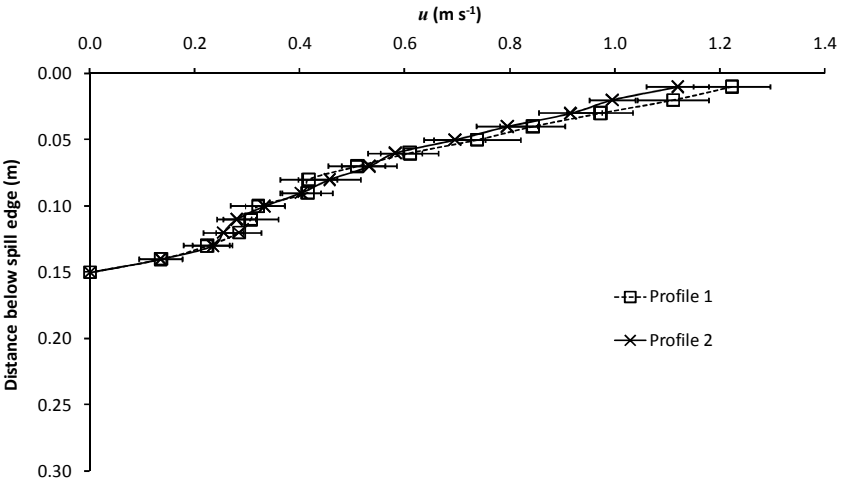

Figure E20: Velocity profiles, Experiment C22

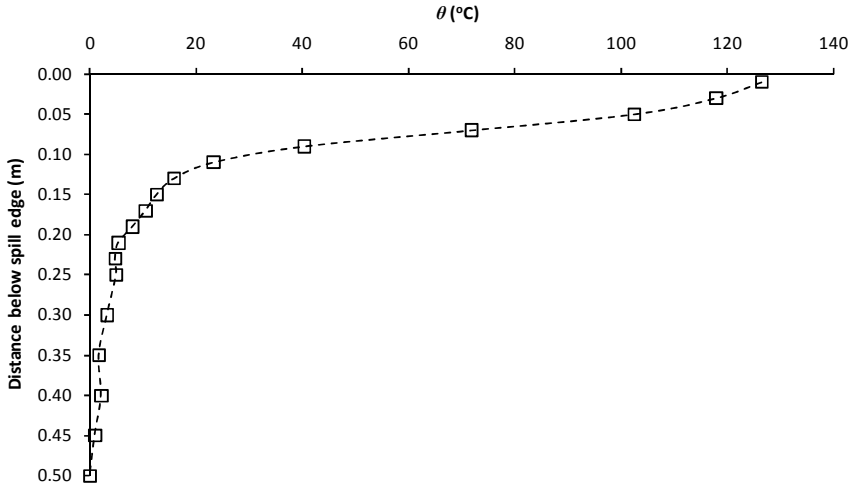

Figure E21: Temperature profile from Column C, Experiment C22

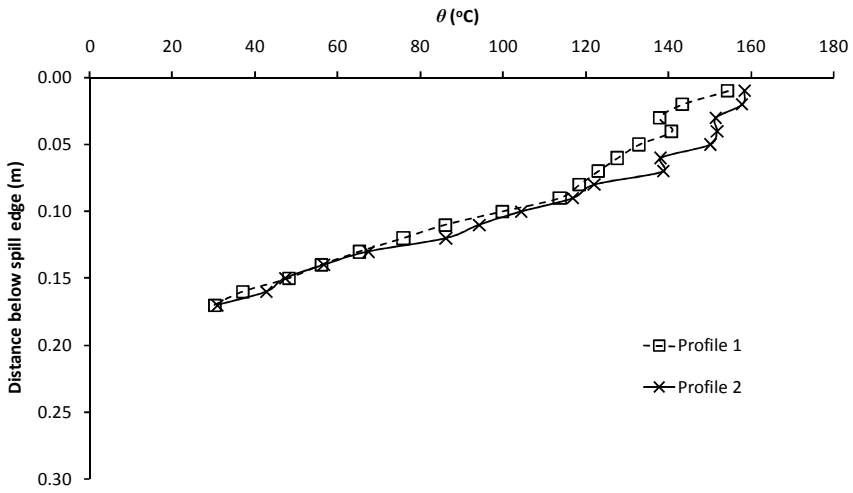

Figure E22: Temperature profiles, Experiment C23

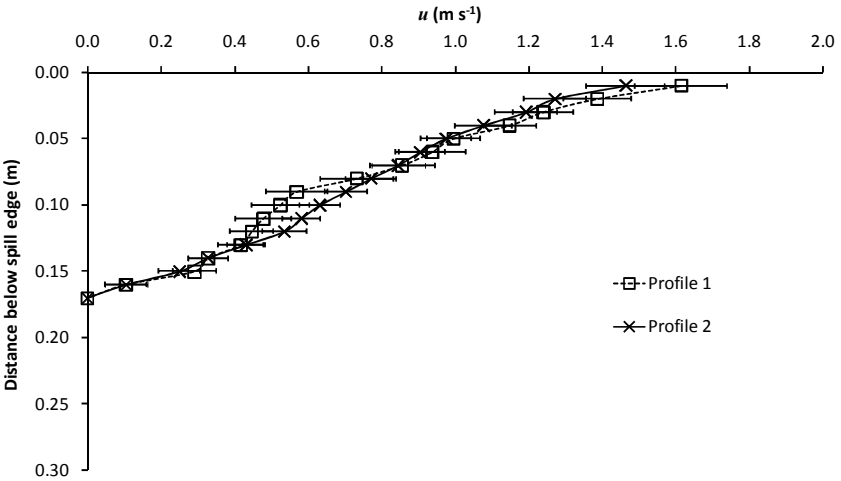

Figure E23: Velocity profiles, Experiment C23

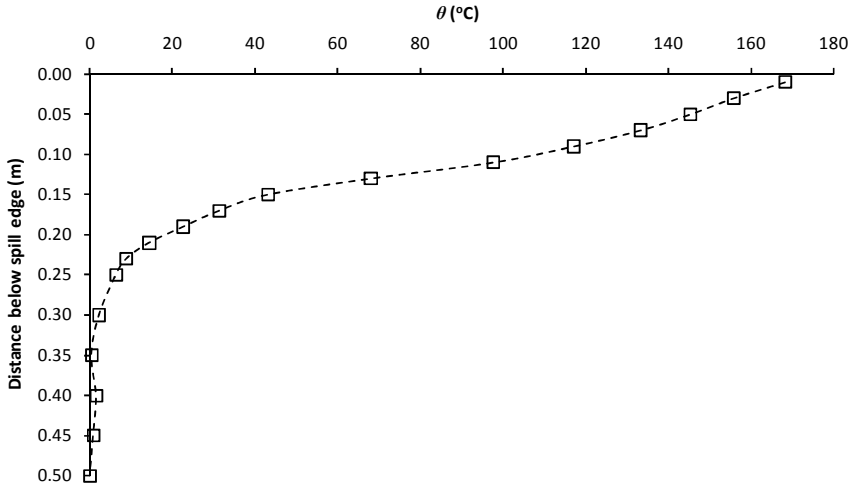

Figure E24: Temperature profile from Column C, Experiment C23

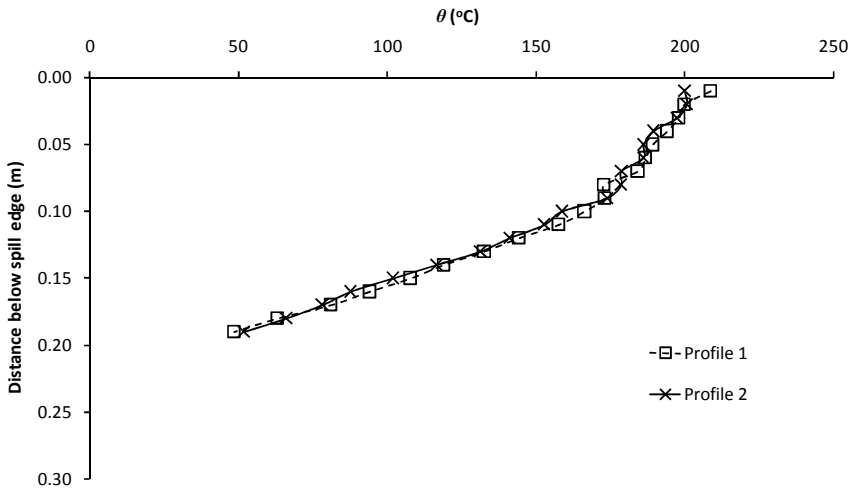

Figure E25: Temperature profiles, Experiment C24

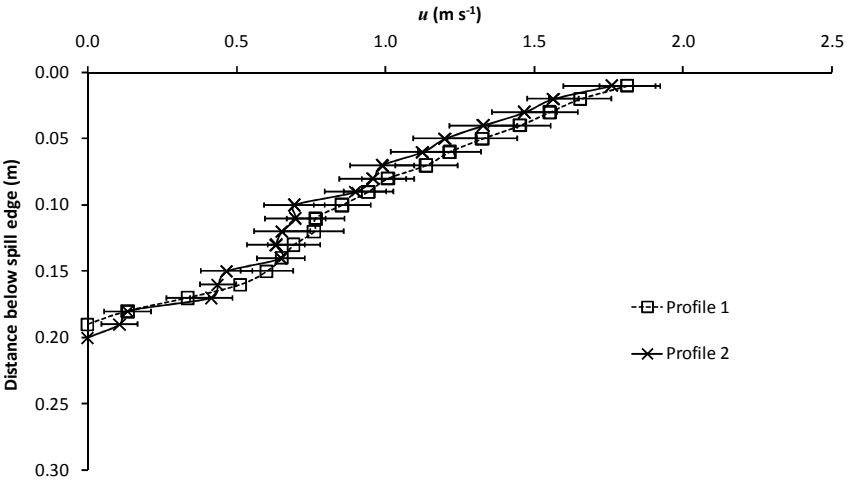

Figure E26: Velocity profiles, Experiment C24

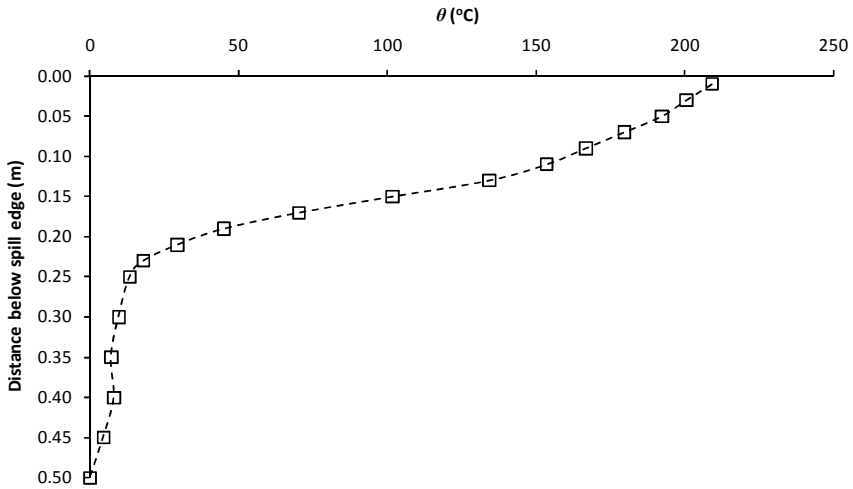

Figure E27: Temperature profile from Column C, Experiment C24

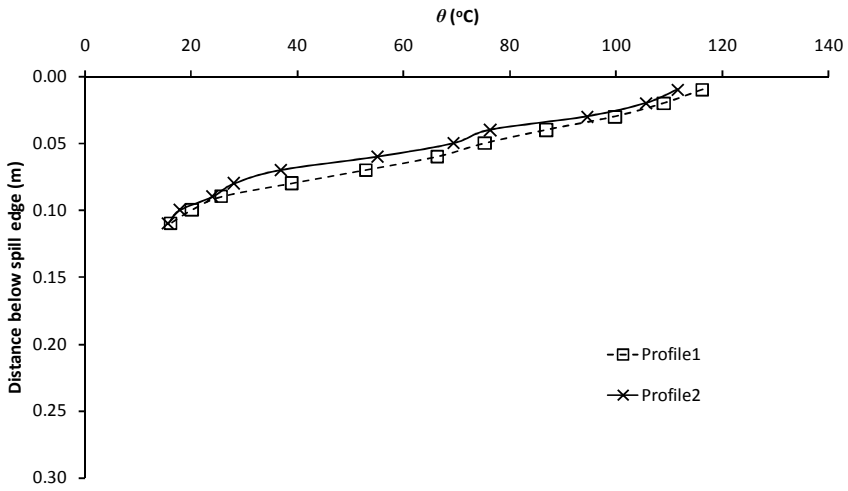

Figure E28: Temperature profiles, Experiment C25

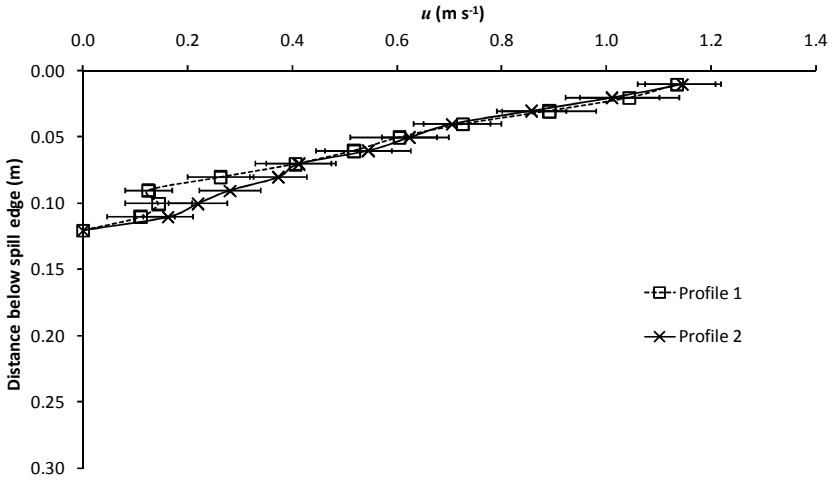

Figure E29: Velocity profiles, Experiment C25

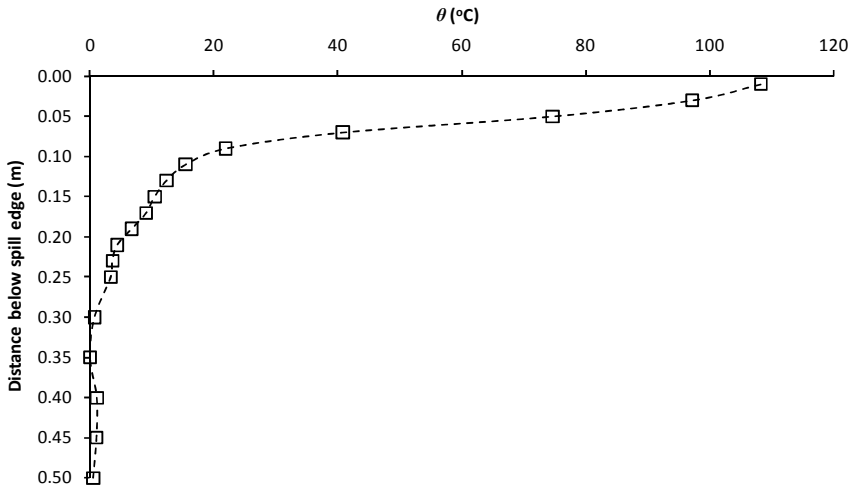

Figure E30: Temperature profile from Column C, Experiment C25

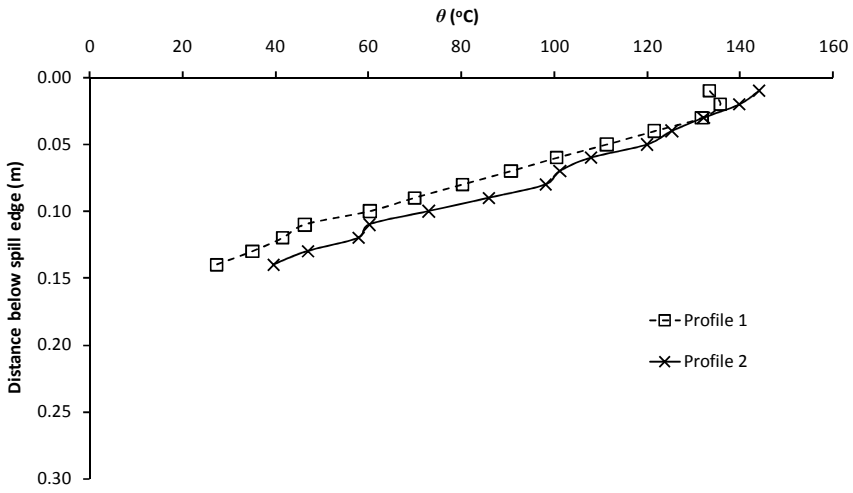

Figure E31: Temperature profiles, Experiment C26

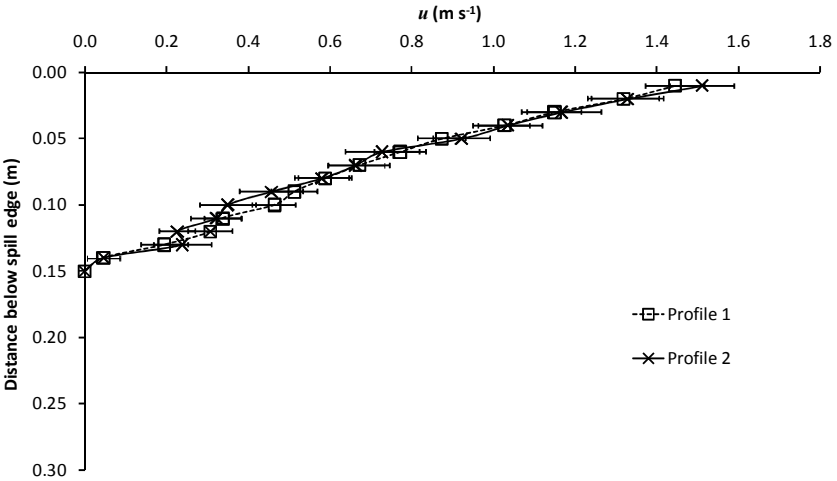

Figure E32: Velocity profiles, Experiment C26

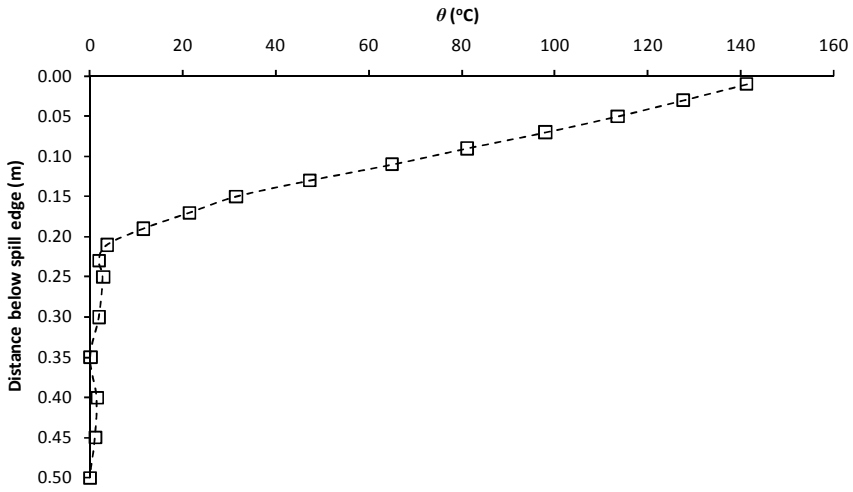

Figure E33: Temperature profile from Column C, Experiment C25

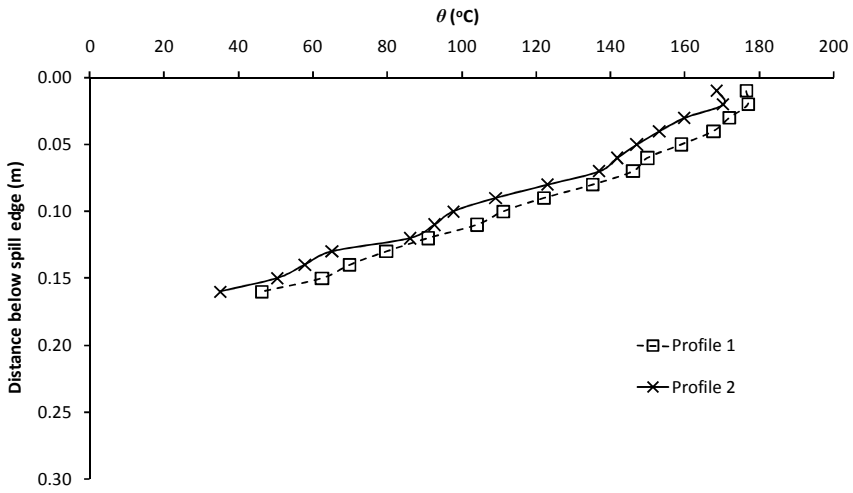

Figure E34: Temperature profiles, Experiment C27

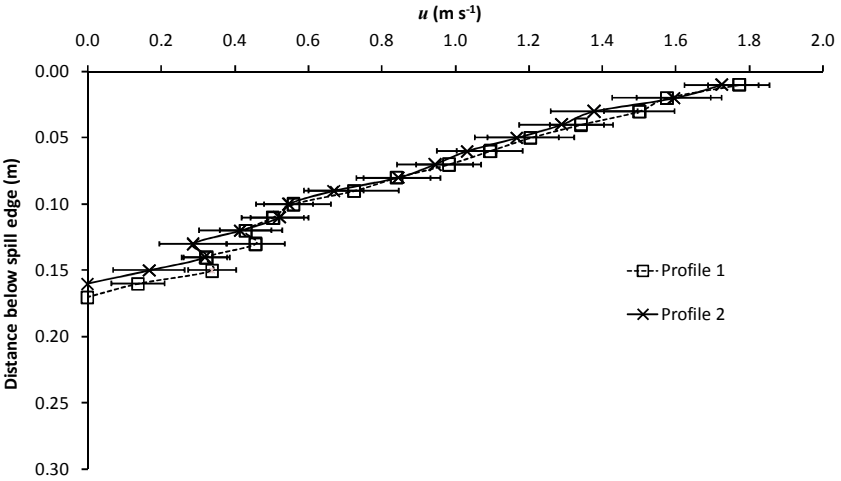

Figure E35: Velocity profiles, Experiment C27

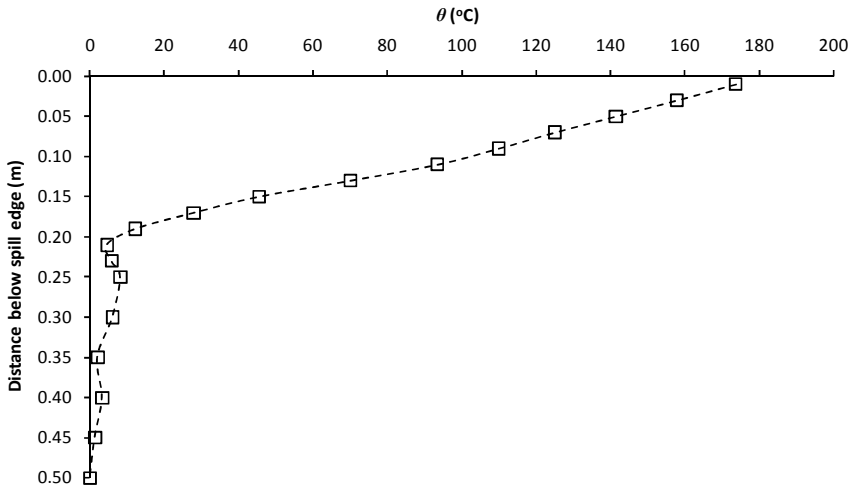

Figure E36: Temperature profile from Column C, Experiment C27

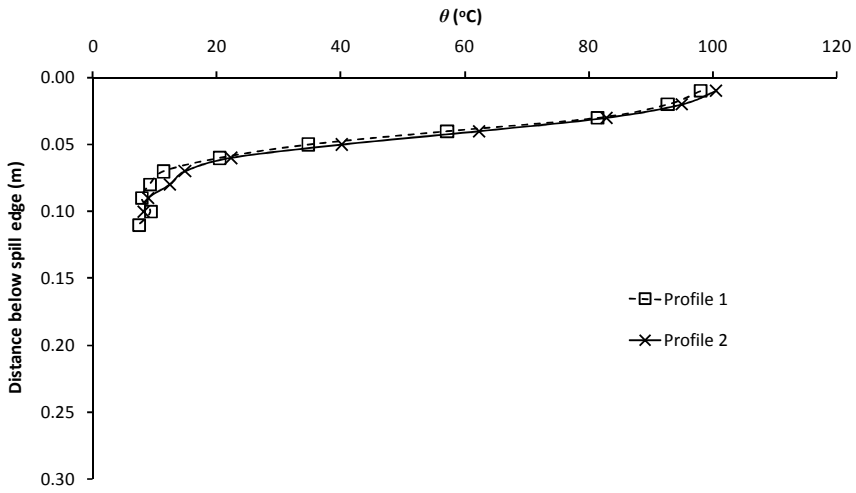

Figure E37: Temperature profiles, Experiment C28

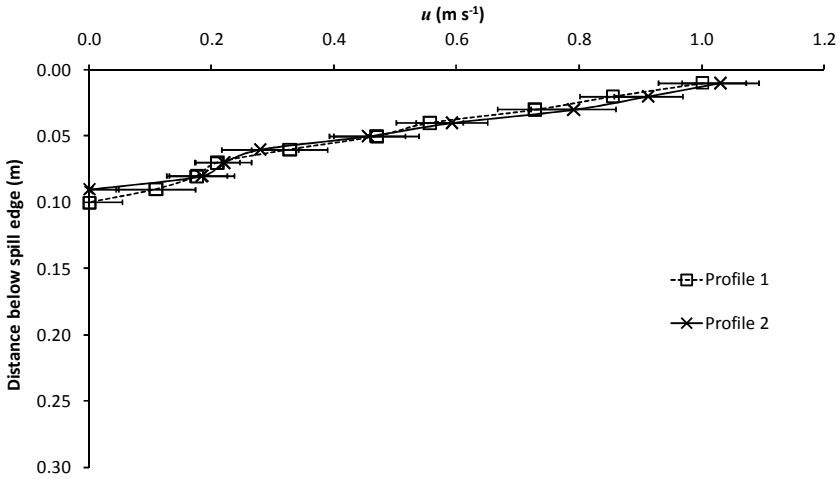

Figure E38: Velocity profiles, Experiment C28

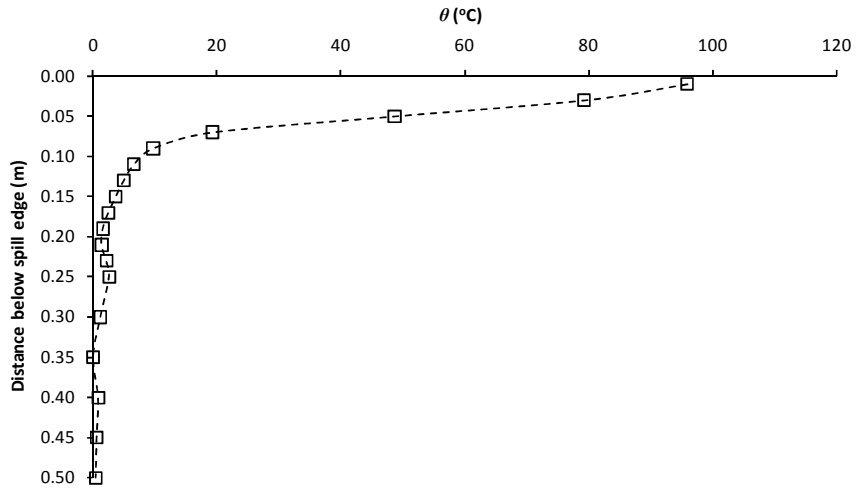

Figure E39: Temperature profile from Column C, Experiment C28

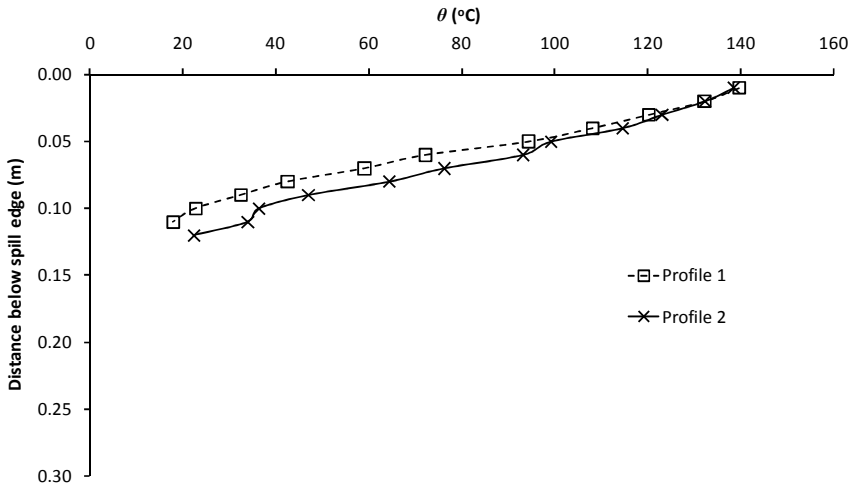

Figure E40: Temperature profiles, Experiment C29

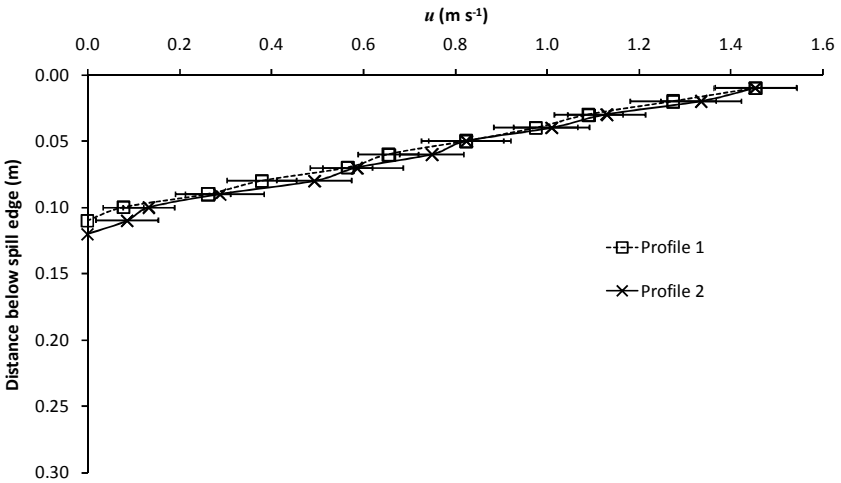

Figure E41: Velocity profiles, Experiment C29

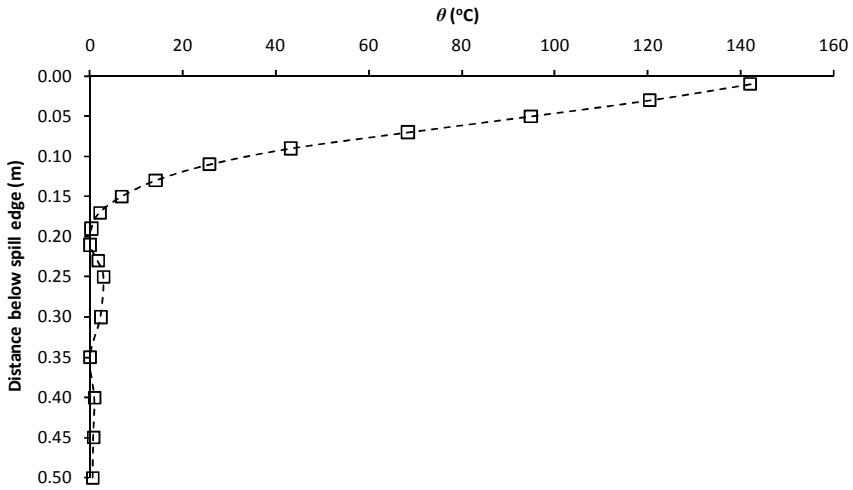

Figure E42: Temperature profile from Column C, Experiment C29

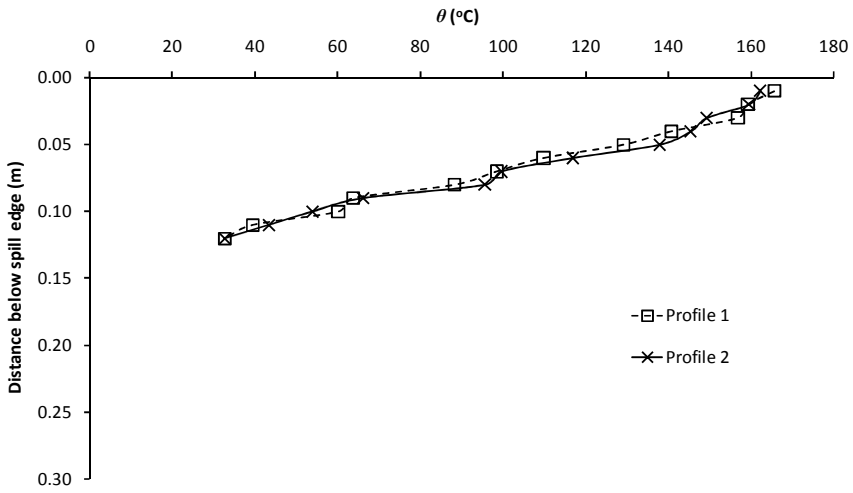

Figure E43: Temperature profiles, Experiment C30

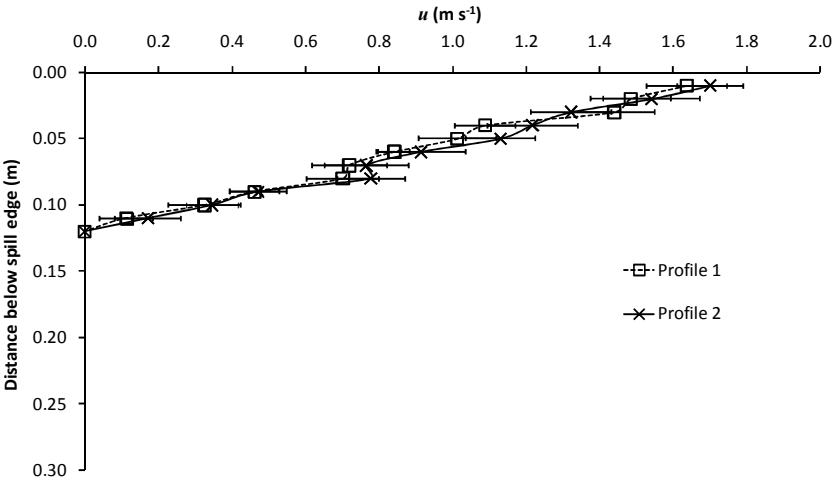

Figure E44: Velocity profiles, Experiment C30

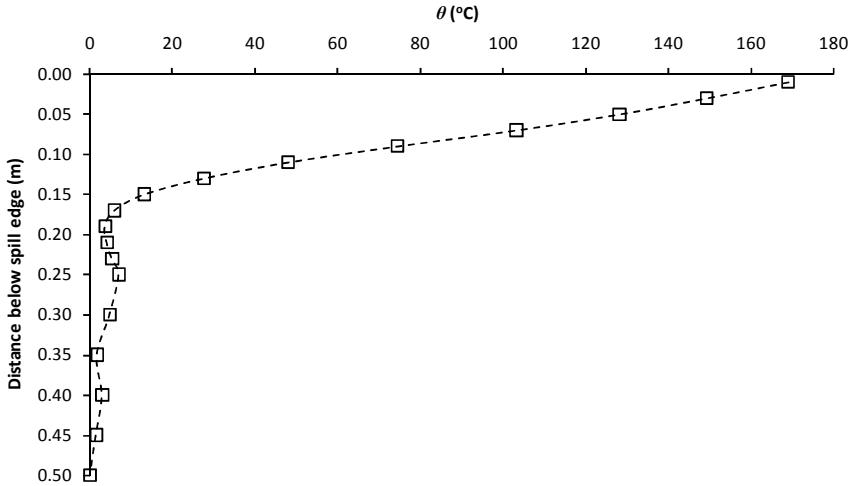

Figure E45: Temperature profile from Column C, Experiment C30

Appendix F: Paper presented at the 9th Symposium on Fire Safety Science, University of Karlsruhe, Germany, September 2008

Characterisation of Balcony Spill Plume Entrainment using Physical Scale Modelling

ROGER HARRISON and MICHAEL SPEARPOINT
Department of Civil and Natural Resources Engineering
University of Canterbury
Christchurch, New Zealand

ABSTRACT

Smoke management design for buildings such as atria and multi-level complexes often requires consideration of smoke produced from a balcony spill plume. This work provides new experimental data to characterise entrainment of air into a balcony spill plume using the approach of physical scale modelling. For a balcony spill plume without entrainment of air into the ends, this work has demonstrated that existing simplified design formulae generally apply for plumes generated from a range of fire compartment geometries. A further simplified design formula is proposed for this type of plume. For a balcony spill plume with entrainment of air into the free ends, the rate of entrainment appears to be specifically dependent on the characteristics of the layer flow below the balcony edge. A simplified design formula is proposed by developing a general empirical expression to describe entrainment of air into the ends of the plume. This work goes some way to explain and reconcile differences in entrainment reported between previous studies and provides improved guidance to designers of smoke management systems.

KEYWORDS: smoke management, balcony spill plume, entrainment

NOMENCLATURE LISTING

Term

C	Coefficient in Equation 2 (kg $m^{1/3}s^{-1}kW^{-1/3}$)
d	Depth of gas layer (m)
$\dot{m}$	Mass flow rate of gases (kgs^{-1})
$\dot{Q}_c$	Convective heat flow of gases (kW)
$\dot{Q}_t$	Total heat output of the fire (kW)
W	Lateral extent of layer at the balcony edge (m)
z	Height of rise of plume above balcony (m)
z_0	Height of virtual source below balcony (m)

Greek

α	Regression coefficient
β	Regression coefficient
γ	Regression coefficient

subscripts

b	Property of layer below balcony edge
ends	Property of the ends of the plume
p	Property of the spill plume
2D	Property of the 2-D plume
3D	Property of the 3-D plume

INTRODUCTION

The design of smoke management systems for buildings such as atria, covered shopping malls and sports arenas require appropriate calculation methods to predict the volume of smoky gases produced in the event of a fire. In design, consideration is often given to entrainment of air into a smoke flow from a compartment opening that subsequently spills at a balcony edge and then rises into an adjacent atrium void. This type of thermal plume is commonly known as a balcony spill plume. There are several calculation methods available for the balcony spill plume, which range from semi-empirical simplified design formulae [1-5] to more complex theories [6,7]. There has been much controversy over the validity of various calculation methods for the balcony spill plume and there are considerable differences in the calculated smoke production rates predicted using these methods [1]. This paper aims to provide information regarding balcony spill plume entrainment using the approach of physical scale modelling. New experimental data has been obtained to rigorously characterise balcony spill plume entrainment by varying the type of plume, fire compartment geometry, fire size and height of rise of plume. Entrainment has been characterised for balcony spill plumes with and without entrainment of air into the ends. In general, this paper seeks to provide a better understanding of spill plume entrainment in an attempt to resolve and reconcile the differences from previous studies and to provide improved guidance to designers of smoke management systems.

PHYSICAL SCALE MODELLING

The approach of physical scale modelling is well established and has been used in many studies of smoke movement in buildings. The approach described in this paper follows that primarily developed at the Fire Research Station in the UK [8,9] and takes the form of reduced scale fires within a physical model. This approach is also described by Klote and Milke [10]. Measurements are generally made of temperature, velocity and gas concentrations, in addition to visual observations. Measurements can be extrapolated to full scale using the appropriate scaling laws. To ensure that the results can be extrapolated to full scale, the physical scale model used in this study was designed to meet the scaling principles set out by Thomas et al [8]. This is effectively a modified Froude number scaling and requires that the equivalent flows are fully turbulent on both full and model scale.

THE EXPERIMENT

The apparatus used for this work was a $1/10^{th}$ physical scale model (see Figure 1). The model simulated a fire within a room adjacent to an atrium void, and consisted of two main units, the fire compartment and a smoke collecting hood. The model employed a similar technique to that used by Zukoski et al [11] to measure entrainment of air into unbounded axisymmetric plumes. The fire compartment was constructed from 25 mm thick Ceramic Fibre Insulation (CFI) board with a 1 mm thick steel substrate on each external face. The dimensions of the fire compartment were 1.0 by 1.0 by 0.5 m high. The height of the compartment opening was equal to the height of the compartment. The width of the compartment opening was varied by inserting walls of equal width at either end of the opening. The inserted walls had widths of 0.1, 0.2, 0.3 and 0.4 m and were constructed from 25 mm thick CFI board with a 1 mm thick steel substrate on the non-fire side of the compartment. A 2.0 m long and 0.3 m broad balcony constructed from 10 mm thick CFI board with a 1 mm thick steel substrate on its upper face was attached to the fire compartment opening. The balcony extended 0.5 m beyond each side of the fire compartment. For those tests examining balcony spill plumes without entrainment of air into the ends (i.e. the 2-D plume), screens were suspended from the ceiling of the collecting hood, in line with each side of the fire compartment opening, to prevent lateral spread of the plume both below and above the balcony. These screens prevented air from entering the ends of the plume over its full height of rise. The dimensions of these screens were 1.2 m wide by 1.4 m high, made from 10 mm thick CFI board with a 1 mm thick steel sheet substrate on the external face. The screens projected across the breadth of the balcony and continued 0.9 m beyond the balcony edge. The screens projected 0.3 m below the balcony and 1.1 m above the balcony. Those tests which examined balcony spill plumes with entrainment of air into the ends of the plume (i.e. the 3-D plume), used channelling screens which were only located beneath the balcony to prevent lateral spread under the balcony. The screens were located in line with each side of the fire compartment opening and projected across the full breadth of the balcony. The screens were made from 10 mm thick CFI board with a 1 mm thick steel substrate on the external face. The screens used were either 0.2 or 0.3 m deep, depending on the compartment geometry and fire size examined. The side walls of the smoke collecting hood were generally constructed from 10 mm thick CFI board with a 1 mm thick steel sheet substrate on each external face. However, one of the side walls was constructed from 10 mm thick transparent acrylic sheet to enable visual observations to be made of the smoke layer within the collecting hood. The model was designed such that the walls could freely move in a vertical direction within a supporting steel frame. This enabled each wall to be moved independently to just below the base of the observed smoke layer in the hood (approximately 60 mm below) allowing unrestricted fresh air to be entrained into the rising plume. This effectively simulated an unbounded balcony spill plume and prevented warming of the air beneath the observed smoke layer. The supporting steel frame was designed such that each side wall could contain up to two, smaller, modular walls each 2.0 m wide by 1.2 m high, which could be bolted together. This would then form a single wall on each face when examining deep smoke layers within the collecting hood. The mechanical smoke exhaust system from the hood consisted of a 0.44 m diameter bifurcated fan attached to the hood exhaust vent using temperature resistant flexible ducting. The gases were exhausted to the outside of the laboratory through flexible ducting connected to the exhaust end of the fan. The fan speed was controllable, which enabled different exhaust rates, and hence, variation in the height of rise of the plume to be examined. The fire source was generated by supplying Industrial Methylated Spirits into a metal tray within the fire compartment at a controlled and measured rate. The tray was 0.25 by 0.25 by 0.015 m high.

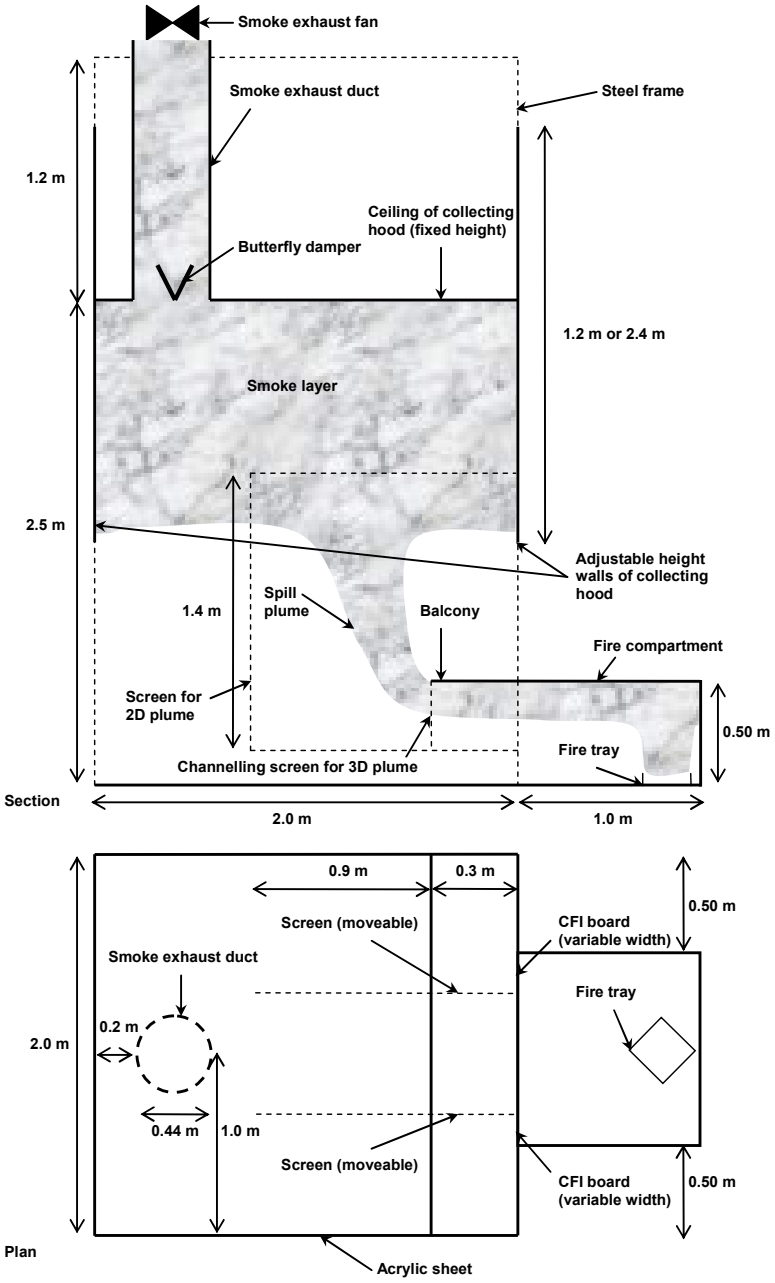

Fig. 1. Schematic Drawing of the 1/10th Physical Scale Model.

The hot gases produced from the fire were visualised by injecting smoke from a commercial smoke generator into the fire compartment. This highlighted the flowing gas layer from the compartment and the subsequent spill plume and smoke layer in the collecting hood. The gas temperatures in the model were measured using 0.5 mm diameter bare wire chromel/alumel (K-type) thermocouples. Thermocouples were positioned at various locations in the model as follows: two columns of 15 thermocouples located within the smoke exhaust hood; one column of 18 thermocouples located centrally beneath the balcony edge; an array of 21 thermocouple across the entire balcony edge, projecting 10 mm below the edge; an array of five thermocouples in the throat of the exhaust vent; one thermocouple located centrally within the smoke exhaust duct, 5.0 m downstream of the exhaust vent; two thermocouples, one located next to each of two

pitot-static tubes, when measuring velocity profiles of the smoke layer below the balcony edge. A perforated gas sampling tube was located in the exhaust duct, 5.0 m downstream of the vent in the smoke exhaust hood. This enabled measurement of the CO_2 gas concentration in the duct to be made using an infra red gas analyser. The mass flow rate of gases entering the buoyant gas layer in the smoke collecting hood and therefore leaving the hood, was found by using a CO_2 tracer gas technique and calculation method described by Marshall [9]. Vertical velocity and temperature profiles of the buoyant gas layer flow below the balcony edge were made using two pitot-static tubes and a thermocouple. The pitot-static tubes were each located a distance of one-third of the compartment opening width from each side of the opening. Each pitot-tube was connected to a sensitive differential pressure transducer. Gas velocity measurements were made every 10 mm below the balcony edge until the base of the smoke layer was reached (i.e. from visual observations and until a negative flow, from the inflow, was measured). This measurement, in addition to the temperature profiles, enabled the mass flow rate and convective heat flow of the gas layer below the balcony edge to be determined. A series of 97 experiments was carried out as part of an extensive parametric analysis to characterise entrainment of air into a balcony spill plume. For the vast majority of the experiments, a balcony spill plume with air entrainment into the free ends was examined. For these experiments examining the 3-D spill plume, the total heat output of the fire was varied, three fire sizes were examined of 5, 10 and 15 kW respectively. This equates to a fire size of 1.6, 3.2 and 4.7 MW respectively for a full scale equivalent using the scaling laws. Varying the total heat output of the fire in turn varied the mass flow rate, convective heat flow and depth of the gas layer below the balcony edge. The height of rise of plume above the balcony was also varied, with six different heights examined between 0 to 1.25 m. The width of the fire compartment opening was varied, with widths of 0.2, 0.4, 0.6, 0.8 and 1.0 m examined. Selected experiments were carried out for a balcony spill plume without air entrainment into the free ends to confirm and extend findings from previous work. For these experiments, the height of rise of plume above the balcony edge was varied, with five different heights examined between 0 to 1.02 m. The width of the fire compartment opening was varied, with widths of 0.2, 0.4, 0.6, 0.8 and 1.0 m examined. The total heat output of the fire remained fixed at 10 kW for the experiments without end entrainment.

ANALYSIS

The analysis of 2-D spill plumes often utilises the weak line plume theory described by Lee and Emmons [12]. The plume is assumed to rise from a virtual line source located at a distance below the balcony edge, and makes the assumption of self-similar profiles across the plume (e.g. Gaussian profiles) in terms of velocity and temperature. A constant entrainment coefficient is assumed, providing linearity between the mass flow rate of gases and the height of rise of the plume. Thomas et al [4] and Poreh et al [5] have determined simplified spill plume design formulae for the 2-D plume. Thomas et al used a rigorous dimensional analysis to develop a simplified spill plume model in the form given by Equation 1. This method does not make the assumption of self-similar flow profiles or a constant entrainment coefficient.

$$\frac{\dot{m}'_p}{\dot{Q}'_c} = \alpha \frac{z}{\dot{Q}'^{2/3}_c} + \beta \frac{\dot{m}'_b}{\dot{Q}'_c} + \gamma \qquad \text{where, } \dot{m}'_p = \frac{\dot{m}_p}{W}, \quad \dot{m}'_b = \frac{\dot{m}_b}{W}, \quad \dot{Q}'_c = \frac{\dot{Q}_c}{W} \tag{1}$$

Poreh et al followed a similar approach to Lee and Emmons, and deduced the following simplified design formula given by Equation 2.

$$\frac{\dot{m}'_p - \dot{m}'_b}{\dot{Q}'_c} = C\left(\frac{z + z_0}{\dot{Q}'^{2/3}_c}\right) \tag{2}$$

When expressed in this form, the Poreh et al method deals with entrainment into the turning region of the plume, as the layer flow rotates at the balcony edge, by assuming it is the same as the entrainment into the virtual region of the plume, with the virtual origin assumed to be located at the base of the gas layer below the balcony edge (i.e. $z_0 = d_b$). These methods will be used to analyse the experimental data from this study for the 2-D plume and the 3-D plume by encompassing the additional entrainment into the ends of the plume into the empirical entrainment coefficient(s).

RESULTS AND DISCUSSION

Balcony Spill Plume without Entrainment of Air into the Ends – The 2-D Plume

Previous 1/10th physical scale modelling work, from separate studies described by Marshall and Harrison [13] has provided data to characterise entrainment of air into a 2-D spill plume. From these data Thomas et al [4] determined, according to Equation 1, that;

$$\frac{\dot{m}'_{p,2D}}{\dot{Q}'_c} = 0.16\frac{z}{\dot{Q}'^{2/3}_c} + 1.2\frac{\dot{m}'_b}{\dot{Q}'_c} + 0.0027 \tag{3}$$

Poreh et al [5] determined from the same data, according to Equation 2, that;

$$\frac{\dot{m}'_{p,2D} - \dot{m}'_b}{\dot{Q}'_c} = 0.16\left(\frac{z + d_b}{\dot{Q}'^{2/3}_c}\right) \tag{4}$$

Equations 3 and 4 were determined for fires with $\dot{Q}_c$ ranging between 6 to 34 kW. However, W was fixed in these experiments at 0.91 m. Therefore, for this study, a selected number of experiments were carried out to determine if Equations 3 and 4 also apply for a range of W. Figure 2 shows the data obtained from this study and previous data by Marshall and Harrison [13], plotted in a form consistent with the dimensional analysis given by Thomas et al [4]. A line representing Equation 3 is also shown for a mid range value of $\dot{Q}_c$ from the Marshall and Harrison data, as it is weakly dependent on $\dot{Q}_c$.

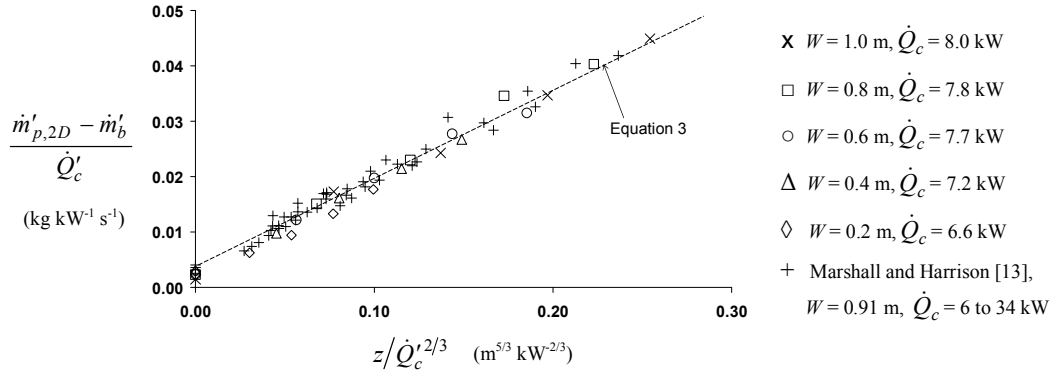

Fig. 2. Comparison of mass flow rate with respect to height of rise according to Thomas et al [4]

Figure 2 shows that all the data follow a common linear relationship, which appears to be independent of $\dot{Q}_c$ and W. The intercept on the vertical axis represents the amount of entrainment in the turning region of the plume. The same data are plotted in Figure 3, according to the method by Poreh et al [5], including a line representing Equation 4. Figures 2 and 3 indicate that the data from this study, obtained from a range of W, is broadly consistent with the data from previous work. Performing linear regression for each complete data set shown in Figures 2 and 3 gives $\alpha = 0.163$ and $C = 0.159$ with standard errors of 0.003 and 0.001 respectively. Therefore, the additional data from this study is consistent with the dominant regression coefficients in Equations 3 and 4 being equal (within 1 standard error), with a value of 0.16. It appears that Equations 3 and 4 can generally be applied for 2-D spill plumes. The difference between them is the term(s) describing the entrainment of air into the flow below the balcony edge (i.e. the mass flow rate in the plume at $z = 0$). Existing experimental data describing entrainment into the plume at $z = 0$ is particularly sparse and has not been characterised in a robust manner. Therefore, in this work, a more extensive data set from 20 experiments was obtained for entrainment at $z = 0$ in an attempt to characterise and decouple entrainment into the flow below the balcony edge. Figure 4 shows a plot of $\dot{m}'_p/\dot{Q}'_c$ versus $\dot{m}'_b/\dot{Q}'_c$ at $z = 0$, consistent with the dimensional analysis by Thomas et al [4].

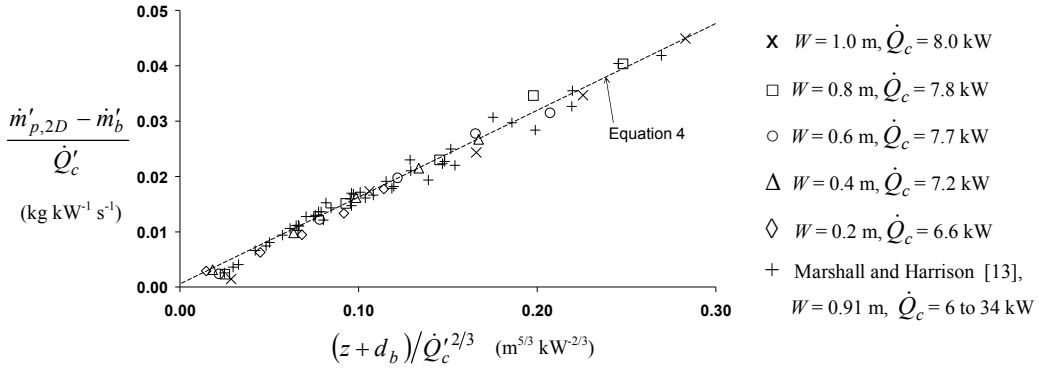

Fig. 3. Comparison of mass flow rate with respect to height of rise according to Poreh et al [5]

The data shown in Figure 4 was from those tests which had channelling screens used for the 2-D plume (screens both above and below the balcony) and those screens used for the 3-D plume (screens only below the balcony), as at z = 0 it is expected that the effect of end entrainment into the rotation region will be negligible for the 3-D plume scenario (also assumed by Thomas et al [4]). Data from previous work by Harrison and Spearpoint [1] and Marshall and Harrison [13], obtained at z = 0, is also included in the analysis. The data is presented in terms of the time averaged mean value with associated standard errors.

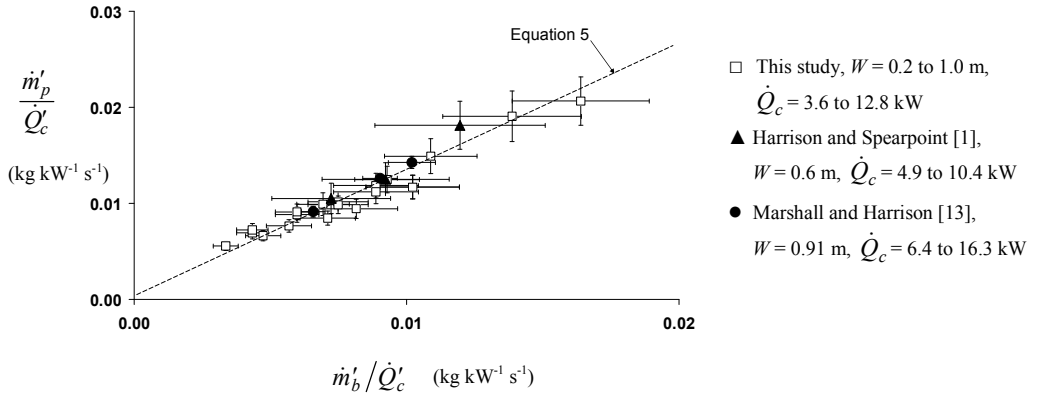

Fig.4. Correlation between $\dot{m}'_p/\dot{Q}'_c$ and $\dot{m}'_b/\dot{Q}'_c$ at z = 0.

Figure 4 shows that all of the data, obtained from a range of $\dot{Q}_c$ and W, generally follow a relationship described by Equation 5, with regression coefficients of β = 1.34 and γ = 0. The standard error of the regression coefficient β is 0.023. This is similar to that suggested by Thomas et al [4] (i.e. β = 1.4) from analysis of much fewer data points. It seems reasonable to use Equation 5 to describe the entrainment of air into the flow below the balcony, instead of the regression coefficients β = 1.2 and γ = 0.0027 given in Equation 3, which were determined using multiple linear regression from data mainly obtained above the balcony. Equation 5 provides a simpler equation, from a more robust data set, which is not determined from data obtained above the balcony, nor is it weakly dependent on $\dot{Q}_c$.

$$\frac{\dot{m}'_p}{\dot{Q}'_c} = 1.34 \frac{\dot{m}'_b}{\dot{Q}'_c} \tag{5}$$

Therefore, Equation 6 is proposed to describe entrainment into 2-D balcony spill plumes, as it is a simpler, modified version of Equation 3 and does not require the calculation of both $\dot{m}_b$ and d_b as required by Equation 4 and appears to generally apply with respect to variation in $\dot{Q}_c$ and W.

$$\frac{\dot{m}'_{p,2D}}{\dot{Q}'_c} = 0.16\frac{z}{\dot{Q}'^{2/3}_c} + 1.34\frac{\dot{m}'_b}{\dot{Q}'_c} \qquad \text{or} \qquad \dot{m}_{p,2D} = 0.16\dot{Q}_c^{1/3}W^{2/3}z + 1.34\dot{m}_b \tag{6}$$

Balcony Spill Plume with Entrainment of Air into the Ends – The 3-D Plume

There is a limited amount of experimental data currently available for 3-D balcony spill plumes. Work by Harrison and Spearpoint [1] and Hansell et al [14], provides data from 1/10th scale model studies, which includes data describing the layer flow below the balcony edge. If the Harrison and Spearpoint data is correlated according to Equation 1, then;

$$\frac{\dot{m}'_{p,3D}}{\dot{Q}'_c} = 0.22\frac{z}{\dot{Q}'^{2/3}_c} + 1.92\frac{\dot{m}'_b}{\dot{Q}'_c} - 0.0042 \tag{7}$$

The Hansell et al data (which forms the basis of the guidance given in [2] and [3]) correlates to;

$$\frac{\dot{m}'_{p,3D}}{\dot{Q}'_c} = 0.34\frac{z}{\dot{Q}'^{2/3}_c} + 2.64\frac{\dot{m}'_b}{\dot{Q}'_c} - 0.0083 \tag{8}$$

The difference in α between Equations 7 and 8 (i.e. the 0.22 and the 0.34) provides significant differences in predicted entrainment. Possible reasons for this may relate to differences in the nature of the plume, fire compartment geometry or smoke reservoir geometry between each experimental study. Thus, there is currently uncertainty concerning an appropriate calculation method to predict the entrainment of air for the 3-D plume. To address this uncertainty, this work provides new data to systematically characterise entrainment of air into 3-D plumes. Figure 5 shows a plot of all the data from this study in a form consistent with the dimensional analysis by Thomas et al [4].

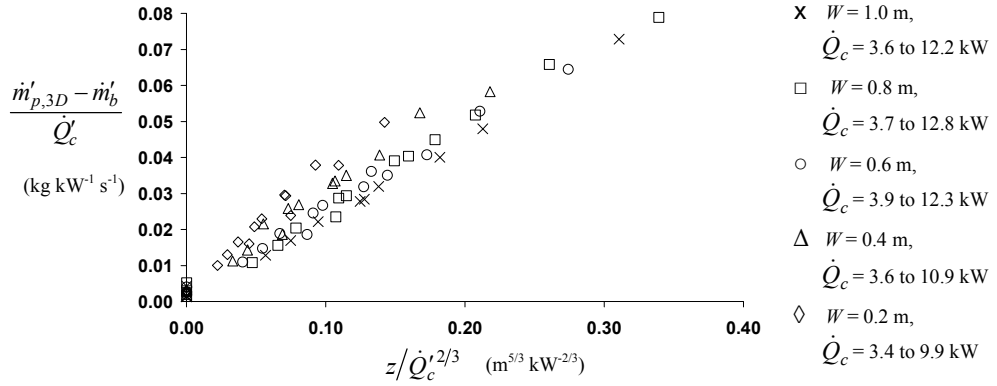

Fig.5. Comparison of mass flow rate with respect to height of rise according to Thomas et al [4]

Figure 5 shows some scatter of the data which appears to be dependent on *W*. The data exhibits linearity, with the representative slope of the line through each data set, for each value of *W*, appearing to increase as *W* decreases. The slope of the line represents the rate of entrainment with respect to height above the balcony. Figure 5 indicates that plumes generated from narrower openings tend to entrain air at a greater rate with respect to height, compared to plumes generated from wider openings. The difference in entrainment appears to be dependent on the nature of the rising plume. Figure 6 shows photographs of plumes generated in the scale model from both a wide and a narrow opening. Figure 6 shows that entrainment into the plume rising above the balcony can be considered in two distinct regions. The first region consists of entrainment into the 2-D region of the plume, rising above, and in line with the compartment opening. The second region is entrainment into both ends of the plume, which, based on visual observations, appeared to be more 3-D in nature, as the lateral extent of the plume increased with height above the balcony. It seems reasonable to expect that the rate of entrainment into the ends of the plume is greater than in the 2-D region of the plume. Figure 6 shows that the majority of the plume from

the wide opening consists of the 2-D region, with entrainment into the ends of the plume being less significant in the overall entrainment process. However, for the narrow opening, entrainment into the ends of the plume is more significant in the overall entrainment process. Therefore, it seems reasonable that narrow plumes entrain air at a greater rate with respect to height compared to wide plumes.

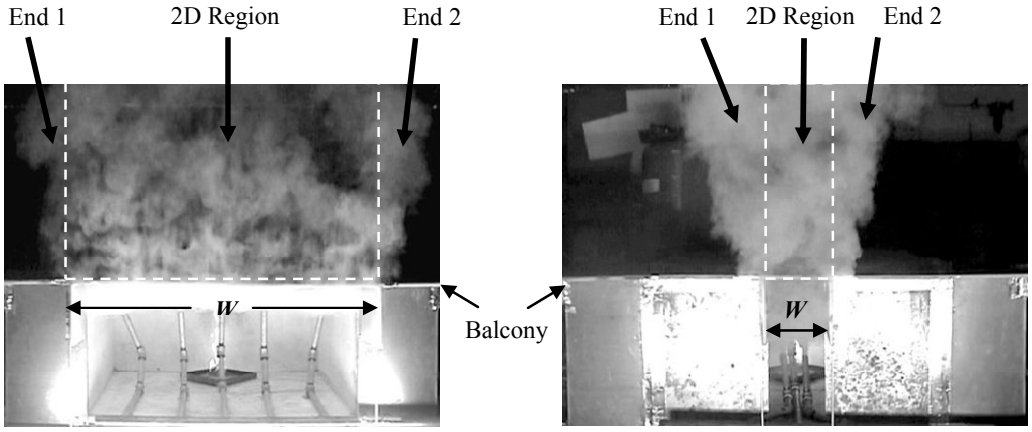

a) plume from a opening with $W = 1.0$ m b) plume from a opening with $W = 0.2$ m

Fig. 6. Photographs of the plume behaviour.

Figure 7 shows a plot of the experimental data according to Poreh et al [4] as given by Equation 2. Figure 7 shows that the general data set does not conveniently pass through the origin (as seen in Figure 3 for the 2-D plume) when an adjustment is made to the height of rise of the plume (assuming $z_o = d_b$).

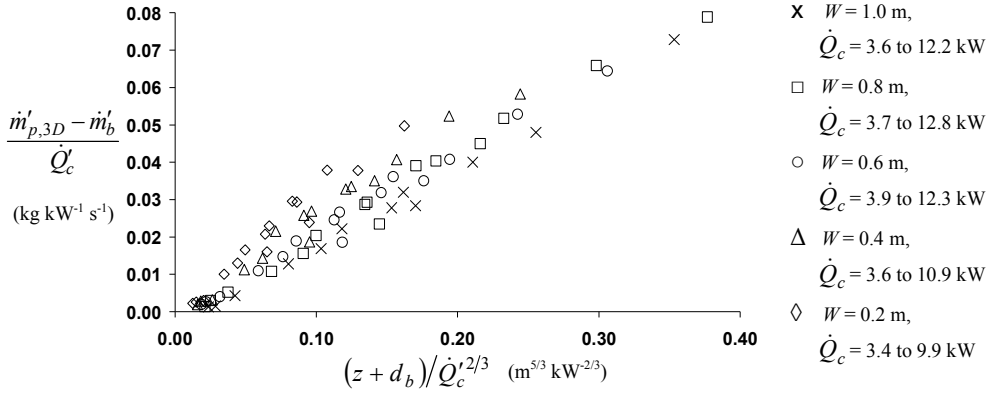

Fig. 7. Comparison of mass flow rates with respect to height of rise according to Poreh et al [5]

Figure 7 indicates that any line of best fit through each data set, for each value of W, would give rise to a negative intercept on the vertical axis. This negative intercept infers negative entrainment in the turning region, which is implausible. It appears that for the 3-D plume, the additional entrainment into the ends of the plume, gives rise to a different location of virtual origin (based on data obtained above the balcony) to that assumed in Equation 2. The location of this virtual origin is likely to be dependent on W as the contribution of the end entrainment changes. The use of Equation 2, which was developed for a 2-D plume, may not be appropriate for a 3-D plume, when encompassing the additional end entrainment into a 'lumped' entrainment coefficient for the entire plume above the balcony. Therefore, the Poreh et al method will not be considered further in this paper for the 3-D plume. The Thomas et al method [4], given by Equation 1, will be used in the analysis of the 3-D plume, as it does not make the fundamental assumption of a virtual origin. If the entrainment into the flow below the balcony is first considered, the values of the relevant regression coefficients β and γ, from previous work (as given in Equations 7 and 8), are dissimilar to those given by Equation 5 (i.e. $\beta = 1.34$ and $\gamma = 0$). However, as the values of β and γ given in Equations

7 and 8 were determined from data mainly obtained above the balcony, it is possible that, in the previous work, the additional entrainment into the ends of the plume (above the balcony) has been taken into account by modifying β and γ (as well as α) when linear regression is performed. It seems reasonable to assume that Equation 5 is appropriate to describe entrainment of air below the balcony for the 3-D plume, as, in the analysis, this entrainment was decoupled from the entrainment of air above the balcony. Because of this, the entrainment of air above the balcony has been treated separately in the analysis. To decouple the entrainment of air above the balcony, the measured mass flow rates were modified by subtracting the mass flow rate in the plume at $z = 0$ for each W and $\dot{Q}_t$ (and hence, $\dot{Q}_c$) examined. Thus, for each W, the data set passes through the origin, with the slope of each line representing the regression coefficient, α. Linear regression was performed to determine α with respect to W and $\dot{Q}_t$. Figure 8 shows the results of the linear regression with values of α (and associated standard errors) plotted with respect to W. The fixed value of α for the 2-D plume (i.e. 0.16 from Equation 6) is also shown.

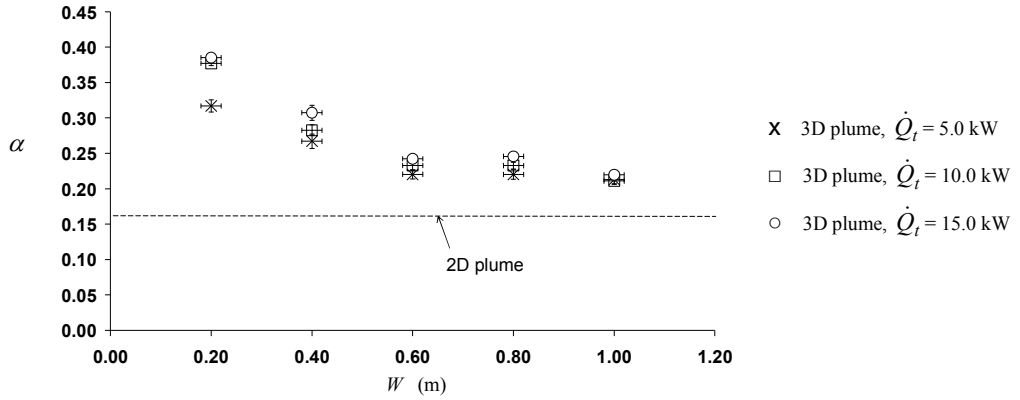

Fig. 8. Plot of α versus W, describing the rate of entrainment into the plume above the balcony edge

Figure 8 shows that when W = 1.0 m, α ≈ 0.21, which is slightly higher than α for the 2-D plume due to the additional end entrainment. As W decreases, α generally increases, with a maximum value of ≈ 0.38. The difference in α between the 3-D and 2-D plumes is representative of the amount of entrainment into the ends of the plume. Figure 8 shows that as W decreases, the contribution of end entrainment in the overall entrainment process increases, thus increasing the value of α, which is consistent with the analysis described above. For W = 1.0 m, Figure 8 shows that α appears to be independent of $\dot{Q}_t$. However, as W decreases, the value of α appears to become somewhat dependent on $\dot{Q}_t$. This is contrary to that observed for the 2-D plume. A possible reason for this may be due to the variation in d_b with respect changes in W and $\dot{Q}_t$. For wide openings, d_b was reasonably insensitive to changes in $\dot{Q}_t$, however, for narrow openings, the observed d_b was more sensitive to changes in $\dot{Q}_t$. It is possible that the amount of end entrainment is directly proportional d_b (also postulated by Thomas et al [4]). A deep layer rotating at the balcony edge will give rise to a plume which rises with broader ends compared to a shallow layer, thus entraining more air. Figure 9 shows a plot of (α_{3D}- α_{2D}) versus (W/d_b) to express the contribution of entrainment into the ends of the plume and to take into account the effect of d_b. Figure 9 shows that the data shown in Figure 8 now collapse to the relationship given by Equation 9.

$$(\alpha_{3D} - \alpha_{2D}) = 0.246\left(\frac{W}{d_b}\right)^{-0.687} \tag{9}$$

The standard errors of the regression coefficients 0.246 and -0.687 are 0.020 and 0.048 respectively. Therefore, for design purposes it seems reasonable and convenient to express Equation 9 by Equation 10.

$$(\alpha_{3D} - \alpha_{2D}) = 0.25\left(\frac{W}{d_b}\right)^{-2/3} \tag{10}$$

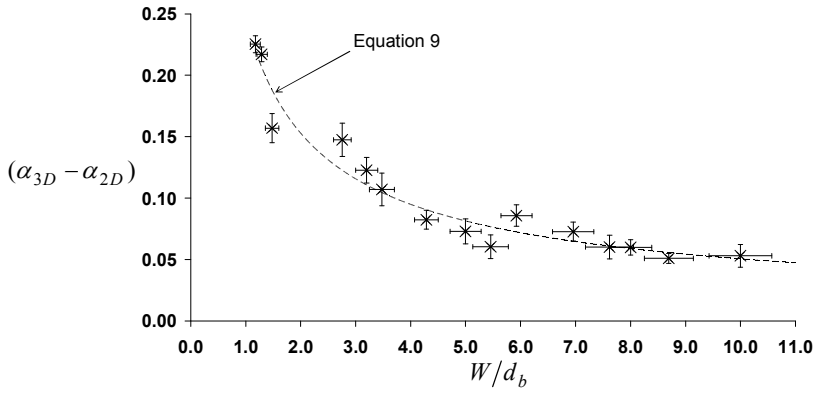

Fig. 9. Plot of (α_{3D}- α_{2D}) versus (W / d_b)

It appears that it is not appropriate to assign a universal value of α to represent the total amount of entrainment above the balcony due to the varying contribution of end entrainment. Therefore, to develop a general simplified design formula for the 3-D plume, an empirical formula was determined to explicitly describe the mass flow rate of gases into the ends of the plume above the balcony, which can be described by Equation 11.

$$\frac{\dot{m}'_{p,3D} - \dot{m}'_{p,2D}}{\dot{Q}'_c} = \frac{\dot{m}'_{ends}}{\dot{Q}'_c} = (\alpha_{3D} - \alpha_{2D})\frac{z}{\dot{Q}'^{2/3}_c} \quad \text{or} \quad \dot{m}_{ends} = (\alpha_{3D} - \alpha_{2D})\dot{Q}_c^{1/3} W^{2/3} z \tag{11}$$

If Equation 10 is substituted into Equation 11, this gives an explicit term to describe the mass flow rate of gases into the ends of the plume (Equation 12), which suggests that the amount of end entrainment is proportional to d_b.

$$\dot{m}_{ends} = 0.25\dot{Q}_c^{1/3} d_b^{2/3} z \tag{12}$$

Equation 12 was determined from data which exhibited linearity. It is expected that at higher heights of rise of plume, the effect of end entrainment will cause the plume to be more axisymmetric in nature and linearity will no longer apply. As Equation 12 is empirical in nature, the limit given by Equation 13 applies for its use.

$$\frac{z}{W} \leq 5 \tag{13}$$

A simplified design formula for the 3-D plume can now be deduced by simply appending Equation 12 to the design formula for the 2-D plume (given by Equation 6). Equation 14 describes the sum of entrainment of air into the flow below the balcony, entrainment into the 2-D region of plume above the balcony and entrainment into the ends of the plume above the balcony. Equation 14 applies to a flow which is channelled by screens beneath the balcony, with the limit given by Equation 13. The overall uncertainty in the use of Equation 14, will be dependent on the nature of the plume and hence, the relative contribution of each term and the associated standard error of each regression coefficient.

$$\begin{aligned} \dot{m}_{p,3D} &= 0.16\dot{Q}_c^{1/3} W^{2/3} z + 1.34\dot{m}_b + 0.25\dot{Q}_c^{1/3} d_b^{2/3} z \\ \Rightarrow \dot{m}_{p,3D} &= 0.16\dot{Q}_c^{1/3}(W^{2/3} + 1.56 d_b^{2/3}) z + 1.34\dot{m}_b \end{aligned} \tag{14}$$

This work suggests that entrainment of air into a 3-D balcony spill plume is dependent on the characteristics of the layer flow below the balcony edge and may explain differences between measured entrainment from previous studies. The Harrison and Spearpoint [1] data was determined from a flow with W = 0.6 m, whereas the Hansell et al [14] data was determined from flow which was narrower with $W \approx 0.43$ m. Thus, it appears that currently available simplified formulae for the 3-D plume, based on these data [given in references 1-3], apply specifically to the range of conditions studied in these experiments and do not apply generally for a wide range of W. Following the analysis of this work, it is not surprising that value of α obtained from Hansell et al [14] is greater than that obtained from Harrison and Spearpoint [1], as the plumes were generated from a narrower opening. This may explain the differences in entrainment between these previous studies and the use of Equation 14 may be appropriate to reconcile these differences. Therefore, Equation 14 was applied to the data from these previous studies, using the measured data for the layer flow below the balcony edge as the input. Figure 10 shows that Equation 14 provides a good prediction of the Harrison and Spearpoint experimental results. Equation 14 also provides a reasonably good prediction of the Hansell et al data for smaller values of mass flow rate, obtained at low heights of rise. However, for larger values obtained at higher height of rise, there is divergence between the experimental results and the prediction, with a general trend to under predict the experimental results. However, the experimental boundary conditions in the Hansell et al work were such that the nature of the plume was different to the unbounded plumes generated in this work and by Harrison and Spearpoint [1]. The plumes generated by Hansell et al were obtained from a model which had four asymmetric openings for inlet air, with the resulting plume having a tendency to become more axisymmetric in nature due to the observed swirling of rising plume in the smoke reservoir [5,14]. Therefore, due to the different nature of the plume, it is possible that the Hansell et al can be considered to be anomalously high (particularly for larger heights of rise of plume) compared to the data obtained from the unbounded spill plumes in this work and by Harrison and Spearpoint [1]. Therefore, it appears that Equation 14 goes some way to reconcile the differences in entrainment between previous work and can be applied more generally compared to currently available simplified design formulae.

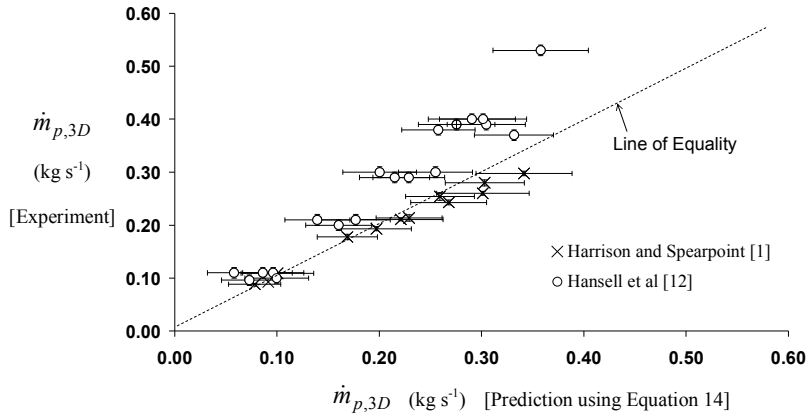

Fig.10. Comparison of experiment and prediction of $\dot{m}_{p,3D}$ (using Equation 14) from previous studies

CONCLUSIONS

This work has provided new experimental data to systematically characterise entrainment of air into a balcony spill plume generated from a flow which is channelled by screens beneath the balcony. This work has demonstrated that existing simplified design formulae, for the 2-D balcony spill plume, apply generally for plumes generated from a range of fire compartment geometries. A further simplified design formula is presented for the 2-D plume. The rate of entrainment into a 3-D balcony spill plume appears to be specifically dependent on the characteristics of the layer flow below the balcony edge. 3-D plumes generated from narrow openings entrain air at a greater rate with respect to height compared to those generated from wider openings. The rate of entrainment appears to be dependent on the contribution of the end entrainment in the overall entrainment process. A simplified design formula is proposed for the 3-D plume, by developing a general empirical expression to explicitly describe the entrainment of air into the

ends of the plume. This simplified formula can be applied more generally compared to currently available formulae for the 3-D plume. This work goes some way to explain and reconcile differences in entrainment reported between previous studies and provides improved guidance to designers of smoke management systems.

ACKNOWLEDGEMENTS

The authors would like to thank the following: Education New Zealand, for awarding the lead author a New Zealand International Doctoral Research Scholarship. The National Fire Protection Association for awarding the lead author the David B. Gratz Scholarship. Bob Wilsea-Smith and Grant Dunlop of the University of Canterbury, for their help with the design and construction of the experimental apparatus. The New Zealand Fire Service Commission for their continued support of the Fire Engineering programme at the University of Canterbury.

REFERENCES

[1] Harrison, R. and Spearpoint, M.J., "Entrainment of Air into a Balcony Spill Plume", Journal of Fire Protection Engineering, Vol. 16, No. 3, 2006, pp 211-245. doi:10.1177/1042391506057954

[2] NFPA 92B, "Smoke Management Systems in Malls, Atria and Large Areas," 2005 Edition, Publication No 92B, National Fire Protection Association, Quincy, MA, USA, 2005.

[3] Chartered Institution of Building Services Engineers, *CIBSE Guide Volume E: Fire Engineering*, London, CIBSE, 2003.

[4] Thomas, P.H., Morgan H.P. and Marshall N.R., "The Spill Plume in Smoke Control Design," Fire Safety Journal, Vol. 30, No. 1, 1998, pp 21-46. doi:10.1016/S0379-7112(97)00037-4

[5] Poreh, M., Morgan, H.P., Marshall N.R. and Harrison R., "Entranment by Two Dimensional Spill Plumes in Malls and Atria," Fire Safety Journal, Vol. 30, No. 1, 1998, pp 1-19. doi:10.1016/S0379-7112(97)00036-2

[6] Morgan, H.P., Ghosh, B.K., Garrad, G., Pamlitschka, R., De Smedt, J-C. and Schoonbaert, L.R., "Design Methodologies for Smoke and Heat Exhaust Ventilation," BRE Report 368, Building Research Establishment, Watford, UK, 1999.

[7] Kumar S., Thomas, P.H., and Cox G., "Revised BRE Method for Spill Plume Entrainment Analysis," *Proceedings of the Second International Conference Fire Bridge*, University of Ulster, May 2005.

[8] Thomas, P.H., Hinkley, P.L., Theobald, C.R. and Simms, D.L., "Investigations into the Flow of Hot Gases in Roof Venting," Fire Research Technical Paper No 7, London, The Stationary Office, 1963.

[9] Marshall, N.R., "The Behaviour of Hot Gases Flowing within a Staircase," Fire Safety Journal, Vol. 9, No 3, 1985, pp 245-255. doi:10.1016/0379-7112(85)90035-9

[10] Klote, J.H., and Milke, J.A., *Principles of Smoke Management,* Chapter 15, Physical Modeling, ASHRAE, Atlanta, GA, 2002.

[11] Zukoski, E.E., Kubota, T. and Cetegen, B., "Entrainment in Fire Plumes," Fire Safety Journal, Vol. 3, No.3, 1981, pp 107-121. doi:10.1016/0379-7112(81)90037-0

[12] Lee, S.L., and Emmons, H.W., "A Study of Natural Convection above a Line Fire," Journal of Fluid Mechanics, Vol. 11, No 3, pp 353-368, 1961. doi:10.1017/S0022112061000573

[13] Marshall, N.R. and Harrison, R., "Experimental Studies of Thermal Spill Plumes", Building Research Establishment Occasional Paper, OP1, 1996.

[14] Hansell, G.O., Morgan, H.P. and Marshall, N.R., "Smoke Flow Experiments in a Model Atrium," BRE Occasional Paper OP55, Building Research Establishment, Watford, UK, 1993.

Appendix G: Temperature profiles in the smoke collecting hood for the series of balcony spill plume experiments

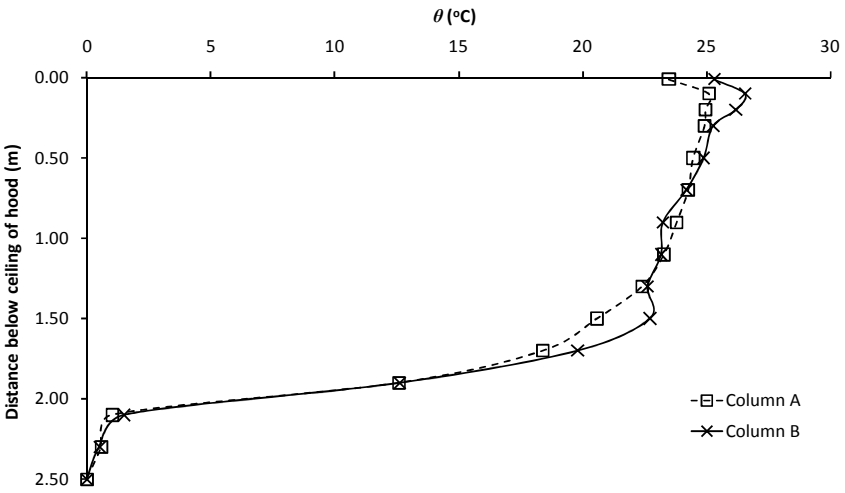

Figure G1: Experiment E1

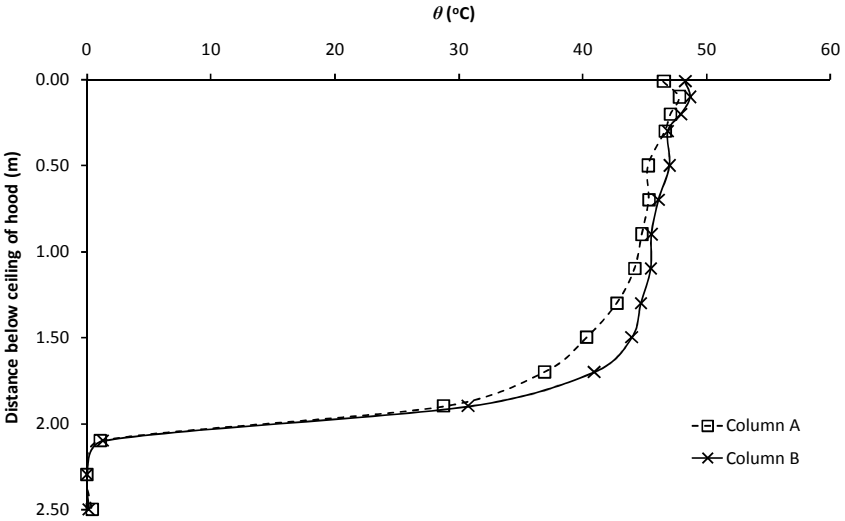

Figure G2: Experiment E2

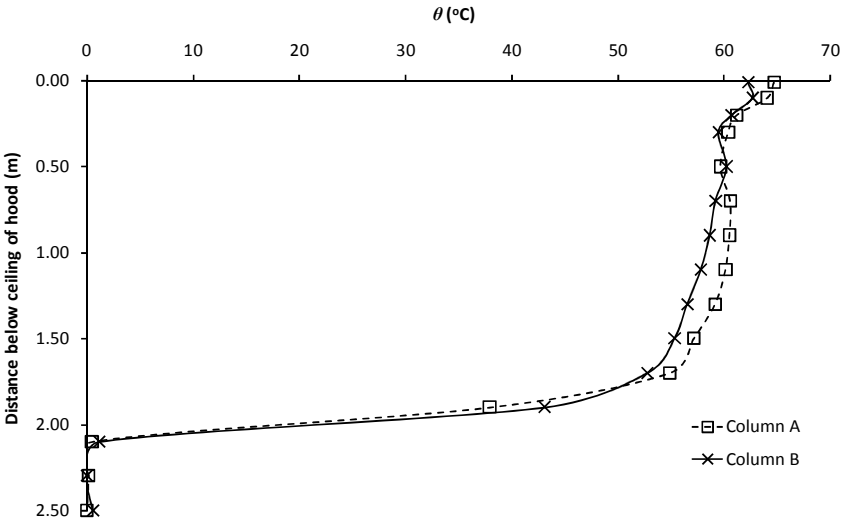

Figure G3: Experiment E3

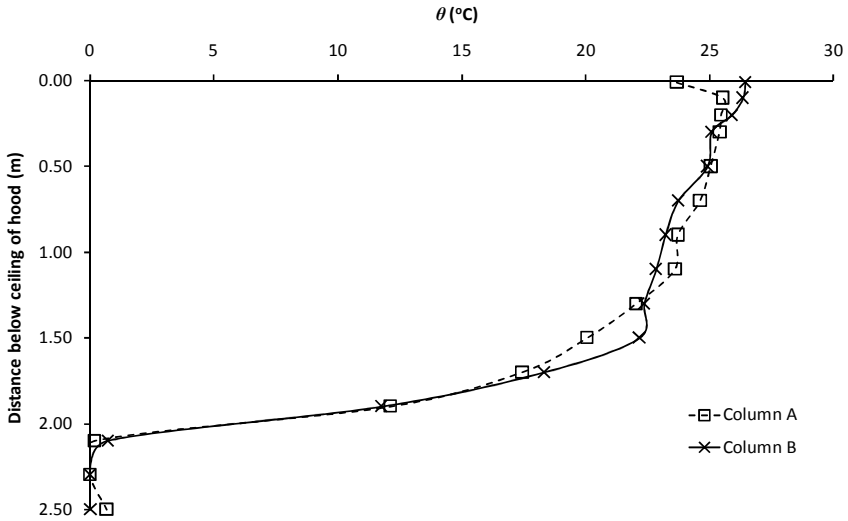

Figure G4: Experiment E4

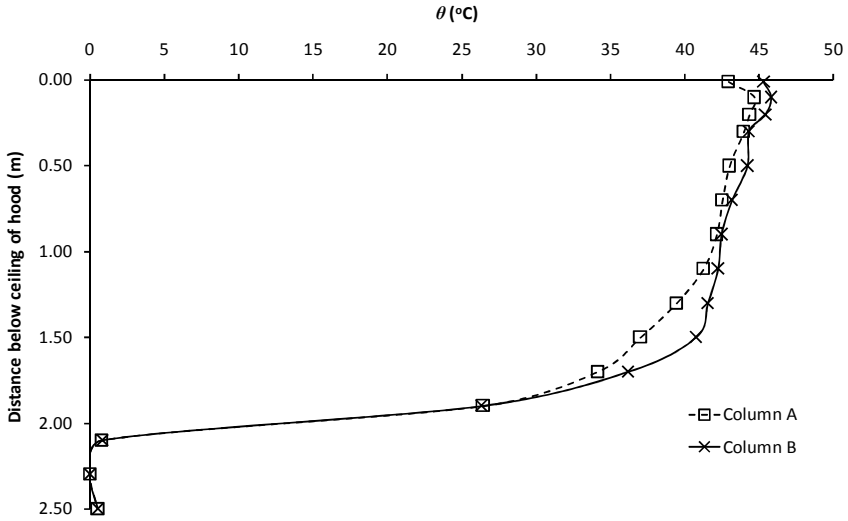

Figure G5: Experiment E5

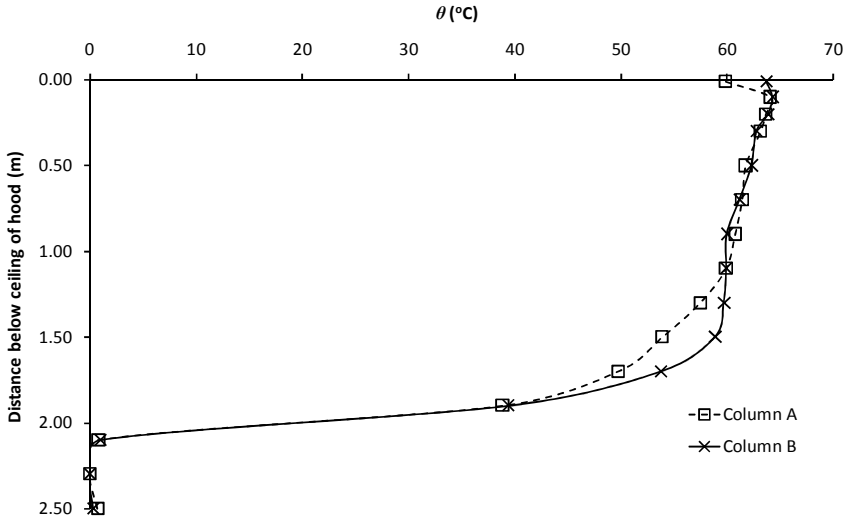

Figure G6: Experiment E6

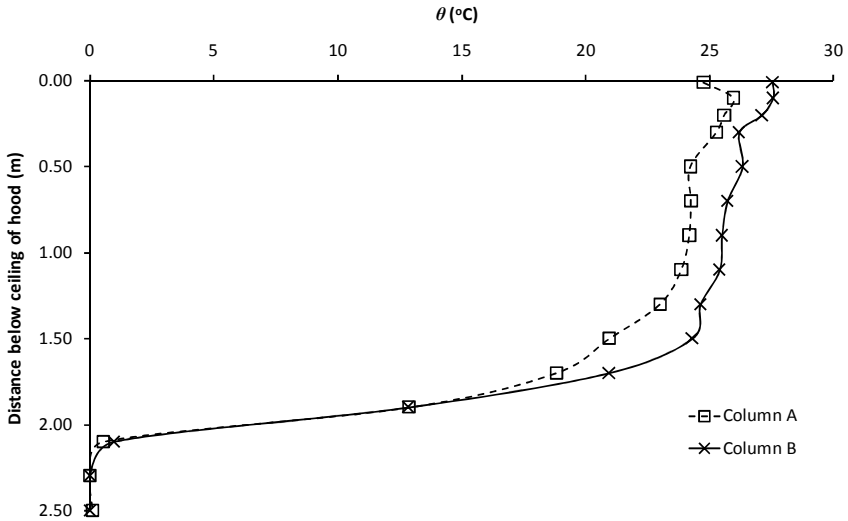

Figure G7: Experiment E7

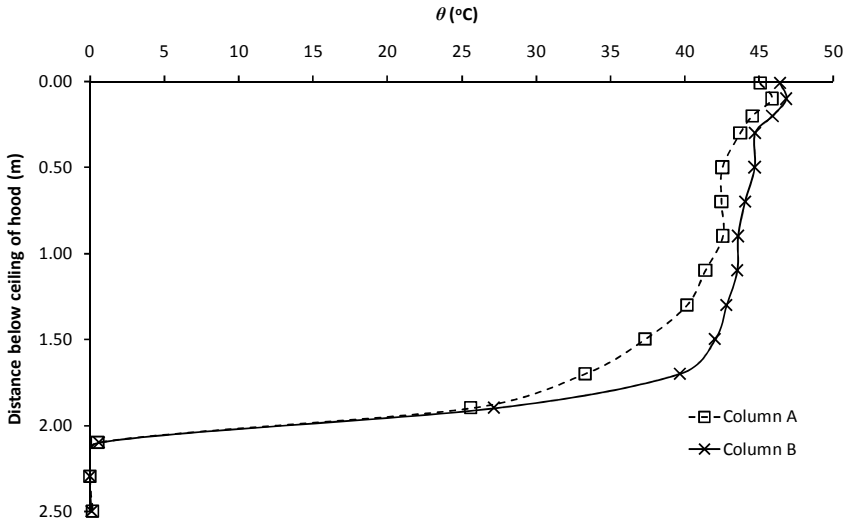

Figure G8: Experiment E8

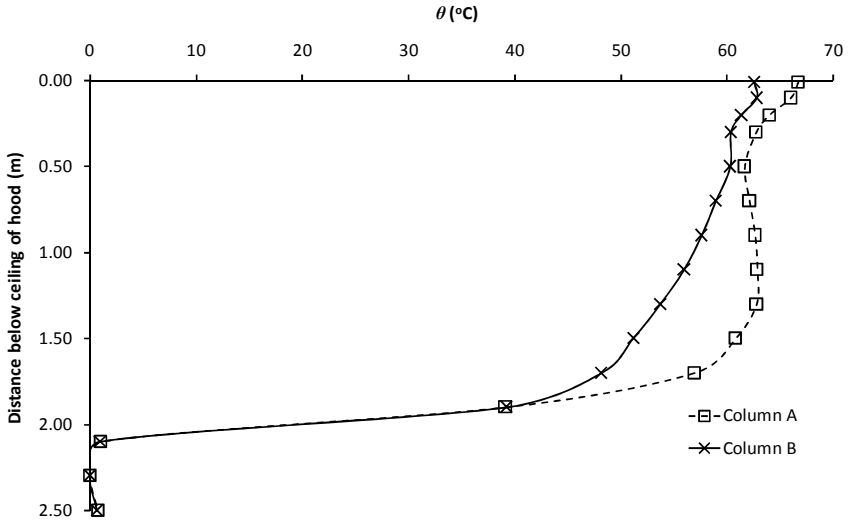

Figure G9: Experiment E9

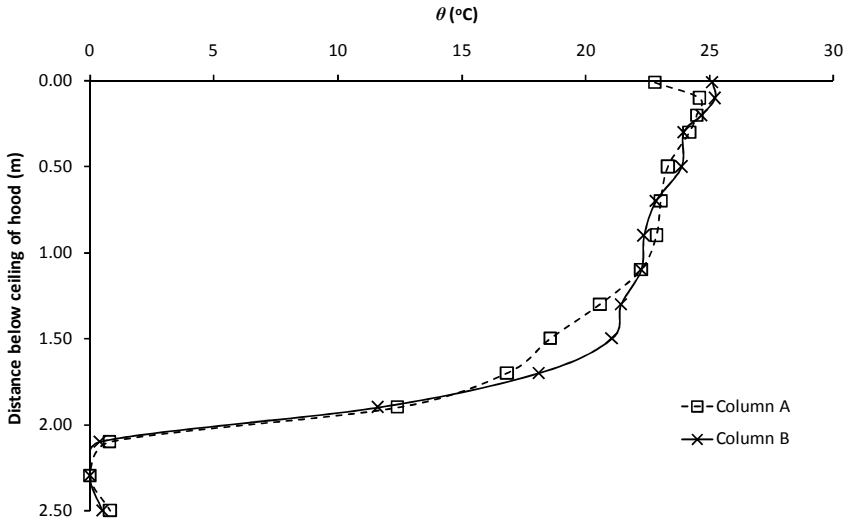

Figure G10: Experiment E10

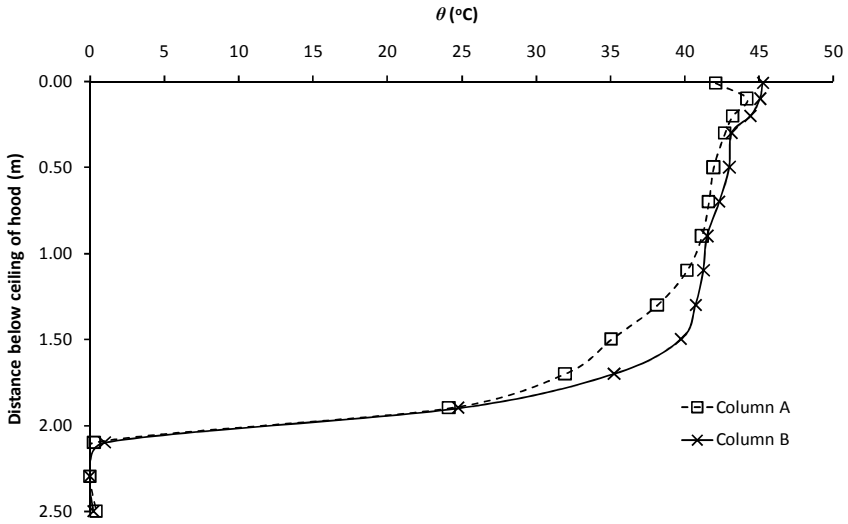

Figure G11: Experiment E11

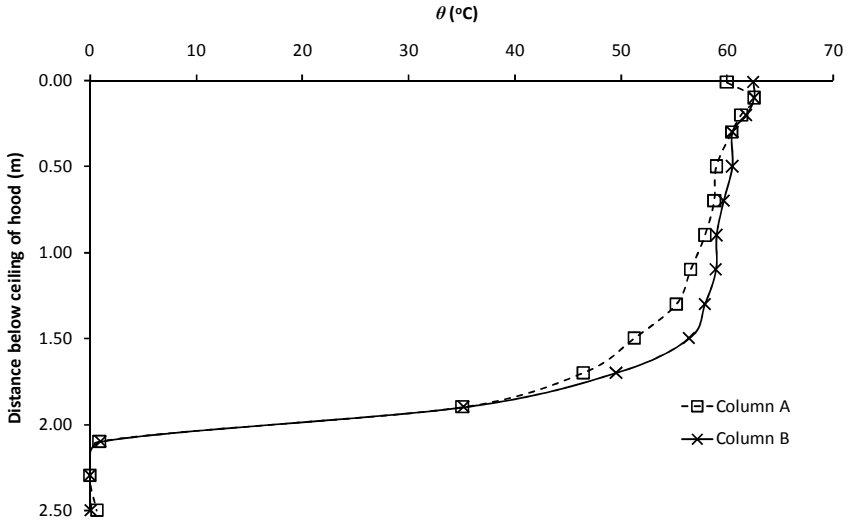

Figure G12: Experiment E12

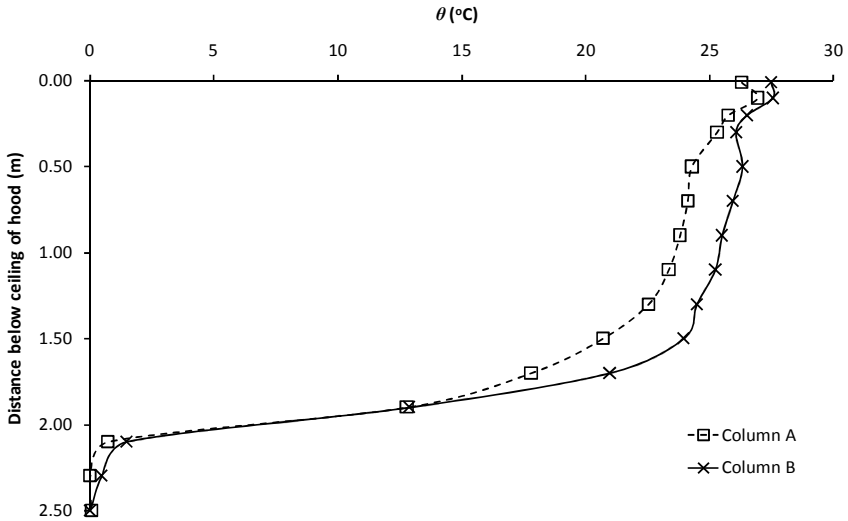

Figure G13: Experiment E13

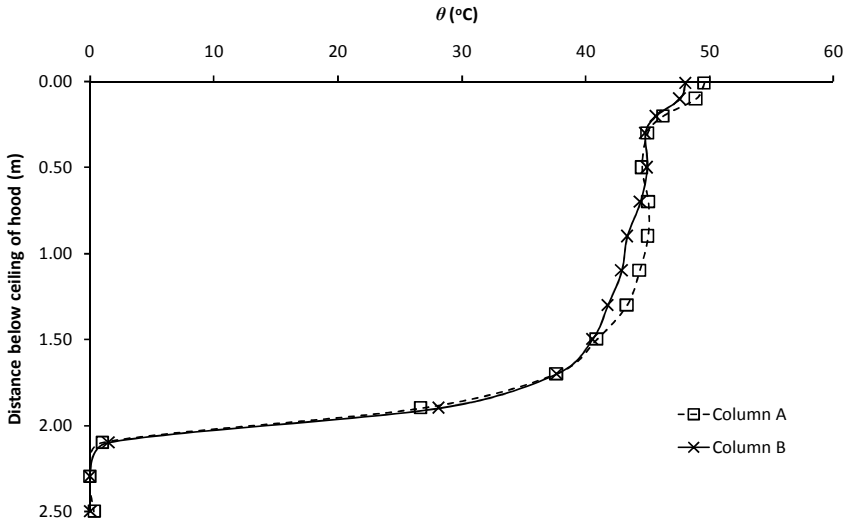

Figure G14: Experiment E14

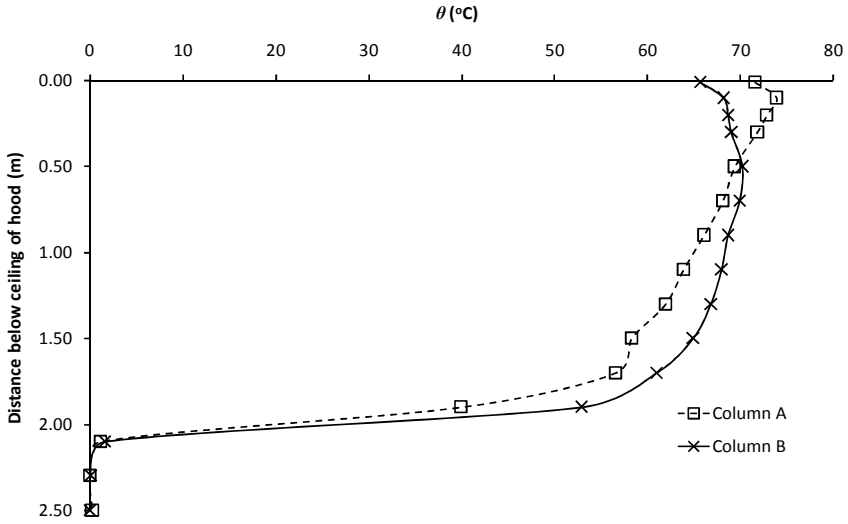

Figure G15: Experiment E15

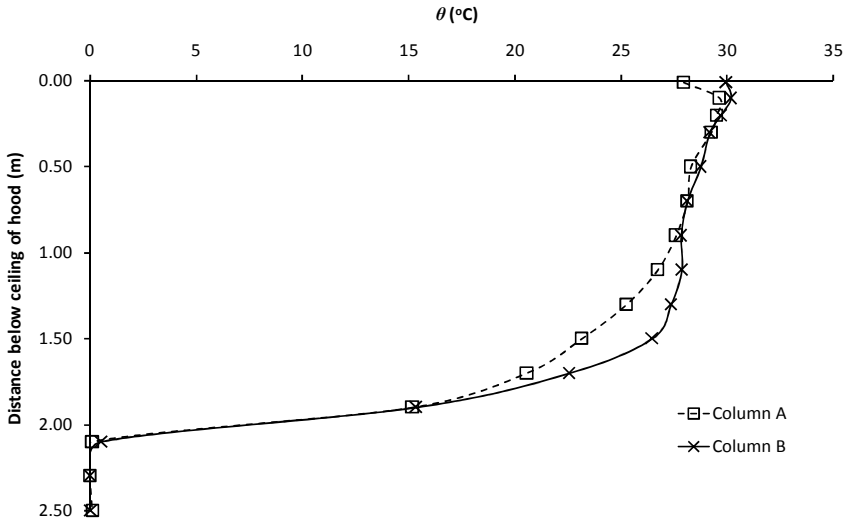

Figure G16: Experiment E16

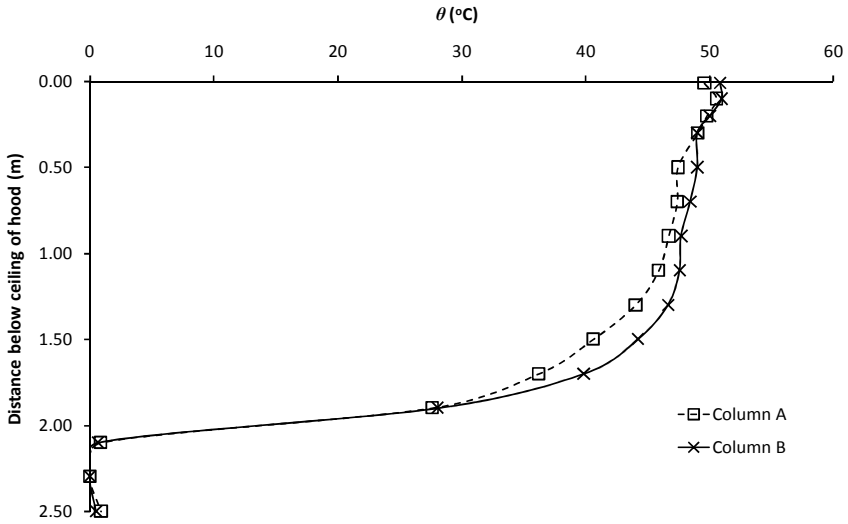

Figure G17: Experiment E17

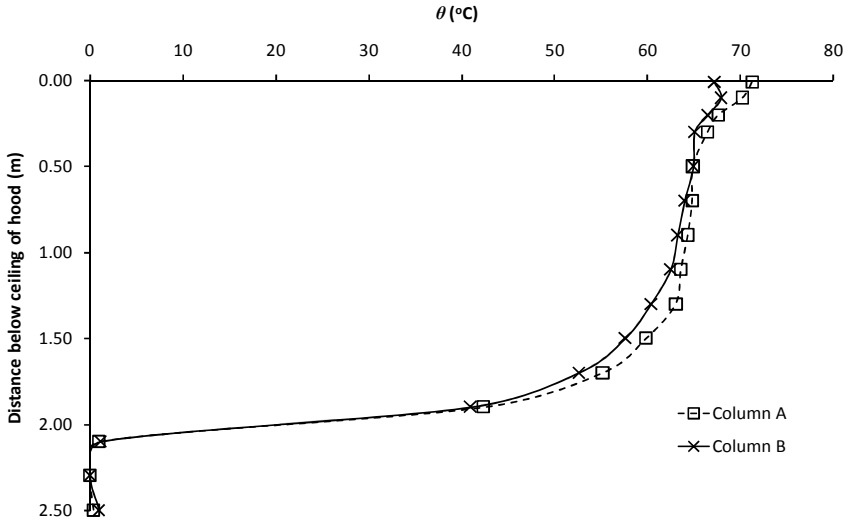

Figure G18: Experiment E18

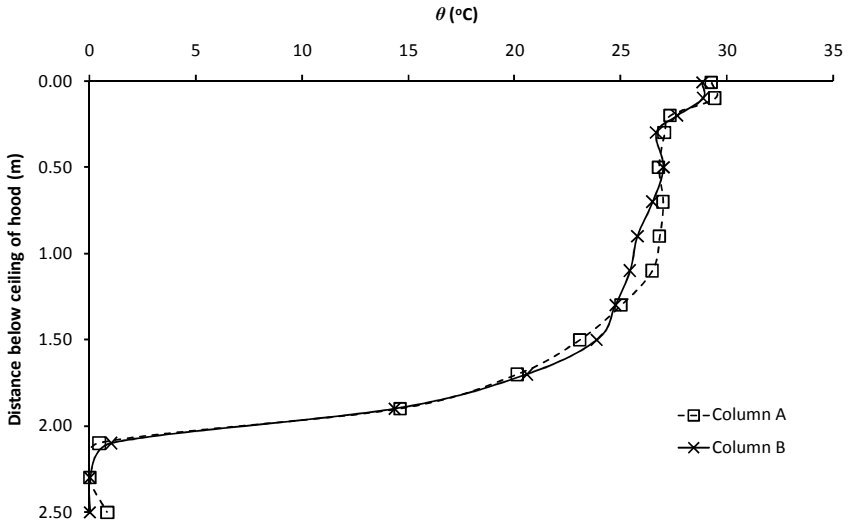

Figure G19: Experiment E19

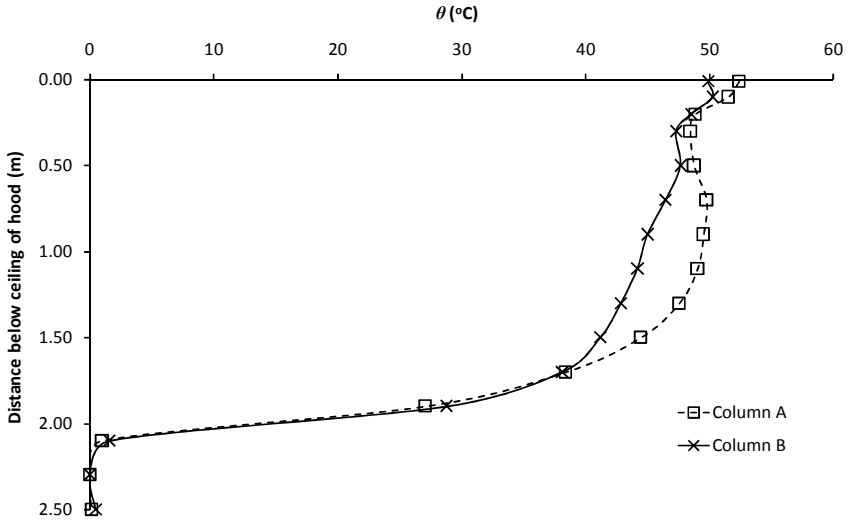

Figure G20: Experiment E21

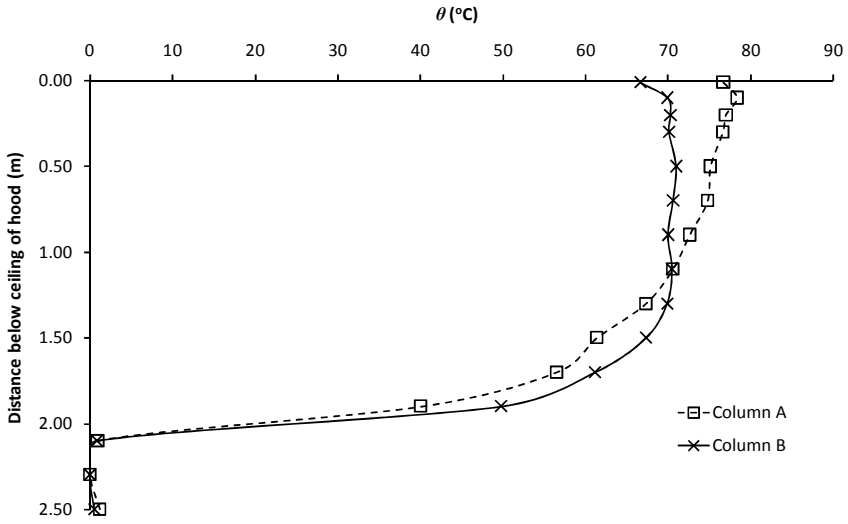

Figure G21: Experiment E21

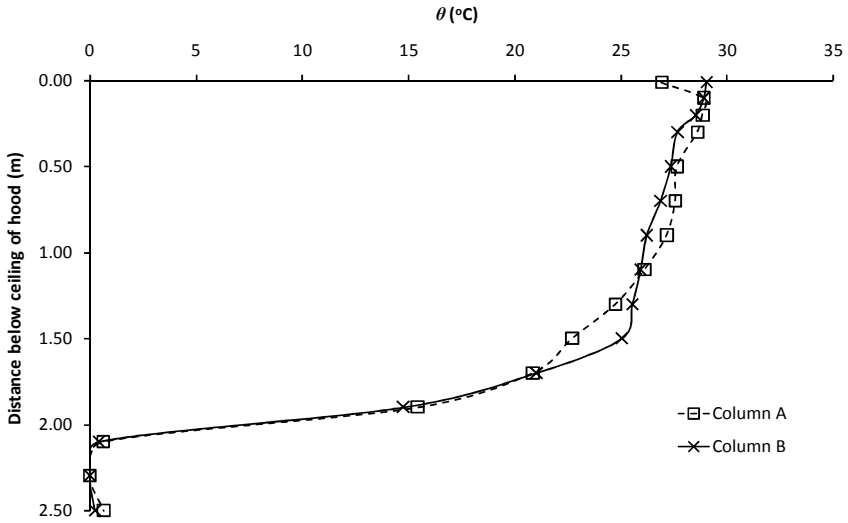

Figure G22: Experiment E22

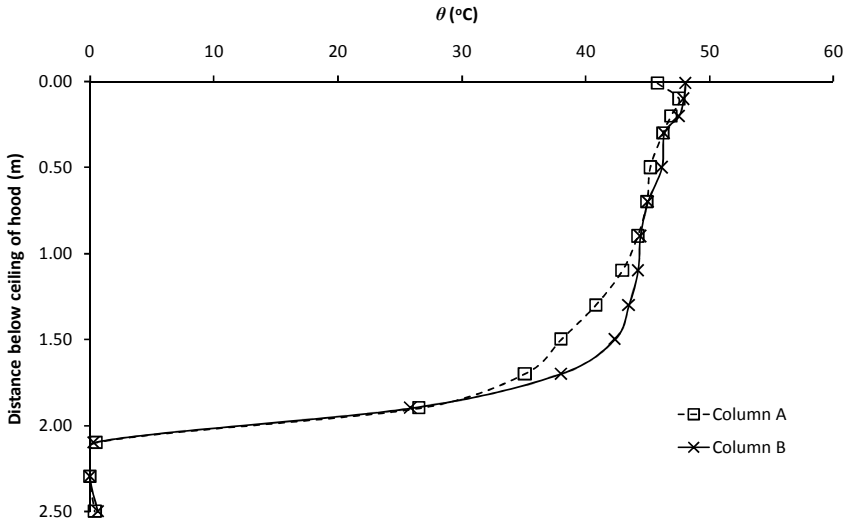

Figure G23: Experiment E23

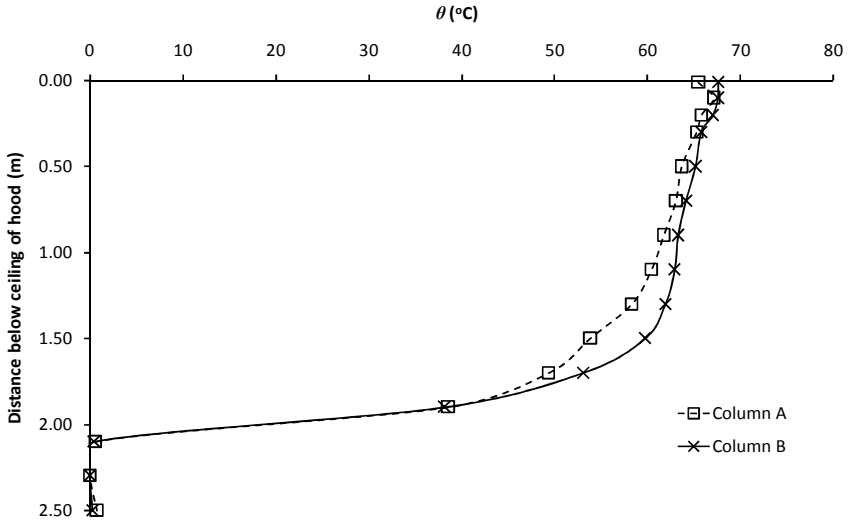

Figure G24: Experiment E24

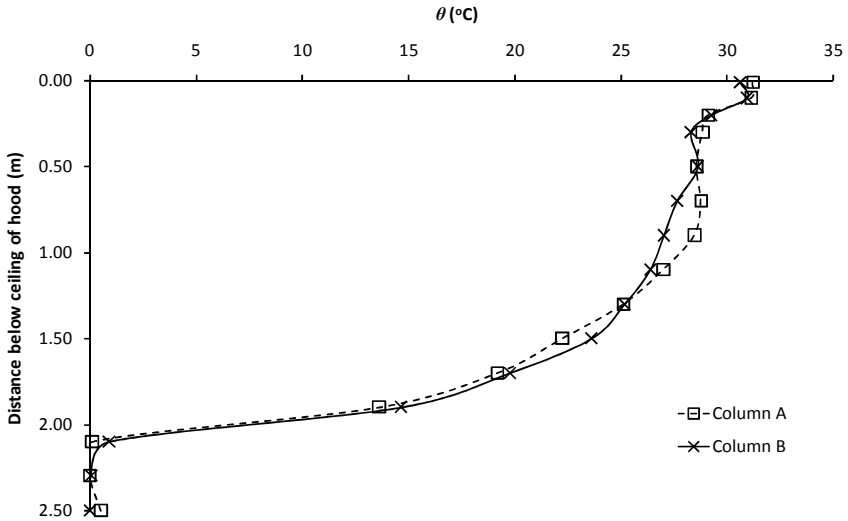

Figure G25: Experiment E25

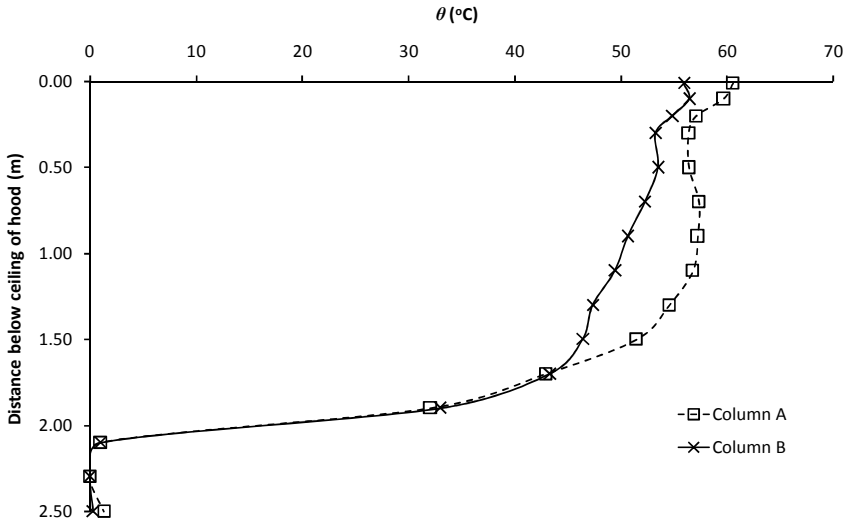

Figure G26: Experiment E26

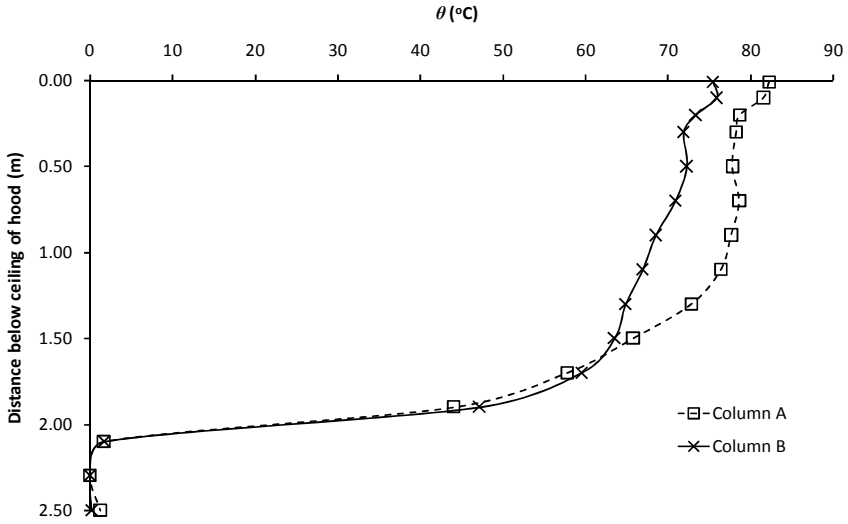

Figure G27: Experiment E27

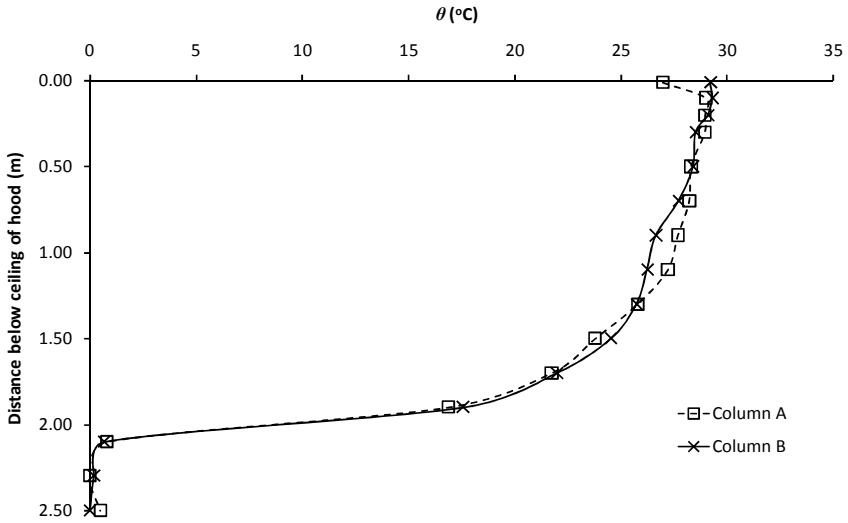

Figure G28: Experiment E28

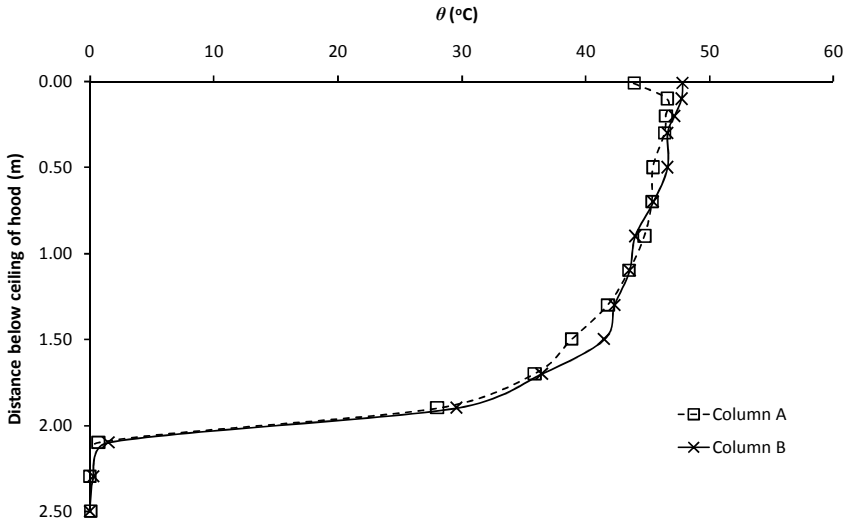

Figure G29: Experiment E29

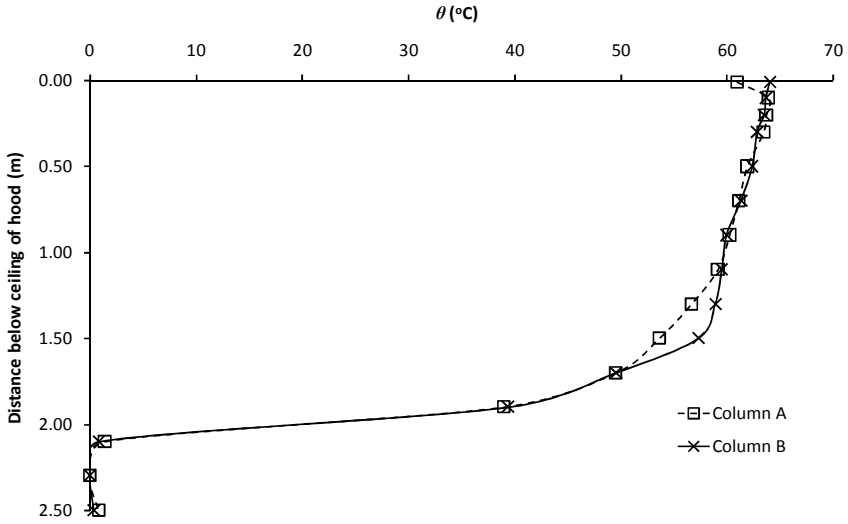

Figure G30: Experiment E30

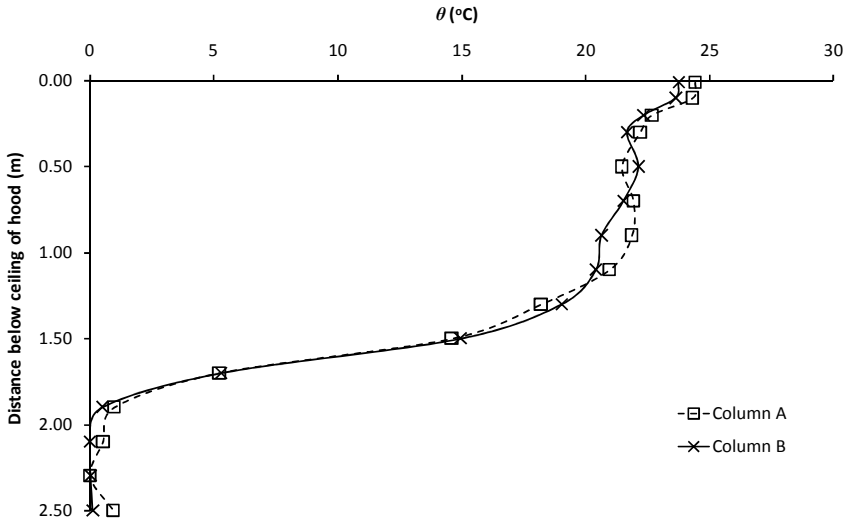

Figure G31: Experiment E61

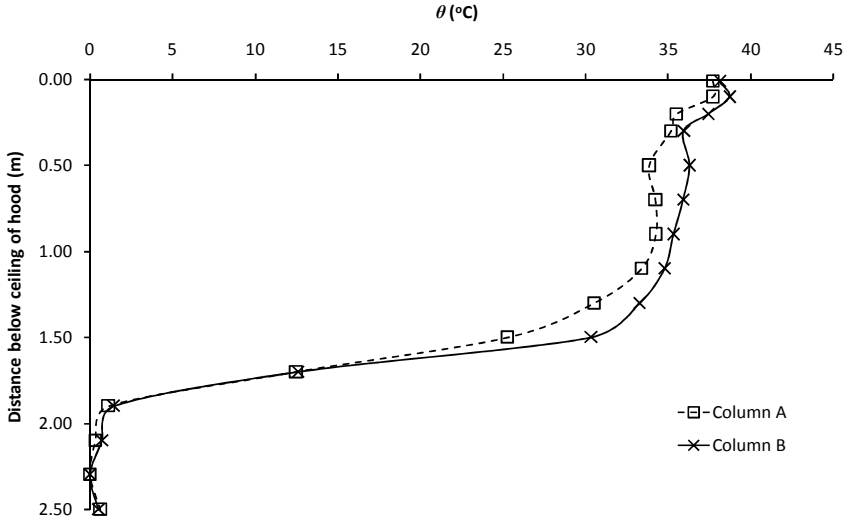

Figure G32: Experiment E62

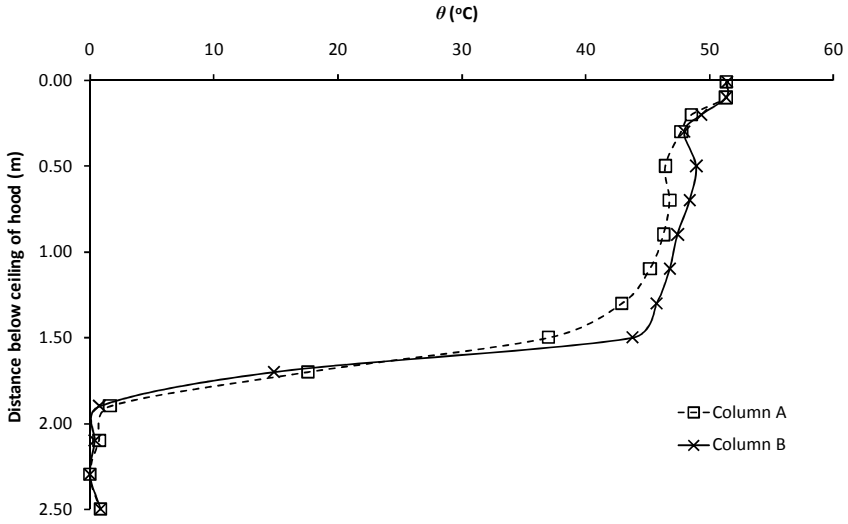

Figure G33: Experiment E63

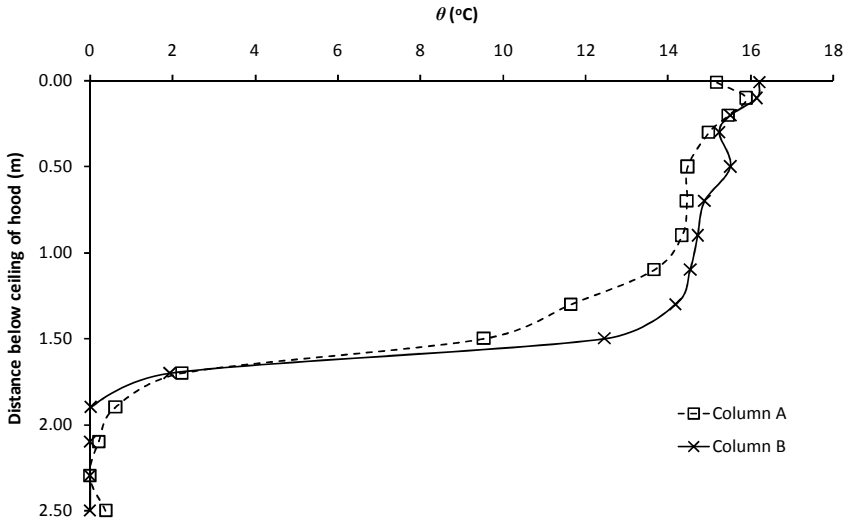

Figure G34: Experiment E64

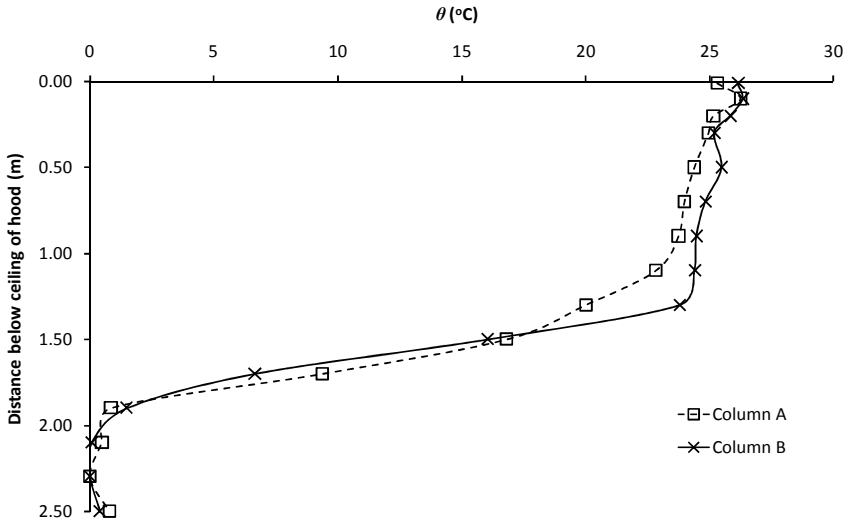

Figure G35: Experiment E65

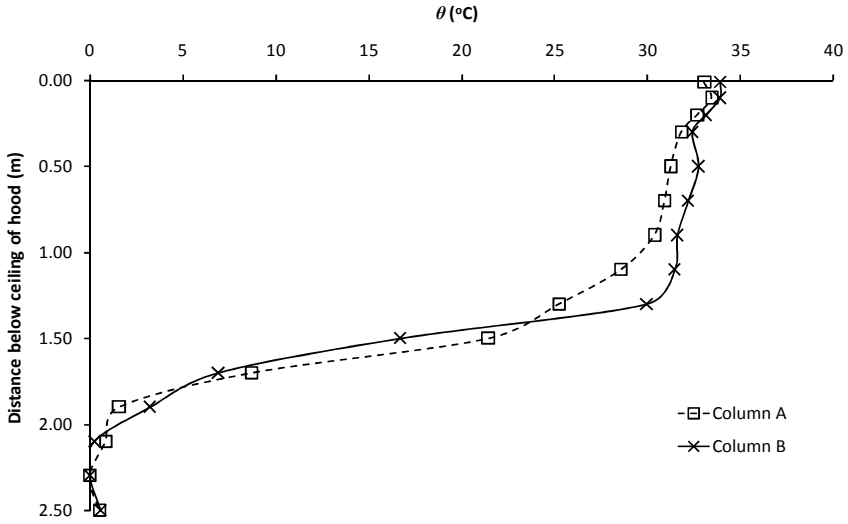

Figure G36: Experiment E66

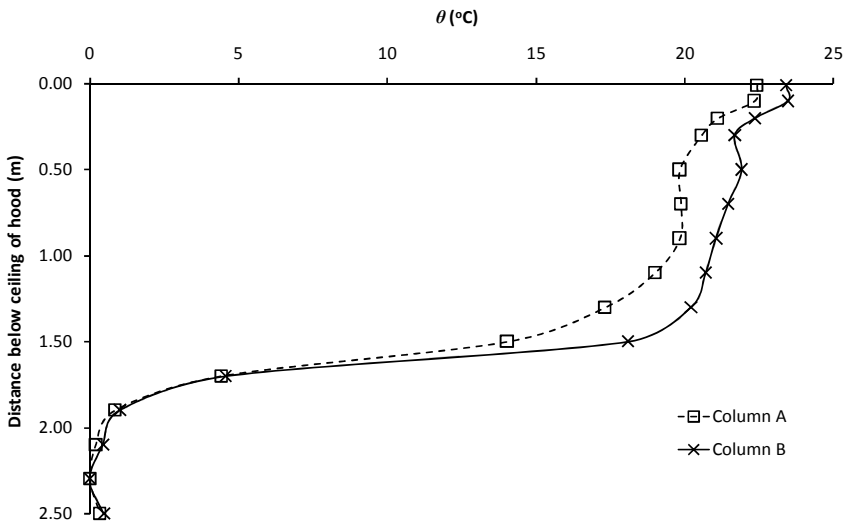

Figure G37: Experiment E67

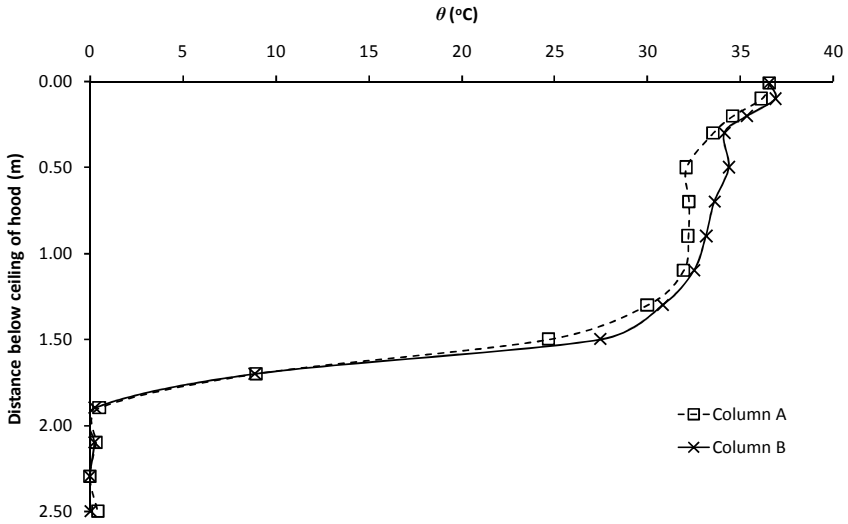

Figure G38: Experiment E68

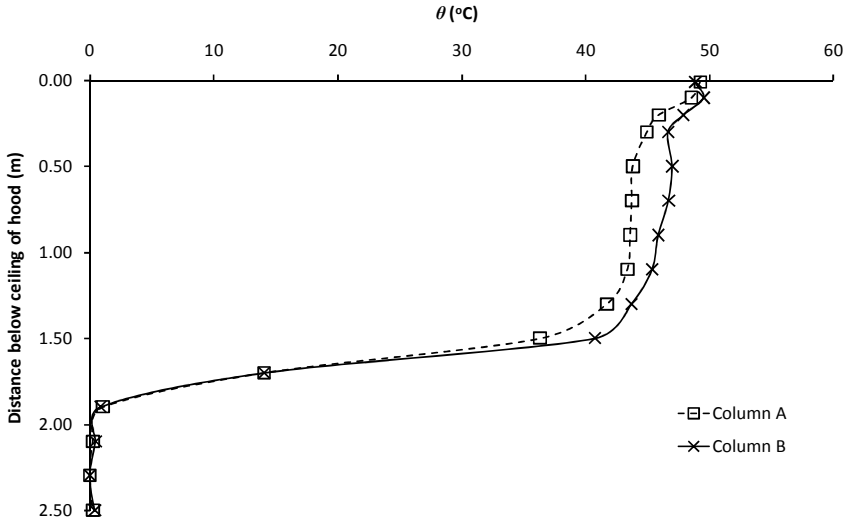

Figure G39: Experiment E69

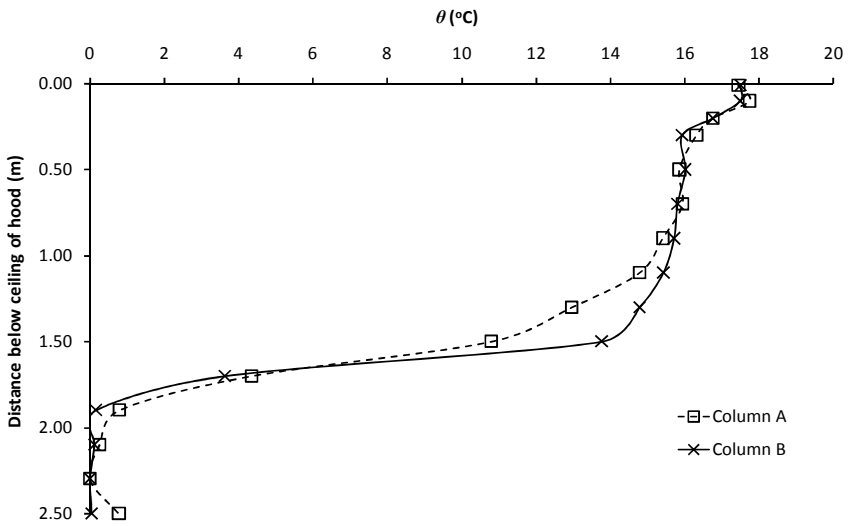

Figure G40: Experiment E70

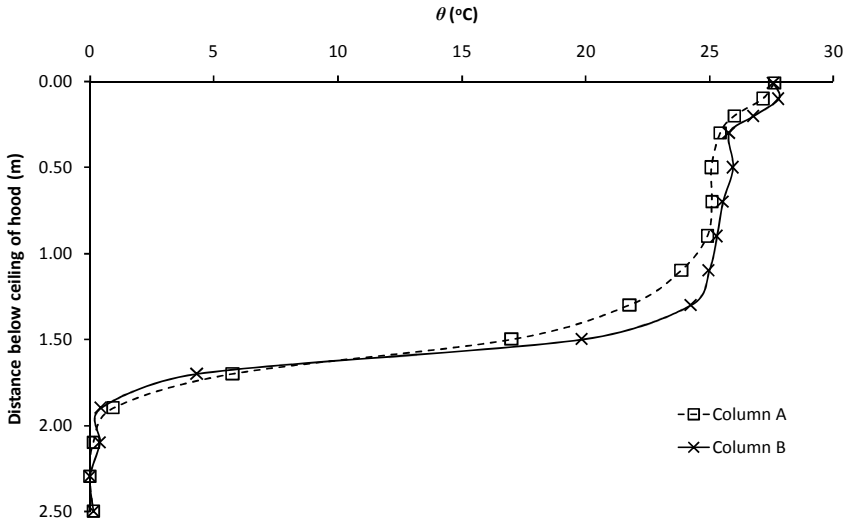

Figure G41: Experiment E71

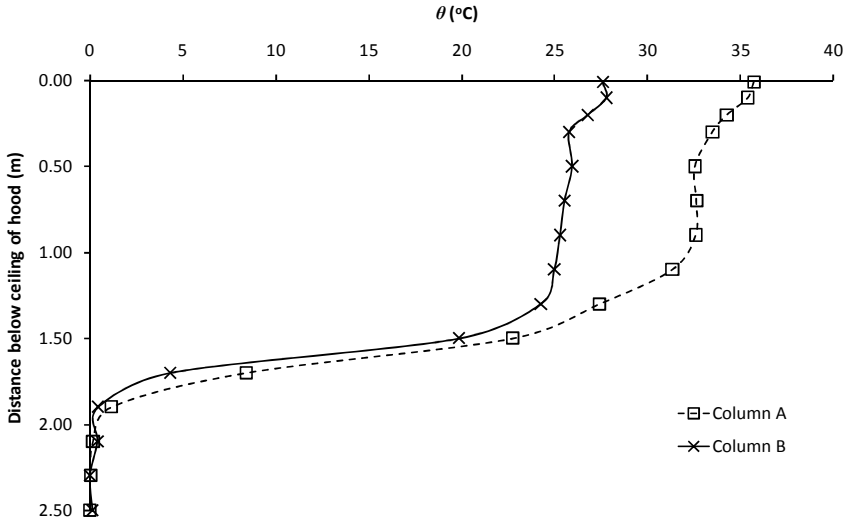

Figure G42: Experiment E72

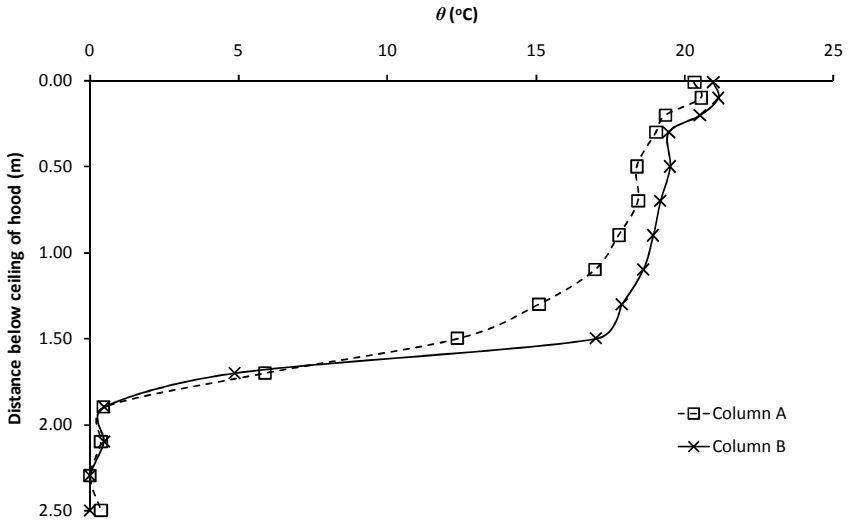

Figure G43: Experiment E73

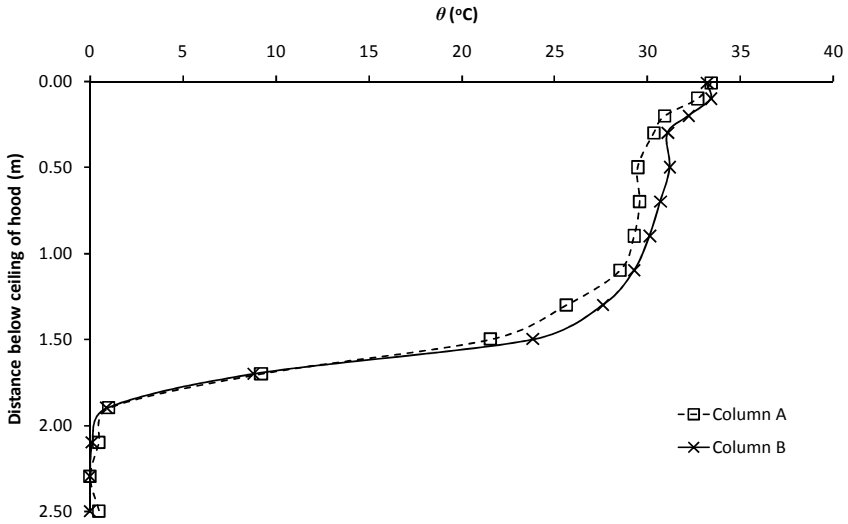

Figure G44: Experiment E74

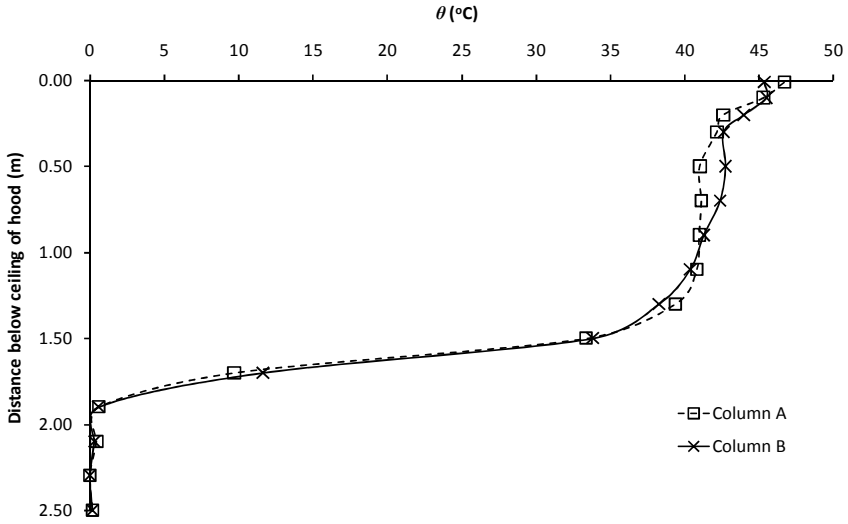

Figure G45: Experiment E75

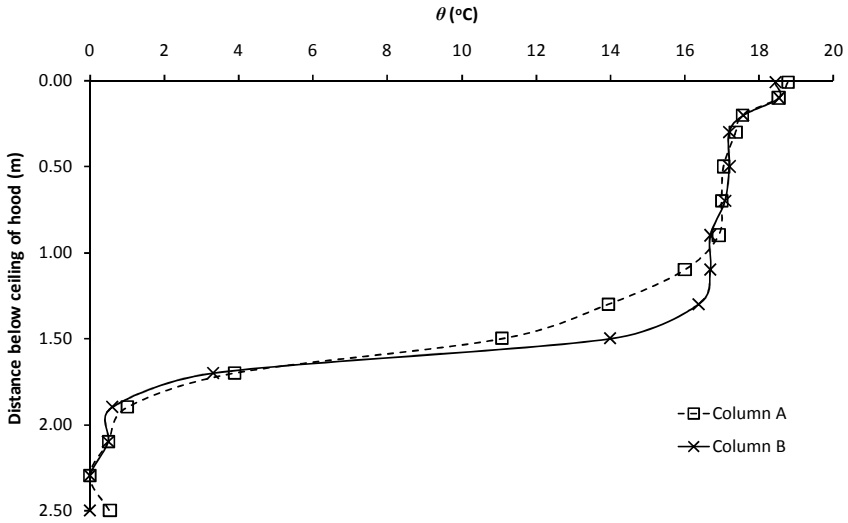

Figure G46: Experiment E76

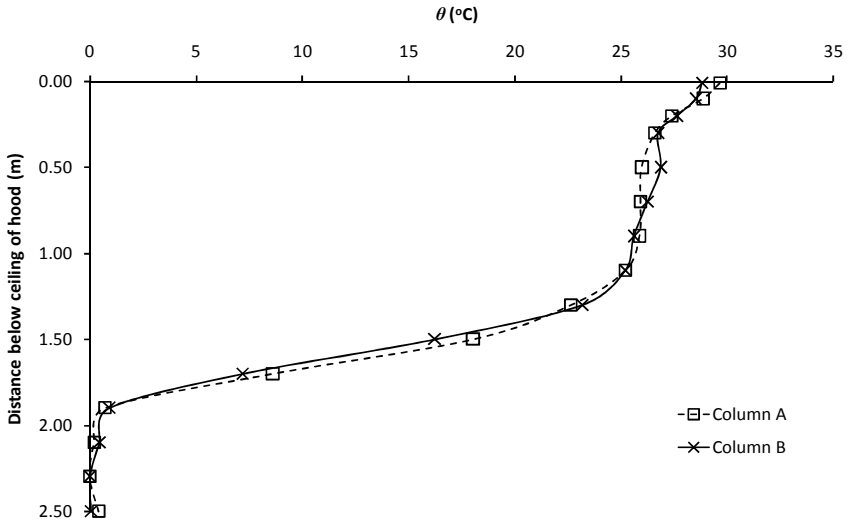

Figure G47: Experiment E77

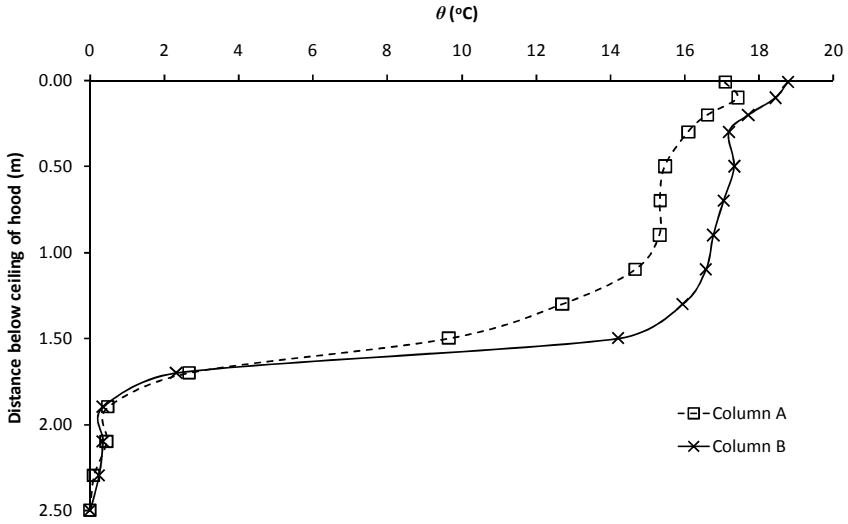

Figure G48: Experiment E78

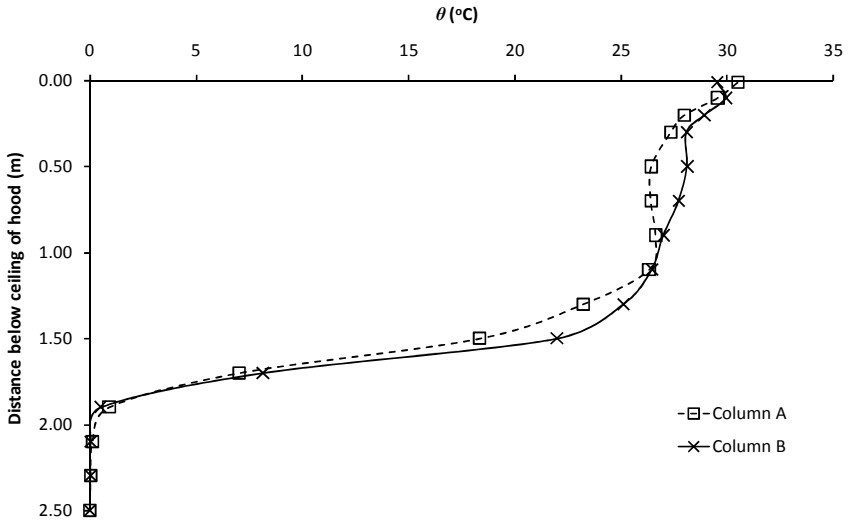

Figure G49: Experiment E79

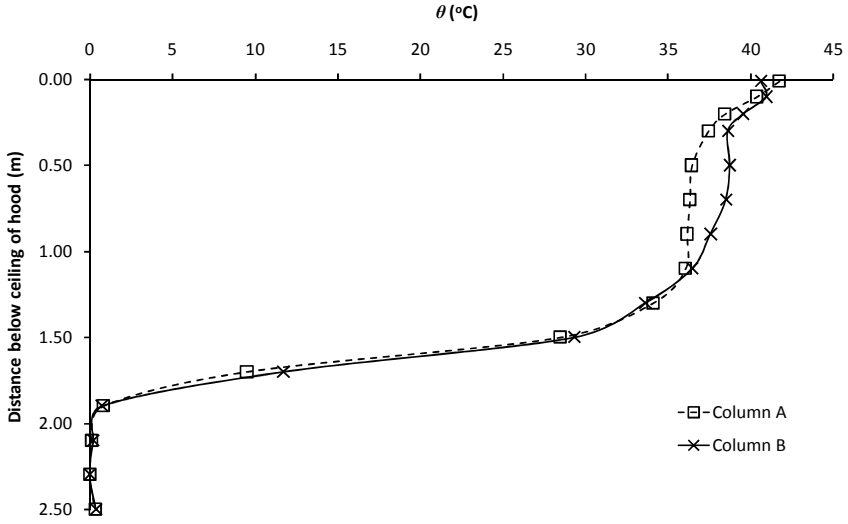

Figure G50: Experiment E80

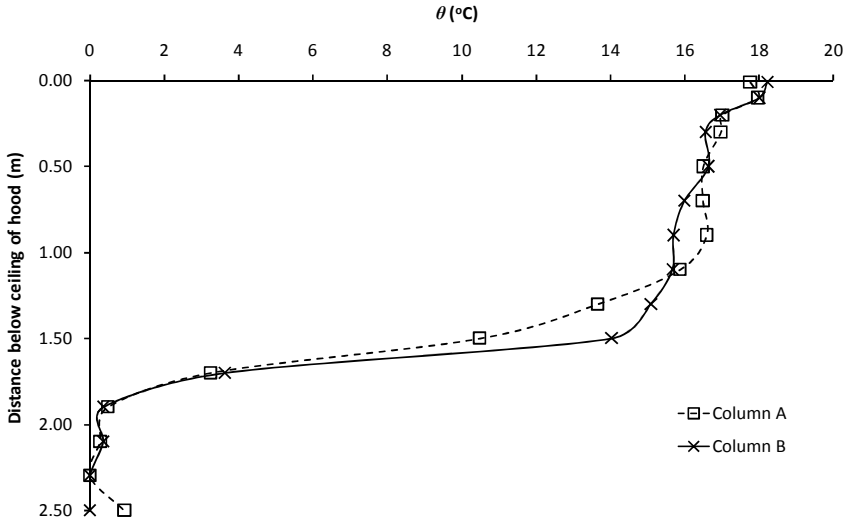

Figure G51: Experiment E81

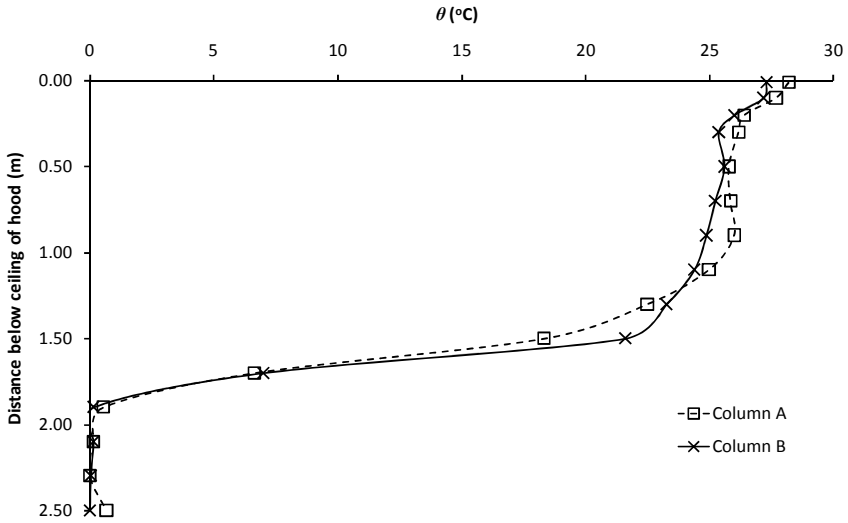

Figure G52: Experiment E82

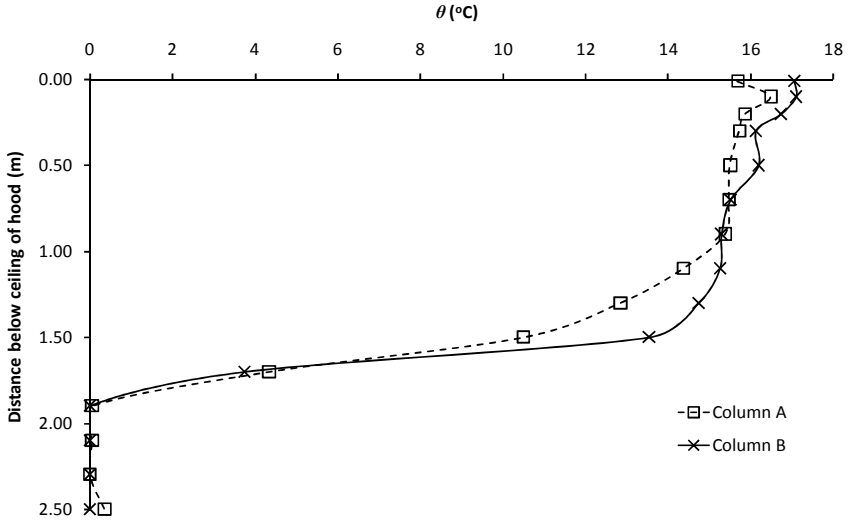

Figure G53: Experiment E83

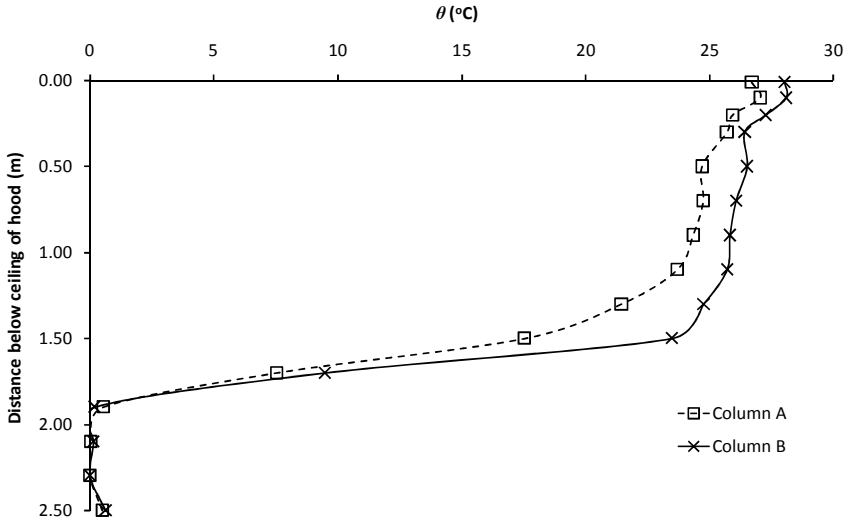

Figure G54: Experiment E84

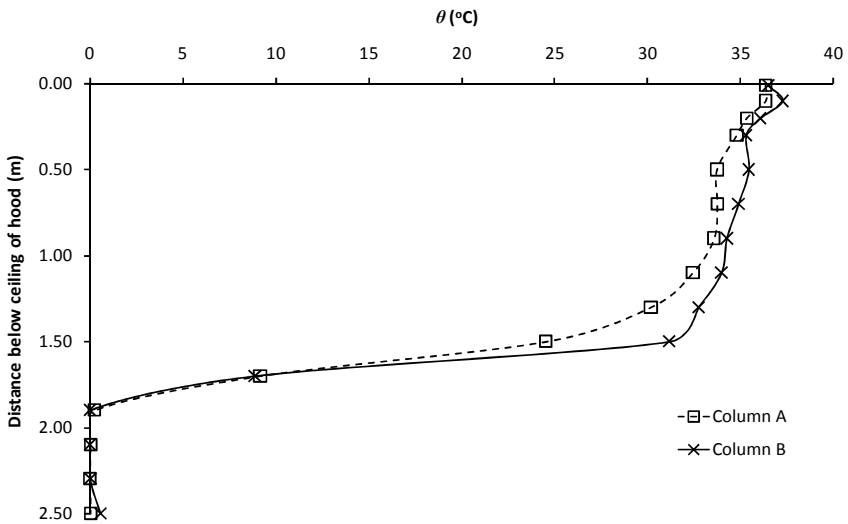

Figure G55: Experiment E85

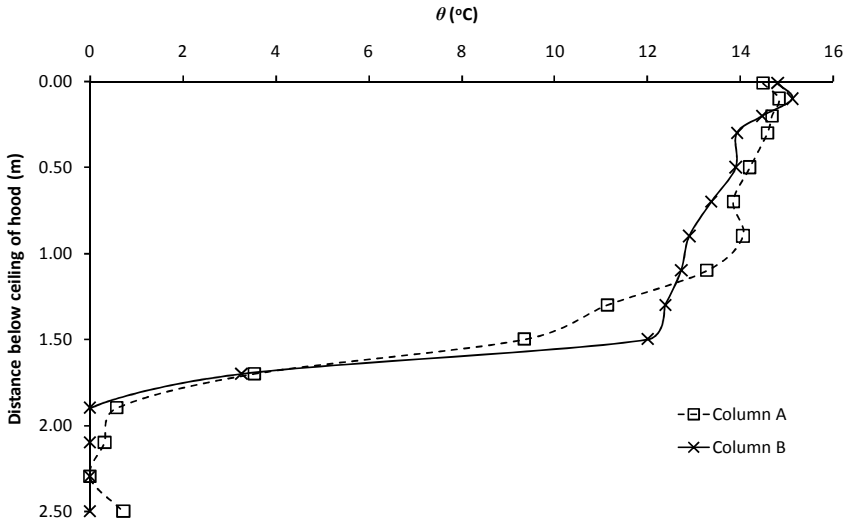

Figure G56: Experiment E86

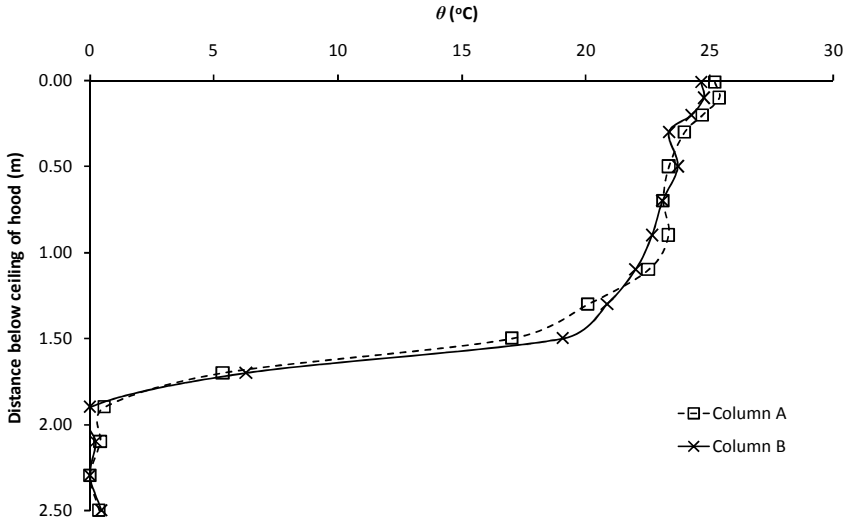

Figure G57: Experiment E87

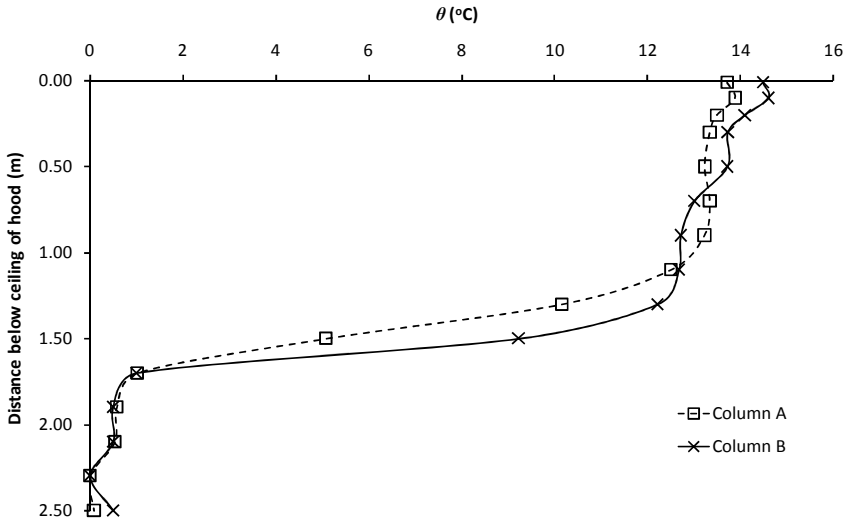

Figure G58: Experiment E88

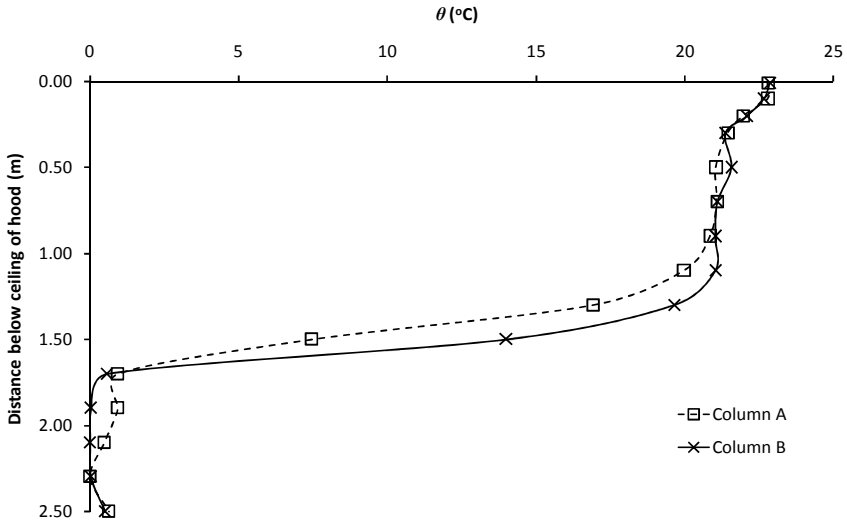

Figure G59: Experiment E89

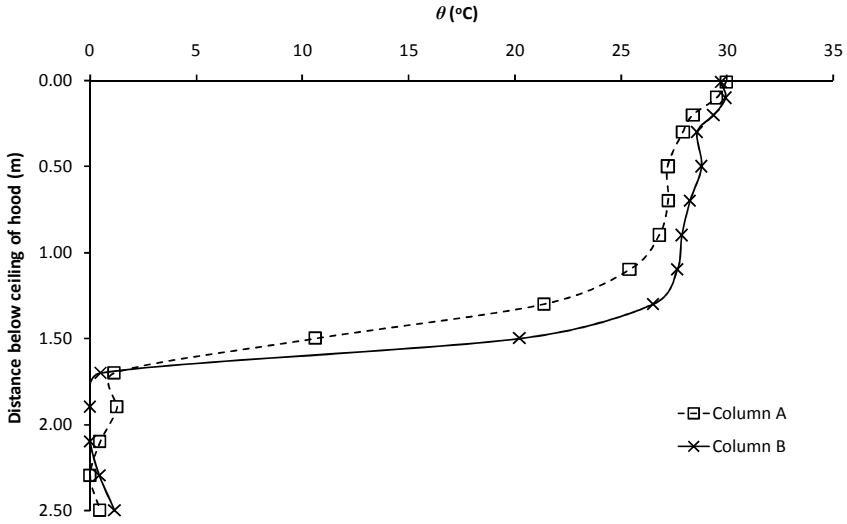

Figure G60: Experiment E90

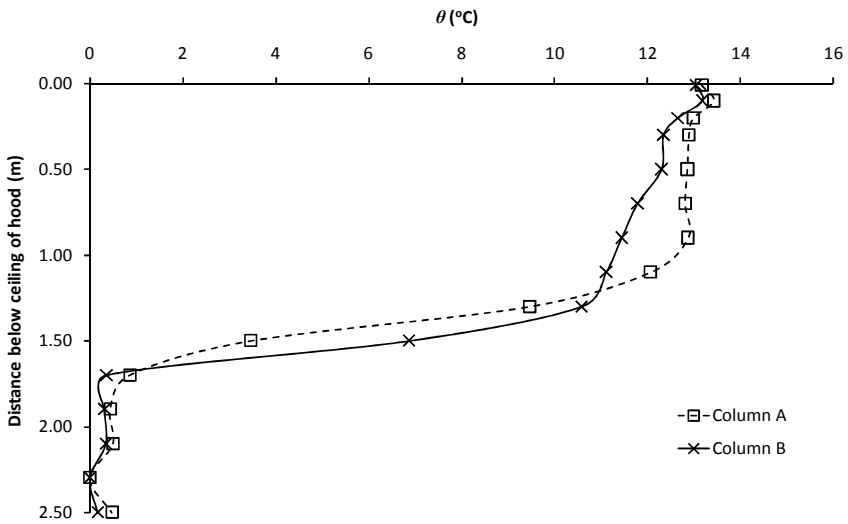

Figure G61: Experiment E91

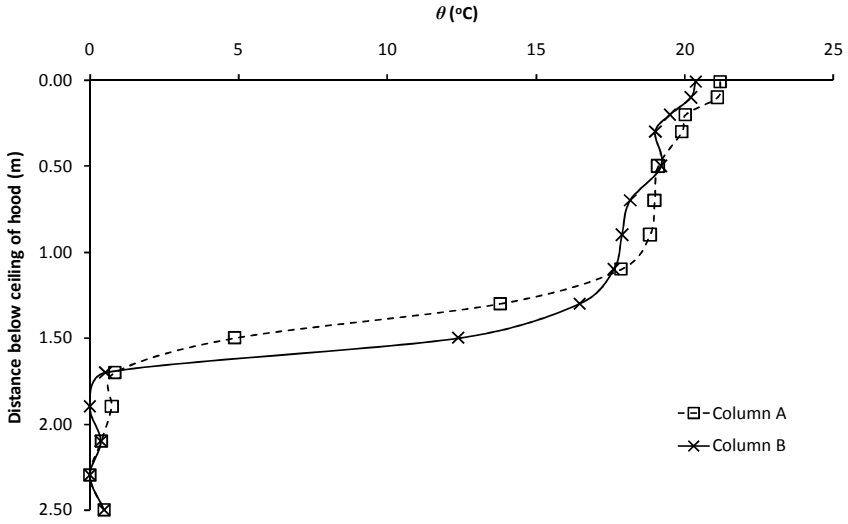

Figure G62: Experiment E92

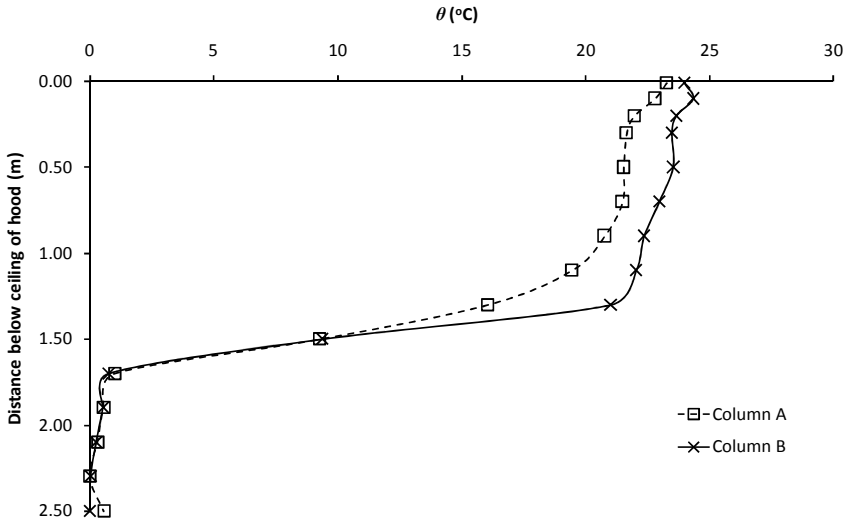

Figure G63: Experiment E93

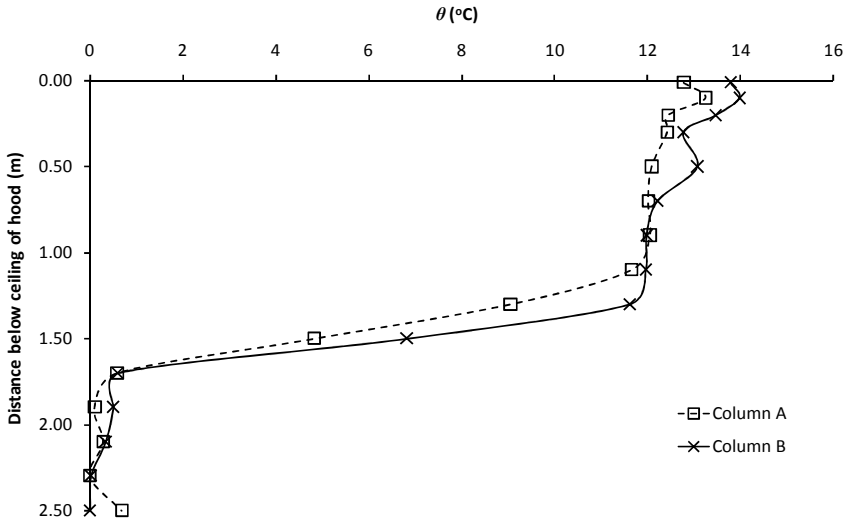

Figure G64: Experiment E94

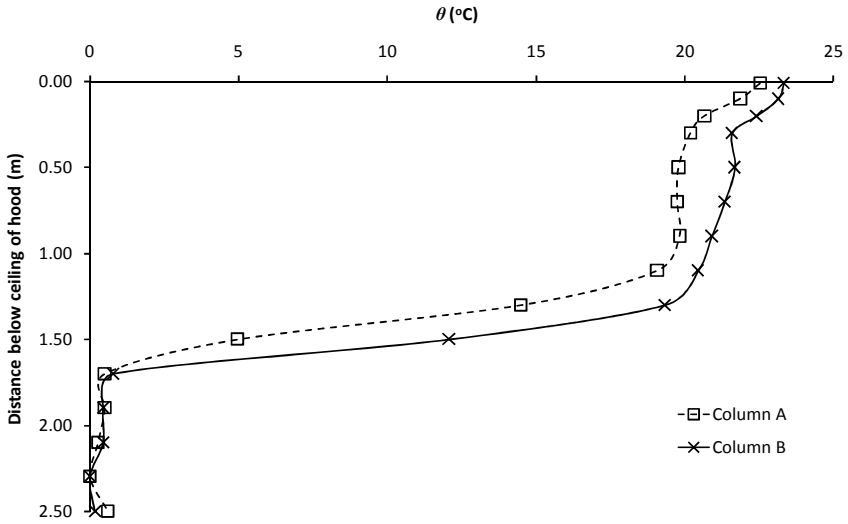

Figure G65: Experiment E95

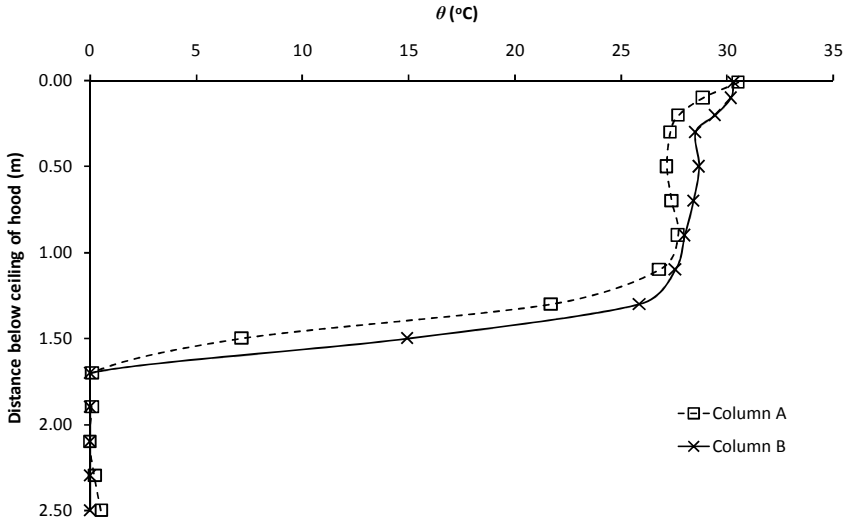

Figure G66: Experiment E96

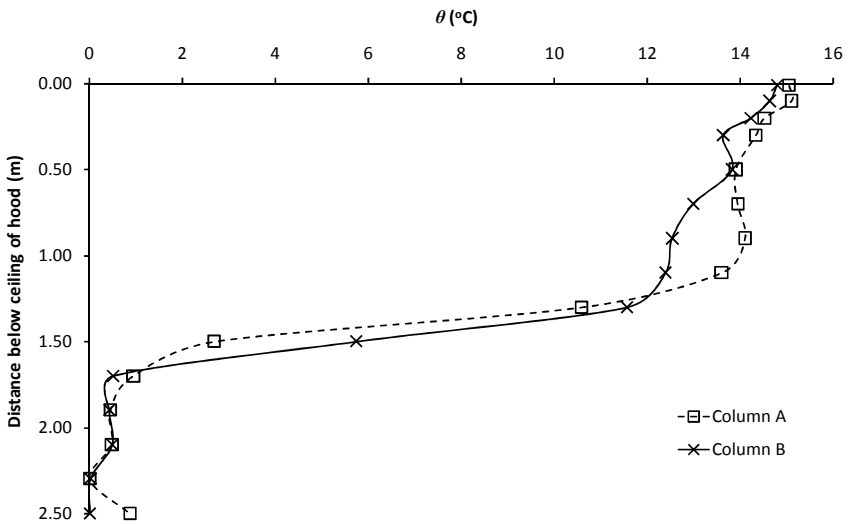

Figure G67: Experiment E97

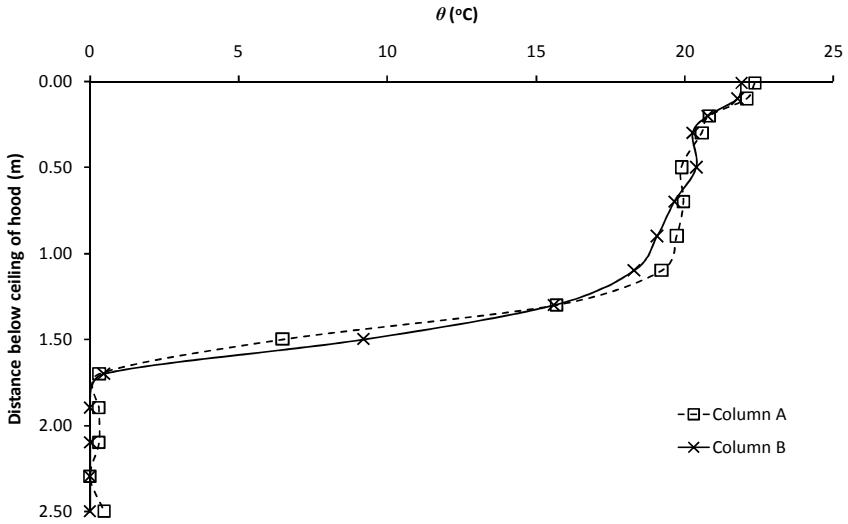

Figure G68: Experiment E98

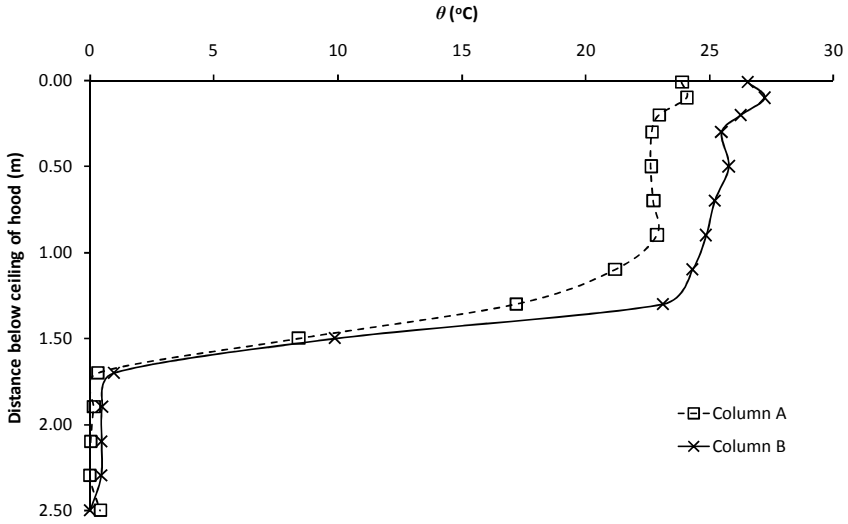

Figure G69: Experiment E99

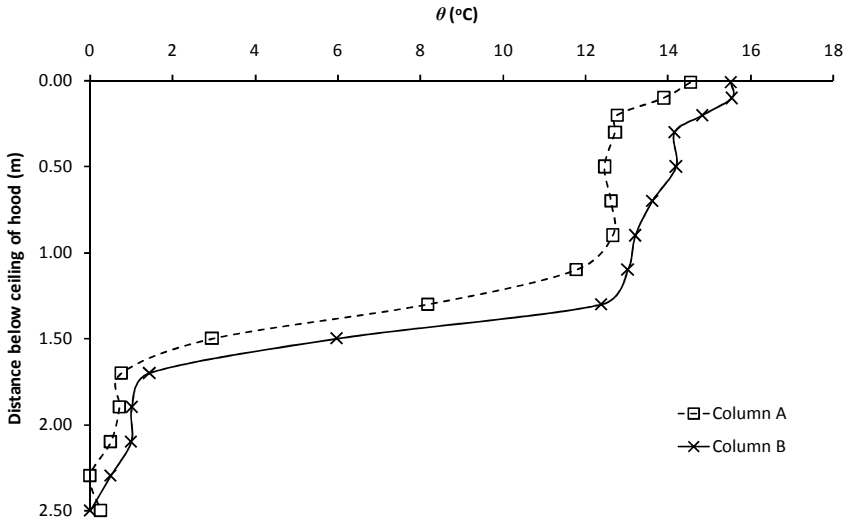

Figure G70: Experiment E100

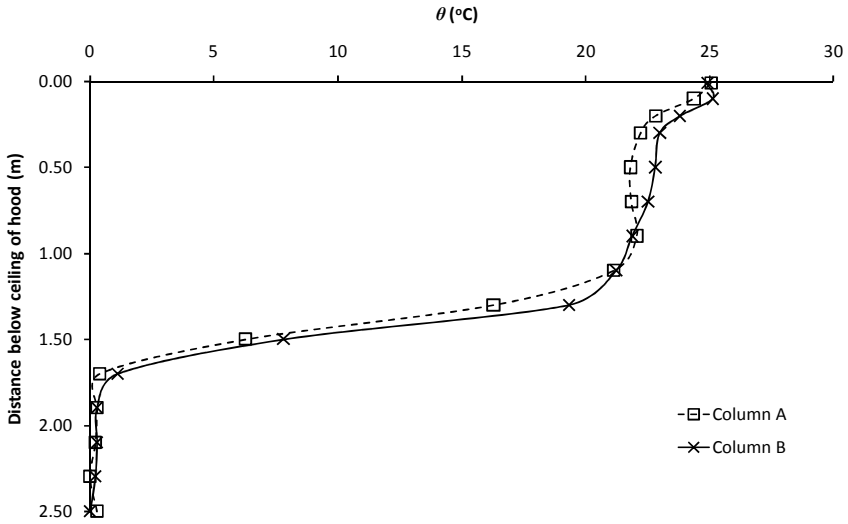

Figure G71: Experiment E101

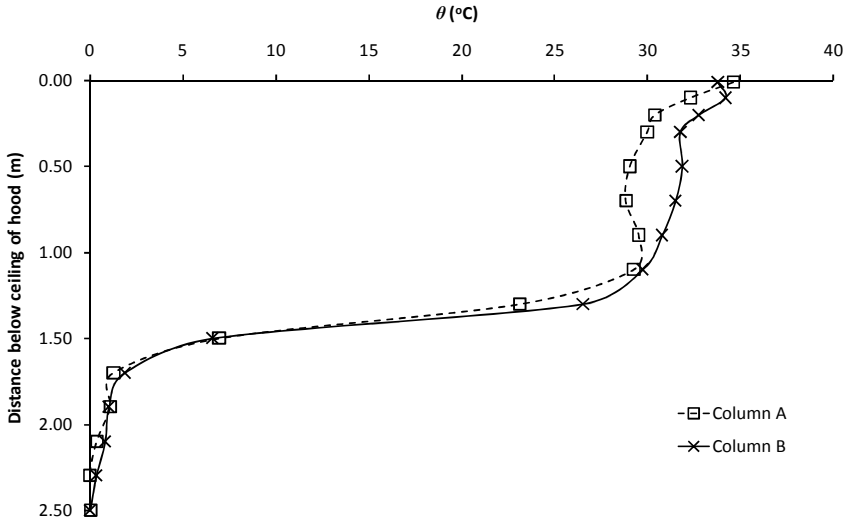

Figure G72: Experiment E102

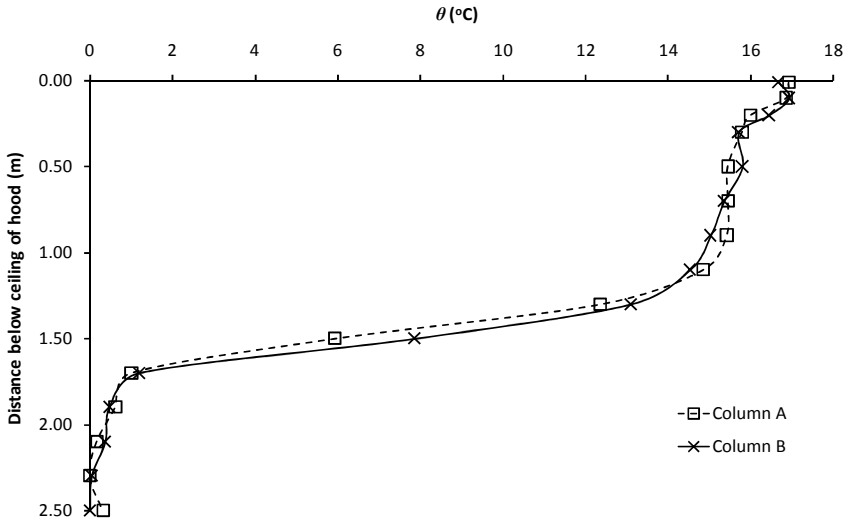

Figure G73: Experiment E103

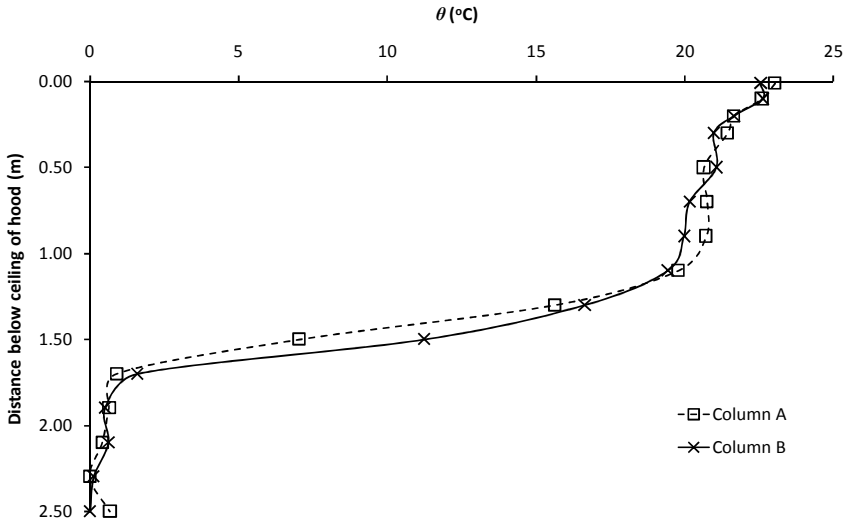

Figure G74: Experiment E104

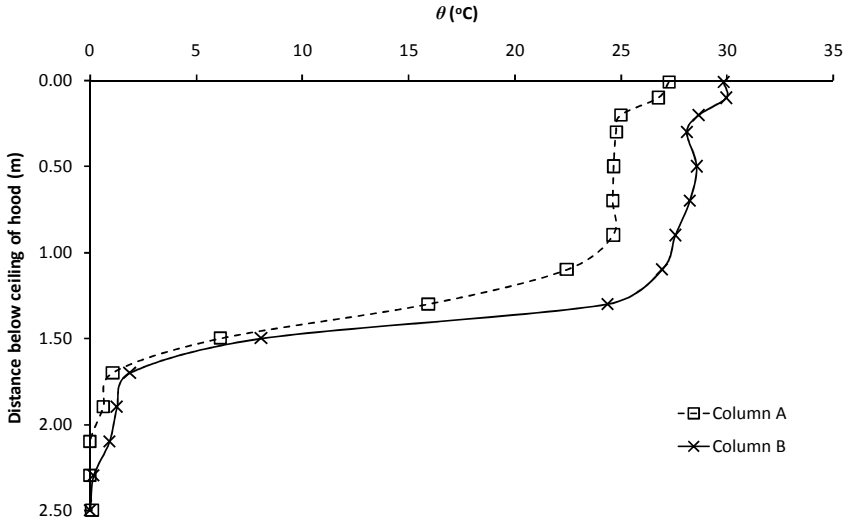

Figure G75: Experiment E105

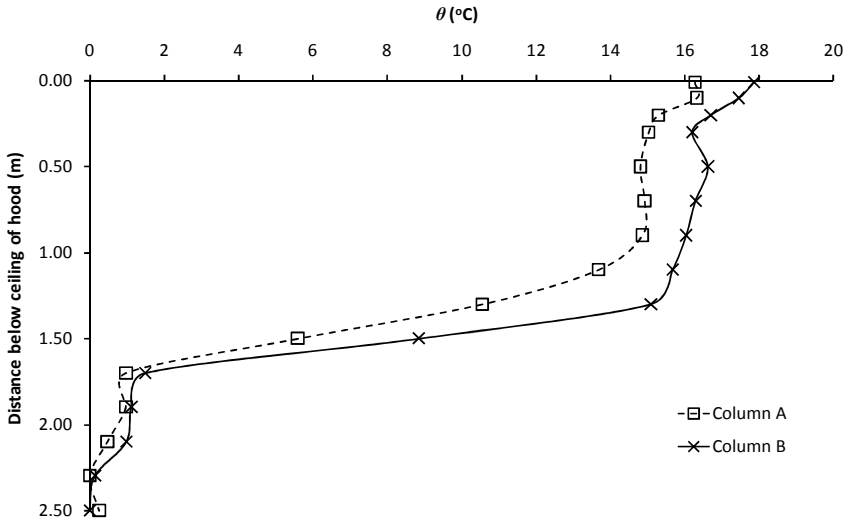

Figure G76: Experiment E106

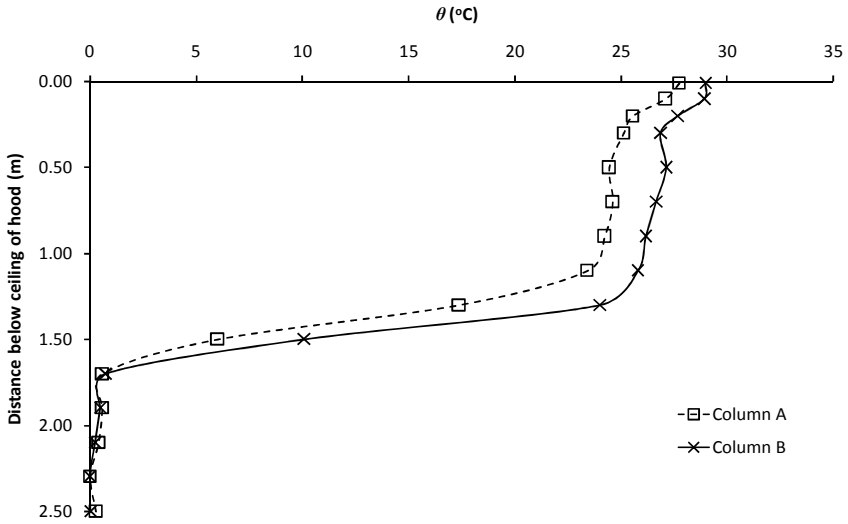

Figure G77: Experiment E107

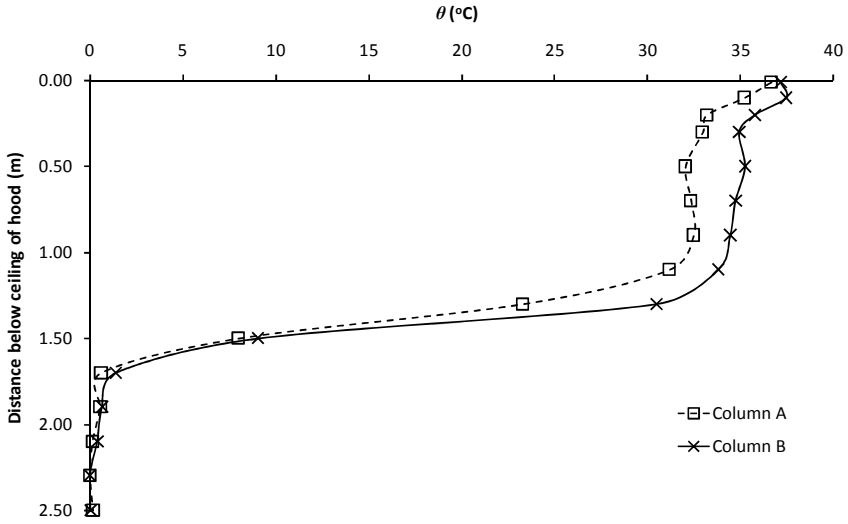

Figure G78: Experiment E108

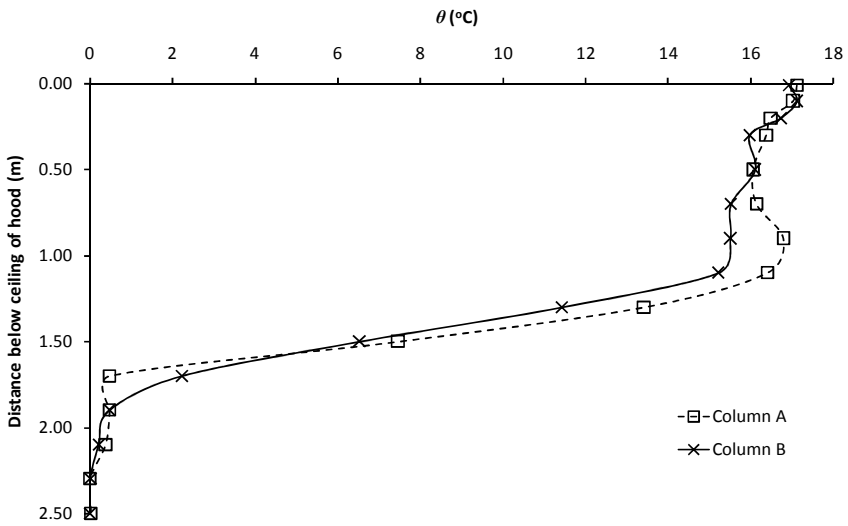

Figure G79: Experiment E109

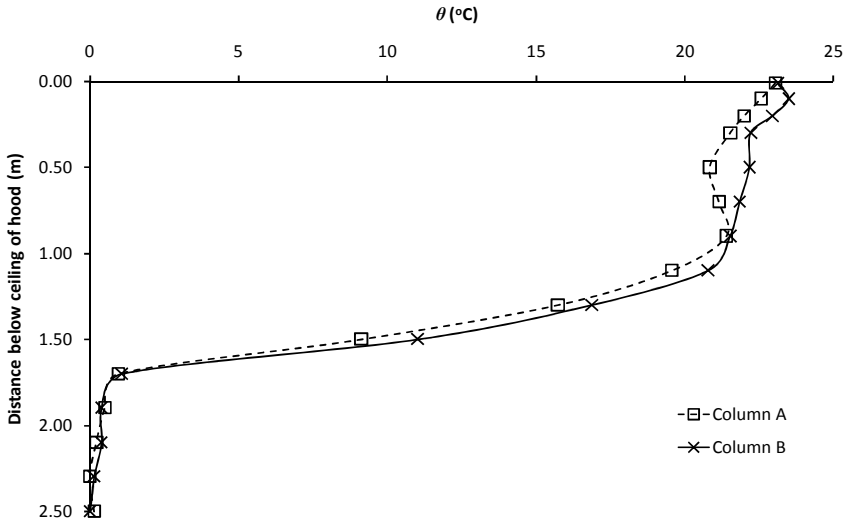

Figure G80: Experiment E110

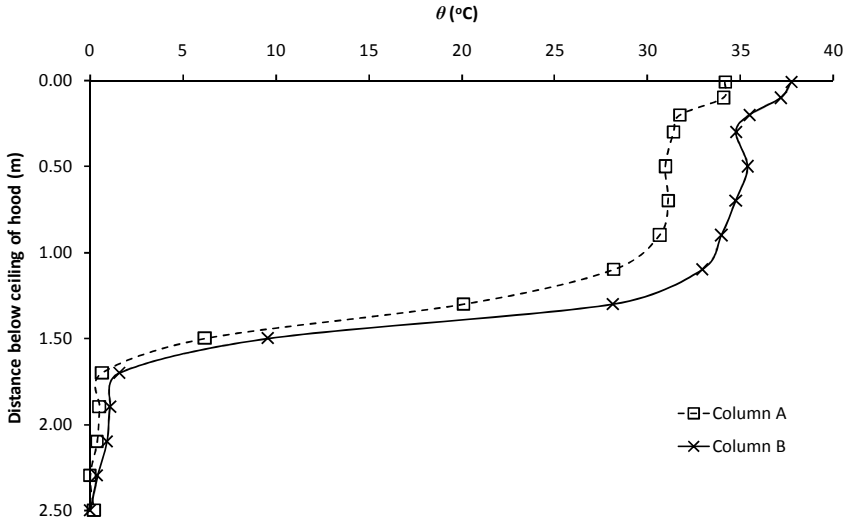

Figure G81: Experiment E111

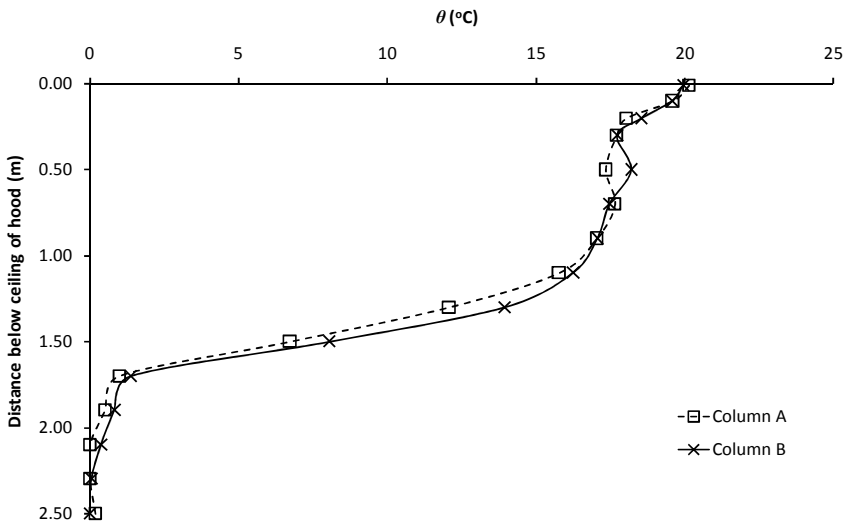

Figure G82: Experiment E112

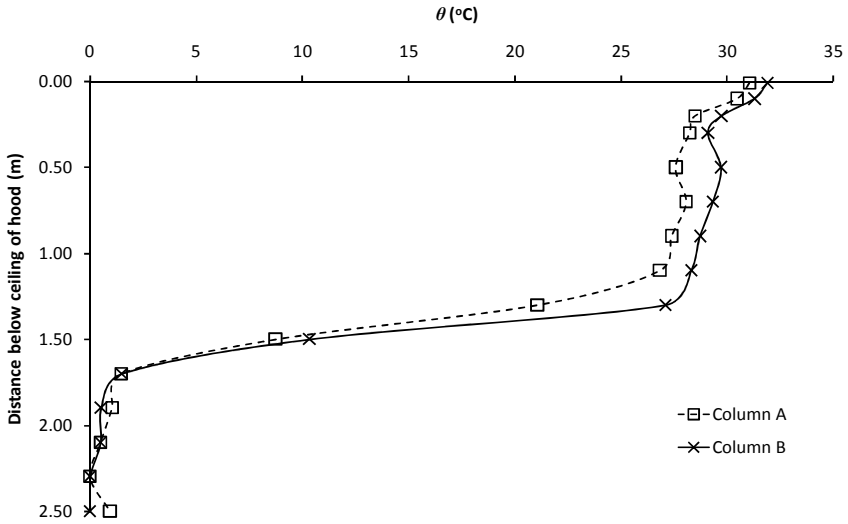

Figure G83: Experiment E113

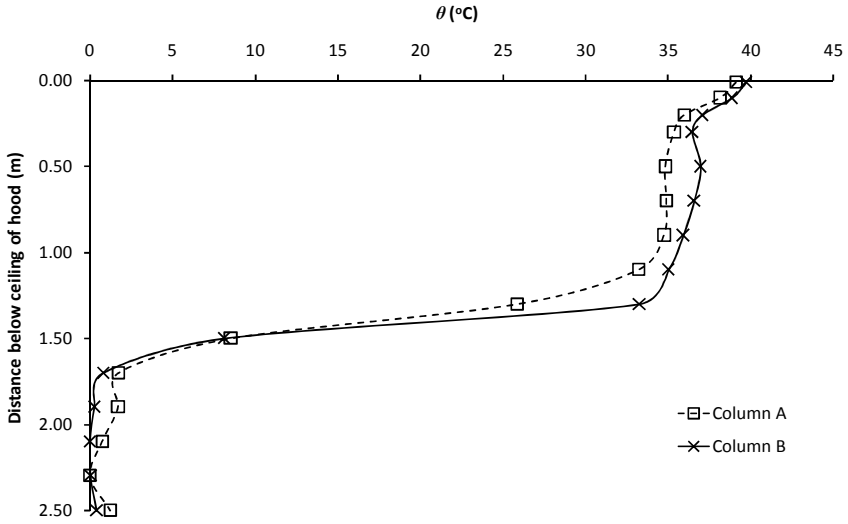

Figure G84: Experiment E114

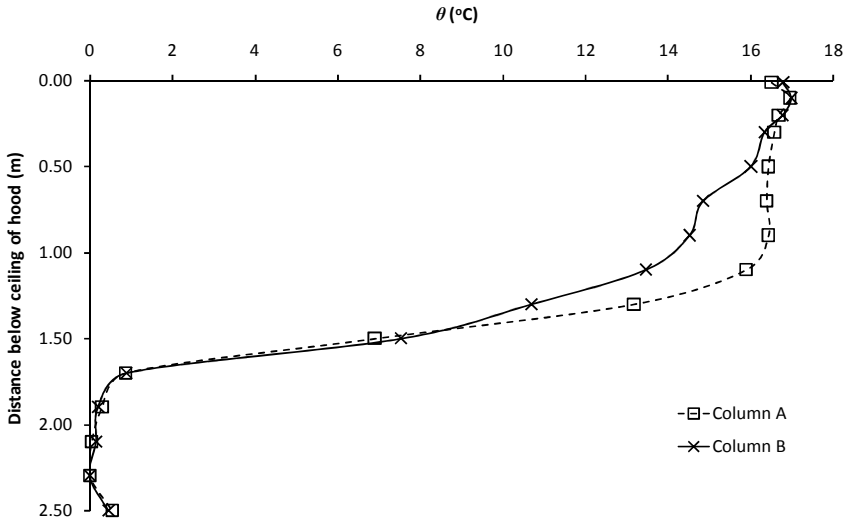

Figure G85: Experiment E115

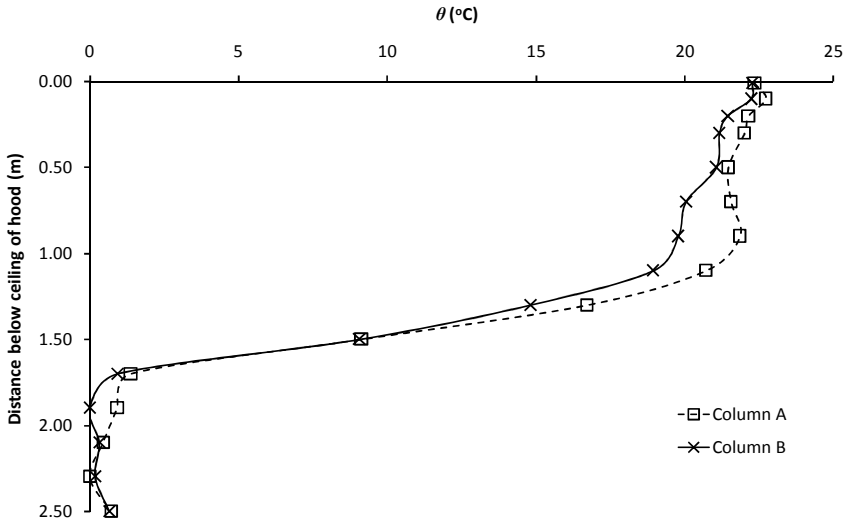

Figure G86: Experiment E116

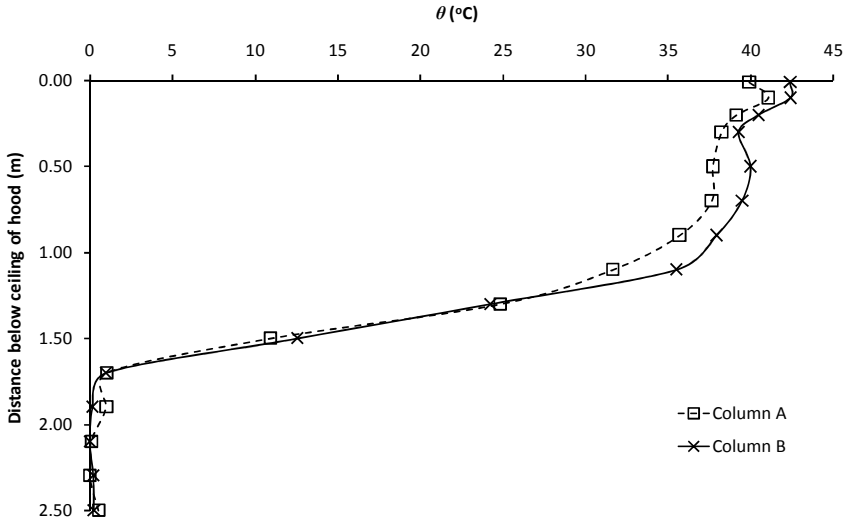

Figure G87: Experiment E117

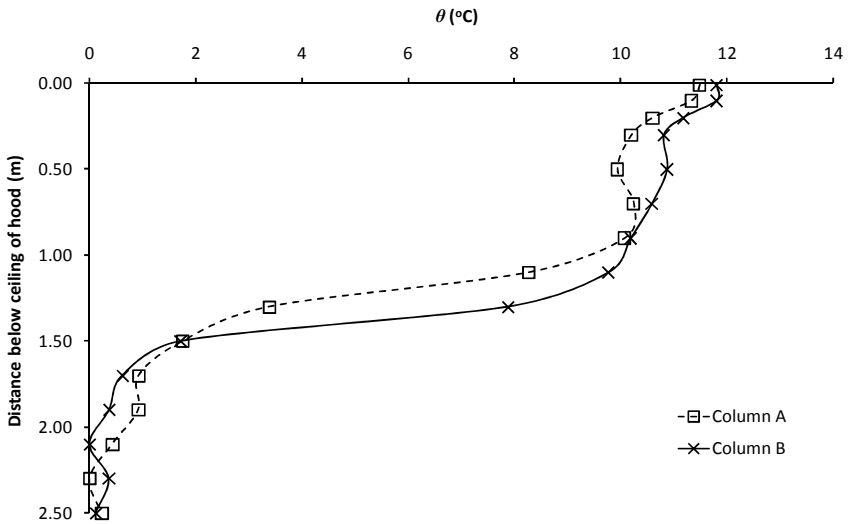

Figure G88: Experiment E158

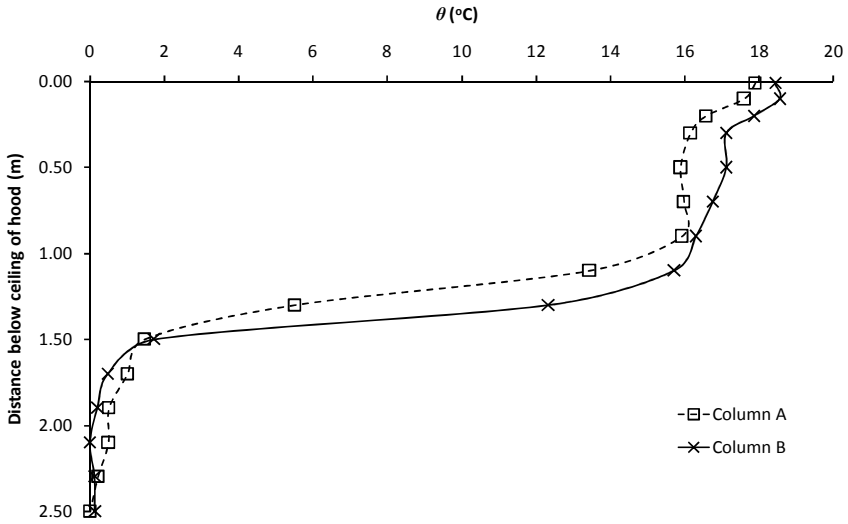

Figure G89: Experiment E159

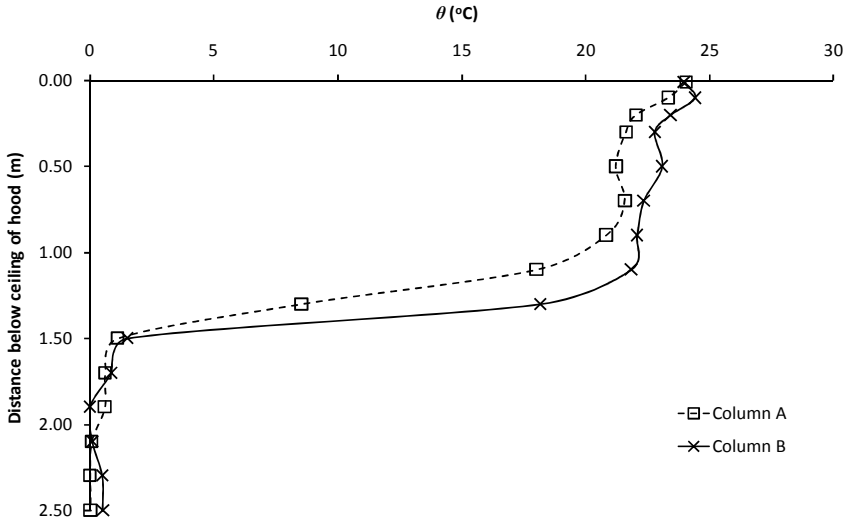

Figure G90: Experiment E160

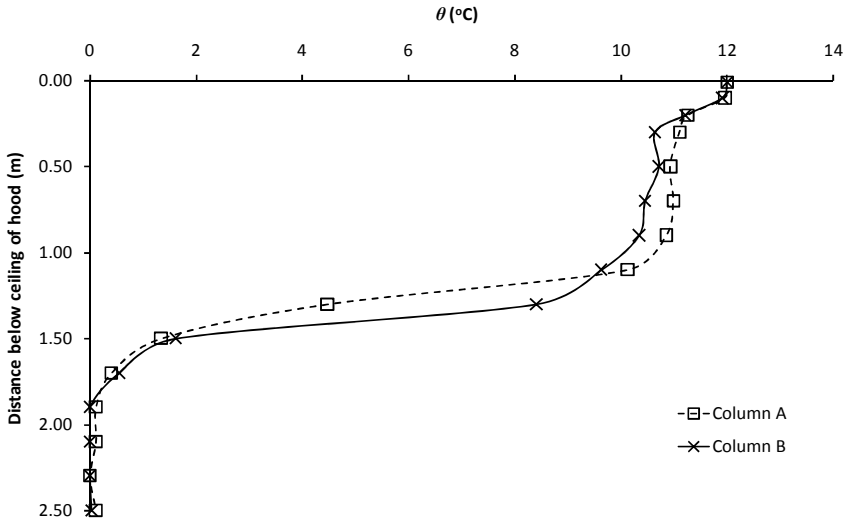

Figure G91: Experiment E161

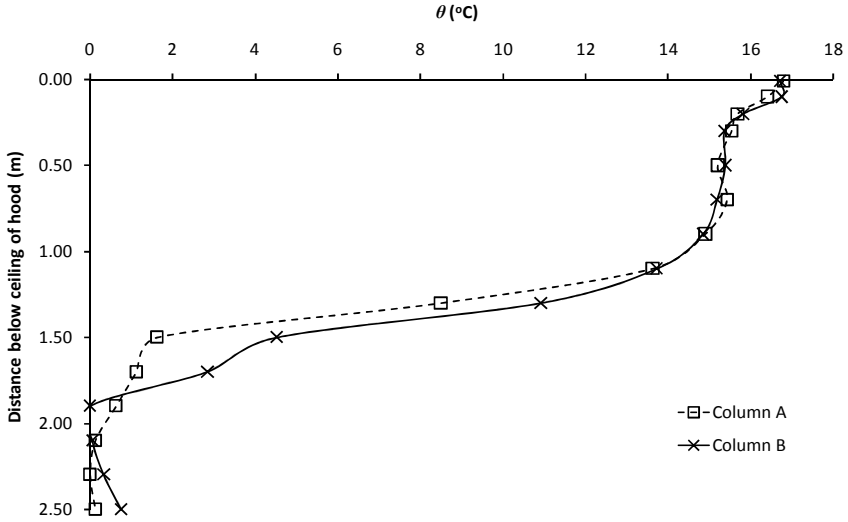

Figure G92: Experiment E162

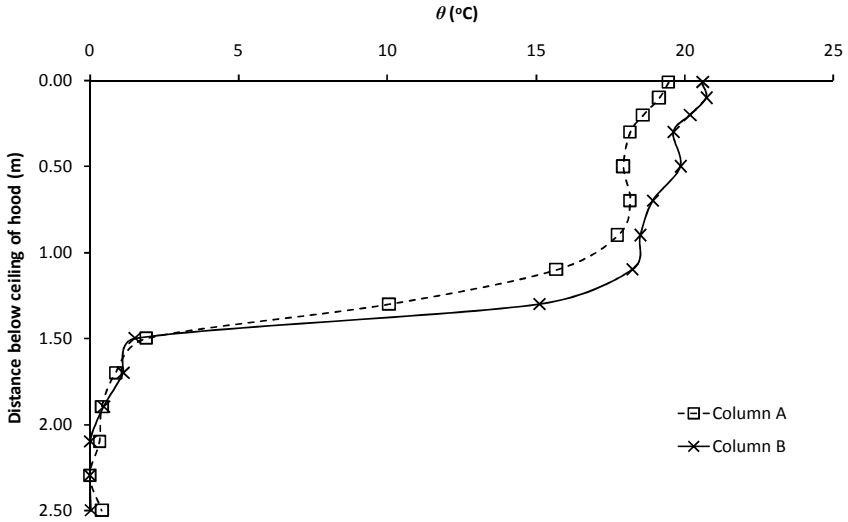

Figure G93: Experiment E163

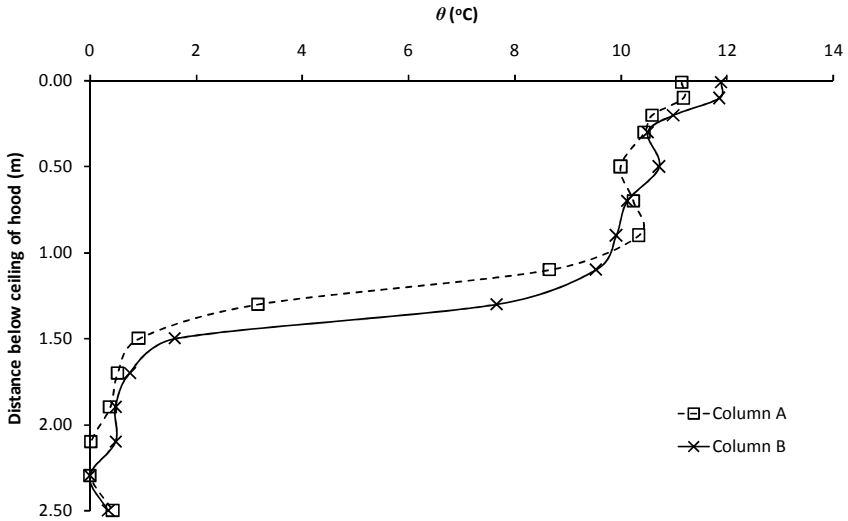

Figure G94: Experiment E164

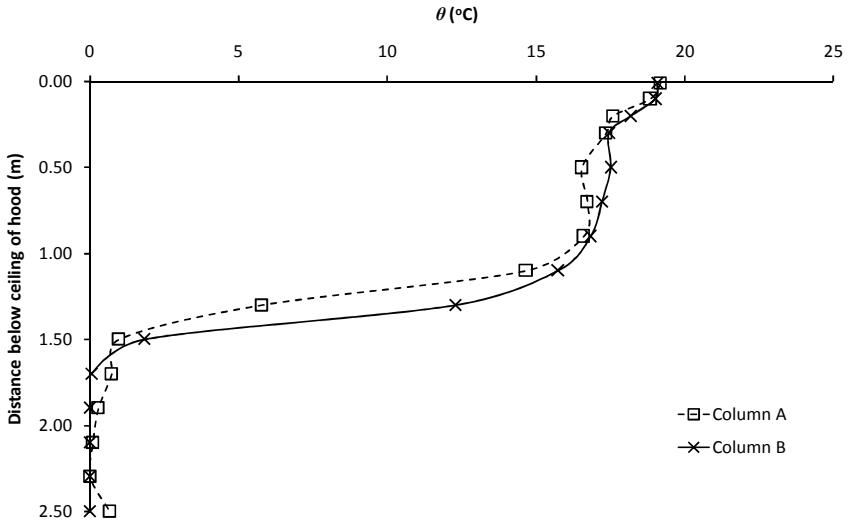

Figure G95: Experiment E165

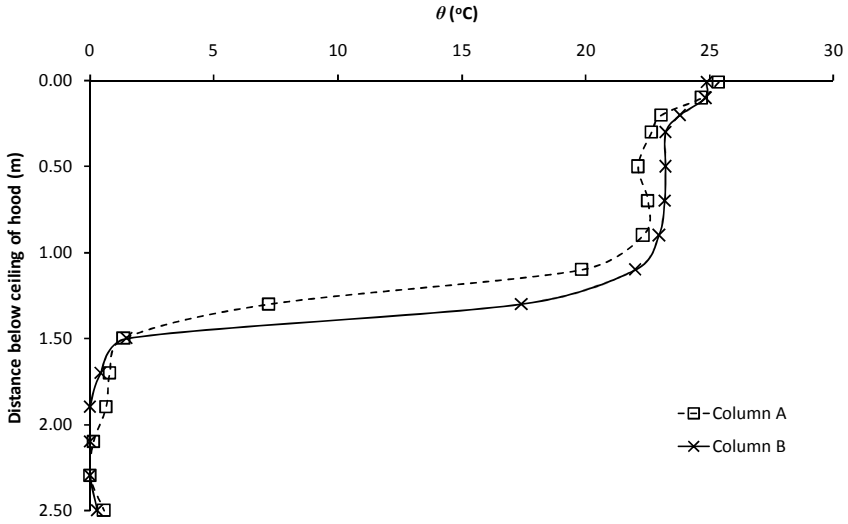

Figure G96: Experiment E166

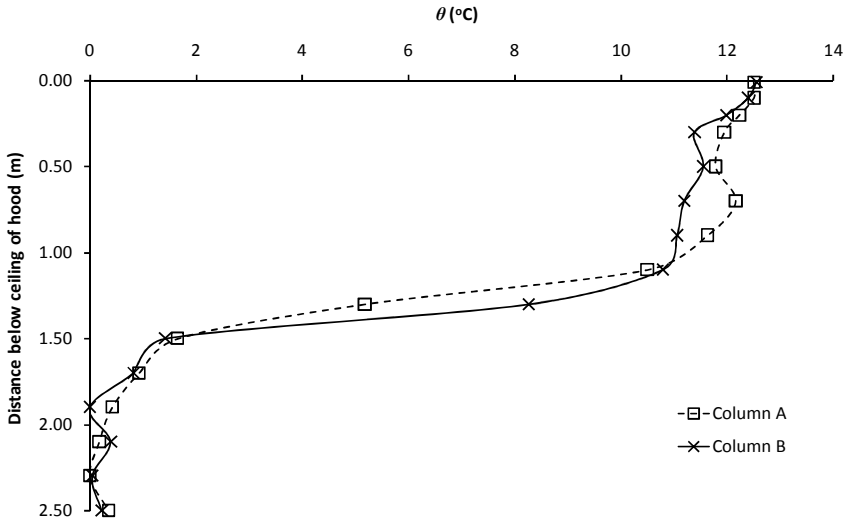

Figure G97: Experiment E167

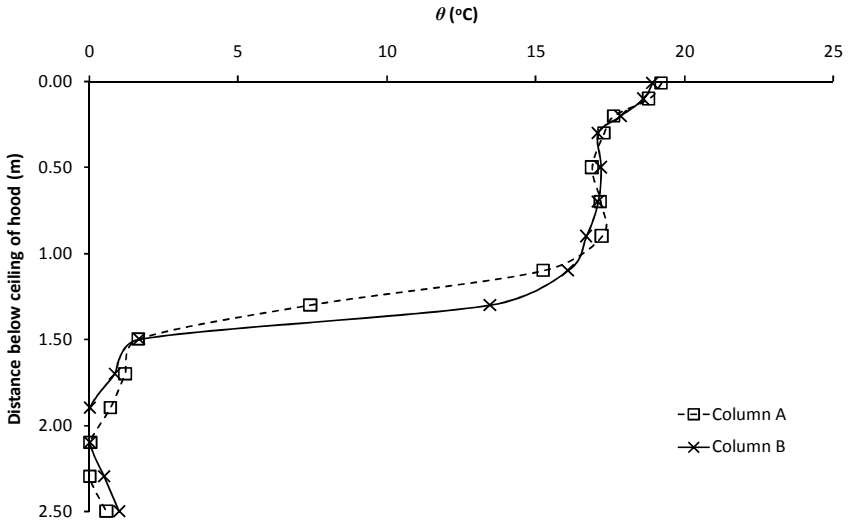

Figure G98: Experiment E168

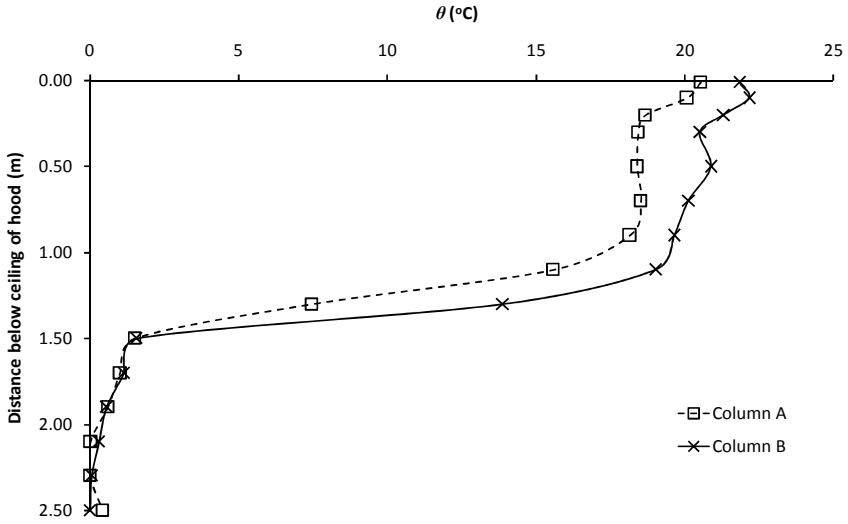

Figure G99: Experiment E169

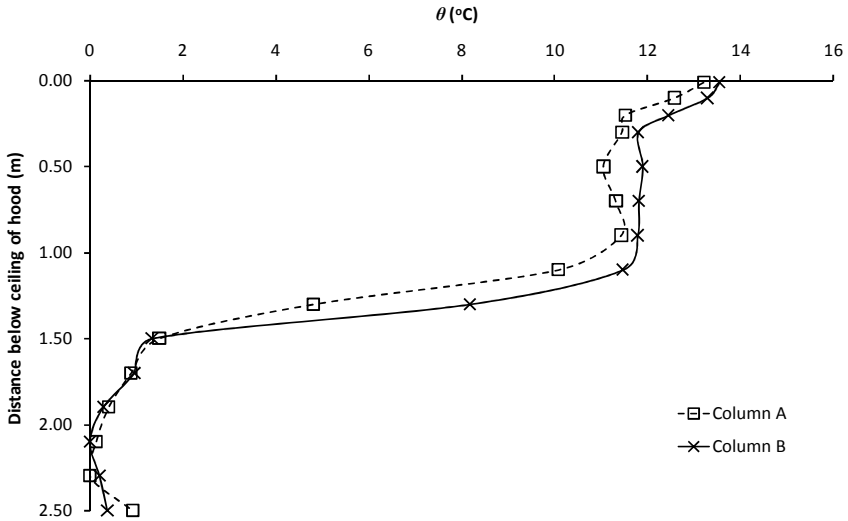

Figure G100: Experiment E170

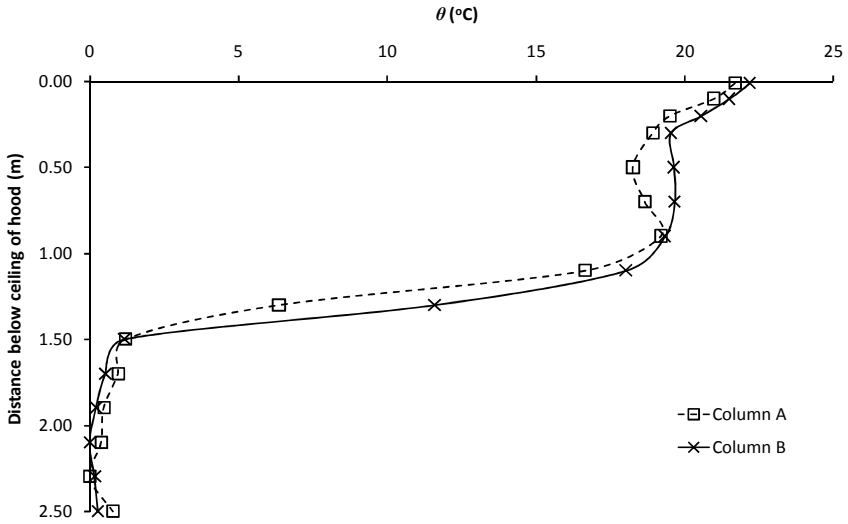

Figure G101: Experiment E171

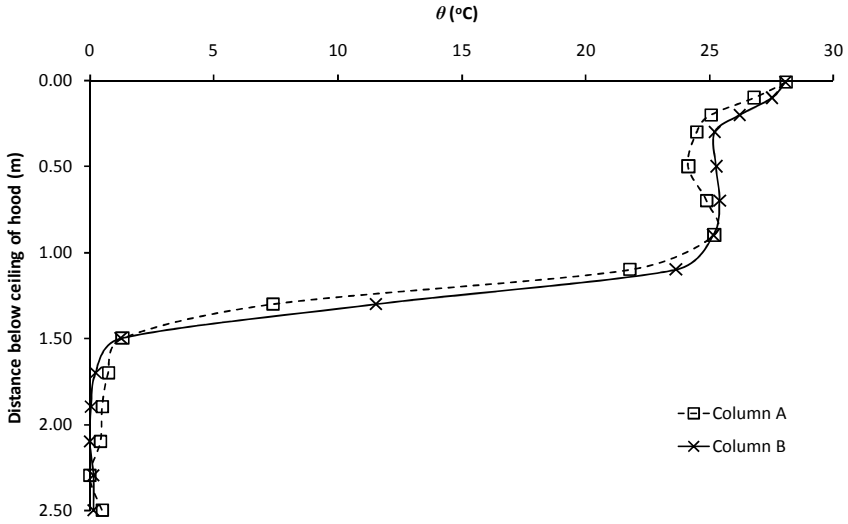

Figure G102: Experiment E172

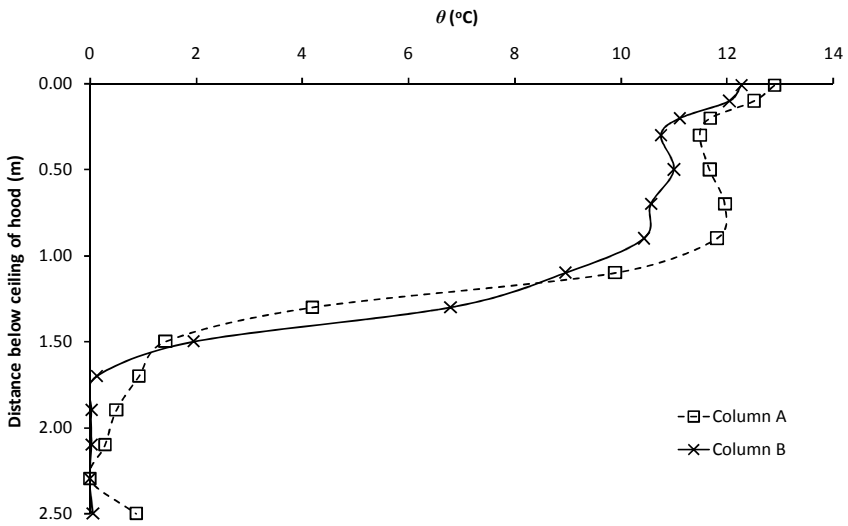

Figure G103: Experiment E173

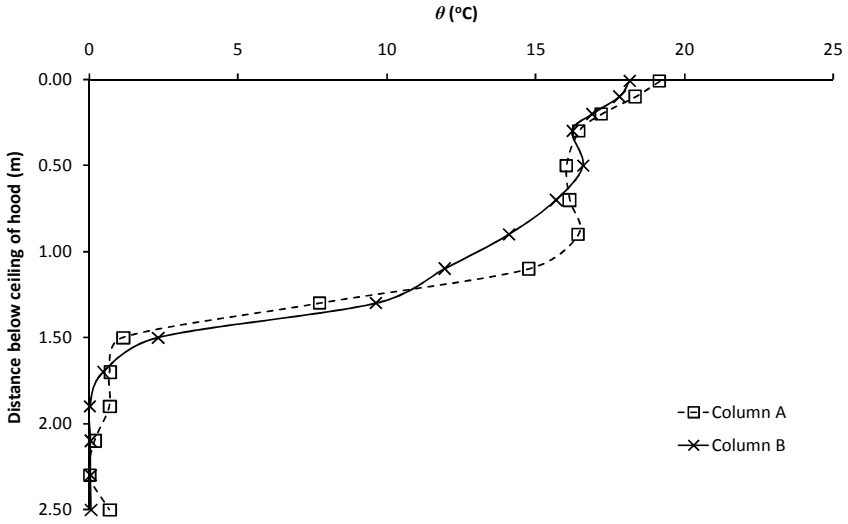

Figure G104: Experiment E174

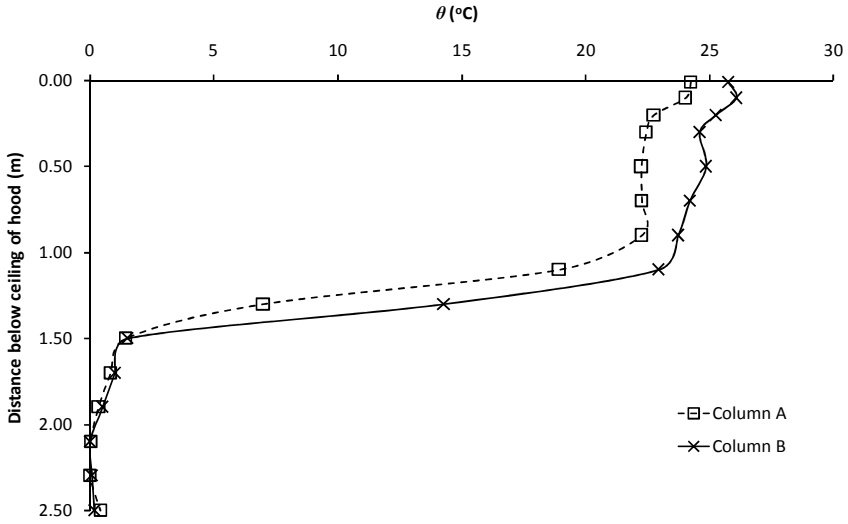

Figure G105: Experiment E175

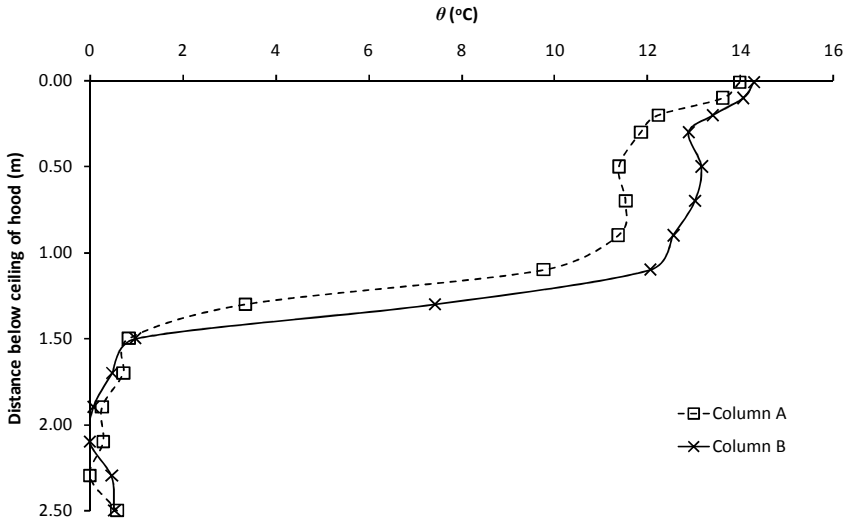

Figure G106: Experiment E176

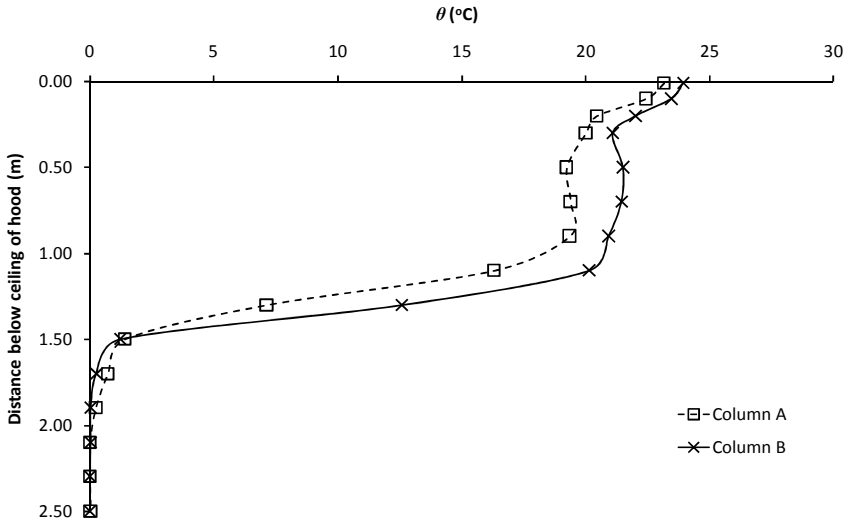

Figure G107: Experiment E177

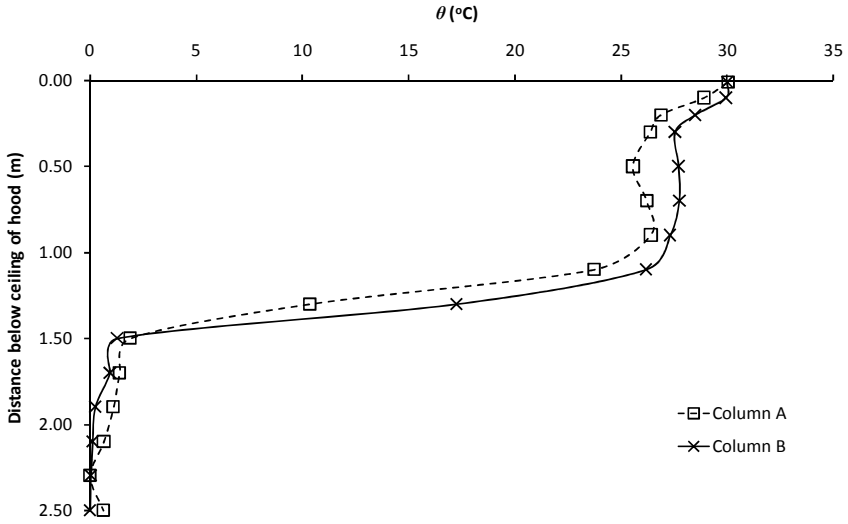

Figure G108: Experiment E178

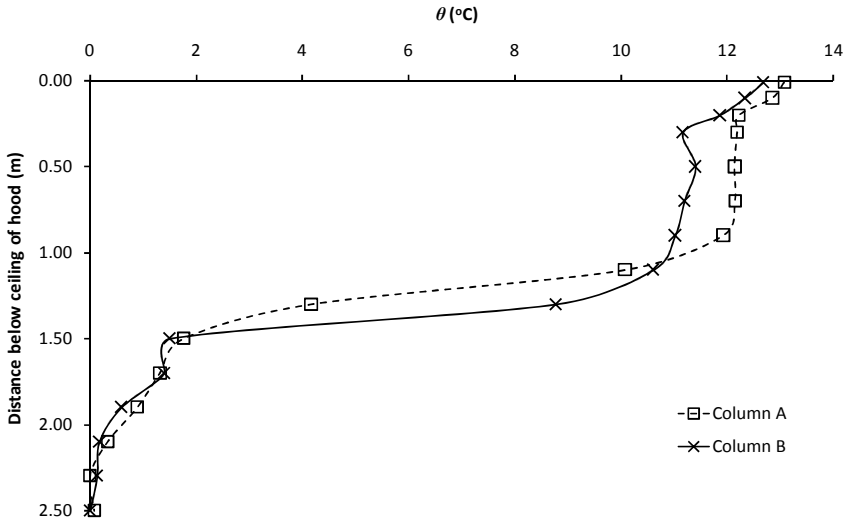

Figure G109: Experiment E179

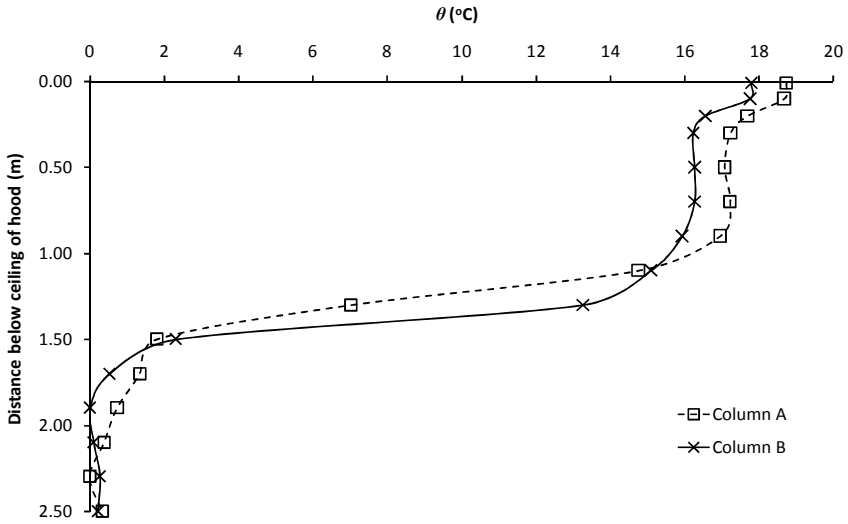

Figure G110: Experiment E180

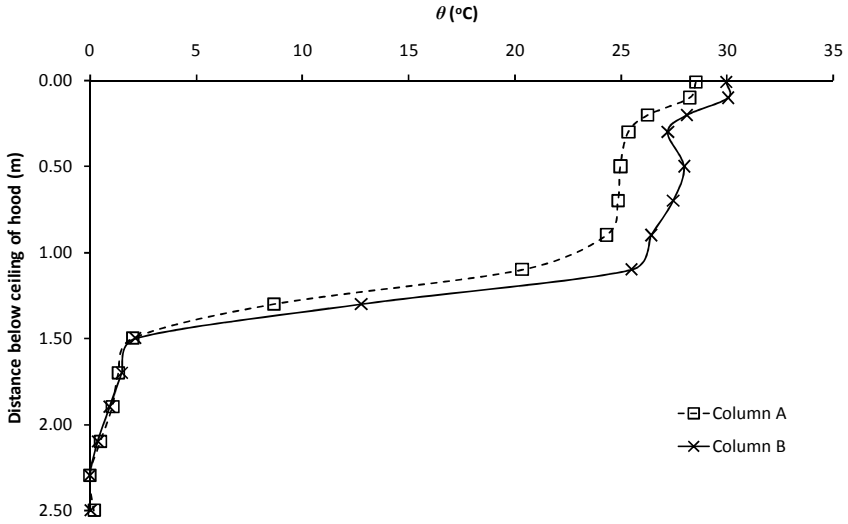

Figure G111: Experiment E181

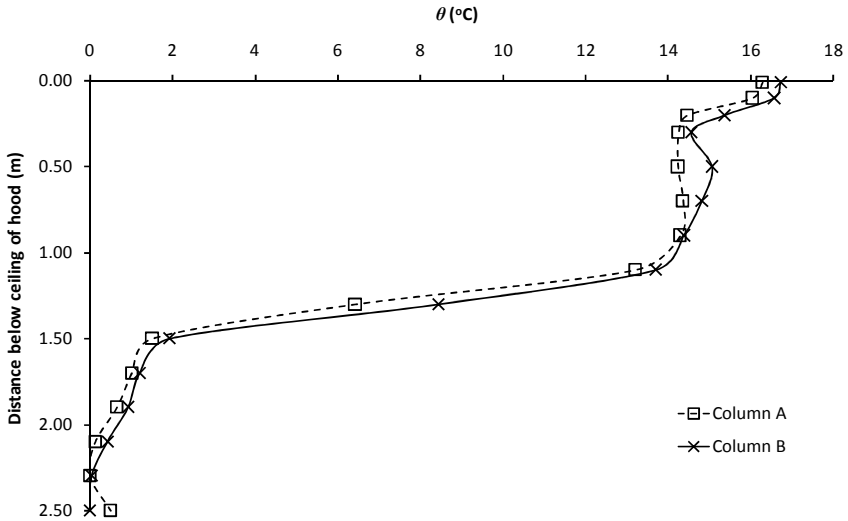

Figure G112: Experiment E182

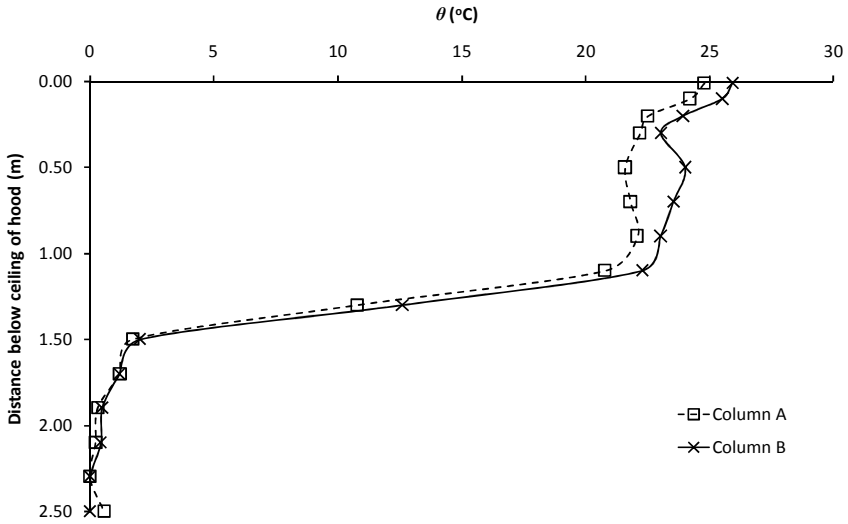

Figure G113: Experiment E183

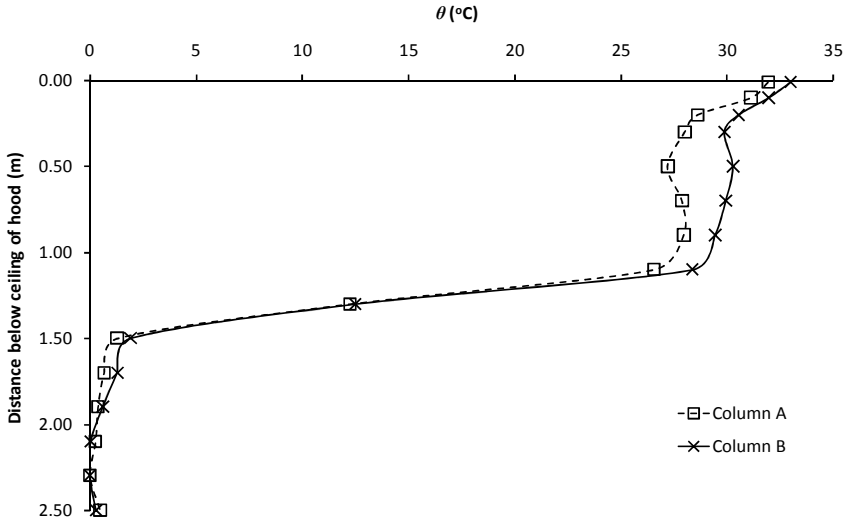

Figure G114: Experiment E184

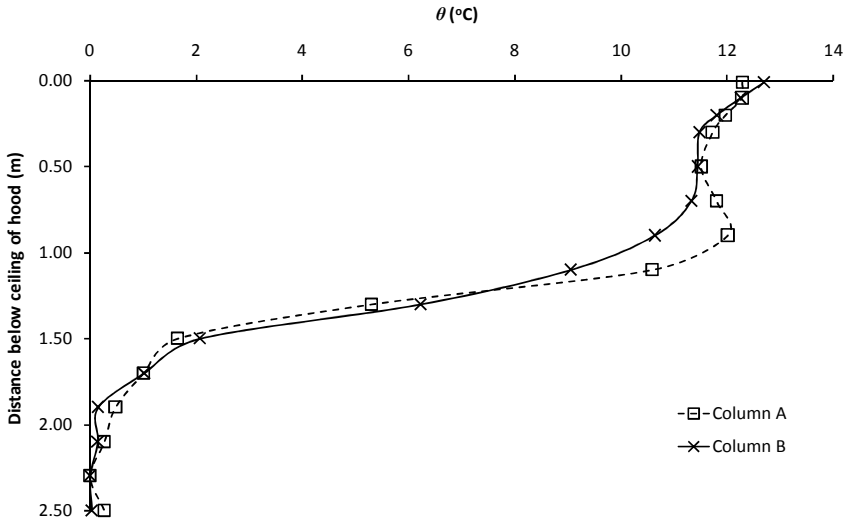

Figure G115: Experiment E185

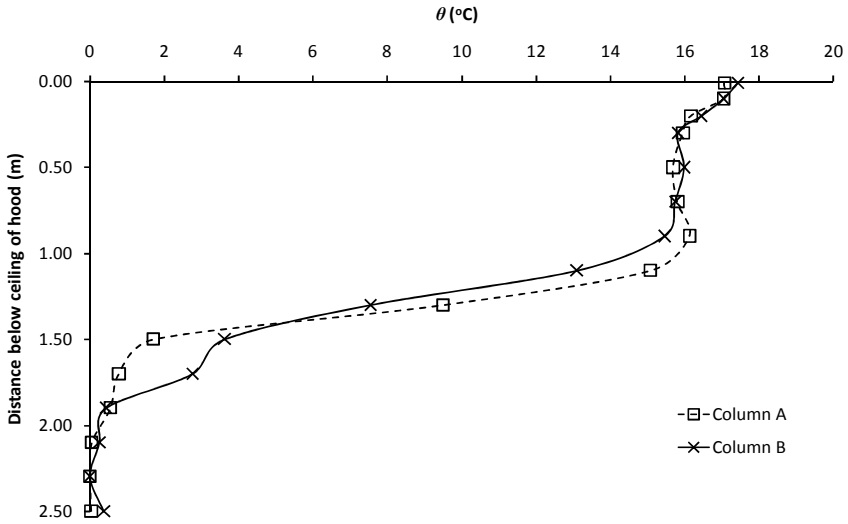

Figure G116: Experiment E186

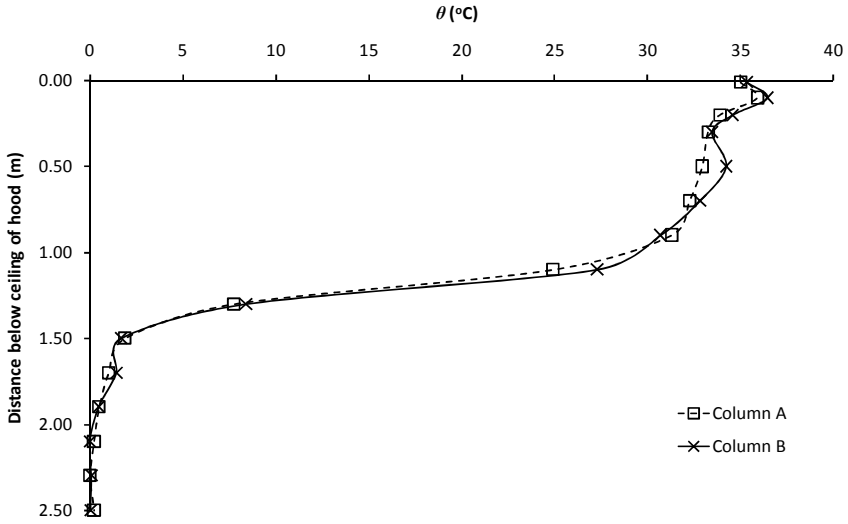

Figure G117: Experiment E187

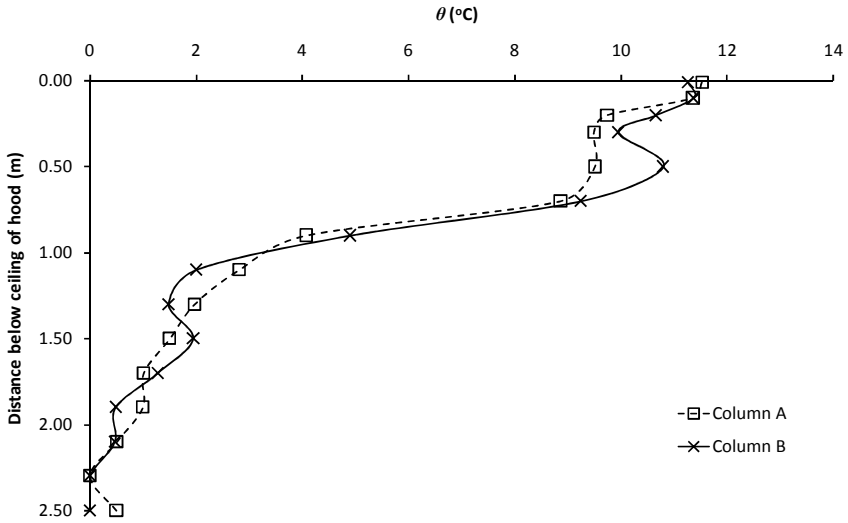

Figure G118: Experiment E223

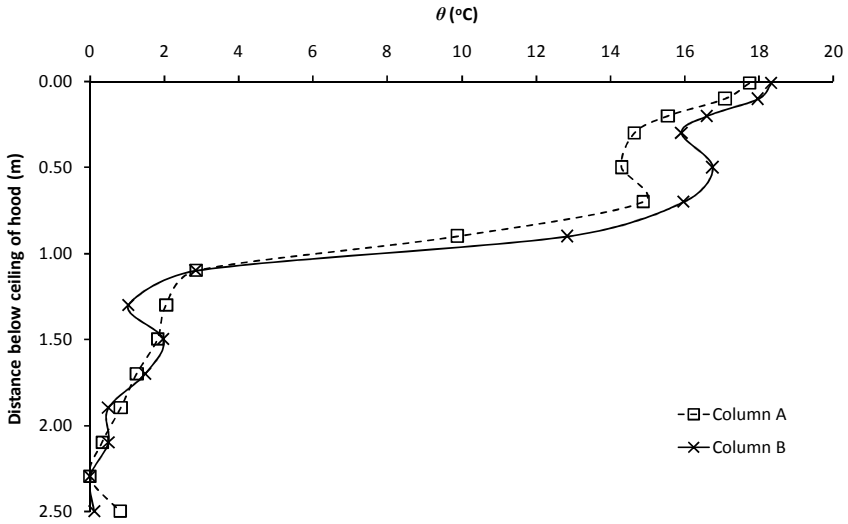

Figure G119: Experiment E224

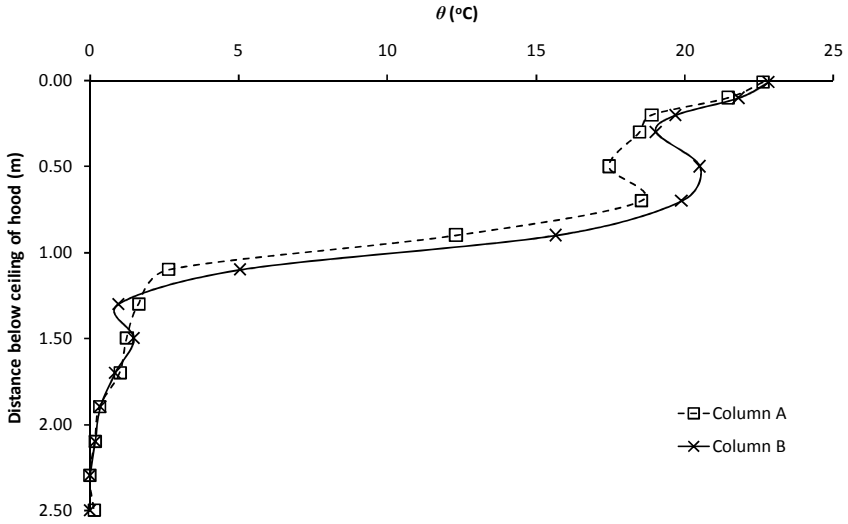

Figure G120: Experiment E225

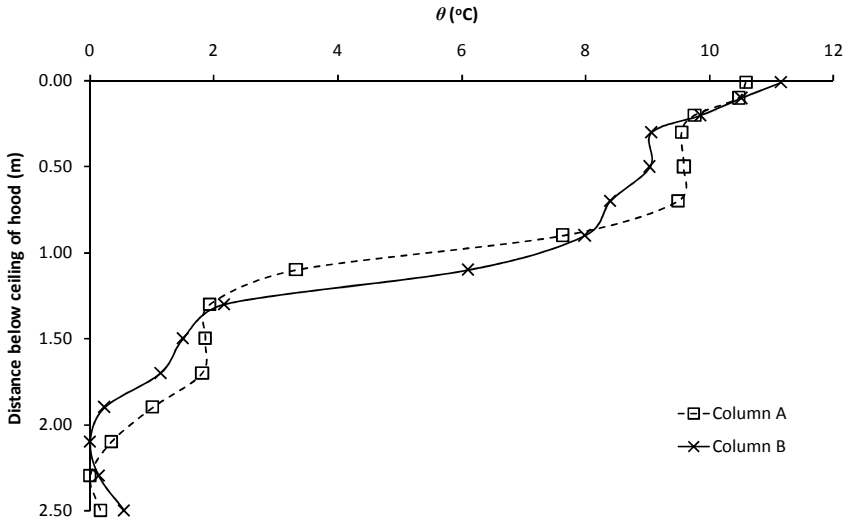

Figure G121: Experiment E226

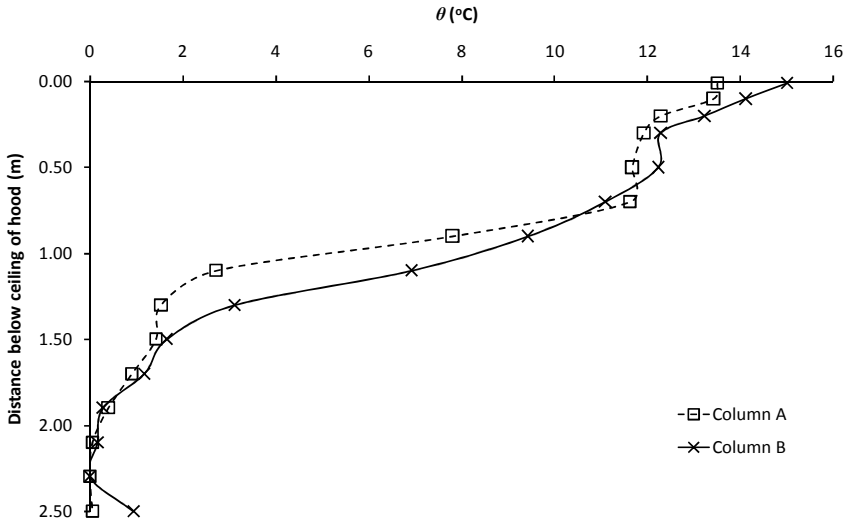

Figure G122: Experiment E227

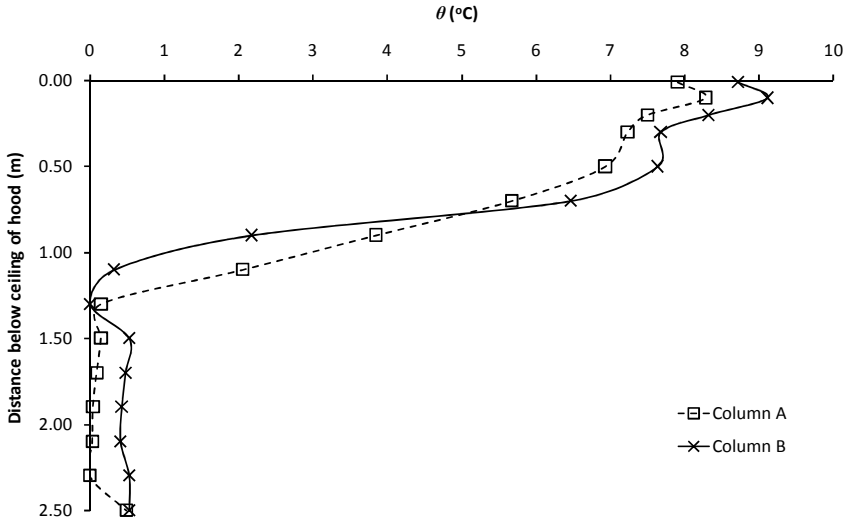

Figure G123: Experiment E228

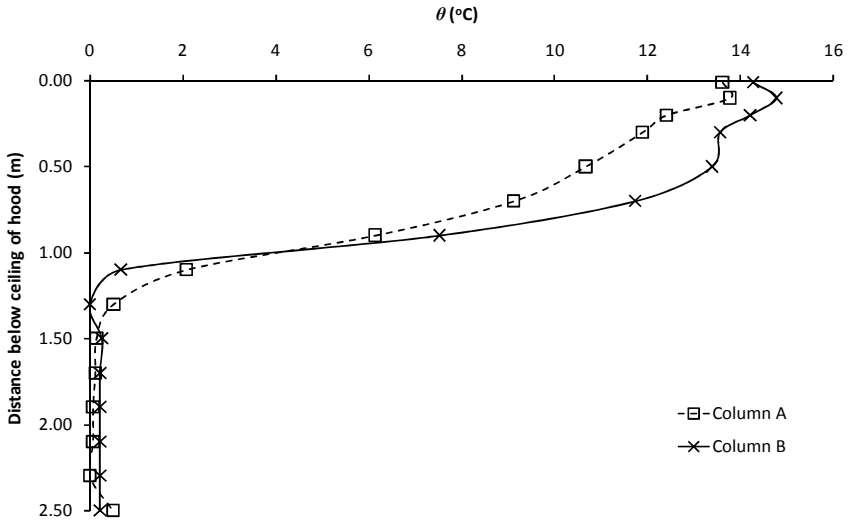

Figure G124: Experiment E229

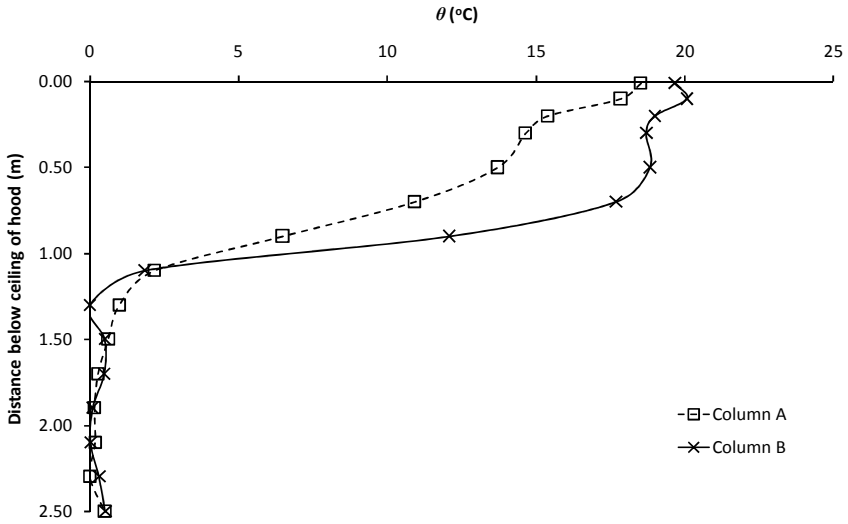

Figure G125: Experiment E230

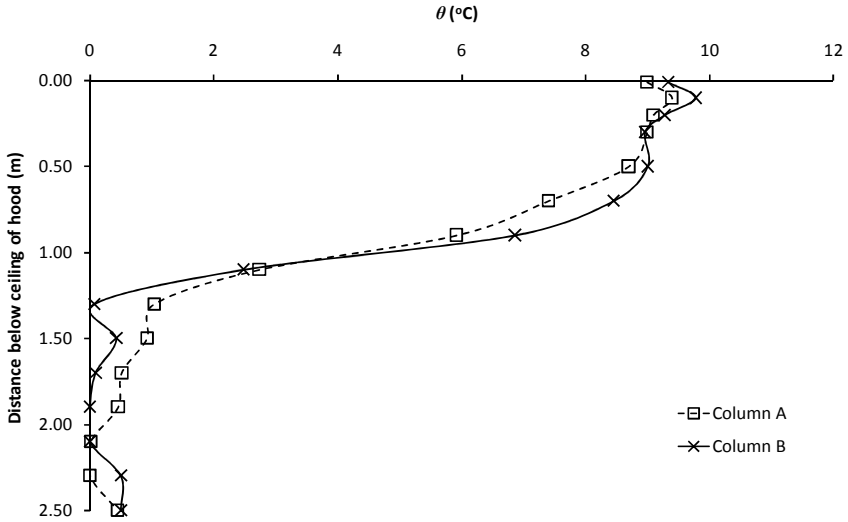

Figure G126: Experiment E231

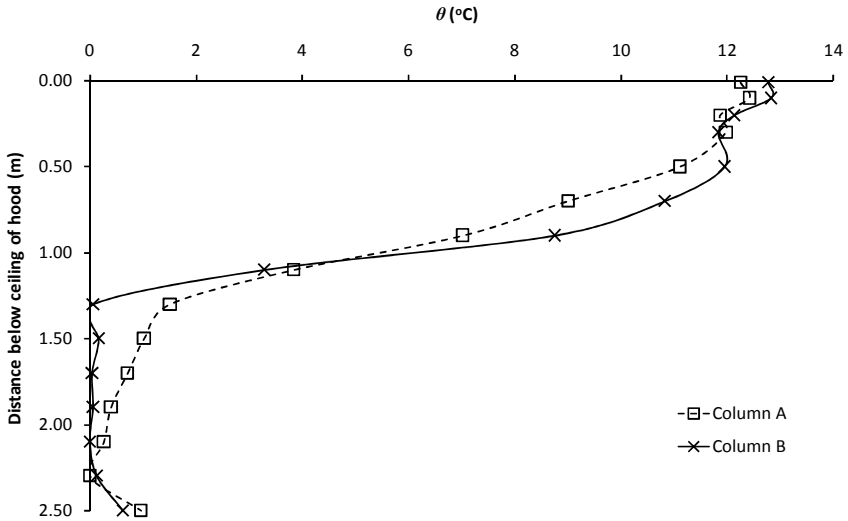

Figure G127: Experiment E232

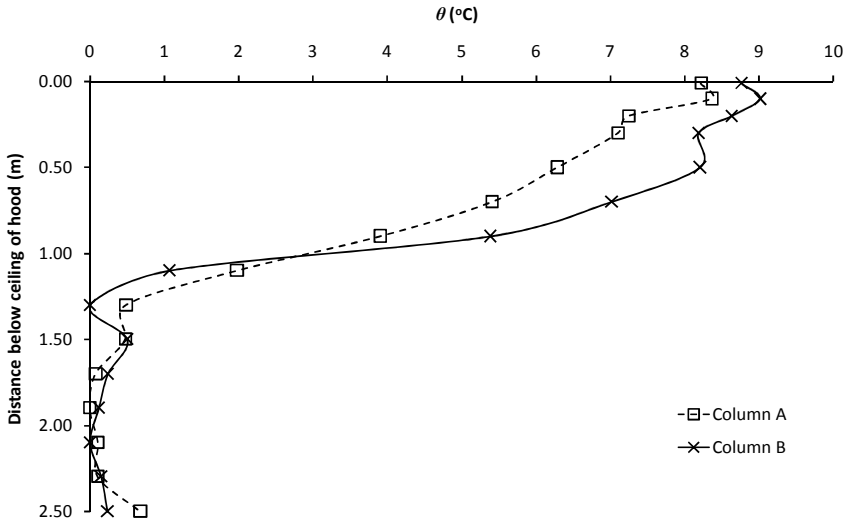

Figure G128: Experiment E233

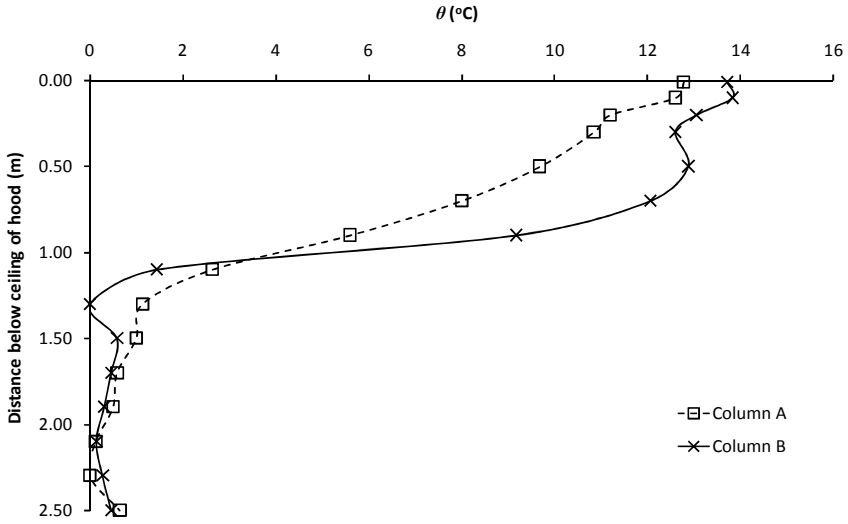

Figure G129: Experiment E234

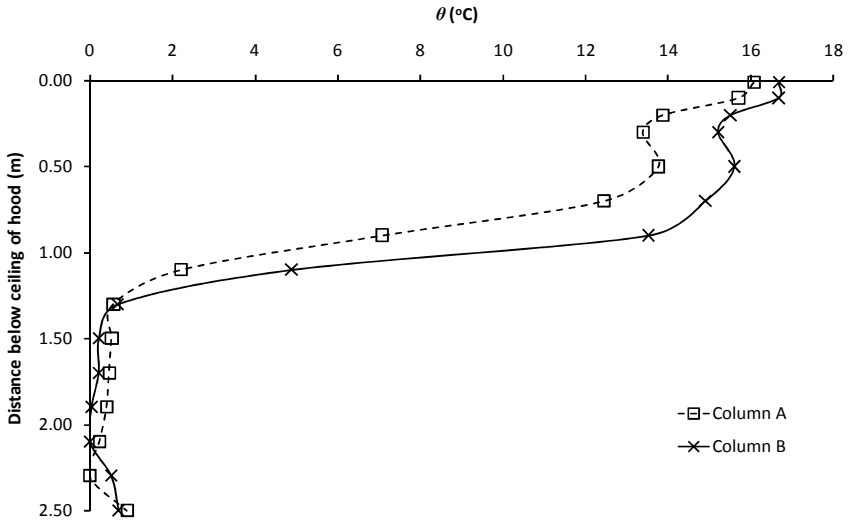

Figure G130: Experiment E235

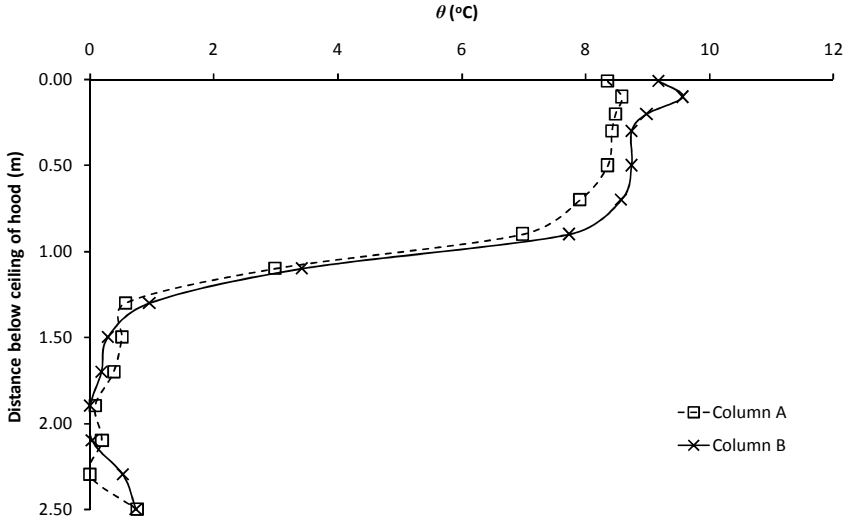

Figure G131: Experiment E236

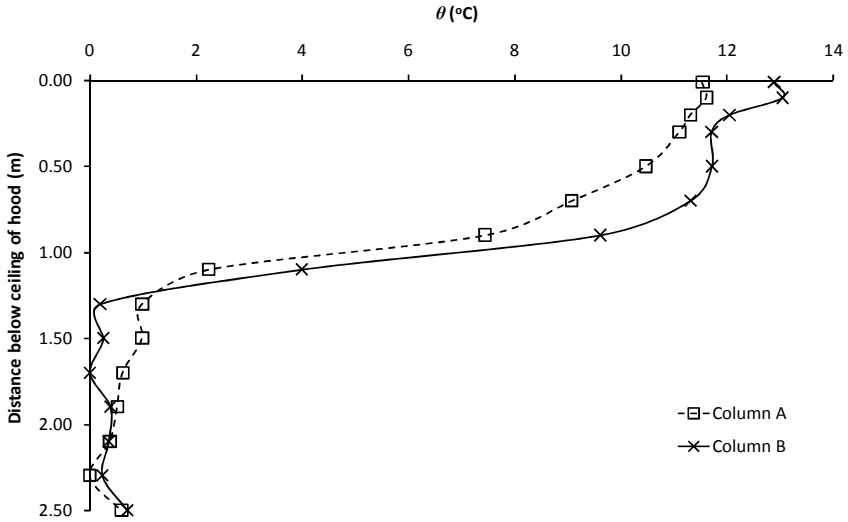

Figure G132: Experiment E237

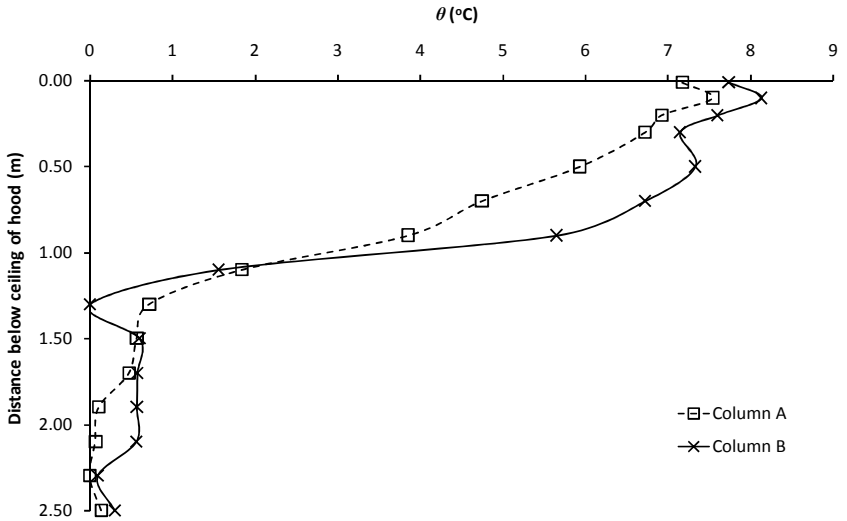

Figure G133: Experiment E238

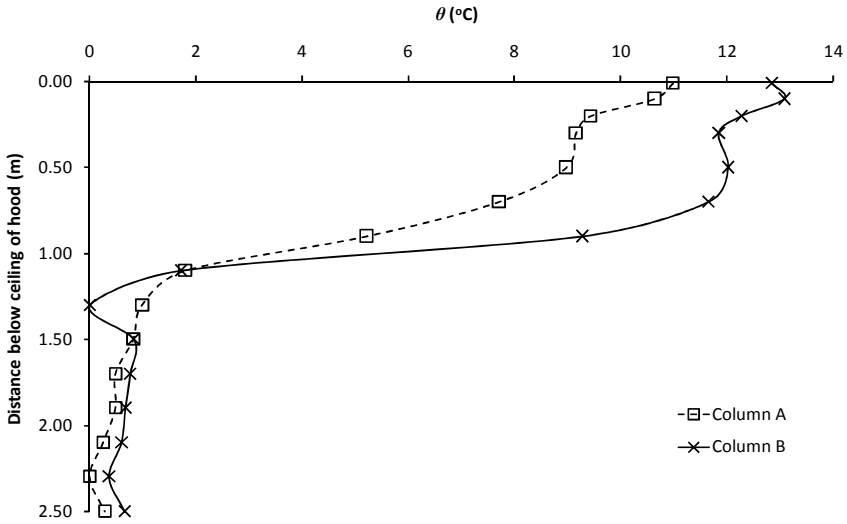

Figure G134: Experiment E239

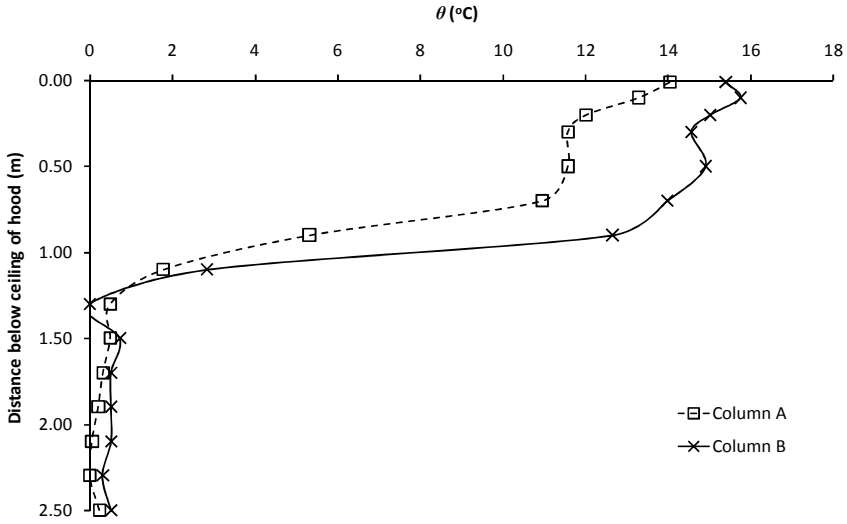

Figure G135: Experiment E240

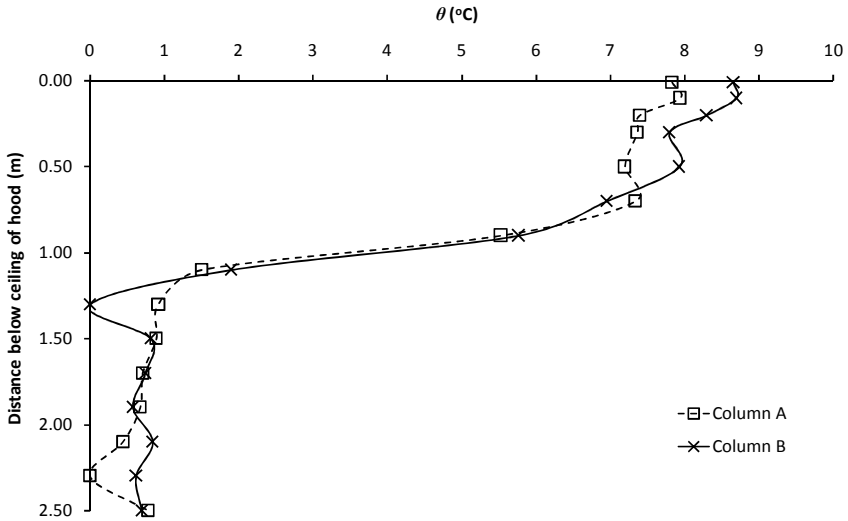

Figure G136: Experiment E241

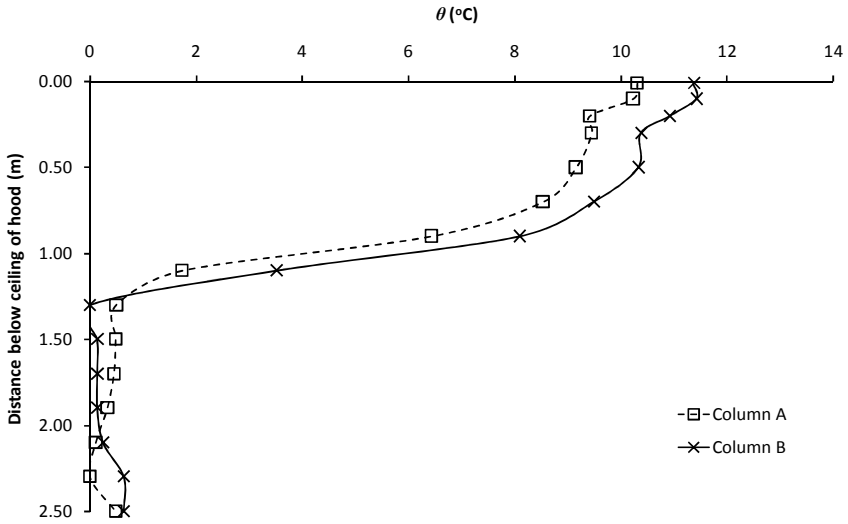

Figure G137: Experiment E242

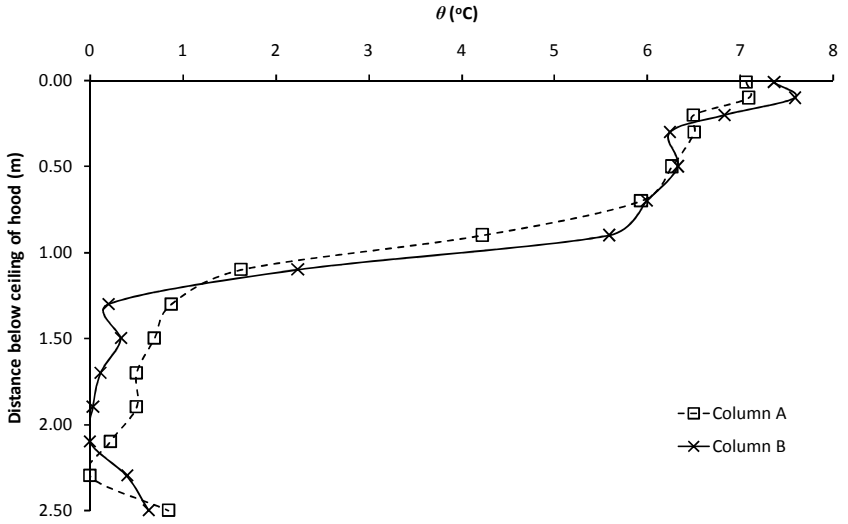

Figure G138: Experiment E243

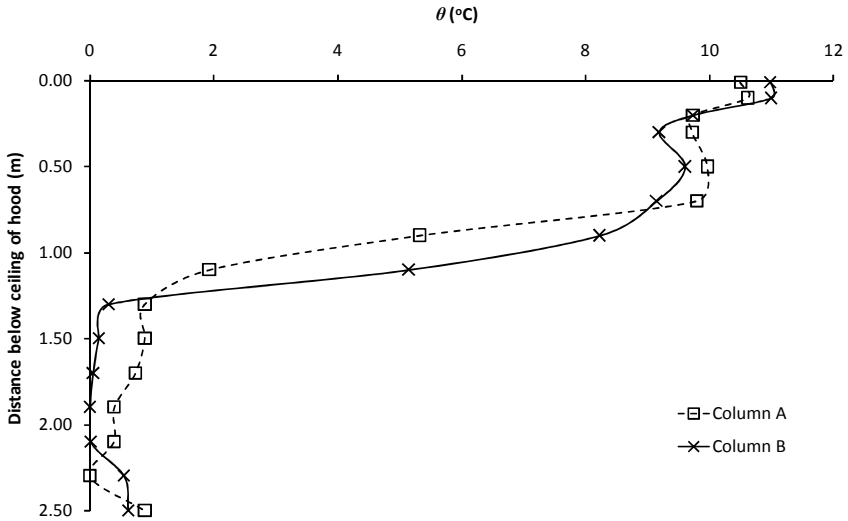

Figure G139: Experiment E244

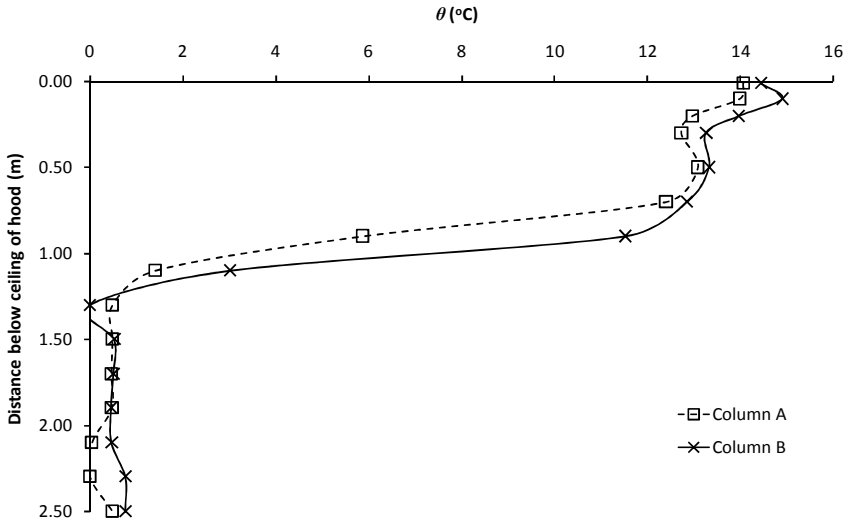

Figure G140: Experiment E245

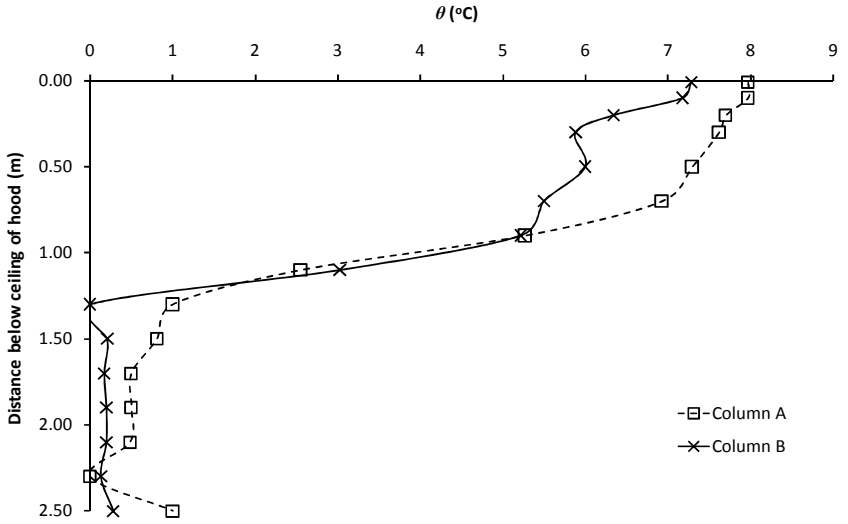

Figure G141: Experiment E246

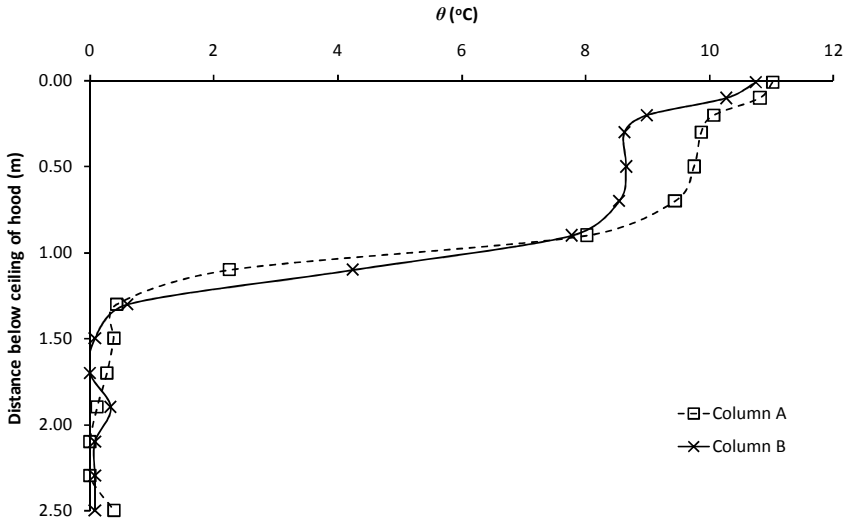

Figure G142: Experiment E247

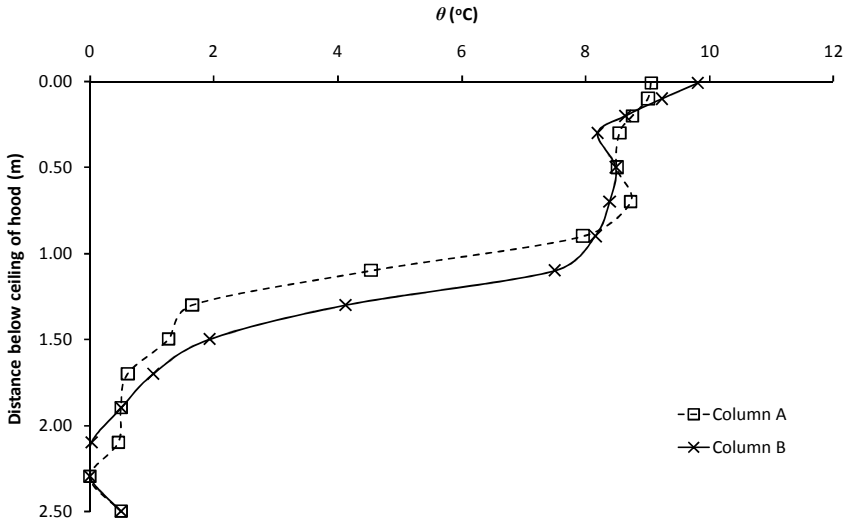

Figure G143: Experiment E248

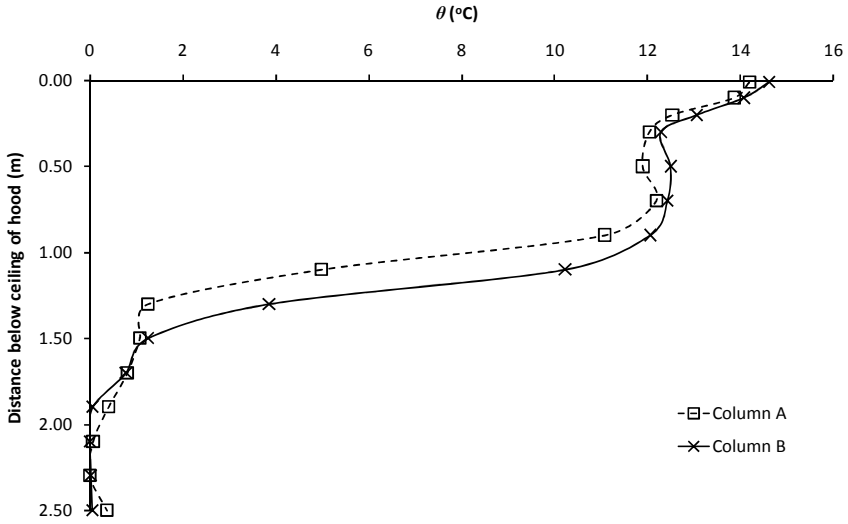

Figure G144: Experiment E249

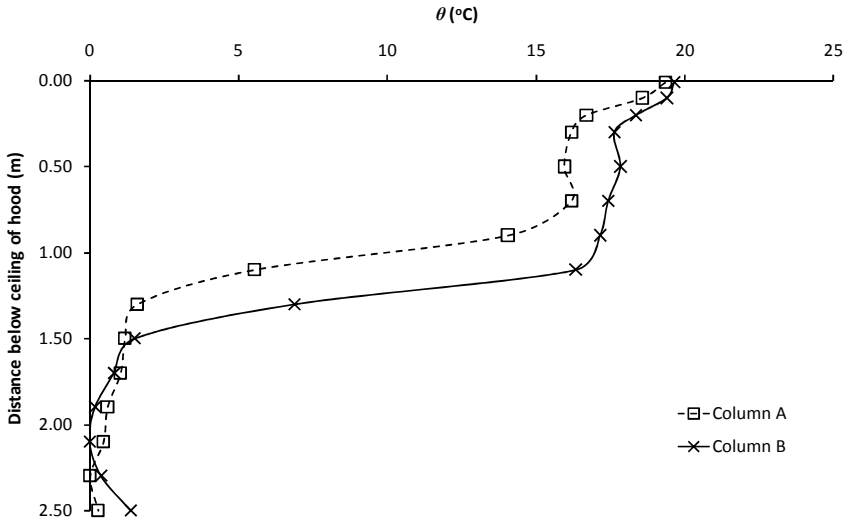

Figure G145: Experiment E250

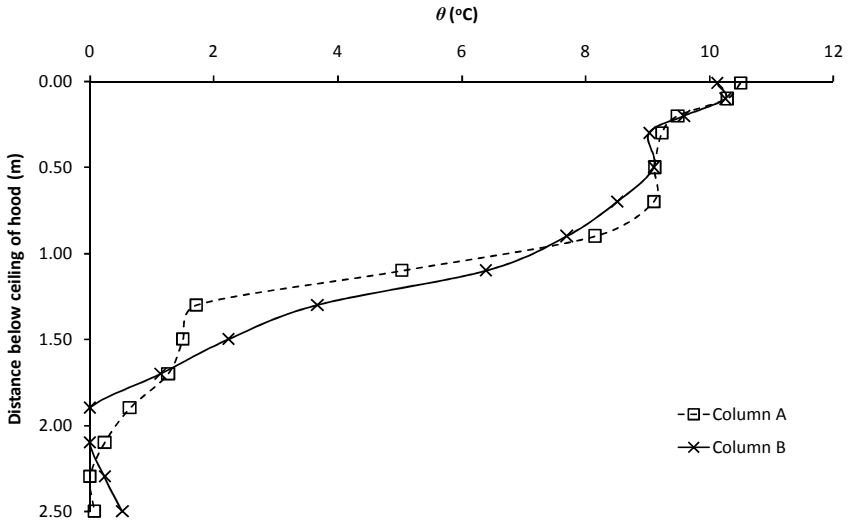

Figure G146: Experiment E251

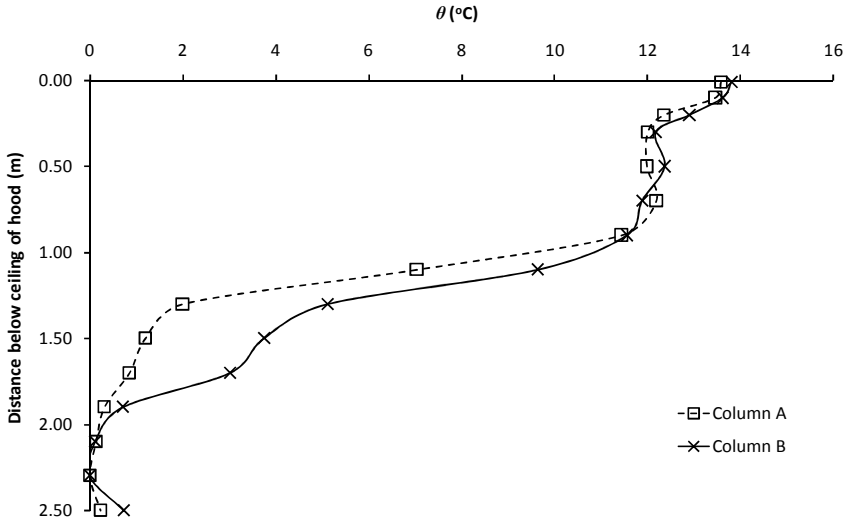

Figure G147: Experiment E252

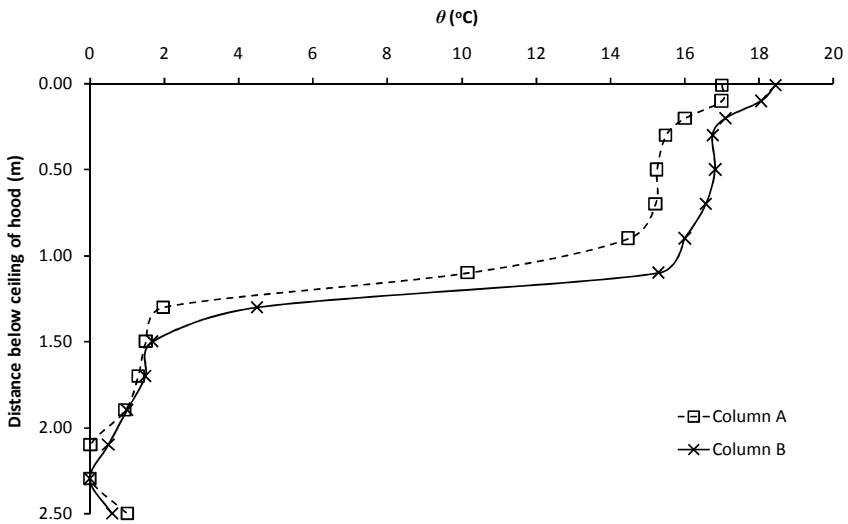

Figure G148: Experiment E253

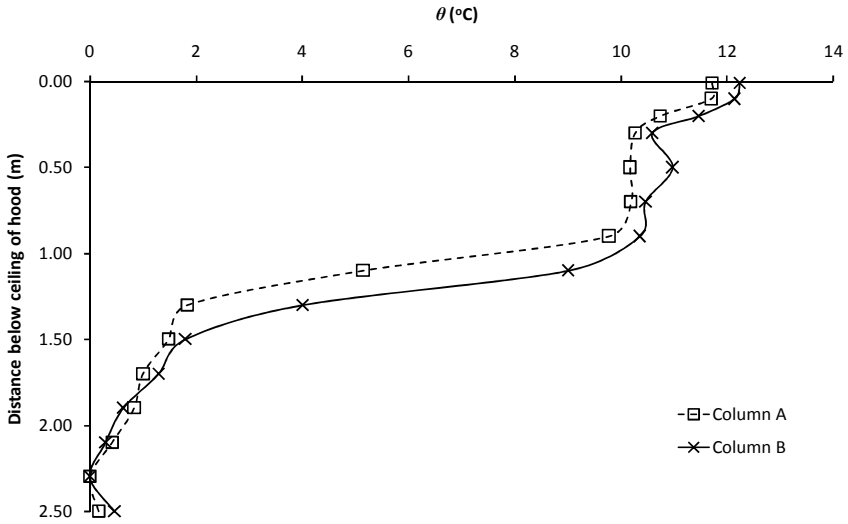

Figure G149: Experiment E254

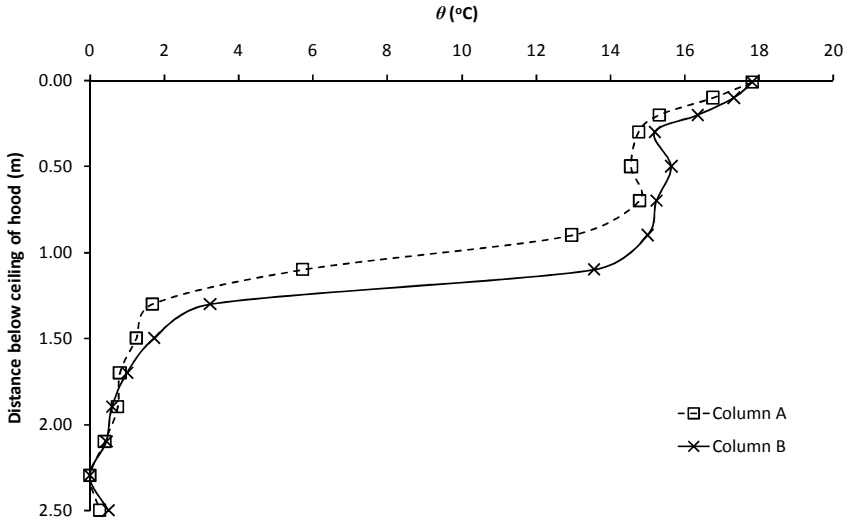

Figure G150: Experiment E255

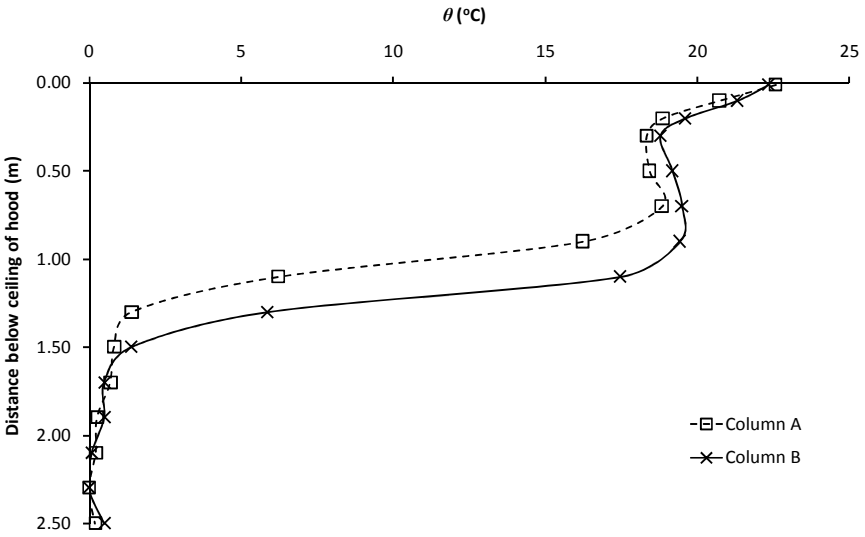

Figure G151: Experiment E256

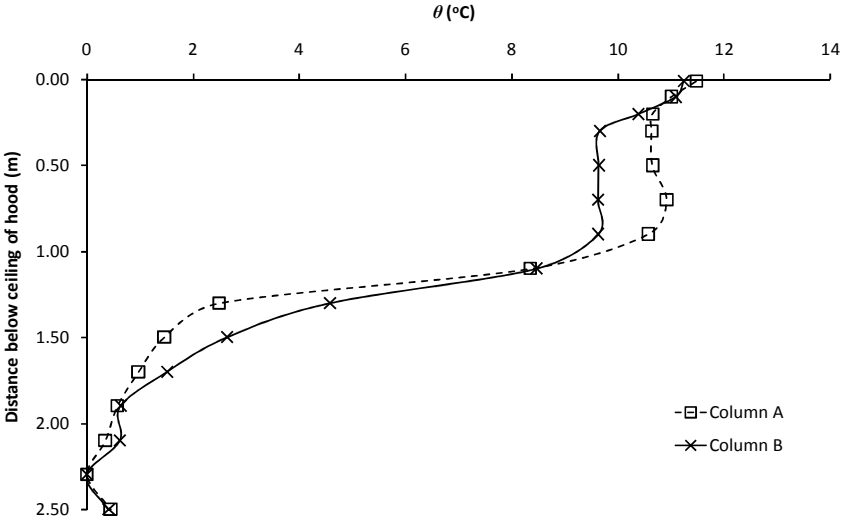

Figure G152: Experiment E257

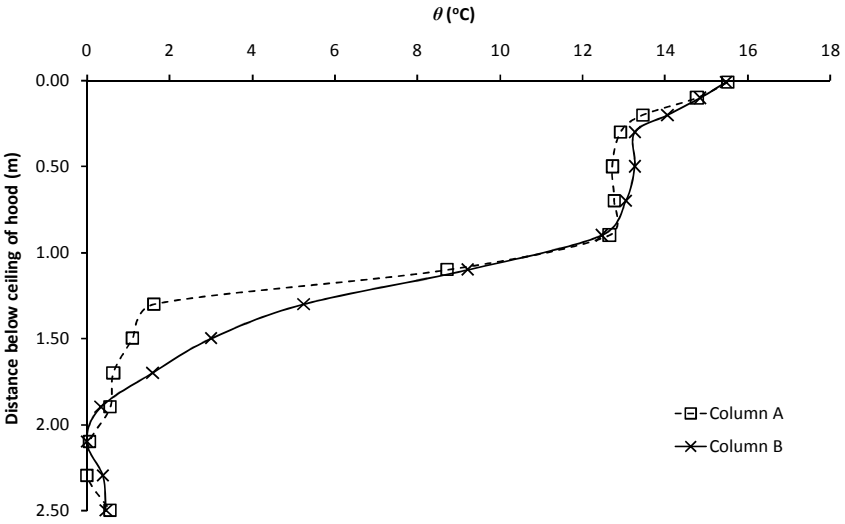

Figure G153: Experiment E258

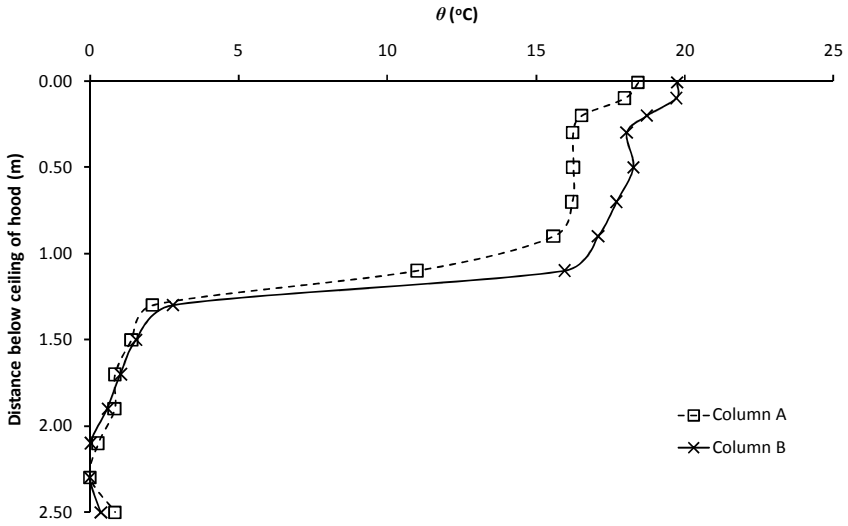

Figure G154: Experiment E259

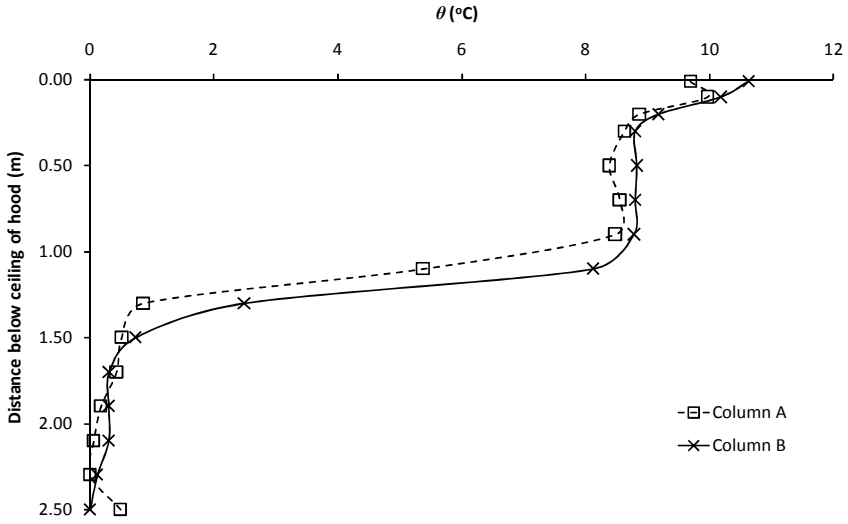

Figure G155: Experiment E260

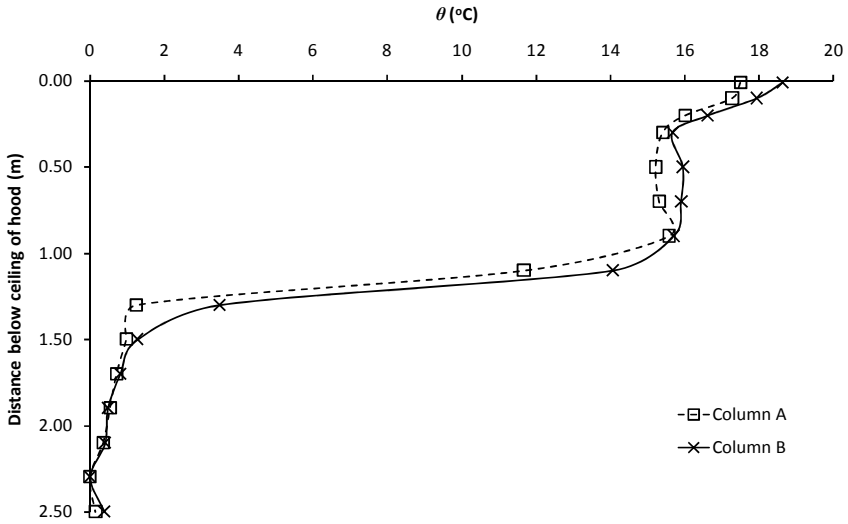

Figure G156: Experiment E261

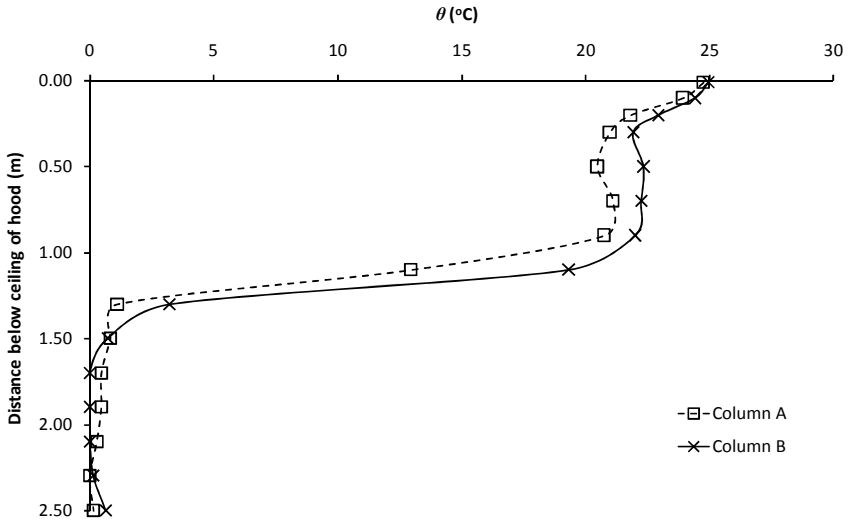

Figure G157: Experiment E262

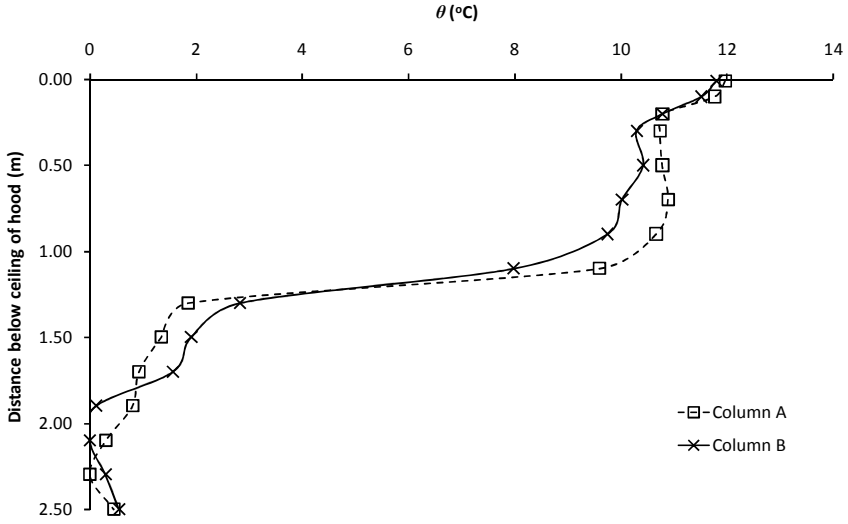

Figure G158: Experiment E263

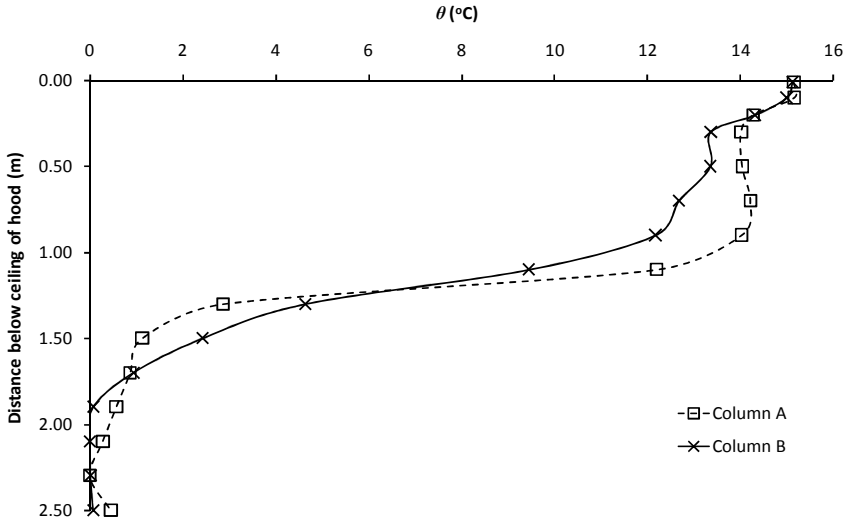

Figure G159: Experiment E264

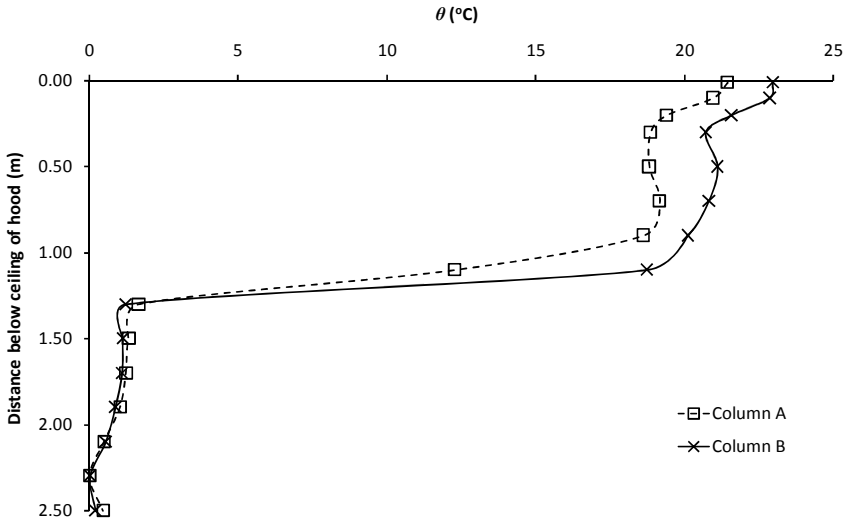

Figure G160: Experiment E265

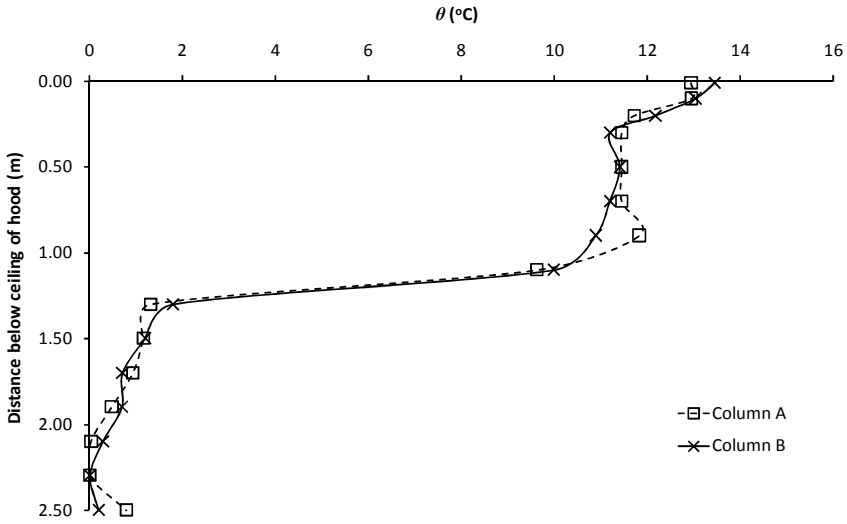

Figure G161: Experiment E266

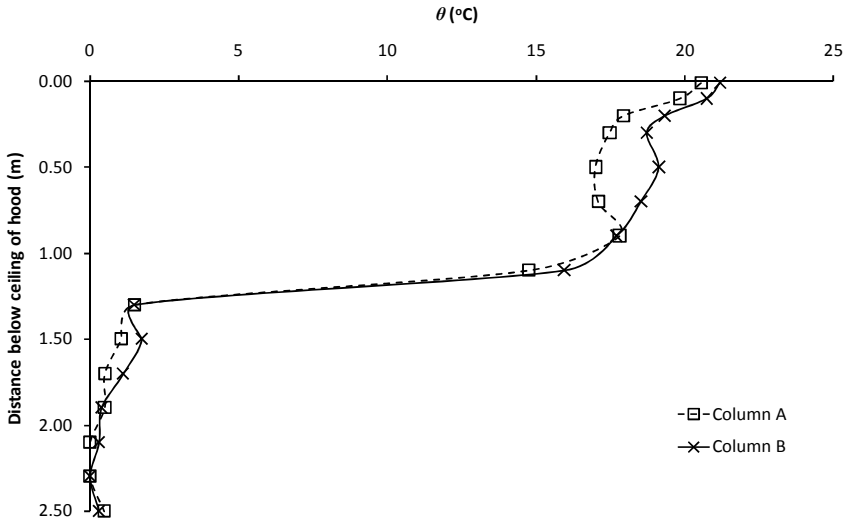

Figure G162: Experiment E267

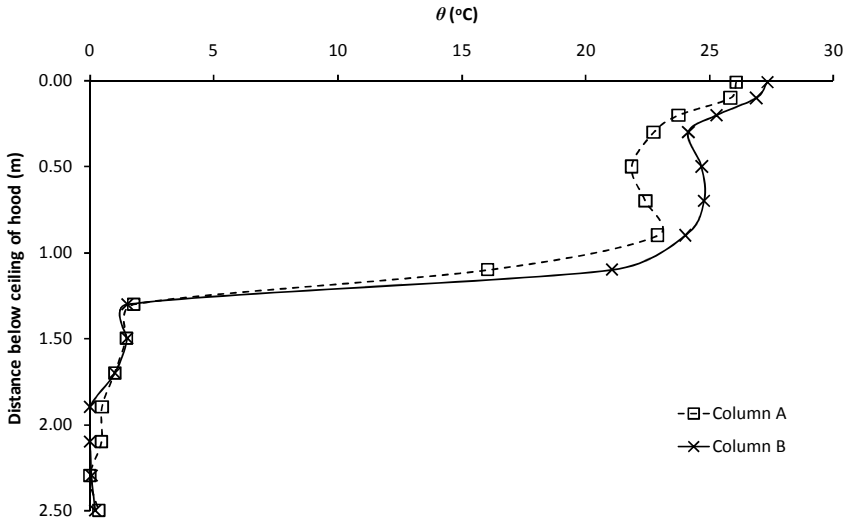

Figure G163: Experiment E268

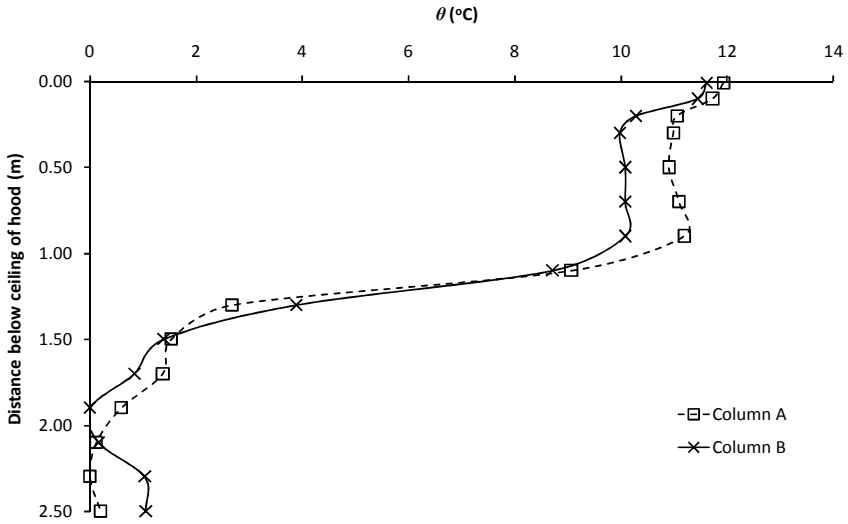

Figure G164: Experiment E269

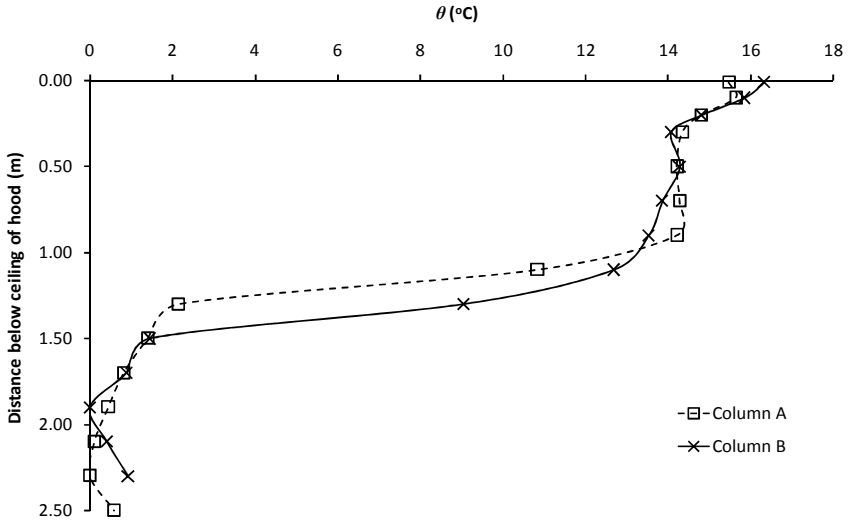

Figure G165: Experiment E270

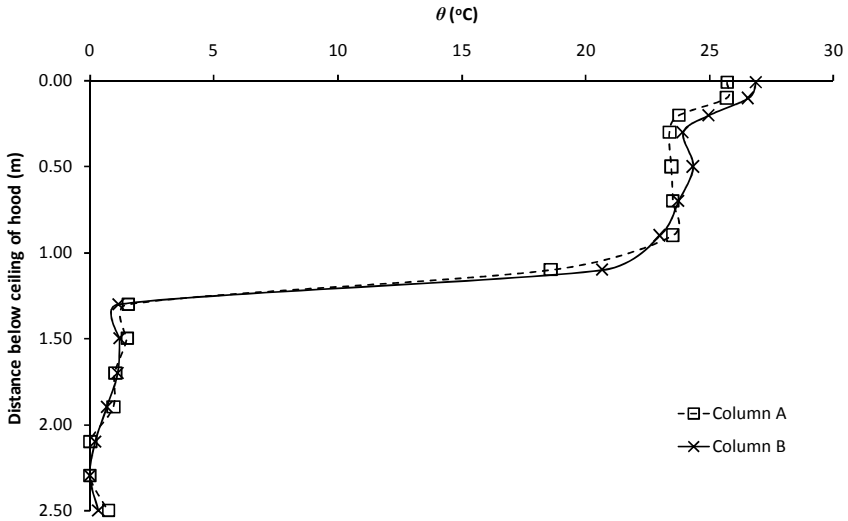

Figure G166: Experiment E271

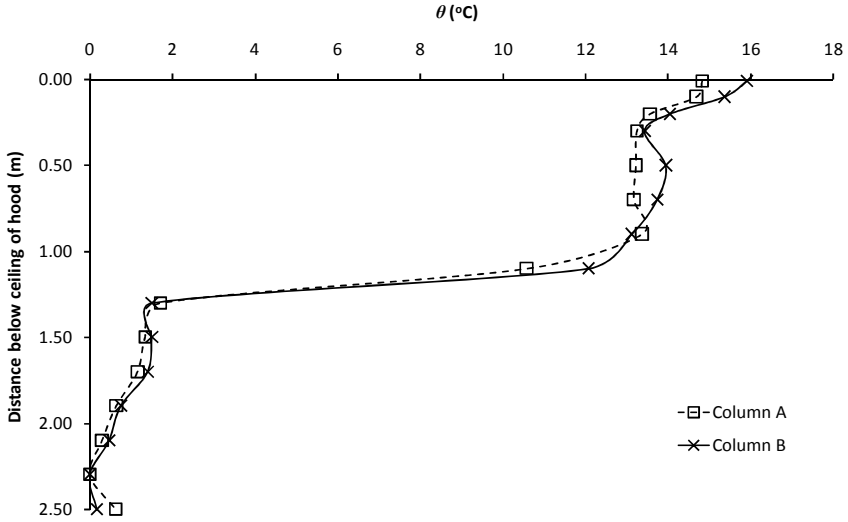

Figure G167: Experiment E272

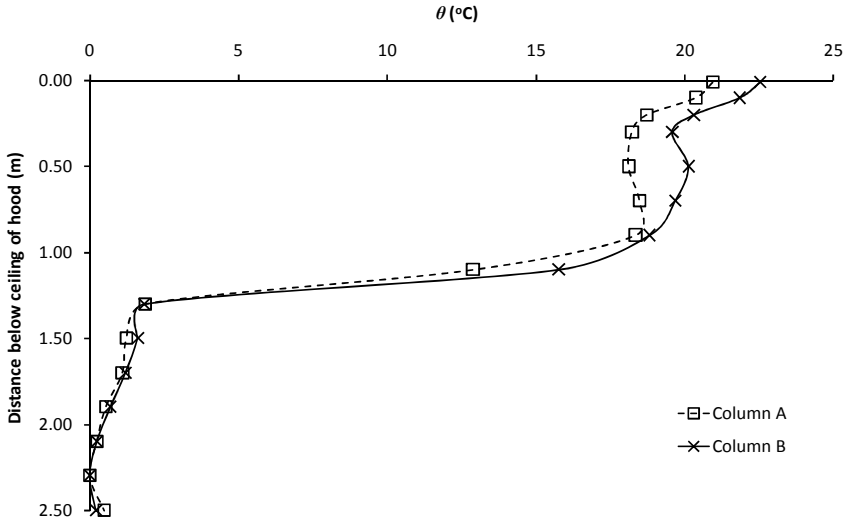

Figure G168: Experiment E273

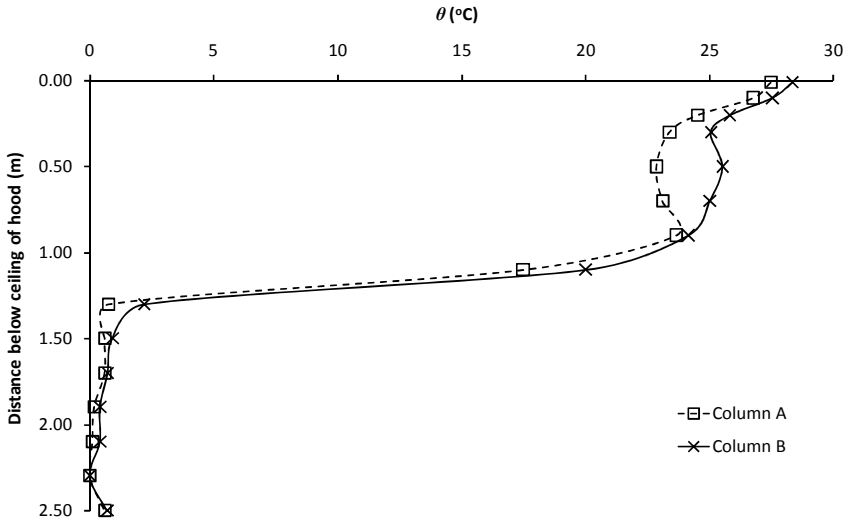

Figure G169: Experiment E274

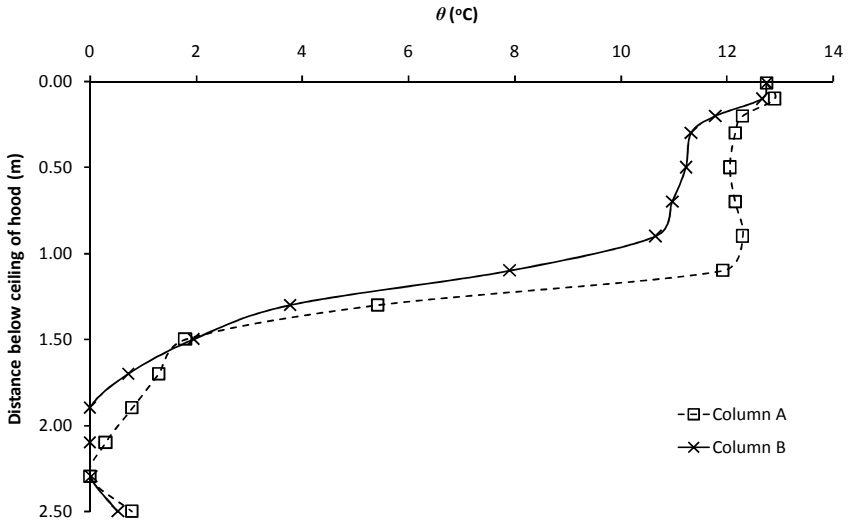

Figure G170: Experiment E275

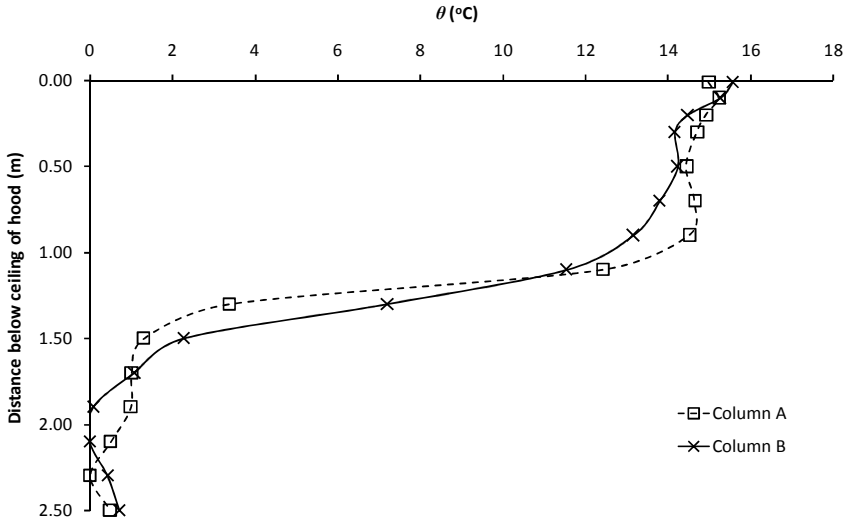

Figure G171: Experiment E276

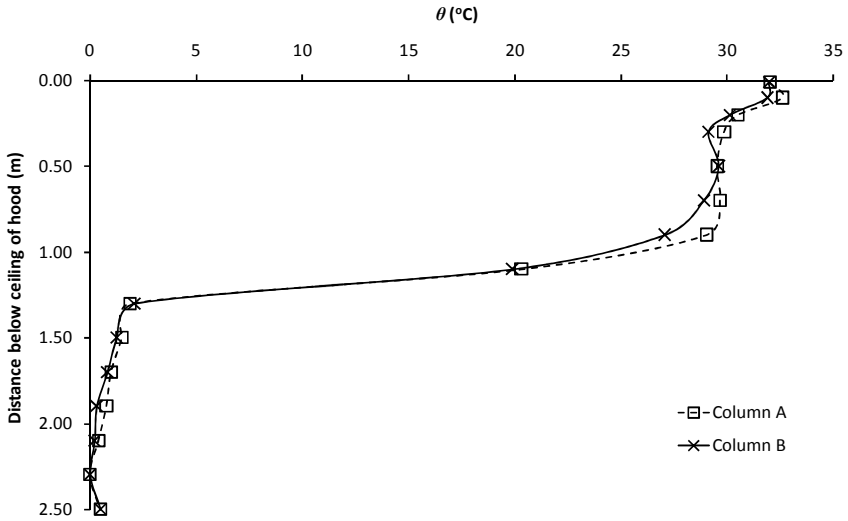

Figure G172: Experiment E277

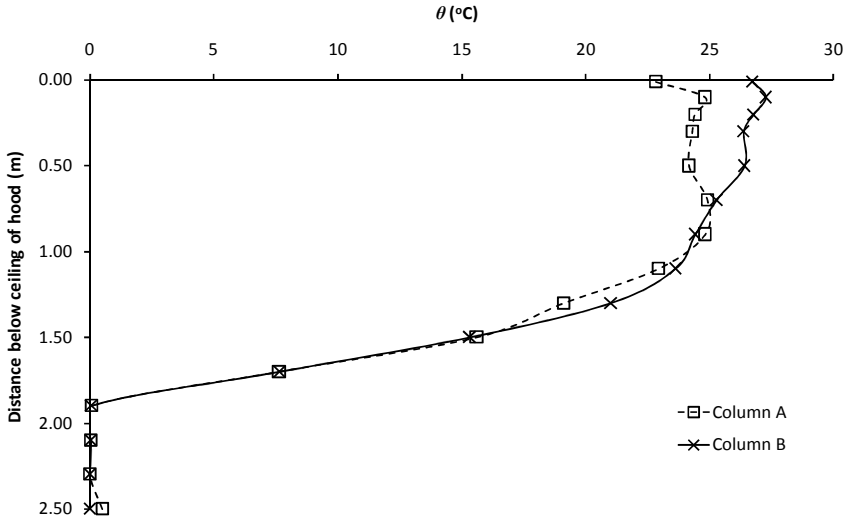

Figure G173: Experiment E278

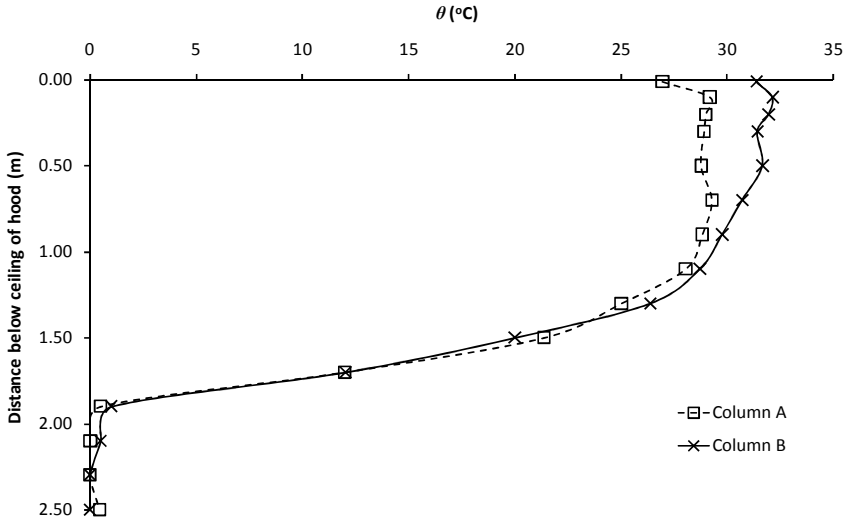

Figure G174: Experiment E279

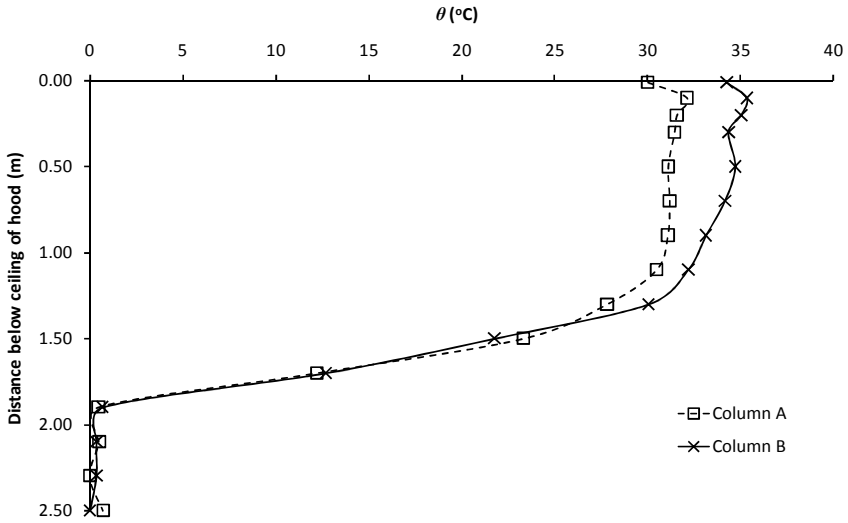

Figure G175: Experiment E280

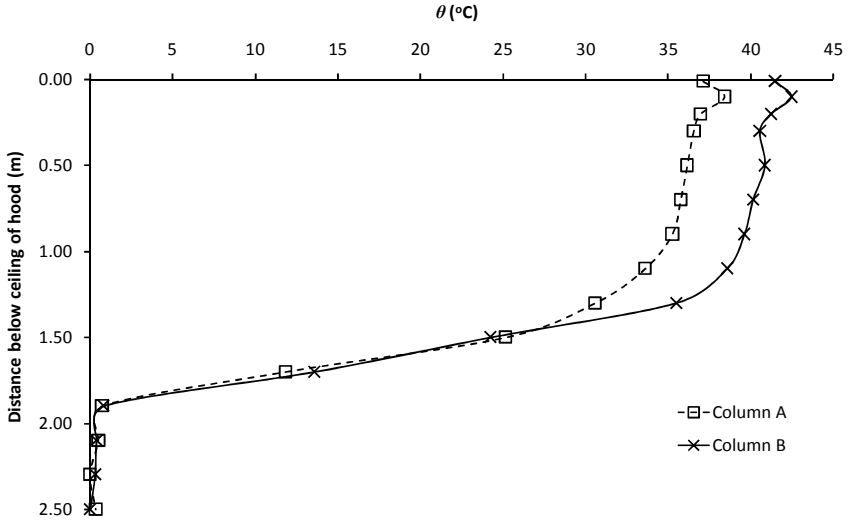

Figure G176: Experiment E281

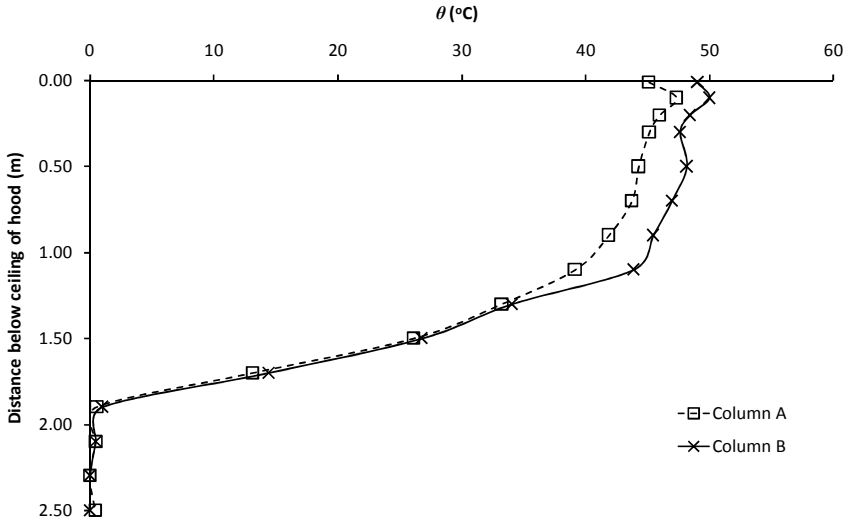

Figure G177: Experiment E282

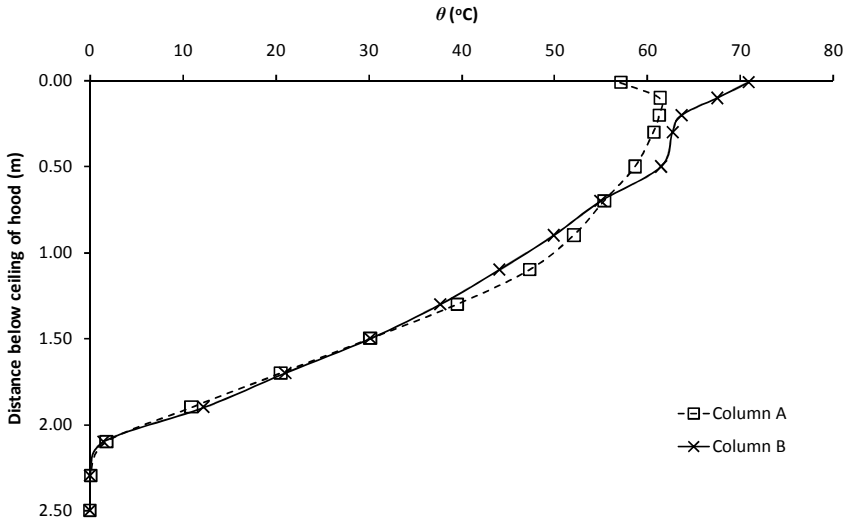

Figure G178: Experiment E288

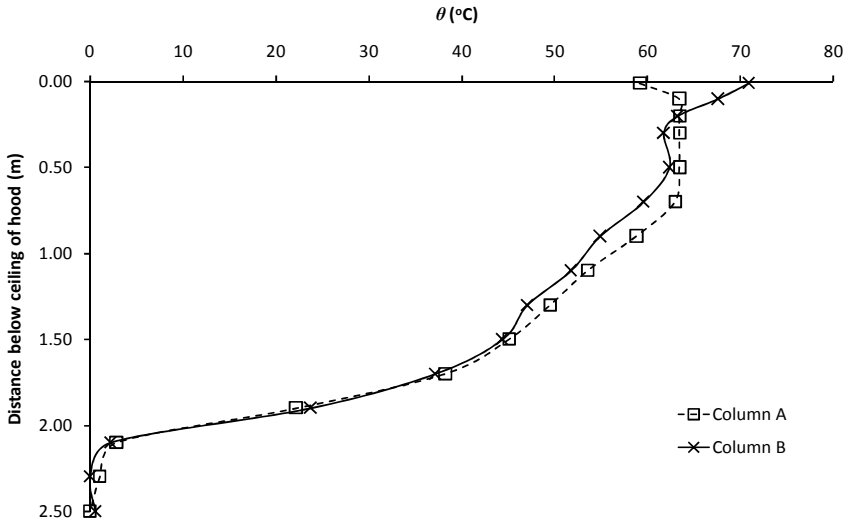

Figure G179: Experiment E289

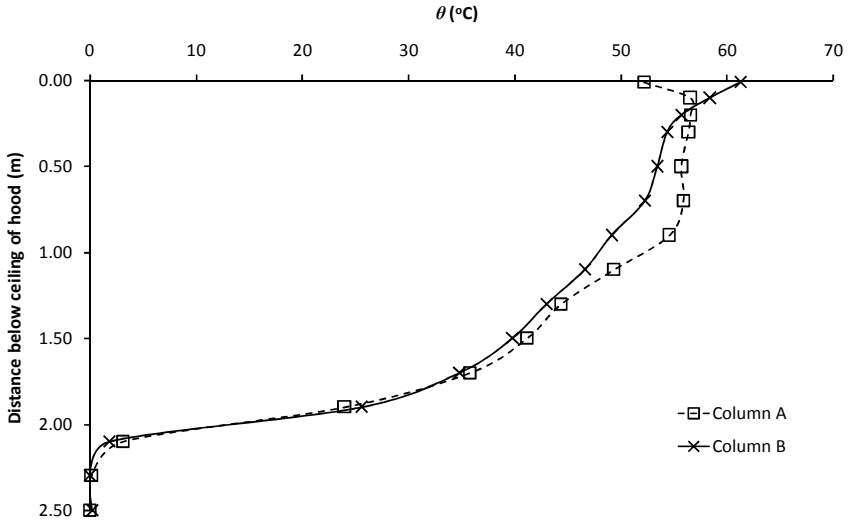

Figure G180: Experiment E290

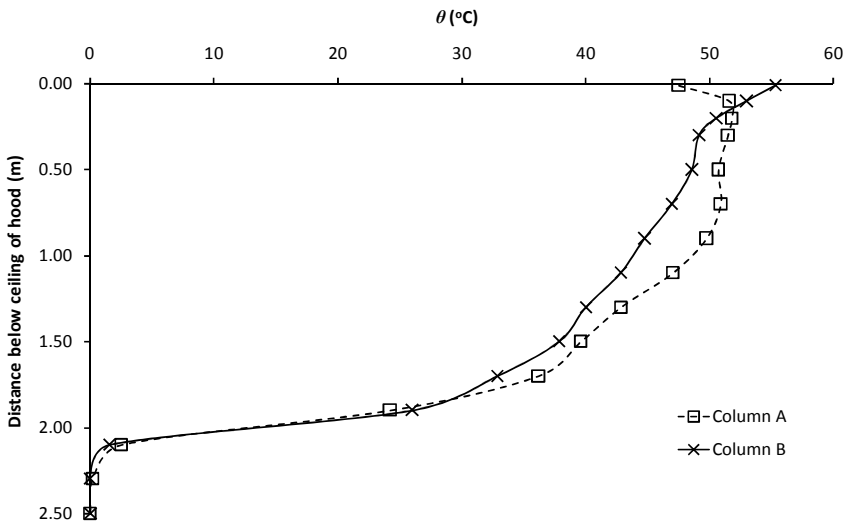

Figure G181: Experiment E291

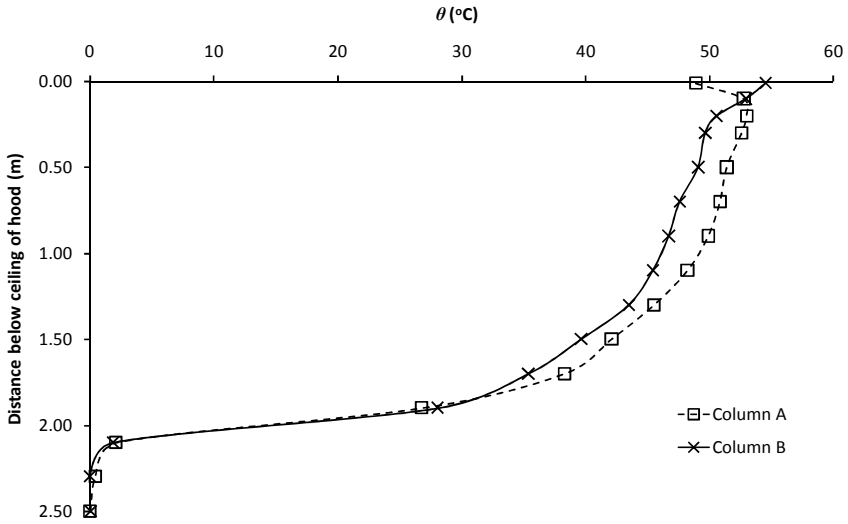

Figure G182: Experiment E292

Appendix H: Temperature profiles for Experiments T1 to T3

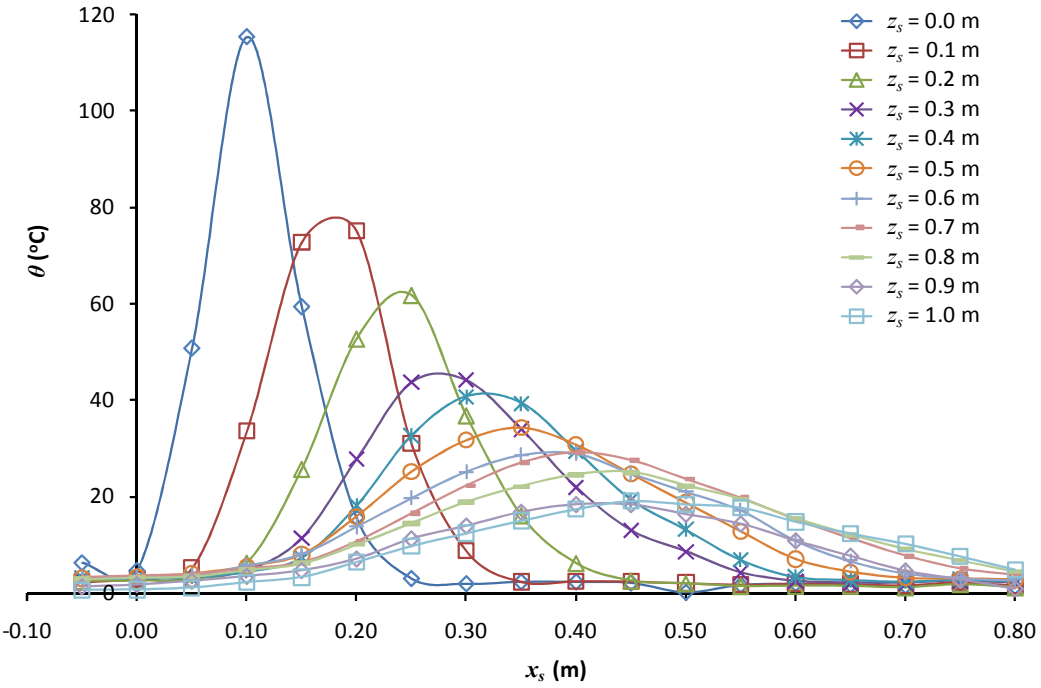

Figure H1: Experiment T1

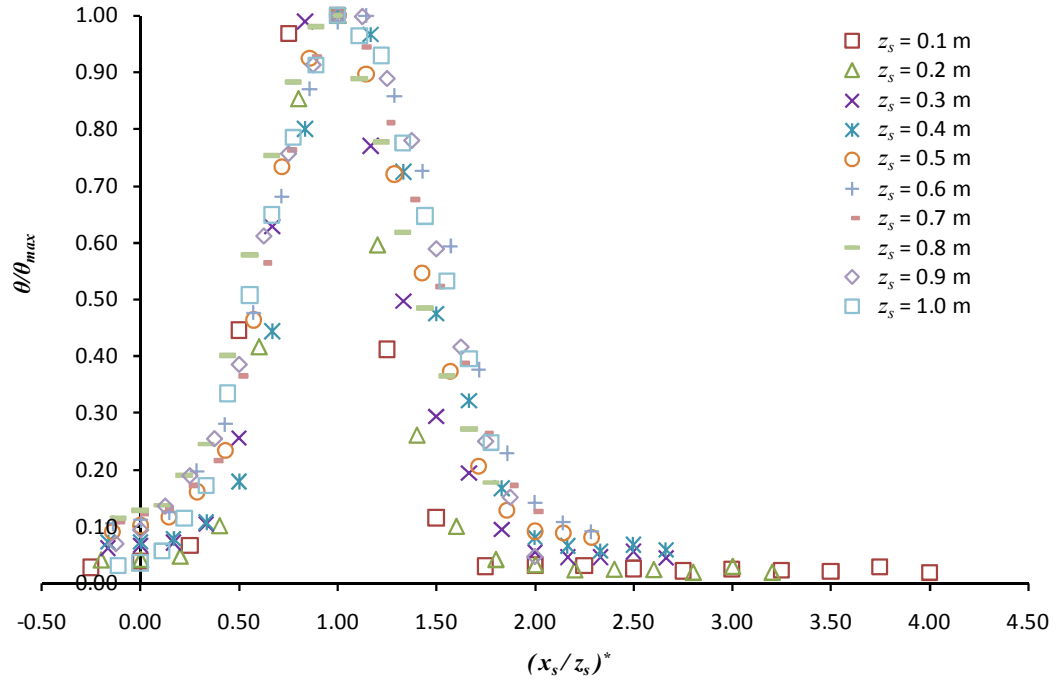

Figure H2: Normalised profiles, Experiment T1

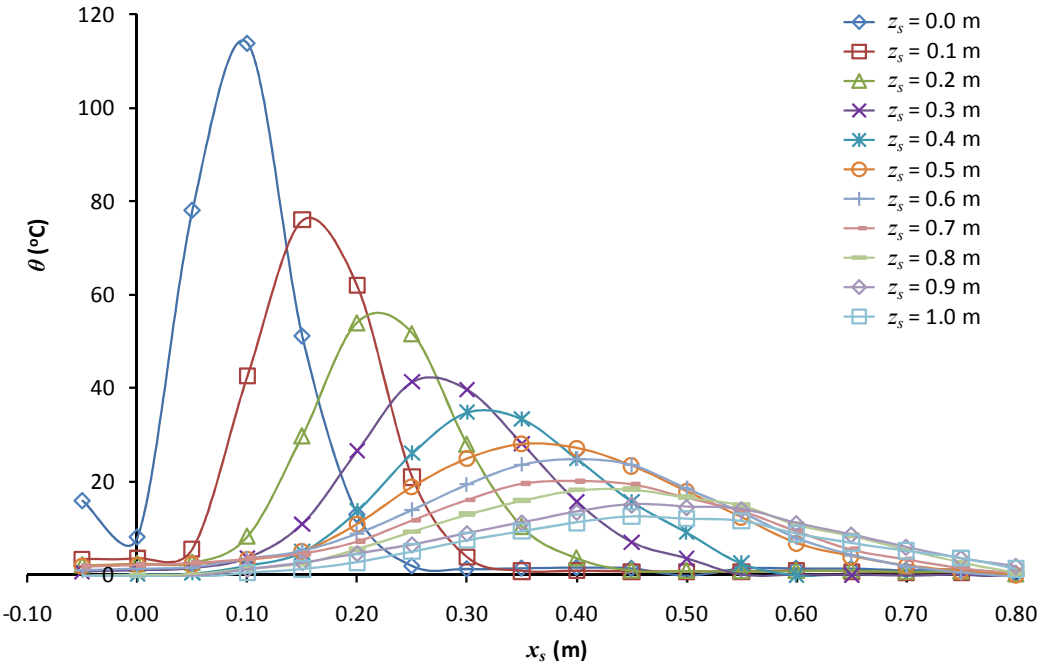

Figure H3: Experiment T2

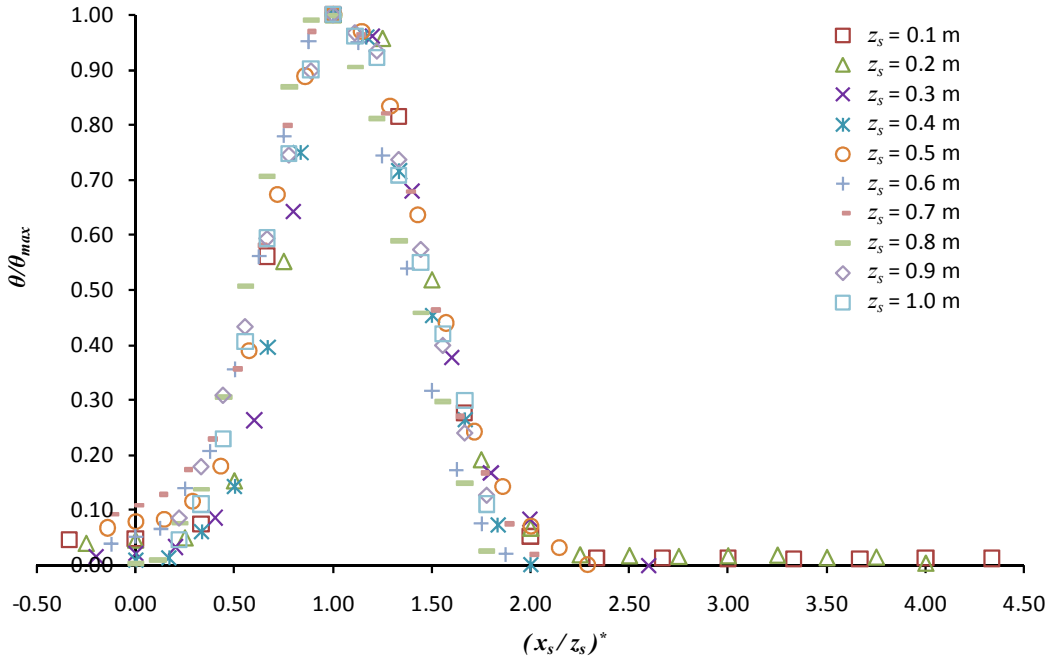

Figure H4: Normalised profiles, Experiment T2

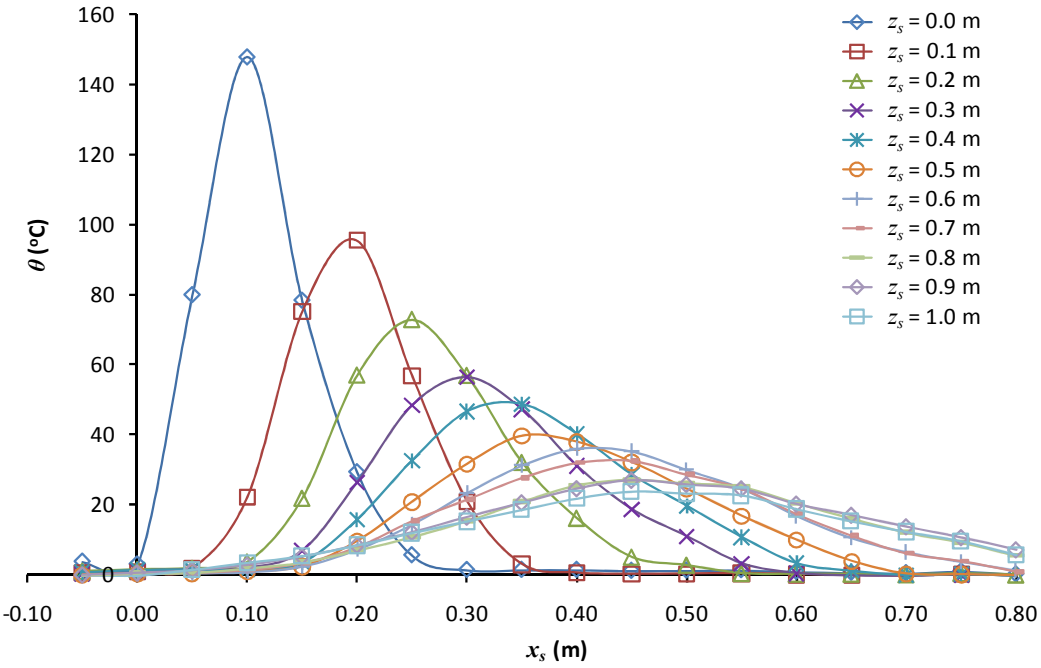

Figure H3: Experiment T3

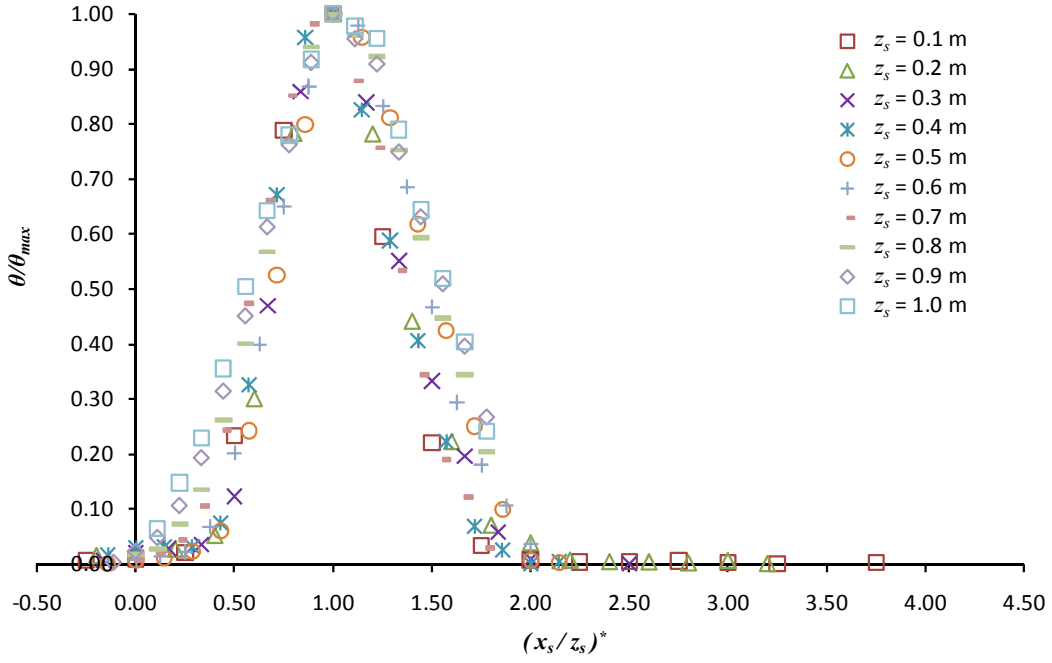

Figure H3: Normalised profiles, Experiment T3

Appendix I: Temperature profiles across and below the spill edge for the unchannelled flows

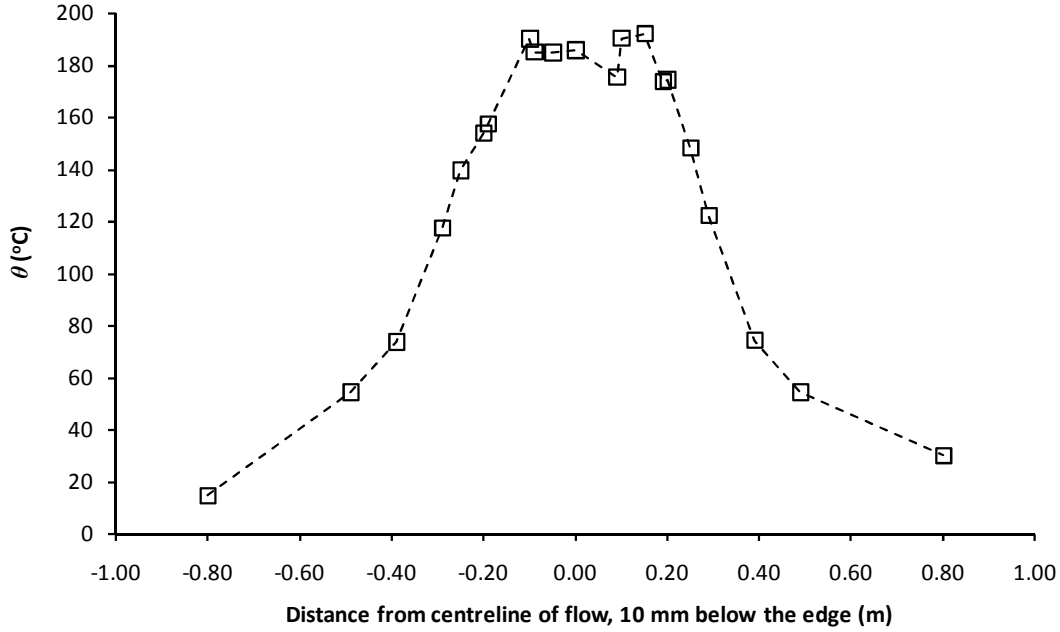

Figure I1: Temperature profile across spill edge, $\dot{Q}_t$ = 5 kW and W_s = 0.2 m

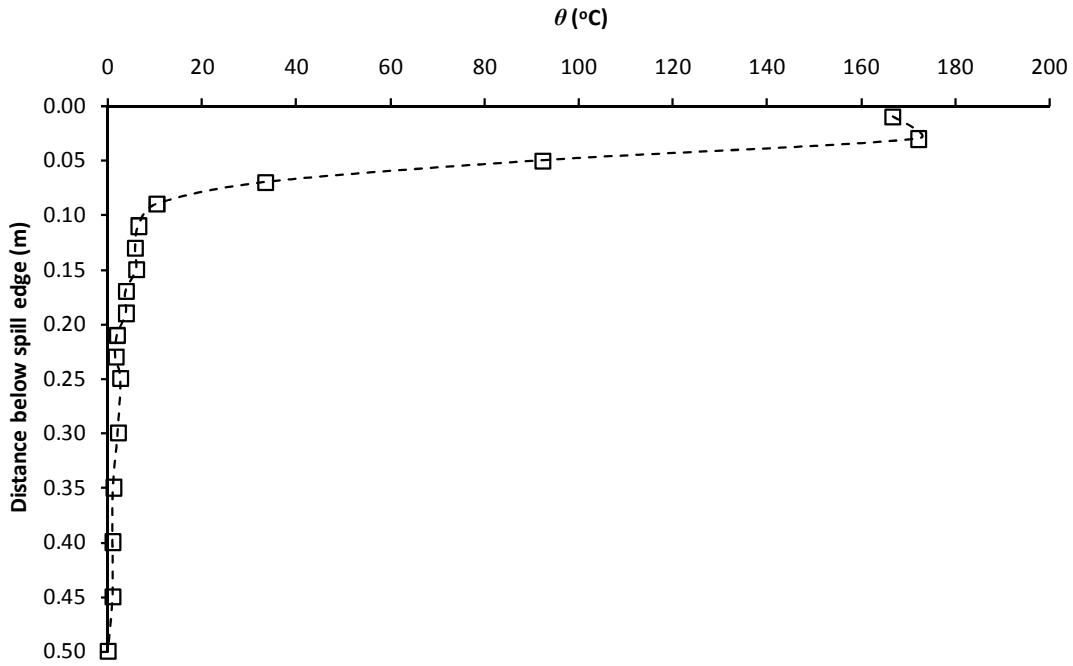

Figure I2: Temperature profile from Column C, $\dot{Q}_t$ = 5 kW and W_s = 0.2 m

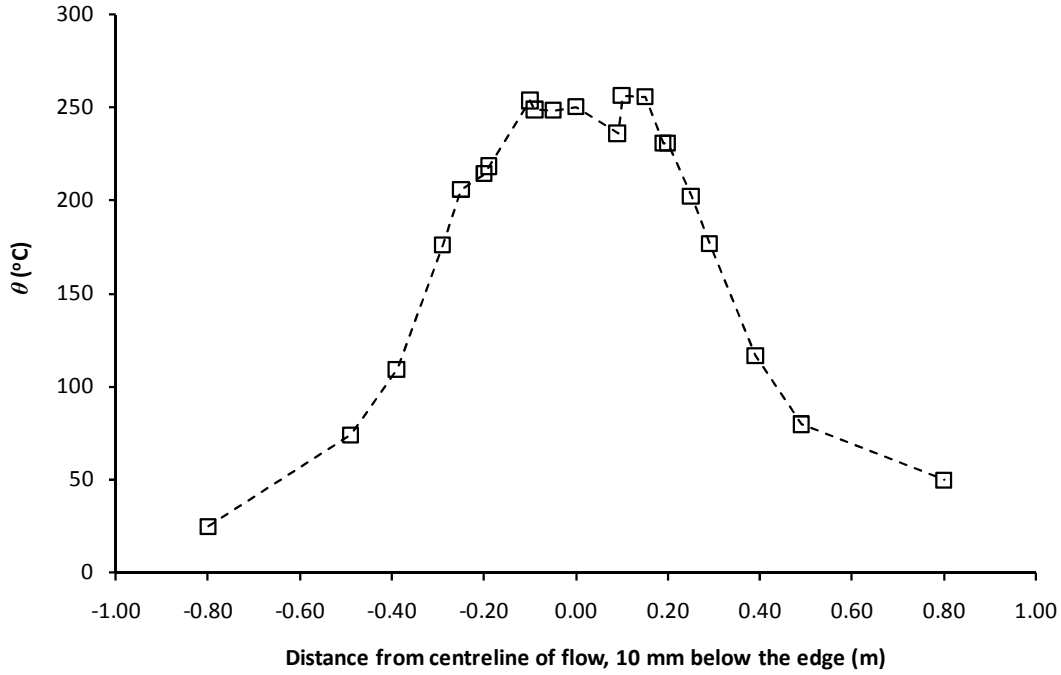

Figure I3: Temperature profile across spill edge, $\dot{Q}_t$ = 10 kW and W_s = 0.2 m

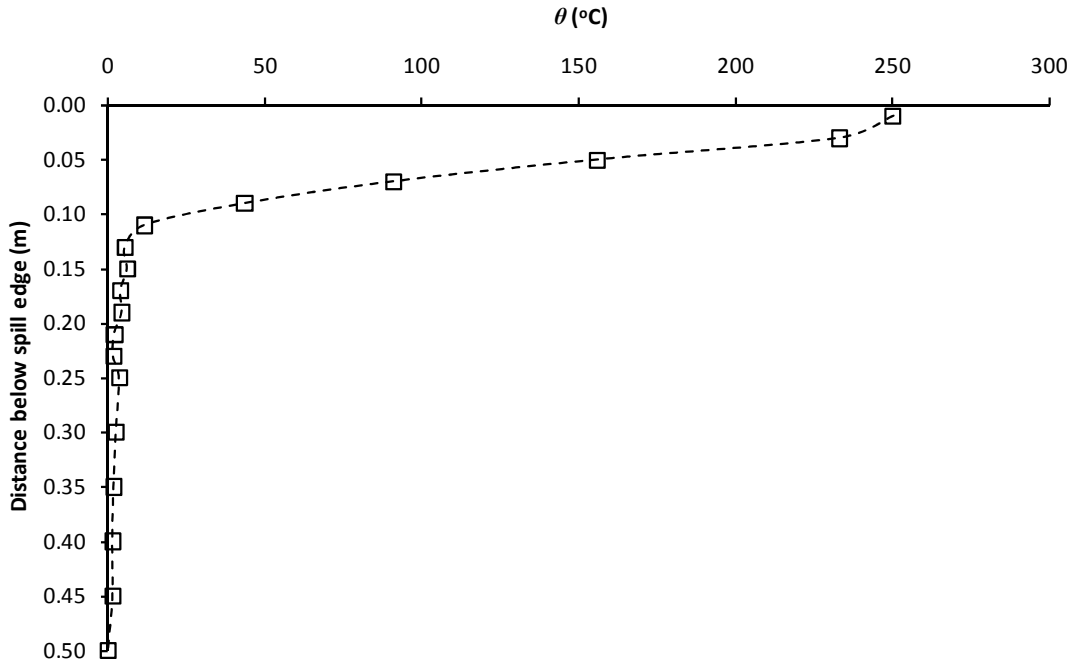

Figure I4: Temperature profile from Column C, $\dot{Q}_t$ = 10 kW and W_s = 0.2 m

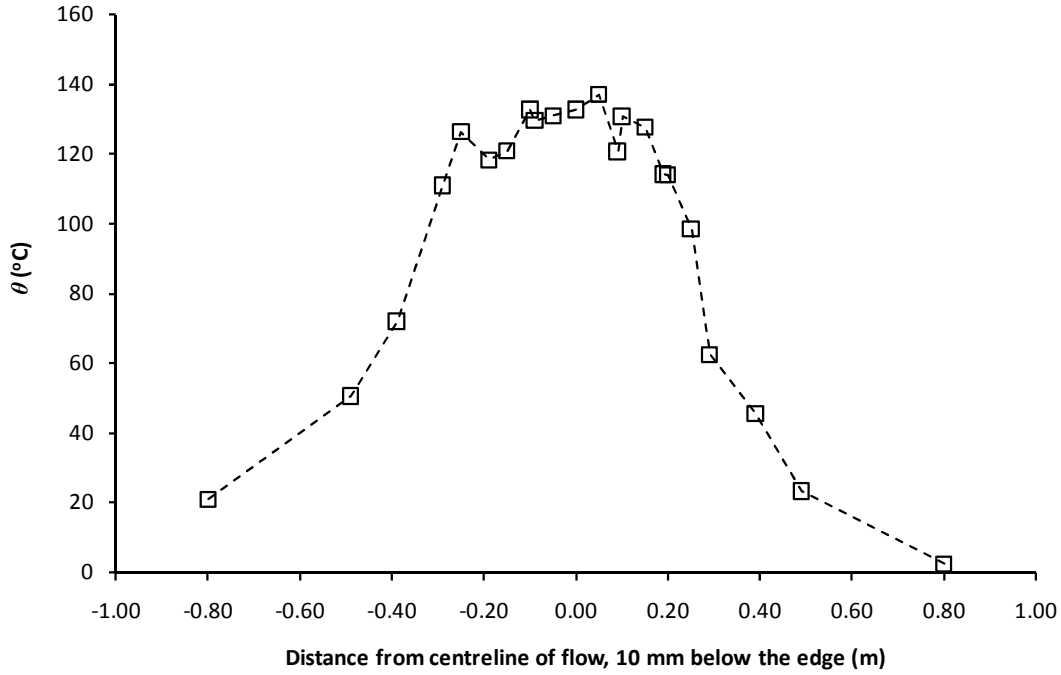

Figure I5: Temperature profile across spill edge, $\dot{Q}_t$ = 5 kW and W_s = 0.4 m

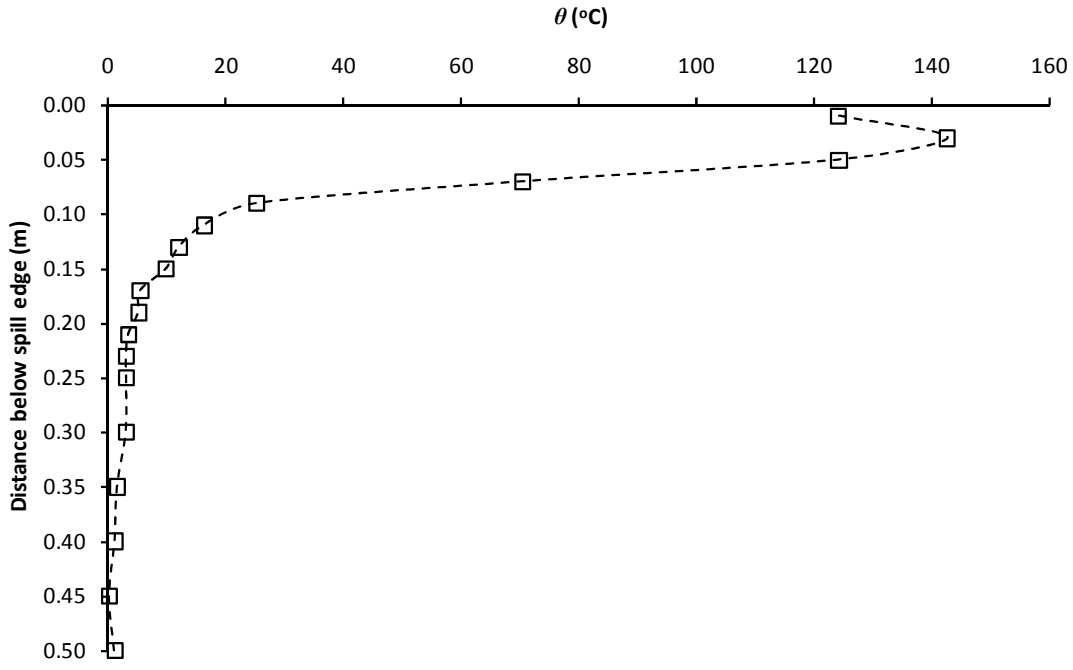

Figure I6: Temperature profile from Column C, $\dot{Q}_t$ = 5 kW and W_s = 0.4 m

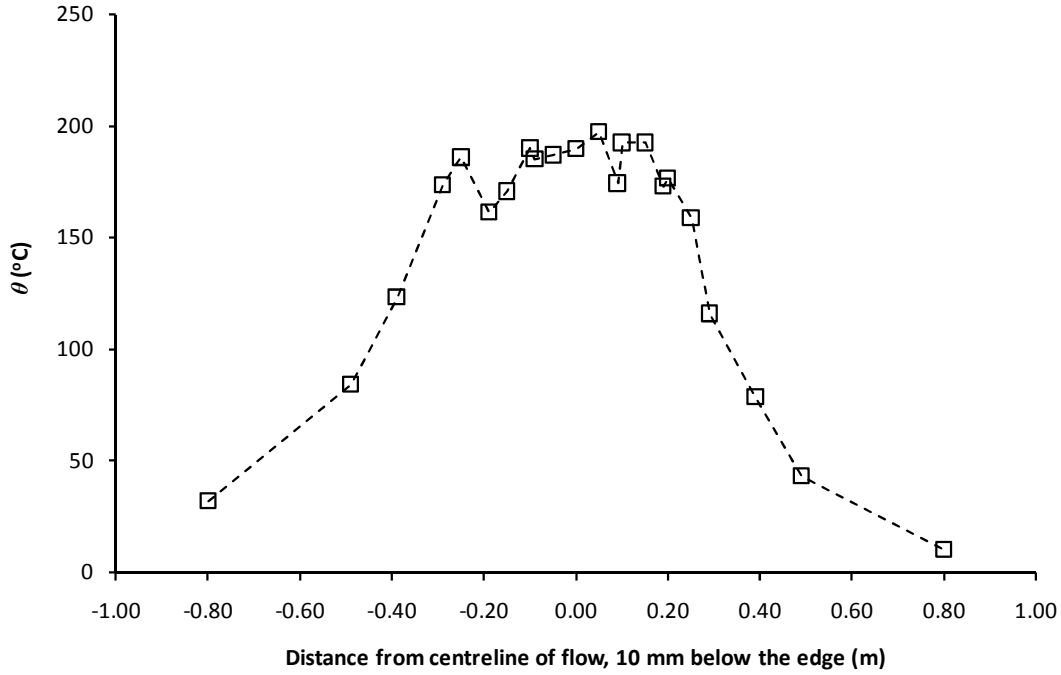

Figure I7: Temperature profile across spill edge, $\dot{Q}_t$ = 10 kW and W_s = 0.4 m

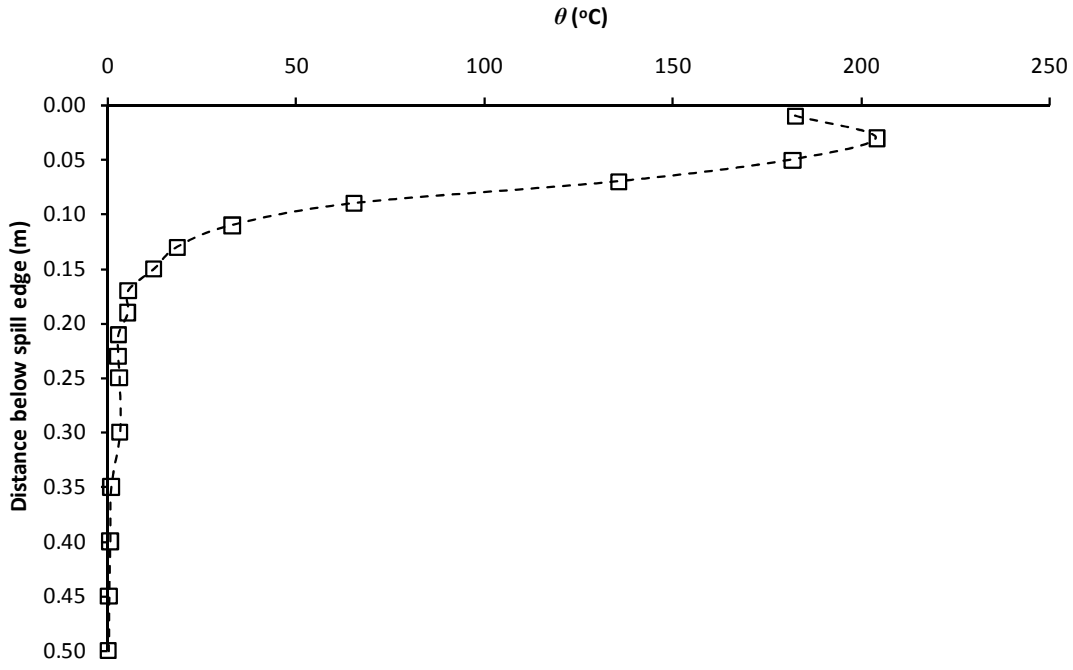

Figure I8: Temperature profile from Column C, $\dot{Q}_t$ = 10 kW and W_s = 0.4 m

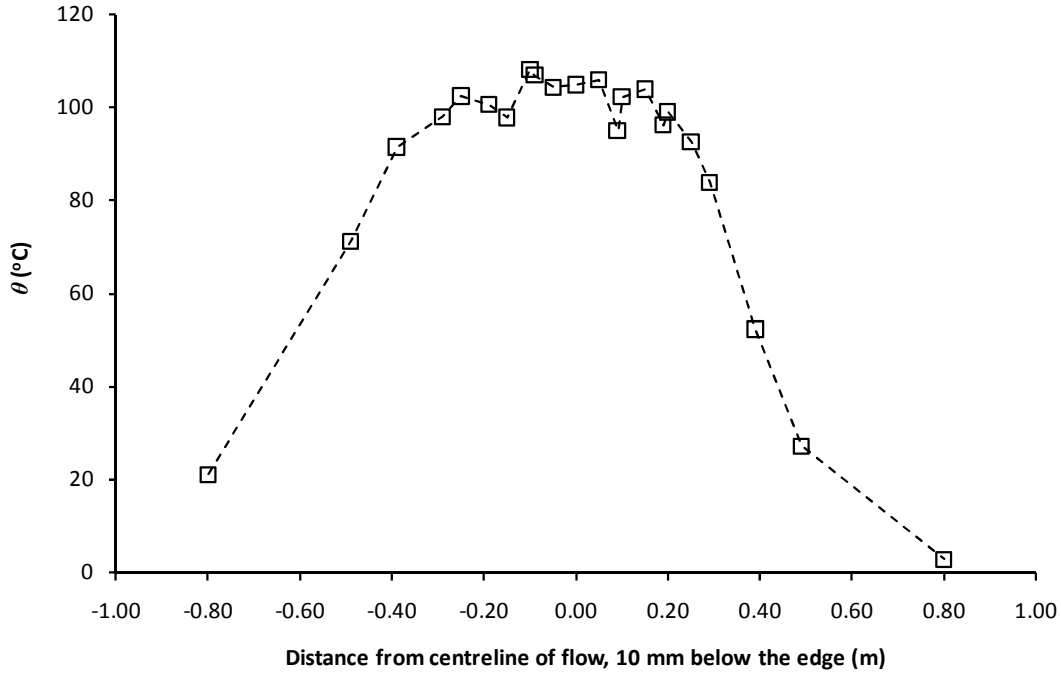

Figure I9: Temperature profile across spill edge, $\dot{Q}_t$ = 5 kW and W_s = 0.6 m

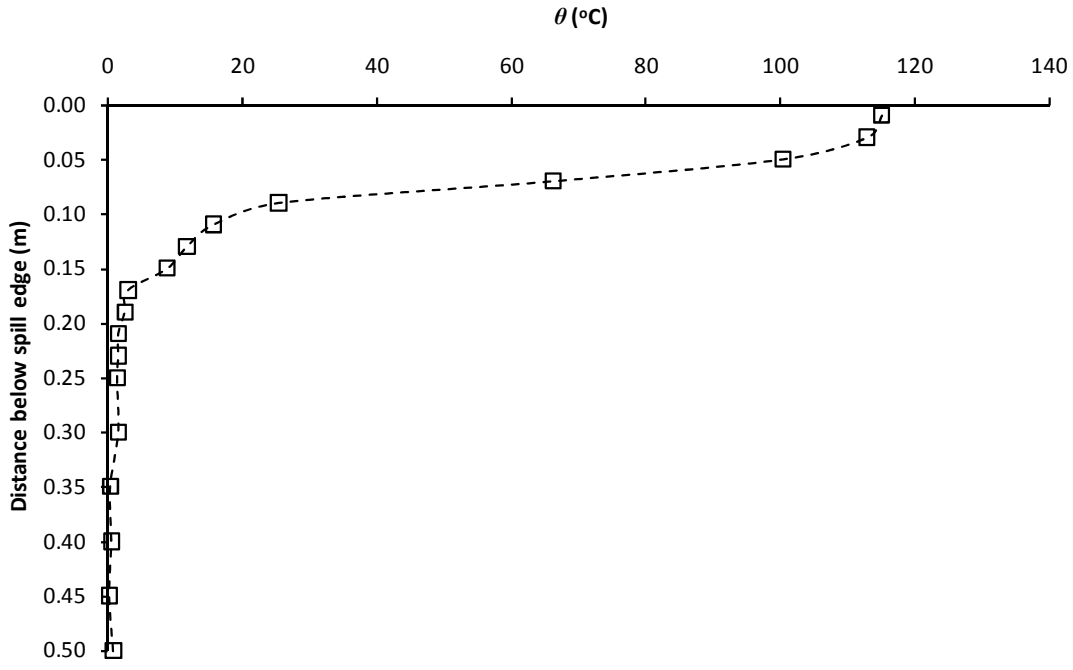

Figure I10: Temperature profile from Column C, $\dot{Q}_t$ = 5 kW and W_s = 0.6 m

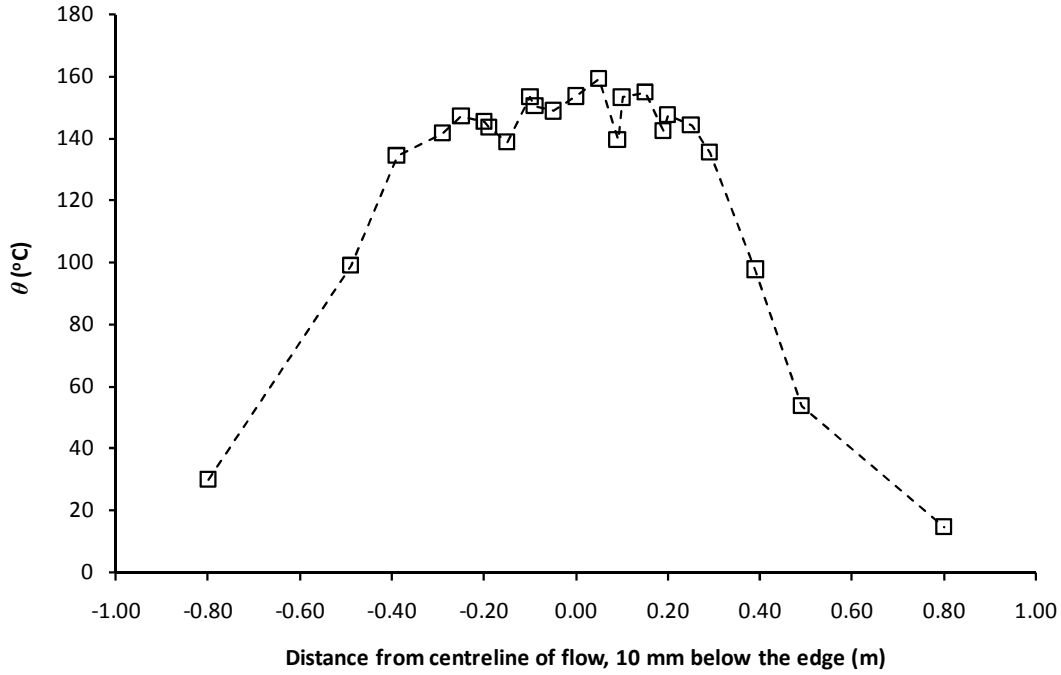

Figure I11: Temperature profile across spill edge, $\dot{Q}_t$ = 10 kW and W_s = 0.6 m

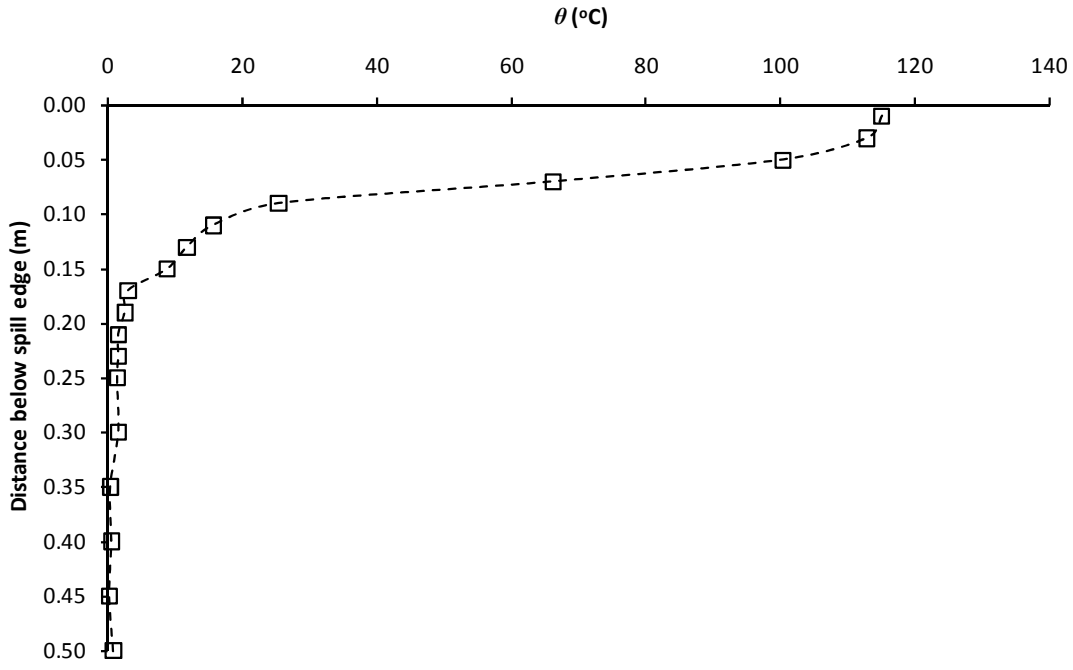

Figure I12: Temperature profile from Column C, $\dot{Q}_t$ = 10 kW and W_s = 0.6 m

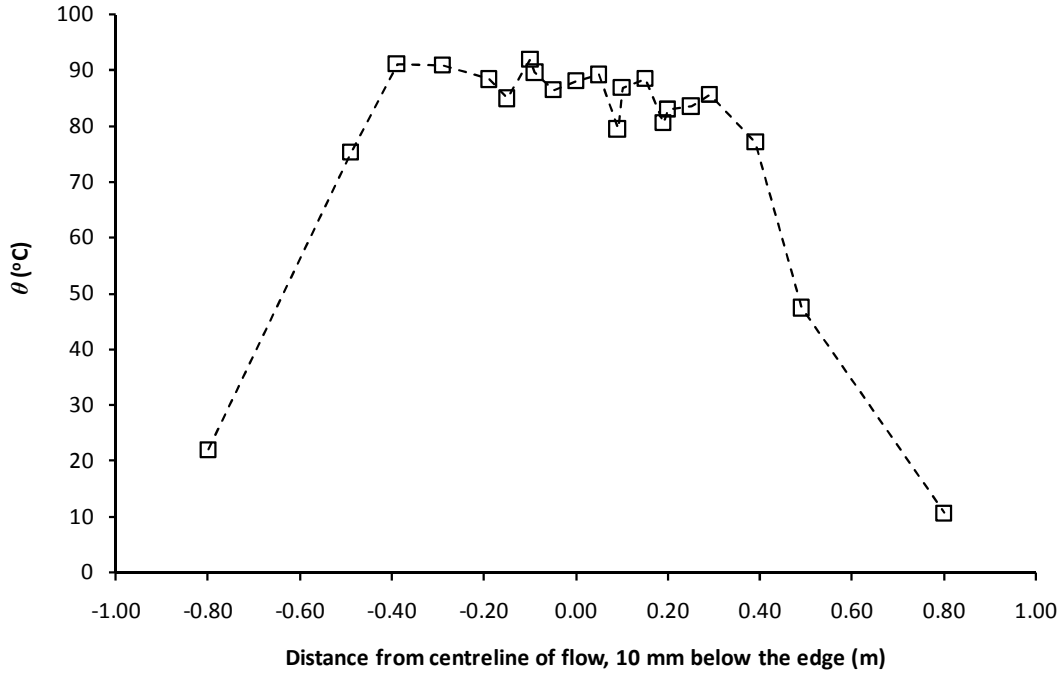

Figure I13: Temperature profile across spill edge, $\dot{Q}_t$ = 5 kW and W_s = 0.8 m

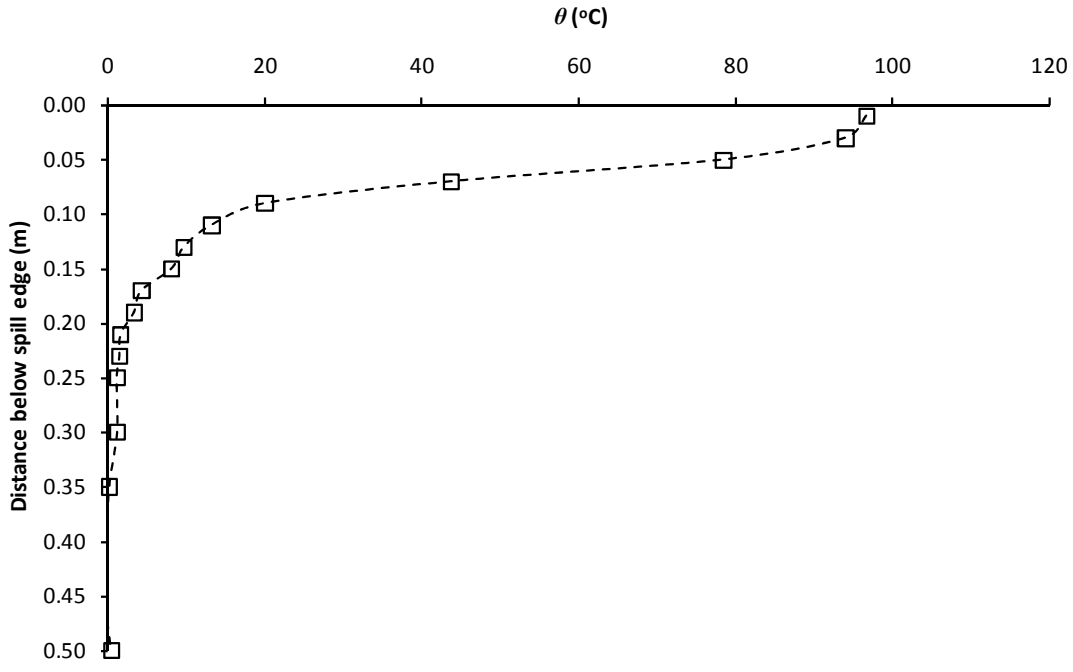

Figure I14: Temperature profile from Column C, $\dot{Q}_t$ = 5 kW and W_s = 0.8 m

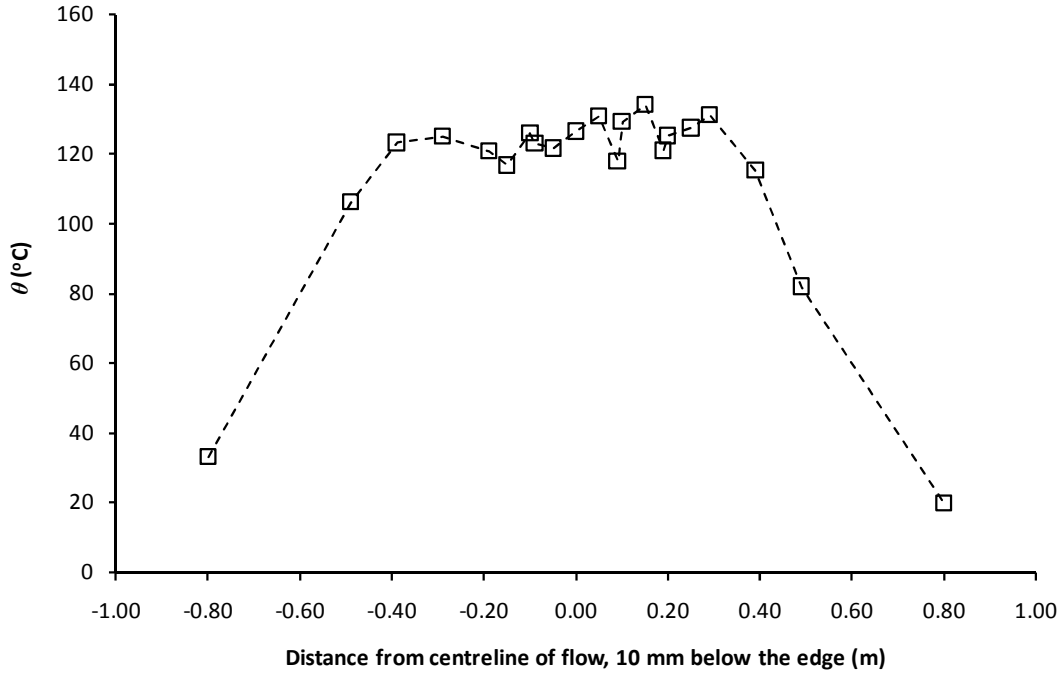

Figure I15: Temperature profile across spill edge, $\dot{Q}_t$ = 10 kW and W_s = 0.8 m

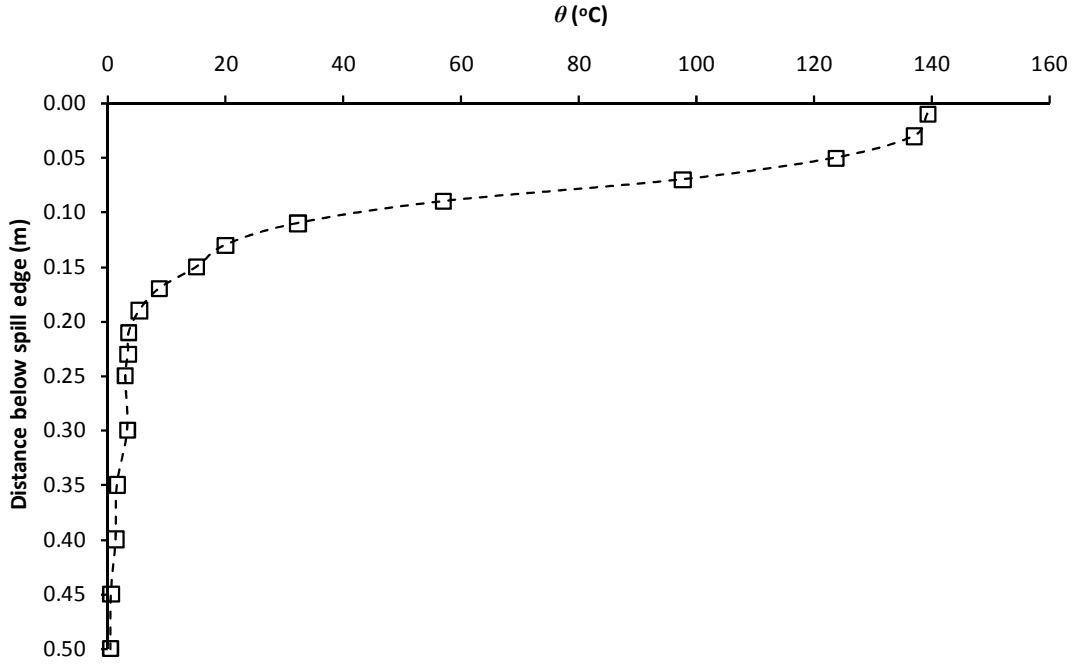

Figure I16: Temperature profile from Column C, $\dot{Q}_t$ = 10 kW and W_s = 0.8 m

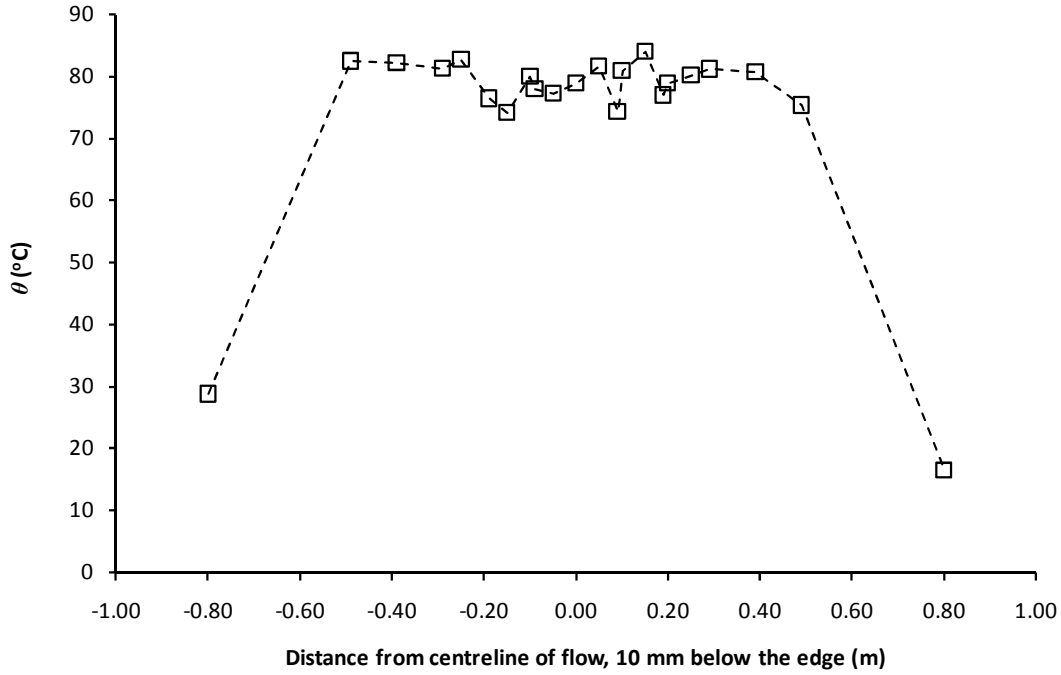

Figure I17: Temperature profile across spill edge, $\dot{Q}_t$ = 5 kW and W_s = 1.0 m

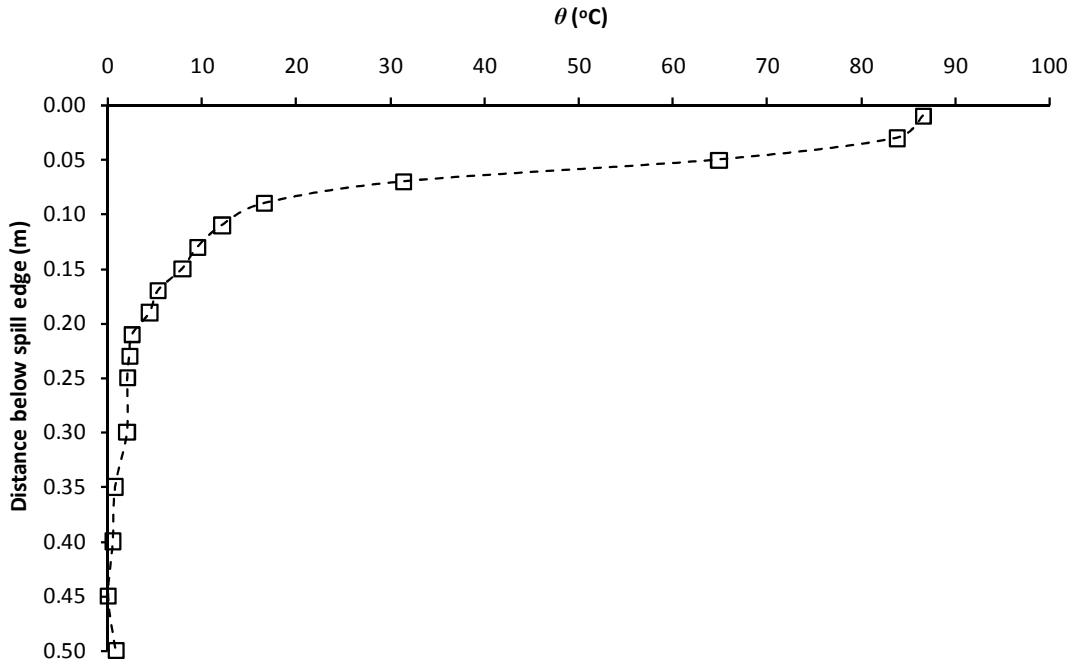

Figure I18: Temperature profile from Column C, $\dot{Q}_t$ = 5 kW and W_s = 1.0 m

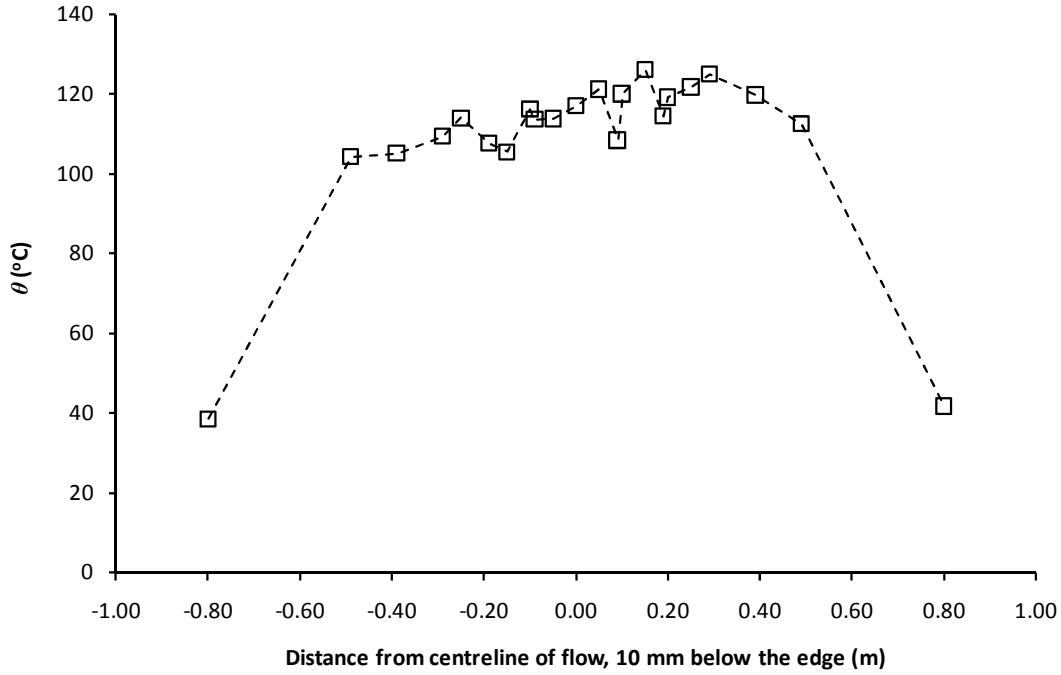

Figure I19: Temperature profile across spill edge, $\dot{Q}_t$ = 10 kW and W_s = 1.0 m

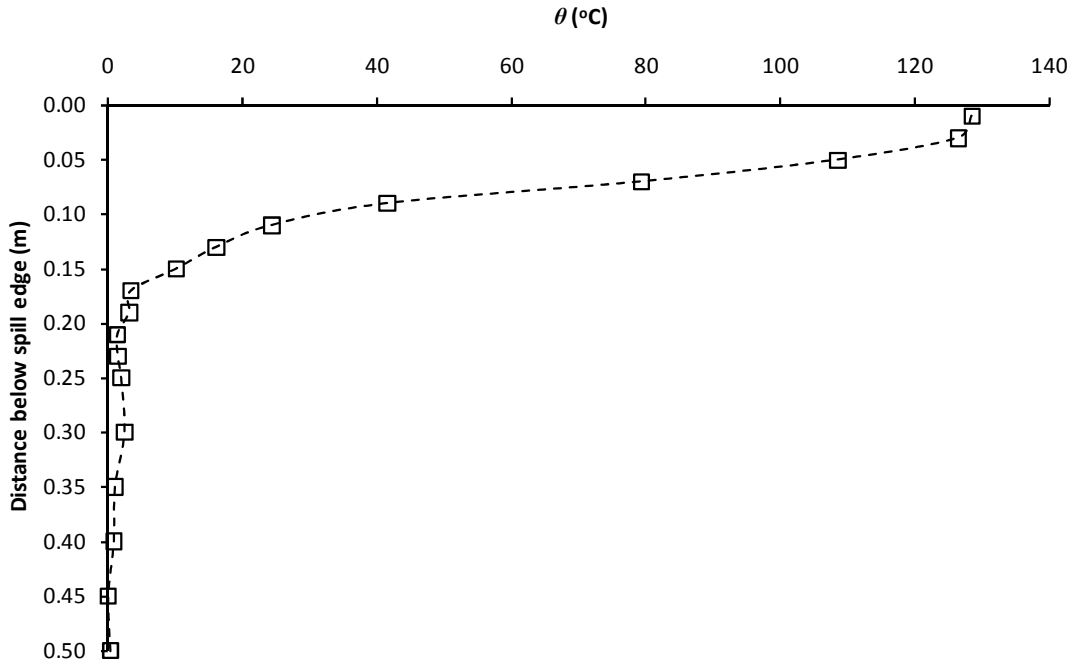

Figure I20: Temperature profile from Column C, $\dot{Q}_t$ = 10 kW and W_s = 1.0 m

Appendix J: Temperature profiles in the smoke collecting hood for the series of adhered spill plume experiments

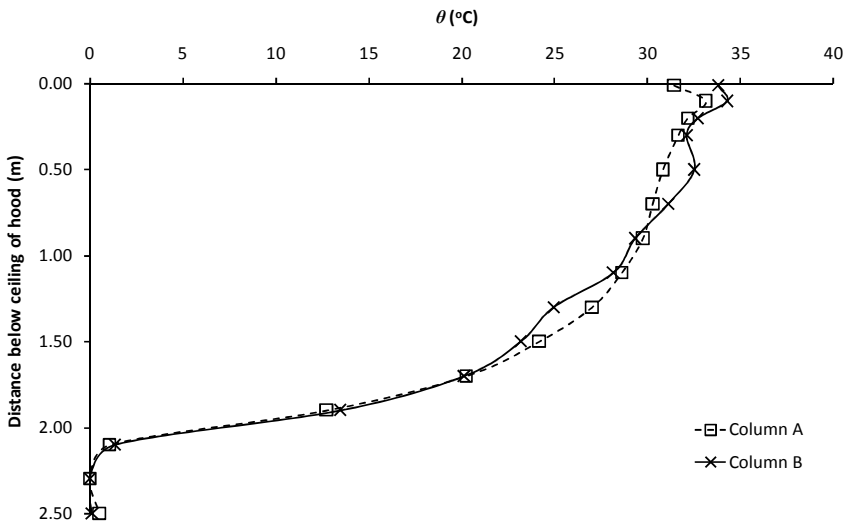

Figure J1: Experiment E31

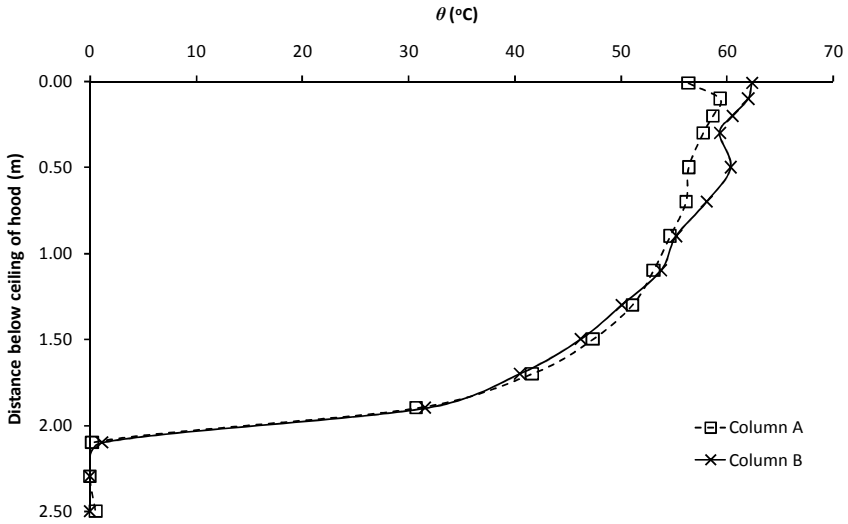

Figure J2: Experiment E32

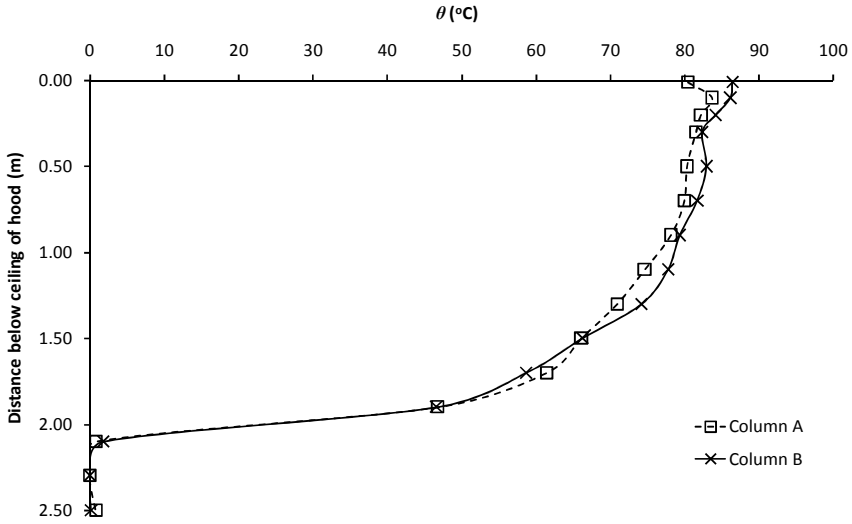

Figure J3: Experiment E33

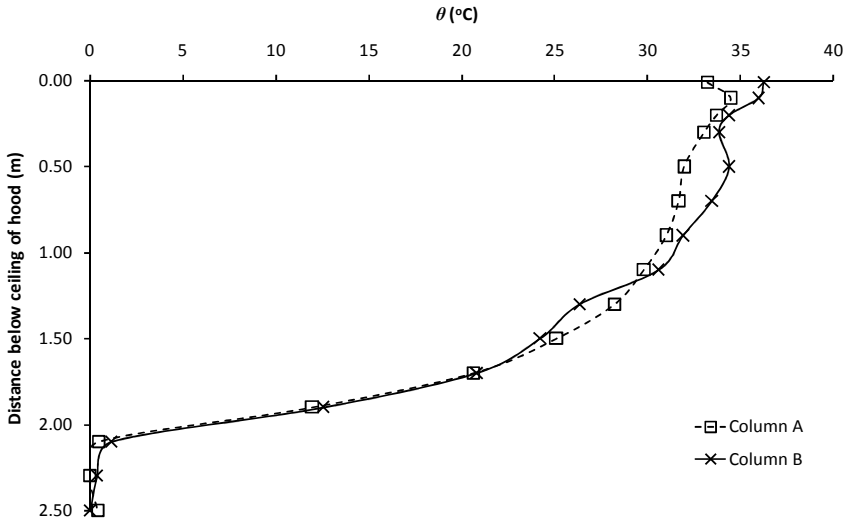

Figure J4: Experiment E34

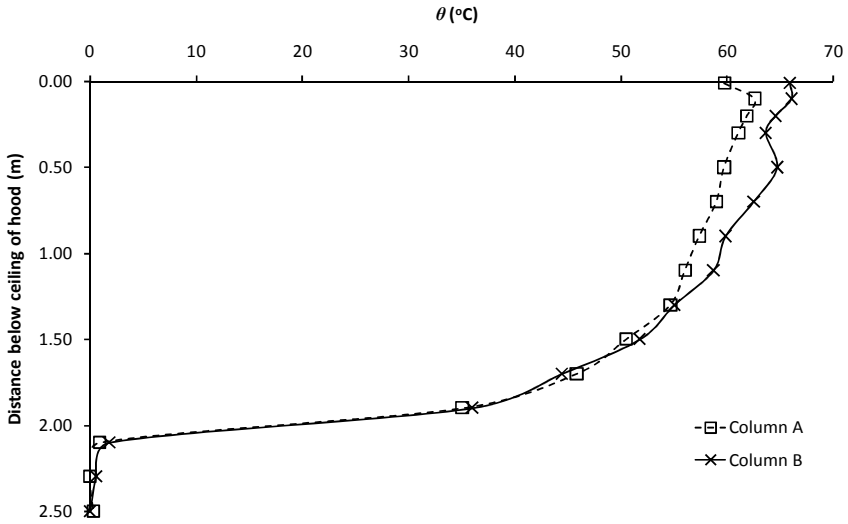

Figure J5: Experiment E35

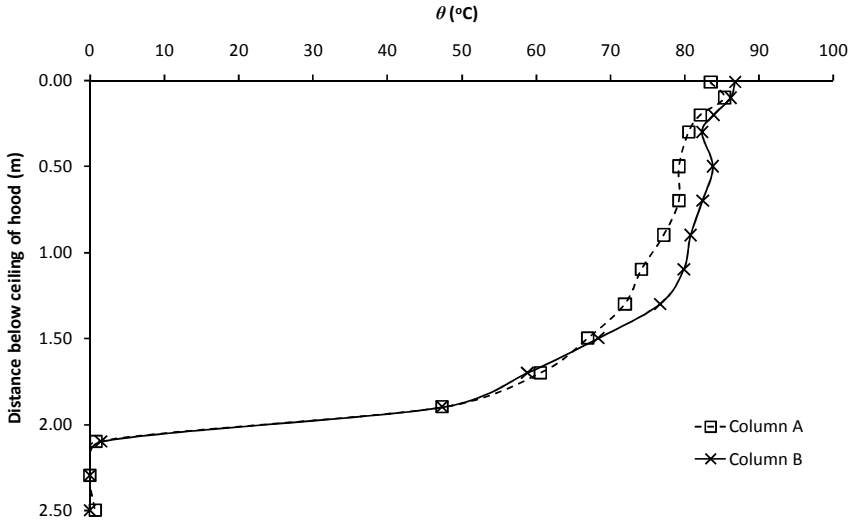

Figure J6: Experiment E36

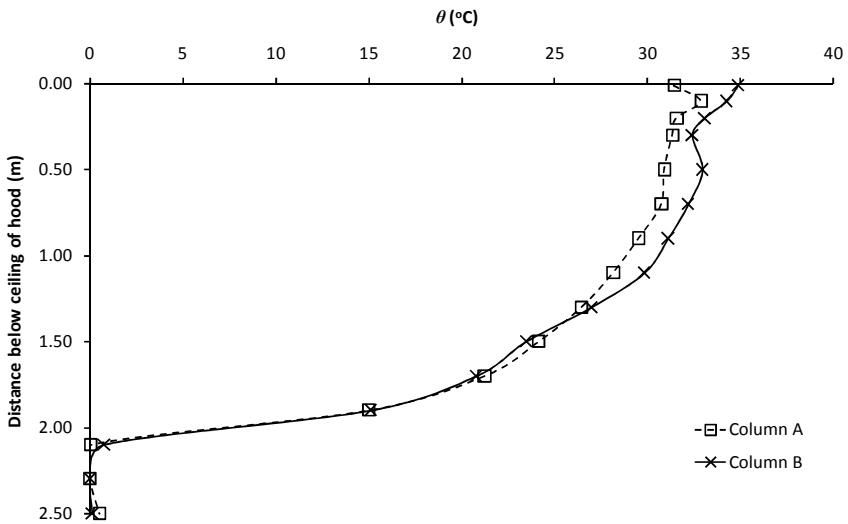

Figure J7: Experiment E37

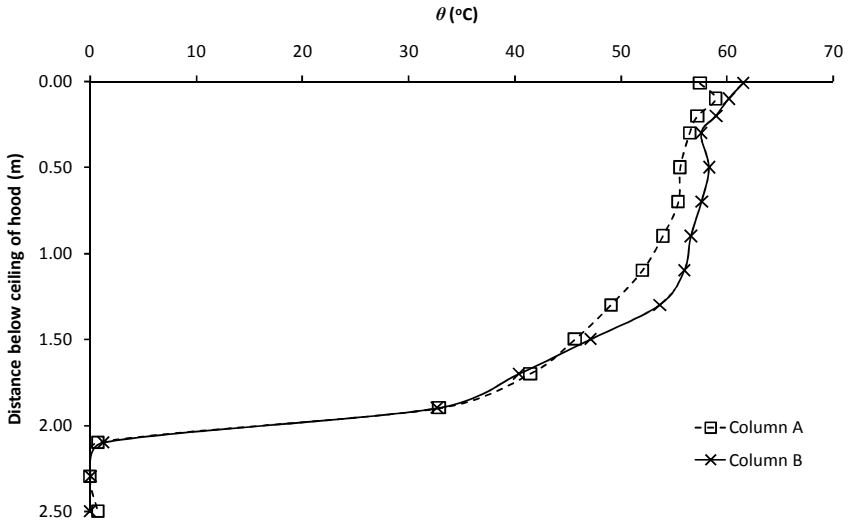

Figure J8: Experiment E38

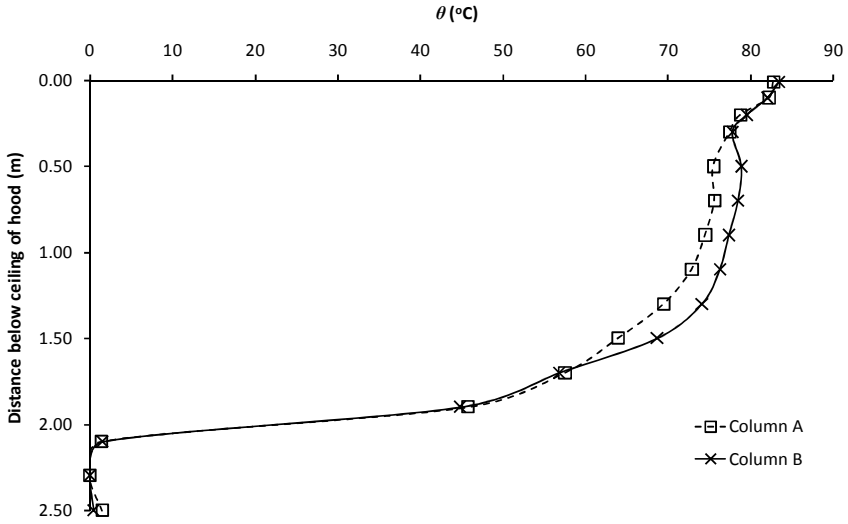

Figure J9: Experiment E39

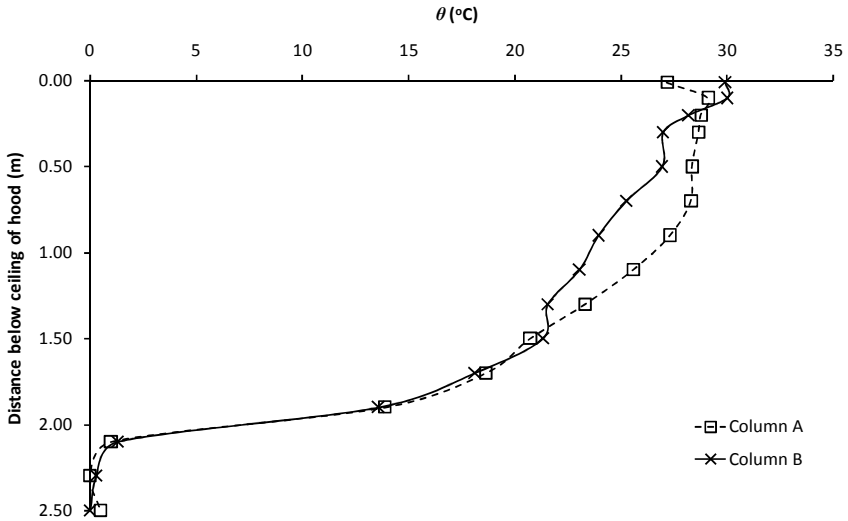

Figure J10: Experiment E40

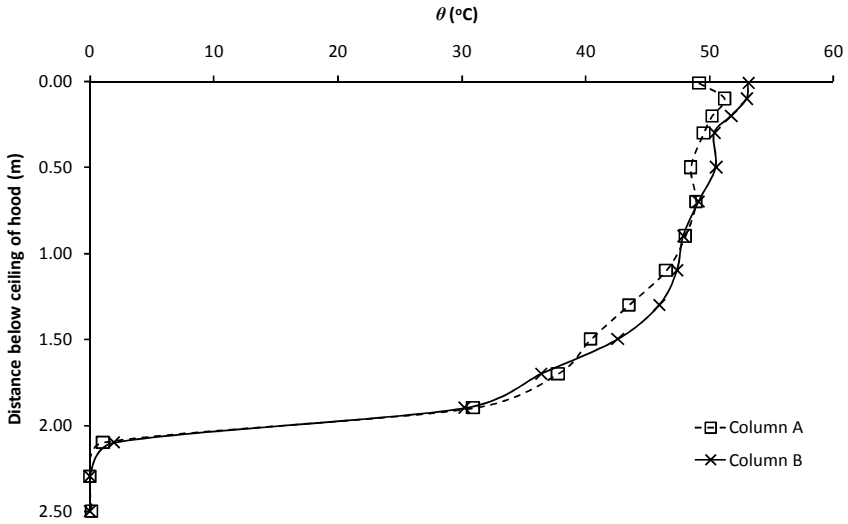

Figure J11: Experiment E41

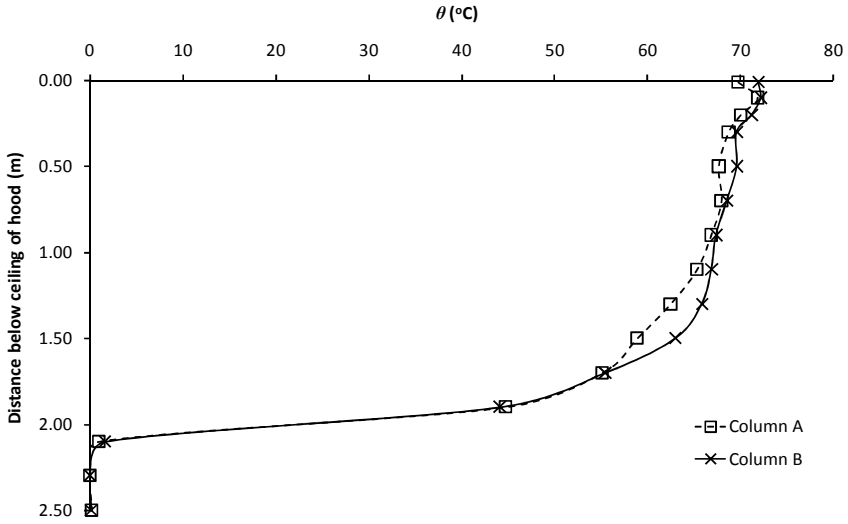

Figure J12: Experiment E42

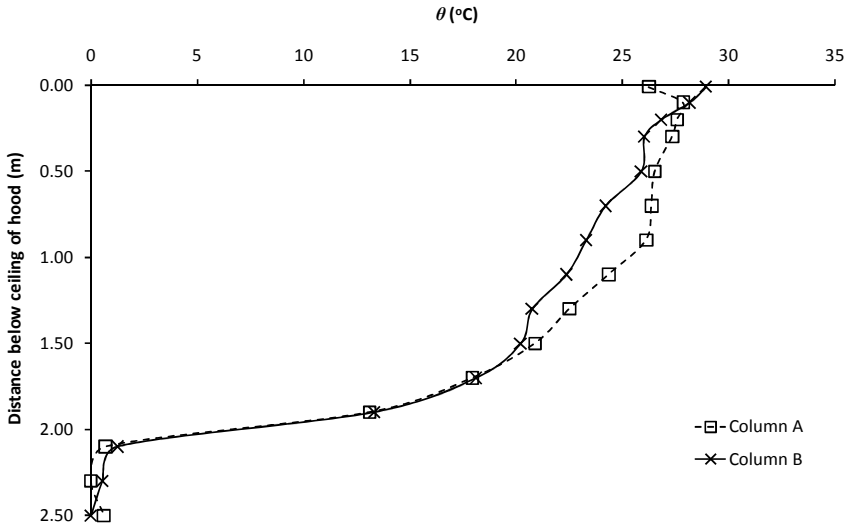

Figure J13: Experiment E43

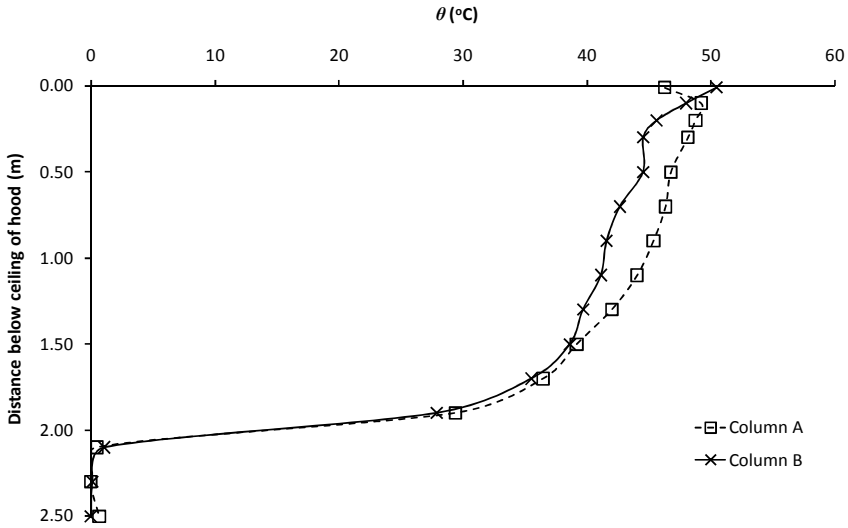

Figure J14: Experiment E44

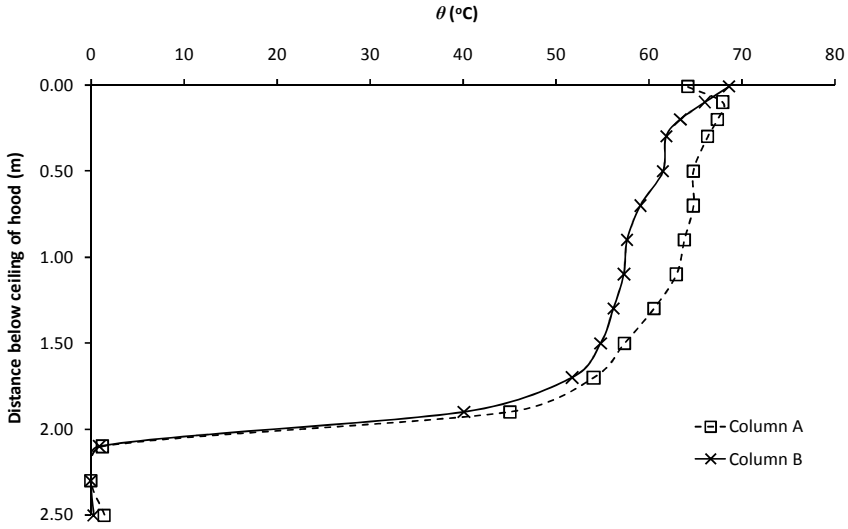

Figure J15: Experiment E45

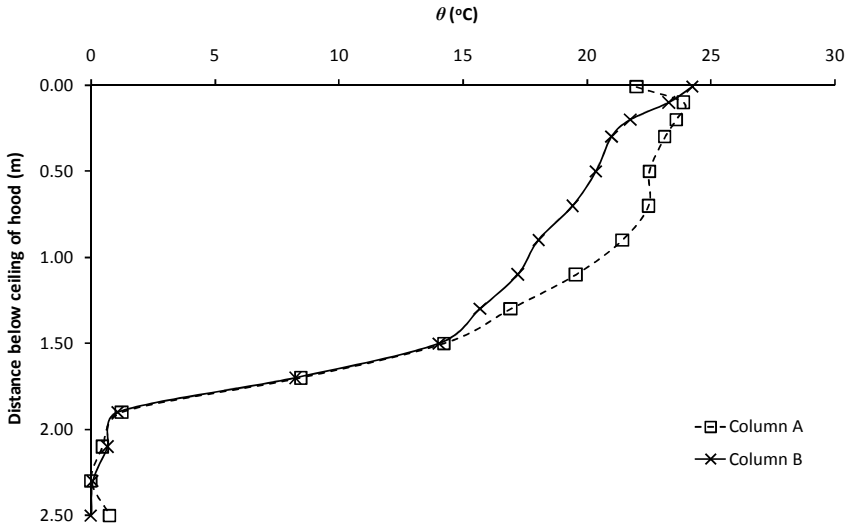

Figure J16: Experiment E46

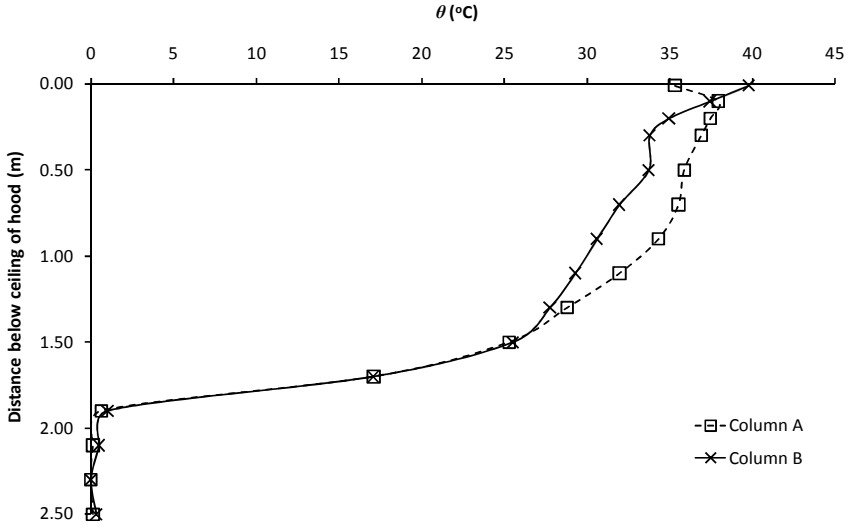

Figure J17: Experiment E47

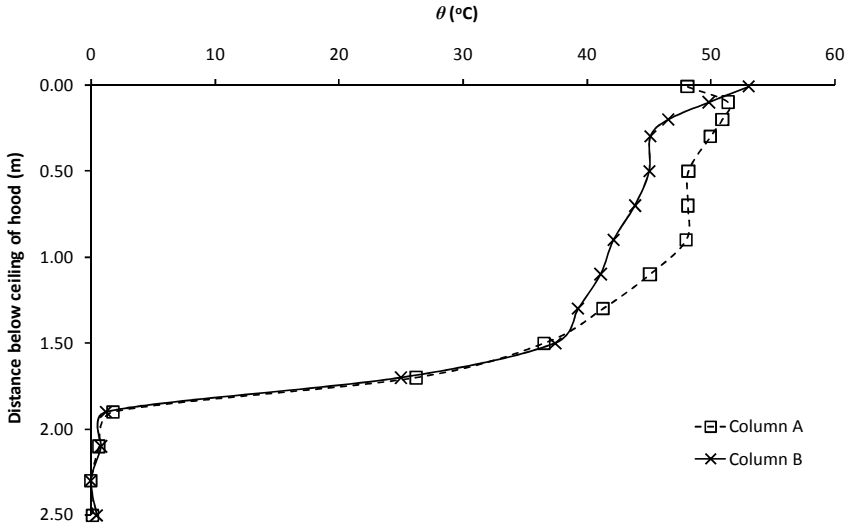

Figure J18: Experiment E48

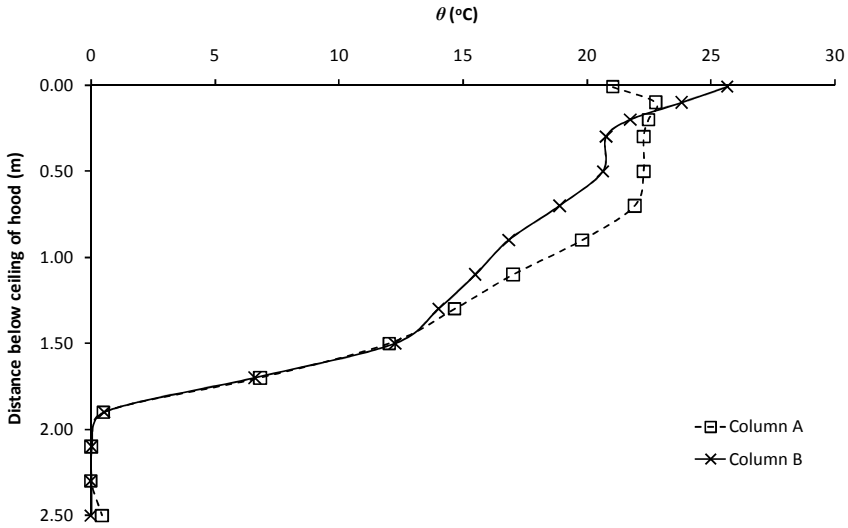

Figure J19: Experiment E49

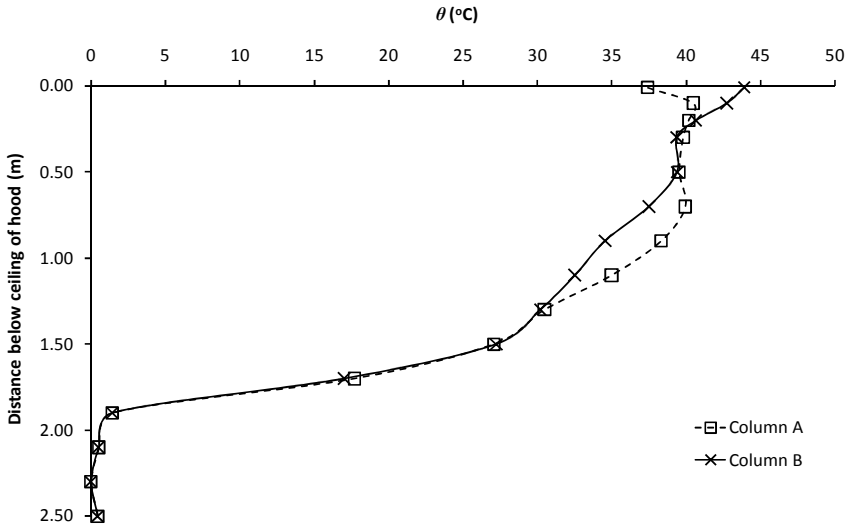

Figure J20: Experiment E50

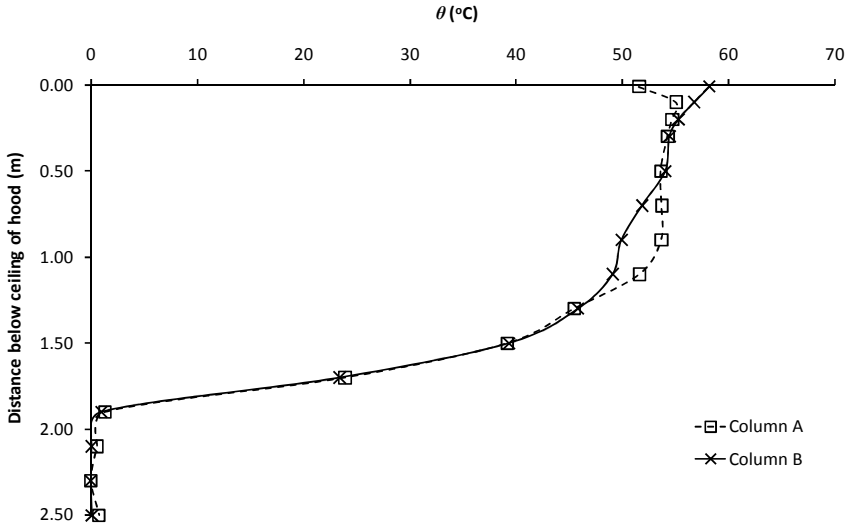

Figure J21: Experiment E51

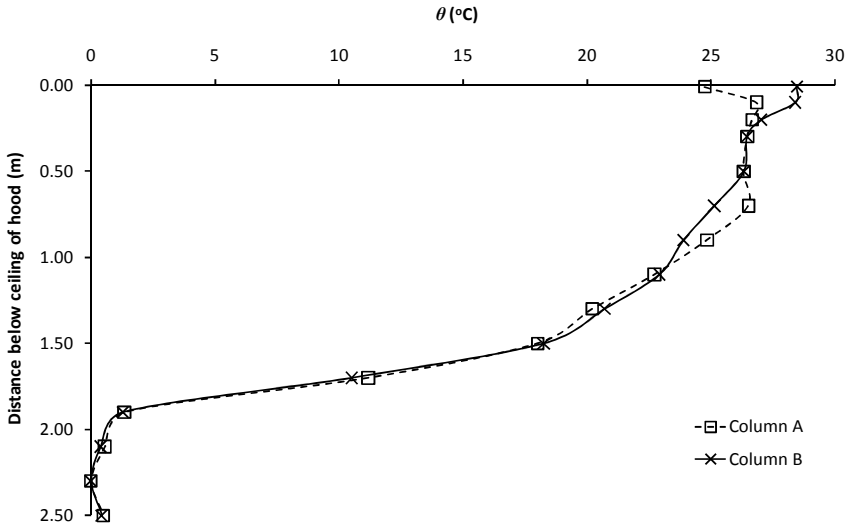

Figure J22: Experiment E52

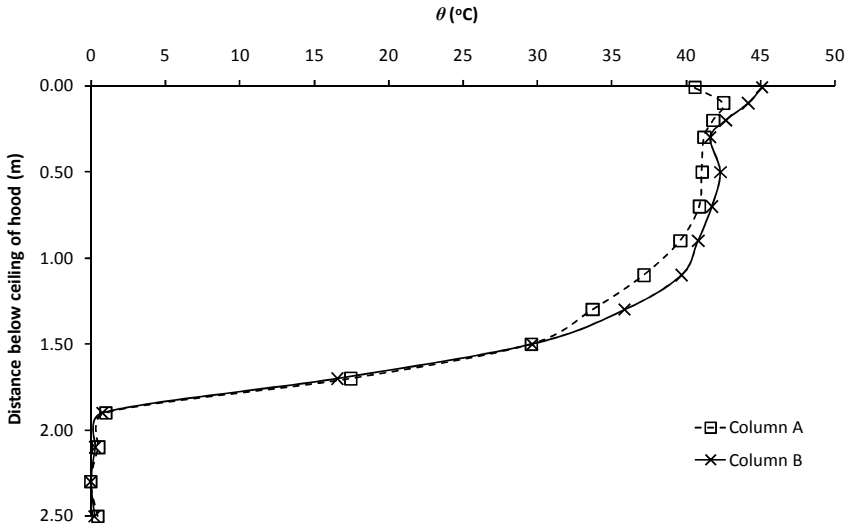

Figure J23: Experiment E53

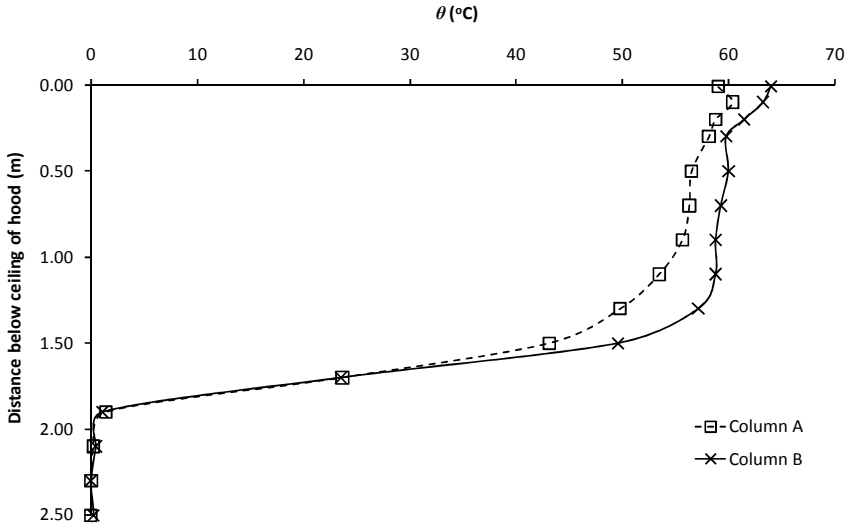

Figure J24: Experiment E54

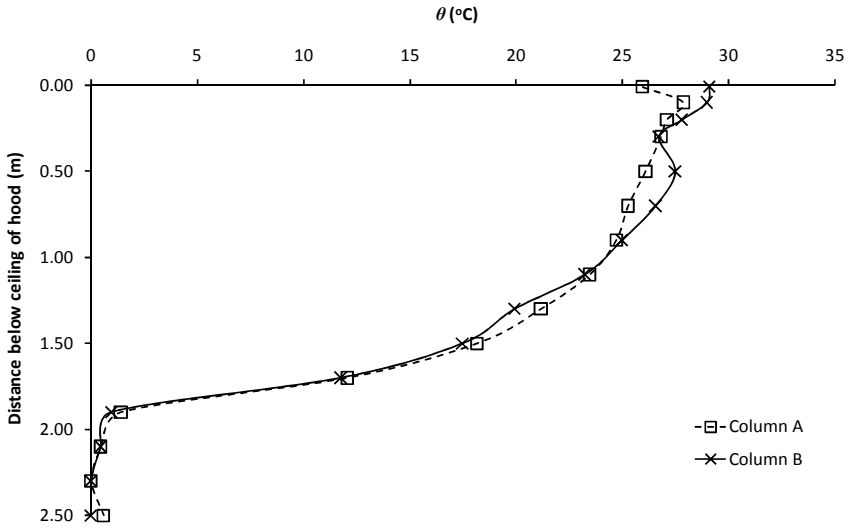

Figure J25: Experiment E55

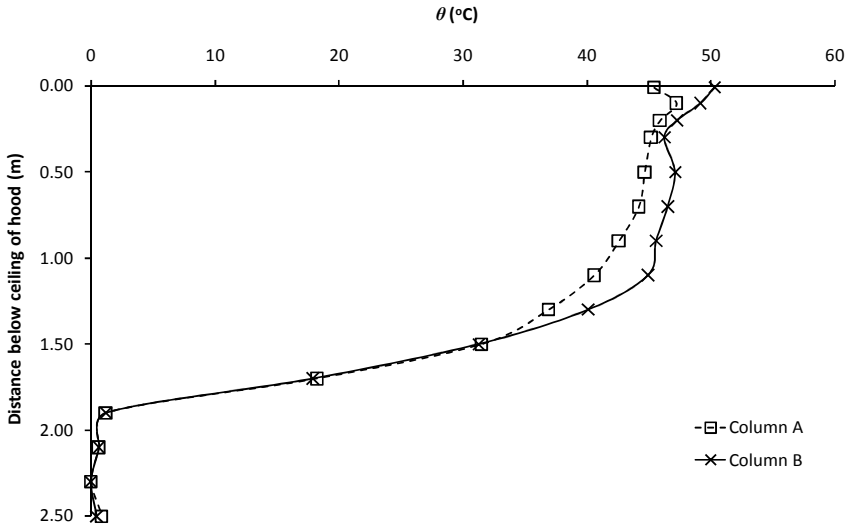

Figure J26: Experiment E56

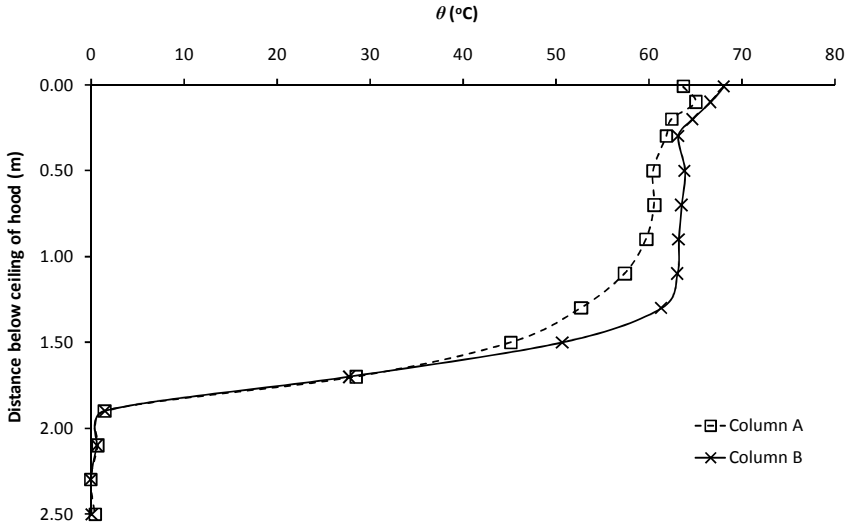

Figure J27: Experiment E57

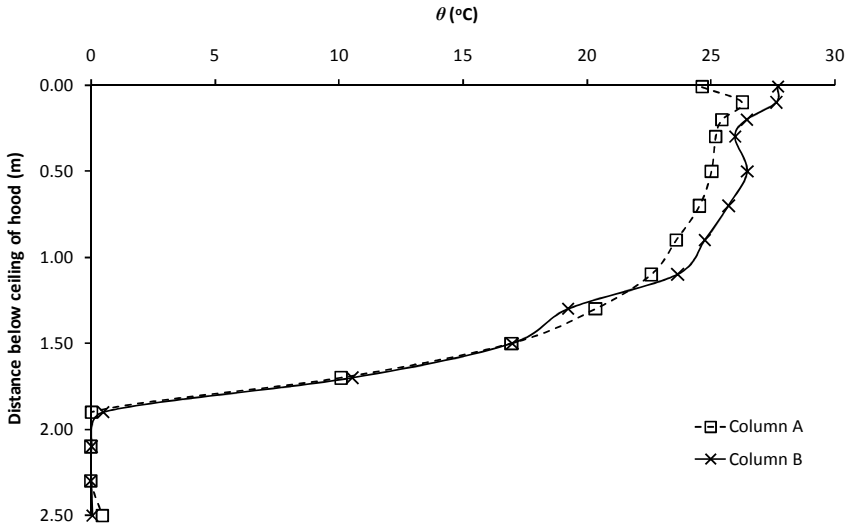

Figure J28: Experiment E58

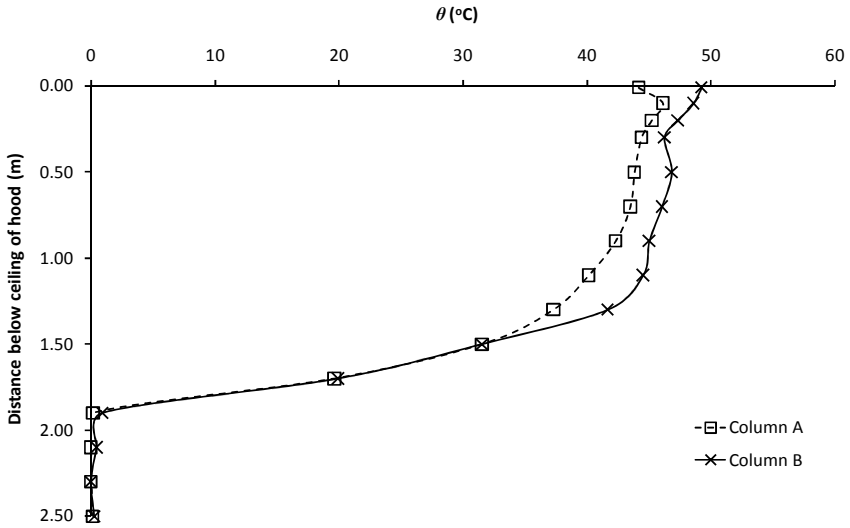

Figure J29: Experiment E59

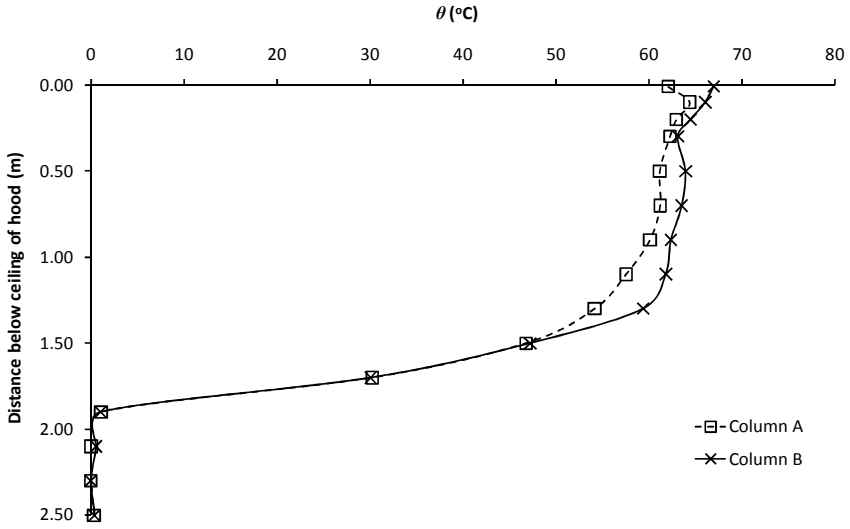

Figure J30: Experiment E60

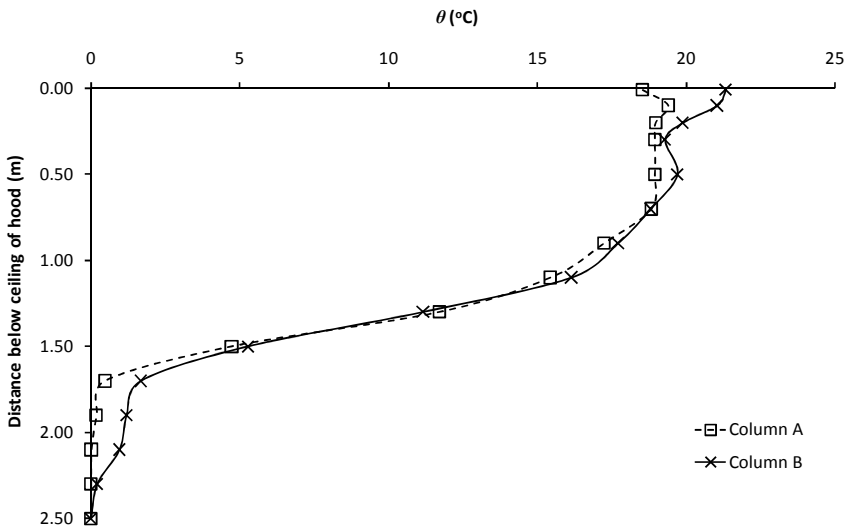

Figure J31: Experiment E118

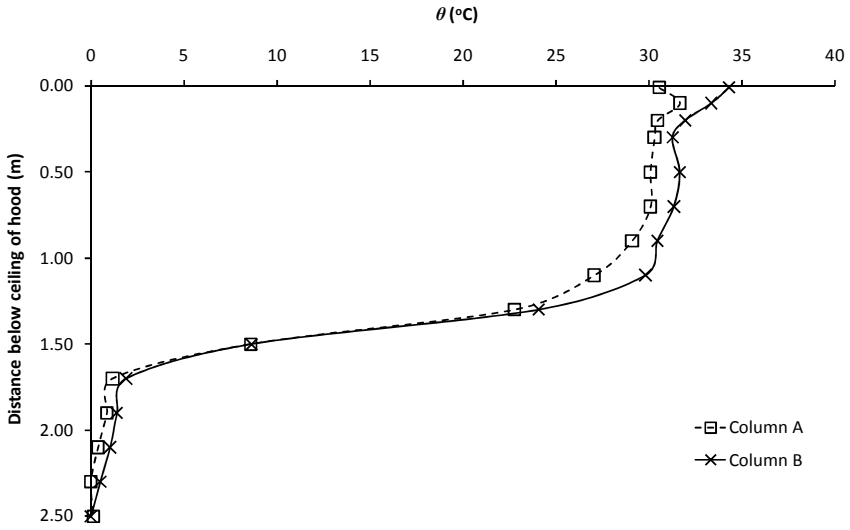

Figure J32: Experiment E119

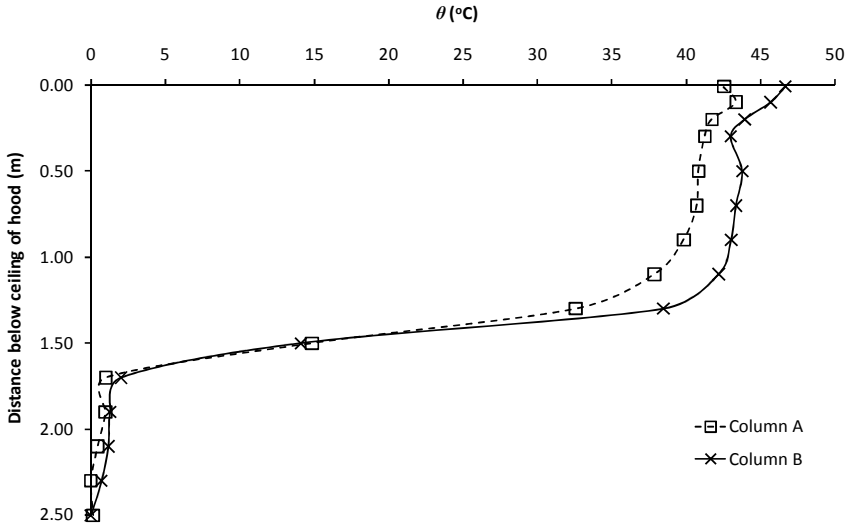

Figure J33: Experiment E120

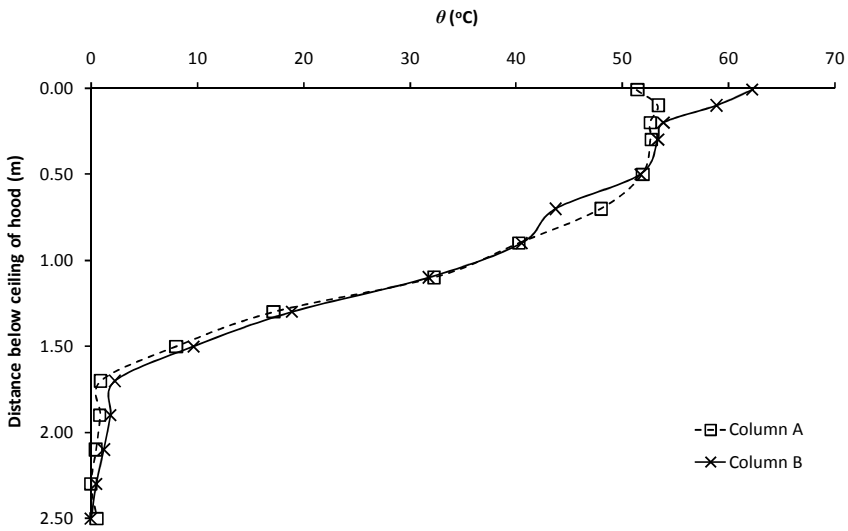

Figure J34: Experiment E121

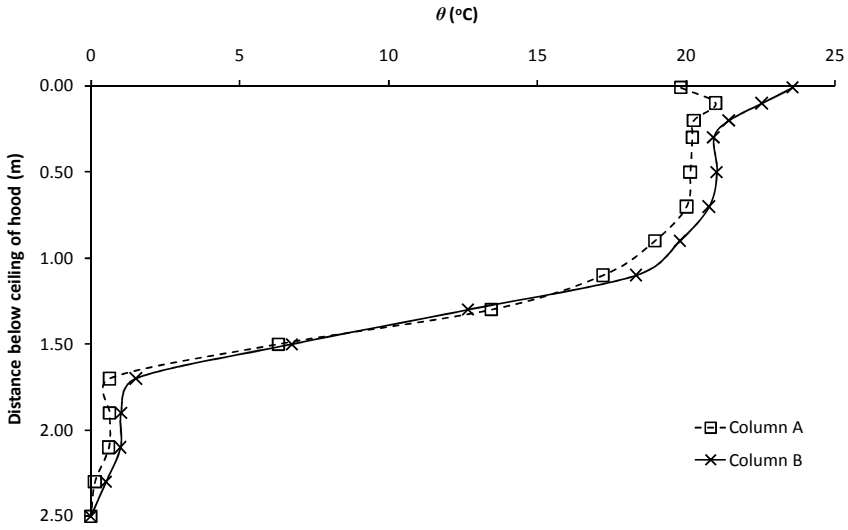

Figure J35: Experiment E122

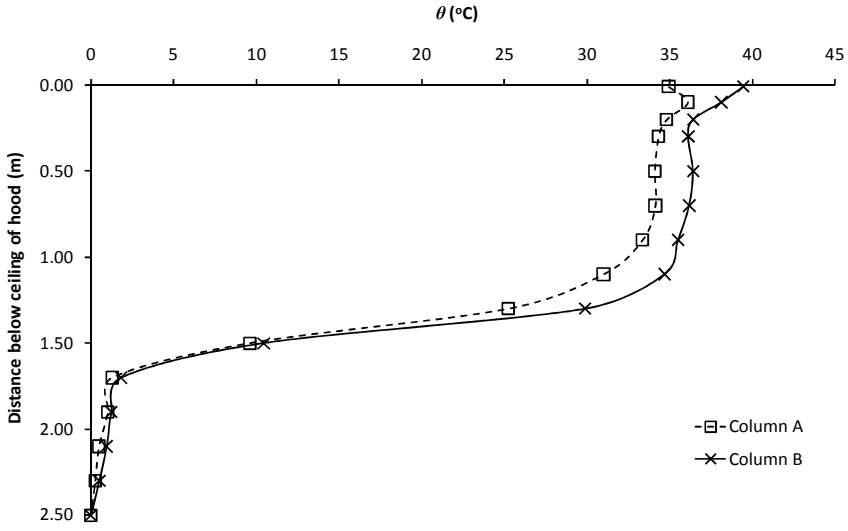

Figure J36: Experiment E123

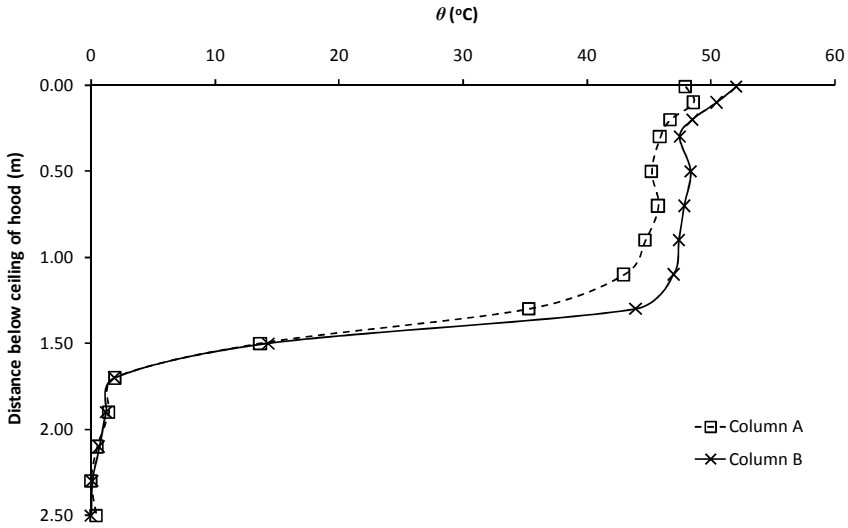

Figure J37: Experiment E124

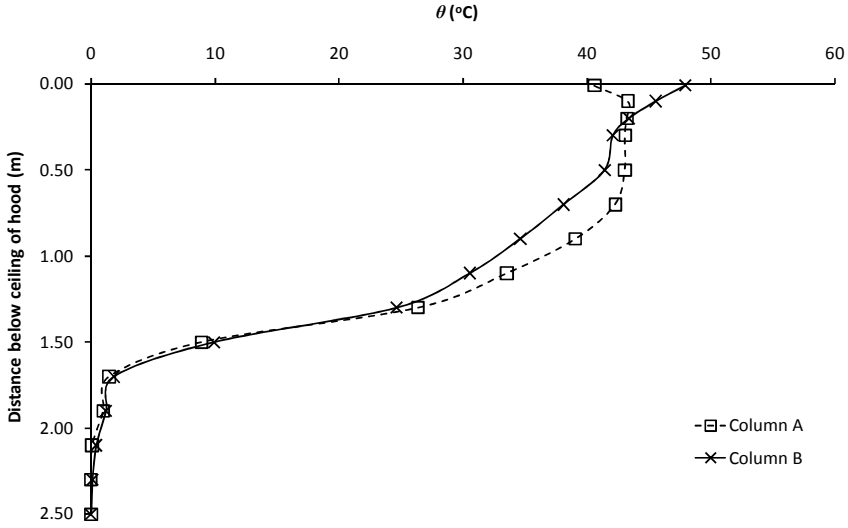

Figure J38: Experiment E125

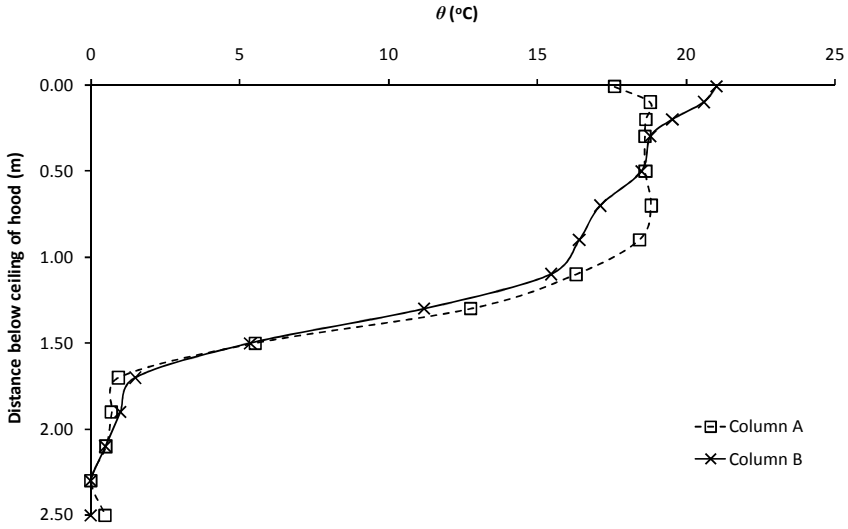

Figure J39: Experiment E126

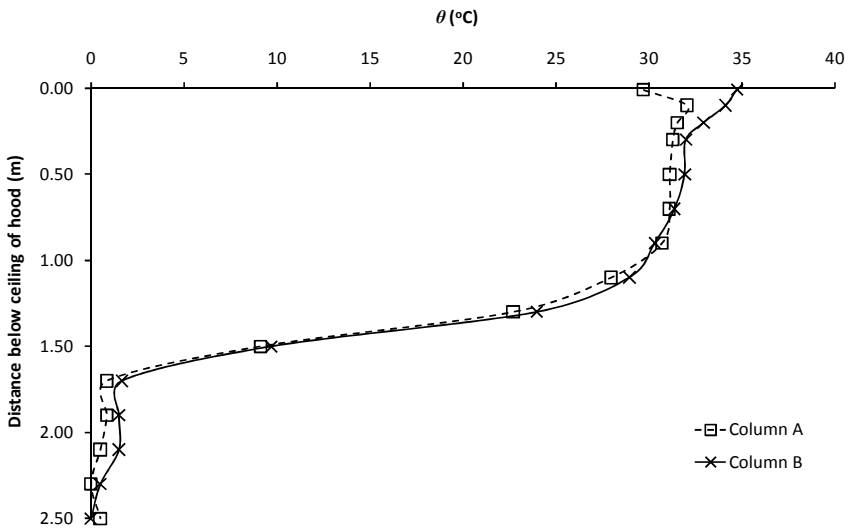

Figure J40: Experiment E127

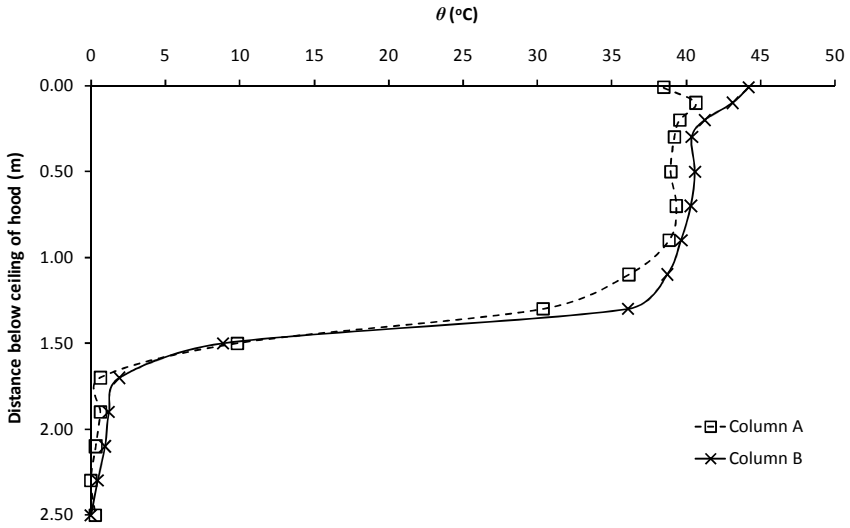

Figure J41: Experiment E128

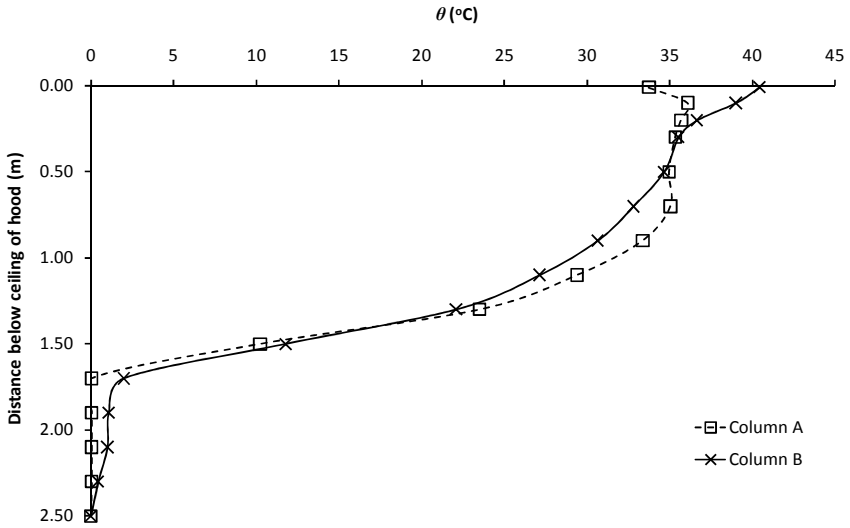

Figure J42: Experiment E129

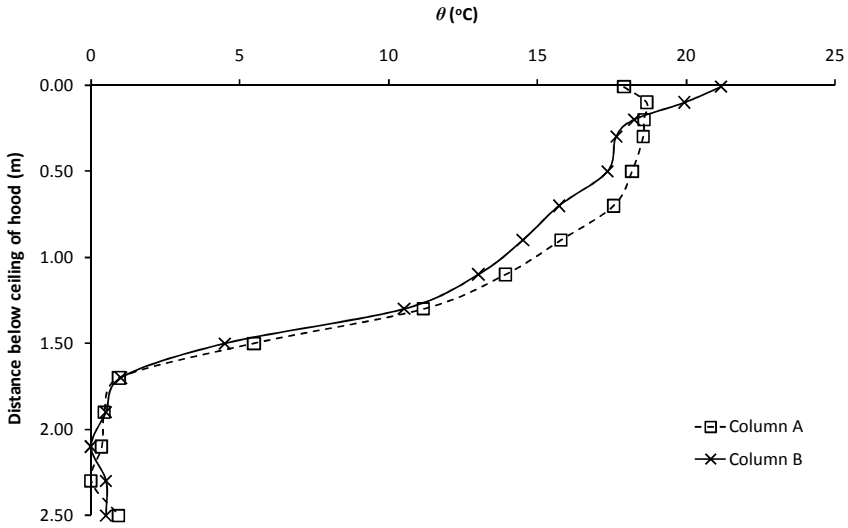

Figure J43: Experiment E130

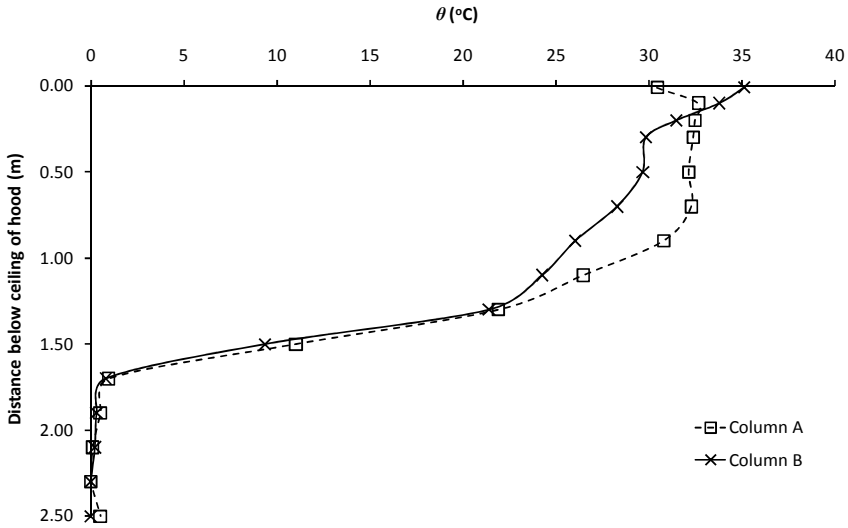

Figure J44: Experiment E131

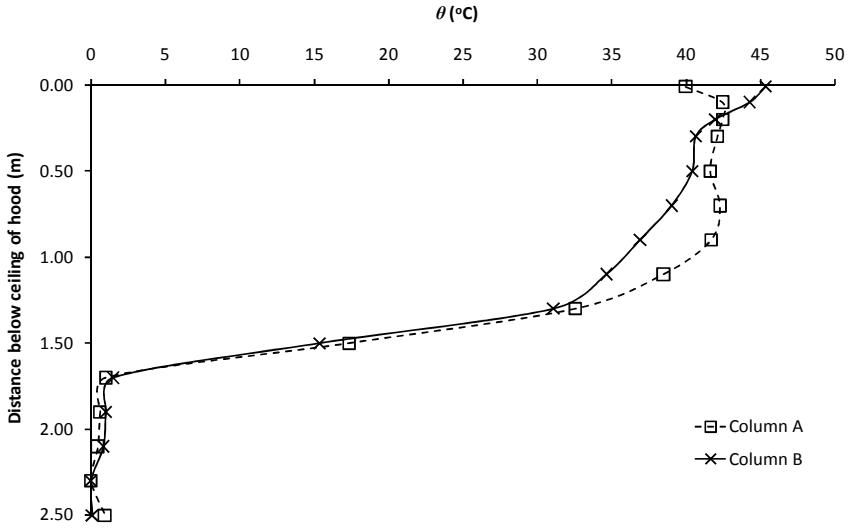

Figure J45: Experiment E132

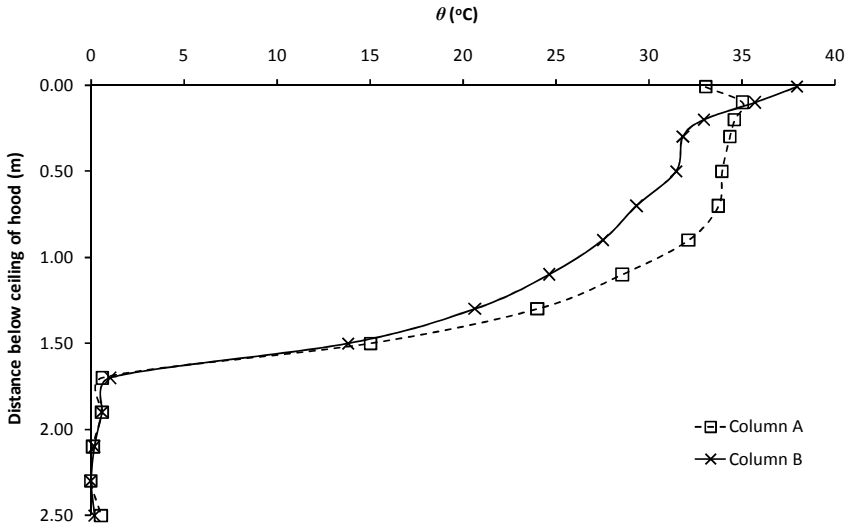

Figure J46: Experiment E133

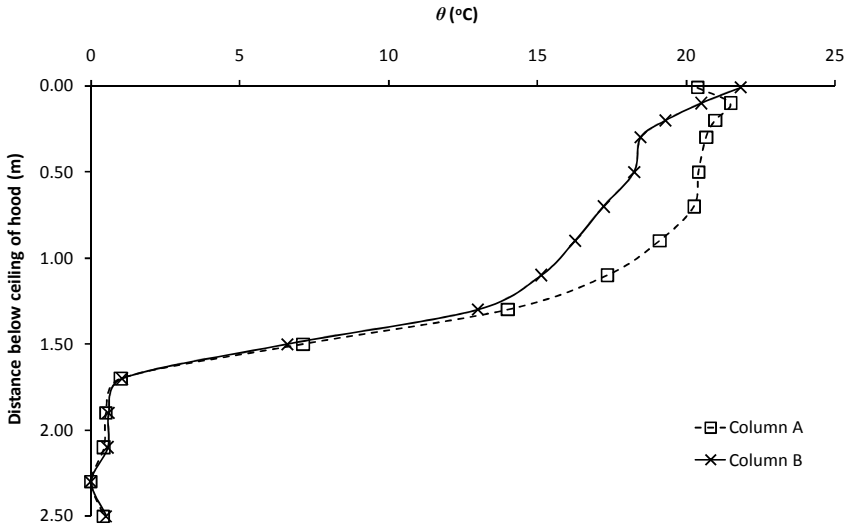

Figure J47: Experiment E134

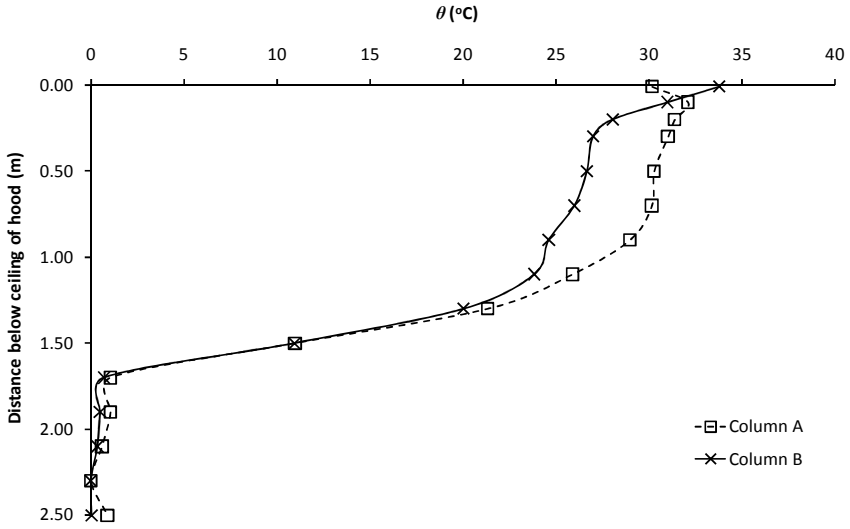

Figure J48: Experiment E135

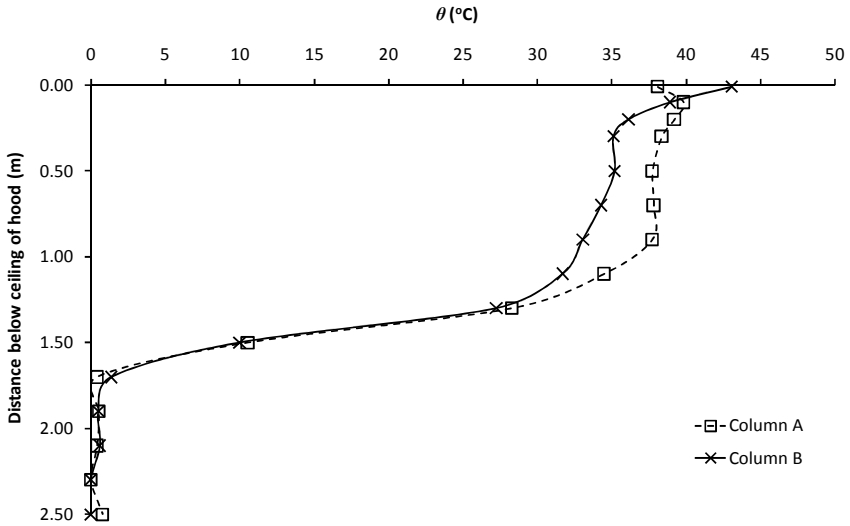

Figure J49: Experiment E136

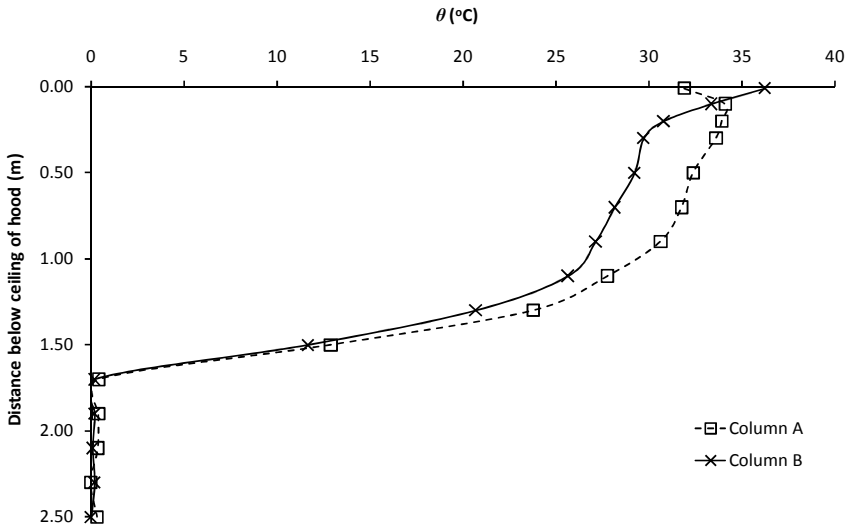

Figure J50: Experiment E137

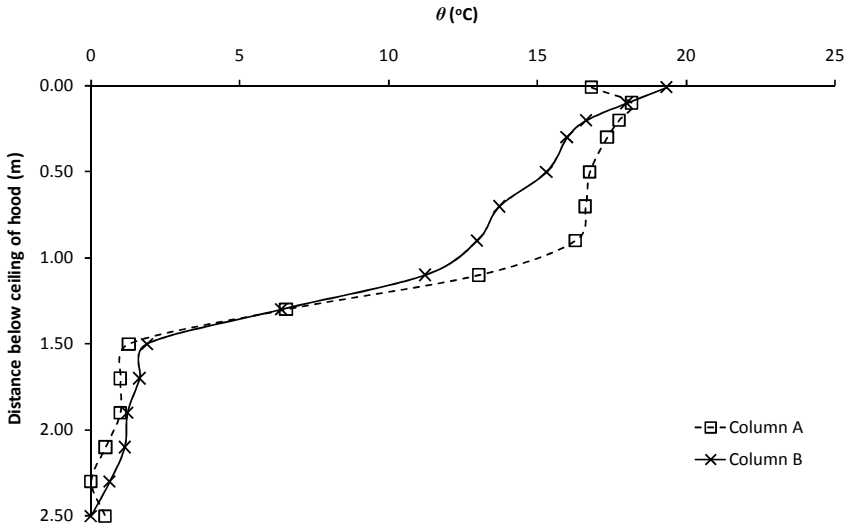

Figure J51: Experiment E138

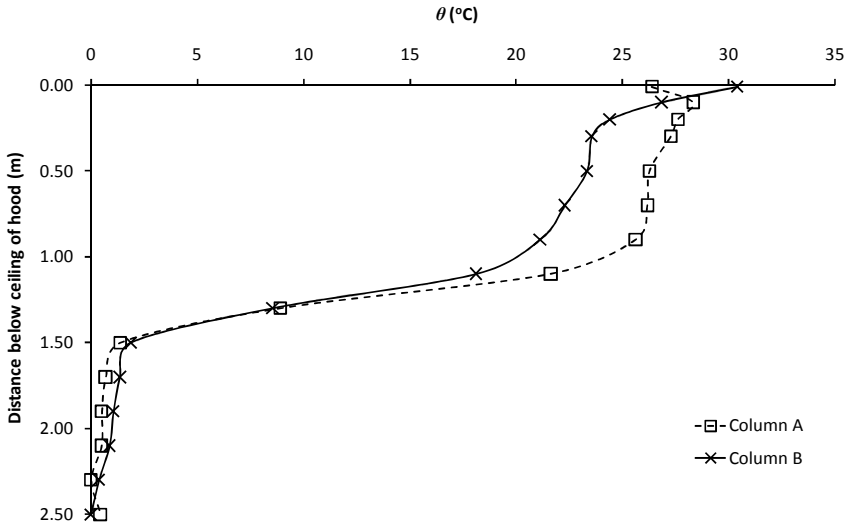

Figure J52: Experiment E139

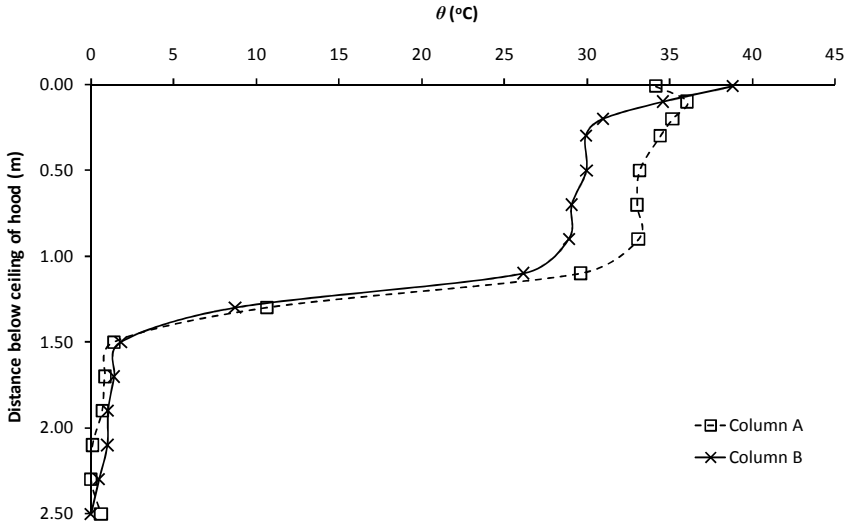

Figure J53: Experiment E140

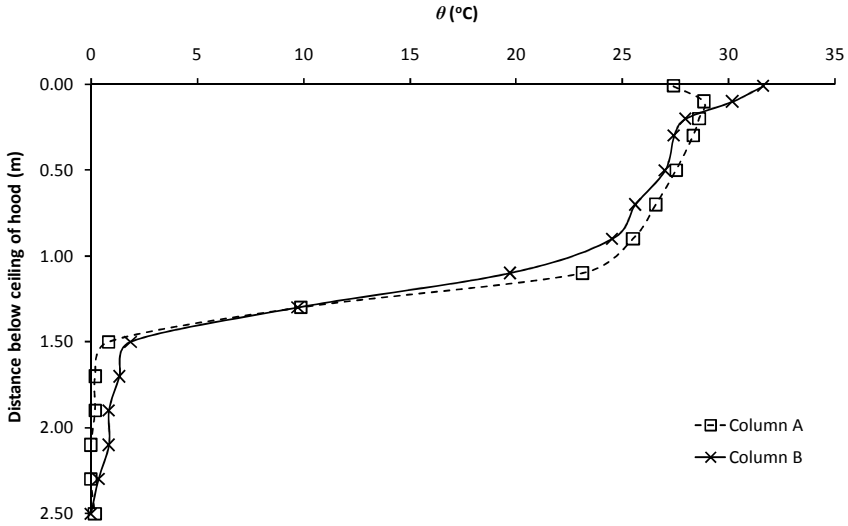

Figure J54: Experiment E141

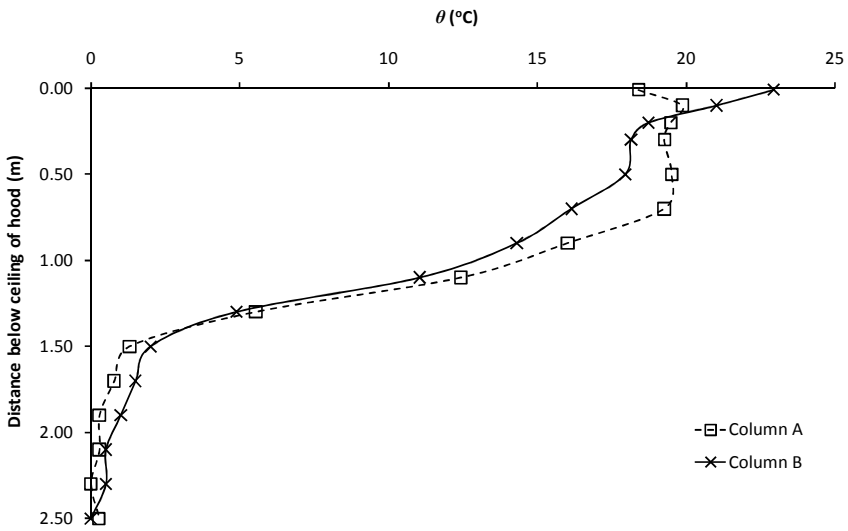

Figure J55: Experiment E142

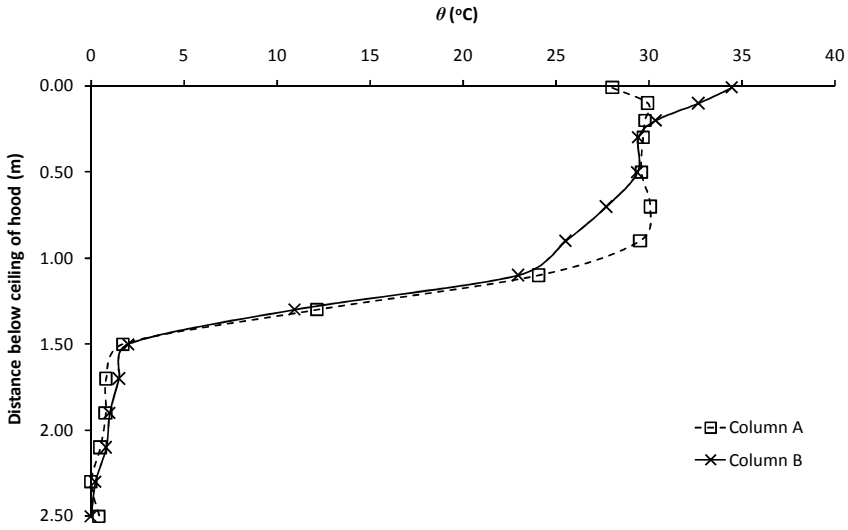

Figure J56: Experiment E143

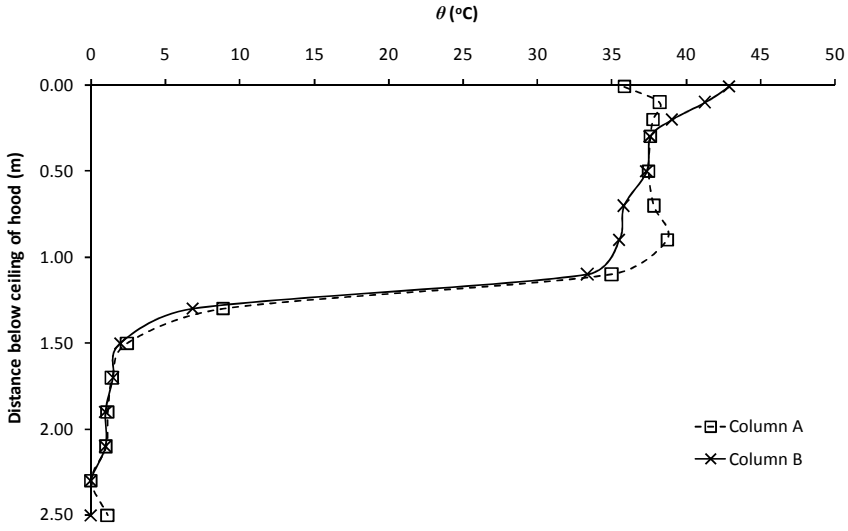

Figure J57: Experiment E144

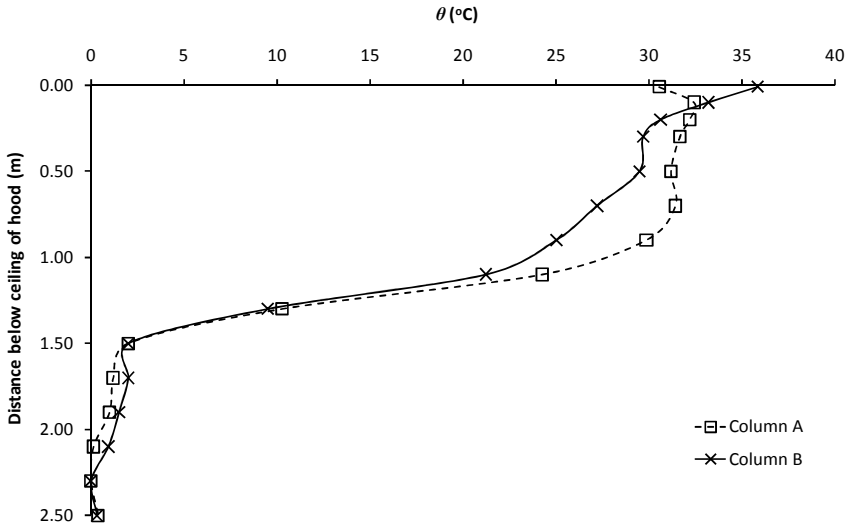

Figure J58: Experiment E145

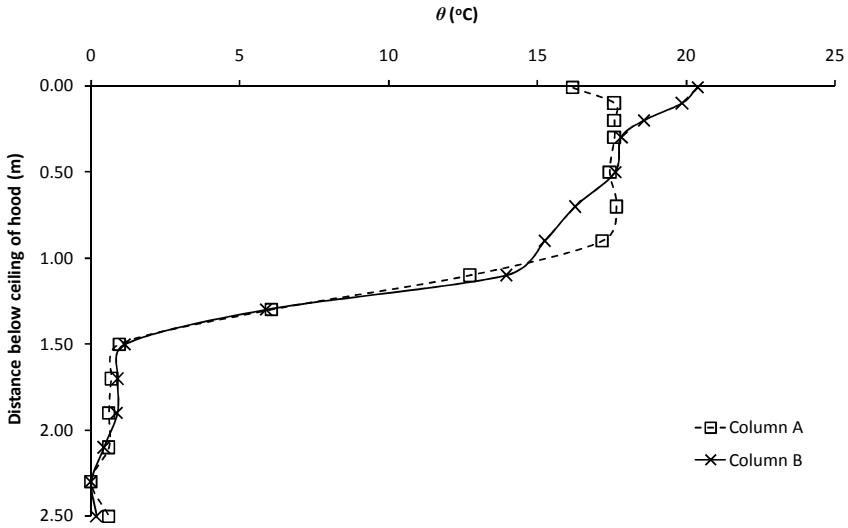

Figure J59: Experiment E146

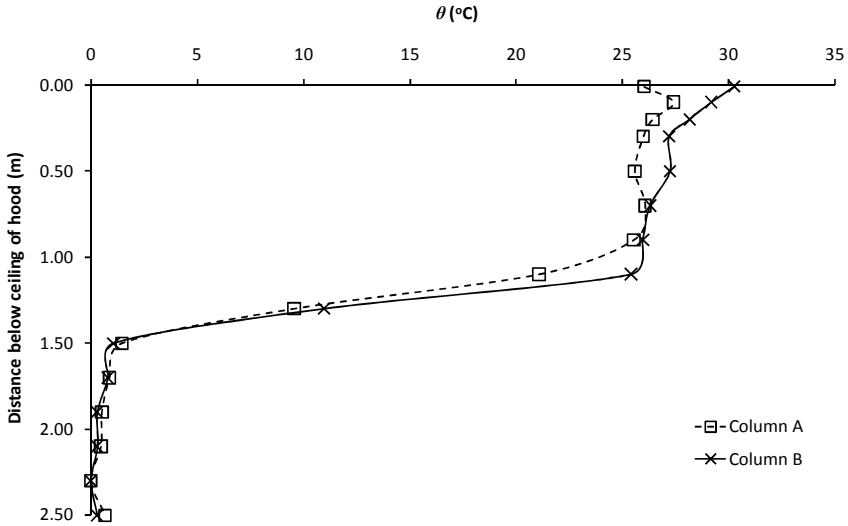

Figure J60: Experiment E147

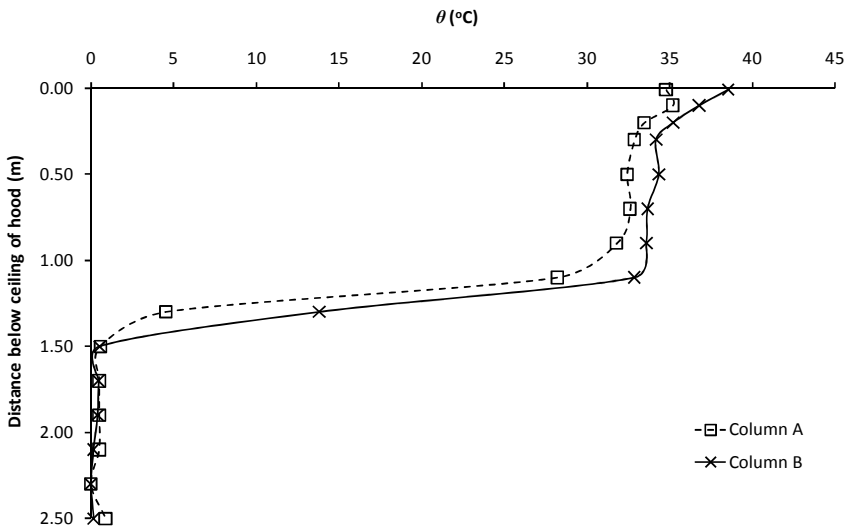

Figure J61: Experiment E148

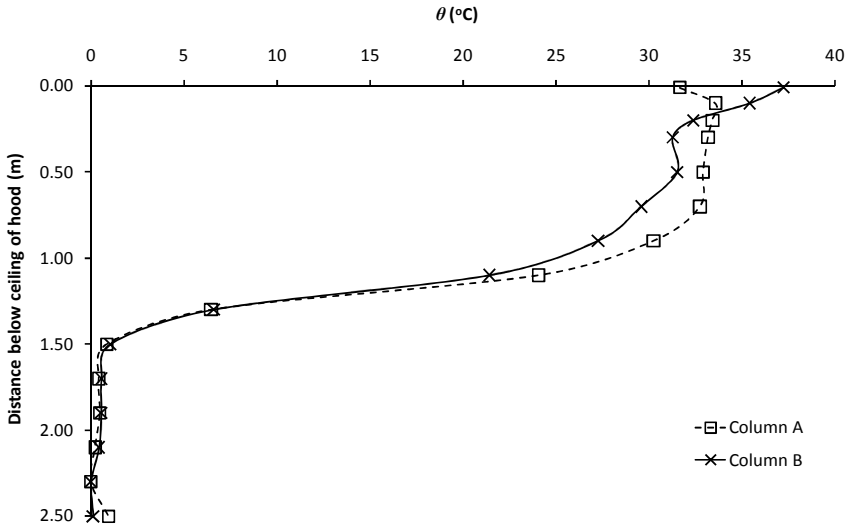

Figure J62: Experiment E149

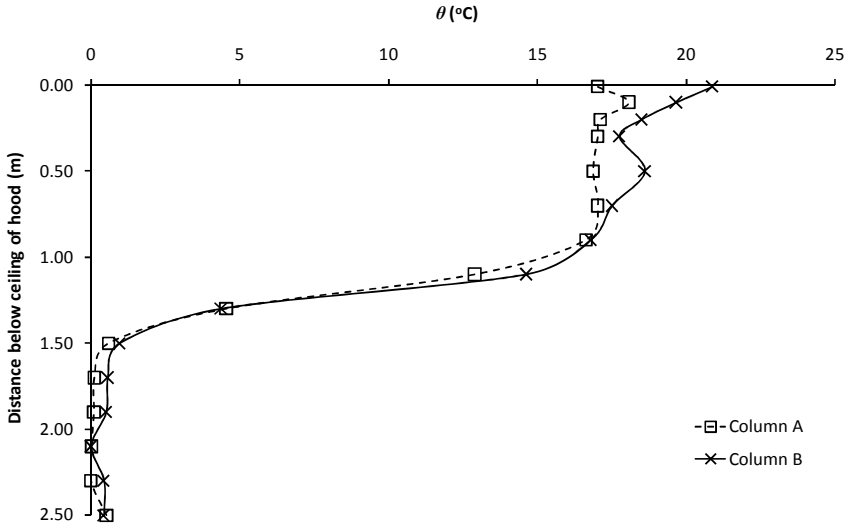

Figure J63: Experiment E150

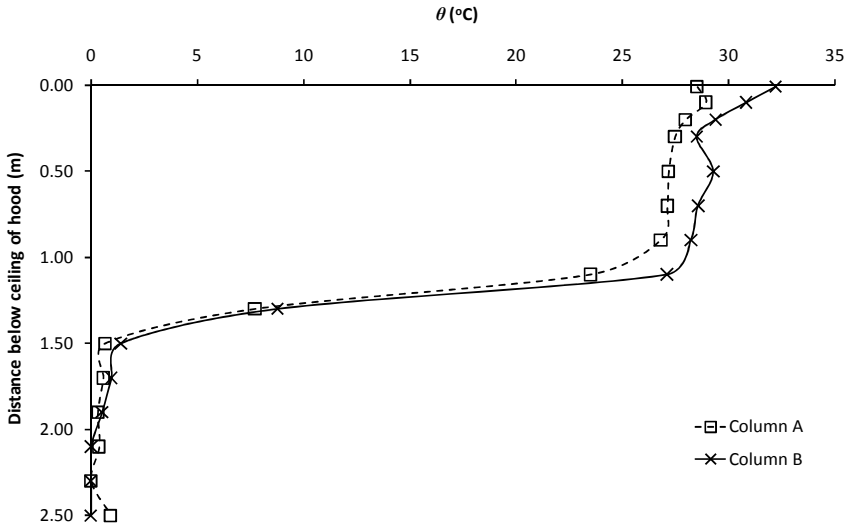

Figure J64: Experiment E151

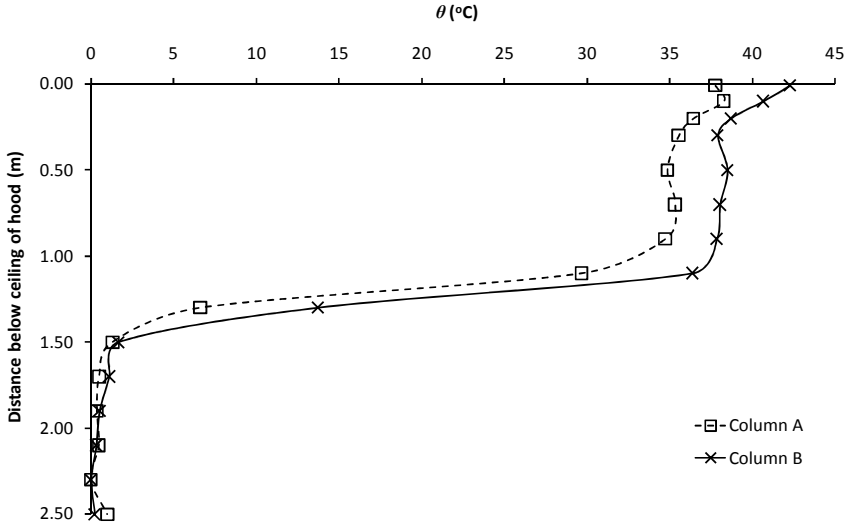

Figure J65: Experiment E152

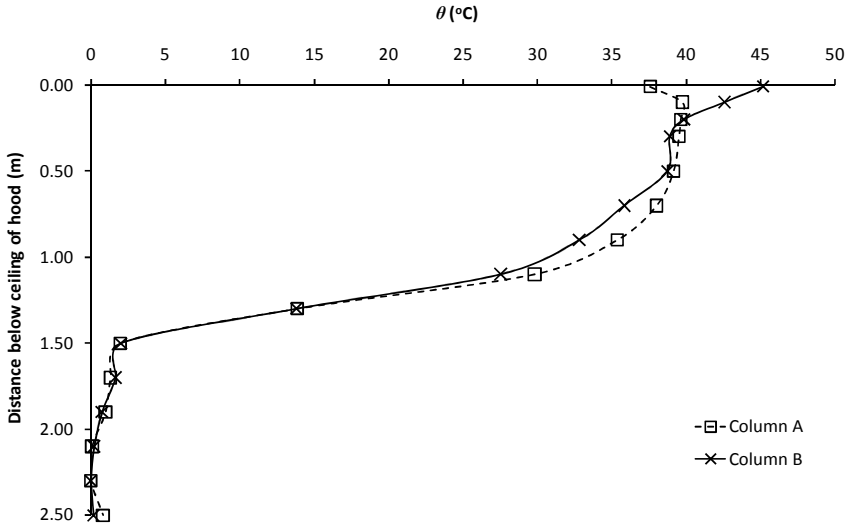

Figure J66: Experiment E153

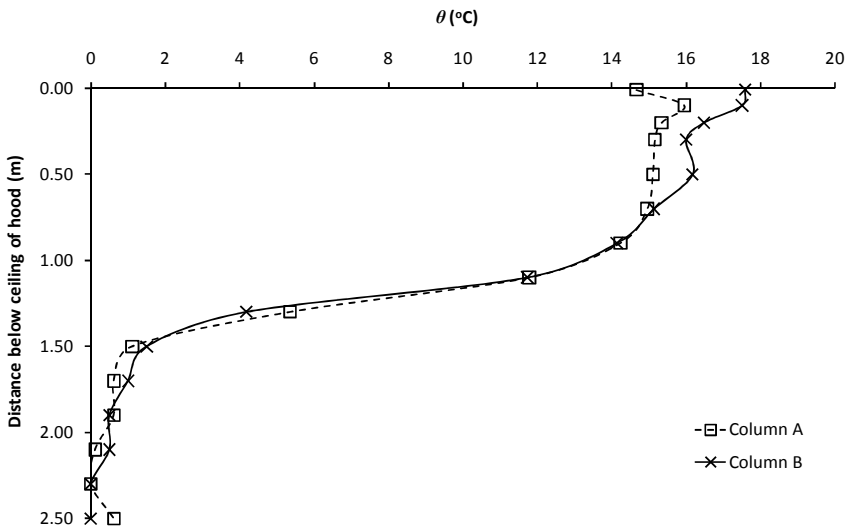

Figure J67: Experiment E154

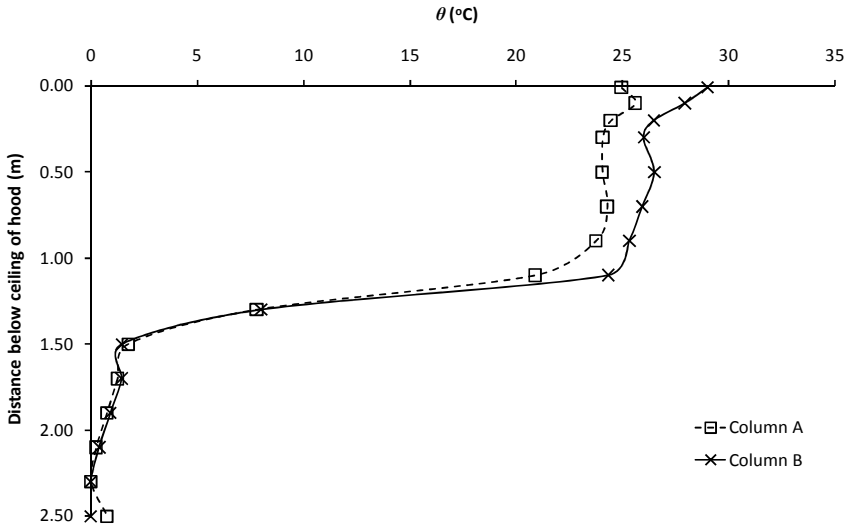

Figure J68: Experiment E155

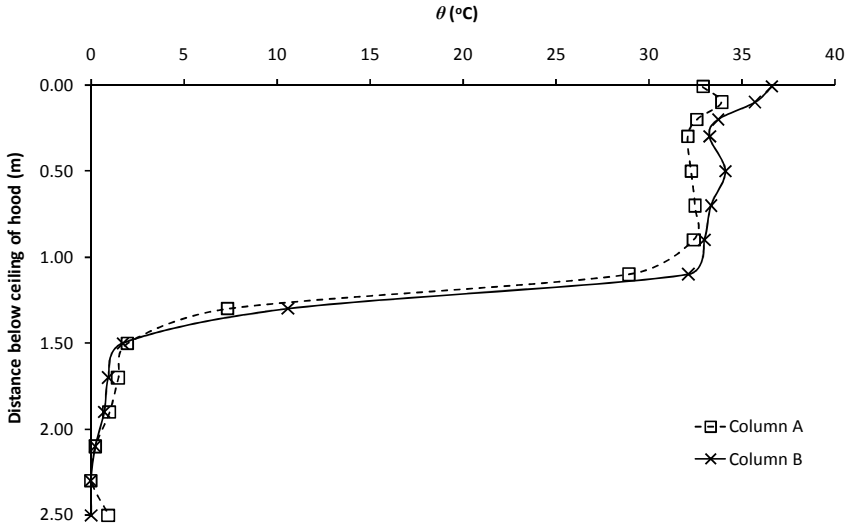

Figure J69: Experiment E156

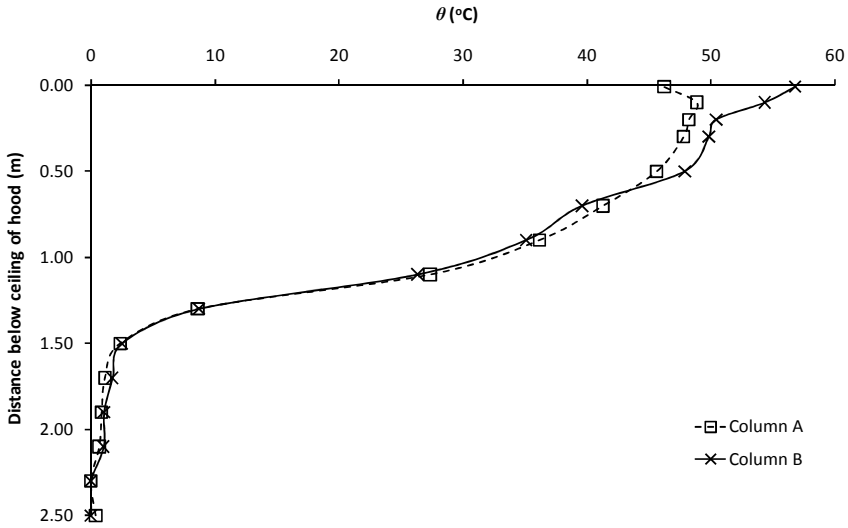

Figure J70: Experiment E157

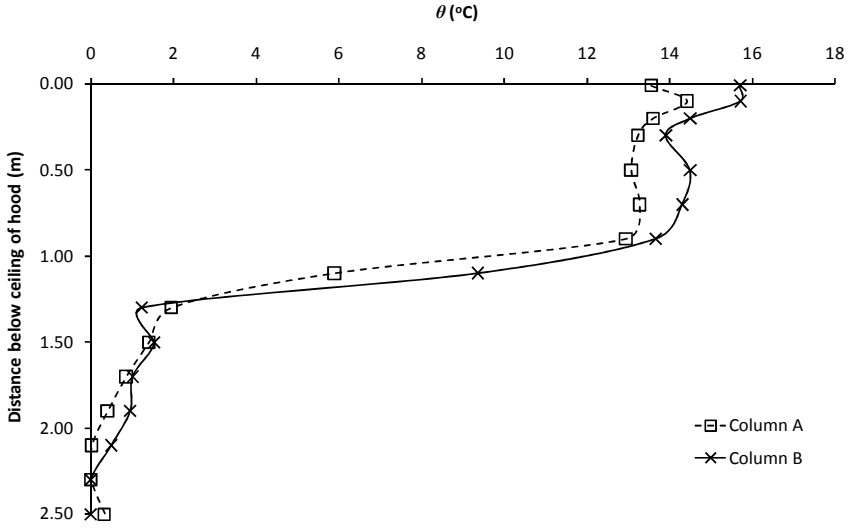

Figure J71: Experiment E188

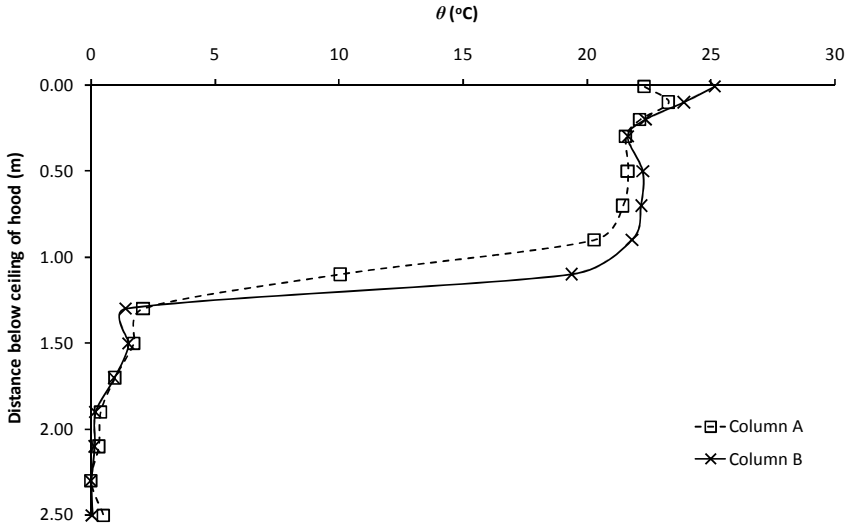

Figure J72: Experiment E189

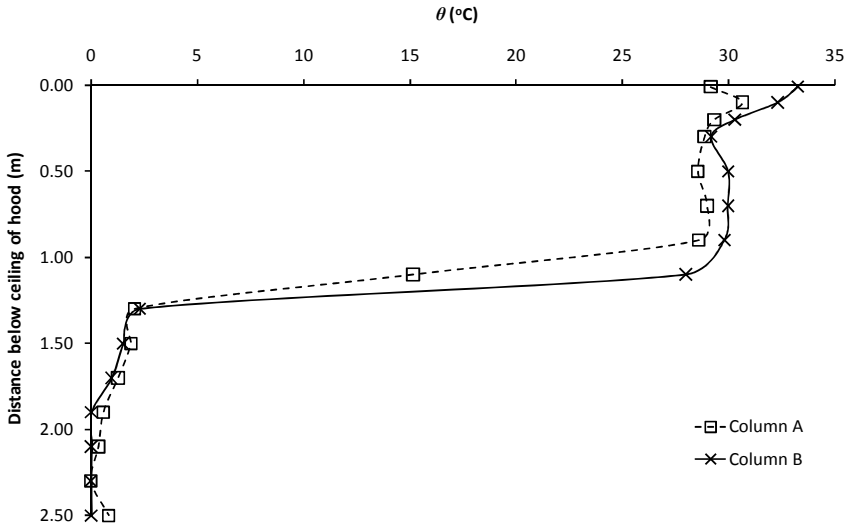

Figure J73: Experiment E190

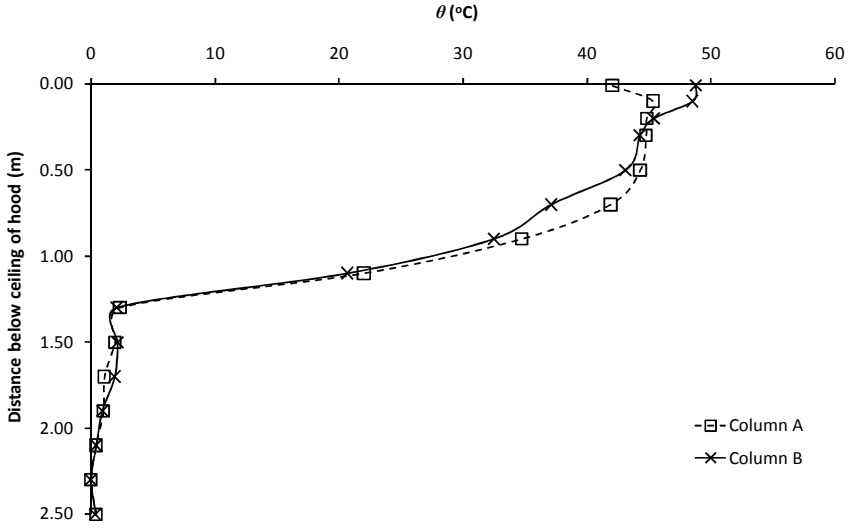

Figure J74: Experiment E191

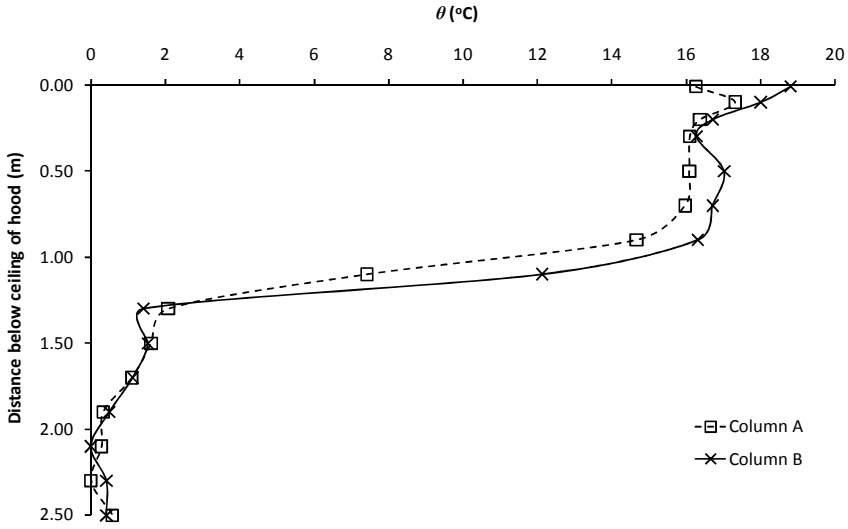

Figure J75: Experiment E192

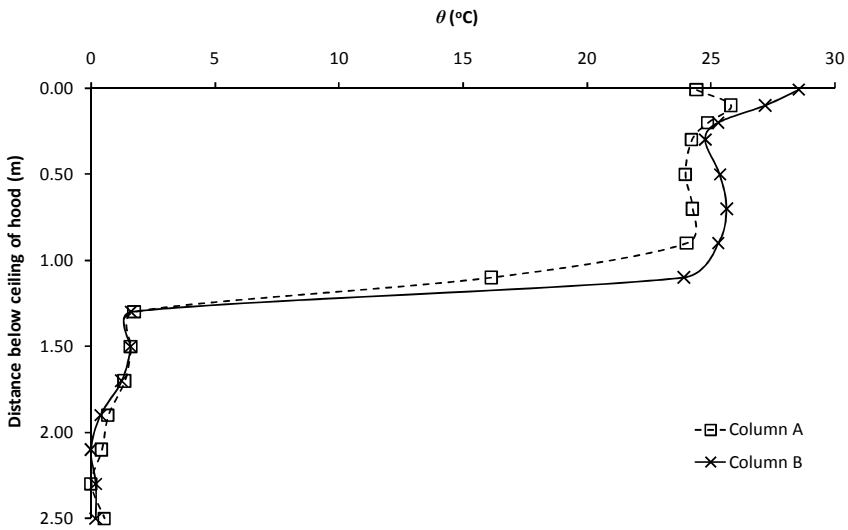

Figure J76: Experiment E193

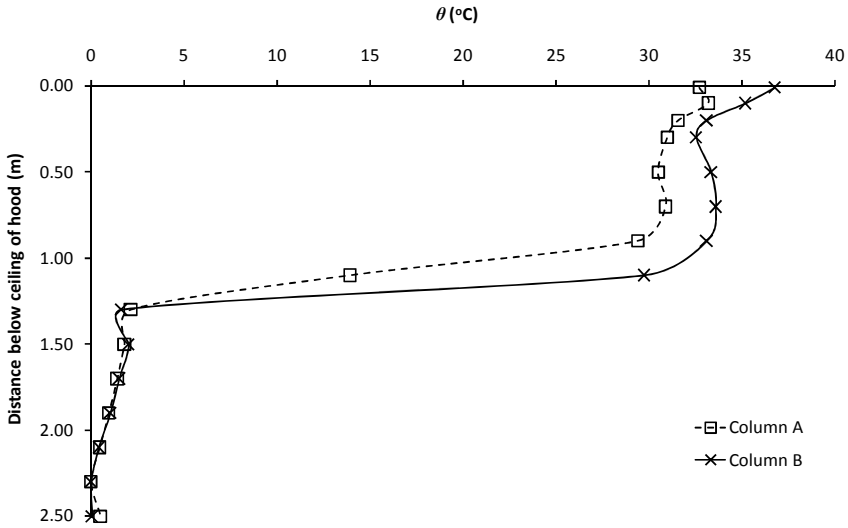

Figure J77: Experiment E194

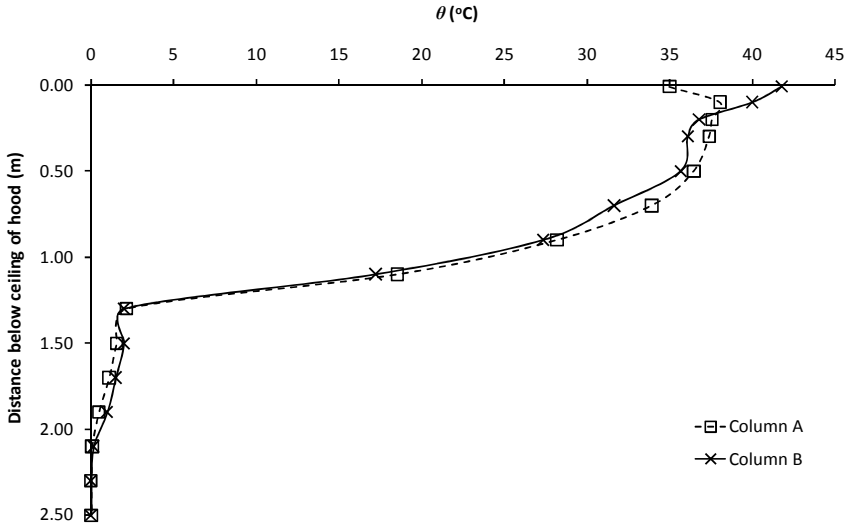

Figure J78: Experiment E195

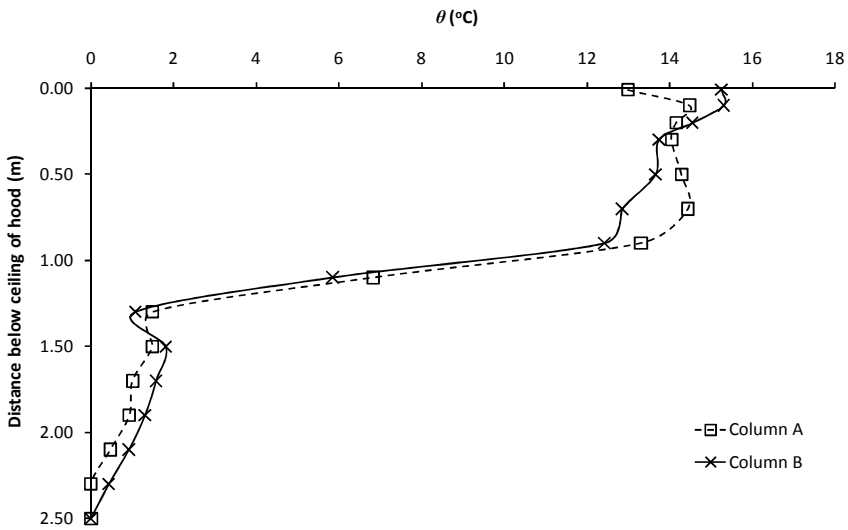

Figure J79: Experiment E196

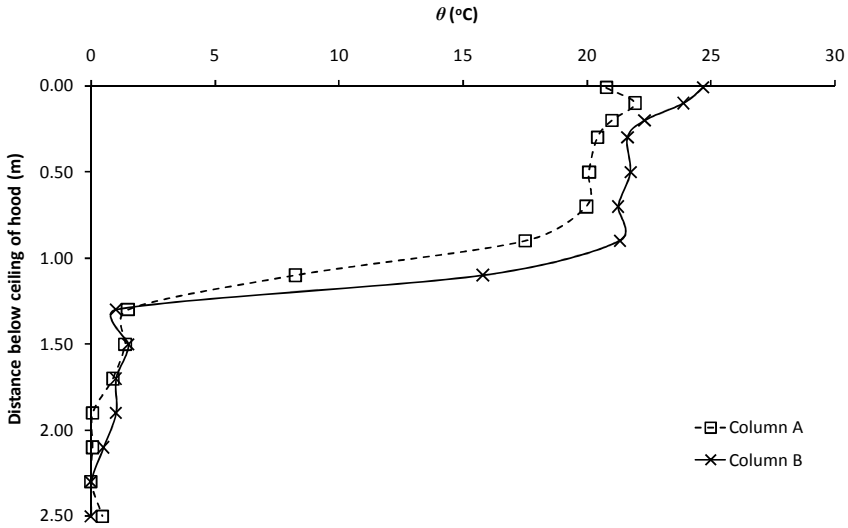

Figure J80: Experiment E197

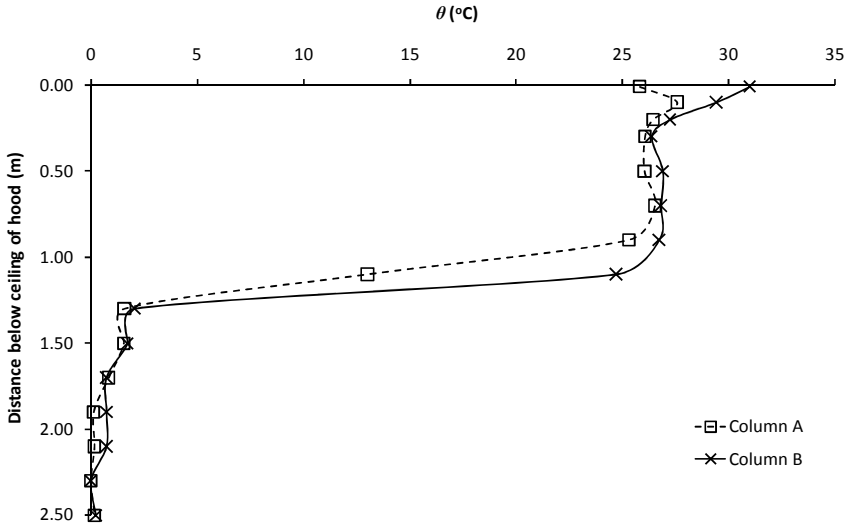

Figure J81: Experiment E198

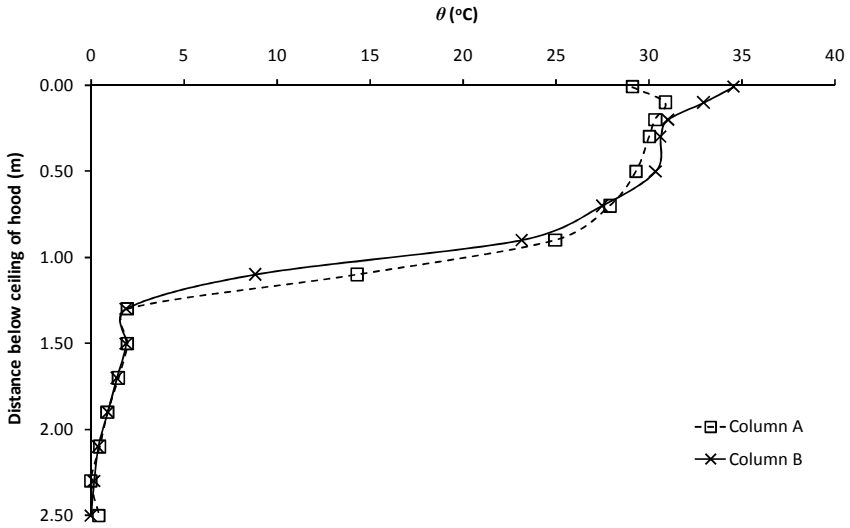

Figure J82: Experiment E199

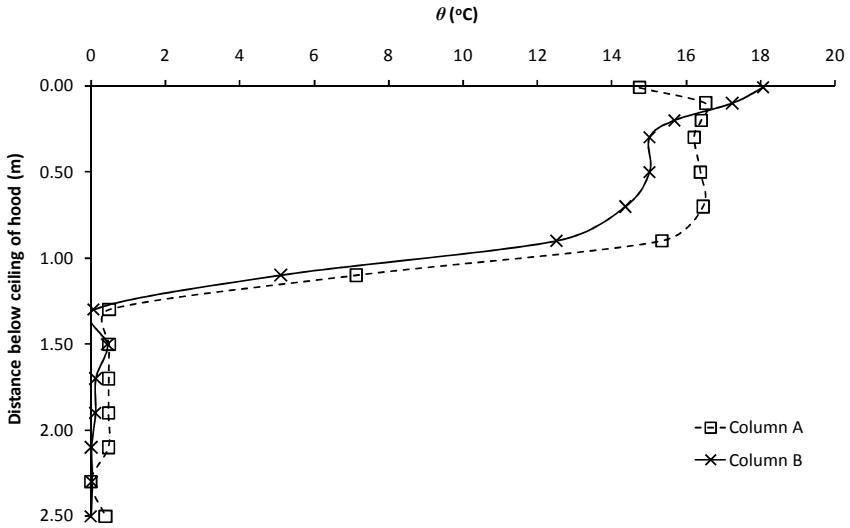

Figure J83: Experiment E200

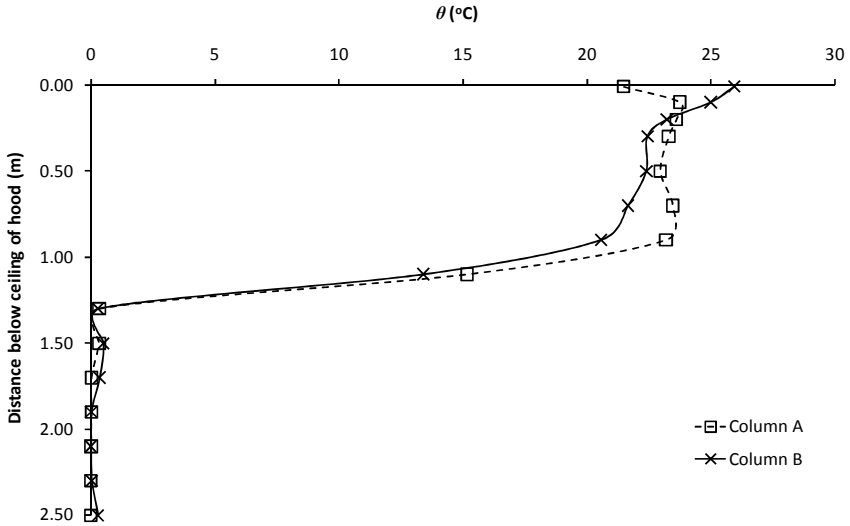

Figure J84: Experiment E201

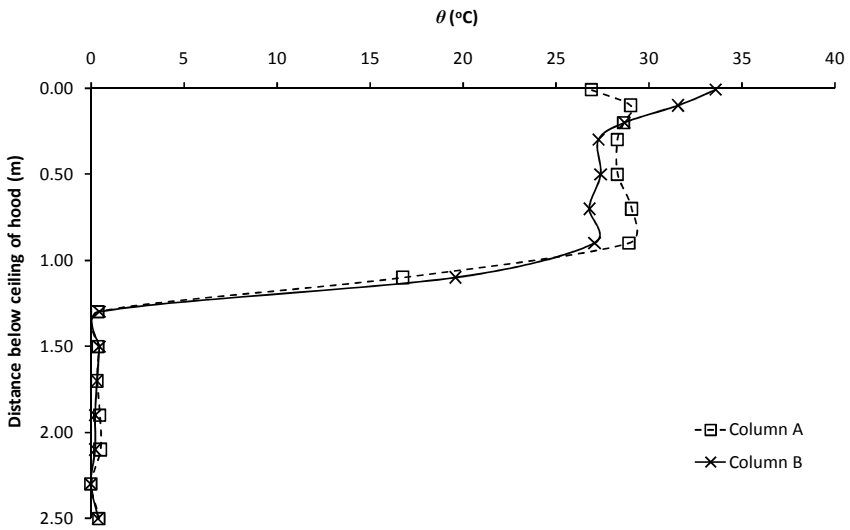

Figure J85: Experiment E202

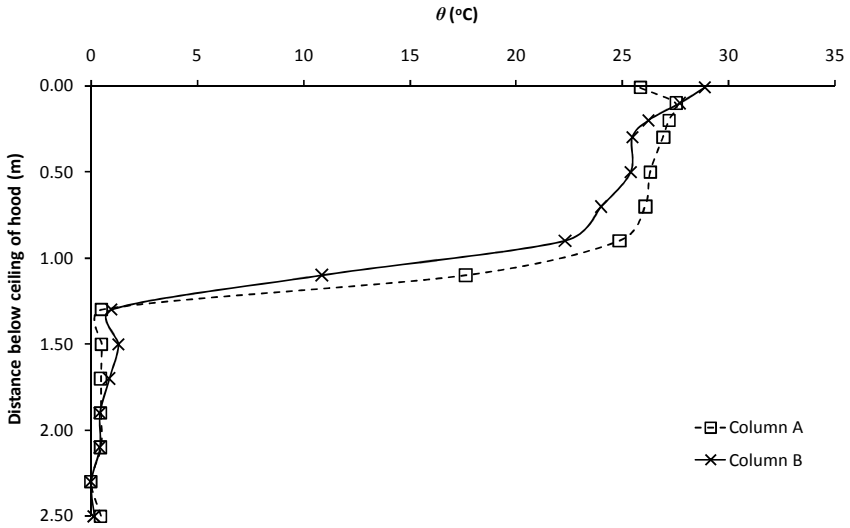

Figure J86: Experiment E203

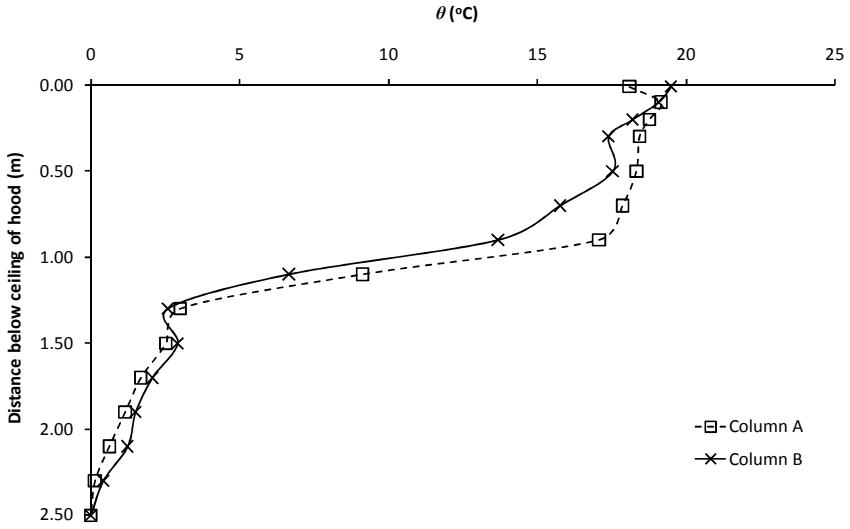

Figure J87: Experiment E204

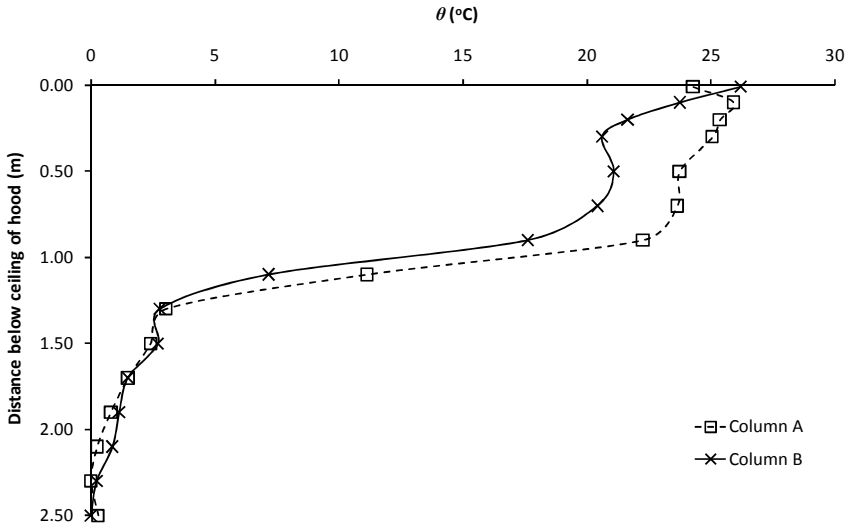

Figure J88: Experiment E205

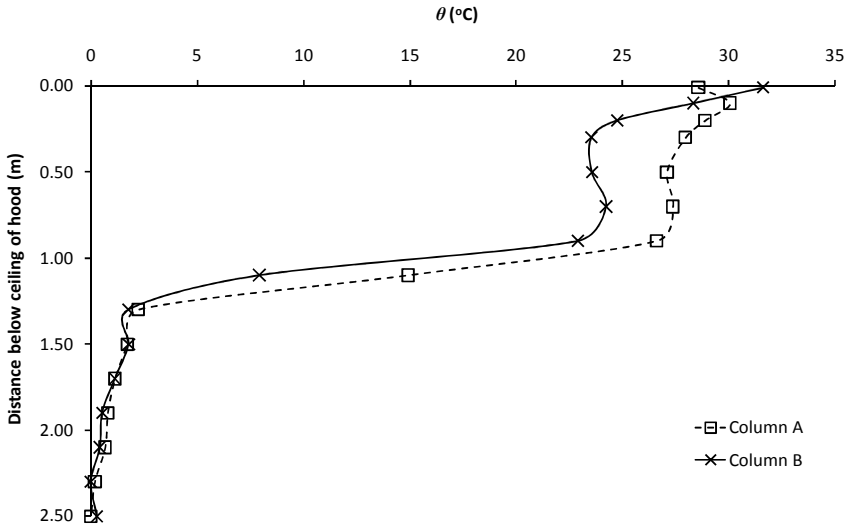

Figure J89: Experiment E206

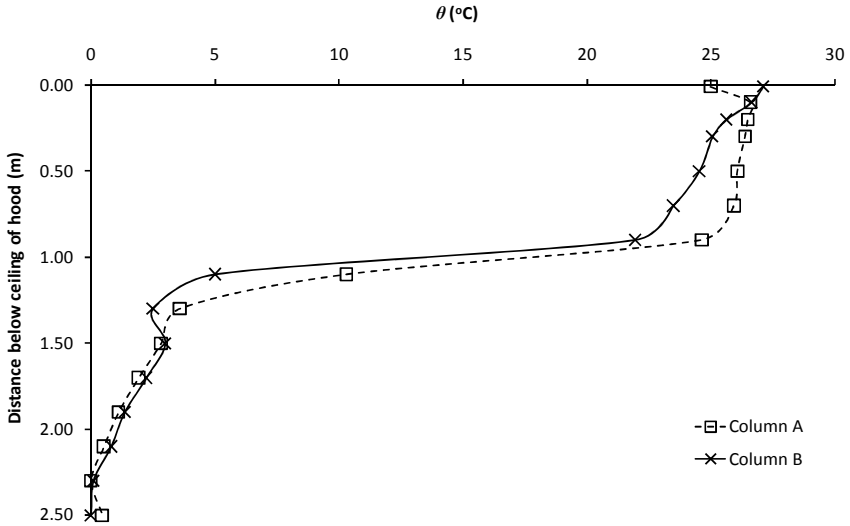

Figure J90: Experiment E207

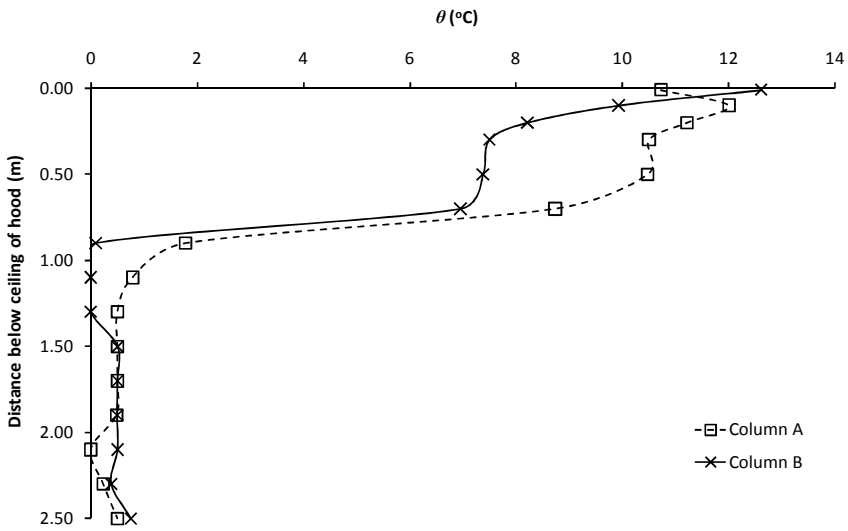

Figure J91: Experiment E208

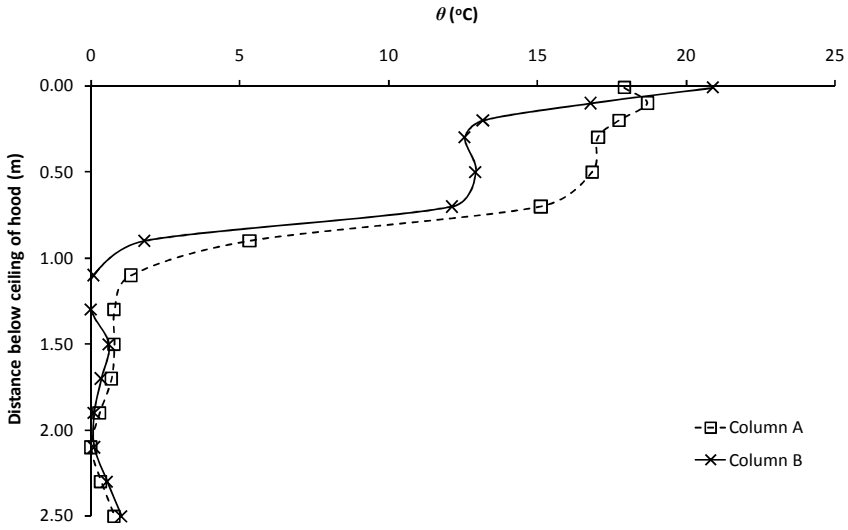

Figure J92: Experiment E209

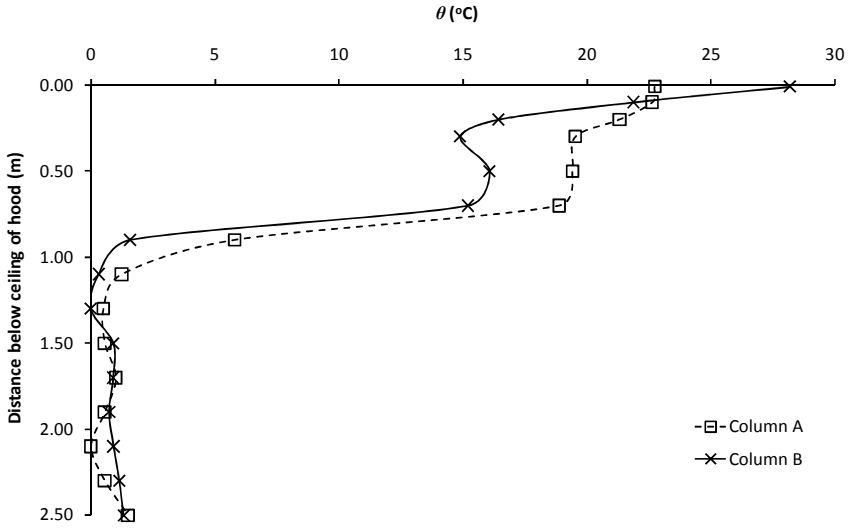

Figure J93: Experiment E210

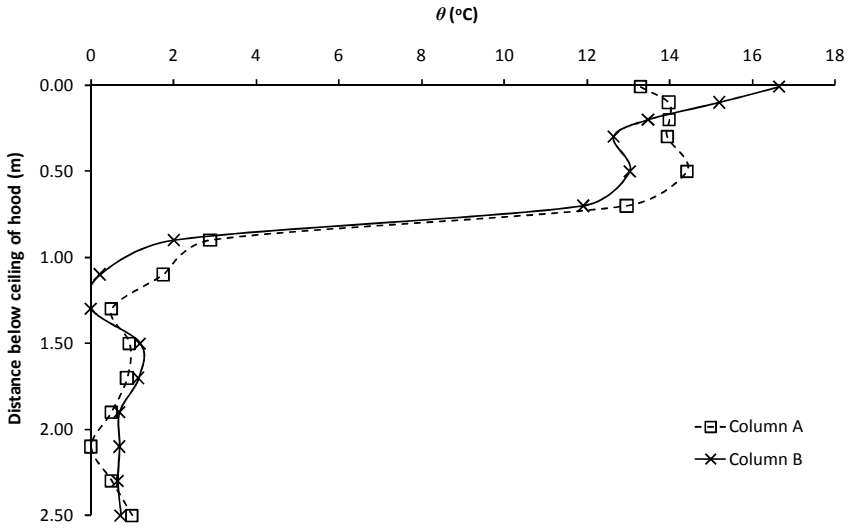

Figure J94: Experiment E211

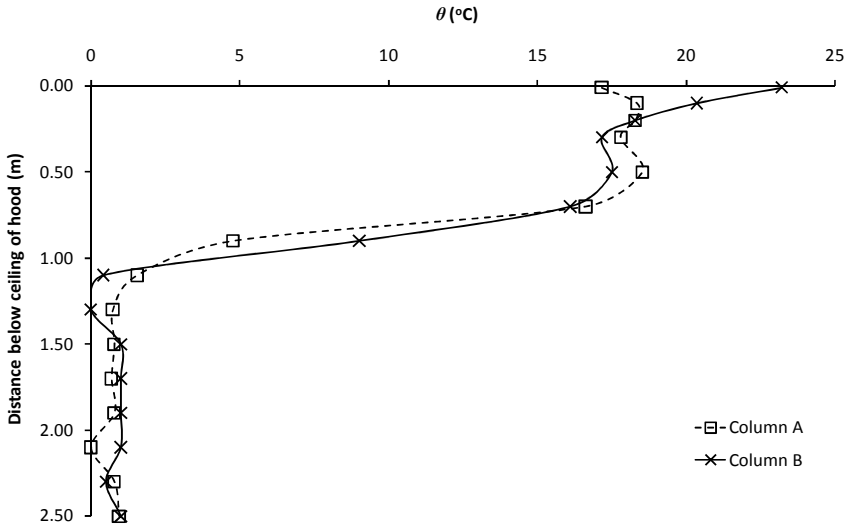

Figure J95: Experiment E212

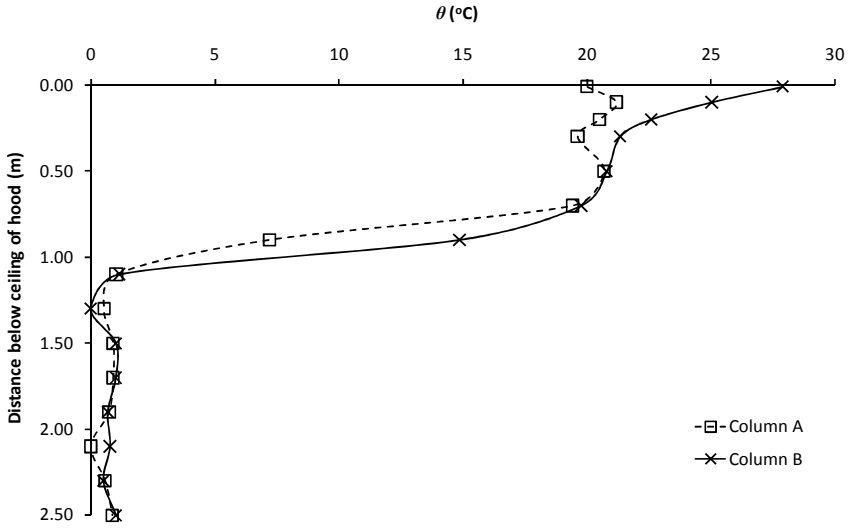

Figure J96: Experiment E213

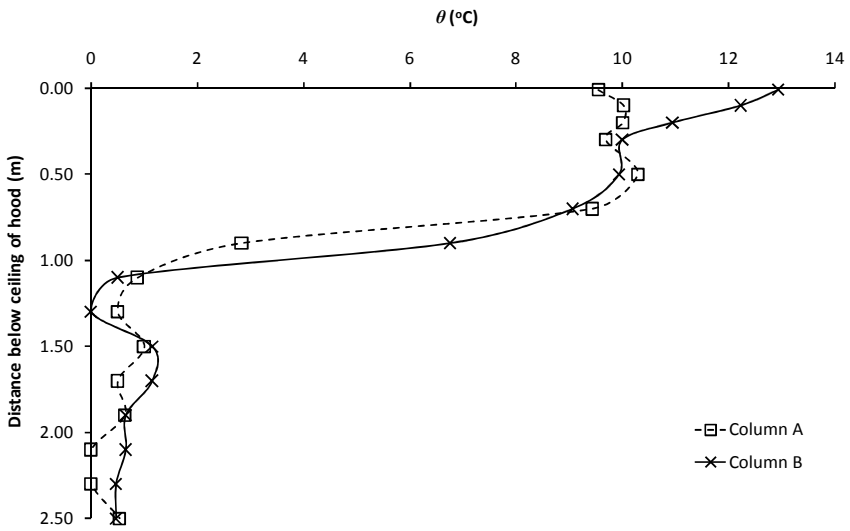

Figure J97: Experiment E214

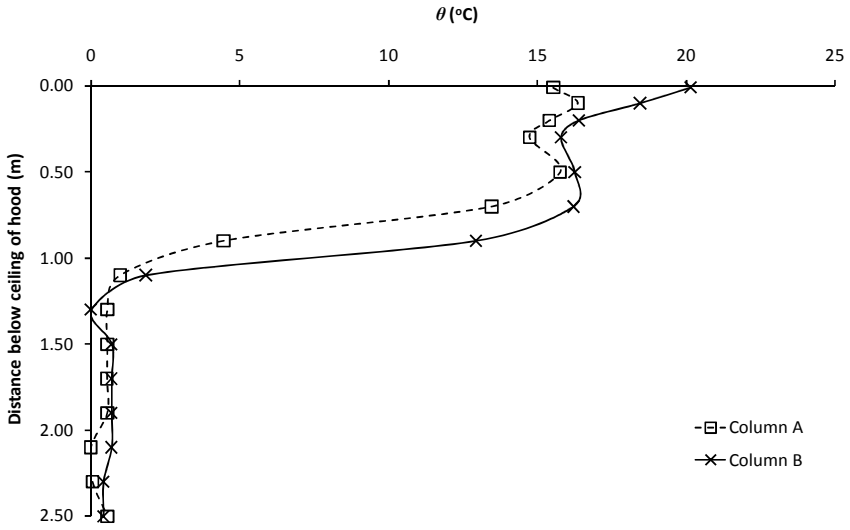

Figure J98: Experiment E215

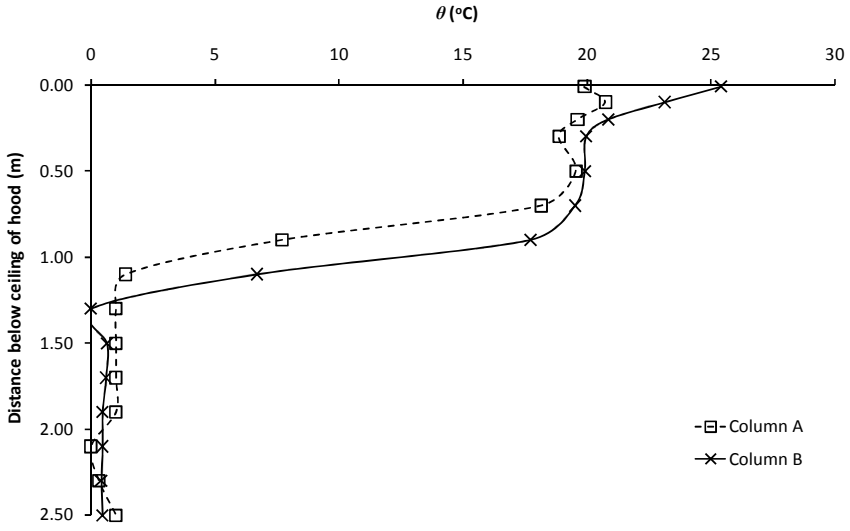

Figure J99: Experiment E216

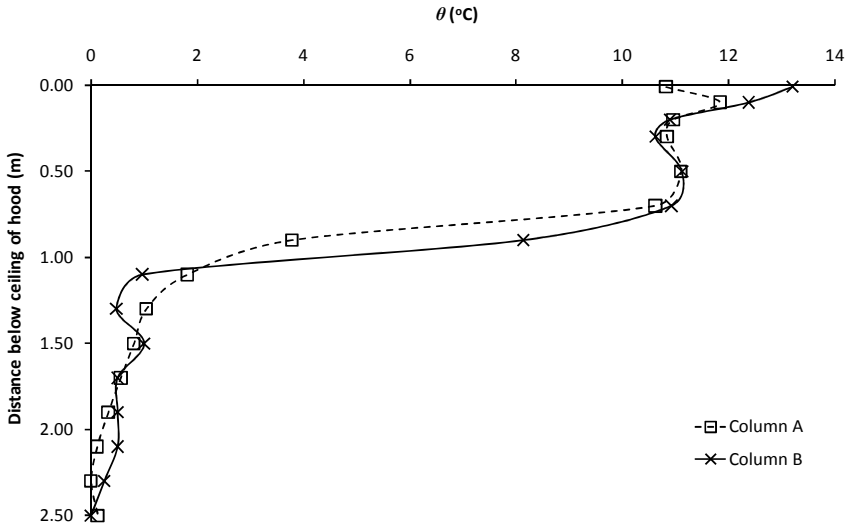

Figure J100: Experiment E217

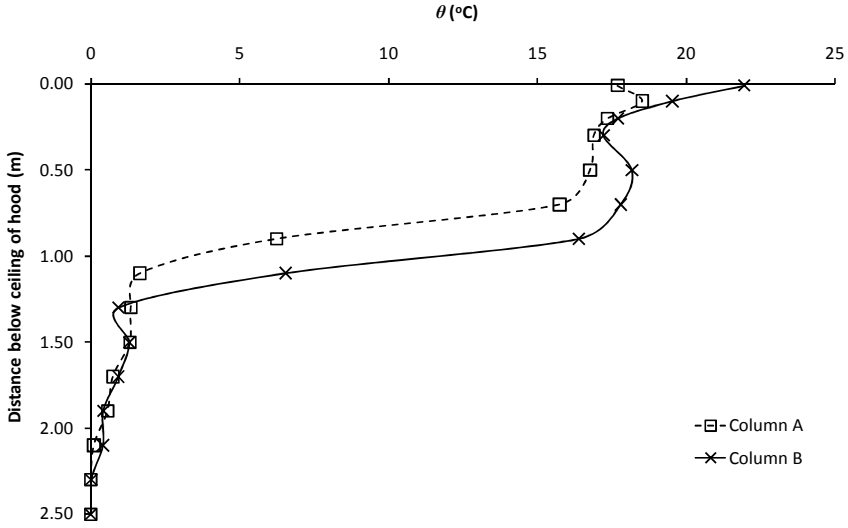

Figure J101: Experiment E218

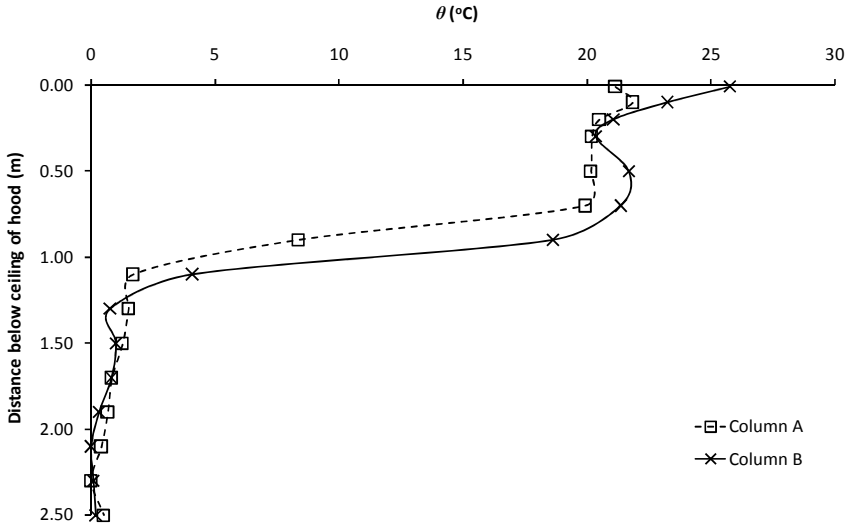

Figure J102: Experiment E219

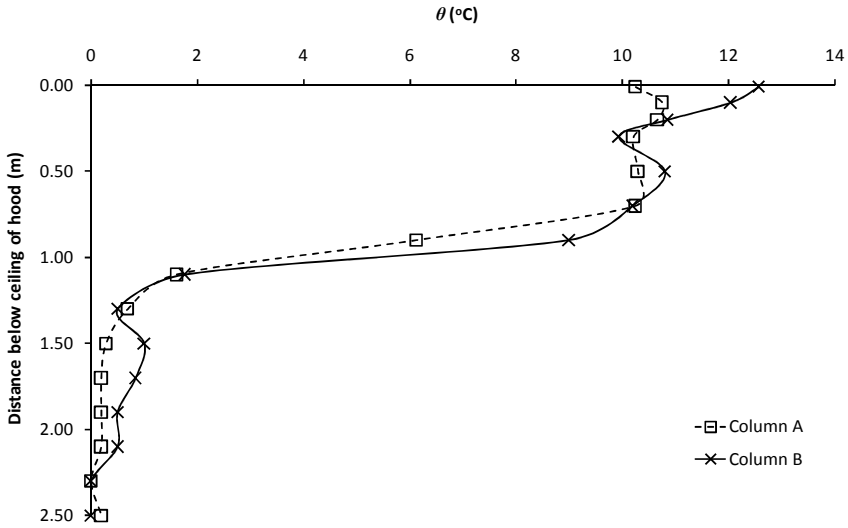

Figure J103: Experiment E220

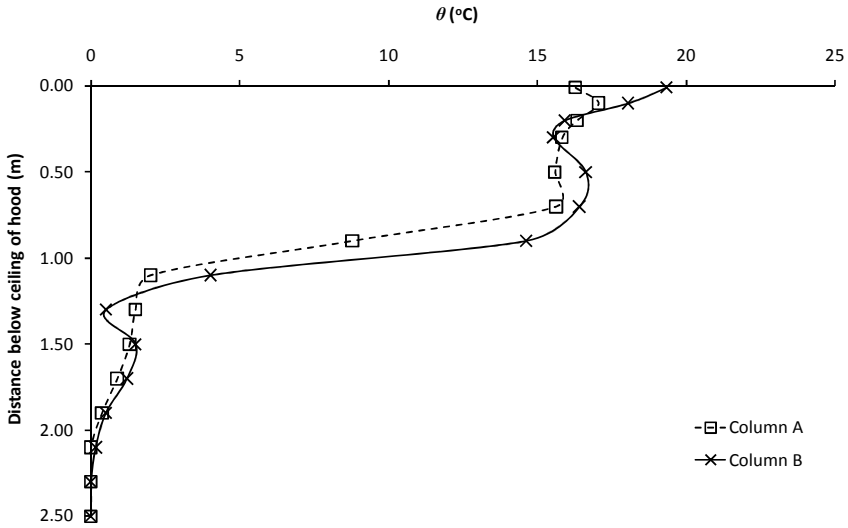

Figure J104: Experiment E221

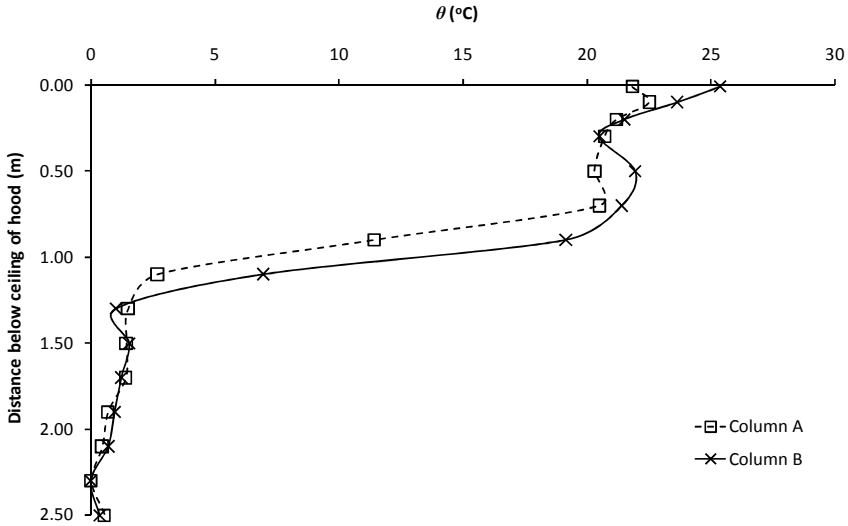

Figure J105: Experiment E222

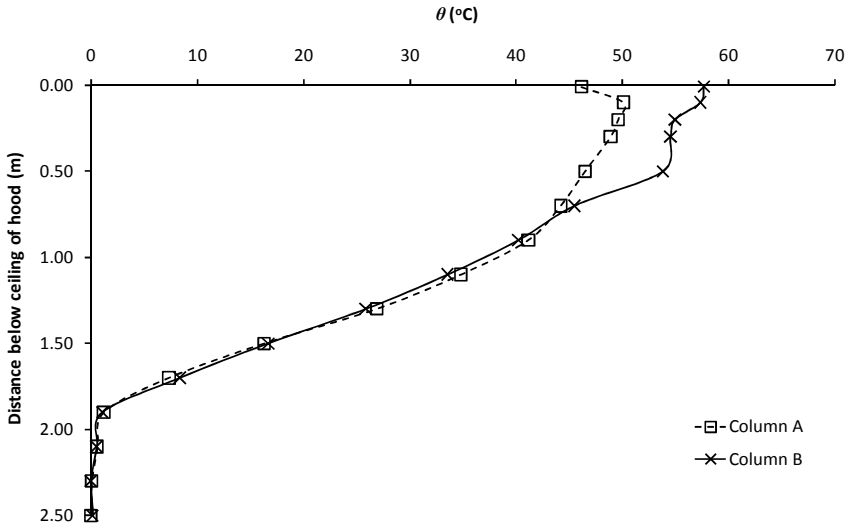

Figure J106: Experiment E283

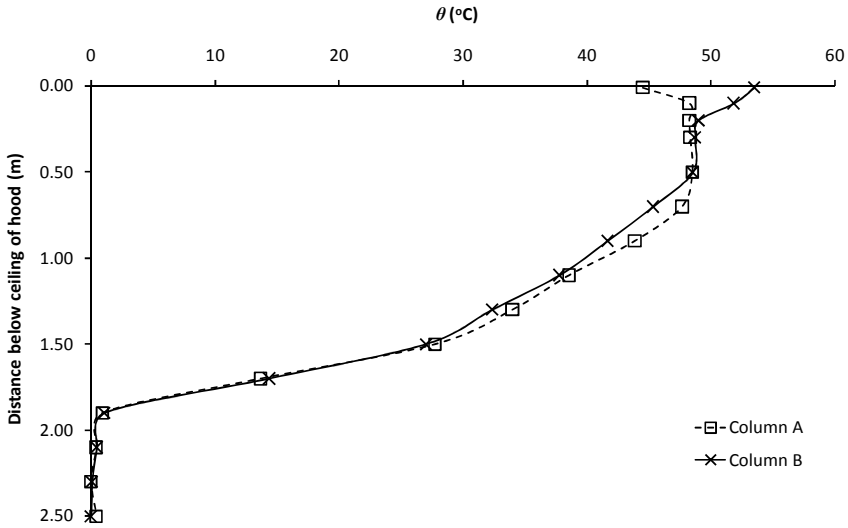

Figure J107: Experiment E284

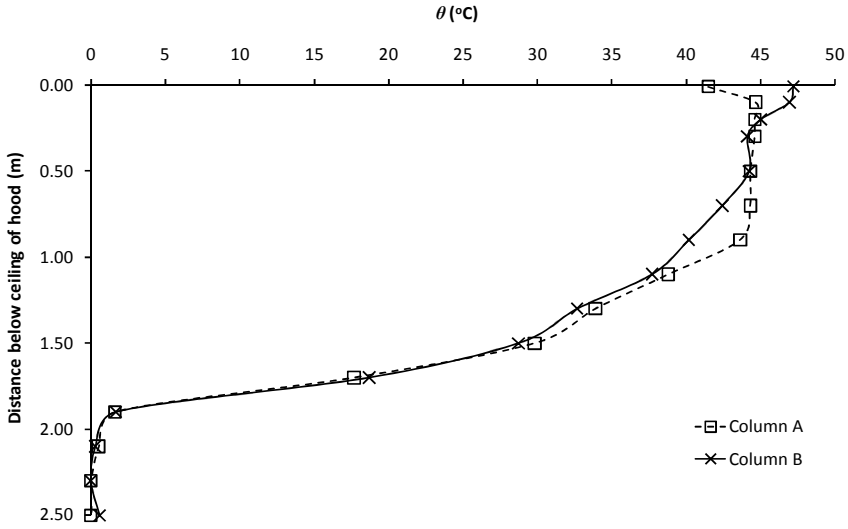

Figure J108: Experiment E285

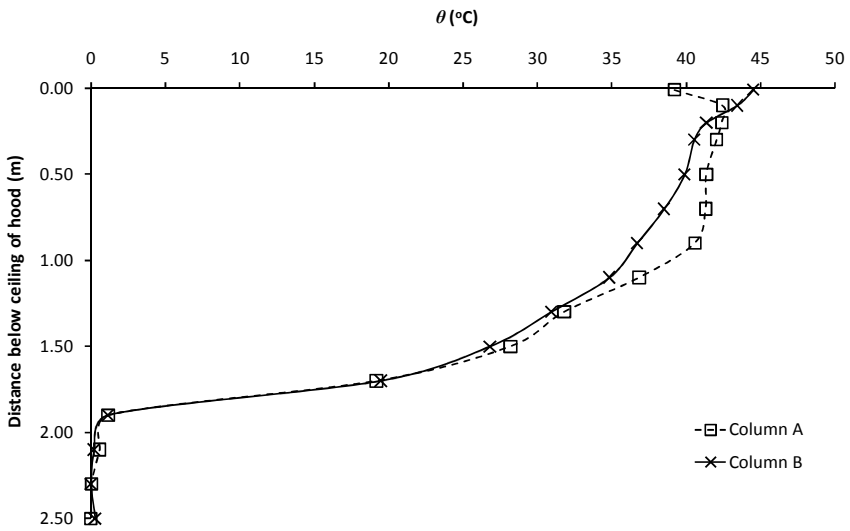

Figure J109: Experiment E286

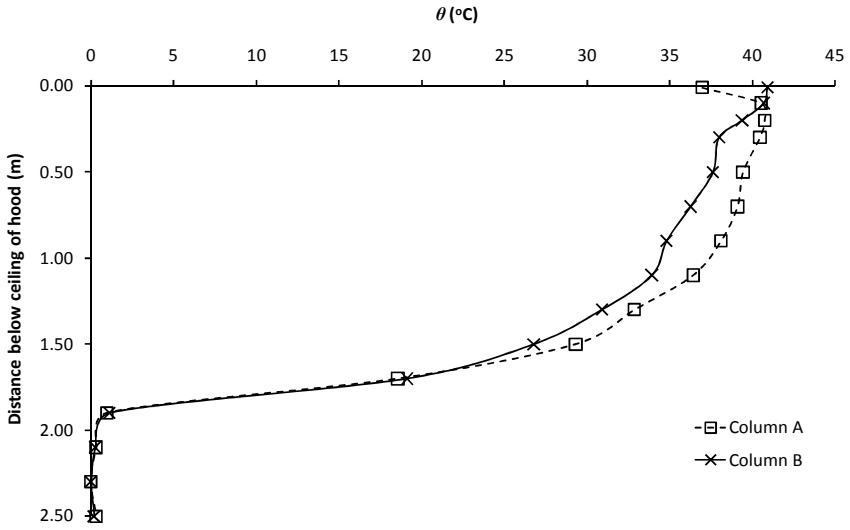

Figure J110: Experiment E287

Appendix K: Temperature profiles above spill edge from Column D, Experiments E208 to E222

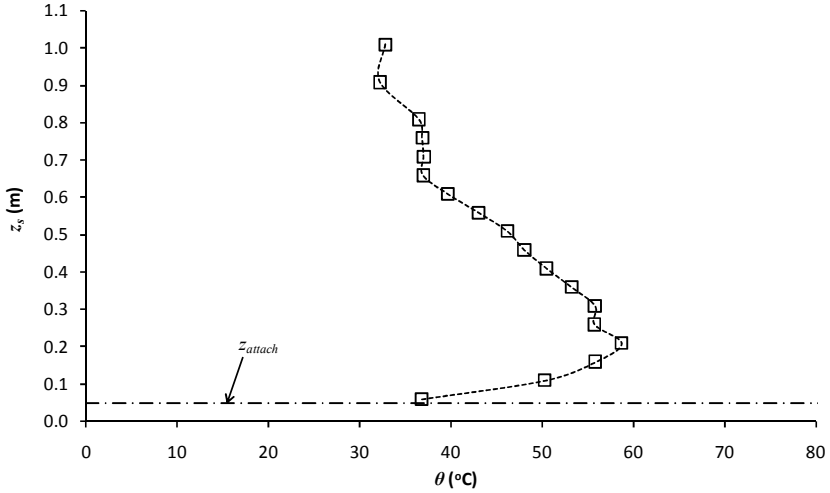

Figure K1: Experiment E208

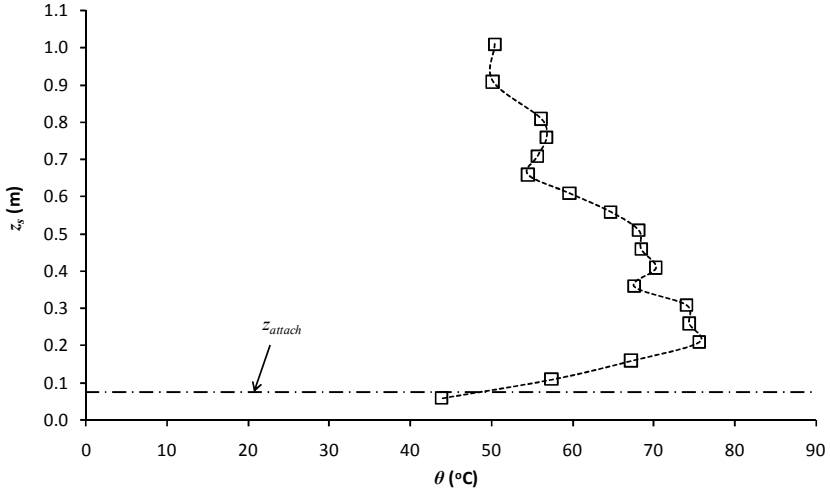

Figure K2: Experiment E209

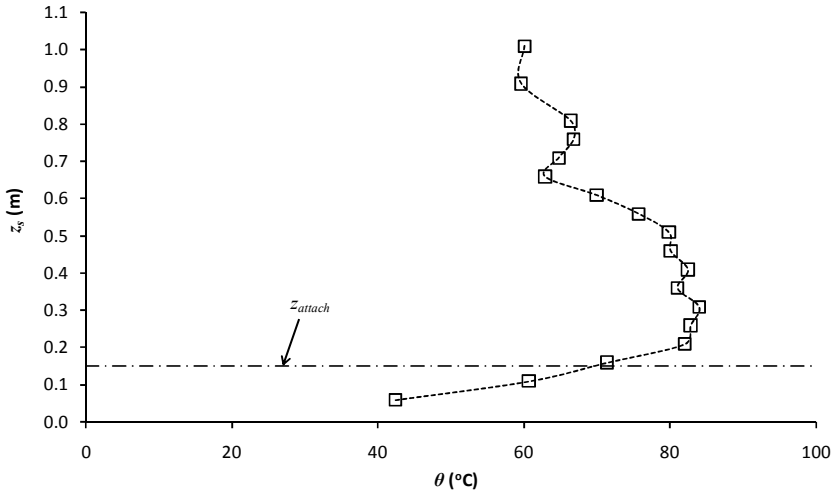

Figure K3: Experiment E210

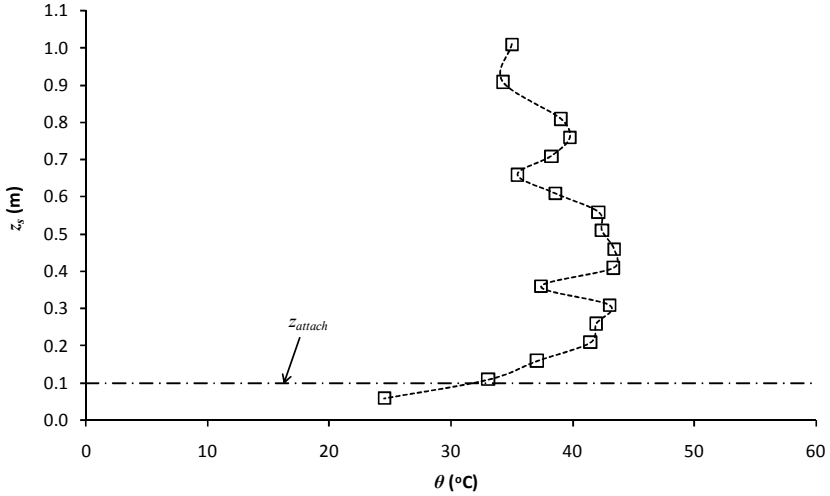

Figure K4: Experiment E211

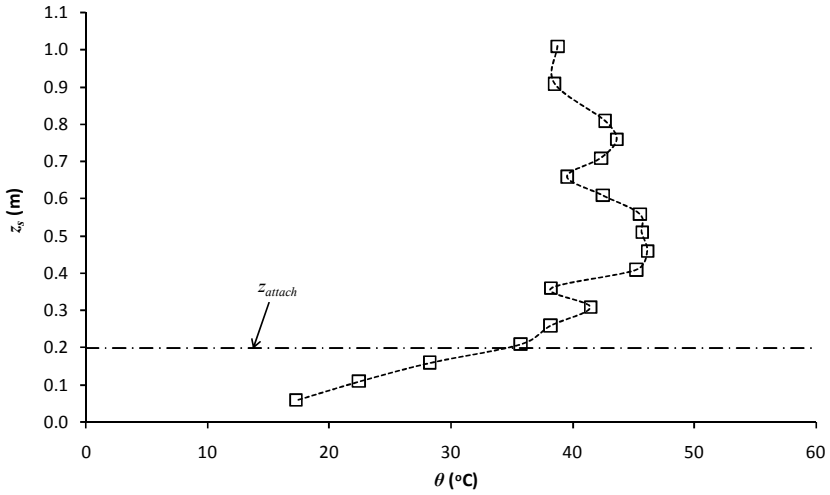

Figure K5: Experiment E212

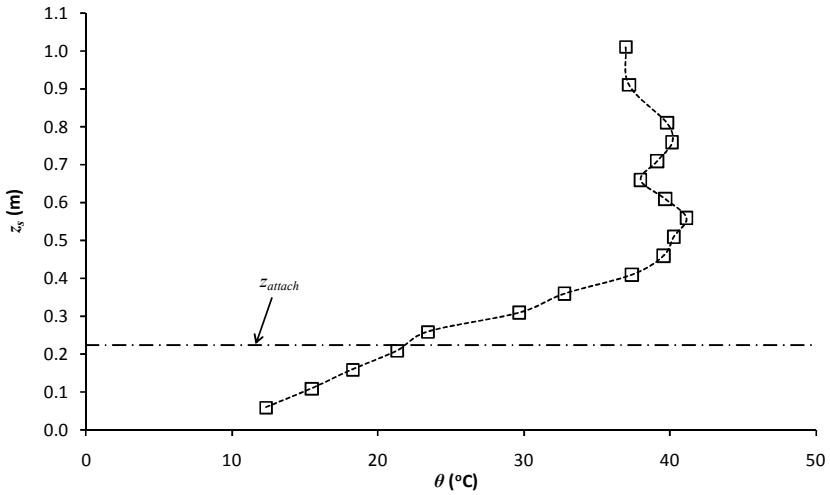

Figure K6: Experiment E213

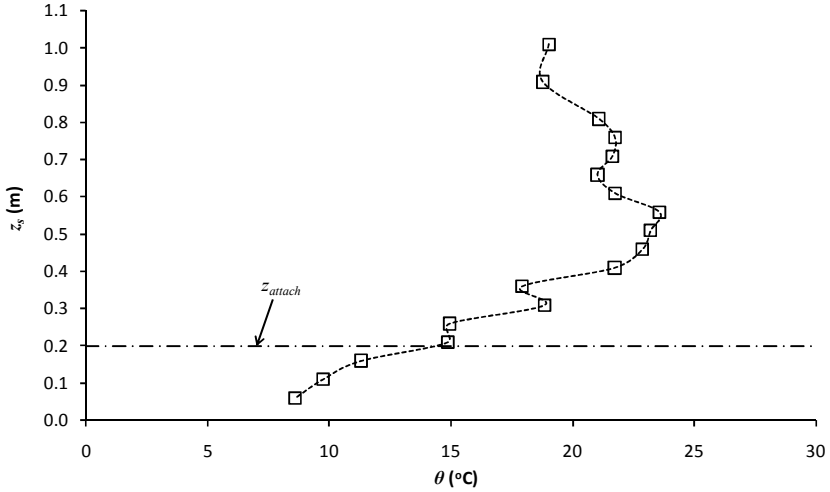

Figure K7: Experiment E214

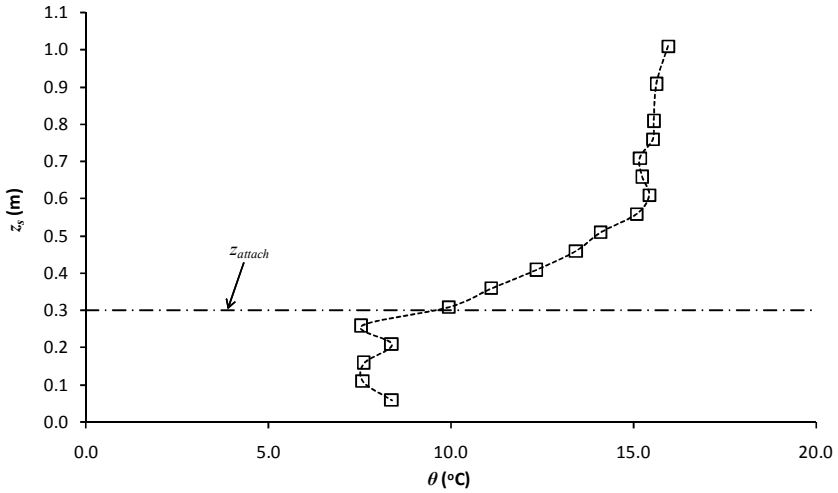

Figure K8: Experiment E215

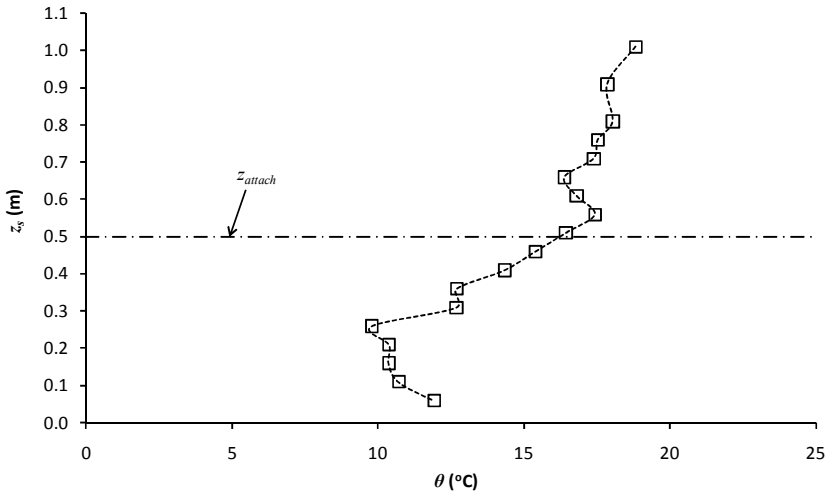

Figure K9: Experiment E216

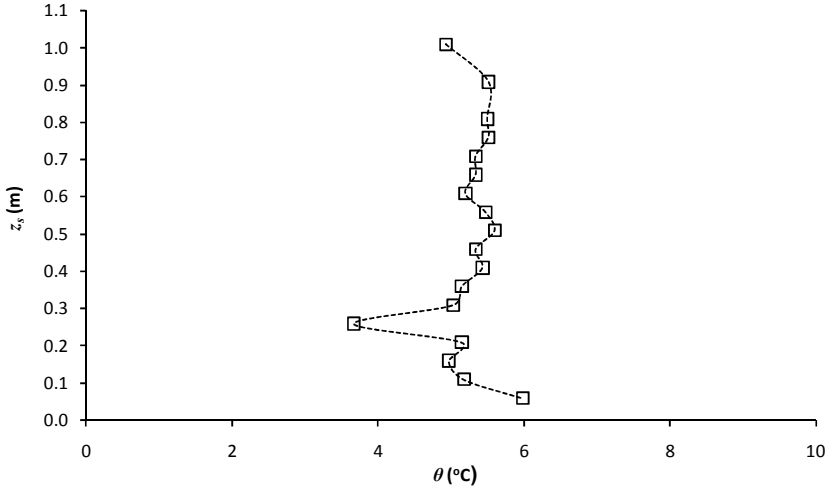

Figure K10: Experiment E217

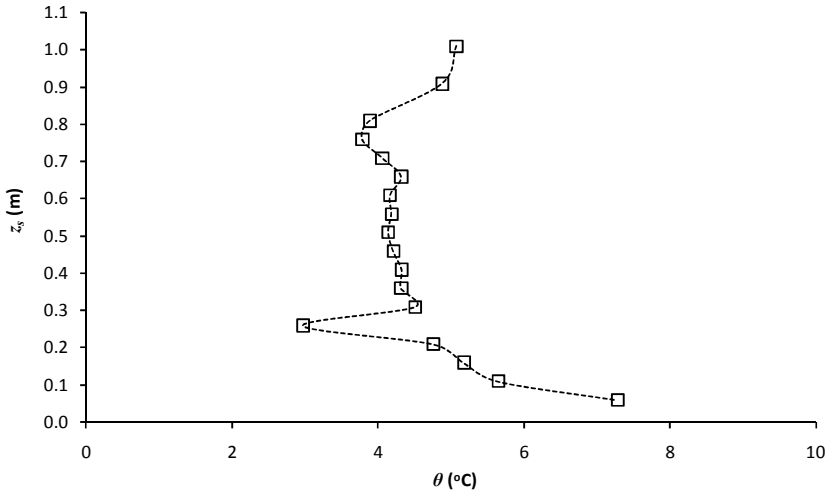

Figure K11: Experiment E218

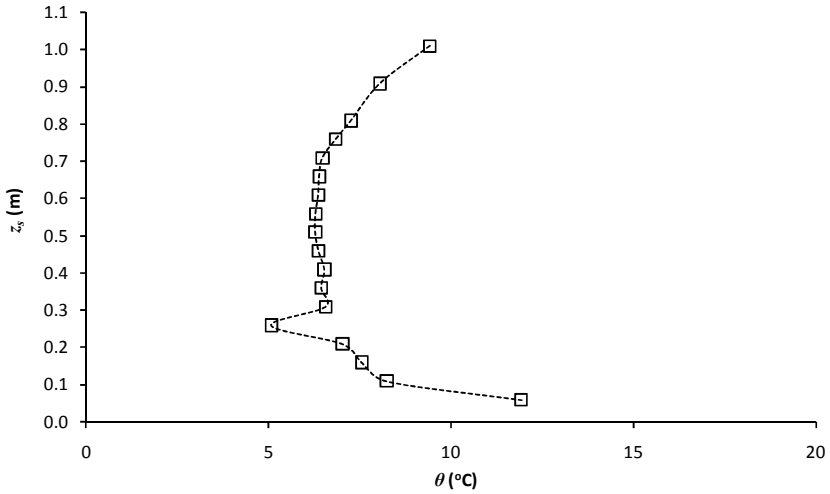

Figure K12: Experiment E219

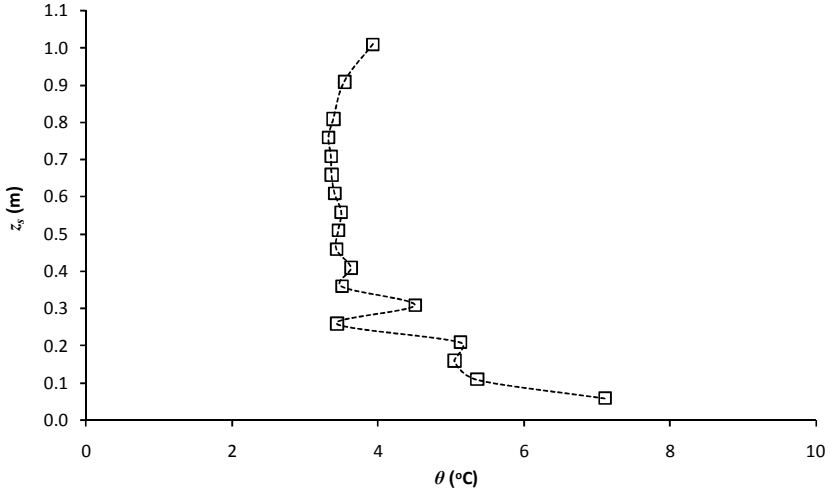

Figure K13: Experiment E220

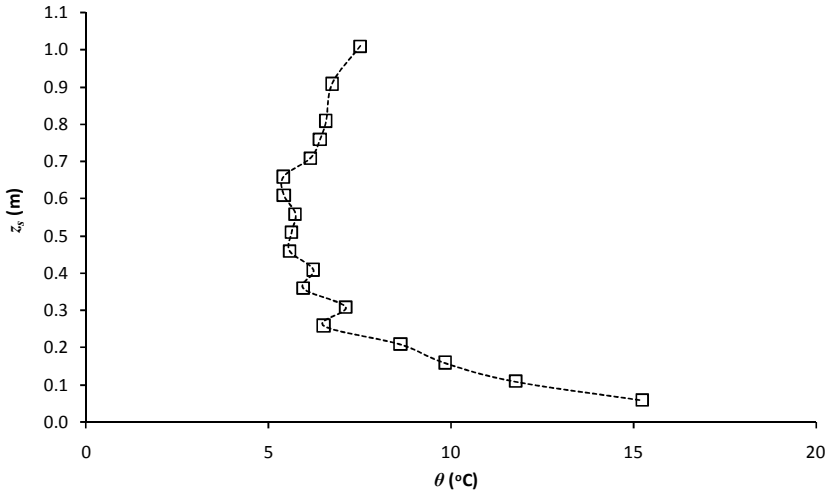

Figure K14: Experiment E221

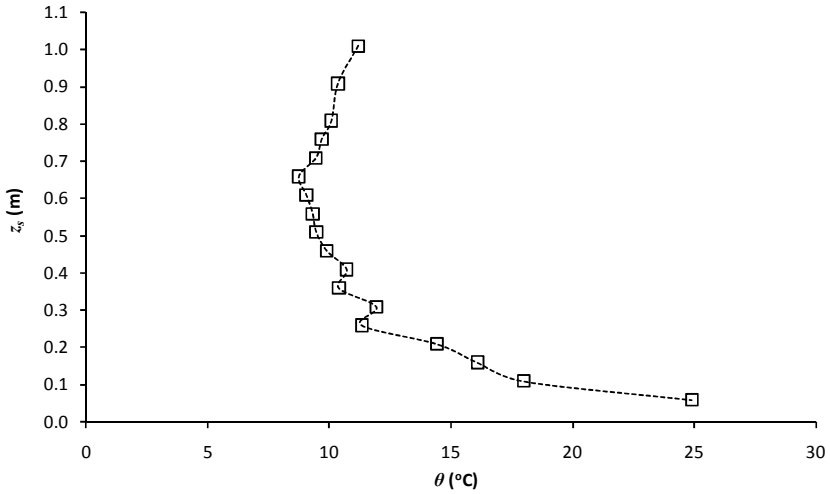

Figure K15: Experiment E222

Appendix L: Temperature profiles for Experiments T4 to T6

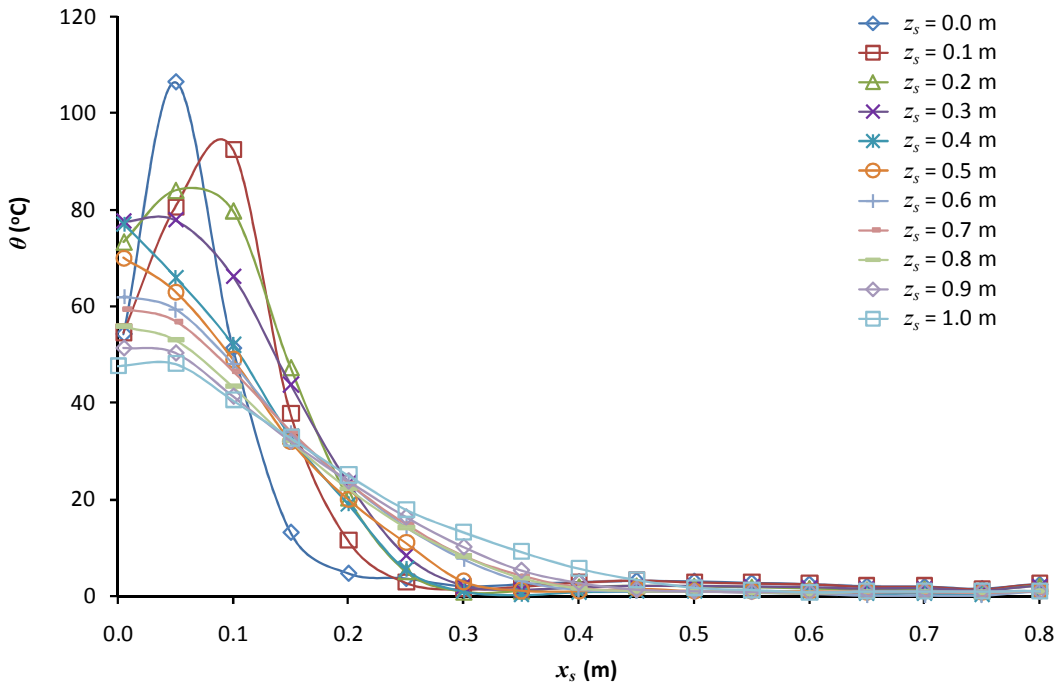

Figure L1: Experiment T4

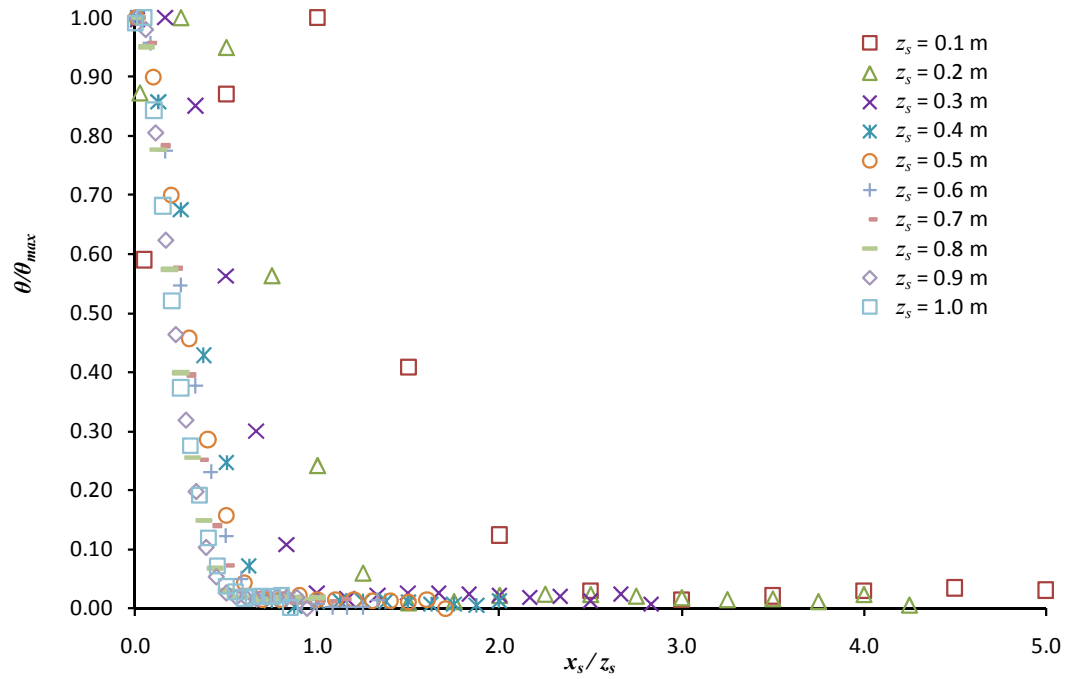

Figure L2: Non-dimensional profiles, Experiment T4

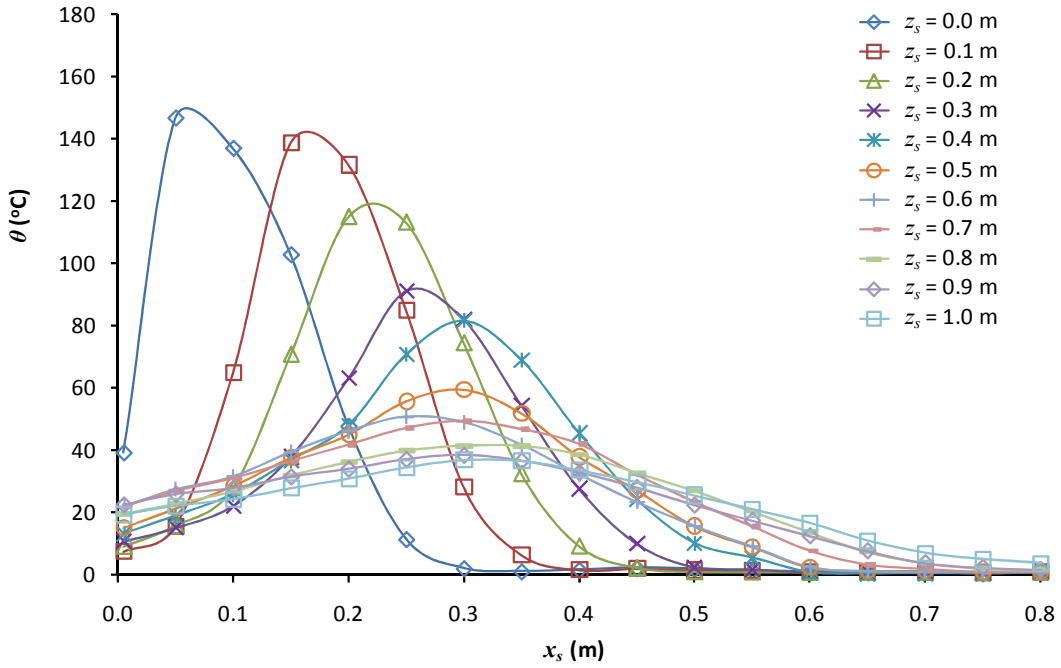

Figure L3: Experiment T5

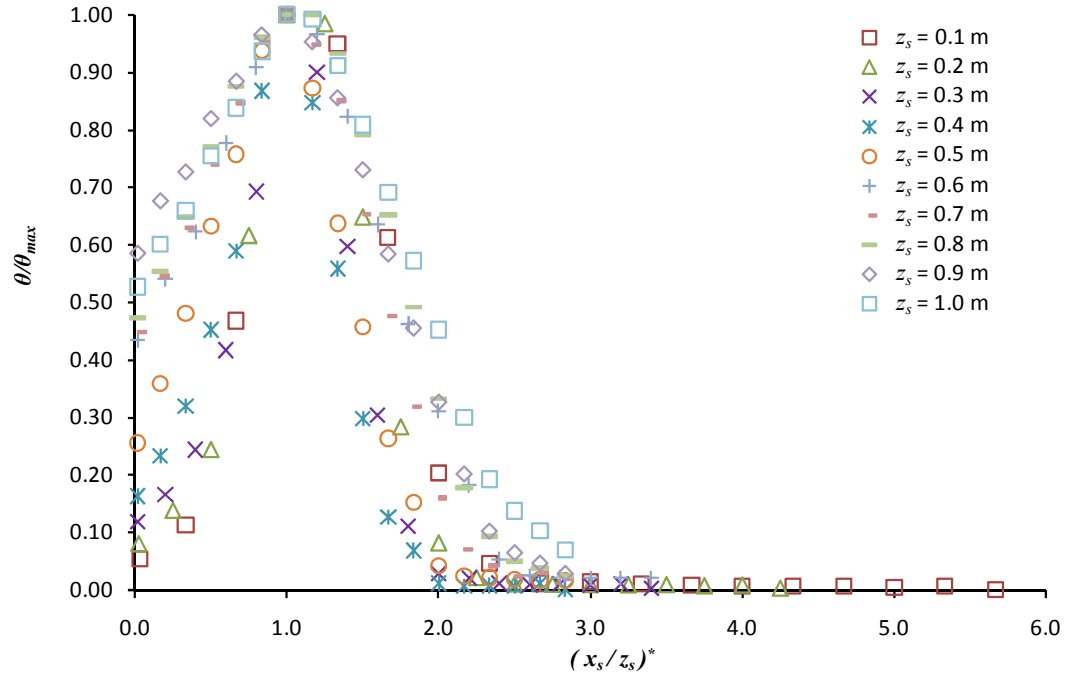

Figure L4: Non-dimensional normalised profiles, Experiment T5

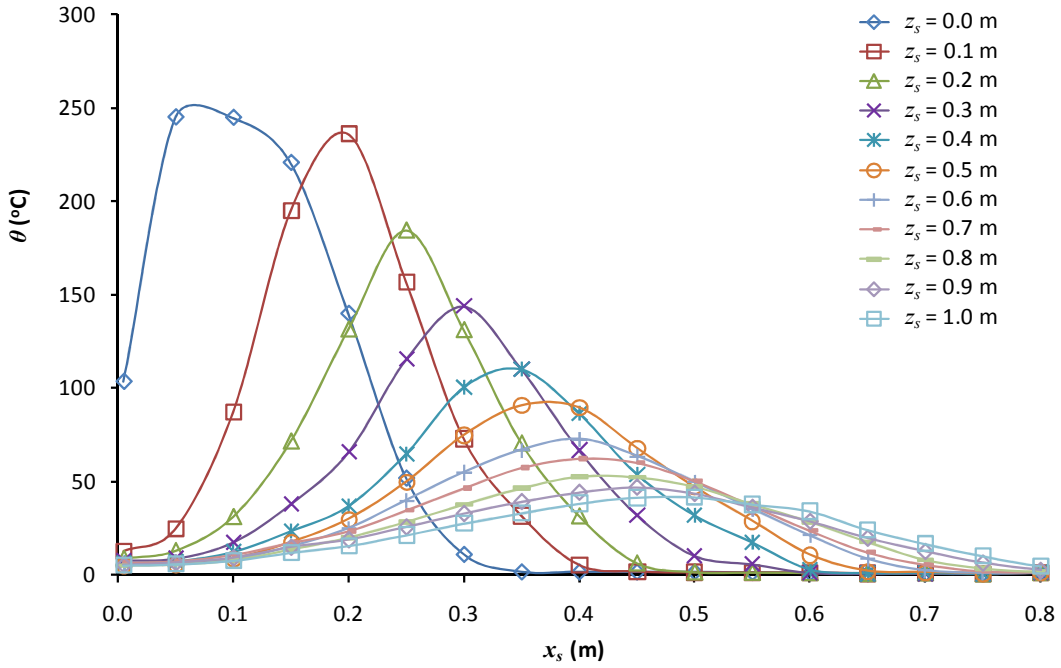

Figure L5: Experiment T6

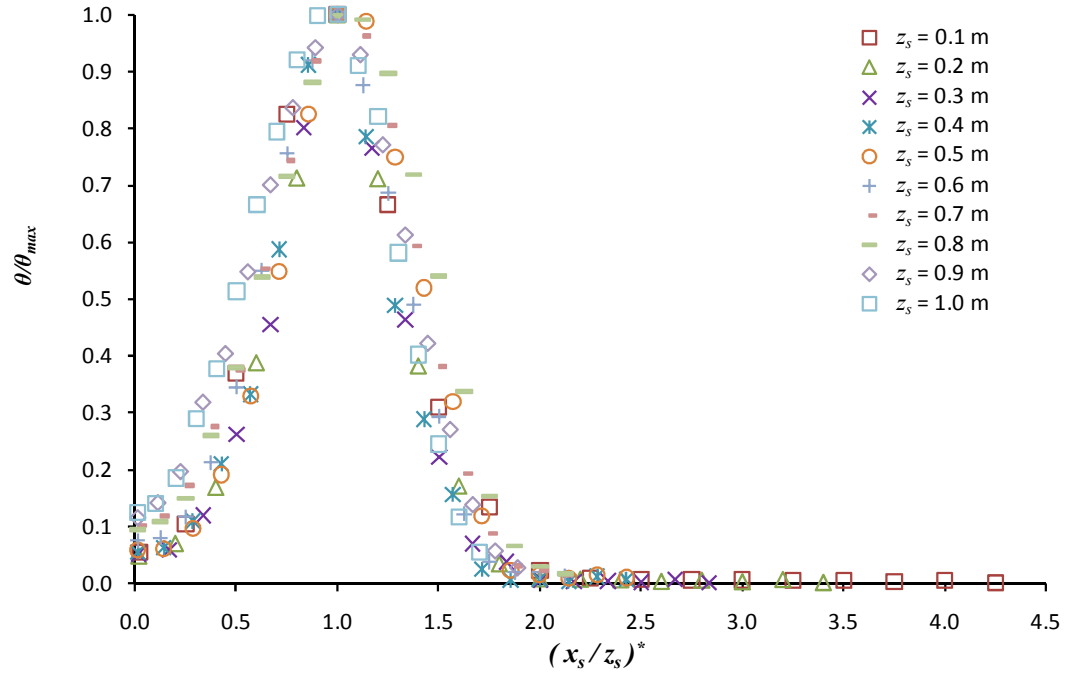

Figure L6: Non-dimensional normalised profiles, Experiment T6

Appendix M: Example FDS input file (Simulation SC6)

```
&HEAD CHID='Simulation SC6',TITLE='Compartment fire,10kW, 0.6 m opening, 25 mm grid'/
&MESH IJK=72,48,24, XB=0,1.8,0,1.2,0,0.6 / 25 mm grid

SIMULATION TIME
**********
&TIME T_END=900. /
&MISC TMPA=20. /
&DUMP NFRAMES=1000, DT_DEVC=1./

CHARACTERISIICS OF THE BURNER FIRE
**********
&SURF ID='fire', HRRPUA=527. /
&OBST XB=0.16,0.30,0.53,0.67,0,0.025, SURF_IDS='fire','INERT','INERT',COLOR='RED' /
&RADI RADIATIVE_FRACTION=0.20 /

CHARACTERISIICS OF THE BOUNDARIES
**********
&VENT MB='XMIN' , SURF_ID='OPEN' /Open domain boundary
&VENT MB='XMAX' , SURF_ID='OPEN' /Open domain boundary
&VENT MB='YMIN' , SURF_ID='OPEN' /Open domain boundary
&VENT MB='YMAX' , SURF_ID='OPEN' /Open domain boundary
&VENT MB='ZMAX' , SURF_ID='OPEN' /Open domain boundary

MATERIAL AND SURFACE PROPERTIES
**********
&MATL ID='CERAMIC BOARD'
    FYI     ='DRYSDALE D, INTRODUCTION TO FIRE DYNAMICS'
    SPECIFIC_HEAT= 2.090
    DENSITY     = 229
    CONDUCTIVITY = 0.041/

&SURF ID      ='COMP WALL'
    MATL_ID  ='CERAMIC BOARD'
    COLOR='GRAY'
    THICKNESS = 0.025 /FIRE COMPARTMENT WALLS

&SURF ID      ='HOOD WALL'
    MATL_ID  ='CERAMIC BOARD'
    COLOR='SLATE GRAY'
    THICKNESS= 0.010 /COLLECTING HOOD WALLS

COMPARTMENT GEOMETRY
**********
&OBST XB=0.1,1.1,0.075,0.1,0.0,0.525,SURF_ID='COMP WALL' /FIRE COMP SIDE WALL
&OBST XB=0.1,1.1,1.1,1.125,0.0,0.525,SURF_ID='COMP WALL' /FIRE COMP SIDE WALL
&OBST XB=0.1,0.125,0.075,1.125,0.0,0.525,SURF_ID='COMP WALL' /FIRE COMP BACK WALL
&OBST XB=1.075,1.1,0.1,0.3,0.0,0.5,SURF_ID='COMP WALL' /FIRE COMP FRONT INSERT 1 (0.6 M OPENING)
&OBST XB=1.075,1.1,0.9,1.1,0.0,0.5,SURF_ID='COMP WALL' /FIRE COMP FRONT INSERT 2 (0.6 M OPENING)
&OBST XB=0.1,1.1,0.075,1.125,0.5,0.525,SURF_ID='COMP WALL' /FIRE COMP CEILING
&OBST XB=1.1,1.4,0.1,1.1,0.5,0.510,SURF_ID='HOOD WALL' /0.3 M BALCONY
&OBST XB=1.1,1.4,0.29,0.3,0.3,0.5,SURF_ID='HOOD WALL' /CHANNELLING SCREEN 1(0.6 M OPENING)
&OBST XB=1.1,1.4,0.9,0.91,0.3,0.5,SURF_ID='HOOD WALL' /CHANNELLING SCREEN 2(0.6 M OPENING)

INSTRUMENTATION AND MEASUREMENTS
**********
&DEVC ID='TC-31', XYZ=1.4,0.6,0.49, QUANTITY='TEMPERATURE' / Thermocouple column C
&DEVC ID='TC-32', XYZ=1.4,0.6,0.47, QUANTITY='TEMPERATURE' /
&DEVC ID='TC-33', XYZ=1.4,0.6,0.45, QUANTITY='TEMPERATURE' /
&DEVC ID='TC-34', XYZ=1.4,0.6,0.43, QUANTITY='TEMPERATURE' /
&DEVC ID='TC-35', XYZ=1.4,0.6,0.41, QUANTITY='TEMPERATURE' /
&DEVC ID='TC-36', XYZ=1.4,0.6,0.39, QUANTITY='TEMPERATURE' /
&DEVC ID='TC-37', XYZ=1.4,0.6,0.37, QUANTITY='TEMPERATURE' /
&DEVC ID='TC-38', XYZ=1.4,0.6,0.35, QUANTITY='TEMPERATURE' /
&DEVC ID='TC-39', XYZ=1.4,0.6,0.33, QUANTITY='TEMPERATURE' /
&DEVC ID='TC-40', XYZ=1.4,0.6,0.31, QUANTITY='TEMPERATURE' /
&DEVC ID='TC-41', XYZ=1.4,0.6,0.29, QUANTITY='TEMPERATURE' /
&DEVC ID='TC-42', XYZ=1.4,0.6,0.27, QUANTITY='TEMPERATURE' /
&DEVC ID='TC-43', XYZ=1.4,0.6,0.25, QUANTITY='TEMPERATURE' /
&DEVC ID='TC-44', XYZ=1.4,0.6,0.20, QUANTITY='TEMPERATURE' /
&DEVC ID='TC-45', XYZ=1.4,0.6,0.15, QUANTITY='TEMPERATURE' /
&DEVC ID='TC-46', XYZ=1.4,0.6,0.10, QUANTITY='TEMPERATURE' /
&DEVC ID='TC-47', XYZ=1.4,0.6,0.05, QUANTITY='TEMPERATURE' /
&DEVC ID='TC-48', XYZ=1.4,0.6,0.00, QUANTITY='TEMPERATURE' /
```

```
&DEVC ID='VEL01,LHS', XYZ=1.4,0.5,0.49, QUANTITY='VELOCITY' / VELOCITY LHS
&DEVC ID='VEL02,LHS', XYZ=1.4,0.5,0.48, QUANTITY='VELOCITY' /
&DEVC ID='VEL03,LHS', XYZ=1.4,0.5,0.47, QUANTITY='VELOCITY' /
&DEVC ID='VEL04,LHS', XYZ=1.4,0.5,0.46, QUANTITY='VELOCITY' /
&DEVC ID='VEL05,LHS', XYZ=1.4,0.5,0.45, QUANTITY='VELOCITY' /
&DEVC ID='VEL06,LHS', XYZ=1.4,0.5,0.44, QUANTITY='VELOCITY' /
&DEVC ID='VEL07,LHS', XYZ=1.4,0.5,0.43, QUANTITY='VELOCITY' /
&DEVC ID='VEL08,LHS', XYZ=1.4,0.5,0.42, QUANTITY='VELOCITY' /
&DEVC ID='VEL09,LHS', XYZ=1.4,0.5,0.41, QUANTITY='VELOCITY' /
&DEVC ID='VEL10,LHS', XYZ=1.4,0.5,0.40, QUANTITY='VELOCITY' /
&DEVC ID='VEL11,LHS', XYZ=1.4,0.5,0.39, QUANTITY='VELOCITY' /
&DEVC ID='VEL12,LHS', XYZ=1.4,0.5,0.38, QUANTITY='VELOCITY' /
&DEVC ID='VEL13,LHS', XYZ=1.4,0.5,0.37, QUANTITY='VELOCITY' /
&DEVC ID='VEL14,LHS', XYZ=1.4,0.5,0.36, QUANTITY='VELOCITY' /
&DEVC ID='VEL15,LHS', XYZ=1.4,0.5,0.35, QUANTITY='VELOCITY' /
&DEVC ID='VEL16,LHS', XYZ=1.4,0.5,0.34, QUANTITY='VELOCITY' /
&DEVC ID='VEL17,LHS', XYZ=1.4,0.5,0.33, QUANTITY='VELOCITY' /
&DEVC ID='VEL18,LHS', XYZ=1.4,0.5,0.32, QUANTITY='VELOCITY' /
&DEVC ID='VEL19,LHS', XYZ=1.4,0.5,0.31, QUANTITY='VELOCITY' /
&DEVC ID='VEL20,LHS', XYZ=1.4,0.5,0.30, QUANTITY='VELOCITY' /

&DEVC ID='VEL01,RHS', XYZ=1.4,0.7,0.49, QUANTITY='VELOCITY' / VELOCITY RHS
&DEVC ID='VEL02,RHS', XYZ=1.4,0.7,0.48, QUANTITY='VELOCITY' /
&DEVC ID='VEL03,RHS', XYZ=1.4,0.7,0.47, QUANTITY='VELOCITY' /
&DEVC ID='VEL04,RHS', XYZ=1.4,0.7,0.46, QUANTITY='VELOCITY' /
&DEVC ID='VEL05,RHS', XYZ=1.4,0.7,0.45, QUANTITY='VELOCITY' /
&DEVC ID='VEL06,RHS', XYZ=1.4,0.7,0.44, QUANTITY='VELOCITY' /
&DEVC ID='VEL07,RHS', XYZ=1.4,0.7,0.43, QUANTITY='VELOCITY' /
&DEVC ID='VEL08,RHS', XYZ=1.4,0.7,0.42, QUANTITY='VELOCITY' /
&DEVC ID='VEL09,RHS', XYZ=1.4,0.7,0.41, QUANTITY='VELOCITY' /
&DEVC ID='VEL10,RHS', XYZ=1.4,0.7,0.40, QUANTITY='VELOCITY' /
&DEVC ID='VEL11,RHS', XYZ=1.4,0.7,0.39, QUANTITY='VELOCITY' /
&DEVC ID='VEL12,RHS', XYZ=1.4,0.7,0.38, QUANTITY='VELOCITY' /
&DEVC ID='VEL13,RHS', XYZ=1.4,0.7,0.37, QUANTITY='VELOCITY' /
&DEVC ID='VEL14,RHS', XYZ=1.4,0.7,0.36, QUANTITY='VELOCITY' /
&DEVC ID='VEL15,RHS', XYZ=1.4,0.7,0.35, QUANTITY='VELOCITY' /
&DEVC ID='VEL16,RHS', XYZ=1.4,0.7,0.34, QUANTITY='VELOCITY' /
&DEVC ID='VEL17,RHS', XYZ=1.4,0.7,0.33, QUANTITY='VELOCITY' /
&DEVC ID='VEL18,RHS', XYZ=1.4,0.7,0.32, QUANTITY='VELOCITY' /
&DEVC ID='VEL19,RHS', XYZ=1.4,0.7,0.31, QUANTITY='VELOCITY' /
&DEVC ID='VEL20,RHS', XYZ=1.4,0.7,0.30, QUANTITY='VELOCITY' /

&DEVC XB=1.4,1.4,0.3,0.9,0.0,0.5, QUANTITY='MASS FLOW +', ID='Massflow under balcony+'/
&DEVC XB=1.4,1.4,0.3,0.9,0.0,0.5, QUANTITY='MASS FLOW -', ID='Massflow under balcony-'/

&TAIL
```

Appendix N: Example FDS input file (Simulation SE5)

```
&HEAD CHID='Simulation SE5',TITLE='3D Balc plume,Q=10kW,W=0.6 m,25 mm grid'/
&MESH IJK=120,80,24, XB=-0.5,2.5,0.2,2.2,0.0,0.6 / 25  mm grid below spill edge
&MESH IJK=120,80,24, XB=-0.5,2.5,0.2,2.2,0.6,1.2/ 25  mm grid above spill edge
&MESH IJK=120,80,24, XB=-0.5,2.5,0.2,2.2,1.2,1.8/ 25  mm grid above spill edge
&MESH IJK=120,80,24, XB=-0.5,2.5,0.2,2.2,1.8,2.4/ 25  mm grid above spill edge

SIMULATION TIME
**********
&TIME T_END=240. /
&MISC TMPA=20. /
&DUMP NFRAMES=240, DT_DEVC=1.,DT_PL3D=210./

CHARACTERISTICS OF THE FIRE
**********
&SURF ID='fire', HRRPUA=527./
&OBST XB=-0.44,-0.3,1.13,1.27,0.0,0.025, SURF_IDS='fire','INERT','INERT',COLOR='RED' /
&RADI RADIATIVE_FRACTION=0.20 /

CHARACTERISIICS OF THE BOUNDARIES
**********
&VENT MB='XMIN' , SURF_ID='OPEN' /Open domain boundary
&VENT MB='XMAX' , SURF_ID='OPEN' /Open domain boundary
&VENT MB='YMIN' , SURF_ID='OPEN' /Open domain boundary
&VENT MB='YMAX' , SURF_ID='OPEN' /Open domain boundary

MATERIAL AND SURFACE PROPERTIES
**********
&MATL ID='CERAMIC BOARD'
    FYI     ='DRYSDALE D, INTRODUCTION TO FIRE DYNAMICS'
    SPECIFIC_HEAT= 2.090
    DENSITY     = 229
    CONDUCTIVITY = 0.041/

&SURF ID      ='COMP WALL'
    MATL_ID  ='CERAMIC BOARD'
    COLOR='GRAY'
    THICKNESS = 0.025 /FIRE COMPARTMENT WALLS

&SURF ID      ='HOOD WALL'
    MATL_ID  ='CERAMIC BOARD'
    COLOR='SLATE GRAY'
    THICKNESS= 0.010 /COLLECTING HOOD WALLS

COMPARTMENT GEOMETRY
**********
&OBST XB=-0.5,0.5,0.675,0.7,0.0,0.525,SURF_ID='COMP WALL' /FIRE COMP SIDE WALL
&OBST XB=-0.5,0.5,1.7,1.725,0.0,0.525,SURF_ID='COMP WALL' /FIRE COMP SIDE WALL
&OBST XB=-0.5,-0.475,0.675,1.725,0.0,0.525,SURF_ID='COMP WALL' /FIRE COMP BACK WALL
&OBST XB=0.475,0.50,0.7,0.9,0.0,0.5,SURF_ID='COMP WALL' /FIRE COMP FRONT INSERT 1 (0.6 M OPENING)
&OBST XB=0.475,0.50,1.5,1.7,0.0,0.5,SURF_ID='COMP WALL' /FIRE COMP FRONT INSERT 2 (0.6 M OPENING)
&OBST XB=-0.5,0.5,0.675,1.725,0.5,0.525,SURF_ID='COMP WALL' /FIRE COMP CEILING
&OBST XB=0.5,0.8,0.7,1.7,0.5,0.510,SURF_ID='HOOD WALL' /0.3 M BALCONY
&OBST XB=0.5,0.8,0.89,0.9,0.3,0.5,SURF_ID='HOOD WALL' /CHANNELLING SCREEN 1(0.6 M OPENING)
&OBST XB=0.5,0.8,1.5,1.51,0.3,0.5,SURF_ID='HOOD WALL' /CHANNELLING SCREEN 2(0.6 M OPENING)

INSTRUMENTATION AND MEASUREMENTS
**********
&DEVC XB=0.8,0.8,0.9,1.5,0.0,0.5, QUANTITY='MASS FLOW +',ID='MSF at balc'/
&DEVC XB=0.8,1.3,0.7,1.7,0.5,0.5, QUANTITY='MASS FLOW', ID='MSF@0HOR'/
&DEVC XB=0.8,1.55,0.65,1.75,0.8,0.8, QUANTITY='MASS FLOW', ID='MSF@0.3HOR'/
&DEVC XB=0.8,1.75,0.65,1.75,1.0,1.0, QUANTITY='MASS FLOW', ID='MSF@0.5HOR'/
&DEVC XB=0.8,1.9,0.6,1.8,1.23,1.23, QUANTITY='MASS FLOW', ID='MSF@0.73HOR'/
&DEVC XB=0.8,2.0,0.55,1.85,1.45,1.45, QUANTITY='MASS FLOW', ID='MSF@0.95HOR'/
&TAIL /
```

Appendix O: Example FDS input file (Simulation SR1)

```
&HEAD CHID='Simulation SR2',TITLE='3D Balcony plume in rig,0.6 m,10kW,0.5 m HOR, 25 mm grid'/
&MESH IJK=124,88,22, XB=0.1,3.2,0.1,2.3,0,0.55/ 25 mm grid for compartment and surroundings
&MESH IJK=124,88,22, XB=0.1,3.2,0.1,2.3,0.55,1.1 / 25 mm grid above spill edge
&MESH IJK=124,88,22, XB=0.1,3.2,0.1,2.3,1.1,1.65 / 25 mm grid above spill edge
&MESH IJK=124,88,22, XB=0.1,3.2,0.1,2.3,1.65,2.2 / 25 mm grid above spill edge
&MESH IJK=124,88,22, XB=0.1,3.2,0.1,2.3,2.2,2.75 / 25 mm grid above spill edge

SIMULATION TIME
********************
&TIME T_END=240. /
&MISC TMPA=20. /
&DUMP NFRAMES=1000, DT_DEVC=1.,DT_SLCF=5. /

CHARACTERISTICS OF EXHAUST
*************************
&SURF ID='fan', MASS_FLUX_TOTAL=1.634, COLOR='INVISIBLE' /
&VENT XB=2.51,2.9,1.005,1.395,2.5,2.5, SURF_ID='fan' /
&OBST XB=2.51,2.9,1.005,1.395,2.5,2.55,COLOR='INVISIBLE'/OBSTRUCTION ATTACHED TO VENT

CHARACTERISIICS OF THE BURNER FIRE
*********************************
&SURF ID='fire', HRRPUA=527. /
&OBST XB=0.16,0.30,1.13,1.27,0.0,0.025, SURF_IDS='fire','INERT','INERT',COLOR='RED' /
&RADI RADIATIVE_FRACTION=0.20 /

CHARACTERISIICS OF THE BOUNDARIES
*********************************
&VENT MB='XMIN' , SURF_ID='OPEN' /Open domain boundary
&VENT MB='XMAX' , SURF_ID='OPEN' /Open domain boundary
&VENT MB='YMIN' , SURF_ID='OPEN' /Open domain boundary
&VENT MB='YMAX' , SURF_ID='OPEN' /Open domain boundary
&VENT MB='ZMAX' , SURF_ID='OPEN' /Open domain boundary

MATERIAL AND SURFACE PROPERTIES
*******************************
&MATL ID='CERAMIC BOARD'
    FYI     ='DRYSDALE D, INTRODUCTION TO FIRE DYNAMICS'
    SPECIFIC_HEAT= 2.090
    DENSITY     = 229
    CONDUCTIVITY = 0.041/

&SURF ID      ='COMP WALL'
    MATL_ID  ='CERAMIC BOARD'
    COLOR='GRAY'
    THICKNESS = 0.025 /FIRE COMPARTMENT WALLS

&SURF ID      ='HOOD WALL'
    MATL_ID  ='CERAMIC BOARD'
    COLOR='SLATE GRAY'
    THICKNESS= 0.010 /COLLECTING HOOD WALLS

&MATL ID         ='ACRYLIC'
    FYI         ='DRYSDALE D, INTRODUCTION TO FIRE DYNAMICS'
    SPECIFIC_HEAT= 1.42
    DENSITY     = 1190
    CONDUCTIVITY = 0.19/

&SURF ID      ='ACRYLIC WALL'
    MATL_ID  ='ACRYLIC'
    COLOR='INVISIBLE'
    THICKNESS= 0.010 /ACRYLIC HOOD WALL


COMPARTMENT GEOMETRY
********************
&OBST XB=0.1,1.1,0.675,0.7,0.0,0.525,SURF_ID='COMP WALL' /FIRE COMP SIDE WALL
&OBST XB=0.1,1.1,1.7,1.725,0.0,0.525,SURF_ID='COMP WALL' /FIRE COMP SIDE WALL
&OBST XB=0.1,0.125,0.675,1.725,0.0,0.525,SURF_ID='COMP WALL' /FIRE COMP BACK WALL
&OBST XB=1.075,1.1,0.7,0.9,0.0,0.5,SURF_ID='COMP WALL' /FIRE COMP FRONT INSERT 1 (0.6 M OPENING)
&OBST XB=1.075,1.1,1.5,1.7,0.0,0.5,SURF_ID='COMP WALL' /FIRE COMP FRONT INSERT 2 (0.6 M OPENING)
&OBST XB=0.1,1.1,0.675,1.725,0.5,0.525,SURF_ID='COMP WALL' /FIRE COMP CEILING
&OBST XB=1.1,1.4,0.2,2.2,0.5,0.510,SURF_ID='HOOD WALL' /0.3 M BALCONY
&OBST XB=1.1,1.4,0.89,0.9,0.3,0.5,SURF_ID='HOOD WALL' /CHANNELLING SCREEN 1(0.6 M OPENING)
&OBST XB=1.1,1.4,1.5,1.51,0.3,0.5,SURF_ID='HOOD WALL' /CHANNELLING SCREEN 2(0.6 M OPENING)
```

```
HOOD GEOMETRY
*************
&OBST XB=1.09,1.1,0.19,2.21,1.335,2.5,SURF_ID='HOOD WALL' /HOOD WALL1 0.9 HOR
&OBST XB=1.09,3.11,0.19,0.2,1.335,2.5,SURF_ID='HOOD WALL' /HOOD WALL2 0.9 HOR
&OBST XB=3.1,3.11,0.19,2.21,1.335,2.5,SURF_ID='HOOD WALL' /HOOD WALL3 0.9 HOR
&OBST XB=1.09,3.11,2.2,2.21,1.335,2.5,SURF_ID='ACRYLIC WALL' /HOOD WALL4 0.9 HOR
&OBST XB=1.09,2.51,0.19,2.21,2.5,2.51,SURF_ID='HOOD WALL' /HOOD CEILING
&OBST XB=2.51,2.90,0.19,1.005,2.5,2.51,SURF_ID='HOOD WALL' /HOOD CEILING
&OBST XB=2.51,2.90,1.395,2.21,2.5,2.51,SURF_ID='HOOD WALL' /HOOD CEILING
&OBST XB=2.90,3.11,0.19,2.21,2.5,2.51,SURF_ID='HOOD WALL' /HOOD CEILING
&OBST XB=1.09,1.1,0.19,2.21,0.935,1.335,SURF_ID='HOOD WALL' /HOOD WALL1 INSERT
&OBST XB=1.09,3.11,0.19,0.2,0.935,1.335,SURF_ID='HOOD WALL' /HOOD WALL2 INSERT
&OBST XB=3.1,3.11,0.19,2.21,0.935,1.335,SURF_ID='HOOD WALL' /HOOD WALL3 INSERT
&OBST XB=1.09,3.11,2.2,2.21,0.935,1.335,SURF_ID='ACRYLIC WALL' /HOOD WALL4 INSERT

INSTRUMENTATION AND MEASUREMENTS
********************************
&DEVC ID='TC-01', XYZ=2.64,0.435,2.49, QUANTITY='TEMPERATURE' / Thermocouple column A
&DEVC ID='TC-02', XYZ=2.64,0.435,2.40, QUANTITY='TEMPERATURE' /
&DEVC ID='TC-03', XYZ=2.64,0.435,2.30, QUANTITY='TEMPERATURE' /
&DEVC ID='TC-04', XYZ=2.64,0.435,2.20, QUANTITY='TEMPERATURE' /
&DEVC ID='TC-05', XYZ=2.64,0.435,2.00, QUANTITY='TEMPERATURE' /
&DEVC ID='TC-06', XYZ=2.64,0.435,1.80, QUANTITY='TEMPERATURE' /
&DEVC ID='TC-07', XYZ=2.64,0.435,1.60, QUANTITY='TEMPERATURE' /
&DEVC ID='TC-08', XYZ=2.64,0.435,1.40, QUANTITY='TEMPERATURE' /
&DEVC ID='TC-09', XYZ=2.64,0.435,1.20, QUANTITY='TEMPERATURE' /
&DEVC ID='TC-10', XYZ=2.64,0.435,1.00, QUANTITY='TEMPERATURE' /
&DEVC ID='TC-11', XYZ=2.64,0.435,0.80, QUANTITY='TEMPERATURE' /
&DEVC ID='TC-12', XYZ=2.64,0.435,0.60, QUANTITY='TEMPERATURE' /
&DEVC ID='TC-13', XYZ=2.64,0.435,0.40, QUANTITY='TEMPERATURE' /
&DEVC ID='TC-14', XYZ=2.64,0.435,0.20, QUANTITY='TEMPERATURE' /
&DEVC ID='TC-15', XYZ=2.64,0.435,0.00, QUANTITY='TEMPERATURE' /

&DEVC ID='TC-16', XYZ=1.56,0.435,2.49, QUANTITY='TEMPERATURE' / Thermocouple column B
&DEVC ID='TC-17', XYZ=1.56,0.435,2.40, QUANTITY='TEMPERATURE' /
&DEVC ID='TC-18', XYZ=1.56,0.435,2.30, QUANTITY='TEMPERATURE' /
&DEVC ID='TC-19', XYZ=1.56,0.435,2.20, QUANTITY='TEMPERATURE' /
&DEVC ID='TC-20', XYZ=1.56,0.435,2.00, QUANTITY='TEMPERATURE' /
&DEVC ID='TC-21', XYZ=1.56,0.435,1.80, QUANTITY='TEMPERATURE' /
&DEVC ID='TC-22', XYZ=1.56,0.435,1.60, QUANTITY='TEMPERATURE' /
&DEVC ID='TC-23', XYZ=1.56,0.435,1.40, QUANTITY='TEMPERATURE' /
&DEVC ID='TC-24', XYZ=1.56,0.435,1.20, QUANTITY='TEMPERATURE' /
&DEVC ID='TC-25', XYZ=1.56,0.435,1.00, QUANTITY='TEMPERATURE' /
&DEVC ID='TC-26', XYZ=1.56,0.435,0.80, QUANTITY='TEMPERATURE' /
&DEVC ID='TC-27', XYZ=1.56,0.435,0.60, QUANTITY='TEMPERATURE' /
&DEVC ID='TC-28', XYZ=1.56,0.435,0.40, QUANTITY='TEMPERATURE' /
&DEVC ID='TC-29', XYZ=1.56,0.435,0.20, QUANTITY='TEMPERATURE' /
&DEVC ID='TC-30', XYZ=1.56,0.435,0.00, QUANTITY='TEMPERATURE' /

&DEVC ID='TC-31', XYZ=1.4,1.2,0.49, QUANTITY='TEMPERATURE' / Thermocouple column C
&DEVC ID='TC-32', XYZ=1.4,1.2,0.47, QUANTITY='TEMPERATURE' /
&DEVC ID='TC-33', XYZ=1.4,1.2,0.45, QUANTITY='TEMPERATURE' /
&DEVC ID='TC-34', XYZ=1.4,1.2,0.43, QUANTITY='TEMPERATURE' /
&DEVC ID='TC-35', XYZ=1.4,1.2,0.41, QUANTITY='TEMPERATURE' /
&DEVC ID='TC-36', XYZ=1.4,1.2,0.39, QUANTITY='TEMPERATURE' /
&DEVC ID='TC-37', XYZ=1.4,1.2,0.37, QUANTITY='TEMPERATURE' /
&DEVC ID='TC-38', XYZ=1.4,1.2,0.35, QUANTITY='TEMPERATURE' /
&DEVC ID='TC-39', XYZ=1.4,1.2,0.33, QUANTITY='TEMPERATURE' /
&DEVC ID='TC-40', XYZ=1.4,1.2,0.31, QUANTITY='TEMPERATURE' /
&DEVC ID='TC-41', XYZ=1.4,1.2,0.29, QUANTITY='TEMPERATURE' /
&DEVC ID='TC-42', XYZ=1.4,1.2,0.27, QUANTITY='TEMPERATURE' /
&DEVC ID='TC-43', XYZ=1.4,1.2,0.25, QUANTITY='TEMPERATURE' /
&DEVC ID='TC-44', XYZ=1.4,1.2,0.20, QUANTITY='TEMPERATURE' /
&DEVC ID='TC-45', XYZ=1.4,1.2,0.15, QUANTITY='TEMPERATURE' /
&DEVC ID='TC-46', XYZ=1.4,1.2,0.10, QUANTITY='TEMPERATURE' /
&DEVC ID='TC-47', XYZ=1.4,1.2,0.05, QUANTITY='TEMPERATURE' /
&DEVC ID='TC-48', XYZ=1.4,1.2,0.00, QUANTITY='TEMPERATURE' /
```

```
&DEVC ID='TC-49', XYZ=1.4,0.71,0.49, QUANTITY='TEMPERATURE' / Thermocouple array A
&DEVC ID='TC-50', XYZ=1.4,0.81,0.49, QUANTITY='TEMPERATURE' /
&DEVC ID='TC-51', XYZ=1.4,0.91,0.49, QUANTITY='TEMPERATURE' /
&DEVC ID='TC-52', XYZ=1.4,0.95,0.49, QUANTITY='TEMPERATURE' /
&DEVC ID='TC-53', XYZ=1.4,1.00,0.49, QUANTITY='TEMPERATURE' /
&DEVC ID='TC-54', XYZ=1.4,1.01,0.49, QUANTITY='TEMPERATURE' /
&DEVC ID='TC-55', XYZ=1.4,1.05,0.49, QUANTITY='TEMPERATURE' /
&DEVC ID='TC-56', XYZ=1.4,1.10,0.49, QUANTITY='TEMPERATURE' /
&DEVC ID='TC-57', XYZ=1.4,1.11,0.49, QUANTITY='TEMPERATURE' /
&DEVC ID='TC-58', XYZ=1.4,1.15,0.49, QUANTITY='TEMPERATURE' /
&DEVC ID='TC-59', XYZ=1.4,1.20,0.49, QUANTITY='TEMPERATURE' /
&DEVC ID='TC-60', XYZ=1.4,1.25,0.49, QUANTITY='TEMPERATURE' /
&DEVC ID='TC-61', XYZ=1.4,1.29,0.49, QUANTITY='TEMPERATURE' /
&DEVC ID='TC-62', XYZ=1.4,1.30,0.49, QUANTITY='TEMPERATURE' /
&DEVC ID='TC-63', XYZ=1.4,1.35,0.49, QUANTITY='TEMPERATURE' /
&DEVC ID='TC-64', XYZ=1.4,1.39,0.49, QUANTITY='TEMPERATURE' /
&DEVC ID='TC-65', XYZ=1.4,1.40,0.49, QUANTITY='TEMPERATURE' /
&DEVC ID='TC-66', XYZ=1.4,1.45,0.49, QUANTITY='TEMPERATURE' /
&DEVC ID='TC-67', XYZ=1.4,1.49,0.49, QUANTITY='TEMPERATURE' /
&DEVC ID='TC-68', XYZ=1.4,1.59,0.49, QUANTITY='TEMPERATURE' /
&DEVC ID='TC-69', XYZ=1.4,1.69,0.49, QUANTITY='TEMPERATURE' /

&DEVC ID='TC-86', XYZ=2.6075,1.2,2.49, QUANTITY='TEMPERATURE' / Thermocouple array in exhaust vent
&DEVC ID='TC-87', XYZ=2.705,1.2,2.49, QUANTITY='TEMPERATURE' /
&DEVC ID='TC-88', XYZ=2.8025,1.2,2.49, QUANTITY='TEMPERATURE' /
&DEVC ID='TC-89', XYZ=2.705,1.2975,2.49, QUANTITY='TEMPERATURE' /
&DEVC ID='TC-90', XYZ=2.705,1.1025,2.49, QUANTITY='TEMPERATURE' /

&SLCF PBY=1.2,QUANTITY='TEMPERATURE'/
&SLCF PBY=1.2,QUANTITY='VELOCITY',VECTOR=.TRUE./

&SLCF PBZ=1.0,QUANTITY='TEMPERATURE'/
&SLCF PBZ=1.0,QUANTITY='VELOCITY',VECTOR=.TRUE./

&DEVC XB=1.4,1.4,0.9,1.5,0.0,0.5, QUANTITY='MASS FLOW +',ID='MSF at balc'/CHANGE FOR DIFFERENT WIDTHS
&DEVC XB=1.4,2.35,0.65,1.75,1.0,1.0, QUANTITY='MASS FLOW', ID='MSF@0.5HOR'/
&DEVC XB=2.51,2.9,1.005,1.395,2.5,2.5, QUANTITY='MASS FLOW'/MASS CHECK AT VENT

&TAIL /
```

Appendix P: Example FDS input file (Simulation SE14)

```
&HEAD CHID='Simulation SE14',TITLE='3D Adhered plume,10kW,0.6 m,25 mm grid'/
&MESH IJK=120,80,24, XB=-0.5,2.5,0.2,2.2,0.0,0.6 / 25  mm grid for the compartment
&MESH IJK=120,80,24, XB=-0.5,2.5,0.2,2.2,0.6,1.2 / 25  mm grid side of compartment below spill edge
&MESH IJK=120,80,24, XB=-0.5,2.5,0.2,2.2,1.2,1.8 / 25  mm grid side of compartment below spill edge
&MESH IJK=120,80,24, XB=-0.5,2.5,0.2,2.2,1.8,2.4 / 25  mm grid side of compartment below spill edge

SIMULATION TIME
*******************
&TIME T_END=240. /
&MISC TMPA=20. /
&DUMP NFRAMES=240, DT_DEVC=1.,DT_PL3D=210./

CHARACTERISTICS OF THE FIRE
*********************************
&SURF ID='fire', HRRPUA=527. /
&OBST XB=-0.44,-0.3,1.13,1.27,0.0,0.025, SURF_IDS='fire','INERT','INERT',COLOR='RED' /
&RADI RADIATIVE_FRACTION=0.20 /

CHARACTERISIICS OF THE BOUNDARIES
*********************************
&VENT MB='XMIN' , SURF_ID='OPEN' /Open domain boundary
&VENT MB='XMAX' , SURF_ID='OPEN' /Open domain boundary
&VENT MB='YMIN' , SURF_ID='OPEN' /Open domain boundary
&VENT MB='YMAX' , SURF_ID='OPEN' /Open domain boundary


MATERIAL AND SURFACE PROPERTIES
******************************
&MATL ID='CERAMIC BOARD'
    FYI     ='DRYSDALE D, INTRODUCTION TO FIRE DYNAMICS'
    SPECIFIC_HEAT= 2.090
    DENSITY     = 229
    CONDUCTIVITY = 0.041/

&SURF ID      ='COMP WALL'
    MATL_ID  ='CERAMIC BOARD'
    COLOR='GRAY'
    THICKNESS = 0.025 /FIRE COMPARTMENT WALLS

&SURF ID      ='HOOD WALL'
    MATL_ID  ='CERAMIC BOARD'
    COLOR='SLATE GRAY'
    THICKNESS= 0.010 /COLLECTING HOOD WALLS

COMPARTMENT GEOMETRY
********************
&OBST XB=0.49,0.5,0.2,2.2,0.525,2.4,SURF_ID='HOOD WALL' /WALL ABOVE OPENING
&OBST XB=-0.5,0.5,0.675,0.7,0.0,0.525,SURF_ID='COMP WALL' /FIRE COMP SIDE WALL
&OBST XB=-0.5,0.5,1.7,1.725,0.0,0.525,SURF_ID='COMP WALL' /FIRE COMP SIDE WALL
&OBST XB=-0.5,-0.475,0.675,1.725,0.0,0.525,SURF_ID='COMP WALL' /FIRE COMP BACK WALL
&OBST XB=0.475,0.50,0.7,0.9,0.0,0.5,SURF_ID='COMP WALL' /FIRE COMP FRONT INSERT 1 (0.6 M OPENING)
&OBST XB=0.475,0.50,1.5,1.7,0.0,0.5,SURF_ID='COMP WALL' /FIRE COMP FRONT INSERT 2 (0.6 M OPENING)
&OBST XB=-0.5,0.5,0.675,1.725,0.5,0.525,SURF_ID='COMP WALL' /FIRE COMP CEILING

INSTRUMENTATION AND MEASUREMENTS
*******************************
&DEVC XB=0.5,0.5,0.9,1.5,0.0,0.5, QUANTITY='MASS FLOW +',ID='MSF at balc'/
&DEVC XB=0.5,0.85,0.8,1.6,0.5,0.5, QUANTITY='MASS FLOW', ID='MSF@0HOR'/
&DEVC XB=0.5,1.05,0.8,1.6,0.8,0.8, QUANTITY='MASS FLOW', ID='MSF@0.3HOR'/
&DEVC XB=0.5,1.1,0.8,1.6,1.0,1.0, QUANTITY='MASS FLOW', ID='MSF@0.5HOR'/
&DEVC XB=0.5,1.2,0.8,1.6,1.23,1.23, QUANTITY='MASS FLOW', ID='MSF@0.73HOR'/
&DEVC XB=0.5,1.3,0.8,1.6,1.45,1.45, QUANTITY='MASS FLOW', ID='MSF@0.95HOR'/
&TAIL /
```

Appendix Q: FDS predictions (Simulations STR1 to STR4)

z_s (m)	$m_{p,3D}$ (kg s^{-1})
0.0	0.05
0.1	0.07
0.2	0.08
0.3	0.10
0.4	0.12
0.5	0.14
0.6	0.16
0.7	0.18
0.8	0.21
0.9	0.23
1.0	0.26
1.1	0.28
1.2	0.31
1.3	0.34
1.4	0.37
1.5	0.40
1.6	0.43
1.7	0.46
1.8	0.50
1.9	0.53
2.0	0.57
2.1	0.60
2.2	0.64
2.3	0.68
2.4	0.72
2.5	0.75
2.6	0.79
2.7	0.83
2.8	0.87
2.9	0.91
3.0	0.95
3.1	0.99
3.2	1.03
3.3	1.07
3.4	1.11
3.5	1.16
3.6	1.20
3.7	1.24
3.8	1.28
3.9	1.33
4.0	1.37
4.1	1.42
4.2	1.47
4.3	1.50
4.4	1.55
4.5	1.60
4.6	1.65
4.7	1.69
4.8	1.74
4.9	1.78
5.0	1.80

Figure Q1: FDS predictions for Simulation STR1

z_s (m)	$m_{p,3D}$ (kg s^{-1})
0.0	0.07
0.1	0.09
0.2	0.11
0.3	0.14
0.4	0.16
0.5	0.19
0.6	0.21
0.7	0.24
0.8	0.26
0.9	0.29
1.0	0.32
1.1	0.35
1.2	0.38
1.3	0.41
1.4	0.45
1.5	0.48
1.6	0.52
1.7	0.56
1.8	0.59
1.9	0.63
2.0	0.66
2.1	0.70
2.2	0.73
2.3	0.77
2.4	0.81
2.5	0.85
2.6	0.89
2.7	0.93
2.8	0.98
2.9	1.02
3.0	1.06
3.1	1.10
3.2	1.14
3.3	1.18
3.4	1.23
3.5	1.27
3.6	1.32
3.7	1.36
3.8	1.41
3.9	1.45
4.0	1.50
4.1	1.55
4.2	1.59
4.3	1.64
4.4	1.68
4.5	1.73
4.6	1.76
4.7	1.81
4.8	1.85
4.9	1.88
5.0	1.89

Figure Q2: FDS predictions for Simulation STR2

z_s (m)	$m_{p,3D}$ (kg s^{-1})
0.0	0.08
0.1	0.11
0.2	0.14
0.3	0.17
0.4	0.20
0.5	0.23
0.6	0.26
0.7	0.29
0.8	0.32
0.9	0.35
1.0	0.38
1.1	0.41
1.2	0.44
1.3	0.47
1.4	0.51
1.5	0.54
1.6	0.58
1.7	0.61
1.8	0.65
1.9	0.68
2.0	0.72
2.1	0.75
2.2	0.79
2.3	0.83
2.4	0.87
2.5	0.90
2.6	0.95
2.7	1.00
2.8	1.04
2.9	1.08
3.0	1.12
3.1	1.17
3.2	1.21
3.3	1.25
3.4	1.29
3.5	1.34
3.6	1.38
3.7	1.42
3.8	1.46
3.9	1.53
4.0	1.57
4.1	1.62
4.2	1.66
4.3	1.72
4.4	1.77
4.5	1.82
4.6	1.86
4.7	1.90
4.8	1.93
4.9	1.98
5.0	2.00

Figure Q3: FDS predictions for Simulation STR3

z_s (m)	$m_{p,3D}$ (kg s^{-1})
0.0	0.10
0.1	0.14
0.2	0.18
0.3	0.22
0.4	0.25
0.5	0.29
0.6	0.32
0.7	0.36
0.8	0.40
0.9	0.43
1.0	0.47
1.1	0.50
1.2	0.54
1.3	0.58
1.4	0.61
1.5	0.65
1.6	0.69
1.7	0.72
1.8	0.76
1.9	0.80
2.0	0.84
2.1	0.88
2.2	0.93
2.3	0.97
2.4	1.01
2.5	1.05
2.6	1.09
2.7	1.15
2.8	1.19
2.9	1.23
3.0	1.27
3.1	1.32
3.2	1.37
3.3	1.41
3.4	1.45
3.5	1.50
3.6	1.57
3.7	1.65
3.8	1.69
3.9	1.73
4.0	1.77
4.1	1.81
4.2	1.85
4.3	1.90
4.4	1.94
4.5	1.99
4.6	2.02
4.7	2.11
4.8	2.15
4.9	2.18
5.0	2.19

Figure Q4: FDS predictions for Simulation STR4

Appendix R: FDS input file for Brussels Airport Hot Smoke Test

```
&HEAD CHID='bairpt',TITLE='Brussels Airport Hot Smoke Test'/
&MESH IJK=56,94,36, XB=0.0,28.0,0.0,47.0,0.0,18.0 / 0.5 m grid
&MESH IJK=54,188,72, XB=28.0,41.5,0.0,47.0,0.0,18.0 / 0.25m grid
&MESH IJK=27,94,36, XB=41.5,55.0,0.0,47.0,0.0,18.0 / 0.5m grid

SIMULATION TIME
**********
&TIME T_END=600. /
&MISC TMPA=19.5 /
&DUMP NFRAMES=600, DT_DEVC=1.,DT_SLCF=5./

CHARACTERISTICS OF EXHAUST
**********
&HOLE XB=4.5,44.5,16.5,17.5,13.25,13.75 /ROOF VENT SIDE 1
&HOLE XB=4.5,44.5,33.5,34.5,13.25,13.75 /ROOF VENT SIDE 2

CHARACTERISIICS OF THE BURNER FIRE
**********
&SURF ID='fire', HRRPUA=527. /
&OBST XB=32.25,33.75,15.5,17.0,0.0,0.0, SURF_ID='fire',COLOR='RED' /
&OBST XB=35.75,37.25,15.5,17.0,0.0,0.0, SURF_ID='fire',COLOR='RED' /
&RADI RADIATIVE_FRACTION=0.20 /

CHARACTERISIICS OF THE BOUNDARIES
**********
&VENT MB='XMIN' , SURF_ID='OPEN' /Open domain boundary
&VENT MB='XMAX' , SURF_ID='OPEN' /Open domain boundary
&VENT MB='YMIN' , SURF_ID='OPEN' /Open domain boundary
&VENT MB='YMAX' , SURF_ID='OPEN' /Open domain boundary
&VENT MB='ZMAX' , SURF_ID='OPEN' /Open domain boundary

MATERIAL AND SURFACE PROPERTIES
**********
&MATL ID='CERAMIC BOARD'
    FYI     ='PROMAT,DATA SHEET'
    SPECIFIC_HEAT= 0.92
    DENSITY     = 870
    CONDUCTIVITY = 0.19/

&SURF ID      ='COMP WALL'
    MATL_ID  ='CERAMIC BOARD'
    COLOR='TAN'
    THICKNESS = 0.01 /FIRE COMPARTMENT WALLS

&MATL ID         ='CONCRETE'
    FYI        ='QUINTIERE,FIRE BEHAVIOR'
    SPECIFIC_HEAT= 0.88
    DENSITY     = 2100
    CONDUCTIVITY = 1.0/

&SURF ID      ='CONCRETE'
    MATL_ID  ='CONCRETE'
    COLOR='GRAY'
    THICKNESS= 0.5 /CONCRETE FLOOR

&MATL ID         ='GLASS'
    FYI        ='DRYSDALE D, INTRODUCTION TO FIRE DYNAMICS'
    SPECIFIC_HEAT= 0.84
    DENSITY     = 2700
    CONDUCTIVITY = 0.76/

&SURF ID      ='GLASS WALL'
    MATL_ID  ='GLASS'
    COLOR='AQUAMARINE'
    TRANSPARENCY=0.3
    THICKNESS= 0.005 /

&MATL ID         ='GLASS FIBRE'
    FYI        ='INCROPERA AND DEWITT'
    SPECIFIC_HEAT= 0.795
    DENSITY     = 105
    CONDUCTIVITY = 0.036/
```

```
&SURF ID      ='CURTAIN'
    MATL_ID  ='GLASS FIBRE'
    COLOR='BLACK'
    TRANSPARENCY=0.3
    THICKNESS= 0.0005 /

COMPARTMENT GEOMETRY
********************
&OBST XB=29.99,39.51,14.49,14.50,0.0,3.5,SURF_ID='COMP WALL' /FIRE BACK WALL
&OBST XB=29.99,30.0,14.49,18.0,0.0,3.5,SURF_ID='COMP WALL' /FIRE COMP SIDE WALL
&OBST XB=39.50,39.51,14.49,18.0,0.0,3.5,SURF_ID='COMP WALL' /FIRE COMP SIDE WALL
&OBST XB=29.99,39.51,14.49,20.0,3.5,3.51,SURF_ID='COMP WALL' /FIRE COMP CEILING
&OBST XB=29.99,39.51,20.00,20.01,3.5,5.0,SURF_ID='COMP WALL' /1.5M FASCIA ABOVE COMP
&OBST XB=29.99,30.0,18.0,20.0,2.3,3.5,SURF_ID='COMP WALL' /CHANNELLING SCREEN
&OBST XB=39.50,39.51,18.0,20.0,2.3,3.5,SURF_ID='COMP WALL' /CHANNELLING SCREEN

COLUMNS
*******
&OBST XB=49.0,49.75,20.25,21.0,0.0,9.5,SURF_ID='CONCRETE', COLOR='LAVENDER' /COLUMN
&OBST XB=49.0,49.75,30.00,30.75,0.0,9.5,SURF_ID='CONCRETE', COLOR='LAVENDER' /COLUMN
&OBST XB=20.00,20.75,20.25,21.0,0.0,9.5,SURF_ID='CONCRETE', COLOR='LAVENDER' /COLUMN
&OBST XB=20.75,21.5,30.00,30.75,0.0,9.5,SURF_ID='CONCRETE', COLOR='LAVENDER' /COLUMN
&OBST XB=12.25,13.0,30.00,30.75,0.0,9.5,SURF_ID='CONCRETE', COLOR='LAVENDER' /COLUMN
&OBST XB=12.25,13.0,20.25,21.00,0.0,9.5,SURF_ID='CONCRETE', COLOR='LAVENDER' /COLUMN

LEVEL 0 GEOMETRY
****************

&OBST XB=30.0,50.0,13.5,14.0,0.0,4.5,SURF_ID='CONCRETE' /WALL
&OBST XB=49.5,50.0,0.0,14.0,0.0,4.5,SURF_ID='CONCRETE' /WALL
&OBST XB=0.0,55.0,0.0,0.005,0.0,4.5,SURF_ID='GLASS WALL' /WALL
&OBST XB=0.0,0.5,0.0,47.0,0.0,4.5,SURF_ID='CONCRETE' /WALL
&OBST XB=0.0,55.0,46.5,47.0,0.0,4.5,SURF_ID='CONCRETE' /WALL

LEVEL 1 GEOMETRY
****************
&OBST XB=0.0,55.0,0.0,20.0,4.5,5.0,SURF_ID='CONCRETE' /FLOOR SLAB
&OBST XB=0.0,12.0,20.0,47.0,4.5,5.0,SURF_ID='CONCRETE' /FLOOR SLAB
&OBST XB=12.0,55.0,31.0,47.0,4.5,5.0,SURF_ID='CONCRETE' /FLOOR SLAB
&OBST XB=50.0,55.0,20.0,31.0,4.5,5.0,SURF_ID='CONCRETE' /FLOOR SLAB
&OBST XB=30.0,30.5,0.0,14.0,5.0,9.5,SURF_ID='CONCRETE' /WALL
&OBST XB=30.0,50.0,13.5,14.0,5.0,9.5,SURF_ID='CONCRETE' /WALL
&OBST XB=49.5,50.0,0.0,14.0,5.0,9.5,SURF_ID='CONCRETE' /WALL
&OBST XB=0.0,55.0,0.0,0.005,5.0,9.5,SURF_ID='GLASS WALL' /WALL
&OBST XB=0.0,0.5,0.0,47.0,5.0,9.5,SURF_ID='CONCRETE' /WALL
&OBST XB=0.0,55.0,46.5,47.0,5.0,9.5,SURF_ID='CONCRETE' /WALL
&OBST XB=0.0,55.0,0.0,20.0,9.5,10.0,SURF_ID='CONCRETE' /CEILING SLAB
&OBST XB=0.0,12.0,31.0,47.0,9.5,10.0,SURF_ID='CONCRETE' /CEILING SLAB
&OBST XB=12.0,55.0,31.0,47.0,9.5,10.0,SURF_ID='CONCRETE' /CEILING SLAB
&OBST XB=0.0,55.0,20.0,21.0,9.5,10.0,SURF_ID='CONCRETE', COLOR='LAVENDER' /CEILING SLAB OVERHANG
&OBST XB=0.0,55.0,30.0,31.0,9.5,10.0,SURF_ID='CONCRETE', COLOR='LAVENDER' /CEILING SLAB OVERHANG
&OBST XB=0.0,55.0,19.5,20.0,9.0,9.5,SURF_ID='CONCRETE', COLOR='LAVENDER' /CEILING SLAB OVERHANG
&OBST XB=0.0,55.0,31.0,31.5,9.0,9.5,SURF_ID='CONCRETE', COLOR='LAVENDER' /CEILING SLAB OVERHANG
&OBST XB=0.0,0.5,16.0,36.0,9.5,12.0,SURF_ID='CONCRETE'/SIDE WALL UNDER GLASS ROOF
&OBST XB=0.0,55.0,16.0,16.5,10.0,12.0,SURF_ID='CONCRETE'/LONG WALL UNDER GLASS ROOF
&OBST XB=0.0,55.0,34.5,35.0,10.0,12.0,SURF_ID='CONCRETE'/LONG WALL UNDER GLASS ROOF
&OBST XB=0.0,55.0,19.0,20.0,10.0,12.0,SURF_ID='CONCRETE'/LONG WALL UNDER GLASS ROOF
&OBST XB=0.0,55.0,31.0,32.0,10.0,12.0,SURF_ID='CONCRETE'/LONG WALL UNDER GLASS ROOF

GLASS ROOF IN BARREL VAULT*************************
&OBST XB=0.0,55.0,23.0,28.000,17.0,17.005,SURF_ID='GLASS WALL',SAWTOOTH=TRUE /ROOF PANEL
&OBST XB=0.0,55.0,23.0,23.005,16.5,17.005,SURF_ID='GLASS WALL',SAWTOOTH=TRUE /ROOF PANEL
&OBST XB=0.0,55.0,21.0,23.005,16.5,16.505,SURF_ID='GLASS WALL',SAWTOOTH=TRUE /ROOF PANEL
&OBST XB=0.0,55.0,21.0,21.005,16.0,16.505,SURF_ID='GLASS WALL',SAWTOOTH=TRUE /ROOF PANEL
&OBST XB=0.0,55.0,19.5,21.005,16.0,16.005,SURF_ID='GLASS WALL',SAWTOOTH=TRUE /ROOF PANEL
&OBST XB=0.0,55.0,19.5,19.505,15.0,16.005,SURF_ID='GLASS WALL',SAWTOOTH=TRUE /ROOF PANEL
&OBST XB=0.0,55.0,18.0,19.505,15.0,15.005,SURF_ID='GLASS WALL',SAWTOOTH=TRUE /ROOF PANEL
&OBST XB=0.0,55.0,18.0,18.005,13.5,15.005,SURF_ID='GLASS WALL',SAWTOOTH=TRUE /ROOF PANEL
&OBST XB=0.0,55.0,16.0,18.005,13.5,13.505,SURF_ID='GLASS WALL',SAWTOOTH=TRUE /ROOF PANEL
&OBST XB=0.0,55.0,16.0,16.005,12.0,13.505,SURF_ID='GLASS WALL',SAWTOOTH=TRUE /ROOF PANEL
&OBST XB=0.0,55.0,27.995,28.0,16.5,17.005,SURF_ID='GLASS WALL',SAWTOOTH=TRUE /ROOF PANEL
&OBST XB=0.0,55.0,27.995,30.0,16.5,16.505,SURF_ID='GLASS WALL',SAWTOOTH=TRUE /ROOF PANEL
&OBST XB=0.0,55.0,29.995,30.0,16.0,16.505,SURF_ID='GLASS WALL',SAWTOOTH=TRUE /ROOF PANEL
&OBST XB=0.0,55.0,29.995,31.5,16.0,16.005,SURF_ID='GLASS WALL',SAWTOOTH=TRUE /ROOF PANEL
&OBST XB=0.0,55.0,31.495,31.5,15.0,16.005,SURF_ID='GLASS WALL',SAWTOOTH=TRUE /ROOF PANEL
```

```
&OBST XB=0.0,55.0,31.495,33.0,15.0,15.005,SURF_ID='GLASS WALL',SAWTOOTH=TRUE /ROOF PANEL
&OBST XB=0.0,55.0,32.995,33.0,13.5,15.005,SURF_ID='GLASS WALL',SAWTOOTH=TRUE /ROOF PANEL
&OBST XB=0.0,55.0,32.995,35.0,13.5,13.505,SURF_ID='GLASS WALL',SAWTOOTH=TRUE /ROOF PANEL
&OBST XB=0.0,55.0,34.995,35.0,12.0,13.505,SURF_ID='GLASS WALL',SAWTOOTH=TRUE /ROOF PANEL

&OBST XB=0.0,0.005,23.0,28.0,12.0,17.005,SURF_ID='GLASS WALL',SAWTOOTH=TRUE /END PANEL PANEL
&OBST XB=0.0,0.005,21.0,23.0,12.0,16.505,SURF_ID='GLASS WALL',SAWTOOTH=TRUE /END PANEL PANEL
&OBST XB=0.0,0.005,19.5,21.0,12.0,16.005,SURF_ID='GLASS WALL',SAWTOOTH=TRUE /END PANEL PANEL
&OBST XB=0.0,0.005,18.0,19.5,12.0,15.005,SURF_ID='GLASS WALL',SAWTOOTH=TRUE /END PANEL PANEL
&OBST XB=0.0,0.005,16.0,18.0,12.0,13.505,SURF_ID='GLASS WALL',SAWTOOTH=TRUE /END PANEL PANEL
&OBST XB=0.0,0.005,28.0,30.0,12.0,16.505,SURF_ID='GLASS WALL',SAWTOOTH=TRUE /END PANEL PANEL
&OBST XB=0.0,0.005,30.0,31.5,12.0,16.005,SURF_ID='GLASS WALL',SAWTOOTH=TRUE /END PANEL PANEL
&OBST XB=0.0,0.005,31.5,33.0,12.0,15.005,SURF_ID='GLASS WALL',SAWTOOTH=TRUE /END PANEL PANEL
&OBST XB=0.0,0.005,33.0,35.0,12.0,13.505,SURF_ID='GLASS WALL',SAWTOOTH=TRUE /END PANEL PANEL

&OBST XB=48.995,49.0,23.0,28.0,12.0,17.005,SURF_ID='GLASS WALL',SAWTOOTH=TRUE /END PANEL PANEL
&OBST XB=48.995,49.0,21.0,23.0,12.0,16.505,SURF_ID='GLASS WALL',SAWTOOTH=TRUE /END PANEL PANEL
&OBST XB=48.995,49.0,19.5,21.0,12.0,16.005,SURF_ID='GLASS WALL',SAWTOOTH=TRUE /END PANEL PANEL
&OBST XB=48.995,49.0,18.0,19.5,12.0,15.005,SURF_ID='GLASS WALL',SAWTOOTH=TRUE /END PANEL PANEL
&OBST XB=48.995,49.0,16.0,18.0,12.0,13.505,SURF_ID='GLASS WALL',SAWTOOTH=TRUE /END PANEL PANEL
&OBST XB=48.995,49.0,28.0,30.0,12.0,16.505,SURF_ID='GLASS WALL',SAWTOOTH=TRUE /END PANEL PANEL
&OBST XB=48.995,49.0,30.0,31.5,12.0,16.005,SURF_ID='GLASS WALL',SAWTOOTH=TRUE /END PANEL PANEL
&OBST XB=48.995,49.0,31.5,33.0,12.0,15.005,SURF_ID='GLASS WALL',SAWTOOTH=TRUE /END PANEL PANEL
&OBST XB=48.995,49.0,33.0,35.0,12.0,13.505,SURF_ID='GLASS WALL',SAWTOOTH=TRUE /END PANEL PANEL

SMOKE CURTAINS
**************
&OBST XB=48.995,49.0,21.0,30.0,7.5,12.0,SURF_ID='CURTAIN' /CURTAIN
&OBST XB=48.995,49.0,20.0,21.0,7.5,9.5,SURF_ID='CURTAIN' /CURTAIN
&OBST XB=48.995,49.0,30.0,31.0,7.5,9.5,SURF_ID='CURTAIN' /CURTAIN
&OBST XB=48.995,49.0,19.5,20.0,7.5,9.0,SURF_ID='CURTAIN' /CURTAIN
&OBST XB=48.995,49.0,14.0,19.5,7.5,9.5,SURF_ID='CURTAIN' /CURTAIN
&OBST XB=48.995,49.0,31.0,31.5,7.5,9.0,SURF_ID='CURTAIN' /CURTAIN
&OBST XB=48.995,49.0,31.5,47.0,7.5,9.5,SURF_ID='CURTAIN' /CURTAIN
&OBST XB=48.995,49.0,20.0,21.0,10.0,12.0,SURF_ID='CURTAIN' /CURTAIN
&OBST XB=48.995,49.0,30.0,31.0,10.0,12.0,SURF_ID='CURTAIN' /CURTAIN
&OBST XB=48.995,49.0,32.0,34.5,10.0,12.0,SURF_ID='CURTAIN' /CURTAIN
&OBST XB=48.995,49.0,16.5,19.0,10.0,12.0,SURF_ID='CURTAIN' /CURTAIN

INSTRUMENTATION AND MEASUREMENTS
********************************
&DEVC ID='TC-01', XYZ=41.0,32.75,14.00, QUANTITY='TEMPERATURE' / Thermocouple column
&DEVC ID='TC-02', XYZ=41.0,32.50,13.75, QUANTITY='TEMPERATURE' / Thermocouple column
&DEVC ID='TC-03', XYZ=41.0,30.00,12.50, QUANTITY='TEMPERATURE' / Thermocouple column
&DEVC ID='TC-04', XYZ=41.0,29.75,12.00, QUANTITY='TEMPERATURE' / Thermocouple column
&DEVC ID='TC-05', XYZ=41.0,29.75,11.50, QUANTITY='TEMPERATURE' / Thermocouple column
&DEVC ID='TC-06', XYZ=41.0,29.75,11.00, QUANTITY='TEMPERATURE' / Thermocouple column
&DEVC ID='TC-07', XYZ=41.0,29.75,10.50, QUANTITY='TEMPERATURE' / Thermocouple column
&DEVC ID='TC-08', XYZ=41.0,29.75,9.50, QUANTITY='TEMPERATURE' / Thermocouple column
&DEVC ID='TC-09', XYZ=41.0,29.75,8.50, QUANTITY='TEMPERATURE' / Thermocouple column
&DEVC ID='TC-10', XYZ=41.0,29.75,7.50, QUANTITY='TEMPERATURE' / Thermocouple column
&DEVC ID='TC-11', XYZ=41.0,29.75,6.50, QUANTITY='TEMPERATURE' / Thermocouple column

&SLCF PBX=34.75,QUANTITY='TEMPERATURE'/
&SLCF PBX=34.75,QUANTITY='VELOCITY',VECTOR=.TRUE./

&SLCF PBY=25.5,QUANTITY='TEMPERATURE'/
&SLCF PBY=25.5,QUANTITY='VELOCITY',VECTOR=.TRUE./

&DEVC XB=29.0,40.5,20.0,24.0,3.5,3.5, QUANTITY='MASS FLOW', ID='MSF@0HOR'/
&DEVC XB=29.0,40.5,20.0,24.5,4.5,4.5, QUANTITY='MASS FLOW', ID='MSF@1HOR'/
&DEVC XB=28.5,41.0,20.0,26.0,5.5,5.5, QUANTITY='MASS FLOW', ID='MSF@2HOR'/
&DEVC XB=28.0,41.5,20.0,27.0,6.5,6.5, QUANTITY='MASS FLOW', ID='MSF@3HOR'/
&DEVC XB=28.0,41.5,20.0,27.5,7.5,7.5, QUANTITY='MASS FLOW', ID='MSF@4HOR'/
&DEVC XB=28.0,41.5,20.0,28.5,8.5,8.5, QUANTITY='MASS FLOW', ID='MSF@5HOR'/
&DEVC XB=28.0,41.5,20.0,28.5,9.5,9.5, QUANTITY='MASS FLOW', ID='MSF@6HOR'/
&DEVC XB=28.0,41.5,20.0,29.5,10.5,10.5, QUANTITY='MASS FLOW', ID='MSF@7HOR'/
&DEVC XB=28.0,41.5,20.0,29.5,11.5,11.5, QUANTITY='MASS FLOW', ID='MSF@8HOR'/
&DEVC XB=28.0,41.5,20.0,30.0,12.5,12.5, QUANTITY='MASS FLOW', ID='MSF@9HOR'/
&DEVC XB=28.0,41.5,20.0,31.0,13.5,13.5, QUANTITY='MASS FLOW', ID='MSF@10HOR'/
&TAIL /
```

Appendix S: FDS input file for European Parliament Hot Smoke Test

```
&HEAD CHID='eparl_25_50_hole',TITLE='European parliament HST'/
&MESH IJK=16,35,56, XB=0.0,8.0,0.0,17.5,0.0,28.0/ 50 mm grid
&MESH IJK=32,70,112, XB=8.0,16.0,0.0,17.5,0.0,28.0/ 25 mm grid
&MESH IJK=64,35,56, XB=16.0,48.0,0.0,17.5,0.0,28.0/ 50 mm grid

SIMULATION TIME
**********
&TIME T_END=600. /
&MISC TMPA=7. /
&DUMP NFRAMES=1000, DT_DEVC=1.,DT_SLCF=5./

CHARACTERISTICS OF EXHAUST
**********
&SURF ID='fan1', VOLUME_FLUX=22.2, COLOR='RED' /
&VENT XB=16.0,17.0,13.5,13.5,26.0,27.0, SURF_ID='fan1' /
&OBST XB=16.0,17.0,13.5,14.0,26.0,27.0,COLOR='INVISIBLE'/OBSTRUCTION ATTACHED TO VENT
&SURF ID='fan2', VOLUME_FLUX=16.7, COLOR='RED' /
&VENT XB=32.0,33.0,12.0,12.0,26.0,27.0, SURF_ID='fan2' /
&OBST XB=32.0,33.0,12.0,12.5,26.0,27.0,COLOR='INVISIBLE'/OBSTRUCTION ATTACHED TO VENT

CHARACTERISTICS OF EXHAUST IN CURTAIN
**********
&HOLE XB=23.5,24.5,13.0,14.0,19.0,25.5 /6.5 M2 HOLE IN CURTAIN ON FOYER LEVEL 3
&HOLE XB=45.0,46.0,7.0,7.5,19.0,22.0 /HOLE IN CURTAIN ON BRIDGE 5

CHARACTERISIICS OF THE BURNER FIRE
**********
&SURF ID='fire', HRRPUA=527. /
&OBST XB=10.25,11.25,1.25,2.25,0.0,0.0, SURF_ID='fire',COLOR='RED' /
&OBST XB=12.75,13.75,1.25,2.25,0.0,0.0, SURF_ID='fire',COLOR='RED' /
&RADI RADIATIVE_FRACTION=0.20 /

CHARACTERISIICS OF THE BOUNDARIES
**********
&VENT MB='XMIN' , SURF_ID='OPEN' /Open domain boundary
&VENT MB='XMAX' , SURF_ID='OPEN' /Open domain boundary
&VENT MB='YMIN' , SURF_ID='OPEN' /Open domain boundary
&VENT MB='YMAX' , SURF_ID='OPEN' /Open domain boundary
&VENT MB='ZMAX' , SURF_ID='OPEN' /Open domain boundary

MATERIAL AND SURFACE PROPERTIES
**********
&MATL ID='CERAMIC BOARD'
    FYI     ='PROMAT,DATA SHEET'
    SPECIFIC_HEAT= 0.92
    DENSITY     = 870
    CONDUCTIVITY = 0.19/

&SURF ID      ='COMP WALL'
    MATL_ID  ='CERAMIC BOARD'
    COLOR='TAN'
    THICKNESS = 0.009 /FIRE COMPARTMENT WALLS

&MATL ID         ='CONCRETE'
    FYI        ='QUINTIERE,FIRE BEHAVIOUR'
    SPECIFIC_HEAT= 0.88
    DENSITY     = 2100
    CONDUCTIVITY = 1.0/

&SURF ID      ='CONCRETE'
    MATL_ID  ='CONCRETE'
    COLOR='GRAY'
    THICKNESS= 0.5 /CONCRETE FLOOR

&MATL ID         ='GLASS'
    FYI        ='DRYSDALE D, INTRODUCTION TO FIRE DYNAMICS'
    SPECIFIC_HEAT= 0.84
    DENSITY     = 2700
    CONDUCTIVITY = 0.76/

&SURF ID      ='GLASS WALL'
    MATL_ID  ='GLASS'
    COLOR='AQUAMARINE'
```

```
    TRANSPARENCY=0.5
    THICKNESS= 0.005 /
&MATL ID         ='GLASS FIBRE'
    FYI        ='INCROPERA AND DEWITT'
    SPECIFIC_HEAT= 0.795
    DENSITY     = 105
    CONDUCTIVITY = 0.036/

&SURF ID      ='CURTAIN'
    MATL_ID  ='GLASS FIBRE'
    COLOR='BLACK'
    TRANSPARENCY=0.4
    THICKNESS= 0.0005 /

COMPARTMENT GEOMETRY
********************
&OBST XB=8.75,15.25,0.0,0.009,0.0,2.75,SURF_ID='COMP WALL' /FIRE BACK SIDE WALL
&OBST XB=8.75,8.759,0.0,3.5,0.0,2.75,SURF_ID='COMP WALL' /FIRE COMP SIDE WALL
&OBST XB=15.241,15.25,0.0,3.5,0.0,2.75,SURF_ID='COMP WALL' /FIRE COMP SIDE WALL
&OBST XB=8.75,15.25,0.0,3.509,2.75,2.759,SURF_ID='COMP WALL' /FIRE COMP CEILING
&OBST XB=8.0,16.0,3.5,3.509,2.75,11.75,SURF_ID='COMP WALL' /CFI BOARD ABOVE FIRE COMPARTMENT
&OBST XB=8.0,8.75,3.5,3.509,0.0,2.75,SURF_ID='COMP WALL' /CFI BOARD SIDE OF FIRE COMPARTMENT
&OBST XB=15.25,16.0,3.5,3.509,0.0,2.75,SURF_ID='COMP WALL' /CFI BOARD SIDE OF FIRE COMPARTMENT

GLAZED OFFICES GEOMETRY
***********************
&OBST XB=0.0,44.0,0.0,0.0,0.0,4.5,SURF_ID='INERT', COLOR='GRAY' /LEVEL 0 BACK WALL
&OBST XB=0.0,44.0,17.5,17.5,0.0,4.5,SURF_ID='INERT', COLOR='GRAY' /LEVEL 0 FRONT WALL
&OBST XB=1.0,1.5,13.5,17.5,0.0,4.5,SURF_ID='INERT', COLOR='GRAY' /LEVEL 0 WALL
&OBST XB=1.0,1.5,0.0,3.5,0.0,4.5,SURF_ID='INERT', COLOR='GRAY' /LEVEL 0 WALL
&OBST XB=43.5,44.0,0.0,3.5,0.0,4.5,SURF_ID='INERT', COLOR='GRAY' /LEVEL 0 WALL
&OBST XB=43.5,44.0,0.0,3.5,0.0,28.0,SURF_ID='CONCRETE' /WALL
&OBST XB=47.0,47.5,0.0,3.5,0.0,28.0,SURF_ID='CONCRETE' /WALL
&OBST XB=1.0,1.5,0.0,3.5,0.0,28.0,SURF_ID='CONCRETE' /WALL
&OBST XB=43.5,44.0,0.0,3.5,0.0,4.5,SURF_ID='INERT', COLOR='GRAY' /WALL
&OBST XB=0.0,16.0,3.5,13.5,27.0,27.005,SURF_ID='GLASS WALL' /GLASS CEILING
&OBST XB=16.0,31.0,1.0,13.5,27.0,27.005,SURF_ID='GLASS WALL' /GLASS CEILING
&OBST XB=31.0,38.5,1.0,12.0,27.0,27.005,SURF_ID='GLASS WALL' /GLASS CEILING
&OBST XB=38.5,48.0,3.5,10.5,27.0,27.005,SURF_ID='GLASS WALL' /GLASS CEILING
&OBST XB=1.0,16.0,3.495,3.5,4.5,28.0,SURF_ID='GLASS WALL' /GLASS WALL ABOVE COMPARTMENT
&OBST XB=15.995,16.0,1.0,3.5,4.5,28.0,SURF_ID='GLASS WALL' /GLASS WALL NEXT TO COMPARTMENT
&OBST XB=16.0,38.5,0.995,1.0,4.5,28.0,SURF_ID='GLASS WALL' /GLASS WALL NEXT TO COMPARTMENT
&OBST XB=38.5,38.505,1.0,3.5,4.5,28.0,SURF_ID='GLASS WALL' /GLASS WALL NEXT TO BRIDGE 2
&OBST XB=38.5,44.0,3.495,3.5,4.5,28.0,SURF_ID='GLASS WALL' /GLASS WALL NEXT TO BRIDGE 2
&OBST XB=47.0,48.0,3.495,3.5,4.5,28.0,SURF_ID='GLASS WALL' /GLASS WALL NEXT TO BRIDGE 2
&OBST XB=0.0,16.0,0.0,3.5,4.5,5.0,SURF_ID='CONCRETE' /FLOOR SLAB LEVEL 1
&OBST XB=16.0,38.5,0.0,1.0,4.5,5.0,SURF_ID='CONCRETE' /FLOOR SLAB LEVEL 1
&OBST XB=38.5,44.0,0.0,3.5,4.5,5.0,SURF_ID='CONCRETE' /FLOOR SLAB LEVEL 1
&OBST XB=47.0,48.0,0.0,3.5,4.5,5.0,SURF_ID='CONCRETE' /FLOOR SLAB LEVEL 1
&OBST XB=0.0,16.0,0.0,3.5,8.0,8.5,SURF_ID='CONCRETE' /FLOOR SLAB LEVEL 2
&OBST XB=16.0,38.5,0.0,1.0,8.0,8.5,SURF_ID='CONCRETE' /FLOOR SLAB LEVEL 2
&OBST XB=38.5,44.0,0.0,3.5,8.0,8.5,SURF_ID='CONCRETE' /FLOOR SLAB LEVEL 2
&OBST XB=47.0,48.0,0.0,3.5,8.0,8.5,SURF_ID='CONCRETE' /FLOOR SLAB LEVEL 2
&OBST XB=0.0,16.0,0.0,3.5,11.5,12.0,SURF_ID='CONCRETE' /FLOOR SLAB LEVEL 3
&OBST XB=16.0,38.5,0.0,1.0,11.5,12.0,SURF_ID='CONCRETE' /FLOOR SLAB LEVEL 3
&OBST XB=38.5,44.0,0.0,3.5,11.5,12.0,SURF_ID='CONCRETE' /FLOOR SLAB LEVEL 3
&OBST XB=47.0,48.0,0.0,3.5,11.5,12.0,SURF_ID='CONCRETE' /FLOOR SLAB LEVEL 3
&OBST XB=0.0,16.0,0.0,3.5,15.0,15.5,SURF_ID='CONCRETE' /FLOOR SLAB LEVEL 4
&OBST XB=16.0,38.5,0.0,1.0,15.0,15.5,SURF_ID='CONCRETE' /FLOOR SLAB LEVEL 4
&OBST XB=38.5,44.0,0.0,3.5,15.0,15.5,SURF_ID='CONCRETE' /FLOOR SLAB LEVEL 4
&OBST XB=47.0,48.0,0.0,3.5,15.0,15.5,SURF_ID='CONCRETE' /FLOOR SLAB LEVEL 4
&OBST XB=0.0,16.0,0.0,3.5,18.5,19.0,SURF_ID='CONCRETE' /FLOOR SLAB LEVEL 5
&OBST XB=16.0,38.5,0.0,1.0,18.5,19.0,SURF_ID='CONCRETE' /FLOOR SLAB LEVEL 5
&OBST XB=38.5,44.0,0.0,3.5,18.5,19.0,SURF_ID='CONCRETE' /FLOOR SLAB LEVEL 5
&OBST XB=47.0,48.0,0.0,3.5,18.5,19.0,SURF_ID='CONCRETE' /FLOOR SLAB LEVEL 5
&OBST XB=0.0,16.0,0.0,3.5,22.0,22.5,SURF_ID='CONCRETE' /FLOOR SLAB LEVEL 6
&OBST XB=16.0,38.5,0.0,1.0,22.0,22.5,SURF_ID='CONCRETE' /FLOOR SLAB LEVEL 6
&OBST XB=38.5,44.0,0.0,3.5,22.0,22.5,SURF_ID='CONCRETE' /FLOOR SLAB LEVEL 6
&OBST XB=47.0,48.0,0.0,3.5,22.0,22.5,SURF_ID='CONCRETE' /FLOOR SLAB LEVEL 6
&OBST XB=0.0,16.0,0.0,3.5,27.0,27.5,SURF_ID='CONCRETE' /FLOOR SLAB LEVEL 7
&OBST XB=16.0,38.5,0.0,1.0,27.0,27.5,SURF_ID='CONCRETE' /FLOOR SLAB LEVEL 7
&OBST XB=38.5,44.0,0.0,3.5,27.0,27.5,SURF_ID='CONCRETE' /FLOOR SLAB LEVEL 7
&OBST XB=44.0,48.0,0.0,3.5,27.0,27.5,SURF_ID='CONCRETE' /FLOOR SLAB LEVEL 7
```

FOYER SIDE GEOMETRY
****
&OBST XB=0.0,31.0,16.0,17.5,4.5,5.0,SURF_ID='CONCRETE' /FLOOR SLAB LEVEL 1
&OBST XB=0.0,8.0,13.5,14.0,4.5,5.0,SURF_ID='CONCRETE' /FLOOR SLAB LEVEL 1
&OBST XB=8.0,31.0,13.5,16.0,4.5,5.0,SURF_ID='CONCRETE' /FLOOR SLAB LEVEL 1
&OBST XB=31.0,38.5,12.0,17.5,4.5,5.0,SURF_ID='CONCRETE' /FLOOR SLAB LEVEL 1
&OBST XB=38.5,44.0,10.5,17.5,4.5,5.0,SURF_ID='CONCRETE' /FLOOR SLAB LEVEL 1
&OBST XB=47.0,48.0,10.5,17.5,4.5,5.0,SURF_ID='CONCRETE' /FLOOR SLAB LEVEL 1

&OBST XB=7.5,8.0,14.0,16.0,4.0,4.5,SURF_ID='CONCRETE',COLOR='CADET BLUE' /STAIR LEVEL 0 TO LEVEL 1
&OBST XB=7.0,7.5,14.0,16.0,3.5,4.0,SURF_ID='CONCRETE',COLOR='CADET BLUE' /STAIR LEVEL 0 TO LEVEL 1
&OBST XB=6.5,7.0,14.0,16.0,3.0,3.5,SURF_ID='CONCRETE',COLOR='CADET BLUE' /STAIR LEVEL 0 TO LEVEL 1
&OBST XB=6.0,6.5,14.0,16.0,2.5,3.0,SURF_ID='CONCRETE',COLOR='CADET BLUE' /STAIR LEVEL 0 TO LEVEL 1
&OBST XB=5.5,6.0,14.0,16.0,2.0,2.5,SURF_ID='CONCRETE',COLOR='CADET BLUE' /STAIR LEVEL 0 TO LEVEL 1
&OBST XB=5.0,5.5,14.0,16.0,1.5,2.0,SURF_ID='CONCRETE',COLOR='CADET BLUE' /STAIR LEVEL 0 TO LEVEL 1
&OBST XB=4.5,5.0,14.0,16.0,1.0,1.5,SURF_ID='CONCRETE',COLOR='CADET BLUE' /STAIR LEVEL 0 TO LEVEL 1
&OBST XB=4.0,4.5,14.0,16.0,0.5,1.0,SURF_ID='CONCRETE',COLOR='CADET BLUE' /STAIR LEVEL 0 TO LEVEL 1
&OBST XB=3.5,4.0,14.0,16.0,0.0,0.5,SURF_ID='CONCRETE',COLOR='CADET BLUE' /STAIR LEVEL 0 TO LEVEL 1

&OBST XB=6.0,10.0,13.5,14.0,0.0,25.5,SURF_ID='CONCRETE',COLOR='LAVENDER' /WALL
&OBST XB=13.0,17.0,13.5,14.0,0.0,25.5,SURF_ID='CONCRETE',COLOR='LAVENDER' /WALL
&OBST XB=21.0,23.0,13.5,14.0,0.0,25.5,SURF_ID='CONCRETE',COLOR='LAVENDER' /WALL
&OBST XB=31.0,32.5,12.0,12.5,0.0,25.5,SURF_ID='CONCRETE',COLOR='LAVENDER' /WALL
&OBST XB=38.5,44.0,10.5,11.0,0.0,25.5,SURF_ID='CONCRETE',COLOR='LAVENDER' /WALL
&OBST XB=38.5,39.0,10.5,17.5,0.0,25.5,SURF_ID='CONCRETE',COLOR='LAVENDER' /WALL
&OBST XB=47.0,48.0,10.5,11.0,0.0,25.5,SURF_ID='CONCRETE',COLOR='LAVENDER' /WALL
&OBST XB=0.5,1.0,13.5,14.0,0.0,25.5,SURF_ID='CONCRETE' /WALL

&OBST XB=1.0,6.0,13.5,13.5,5.0,11.5,SURF_ID='CURTAIN' /CURTAIN LEVEL 1
&OBST XB=10.0,13.0,13.5,13.5,5.0,11.5,SURF_ID='CURTAIN' /CURTAIN LEVEL 1
&OBST XB=17.0,21.0,13.5,13.5,5.0,11.5,SURF_ID='CURTAIN' /CURTAIN LEVEL 1
&OBST XB=23.0,31.0,13.5,13.5,5.0,11.5,SURF_ID='CURTAIN' /CURTAIN LEVEL 1
&OBST XB=31.0,31.0,12.0,13.5,5.0,11.5,SURF_ID='CURTAIN' /CURTAIN LEVEL 1
&OBST XB=32.5,38.5,12.0,12.0,5.0,11.5,SURF_ID='CURTAIN' /CURTAIN LEVEL 1

&OBST XB=0.0,31.0,15.5,16.0,11.5,12.0,SURF_ID='CONCRETE' /FLOOR SLAB LEVEL 2
&OBST XB=0.0,8.0,16.0,17.5,11.5,12.0,SURF_ID='CONCRETE' /FLOOR SLAB LEVEL 2
&OBST XB=0.0,22.0,13.5,16.0,11.5,12.0,SURF_ID='CONCRETE' /FLOOR SLAB LEVEL 2
&OBST XB=22.0,31.0,13.5,17.5,11.5,12.0,SURF_ID='CONCRETE' /FLOOR SLAB LEVEL 2
&OBST XB=31.0,38.5,12.0,17.5,11.5,12.0,SURF_ID='CONCRETE' /FLOOR SLAB LEVEL 2
&OBST XB=38.5,44.0,10.5,17.5,11.5,12.0,SURF_ID='CONCRETE' /FLOOR SLAB LEVEL 2
&OBST XB=47.0,48.0,10.5,17.5,11.5,12.0,SURF_ID='CONCRETE' /FLOOR SLAB LEVEL 2

&OBST XB=21,22,16.0,17.5,11.0,11.5,SURF_ID='CONCRETE',COLOR='CADET BLUE' /STAIR LEVEL 1 TO LEVEL 2
&OBST XB=20,21,16.0,17.5,10.5,11.0,SURF_ID='CONCRETE',COLOR='CADET BLUE' /STAIR LEVEL 1 TO LEVEL 2
&OBST XB=19,20,16.0,17.5,10.0,10.5,SURF_ID='CONCRETE',COLOR='CADET BLUE' /STAIR LEVEL 1 TO LEVEL 2
&OBST XB=18,19,16.0,17.5,9.5,10.0,SURF_ID='CONCRETE',COLOR='CADET BLUE' /STAIR LEVEL 1 TO LEVEL 2
&OBST XB=17,18,16.0,17.5,9.0,9.5,SURF_ID='CONCRETE',COLOR='CADET BLUE' /STAIR LEVEL 1 TO LEVEL 2
&OBST XB=16,17,16.0,17.5,8.5,9.0,SURF_ID='CONCRETE',COLOR='CADET BLUE' /STAIR LEVEL 1 TO LEVEL 2
&OBST XB=15,16,16.0,17.5,8.0,8.5,SURF_ID='CONCRETE',COLOR='CADET BLUE' /STAIR LEVEL 1 TO LEVEL 2
&OBST XB=14,15,16.0,17.5,7.5,8.0,SURF_ID='CONCRETE',COLOR='CADET BLUE' /STAIR LEVEL 1 TO LEVEL 2
&OBST XB=13,14,16.0,17.5,7.0,7.5,SURF_ID='CONCRETE',COLOR='CADET BLUE' /STAIR LEVEL 1 TO LEVEL 2
&OBST XB=12,13,16.0,17.5,6.5,7.0,SURF_ID='CONCRETE',COLOR='CADET BLUE' /STAIR LEVEL 1 TO LEVEL 2
&OBST XB=11,12,16.0,17.5,6.0,6.5,SURF_ID='CONCRETE',COLOR='CADET BLUE' /STAIR LEVEL 1 TO LEVEL 2
&OBST XB=10,11,16.0,17.5,5.5,6.0,SURF_ID='CONCRETE',COLOR='CADET BLUE' /STAIR LEVEL 1 TO LEVEL 2
&OBST XB=9,10,16.0,17.5,5.0,5.5,SURF_ID='CONCRETE',COLOR='CADET BLUE' /STAIR LEVEL 1 TO LEVEL 2
&OBST XB=8,9,16.0,17.5,4.5,5.0,SURF_ID='CONCRETE',COLOR='CADET BLUE' /STAIR LEVEL 1 TO LEVEL 2

&OBST XB=1.0,6.0,13.5,13.5,12.0,18.5,SURF_ID='CURTAIN' /CURTAIN LEVEL 2
&OBST XB=10.0,13.0,13.5,13.5,12.0,18.5,SURF_ID='CURTAIN' /CURTAIN LEVEL 2
&OBST XB=17.0,21.0,13.5,13.5,12.0,18.5,SURF_ID='CURTAIN' /CURTAIN LEVEL 2
&OBST XB=23.0,31.0,13.5,13.5,12.0,18.5,SURF_ID='CURTAIN' /CURTAIN LEVEL 2
&OBST XB=31.0,31.0,12.0,13.5,12.0,18.5,SURF_ID='CURTAIN' /CURTAIN LEVEL 2
&OBST XB=32.5,38.5,12.0,12.0,12.0,18.5,SURF_ID='CURTAIN' /CURTAIN LEVEL 2

&OBST XB=0.0,31.0,16.0,17.5,18.5,19.0,SURF_ID='CONCRETE' /FLOOR SLAB LEVEL 3
&OBST XB=0.0,22.0,13.5,14.0,18.5,19.0,SURF_ID='CONCRETE' /FLOOR SLAB LEVEL 3
&OBST XB=0.0,9.0,14.0,16.0,18.5,19.0,SURF_ID='CONCRETE' /FLOOR SLAB LEVEL 3
&OBST XB=22.0,31.0,13.5,17.5,18.5,19.0,SURF_ID='CONCRETE' /FLOOR SLAB LEVEL 3
&OBST XB=31.0,38.5,12.0,17.5,18.5,19.0,SURF_ID='CONCRETE' /FLOOR SLAB LEVEL 3
&OBST XB=38.5,44.0,10.5,17.5,18.5,19.0,SURF_ID='CONCRETE' /FLOOR SLAB LEVEL 3
&OBST XB=47.0,48.0,10.5,17.5,18.5,19.0,SURF_ID='CONCRETE' /FLOOR SLAB LEVEL 3

```
&OBST XB=21,22,14.0,15.5,18.0,18.5,SURF_ID='CONCRETE',COLOR='CADET BLUE' /STAIR LEVEL 1 TO LEVEL 2
&OBST XB=20,21,14.0,15.5,17.5,18.0,SURF_ID='CONCRETE',COLOR='CADET BLUE' /STAIR LEVEL 1 TO LEVEL 2
&OBST XB=19,20,14.0,15.5,17.0,17.5,SURF_ID='CONCRETE',COLOR='CADET BLUE' /STAIR LEVEL 1 TO LEVEL 2
&OBST XB=18,19,14.0,15.5,16.5,17.0,SURF_ID='CONCRETE',COLOR='CADET BLUE' /STAIR LEVEL 1 TO LEVEL 2
&OBST XB=17,18,14.0,15.5,16.0,16.5,SURF_ID='CONCRETE',COLOR='CADET BLUE' /STAIR LEVEL 1 TO LEVEL 2
&OBST XB=16,17,14.0,15.5,15.5,16.0,SURF_ID='CONCRETE',COLOR='CADET BLUE' /STAIR LEVEL 1 TO LEVEL 2
&OBST XB=15,16,14.0,15.5,15.0,15.5,SURF_ID='CONCRETE',COLOR='CADET BLUE' /STAIR LEVEL 1 TO LEVEL 2
&OBST XB=14,15,14.0,15.5,14.5,15.0,SURF_ID='CONCRETE',COLOR='CADET BLUE' /STAIR LEVEL 1 TO LEVEL 2
&OBST XB=13,14,14.0,15.5,14.0,14.5,SURF_ID='CONCRETE',COLOR='CADET BLUE' /STAIR LEVEL 1 TO LEVEL 2
&OBST XB=12,13,14.0,15.5,13.5,14.0,SURF_ID='CONCRETE',COLOR='CADET BLUE' /STAIR LEVEL 1 TO LEVEL 2
&OBST XB=11,12,14.0,15.5,13.0,13.5,SURF_ID='CONCRETE',COLOR='CADET BLUE' /STAIR LEVEL 1 TO LEVEL 2
&OBST XB=10,11,14.0,15.5,12.5,13.0,SURF_ID='CONCRETE',COLOR='CADET BLUE' /STAIR LEVEL 1 TO LEVEL 2
&OBST XB=9,10,14.0,15.5,12.0,12.5,SURF_ID='CONCRETE',COLOR='CADET BLUE' /STAIR LEVEL 1 TO LEVEL 2
&OBST XB=8,9,14.0,15.5,11.5,12.0,SURF_ID='CONCRETE',COLOR='CADET BLUE' /STAIR LEVEL 1 TO LEVEL 2

&OBST XB=1.0,6.0,13.5,13.5,19.0,25.5,SURF_ID='CURTAIN' /CURTAIN LEVEL 3
&OBST XB=10.0,13.0,13.5,13.5,19.0,25.5,SURF_ID='CURTAIN' /CURTAIN LEVEL 3
&OBST XB=17.0,21.0,13.5,13.5,19.0,25.5,SURF_ID='CURTAIN' /CURTAIN LEVEL 3
&OBST XB=23.0,31.0,13.5,13.5,19.0,25.5,SURF_ID='CURTAIN' /CURTAIN LEVEL 3
&OBST XB=31.0,31.0,12.0,13.5,19.0,25.5,SURF_ID='CURTAIN' /CURTAIN LEVEL 3
&OBST XB=32.5,38.5,12.0,12.0,19.0,25.5,SURF_ID='CURTAIN' /CURTAIN LEVEL 3

&OBST XB=0.0,31.0,13.5,17.5,25.5,26.0,SURF_ID='CONCRETE' /FLOOR SLAB LEVEL 4
&OBST XB=31.0,38.5,12.0,17.5,25.5,26.0,SURF_ID='CONCRETE' /FLOOR SLAB LEVEL 4
&OBST XB=38.5,48.0,10.5,17.5,25.5,26.0, SURF_ID='CONCRETE' /FLOOR SLAB LEVEL 4
&OBST XB=47.0,48.0,10.5,17.5,25.5,26.0, SURF_ID='CONCRETE' /FLOOR SLAB LEVEL 4

&OBST XB=0.0,16.0,13.5,14.0,26.0,28.0,SURF_ID='CONCRETE' /WALL SLAB LEVEL 4
&OBST XB=16.0,17.0,13.5,14.0,27.0,28.0,SURF_ID='CONCRETE' /WALL SLAB LEVEL 4
&OBST XB=17.0,31.0,13.5,14.0,26.0,28.0,SURF_ID='CONCRETE' /WALL SLAB LEVEL 4
&OBST XB=31.0,31.5,12.0,14.0,26.0,28.0,SURF_ID='CONCRETE' /WALL SLAB LEVEL 4
&OBST XB=31.0,32.0,12.0,12.5,26.0,28.0,SURF_ID='CONCRETE' /WALL SLAB LEVEL 4
&OBST XB=32.0,33.0,12.0,12.5,27.0,28.0,SURF_ID='CONCRETE' /WALL SLAB LEVEL 4
&OBST XB=33.0,38.5,12.0,12.5,26.0,28.0,SURF_ID='CONCRETE' /WALL SLAB LEVEL 4
&OBST XB=38.5,39.0,10.5,12.0,26.0,28.0,SURF_ID='CONCRETE' /WALL SLAB LEVEL 4
&OBST XB=38.5,44.0,10.5,11.0,26.0,28.0,SURF_ID='CONCRETE' /WALL SLAB LEVEL 4
&OBST XB=44.0,48.0,10.5,11.0,26.0,28.0,SURF_ID='CONCRETE' /WALL SLAB LEVEL 4

BRIDGE 1 GEOMETRY
*****************
&OBST XB=0.0,1.0,3.5,13.5,4.5,5.0,SURF_ID='CONCRETE' /FLOOR SLAB LEVEL 1
&OBST XB=0.0,1.0,3.5,13.5,11.5,12.0,SURF_ID='CONCRETE' /FLOOR SLAB LEVEL 2
&OBST XB=0.0,1.0,3.5,13.5,18.5,19.0,SURF_ID='CONCRETE' /FLOOR SLAB LEVEL 3
&OBST XB=1.0,1.0,3.5,13.5,5.0,11.5,SURF_ID='CURTAIN' /CURTAIN LEVEL 1 FOYER
&OBST XB=1.0,1.0,3.5,13.5,12.0,18.5,SURF_ID='CURTAIN' /CURTAIN LEVEL 2 FOYER
&OBST XB=0.995,1.0,3.5,13.5,19.0,27.0,SURF_ID='GLASS WALL' /GLASS WALL LEVEL 3 FOYER

BRIDGE 2 GEOMETRY
*****************
&OBST XB=44.0,47.0,0.0,17.5,4.5,5.0,SURF_ID='CONCRETE' /FLOOR SLAB LEVEL 1
&OBST XB=44.0,47.0,0.0,17.5,11.5,12.0,SURF_ID='CONCRETE' /FLOOR SLAB LEVEL 2
&OBST XB=44.0,47.0,0.0,17.5,18.5,19.0,SURF_ID='CONCRETE' /FLOOR SLAB LEVEL 3
&OBST XB=45.5,45.5,3.5,10.5,5.0,11.5,SURF_ID='CURTAIN' /CURTAIN LEVEL 1 FOYER
&OBST XB=44.0,45.5,3.5,3.5,5.0,11.5,SURF_ID='CURTAIN' /CURTAIN LEVEL 1 FOYER
&OBST XB=44.0,45.5,10.5,10.5,5.0,11.5,SURF_ID='CURTAIN' /CURTAIN LEVEL 1 FOYER
&OBST XB=45.5,45.5,3.5,10.5,12.0,18.5,SURF_ID='CURTAIN' /CURTAIN LEVEL 1 FOYER
&OBST XB=44.0,45.5,3.5,3.5,12.0,18.5,SURF_ID='CURTAIN' /CURTAIN LEVEL 1 FOYER
&OBST XB=44.0,45.5,10.5,10.5,12.0,18.5,SURF_ID='CURTAIN' /CURTAIN LEVEL 1 FOYER
&OBST XB=45.5,45.5,3.5,10.5,19.0,27.0,SURF_ID='CURTAIN' /CURTAIN LEVEL 1 FOYER
&OBST XB=44.0,45.5,3.5,3.5,19.0,27.0,SURF_ID='CURTAIN' /CURTAIN LEVEL 1 FOYER
&OBST XB=44.0,45.5,10.5,10.5,19.0,27.0,SURF_ID='CURTAIN' /CURTAIN LEVEL 1 FOYER
```

INSTRUMENTATION AND MEASUREMENTS
****
```
&DEVC ID='TC-01', XYZ=17.0,13.0,26.56, QUANTITY='TEMPERATURE' / Thermocouple column
&DEVC ID='TC-02', XYZ=17.0,13.0,23.56, QUANTITY='TEMPERATURE' / Thermocouple column
&DEVC ID='TC-03', XYZ=17.0,13.0,20.56, QUANTITY='TEMPERATURE' / Thermocouple column
&DEVC ID='TC-04', XYZ=17.0,13.0,18.56, QUANTITY='TEMPERATURE' / Thermocouple column
&DEVC ID='TC-05', XYZ=17.0,13.0,16.56, QUANTITY='TEMPERATURE' / Thermocouple column
&DEVC ID='TC-06', XYZ=17.0,13.0,15.56, QUANTITY='TEMPERATURE' / Thermocouple column
&DEVC ID='TC-07', XYZ=17.0,13.0,14.56, QUANTITY='TEMPERATURE' / Thermocouple column
&DEVC ID='TC-08', XYZ=17.0,13.0,13.56, QUANTITY='TEMPERATURE' / Thermocouple column
&DEVC ID='TC-09', XYZ=17.0,13.0,12.56, QUANTITY='TEMPERATURE' / Thermocouple column
&DEVC ID='TC-10', XYZ=17.0,13.0,11.56, QUANTITY='TEMPERATURE' / Thermocouple column
&DEVC ID='TC-11', XYZ=17.0,13.0,9.56, QUANTITY='TEMPERATURE' / Thermocouple column
&DEVC ID='TC-12', XYZ=17.0,13.0,7.56, QUANTITY='TEMPERATURE' / Thermocouple column
&DEVC ID='TC-13', XYZ=17.0,13.0,5.56, QUANTITY='TEMPERATURE' / Thermocouple column

&DEVC ID='TC-14', XYZ=8.8,3.5,2.65, QUANTITY='TEMPERATURE' / Thermocouple array across compartment
&DEVC ID='TC-15', XYZ=10.4,3.5,2.65, QUANTITY='TEMPERATURE' / Thermocouple array across compartment
&DEVC ID='TC-16', XYZ=12.0,3.5,2.65, QUANTITY='TEMPERATURE' / Thermocouple array across compartment
&DEVC ID='TC-17', XYZ=13.6,3.5,2.65, QUANTITY='TEMPERATURE' / Thermocouple array across compartment
&DEVC ID='TC-18', XYZ=15.2,3.5,2.65, QUANTITY='TEMPERATURE' / Thermocouple array across compartment

&DEVC ID='TC-19', XYZ=12.0,3.509,2.75, QUANTITY='TEMPERATURE' / Thermocouple array above compartment
&DEVC ID='TC-20', XYZ=12.0,3.509,6.25, QUANTITY='TEMPERATURE' / Thermocouple array above compartment
&DEVC ID='TC-21', XYZ=12.0,3.509,11.75, QUANTITY='TEMPERATURE' /Thermocouple array above compartment

&SLCF PBX=12,QUANTITY='TEMPERATURE'/
&SLCF PBX=12,QUANTITY='VELOCITY',VECTOR=.TRUE./
&SLCF PBY=3.75,QUANTITY='TEMPERATURE'/
&SLCF PBY=3.75,QUANTITY='VELOCITY',VECTOR=.TRUE./

&DEVC XB=8.75,15.25,3.5,3.5,0.0,2.75, QUANTITY='MASS FLOW +',ID='MSF at balc'/
&DEVC XB=8.0,16.0,3.5,7.0,2.75,2.75, QUANTITY='MASS FLOW', ID='MSF@0.0HOR'/
&DEVC XB=8.0,16.0,3.5,8.5,5.75,5.75, QUANTITY='MASS FLOW', ID='MSF@3.0HOR'/
&DEVC XB=8.0,16.0,3.5,9.0,7.75,7.75, QUANTITY='MASS FLOW', ID='MSF@5.0HOR'/
&DEVC XB=8.0,16.0,3.5,9.5,9.75,9.75, QUANTITY='MASS FLOW', ID='MSF@7.0HOR'/
&DEVC XB=8.0,16.0,3.5,10.5,11.75,11.75, QUANTITY='MASS FLOW', ID='MSF@9.0HOR'/
&DEVC XB=8.0,16.0,3.5,10.5,15.0,15.0, QUANTITY='MASS FLOW', ID='MSF@12.25HOR'/

&DEVC XB=8.0,16.0,3.5,7.0,2.75,2.75, QUANTITY='VOLUME FLOW', ID='VF@0.0HOR'/
&DEVC XB=8.0,16.0,3.5,8.5,5.75,5.75, QUANTITY='VOLUME FLOW', ID='VF@3.0HOR'/
&DEVC XB=8.0,16.0,3.5,9.0,7.75,7.75, QUANTITY='VOLUME FLOW', ID='VF@5.0HOR'/
&DEVC XB=8.0,16.0,3.5,9.5,9.75,9.75, QUANTITY='VOLUME FLOW', ID='VF@7.0HOR'/
&DEVC XB=8.0,16.0,3.5,10.5,11.75,11.75, QUANTITY='VOLUME FLOW', ID='VF@9.0HOR'/
&DEVC XB=8.0,16.0,3.5,10.5,15.0,15.0, QUANTITY='VOLUME FLOW', ID='VF@12.25HOR'/

&TAIL /
```